

LOAN DOCUMENT

<p style="font-size: 2em; transform: rotate(-90deg); transform-origin: left top;">AD-A225 738</p> <p style="font-size: 1.5em; transform: rotate(-90deg); transform-origin: left top;">DTIC FILE COPY</p>	<p style="text-align: center;">PHOTOGRAPH THIS SHEET</p>	<p style="text-align: center;">LEVEL</p>	<p style="text-align: right;">INVENTOR</p>																								
<p style="font-size: 1.5em;">AFOSR-TR 90 0784</p> <p style="font-size: 1.2em;">DOCUMENT IDENTIFICATION</p> <p style="font-size: 1.5em;">30 JULY 1985</p>																											
<div style="border: 1px solid black; padding: 5px; width: fit-content; margin: 0 auto;"> <p style="margin: 0;">DISTRIBUTION STATEMENT A</p> <p style="margin: 0;">Approved for public release;</p> <p style="margin: 0;">Distribution Unlimited</p> </div>																											
<p style="font-size: 0.8em;">DISTRIBUTION STATEMENT</p>																											
<table border="1" style="width: 100%; border-collapse: collapse;"> <tr> <td colspan="2" style="font-size: 0.7em;">ACCESSION FOR</td> </tr> <tr> <td style="font-size: 0.7em;">NTIS</td> <td style="font-size: 0.7em;">GRI&I</td> </tr> <tr> <td style="font-size: 0.7em;">DTIC</td> <td style="font-size: 0.7em;">TRAC</td> </tr> <tr> <td style="font-size: 0.7em;">UNANNOUNCED</td> <td style="font-size: 0.7em;">JUSTIFICATION</td> </tr> <tr> <td colspan="2" style="height: 20px;"></td> </tr> <tr> <td colspan="2" style="height: 20px;"></td> </tr> <tr> <td colspan="2" style="height: 20px;"></td> </tr> <tr> <td colspan="2" style="font-size: 0.7em;">BY</td> </tr> <tr> <td colspan="2" style="font-size: 0.7em;">DISTRIBUTION/</td> </tr> <tr> <td colspan="2" style="font-size: 0.7em;">AVAILABILITY CODES</td> </tr> <tr> <td style="font-size: 0.7em;">DISTRIBUTION</td> <td style="font-size: 0.7em;">AVAILABILITY AND/OR SPECIAL</td> </tr> <tr> <td style="height: 40px; vertical-align: bottom; font-size: 1.5em;">A-1</td> <td style="height: 40px; vertical-align: bottom; font-size: 1.5em;">21</td> </tr> </table>	ACCESSION FOR		NTIS	GRI&I	DTIC	TRAC	UNANNOUNCED	JUSTIFICATION							BY		DISTRIBUTION/		AVAILABILITY CODES		DISTRIBUTION	AVAILABILITY AND/OR SPECIAL	A-1	21	<div style="border: 1px solid black; padding: 10px; text-align: center; margin: 0 auto; width: 150px;"> <p style="font-size: 2em; margin: 0;">DTIC</p> <p style="font-size: 1.5em; margin: 0;">ELECTE</p> <p style="font-size: 1.2em; margin: 0;">JUL 30 1990</p> <p style="font-size: 2em; margin: 0;">S E D</p> </div> <p style="text-align: center; font-size: 0.8em;">DATE ACCESSIONED</p> <div style="border: 1px solid black; height: 80px; margin-top: 10px;"></div> <p style="text-align: center; font-size: 0.8em;">DATE RETURNED</p> <div style="border: 1px solid black; height: 80px; margin-top: 10px;"></div> <p style="text-align: center; font-size: 0.8em;">REGISTERED OR CERTIFIED NUMBER</p>		
ACCESSION FOR																											
NTIS	GRI&I																										
DTIC	TRAC																										
UNANNOUNCED	JUSTIFICATION																										
BY																											
DISTRIBUTION/																											
AVAILABILITY CODES																											
DISTRIBUTION	AVAILABILITY AND/OR SPECIAL																										
A-1	21																										
<p style="font-size: 1.2em; margin: 0;">90 07 25 091</p> <p style="text-align: center; font-size: 0.8em;">DATE RECEIVED IN DTIC</p>																											
<p style="font-size: 0.8em;">PHOTOGRAPH THIS SHEET AND RETURN TO DTIC-FDAC</p>																											

HANDLE WITH CARE

LORENTS
MEYERHOF
PETERSON
editors

D.C. LORENTS
W.E. MEYERHOF
J.R. PETERSON editors

ELECTRONIC AND
ATOMIC COLLISIONS

AD-A225 738

ELECTRONIC
AND ATOMIC
COLLISIONS

invited papers



NORTH-
HOLLAND



REPORT DOCUMENTATION PAGE

Form Approved
OMB No. 0704-0188

1. AGENCY USE ONLY (Leave blank)		2. REPORT DATE		3. REPORT TYPE AND DATES COVERED	
4. TITLE AND SUBTITLE Electronic and atomic collisions.				5. FUNDING NUMBERS	
6. AUTHOR(S) D.C. Lorents					
7. PERFORMING ORGANIZATION NAME(S) AND ADDRESS(ES) Physics of Electronic and Atomic Collision Palo Alto, California AFOSR-TR-				8. PERFORMING ORGANIZATION REPORT NUMBER 00 0784	
9. SPONSORING / MONITORING AGENCY NAME(S) AND ADDRESS(ES) US AIR FORCE				10. SPONSORING / MONITORING AGENCY REPORT NUMBER	
11. SUPPLEMENTARY NOTES					
12a. DISTRIBUTION / AVAILABILITY STATEMENT Approved for public release; distribution unlimited.				12b. DISTRIBUTION CODE	
13. ABSTRACT (Maximum 400 words) <i>See also Abstracts</i> <i>AD-H163497</i>					
14. SUBJECT TERMS				15. NUMBER OF PAGES	
				16. PRICE CODE	
17. SECURITY CLASSIFICATION OF REPORT <i>Unclassified</i>		18. SECURITY CLASSIFICATION OF THIS PAGE <i>Unclassified</i>		19. SECURITY CLASSIFICATION OF ABSTRACT <i>Unclassified</i>	
				20. LIMITATION OF ABSTRACT <i>Unclassified</i>	

NSN 7540-01-280-5500

Standard Form 298 (890104) Draft:
Revised by GSA Vol. 135-10
770-01

AEOSR-TR- 00 0784

Approved for public release
distribution unlimited.

ADVANCED OFFICE OF SCIENTIFIC RESEARCH (AESR)
1000 ...
...
...
...

ELECTRONIC AND ATOMIC COLLISIONS

Electronic and Atomic Collisions

Invited Papers of the XIV International Conference on
the Physics of Electronic and Atomic Collisions
Palo Alto, California, 24–30 July, 1985

Edited by

Donald C. LORENTS
SRI International

Walter E. MEYERHOF
Stanford University

James R. PETERSON
SRI International



1986

NORTH-HOLLAND
AMSTERDAM · OXFORD · NEW YORK · TOKYO

© Elsevier Science Publishers B.V., 1986

All rights reserved. No part of this publication may be reproduced, stored in a retrieval system, or transmitted, in any form or by any means, electronic, mechanical, photocopying, recording or otherwise, without the prior permission of the publisher, Elsevier Science Publishers B.V. (North-Holland Physics Publishing Division), P.O. Box 103, 1000 AC Amsterdam, The Netherlands.

Special regulations for readers in the USA: This publication has been registered with the Copyright Clearance Center Inc. (CCC), Salem, Massachusetts. Information can be obtained from the CCC about conditions under which photocopies of parts of this publication may be made in the USA. All other copyright questions, including photocopying outside of the USA, should be referred to the publisher.

ISBN: 0-444-86998-0

Published by:

NORTH-HOLLAND PHYSICS PUBLISHING

a division of

Elsevier Science Publishers B.V.

P.O. Box 103

1000 AC Amsterdam

The Netherlands

Sole distributors for the U.S.A. and Canada:

ELSEVIER SCIENCE PUBLISHING COMPANY, INC.

52 Vanderbilt Avenue

New York, N.Y. 10017

U.S.A.

Library of Congress Cataloging-in-Publication Data

International Conference on the Physics of Electronic
and Atomic Collisions (14th : 1985 : Palo Alto,
Calif.)

Electronic and atomic collisions.

Includes index.

I. Collisions (Physics)--Congresses. I. Lorents,
Donald C. II. Meyerhof, Walter E. (Walter Ernst),
1922- . III. Peterson, James R. IV. Title.

QC794.6.C6157 1985 539.7154 86-2530

ISBN 0-444-86998-0 (U.S.)

PRINTED IN THE NETHERLANDS

PREFACE

The XIV International Conference on the Physics of Electronic and Atomic Collisions was held on the campus of Stanford University July 24 - 30, 1985, and was hosted by the Molecular Physics Department of SRI International and the Department of Physics at Stanford University. The conference was attended by about 740 scientists from about 35 nations, indicating the strong worldwide interest and vitality of this field. The 720 contributed papers presented at poster sessions showed that the research activity is continuing at about the same level as in the past few years. Eight satellite meetings devoted to more intense discussions of individual topics were held in conjunction with this conference.

This book contains the papers of the invited lectures given at the conference, the program of invited lectures having been selected by the program committee from suggestions by the general committee. N.F. Ramsey gave the opening lecture, reviewing the history of molecular beams, and plenary lectures by R. Gentry, G. Dunn, and U. Heinzmann followed on successive days. The major fraction of the invited program consisted of review talks and progress reports on topics of long standing interest to the participants.

Symposia on topics of strong current interest included "Dynamics of Photo- and Electron-Capture Dissociation, Energy Transfer Processes Involving Polarized Atom Collisions, State Resolved Capture by Multicharged Ions, and Multiphoton Ionization". These topics reflect some of the most intense current activity and interest of the conference participants and provide an assessment of the status of these areas. Finally, Hot Topic papers selected from the contributed papers to be presented orally are also included here.

New techniques and applications also continue to be developed that provide vitality and new directions to the field. For example, the recent progress on the laser cooling of atoms and its possible application to collision physics was described as well as progress in producing beams of low energy positrons and polarized electrons.

The scope of the conference has broadened in a natural way as the field has progressed, the problems of interest have changed, and the tools at our disposal have improved. This evolution was particularly evident at this conference from the increased attention being given to the role of exit channel spectroscopy and decay processes in all types of collisions whether they were excited with ions, electrons, or photons. It is exemplified by the photo excitation processes in which it is possible to prepare well-specified systems on which to conduct "half-collision" experiments. Thus, the exit channels of many types of collision processes, such as autoionization, dissociation, and detachment, are being investigated on a detail previously unavailable. This research is possible in part because photon sources such as synchrotrons and lasers have become generally available and useful to many researchers. Thus, ICPEAC is recognizing the close relationship of the collisions and spectroscopy fields and the important interdependence of these areas of research to each other. These developments provide new and exciting avenues of investigation and lead to improved understanding of the basic problems of atomic and molecular collisions.

The editors are grateful to the authors for their cooperative efforts in completing the manuscripts in a timely manner to allow early publication of these papers. We are also indebted to Faye Knowles and Gabriella Huff of the SRI Molecular Physics Department for their painstaking work on correcting the final manuscripts.

A noteworthy original contribution to ICPEAC XIV was due to M.J. Coggiola who composed appropriate lyrics to a number of folk-songs that were sung on this occasion. Three of these songs are included in this book at places appropriate to their topical significance.

D.C. LORENTS
W.E. MEYERHOF
J.R. PETERSON

This conference is indebted to the following sponsors:

The National Science Foundation (NSF)
The Department of Energy (DOE)
International Union of Pure and Applied Physics (IUPAP)
The Office of Naval Research (ONR)
The Air Force Office of Scientific Research (AFOSR)
The National Aeronautics and
Space Administration Goddard Space Flight Center (NASA)
EG&G Princeton Applied Research
Leisk Instruments
McPherson, a division of S.I. Corporation
Extrel Corporation

**The Institutional support of SRI International and Stanford University
in providing facilities, resources, and personnel
is gratefully acknowledged.**

**INTERNATIONAL CONFERENCE ON THE PHYSICS OF
ELECTRONIC AND ATOMIC COLLISIONS
ORGANIZATION 1983 - 1985**

EXECUTIVE COMMITTEE

CHAIRMAN

B. Bederson - USA

VICE CHAIRMAN

W.O. Mehlhorn - Germany

SECRETARY

J.S. Risley - USA

TREASURER

G.C. Watel - France

TREASURER-ELECT

R. Morgenstern - The Netherlands

ADMINISTRATIVE SECRETARY

L. Roos - The Netherlands

MEMBERS

J. Eichler - Germany

F.A. Gianturco - Italy

H.B. Gilbody - UK

Y.S. Gordeev - USSR

F. Gounand - France

I.V. Hertel - Germany

Y. Kaneko - Japan

D.C. Lorents - USA

T. Lucatorto - USA

M. Lubell - USA

W.E. Meyerhof - USA

F.H. Read - UK

L. Spruch - USA

N. Stolterfoht - Germany

N. Tolk - USA

GENERAL COMMITTEE

ARGENTINA*C.R. Garibotti***AUSTRALIA***I.E. McCarthy***AUSTRIA***T.D. Märk***BELGIUM***J. Momigny***CANADA***D. Roy***DENMARK***P. Hvelplund***FRANCE***J.F. Chemin**J.F. Delpech**F. Gounand**V. Sidis**G.C. Watel***GERMANY***J. Eichler**H. Haberland**I.V. Hertel**W.O. Mehlhorn**W. Raith**H.W. Schmidt-Böcking**N. Stolterfoht***INDIA***S.C. Mukherjee***ITALY***F.A. Gianturco**A. Giardini-Guidoni***JAPAN***T. Arikawa**Y. Kaneko**M. Matsuzawa***THE NETHERLANDS***R. Morgenstern**M.J. van der Wiel***SPAIN***A. Riera***SWITZERLAND***W. Wölfli***UNITED KINGDOM***J. Comer**H.B. Gilbody**C.L. Latimer**M.R.C. McDowell**F.H. Read***UNITED STATES***B. Bederson**R.L. Champion**A. Dalgarno**D.C. Lorents**M. Lubell**T. Lucatorto**K.B. MacAdam**W.E. Meyerhof**T.M. Miller**R.A. Phaneuf**J.S. Risley**I.A. Sellin**L. Spruch**N. Tolk**S. Trajmar***USSR***R.J. Damburg**Y.S. Gordeev**N.P. Penkin**A.M. Urnov***YUGOSLAVIA***S.V. Cvejanović*

LOCAL COMMITTEE

CHAIRMEN

Donald C. Lorents
Molecular Physics Department
SRI International

Walter E. Meyerhof
Department of Physics
Stanford University

MEMBERS

Robert E. Anholt - Stanford University
Christopher H. Becker - SRI International
William K. Bischel - SRI International
Michael J. Coggiola - SRI International
Richard A. Copeland - SRI International
Philip C. Cosby - SRI International
Keith T. Gillen - SRI International
Hanspeter Helm - SRI International
A. Peet Hickman - SRI International
Robert M. Hill - SRI International
David L. Huestis - SRI International
Jay B. Jeffries - SRI International
Ravinder Kachru - SRI International
James R. Peterson - SRI International
Roberta P. Saxon - SRI International
Christian Stoller - Stanford University

PROGRAM COMMITTEE

Executive Committee

and

R. Anholt
M. Coggiola
K. Gillen
R. Hill
J. Peterson
R. Saxon

TABLE OF CONTENTS

Preface	v
Sponsors	vii
Executive Committee	viii
General Committee	ix
Local Committee, Program Committee	x
<i>Rush to Publish (song text)</i> <i>M.J. COGGIOLA</i>	1
PLENARY AND GENERAL LECTURES	
Oscillations in the History of Molecular Beams N.F. RAMSEY	3
State-to-State Energy Transfer in Collisions of Neutral Molecules W.R. GENTRY	13
Radiatively Stabilized Collisions: Dielectric Recombination and Radiative Association G.H. DUNN	23
Angle- and Spin-Resolved Photoelectron Spectroscopy with Atoms and Molecules U. HEINZMANN	37
Alignment and Orientation of Atomic Outer Shells induced by Electron and Ion Impact: Some Recent Developments and Remaining Problems N. ANDERSEN, J.W. GALLAGHER and I.V. HERTEL	57
ELECTRON COLLISIONS	
Electron Impact Excitation of Molecules S. TRAJMAR	77
Rotational Excitation of Molecules by Slow Electrons I. SHIMAMURA	93

Positron (and Electron) Scattering by Atoms and Molecules T.S. STEIN and W.E. KAUPPILA	105
The Coulomb Three-Body Problem: The Electron Hydrogen System E. WEIGOLD	125
e - 2e Collisions near Ionization Threshold — Electron Correlations J. MAZEAU, A. HUETZ and P. SELLES	141
Electron Attachment to van der Waals Molecules Y. HATANO	153
Aspects of Electron Detachment in Negative Ion Collisions V.A. ESAULOV	175
Collision Dynamics with Nonlocal Potentials W. DOMCKE and C. MÜNDEL	195
The Role of Indirect Processes in Electron-Impact Ionization of Multicharged Ions D.C. GREGORY	205
Inner Shell Excitation in Atoms and Molecules by High Resolution Electron Impact G.C. KING	215
Hot Topics	
Description of the Intense, Low Energy, Monoenergetic Positron Beam at Brookhaven K.G. LYNN, A.P. MILLS, Jr., L.O. ROELLIG and M. WEBER	227
Ionization of Helium by Positron Impact D. FROMME, W. RAITH and G. SINAPIUS	233
Observations of Spin Dependence in Superelastic Scattering of Polarized Electrons from Na(3P) J.J. McCLELLAND, M.H. KELLEY and R.J. CELOTTA	239

ION COLLISIONS

<i>This Beam is Your Beam (song text)</i> M.J. COGGIOLA	244
Relativistic Atomic Collisions R. ANHOLT	245
Relativistic Eikonal Theory of Electron Capture J. EICHLER	257
Atomic Collisions in the Time-Dependent Hartree-Fock Approach K.R. Sandhya DEVI, J.D. GARCIA and N.H. KWONG	263
Inner-Shell Excitation in Slow Ion-Atom Collisions U. WILLE	273
Collision Physics with Highly Stripped Slow Ions R. SCHUCH	297
Laser-Induced Charge Exchange in Ion-Atom Collisions A. RIERA	319
Doubly Differential Cross Sections of Collision-Produced Forward Electron Emission S.B. ELSTON	331
Multiple Scattering Contributions in Electron Capture Theories L.J. DUBÉ	345
Correlated Electron Effects in Electron-Transfer Processes for Highly Charged Ion-Atom Collisions L.H. ANDERSEN	365
United Atom X-Rays from Nuclear Fusion Reactions J.F. CHEMIN, S. ANDRIAMONJE, D. GUEZET, J.N. SCHEURER, J.P. THIBAUD, P. AGUER, F. HANNACHI and J.F. BRUANDET	377

Positron Creation in Supercritical Heavy Ion Collisions J. REINHARDT, T. de REUS, W. GREINER, B. MÜLLER, U. MÜLLER, A. SCHÄFER, P. SCHLÜTER, S. SCHRAMM and G. SOFF	389
Hot Topics	
Anomalous Positron Peaks from Superheavy Collision Systems J. SCHWEPPE	405
Production of Multiply Charged Ions from Molecular Targets in Heavy Ion Impact H. TAWARA, T. TONUMA, S.H. BE, H. SHIBATA, M. KASE, T. KAMBARA, H. KUMAGAI and I. KOHNO	417
Correlated Electron Capture and Inner-Shell Excitation Measurements in Ion-Atom Collisions J.A. TANIS, E.M. BERNSTEIN, M.W. CLARK, W.G. GRAHAM, R.H. McFARLAND, T.J. MORGAN, A. MULLER, M.P. STOCKLI, K.H. BERKNER, P. GOHIL, A.S. SCHLACHTER, J.W. STEARNS, B.M. JOHNSON, K.W. JONES, M. MERON and J. NASON	425
SYMPOSIUM: STATE RESOLVED CAPTURE BY MULTICHARGED IONS	
Theoretical Treatment of Electron Capture and Excitation in Two-Electron System Ion-Atom, Atom-Atom Collisions at Low to Intermediate Energy M. KIMURA	431
State-Resolved Single Electron Capture in Slow Collisions of Multi-Charged Ions with One- and Two-Electron Atoms D. DIJKKAMP, D. ĆIRIĆ and F.J. de HEER	445
Translational Energy Spectroscopy and Angular Distributions for Low Energy Capture by Multiply Charged C, Ne and Ar from He, D₂, and D Targets C.L. COCKE, J.P. GIESE, L.N. TUNNELL, W. WAGGONER and S.L. VARGHESE	453

State-Selective Electron Capture by Slow Multiply Charged Ions in Atomic Hydrogen using Translational Energy Spectroscopy R.W. McCULLOUGH	463
Electron Capture by Slow and Highly Stripped Iodine Ions from Helium Atoms Masahiro KIMURA	471
EXCITED ATOM AND ION-MOLECULE COLLISIONS	
Expanding Overcooled Laser Plasma as a Promising Medium for Atomic Collision Studies S.V. BOBASHEV and L.A. SHMAENOK	479
Electron Spectra and Ion Analysis in Laser-Excited Metallic Vapors B. CARRÉ, J.M. BIZAU, P. BREGER, D. CUBAYNES, P. GÉRARD, J.L. PICQUÉ, F. ROUSSEL, G. SPIESS and F.J. WUILLEUMIER	493
Excited Atom-Molecule Collisions at Thermal and Suprathermal Energies J.-M. MESTDAGH	507
Negative Ion Formation by Collision of Rydberg Atoms with Clusters T. KONDOW	517
State Selected Ion-Molecule Reactions by TESICO I. KOYANO, K. TANAKA and T. KATO	529
Low Energy Ion Reactions measured with Guided Beams D. GERLICH	541
Atom Capture and Loss in Ion Molecule Collisions M. BREINIG, S.E. LASLEY, C.C. GAITHER, III	555
SYMPOSIUM: ENERGY TRANSFER PROCESSES INVOLVING POLARIZED ATOM COLLISIONS	
Inelastic and Reactive Collisions with Polarized Excited Na Atoms H. SCHMIDT, I.V. HERTEL and Y.T. LEE	561

Polarization Effects in Associative Ionization of Excited Sodium Atoms G. NIENHUIS	569
Polarization Effects in Ionizing Collisions of Excited Neon Atoms T. BREGEL, W. BUßERT, J. GANZ, H. HOTOP and M.-W. RUF	577
Energy Transfer Processes of Aligned Excited States of Ca Atoms D. NEUSCHÄFER, M.O. HALE, I.V. HERTEL and S.R. LEONE	585
Hot Topics	
<i>Alkaline (song text)</i> M.J. COGGIOLA	592
Trapping and Cooling Neutral Atoms D.E. PRITCHARD	593
The Electronic and Molecular Structure of Free Liquid Surfaces. Electron Spectroscopy under He(2^3S) versus HeI-Photon Impact W. KELLER, H. MORGNER and W.A. MÜLLER	605
EXCITED STATE DECAY PROCESSES	
Doubly Excited Autoionizing States T.F. GALLAGHER	609
Progress on Quantum Defect Theory – Dynamics of Excited Atoms and Molecules J.-M. LI	621
Mechanisms of Atomic and Molecular Autoionization J. BERKOWITZ	631
Classification of Doubly Excited States C.D. LIN	643
Coherence Effects in Electron Emission from Ion-Atom Collisions A. NIEHAUS	657

Auger Spectroscopy of Highly Stripped Ions D. SCHNEIDER, N. STOLTERFOHT, A. ITOH, T. SCHNEIDER, G. SCHIWETZ, W. ZEITZ and T. ZOUROS	671
Spectroscopy of Hydrogenlike and Heliumlike Krypton Ions J.P. BRIAND	685
SYMPOSIUM: THE DYNAMICS OF PHOTO- AND ELECTRON-CAPTURE DISSOCIATION	
Dissociation of H_2^* Products of Electron Capture D.P. de BRUIJN	697
Photodissociation and Photoionization in Triplet Molecular Hydrogen H. HELM	705
Quantum Mechanical Time-Independent Theory of Molecular Photodissociation J.A. BESWICK	717
Analytic Multichannel Theory of Molecular Dissociation P.S. JULIENNE and F.H. MIES	725
SYMPOSIUM: MULTI-PHOTON IONIZATION	
Transitions within the Continuum in High-Intensity Laser Fields M.J. van der WIEL and H.-G. MULLER	735
Multiphoton Multiple Ionization of Alkaline-Earth Atoms P. AGOSTINI and G. PETITE	743
Multiphoton Inner-Shell Atomic Excitation and Multiple Ionization U. JOHANN, T.S. LUK and C.K. RHODES	751
Multiphoton Stripping of Atoms M. CRANCE	757
Theory of Multiphoton Ionization and Autoionization of Xe P. GANGOPADHYAY, X. TANG, P. LAMBROPOULOS and R. SHAKESHAFT	765

Two Photon Ionization of Metastable Helium H. HABERLAND, J. HÖHNE, M. OSCHWALD and J. BROAD	771
Hot Topics	
The Highly Excited Hydrogen Atom in Strong Magnetic Fields K.H. WELGE and A. HOLLE	779
State Selective Laser Detection of Rydberg Atoms W. SANDNER	785
Photodetachment Spectroscopy of FeO^- T. ANDERSEN, K.R. LYKKE, D.M. NEUMARK and W.C. LINEBERGER	791
Modified Photodetachment Threshold Behavior near Resonances Y.K. BAE and J.R. PETERSON	799
Experiments on Mass-Resolved Clusters of Semiconductors L.A. BLOOMFIELD, M.E. GEUSIC, R.R. FREEMAN and W.L. BROWN	807
The Vibrational Predissociation Spectroscopy of Hydrogen Cluster Ions L.I. YEH, M. OKUMURA and Y.T. LEE	813
AUTHOR INDEX	819

RUSH TO PUBLISH

By M. J. Coggiola

Tune: Glory, Glory, Hallelujah

Mine eyes have seen the X-ray from the inner shell decay;
It is bouncing off the grating in a most peculiar way;
We can hardly stop to contemplate, just write to Phys Rev A:
Our grant is running out.

Hurry, hurry, rush to publish!
Hurry, hurry, rush to publish!
Hurry, hurry, rush to publish!
Our grant is running out.

We will overwhelm the editors with data nice and neat;
So who cares that these are measurments we never shall repeat.
Oh, what use is it to worry, it's a truly major feat!
Our grant is coming through.

Hurry, hurry, rush to publish!
Hurry, hurry, rush to publish!
Hurry, hurry, rush to publish!
Our grant is coming through.

OSCILLATIONS IN THE HISTORY OF MOLECULAR BEAMS

Norman F. RAMSEY

Lyman Physics Laboratory, Harvard University, Cambridge, MA 02138

1. INTRODUCTION

The subject of molecular beams is now just 75 years old. The first publication on molecular beams was by Dunoyer (1) in 1911, but even in those early days there must have been an interval of about a year from the beginning of a first molecular beam experiment to its publication so work in the field must have begun in 1910, just 75 years ago.

The earliest molecular beam experiments were primarily tests of kinetic theory, followed by measurements of atomic and molecular collision cross sections. Since then the history of molecular beams has followed an oscillatory path as newly invented techniques shifted and even excessively shifted the primary interest from one field to another. Studies of atomic collisions, for example, at one time dominated the field but were later mostly abandoned in favor of magnetic deflection experiments for the measurement of atomic and nuclear magnetic moments. Subsequently the interest in scattering experiments revived. The history of molecular beams since then has been oscillatory with primary attention oscillating between collision experiments and spectroscopic experiments up to the present time when a merger between the two kinds of experiments seems to be taking place with many of the most interesting experiments involving both collision techniques and laser spectroscopy to identify the atomic states involved in a collision.

2. KINETIC THEORY

The original molecular beam experiment by Dunoyer (1) in 1911 used the simple apparatus of Fig. 1, but it contained the characteristic features of most subsequent atomic and molecular beam apparatus: a source (of Na atoms), a region sufficiently well evacuated for the atoms to traverse the apparatus without collision, a collimator and a detector region (in this case a cooled surface on which visible amounts of Na atoms would deposit).

The objective of Dunoyer's original experiment was to confirm one of the simplest predictions of kinetic theory: that atoms in a low pressure region travel in straight lines.

In subsequent years a number of other kinetic theory experiments were carried out -- with a peak of such activity during the period 1920-1930. Stern, Eldridge and others (2) did a number of experiments to measure the velocity distributions of the molecules emerging from a source. Some of the earliest experiments utilized an atomic beam apparatus that was rotated about an axis perpendicular to the beam to measure the atoms velocity by the shift of the beam deposit from the position of deposit when there was no rotation. Other experiments used choppers and free fall under gravity. All of the experiments provided good general confirmation of the Maxwell velocity distribution but the experiments were not sensitive to the number at extremely low velocities such as a few meters per second.

The angular distribution of molecules emerging from a source with thin defining apertures were studied by Knudsen, Stern and others (2). They showed that a cosine distribution law was followed such that the number dQ of molecules

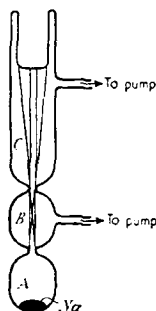


FIGURE 1
Schematic diagram of Dunoyer's original
atomic beam apparatus (1).

moving per second into solid angle $d\Omega$ from a source aperture of area A_s was given by

$$dQ = \left(\frac{d\Omega}{4\pi}\right) n\bar{v} \cos\theta$$

where θ was the angle of the emerging atoms relative to a perpendicular to the aperture.

Claussing and others (2) during this period studied the effect of source channels whose thickness exceeded their width and showed that beams were concentrated more in the forward direction than expected from a cosine law.

3. EARLY SCATTERING EXPERIMENTS

One of the earliest applications of atomic and molecular beams was to study scattering. Mean free paths, λ , of atoms passing through gases at suitable pressures, p , were measured from the relation

$$I_p = I_0 e^{-\ell/\lambda} p$$

where I_p is the intensity transmitted at pressure p and ℓ is the length of the scattering region.

Soon thereafter, molecular beam measurements of the angular distribution of molecular scattering were carried out by Born, Estermann and others.

Also during the 1930's interactions of atomic beams with solid surfaces were studied by Knauer, Estermann, Stern and others.

4. OPTICAL SPECTROSCOPY WITH ATOMIC BEAMS

One of the principal sources of the width of spectral lines in early optical spectroscopy was first order Doppler shift. Soon after the molecular beam technique was invented it was realized that the high directivity of the beam could greatly reduce the first order Doppler broadening by viewing the atoms from the side, perpendicular to their line of motion. As a result, beginning in 1913 atomic beam sources were used in optical spectroscopy by Dunoyer, Jackson, Kuhn, Kopfermann and many others (2), but their use was limited by their limited intensity of the beam technique.

5. MAGNETIC DEFLECTION EXPERIMENTS

A major revolution in atomic and molecular beam experiments was initiated with the use of inhomogeneous magnetic fields to deflect the beams. In a homogeneous magnetic field, an atom with a magnetic moment is not deflected since the force on the north pole of the magnet is equal and opposite to that on the south pole leading to no net force on the atom. On the other hand in an inhomogeneous magnetic field the force on the north pole is different from that on the south pole and the atom is deflected in its passage through the inhomogeneous magnetic field. This technique was first used by Stern and Gerlach (2) in their great experiment which gave a clear demonstration of the reality of space quantization and which also clearly demonstrated experimentally that the spin angular momentum of the electron was $1/2$ in units of $\hbar = h/2\pi$. Additional experiments on the process of space quantization including the effects of changing magnetic field directions were carried out by Stern, Frisch, Estermann and others.

Although the deflections were largest with electron magnetic moments, Stern soon realized that nuclear magnetic moments could be deflected in a similar fashion even though the nuclear magnetic moments were approximately 2000 times smaller than atomic or electron moments. Stern, Estermann and others during the late 1920's used this technique to measure the magnetic moments of the proton and deuteron in the molecules H_2 and D_2 . Since both of these molecules were 1: the electron spin magnetic moments were oppositely directed and cancelled. A major difficulty of the experiment was to distinguish between the nuclear magnetic moments and the molecular rotational magnetic moments due to the circulating electrical charges of the rotating molecule. These could be distinguished, however, by separately studying para-hydrogen for which the nuclear magnetic moments cancelled and the deflection was due only to the rotational magnetic moments. With the value of the rotational magnetic moment inferred from the para-hydrogen experiments, the deflection experiments with a normal mixture of ortho- and para-hydrogen could be analyzed for the contribution due to the nuclear magnetic moments alone. The accuracy of the experiments in measuring the proton and deuteron magnetic moments, however, was severely limited both by the smallness of the deflection and by the need to adjust the direct observations for the contribution of the rotational magnetic moments of the molecules. The result was exciting and surprising: the proton magnetic moment was not equal to one nuclear magneton ($e\hbar/2Mc$ with M = proton mass) but was considerably larger.

The interest and excitement of the magnetic deflection experiments necessarily drew attention away from scattering experiments which started a decline in the interest in scattering and interaction experiments which continued until well after World War II.

6. BREIT-RABI FORMULA

Although the early experiments of Stern, Gerlach, Frisch and others (2) confirmed many of the quantum mechanical predictions about the behavior of electron spins in magnetic fields, there were also experimental anomalies that did not fit well with theory. I. I. Rabi (2) pointed out that these apparent disagreements between theory and experiment were due to the neglect in previous theories of the effects of nuclear magnetic moments in paramagnetic atoms, i.e. atoms with electron magnetic moments. Since the electron magnetic moment is about 2000 times greater than a nuclear magnetic moment, it had seemed reasonable to neglect the effect of the nuclear magnetic moment. However, Rabi pointed out that in low external magnetic fields the nuclear magnetic moment and the electron magnetic moment are coupled together magnetically so that the small nuclear magnetic moment partially controls the large effective magnetic moment of the atom. Breit and Rabi in 1931 quantitatively demonstrated this effect in the now famous Breit-Rabi formula which shows, for example, that in an atom with electronic spin $1/2$ and nuclear spin $3/2$ the effective magnetic moment of the atom varies with external magnetic field as shown in Fig. 2.

7. ATOMIC BEAM DEFLECTION MEASUREMENTS OF NUCLEAR SPINS AND MAGNETIC MOMENTS

The Breit-Rabi formula became the basis of a long series of important measurements of nuclear spins and magnetic moments in Rabi's laboratory at Columbia University in the period between 1933-1940 by Rabi, Cohen, Kelloq, Zacharias and others (2).

In the initial experiments the deflections were by weak magnetic fields such that μ_{eff}/μ_0 in fig. 2 was intermediate between zero and 1 and the beam was correspondingly deflected. From an analysis of the deflection pattern the

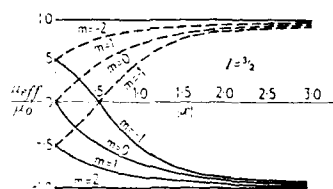


FIGURE 2

Effective magnetic moment of an atom with electronic spin $1/2$ and nuclear spin $3/2$ as a function of $X = -(M_J/J)H_0/\Delta W$ where M_J/J is the atomic magnetic moment in a strong field divided by the electron spin $J = 1/2$ and where W is the atomic hyperfine separation when $H_0 = 0$.

value of the nuclear spin and the x could be inferred. From x and the value of H_0 the value of ΔW could be calculated and from this and the atomic wave function the nuclear magnetic moment could be determined. The experiments, however, suffered from the disadvantage that the velocity distribution of the molecules

smearing out the deflection pattern in a manner that both made the analysis difficult and diminished the accuracy of the magnetic moment determinations.

A major improvement was the invention by Rabi of the zero moment method. From Fig. 2 it can be seen that for a specific value of x the effective magnetic moment μ_{eff} is zero. At this value, there is no deflection. Consequently if the undeflected beam intensity is measured as H_0 and hence x is varied, the intensity will rise to a peak at the value of x corresponding to a zero moment. Since the zero of deflection is zero for all molecules independent of the velocity, the peak can be both intense and narrow. The number of peaks gives the value of the nuclear spin and the spacing of the peaks gives the value of hW from which the nuclear magnetic moment can be inferred.

In the atomic deflection methods the sign of hW could also be determined by allowing the atoms to pass through regions in which the magnetic field was successively reversed, thereby inducing transitions between states with different magnetic quantum numbers m .

In the period from 1935 to 1940, Rabi, Millman, Fox, Manley, Zacharias, Hamilton, Renzetti, and others (2) in Rabi's laboratory at Columbia made many measurements of nuclear spins and magnetic moments by the atomic deflection and zero moment methods. The focussing of interest on these experiments led to a further decline in the emphasis on scattering and collision experiments.

8. MAGNETIC RESONANCE METHOD

The measurements of the signs of nuclear magnetic moments, required transitions between atomic states of different m values. To aid in analyzing these transitions, Rabi considered the theoretical problem of a magnetic moment with an associated angular momentum in a fixed magnetic field about which a smaller perpendicular magnetic field rotated with angular frequency ω ; the title of his theoretical paper was "Space Quantization in a Gyration Magnetic Field." This paper provides the fundamental equation for the transition probabilities of the molecular beam magnetic resonance method and of subsequent nuclear magnetic resonance methods. Nevertheless at the time the paper was written the objective was to account for transitions induced in atoms on passage through regions in which the direction of the field successively changed. Since the molecules had a wide distribution in velocities the sharp resonances predicted by the formulae in that paper for a single frequency were lost when the formulae were averaged over the velocity distribution. As a result, this paper was not immediately followed by the invention of the molecular beam magnetic resonance method. Instead Rabi's fundamental theoretical paper was first submitted for publication on March 1, 1937 and it was eight months later before experiments were started using oscillatory fields which preserved the sharp resonances, even though Rabi had some informal discussions with his colleagues in the intervening months on the possibility of using oscillatory fields. A year earlier, Gorter (3) had published a report on his unsuccessful attempt to detect nuclear magnetic resonance by absorption by microwave absorption and he described these unsuccessful experiments to Rabi on a visit to Columbia in September of 1947. Soon thereafter, Rabi made a major change in the program in his molecular beam laboratory and two of the major research groups in that laboratory began converting their apparatus to a form in which the transitions were induced by a magnetic field driven by a radiofrequency oscillator. The form of apparatus used is shown schematically in Fig. 3. Molecules from the source O are deflected by inhomogeneous magnetic field A , pass through collimator S and are refocussed to detector D by the inhomogeneous field B , whose direction of inhomogeneity is opposite to that of A . A uniform fixed magnetic field H_0 and a small perpendicular field H_1 oscillating at angular frequency ω are applied in region C . When the frequency ω is close to the nuclear Larmor precession frequency $\omega_0 = (h\gamma/h)H_0$ transitions are induced and the detected beam intensity is reduced by a failure of the refocussing for molecules whose

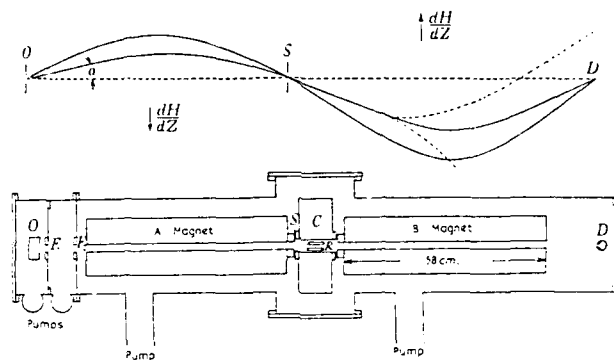


FIGURE 3
Schematic diagram of molecular beam magnetic resonance experiment.

orientation state has been changed by the transitions. The peak of the reduction in refocused beam is for $\omega = \omega_0$. The nuclear magnetic moment μ_I can therefore be determined by a measurement of $\omega = \omega_0$ and by a determination of H_0 .

The first experiment to show a molecular beam magnetic resonance curve was that obtained for Li in LiCl_2 by Rabi, Zacharias, Millman and Kusch (4) and is shown in Fig. 4.

The other resonance experiment by Kellogg, Rabi, Ramsey and Zacharias (5) yielded results that at first sight were disappointing but ultimately proved to be much more interesting. The intent was to measure the magnetic moments of the proton and deuteron and a single sharp resonance as in Fig. 4 was antici-

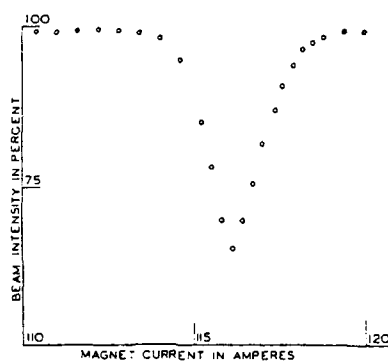


FIGURE 4
First molecular beam nuclear magnetic resonance curve (4). Li in LiCl_2

pated. Instead the peculiarly shaped curve in Fig. 5(a) was observed for the molecule H_2 . Eventually, sharp proton and deuteron resonances were obtained in HD and the proton and deuteron magnetic moments were obtained from these values. The problem of the peculiar structure of the H_2 and D_2 curves was initially left as a thesis project for Ramsey, the one graduate student in the group. He found that the curve became more interpretable if the radiofrequency power were drastically reduced but that the structure remained and became even more pronounced. The structure was similar to curves characteristic of spectroscopy as shown in Fig. 5(b) with resonances occurring at the Bohr frequencies $\nu_0 = (E_i - E_f)/h$. The curves could be interpreted in terms of additional interactions in the H_2 molecule such as spin-spin and spin-rotational interactions as well as the interaction of the nuclei with external magnetic fields. He also found that the width of the D_2 resonance curves was greater than that expected from D_2 , which suggested the possibility of a deuteron quadrupole moment which had been discussed as a possibility by Rabi. It therefore became apparent that the detailed study of the structure of the curves was more appropriate for the whole group that had built the apparatus and Ramsey took for his thesis project measurements of rotational magnetic moments of H_2 , D_2 and HD. The group of Kellogg, Rabi, Ramsey and Zacharias (5) then lengthened the apparatus and obtained the much clearer spectrum shown in Fig. 5(c). They also clearly confirmed that the extended spectrum with D_2 arose from a deuteron quadrupole moment. Radiofrequency spectroscopy began with these studies and the subtitle "Radiofrequency Spectroscopy" was used on the papers (5).

In 1940, Kusch, Millman and Rabi (6) studied the paramagnetic atom 7Li by the molecular beam resonance method and thereby observed the first electronic paramagnetic resonances. Resonances were observed both for $\Delta F = 0$, $\Delta m = \pm 1$ transitions and for $\Delta F = \pm 1$ transitions where F is the quantum number associated with \vec{F} , the vector sum of the electronic angular momentum \vec{J} and the nuclear angular momentum \vec{I} ($\vec{F} = \vec{I} + \vec{J}$). During the same year the $\Delta F = \pm 1$ transitions in Cs were studied, one of which later became the basis of the Cs atomic beam clocks in terms of which the second and the meter are now defined.

With the great activity devoted to the molecular beam magnetic resonance method, other molecular beam studies such as scattering became only a small fraction of the total molecular beam activity and during World War II almost all molecular beam research came to a temporary end.

9. MOLECULAR BEAM RESONANCE EXPERIMENTS FOLLOWING WORLD WAR II

Shortly after World War II there was a dramatic resurgence of atomic and molecular beam research, mostly devoted to resonance experiments and radiofrequency spectroscopy.

In 1947 Rabi and Hughes (2) carried out the first molecular beam electric resonance experiments. The technique was essentially the same as for the magnetic resonance experiments except the atoms were deflected and refocused by inhomogeneous electric fields and the transitions were induced by oscillatory electric fields. In the subsequent years the electric resonance spectra of many molecules were studied by Rabi, Trischka, Grabner, Carlson, Lee, Fabricand, Zeiger, Bolef, Ramsey and others (2). Since individual rotational and vibrational states of molecules were ordinarily resolved by this technique, accurate measurements of the internal molecular interactions were made with the electric resonance method for a number of different molecules in specific rotational and vibrational states.

In 1946 and 1947 Lamb and Retherford (2) studied the fine structure of atomic hydrogen by an atomic beam resonance method and discovered that the $2^2S_{1/2}$ and $2^2P_{1/2}$ states of atomic hydrogen were not degenerate. Accounting for this observed Lamb shift was a major stimulus to the development of quantum electrodynamics.

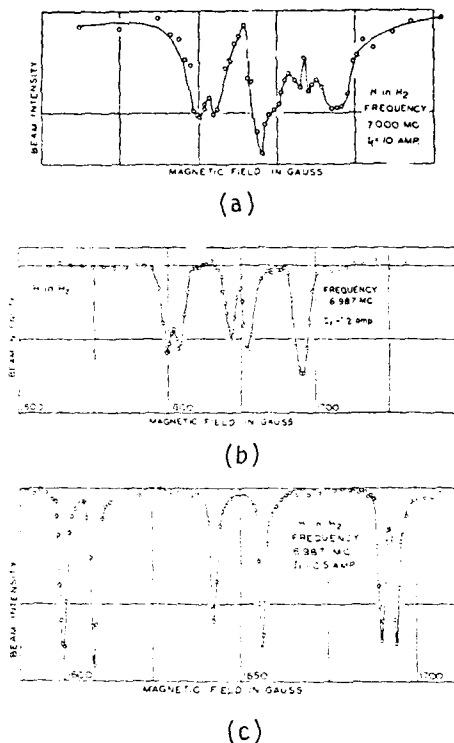


FIGURE 5

(a) Early nuclear magnetic resonance curve with H_2 . (b) Magnetic resonance curve with reduced radiofrequency power. (c) H_2 magnetic resonance curve with reduced power and longer resonance region.

In 1947 Nofe Nelson and Rabi (2) measured accurately the hyperfine interaction in atomic hydrogen and showed it was different from that expected theoretically. This was the first indication that the electron magnetic moment was different from the prediction of the Dirac theory. This discovery stimulated the development of relativistic quantum electrodynamics which was the first successful quantum field theory and the model for other field theories such as quantum chromodynamics. The anomalous magnetic moment of the electron was measured directly by Kusch (2) and others (2) in a series of experiments extending from 1948 to 1952.

In 1950, Ramsey (2) proposed the method of separated oscillatory fields in which the single oscillatory field region of the Rabi method was replaced by two separated but coherent oscillatory fields, one at the beginning of the transition region and the other at the end. This method not only provides resonances that are almost twice as narrow as the Rabi resonances in favorable circumstances for the latter but also can provide narrowing of the resonances by factors of ten or more when the static magnetic fields are not

sufficiently uniform. The separated oscillatory field method also overcomes first order Doppler shifts, is applicable to high frequencies where the wave length of the radiation is small compared to the length of the transition region, provides a narrowing of the line even below that expected by a simple application of the Heisenberg uncertainty principle, etc.

From 1950 onward, nuclear interactions in many molecules were made by molecular beam resonance methods by Ramsey, Ozier, Anderson, Cederberg, Klemperer and many others.

An important advance in molecular beam techniques was introduced in 1951 by Friedburg, Paul (2) and others (2). This was the use of magnetic hexapoles and electric quadrupoles both for state selection and for achieving space focusing which markedly increased the intensity of the beams.

In 1951 Kantrowitz and Grey (2) pointed out the possibility of using hydrodynamic jet sources both for increasing the effective beam intensity and to provide cooling of the beam and its rotational states. Slichter, Smalley, Ross, Zewail, Miller and Levy and others (2) have extensively used jet sources in molecular beam studies. From some points of view the tendency of such beams to form polymers and van der Waals complexes complicates the interpretation of experiments, but from other views it is an advantage since it permits the study of van der Waals complexes, molecular clusters, droplets, radicals, and chemical intermediates. Seeing a beam with a mixture of two molecules extends the scope of the technique.

In 1954 the first maser of Townes and others (2), was based on molecular beam techniques. NH_3 passed through electric quadrupoles which focussed molecules in the higher inversion on a tuned cavity amplifier and oscillator.

In 1960 Ramsey and Kleppner (2) developed the first atomic hydrogen maser. In this device a beam of atoms in the higher hyperfine state are focussed by a six pole magnet into a teflon coated storage bottle inside a cavity tuned to the hyperfine transition frequency of atomic hydrogen. This device not only permits highly accurate measurements on atomic hydrogen, deuterium and tritium but it also provides the most stable clock so far built. For this reason it is extensively used in long base line radioastronomy and other applications requiring a clock of high stability. Stabilities of 5×10^{-16} over several hours are achieved.

In the period following the invention of the laser there have been many applications of lasers to atomic and molecular beam research. Lasers have been used with atomic and molecular beams for (a) Laser spectroscopy, (b) Excitation of molecules to high states, (c) Beam detection, (d) State selection, (3) Laser fluorescence spectroscopy, (f) Separated oscillatory laser fields, (g) Study of short lived isotopes, (h) Collinear fast beam laser spectroscopy, etc.

10. ATOMIC AND MOLECULAR BEAM SCATTERING AND INTERACTION EXPERIMENTS

As mentioned earlier, few atomic beam scattering experiments were carried out in the period immediately preceding World War II and even fewer during World War II. Likewise in the immediate post war period, scattering experiments did not share the dramatic recovery made by molecular beam magnetic and electric resonance experiments. However, a new era of atomic beam scattering and interaction experiments began soon thereafter. Elastic scattering experiments were undertaken at many places. Quantum effects in scattering were observed and studies were made of rainbow and glory scattering.

Inelastic and reactive scatterings were studied extensively and became powerful tools for studying chemical processes in detail.

Photofragment and photo chemistry spectroscopy was studied by atomic beam techniques. As a result, during the decades following World War II there has been a dramatic (but still somewhat oscillatory) growth in the molecular beam studies of collisions and interactions.

In the past few years the study of scattering and interactions have been marked by the great power brought by a combination of techniques: lasers, jet beams, atomic beams, pulse techniques and spectroscopy. With these combinations, it is possible to identify the initial and final states of molecules and atoms that interact.

11. CONCLUSION

Molecular beams has had a rich 75 year history. Many fundamental discoveries have been made with atomic beams and important devices like the maser were first developed with this technique. The progress has been more by oscillatory stages rather than by steady advancement but the advances have been large.

We have recently witnessed a joining of many techniques: molecular beams, scattering, jets, lasers, spectroscopy and pulse techniques. With this powerful combinations, the field should have a bright future. The accomplishments of the molecular beams in the past 75 years make these years a hard act to follow, but there is every reason to believe that the next 75 years will also be exciting.

REFERENCES

- 1) Dunoyer, Comptes. Rendus, 152 (1911) 594.
- 2) A list of references for the early atomic and molecular beam experiments is given in N. F. Ramsey, Molecular Beams, Oxford University Press (1958 and 1985).
- 3) C. J. Gorter, Physica 3 (1936) 503 & 995.
- 4) I. I. Rabi, J. R. Zacharias, S. Millman and P. Kusch, Phys. Rev. 53 (1938) 318 and 55 (1939) 526.
- 5) J. M. B. Kellogg, I. I. Rabi, N. F. Ramsey and J. R. Zacharias. Phys. Rev. 55 (1939) 526; 55 (1939) 595; 57 (1940) 677 and 58 (1940) 226.
- 6) P. Kusch, S. Millman and I. I. Rabi, Phys. Rev. 57 (1940) 765.

STATE-TO-STATE ENERGY TRANSFER IN COLLISIONS OF NEUTRAL MOLECULES*

W. Ronald GENTRY

Chemical Dynamics Laboratory, University of Minnesota, 207 Pleasant Street,
S.E., Minneapolis, Minnesota 55455, U.S.A.

The kinetic energy dependences of cross sections for state-to-state rovibrational transitions in collisions of neutral molecules have been measured with a novel instrument combining crossed, pulsed molecular beams and laser-induced fluorescence detection. The results may be understood qualitatively in some cases by comparison with simple dynamical models, but the quantitative details depend on subtle features of the interactions which will require more sophisticated theoretical interpretation.

1. INTRODUCTION

Of all the principal categories of molecular collision phenomena, vibrational transitions in collisions of neutral molecules are the last to be studied by molecular beam techniques at a state-resolved level of detail. The main reason for this is that the cross sections for vibrational transitions tend to be much smaller than those for elastic or for rotationally inelastic scattering, while the interfering background signal from the primary beams is more severe than in the case of reactive scattering, where the products are structurally distinguishable from the reactants. The signal-to-background problems are compounded by the fact that vibrational transitions are nearly always accompanied by rotational transitions, so that very high energy resolution is required to distinguish between the two. Thus, one must deal with the worst of both circumstances and search for a low intensity signal with high resolution.

The observation of vibrational excitation in ion-molecule collisions is much easier, and in fact it has now been about fifteen years since the first measurements of total and differential cross sections for state-resolved vibrational excitation, in the $H^+ + H_2$ and $Li^+ + H_2$ systems (1-4). The dynamics of the ion-molecule excitation processes, however, are quite different from those expected for neutral systems. In the first place, high probabilities for vibrational transitions in ion-molecule collisions are generally obtained by accelerating the ions to kinetic energies which are much larger than the vibrational excitation energy--typically about 10eV or more. Secondly, extensive rotational excitation is usually avoided by observing the scattering at small center-of-mass (c.m.) scattering angles, where vibrational transitions may be induced by long-range electrostatic interactions, and where nonpolar molecules experience only a small net torque (5). For neutral molecules, such high kinetic energies are not readily available, and long-range electrostatic forces are generally much less important than the shorter-range valence contributions.

Despite the technical difficulties in studying the microscopic details of vibrational energy transfer in neutral systems, these phenomena are of great theoretical and practical significance. Exoergic chemical reactions tend to form products with highly excited non-Boltzmann vibrational populations, and the rates of subsequent reaction steps may depend strongly on the vibrational

*The research described in this review has been supported by the Division of Chemical Sciences, U.S. Department of Energy, contract no. DE-AC02-83ER13063.

state distribution and hence on the rates of the energy transfer processes. In another example, the performance of infrared chemical lasers depends critically on the microscopic rates of formation and depletion of individual vibrational states. As with other types of molecular collision processes which have been investigated by molecular beam techniques over the last twenty-five years, one expects single-collision experiments, with selection of initial and final states and control of the kinetic energy, to yield more insight into the dynamical mechanisms responsible for vibrational energy transfer than is available from measurements of thermally averaged rate coefficients (6).

Although crossed molecular beam studies of state-resolved rotational excitation in neutral systems were first performed about eight years ago (7-9), and have now been extended to many systems (10), there have been only a few very recent experiments in which vibrational transitions were observed. These include Na_2 excitation observed by laser-induced fluorescence by Serri et al. (11) and more recently by Bergmann and coworkers (12), and the singular experiment by Ryali et al. (13) on bending-mode excitation of CO_2 detected by a Fourier transform infrared spectrometer. It is the purpose of the present report to describe the experiments in our laboratory which have made possible the measurement of cross sections for state-resolved vibrational excitation as functions of the kinetic energy of collision for a relatively broad range of energies and chemical systems. Examples will include the state-to-state vibrational excitation of I_2 and the mode-specific vibrational excitation of two "large" polyatomic molecules, p-difluorobenzene and aniline. The signal-to-background problems in these experiments were ameliorated by the use of a novel crossed, pulsed beam apparatus, and the high resolution necessary to observe vibrational transitions in the presence of the much more probable rotational excitation was provided by a laser-induced fluorescence (LIF) detection scheme.

2. PULSED MOLECULAR BEAM APPARATUS

The molecular beam sources used in this work are very fast electromechanical valves with open times of approximately 20 μsec (14,15). The instantaneous intensities of the supersonic molecular beams from these sources, operated at total pressures of 15-19 atm and nozzle diameters of about 0.6mm, are orders of magnitude higher than those which are typical for continuous beams. The instantaneous scattered signal, which is proportional to the product of the two primary beam intensities, is also correspondingly larger. At the same time, the residual background pressure of the sample molecule is extremely small. The primary molecular beam pulse, which is physically only a few cm long, does not contribute to this background until it traverses the scattering chamber and is reflected from the vacuum chamber wall. The real scattered signal is measured with a pulsed laser while the two primary beam pulses are at the crossing point, and before the background signal rises. In the interval between pulses, which is typically 100-125ms, the background gas is removed by the vacuum pumps with a pumpout time constant of about 30ms.

Figure 1 shows a cutaway drawing of the apparatus, with the important features drawn approximately to scale. The main vacuum chamber is a horizontal cylinder about 50cm in diameter and 85cm long. This chamber is divided into three sections by two internal partition disks, each of which forms a rotating o-ring seal with the inside of the cylinder, and each of which is rigidly connected to a rotating lid at one end of the cylinder. The two molecular beam sources are mounted in chambers attached to these partition disks, so that each source can be independently rotated in a vertical plane through the center of the apparatus, by turning its respective rotating lid. At any angle of rotation, differential pumping of the source chamber is provided through a port in the partition disk at the base of the source chamber. The kinetic energy of collision in this instrument can therefore be conveniently and continuously varied, without changing the source conditions, by simply varying the intersec-

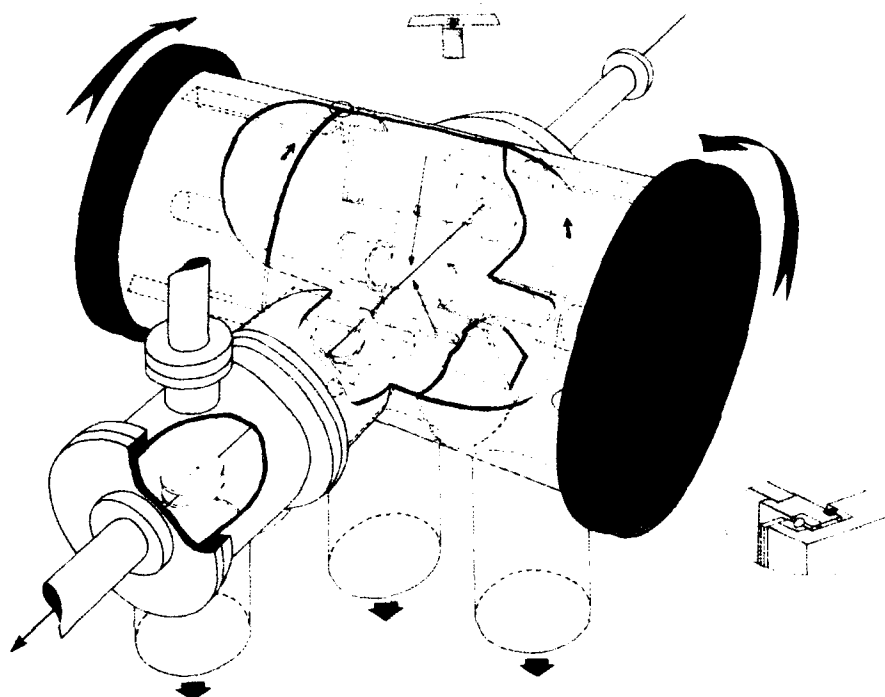


FIGURE 1
Cutaway drawing of the crossed, pulsed molecular beam apparatus with LIF detection at the University of Minnesota (17).

tion angle of the two beams.

The detector in this apparatus is a photomultiplier tube which images the center of the crossing region with a spherical mirror and lens system. The laser beam enters and leaves the vacuum system through Brewster's angle windows and long light baffles which reduce the scattered light background to about 1 in 10^4 photons. In operation, the molecular beam pulses are collimated with multiple skimmers to angular widths of $2-3^\circ$. The laser is tuned to the appropriate spectral frequency for detecting the selected state of the scattered molecules, and timed to intersect the molecular beam pulses at the crossing point. The LIF signal, proportional to the collision-induced population of that state, is then measured as a function of the molecular beam intersection angle. The result is transformed into the total cross section for populating that state as a function of c.m. kinetic energy. Relative cross sections for various transitions are all normalized to a single value, called the "attenuation cross section" σ_a , which represents the total rotationally and vibrationally inelastic cross section for scattering of the primary beam molecules out of the small range of rotational states detected at a convenient $v=0$ bandhead at a selected high value of collision energy. For I_2 collisions, σ_a is essentially the total gas kinetic cross section, about 45\AA^2 , and for p-difluorobenzene and aniline collisions σ_a is expected to be close to the gas kinetic value, since virtually every collision results in scattering of the internally cold primary beam molecules out of the narrow range of rotational states viewed by the detector at the bandhead.

Additional details of the apparatus and data analysis can be found in previous reports (16-18).

3. VIBRATIONAL EXCITATION OF I_2 IN COLLISIONS WITH He

The first example which will be presented is that of vibrational excitation in a relatively "simple" system, $I_2 + \text{He}$ (16,17). In a typical experiment, I_2 was seeded at about 1 torr partial pressure in He carrier gas at a total pressure of 10^{-4} torr. The resulting supersonic expansion cools the I_2 rotational degree of freedom to about 1-2K, and the $v=1/v=0$ population ratio to about 10^{-4} . Figure 2 shows the cross sections for excitation of $v=1, 2$ and 3 from $v=0$ as functions of kinetic energy, over the range from the $v=1$ threshold to about 16 vibrational quanta. The laser in each of these cases was tuned to a convenient vibrational bandhead of the $B(^3\Pi_u) \rightarrow X(^1\Sigma_g^+)$ transition, where only the $J \leq 5$ states were detected. An analysis of the rotational bandshapes for the LIF spectra show that vibrational excitation in this system occurs with very little concomitant rotational excitation. For each of the final excited vibrational states the most probable change of rotational quantum number is about 5. Nevertheless, at 100meV collision energy the total rotationally inelastic cross section σ_a is about 10^3 times the total vibrationally inelastic cross section.

Perhaps the most striking feature of the data shown in Fig. 2 is the qualitatively different energy dependences for the different final vibrational quantum numbers. The $\sigma_{a,1}$ cross section shows a sharp onset at threshold, with a linear kinetic energy dependence, while $\sigma_{a,2}$ and $\sigma_{a,3}$ have accurately quadratic and cubic energy dependences, respectively. This behavior is very reminiscent of that which we observed many years ago in the state-resolved differential cross sections for vibrational excitation in $\text{H}^+ + \text{H}_2(v=0)$ collisions (2,3). Figure 3 shows the $\text{H}^+ + \text{H}_2$ scattering data for several collision energies and scattering angles plotted as ratios P_v/P_0 of the probability of the inelastic to the elastic channel. The same simple dependences--linear for P_1 , quadratic for P_2 and cubic for P_3 --are seen when these probability ratios are plotted as functions of the parameter $\epsilon = -\lambda n P_0$. These dependences are easily derived from the correspondence between the classical and quantal equations of motion for a harmonic oscillator which is excited by an arbitrary time-dependent force

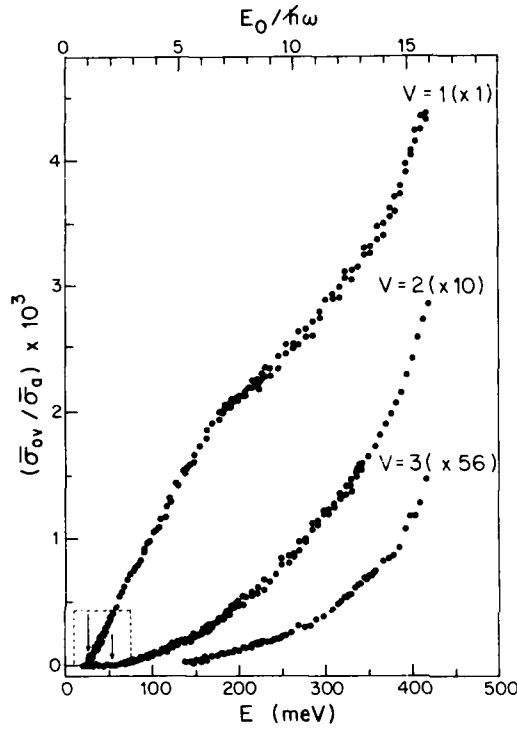


FIGURE 2
Cross sections as functions of relative kinetic energy E_0 for $I_2(v=0)$ excitation in collisions with He. The cross sections are normalized to the attenuation cross section σ_a (about 45\AA^2) as described in the text.

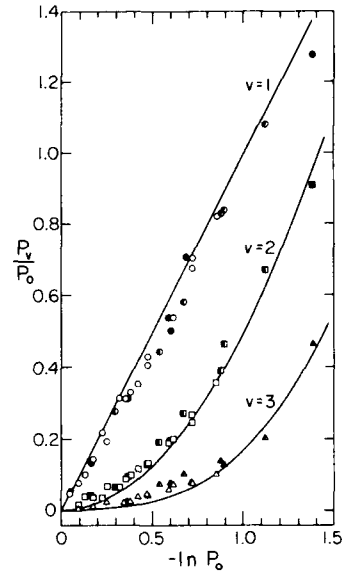


FIGURE 3
Probabilities P_v for vibrational excitation in $H^+ + H_2 (v=0)$ collisions plotted as functions of the parameter $\varepsilon = -\ln P_0$. Data are combined from measurements of the state-resolved differential cross sections at several c.m. kinetic energies in the range 4-21 eV and c.m. scattering angles in the range $6-36^\circ$ (3). The solid lines are linear, quadratic and cubic fits.

(19). An initially stationary classical oscillator driven by the force $F(t)$ gains the vibrational energy ΔE , given by

$$\Delta E = \frac{1}{2\mu} \int_{-\infty}^{\infty} F(t) e^{-i\omega t} dt, \quad (1)$$

where μ is the oscillator reduced mass and ω is the vibrational frequency. Quantum mechanically, the same oscillator subjected to the same driving force will undergo discrete transitions from the ground state having a Poisson distribution of probabilities,

$$P_{OV} = \frac{\epsilon^v e^{-\epsilon}}{v!}, \quad (2)$$

where v is the vibrational quantum number, and $\epsilon = \Delta E / \hbar \omega$ is simply the classical energy transfer in units of the vibrational quantum. In real molecular collisions, each set of initial conditions (kinetic energy, impact parameter and molecular orientation angles) leads in general to a different value of ΔE and ϵ , but the general form of Eq. (2) is preserved for the quantum number dependence. Equation (2) gives directly the P_v/P_0 ratios for $H^+ + H_2$ collisions shown in Fig. (3). To obtain the kinetic energy dependences observed experimentally for $I_2 + He$ collisions, two additional conditions are sufficient. First, the transition probabilities must be small, making $e^{-\epsilon} \sim 1$ and $P_{OV} \approx \epsilon^v$. Second, ΔE and ϵ must be proportional to kinetic energy. This is the result expected for impulsive collisions, for which the classical energy transfer for given initial conditions will depend only on the kinetic energy and the atomic masses. For example, an atom (mass m_1) colliding collinearly and impulsively with a homonuclear diatom (masses m_2) will vibrationally excite an initially stationary molecule by the classical energy

$$\Delta E_{1D} = ME_0, \quad (3)$$

$$\text{where } M = \frac{m_1(m_1 + 2m_2)}{(m_1 + m_2)^2}. \quad (4)$$

Perhaps the simplest extension of this model to three spatial dimensions is shown in Fig. 4. Here an atom with initial momentum p_0 transfers the momentum

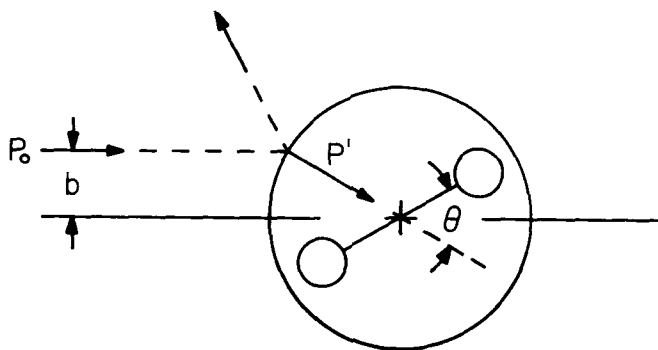


FIGURE 4

Simple three-dimensional hard-sphere model for vibrational excitation in atom-diatom collisions. The momentum transfer to the oscillator is the projection on the oscillator axis of the impulsive momentum transfer normal to the surface of the sphere.

p' normal to the surface of a hard sphere, and the momentum transfer to the oscillator is taken to be $p' \cos \theta$. Averaging over impact parameter and orientation angles then gives the average energy transfer

$$\overline{E_{3D}} = ME_0/6 \quad (5)$$

It is interesting that this simple model, together with the classical-quantal correspondence relation, Eq. (2), predicts the correct dependence on v of the cross sections $\sigma_{0v}(E_0)$, and also predicts the experimental cross section ratios $\sigma_{0,2}/\sigma_{0,1}$ and $\sigma_{0,3}/\sigma_{0,1}$ to within about a factor of two. Nevertheless, the actual details of the collision dynamics are much more subtle, as shown by the quantum scattering calculations performed for this system by Schwenke and Truhlar (20). Because of the large rotational excitation in the vibrationally elastic channel, a quantitative interpretation of the scattering data depends very sensitively on the anisotropy of the potential energy surface and on the dynamical coupling between vibration and rotation. A very recent extension by Schwenke and Truhlar of their previous calculation shows that the break in the $\sigma_{0,1}(E_0)$ cross section at $E_0 = 180\text{meV}$ is due to the shift of a prominent feature in the rotational state distribution (perhaps a "rotational rainbow") from inside the $0 \leq J \leq 5$ range viewed by the detector to outside this range. The impulsive collision model also fails to explain the smaller vibrational excitation cross sections which we observed for $\text{I}_2 + \text{D}_2$ collisions compared to $\text{I}_2 + \text{He}$. Since the mass parameters are essentially identical for the two cases, and since we do not expect coupling to D_2 rotation and vibration to be important, a softer repulsive interaction for $\text{D}_2 + \text{I}_2$ compared to $\text{He} + \text{I}_2$ is likely to be the origin of the smaller excitation cross sections.

4. VIBRATIONAL EXCITATION IN ATOM COLLISIONS WITH LARGE POLYATOMIC MOLECULES

We now turn to the vibrational excitation of polyatomic molecules having many vibrational degrees of freedom. At high levels of excitation the various normal modes in such molecules will be strongly mixed by anharmonic coupling, so that even if energy were localized in one normal mode at some initial time, rapid and more-or-less statistical redistribution of the vibrational energy among accessible levels would be expected. At low levels of excitation, however, energy deposited in one normal mode should remain in that mode for long periods. Under these conditions there would appear to be no reason why one should expect a dynamical process such as collision with an atom at some particular value of kinetic energy to populate all energetically accessible modes with statistical probabilities. The possibility of mode-selective vibrational energy transfer is intimately related to the question of whether mode-selective chemistry will occur (for example, upon laser excitation of some specific reactant state) since vibrational energy transfer will generally compete kinetically with reaction.

So far we have results on two similar systems, aniline ($\text{C}_6\text{H}_5\text{NH}_2$) and *p*-difluorobenzene ($\text{C}_6\text{H}_4\text{F}_2$), both excited by collisions with He. In both cases, supersonic expansion of 0.1 to 1 torr of the sample molecule in about 10^4 torr of He carrier gas resulted in a primary beam rotational temperature of about 1K. The attenuation cross sections were measured at the RQ (low J , low K) bandheads of the $\text{S}_1(0_0^+)$ band origins, which were essentially featureless at our primary beam temperature and laser bandwidths. Figure 5 shows the single-quantum vibrational excitation cross sections measured for aniline + He collisions for two modes (18). The NH_2 inversion mode I has a $v=0+1$ transition energy of only 41cm^{-1} , and corresponds to flipping of the NH_2 hydrogens from one side of the benzene plane to the other. Mode T, also called mode 11, corresponds to the out-of-plane vibration of the entire NH_2 group relative to the benzene ring, and has a $v=0+1$ transition energy of 233cm^{-1} . The threshold energies for $v=0+1$ excitation of these and several other low-frequency normal modes are indicated by arrows in Fig. 5.

Excitation of mode 11 shows a linear dependence on collision energy above threshold, just as was seen for $v=0+1$ excitation of I_2 , then a leveling off which is at least qualitatively what one expects from the Poisson distribution

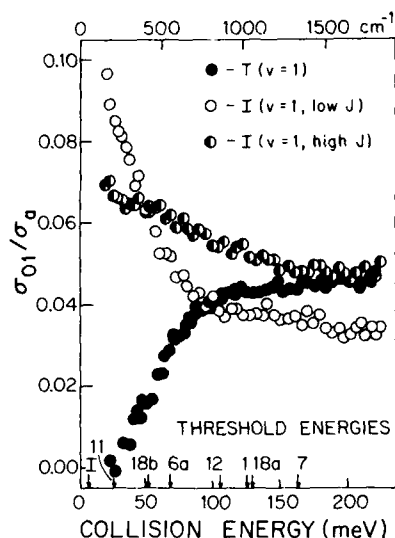


FIGURE 5

Normalized cross sections as functions of the c.m. kinetic energy for excitation of modes I and 11 in aniline + He collisions. Arrows mark the $v=1$ excitation thresholds for modes I and 11, and for six other low-frequency modes for which excitation was not observed.

of Eq. (2) as ϵ increases. Note that the normalized excitation cross sections are much larger than for $I_2 + He$ at similar collision energies, even though the mode 11 vibrational spacing in aniline (233cm^{-1}) is about the same as the I_2 vibrational spacing (213cm^{-1}).

The inversion mode I was observed at two spectroscopic features, corresponding to low-J and high-J peaks of the RQ-branch transitions. Quite remarkably, both features show $v=0 \rightarrow 1$ excitation cross sections which increase with decreasing kinetic energy down to the lowest kinetic energy (about 160cm^{-1}) accessible in the experiment. This kinetic energy dependence is very different from that of mode 11, and of course it indicates highly mode-specific behavior. Although theoretical modeling of these data has not yet been attempted, it seems likely that the origin of this kinetic energy dependence can be found in Eq. (1). Given a time-dependent driving force $F(t)$, it is only the Fourier component of that force at the oscillator frequency ω which is effective in inducing transitions in that particular oscillator. Excitation of the extremely low-frequency inversion mode is apparently favored by slow collisions which contain larger low-frequency Fourier components of the interaction.

Perhaps the most surprising feature of the aniline excitation data is that

none of the other modes for which $v=0 \rightarrow 1$ thresholds are given in Fig. 5 were observed at all. In each of these cases the experimental sensitivity was comparable to the scatter in the data in Fig. 5, making the probability of excitation of each of these modes at least one to two orders of magnitude less than the excitation probabilities for modes I and 11. This degree of mode specificity is quite striking. There are two apparent differences between the modes in which we observe excitation and all of the other modes in which we do not. First, modes I and 11 are the two lowest-frequency modes of aniline, and one generally expects the probabilities of low-frequency transitions to be favored over those of high-frequency transitions simply because the kinetic energy defect is smaller. However, the frequency differences do not seem to be large enough to account for the observations. Modes I and 11 are excited with comparable probabilities in this kinetic energy range even though the ω_{11}/ω_I frequency ratio is greater than 5. By way of comparison, the ω_{10b}/ω_{11} ratio is only about 2, and 10b is not observed at all. The second difference is one of geometry: all of the unobserved modes are in-plane motions while modes I and 11 are out-of-plane bends. This suggests that some symmetry or other geometrical feature of the interaction potential may be responsible for the mode selectivity in this system.

Additional information is provided by the data on p-difluorobenzene + He collisions (21). This molecule, of course, has no mode analogous to the inversion mode of aniline, but its lowest frequency mode, designated 30, is quite comparable to mode 11 in aniline. Mode 30 of p-difluorobenzene corresponds to the in-phase out-of-plane bend of both C-F bonds, and has a $v=0 \rightarrow 1$ transition energy of 160cm^{-1} . Mode 30 excitation is observed to both $v=1$ and $v=2$, but none of the other low-frequency modes are excited within our detection sensitivity, including the out-of-phase out-of-plane C-F bend at 374cm^{-1} . The exceptional activity of mode 30 which we observe in our crossed-beam experiments with S_0 p-difluorobenzene has also been observed in collisional relaxation rate measurements for both the S_0 and S_1 electronic states, and even in collision-free vibration energy redistribution within the molecule following excitation of selected combination bands in S_1 involving mode 30 (22-24). It is not clear at present whether the apparently ubiquitous role which mode 30 plays in the energy flow dynamics in this molecule is merely a consequence of its low frequency or is related instead to some specific dynamical coupling mechanism.

It is intriguing that the first two polyatomics which we studied show such strong and similar mode specificity. However, two systems constitute much too small a set from which to draw general conclusions. It is also evident that a great deal of theoretical work is needed on both the potential energy surfaces and the collision dynamics in order to provide a more rigorous basis for interpretation of the data. Nevertheless, it appears that state-resolved single-collision experiments on vibrational excitation in a wide variety of neutral molecular systems are now feasible, and one can look forward finally to the same kind of detailed insights into the microscopic dynamics of vibrational energy transfer of neutrals that molecular beam experiments have previously yielded for other categories of molecular collision phenomena.

ACKNOWLEDGEMENT

The author has enjoyed the benefit of many excellent collaborators on the work described in this report: these include Dr. Gregory Hall, Dr. Kopin Liu, Dr. Michael McAuliffe, Dr. Michel Costes, Mr. Vasgen Shamamian, and Professor Clayton Giese.

REFERENCES

- 1) J. H. Moore and J. P. Doering, *Phys. Rev. Lett.* 23 (1969) 584.

- 2) H. Udseth, C. F. Giese and W. R. Gentry, *J. Chem. Phys.* 54 (1971) 3642.
- 3) H. Udseth, C. F. Giese and W. R. Gentry, *Phys. Rev. A* 8 (1973) 2483.
- 4) H. E. van den Bergh, M. Faubel and J. P. Toennies, *Faraday Discuss. Chem. Soc.* 55 (1973) 203.
- 5) For example, see T. Ellenbroek, U. Gierz, M. Noll and J. P. Toennies, *J. Phys. Chem.* 86 (1982) 1153.
- 6) R. B. Bernstein, *Chemical Dynamics via Molecular Beam and Laser Techniques* (Oxford, New York, 1982).
- 7) U. Buck, F. Huisken, J. Schleusener and H. Pauly, *Phys. Rev. Lett.* 38 (1977) 680.
- 8) W. R. Gentry and C. F. Giese, *J. Chem. Phys.* 67 (1977) 5389.
- 9) W. R. Gentry and C. F. Giese, *Phys. Rev. Lett.* 39 (1977) 1259.
- 10) For example, see U. Buck, M. Faubel, K. H. Kohl, A. Kohlhaase and V. Staemmler, *Mol. Phys.* (1985) in press.
- 11) J. A. Serri, C. H. Becker, M. B. Elbel, J. L. Kinsey, W. P. Moskowitz and D. E. Pritchard, *J. Chem. Phys.* 74 (1981) 5116.
- 12) K. Bergmann (1985) private communication.
- 13) S. B. Ryali, J. B. Fenn, C. E. Kolb and J. A. Silver, *J. Chem. Phys.* 76 (1982) 5878.
- 14) W. R. Gentry and C. F. Giese, *Rev. Sci. Instr.* 49 (1978) 595.
- 15) W. R. Gentry, in *Atomic and Molecular Beam Methods*, Ch. 3, edited by G. Scoles (Oxford, New York, in press).
- 16) G. Hall, K. Liu, M. J. McAuliffe, C. F. Giese and W. R. Gentry, *J. Chem. Phys.* 78 (1983) 5260.
- 17) G. Hall, K. Liu, M. J. McAuliffe, C. F. Giese and W. R. Gentry, *J. Chem. Phys.* 81 (1984) 5577.
- 18) K. Liu, G. Hall, M. J. McAuliffe, C. F. Giese and W. R. Gentry, *J. Chem. Phys.* 80 (1984) 3494.
- 19) W. R. Gentry, in *Atom-Molecule Collision Theory--A Guide for the Experimentalist*, Ch. 12, edited by R. B. Bernstein (Plenum, New York, 1979).
- 20) D. W. Schwenke and D. G. Truhlar, *J. Chem. Phys.* 81 (1984) 5586, and additional unpublished results.
- 21) G. Hall, C. F. Giese and W. R. Gentry, to be published; G. Hall, Ph.D. thesis, University of Minnesota (1985).
- 22) W. D. Lawrance and A. E. W. Knight, *J. Chem. Phys.* 76 (1982) 5637.
- 23) D. J. Muller, W. D. Lawrance and A. E. W. Knight, *J. Phys. Chem.* 87 (1983) 4952.
- 24) D. L. Catlett, K. W. Holtzclaw, D. Krajnovich, D. B. Moss, C. S. Parmenter, W. D. Lawrance and A. E. W. Knight, *J. Phys. Chem.* 89 (1985) 1577.

RADIATIVELY STABILIZED COLLISIONS: DIELECTRONIC RECOMBINATION AND RADIATIVE ASSOCIATION

Gordon H. DUNN*

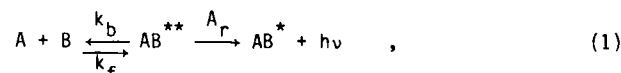
Joint Institute for Laboratory Astrophysics, National Bureau of Standards
and University of Colorado, and Departments of Physics and Chemistry,
University of Colorado, Boulder, Colorado 80309

Radiatively stabilized collisions are a class to which relatively little attention has been given -- especially experimentally. In this paper two processes representative of radiatively stabilized collisions -- dielectronic recombination and radiative association -- are discussed, and recent experimental measurements on both collision types are described. Radiative association rate measurements have been carried out in a Penning ion trap at 11 K. Dielectronic recombination measurements have been made which show definitively the dependence of cross sections on extrinsic fields in the collision region and also demonstrate the dependence of cross sections on principal quantum numbers of the product Rydberg atoms.

1. INTRODUCTION

Consider the collision of two particles which, upon collision, form a complex with the excess initial kinetic energy distributed to internal modes of the complex. If the energy becomes redistributed to translational energy, the particles separate, and there is little evidence of the complex having formed except for, perhaps, some structure in the elastic scattering cross section. If, on the other hand, a radiative transition occurs between states of the complex, then sufficient energy may be carried off by the photon to leave behind a stable combined particle. We will refer to this latter case as a radiatively stabilized collision.

We may represent this by



where k_f is the rate for complex formation, k_b is the rate for the complex's coming apart again, and A_r is the radiative stabilization rate. Clearly, the rate for the radiatively stabilized collision is the forward rate k_f times the branching ratio for stabilization,

$$k_r = k_f \left(\frac{A_r}{A_r + k_b} \right) \quad . \quad (2)$$

Often, $k_b \gg A_r$, so that Eq. (2) becomes $k_r = k_f/k_b(A_r)$. Further, recognizing that k_f and k_b are related by detailed balancing, we have

$$k_r = V_{sp} A_r \quad , \quad (3)$$

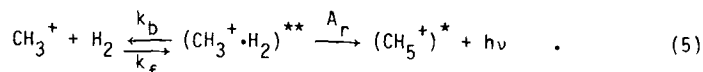
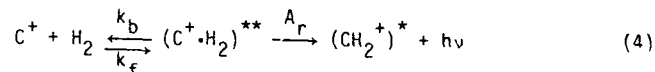
where V_{sp} is a function of the phase space in the collision.

*Staff Member, Quantum Physics Division, National Bureau of Standards.

Two very important examples of radiatively stabilized collisions are radiative association (RA) and dielectronic recombination (DR). The first of these is important, perhaps crucial, in the ion-molecule reaction chains leading to synthesis of molecules in cold interstellar gas clouds (1-5). Dielectronic recombination has long been recognized (6) as essential to modeling of the hot plasmas occurring in fusion devices, stellar atmospheres, high power lasers, and etc.

2. RADIATIVE ASSOCIATION

In an ion-molecule collision, a complex may be formed where translational energy becomes tied up in electronic-vibrational-rotational energy of the complex molecule comprised of the colliding partners. If a photon of sufficient energy is emitted prior to the energy's being redistributed to translational energy, then radiative association will have taken place. Examples which serve to demonstrate the process are



The first of these, Eq. (4), is hypothesized (3) to be a crucial initial step in carbon molecule synthesis in the interstellar medium. The second, Eq. (5), is thought (7) to be a key reaction in the chain leading to formation of methane in these clouds.

Because of the importance of radiative association, a substantial amount of work has gone into the theory for the process (8-19). It is beyond the scope of this paper to deal with the details of the theory, but the developments follow arguments such as those leading to Eq. (3). Generally, the process is so complex that one doesn't know the details of states involved, so the best one can do is to make reasonable estimates (20) for the value of A_r . Values between 10^2 and 10^3 s^{-1} are usually assumed. For the assumption that thermodynamic equilibrium prevails, we have (10,11) for V_{sp}

$$V_{sp} = \frac{h^3}{(2\pi\mu kT)^{3/2}} \frac{f(AB^{**})}{f(A)f(B)} \quad (6)$$

where the f 's are the internal partition functions indicated. Again -- particularly as it pertains to the complex AB^{**} -- detailed knowledge may not be available for specifying the f 's and an assortment of estimates and approximations must be resorted to.

Brief examination of Eq. (1) [or Eqs. (4) and (5)] leads one to realize that collision of the complex AB^{**} with another body may also lead to stabilizing the complex, as the third body, rather than a photon, carries away the excess energy. Thus, any efforts to observe the radiative process experimentally must take into account this prospect of collisionally-assisted association.

When a third body M enters into Eq. (1), we have a new form for Eq. (2)

$$k_a = k_f \frac{A_r + k_s [M]}{k_b + A_r + k_s [M]} \quad (7)$$

where k_a is the total association rate coefficient, k_s is the rate coefficient for stabilization of AB^{**} , and $[M]$ is the density of M . If $A_r \approx 10^3 \text{ s}^{-1}$ and

$k_s \approx 10^{-9} \text{ cm}^3 \text{ s}^{-1}$, then for $[M] > 10^{12} \text{ cm}^{-3}$ the collisional process may dominate. In the range of densities $A_r/k_s \ll [M] \ll k_b/k_s$ we have $k_a \approx k_f \tau_b k_s [M]$. Thus, over some range of $[M]$, if k_a is measured, then combined with reasonable estimates (Langevin) of k_f and k_s , $\tau_b = 1/k_b$ can be obtained. In combination with Eq. (2), then, and estimates of k_f (again, Langevin) and A_r , estimates of k_r may be obtained. This procedure has been used for a number of cases. However, τ_b is a very steep function of temperature, and to get from the temperatures ($T > 80 \text{ K}$) at which such measurements of τ_b have been made to temperatures (10 K) of the interstellar medium requires uncertain extrapolation.

There seem to be only two direct measurements of RA. Woodin and Beauchamp (21) used an ICR cell at 300 K and gas densities the order of 10^9 cm^{-3} and greater to observe association reactions of the type



where (LPM) means "large polar molecule," e.g. $(\text{C}_2\text{H}_5)_2\text{CO}$, $\text{CH}_3\text{COC}_2\text{H}_5$. Here k_b is estimated to be small (the energy gets "lost" in all the degrees of freedom of the complex), the gas density is small, and it is almost certain that their measurements are primarily due to radiative association.

Barlow, Dunn, and Schauer (22) used a technique introduced by Luine and Dunn (23,24) to make measurements at 13 K for the reaction in Eq. (5). Here the temperature is low (characteristic of the interstellar clouds), and the reaction involves a small nonpolar molecule and a complex with a relatively short lifetime.

The measurements were made using a Penning ion-trap technique which is described elsewhere (22-27). The trap, schematically illustrated in Fig. 1, is made up of two end caps and a ring which are hyperboloids of revolution. It is cooled to 11 K and centered and aligned in the 2.4 T field of a superconducting solenoid. A negative potential on the ring produces a harmonic

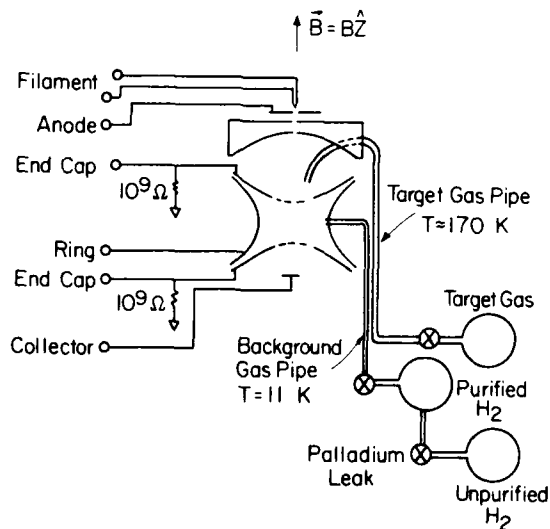


FIGURE 1
Schematic of cold Penning ion trap used for radiative association measurements.

well along the z axis, thus leading to positive ion confinement along z . The ions of charge q and mass m are radially confined by the magnetic field. In the trap, ions move with simple harmonic motion along the z axis at frequency ν_z , the ion cloud rotates uniformly about the z axis with the magnetron frequency ν_- , and the ions execute cyclotron motion in the B field with the off-set cyclotron frequency $\nu_+ = \nu_c - \nu_-$, where $\nu_c = qB/2\pi m$.

Ion clouds of CH_3^+ were made with densities of $10^5 - 10^6 \text{ cm}^{-3}$ and trapping lifetimes of order 10^7 s . Hydrogen gas was then introduced through the background gas pipe (Fig. 1) to bring the neutral density to $\sim 10^7 \text{ cm}^{-3}$ and the trapping lifetime to $\sim 10^4 \text{ s}$.

Ions are nondestructively detected by measuring the noise power at ν_z in image currents to the endcaps. The area S_z under the spectral feature at ν_z is proportional to the product of the number of ions and their axial temperature. The relative number of ions of a particular q/m is measured by applying a small amount of rf power at $\nu_+ - \nu_-$; ion-ion collisions rapidly bring the ion cloud into thermal equilibrium, and one observes an increase in signal proportional to the number of resonant absorbers, the square of rf amplitude, and the heating time.

Sequential heating of each species in a period short compared to the reaction time is used to establish the relative number of each ion at the measurement time. Figure 2 shows a typical measurement cycle. The cooling or equilibration rate after each heating is also determined to give a measurement of the neutral density (gas densities at 11 K and at the trapping site are not measurable by conventional techniques).

Both parent and daughter ions and neutral colliders are thus monitored at intervals over $\sim 10^4 \text{ s}$ and the total ion number $N_T(t) = \sum_i N_i(t)$ is least-squares fitted to $N_T(t) = N_0 \exp(-t/\tau_a)$ to determine the attrition time τ_a of ions in the trap. The number of product ions is given by $N_p(t) = N_0 \exp(-t/\tau_a) [1 - \exp(-t/\tau_r)]$; so that a plot of $X_p(t) = \ln\{[1 - N_p(t)/N_0] \exp(t/\tau_a)\}$ versus time yields a line of slope $1/\tau_r$, where τ_r is the reaction time constant.

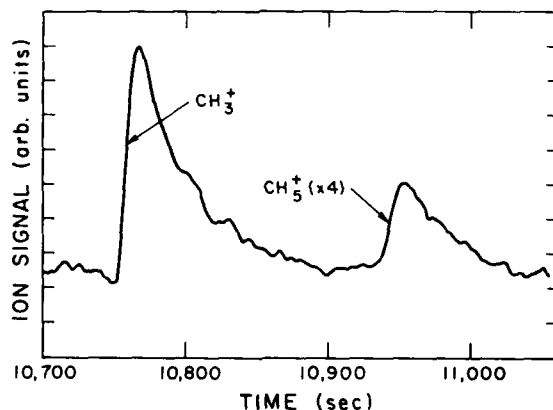


FIGURE 2

Demonstration of ion signal versus time. The observed signal, the noise power in image currents at ν_z , is proportional to product of ion number and temperature. The signal increases sharply (arrows) when cyclotron resonant power is applied, thus increasing the temperature. The power input $[(\text{rf amplitude})^2 \times \text{time}]$ for heating CH_5^+ was 4 times greater than for CH_3^+ . From Ref. 22.

The reaction probability $P_r(T)$ is the ratio of the ion-neutral collision time to the reaction time; $P_r(T) = \tau_c/\tau_r$. The ion-neutral collision time τ_c is related (28) to the observed equilibration time τ_e by $\tau_c = (8/3) \times [m_i m_n / (m_i + m_n)^2] \tau_e$, where m_i and m_n are the ion and neutral masses, respectively. The reaction rate coefficient is then simply $k_r(T) = k_c(T) P_r(T)$ where $k_c(T)$ is the collision rate coefficient. Assuming that the contribution of the quadrupole moment of H_2 is small, one can take $k_c(T)$ to be simply the Langevin value $k_L(T) = 2\pi q(\alpha/u)^{1/2}$, where q is the ion charge and α the molecular polarizability. Then we have

$$k_r(T) = \frac{8}{3} \frac{m_i m_n}{(m_i + m_n)^2} \frac{\tau_e}{\tau_r} k_L(T) \quad (9)$$

as the final relationship for obtaining the reaction rate coefficient.

With this method, Barlow et al. (22) found for the reaction of Eq. (5)

$$k_{r5}(13 \text{ K}) = 1.1^{+0.4}_{-0.2} \times 10^{-13} \text{ cm}^3 \text{ s}^{-1},$$

and Luine and Dunn (23,24) established an upper limit for Reaction (4) of

$$k_{r4}(13 \text{ K}) < 1.5 \times 10^{-15} \text{ cm}^3 \text{ s}^{-1}.$$

The measured value of $k_{r5}(13 \text{ K})$ is about an order of magnitude larger than theoretical values in the literature (16,29).

A more recent calculation of Bates (17) giving V_{sp} together with the measured k_{r5} and using Eq. (3) yields $A_r = 3 \times 10^3 \text{ s}^{-1}$. Extrapolating three body data of Smith and Adams (30) for k_b , and assuming 50% of collisions result in stabilization, gives $A_r = 529 \text{ s}^{-1}$ when taken with Eq. (2) and the measured k_{r5} . The extrapolation of the three body data to low temperatures is a very uncertain procedure, so the disagreement by nearly a factor of 6 is not reason for concern; rather it points up the difficulties of extrapolating.

From the above brief discussion of RA, we can conclude that

1) The basic problem seems reasonably well understood, but ways to theoretically get at A_r are inadequate. The calculation of V_{sp} is very difficult -- especially as it involves unknown states of the intermediate complex.

2) Experiments are woefully few in number. More experiments are needed. However, drift tube techniques operate at densities where typically $[M] > A_r/k_s$ for reasonable A_r , so results with these methods will be looked at with some skepticism.

3) The stabilizing photons should be looked for experimentally. This promises to be a Herculean task that will not likely be accomplished in the near future.

4) For purposes of more directly relating to the interstellar medium, measurements at low temperatures on H_2 should be done using pure para-hydrogen, since V_{sp} [Eq. (6)] depends on the ortho/para mix.

3. DIELECTRONIC RECOMBINATION

Dielectronic recombination is the other example of a radiatively stabilized collision which we will discuss here. The DR process has been recognized (6) for more than twenty years as important in hot plasmas; but interest in DR has intensified over the past three years since the first direct cross section measurements were made (31-34).

For this case, the form for Eq. (1) becomes

$$e + X^{n+} \rightleftharpoons (X^{(n-1)+})^{**} \rightarrow (X^{(n-1)+})^* + h\nu, \quad (10)$$

and is represented pictorially in Fig. 3. An electron with energy ϵ less than

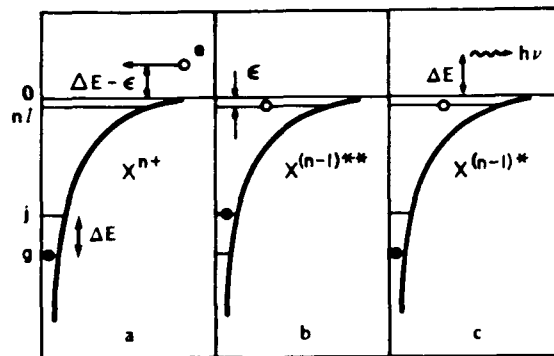


FIGURE 3
Cartoon showing the sequential "steps" in dielectronic recombination.

ΔE , that is necessary to excite level j of the target ion, gains kinetic energy from the Coulomb field as it approaches the ion. Close to the ion core, the electron has more than enough kinetic energy to excite the core, but having done so, it finds itself bound with energy ϵ . The complex AB^{**} of Eq. (1) is thus formed. The two electrons can communicate, and the reverse process or autoionization will occur with rate $k_b \approx A_a$. The only evidence of anything's having happened will be some structure in the elastic scattering cross section. If, however, the excited core electron (or the trapped Rydberg electron) radiates before autoionization occurs, then one is left with a Rydberg state of a once less charged ion -- DR will have occurred.

Because of the importance to fusion, astrophysical, and other hot plasmas, there has been extensive theoretical work on DR (35-49), so much in fact that complete literature citations are beyond the scope of this paper. The excellent review by Seaton and Storey (35) is a good place to start, though much has been done since that time.

No measurements existed for DR until 1978 when breakthroughs by Brooks et al. (50) and Breton et al. (51) provided the first plasma rate measurements for the process. Other measurements have since been made (52), and another important new plasma method was introduced by Bitter et al. (53) in 1982. The breakthrough in 1982-1983 leading to colliding-beams cross section measurements (31-34,54) has allowed more direct comparisons between theory and experiment. In a nutshell, the results of the beams measurements can be summarized with the statement that all give measured cross sections significantly larger than theoretically predicted. The hypothesis has been made (42) that there is in effect a "knob" on the reaction which can be turned to adjust the size of the cross sections. The control spoken of is the extrinsic electric field in the collision region. We emphasize here that this "knob" adjusts the actual reaction cross section, and not just some apparent or detected cross section.

Before describing recent experiments to explore this seemingly bizarre hypothesis, it is useful to consider some more details of the radiatively stabilized collision process for the specific case of DR.

Rewriting Eq. (2) for DR in terms of cross section, we have

$$\sigma_{DR} = M \cdot (2\ell + 1) \frac{A_a(n, \ell) A_r(n, \ell)}{A_a(n, \ell) + A_r(n, \ell)} \quad (11)$$

Now, generally $A_r(n, \ell)$ is nearly constant with n and ℓ , while $A_a(n, \ell)$, varies as $1/n^3$. For "low" n 's and ℓ 's, $A_a \gg A_r$, where the inequality defines what we mean by "low." Numbers may be $A_a \sim 10^{14} \text{ s}^{-1}$, $A_r \sim 10^8 \text{ s}^{-1}$. Under these conditions, as already seen in Eq. (3), $\sigma_{DR}(n, \ell) \propto A_r(n, \ell)$. At high enough n 's, $A_a = A_r$, and beyond that, $A_r > A_a$, so $\sigma_{DR}(n, \ell) \propto A_a(n, \ell) \propto 1/n^3$.

Similarly, $A_a(n, \ell)$ decreases rapidly with ℓ (e.g. $A_a \propto \exp(-\alpha \ell^2)$, where α is a constant). The total DR cross section is a sum over the resonances covering the combinations of n and ℓ . For a given (low to moderate) n , and for low ℓ , again $A_a \gg A_r$ so $\sigma_{DR}(n, \ell) \propto (2\ell+1)A_r$ and for high ℓ , $\sigma_{DR}(n, \ell) \propto (2\ell+1)\exp(-\alpha \ell^2)$. This is visualized with the aid of Figure 4 which shows a hypothetical A_r and A_a versus ℓ for constant n as well as the resultant $\sigma_{DR}(n, \ell)$ from Eq. (11). Thus, though the number of resonances which could contribute to DR increases as

$$\sum_{\ell=0}^{n-1} 2(2\ell+1) = 2n^2, \quad ,$$

only ℓ 's for $\ell \leq \ell_c$ will typically contribute.

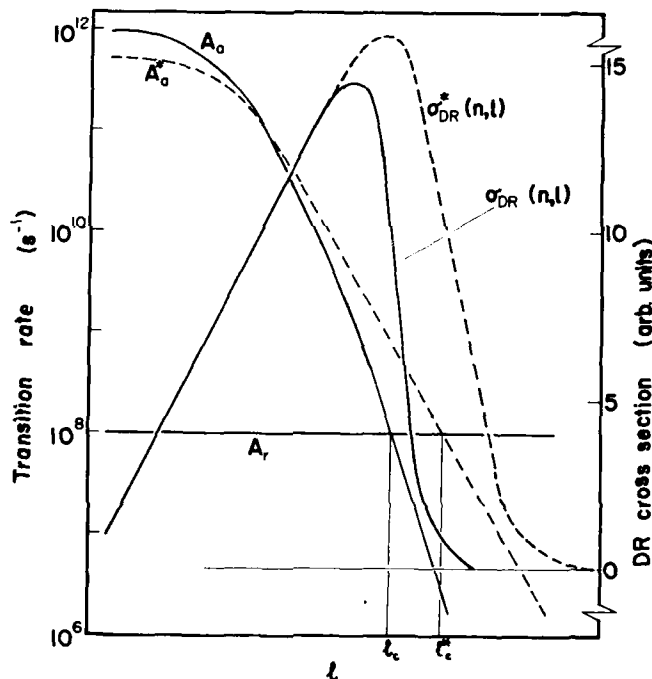


FIGURE 4

Schematic illustration showing variation of the autoionization rate A_a and the radiative stabilization rate A_r as functions of ℓ for fixed n (read log ordinate scale on left). Solid curves are for no ℓ mixing, dashed curves for small amount of ℓ mixing by fields or other mechanisms. Also shown are cross sections σ_{DR} [see Eq. (11)] resulting from the rates (read linear scale on right).

While this is no limitation for small n 's where $\ell_{\max} = n-1 < \ell_c$, already for moderate n 's all possible contributions from ℓ 's with $\ell_c \leq \ell \leq n-1$ are suppressed because of the strong decrease of A_ℓ with ℓ . This becomes even more dramatic with high n 's where the relation $A_\ell \sim 1/n^3$ leads to a strong decrease of the cutoff angular momentum ℓ_c and hence the DR cross section.

Thus, a plot of σ versus n will appear as the solid curve in Fig. 5, whereas if all the ℓ states at each n could contribute equally, there would result a curve similar to the dashed curve in Fig. 5. The effect of the electric field "knob" is to "tune" in or out the ℓ resonances which contribute significantly to the collision. One may visualize this crudely by referring again to Fig. 4. Introducing an electric field will mix states for $\ell > \ell_c$ with states for $\ell < \ell_c$ with the result that the dashed curve for A_ℓ^* results. Since ℓ_c is extended to ℓ_c^* , the states between ℓ_c and ℓ_c^* now add to the cross section; and $\sigma_{DR}(n, \ell)$ results as depicted by the dashed curve in the figure. In Fig. 5, a curve between the solid and dashed curves would result. Though proper theoretical description must make use of Stark states, this qualitative picture in terms of spherical states relays the general physical picture in terms perhaps more familiar to most.

It has been recognized for some time that mixing of angular momentum states by mechanisms such as collisions (55), plasma microfields (56), and magnetic fields (57) may affect DR. More recently, in an effort to rationalize the disparity between results of beams experiments and theoretical calculations, the effects of extrinsic electric fields have been treated theoretically (42,47,58,59).

Recently, experiments were carried out at JILA (60) to explore the hypothesis that the cross section for DR can be varied by controlling the electric field in the collision region. In the experiments cross sections were measured as a function of electron energy for a fixed value of principal quantum number of the final Rydberg atom, and these measurements were made for

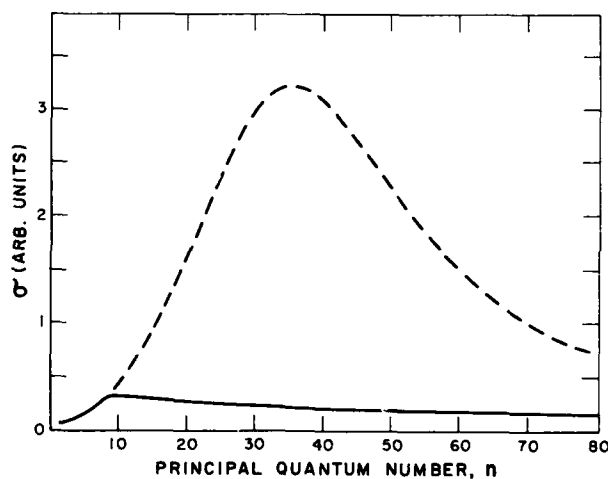
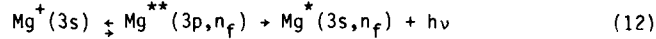


FIGURE 5

Illustration showing anticipated dependence of dielectronic recombination cross section on the principal quantum number of the final Rydberg state. Solid curve is for no ℓ mixing; dashed curve is for full ℓ state mixing.

two values of electric field in the collision region. Also, at a fixed value of electron energy, cross sections were measured as a function of principal quantum number of the final Rydberg state, and these measurements were done for three values of electric field in the collision region.

The experiments were performed for the process,



with an arrangement schematically illustrated in Fig. 6. A beam of mass selected $^{24}\text{Mg}^+$ ions (2 keV, ~ 300 nA) is crossed by a magnetically confined, variable-energy beam of electrons (~ 25 μA , ~ 0.5 eV energy width). Dielectronic recombination processes occur in an electric field $\vec{E}_c = \vec{v}_i \times \vec{B}$ (y direction) which can be changed by variation of the ion velocity v_i or the magnetic field B . With v_i between 0.64×10^7 cm s $^{-1}$ and 1.27×10^7 cm s $^{-1}$ the doubly excited Mg atoms formed by the capture of a free electron into a bound Rydberg state, with simultaneous excitation of the ground state 3s-electron into 3p states, can stabilize by the emission of a 3p-3s photon within a flight path of less than 0.25 mm, thus completing the DR process. Rydberg atoms surviving the field in the interaction region then enter a field \vec{E}_s which separates Mg^+ ions from the neutral beam. The field plates extend from about 6 cm to 21 cm down beam from the collision region. The field \vec{E}_s in the separator is parallel to \vec{E}_c , and considering an additional contribution from the fringe magnetic field of the electron gun, E_c was kept to a maximum of about 40 V cm $^{-1}$, a field such that classically all atoms with $n > 53$ are field ionized.

Field ionization has been used in these measurements to distinguish between Rydberg atoms in different quantum states. The field needed to ionize a given quantum state depends generally on all its quantum numbers, not just n . However, in the experiment there is only the field E_i to distinguish states. Thus, we have adopted an operational definition and use the formula for the classical saddle point

$$n_f = (3.2 \times 10^8 / E_i)^{1/4} \quad (13)$$

to label the Rydberg states detected at an electric field E_i (V cm $^{-1}$).

The Rydberg atoms surviving the separation field \vec{E}_s are introduced into a region with an electric field in the x-z plane given by $\vec{E}_i = V/(\alpha R)\hat{\theta}$, where a voltage of $\pm V$ is applied to plates at an angle 2θ with respect to each other ($\theta = 15^\circ$ in this experiment), R is the distance from the apex of the wedge, and $\hat{\theta}$ is the cylindrical coordinate unit vector. (The wedge field is shown rotated 90° about the z-axis in Fig. 6.) Because the field changes with z ,

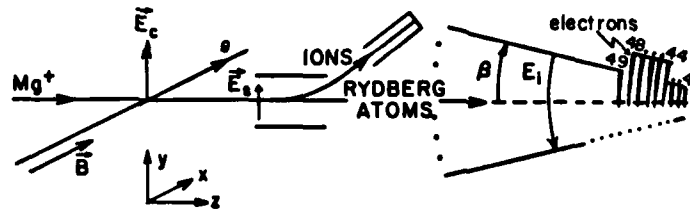


FIGURE 6

Schematic of the crossed beams apparatus with wedge field Rydberg state detector used for DR measurements.

Rydberg atoms in different quantum states are field ionized at different values of z , presenting the opportunity to selectively detect the electrons or ions produced from different states. In one plate (the top in Fig. 6) about 72 cm down beam from the collision region, a 29 mm gridded square aperture is cut, behind which is located a position-sensitive detector (multichannel plates with resistive anode). This detects particles in a given range of n_f , as shown in the figure for electrons between $n_f = 44$ and 48. By changing the voltage on the plates and/or the angle, a large range of n_f 's can be detected. By choosing the polarity of voltages on the plates, one can observe either electrons or ions.

Proper measurements of beam current, signal counts, beam overlap factor, and detector efficiency then allowed the determination of the cross section $\sigma(n_f)$. Variation of electron energy E_e for fixed V on the wedge field plates gave $\sigma_{n_f}(E_e)$ versus E_e with results shown in Fig. 7. Variation of the voltage V on the wedge field plates for fixed E_e gave $\sigma(n_f)$ vs. n_f with results shown in Fig. 8.

These results clearly demonstrate the strong influence of extrinsic electric fields on DR cross sections and on the final Rydberg state distribution. The observed trends are in qualitative agreement with predictions of LaGattuta and Hahn (42) and recent calculations of Griffin, Pindzola and Bottcher (61); however, a direct comparison between experimental and theoretical results is complicated by the fact that the label n_f used in the experiment to identify Rydberg states is not the same as the principal quantum number n . Further work must be done on this "mapping," but this is seen more as a detail that will affect the shapes of the $\sigma(n_f)$ vs. n_f curves, but not the total cross sections.

As intriguing and interesting as this "knob" on the cross section is, it has serious implications for future experiments to study DR, since a "dial" must be included with the "knob," i.e. provision should be made to determine what the extrinsic fields are. Similarly, this behavior of DR must be thought

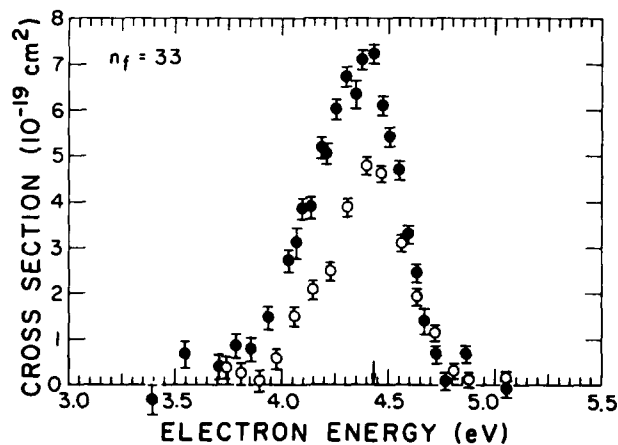


FIGURE 7

Cross section $\sigma(n_f=33)$ versus electron energy for two different extrinsic fields; solid circles, $E_c = 23.5 \text{ V cm}^{-1}$; open circles, $E_c = 7.24 \text{ V cm}^{-1}$. Uncertainties are one statistical standard deviation. Arrow indicates excitation threshold energy. From Ref. 60.

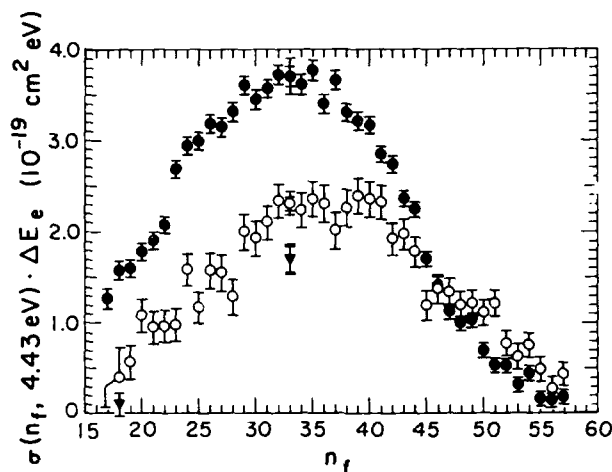


FIGURE 8

Cross section times width ΔE_e of electron energy distribution versus field ionization quantum number n_f [see Eq. (13)]. Solid circles, $E_c = 23.5 \text{ V cm}^{-1}$, open circles, $E_c = 7.24 \text{ V cm}^{-1}$; triangles, $E_c = 3.62 \text{ V cm}^{-1}$. Uncertainties are one statistical standard deviation. For $n_f = 33$ the relative uncertainties are also indicated. Absolute uncertainties at $n_f = 33$ are within 10%. From Ref. 60.

about and dealt with in applications areas. For some cases the effects of fields may be quite minimal. For example, A_r generally scales as Z^4 , so for high z we may have $A_a > A_r$ only for a few low n ; and since for low n , $\lambda_{\max} < \lambda_c$ there is no reservoir of states which electric fields can "turn on." Thus, depending on the specific circumstances of applications, the field-effects issues may or may not be important, but need to be considered.

The earlier beams experiments on DR seem to be at least qualitatively explained by the field effects. For the merged beams experiments at Oak Ridge National Laboratory (33,62), the DR results may provide a measurement of average electric field in the 1 m long interaction region, since a hypothesized field of 25 V/cm gives reasonable agreement between theory (58,61) incorporating fields and the experiments for most species studied. No independent methods of determining the fields in the collision region are yet available.

Figure 9 shows results from the Oak Ridge experiments (62) for the sodium-like ion S^{5+} compared to calculations with no fields (lower curve) and complete Stark mixing (upper curve). The experimental points lie in the intermediate area; and, as noted above, a theoretical curve (61) incorporating a field of 25 V/cm passes quite nicely through the measurements.

In summary, for dielectronic recombination, we note that

- 1) The gap between experiment and theory is closing; the process seems reasonably well understood.
- 2) Extrinsic electric fields must be considered part of the collision system, since they mix angular momenta leading to dramatic enhancement of DR cross sections. Fields needed for such mixing are relatively small.
- 3) Though the role of possible field enhancement needs to be looked at for each applications case, the field enhancement of DR cross sections may not be important for most highly charged ions.

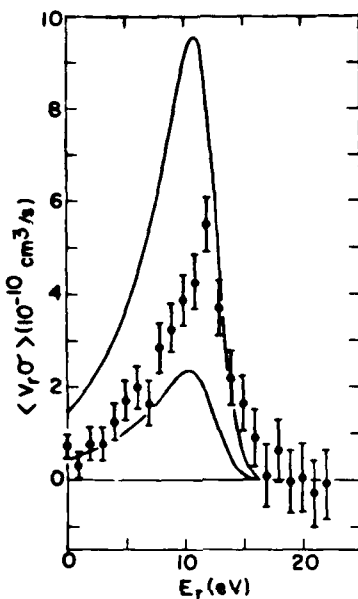


FIGURE 9

The DR rate $\langle \nu_r \sigma \rangle$ versus E_r for S^{5+} from Ref. 62. Upper curve (full mixing) and lower curve (no mixing) were calculated from cross sections in Ref. 58.

4) The theoretical work on plasma microfield enhancement and collisional enhancement of DR cross sections needs to be taken seriously by workers in applications areas. Experiments are needed to demonstrate and verify these effects.

5) The roles of fine structure and other state interference effects need more work; there are no good experimental observations so far.

6) There is a need for experiments on multiply charged ions where fields are defined, measured, etc.

7) Experiments separating low-lying resonances (final Rydberg states) would be valuable in testing the relationship between radiative and dielectronic recombination and the presence of possible interference.

4. SUMMARY

Radiatively stabilized collisions are a unique class of collisions to which relatively little attention has been devoted until quite recently. Yet, they play critical roles in the behavior of plasmas in the coldest (interstellar clouds) and hottest (stars, fusion plasmas), parts of the universe. Though the past few years can boast much progress in understanding these processes, much work remains in uncovering the intricacies of these elegant and fragile collisions.

The author emphasizes with gratitude the role of colleagues in the work at JILA. The experiments on radiative association were supported by the National

Science Foundation and were done in collaboration with J. Luine, S. Barlow, and M. Schauer. The recent work on field effects in dielectronic recombination was carried on with A. Müller, D. Belic, B. DePaola, N. Djuric, D. Mueller, and C. Timmer, and was supported by the Office of Fusion Energy, U. S. Department of Energy.

REFERENCES

- 1) D. R. Bates and L. Spitzer, *Astrophys. J.* 113 (1951) 441.
- 2) E. Herbst and W. Klemperer, *Astrophys. J.* 185 (1973) 505.
- 3) J. H. Black and A. Dalgarno, *Astrophys. J. Letters* 15 (1973) 79;
Astrophys. J. Suppl. 34, (1977) 405.
- 4) W. T. Huntress and S. S. Prasad, *Astrophys. J.* 236 (1980) 318.
- 5) T. E. Graedel, W. D. Langer, and M. A. Frerking, *Astrophys. J. Suppl.* 48 (1982) 321.
- 6) A. Burgess, *Astrophys. J.* 139 (1964) 776.
- 7) E. Herbst, *Astrophys. J.* 205 (1976) 94.
- 8) E. Herbst, J. G. Schubert, and P. R. Certain, *Astrophys. J.* 213 (1977) 696.
- 9) D. R. Bates, *J. Phys. B*, 12 (1979) 4135.
- 10) D. R. Bates, *J. Chem. Phys.* 71 (1979) 2318.
- 11) E. Herbst, *J. Chem. Phys.* 70 (1979) 2201.
- 12) L. Bass, W. J. Chesnavich, and M. T. Bowers, *J. Am. Chem. Soc.* 101 (1979) 5493.
- 13) E. Herbst, *J. Chem. Phys.* 72 (1980) 5284.
- 14) L. M. Bass, P. R. Kemper, V. G. Anicich, and M. T. Bowers, *J. Am. Chem. Soc.* 103 (1981) 5283.
- 15) E. Herbst, *Astrophys. J.* 252 (1982) 810.
- 16) D. R. Bates, *Astrophys. J.* 270 (1983) 564.
- 17) D. R. Bates, *Astrophys. J.* (1985) in press.
- 18) W. Roberge and A. Dalgarno, *Astrophys. J.* 255 (1982) 489.
- 19) M. M. Graff and J. T. Moseley, *Astrophys. J.* 269 (1983) 796.
- 20) E. Herbst, *Chem. Phys.* 65 (1982) 185.
- 21) R. L. Woodin and J. L. Beauchamp, *Chem. Phys.* 41 (1979) 1.
- 22) S. E. Barlow, G. H. Dunn, and M. Schauer, *Phys. Rev. Lett.* 52 (1984) 902.
- 23) J. A. Luine and G. H. Dunn, in: *Electronic and Atomic Collisions, Abstracts of Papers, XIth ICPEAC*, ed. S. Datz (Gatlinburg, Tenn., 1981), pp. 1035-1036.
- 24) J. A. Luine and G. H. Dunn, *Astrophys. J. Letters*, in press.
- 25) J. A. Luine, Ph.D Thesis, University of Colorado, Boulder (1981), available through University Microfilms, Inc., Ann Arbor, Michigan 48106, Order No. 81-22304.
- 26) S. E. Barlow, Ph.D Thesis, University of Colorado, Boulder (1984), available through University Microfilms, Inc., Ann Arbor, Michigan 48106, Order No. 84-28636.
- 27) S. E. Barlow, J. A. Luine, and G. H. Dunn, in preparation.
- 28) A. M. Cravath, *Phys. Rev.* 36 (1930) 248.
- 29) E. Herbst, *Astrophys. J. Suppl.* 53 (1983) 41.
- 30) D. Smith and N. Adams, *Chem. Phys. Lett.* 79 (1981) 563.
- 31) J. B. A. Mitchell, C. T. Ng, J. L. Foraud, D. P. Levac, R. E. Mitchell, A. Sen, D. B. Miko and J. W. McGowan, *Phys. Rev. Lett.* 50 (1983) 335.
- 32) D. S. Belic, G. H. Dunn, T. J. Morgan, D. W. Mueller, C. Timmer, *Phys. Rev. Lett.* 50 (1983) 339.
- 33) P. F. Dittner, S. Datz, P. D. Miller, C. D. Heath, P. A. Stelson, C. Bottcher, W. B. Dress, G. D. Alton and N. Neskovic, *Phys. Rev. Lett.* 51 (1983) 31.
- 34) J. F. Williams, *Phys. Rev. A* 29 (1984) 2936.

- 35) M. J. Seaton and P. J. Storey, in: Atomic Processes and Applications, eds. P. G. Burke and B. L. Moiseiwitsch (North-Holland, Amsterdam, 1977), pp. 134-197.
- 36) R. D. Cowan, The Theory of Atomic structure and Spectra (University of California Press, Berkeley, 1981), pp. 549-563.
- 37) L. J. Roszman, in: Physics of Electronic and Atomic Collisions, ed. S. Datz (North-Holland, Amsterdam, 1982), p. 641.
- 38) J. Dubau and S. Volante, Rep. Prog. Phys. 43 (1980) 199.
- 39) K. LaGattuta and Y. Hahn, J. Phys. B 15 (1982) 2101.
- 40) D. J. McLaughlin and Y. Hahn, Phys. Rev. A 28 (1983) 493.
- 41) D. J. McLaughlin and Y. Hahn, Phys. Rev. A 27 (1983) 1389.
- 42) K. LaGattuta and Y. Hahn, Phys. Rev. Lett. 51 (1983) 558.
- 43) S. Geltman, J. Phys. B 18 (1985) 1425.
- 44) R. H. Bell and M. J. Seaton, J. Phys. B 18 (1985) 1589.
- 45) A. P. Hickman, J. Phys. B 18 (1985) 3219.
- 46) D. C. Griffin, M. S. Pindzola, and C. Bottcher, Phys. Rev. A 31 (1985) 568.
- 47) A. P. Hickman, J. Phys. B 17 (1984) L101.
- 48) G. Alber, J. Cooper, and A. R. P. Rau, Phys. Rev. A 30 (1984) 2845.
- 49) A. Pradhan, Phys. Rev. A 30 (1984) 2141.
- 50) R. L. Brooks, R. V. Datta, and H. R. Griem, Phys. Rev. Lett. 41 (1978) 107; R. L. Brooks, R. V. Datta, A. D. Krumbein and H. R. Griem, Phys. Rev. A 21 (1980) 1387.
- 51) C. Breton, C. DeMichelis, M. Finkenthal, and M. Mattioli, Phys. Rev. Lett. 41 (1978) 110.
- 52) R. C. Isler, E. C. Crume, D. E. Arnurius, Phys. Rev. A 26 (1982) 2105.
- 53) M. Bitter, S. Cohen, K. Wittill, S. Sesnic, F. Tenny, J. Timberlake and S. von Goeller, Bull. Am. Phys. Soc. 27 (1982) 1083; F. Bely-Dubau et al. Phys. Lett. 93A (1983) 189.
- 54) See series of papers in: Electronic and Atomic Collisions, eds. J. Eichler, I. V. Hertel, N. Stolterfoht (North-Holland, Amsterdam, 1983). S. Datz, p. 795; Y. Hahn, p. 801; G. Dunn et al., p. 809; P. F. Dittner et al., p. 819; J. P. Briand et al., p. 827; A. P. Hickman, p. 833.
- 55) A. Burgess and H. P. Summers, Astrophys. J. 157 (1969) 1007.
- 56) V. L. Jacobs, J. Davis, and P. C. Kepple, Phys. Rev. Lett. 37 (1976) 1390.
- 57) W. A. Huber and C. Bottcher, J. Phys. B 13 (1980) L399.
- 58) D. C. Griffin, M. S. Pindzola and C. Bottcher, Oak Ridge National Laboratory Report ORNL/TM-9478 (1985); in: XIV ICPEAC, Abstracts of Contributed Papers (1985), p. 308.
- 59) D. Harmin, private communication
- 60) A. Müller, D. S. Belic, B. D. DePaola, N. Djuric, G. H. Dunn, D. W. Mueller, and C. Timmer, Phys. Rev. Lett., submitted.
- 61) D. C. Griffin, M. S. Pindzola, and C. Bottcher, private communication.
- 62) P. F. Dittner, S. Datz, P. D. Miller, and P. L. Pepmiller, in: XIV ICPEAC, Abstracts of Contributed Papers (1985), p. 306; private communication.

ANGLE- AND SPIN-RESOLVED PHOTOELECTRON SPECTROSCOPY WITH ATOMS AND MOLECULES

Ulrich HEINZMANN

Fakultät für Physik, Universität Bielefeld, 4800 Bielefeld 1, West Germany

1. INTRODUCTION

Up to 1984 experimental analysis of the electron-spin polarization (ESP) in photoionization and photoemission using circularly polarized light (Fano effect (1)) was restricted to angle-integrated measurements (2, 3) without resolution of the kinetic energy of the photoelectrons ejected. With the development of the new German dedicated electron storage ring for synchrotron radiation BESSY in Berlin, a light source of circularly polarized vacuum ultra-violet (vuv) radiation with sufficiently high intensity has become available, making angle- and energy-resolved spin-polarization transfer studies from circularly polarized radiation onto photoelectrons feasible. These measurements have been performed with free atoms (4, 5), atoms adsorbed on solid surfaces (6) as well as with a solid state system (7) even in a photon energy range ≥ 10 eV, where conventional methods for producing circularly polarized radiation break down because no transparent or even double refracting material exists. These studies using circularly polarized radiation complement recent photoelectron spectroscopy measurements with free randomly oriented (8) as well as free oriented molecules (9). One of the reasons why these experiments have been done is to find a set of parameters measured in the experiments which characterize the photoemission process quantummechanically completely. It builds a bridge from the atoms via the molecules via the adsorbates to the three-dimensional crystal. It makes this cross comparison not only in terms of intensities and polarizations but also by means of dipole matrix elements and phase-shift differences of continuum-wave functions for single channels, which are energy degenerate but have been isolated by the data-combination of different non-redundant experiments.

The reaction plane of symmetry for an angle- and spin-resolved photoionization process of an unpolarized atom or unoriented molecule using circularly polarized radiation is shown in Fig. 1. Because the momentum of the photon is negligibly small compared with the momentum of the photoelectron (valid in nonrelativistic approximation for photon energies ≤ 100 eV) there is a forward-backward symmetry in the reaction plane of Fig. 1. It also makes no difference whether right handed circularly polarized radiation comes from the left or left handed comes from the right. The rotational symmetry around the direction of the photon momentum causes both ESP components perpendicular to the photon spin to vanish for photoelectron emission angles $\theta = 0, \pi/2, \pi$. This is shown in Fig. 2, where the angle dependences of intensity $I(\theta)$ and spin polarization components are shown for a certain atomic photoionization process (xenon), which has been simultaneously resolved with respect to all relevant variables i.e.: radiation wavelength 80 nm, radiation polarization σ^+ , electron emission angle θ , electron kinetic energy corresponding to the final ionic state $Xe^+ 2p_{1/2}$, the 3 components of the electron spin polarization vector $\vec{P}(\theta)$: $P_{\perp}(\theta)$ perpendicular to the reaction plane, $A(\theta)$ parallel to the photon spin, $P_{\parallel}(\theta)$ perpendicular to the photon spin but in the reaction plane.

The curves in Fig. 2 are fits to the experimental points (4, 5) (the size of a typical error-bar cross is given in the middle part) and are in accordance with the theoretical predictions by Cherepkov (10) and Lee (11):

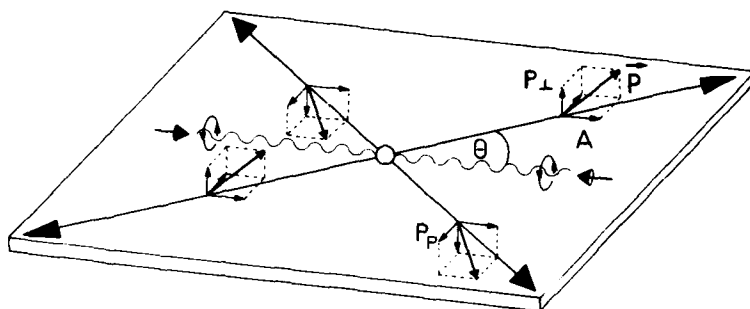


FIGURE 1
Photoionization reaction plane in the case of circularly polarized radiation

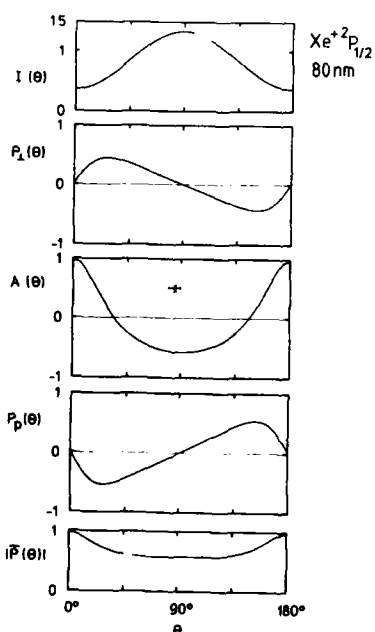


FIGURE 2
Fit-curves of the experimental results (the size of a typical error-bar cross is given in the middle part) describing the angular dependences of the photoelectron intensity $I(\theta)$, of the 3 components and the length of the ESP vector for photoionization of Xe atoms at 80 nm; the photoelectrons leave the ion in the $^2P_{1/2}$ state. (4, 5)

$$\begin{array}{lcl}
 I(\theta) = 1 - \frac{\beta}{2} \left(\frac{3}{2} \cos^2 \theta - \frac{1}{2} \right) & \left. \vphantom{\begin{array}{l} I(\theta) \\ P_{\perp}(\theta) \end{array}} \right\} & \text{independent on helicity} \\
 P_{\perp}(\theta) = 2 \xi \sin \theta \cos \theta / I(\theta) & & \text{of light} \\
 A(\theta) = \pm (A - \alpha \left(\frac{3}{2} \cos^2 \theta - \frac{1}{2} \right)) / I(\theta) & \left. \vphantom{\begin{array}{l} A(\theta) \\ P_p(\theta) \end{array}} \right\} & \begin{array}{l} + \text{ for } \sigma^+ \text{ light} \\ - \text{ for } \sigma^- \text{ light} \end{array} \\
 P_p(\theta) = \pm \alpha \sin \theta \cos \theta / I(\theta) & &
 \end{array}$$

β , ξ , A , α and the total photoionization-cross section Q are the so called dynamical parameters of the photoionization process, which are energy dependent and which are one possible set for a complete quantummechanical characterization.

$A(\theta)$ and $P_p(\theta)$ vanish, if linearly polarized or unpolarized instead of circularly polarized radiation is used. (12, 13) All five curves in Fig. 2 show a reflection symmetry with respect to $\theta = \pi/2$, but $P_{\perp}(\theta)$ and $P_p(\theta)$ with changing sign. Thus, the polarizations of opposite sign cancel one another, if the photoelectrons ejected are extracted by an electric field regardless of their direction of emission. The only non-vanishing component of the spin polarization in an angle-integrated measurement is $A(\theta)$ which yields A as the average value. This Fano-effect value A is identical with $A(\theta)$ for the so called magic angle $\theta = 54^\circ$, where the second Legendre polynomial vanishes. To determine A in an angle-resolved experiment yields the advantage, that it can be now also studied as function of the electron energies by use of an electron spectrometer in the experiment, which was impossible in the former original type of experiment to determine A angle integrated. It is also worth noting that within the error limits the photoelectrons emitted into forward direction $\theta = 0$ have been found (4) to be completely spin polarized (Fig. 2 middle part), which has been explicitly theoretically predicted for this final ionic state one and a half decades ago. (14) This complete ESP in forward direction parallel to the photon spin as well as the fact, that the electron polarization is proportional to the degree of photon polarization if partly polarized radiation is used, allows to characterize the process by the phrase "spin-polarization transfer" from spin polarized photons onto photoelectrons.

The bottom part of Fig. 2 demonstrates that the length of the ESP vector never vanishes as function of the emission angle θ . This can be generalized by the experimentally confirmed rule, that in an angular resolved photoemission experiment on atoms, molecules, adsorbates or solids it is very common rather than exceptional to get spin polarized photoelectrons.

2. EXPERIMENTAL TECHNIQUES

The main components of the two apparatus built at the new German electron storage ring BESSY – one for the studies of atomic and molecular photoionization (4) and one for photoemission experiments with solid surfaces (7) and adsorbates (6) – are briefly discussed here. The synchrotron radiation is dispersed by a 6.5 m N.I. UHV monochromator of the Gillieson type (15) with the electron beam in the storage ring being the virtual entrance slit. A spherical mirror and a plane holographic grating (1200 lines/mm) form a 1 : 1 image of the tangential point in the exit slit. With a slit width of 2 mm a bandwidth of 0.5 nm has been achieved. Apertures movable in vertical direction are used to select radiation emitted above and below the storage ring plane, which has positive or negative helicity, respectively. In the plane, the synchrotron radiation is linearly polarized.

The optical degrees of polarization of the synchrotron radiation have been measured (4) by means of a rotatable four-mirror analyzer (16). Fig. 3 shows the results for the circular polarization P_{circ} and the linear polarization P_{lin} as functions of the vertical angle ψ (± 0.1 mrad). The solid lines which represent the theoretical predictions according to Schwinger's theory show excellent agreement with the experimental results demonstrating a complete linear polarization and a vanishing circular polarization of radiation emitted in the plane of the BESSY-storage ring. Under the conditions of radiation accepted in the vertical angular range from 1 to 5 mrad out of the storage ring plane, a photon flux of 10^{11} to 10^{12} photons s^{-1} with a degree of circular polarization $P_{\text{circ}} = 93\%$ passes the monochromator exit slit and hits the phototarget.

The monochromatized and in general elliptically polarized light produces photoelectrons in a region free of electric or magnetic fields. As shown in Fig. 4 the photoelectrons emitted in the reaction plane at an angle θ are energy analyzed in a simulated hemispherical electron spectrometer (17), which is rotatable around the normal of the reaction plane. An electrostatic deflection by 90° directs the electron beam along the axis of rotation of the electron spectrometer. After a second deflection by 90° the electron beam is accelerated to 120 keV and scattered at the gold foil of the Mott detector (18). $A(\theta)$ and $P_\perp(\theta)$ both being transverse components, are simultaneously determined from the left-right scattering asymmetry measured by two pairs of detectors as shown in Fig. 4. Instrumental asymmetries could be easily eliminated by taking advantage of the reversal of light helicity and of the change of the emission angle from θ to $-\theta$ as well as by use of 4 additional detectors in forward scattering directions in the Mott detector, not shown in Fig. 4.

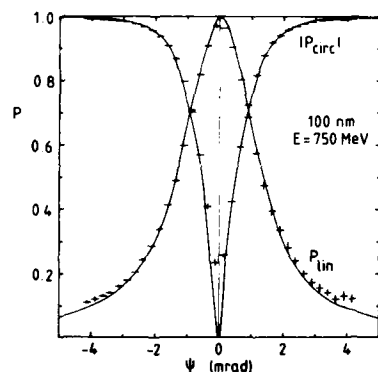


FIGURE 3

Degree of circular and linear polarization P_{circ} and P_{lin} , respectively, of vuv synchrotron radiation emitted from the BESSY-storage ring plane as function of the vertical angle ψ (± 0.1 mrad) (4)

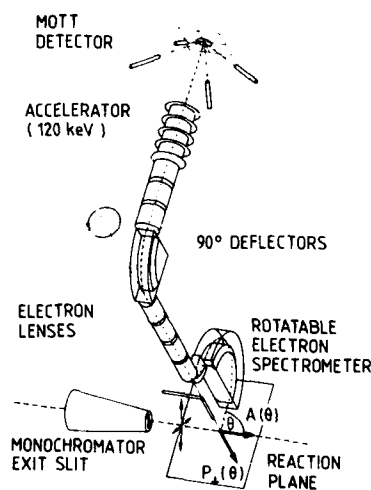


FIGURE 4

Schematic diagram of the apparatus, built up at BESSY (4)

In the solid state apparatus, the sample is cleaned by ion bombardment, heating in oxygen, and flashing; it is characterized by low energy electron diffraction (LEED) and scanning Auger electron spectroscopy in a separate preparation chamber. The crystal on top of a three-axis manipulator movable between preparation and photoemission chamber, can be cooled by use of a temperature-controlled liquid He-Cryostat to temperatures of less than 40 K. The adsorbate is introduced via a doser nozzle which kept the background pressure below 10^{-9} mbar (base pressure $5 \cdot 10^{-11}$ mbar), allowing the continuous monitoring of the photoelectron spectra and LEED pattern as function of coverage. The photoelectrons emitted into a cone $\pm 3^\circ$ are energy analyzed at a resolution of 90 meV FWHM.

3. ATOMIC PHOTOIONIZATION

All photoelectron spin polarization effects in atoms arise due to the existence of the spin-orbit interaction. Because of that the l and m_l quantum numbers are no longer good and thus the "spin momentum transfer" is no longer performed from the photon spin to the orbital angular momentum l and m_l but to the total angular momentum j and m_j of which the photoelectron spin is a part. Discussing this influence of the spin-orbit interaction quantitatively, however, one has to distinguish between two cases:

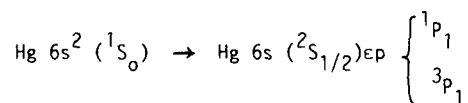
1. Photoionization of atoms, where the discrete atomic or ionic states involved show a fine structure splitting induced by the spin-orbit coupling.
2. Photoionization of an atomic s-subshell, where neither the ground-state nor the final ionic state shows a splitting.

Case 1, the more general one, is fulfilled for photoionization of rare gas atoms. Two peaks in the photoelectron spectrum correspond with the ionic states $^2P_{1/2}$ and $^2P_{3/2}$, split by the existence of the spin-orbit interaction.

Both peaks in the spectrum yield spin-polarized photoelectrons but with a spin-polarization degree of opposite sign. In other words, in case the spin-orbit interaction is not resolved by use of an appropriate electron spectrometer, the polarizations of opposite sign for both unresolved peaks would almost cancel one another. A quantitative example is shown in Fig. 5 as the wavelength dependences of the dynamical spin parameters α and A for photoionization of xenon. The agreement of the experimental data (error bars (4)) with the theoretical predictions (RRPA solid curves (19), RPAE dashed curve (20)) is good.

One needs the spin-orbit interaction and the fine-structure splitting in order to get polarized photoelectrons. It is, however, worth noting that the magnitude of the ESP in both peaks does not depend on whether the spin-orbit interaction is strong or weak. While the fine-structure splitting in Xe^+ is seven times larger than in Ar^+ , the magnitudes of the polarizations given by height and shape of the wavelength dependence of the dynamical spin parameters are nearly the same for Ar, Kr and Xe. (2, 12, 16)

Case 2 is fulfilled in the photoionization of mercury atoms for example:



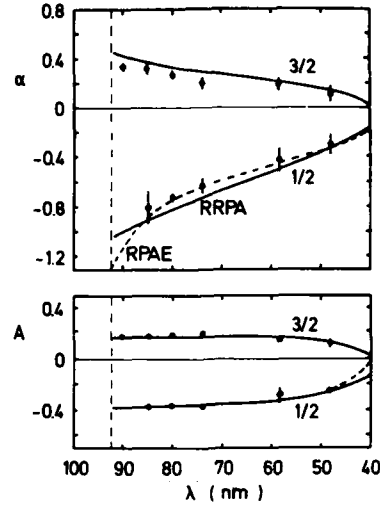


FIGURE 5

Experimental results of the spin parameters α and A (4), upper and lower part, respectively, as functions of the radiation wavelength for photoelectrons leaving the xenon ion in the $^2P_{3/2}$ and $^2P_{1/2}$ final states in comparison with theoretical predictions: RRPA (19), solid curve; and RPAE (20), dashed curve (RRPA = relativistic random phase approximation, RPAE = RPA with exchange).

The photoionization transitions into the two energy-degenerate continuum final states 1P_1 and 3P_1 are described by the singlet and triplet amplitudes D_S and D_T , respectively, as well as by the difference of the continuum-phase shifts $\delta_S - \delta_T$. In terms of the transition amplitudes and phases, the dynamical parameters read (11, 21, 22):

$$Q = \frac{4}{3}\pi^2 \alpha_0^2 \omega (D_S^2 + D_T^2)$$

$$\beta = \frac{2D_S^2 - D_T^2}{D_S^2 + D_T^2}$$

$$\xi = \frac{3\sqrt{2}D_S D_T \sin(\delta_S - \delta_T)}{4(D_S^2 + D_T^2)}$$

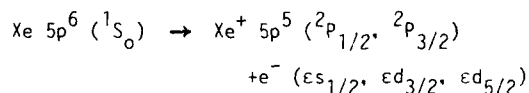
$$A = \frac{D_T^2 - 2\sqrt{2}D_S D_T \cos(\delta_S - \delta_T)}{2(D_S^2 + D_T^2)}$$

$$\alpha = \frac{-D_T^2 - \sqrt{2}D_S D_T \cos(\delta_S - \delta_T)}{D_S^2 + D_T^2}$$

It is remarkable that the asymmetry parameter β depends incoherently upon the matrix elements with the consequence that neglecting the spin-orbit interaction ($D_T \equiv 0$) the "parity-favored" transition D_S yields $\beta = 2$. The spin parameter ξ is given by a single interference term containing the sine of the phase-shift difference. It is worth noting that all 3 spin-parameters ξ , A , α which are a measure for the 3 components of the spin-polarization vector are proportional to the "parity-unfavored" matrix element D_T . This means, that in this case the magnitude of the electron polarization is a measure of the strength of the spin-orbit interaction, which influences the photoionization process here in the final continuum state without a fine-structure splitting. Neglecting the spin-orbit coupling, all three spin parameters must vanish. These effects have been studied in detail for mercury (23 - 28). The experimental results of all 5 dynamical parameters allow to determine the matrix elements D_S and D_T as well as the phase-shift difference $\delta_S - \delta_T$ separately (27).

A strong enhancement of the influence of the spin-orbit interaction and thus a pronounced ESP has been seen in resonance regions, where effects of configuration interaction, channel mixing and many-electron correlations play an important role. Fig. 6 gives an example for the photoionization of xenon in the autoionization region between the $^2P_{3/2}$ and $^2P_{1/2}$ thresholds with respect to the total photoionization cross section Q (29), the asymmetry parameter β (30), the spin parameters A , ξ and α (5), respectively. All five dynamical parameters show a pronounced variation as function of the wavelength. Earlier results for the spin parameter A (16) (dotted curve) employing a method which yields the ESP of the angle-integrated flux are also given and show good agreement with the data obtained angular resolved. For comparison the results of an RRPA calculation (31) and a semiempirical MQDT-analysis* (11), convoluted with the experimental bandwidth, are shown as full and dashed curves, respectively. The wavelength dependences of the spin parameters measured are in reasonable agreement with both theories.

The combination of the data given in Figs. 5 or 6 allows to determine all matrix elements as well as all phase-shift differences of the continuum wavefunctions separately. The procedure of this uses formulae (16) similar to those of mercury mentioned above which are, however, more complicated than in the 6s photoionization of mercury because 5 instead of 2 channels are open:



The influence of the relativistic effects clearly shows up in the matrix elements for transitions into the partial energy-degenerate continua. The phase-shift difference between $d_{5/2}$ and $d_{3/2}$ continuum states, for example, is significantly different from zero. The importance of relativistic and correlation effects, however, can be visualized in a more convenient way by application of the angular momentum transfer formalism (32, 33). The continuum states are classified by the angular momentum of the photon and the orbital angular momentum of the photoelectron. In the case of the $\text{Xe}^+ {}^2P_{3/2}$ final ionic state, there are two "parity-favored" transitions with $t = 1$ into s- and d-continua and one "parity-unfavored" transition with $t = 2$ into a d-continuum (21). "Parity-unfavored" contributions to the photoionization process are caused by anisotropic interactions in the photoelectron emission.

*MQDT = Multichannel quantum defect theory.

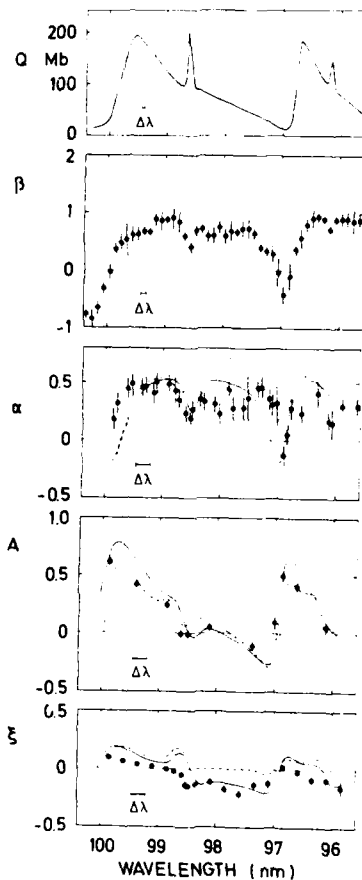


FIGURE 6

Photoionization cross section Q (29), asymmetry parameter β (30) and spin-polarization parameter (5, 16) in the autoionization range of xenon. The bandwidths used are shown as horizontal error bars. Theoretical values for α , A and ξ are represented by the full (RRPA (31)) and dashed (semiempirical (11)) curves

Some selected results (34) are shown in Figs. 7 and 8. Fig. 7 shows the transitions amplitude S_2 for the parity unfavored d-channel $t = 2$ together with the phase-shift difference between the matrix elements for the d ($t = 2$) transition and the s ($t = 1$) transition after elimination of the coulomb-phase-shift. The parity-unfavored transition reaches up to 50 % of the values of the two parity-favored amplitudes which shows the importance of anisotropic interactions in the photoionization investigated. It is interesting to note that the enhancement of the matrix element at about 17 eV only appears in the parity-unfavored channel. All parity-favored matrix elements monotonically decrease with increasing photon energy above the 2 photoionization thresholds (dashed vertical lines in Fig. 7).

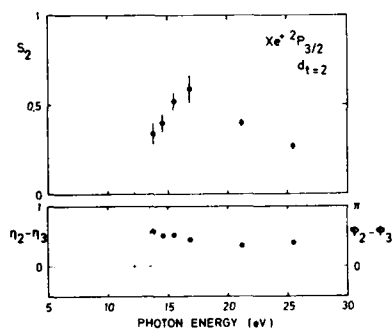


FIGURE 7

Parity-unfavored 5p- ϵ d transition of Xe; upper part: reduced dipole matrix element; lower part: phase shift of the unfavored d-transition with reference to the phase of the favored 5p- ϵ s transition (34)

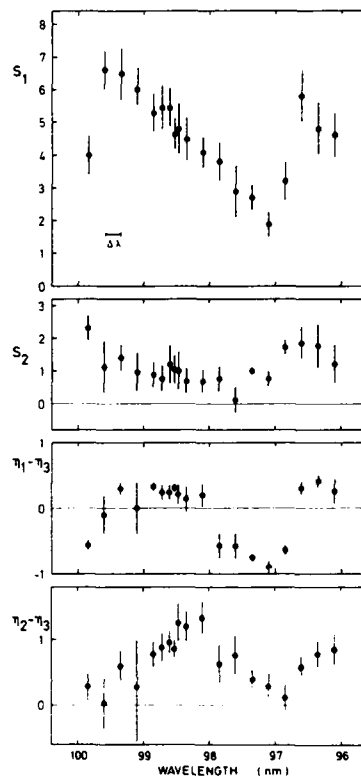


FIGURE 8

Parity-favored (S_1) and unfavored (S_2) 5p- ϵ d transition of Xe and the corresponding phase shifts (η_1 and η_2 , respectively) with reference to the phase of the favored 5p- ϵ s transition (η_3) in the autoionization range between the two thresholds shown in Fig. 7 (34)

Fig. 8 shows the corresponding results but obtained in the autoionization range (between the thresholds shown in Fig. 7) by use of the experimental data of Fig. 6. S_1 the parity-favored d-matrix element follows the energy dependence of the photoionization-cross section showing the pronounced d-resonance structure of the autoionization, while the resonance character of the parity-unfavored d-matrix element S_2 is less dominant. On the other hand it is vice versa in the corresponding phases, where the phase-shift difference $\eta_2-\eta_3$ of the unfavored d-matrix and the favored s-matrix element shows a more pronounced enhancement than in the case of the pure "favored" d-s phase shift difference $\eta_1-\eta_3$. It is worth noting that the enhancement shown in the bottom of Fig. 8 is close to the here not completely resolved narrow s-autoionization resonance seen in the cross section in Fig. 6. This indicates the importance of interchannel interactions in the autoionization region of xenon.

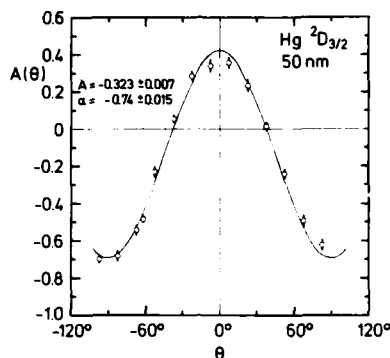


FIGURE 9

Angular dependence of the spin-polarization component $A(\theta)$ in the Hg 5d photoionization (35)

A similar case as for xenon is given for the Hg 5d photoionization. The photoelectron spectrum shows a fine-structure splitting corresponding to the ionic states $^2D_{3/2}$ and $^2D_{5/2}$. Fig. 9 demonstrates the angular dependence of $A(\theta)$ for a wavelength of 50 nm and the $^2D_{3/2}$ final ionic state (35); the solid curve in Fig. 9 is the least squares fit of the experimental values yielding A and α . The energy dependences of $A = A(\theta_m)$ and α are given for both ionic states $^2D_{5/2}$ (closed circles) and $^2D_{3/2}$ (open circles) (35) in Figs. 10 and 11, respectively. The RRPA calculations (36) (solid curves) which include correlations between 5d and 6s (8 channels) and uses experimental thresholds (vertical dashed lines) are in reasonable agreement with experiment. The RPAE-curve (dashed) was calculated from non-relativistic matrix elements and phase shifts (35, 37) and is shifted by 2.6 eV to fit the experimental threshold.

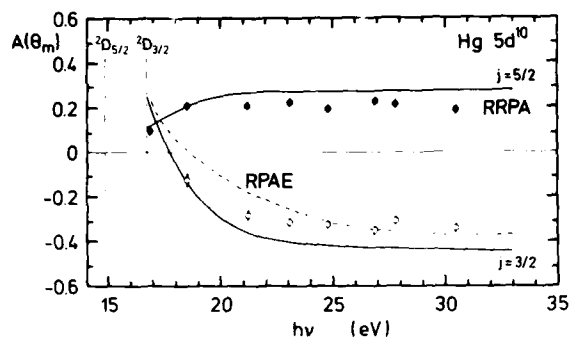


FIGURE 10
Energy dependence of the spin parameter A ($A(\theta)$ at the magic angle θ_m) in the Hg 5d photoionization; experimental results (35) in comparison with theories (solid (36), dashed (37))

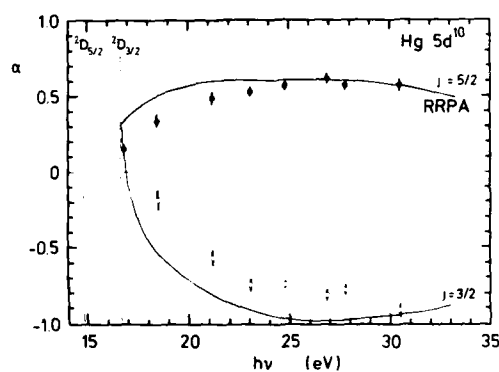


FIGURE 11
As Fig. 10 but the spin parameter α

4. MOLECULAR PHOTOIONIZATION WITH SPIN ANALYSIS

In molecular photoionization one has to take into account that the intramolecular Coulomb interaction is usually much stronger than the spin-orbit interaction. Therefore, it was believed over a period of several years that an ESP cannot occur in the photoionization of a randomly oriented molecular beam if one assumes the intramolecular axis as quantization axis the spin-polarization vector follows. But nevertheless, pronounced ESP effects have been found (8) in the photoionization of randomly oriented halogen molecules by unpolarized radiation. Both cases discussed for atoms exist for molecular photoionization, too. Fig. 12 shows in the lower part the spin parameter ξ for photoelectrons leaving Br_2^+ (squares) and I_2^+ (circles) in their $2\Sigma_g^+$ ionic state, where neither the ground neutral nor the final ionic state has any fine-structure splitting. The spin polarization, which occurs close to the photon energy where the cross section (Fig. 12 upper part) strongly decreases, is analogous to the well known Fano effect (1) in s-subshell ionization of alkali atoms. There the dynamical spin parameters are direct measure for the evidence of the spin-orbit interaction in the continuous spectrum.

Ionizing a π -orbital of halogens yields photoelectron spectra, which show a spin-orbit fine-structure splitting corresponding to the ionic total angular momentum $3/2$ and $1/2$ as in the rare-gas analogon. The behavior of spin polarizations and photoelectron intensities for the outermost orbitals of Br_2 , I_2 , CH_3Br , and CH_3I is the most striking example studied in atomic and molecular photoionization with respect to the fact that photoelectron intensity data follow a certain theoretical prediction (38) - in our case the non-relativistic model neglecting the influence of the spin-orbit interaction onto the molecular continuum states - whereas spin polarizations do not. Fig. 13 summarizes all experimental ratios of the spin parameter ξ , the asymmetry parameter β (8) and the partial cross section σ (39) for the spin-

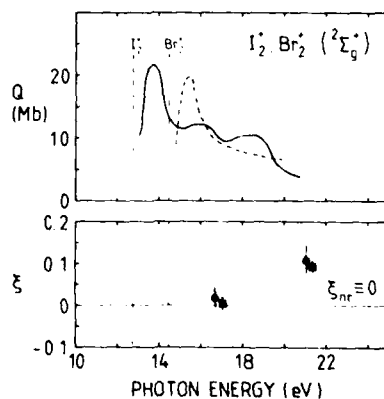


FIGURE 12

Experimental results of the spin parameter ξ for photoelectrons leaving Br_2^+ (squares) and I_2^+ (circles) in their $2\Sigma_g^+$ states (8) in comparison with the corresponding partial cross sections σ (39) (Br_2 dashed, I_2 solid). The vertical lines indicate the adiabatic ionization thresholds

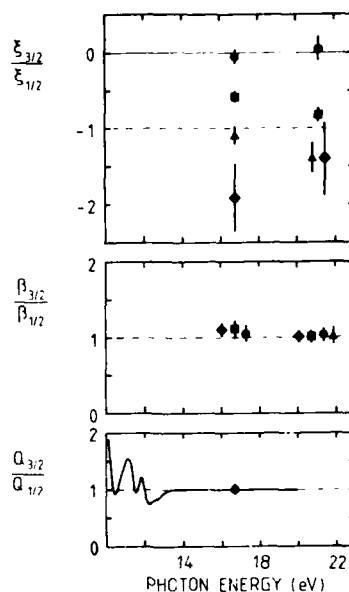


FIGURE 13

Comparison of the ratios of the spin parameter ξ , asymmetry parameter β (8) and partial photoionization cross section Q (39) (for I_2 only) with the non-relativistic predictions (38) (chain lines) for photoelectrons from the outermost orbitals of Br_2 , I_2 , CH_3Br , and CH_3I (squares, circles, triangles, and diamonds, respectively). The results correspond to photon energies of 16.85 and 21.22 eV.

orbit components of these lone-pair orbitals. In all cases the ratio of β agrees with the theoretical prediction of +1 and the branching ratio $Q_{3/2}/Q_{1/2}$ (for I_2 only) is also identical to the statistical value over the energy range outside the threshold region. In contrast to this behavior of the differential cross section, the ratios of the spin parameters show a significant systematic deviation. While $\xi_{3/2}/\xi_{1/2}$ is close to -1 for CH_3Br (triangles) and not far from -1 for Br_2 (squares), it is zero for I_2 (circles), and tends to -2 for CH_3I (diamonds). In contrast to the cross sections, the spin polarizations are very sensitive to any phase shift of the continuum-wave functions induced by the spin-orbit interaction. This, however, is stronger for heavier atoms in molecules than for lighter.

5. ANGLE-RESOLVED PHOTOELECTRON SPECTROSCOPY WITH A FREE ORIENTED MOLECULE

An experiment of angular-resolved photoelectron spectroscopy of free oriented CH_3I molecules has been performed for the first time very recently (9). As indicated in the schematic diagram of the apparatus used shown in Fig. 14 CH_3I molecules in a supersonic beam have been oriented with respect to the molecular axis parallel to an external field by use of an electric hexapole in a "Stern-Gerlach" type analogous experiment. The oriented molecules have to be brought from a region of high electric fields (10^5 V/cm in the hexapole) to very weak fields (0.3 V/cm) in order to study the photoelectron emission angular and energy resolved. To avoid deorientation this has been performed by means of a buffer field and a guiding field of slow decrease of the local electric field (9). The photoelectrons ejected by vuv radiation from the lone-pair orbital at the iodine atom show a pronounced asymmetry in intensities depending on whether they are emitted parallel or antiparallel to the intramolecular axis. If the methyl group is directed toward the electron spectrometer, a photoelectron current I^+ is detected, if the iodine atom is directed, a current I^- as shown in Fig. 15. Fig. 16 shows the asymmetries I^-/I^+ measured for both spin-orbit components in the photoelectron spectrum and for two vuv photon energies (NeI and HeI light) as function of the focussing voltage in the hexapole (9). The heights of the full points with error bars are roughly proportional to the degree of molecular orientation which has been estimated to be between 0.24 and 0.40. Comparing this degree of orientation with the asymmetry ratios found, the forward/backward photoelectron-emission asymmetry parallel to the molecular axis must be a pronounced effect for a complete orientation of the molecules.

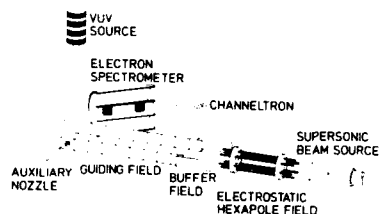


FIGURE 14
Schematic diagram of the apparatus
to study the photoionization of
free oriented molecules (9)

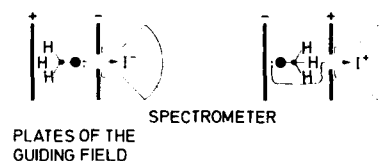


FIGURE 15
Schematic diagram of the molecular
orientation in reference with the
direction of observation, to define
 I^+ and I^- (9)

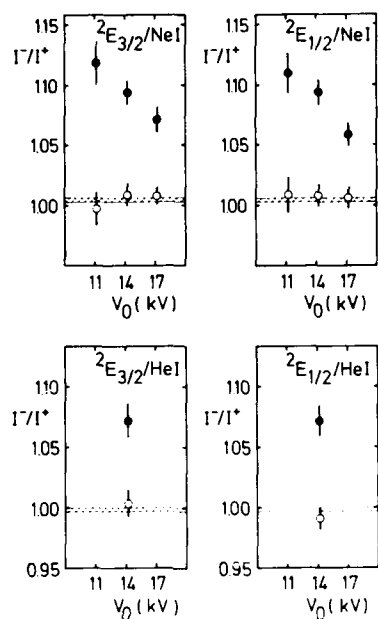


FIGURE 16

Experimental results of the intensity asymmetry of photoelectrons emitted angular resolved parallel or antiparallel to the molecular axis of a free oriented CH_3I molecule (full points with error bars). The open points and the dashed areas represent the corresponding results with a randomly oriented molecular beam showing the apparatus-related asymmetries. (9)

6. PHOTOEMISSION FROM ATOMS ADSORBED ON SOLID SURFACES

Using circularly polarized synchrotron radiation at BESSY spin polarized photoemission from the valence orbitals of Xe and Kr atoms physisorbed on the Pt(111) single-crystal surface has been studied for normal light incidence and normal (angular resolved) emission. Two spin-resolved photoemission spectra (6) are shown in Fig. 17 for Kr and Xe monolayers adsorbed on Pt(111). The peak at lowest binding energy (1) has nearly complete negative spin polarization and corresponds to the $p_{3/2}|m_j| = 3/2$ hole state of the rare gas atoms, whereas peaks 2 and 3 are highly positive polarized ($|m_j| = 1/2$). These polarization values quantitatively correspond to the experimental results in the gas phase (Fig. 2 middle part, $\theta = 0$) except that for free atoms there is no energetic splitting of the m_j substates. These spin-polarization results confirm experimentally the peak assignment proposed in the literature (40) as shown in Fig. 17 including that the m_j splitting is caused by lateral Xe-Xe interactions.

Fig. 18 gives two examples of spin-polarization data obtained for the different peaks in Fig. 17 plotted as function of the photon energy for an incommensurate hcp and a commensurate $\sqrt{3}$ layer of Xe. The polarization shows pronounced resonance structures which partly correspond with structures of the photoelectron intensities measured and shown in the upper part of Fig. 18.

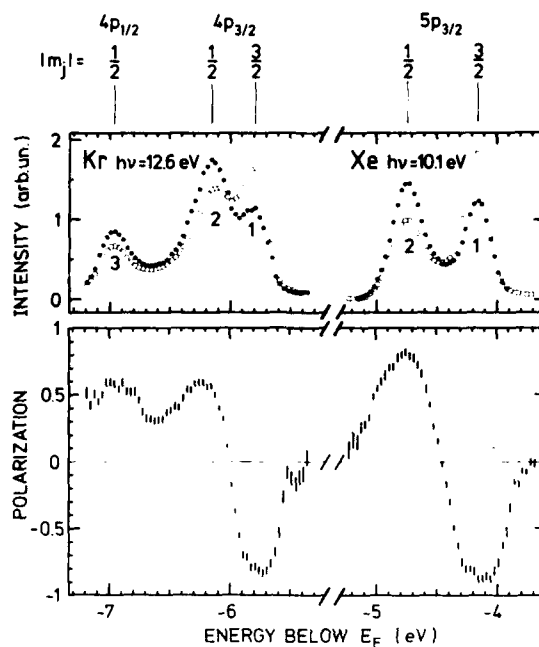


FIGURE 17

Spin-resolved photoelectron spectra of Kr and Xe monolayers at full coverage on Pt(111) in normal photoemission. Upper part, intensities scattered into two counters of the Mott detector as full and open circles. Lower part, photoelectron-spin polarization obtained from the count rates in the upper part, normalized to a complete circular photon polarization (6)

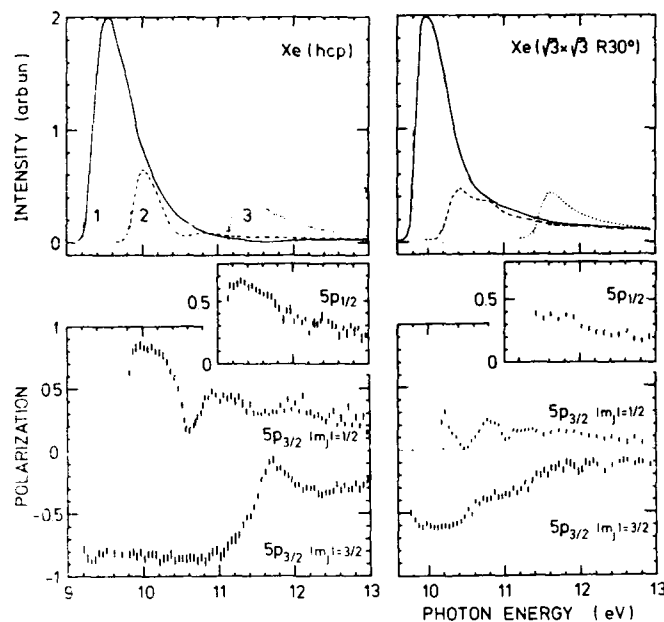


FIGURE 18

Photoelectron intensities (upper part) and spin polarizations (lower part) of the Xe adsorbate photoemission peaks (normal emission) as function of the photon energies for hcp (incommensurate layer) and the $\sqrt{3}$ commensurate layer. Peaks 1, 2, 3 are numbered within increasing binding energies (vertical dashed lines) corresponding to the rare gas hole states $5p_{3/2}$, $1/2$, (6)

These structures which are discussed in more detail elsewhere (6, 41), may partly be due to atomic effects like autoionization resonances (the spin parameters of free xenon atoms measured in comparison with theoretical curves and the photoionization-cross section are shown in Fig. 6) or Cooper minima (6) due to typical surface effects like electron diffraction patterns or resonances induced by the surface barrier. It is worth noting that angular resolved photoemission from the clean substrate Pt(111) yields polarized photoelectrons as recently studied at BESSY using circularly polarized synchrotron radiation (7, 42). In order to get high degrees of polarization one has, as shown in Fig. 19 upper part, to resolve the fine-structure splitting in the photoelectron spectra, as in the atomic photoionization discussed. Peak one and two give ESP of opposite sign corresponding to optical transitions from valence bands of different symmetries. Thus, the ESP results allowed to perform a symmetry-resolved band mapping of the electronic structure. Fig. 19 also shows that the ESP strongly depends upon the temperature of the crystal due to spin-dependent (inelastic) background effects (42). Although some atomic effects are also hidden in the photoemission of a nonmagnetic solid, a detailed review of these solid-state properties is out of the scope of this article and is given, therefore, elsewhere (41).

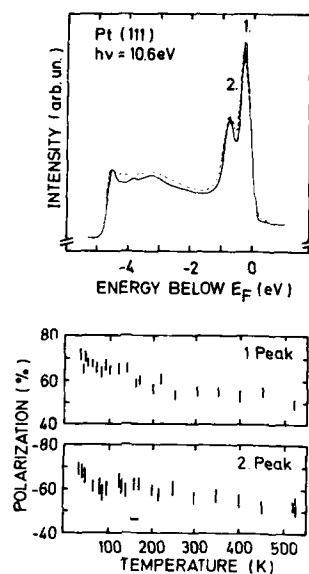


FIGURE 19

Photoelectron spectroscopy of Pt(111) using circularly polarized radiation in normal incidence and normal photoemission (42); Upper part: photoelectron spectrum, energy with respect to the Fermi energy; Lower part: dependences of the ESP upon the crystal temperature for the first two peaks

7 CONCLUSION AND ACKNOWLEDGEMENT

It is the purpose of the angle- and spin-resolved photoelectron spectroscopy to find a set of non-redundant experimental data which characterize the photoeffect quantummechanically completely. This has been shown for atoms successfully. To build a quantitative bridge from the free atoms, via the free randomly oriented molecules, via the atoms adsorbed and the free oriented molecules up to the three dimensional crystal will be the main topic of the angle- and spin-resolved photoemission studies in the future. Thus atomic physics can become an applied method to study and to understand more complicated systems like condensed matter. There is no doubt, that correlation effects studied in details for atoms play an important role there, too.

The author wishes to express his thanks to the coworkers Drs. A. Evers, Ch. Heckenkamp, S. Kaesdorf, F. Schafers, and G. Schonhense for the measurements performed and many intensive discussions. Support by the BMFT, DFG, and MPG is gratefully acknowledged.

REFERENCES

- 1) U. Fano, Phys. Rev. 178 (1969) 131.
- 2) U. Heinzmann, Appl. Opt. 19 (1980) 4087.
- 3) U. Heinzmann, B. Osterheld, F. Schafers and G. Schonhense, J. Phys. B14 (1981) L79.

- 4) Ch. Heckenkamp, F. Schäfers, G. Schonhense and U. Heinzmann, *Phys. Rev. Lett.* 52 (1984) 421.
- 5) Ch. Heckenkamp, F. Schäfers, G. Schonhense and U. Heinzmann, *Phys. Rev. A* (1985) in print.
- 6) G. Schonhense, A. Evers, U. Friess, F. Schäfers and U. Heinzmann, *Phys. Rev. Lett.* 54 (1985) 547.
- 7) A. Evers, F. Schäfers, G. Schonhense, U. Heinzmann, H.P. Oepen, K. Hünlich, J. Kirschner and G. Borstel, *Phys. Rev. Lett.* 52 (1984) 1559.
- 8) G. Schonhense, V. Dzidzonou, S. Kaesdorf and U. Heinzmann, *Phys. Rev. Lett.* 52 (1984) 811.
- 9) S. Kaesdorf, G. Schonhense and U. Heinzmann, *Phys. Rev. Lett.* 54 (1985) 885.
- 10) N.A. Cherepkov, *Zh. Eksp. Teor. Fiz.* 65 (1973) 933; (*Sov. Phys. JETP* 38 (1974) 463).
- 11) C.M. Lee, *Phys. Rev. A* 10 (1974) 1598.
- 12) U. Heinzmann, G. Schonhense and J. Kessler, *Phys. Rev. Lett.* 42 (1979) 1603 and *J. Phys.* B13 (1980) L153.
- 13) G. Schonhense, *Phys. Rev. Lett.* 44 (1980) 640.
- 14) B. Brehm, *Z. Phys.* 242 (1971) 195.
- 15) A. Evers, Ch. Heckenkamp, F. Schäfers, G. Schonhense and U. Heinzmann, *Nucl. Instrum. Meth.* 208 (1983) 303.
- 16) U. Heinzmann, *J. Phys.* B13 (1980) 4353 and 4367.
- 17) K. Jost, *J. Phys.* E12 (1979) 1006.
- 18) J. Kessler, *Polarized Electrons*, Springer, Berlin (1976).
- 19) K.N. Huang, W.R. Johnson and K.T. Cheng, *At. Data Nucl. Data Tabl.* 26 (1981) 33.
- 20) N.A. Cherepkov, *J. Phys.* B12 (1979) 1279.
- 21) H. Klar, *J. Phys.* B13 (1980) 3117.
- 22) K.N. Huang and A. Starace, *Phys. Rev. A* 21 (1980) 697.
- 23) B. Brehm, *Z. Naturforsch.* 21a (1966) 196.
- 24) B. Brehm and K. Höfler, *Phys. Lett.* 68A (1978) 437.
- 25) K. Höfler, PhD-thesis, University Hannover (1979), unpublished.
- 26) F. Schäfers, G. Schonhense and U. Heinzmann, *Z. Phys.* A304 (1982) 41.
- 27) G. Schonhense, F. Schäfers, Ch. Heckenkamp, U. Heinzmann and A.M. Baig, *J. Phys.* B17 (1984) L771.
- 28) F. Schäfers, Ch. Heckenkamp and U. Heinzmann, contributed paper XIV. ICPEAC (1985) book of abstracts.
- 29) R.E. Hufmann, Y. Tanaka and J.C. Larrabee, *J. Chem. Phys.* 39 (1963) 902.
- 30) J.A.R. Samson and J.L. Gardner, *Phys. Rev. Lett.* 31 (1973) 1327.
- 31) W.R. Johnson, K.T. Cheng, K.N. Huang and M. LeDourneuf, *Phys. Rev. A* 22 (1980) 989.
- 32) D. Dill and U. Fano, *Phys. Rev. Lett.* 29 (1972) 1203.
- 33) C.H. Greene and R.N. Zare, *Ann. Rev. Phys. Chem.* 33 (1982) 119.
- 34) Ch. Heckenkamp, F. Schäfers and U. Heinzmann, contributed paper 2. ECAMP Amsterdam and XIV. ICPEAC (1985) book of abstracts.
- 35) F. Schäfers, Ch. Heckenkamp, G. Schonhense and U. Heinzmann, contributed paper 2. ECAMP Amsterdam and XIV. ICPEAC (1985) book of abstracts.
- 36) W.R. Johnson, V. Radojević, P. Deshmukh, K.T. Cheng, *Phys. Rev. A* 25 (1982) 337.
- 37) V.K. Ivanov, S.Yu. Medvedev, V.K. Sosnivker, Preprint 615 A.F. Ioffe Phys. Techn. Inst. Leningrad (1979) and N.A. Cherepkov, priv. com. (1981)
- 38) N.A. Cherepkov, *J. Phys.* B14 (1981) 2165.
- 39) J.H. Carver and J.L. Gardner, *J. Quant. Spectrosc. Radiat. Transfer* 12 (1972) 207.
- 40) K. Horn, M. Scheffler and A.M. Bradshaw, *Phys. Rev. Lett.* 41 (1978) 822.
- 41) U. Heinzmann and G. Schonhense in *Polarized Electrons in Surface Physics*, ed. R. Feder (World Scient. Publ., Singapore 1985).
- 42) A. Evers, G. Schonhense, U. Friess, F. Schäfers and U. Heinzmann, *Surface Science* (1985) in print.

ALIGNMENT AND ORIENTATION OF ATOMIC OUTER SHELLS INDUCED BY ELECTRON AND
ION IMPACT: SOME RECENT DEVELOPMENTS AND REMAINING PROBLEMS

Nils ANDERSEN,^{*} Jean W. GALLAGHER and Ingolf V. HERTEL[†]

Joint Institute for Laboratory Astrophysics, National Bureau of Standards
and University of Colorado, Boulder, Colorado 80309 USA

Alignment and orientation of atoms in collision experiments with planar symmetry have now been studied for about 15 years and close to 500 papers have been produced, mainly devoted to S+P excitation. Despite the large variety of electron-atom, ion-atom and atom-atom collision systems considered, a unified framework for description of these phenomena is now emerging. This framework is a generalization of the original ideas of Macek and Jaecks and is based on consideration of symmetries, conservation laws, etc. The key parameters are directly related to the shape and dynamics of the charge cloud of the excited electron as well as to experimental observables. A brief review is given of this framework, and some current problems and prospects for the future are discussed.

1. INTRODUCTION

The field of alignment and orientation in atomic collisions is devoted to the study of the shape and dynamics of the electronic charge clouds excited in a collision process. Obviously this kind of information, most effectively obtained from experiments with planar symmetry, provides a much more severe test of our understanding of the excitation mechanisms than determination of, say, a probability or a cross section for excitation. As will be detailed below, in favorable cases a complete determination of the quantum-mechanical state of the system may be obtained, thereby providing a so-called "perfect scattering experiment," the most fundamental level at which experiment and theory can be compared. The shape and dynamics are expressible in dimensionless parameters based on relative measurements, thereby eliminating the otherwise often serious problem of accurate determination of absolute units. Furthermore, they may be very sensitive to details in the theoretical description in cases where the cross sections show only minor variations.

At previous ICPEAC's several symposia (1,2) review papers (3,4) and progress reports (5), and a large number of contributed papers have dealt with various particular aspects of this field. The Data Center of the Joint Institute for Laboratory Astrophysics is currently undertaking a critical review of this whole flourishing field, restricted to excitation of outer shells of atoms in planar scattering experiments using unpolarized beams. During this review several parallel lines of thought within the otherwise traditionally separated fields of electron-atom and atom-atom collisions became evident. In

^{*}Permanent address: Physics Laboratory 11, H.C. Ørsted Institute, DK-2100 Copenhagen, and Institute of Physics, University of Aarhus, DK-8000 Aarhus, Denmark.

[†]Permanent address: Institut für Molekülphysik, Fachbereich Physik, Freie Universität Berlin, Arnimallee 14, D-1000 Berlin 33, West Germany.

particular a unified framework, or language for description of these phenomena, is developing though several "local dialects" still exist and probably will persist, partly due to differences in nature of the underlying physics for specific problems. Below we shall first try to summarize this framework, mainly concentrating on S+P excitation to which about 95% of the literature is devoted. Then some selected current problems will be discussed within this framework and conclusions drawn concerning areas where future efforts might be most fruitfully concentrated. The discussion will be restricted to excitation of states decaying by photon emission, though most of the ideas can be easily modified to include electron emission as well, cf. Niehaus (6).

2. FRAMEWORK

2.1. Coordinate frames, basis functions, symmetries and time scales

In an experiment, the collision plane is determined by e.g. the two directions of incoming and outgoing particles, thereby fixing the scattering angle. Excitation processes corresponding to this scattering angle are then studied by analysis of either the polarization properties or the angular distribution of the secondary photons emitted when the excited state decays, detected in coincidence with the scattered particle, or, in time reversed experiments, analysis of the scattered particles as function of the polarization properties of the laser light used to prepare the target atoms prior to the collision. These procedures are detailed in recent reviews (7-9), so we shall just briefly outline the principles here.

Since the symmetry properties of the force(s) determining the excitation and time evolution of the charge cloud will be seen to play an essential role, we shall recall the symmetry properties of the three eigenstates corresponding to a P-level, neglecting at first the effect of fine and hyperfine structure, which will be included later. The upper panel of Fig. 1 shows the angular parts of the charge clouds for the so-called "atomic physics basis" ($|p_{+1}\rangle$, $|p_{-1}\rangle$, $|p_0\rangle$), with $|p_M\rangle$ labeled according to the magnetic quantum number M. Here we quantize along the axis perpendicular to the collision plane since this choice simplifies the subsequent mathematical description considerably. The lower panel of Fig. 1 shows the alternative "molecular physics basis" corresponding to real-valued wave functions ($|p_x\rangle$, $|p_y\rangle$, $|p_z\rangle$), describing p-orbitals along the three coordinate axes. The state $|p_0\rangle = |p_z\rangle$ has negative reflection symmetry with respect to this plane, while the other ones have positive reflection symmetry.

Notation for circularly polarized light varies in the literature. We here use the definition of classical optics (10), which uses the term left hand-circularly (LHC) polarized light, if the electric vector is seen to rotate counter-clockwise when looking toward the light source, i.e. LHC-photons have positive helicity. Referring to Fig. 1, decay of the state $|p_{+1}\rangle$ will thus lead to emission of LHC-photons in the +z (RHC-photons in the -z) direction.

At this point it is useful to recall some important time scales:

- (i) τ_c , the collision time, during which the excitation takes place; $\tau_c \sim a/v$, where a is a characteristic interaction length and v the collision velocity.
- (ii) τ_{fs} , the characteristic time for the fine structure; $\tau_{fs} \sim 1/\omega_{fs}$, where $\hbar\omega_{fs}$ is the fine structure splitting.
- (iii) τ_{hfs} , the characteristic time for the hyperfine structure; $\tau_{hfs} \sim 1/\omega_{hfs}$, where $\hbar\omega_{hfs}$ is the hyperfine structure splitting.
- (iv) τ_{nat} , the (natural) lifetime; $\tau \sim 1/A$, where A is the decay probability.
- (v) τ_{obs} , the observation time for an atom in the actual experimental setup.

Each specific situation requires consideration of these magnitudes. An atom that is initially in an S state has positive reflection symmetry.

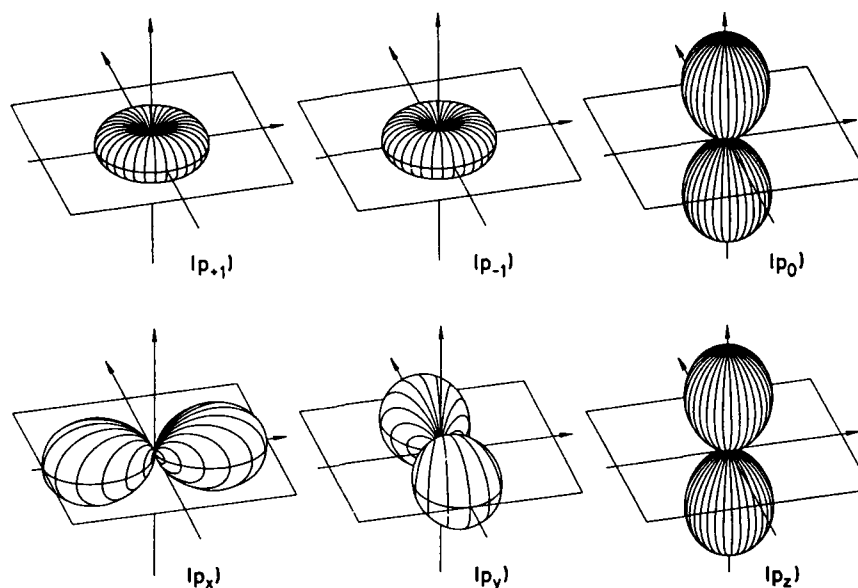


FIGURE 1

The total wave function describing the collision event conserves its reflection symmetry with respect to the scattering plane. Often fine and hyperfine forces are so weak, they can be neglected during the collision so that the excitation is caused by Coulomb interaction only. In the simple case where the collision partner acts as a spinless, structureless particle, this implies that the (spatial part of the) wave function of the atom that is excited preserves its reflection symmetry during the collision. Thus excitation to a P-level can only take place to two of the three states of Fig. 1: "Out-of-plane" excitation of $|p_0\rangle$ is forbidden.

After the collision the isolated, excited atom may develop further under the influence of the fine structure (and possibly hyperfine structure) force, which does not conserve reflection symmetry of the spatial part of the wave function, thereby allowing the charge cloud to change shape in time until the decay takes place. We shall treat these two regimes -- excitation and time development -- separately, and see how it is possible to reconstruct the nascent charge cloud, the object of interest to collision physics, from the actual observed radiation pattern and a knowledge of τ_{fs} , τ_{hfs} , τ_{nat} and τ_{obs} .

2.2. S+P excitation

2.2.1. The simplest case: Full coherence -- the Poincaré sphere

We shall first analyze the properties of the radiation pattern in the simplest case in which the excited P-level of the atom can be described by a state vector, i.e. its coordinates (a_{+1}, a_{-1}, a_0) in the basis of Fig. 1. Reflection symmetry conservation implies $a_0 = 0$. This situation may be encountered in, e.g., electron impact excitation of a $\text{He}(n^1P)$ level.

Figure 2(a) shows an example of the angular part of the P-state electron density. Three coordinate frames are shown: (i) the collision frame $(x^C, y^C,$

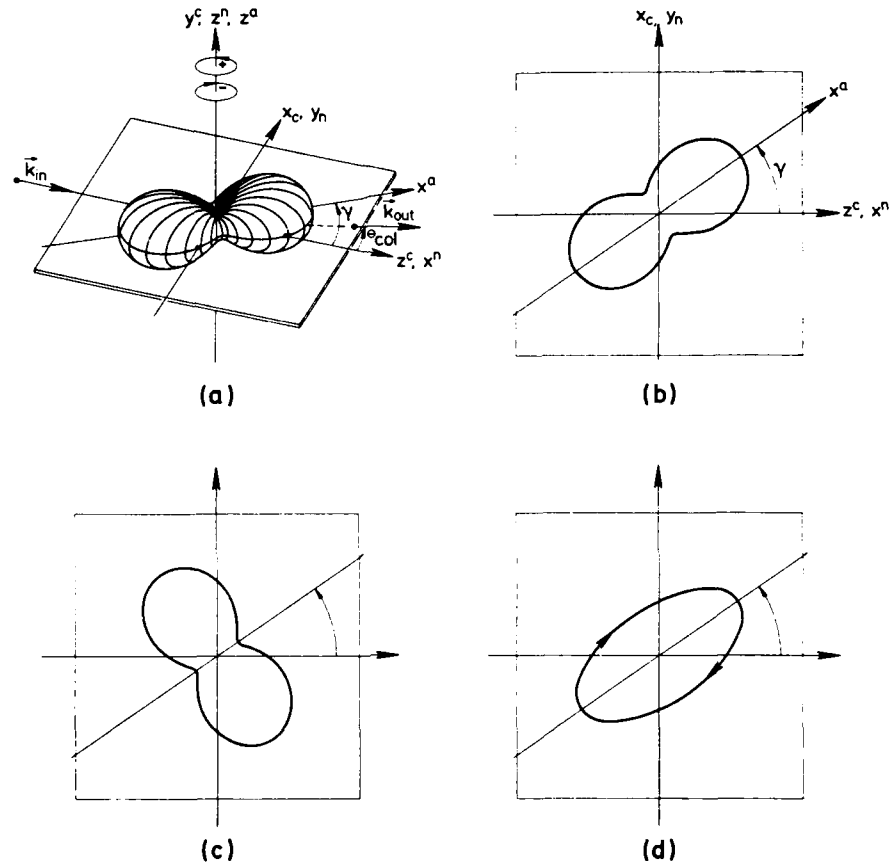


FIGURE 2

z^c) with z^c in the direction \vec{k}_{in} of the incident particles, (x^c, z^c) is the collision plane, and y^c is parallel to $\vec{k}_{in} \times \vec{k}_{out}$. θ_{col} is the scattering angle; (ii) the natural frame (x^n, y^n, z^n) with $x^n = z^c$, $y^n = x^c$, $z^n = y^c$; finally, another convenient frame (iii) is the atomic frame (x^a, y^a, z^a) obtained from the natural frame by rotation through an angle γ around $z^n = z^a$ so that x^a parallels the major symmetry axis of the charge cloud, which is also a symmetry axis for the radiation pattern. Assuming normalization, $a_{+1}^2 + a_{-1}^2 = 1$, then, apart from an arbitrary common phase factor, the wave function is completely characterized by the two parameters (γ, L_1) , where γ is the alignment angle and $L_1 = a_{+1}^2 - a_{-1}^2$ is the angular momentum, pointing along z^n . In the atomic frame the wave function takes the simple form

$$|\psi\rangle^a = 2^{-1/2} [(1+L_1)^{1/2} |p_{+1}\rangle^a - (1-L_1)^{1/2} |p_{-1}\rangle^a] \quad (1)$$

Using polar coordinates (θ, ϕ) in the natural frame, the angular part τ of the charge cloud may be written as (omitting a $3/4\pi$ normalization factor)

$$\tau(\theta, \phi) = \frac{1}{2} [1 + P_\ell \cos 2(\phi - \gamma)] \sin^2 \theta \quad . \quad (2)$$

Figure 2(b) shows a cut through the charge cloud in the collision plane, given by

$$\tau(\frac{\pi}{2}, \phi) = \frac{1}{2} [1 + P_\ell \cos 2(\phi - \gamma)] \quad . \quad (3)$$

P_ℓ , the linear polarization, is thus a width parameter, with $(1+P_\ell)/2$ and $(1-P_\ell)/2$ determining the major and minor axes of the charge cloud in the collision plane.

The angular correlation pattern of the photons emitted from the excited atoms and detected in the collision plane is given by $(\theta = \pi/2)$

$$I(\phi) = 1 - P_\ell \cos 2(\phi - \gamma) \quad . \quad (4)$$

This pattern, Fig. 2(c), is thus identical to the shape of the charge cloud, Eq. (3) and Fig. 2(b), rotated by 90° , as expected from the properties of electric dipole radiation.

Alternatively one may measure the polarization ellipse observed in the $+z^n$ direction with a linear and circular polarizer, Fig. 2(d), or equivalently, the three Stokes parameters (P_1, P_2, P_3) defined by

$$I \cdot P_1 = I(0^\circ) - I(90^\circ)$$

$$I \cdot P_2 = I(45^\circ) - I(135^\circ)$$

$$I \cdot P_3 = I(\text{RHC}) - I(\text{LHC})$$

where I is the total light intensity in the z^n direction, and $I(\theta)$ is the light transmitted through an ideal linear polarizer tilted at an angle θ with respect to x^n [sometimes one may find the alternative notation $(n_1, n_2, n_3) = (P_2, -P_3, P_1)$]. Evidently

$$\vec{P} = (P_1, P_2, P_3) = (P_\ell \cos 2\gamma, P_\ell \sin 2\gamma, -L_\perp) \quad (5)$$

with the linear polarization $P_\ell = (P_1^2 + P_2^2)^{1/2}$ being invariant under rotation around z^n . Furthermore, the light emitted is fully coherent, such that the degree of polarization

$$P = |\vec{P}| = (P_1^2 + P_2^2 + P_3^2)^{1/2} = (P_\ell^2 + L_\perp^2)^{1/2} \quad (6)$$

in this case is unity, and P_ℓ thus fully determined from L_\perp .

The Stokes vector (P_4, P_5, P_6) measured in the y^n direction is $(1, 0, 0)$ and adds no further information in this case.

A correlation experiment, Fig. 2(c), determines (γ, P_ℓ) while a coherence experiment, Fig. 2(d), determines (γ, L_\perp) . Thus, here, a coherence experiment is a "perfect scattering experiment" in the sense discussed in the introduction, while a correlation experiment only determines P_ℓ , leaving the sign of L_\perp undetermined. The parameters used in Fig. 2 are $\gamma = 35^\circ$, $L_\perp = 0.8$ and $P_\ell = 0.6$.

For later generalization we also state the density matrix $\rho_{mn} = a_m a_n^*$ in the natural frame ($\text{tr } \rho = 1$)

$$\begin{Bmatrix} \rho_{11}^n & 0 & \rho_{1-1}^n \\ 0 & \rho_{00}^n & 0 \\ \rho_{-11}^n & 0 & \rho_{-1-1}^n \end{Bmatrix} = \frac{1}{2} \begin{Bmatrix} 1-P_3 & 0 & -P_1 + iP_2 \\ 0 & 0 & 0 \\ -P_1 - iP_2 & 0 & 1+P_3 \end{Bmatrix} \quad . \quad (7)$$

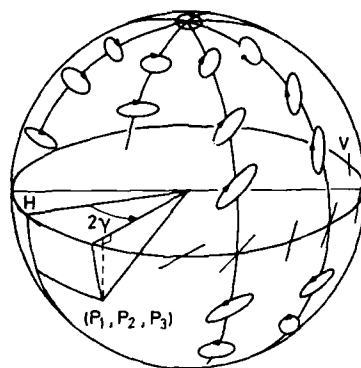


FIGURE 3

A succinct way of summarizing this situation is by introducing the Poincaré sphere (11), making use of the fact that the point $\vec{P} = (P_1, P_2, P_3)$ is located on a unit sphere, cf. Eq. (6). Figure 3 illustrates the polarization ellipse corresponding to various points on the sphere, with $H=(1,0,0)$ corresponding to $|p_x\rangle$ or horizontal linear polarization in Fig. 2(d), $V=(-1,0,0)$ corresponding to $|p_y\rangle$ or vertical linear polarization, the north pole to $|p_{+1}\rangle$, and the south pole to $|p_{-1}\rangle$. Two opposite points on the sphere correspond to orthogonal states. In this language, a coherence experiment determines a point on the Poincaré sphere, while a correlation experiment only determines its projection on the equatorial plane, $P_1 + iP_2 = P_3 \cdot e^{2i\gamma} = -2 \cdot \rho_{11}$.

2.2.2. Loss of full coherence

Where several processes which are in principle distinguishable contribute, the excitation may no longer be coherent. For instance, in the low energy electron impact excitation of a $H(n^2P)$ level, exchange effects lead to different amplitudes for singlet and triplet scattering, and if no spin analysis is performed before or after the collision the corresponding density matrix elements have to be added incoherently. This situation can no longer be represented by a wave function. Positive reflection symmetry is still conserved. The light emitted in the $+z^n$ direction is no longer fully coherent so that $P < 1$. All Eqs. (2)-(7) remain valid. However, P_3 and $L_1 = -P_3$ are now independent parameters. Thus, in this case three parameters are needed to specify the situation completely, namely (γ, L_1, P_3) . A correlation experiment only determines shape (P_3) and alignment angle γ , but gives no information about dynamics (L_1), while coherence analysis still provides complete information.

2.2.3. The general case

In the general case the assumption for the atomic wave function of positive reflection symmetry only cannot be maintained. This may happen, for example, in electron impact excitation of P levels of the heavy rare gases for which spin-orbit effects are so strong that they play a role during the collision ($\tau_{fs} \sim \tau_c$), at least at low energies. Equation (7) must then be replaced by

$$\begin{pmatrix} \rho_{11}^n & 0 & \rho_{-1-1}^n \\ 0 & \rho_{00}^n & \\ \rho_{-11}^n & 0 & \rho_{-1-1}^n \end{pmatrix} = (1 - \rho_{00}^n) \frac{1}{2} \begin{pmatrix} 1 - P_3 & 0 & -P_1 + iP_2 \\ 0 & 0 & 0 \\ -P_1 - iP_2 & 0 & 1 + P_3 \end{pmatrix} + \rho_{00}^n \begin{pmatrix} 0 & 0 & 0 \\ 0 & 1 & 0 \\ 0 & 0 & 0 \end{pmatrix}. \quad (8)$$

Equation (8) shows the decomposition of the density matrix into two parts, one having positive and one negative reflection symmetry. While Eq. (5) still holds, Eq. (2) is replaced by

$$T(\theta, \phi) = (1 - \rho_{00}) \frac{1}{2} [1 + P_L \cos 2(\phi - \gamma)] \sin^2 \theta + \rho_{00} \cos^2 \theta \quad (9)$$

ρ_{00} is thus a height parameter, the determination of which requires observation from a direction different from z^n . Here and below we abbreviate $\rho_{00} = \rho_{00}^+ = \rho_{00}^-$. Within the positive reflection symmetry we define explicitly $P_L^+ = (P_1^2 + P_2^2)^{1/2}$, $L_1^+ = -P_3$ and $P^+ = (P_1^2 + P_2^2 + P_3^2)^{1/2} = (P_L^{+2} + L_1^{+2})^{1/2}$. In the y^n direction the Stokes parameters are now $(P_4, 0, 0)$ with $P_4 < 1$. Then

$$\rho_{00} = \frac{(1 + P_1)(1 - P_4)}{4 - (1 - P_1)(1 - P_4)} \quad (10)$$

The angular momentum is given by

$$L_L = -P_3(1 - \rho_{00}) = L_L^+(1 - \rho_{00}) \quad (11)$$

Similarly, in a correlation experiment, determination of ρ_{00} requires observations from at least two θ angles. The angular distribution of the total intensity is given by

$$I(\theta, \phi) \propto (1 - \rho_{00}) \frac{1}{2} [1 + \cos^2 \theta - P_L \cos 2(\phi - \gamma) \sin^2 \theta] + \rho_{00} \sin^2 \theta \quad (12)$$

replacing Eq. (4). Equation (12) may be written as

$$I(\theta, \phi) \propto B(\theta) [1 - A(\theta) \cos 2(\phi - \gamma)] \quad (13)$$

where

$$A(\theta) = \frac{(1 - \rho_{00}) \cdot P_L \cdot \sin^2 \theta}{(1 + \rho_{00}) + (1 - 3\rho_{00}) \cdot \cos^2 \theta} \quad (14)$$

The value of A in the scattering plane is

$$A(\frac{\pi}{2}) = \frac{1 - \rho_{00}}{1 + \rho_{00}} \cdot P_L < P_L \quad (15)$$

i.e., a smaller amplitude than the amplitude P_L for the corresponding coherence analysis along z^n , see Eq. (9). Equation (14) also implies that

$$A(\frac{\pi}{4}) = P_L(1 - \rho_{00}) / (3 - \rho_{00}) \quad (16)$$

Defining the ratio $R = A(\pi/4)/A(\pi/2)$ one obtains

$$\rho_{00} = (3R - 1) / (R + 1) \quad (17)$$

The general case is thus described by four parameters $(\gamma, L_1^+, P_L^+, \rho_{00})$ of which the three first can be determined from coherence analysis along z^n . Notice that one may still have full coherence within the positive reflection symmetry, $P^+ = 1$.

The situation is summarized in Fig. 4, which shows the shapes of the charge clouds and below, in comparable scales, cuts along the principal axes in the atomic frame. In both cases (a) and (b) the alignment angle is 35° and the width parameter $P_L = 0.6$, but the height parameter in (a) is $\rho_{00} = 0$, i.e. positive reflection symmetry, while $\rho_{00} = 1/3$ in (b). The angular momentum has no influence on the shape, and P_3 can be anywhere in the region $-0.8 < P_3 < 0.8$, so that $P^+ < 1$. The parametrization suggested above is a natural development of

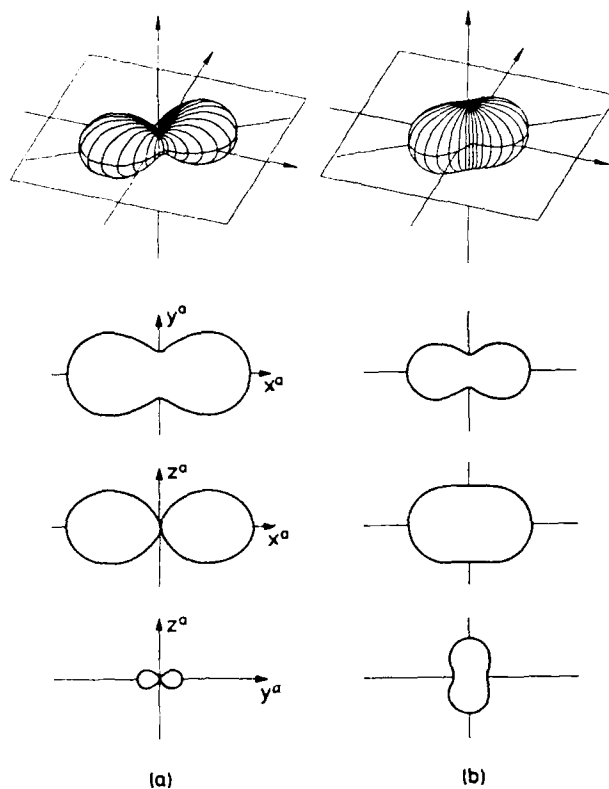


FIGURE 4

the semiclassical model put forward by Macek and Jaeckl in Sec. III of their fundamental paper (12).

2.2.4. Relations to L. Blum-Paixão parameters

Blum, Paixão and collaborators (13) were the first to realize and formulate a parametrization for the general case. Here we summarize their mathematics and give relations to the parameters defined above. Again the atomic basis of fig. 1 is used, however this time quantized along $z^C = x^D$. The density matrix may be decomposed into two components with positive and negative reflection symmetry with respect to the scattering plane, expressible in terms of the Stokes parameters in the following way (tr $\rho = 1$)

$$\left\{ \begin{array}{ccc} \rho_{11}^C & \rho_{10}^C & \rho_{1-1}^C \\ \rho_{01}^C & \rho_{00}^C & \rho_{0-1}^C \\ \rho_{-11}^C & \rho_{-10}^C & \rho_{-1-1}^C \end{array} \right\} = \left\{ \begin{array}{ccc} \frac{1}{2} (\rho_{11}^C - \rho_{-11}^C) & \rho_{10}^C & -\frac{1}{2} (\rho_{11}^C - \rho_{-11}^C) \\ \rho_{10}^{C*} & 1-2\rho_{11}^C & -\rho_{10}^{C*} \\ -\frac{1}{2} (\rho_{11}^C - \rho_{-11}^C) & -\rho_{10}^C & \frac{1}{2} (\rho_{11}^C - \rho_{-11}^C) \end{array} \right\}$$

$$\begin{aligned}
& + (\rho_{11}^C + \rho_{-11}^C) \frac{1}{2} \begin{Bmatrix} 1 & 0 & 1 \\ 0 & 0 & 0 \\ 1 & 0 & 1 \end{Bmatrix} \\
& = (1 - (\rho_{11}^C - \rho_{-11}^C)) \cdot \frac{1}{2} \begin{Bmatrix} \frac{1}{2} (1 - P_1) & \frac{1}{\sqrt{2}} (-P_2 + iP_3) & -\frac{1}{2} (1 - P_1) \\ \frac{1}{\sqrt{2}} (-P_2 - iP_3) & 1 + P_1 & \frac{1}{\sqrt{2}} (P_2 + iP_3) \\ -\frac{1}{2} (1 - P_1) & \frac{1}{\sqrt{2}} (P_2 - iP_3) & \frac{1}{2} (1 - P_1) \end{Bmatrix} \\
& + (\rho_{11}^C + \rho_{-11}^C) \frac{1}{2} \begin{Bmatrix} 1 & 0 & 1 \\ 0 & 0 & 0 \\ 1 & 0 & 1 \end{Bmatrix},
\end{aligned}$$

where $\rho_{11}^C + \rho_{-11}^C = \rho_{00}^n$ is determined by P_1 and P_4 ; cf. Eq. (10). Following Blum and Paixão we now define

$$\lambda \equiv \rho_{00}^C$$

$$\bar{\chi} \equiv \arg(\rho_{10}^C) = -\arg(\rho_{01}^C)$$

$$\cos \Delta \equiv |\rho_{10}^C| / (\rho_{00}^C \rho_{11}^C)^{1/2} = |\rho_{01}^C| / (\rho_{00}^C \rho_{11}^C)^{1/2}$$

$$\cos \epsilon \equiv -\rho_{1-1}^C / \rho_{11}^C = -\rho_{-11}^C / \rho_{11}^C$$

so that

$$(1 - \rho_{00}) \cdot P_1 = \frac{1}{2} \{ \lambda (3 + \cos \epsilon) - (1 + \cos \epsilon) \}$$

$$(1 - \rho_{00}) \cdot P_2 = -2(\lambda(1 - \lambda))^{1/2} \cdot \cos \Delta \cdot \cos \bar{\chi}$$

$$(1 - \rho_{00}) \cdot P_3 = 2(\lambda(1 - \lambda))^{1/2} \cdot \cos \Delta \cdot \sin \bar{\chi}$$

where $\rho_{00} = (1 - \lambda)(1 - \cos \epsilon)/2$. Here $0 < \lambda < 1$, $0 < \bar{\chi} < 2\pi$, $0 < \cos \Delta < 1$, $-1 < \cos \epsilon < 1$. We may require $0 < \Delta < \pi/2$ since $\sin \Delta$ has no physical meaning. Similarly $0 < \epsilon < \pi$ since $\sin \epsilon$ has no meaning. If $\rho_{00} = 0$ then $\epsilon = 0$.

2.3. Time evolution due to internal forces. Depolarization

2.3.1. The effect of fine structure

When the collision is over, the isolated atom develops under the influence of internal forces until the optical decay. Again, restricting ourselves to an excited P state, we shall first analyze the simplest case of electron spin $S=1/2$, and see how the shape and dynamics of the charge cloud changes in time, resulting in a modification of the observed radiation compared to the unperturbed case, $S=0$.

Consider first the shape: Referring to Fig. 4 it is most conveniently analyzed in terms of the molecular basis in the atomic frame for which the relevant density matrix elements at the time of excitation $t=0$ are given by

$$\rho_{xx}^d(0) = \frac{1}{2} (1 + P_x), \quad \rho_{yy}^d(0) = \frac{1}{2} (1 - P_x), \quad \rho_{zz}^d(0) = 0$$

which directly measure the relative length, width and height of the charge cloud. The shape now develops in time according to [see, e.g., Ref. (14)]

$$\rho_{xx}^a(t) = \rho_{xx}^a(0) \cdot G_2 + \frac{1}{3} (G_0 - G_2)$$

$$\rho_{yy}^a(t) = \rho_{yy}^a(0) \cdot G_2 + \frac{1}{3} (G_0 - G_2)$$

$$\rho_{zz}^a(t) = 0 \cdot G_2 + \frac{1}{3} (G_0 - G_2)$$

where $G_0 = G_0(t) = 1$ and $G_2 = G_2(t) = 1/3 \cdot [1 + 2 \cos(\omega_{fs}t)]$; $\hbar\omega_{fs}$ is the energy splitting between the fine structure levels $^2P_{1/2}$ and $^2P_{3/2}$. Thus, as long as we assume $\rho_{00}(0) = 0$, the height varies in time as

$$\rho_{00}(t) = \rho_{zz}^a(t) = \frac{2}{9} [1 - \cos(\omega_{fs}t)] \quad (18)$$

independent of $\rho_{xx}^a(0)$ and $\rho_{yy}^a(0)$. For the simple shape discussed previously in Fig. 2 and Fig. 4(a) having $P_k=0.6$, Fig. 5(a) shows the (reversible) change in time of the shape, where the five situations correspond to $\omega_{fs}t=0, \pi/2, \pi, 3\pi/2, 2\pi$, respectively, showing the quantum-beat phenomenon well known in e.g. beam-foil spectroscopy. Since the symmetry axes stay fixed in time the plot has been made for $\gamma=0^\circ$.

Most collision experiments only monitor the time average of these beats, i.e. the limit $\tau_{fs} \ll \tau_{obs}$, though some intermediate situations, displaying various aspects of this beat phenomenon, have been reported (15,16). Averaging over time yields a charge cloud corresponding to $\omega_{fs}t = \pi/2$ or $3\pi/2$ (here we assume that $\tau_{fs} \ll \tau_{nat}$, so that the pattern has time to develop before decay); i.e.,

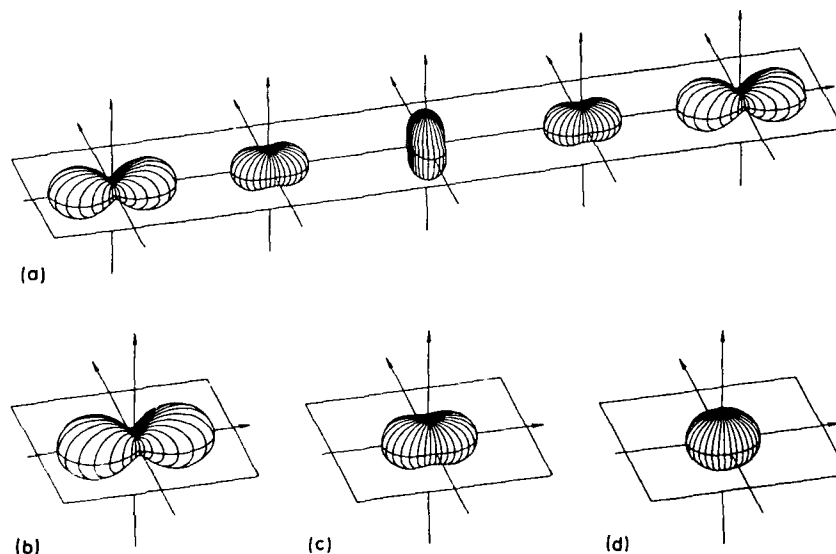


FIGURE 5

$$\langle \rho_{xx}^a \rangle_t = \frac{1}{3} \rho_{xx}^a(0) + \frac{2}{9} = \frac{7}{18} (1 + \frac{3}{7} P_z)$$

$$\langle \rho_{yy}^a \rangle_t = \frac{1}{3} \rho_{yy}^a(0) + \frac{2}{9} = \frac{7}{18} (1 - \frac{3}{7} P_z)$$

$$\langle \rho_{zz}^a \rangle_t = \frac{2}{9} = \frac{2}{9} ,$$

thereby modifying the linear polarizations

$$P_{1,2}(S=1/2) = \frac{3}{7} \cdot P_{1,2}(S=0) ,$$

provided that the sum of the two fine structure components, $2P_{3/2} + 2S_{1/2}$ and $2P_{1/2} + 2S_{1/2}$, is monitored.

The time evolution of the angular momentum $L_1(t)$ is best analyzed in the atomic basis, where the initial conditions are

$$\rho_{11}^a(0) = \frac{1}{2} (1 + L_1)$$

$$\rho_{-1-1}^a(0) = \frac{1}{2} (1 - L_1) .$$

The time evolution is governed by (14)

$$\rho_{11}^a(t) = \frac{1}{2} L_1 \cdot G_1 + \frac{1}{3} (G_0 + \frac{1}{2} G_2)$$

$$\rho_{-1-1}^a(t) = -\frac{1}{2} L_1 \cdot G_1 + \frac{1}{3} (G_0 + \frac{1}{2} G_2)$$

with $G_1 = G_1(t) = 1/9 \cdot [7 + 2 \cos(\omega_{fs}t)]$. Thus the spin-orbit coupling causes the angular momentum component along z^0 to vary in time as

$$L_1(t) = \rho_{11}^a - \rho_{-1-1}^a = L_1 \cdot \frac{1}{9} [7 + 2 \cos(\omega_{fs}t)] . \quad (19)$$

The photon intensity $I_1(t)$ in the z direction varies in time as

$$I_1(t) \propto \rho_{11}^a + \rho_{-1-1}^a = \frac{1}{9} [7 + 2 \cos(\omega_{fs}t)] \quad (20)$$

in agreement with Eq. (18). Equations (19) and (20) show that $L_1(t)$ and $I_1(t)$ vary with the same amplitude, implying that $P_3 = (\rho_{-1-1} - \rho_{11}) / (\rho_{-1-1} + \rho_{11}) = -L_1 = -L_1^+$ stays constant in time and is thus not affected by the fine structure:

$$P_3(S=1/2) = P_3(S=0) .$$

So, a measurement of the Stokes parameters for a $2p \rightarrow 2s$ transition allows reconstruction of the shape and dynamics of the charge cloud created in the collision by multiplying the linear polarizations by a factor $7/3$, while P_3 is unchanged. The average intensity $I_1 = \langle I_1(t) \rangle = 7/9$ is reduced because of the change in photon angular distribution.

Table 1 summarizes the (average) intensity and the depolarization factors c_1 for circular and c_2 for linear polarization in the z^0 direction for the cases $S=1/2$ and $S=1$, including also the individual fine structure components. General formulas may be found in (17).

2.3.2. The effect of hyperfine structure

In analogy to the fine structure effect, the presence of nuclear spin will cause further oscillatory behavior. We shall not present the details in general but refer to the literature (14) and here just give as an example the effect of further adding a nuclear spin $I=3/2$. The effect on the (time averaged) circular polarization is a reduction to almost half the size, while the linear polarization is reduced by almost a factor of eight, cf. Table 1.

TABLE 1

Transition		I_1	c_1	c_2
$I = 0$:	$1p \rightarrow 1s$	1	1	1
	$2p \rightarrow 2s$	7/9	1	3/7
	$2p_{1/2} \rightarrow 2s_{1/2}$	2/9	1	0
	$2p_{3/2} \rightarrow 2s_{1/2}$	5/9	1	3/5
	$3p \rightarrow 3s$	41/54	27/41	15/41
	$3p_0 \rightarrow 3s_1$	2/27	0	0
	$3p_1 \rightarrow 3s_1$	1/4	1/3	1/3
	$3p_2 \rightarrow 3s_1$	47/108	45/47	21/47
	$2p \rightarrow 2s$	209/300	325/627	27/209

Figure 5 illustrates the effect on the (time-averaged) shape by subsequently adding an electron spin $S=1/2$, (b) \rightarrow (c), and a nuclear spin $I=3/2$, (c) \rightarrow (d), leading to an almost isotropic charge distribution. This situation is close to the case of the ${}^7\text{Li}(2^2p)$ state, where, however, effects due to a finite lifetime, etc., also show up (16).

Fine and hyperfine structure may thus cause a severe reduction in measured anisotropy compared to the nascent charge cloud, provided of course that they have time to develop.

2.4. S+D excitation

S+D excitation has so far only been studied in a few cases. A D state has five substates of which, in the natural frame, the atomic basis states with $M=2, 0, -2$ have positive reflection symmetry with respect to the scattering plane, while $M=1, -1$ yield negative reflection symmetry. In the simple case where the excitation is fully coherent and the system possesses positive reflection symmetry, three amplitudes (a_2, a_0, a_{-2}) thus come into play. The normalization condition $|\vec{a}|=1$ and an arbitrary phase factor leave four real parameters to be determined. The dipole radiation pattern for a subsequent D+F decay is completely determined by the four parameters P_1, P_2, P_3, P_4 introduced above. One might think that a coherence analysis giving these four Stokes parameters determines the D state completely. However, this turns out not to be the case (18). Though characteristic parameters for the shape and dynamics of the charge cloud, like γ, L_1, P_2 and the relative height, still given by Eq. (10), can be evaluated, analysis shows that in general two D-states exist having identical dipole radiation patterns, one charge cloud being the mirror of the other one in the (x^a, z^a) plane. Here x^a is still the symmetry axis of the radiation pattern, but the charge cloud does not exhibit reflection symmetry with respect to this plane (18). Application of external fields, which break the symmetry even further and influence the time development of the charge cloud during the time from excitation to decay, is necessary in order to distinguish between the two possibilities (19).

3. ORIENTATION EFFECTS

We shall now address some central, not yet resolved problems of current interest, which may conveniently be discussed within the framework presented above. Our aim is to attempt to understand orientation effects, a feature unique for planar scattering experiments.

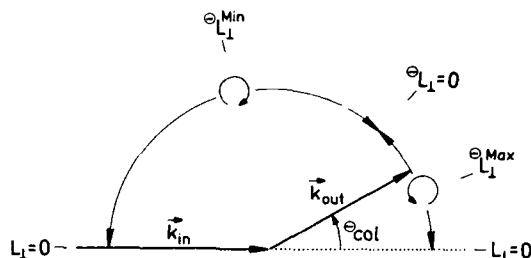


FIGURE 6

3.1. Orientation in electron-atom collisions

3.1.1. He excitation

Starting out with the simplest case, excitation of the He(2¹P) level, a great number of theoretical and experimental investigators have studied this process for electron impact energies around 80 eV. The situation is schematically summarized in Fig. 6.

For scattering angles $\theta_{col}=0^\circ$ and 180° we have $L_1=0$ and $\gamma=0^\circ$ for symmetry reasons. For small scattering angles $L_1>0$, and γ follows the direction of momentum transfer, as predicted by the First Born Approximation (FBA), while L_1 (FBA)=0. L_1 goes through a maximum where the state is almost circular, and from about there also the alignment angle differs greatly from the FPA prediction. L_1 then decreases and goes through zero at some intermediate angle $\theta_{L1}=0$, beyond which the sense of rotation of the electron changes. The shape approaches again a circular state, now with a negative angular momentum, which subsequently is reduced in size when θ_{col} approaches 180° .

Generally speaking, there is now reasonable agreement between theory and experiment up to the angle $\theta_{L1}=0$, while the situation beyond this point is still unclear, with disagreements among the various theories and among the experimental results. And the qualitative physics behind the behavior shown in Fig. 6 still needs to be clarified. One suggestion is that at small angles the scattering is dominated by attractive polarization forces, leading to $L_1>0$, while at larger angles repulsive electron-electron forces dominate, hence $L_1<0$. However, this argument alone cannot be the whole story, because calculations for positron scattering give $L_1<0$ at small angles, although the polarization forces are still attractive (20). Analysis in terms of Born series shows that, in general, for small q the leading term of L_1 is proportional to q^3 and a product of a first and second order term, while at larger angles a term proportional to q^4 and a product of two second order terms become important, q being the projectile charge (20).

Going toward lower energies where the de Broglie wavelength begins to exceed the size of the He atom, the situation is even more unclear, and whether the picture outline in Fig. 6 can be maintained (21) is still being debated. Fortunately, agreement between theory and experiment is now very good at energies very close to threshold, though a typical data point here takes about 1000 hours to measure (22).

One problem on the experimental side is that mainly the photon pattern of the HeI 1¹S-2¹P 584 Å line, being in the vacuum ultraviolet (VUV) region, has been studied with correlation techniques, by which the sign of L_1 cannot be directly determined. We refer to Ref. 23 for a detailed analysis of the situation, and will here just sketch an illuminating way of analyzing the problem making use of the Poincaré sphere introduced above. Figure 7 shows a recent calculation of Madison (24) for He(2¹P) excitation at 80 eV impact energy, illustrating quantitatively the behavior summarized in Fig. 6.

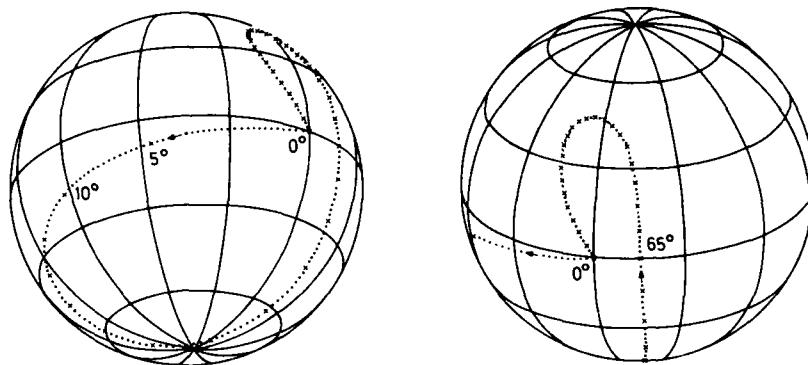


FIGURE 7

Crosses mark 5° steps in θ_{col} . The curve starts out at $\vec{P}=(1,0,0)$ for $\theta_{\text{col}}=0^\circ$ and then moves westward, slightly below the equator, with increasing θ . In contrast, FBA predicts a curve restricted to the equator since $L_\perp(\text{FBA})=0$. Then it makes a loop passing near the south pole at the angle $\theta_{\text{L}}^{\text{max}}$; then a rapid movement in the northern direction, crossing the equator at $\theta_{\text{L}}=0=65^\circ$. After an approach to the north pole at $\theta_{\text{L}}^{\text{min}}$ it returns to the starting point at $\theta=180^\circ$. Why a study of angular momentum sign changes is particularly difficult using correlation analysis is now evident when we bear in mind that this technique only determines the projection $P_1+iP_2=P_2 \cdot e^{2i\gamma}$ onto the equatorial plane, as shown in Fig. 8 for the curve of Fig. 7. Crosses correspond to $L_\perp > 0$, i.e. the southern hemisphere, circles to $L_\perp < 0$. The lower part of Fig. 7 shows that when L_\perp changes from $0.5 \hbar$ to $-0.5 \hbar$, corresponding to the region from 30° southern to 30° northern latitude and $55^\circ < \theta_{\text{col}} < 85^\circ$, the longitude 2γ stays almost constant, so the projection, Fig. 8, varies little.

Thus despite the fact that \vec{P} moves rapidly, the angular correlation pattern is almost stationary, as further illustrated in Fig. 9. This figure, symmetric with respect to the equator and based on Eqs. (3), (4) and (6), shows the change in shape of the charge cloud, and thereby the correlation pattern when moving from the north pole to the south pole on the Poincaré sphere. Some numerical examples are given in Table 2, highlighting the difficulty of studying L_\perp sign changes based on measurement of P_2 .

Trapping of resonance radiation in the target gas will tend to reduce the anisotropy, and thereby P_2 , but leaves the angle γ unchanged. This effect might be difficult to exclude on the $\sim 1\%$ level which is required (25). So, though being difficult, circular polarization measurements in the VUV range at carefully selected angles would be highly desirable, and much larger error bars can be tolerated if one just wants to determine the sign unambiguously (26).

Another way of exploring this problem is to study the $\text{He}(3^1\text{P})$ level instead. This level has two decay modes, one leading to VUV emission (537 Å) and one in the visible (5016 Å), see Fig. 10. So, here systematic comparison of correlation analysis in the VUV and coherence analysis in the visible (27) serves as a good consistency check.

3.1.2. He, Ar, Kr, Xe excitation

Much less work has been done for the heavier rare gases, so little in fact that no picture like Fig. 6 for He can be drawn. Some studies of the resonance levels $\text{He}(3s,3s')$, $\text{Ar}(4s,4s')$, $\text{Kr}(5s,5s')$ and $\text{Xe}(6s,6s')$ have been

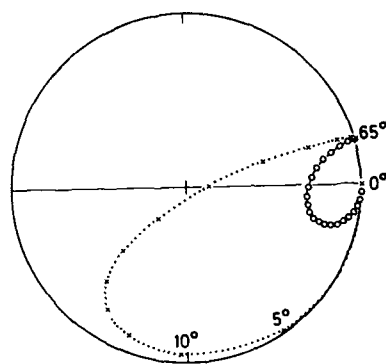


FIGURE 8

TABLE 2

L_z	P_z	Length	Width
0.0	1.000	1.000	0.000
± 0.1	0.995	0.9975	0.0025
± 0.2	0.980	0.990	0.010
± 0.5	0.866	0.933	0.067

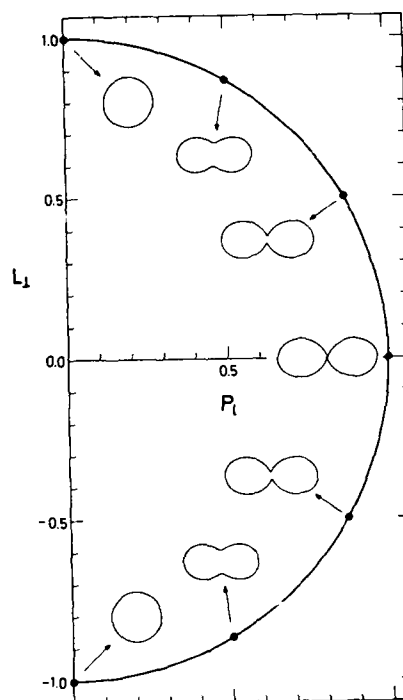


FIGURE 9

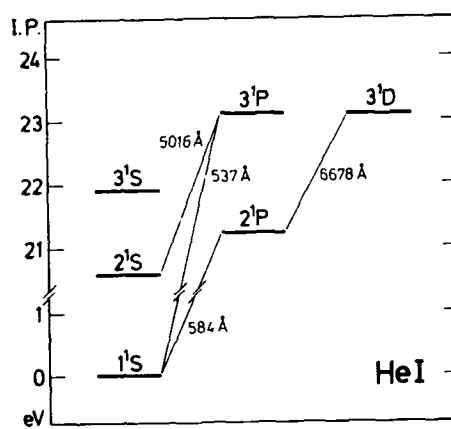


FIGURE 10

performed, but more systematic work is needed. This series of levels shows the effect at low energies of spin-orbit coupling during the collision, leading to charge clouds where p_{00} becomes significant. Also here VUV circular polarization measurements are very desirable to see, e.g., whether the small-angle behavior is similar to that for He, or the physics is different. This has not been done yet, but there are reasons to believe that at small scattering angles L_1 might have the opposite sign of the He(n^1P) case, since for He a p electron is created, while for the heavy rare gases one creates a p hole.

3.2. Orientation in heavy atom collisions

Turning now to the topic of heavy atom collisions we shall again try to speculate on some directions of research which fruitfully could be investigated in the future, being well aware that this might be a risky business.

Excitation in heavy atom collisions is known to take place in essentially two ways: (i) at short distances through radial and rotational couplings at potential curve crossings (or approaches) of the transient quasi-molecule, and (ii) at large distances excitation also may take place via direct transitions, and this with appreciable probabilities at velocities where the Massey criterion or "the maximum rule" is fulfilled: $\Delta E a / \hbar v = \pi$, ΔE being the excitation energy, a the effective interaction length, and v the collision velocity (22). While the orientation may vary in sign for mechanism (i), depending on details of the molecular curves (18,29) there seems to be a preferred direction of rotation over a large velocity range for mechanism (ii), which we shall now briefly discuss.

3.2.1. Direct excitation: A propensity rule for orientation?

Large impact parameter direct excitation of the resonance S+P transitions of alkali or alkali-like atoms in collisions with rare gases shows that L_1 consistently has a large negative value in the region of maximum excitation where the Massey criterion is fulfilled (28,30). To analyze this problem further we model the alkali-rare gas system as a quasi-one electron system, i.e. effectively a three-body system consisting of the alkali core, the valence electron, and the rare gas atom, with the electronic excitation induced by the electron-rare gas interaction V for which various simple models have been proposed (28). If we select as basis the set of three states consisting of the ground state $|s\rangle$ and the two atomic basis states $|p_{+1}\rangle$ and $|p_{-1}\rangle$ of Fig. 1, all having positive reflection symmetry, the following close-coupling equations are obtained for the amplitudes $a = (a_s, a_{+1}, a_{-1})$

$$i\hbar \frac{d}{dx} \underline{a} = \underline{A} \underline{a} \quad (21)$$

with x being the position along the trajectory, b the impact parameter, and $R = (z^2 + b^2)^{1/2}$ the internuclear distance

$$\underline{a} = F_{sp}(R) \begin{pmatrix} 0 & \text{c.c.} & \text{c.c.} \\ \exp i(\frac{\Delta E x}{\hbar v} - \pi) & 0 & 0 \\ -\exp i(\frac{\Delta E x}{\hbar v} + \pi) & 0 & 0 \end{pmatrix} + F_{+-}(R) \begin{pmatrix} 0 & 0 & 0 \\ 0 & 0 & \text{c.c.} \\ 0 & e^{i2\pi} & 0 \end{pmatrix} \quad (22)$$

Here ΔE is the (x -dependent) S-P energy difference, and π the rotation angle of the internuclear axis (31). The valence electron potential V only enters through the common factors $F_{sp}(R)$ describing the S+P coupling, and $F_{+-}(R)$, describing the $|p_{+1}\rangle \leftrightarrow |p_{-1}\rangle$ coupling, respectively equal to the matrix elements $\langle s | V | - \rangle = -\langle s | V | + \rangle$ and $\langle + | V | - \rangle$, referred to the body-fixed system. The interior of the matrices depend on the dynamics only, allowing us to state general conclusions. We can now easily see what happens. Starting the system in the ground state, i.e. $(1,0,0)$, one gets in first order:

$$\underline{a}_1 = \frac{1}{i\hbar} \underline{A} \underline{a}_0 = \exp i(\frac{\Delta E x}{\hbar v} - \pi) \underline{a}_0 \quad (23)$$

$$a_{+1} = -\frac{1}{i v} \int F_{sp} \cdot \exp i\left(\frac{\Delta E x}{\hbar v} + \theta\right) dx \quad (23h)$$

The angle θ changes by π during the collision. Thus, if the velocity is such that the change in phase over the effective interaction length a , $\Delta E a / \hbar v \approx \pi$, then a_{-1} has a stationary phase and its maximum value is obtained. For a_{+1} , however, the total phase changes by 2π , giving a near cancellation of the integral, so that a_{+1} is small. Thus a propensity rule (32,33) for circular polarization seems to hold in the region of maximum excitation. To illustrate the development of the circular state along the trajectory, Fig. 11 shows a calculation for the Na-He system (31) at an energy $E_{CM} = 2$ keV and impact parameter $b = 2.2$ a.u. using for V a Baylis-type (28) potential. This system is particularly interesting since a study of the time-inverse process, scattering of He on laser-excited, oriented sodium atoms may be feasible (34): Eqs. (21) and (22) predict that in the usual geometry the $|p_{-1}\rangle$ state should be easily deexcited, while the $|p_{+1}\rangle$ state should be quite stable.

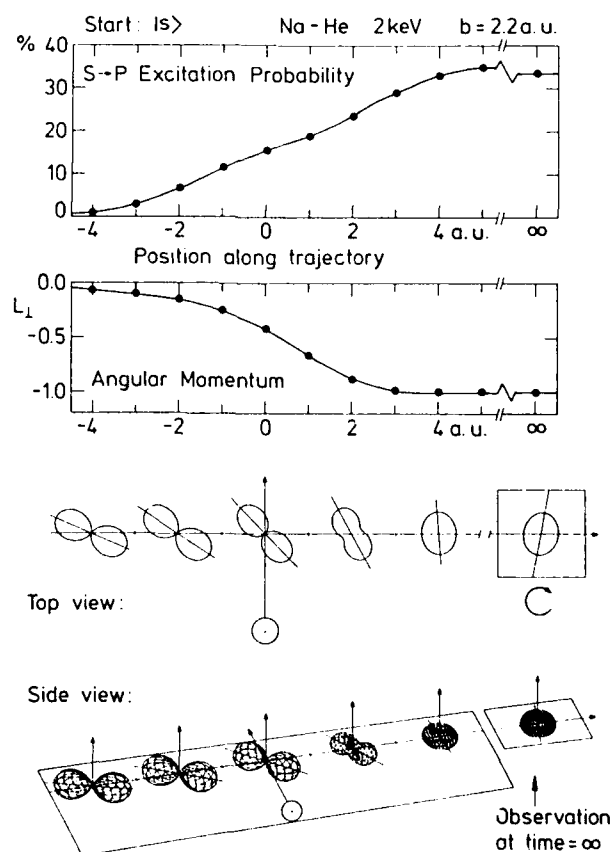


FIGURE 11.

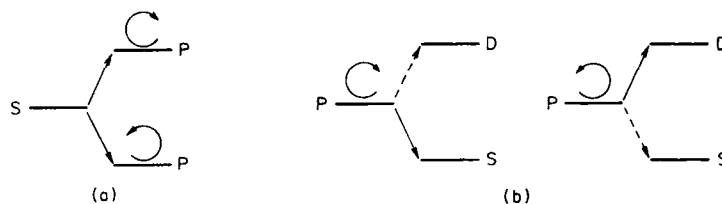


FIGURE 12

These ideas can be further generalized, admittedly now becoming even more speculative: Inspection of Eqs. (23) shows that if $\Delta E < 0$ then the roles of a_{-1} and a_{+1} will be interchanged. Thus the situation of Fig. 12(a) might be possible: Excitation from an $|s\rangle$ state will lead to a $|p_{-1}\rangle$ state, deexcitation to $|p_{+1}\rangle$. Furthermore, Fig. 12(b) shows another configuration that might be accessible: An atom in a $|p_{-1}\rangle$ state is easy to deexcite (to the S state) but hard to excite (to the D state). Changing the sense of rotation, i.e. to a $|p_{+1}\rangle$ state, will now give an atom unwilling to get deexcited (to the S state) but readily excited (to D). In other words, if an atom in the $|p_{-1}\rangle$ state is hit on its left side [Fig. 2(a)] it preferably gets deexcited, while hitting its right side triggers excitation!

To what extent such experiments, in which the dynamics of the active electron is strictly controlled, are feasible, the future will show.

4. CONCLUSIONS

We have suggested a common framework for description of alignment and orientation of atoms excited in planar scattering experiments, quantizing along the axis perpendicular to the scattering plane. Analysis of symmetry properties of the atomic states and the forces responsible for the evolution of the charge cloud suggest a parametrization of the shape (i.e., length, width, and height) and dynamics of the excited charge cloud, which is directly related to experimental observables as well as to the atomic scattering amplitudes and density matrix elements.

Considering the often very extensive investments of time and equipment needed for these investigations, one must carefully consider which systems are worth understanding. Obviously, it is worthwhile to see if we can understand the simplest and/or most fundamental systems at this level of accuracy.

Concentrating on orientation effects -- unique for planar scattering geometry -- we conclude that electron impact excitation of He is now quite well understood at small and intermediate scattering angles while the experimental and theoretical situation still needs to be improved at large angles. For the heavier rare gases, much remains to be done before a consistent picture emerges. Circular polarization measurements in the VUV would be particularly useful.

For heavy atom collisions a few simple systems have now been understood in the molecular regime. For direct excitation a propensity rule has been suggested, but it needs further experimental attention.

In this short overview we have omitted discussion of the now rapidly developing field of application of spin-polarized particles, which promises much information about spin-dependent forces (35) in the future. Also experiments involving coherent superposition of states with opposite parity, using hydrogen targets for photon emission (36) and, e.g., helium for electron emission (37) are interesting new developments.

ACKNOWLEDGEMENTS

During the preparation of this review the authors acknowledge stimulating discussions, collaborations, correspondence, and communication of results prior to publication on some of the topics presented here with M. Barat, A. Bähring, J. P. M. Beijers, D. Burns, D. Döwck, W. Fritsch, H. G. M. Heideman, C. J. Joachain, H. Kleinpoppen, D. Madison, S. E. Nielsen, F. da Paixão, M. J. Roberts, H. Schmidt, and V. Sidis. Two of us (NA, IVH) are grateful for the facilities and financial support provided by JILA and the NBS office of Standard Reference Data to conduct this study. Two of us acknowledge travel grants from the Danish Natural Science Research Council and NATO (NA) as well as from the Deutsche Forschungsgemeinschaft (IVH).

REFERENCES

Space permits inclusion only of references directly related to topics discussed in the text.

1. H. Kleinpoppen, XI ICPEAC, Book of Invited Papers, p. 557.
2. D. H. Jaecks, XIII ICPEAC, Book of Invited Papers, p. 663.
3. M. R. C. McDowell, XII ICPEAC, Book of Invited Papers, p. 19; D. H. Jaecks et al., *ibid.*, p. 97.
4. J. Stevin, XIII ICPEAC, Book of Invited Papers, p. 85.
5. I. V. Hertel, XII ICPEAC, Book of Invited Papers, p. 513; H. H. Folt et al., *ibid.*, p. 833.
6. A. Niehaus et al., *this volume*.
7. K. Blum and H. Kleinpoppen, Phys. Rep. 52 (1979) 203, *ibid.*, 96 (1983) 251; Adv. At. Mol. Phys. 19 (1983) 187.
8. H. W. Herman and I. V. Hertel, Adv. At. Mol. Phys. 13 (1979) 113.
9. J. Stevin, Rep. Prog. Phys. 47 (1984) 461.
10. H. Born and E. Wolf, Principles of Optics, 4th Ed. (Pergamon, New York, 1970).
11. H. Poincaré, Théorie Mathématique de la Lumière (G. Carré, Paris, 1889), Chap. 12.
12. J. Macek and D. H. Jaecks, Phys. Rev. 4 (1971) 2288.
13. F. J. da Paixão et al., Phys. Rev. Lett. 45 (1980) 1164; K. Plum, F. J. da Paixão and G. Csank, J. Phys. B 13 (1980) L257.
14. K. Blum, Density Matrix Theory and Applications (Plenum, New York, 1981).
15. P. J. O. Teubner et al., Phys. Rev. Lett. 46 (1981) 1569.
16. H. Andersen et al., J. Phys. B 18 (1985) 2247.
17. H. W. Hermann and I. V. Hertel, Comm. At. Mol. Phys. 12 (1982) 61; *ibid.* 127.
18. H. Andersen et al., J. Phys. B 16 (1983) 817.
19. T. Andersen and H. P. Neitzke, J. Phys. B 17 (1984) 1559.
20. D. H. Madison and K. H. Winters, Phys. Rev. Lett. 47 (1981) 1985; H. F. Fargher and M. J. Roberts, J. Phys. B 17 (1984) L587; C. J. Joachain and R. M. Potvliege, private communication.
21. J. P. M. Beijers, J. van Eck and H. G. M. Heidemann, J. Phys. B 17 (1984) L265, and private communication.
22. P. A. Heill and A. Crowe, J. Phys. B 17 (1984) L791.
23. H. Andersen, J. W. Gallagher, and I. V. Hertel, Phys. Rep., to be published.
24. D. H. Madison, private communication.
25. M. Lminyan et al., J. Phys. B 7 (1984) 1519.
26. J. F. Williams, XII ICPEAC, Book of Abstracts (Berlin, 1983), p. 132.
27. K. S. Ibraheim, H.-J. Beyer and H. Kleinpoppen, II ECAMP, Book of Abstracts (Amsterdam, 1985), p. 298.
28. H. Andersen and S. E. Nielsen, Adv. At. Mol. Phys. 18 (1982) 265.

- 29. H. Schmidt, this volume; R. J. Allan et al., Chem. Phys. Lett., in press; M. Kimura, this volume, and private communication.
- 30. N. Andersen et al., Phys. Rev. Lett. 42 (1979) 1134.
- 31. N. Andersen and S. E. Nielsen, XIV ICPAC, Book of Abstracts (Palo Alto, 1985), p. 359, and to be published,.
- 32. R. S. Berry, J. Chem. Phys. 45 (1966) 1228.
- 33. J. Fano, Phys. Rev. A 32 (1985) 617.
- 34. D. Dowek, private communication.
- 35. A. Wolcke et al., Phys. Rev. Lett. 52 (1984) 1108.
- 36. C. C. Havener et al., Phys. Rev. Lett. 48 (1982) 926; J. Burgdörfer and E. J. Dubé, Phys. Rev. Lett. 52 (1984) 2225; C. G. Rack et al., J. Phys. B 17 (1984) 2695.

ELECTRON IMPACT EXCITATION OF MOLECULES

Sandor TRAJMAR

Jet Propulsion Laboratory, California Institute of Technology, Pasadena,
CA 91109, U.S.A.

1. INTRODUCTION

Although a great deal of qualitative information has been generated for molecules, our knowledge of cross section data is rather meager and theoretical methods for calculating cross sections are not yet as reliable as for atoms.

Here, we are going to give a brief overview on electron impact excitation of molecules with emphasis on elastic scattering, rotational, vibrational and electronic excitations. A few general remarks on dissociation and ionization will be made. Recent developments in the electron-photon coincidence area will be mentioned only for completeness. Practically no cross section data are available for innershell excitations and for electron collisions with excited molecules. We will briefly discuss presently used experimental techniques and difficulties related to cross section measurements, *survey* available differential, integral, momentum transfer and total electron scattering cross section data, and compare experimental and theoretical results in the near threshold to few hundred eV impact energy range.

There are several complications associated with quantitative characterization of electron molecule collision processes. In general a very large variety of reactions can take place as the result of electron-molecule collision. For example, excitation of an electronic state can be accompanied by various combinations of rotational and vibrational transitions or the excitation can lead to dissociation into neutral, positive and/or negative ion fragments in their ground or various excited states. In compiling the energy and angular dependencies of all these processes, we are faced with an overwhelming body of cross section data. In addition the scattering probability may depend on molecular orientation, fine, hyperfine, and magnetic sublevel quantum numbers, the spin of the continuum electron etc. Fortunately some simplification results from the fact that we average over many of the events which are difficult or impossible to resolve experimentally. Furthermore, the Born-Oppenheimer separation of nuclear and electronic motions and the Franck-Condon principle appears to be applicable in most of the electron scattering cases (when no resonances or long range forces are present). Another difficult problem in cross section measurements is related to the establishment of the absolute scale at low and intermediate impact energies. This question will be discussed in more detail below.

2. DEFINITION OF CROSS SECTIONS

The quantity that characterizes a scattering process is the cross section. Experimental measurements usually do not yield cross sections for the most fundamental scattering processes (for which the initial and final quantum states are fully specified) but for a number of experimentally indistinguishable processes. In addition, the measuring apparatus has a finite energy and angular resolution and the measured quantity is a cross section averaged over these instrumental functions. When cross sections are

obtained from theoretical calculations, similar averaging is required to make a comparison between experiment and theory possible. This all sounds trivial but in practice, both experimentalists and theoreticians are frequently guilty in not specifying precisely what kind of cross sections they are presenting.

Most of the experimental work have been carried out in recent years in a molecular-beam/electron-beam arrangement and differential cross sections are obtained at fixed impact energies as:

$$[\overline{DCS_n(\theta)}]_{E_0} = \sum_i \sum_f N_i \left[\frac{d\sigma_{if}}{d\Omega} \right]_{E_0} \quad (1)$$

Here n refers to the collection of unresolved channels, E_0 is the impact energy, and θ is the scattering angle (polar angle). The azimuthal angle dependence disappears because we are dealing with an ensemble of rotating (randomly oriented) target molecules. The bar above the right hand side term refers to the averaging over instrumental energy and angular resolution functions.

Integration of the differential cross sections (DCS) over all angles yields the integral and, in the case of elastic ($n = 0$) scattering, the momentum transfer cross sections:

$$\sigma_n(E_0) = 2\pi \int_0^\pi [\overline{DCS_n(\cdot)}]_{E_0} \sin \theta \, d\theta \quad (2)$$

$$\sigma_n^M(E_0) = \sigma_0^M(E_0) = 2\pi \int_0^\pi [\overline{DCS_0(\cdot)}]_{E_0} (1 - \cos \theta) \sin \theta \, d\theta \quad (3)$$

The total electron scattering cross section is defined as:

$$\sigma_{TOT}(E_0) = \sum_n \sigma_n(E_0) \quad (4)$$

(The summation includes elastic and all inelastic processes.)

3. CROSS SECTION MEASUREMENT TECHNIQUES AND DATA

3.1 Total Electron Scattering Cross Sections

There are three widely utilized methods for determining $\sigma_{TOT}(E_0)$:

- a. Electron transmission measurements
- b. Measurement of electron-transmission-with-time-of-flight analysis
- c. Recoil measurements

In addition, some total cross sections have been generated by indirect methods and can, in certain cases, be deduced from swarm measurements.

The transmission and transmission with time-of-flight methods have been extensively used in recent years for determining highly accurate (~1-3%) total scattering cross sections ranging from impact energies of 20 meV to 2,000 eV for a number of molecular species. The recoil method has been applied in the case of diatomic alkali and alkali halide molecules. Table I summarizes the total cross section data available since about 1970.

More detailed discussion of the techniques and data have been published by Trajmar and Register (1) and Trajmar et al. (2), respectively. Although possible in principle, the approach of obtaining $\sigma_{TOT}(E_0)$ from $\sum_n \sigma_n(E_0)$ is

not feasible in practice due to lack of cross section data. Total scattering cross sections are needed in modeling

Table I. Summary of Recent Total Cross Section Data

Molecule	Energy Range (eV)	Method (a)	Molecule	Energy Range (eV)	Method (a)
H ₂	0.02-2,000	T	H ₂ O	0-10	T
N ₂	0.25-1,600	T	CO ₂	0.07-700	T
CO	0.3-8	T	N ₂ O	0.5-10	T
O ₂	100-1,600	T	SO ₂	0-10	T
NO	100-1,600	T	H ₂ S	0-10	T
Li ₂	0.5-10	R	OCS	1-8	T
Na ₂	0.5-50	R	CH ₄	0.5-100	T
K ₂	0.5-50	R	SF ₆	0.036-100	T
KI	0.81-15.7	R	C ₂ H ₂	0.3-5	T
CsF	0.69-6.81	R	CCl ₄ , CCl ₃ F		
CsCl	0.47-15.7	R	CCl ₂ F ₂ , CClF ₃ , CF ₄	0.6-50	T

(a) T = transmission; R = recoil

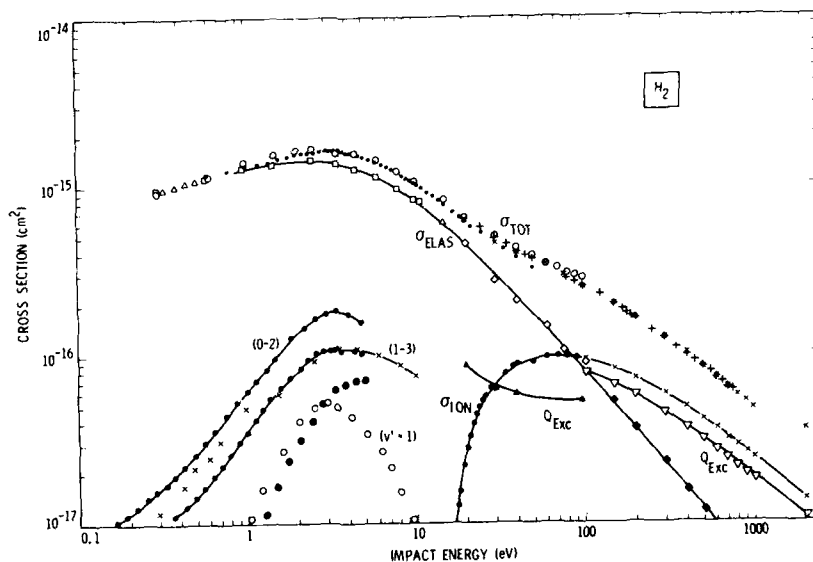


FIGURE 1.

Total scattering, elastic scattering, rotational, vibrational and electronic excitation, and ionization cross sections are shown. σ_{EXC} above 100 eV is the empirically estimated sum of all electronic excitation cross sections while below 100 eV it refers to the sum of the cross sections measured for the excitation of the six lowest electron states (Ref. 3).

various plasma systems and are very useful for setting upper limits and for

normalization of integral and differential cross sections as will be pointed out later.

It is interesting to see how the more specific cross sections contribute to the total electron scattering cross section. This is demonstrated for H_2 in Fig. 1.

3.2 Integral Cross Sections

General Remarks: Integral cross sections could be obtained by measuring, over all angles, the electron scattering signal associated with a given process. Although some efforts in this direction were made, most of the integral electron scattering cross sections, that we are concerned with, have been obtained from DCS measurements. There are two exceptions: optical excitation functions and total electron impact ionization cross sections. In these cases the photon emission rate by the electron impact excited molecules and the total ion current can be measured.

Optical Excitation Functions: Optical excitation functions are obtained by measuring the light emission intensity between two quantum states at particular wave lengths as a function of electron impact energy. The experimental procedure requires quantitative measurement of emission intensity, electron beam flux, target density and geometrical factors and the knowledge of angular distribution or polarization character of the emitted radiation. Optical excitation functions in general represent electron impact induced photon emission probabilities as a function of electron impact energy. If they are corrected for cascade effects, branching ratios, and other competing decay processes, they become equivalent to electron impact excitation cross sections and are frequently called level excitation functions. If no correction is made for cascade, they are called line excitation functions or apparent electron impact excitation cross sections and they represent upper limits to the true excitation cross sections.

A large body of data is available in the form of optical excitation functions in the visible region and considerable progress was made recently in the VUV region. For example, it was found very recently that the cross section for production of Lyman- α radiation in electron H_2 collisions was incorrect (4-6) and it had to be lowered by a factor of 0.64. This has affected a large fraction of the VUV optical excitation functions since the Lyman- α cross section has been commonly used as a calibration standard. The availability of VUV circular polarizer (7) represents a new important capability.

A short overview on optical excitation cross sections was presented by McConkey (8) but the field has not been critically reviewed for many years and it is certainly ready for such review.

Total Ionization Cross Sections: There have been no major developments in recent years concerning total ionization cross sections. Kieffer and Dunn (9) summarized the experimental techniques and data on diatomic molecules up to 1966. For a recent review of this subject see Ref. 10. The situation can be briefly summarized as follows. For H_2 , D_2 , N_2 , O_2 , CO, NO, CO_2 , N_2O , CH_4 , SF_6 and C_2H_4 , the results of Rapp and England-Golden (11) are most likely to be correct within the specified error limits. The progress in the last decade was mainly in the sense of extending the measurements to other molecular species like F_2 , Cl_2 , H_2O , BF_3 , NH_3 , UF_6 , O_3 and many hydrocarbons.

The integral elastic scattering and excitation cross section data obtained from electron scattering experiments will be reviewed under Differential Cross Sections.

3.3 Differential Cross Sections

General Remarks: Differential (in angle) scattering cross sections (DCS's) represent information one level more detailed than integral cross sections. These type of data are needed for obtaining momentum transfer cross sections at impact energies higher than inelastic thresholds, for stringent testing of theoretical models in cross section calculations, and for understanding the physics of scattering. Differential cross sections

also explicitly enter terms higher than second order in the spherical harmonic expansion solution of the Boltzmann equation for electrons in molecular gases. Integral cross sections obtained by direct integration of differential cross sections are free from many of the deficiencies encountered in measurement of the integral cross section (e.g., cascade effects) but are subject to some errors due to the need for extrapolation of the measured data beyond the experimentally accessible regions (to 0° and 180° scattering angles).

The customary first step in obtaining DCS's is to generate energy-loss spectra at various scattering angles and impact energies. The experimental arrangement is schematically shown in Fig. 2. An energy selected, well collimated electron beam of desired kinetic energy is produced and focused on the target molecules. The target is either a beam or a static gas sample.

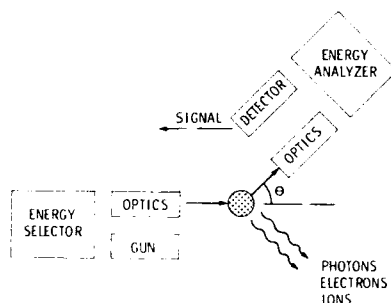


FIGURE 2.

Schematic diagram for differential scattering cross section measurements.

Electrons scattered into a small solid angle at a given scattering angle with respect to the incoming electron beam are energy analyzed and detected as a function of energy loss. A typical energy-loss spectrum generated this way is shown in Fig. 3. The location of the spectral features characterizes the energy-level scheme of the target and the scattering intensities are related to the corresponding DCS's. Determination of DCS from such spectra requires a decomposition of the overlapping structures into individual contributions.

A large number of studies have been carried out leading to energy-loss spectra e.g. for the purpose of identifying optically forbidden excitations. However, only in a few cases have the energy-loss spectra been converted to absolute cross sections.

The general relationship between the scattered electron signal and the cross section is rather complex

$$I_n(E_0, \Delta E, \Omega) = \int_{\vec{r}} \int_{E'_0} \int_{\Delta E'} \int_{\Omega'(\vec{r})} \rho(\vec{r}) f(E'_0, \vec{r}) F(E'_0, \Delta E', \vec{r}, \Omega') \times$$

$$\sum_i \sum_f N_i \left[\frac{\partial^3 \sigma(E'_0, \Delta E', \Omega')}{\partial E'_0 \partial \Delta E' \partial \Omega'} \right]_{if} d\Omega' d\Delta E' dE'_0 d\vec{r} \quad (5)$$

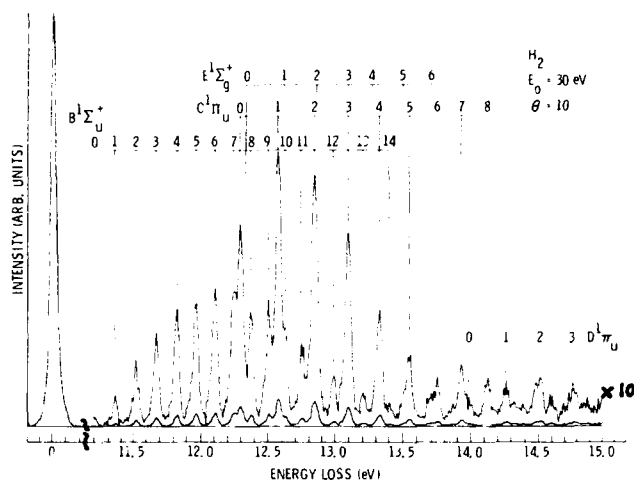


FIGURE 3.
Electron-impact energy-loss spectrum for H_2 . The prominent singlet state excitations and the elastic peak are shown (from Ref. 3).

where:

$I_n(E_0, \Delta E, \Omega)$ is the scattering signal (counts/sec) measured by the instrument at a nominal impact energy E_0 , energy-loss ΔE , and scattering polar angles (θ, ϕ) for a collection of processes indicated by n ; $\rho(\vec{r})$ is the spatial density distribution of the target molecules (cm^{-3}); $f(E_0, \vec{r})$ is the distribution (both energy and spatial) function of the electron flux; $F(E_0, \Delta E', \Omega')$ is the response function of the detector; $\partial^3 \sigma(E_0, \Delta E', \Omega') / \partial E_0 \partial \Delta E' \partial \Omega'$ is the triply differential cross section for the process $(i \rightarrow f)$ with energy loss $\Delta E'$ at impact energy E_0 and scattering angle Ω' ; \vec{r} is the position coordinate of the individual scattering points which contribute to the observed signal and θ' and ϕ' are the polar angles of scattering from these points. The extraction of the desired cross section from Eqn. (5) is complicated. It requires detailed knowledge of the target density and electron beam flux distributions and the overall instrument function. The situation becomes much more manageable if a DCS averaged over the energy and angular resolution of the apparatus, is removed from the integrand. Then the relationship for the indistinguishable scattering processes becomes

$$I_n(E_0, \theta) = DCS_n(E_0, \theta) V_{eff} \quad (6)$$

Here all the flux, geometrical, and instrumental functions are included in the "effective scattering path length" V_{eff} which can be obtained by the appropriate integrations. The values of the "effective scattering path length" could be calculated at each impact energy as a function of the scattering angle and, therefore, the absolute values of the DCS can, in principle, be obtained. At high impact energies Lassettre and Bromberg determined the effective path length experimentally and produced absolute

elastic cross sections this way. At low impact energies this procedure becomes hopeless. It is very difficult to measure these parameters accurately and even more difficult to keep them constant during the entire measurement. An easier and more reliable procedure is to measure relative cross sections and normalize them by other methods. Let us now summarize the various methods by which absolute cross sections can be generated.

One approach to normalization utilizes total electron scattering, excitation, and ionization cross sections. The integral elastic cross section is obtained from the expression

$$\sigma_0 = \sigma_{TOT} - \sigma_{INEL} = \sigma_{TOI} - \sigma_{EXC} - \sigma_{ION} \quad (7)$$

and is used to normalize the relative experimental elastic data, which in turn can be used to normalize the inelastic data. Total cross sections can be measured with 1-3% accuracy and have recently become available for a large number of molecules. The ionization cross section σ_{ION} is usually available to an accuracy of about 5%. The total excitation cross section, σ_{EXC} is usually not available, but can be, at low energies, estimated with acceptable accuracy. At higher impact energies, σ_{EXC} is comparable to the other quantities in Eq. (7) and the estimation accuracy will greatly influence the calibration.

High-energy and low-angle electron-impact measurements have been used to generate optical f-values by extrapolation of the generalized oscillator strength $f^G(K)$ to zero momentum transfer (K). This is the basis of generating optical absorption and photoionization data by electron impact techniques. One can, however, reverse the procedure and utilize available optical f-values to normalize relative generalized oscillator strengths which were obtained from, and are equivalent to, the experimentally measured inelastic DCS. This is usually performed by plotting the relative $f^G(K)$ against K^2 , observing the small K^2 tendency in the curve and extrapolating to $K = 0$. The problem, however, is that for an inelastic process the momentum transfer is finite even at zero scattering angle and the extrapolation to the zero limit is unphysical. Another problem is that the most important points in this extrapolation are the low-angle DCS points, which are experimentally the most uncertain. This uncertainty in the low-angle data arises mainly from the interference of the parent electron beam, and the rapid change of the DCS and the effective path length with scattering angle at small scattering angles.

Optical excitation functions, if properly corrected for cascade, can also be used to normalize selective integral electron-impact excitation cross sections. Since absolute optical excitation function measurements face most of the problems one encounters in absolute electron-impact cross section measurements and more, this normalization procedure is not very practical.

In principle, theoretical calculations could also serve as the basis for normalizing relative cross section data. In general, however, the theoretical calculations have not been accurate enough for this purpose.

The most practical and reliable method for normalizing elastic scattering cross sections is the "relative flow" technique. In this approach one measures relative elastic scattering intensities for the gas in question with respect to H_2 under "identical experimental conditions". On the basis of Eqn. (6), the relative intensities are given as

$$\frac{I(E_0, \theta; x)}{I(E_0, \theta; He)} = \frac{DCS(E_0, \theta; x)}{DCS(E_0, \theta; He)} \frac{V_{eff}(x)}{V_{eff}(He)} \quad (8)$$

He is selected as a standard since elastic DCS for He are the most accurately known cross sections and the identical experimental conditions cancel the effective scattering path lengths. In practice, no complete cancellation is achieved but the ratio of the effective path lengths is determined. (For details see Refs. 1, 12 and 13.) We have spent a considerable amount of time in our laboratory to refine this technique and we feel that it can now yield cross sections accurate to about 10% at intermediate impact energies. The major points of concerns are: identical relative density distributions for the two gas targets, accurate knowledge of the relative gas flow rates, avoidance of cross contamination, and the overall stability of the apparatus during the measurement. Once elastic DCS are determined for a given molecule, the inelastic cross sections can be normalized against it. Some problems arise at low (near threshold) impact energies in evaluating energy-loss spectra and converting the measured scattering signals to cross sections. For the unfolding of individual vibrational band intensities associated with an electronic transition from an energy-loss spectrum, we can no longer assume (as at higher impact energies) that the relative scattering intensities of these bands are given by the Franck-Condon factors. The rapid change of the cross section near threshold now has to be considered (since each vibrational excitation occurs at a different energy above its own threshold). This effect was nicely demonstrated by Ajello and Shemansky (14) for the electron impact excitation of N_2 . In addition special problems are presented by the low-energy background electrons and the need to calibrate the response function of the detector as a function of electron energy.

Elastic Scattering and Rotational Excitation: Elastic cross section data, with very few exceptions always include elastic and rotational excitation together. In this composite "vibrationally elastic" cross section usually the true elastic $\Delta J = 0$ contribution dominates. The exceptions are high angle scattering where $\Delta J = \pm 2, \pm 4$ type transitions also become important and highly polar molecules where the $\Delta J = \pm 1$ dipole processes dominate especially at low angles.

The electron energy and scattering angle dependence of vibrationally elastic electron scattering is illustrated in Fig. 4 for the case of N_2 .

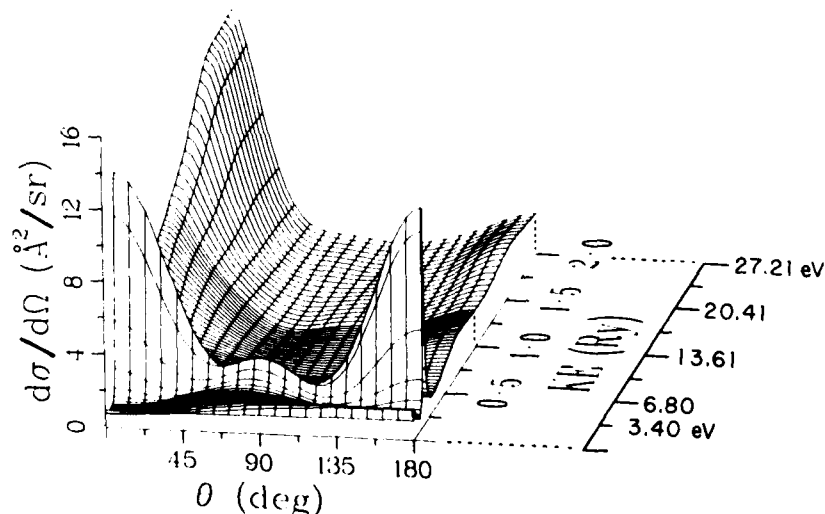


FIGURE 4.
Energy and angular dependence of elastic DCS for N_2 (from Ref. 15).

This figure is based on the calculations of Siegel et al., (15) and it displays the important characteristics of elastic scattering. At very low incident electron energies, the DCS for elastic scattering is nearly isotropic (because the centrifugal barrier excludes all but S-wave scattering). As the incident electron energy increases, the DCS generally becomes more and more forward-peaked which is a manifestation of the fact that more and more partial waves contribute to the scattering process and the fact that the electron transfers less and less momentum to the molecules. N_2 has the interesting d-wave shape resonance centered near 2.4 eV that dramatically alters the general characteristics just described, and which stands-out in this figure. In the case of resonances, the shape of the DCS is determined by the properties of the intermediate ion state and does not follow the qualitative arguments that apply in the nonresonant region.

Figure 5 displays the incident electron energy dependence of the measured integral vibrationally "elastic" scattering cross section for a variety of molecules, ranging from H_2 to SF_6 . The purpose of this figure is to illustrate the substantial variation, in both the magnitude and electron energy dependence of the integral cross sections.

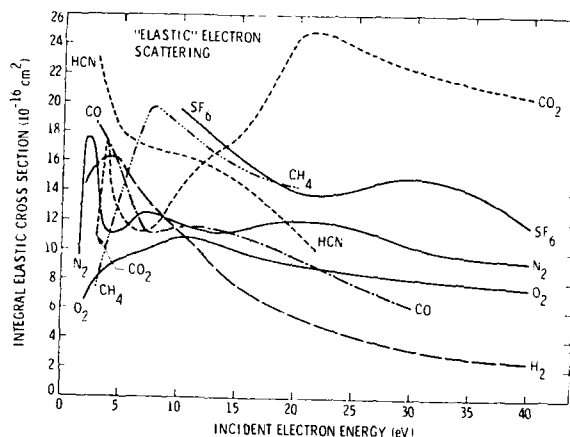


FIGURE 5.

Integral elastic scattering cross sections (from Ref. 12).

Reasonably complete sets of differential and integral elastic cross sections are available for H_2 and N_2 at impact energies ranging from about 0.1 to 1,000 eV. Fragmentary data is available for O_2 , CO, NO, HF, HCl, HBr, LiF, KI, CsF, CsCl, H_2O , H_2S , HCN, CO_2 , N_2O , SO_2 , NH_3 , As_4 , CH_4 , C_2H_2 , C_2H_4 , C_2H_6 , C_3H_8 , CCl_2F_2 , CCl_3F , CCl_4 , SF_6 and UF_6 . (See Refs. 2 and 12.)

Pure rotational excitation cross section has been measured for H_2 and obtained by unfolding technique for N_2 , CO and H_2O but only over very limited angular and energy ranges. (See Refs. 2 and 12.)

Vibrational Excitation: Electrons are quite effective in producing vibrational excitation, particularly at low impact energies, by interacting with the molecular electron distribution, which is coupled with the nuclear vibrational motion. Especially effective are the resonance mechanisms for vibrational excitation which involve temporary electron capture. The

increased electromagnetic interaction causes a substantial distortion of the molecular charge distribution and this distortion leads to efficient energy transfer into vibrational modes. At low energies typical integral cross sections are about 10^{-16} cm².

The energy and angular dependence of vibrational excitation cross sections in the resonance region depends critically on the lifetime and the properties of the negative ion state. Vibrational excitations to high vibrational levels, far outside the Franck-Condon region, can occur through formation of negative molecular ion states which are unstable with respect to dissociation. As the nuclei fly apart, decay to the vibrational levels of the ground electronic state takes place in competition with the dissociation. In the case of polyatomic molecules the resonance excitation can be selective with respect to vibrational modes.

The direct electron-impact excitation of molecular vibration, especially at high impact energies, tends to approximate the $\Delta v = 1$ selection rule. These direct-excitation integral cross sections are of the order of 10^{-18} cm², change smoothly with impact energy and are usually forward peaked. Excitation to overtone or combination bands decrease by about an order of magnitude with increasing vibrational quantum numbers. The angular behavior of the cross sections depends on the relative importance of short and long range interaction terms and is usually similar for the fundamental and overtone bands.

Most of the vibrational excitation cross sections available are for H₂ and N₂. Some fragmentary data exist for O₂, CO, HF, HCl, HBr, H₂O, H₂S, CO₂, SO₂, CH₄, C₂H₄, C₂D₄, CCl₃F and CCl₂F₂. (See Refs. 2 and 16 for details.)

Electronic Excitation: In excitation of electronic states, resonance mechanisms do not appear to play a significant role. Only core-excited shape resonances cause significantly increased cross sections but then only over an energy region which is small (a few electron volts) compared to the energy region over which direct excitation is effective.

The largest cross sections for electronic excitation are associated with optically allowed transitions at intermediate impact energies (and small scattering angles). The value of these cross sections increase gradually with increasing impact energy from threshold to about ten times threshold energy and then slowly decrease at high energies. The angular distributions are forward peaked and this character becomes more enhanced with increasing impact energy.

At low impact energies (within a few electron volts of threshold) forbidden transitions dominate the energy-loss spectra and, therefore, represent the important cross sections. Particularly significant are the spin-forbidden processes that readily occur by electron exchange and produce metastable species. This property of electron-impact excitation has been widely utilized to generate metastable atoms and molecules. Integral cross sections for spin-forbidden processes rise steeply near threshold, reach their peak value within a few electron volts and then decrease sharply with increasing energy. The DCS's associated with these processes are nearly isotropic, reflecting the short-range nature of the spin exchange reaction. No simple characteristics can be identified for symmetry-forbidden excitations. The integral cross sections for these processes are usually smaller than for optically allowed excitations, reach their peak value at lower impact energies, and their DCS's show a large variety of behaviors. There is, however, a very unique character associated with parity-unfavored transitions ($\Sigma^+ \leftrightarrow \Sigma^-$). The DCS for this excitation goes to zero at 0° and 180° scattering angles (17).

Until very recently, a reasonably complete coverage of electronic state excitation cross section was available only for N₂ and some fragmentary data was available for H₂, O₂, SO₂ and CH₄ (see Refs. 2 and 16). An extensive study has now been reported for H₂ (Ref. 3).

Excitation to repulsive electronic states leads to dissociation of the

molecule. A large variety of processes are possible and a considerable amount of general information and cross section data exist for dissociative attachment and for dissociation into excited or charged products. Very little information is available, however, on dissociation into neutral fragments. For recent reviews on this subject see Ref. 18.

Ionization: Differential cross section for ionization are more difficult to determine than for processes discussed so far. The cross section now depends not only on the impact energy but also on the energy and angle of the primary and secondary electrons. Some investigations for atomic species have been carried out but no comparable data exist for molecules. From a practical point of view the single (with respect to the energy of one of the electron) differential cross sections are the most important quantities while from a theoretical point of view the multiple differential cross sections and angular correlations represent the most stringent tests of models and approximations. (See Ref. 10.)

3.4 Momentum Transfer Cross Sections

Elastic momentum transfer cross sections at low energies (below a few eV) are commonly and most accurately determined by electron swarm techniques. Beam/beam experiments are mandatory at higher energies. The swarm and the beam/beam measurements cover complementary energy ranges and the comparison of the cross section data obtained by these two methods in the overlapping energy range can serve as an important check. For discussions and compilation of momentum transfer cross section data see References 2, 19, 20 and 21.

A great deal of progress has been made recently through detailed comparisons between the results of swarm experiments and experimental and theoretical cross section data for electron-molecule collision processes. These comparisons make it possible to judge the consistency of available data and allows us to deduce such data from swarm parameters. At the Joint Meeting of the 4th International Swarm Seminar and the Inelastic Electron-Molecule Collision Symposium (Satellite Meeting of the XIVth ICPEAC), Tahoe City, California, July 19-23, 1985 detailed discussions on these matters were presented. (See especially the abstracts by M. Hayashi and A. V. Phelps, Proceedings pp. 8 and 6, respectively.)

5. COMPARISON OF EXPERIMENTAL AND THEORETICAL CROSS SECTIONS

It is important to develop theoretical methods which can reliably predict electron collision cross sections. Such methods would enable us to generate a large body of cross sections which would take decades of extensive laboratory work to measure. Especially important are calculations for molecular species which are difficult to study in a laboratory (free radicals, excited and corrosive molecules). In addition the development of these methods helps us to understand the basic nature of electron molecule collisions.

Comparison of experimental data with theoretical calculations provides information about the validity of various approximations and allows some insight into the physics of the scattering process. The type of questions one should ask about the physics of the scattering processes in case of molecules are:

1. What is the role of nuclear motion in the scattering process. Under what conditions can we take the nuclei fixed (Adiabatic Nuclei Approximation)?
2. Is it necessary to solve the complete Laboratory Frame Close Coupled or Body Frame Close Coupled equations or do the Distorted Wave, Glauber, or Born Approximation suffice?
3. What is the importance of the various terms in an interaction potential; such as static, exchange, polarization and absorption terms?

In Fig. 6 cross sections for excitation of the B^1_u state of H_2 are compared. The Born type calculations (22) predict qualitatively correct DCS only at small scattering angles. The distorted wave results (23) are in good agreement with experiment shape wise but differ in magnitude by about a factor of two. Figure 7 shows the integral cross sections. The theoretical

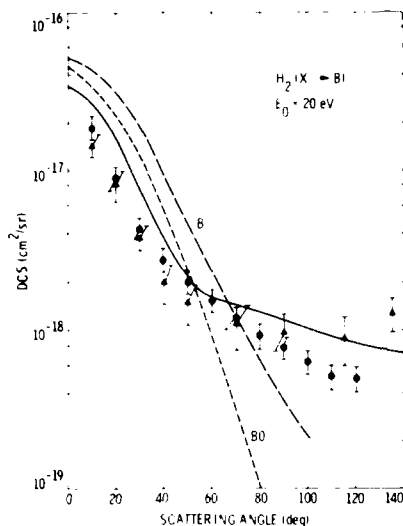


FIGURE 6.

Differential cross sections for the excitation of the B^1_u state of H_2 at 20 eV impact energy. Experimental results: \bullet , Ref. 3; Δ , Refs. 2 and 24. Theoretical results: —, Ref. 22 (Born); ---, Ref. 22 (Born-Ochkur); —, Ref. 23 (distorted wave).

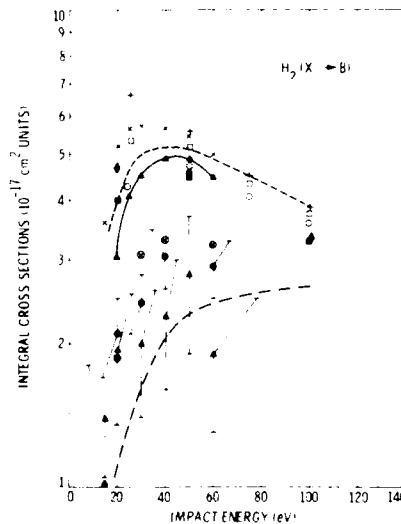


FIGURE 7.

Integral cross sections for the excitation of the B^1_u state of H_2 . Experimental data: \bullet , Ref. 3; Δ , Refs. 2 and 24; \times , Ref. 25 (optical); ---, Ref. 26 (optical); Theoretical results: +, Ref. 27 (Born); \square Ref. 27 (Born-Ochkur); \diamond , Ref. 22 (Born); \blacksquare , Ref. 22 (Born-Ochkur); \times , Ref. 23 (Born); ---, Ref. 28 (semi-classical impact parameter); \blacktriangle , Ref. 23 (distorted wave); \circ , Ref. 27 (2 state close coupling).

results all fall into a group and are larger than the group formed by the experimental data. For the excitation of the a^3_g and c^3_u states the experimental results (3) are compared with two state close coupling (29) and distorted wave (30) calculations in Figs. 8 and 9, respectively. The close coupling results for the a^3_g state are in good agreement with experiment at 20 eV, but substantial differences exist at 30 eV. In the case of the c^3_u state the distorted wave and experimental results agree shape wise but not in magnitude. These and other comparisons of various cross sections in H_2 and N_2 (12, 16) lead us to the following general conclusions: 1) The treatment of the nuclear motion by different methods, as far as vibrational excitation is concerned, yields similar results (with the same potentials); 2) Exchange and polarization effects have to be included in the interaction potential to get even qualitatively correct results; 3) Born and

various first order theories yield incorrect angular distributions (although

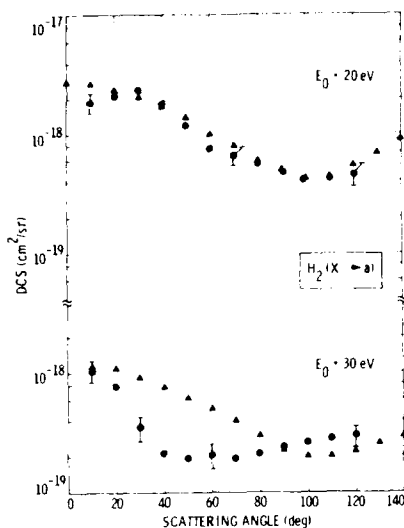


FIGURE 8.
Differential cross sections for excitation of the $a^3\sigma^+$ state in H_2 at 20 and 30 eV impact energies. \blacklozenge , Ref. 3 (experiment); \blacktriangle , Ref. 29 (two state close coupling calculation).

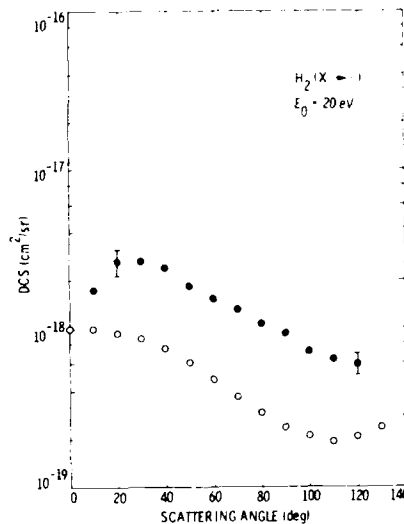


FIGURE 9.
Differential cross sections for excitation of the $c^3\sigma^+$ state in H_2 at 20 eV impact energy. \blacklozenge , Ref. 3 (experiment); \circ , Ref. 30 (distorted wave).

sometimes correct integral cross sections by accidental cancelation of low- and high-angle errors); 4) Further improvements in theoretical methods are required before quantitative agreement between theory and experiment can be achieved. For example, the effect of including more than two open channels in calculating electronic state excitations by the close coupling method would be very important.

Recent electron-photon coincidence measurements on molecular targets (31) indicate that information at a deeper level than DCS can be obtained concerning electron molecular collision processes. This, like in the case of electron-atom scattering, will subject the theoretical models to even more stringent tests.

ACKNOWLEDGEMENT

This article was prepared at the Jet Propulsion Laboratory, California Institute of Technology and has been supported by the National Aeronautics and Space Administration and by the National Science Foundation. Helpful discussions with D. C. Cartwright and V. McKoy are gratefully acknowledged.

REFERENCES

- 1) S. Trajmar and D. F. Register, "Experimental Techniques for Cross Section Measurements", Chapter 6 in Electron-Molecule Collisions, eds. I.

- Shimamura and K. Takayanagi (Plenum Publishing Corp., 1984).
- 2) S. Trajmar, D. F. Register and A. Chutjian, *Physics Reports* 97 (1983) 219.
- 3) M. A. Khakoo and S. Trajmar (Three articles to be published in *Phys. Rev. A*, 1985).
- 4) B. van Zyl, M. W. Beaby and H. Neumann (submitted to *Phys. Rev. A* 1985).
- 5) D. E. Shemansky, J. M. Ajello and D. T. Hall (submitted to *The Astrophys. J.*, 1985).
- 6) R. C. G. Lichtenberg, A. McPherson, N. Rouze, W. B. Westerweld and J. S. Risley, 16th Annual Meeting of Div. of Electron and Atomic Phys., Am. Phys. Soc., May 29-31, 1985, Norman, OK (Abstract ED7).
- 7) W. B. Westerweld, K. Becker, P. Zetner, J. J. Carr and J. W. McConkey, *J. Appl. Optics*, (to appear, 1985).
- 8) J. W. McConkey, in "Workshop on Electronic and Ionic Collision Cross Sections Needed in the Modeling of Radiation Interaction with Matter", Argonne National Laboratory Report, ANL-84-28, ed. M. Inokuti, May 1984.
- 9) L. J. Kieffer and G. H. Dunn, *Rev. Mod. Phys.* 38 (1966) 1.
- 10) T. D. Mark, "Ionization of Molecules by Electron Impact", Chapter 3 in Electron Molecule Interactions and Their Applications, Vol. 1, ed. L. G. Christophorou (Academic Press, New York, 1984); T. D. Mark and G. H. Dunn, Electron Impact Ionization (Springer-Verlag, Wien, 1984).
- 11) D. Rapp and P. Englander-Golden, *J. Chem. Phys.* 43 (1965) 1464.
- 12) G. Csanak, D. C. Cartwright, S. K. Srivastava and S. Trajmar, "Elastic Scattering of Electrons by Molecules", Chapter 1 in Electron-Molecule Interactions and Their Applications, Vol. 1, ed. L. G. Christophorou (Academic Press, 1984).
- 13) R. T. Brinkmann and S. Trajmar, *J. Phys. E: Sci. Instrum.* 14 (1981) 245.
- 14) J. M. Ajello and D. E. Shemansky, *J. Geophys. Res.* (to appear, 1985).
- 15) J. Siegel, D. Dill and J. L. Dehmer, *Phys. Rev. A* 17 (1978) 2106.
- 16) S. Trajmar and D. C. Cartwright, "Excitation of Molecules by Electron Impact", Chapter 2 in Electron Molecule Interactions and Their Applications, Vol. 1, ed. L. G. Christophorou (Academic Press, New York, 1984).
- 17) D. C. Cartwright, S. Trajmar, W. Williams and D. L. Huestis, *Phys. Rev. Lett.* 27 (1971) 704 and W. A. Goddard III, D. L. Huestis, D. C. Cartwright and S. Trajmar, *Chem. Phys. Lett.* 11 (1971) 329.
- 18) R. N. Compton and J. N. Bardsley, "Dissociation of Molecules by Slow Electrons", Chapter 4 in Electron Molecule Collisions, eds. I. Shimamura and K. Takayanagi (Plenum Press, New York 1984); E. C. Zipf., "Dissociation of Molecules by Electron Impact", Chapter 4 in Electron Molecule Interactions and Their Applications, Vol. 1, ed. L. G. Christophorou (Academic Press, New York, 1984).
- 19) Y. Itikawa, Momentum Transfer Cross Sections for Electron Collisions on Atoms and Molecules and their Application to Effective Collision Frequencies, Argonne National Laboratory Report, ANL-77939, April, 1972; Atomic Data and Nuclear Data Tables 14 (1974) 1; *ibid* 21 (1978) 69.
- 20) M. Hayashi, Recommended Values of Transport Cross Sections for Elastic Collision and Total Collision Cross Section for Electrons in Atomic and Molecular Gases, Report IPPJ-AM-19, Inst. Plasma Phys., Nagoya Univ., Japan, November 1981.
- 21) J. W. Gallagher, E. C. Beaty, J. Dutton and L. C. Pitchford, "A Compilation of Electron Swarm Data in Electro Negative Gases", JILA Report No. 22, Aug. 1, 1982 and *J. Phys. Chem. Ref. Data* 12 (1983) 109.
- 22) G. P. Arrighini, F. Biondi and C. Guidotti, *Mol. Phys.* 41 (1980) 1501.
- 23) A. W. Fiflet and V. McKoy, *Phys. Rev. A* 21 (1980) 1863.
- 24) S. K. Srivastava and S. Jensen, *J. Phys. B: Atom. Molec. Phys.* 10 (1977) 3341.

- 25) D. E. Shemansky, J. M. Ajello and D. T. Hall (submitted to *The Astrophys. J.*, 1985).
- 26) I. C. Malcolm, H. W. Dassen and J. W. McConkey, *J. Phys. B: Atom. Molec. Phys.* 12 (1979) 1003; J. W. McConkey, *J. Chem. Phys.* 74 (1981) 6224.
- 27) S. Chung and C. C. Lin, *Phys. Rev. A* 17 (1978) 1874.
- 28) A. N. Hazi, *Phys. Rev. A* 23 (1981) 2232.
- 29) M. A. P. Lima, T. L. Gibson, W. Huo and V. McKoy (private communication, to be published, 1985).
- 30) L. Mu-Tao, R. R. Lucchese and V. McKoy, *Phys. Rev. A* 26 (1982) 3240.
- 31) I. C. Malcolm and J. W. McConkey, *J. Phys. B: Atom. Molec. Phys.* 12 (1979) L67; K. Becker, H. W. Dassen and J. W. McConkey, *J. Phys. B: atom. Molec. Phys.* 16 (1983) L177 and *ibid* 17, (1984) 2535; J. W. McConkey, S. Trajmar, J. C. Nickel and R. McAdams, *J. Phys. B: Atom. Molec. Phys.* 18 (1985) L207; J. W. McConkey, S. Trajmar, J. C. Nickel and G. Csanak (private communication, to be published, 1985).

ROTATIONAL EXCITATION OF MOLECULES BY SLOW ELECTRONS

Isao SHIMAMURA

RIKEN (Institute of Physical and Chemical Research)
Wako, Saitama 351-01, Japan*
and
Institute for Molecular Science
Okazaki, Aichi 444, Japan**

Abstract. The electron-molecule collision time is usually much shorter than the molecular rotational period, and the rotational motion may be treated adiabatically. Then follow a number of useful relations between cross sections for different rotational transitions. These relations are independent of the interaction potential or the collision dynamics. In some cases to be discussed these relations must be modified or abandoned. Most results apply also to collisions of molecules with positrons, atoms, and ions and to molecular photoabsorption and photoionization.

1. INTRODUCTION

An electron that penetrates molecular gas loses its kinetic energy by exciting the internal motion of the molecules. When the electron energy becomes low, the main energy-loss mechanism is rotational-vibrational excitation in electron-molecule collisions. Therefore, rotational-vibrational transitions are important in any branch of physics in which the behavior of secondary electrons plays a significant role, e.g., in the physics of gas discharges, in radiation physics and chemistry, in the physics of the earth's upper atmosphere and planetary atmospheres, and so on.

In this article I discuss our present understanding of the physics of rotational motion in low-energy electron-molecule collisions in which rotational-vibrational transitions and even electronic transitions and ionization occur. Most of the results to be discussed below apply also to positron scattering, photoionization, and heavy-particle collision with a molecule.

Many diatomic and linear polyatomic molecules in a $^1\Sigma$ state may be regarded as linear rigid rotators. The molecular wave function may be written as the product of a vibronic (or vibrational-electronic) wave function and a rotational wave function represented by a spherical harmonic function $Y_{jm}(\hat{R})$ of the molecular orientation \hat{R} . The linear-rotator levels are specified by two quantum numbers, namely, the magnitude j of the rotational angular momentum \mathbf{j} and its projection m onto a space-fixed quantization axis. The rotational levels are degenerate in m , and rotational transition cross sections are usually averaged over the initial m sublevels and summed over the final m sublevels. The rotational energies are given by

$$E(j) = B j(j+1). \quad (1)$$

B is the rotational constant, which is inversely proportional to the moment of inertia of the rotator. B is very small, and is smaller for heavier molecules. For example, $B=7.4\text{meV}$ for H_2 , 0.25meV for N_2 , 0.17meV for LiF , and 0.008meV for

*Permanent address.

**Adjunct member of staff from April 1984 to March 1986.

KI.

Because B is small, the rotational level spacings are small. Therefore, molecules in a gas are distributed over many different rotational levels, most of which being high- j levels. Then, in a real molecular gas, transitions from many different initial j to many different final j' are taking place. One has to take all of them into account in discussing physical phenomena occurring in a gas.

Experimentally, small level spacings make it difficult to resolve each rotational transition. Rotational lines in electron-energy-loss spectra, for example, are resolvable only for H_2 and its isotopes, and unresolvable for heavier molecules. This attaches a particular importance to theoretical investigations of rotational transitions in electron-molecule collisions.

Another aspect of electron-molecule collisions is that the electron mass is much smaller than the molecular mass. This leads us to two questions. The first concerns the small momentum of a slow electron. Can an electron really give an enough torque to a very heavy molecule and excite (or deexcite) its rotational motion? The second question concerns the high velocity of the light electron with even a small kinetic energy. The electronic motion is often much faster than the rotational motion, and the latter is often separable from any other motions. Then, what physics of rotational motion emerges from this separability? When and how this separability breaks down? This article is mostly concerned with the separation of rotational motion from vibronic motion and its consequences and limitations [1].

For characterizing the rotational transitions we often use the difference $\Delta j = j' - j$ between the final and initial rotational quantum numbers and the difference $\Delta E = E - E' = \frac{1}{2}h^2(k'^2 - k^2)$ between the initial and final electron energies. These physical quantities are useful for practical purposes. For example, an electron-energy-loss spectrum as a function of ΔE may be decomposed into different Δj components that we may call P branch ($\Delta j = -1$), Q branch ($\Delta j = 0$), R branch ($\Delta j = +1$), and so on, as in optical spectroscopy. Physically more relevant quantities, however, are the vectorial differences $\mathbf{j}_t = \mathbf{j}' - \mathbf{j}$ and $\mathbf{q} = \mathbf{k} - \mathbf{k}'$ between the final and initial rotational angular momenta and between the initial and final linear momenta of the electron, as will become clear later (Fig.1). These differences are the angular and linear momenta transferred from the electron to the molecule during the collision.

The rest of this section answers the first question posed above on the small electron momentum and rotational excitation of heavy molecules. See Fig.2 that summarizes the total cross sections for electron scattering by several molecules measured by crossed-beam experiments. The total cross sections in this figure are nearly the same as rotational transition cross sections except for H_2 . In the energy region between 1 and 20 eV the cross sections for molecules

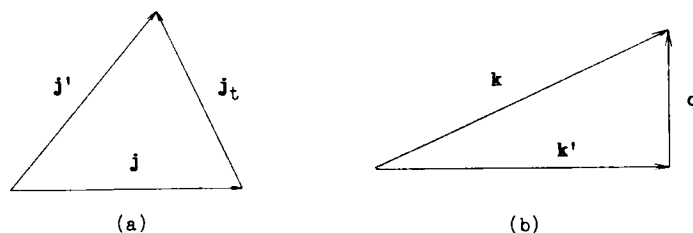


FIGURE 1

(a) Transfer of an angular momentum \mathbf{j}_t to a linear rotator with a rotational angular momentum \mathbf{j} . (b) Transfer of a linear momentum \mathbf{q} to a rotator from an electron with a momentum \mathbf{k} .

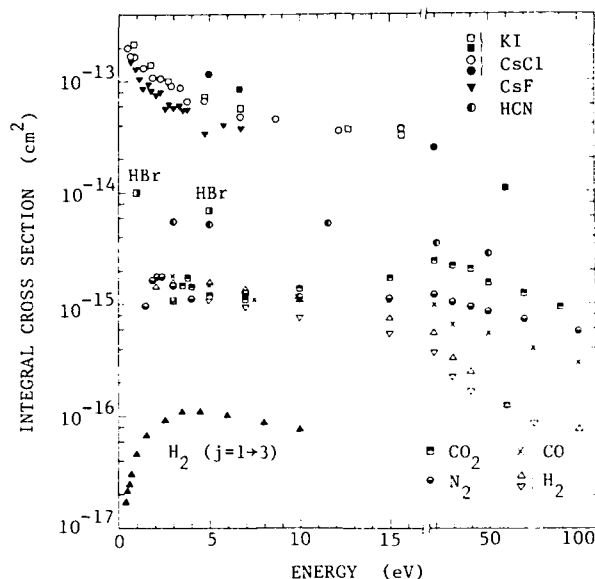


FIGURE 2

Integral cross sections for scattering of electrons by several molecules obtained by integrating differential cross sections measured by the crossed-beam technique. All transitions or electronically elastic processes for KI, CsCl, CsF; vibrationally elastic and $0 \rightarrow 1$ v_2 vibrational excitation processes for HCN; vibrationally elastic processes for HBr, CO, CO₂, N₂; vibrationally elastic, vibrationally and rotationally elastic, or rotational transition $j=1 \rightarrow 3$ for H₂. See Ref.(1), p.147 for data source. (Taken from Ref.(1).)

having a dipole moment D of about 10 debyes are of the order of 10^{-13} cm^2 , those for molecules with a D of a few debyes are of the order of 10^{-14} cm^2 , and those for nonpolar molecules with a quadrupole moment are of the order of 10^{-15} to 10^{-16} cm^2 .

These cross sections are huge, and especially so for large dipole moments, due to the charge-dipole interaction that decays as r^{-2} at large electron-molecule distances r . The charge-quadrupole interaction decaying as r^{-3} plays a dominant role in the absence of a dipole moment. These long-range electrostatic interactions depend on the molecular orientation, and give the molecules an enough torque or angular momentum to change their rotational motion even in the distant collisions. This makes the cross section huge.

2. ADIABATIC-ROTATION RELATION FOR CROSS SECTIONS

A typical electron-molecule collision time is shorter than 10^{-15} s for electron energies higher than 1 eV. It is much shorter than the characteristic period ($\sim 10^{-12} \text{ s}$) of molecular rotation. Therefore, the molecular orientation is almost stationary during the collision irrespective of the initial and final

rotational angular momenta, unless the molecular gas is at extremely high temperature. Because the molecular orientation is almost fixed, there is hardly any effect of molecular rotation on the collision dynamics, and the cross section $d\sigma^{AMT}(j_t; v, v')/d\omega$ for angular-momentum transfer j_t is independent of j and j' , though it may depend on the initial and final vibrational quantum numbers v and v' [1].

A rotational-vibrational transition $v_j \rightarrow v'j'$ has contributions from those angular-momentum transfers j_t which satisfy the triangular relation of Fig. 1a. The contribution from each j_t is proportional to the angular-momentum-transfer cross section and to the probability $p(jj_tj')$ of finding j' with a magnitude j' when adding j and j_t with fixed magnitudes j and j_t . Thus it follows that [1]

$$d\sigma(v_j \rightarrow v'j')/d\omega = \sum_{j_t} p(jj_tj') d\sigma^{AMT}(j_t; v, v')/d\omega. \quad (2)$$

If the molecular rotational motion is initially at rest, i.e., if $j=0$, then $j'=j_t$. Hence, the angular-momentum-transfer cross section $d\sigma^{AMT}(j_t; v, v')/d\omega$ is the same as the cross section for the transition $v_0 \rightarrow v'j_t$, and we have [1]

$$d\sigma(v_j \rightarrow v'j')/d\omega = \sum_{j_t} p(jj_tj') d\sigma(v_0 \rightarrow v'j_t)/d\omega. \quad (3)$$

The quantum mechanical angular-momentum coupling theory leads to a probability [2]

$$p(jj_tj') = [C(jj_tj'; 000)]^2 \quad (4)$$

in terms of a Clebsch-Gordan coefficient. Equations (2) and (3) are valid also for classical collisions; in this case the probability $p(jj_tj')$ is the classical Clebsch-Gordan coefficient squared [3,4].

A virtue of Eqs. (2) and (3) is that the cross section is factored into two parts, one being a known quantity that is independent of the collision dynamics and the other being dependent on the dynamics but independent of j and j' . The dependence of the cross section on j and j' is contained solely in the known probability $p(jj_tj')$. All cross sections $d\sigma(v_j \rightarrow v'j')/d\omega$ are expressible as linear combinations of those for the transitions from the ground rotational state. The collision dynamics is most efficiently studied by looking into only the cross sections $d\sigma(v_0 \rightarrow v'j')/d\omega$ rather than all the cross sections $d\sigma(v_j \rightarrow v'j')/d\omega$. Also to be noted is that usually only a small number of units of angular momentum is transferred in electron-molecule collisions. This limits the range of summation in Eqs. (2) and (3) over only a few terms, which is convenient for practical purposes.

We have dealt with the molecular rotation adiabatically, and have seen that the angular-momentum transfer j_t plays a much more important part in rotational transitions than the rotational-quantum-number difference Δj .

A relation of the same type as Eq. (3) is satisfied by any physical quantity that is defined by summing or integrating the differential cross section, with or without a weight function, over any variables or indices other than j , j' , and j_t ; both sides of Eq. (3) may be summed or integrated over these variables or indices to derive an adiabatic-rotation relation for such a physical quantity. The integral and momentum-transfer cross sections and the rate coefficient, for example, satisfy a relation similar to Eq. (3).

I have discussed only rotational-vibrational transitions so far. Equation (3) applies, however, also to the case where an electronic transition or ionization occurs simultaneously with rotational or rotational-vibrational transitions, provided that both the initial and final states may be regarded as linear rotators.

The fact that the incident particle is an electron has been used in the derivation of Eq. (3) only to justify the adiabatic-rotation approximation. Equation (3) is equally valid for the collision of a molecule with any incident particle with or without an internal structure, if the rotational period is

much longer than the interaction time [5]. For example, if the incident particle is a photon and the outgoing particle is an electron, the process is photoionization [6].

The differential cross section for photoionization by linearly polarized light is expressible as

$$d\sigma(vj \rightarrow v'j')/d\omega = (4\pi)^{-1} \sigma(vj \rightarrow v'j') [1 + B(vj \rightarrow v'j') P_2(\cos \theta)] \quad (5)$$

in terms of the integral cross section σ and the anisotropy parameter B . The direction θ , in the Legendre function, of the photoelectron is measured from the direction of polarization of the light. The differential cross section satisfies Eq.(3) at any θ in the adiabatic-rotation approximation. Therefore, σ and B separately satisfy Eq.(3) with $d\sigma/d\omega$ replaced by σ or by $B\sigma$. One may derive from these relations a formula that $B(vj \rightarrow v'j')$ parameters must satisfy. This formula is particularly useful, if a small number of j_t values only contribute to the cross section, or if the j and j' values involved are large [6].

Drozdov first derived Eq.(3) with the probability (4) by introducing an adiabatic-rotation theory for quantum mechanical collision problems [7]. Equation (3) is implicit in an expression for electron-molecule collision cross sections given, e.g., by Hara [8] and by Chang and Temkin [9]. The latter authors discussed a special case of Eq.(3) to which only one value of j_t contributes. Equation (3) for photoionization was studied by Buckingham et al. [10] and by Sichel [11]. Fano and Dill [12] detailed the significance of angular-momentum transfer in a more general context. Discussion of Eq.(3) for atom-molecule collisions was started rather late without reference to earlier work and with some detour [13].

3. APPLICATIONS OF THE ADIABATIC-ROTATION RELATION

3.1. High- j behavior

Most molecules in a gas are usually in high- j states as I have explained in Sec.1. I have also mentioned in Sec.2 that only small angular momenta are transferred in electron-molecule collisions. Therefore, a high- j expansion of Eq.(3) with $|\Delta j|$ fixed at a small value would be useful. Expansion of Eq.(4) in terms of inverse powers of j after writing $j' = j + \Delta j$ leads to an expression [14,15]

$$p(j, j_t, j + \Delta j) = c[1 + (\Delta j/2j) + O(j^{-2})], \quad (6)$$

where c is a function only of j_t and $|\Delta j|$. If we neglect the term of order j^{-2} , the quantity in the square brackets is independent of j_t and may be taken out of the summation over j_t in Eq.(3). Then, Eq.(3) reduces to a form [6,15]

$$d\sigma(vj \rightarrow v', j + \Delta j)/d\omega = A(v \rightarrow v'; |\Delta j|) [1 + (\Delta j/2j)], \quad (7)$$

where A , which contains information on the collision dynamics, is a function of $|\Delta j|$ but not of j .

Equation (7) expresses the cross sections for the transitions $j \rightarrow j + \Delta j$ for any high j in terms of a single parameter independent of j . This makes it easy to take all rotational transitions into account to analyze physical phenomena occurring in molecular gas.

The two cross sections $d\sigma(vj \rightarrow v', j \pm |\Delta j|)/d\omega$ plotted versus j approach a value $A(v \rightarrow v'; |\Delta j|)$ common to both as $j \rightarrow \infty$, one from above and the other from below in a nearly symmetric manner.

Figure 3 shows examples of the high- j behavior (7) for electron scattering by N_2 as compared with the j dependence of experimental cross sections (which have been obtained by use of the technique to be explained in Sec.3.3). The

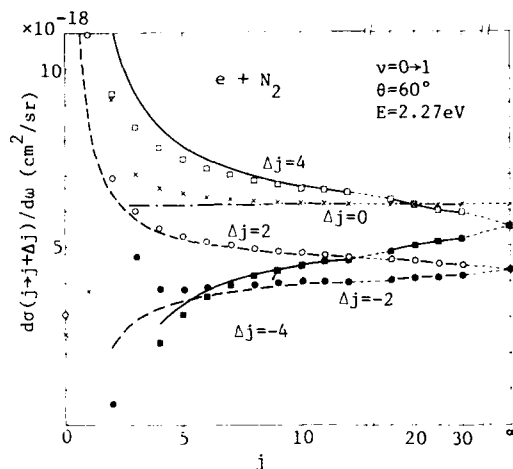


FIGURE 3

Example of the j dependence of the differential cross sections for the vibrational-rotational transitions $(v,j)=(0,j) \rightarrow (1,j+\Delta j)$. Scattering of electrons of energy $E=2.27\text{eV}$ by N_2 into a scattering angle of 60 degrees. Circles, squares, and crosses show experimental data. Curves show the results of the high- j formula (7). (Taken from Ref.(6).)

high- j formula (7) is reasonably accurate even for a j value of as small as five.

3.2. Sum rules

The probability $p(jj_t j')$ is normalized so that, if summed over j' , it is unity. Therefore, summation of both sides of Eq.(3) over j' leads to a sum rule [7,16]

$$\begin{aligned} S_0(j) &= \sum_{j'} d\sigma(vj \rightarrow v'j')/d\omega \\ &= \sum_{j_t} d\sigma(v0 \rightarrow v'j_t)/d\omega = S_0(0) = \text{independent of } j. \end{aligned} \quad (8)$$

The rotationally averaged cross section for the energy loss by the incident electron is defined by the sum over j' of the product of the transition energy ΔE and the cross section. A sum rule

$$\begin{aligned} S_1(j) &= \sum_{j'} \Delta E(vj \rightarrow v'j') d\sigma(vj \rightarrow v'j')/d\omega \\ &= \sum_{j_t} \Delta E(v0 \rightarrow v'j_t) d\sigma(v0 \rightarrow v'j_t)/d\omega = S_1(0) = \text{independent of } j \end{aligned} \quad (9)$$

for the rotationally averaged energy-loss cross section was also derived [14,17,18] and confirmed [19]. $S_1(j)$ includes negative contributions from rotational deexcitation, if $v'=v$ and $j>0$ (or $j>1$ for homonuclear diatomic molecules). The positive contributions from rotational excitation, however, overcome the negative contributions; this is seen by noting that $S_1(0)$ is positive if $v=v'$. The rotationally averaged energy loss by the electron is always positive for $v \leq v'$, unless the electron energy is too low for the adiabatic-rotation approximation to be valid.

Because the rotationally summed cross section $S_0(j)$ and the rotationally

averaged energy-loss cross section $S_1(j)$ are independent of j , their Boltzmann averages $\langle S_0 \rangle$ and $\langle S_1 \rangle$ are independent of the rotational distribution or the rotational temperature T . This result is particularly useful for applications, because the average energy loss is now a function only of the electron energy E rather than a function of two variables E and T .

The average energy-loss cross section is the moment of ΔE of first order. Moments of higher orders are discussed in Ref.(5). The principle of detailed balance transforms the sum rules into those for the sums over the initial rotational state, giving useful information on transitions to a specified rotational state in a further approximation [20].

3.3. Line-shape analysis of energy-loss spectra

Rotational transition lines in energy-loss spectra have been resolved so far only for H_2 , for which the typical line spacings ΔB are about 30 meV, and for D_2 , for which the typical spacings are 15 meV. With the electron spectrometers now available scattering experiments with energy resolution better than about 10 meV are difficult. Therefore, many rotational transition lines for N_2 overlap each other and form a broad feature because of small line spacings of 1 meV. It is impossible to deconvolute the broad feature to determine the cross sections for all transitions involved in this feature.

We have seen, however, that not all the cross sections are linearly independent. Equation (3) usually reduces the number of independent cross sections to only a few, and these cross sections may be treated as fitting parameters to reproduce the shape of the broad feature [14,15,21]. This line-shape analysis yields the cross sections for transitions from the ground rotational state. Then, one may use them in Eq.(3) to obtain the cross sections for all transitions. The experimental cross sections shown in Fig.3 were obtained in this manner [15]. Note that for molecules heavier than the hydrogen the adiabatic-rotation approximation is valid at collision energies at which crossed-beam experiments are possible, i.e., at energies higher than about 10^{-1} eV.

This line-shape analysis produces meaningful results on rotationally inelastic collisions, only if rotational broadening compared with the apparatus function is clearly observed in the energy-loss spectrum. The rotational broadening is appreciable for molecules with a fairly large rotational constant B . For molecules much heavier than N_2 , however, the rotational broadening is unobservable with an energy resolution of about 10 meV, and the line-shape analysis mentioned above does not work.

Read [22] proposed another method of line-shape analysis. He assumed that most molecules are in such high- j states that cross sections for a given $|\Delta j|$ value are practically independent of j . Thus he could determine the cross sections in the limit as j becomes large but not low- j cross sections. A slightly improved method was used by Wong and Dubé [23] and by Jung et al.[24], but it is essentially the same as Read's method, and cannot produce low- j cross sections without the theory discussed in Sec.2. Reference (21) discusses a relation between Read's method and the method of this subsection.

4. SCATTERING AMPLITUDE IN THE ADIABATIC-ROTATION APPROXIMATION

In this section I discuss, just for simplicity of notation, purely rotational transitions only and neglect the vibronic motion of the molecule. In the adiabatic-rotation approximation the rotational motion is separated from the motion of the scattered electron. In other words the wave function ψ for the total collision system is expressed as the product of the wave function $Y_{jm}(\hat{R})$ of the initial rotational state and the wave function of the scattered electron. Therefore, the asymptotic form of ψ is

$$\psi \sim [\exp(i\mathbf{k}\cdot\mathbf{r}) + F(\mathbf{k}\rightarrow\mathbf{k}';\hat{R})r^{-1}\exp(ik'r)]Y_{jm}(\hat{R}). \quad (10)$$

The molecular orientation \hat{R} in the rotational wave function is a variable, but that in the scattering amplitude F is merely a parameter. In other words F is the scattering amplitude for a fictitious collision problem in which the molecular orientation is held fixed during the collision.

The true wave function behaves asymptotically as

$$\psi \sim \exp(i\mathbf{k} \cdot \mathbf{r}) Y_{jm}(\hat{R}) + \sum_{j'm'} f(\mathbf{k}_{jm} \rightarrow \mathbf{k}'_{j'm'}) r^{-1} \exp(ik'r) Y_{j'm'}(\hat{R}). \quad (11)$$

The initial wave vector \mathbf{k} is the same for both Eqs.(10) and (11). The final wave vector \mathbf{k}' in Eq.(11) depends on the rotational channel. In Eq.(10), however, \mathbf{k}' is the final wave vector for the fixed-orientation problem. Comparison of Eqs.(10) and (11) reveals that the scattering amplitude f in the adiabatic-rotation approximation follows if $F Y_{jm}$ is equated to the sum of $f Y_{j'm'}$; we assume that the spherical scattered waves $\exp(ik'r)$ in both Eqs. (10) and (11) are practically the same in accordance with the adiabatic-rotation approximation. Then, the scattering amplitude f for a transition $jm \rightarrow j'm'$ is a coefficient of expansion of $F Y_{jm}$ in terms of the complete set of functions $Y_{j'm'}$:

$$f(\mathbf{k}_{jm} \rightarrow \mathbf{k}'_{j'm'}) = \langle Y_{j'm'} | F(\mathbf{k} \rightarrow \mathbf{k}'; \hat{R}) | Y_{jm} \rangle_{\hat{R}}. \quad (12)$$

This expression was derived by Drozdov [7] and later by Chase [25].

If the correct \mathbf{k}' that depends on the rotational channel is used for the calculation of F in Eq.(12), I would call it an adiabatic-rotation approximation in a broad sense. The Born approximation for the scattering amplitude f follows, if F is calculated to the first-order in the interaction potential. The Glauber approximation follows, if F is calculated in the eikonal approximation.

Use of a common \mathbf{k}' for all rotational channels greatly simplifies the computation of Eq.(12). This is often simply called adiabatic-rotation approximation, but I would call it that in a narrow sense. In this case the adiabatic-rotation relation for the cross sections may be proved by using Eq.(12) with no further approximation [1,7]. In fact the correct relation is slightly different from Eq.(3). Returning to the general rotational-vibrational transitions, we obtain

$$\begin{aligned} (k/k'_{vj}) d\sigma(vj \rightarrow v'j'; \theta) / d\omega \\ = \sum_{jt} (k/k'_{vj_t}) p(jj_t j') d\sigma(v0 \rightarrow v'j_t; \theta) / d\omega. \end{aligned} \quad (13)$$

The wave-number ratio on each side is the initial-to-final wave-number ratio for the process on each side. This factor stems from the expression for the differential cross section in terms of the scattering amplitude; Eq.(3) actually applies to the square of the absolute value of the scattering amplitude. We recover Eq.(3) if we neglect the rotational-channel dependence of the final wave numbers in Eq.(13), just as we did in the derivation of the adiabatic-rotation scattering amplitude in a narrow sense.

5. BREAKDOWN OF THE ADIABATIC-ROTATION APPROXIMATION

5.1. Cases of long collision time

The adiabatic-rotation approximation breaks down, if the collision time is comparable to or longer than the characteristic period of molecular rotation. This occurs in the following three cases:

(A) For narrow resonances, because the resonance lifetime, which may be regarded as the collision time, can be longer than 10^{-12} s, a typical rotational period. This occurs for resonance widths smaller than 1 meV, and could be a serious problem in Feshbach resonance regions. Shape resonances, which are found frequently in low-energy electron-molecule collisions, are usually much

broadener than 1meV, and the adiabatic-rotation theory may be safely applied to most shape resonances.

(B) Close to a threshold of excitation, because the outgoing electron can be very slow then. I will discuss this case in Sec. 5.3 into some details.

(C) For small-angle scattering of an electron by a polar molecule in which purely rotational transitions occur. This case corresponds to distant collisions in which the electron keeps feeling the weak long-range dipole potential, proportional to r^{-2} , for an extended distance along its trajectory. Thus the effective collision time is long. In fact the differential cross section diverges at a zero scattering angle in the adiabatic-rotation approximation in the narrow sense. I will discuss this case in Sec. 5.2.

5.2. Small-angle scattering by a polar molecule

Case C raises no serious problem with the adiabatic-rotation relation. The Born approximation is known to apply to this case because of the weak interaction. The scattering amplitude in the Born approximation takes the form of Eq. (12) in which the correct \mathbf{k}' is used. Partly for this reason the differential cross sections in the Born approximation in this case satisfy a relation

$$\begin{aligned} & (k/k'_{v',j'}) d\sigma(vj \rightarrow v'j'; q)/d\omega \\ &= \sum_{j_t} (k/k'_{v',j_t}) p(jj_t j') d\sigma(v0 \rightarrow v'j_t; q)/d\omega \end{aligned} \quad (14)$$

similar to Eq.(13) but with the same momentum transfer q on both sides rather than the same scattering angle θ . The difference between Eqs.(13) and (14) is significant in case C. It is negligible, however, at larger scattering angles where the adiabatic-rotation approximation in the narrow sense is valid. The difference is also negligible at all scattering angles for nonpolar molecules. Therefore, Eq.(14) applies to both polar and nonpolar molecules at all scattering angles from zero to 180 degrees. In this way the momentum transfer q of Fig. 1b is important particularly in case C.

The range $0 \leq \theta \leq \pi$ of integration over the scattering angle to calculate the integral cross section transforms into the range $|k-k'| \leq q \leq k+k'$ of integration over the momentum transfer. The latter range differs depending on the rotational channel. In particular a small change in the lower limit, which corresponds to forward scattering, changes the integral significantly for pure rotational transitions of a polar molecule (with a dipole moment D), because the differential cross section is strongly peaked towards a zero scattering angle. Near the lower limit of integration we may use an explicit form of the Born cross section for the dipole interaction; other interactions are negligible there. We may use Eq.(13) at larger scattering angles. Regardless of exactly where we switch from the Born approximation into the adiabatic-rotation approximation in the narrow sense, we obtain a relation

$$\begin{aligned} \sigma(j \rightarrow j') &= \sum_{j_t \neq 1} (k'_{j_t}/k'_{j_t}) p(jj_t j') \sigma(0 \rightarrow j_t) \\ &+ p(j1j') [\sigma(0 \rightarrow 1) - (8\pi D^2/3k^2) \ln[(k-k'_{j_t})/(k-k'_1)]] \end{aligned} \quad (15)$$

in atomic units. Only the $j_t=1$ term needs to be modified, because this is the only possible angular-momentum transfer to the first order in the dipole potential. This term vanishes unless $j'=j \pm 1$; $p(j1j')$ is $(j+1)/(2j+1)$ for $j'=j+1$, $j/(2j+1)$ for $j'=j-1$, and zero otherwise.

Sum rules for polar molecules follow from Eq.(15) as

$$S_0(j) = S_0(0) - (8\pi D^2/3k^2) [(j+1)\ln(j+1) + j\ln j]/(2j+1) \quad (16)$$

$$S_1(j) = S_1(0) - 2B(8\pi D^2/3k^2) [(j+1)^2 \ln(j+1) - j^2 \ln j]/(2j+1) \quad (17)$$

on the assumption that the wave-number ratios are negligible. Boltzmann ave-

rages of Eqs.(16) and (17) show temperature dependence

$$\langle S_0 \rangle = \langle S_0 \rangle_{T=0} - \frac{1}{2} (8 \pi D^2 / 3 k^2) \ln(k_B T / B) \quad (18)$$

$$\langle S_1 \rangle = \langle S_1 \rangle_{T=0} - B (8 \pi D^2 / 3 k^2) \ln(k_B T / B) \quad (19)$$

for $k_B T \gg B$, k_B being the Boltzmann constant.

A computational procedure closely related to the discussion in this subsection has been applied by Norcross, Padial, and Jain to calculate the cross sections for rotational-vibrational transitions of polar molecules HCl, HCN, and CO [26]. They use the adiabatic-rotation approximation in the narrow sense for close collisions (low partial waves) and the Born approximation for distant collisions (high partial waves).

5.3. Close to excitation threshold

The scattering amplitude is small at energies very close to a threshold of rotational excitation. This allows the first-order perturbation theory or the Born approximation to be applied at these energies. Unfortunately, the adiabatic-rotation approximation breaks down at higher energies than the energies at which the Born approximation is valid. More sophisticated calculations are necessary to fill in the gap between the energy regions of applicability of these two simple methods.

Simple modifications of the adiabatic-rotation approximation in the narrow sense (ARA) have been considered such that the dependence of the wave number on the rotational channel may be taken into account. Nesbet [27] has proposed an "energy-modified adiabatic" approximation (EMA), and Feldt and Morrison [28] have proposed a "scaled adiabatic-rotation" approximation.

Morrison et al. [29] have studied the breakdown of ARA by comparing it on electron scattering by H_2 with laboratory-frame close-coupling calculations (LFCC), which should really be done close to a threshold. Figure 4 shows the percentage deviation of the ARA and EMA cross sections for rotational excitation $j=0 \rightarrow 2$ from the accurate LFCC results. The excitation energy ΔE is 44 meV. ARA begins to deviate from LFCC at about $E=100\Delta E$, but the relative error in ARA is 10% at $E=4\Delta E$ and 30% at energies very close to the threshold. The $j=1 \rightarrow 3$ cross section satisfies to a good accuracy the adiabatic-rotation relation (3) in terms of the $j=0 \rightarrow 2$ and $0 \rightarrow 4$ cross sections. The deviation from Eq.(3) is

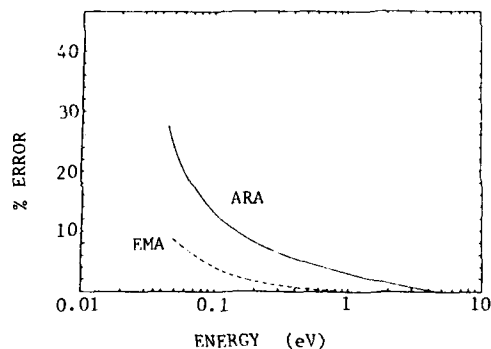


FIGURE 4

Percentage errors of approximate $e-H_2$ integral cross sections for $j=0 \rightarrow 2$ excitation. ARA: adiabatic-rotation approximation in the narrow sense. EMA: energy-modified adiabatic approximation (taken from Ref.(29)).

only 10% at $E=2\Delta E$ ($\Delta E=73\text{meV}$) and 20% at $E=1.1\Delta E$. On the other hand the accuracy of the ARA differential cross sections depends strongly on the scattering angle. The $j=0\rightarrow 2$ cross section at 0.1eV at a zero scattering angle, for example, deviates from the LFCC result by a factor of three [29].

Extension of the study of the breakdown of ARA to other molecules is highly desirable, because H_2 is too special a molecule; it is a nonpolar molecule, it has only two electrons, the nuclear charge is small and the potential singularity at the nuclear positions is weak, and the potential field is nearly spherical.

6. EXTENSION TO NONLINEAR MOLECULES

Linear molecules in non- Σ states and many nonlinear molecules may be regarded as nonlinear rigid rotators. They have three principal moments of inertia. If all of them are unequal, the rotator is called an asymmetric top. An example of an asymmetric top is the H_2O molecule. If two principal moments of inertia are equal, the rotator is a symmetric top, of which an example is the NH_3 molecule. If all principal moments of inertia are equal, the rotator is a spherical top, of which an example is the CH_4 molecule.

Many of the results I have discussed so far in this talk are generalizable for nonlinear rigid rotators. The sum rules (8) and (9), for example, have been generalized for all kinds of rigid rotators [17]; the rotationally summed cross section and the rotationally averaged energy-loss cross section are independent of the initial rotational state, if they are averaged over the degenerate initial sublevels.

The adiabatic-rotation relation (3) has been generalized for symmetric tops [7] and for spherical tops [15,18]. The result for the latter rotators takes a form (3) with a probability

$$p(jj_tj') = (2j'+1)/[(2j+1)(2j_t+1)]. \quad (20)$$

No simple adiabatic-rotation relation for the real cross sections is known for asymmetric tops, but the complex scattering amplitudes satisfy a relation similar to but more complicated than Eq.(3) [30].

Müller et al. have used Eq.(20) for line-shape analysis of electron energy-loss spectra for CH_4 according to the prescription in Refs.(15) and (21) [31].

High- j relation (7) has been generalized for symmetric-top rotators [32], but not yet for asymmetric-top rotators.

7. CONCLUSIONS

The adiabatic-rotation theory has a wide applicability in electron-molecule collisions. It leads to many simple and useful relations for cross sections. There are some cases, however, where this theory has to be either modified or replaced by more accurate theory. One has to carefully examine in what cases and how the adiabatic-rotation theory deviates from the reality. Although the relations derived from the adiabatic-rotation theory apply also to photoionization and heavy-particle collisions, different modifications have to be made for different classes of processes when the theory in the simplest form breaks down. I have not mentioned those references which are closely related to the present subject but are specific to atom-molecule and ion-molecule collisions.

REFERENCES

- 1) I. Shimamura, Rotational excitation of molecules by slow electrons, in: *Electron-Molecule Collisions*, eds. I. Shimamura and K. Takayanagi (Plenum,

- New York, 1984) pp.89-189.
- 2) For example, M.E. Rose, *Elementary Theory of Angular Momentum* (John Wiley, New York, 1957).
 - 3) P.J. Brussaard and H.A. Tolhoek, *Physica* **23** (1957) 955.
 - 4) S.S. Bhattacharyya and A.S. Dickinson, *J. Phys.* **B12** (1979) L521.
 - 5) I. Shimamura, *Zeit. f. Phys.* **A309** (1982) 107.
 - 6) I. Shimamura, *Phys. Rev. A* **28** (1983) 1357.
 - 7) S.I. Drozdov, *Sov. Phys. JETP* **1** (1955) 591; *ibid.* **3** (1956) 759.
 - 8) S. Hara, *J. Phys. Soc. Jpn.* **27** (1969) 1592.
 - 9) E.S. Chang and A. Temkin, *Phys. Rev. Lett.* **23** (1969) 399.
 - 10) A.D. Buckingham, B.J. Orr, and J.M. Sichel, *Phil. Trans. Roy. Soc. London* **A268** (1970) 147.
 - 11) J.M. Sichel, *Mol. Phys.* **18** (1970) 95.
 - 12) U. Fano and D. Dill, *Phys. Rev. A* **6** (1972) 185.
 - 13) For example, R. Goldflam, D.J. Kouri, and S. Green, *J. Chem. Phys.* **67** (1977) 5661; V. Khare, *J. Chem. Phys.* **68** (1978) 4631.
 - 14) I. Shimamura, Systematics in the cross sections for excitation of molecules by electrons, in: *Symposium on Electron-Molecule Collisions*, eds. I. Shimamura and M. Matsuzawa (Univ. Tokyo, Tokyo, 1979) pp.13-30.
 - 15) I. Shimamura, *Chem. Phys. Lett.* **73** (1980) 328.
 - 16) S. Altshuler, *Phys. Rev.* **107** (1957) 114.
 - 17) I. Shimamura, *Phys. Rev. A* **23** (1981) 3350.
 - 18) I. Shimamura, *J. Phys.* **B15** (1982) 93.
 - 19) D.W. Norcross, *Phys. Rev. A* **25** (1982) 764.
 - 20) I. Shimamura, *Progr. Theor. Phys. (Kyoto)* **68** (1982) 178.
 - 21) I. Shimamura, Line-shape analysis of energy-loss spectra and photoelectron spectra, in: *Wavefunctions and Mechanisms from Electron Scattering Processes*, eds. F.A. Gianturco and G. Stefani (Springer, Berlin, 1984) pp.210-214.
 - 22) F.H. Read, *J. Phys.* **B5** (1972) 255.
 - 23) S.F. Wong and L. Dubé, *Phys. Rev. A* **17** (1978) 570.
 - 24) K. Jung, Th. Antoni, R. Müller, K.-H. Kochem, and H. Ehrhardt, *J. Phys.* **B15** (1982) 3535.
 - 25) D.M. Chase, *Phys. Rev.* **104** (1956) 838.
 - 26) D.W. Norcross and N.T. Padial, *Phys. Rev. A* **25** (1982) 226; N.T. Padial and D.W. Norcross, *ibid.* **29** (1984) 1590; A. Jain and D.W. Norcross, *ibid.* **32** (1985) 134; A. Jain and D.W. Norcross, *ibid.*, to be published.
 - 27) R.K. Nesbet, *Phys. Rev. A* **19** (1979) 551.
 - 28) A.N. Feldt and M.A. Morrison, *Phys. Rev. A* **29** (1984) 401.
 - 29) A.N. Feldt and M.A. Morrison, *J. Phys.* **B15** (1982) 301; M.A. Morrison, A.N. Feldt, and D. Austin, *Phys. Rev. A* **29** (1984) 2518.
 - 30) S. Green, *J. Chem. Phys.* **70** (1979) 816.
 - 31) R. Müller, K. Jung, and H. Ehrhardt, in: *Electronic and Atomic Collisions, XIV ICPEAC, Abstracts of Contributed Papers*, eds. M.J. Coggiola et al. (1985) p.234.
 - 32) I. Shimamura and A.C. Roy, in: *Electronic and Atomic Collisions, XIV ICPEAC, Abstracts of Contributed Papers*, eds. M.J. Coggiola et al. (1985) p.211.

POSITRON (AND ELECTRON) SCATTERING BY ATOMS AND MOLECULES

Talbert S. STEIN and Walter E. KAUPPILA

Department of Physics and Astronomy, Wayne State University,
Detroit, Michigan 48202, U.S.A.

In this paper, attention is focused upon recent developments in the general area of positron-gas scattering experiments, with an emphasis on the intriguing differences and similarities between the scattering of positrons and electrons by the same target gases.

1. INTRODUCTION

The study of electron (e^-)-atom (molecule) collisions has been a lively area of research for the past several decades, and has played a vital role in the development of our present understanding of atomic and molecular physics. Considering the positron (e^+) as a complementary probe, the combination of intriguing differences (opposite sign of the projectile charge, and absence of the exchange interaction in the case of the e^+) and similarities (same magnitudes for the mass, charge, and spin) of the e^+ and the e^- has stimulated numerous experimental and theoretical investigations of e^+ -atom (molecule) collisions since the development of the first practical low energy e^+ beam [1] for scattering experiments in 1972. Some simple theoretical considerations help to provide insight into the interesting differences and similarities between e^+ and e^- scattering from the same atoms and molecules. The static interaction (associated with the interaction of the projectile with the Coulomb field of the undistorted atom) is attractive for the e^- and repulsive for the e^+ , while the polarization interaction (resulting from the distortion of the atom by the passing charged projectile) is attractive for both projectiles. The exchange interaction contributes to e^- scattering (due to the indistinguishability of the projectile and electrons in the target atoms) but does not play a role in e^+ scattering. The net effect of the static and polarization interactions is that they add to each other in e^- scattering whereas they tend to cancel each other in e^+ scattering. In general, this results in smaller total scattering cross sections for positrons than for electrons at low energies. As the projectile energy is increased, the polarization and exchange interactions eventually become negligible compared with the static interaction, and since the static interaction has the same magnitude for positrons and electrons, the result is a merging of the corresponding e^+ and e^- scattering cross sections at sufficiently high projectile energies. Two additional scattering processes which occur for positrons are annihilation and positronium (Ps) formation (real and virtual). Annihilation is not expected [2] to play a significant role in scattering at the energies which have been used in e^+ scattering experiments (>0.2 eV). However, Ps formation has been found to be an important factor in e^+ -gas collisions [3-8].

In a number of ways, e^+ -gas scattering experiments have been following a path similar to that followed by early e^- -gas scattering experiments. During the first decade of scattering experiments using low energy e^+ beams, attention was focused primarily on measuring total scattering cross sections (Q_T) for positrons colliding with room temperature gases, including the inert gases and a variety of molecules [3-9]. In recent years, as e^+ beam

technology has improved, the first steps have been taken toward directly measuring the cross sections for the separate processes [10] (including Ps formation [11-14], atomic excitation [15-17], and ionization cross sections [17-19]) which contribute to Q_T , and toward making direct measurements of differential elastic cross sections (DCS) [20,21] for e^+ -gas collisions. In addition, Q_T measurements for positrons are now being extended to non-room-temperature gases (the alkali atoms) [22]. One of the side-benefits of having the e^+ experiments retracing some of the steps taken by the corresponding earlier e^- experiments, is that new experimental apparatuses and approaches developed for positrons are sometimes "tested" by applying the same approaches to electrons to see if one obtains the "accepted" e^- results. However, it is not always clear which of the sets of e^- results are the "accepted" results, since not all of the discrepancies involving e^- -gas scattering measurements and theories have been resolved. The "testing" of e^+ experimental techniques by applying them to electrons thus provides an incentive for redoing some of the e^- -gas scattering measurements which has potential for helping to clear up some of the "unfinished business" that still remains in that area of research.

Aside from the connections between e^+ and e^- -gas scattering, e^+ -atom scattering is intrinsically interesting because it involves interactions of antimatter with matter. Interest in such interactions has been intensified by a series of balloon and satellite experiments dating back to the early 1970's which have detected e^+ annihilation gamma rays coming from solar flares [23], and have also established the existence of a powerful, compact source of e^+ annihilation radiation which appears to be located at the center of our own Milky Way galaxy [24]. After having been "on" for most of the decade of the 1970's, the source was observed to turn "off" rather abruptly at the end of the last decade and appears to have remained "off" through the most recent observations made in November of 1984 [25]. If the latter source is indeed located at the galactic center, the observed intensity of the annihilation gamma ray line would imply an annihilation rate of 10^{43} annihilations per second which corresponds to approximately 10^{38} ergs per second in annihilation radiation which amounts to about 10^5 solar luminosities. From the short period of time over which the source was observed to turn off, the size of the source is estimated to be less than six light-months in extent which is compact on a galactic scale (considering that the solar system is approximately 30,000 light-years from the galactic center) [25]. Annihilation gamma ray observations such as those referred to above can provide considerable information on the type of environment which exists at the site of their origin if sufficient information can be obtained on the ways in which positrons interact with H, H_2 , and other atoms and molecules of astrophysical interest [25-27].

Several comprehensive review papers and progress reports have been published [3-9] which have included detailed surveys, assessments, and comparisons of the various experiments and theoretical calculations related to total cross sections for positrons colliding with room temperature gases. Rather than attempt a comprehensive extension of such assessments and comparisons in this paper, we will point out what we feel are some of the most significant developments in the general area of e^+ -gas scattering research including total scattering cross sections for room temperature gases as well as some of the more recent developments which go beyond that specific area. Comparisons between positrons and electrons scattering from various gases will be emphasized in these discussions.

2. EXPERIMENTAL POSITRON BEAM TECHNIQUES

The methods for producing low, and well-defined energy- e^+ beams have been discussed extensively elsewhere [3,5-8,28]. We will just emphasize a few of

the considerations which we feel are most relevant to e^+ -gas scattering experiments. The most widely used e^+ source has been ^{22}Na , primarily because of its relatively long half-life (2.6 years) coupled with the commercial availability of high intensity ^{22}Na sources in useful configurations. Other approaches to obtaining positrons for e^+ -gas scattering experiments have included the use of a 55 MeV e^- linear accelerator [1] to produce positrons by pair production, and the use of a 4.75 MeV proton beam of a Van de Graaff accelerator to produce an ^{11}C e^+ source [29] by the reaction $^{11}\text{B}(p,n)^{11}\text{C}$. A variety of moderators used in either a backscattering or transmission mode have been found to yield low-energy positrons with relatively narrow energy distributions when exposed to the high-energy, broad energy-width fluxes resulting from e^+ sources [28].

Two properties of moderators which are of particular interest in e^+ -gas scattering experiments are (1) the energy width of the emitted slow e^+ beam (full-width at half-maximum), and (2) the "conversion efficiency" defined as the ratio of the slow e^+ emission rate of the moderator to the total rate of e^+ production by the radioactive source. A moderator with one of the highest available conversion efficiencies (10^{-3}) which can be readily used in e^+ -gas scattering experiments, is relatively stable over long periods of time, and can be exposed to air without appreciable degradation, is annealed tungsten [30,31]. Although the energy width of the low energy e^+ beam emitted by annealed tungsten in a backscattering mode is relatively broad [31] (of the order of 2 eV), there are many different types of e^+ scattering experiments which can be performed with such a source without the need for any further energy monochromatization [14,19,21]. The ^{11}C source referred to above, used in a self-moderating mode, has a much narrower energy width [32] (less than 0.1 eV), but it also has a much lower conversion efficiency (10^{-6}) than an external annealed tungsten moderator. However, for experiments which demand a better energy resolution, such a moderator has been found to be very useful [8,33].

Some recent developments in low energy e^+ beam technology may have potential for applications in the area of e^+ -gas scattering experiments. The highest reported low-energy e^+ beam intensities up to the present time have been produced at Lawrence Livermore National Laboratory (LLNL) and at Brookhaven National Laboratory (BNL). The LLNL e^+ beam has an intensity of 7×10^9 slow e^+ /sec instantaneous (2×10^7 slow e^+ /sec time averaged), and is derived by moderation (using tungsten vanes) of high-energy positrons produced by pair production in a tungsten target irradiated by electrons at the LLNL 100 MeV e^- linac [34]. An e^+ beam with 10^7 slow e^+ /sec has been produced at the BNL using a reactor produced ^{64}Cu e^+ source [35]. The ^{64}Cu is evaporated in situ onto a W(110) substrate prepared by heating to form a self-moderating source. With a much less elaborate experimental set-up, an e^+ beam of intensity, 5×10^5 slow e^+ /sec has been generated by Van House and Zitzewitz [31] using a ^{22}Na source and an annealed tungsten moderator. It has also been found that positrons emitted from moderators are, in general, polarized [31,36] and a degree of polarization as high as 0.69 \pm 0.04 has been achieved using an MgO moderator [31].

Techniques [8] which have been used for analyzing the energy of e^+ beams are basically the same as those used for electrons, and include the use of time-of-flight, 90° electrostatic analyzers, a transverse magnetic field with beam-defining apertures, and retarding electrostatic fields. Methods which have been used for e^+ detection [3,5-8] include (1) observing the two coincident annihilation gamma rays with two NaI scintillation counters, (2) observing one or both annihilation gamma rays with a single NaI well counter, and (3) using a Channeltron electron multiplier (CEM). The CEM has become the preferred detector in many experiments due to its high e^+ detection efficiency and its relatively small size and ease of use.

3. TOTAL CROSS SECTION MEASUREMENTS

The basic experimental method used by all of the groups which have measured Q_T for positrons is to study the attenuation of the e^+ beam as it passes through a gas scattering region. Under "ideal" experimental conditions, Q_T can be obtained from the expression,

$$I = I_0 e^{-nLQ_T}$$

where I_0 is the detected beam intensity with no gas in the scattering region, I is the detected beam intensity with gas of number density n in the scattering region, and L is the path length of the e^+ beam through the scattering region.

Recent review papers and progress reports [3,5-9] have included detailed discussions of the various techniques used to measure e^+ -gas Q_T values and have also included discussions of nearly all the results (including He, Ne, Ar, Kr, Xe, H₂, D₂, N₂, O₂, CO, CO₂, CH₄, and N₂O) obtained up to the early part of 1983.

The qualitative features of the low energy e^+ Q_T curves for the inert gases are summarized in Fig. 1 where they are compared with the corresponding e^- Q_T curves. Ramsauer-Townsend effects (minima in Q_T due to quantum mechanical effects associated with a net attractive interaction between the projectile and the target atom) are observed for positrons colliding with the lighter inert gases (He, Ne, and possibly a shallow minimum for Ar), whereas the situation is reversed for electrons which exhibit Ramsauer-Townsend effects only for the heavier inert gases (Ar, Kr, and Xe). Another qualitative feature of the e^+ curves is the dramatic increase in Q_T at the thresholds for Ps formation in each of the gases. The e^+ curves in Fig. 1 can be used to estimate Ps formation cross sections (Q_{Ps}) (crosshatched regions) for e^+ energies between the thresholds for Ps formation and atomic excitation, assuming that the elastic scattering cross sections are smoothly varying as the e^+ energy increases through the Ps formation thresholds. However there is now evidence [37] that such an assumption may not necessarily be valid. (For a further discussion of Q_{Ps} , refer to Sec. 5.1).

The e^+ -He Q_T comparison measurements [38] (up to intermediate energies) shown in Fig. 2 provide a striking illustration of some of the differences and similarities in e^+ and e^- scattering. At low energies, the e^+ cross section is about two orders of magnitude smaller than the e^- cross section. This is consistent with the fact that the static and polarization interactions are both attractive in the e^- case, whereas there is a tendency toward cancellation of these interactions in the e^+ case. In contrast to the large difference between the cross sections at low energies there is an observed merging (to within 2%) of the e^- and e^+ results above 200 eV. Although as was mentioned in the introduction, a merging of the e^+ and e^- cross sections is expected at sufficiently high projectile energies, when the polarization and the exchange interactions (for electrons) are negligible compared to the static interaction, the merging of the Q_T curves was not expected to occur at such low energies. The e^+ and e^- distorted wave second Born approximation (DW) calculations of Dewangan and Walters [39] do not merge (to within 2%) until 2000 eV. At 200 eV, where the measurements of Kauppila et al. indicate a merging to within 2%, the DW e^- calculations are 21% higher than the corresponding e^+ calculations. Another curious aspect of the observed merging of the e^+ and e^- Q_T values above 200 eV is that recent theoretical estimates [40] suggest that at 200 eV, the e^- total elastic cross section is nearly four times as large as the e^+ total elastic cross section. This raises the question of how Q_T for e^+ and e^- -He collisions can merge near 200 eV when these projectiles appear to be behaving much differently with respect to elastic scattering at that energy. Is there some overriding consideration that governs the merging of e^+ and

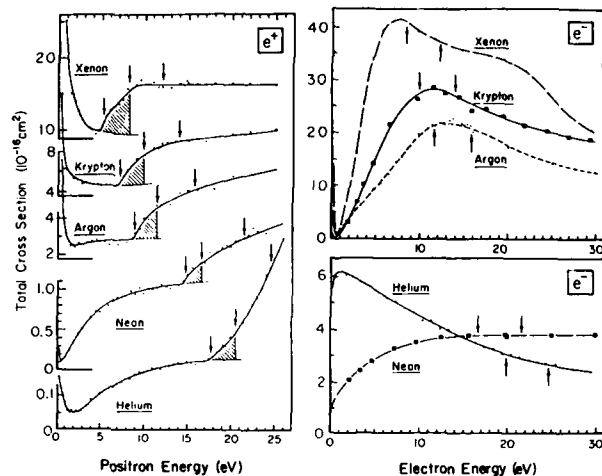


FIGURE 1

Q_T curves for low-energy e^+ -inert gas and e^- -inert gas scattering. The arrows, in order of increasing energy, refer to the thresholds for Ps formation, atomic excitation and ionization for e^+ scattering, and atomic excitation and ionization for e^- scattering. (From Stein and Kauppila, Ref. 8)

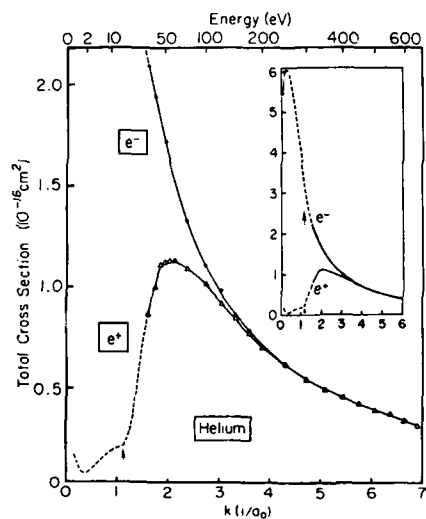


FIGURE 2

Comparison of measured e^+ -He and e^- -He total cross sections up to intermediate energies. The lowest inelastic thresholds for each projectile are indicated by arrows. (From Kauppila et al., Ref. 38)

e^- Q_T values at an energy where the separate processes that contribute to Q_T may still be exhibiting very dissimilar behavior? It should be noted that comparison $e^+,-$ Q_T measurements [38,41] for Ne, Ar, Kr, and Xe indicate a tendency toward a merging but an actual merging of the cross sections has not been observed at the highest energies studied.

The first Q_T measurements for e^+-N_2O collisions, recently reported by Kwan et al. [42] are shown in Fig. 3 with the corresponding e^- measurements and with prior $(e^+,-)CO_2$, $(e^+,-)N_2$, and $(e^+,-)CO$ Q_T measurements [37,44]. It has been known for some time that the isoelectronic pair, N_2 and CO , scatter electrons in remarkably similar ways because of their similar structure, in spite of their very different chemical behavior. Since the isoelectronic pair of molecules, N_2O and CO_2 are obtained by adding a single oxygen atom to N_2 and CO , it is of interest to determine whether these molecules also exhibit similar scattering characteristics. It is observed that above 5 eV, the shape and magnitude of the Q_T results for both N_2O and CO_2 are very similar for each projectile. The e^- Q_T curves are within a few percent of each other above 5 eV, while the e^+-N_2O Q_T results are slightly but noticeably higher than those for the e^+-CO_2 system. Although the differences between the molecules become more pronounced at the lowest energies, due to the greater role played by the internal structures of the respective molecules, there are similarities in the qualitative behavior even at low energies. For e^- scattering, there are prominent shape resonances at 2.3 and 3.8 eV for N_2O and CO_2 respectively, and broad maxima around 25 eV for N_2O and 30 eV for CO_2 . For positrons, there are also similar features in the Q_T curves for N_2O and CO_2 . The shape resonances observed at low energies in the e^- case are absent for e^+ scattering from these gases. The e^+ Q_T 's increase rapidly below 2 eV.

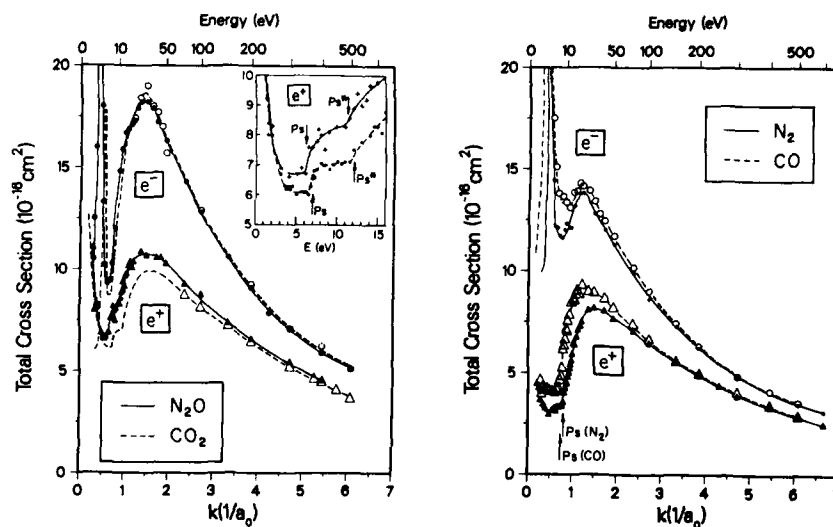


FIGURE 3

Comparison of $(e^+,-)N_2O$, CO_2 , N_2 , and CO Q_T values up to intermediate energies. The threshold energies for formation of Ps in the ground and first excited states are indicated by arrows labeled Ps and Ps*, respectively. (From Kwan et al., Ref. 42)

Both e^+ curves show an abrupt increase at the respective Ps formation thresholds, suggesting a significant increase of inelastic scattering (due to Ps formation) at these energies. There appears to be a second increase in the Q_T curves for N_2O and CO_2 about 5 eV above each Ps formation threshold (see insert of Fig. 3). These latter increases in the Q_T curves may be associated with formation of Ps in the first excited state, although recent experimental investigations [45] of this possibility for CO_2 have not provided evidence of appreciable Ps being formed in the first excited state.

Comparisons between e^- and e^+ measurements [43,44] of Q_T for N_2 and CO indicate a very similar situation as has been observed for N_2O and CO_2 with respect to striking similarities and some small differences in the shapes and magnitudes of the respective Q_T curves. For e^- scattering, both gases exhibit shape resonances at low energies and agree to within a few percent of each other for e^- energies above 10 eV. For e^+ scattering, the shape resonances are absent and both gases exhibit very similar shapes. An interesting feature of the curves shown in Fig. 3 that was pointed out by Kwan et al. [42] is that both of the polar molecules, CO and N_2O have noticeably larger Q_T 's for e^+ scattering than the corresponding nonpolar molecules, N_2 and CO_2 , while the Q_T 's for e^- scattering by these two pairs of molecules are much closer to each other than for e^+ scattering. Kwan et al. [42] have speculated that the larger differences in the Q_T measurements for e^+ scattering than for e^- scattering by N_2O and CO_2 and by N_2 and CO, may result from the permanent dipole moments of N_2O and CO having a greater effect on e^+ scattering.

As an illustration of some possibly "unfinished business" in e^- -atom (molecule) scattering measurements alluded to in the introduction to this paper, which can be encountered when e^+ -experimenters redo e^- scattering measurements to "test" their e^+ apparatuses and techniques, the Q_T measurements of Kwan et al. [42] for low energy e^- - N_2O collisions are shown in Fig. 4 with prior measurements. It is interesting to see how similar the three sets of measurements are away from the peak of the shape resonance, but how different they are in the vicinity of the peak of that resonance. This is not an isolated case, as the low energy e^- - CO_2 and e^- -CO Q_T curves in Refs. 43 and 44 respectively, show. In all three cases, the measurements of the Wayne State University group [42-44] are higher than the other measurements in the vicinity of the peak of the respective shape resonances and in better agreement with the prior measurements away from the respective peaks. One possible explanation for a discrepancy of this type would be that small angle scattering becomes more pronounced in the vicinity of the peak of the shape resonance, and the lower results are being influenced more by a lack of sufficient angular discrimination, but we have no basis at this time for suggesting that this is indeed the explanation for the observed experimental discrepancies.

The first Q_T measurements for positrons colliding with a non-room-temperature gas (potassium) have recently been reported by Stein et al. [22] using a thermally isolated oven as the scattering cell (shown in Fig. 5) in a beam transmission experiment. Determinations of (1) the attenuation of the beam by the K vapor, (2) the number density, n , of K atoms in the oven, which is obtained by measuring the oven temperature at three different locations in the oven walls and in the oven's interior and by using published vapor pressure data, and (3) the path length, L , of the projectiles through the oven, are used to obtain absolute Q_T values. A unique feature of e^+ -alkali collisions is that since the alkalis all have ionization potentials less than the binding energy (6.8 eV) of Ps in its ground state, an e^+ with arbitrarily small kinetic energy can form Ps. Another distinguishing feature of the alkalis is that their polarizabilities are considerably larger than those of any of the gases which have been studied for positrons. Q_T values for e^+ -K collisions [22] are shown in Fig. 6 along with theoretical estimates of the elastic cross sections [46,47] (Q_E), and

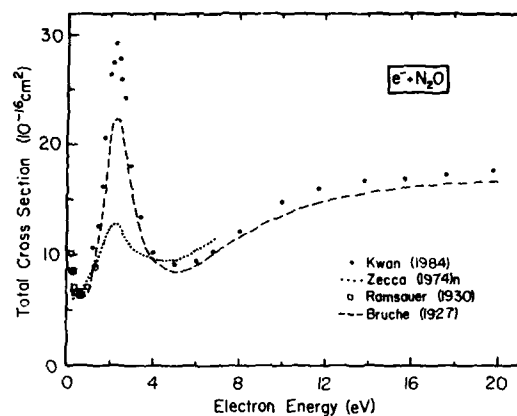


FIGURE 4
Low energy e^- - N_2O Q_T measurements. For references to all of the work displayed in this figure, please see Ref. 42. (From Kwan et al., Ref. 42.)

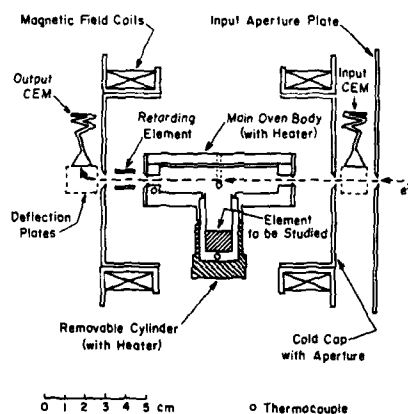


FIGURE 5
(e^+ , -)-alkali scattering apparatus.
(From Stein et al., Ref. 22)

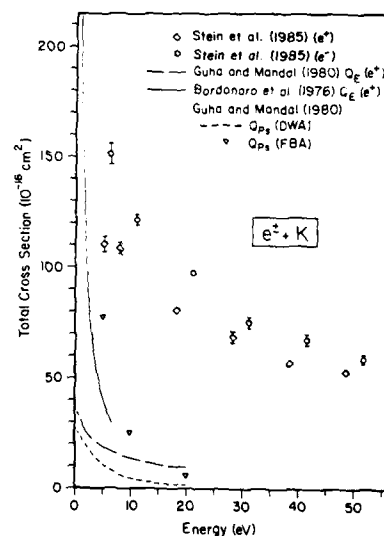


FIGURE 6
(e^+ , -)-K Q_T values.
(From Stein et al., Ref. 22)

Q_{ps} [47], and for comparison, the corresponding $e^- Q_T$ results. The direct comparisons of e^+ and $e^-K Q_T$ values indicate that the $e^+ Q_T$ values are lower than the e^- values from 5 to 50 eV, but it is intriguing that they are closer to the corresponding e^- values (within 25%) over this energy range than has been the case for any other gases for which such comparisons have been made. The measured $e^+ Q_T$ values are more than twice as large as the theoretical estimates of Q_E by Bordonaro et al. [46] at the only energy of overlap (5 eV) and are more than five times as large as the theoretical estimates of Q_E by Guha and Mandal [47] at all energies of overlap. The discussion above suggests the possibility that for positrons between 10 and 50 eV, excitation or perhaps ionization (for both of which no measurements or calculations of cross sections yet exist for K) may make the major contribution to Q_T (as is the case for e^-K collisions [48]).

One possible interpretation [22] of the proximity of the e^+ and $e^- K Q_T$ results at low energies is that the polarizability of K is so large that it could be overwhelming the static interaction at the low energies used in these experiments, even when dynamical (non-adiabatic) effects [48] are taken into account. As a result, the tendency of the static and polarization interactions to cancel each other in the case of e^+ scattering and to add in the case of e^- scattering may not differentiate between these projectiles to the same degree for K as it does in scattering from targets of much lower polarizability. Extending this train of thought, there could be a diverging of the e^+ and $e^- Q_T$ values at intermediate energies due to a more complete cancellation of the polarization and static interactions in the e^+ case (in contrast to an addition of these interactions in the e^- case) where the polarization interaction diminishes to become more comparable in magnitude to the static interaction. Finally, at sufficiently high energies where the polarization interaction has become relatively insignificant, the e^+ and $e^- Q_T$ values would be expected to merge and would be given by the first Born approximation.

4. DIFFERENTIAL SCATTERING CROSS SECTIONS

The first measurements of differential cross sections (DCS) for positrons were reported by Coleman and McNutt [20] for the elastic scattering of 2-9 eV positrons by Ar for angles from 20-60°, using a time-of-flight (TOF) spectrometer shown schematically in Fig. 7. In their experiment, slow positrons pass through a 1-cm-long gas cell and then travel approximately 25 cm through an evacuated straight flight tube in a strong axial magnetic field to a detector (Channeltron electron multiplier). The larger the angle through which an e^+ is scattered in the gas cell, the longer its TOF will be in the axial magnetic field, and it is this correlation that is used to determine DCS's for positrons. The DCS's measured by Coleman and McNutt for e^+-Ar collisions are compared with the calculations of Schrader [50] (solid lines) and "scaled-down" calculations of McEachran et al. [51] (broken lines) in Fig. 8. The agreement between experiment and theory is reasonable.

Direct measurements of relative DCS's for the elastic scattering of positrons (and electrons) by Ar have recently been reported by Kauppila et al. [21] using a differentially-pumped crossed-beam scattering system shown in Fig. 9. The scattering occurs in a "field-free" region where the projectile e^+ beam passes through a target gas beam (effusing from a multi-channel capillary array source) and the scattered positrons are detected at angles ranging from 30 to 135°. The retarding elements preceding detector #2 are used to reject any inelastically scattered positrons. Detector #1 is offset from the primary beam direction so that it will not respond to any high energy positrons that may be coming directly from the ^{22}Na e^+ source. In order to obtain relative DCS results, a constant "head" pressure is maintained on the capillary array atom source and the ratio of the scattered positron beam

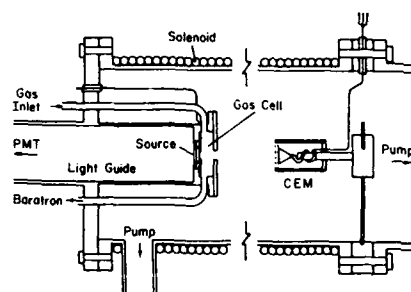


FIGURE 7
Texas TOF spectrometer.
(From Coleman et al., Ref. 49)

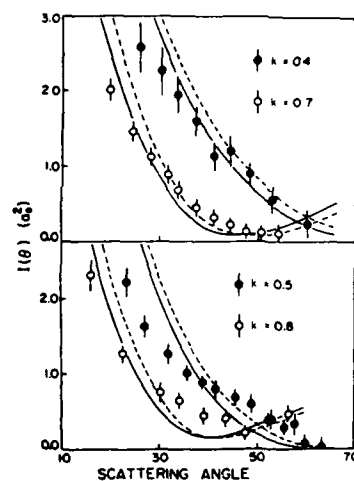


FIGURE 8
DCS results for e^+ -Ar scattering.
(From Coleman and McNutt, Ref. 20)

intensity to the primary beam intensity is measured. The initial DCS measurements of Kauppila et al. for 100 eV positrons and electrons elastically scattered by Ar are shown in Fig. 10 where they are normalized to prior work at either 60 or 90° (indicated by an "N" in the figure) and compared with other experimental [52] and theoretical [53,54] results. The relative shapes of the respective e^+ , e^- results of Kauppila et al. [21] are in good agreement with the prior results. Unfortunately, the measurements for positrons do not extend down to sufficiently small angles to provide a check of the structure

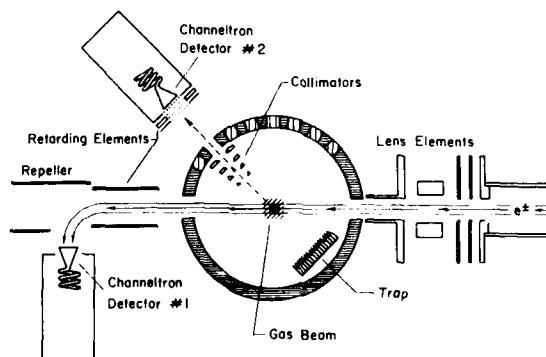


FIGURE 9
Experimental setup for DCS measurements. (From Kauppila et al., Ref. 21)

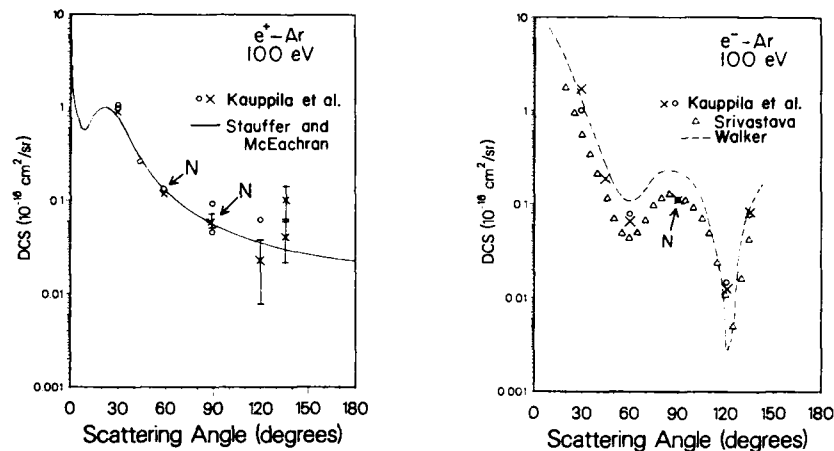


FIGURE 10
Elastic DCSs for $e^+-\text{Ar}$ at 100 eV. (From Kauppila et al., Ref. 21)

predicted by the polarized orbital calculations of McEachran and Stauffer [54] for angles less than 30° . However, since the predicted structure shifts to larger angles for lower e^+ energies [54], it should be somewhat easier to check for the presence of such structure at lower energies. It is also to be noted that the shape of the theoretically predicted [54] DCS curve for positrons at 100 eV is appreciably different from that for electrons [53].

5. INELASTIC SCATTERING INVESTIGATIONS

5.1 Cross Sections for Ps Formation and Ionization by Positron Impact

In this section we will focus our attention on recent relatively direct approaches for measuring Q_p and ionization cross sections and we refer the reader to Refs. 6-8, 10, and 55 for discussions of earlier indirect approaches. The first direct measurements of the energy dependence of the ortho-positronium (o-Ps) formation cross section in He, Ar, H_2 , and CH_4 were made by Charlton et al. [11] by passing a slow e^+ beam through a scattering chamber and counting triple coincidences from the 3 gamma decay of o-Ps. Using a higher e^+ beam intensity and an improved data collection and analysis system, Charlton et al. [12] and Griffith [13] have respectively reported more recent Q_p values in the noble gases [12] and some molecular gases [13] from threshold to 150 eV. Their relative measurements were put on an absolute scale by normalizing to $Q_T - Q_E$ below the respective excitation thresholds.

Experiments have been set up at the University of Texas at Arlington [14,18,56] and at the University of Bielefeld [19] which can provide cross sections for Ps formation and for ionization by e^+ impact. At the University of Texas at Arlington, Fornari et al. [14], and more recently, Diana et al. [56] have measured absolute cross sections for Ps formation in $e^+-\text{He}$, Ar, and H_2 collisions using a technique which is complementary to that of Charlton et al. [11,12]. Rather than detecting Ps formed in a gas cell, Fornari et al. and Diana et al. detect all the positrons which leave the gas cell without forming Ps. The earlier approach by Fornari et al. [14]

employed a TOF spectrometer. In the most recent version of the University of Texas at Arlington Q_{PS} experiments [56,57] (shown schematically in Fig. 11), some simple modifications were made so that the apparatus could be used without timing to directly measure Q_{PS} . The gas to be studied fills the entire region between the source and detector (CEM). The constant 210 G axial magnetic field in the scattering region constrains essentially all positrons to helical paths that eventually reach the CEM detector. The moderator mesh to which the potential that determines the e^+ beam energy is applied, reflects backscattered positrons. The cylindrical retarding field analyzer permits the accumulation of integral spectra. Q_{PS} is calculated using

$$Q_{PS} = F_{PS} Q_T / F_T$$

where F_{PS} is the fraction of positrons forming Ps in a given time period, Q_T values are obtained from the direct measurements of that quantity by other groups, and F_T is the fraction of incident positrons scattered through any channel.

The group at the University of Texas at Arlington has used the same apparatus as used in their Q_{PS} measurements to measure ionization cross sections [18] (Q_{ion}). Q_{ion} is determined using

$$Q_{ion} = F_{ion} Q_T / F_T,$$

where F_{ion} is the fraction of incident positrons that produce ions, which is determined from counting rates obtained with the CEM potentials set for counting electrons, Q_T is obtained from prior Q_T measurements, and F_T is the fraction of incident positrons that are scattered through any channel.

At the University of Bielefeld, the apparatus shown schematically in Fig. 12 has been used to measure [19] cross sections for the ionization of helium by e^+ impact both with and without Ps formation. The same apparatus is also used to measure e^- impact ionization cross sections. Beam transport is accomplished by a 200 to 350 G longitudinal magnetic guiding field and electrostatic lenses. The scattering tube consists of a 1 cm diameter, 50 cm

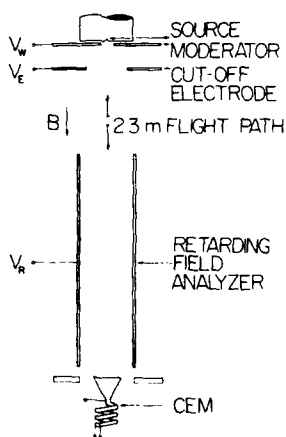


FIGURE 11
Experimental set-up for measuring Q_{PS} and Q_{ion} (From Diana, Ref. 57)

long glass cylinder lined with a tungsten spiral. In order to extract the ions, a potential gradient is established in the cylinder by passing current through the tungsten spiral. The target gas is supplied at the center of the tube which is differentially pumped at both ends. After leaving the gas target, transmitted positrons and ions are accelerated and enter an EXB mass analyzer. The positrons are not strongly affected and pass on toward a microchannel plate (detector 1) whereas the ions are deflected upwards and pass through a mesh onto a second microchannel plate (detector 2). The ion production rate is measured as a function of the projectiles' energy. The e^+ and the ion signals are processed by a time-to-amplitude converter (TAC). Ions which are time correlated with an e^+ originate from ionization without Ps formation. Uncorrelated ions are due to Ps formation. By counting all ions produced, e^+ impact ionization cross sections, with and without Ps formation, $(Q_{\text{ion}}^+ + Q_{\text{Ps}})$ are measured. To determine absolute values of $(Q_{\text{ion}}^+ + Q_{\text{Ps}})$, a normalization procedure was used where the ratio of the ion rates produced by e^+ and e^- was formed and normalized to unity between 200 and 400 eV based upon the known merging of e^+ and e^- total cross sections above 200 eV. Then the ratios were multiplied with the e^- ionization cross sections from the literature. One possible difficulty with this normalization procedure is that although the e^+ -He and e^- -He Q_T values have been observed to merge near 200 eV, there are indications (refer to Sec. 3) that the separate processes (inelastic and elastic) that contribute to Q_T are not even close to merging at 200 eV, so the assumption that the ionization cross sections for e^+ and e^- He impact are merged at 200 eV and above can be questioned. The cross sections for ionization without Ps formation, Q_{ion}^+ , were derived from the MCA spectra using a normalization procedure essentially the same as that described above. From the difference between $(Q_{\text{ion}}^+ + Q_{\text{Ps}})$ and Q_{ion}^+ , Q_{Ps} was obtained.

Measurements [12,14,19,56] of Q_{Ps} for e^+ -He collisions are shown in Fig. 13 along with a recent polarized orbital calculation [58]. There is reasonable agreement between the measurements of Fornari et al. [14], Diana et al. [56], and Sinapius et al. [19] below 40 eV, while above 40 eV, the

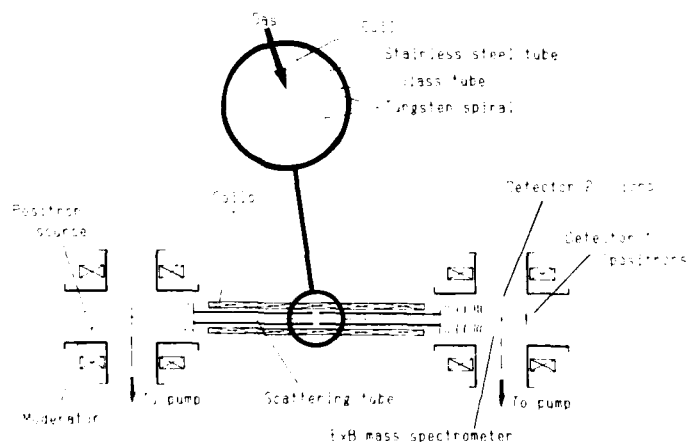


FIGURE 12
Schematic diagram of the apparatus used for measuring e^+ and e^- impact ionization cross sections. (From Sinapius et al., Ref. 19)

measurements of Diana et al. are somewhat higher than those of Sinapius et al. The measurements of Charlton et al. [12] are much lower than the measurements of the other groups over most of the energy range. The polarized orbital calculation of Khan and Ghosh [58] agrees quite well with the measurements of Sinapius et al.

Measurements [17-19] of e^+ impact ionization cross sections without Ps formation (Q^+_{ion}) for e^+ -He collisions are shown in Fig. 14 along with a theoretical calculation [59] of Q^+_{ion} and measurements [60] of e^- impact ionization cross sections, Q^-_{ion} . The preliminary results of Sinapius et al. [19] shown in Fig. 14 indicate that Q^+_{ion} is significantly higher than Q^-_{ion} below 200 eV. This is in contradiction to Sueoka's results [17] for Q^+_{ion} which are close to the values of Q^-_{ion} . The calculations of Basu et al. [59] (approximations DW2 and FBA in Ref. 59) agree well with the data of Sinapius et al. [19].

A comparison of the results of Sinapius et al. [19] shown in Figs. 13 and 14 indicates [19] that below 50 eV, He impact ionization is dominated by Ps formation. The cross sections for both reaction channels that lead to ionization reach roughly the same maximum value ($0.4 \times 10^{-16} \text{ cm}^2$) but at different energies (40 eV for Q_{Ps} and 90 eV for Q^+_{ion}).

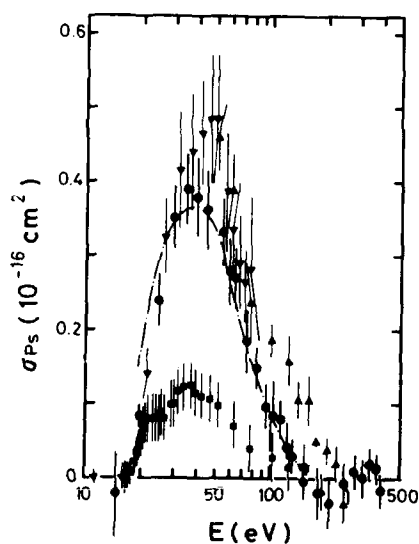


FIGURE 13

Ps formation cross sections (Q_{Ps}). Symbols: closed circles - Sinapius et al. [19], inverted triangles - Fornari et al. [14], normal triangles - Diana et al. [56], squares - Charlton et al. [12], dash-dot curve - Khan and Ghosh (polarized orbital calculation) [58]. (From Sinapius et al., Ref. 19)

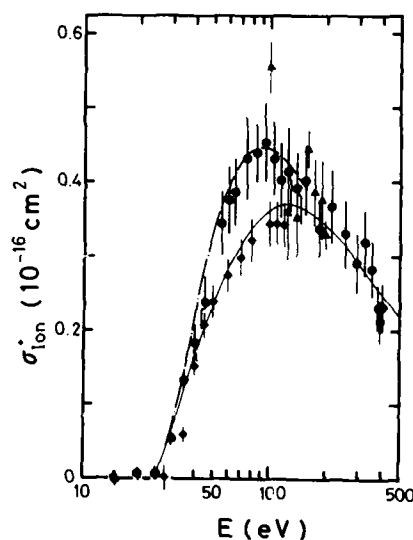


FIGURE 14

Positron impact ionization cross sections without Ps formation (Q^+_{ion}). Symbols: closed circles - Sinapius et al. [19], diamonds - Sueoka [17], triangles - Diana et al. [18], dash-dot curve - Basu et al. (DW2) [59], solid line - Montague et al. (Q^-_{ion}) [60]. (From Sinapius et al., Ref. 19)

5.2 Excitation Cross Sections

Using the TOF apparatus shown in Fig. 7 (the same apparatus used for measurements of differential cross sections), Coleman and Hutton [15] have obtained lower bounds on total excitation cross sections for 23-31 eV e^+ -He collisions. Well-defined secondary peaks were observed in the TOF spectra corresponding to e^+ which have lost 20.6 eV of energy and have been scattered in the forward direction at angles less than 70° . At incident e^+ energies above 30 eV, a secondary peak associated with ionization overlaps the excitation peak, making it difficult to assign excitation cross sections. According to the interpretation of Coleman and Hutton, the secondary peak corresponding to a 20.6 eV energy loss indicates that in the projectile energy range from 23 to 31 eV, the total excitation cross section is dominated by excitation of the 2^1S state and that there is appreciable small angle scattering associated with this excitation process. However, there is some question [61] as to whether a significant part of the signal observed by Coleman and Hutton could be associated with the 2^1P state and/or with appreciable elastic scattering at an appropriate angle. The work of Coleman and Hutton was extended to Ne and Ar and lower bounds on "excitation plus ionization" cross sections have been measured for He, Ne, and Ar [16]. Sueoka [17] has extended the technique of Coleman and Hutton to obtain excitation cross sections in He to 120 eV by employing retarding field analysis to discriminate against positrons losing energy through ionization.

A possible partition scheme [62] for Q_T in He is shown in Fig. 15. The Q_T curve (labeled $Q_{T\text{tot}}$ in Fig. 15) is a smoothed line through available experimental data [6]. The total elastic cross section (Q_{el}) is extrapolated from below the first inelastic threshold (17.8 eV) to match calculated values [63] for energies greater than 150 eV. Q_{ps} in Fig. 15 represents the smoothed data of Fornari et al. [14]. Q_{ion} is the total ionization cross section for e^- -He scattering [60,64]. Up to the broken vertical line, the Q_{ion}^+ measurements of Sueoka [17] agree with the e^- values to within experimental uncertainties. Q_{ex} is the total cross section for the singlet excitation of He by e^- impact [62]. Contributions to Q_{ex} from triplet excitations are neglected since they proceed primarily via exchange, which is absent in e^+ scattering. The vertically hatched region is the $1^1S - 2^1S$ excitation cross section measured by Sueoka [17] and the black region is the same cross section measured by Coleman et al. [65]. Finally, the horizontally hatched region is based on the experimental values for the total cross section for excitation + ionization of Coleman et al. [65]. The partitioning scheme shown in Fig. 15 suggests [62] that considering the experimental uncertainties, the partial cross sections shown in Fig. 15 essentially add to give a result close to the directly measured Q_T values [6], suggesting a consistency between the measured Q_T values and the partial cross sections shown in Fig. 15. The Q_{ps} values of Charlton et al. [12] on the other hand would not lead to such a consistency.

6. SOME FUTURE DIRECTIONS

In the area of e^+ Q_T measurements, atomic hydrogen has not yet been studied experimentally. This system is of particular theoretical interest because of the relatively simple structure of atomic hydrogen. Positron-H Q_T measurements present a challenge to experimenters because of the difficulty of producing sufficiently intense low energy e^+ beams coupled with the difficulty of producing an atomic hydrogen gas target with a sufficiently high number density. In addition to the intriguing possibility of making direct comparisons between e^+ -H and e^- -H scattering in the same experimental system using the same technique, there would be definite interest in searching for scattering resonances for this system, since such resonances

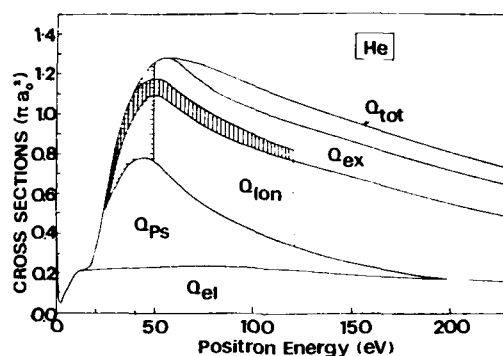


FIGURE 15
Partial cross sections for e^+ -He scattering. (From Coleman et al., Ref. 62)

have been predicted to exist for e^+ -H scattering just below the $n = 2$ atomic excitation threshold [66] and associated with the first excited state of Ps in the e^+ -H system [67]. Up to the present time, there have not been any experimental observations of e^+ scattering resonances. Stein et al. [33] have used their narrow energy width (<0.1 eV) e^+ beam in a transmission experiment to search for e^+ scattering resonances over 1.0 eV ranges centered near the Ps formation threshold (9.0 eV) and the lowest atomic excitation threshold (11.5 eV) for Ar and near 20.375 eV in He (above the Ps formation threshold and just below the first singlet excitation of He) where some possible theoretical evidence of a resonance in the e^+ -He system has been provided by Ho and Fraser [68]. However, up to the present time there have been no observations of e^+ scattering resonances. Positron beam technology has improved to the point where it should be feasible to measure e^+ -H Q_T values, and search for resonances, using standard techniques for producing atomic hydrogen.

There is clearly much more work to be done in measuring Q_T values for e^+ -alkali metal atom collisions, since the only such atom which has been studied thus far for positrons is potassium [22]. Lithium and sodium, being relatively simple in structure, would be interesting candidates for e^+ Q_T measurements from a theoretical point of view. It would be of interest in the case of the other alkali atoms (besides K) to see to what extent (if any) the tendency is present for the e^+ and e^- Q_T values to be close together over the entire energy from a few eV up to 50 eV as it is in the case of K.

In the area of differential scattering cross section measurements, it would be interesting to see if critical points [69] (minima in the differential scattering cross section where a small change in either the incident electron energy or the scattering angle is associated with an appreciable increase in the differential scattering cross section) exist for e^+ -atom scattering as they do for e^- -atom scattering. Wadehra et al. [70] have theoretically predicted that critical points exist for the elastic scattering of low energy positrons by Ar, Kr, and Xe, between 1 and 2 eV and between 95° and 96° and have demonstrated that these points arise due to low-energy diffraction effects. A determination of the critical points could provide a sensitive test for the atomic potential used in the calculations, and an experimental verification of the critical points for heavier atoms could provide a means for improving our knowledge of the atomic potentials for these atoms which are

generally not known very accurately [70].

Now that the first steps have been taken towards making direct measurements of Q_{ion} , it would be of interest to investigate the threshold behavior for ionization by electrons and positrons in view of the prediction by Geltman [71] that there is a very large difference between the threshold behavior for atomic ionization by e^- and e^+ impact. The experimental approach developed by the University of Bielefeld group [19] may be suitable for conducting such investigations in the future.

ACKNOWLEDGEMENT

We would like to acknowledge, with gratitude, the support of the National Science Foundation for our research program.

REFERENCES

- 1) D.G. Costello, D.E. Groce, D.F. Herring, and J.W. McGowan, *Can. J. Phys.* 50 (1972) 23.
- 2) H.S.W. Massey, *Phys. Today* 29 (3) (1976) 42.
- 3) T.C. Griffith and G.R. Heyland, *Phys. Rep.* 39 (1978) 169.
- 4) J.W. Humberston, *Adv. Atom. Mol. Phys.* 15 (1979) 101.
- 5) T.C. Griffith, *Adv. Atom. Mol. Phys.* 15 (1979) 135.
- 6) W.E. Kauppila and T.S. Stein, *Can. J. Phys.* 60 (1982) 471.
- 7) T.S. Stein and W.E. Kauppila, in: *Physics of Electronic and Atomic Collisions*, ed. S. Datz (North-Holland, Amsterdam, 1982) pp. 311-329.
- 8) T.S. Stein and W.E. Kauppila, *Adv. Atom. Mol. Phys.* 18 (1982) 53.
- 9) W. Raith, in: *Positron Scattering in Gases*, eds. J.W. Humberston and M.R.C. McDowell (Plenum, New York, 1984) pp. 1-13.
- 10) W.E. Kauppila and T.S. Stein, in: *Positron Scattering in Gases*, eds. J.W. Humberston and M.R.C. McDowell (Plenum, New York, 1984) pp. 15-25.
- 11) M. Charlton, T.C. Griffith, G.R. Heyland, K.S. Lines, and G.L. Wright, *J. Phys. B* 13 (1980) L757.
- 12) M. Charlton, G. Clark, T.C. Griffith, and G.R. Heyland, *J. Phys. B* 16 (1983) L465.
- 13) T.C. Griffith, in: *Positron Scattering in Gases*, eds. J.W. Humberston and M.R.C. McDowell (Plenum, New York, 1984), pp. 53-63.
- 14) L.S. Fornari, L.M. Diana, and P.G. Coleman, *Phys. Rev. Lett.* 51 (1983) 2276.
- 15) P.G. Coleman and J.T. Hutton, *Phys. Rev. Lett.* 45 (1980) 2017.
- 16) P.G. Coleman, J.T. Hutton, D.R. Cook, L.M. Diana, and S.C. Sharma, *Proc. Int. Conf. Phys. Electron. Atom. Collisions*, 12th Abstr., (1981) p. 426.
- 17) O. Sueoka, *J. Phys. Soc. Jpn.* 51 (1982) 3757.
- 18) L.M. Diana, L.S. Fornari, S.C. Sharma, P.K. Pendleton, and P.G. Coleman, to be published in: *Positron Annihilation -- Proceedings of the 7th International Conference on Positron Annihilation*, Jan. 6-11, 1985, New Delhi, India, eds. P.C. Jain, R.M. Singru, and K.P. Gopinathan (World Scientific, Singapore).
- 19) G. Sinapius, D. Fromme, and W. Raith, to be published in: *Positron (Electron)-Gas Scattering -- Proceedings of the Third International Workshop on Positron (Electron)-Gas Scattering*, July 16-18, 1985, Detroit, Michigan, eds. W.E. Kauppila, T.S. Stein, and J.M. Wadehra (World Scientific, Singapore).
- 20) P.G. Coleman and J.D. McNutt, *Phys. Rev. Lett.* 42 (1979) 1130.
- 21) W.E. Kauppila, G.M.A. Hyder, M.S. Dababneh, Y.-F. Hsieh, C.K. Kwan, and T.S. Stein, to be published in: same as for Ref. 19.
- 22) T.S. Stein, R.D. Gomez, Y.-F. Hsieh, W.E. Kauppila, C.K. Kwan, and Y.J. Wan, *Phys. Rev. Lett.* 55 (1985) 488.

- 23) E.L. Chupp, D.J. Forrest, P.R. Higbie, A.N. Suri, C. Tsai, and P.P. Dunphy, *Nature* (London) 241 (1973) 333.
- 24) C.J. MacCallum and M. Leventhal, in: *Positron-Electron Pairs in Astrophysics*, eds. M.L. Burns, A.K. Harding and R. Ramaty, AIP Conference Proceedings Number 101, (1983) p. 211.
- 25) M. Leventhal and B.L. Brown, to be published in: same as for Ref. 19.
- 26) C.J. Crannell, G. Joyce, R. Ramaty, and C. Werntz, *Astrophys. J.* 210 (1976) 582.
- 27) R.W. Bussard, R. Ramaty, and R.J. Drachman, *Astrophys. J.* 228 (1979) 928.
- 28) A.P. Mills, Jr., in: *Proceedings of the International School of Physics, "Enrico Fermi", Course LXXXIII, Varenna, 1981*, eds. W. Brandt and A. Dupasquier (Academic, New York, 1982).
- 29) T.S. Stein, W.E. Kauppila, and L.O. Roellig, *Rev. Sci. Instrum.* 45 (1974) 951.
- 30) J.M. Dale, L.D. Hulet, and S. Pendyala, *Surf. Interface Anal.* 2 (1980) 199.
- 31) J. Van House and P.W. Zitzewitz, *Phys. Rev. A* 29 (1984) 96.
- 32) T.S. Stein, W.E. Kauppila, and L.O. Roellig, *Phys. Lett.* 51A (1975) 327.
- 33) T.S. Stein, F. Laperriere, M.S. Dababneh, Y.-F. Hsieh, V. Pol, and W.E. Kauppila, in: *Proc. Int. Conf. Phys. Electron. Atom. Collisions*, 12th Abstr. (1981) p. 424.
- 34) R.H. Howell, P. Meyer, I.J. Rosenberg, and M.J. Fluss, *Phys. Rev. Lett.* 54 (1985) 1698.
- 35) K.G. Lynn, A.P. Mills, Jr., R.N. West, S. Berko, K.F. Canter, and L.O. Roellig, *Phys. Rev. Lett.* 54 (1985) 1702.
- 36) P.W. Zitzewitz, J. Van House, A. Rich, and D.W. Gidley, *Phys. Rev. Lett.* 43 (1979) 1281.
- 37) J.W. Humberston, to be published in: same as for Ref. 19.
- 38) W.E. Kauppila, T.S. Stein, J.H. Smart, M.S. Dababneh, Y.K. Ho, J.P. Downing, and V. Pol, *Phys. Rev. A* 24 (1981) 725.
- 39) D.P. Dewangen and H.R.J. Walters, *J. Phys. B* 10 (1977) 637.
- 40) R.P. McEachran and A.D. Stauffer, to be published in: same as for Ref. 19.
- 41) M.S. Dababneh, Y.-F. Hsieh, W.E. Kauppila, V. Pol, and T.S. Stein, *Phys. Rev. A* 26 (1982) 1252.
- 42) Ch.K. Kwan, Y.-F. Hsieh, W.E. Kauppila, Steven J. Smith, T.S. Stein, M.N. Uddin, and M.S. Dababneh, *Phys. Rev. Lett.* 52 (1984) 1417.
- 43) K.R. Hoffman, M.S. Dababneh, Y.-F. Hsieh, W.E. Kauppila, V. Pol, J.H. Smart, and T.S. Stein, *Phys. Rev. A* 25 (1982) 1393.
- 44) Ch.K. Kwan, Y.-F. Hsieh, W.E. Kauppila, S.J. Smith, T.S. Stein, M.N. Uddin, and M.S. Dababneh, *Phys. Rev. A* 27 (1983) 1328.
- 45) M. Charlton and G. Laricchia, to be published in: same as for Ref. 19.
- 46) G. Bordonaro, G. Ferrante, M. Zarccone, and P. Cavaliere, *Nuovo Cimento Soc. Ital. Fis.* 35B (1976) 349.
- 47) S. Guha and P. Mandal, *J. Phys. B* 13 (1980) 1919.
- 48) H.R.J. Walters, *J. Phys. B* 9 (1976) 227.
- 49) P.G. Coleman, J.D. McNutt, J.T. Hutton, L.M. Diana, and J.L. Fry, *Rev. Sci. Instrum.* 51 (1980) 935.
- 50) D.M. Schrader, *Phys. Rev. A* 20 (1979) 918.
- 51) R.P. McEachran, A.G. Ryman, and A.D. Stauffer, *J. Phys. B* 12 (1979) 1031.
- 52) S.K. Srivastava, H. Tanaka, A. Chutjian, and S. Trajmar, *Phys. Rev. A* 23 (1981) 2156.
- 53) D.W. Walker, private communication with Srivastava et al. (Ref. 52) and *J. Phys. B* 3 (1970) 788.
- 54) A.D. Stauffer and R.P. McEachran, private communication: also see R.P. McEachran and A.D. Stauffer, to be published in: same as for Ref. 19.
- 55) P.G. Coleman, to be published in: same as for Ref. 19.
- 56) L.M. Diana, S.C. Sharma, L.S. Fornari, P.G. Coleman, P.K. Pendleton, D.L. Brooks, and B.E. Seay, to be published in: same as for Ref. 18.
- 57) L.M. Diana, private communication, 1985.

- 58) P. Khan and A.S. Ghosh, *Phys. Rev. A* 28 (1983) 2181.
- 59) M. Basu, P.S. Mazumdar, and A.S. Ghosh, *J. Phys. B* 18 (1985) 369.
- 60) R.G. Montague, M.F.A. Harrison, and A.C.H. Smith, *J. Phys. B* 17 (1984) 3295.
- 61) R.P. McEachran, L.A. Parcell, and A.D. Stauffer, to be published in: same as for Ref. 19.
- 62) P.G. Coleman, L.S. Fornari, and L.M. Diana, to be published in: same as for Ref. 18.
- 63) C.J. Joachain, in: *Positron Scattering in Gases*, eds. J.W. Humberston and M.R.C. McDowell (Plenum, New York, 1984) pp. 39-52.
- 64) F.J. de Heer and R.H.J. Jansen, *J. Phys. B* 10 (1977) 3741.
- 65) P.G. Coleman, J.T. Hutton, D.R. Cook, and C.A. Chandler, *Can. J. Phys.* 60 (1982) 584.
- 66) G.D. Doolen, J. Nuttall, and C.J. Wherry, *Phys. Rev. Lett.* 40 (1978) 313.
- 67) G.D. Doolen, *Int. J. Quant. Chem.* 14 (1978) 523.
- 68) Y.K. Ho and P.A. Fraser, *J. Phys. B* 9 (1976) 3213.
- 69) W. Buhring, in: *Proceedings of the Fourth International Conference on Atomic Physics, Abstracts of Contributed Papers*, eds. J. Kowalski and H.G. Weber (Heidelberg Univ. Press, Heidelberg, 1974) p. 417.
- 70) J.M. Wadehra, T.S. Stein, and W.E. Kauppi, *Phys. Rev. A* 29 (1984) 2912.
- 71) S. Geltman, *J. Phys. B* 16 (1983) L525.

THE COULOMB THREE-BODY PROBLEM : THE ELECTRON HYDROGEN SYSTEM

Erich WEIGOLD

Flinders University of S.A., Adelaide, South Australia, 5042.

Triple differential cross sections for the ionization of atomic hydrogen in the intermediate energy regime are discussed in terms of theoretical approximations based on the Born series (B1, B2, EBS, and DWBA) and on the multiple scattering expansion (DWIA). First order plane wave theories are incapable of describing the data, and the inclusion of higher order effects is essential. The impulse approximation works very well in the high momentum transfer region, whereas the Born series approach works best in the region of very small momentum transfer. Some fundamental difficulties remain in the intermediate region.

1. INTRODUCTION

The ionization of atoms by electron impact is one of the most interesting processes in the field of atomic collisions. Besides being a process of great interest in plasma physics and astrophysics, it has led to the development of a new spectroscopy - electron momentum spectroscopy - which has yielded a much deeper understanding of the structure of atoms and molecules. It also provides an extremely interesting and challenging problem in the basic understanding of collision problems. The breakup channel exhibits all the difficulties of many-body scattering theory coupled with the special problems of the infinite range of the Coulomb interaction.

The most detailed information on the dynamics of electron impact ionizing collisions is obtained by means of the triple differential or (e,2e) cross section, in which the kinematics are completely determined. The energy E_0 of the incident electron is known, and the energies E_A and E_B and directions of motion (θ_A, ϕ_A) and (θ_B, ϕ_B) relative to the incident direction are determined for the two emitted electrons. The experiments may conveniently be divided into two broad kinematic regimes, depending on the magnitude of the momentum transfer $\vec{K} = \vec{k}_0 - \vec{k}_A$, where electron A is conventionally assumed to be the "scattered" electron with $E_A \geq E_B$.

First we have the regime of high momentum transfer ($K \geq 6$ a.u.) between the "scattered" electron and the target. The most important class of experiments in this category are those using symmetric kinematics, i.e. $E_A = E_B$ and $\theta_A = \theta_B = \theta$ at high incident energies. These high momentum transfer experiments are dominated by close encounters between the incident and struck electron and they yield structure information on the target and ion in the form of target electron momentum probability distributions and electron separation energy spectra. They are sometimes referred to as binary (e,2e) experiments or electron momentum spectroscopy (EMS)(1).

The other broad category of (e,2e) collisions consists of those having low momentum transfer. Such collisions dominate the total ionization cross section. These experiments generally involve asymmetric kinematics in which $E_A \gg E_B$ and $\theta_A \ll \theta_B$. At high incident energies and $\theta_A \approx 0$, $k_A \approx k_0$, $K \approx 0$, these experiments, known as dipole (e,2e) experiments, also give structure information(2). In the limit as $K \rightarrow 0$ these experiments simulate photo-electron spectroscopy, with the absorbed photon having energy " $h\nu$ " = $E_0 - E_A$.

Measurements of the triple differential cross section in the asymmetric

regime provide a fundamental testing ground for various theoretical approaches to the ionization problem. These experiments were pioneered by Ehrhardt and coworkers(3), who have produced extensive measurements of the triple differential cross section for helium as well as some other targets. With a target of atomic hydrogen the ionization problem is greatly simplified, since the bound-state wave functions are known exactly, as are the two-body potentials within the three-body system. We have a pure three-body problem with known forces, namely the three-body Coulomb problem. Unfortunately it is difficult to formulate the Coulomb three-body problem in a way that leads to a manifestly convergent approximation scheme for ionization.

The detailed understanding of electron impact ionization of atomic hydrogen is therefore of great fundamental interest. It provides the simplest testing ground for any theory of ionization, and provides a tool for investigating any general three-body theory involving the electromagnetic interaction. In practical terms, the major theoretical thrust required in improving our understanding of the ionization process must be concerned with developing a better description of the incident channel, of the three-body final state, and of the collision process.

2. THEORY

2.1 Electron-Hydrogen Scattering

In order to describe even the first of the above three aspects of the ionization problem we must be able to describe electron-hydrogen scattering. It is outside the scope of this review to discuss in detail the progress achieved in this problem, which of course is also a three-body problem. However, it is relevant to point out that our understanding is still incomplete, especially in the intermediate energy region. For instance the coupled channel optical model (CCO) method of McCarthy and coworkers(4) is one of the most ambitious theoretical approaches to electron-hydrogen scattering. In CCO method the set of reaction channels (defined by the target states) is divided into two sets P and Q projected by operators P and Q. The discrete set P is treated by solving the coupled integral equations of the momentum representation using the electron-electron potential operator

$$v^{(Q)} = v(1+(-)S_{P_r}) + v(1+(-)S_{P_r})Q \frac{1}{E(+)-H} Q(1+(-)S_{P_r})v, \quad (1)$$

where v is the actual electron-electron potential, S is the total spin, P_r is the space-exchange operator and H is the Hamiltonian for the scattering problem. The last term in (1) is a complex polarization potential for which (1) gives a formally-exact rearrangement of the scattering problem for states in the P set. It mainly takes care of ionized channels, which are treated approximately by integrating over the kinematic degrees of freedom using the second-order approximation with the screening correlation. This treatment, unlike methods that treat the continuum as a set of normalized pseudostates, gives a good description of the total reaction (inelastic plus ionization) cross section.

Figure 1 shows the calculated differential cross sections at 54 eV for elastic scattering and excitation of the $n=2$ states(4) compared with the measured values of Williams(5,6) and in the case of elastic scattering also with the measurements of Lloyd et al(7). The agreement appears to be excellent. However, I should point out that for elastic scattering the theory has been normalized to the data, the theoretical cross sections being too large by a factor of about 1.2. In addition for the excitation of the 2p state the calculation gives the wrong values for the λ and R parameters for angles greater than about 60° . Other approaches, such as coordinate space coupled-channels calculations(8) and calculations using pseudostates to mimic the effects of higher energy channels (e.g. ref. 9), give results in similar disagreement with

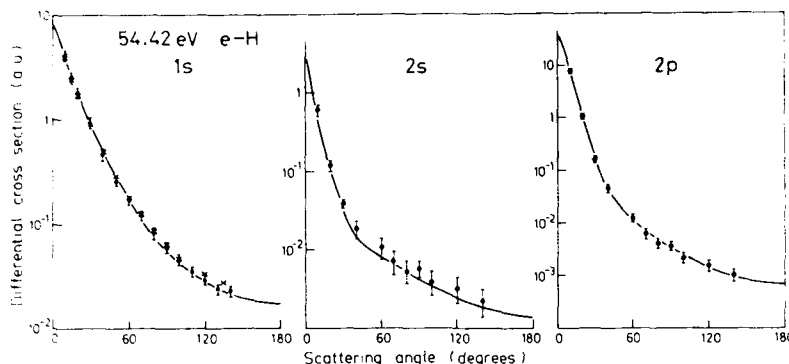


FIGURE 1

The coupled channel optical model (ref 4) cross sections for elastic and inelastic electron scattering of 54 eV electrons from atomic hydrogen compared with the data of Williams(5,6) (●) and Lloyd et al(7) (×).

experiment. The large angle λ and R parameters describing the excitation of the 2p magnetic substates depend sensitively on the details of the approximation used. However, it is rather surprising that there is significant disagreement between the calculated and measured absolute elastic cross sections. It is obviously important to repeat the experiments. New independent measurements we are making at Flinders, although only preliminary, support the earlier measurements. The new measurements concentrate on measuring accurately the ratio of $n=2$ excitation to elastic scattering, since this ratio can be measured more accurately than absolute cross sections. Therefore I believe it is still too early to say that this relatively simple part of the ionization problem is completely understood.

2.2. The (e,2e) cross section

Let me now turn to a discussion of the (e,2e) cross section itself. The scattering amplitude for the three-body problem of ionization of atomic hydrogen is defined by

$$M = \langle \psi^{(-)} | T | \psi^{(+)} \rangle, \quad (2)$$

where T is the three-body T matrix for the electron-hydrogen system. The wave functions $\psi^{(\pm)}$ indicate incoming and outgoing boundary conditions, respectively. In order to solve this problem we must make approximations to the three-body T matrix as well as for $\psi^{(\pm)}$. We can make approximations for T using various expansions and two-body operators.

For the electron hydrogen problem it is convenient to label the incident electron-proton system by 1, the target electron system by 2, and the electron-electron system by 3. We indicate the incoming electron by the subscript 1 and the bound electron by subscript 2.

2.2.1. The Born Series

In our notation the two-body potentials in the system are v_1 , v_2 , and v_3 , where v_1 is the potential between the incident electron and the ion, v_2 is the potential between the bound electron and the ion, and v_3 is the interelectron potential. Using the Lippmann-Schwinger equation, the three-body T matrix may be written in terms of these potentials and the Green's function G for the system as

$$T = V + VGV \quad (3)$$

$$= (v_1 + v_3) + (v_1 + v_3)G(v_1 + v_3), \quad (4)$$

where we have partitioned the Hamiltonian such that

$$V = v_1 + v_3. \quad (5)$$

Introducing the Green's function G_0 for the interaction of the target electron with the proton, we may iterate this equation to produce

$$T = (v_1 + v_3) + (v_1 + v_3)G_0(v_1 + v_3) + (v_1 + v_3)G_0(v_1 + v_3)G_0(v_1 + v_3) + \dots \quad (6)$$

which is simply the Born series expansion for the three-body T matrix. Taking as an approximation to the T matrix the first term of the above expansion yields the first-order Born (B1) approximation.

The scattering amplitude in this approximation may be written

$$M_{B1} = \langle \vec{k}_A \chi^{(-)}(\vec{k}_B) | v_1 + v_3 | \psi_2 \vec{k}_0 \rangle, \quad (7)$$

where ψ_2 is the bound state of the target, in this case the ground state of atomic hydrogen. $\chi^{(-)}(\vec{k}_B)$ is a distorted wave which in practice may be approximated by a plane wave (plane wave Born approximation) or Coulomb wave (Coulomb-Born approximation) and \vec{k}_A, \vec{k}_0 represent plane waves.

Including both first- and second-order terms of the Born expansion in the approximation to the T matrix yields the second Born approximation (B2)

$$M_{B2} = \langle \vec{k}_A \chi^{(-)}(\vec{k}_B) | [(v_1 + v_3) + (v_1 + v_3)G_0(v_1 + v_3)] | \psi_2 \vec{k}_0 \rangle. \quad (8)$$

The eikonal-Born-series (EBS) calculation attempts the logical extension to third order in the Born expansion by approximating the third-order Born term in the scattering amplitude by the third-order term of an eikonal multiple scattering (Glauber) expansion. The eikonal Born Series has been developed by Joachain and Byron⁽¹⁰⁾, and applied by them and coworkers to the triple differential ionization cross sections in helium⁽¹¹⁾ and more recently hydrogen^(12,13).

The distorted wave Born approximation (DWBA) which takes the incident and fast outgoing electron waves in the matrix element (7) to be fully distorted waves, has also been applied to the calculation of triple differential cross sections for both atomic hydrogen and helium targets⁽¹⁴⁻¹⁸⁾.

2.2.2. The Impulse Approximation

The multiple scattering series for T arises from iterating the three-body equations for finite-range potentials⁽¹⁹⁾, and up to second order it is

$$T = (t_3 + t_2 G_0 t_3) + (t_1 + t_2 G_0 t_1) + t_1 G_0 t_3 + t_3 G_0 t_1, \quad (9)$$

where t_i is the two-body t-matrix in the three-body space for the interaction of the pair i ($t_i = v_i + v_i G_0 t_i$). In the impulse approximation the three-body T matrix is approximated by the first order term in (9), that is

$$T = t_3 + t_1 \quad (10)$$

The operators in (9) are grouped to show the relationship to the distorted-wave impulse approximation, which involves some terms up to fourth order.

$$M_{DWIA} = \langle \chi^{(-)}(\vec{k}_A) \chi^{(-)}(\vec{k}_B) | t_3 + t_1 | \psi_2 \chi^{(+)}(\vec{k}_0) \rangle \quad (11)$$

$$| \chi^{(+)}(\vec{k}_i) \rangle = (1 + G_0 t_i) | \vec{k}_i \rangle \quad (12)$$

Neglecting the proton kinetic energy, the t_1 term vanishes if $\chi^{(-)}(\vec{k}_B)$ is calculated with the bare Coulomb potential since it is then orthogonal to ψ_2 .

The t_1 term can also be neglected in the case where we can treat the proton (or ion) as a spectator in first order. This is generally assumed to be the case in the kinematic region involving a large momentum transfer to particle 2. This approximation $T = t_3$ which takes the T-matrix to be independent of the ion coordinates is the binary encounter approximation. The above form of the scattering amplitude, even in the binary encounter approximation, involves a nine-dimensional integral. Numerical implementation of Eq. (11) involves using the factorization approximation which yields

$$M = \langle \vec{k}' | t_m | \vec{k} \rangle \langle \chi^{(-)}(\vec{k}_A) \chi^{(-)}(\vec{k}_B) | \psi_2(\vec{q}) \chi^{(+)}(\vec{k}_0) \rangle \quad (13)$$

where \vec{q} is the ion (proton) recoil momentum $\vec{k}_0 - \vec{k}_A - \vec{k}_B$, t_m is the half-off-shell two-body electron-electron Coulomb t matrix with exchange for spin state m , and

$$\vec{k}' = \frac{1}{2}(\vec{k}_A - \vec{k}_B) \text{ and } \vec{k} = \frac{1}{2}(\vec{k}_0 + \vec{q}) \quad (14)$$

2.3. Coulomb Three-Body Boundary Conditions

The main difficulty with the above approach for Coulomb interactions is the three-body boundary condition, a problem related to the logarithmic dependence of the phase of the screened two-body Coulomb t-matrix on the screening parameter (20). If the three-body wave function is approximated by a product of two distorted waves, a necessary condition for choosing effective charges to eliminate the logarithmic singularity in the phase has been given by Rudge (21). It is a constraint on the effective charges Z_A and Z_B for the electrons detected at A and B, and the condition is

$$\frac{Z_A}{k_A} + \frac{Z_B}{k_B} = \frac{1}{k_A} + \frac{1}{k_B} - \frac{1}{|\vec{k}_A - \vec{k}_B|} \quad (15)$$

The same result is obtained classically by requiring the energy of the two effective charges interacting with the ion, but not with each other, to be the same as the energy of the system of two electrons and the ion with Coulomb forces between all pairs. However, the asymptotic condition (15) does not define the effective charges uniquely, and a suitable choice still has to be made. In the case of hydrogen, with a proton and two free electrons in the final state, the distorted waves $\chi_{A(B)}^{(-)}$ are simply Coulomb waves with the effective charges Z_A and Z_B .

The differential cross section is

$$\frac{d^3\sigma}{d\Omega_A d\Omega_B dE_A} = |f(\vec{k}_A, \vec{k}_B)|^2 + |f(\vec{k}_B, \vec{k}_A)|^2 - \text{Re}[f(\vec{k}_A, \vec{k}_B) * f(\vec{k}_B, \vec{k}_A)] \quad (16)$$

where

$$f(\vec{k}_A, \vec{k}_B) = (2\pi)^{-2} M'(\vec{k}_A, \vec{k}_B) e^{i\Delta},$$

the matrix element M' is equivalent to the direct term of M , and

$$\Delta(\vec{k}_A, \vec{k}_B) = 2[(Z_A/k_A) \ln(k_A/X) + (Z_B/k_B) \ln(k_B/X)],$$

where

$$X^2 = k_A^2 + k_B^2.$$

2.4. Low-order Structure of the Approximations

For extremely asymmetric conditions $k_B \ll k_A$ the asymptotic condition (15) shows that it is reasonable to take $Z_A = 0$ and $Z_B = 1$. This solution corresponds to a completely screened fast ("scattered") electron A and an unscreened slow ("ejected") electron B. Then if we neglect the kinetic energy of the proton the t_1 term of (11) vanishes since the Coulomb wave $\chi^{(-)}(\vec{k}_B)$ is orthogonal to ψ_2 . We can then write the matrix element (11) for the DWIA using the form (12) for the distorted waves as

$$M_{\text{DWIA}} = \langle \vec{k}_A \vec{k}_B | (1+t_1 G_0)(1+t_2 G_0) t_3 (1+G_0 t_2) | \psi_2 \vec{k}_0 \rangle \quad (17)$$

This is the DWIA written as a plane wave approximation with an effective T-matrix. The second order approximation to this effective T-matrix is just the second order multiple scattering approximation.

$$T_{\text{DWIA}}^{(2)} = t_3 + t_2 G_0 t_3 + t_1 G_0 t_3 + t_3 G_0 t_1 \quad (18)$$

It is interesting to compare this with the corresponding sum from the second Born approximation. Again assuming the bare potential on the proton for $\chi_B^{(-)}(\vec{k}_B)$, we have to second order in the potentials

$$T_{\text{2BA}}^{(2)} = (v_3 + v_3 G_0 v_3) + v_2 G_0 v_3 + v_1 G_0 v_3 + v_3 G_0 v_1 \quad (19)$$

This is identical to the second order potential expansion of eq. (18), although the expansions are different in third order in the potentials. There are significant differences in the numerical implementation of the two approximations. The second Born approximation utilizes the closure approximation (see ref. 11), whereas the implementation of the distorted-wave impulse approximation requires factorization.

3. COMPARISON WITH EXPERIMENT

The asymptotic condition (15) does not determine Z_A and Z_B uniquely, and a further constraint is required before a calculation can be made and compared with experiment. The additional condition that the field strength at the nucleus be changed only minimally by the introduction of the effective charges is one constraint that has been used (22,23). This gives effective charges which differ at every angle. The computation must therefore be done completely at each angle and energy. This was carried out by Weigold et al (23) in the DWIA who compared their calculated cross sections with their measurements at several incident energies. The optical potential used by them to calculate the incident wave was energy dependent and had polarization and exchange terms as well as an absorption part.

Since the effective charges appear in the asymptotic region in the combination Z_{eff}/k , for extreme asymmetric conditions $k_B/k_A \rightarrow 0$ and it is sensible to take $Z_A = 0$ and $Z_B = 1$. The faster electron sees essentially a neutral atom, which is however in a continuum orbital. This is the approximation used in the Born series calculations by Byron, Joachain and Piraux (11-13) for asymmetric collisions, the incident and fast outgoing electrons being treated as plane waves. In the DWIA the fast outgoing wave is treated as a fully distorted wave. It is generally calculated using the same form for the optical potential as the incoming wave. Since the potential used by Weigold et al (23) was energy dependent, it differed in the incident and exit channels.

Figure 2 shows the coplanar 400 eV relative cross sections of Weigold et al compared with their DWIA calculations. The solid curve (DWIA-1) is obtained using $Z_A = Z_B = 1$, which violates the asymptotic conditions although it satisfies it in the limit $|\vec{k}_A - \vec{k}_B| \gg 1$, i.e. the high energy large angle, symmetric limit. The curve labelled DWIA-2 is obtained by setting $Z_A = Z_B$ (since $k_A = k_B$) and using the asymptotic condition (15), which in this case uniquely gives angle dependent effective charges. Since the cross sections shown in figure 2 are obtained under nearly symmetric conditions, the complete screening approximation is obviously invalid. The figure shows that DWIA-1 gives a better description at small angles and DWIA-2 at the larger angles. The plane wave cross sections are much too large at small θ_A and too small at large θ_A .

Figure 3 shows the more asymmetric data obtained at 250 eV compared with the "fully screened" approximation ($Z_A = 0$ and $Z_B = 1$, DWIA-4) and the totally bare

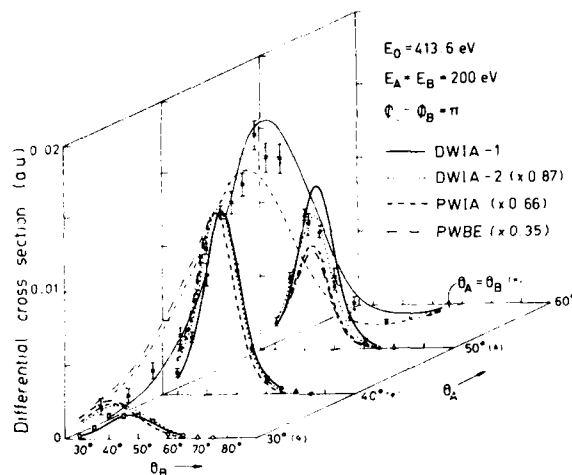


FIGURE 2

The $H(e,2e)H^+$ cross section at $E_0=413.6\text{eV}$, $E_A=E_B=200\text{eV}$ and $\phi_A-\phi_B=\pi$. The calculated cross sections are: — DWIA-1 ($Z_A=Z_B=1$), DWIA-2 $\times 0.87$ ($Z_A=Z_B$), ---- PWIA ($\times 0.66$), ---- and - - - - - PWBE ($\times 0.35$). The data are normalized to DWIA-1 at $\theta_A=40^\circ$.

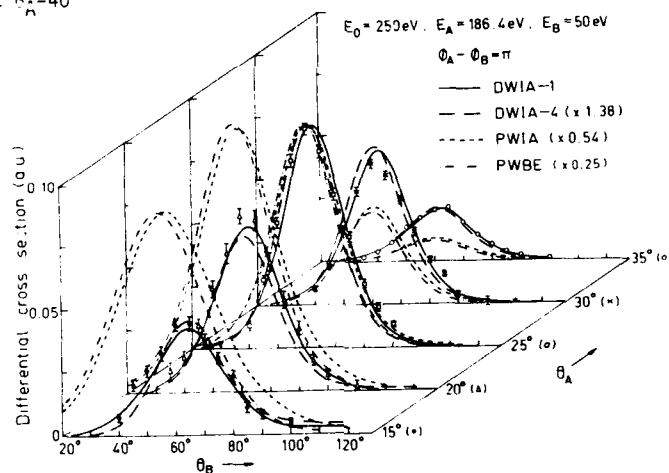


FIGURE 3

The $H(e,2e)H^+$ cross section at $E_0=250\text{eV}$, $E_B=50\text{eV}$, $\phi_A-\phi_B=\pi$ normalized to DWIA-1 ($Z_A=Z_B=1$) (solid curve) at $\theta_A=25^\circ$. — DWIA-4 ($Z_A=0$, $Z_B=1$) ($\times 1.38$), ---- PWIA ($\times 0.54$), - - - - - PWBE ($\times 0.25$).

approximation ($Z_A=Z_B=1$, DWIA-1). Both DWIA calculations give an excellent fit to the data, although the "screened" version is somewhat more successful at larger values of $\theta_A+\theta_B$, and the unscreened version at smaller $\theta_A+\theta_B$.

Smith, Winters and Bransden(17) compared a variety of DWBA calculations with

the 250 eV, 113.6 eV, and 100 eV data of Weigold et al(23). They employed local forms for the second-order complex potential and spin dependent exchange potentials for calculating the incident distorted wave. This potential (and the one used by Weigold et al in their DWIA calculations) allowed for polarization of the target and the loss of flux from the elastic scattering channel. Several different choices were considered for the final-state distorted wave functions. The wave function for the slow ejected electron B was always represented by a Coulomb wave with $Z_B=1$, while the fast electron was taken to be: (1) a Coulomb wave with $Z_A=1$, (2) a fully distorted wave with $Z_A=0$ and (3) Z_A determined by the asymptotic condition(15) with $Z_B=1$ ($Z_A=1-k_A(|\vec{k}_A-\vec{k}_B|)^{-1}$). No single approximation successfully reproduced the position and shape of the cross section over the entire angular range.

In both the DWIA and DWBA calculations an overall comparison between all the data and the calculations indicates that for angles where the sum $\theta_A+\theta_B$ is small, the completely unscreened model with $Z_A=Z_B=1$ gives the best fit to the data, whereas where $\theta_A+\theta_B$ is large the completely screened model ($Z_A=0$) works best. On purely physical grounds this appears a somewhat surprising result. It might have been expected, especially as $E_A \gg E_B$ that when the two final-state electrons leave after ionisation in approximately the same direction the slower electron would largely 'shield' the faster electron from the charge of the proton. As the angle between the two electrons increases the 'shielding' of the faster electron should reduce, until when the electrons move in opposite directions they both 'see' the full charge of the proton. The exact opposite is observed. The use of asymptotic arguments to determine electron wave functions in the small r region is obviously not correct. The effective charge must vary with distance as well as angle.

A large range of more asymmetric experiments at 250 eV was carried out recently by the Flinders group(24). In these experiments the slow outgoing electron was detected at energies E_B of 5, 11, and 14 eV for scattering angles θ_A of the fast outgoing electron of 3° , 5° and 8° . Although the data are not absolute, relative normalization between the different energies E_B and angles θ_A is maintained. Thus the data need be normalized to the cross sections given by the various theoretical approximations at only one point when compared with theory. A selection of the data is shown in figures 4 and 5 where they are compared with the Born series calculations of Byron, Joachain and Piraux(12), and various impulse approximation calculations. The data show the typical structure observed for ionization of atoms from S states, such as that observed by Erhard et al(3) from helium, namely the triple differential cross section is characterized by the presence of two lobes. These are usually referred to as the binary and recoil peaks. The binary peak is located in a direction close to the momentum transfer direction, and the presence of the peak can be attributed to binary collisions between the incident and ejected electrons. The recoil peak is observed in a direction roughly opposite to the momentum transfer direction, and can be attributed to collisions where significant momentum is transferred to the recoiling ion. If the ejected energy E_B and the momentum transfer K are reasonably large, the recoil peak is very small.

In figure 4 the data are normalized to the B2 calculation at $E_B = 10$ eV and $\theta_A = 5^\circ$ (solid curve). The EBS result is shown by the dot-dash curve and B1 by the dashed curve. The EBS and second Born calculations give an excellent description of the position and relative magnitudes of the "binary" peak. They also give a good fit to the recoil peak for the case of lowest momentum transfer ($K = 0.27$ a.u.) i.e. $E_B = 5$ eV $\theta_A = 3^\circ$. For higher momentum transfer, the magnitude of the recoil peak is somewhat underestimated.

In contrast to the Born approximation, which is expected to be most accurate for the low momentum transfer situations, the impulse approximation is expected to be most valid for the large momentum transfer situations, i.e., close electron-electron collisions. In the experiments of Lohmann et al(24) the momentum transfers were about an order of magnitude below those for which the impulse approximation was designed. Nevertheless they compared their data with a number

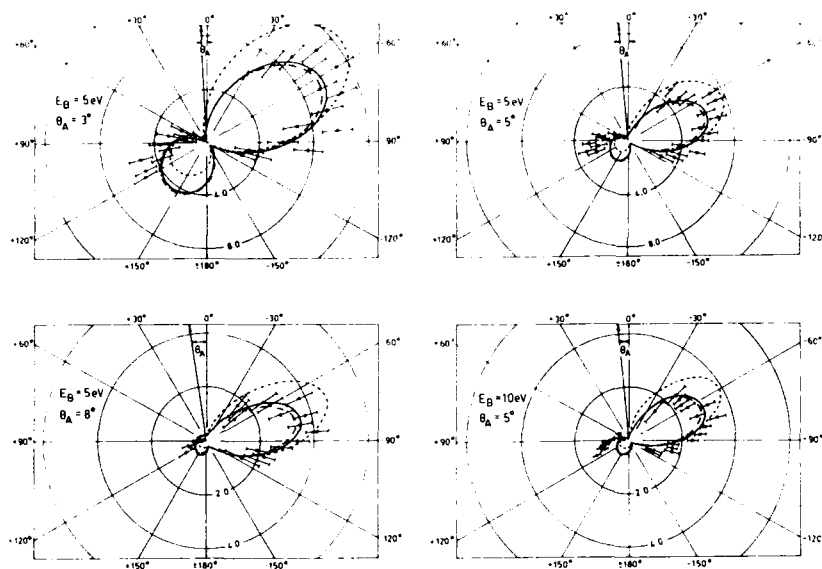


FIGURE 4

Polar diagrams of the differential coplanar asymmetric (e,2e) cross sections measured for atomic hydrogen at $E_0 = 250$ eV with $E_B = 5$ eV and $\theta_A = 3^\circ, 5^\circ$ and 8° and $E_B = 10$ eV and $\theta_A = 5^\circ$ (ref. 24). Data has been normalized to the second order Born calculation at $E_B = 10$ eV, $\theta_A = 5^\circ$. Calculated cross sections are - - -, first-order Born approximation; —, second-order Born approximation; - · - · - ·, eikonal Born series (Ref. 12). Cross sections are in atomic units.

of DWIA calculations (fig. 5). In all their calculations the distorted wave for the slow electron (B) is a Coulomb wave with a bare charge, and the incident wave is obtained by using the ground state average potential (including exchange). The distorted wave representing the fast outgoing electron is calculated in three different ways: DWIA-I in the same way as the incident electron (solid curves); DWIA-II as a plane wave (short dashed curves); and DWIA-III as a Coulomb wave. Also shown is a PWIA calculation, which does not give rise to a recoil peak since the IA does not include ion coordinates directly. The effect of the ion enters through the distorted waves as shown in Eq. (17).

The DWIA calculations give a surprisingly good fit to the data. The DWIA-I approximation, which takes $Z_B = 1$ and calculates the distorted wave for electron A in the groundstate potential of the atom is the most successful of the approximations.

It appears therefore that the EBS method and the DWIA can both describe the main features of the asymmetric triple differential cross sections. In fact the DWIA appears to do rather better in describing the relative magnitudes of the binary and recoil peaks. The two methods differ significantly, however, in the absolute magnitudes of the cross sections, the DWIA cross sections being generally smaller than the B2 and EBS cross section by a factor of about 3. It is interesting to note that the DWIA cross sections are very much smaller than the first order PWIA cross sections (by a factor of about 20), whereas the B2

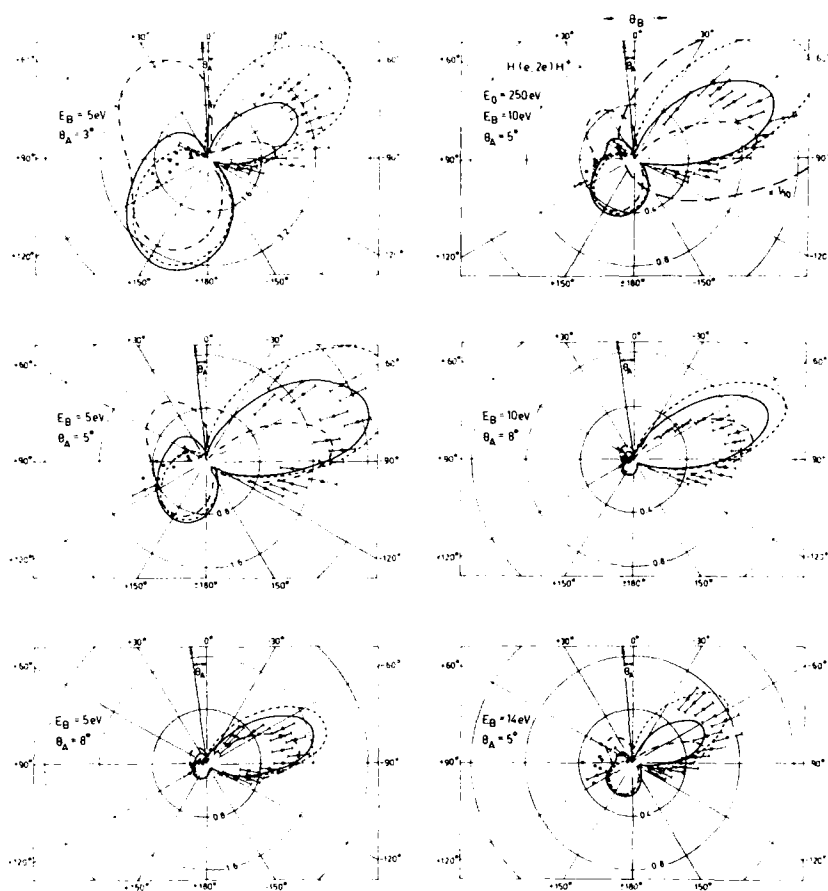


FIGURE 5

Polar diagrams of the differential coplanar asymmetric (e,2e) cross sections (ref. 24) measured for atomic hydrogen at $E_0 = 250$ eV with $E_B = 5, 10$ and 14 eV and $\theta_A = 3^\circ, 5^\circ$, and 8° . Data have been normalized to DWIA-I at $E_B = 10$ eV and $\theta_A = 5^\circ$. Calculated cross sections are —, DWIA-I; ---, DWIA-II; - · - · -, DWIA-III (fast electron respectively a fully distorted wave, plane wave, and Coulomb wave); ----, PWIA.

and EBS cross sections are only a little smaller than those given by their corresponding first order term, namely B1. This suggests, not unexpectedly, that in this kinematic regime the Born series expansion is likely to be much more reliable. The DWIA results obviously depend extremely sensitively on the details of the distorted waves used in the calculation. Absolute measurements are obviously required to clear this up.

Ehrhardt and coworkers⁽²⁵⁾ have recently reported some very interesting asymmetric triple differential cross section measurements for atomic hydrogen

at $E_0 = 250$ eV, $E_B = 5$ eV and $\theta_A = 3^\circ$, one of the cases studied by Lohmann et al(24). The new feature in their measurement is that they normalize their cross section by an extrapolation to the optical limit. At high enough incident energies and in the limit $K \rightarrow 0$, electron impact ionization simulates photoionization and the first Born approximation is a good description. From equations (7) and (16) the first Born TDCS (ignoring exchange) is given by

$$\frac{d^3\sigma_{B1}}{d\Omega_A d\Omega_B dE} = \frac{k_A k_B}{k_0} |f_{B1}(\vec{k}_A, \vec{k}_B)|^2 = \frac{k_A k_B}{k_0} \frac{4}{K^4} |M(\vec{k}, \vec{k}_B)|^2 \quad (20)$$

where

$$M(\vec{k}, \vec{k}_B) = \langle \psi_{CK_B}^{(-)}(\vec{r}_2) | \exp(i\vec{k} \cdot \vec{r}_2) | \psi_2 \rangle \quad (21)$$

The term in $\psi_1 (= -r_{13}^{-1})$ does not contribute because of the orthogonality of the initial and final target states. This quantity, which can be readily evaluated, can be expressed in the form

$$M(\vec{k}, \vec{k}_B) = \sum_{n=1}^{\infty} A_n(\vec{k}_B, \vec{k}_B \cdot \hat{K}) K^n, \quad (22)$$

where the coefficients A_n are linear combinations of Legendre polynomials. In the limit of small momentum transfer f_{B1} behaves like K^{-1} , reflecting the fact that at small momentum transfers ionization is mainly into continuum p states. Considering only the intensities parallel or antiparallel to the momentum transfer direction K ,

$$d^3\sigma = \frac{4k_A k_B}{k_0 K^2} (a_0 \pm a_1 K + a_2 K^2 + a_3 K^3 + \dots) \quad (23)$$

where \pm signs correspond to the parallel and antiparallel directions respectively.

The Born triple differential cross section can be related to the generalized oscillator strength by (26)

$$\frac{df}{dE} = d^3\sigma K^2 \frac{k_0}{2k_A} (E_B + IP) \quad (24)$$

Relative values of a_i up to $i=5$ are obtained by Ehrhardt and coworkers by fitting expression (23) to relative values of the generalized oscillator strength obtained from the measured relative cross sections. Extrapolation to $K=0$ and the known absolute oscillator strength yields the coefficient a_0 in absolute units, and therefore the other a_i and the TDCS. An additional constraint is that the intensities of the binary and recoil peaks have to be equal at $K=0$ (ionization into the p continuum). There are some uncertainties about this extrapolation procedure. It assumes that the first Born approximation gives the correct K dependence of the cross section in the $\pm K$ direction in the region being measured. However this may not be so. For instance the first Born approximation predicts a maximum in the direction \vec{K} the binary peak, and for small K and k_B a recoil peak with a maximum in the direction $-\vec{K}$. This is manifestly not the case. However, it is likely that the parametrization involved in expression (23) still adequately describes the actual cross section. The extrapolation procedure used by Ehrhardt et al(25) is shown in figure 6, where the measured intensities in the binary peak in the \vec{K} direction and in the recoil peak in the $-\vec{K}$ direction are used to extrapolate to the $K=0$ region. The dipole oscillator strength at $K=0$ was taken from Samson(27). They estimate their error to be less than 15%.

The dashed curve in figure 6 shows the expected intensities in the $\pm K$ directions in the B1 approximation. This shows quite clearly that the first Born approximation breaks down even in this domain of relatively high incident

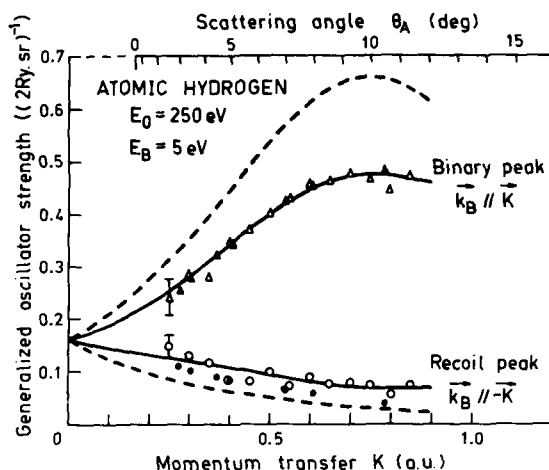


FIGURE 6

Generalized oscillator strength in the directions $+\hat{K}$ and $-\hat{K}$ as a function of momentum transfer K and scattering angle θ_A (ref. 25). The dashed curve shows the B1 result, the Δ and \bullet a B2 result, and the solid curve is the polynomial fit to the data.

energy ($\geq 181P$) and low momentum transfer. The results of a second Born calculation give a much better description of the data (triangles and dots).

Figure 7 shows a polar and cartesian plot of their TDCS compared with B1 (dash-dot curve) B2 (dashed curve) and EBS (solid curve) cross sections. The data again clearly demonstrates the need for higher order approximations to adequately describe the dynamics of the collision process. Although the Flinders data are not shown in figure 7, they are in excellent agreement with the Kaiserslautern data after suitable normalization.

Finally let me discuss briefly the high momentum transfer region. In this region the impulse approximation should be valid, and at high enough energies we can replace the distorted waves by plane waves (PWIA). The PWIA cross section for atomic hydrogen is simply

$$d^3\sigma = (2\pi)^4 \frac{k_A k_B}{k_0} f_{ee} |\phi_{1s}(p)|^2, \quad (25)$$

where $\vec{p} = -\vec{q} = \vec{k}_A + \vec{k}_B - \vec{k}_0$ is the momentum of the struck electron and f_{ee} is the half-off-shell Mott scattering cross section. In the symmetric geometry f_{ee} varies rapidly with θ but is nearly independent of ϕ . Thus in the noncoplanar symmetric geometry, where $k_A = k_B$, θ is fixed, and the out of plane azimuthal angle $\phi = \phi_A - \phi_B - \pi$ is varied, the cross section should be directly proportional to the square of the momentum space ground state wave function of atomic hydrogen, i.e. the one electron momentum probability distribution. Figure 8 shows the 400 eV, 800 eV, and 1200 eV data of Lohmann and Weigold(28) compared with the absolute square of the ground state Schrödinger wave function. This is the first direct measurement of the probability distribution of an electron in atomic hydrogen, a case which is discussed in most introductory texts on quantum mechanics by means of "thought" experiments. This type of

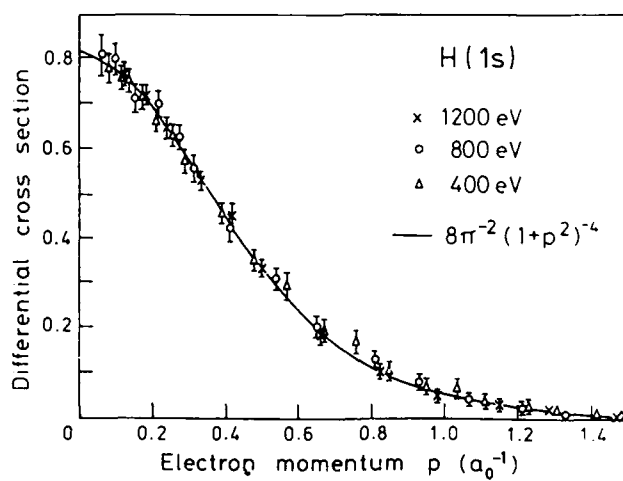
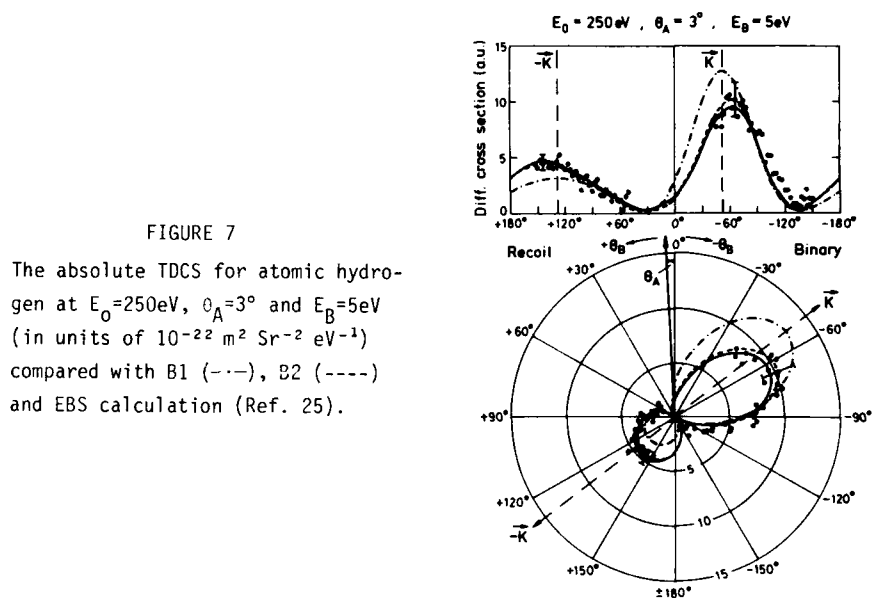


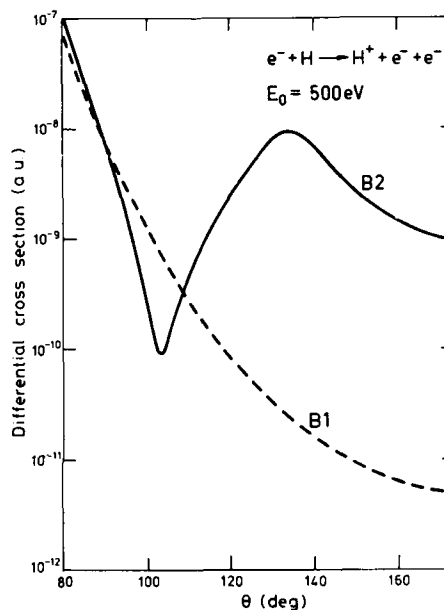
FIGURE 8

The noncoplanar symmetric (e,2e) cross section for atomic hydrogen at the indicated energies compared with $|\phi_{1s}(1p)|^2 = 8\pi^{-2}(1+p^2)^{-4}$, the Schrödinger momentum probability distribution.

measurement, which gives information on the structure of the target, has given rise to the field of electron momentum spectroscopy.

Second order or distortion effects are small in the high energy high momentum transfer region. Byron, Joachain and Piraux⁽²⁹⁾ have calculated some of these effects, and figure 9 shows their results at large angles θ for the

FIGURE 9
The large angle coplanar symmetric TDCS for atomic hydrogen at $E_0=500\text{eV}$ in the first (B1) and second (B2) Born approximations (ref. 29).



coplanar symmetric (e,2e) collision on atomic hydrogen at 500 eV. The cross section for $\theta > 80^\circ$ is very small compared to that in the region of the peak at $\theta \sim 45^\circ$, and so these effects are difficult to observe.

They have, however, been observed in the case of helium, where the effects are expected to be larger and the experiments are a lot easier to carry out. Pochat et al⁽³⁰⁾ in a coplanar symmetric experiment at 200 eV found that the B2 calculation described the trends in the measured cross section quite well, although the B1 cross section was nevertheless adequate over the entire range of backward angles ($\theta > 45^\circ$) studied. Cook et al carried out a detailed study of the (e,2e) process in helium in a 1200 eV noncoplanar symmetric experiment⁽³¹⁾. Their data for the ground state transitions are shown in figure 10 plotted as a function of struck electron momentum p . A logarithmic scale is used to highlight the small cross section region. The DWIA gives an excellent description of the data, while the PWIA does quite well for p less than about 1.3 a.u. Two different He ground state wave functions are used in the PWIA calculations, an accurate correlated wave function due to Joachain and Vanderpoorten (indicated by JV) and the Hartree-Fock wave function. For the DWIA calculation only the H-F wave function was used. Absolute symmetric coplanar (e,2e) cross sections have also been obtained for helium⁽³²⁾, and they are in excellent agreement with the DWIA results and at higher energies with the PWIA.

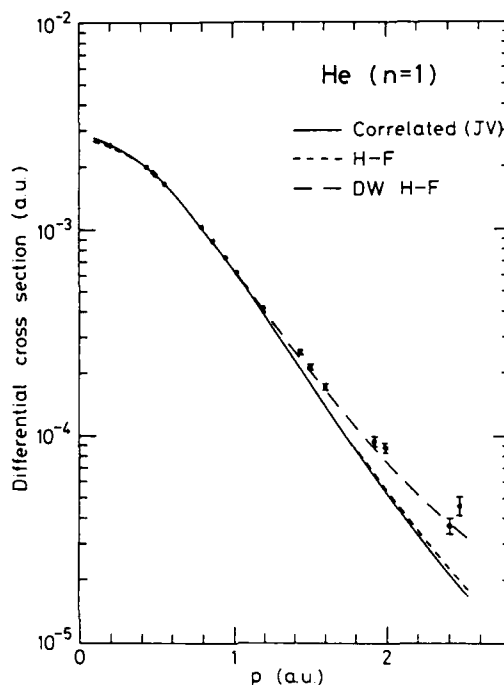


FIGURE 10

The 1200eV noncoplanar symmetric (e,2e) cross section for He plotted as a function of recoil momentum. The PWIA curves are obtained using an accurate correlated He ground state wave function (full curve) and the H-F wave function (broken curve). The DWIA (chain curve) uses the HF wave function.

4. SUMMARY

The understanding of ionization, which proceeds by an iterative interaction between theory and experiment, has reached an interesting stage. For symmetric noncoplanar geometry at high energy the simplest form of the impulse approximation, the PWIA, is sufficient. The DWIA describes even the fine details of these cross sections. The PWIA is the basis of the enormously successful application of the noncoplanar symmetric (e,2e) reaction to the understanding of many-electron atoms and molecules - namely electron momentum spectroscopy(1).

In the case of asymmetric kinematics and low momentum transfer, the collisions which dominate the ionization process, the PWIA approximation fails completely. The DWIA does considerably better, obtaining the correct shapes and relative magnitudes of the binary and recoil peaks, but it becomes unreliable in predicting the absolute magnitudes. Higher order Born expansions, such as the EBS method, give the correct absolute cross sections and give a good description of the data at the lowest values of momentum transfer and energy "loss" ($E_0 - E_A$) studied to date. At higher but still relatively low values of K even the EBS method does not appear to describe some of the details of the recoil peaks reliably.

As $E_0 - E_A$ and K increase no single approximation adequately describes the data over the entire range of angles. The asymptotic constraint on the effec-

tive charges seen by the emitted electrons gives the wrong values of the "effective" charges in the interaction region. In this intermediate regime it might require a more fundamental theory to devise successful approximations.

ACKNOWLEDGEMENTS

I am grateful to Ian McCarthy for many useful discussions and to Professors H. Ehrhardt and C. Joachain for sending me their experimental and theoretical results respectively prior to publication. I am also grateful to the Australian Research Grants Scheme for supporting my work.

REFERENCES

- (1) I.E. McCarthy and E. Weigold, *Phys. Rep.* **27C** (1976).
- (2) A. Hamnett, W. Stoll, G. Branton, C. Brion, and M.J. Van der Wiel, *J. Phys. B* **9** (1976) 945.
- (3) H. Ehrhardt, M. Schultz, T. Tekaas and K. Willmann, *Phys. Rev. Lett.* **22** (1969) 89; H. Ehrhardt, K.H. Hesselbacher, K. Jung, and K. Willmann, *Case Studies in Atomic Physics* (North Holland, Amsterdam) **2** (1971) 159.
- (4) I.E. McCarthy and A.T. Stelbovics, *Phys. Rev.* **28A** (1983) 2693.
- (5) J.F. Williams, *J. Phys. B.* **8** (1975) 2191.
- (6) J.F. Williams, *J. Phys. B.* **14** (1981) 1197.
- (7) C.R. Lloyd, P.J.O. Teubner, E. Weigold and B.R. Lewis, *Phys. Rev. A* **10** (1974) 175.
- (8) A.E. Kingston, W.C. Fon, and P.G. Burke, *J. Phys. B.* **9** (1976) 605.
- (9) B.H. Bransden, T. Scott, R. Shingal, and R.K. Roychoudhury, *J. Phys. B.* **15** (1982) 4605.
- (10) F.W. Byron, Jr. and C.J. Joachain, *Phys. Rep.* **34C** (1977) 233.
- (11) F.W. Byron, Jr., C.J. Joachain, and B. Piraux, *J. Phys. B.* **15** (1982) L293.
- (12) F.W. Byron, Jr., C.J. Joachain, and B. Piraux, *Phys. Lett.* **99A** (1983) 427.
- (13) F.W. Byron, Jr., C.J. Joachain, and B. Piraux, *J. Phys. B.* (in press).
- (14) K.L. Baluja and H.S. Taylor, *J. Phys. B.* **9** (1976) 829.
- (15) D.H. Madison, R.V. Calhoun and W.N. Shelton, *Phys. Rev. A* **16** (1977) 552.
- (16) B.H. Bransden, J.J. Smith, and K.H. Winters, *J. Phys. B.* **11** (1978) 3095.
- (17) J.J. Smith, K.H. Winters, and B.H. Bransden, *J. Phys. B.* **12** (1979) 1723.
- (18) R.J. Tweed, *J. Phys. B.* **13** (1980) 4467.
- (19) E. Alt, P. Grassberger, and W. Sandhas, *Nuclear Physics* **82** (1967) 167.
- (20) J.C.Y. Chen and A.C. Chen, *Adv. At. Mol. Phys.* **8** (1972) 71.
- (21) M.R.H. Rudge, *Rev. Mod. Phys.* **40** (1968) 564.
- (22) M. Schulz, *J. Phys. B.* **6** (1973) 2580.
- (23) E. Weigold, C.J. Noble, S.T. Hood and I. Fuss, *J. Phys. B.* **12** (1979) 291.
- (24) B. Lohmann, I.E. McCarthy, A.T. Stelbovics and E. Weigold, *Phys. Rev. A* **30** (1984) 758.
- (25) H. Ehrhardt, G. Knoth, P. Schlemmer and K. Jung, *Physics Lett.* (to be published).
- (26) M. Inokuti, *Rev. Mod. Phys.* **43** (1971) 297.
- (27) J.A.R. Samson, *Adv. At. Mol. Phys.* **2** (1966) 177.
- (28) B. Lohmann and E. Weigold, *Phys. Lett.* **86A** (1981) 139.
- (29) F.W. Byron, C.J. Joachain, and B. Piraux, *J. Phys. B.* (in press).
- (30) A. Pochat, R.J. Tweed, J. Peresse, C.J. Joachain, B. Piraux, and F.W. Byron, Jr., *J. Phys. B.* (in press).
- (31) J.P.D. Cook, I.E. McCarthy, A.T. Stelbovics and E. Weigold, *J. Phys. B.* **17** (1984) 2339.
- (32) B. Van Wingerden, J.T. Kimman, M. Van Tilbury, E. Weigold, C.J. Joachain, B. Piraux, and F.J. de Heer, *J. Phys. B.* **12** (1979) L627.

e - 2e COLLISIONS NEAR IONIZATION THRESHOLD - ELECTRON CORRELATIONS

J. MAZEAU, A. HUETZ and P. SELLES
Lab. de Physique et Optique Corpusculaires T.12
Université Pierre et Marie Curie
4, place Jussieu
75230 PARIS Cedex 05 - FRANCE

1. INTRODUCTION

When two electrons move in the field of a positive ion, because of the long range Coulomb interaction, correlation effects are expected to be more and more dominant as their kinetic energies decrease. This situation occurs near the threshold for double photoionization as well as for electron impact ionization processes, the latter appearing easier to study experimentally.

A fundamental contribution to the understanding of these processes is the work of Wannier (1) who has shown that they would occur most probably in a configuration where both electrons are at equal distances from the ion and in opposite directions. This configuration corresponds to the center of the flat saddle potential surface which represents the fixed R interaction between the 3 particles when hyperspherical coordinates $[R = \sqrt{r_1^2 + r_2^2}, \alpha = \tan^{-1}(r_2/r_1), \Theta_{12} = \cos^{-1}(\hat{r}_1 \cdot \hat{r}_2)]$ are used. The radial correlation (which tends to determine the energy distribution between the two electrons) is related to the instability in α around $\alpha = \pi/4$, while the angular correlation is related to the stability in Θ_{12} around $\Theta_{12} = \pi$.

So when dealing with electron correlations in electron impact ionization (only the e-He system will be considered here) two important questions have to be answered :

i) What is the probability for partitioning the excess energy E above threshold between the two outgoing electrons with energy E_1 and E_2 ? Up to 3.6 eV above threshold it has been found experimentally (2) (3) (4) that all the couples (E_1, E_2) are equiprobable. This is in agreement with the Wannier theory and ergodic hypothesis (1) (5) but in contradiction with some results of the rival Coulomb dipole theory of Temkin (6) (7) in which the faster electron sees the attractive field of the dipole formed by the slower electron and the positive ion. Very recently the energy partitioning problem has been reexamined by Read (8). Still admitting the ergodic hypothesis and analysing more carefully the classical trajectories in the Coulomb zone, he obtained a distribution function where equal sharing ($E_1 = E_2$) is slightly more probable by 5%, a result which has been confirmed experimentally (9).

ii) Is there an angular correlation between the two outgoing electrons ? The prediction of Wannier (which was limited to a total angular momentum $L = 0$) is that the angular distribution has a maximum for $\Theta_{12} = \pi$ with a gaussian shape the width of which varies as $E^{1/4}$. On the experimental side, by coincidence measurements in a plane perpendicular to the incident beam, Cvejanovic and Read (2) have confirmed the $E^{1/4}$ law but as the angular resolution was poor, the determination of the width was not very accurate. More recently, Schubert et al. (10) have measured in a coplanar geometry the angular correlation between the two outgoing electrons at 6 eV above threshold. They observed a correlation with maximum at about $\Theta_{12} = 220^\circ$.

and not at 180° as predicted by the $L = 0$ Wannier theory (1). This can mean that 6 eV is too high for threshold theory to be applied and/or as pointed out by Greene and Rau (11), that other $L S \Pi$ states contribute to the ionization process.

This is why we have undertaken coplanar measurements from 6 eV down to 0.5 eV above threshold (12) with the goal to look for an eventual contribution of a few $L S \Pi$ states, to test the threshold theories and try to determine the energy range of validity.

2. EXPERIMENT

The experimental set up consists essentially of a single selector and two double analysers similar to those described elsewhere (13). The selector and one of the analysers can rotate individually or simultaneously by means of two stepping motors so that the angles of the two detected electrons with respect to the incident beam can be scanned. To avoid small drifts with time, accumulation at different angles is done cyclically. The difficulty at low energy is that there are a lot of unwanted scattered electrons; the use of two electrostatic analysers in series as well as an appropriate set of potentials on the optics reduces this noise. When both electrons have the same energy, invariance of the coincidence signal when interchanging the angles of the two analysers is checked throughout the measurements. In particular, it has been verified that when $\Theta_2 = \Pi$ (2 detectors in opposite directions) the curve obtained by plotting the coincidence signal as a function of the angle Θ_1 (angle between the incident beam and one of the 2 detectors) is symmetric with respect to $\Theta_1 = 90^\circ$. The invariance of the position and width of the coincidence peak, when the selector and the detector are rotated is also, at low energy, a test for a good angular response of the equipment. Finally because of the need for high incident intensity due to the decrease of the cross section near threshold, the resolution in energy is about 0.2 eV and the acceptance of each analyser is rather large (about 10°). The statistical accuracy, when random coincidence and normalisation procedures are taken into account is typically 10%.

3. RESULTS

In the following we adopt the convention that the two outgoing electrons are located by their spherical angles $\Theta_1, \varphi_1, \Theta_2, \varphi_2$, the z axis being taken along the incident beam direction. In the present coplanar measurements $\varphi_1 - \varphi_2 = 180^\circ$ and the mutual angle Θ_2 is equal to $\Theta_1 + \Theta_2$.

Figures 1, 2 and 3 show the measured triple differential cross section plotted in polar coordinates for equal sharing of the energy between the 2 electrons ($E_1 = E_2$) at 3 energies above threshold ($E = 2, 1$ and 0.5 eV) and for 5 values of Θ_1 ($30^\circ, 60^\circ, 90^\circ, 120^\circ$ and 140°). The incident electron comes from the left and the direction of the first detected electron is represented by the second arrow. It is clear that whatever the direction of the first electron is, the second one is detected roughly around the opposite direction especially as E decreases. But it is only for $\Theta_1 = 90^\circ$ that the maximum of intensity is exactly located at $\Theta_2 = 180^\circ$. When going from 2 eV down to 0.5 eV it is also seen that the width of the lobes (in particular for $\Theta_1 = 90^\circ$) decreases which is consistent with the energy behaviour of the gaussian factor mentioned above. At 0.5 eV above threshold the lobes are still not invariant with respect to the direction of the first electron detected, consequently they cannot be interpreted within a $L = 0$ theory.

Indeed this is not so surprising as in the ionization process the Coulomb interaction dominates in the asymptotic region in opposition to threshold excitation where there is always a small energy range in which the centrifugal potential rules the cross section and thus depresses all the $\ell \neq 0$ with respect to s wave. Nevertheless we will see that these complicated shapes (double lobe for instance) still remain consistent with the Wannier theory when the rotation of the two electrons is taken into account.

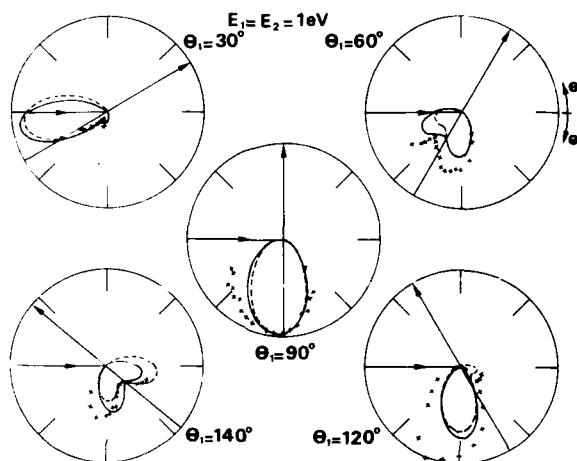


FIGURE 1

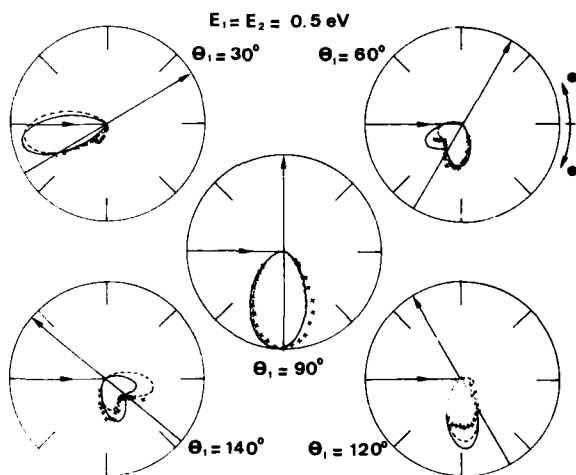


FIGURE 2

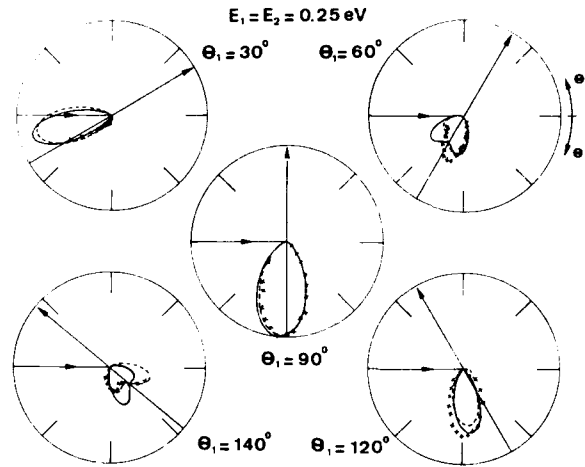


FIGURE 3

The contribution of $L \neq 0$ can also be directly seen by measuring the coincidence signal as a function of the angle Θ_1 when both detectors are kept in opposite directions (to be called Wannier geometry). This is clearly demonstrated in figure 4 for $E = 0.5$ eV and 1 eV and $E_1 = E_2$. It is first seen that, within the experimental uncertainties, the angular dependence of the signal is symmetric with respect to $\Theta_1 = 90^\circ$ as expected from the symmetry of revolution around the incident beam direction. Now in this configuration ($\Theta_2 = \pi$) and from only geometrical properties of the two electron wave function, the partial cross section varies as $|P_L(\cos \theta_1)|^2$ (14), thus the strong variations which are observed on figure 4 imply the participation of $L \neq 0$.

The quasi identity of the two experimental curves in figure 4 is an indication that the L mixing does not change from $E = 0.5$ eV to $E = 1$ eV. This is still approximatively true up to 2 eV while at higher energy (4 eV for instance) there is a significant change (in particular a spectacular enhancement in the small Θ_1 region).

Figure 5 shows the coincidence signal as a function of Θ_1 when both electrons are detected symmetrically with respect to the incident beam (symmetric geometry, $\Theta_1 = \Theta_2$) and for 2 different energies $E = 0.5$ and 1 eV. The enhancement of the width from the lower to the upper energy curve is again in qualitative agreement with the energy dependence of the angular correlation factor mentioned above.

A quantitative analysis of figures 4 and 5 will be presented in the following.

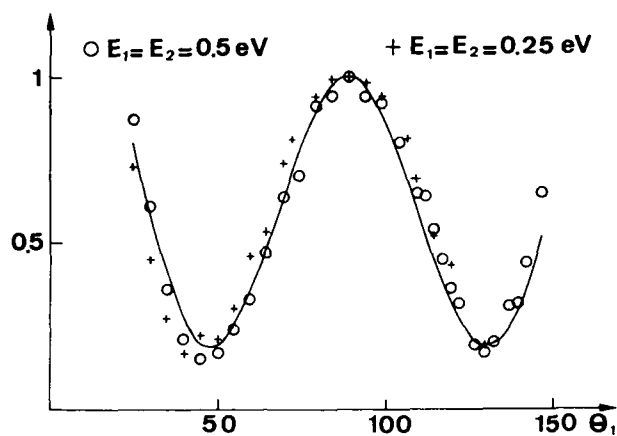


FIGURE 4 : $\theta_{12} = \pi$ — Fit

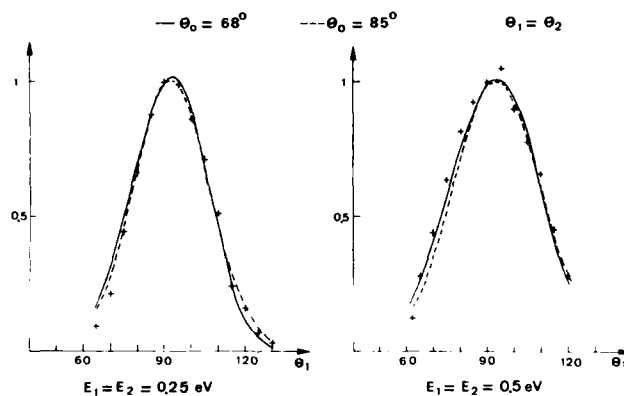


FIGURE 5

4. DISCUSSION

4.1. Derivation of the triple differential cross section for helium in the Wannier-Peterkop-Rau theory.

When dealing with the electron impact ionization of helium in its ^1Se ground state and limiting the angular momentum of the incident electron to $\ell \leq 2$, it follows from the conservation of parity, total angular momentum and its projection that 6 states for the two outgoing electrons can contribute, namely the ^1Se , ^3Se , ^1Po , ^3Po , ^1De , ^3De states.

Because of the strong correlation predicted by the Wannier theory a judicious choice of coordinates is required to describe the motion of the two electrons. The hyperspherical coordinates (R, α, θ_{12}) are well adapted to such a problem. They completely define the shape of the triangle formed by the 3 particles and three Euler angles can then be used to specify its orientation in space, such as $(\theta_1, \varphi_1, \psi)$, ψ being the angle between the planes (\vec{r}_1, \vec{r}_2) and (\vec{r}_1, \vec{z}) (15) (16).

As each $L S \Pi$ state has a specific angular dependence, the coherent superposition of a few of them leads to a complicated angular behaviour. Let us summarize the different steps which lead to the cross section formula.

Each $L S \Pi$ wave function $\Psi_{LS\Pi}^{M=0}$ is expanded on the rotational wave functions $D_{M=0,K}^L(\theta_1, \varphi_1, \psi)$

$$\Psi_{LS\Pi}^{M=0} = \sum_K G_K^{LS\Pi}(R, \alpha, \theta_{12}) D_{M=0,K}^L(\theta_1, \varphi_1, \psi)$$

After antisymmetrisation of the total wave function the following expressions are obtained (17) (18) :

$$^1S^0: F \quad \text{with} \quad F(R, \alpha, \theta_{12}) = F(R, \frac{\pi}{2} - \alpha, \theta_{12}) = \bar{F}$$

$$^3S^0: F \quad \text{with} \quad \bar{F} = -F$$

$$^1P^0: F \cos \theta_1 + \bar{F} \cos \theta_2$$

$$^3P^0: F \cos \theta_1 - \bar{F} \cos \theta_2$$

$$^1D^0: F_1(3\cos^2\theta_1 - 1) + \bar{F}_1(3\cos^2\theta_2 - 1) + F_3(3\cos\theta_1\cos\theta_2 - \cos\theta_{12}) \quad \text{with} \quad \bar{F}_3 = F_3$$

$$^3D^0: F_1(3\cos^2\theta_1 - 1) - \bar{F}_1(3\cos^2\theta_2 - 1) + F_3(3\cos\theta_1\cos\theta_2 - \cos\theta_{12}) \quad \text{with} \quad \bar{F}_3 = -F_3$$

where the F_i functions which are related to the G_K are solutions of "radial" equations in which only the three hyperspherical coordinates (R, α, θ_{12}) remain. For $L \geq 2$ they form a set of coupled differential equations.

Following the Wannier (1) Peterkop (19), Rau (20) theory, only configuration space near the Wannier saddle point is taken into account and only the asymptotic part of the wave function in the exit channel critically depends on the energy in the threshold region. Then the small E Schrödinger radial equations are resolved near the Wannier point and at large R . For each $L S \Pi$ one expects to obtain the partial cross section to within complex constants related to the connection with the unknown smaller R solution.

To be consistent this linearization of the radial equations requires the retention of all the terms up to β^2/R , V^2/R and $1/R^{3/2}$ (21)

where $\beta = \pi/4 - \alpha$ and $\gamma = \pi - \theta_{12}$ represent the distance to the Wannier point. Then two groups of consequences can be distinguished. Firstly, annulling $1/R$ terms has the same consequences for all the various $L S \Pi$ and thus the properties which have been demonstrated initially for the 1Se state (22) extend to the others. There are the following :

- i) each partial cross section is independent of the sharing of energy (E_1, E_2),
- ii) each partial cross section contains the angular correlation factor

$$\exp \left[-4 \ln 2 \left((\theta_{12} - \pi) / \theta_{1/2} \right)^2 \right] \quad \text{where } \theta_{1/2} \text{ depends on } E \text{ as } \theta_{1/2} = \theta_0 E^{1/4}.$$

Secondly, annulling $1/R^{3/2}$ terms yields the R and E dependence of the radial wave functions, and leads to a fundamental classification according to the parity under radial interchange ($\alpha \rightarrow \pi/2 - \alpha$). The partial cross section associated with the 1Se state which is purely symmetric ($F = \bar{F}$) behaves as $E^{1.127}$ which is the Wannier law, while that of 3Se which is purely antisymmetric ($F = -\bar{F}$) follows a E^n law where n is greater than 1.127 (the value $n = 3.881$ has been proposed by Greene and Rau (11) (23) and $n = 3.381$ by Peterkop (24) and Feagin (25)) and then is suppressed at threshold. The single radial wave function F of the $^1P^0$ and $^3P^0$ states which have been analysed by Roth (26) and Klar and Schlecht (27) can be split into a symmetric F^s plus an antisymmetric F^a component (11) (23) so that from the preceding their wave functions can be written :

$$\begin{aligned} ^1P^0 &= F^s (\cos \theta_1 + \cos \theta_2) + F^a (\cos \theta_1 - \cos \theta_2) \\ ^3P^0 &= F^s (\cos \theta_1 - \cos \theta_2) + F^a (\cos \theta_1 + \cos \theta_2) \end{aligned}$$

and the symmetric partial cross sections follow the Wannier law while the antisymmetric ones are suppressed at threshold.

For $L \geq 2$ the splitting $F_i = F_i^s + F_i^a$ of each radial component is still necessary but a new characteristic occurs. As mentioned above one is faced with a set of coupled radial equations that would be decoupled if limited to the order $1/R$ (17) but which are not when going to $1/R^{3/2}$. Thus one can expect, apart from determining the energy behaviour of the $L S \Pi$ partial cross section, to obtain some relationships between the F_i . In the case of the 1De state a detailed study indicates (18) that this relation is $F_3^s = -2 F_1^s$, but presently this remains an open theoretical question.

Using all these results, one finally obtains the following triple differential cross section (DCS) :

$$\frac{d\sigma}{d\Omega}(\theta_1, \varphi_1, \theta_2, \varphi_2, E) = \left[\frac{1}{4} |f_0|^2 + \frac{3}{4} |f_1|^2 \right] \exp \left[-4 \ln 2 \left((\theta_{12} - 180) / \theta_{1/2} \right)^2 \right]$$

with

$$f_0 = a_{1Se} + a_{p0}(\cos \theta_1 + \cos \theta_2) + a_{D0}(3/2 \cos^2 \theta_1 + 3/2 \cos^2 \theta_2 - 1)$$

$$- 2 \cos \theta_1 \cos \theta_2 + \cos \theta_{12})$$

$$f_1 = a_{3p0}(\cos \theta_1 - \cos \theta_2) + a_{3D0}(3/2 \cos^2 \theta_1 - 3/2 \cos^2 \theta_2)$$

$$\theta_{12} = \cos^{-1} [\cos \theta_1 \cos \theta_2 + \sin \theta_1 \sin \theta_2 \cos(\varphi_1 - \varphi_2)]$$

where the a_i are complex numbers. As long as the threshold region is concerned and following Peterkop (24) and Feagin (25) all the a_i which correspond to $L S \Pi$ states with no angular node for $\theta_{1/2} = \Pi$ (1Se , 1De , 3Po) have a $(E-0.5 E_0^{1.27})^{1/2}$ energy dependence while an angular node (such as in the above 1Po and 3De contributions) yields an additional $E^{-0.25}$ factor. Then integration over angles and energy E_1 leads to an integral cross section which varies as $E^{1.127}$ (11) (23) (24) (25).

The last missing point concerns the exact value of θ_0 in the law

$\theta_{1/2} = \theta_0 E^{1/4}$ giving the width of the gaussian factor. Some discrepancies exist in the literature between the values which have been obtained from the Wannier theory, due to the fact that different methods have been used. From a pure quantal formalism Rau (22) has obtained $\theta_0 = 85^\circ$, while $\theta_0 = 89^\circ$ comes out of the classical trajectories of Read (8) and $\theta_0 = 68^\circ$ from the JWKB formalism of Feagin (25) and Crothers (28). Besides these results an alternative asymptotic theory where the electron-electron interaction is taken into account separately has led Altick (17) to propose $\theta_0 = 67^\circ$ with no Z dependency. Note that in the Wannier theory the angular correlation factor completely disappears for $Z \geq 3$.

4.2. Analysis of the results

4.2.1. Analysis of the curve

The theoretical DCS which was derived in the last section contains 7 parameters concerning the mixing of states, which become 8 if θ_0 is included. A direct fit to the complete set of data, although possible, would link the determination of the mixing together with the testing of the Wannier theory. We find it preferable to separate the two as far as possible and to follow a step by step method which has been described elsewhere (12).

From pure geometrical and symmetry properties and without using any ionization theory it can be shown (14) that when $\phi_1 - \phi_2 = \pi$, $\theta_1 + \theta_2 = \pi$ (Wannier geometry) the DCS can be written :

$$\sum_{s=0,1} \frac{2s+1}{4} \left| \sum_{L \Pi} C_{LS\Pi}(E_1, E_2) P_L(\cos \theta_1) \right|^2$$

where all the $C_{LS\Pi}$ with $L + S$ odd cancel when $E_1 = E_2$ (18). This latter property then ensures that the summation contains only even powers of $\cos \theta_1$, which is called for by the symmetry of revolution around the incident beam axis.

When limiting $L \leq 2$ only the 1Se , 3Po and 1De states (the following would be the 3Po state) contribute and the DCS takes on the simple form $b_0 + b_2 \cos^2 \theta_1 + b_4 \cos^4 \theta_1$, where b_0, b_2, b_4 are real. It is straightforward to verify that the formula derived in the preceding section satisfies this property and to obtain the relations with the complex a_{1Se} , a_{3Po} and a_{1De} .

The above expression was fitted to the curve corresponding to $E_1 = E_2 = 0.5$ eV (figure 4) using a least squares method and $L \leq 2$ was found to be enough to get a good fit. The following values were obtained : $b_0 = 1$; $b_2 = -3.72 \pm 0.04$ and $b_4 = 4.26 \pm 0.07$. From these values it can be shown that a_{3Po} is weak and will be taken as zero. Under this condition the modulus and the argument of the ratio a_{1De}/a_{1Se} were found to be 0.7 and 2 rad, respectively.

4.2.2. Confrontation with the WPR theory.

As mentioned in § 4.1. the coefficients a_{1s^e} , a_{1p^e} and a_{3p^e} should have the same energy dependence in the threshold region thus giving a frozen curve shape in the Wannier geometry. This first prediction is indeed confirmed by the measurements up to $E = 2\text{ eV}$ (see §3).

Now another specific geometry, namely the symmetric one ($\Theta_1 = \Theta_2$, $\varphi_1 - \varphi_2 = \pi$), has the property of eliminating the contribution of triplet states as can be verified in the formula derived in section 4.1. So as the $1s^e$ and $1p^e$ states parameters have been obtained already, the comparison of the Wannier theory triple DCS with the $\Theta_1 = \Theta_2$ data of figure 5 only involves the two unknown quantities a_{1p^e} and θ_0 . Systematic fits to the curve with $E_1 = E_2 = 0.5\text{ eV}$ have shown that a reasonable agreement can only be obtained when $60^\circ < \theta_0 < 110^\circ$. Unfortunately a more precise determination cannot be achieved, as illustrated by the two curves reported in figure 5 corresponding to $\theta_0 = 68^\circ$, $|a_{1p^e}|/|a_{1s^e}| = 2.1$, $\arg(a_{1p^e}/a_{1s^e}) = 3.9\text{ rad}$ (full curve) and $\theta_0 = 85^\circ$, $|a_{1p^e}|/|a_{1s^e}| = 0.65$, $\arg(a_{1p^e}/a_{1s^e}) = 3.5\text{ rad}$ (dashed curve) respectively, which both fit satisfactorily. It should be noted that with only $1s^e$ and $1p^e$ states the DCS would be symmetric with respect to $\Theta_1 = 90^\circ$ (see formula of § 4.1). Thus the weak asymmetry which is seen in figure 5 is the signature of the $1p^e$ (or eventually $1f^e$) state. Its precise determination and that of Θ_0 would require better angular resolution and better statistical accuracy than in the present experiment.

In figure 5 the theoretical DCS for the two values of Θ_0 and for $E = 0.5\text{ eV}$ has also been presented. The observed enhancement of the width when E increases appears to be correctly reproduced, thus confirming in both cases the $E^{1/4}$ energy dependence of $\Theta_{1/2}$.

To summarize, the above analysis of only two curves ($\Theta_1 + \Theta_2 = \pi$ and $\Theta_1 = \Theta_2$ at $E_1 = E_2 = 0.5\text{ eV}$) has yielded quantitative information on $1s^e$, $1p^e$, $1d^e$ and $3p^e$ mixing. It is now possible to perform a comparison of the DCS for all the available (Θ_1, Θ_2) and $0.5 \leq E \leq 2\text{ eV}$ values (fig. 1, 2, 3). The general agreement is slightly improved with a small contribution from the $3d^e$ state ($a_{3d^e}/a_{1s^e} = 0.4$). For the 5 angles and for both $\Theta_0 = 68^\circ$ and 85° the agreement appears to be satisfactory for the 2 lowest values of E . For $\Theta_1 = 60^\circ$ and 140° , the double lobe structures ($E = 1$ and 2 eV) come out correctly from the calculations but differ in orientation and intensity from the experimental results. Some marked discrepancies which do not exist at $E = 0.5$ and 1 eV appear at 2 eV (see for instance $\Theta_1 = 120^\circ$ on figure 1). Of course a better comparison would need measurements in regions which are forbidden in the present experiment.

Finally it is interesting to point out that independently Altick (17) has fitted the data at $E = 1$ and 2 eV (fig. 2 and 1) with a theoretical DCS which is similar to that of § 4.1. with $\Theta_0 = 67^\circ$ but containing 9 parameters as the $1d^e$ state contribution has been written:

$$a_{1d^e}(3/2 \cos^2 \theta_1 + 3/2 \cos^2 \theta_2 - 1) + a_{1d^e}'(1/2 \cos \theta_{12} - 3/2 \cos \theta_1 \cos \theta_2)$$

A better agreement is obtained with the experiment while the deduced values of the modulus and phase of $(a_{1d^e} + a_{1d^e}'/2)$ which represent the contribution of $1d^e$ in the Wannier geometry and the triplet state coefficients are close to ours.

4.3. Ab-initio calculations of Crothers (28).

Very recently on the theoretical side, important progress has been accomplished by Crothers (28) who has given the absolute triple DCS for near threshold ionization of helium by following the lines of the Wannier Peterkop Rau theory but using a JWKB formalism which allows the determination of the

unknown constants. As mentioned in his paper, as a first order perturbation theory is used, some approximations are made on the final state angular dependence. In particular this leads in the notations of § 4.1. to phases of each $a_{LS\pi}$ equal to iL and to the elimination of terms such as the $(3 \cos \theta_1 \cos \theta_2 - \cos \theta_{12})$ component of $^1D^e$ state. However these calculations restricted to singlet states and $L \leq 3$ are in remarkable agreement with the data of fig 1 and 2 for $\theta_1 = 60, 90$ and 120° . Some discrepancies still exist elsewhere.

4.4. Dependence of the DCS on E_1, E_2 partitioning.

All the preceding experimental results were performed for equal sharing of the energy ($E_1 = E_2$) but as mentioned above the Wannier theory cross section is either independent or only very slightly dependent (8) on the partitioning of energy. This has been verified in integral (4) and double differential (2), (3), (9) cross section measurements but the triple DCS yields a finer test. A first confirmation involving the triple DCS at $E = 6$ eV, $E_1 = 4$ eV, $E_2 = 2$ eV has been reported by Schubert et al. (10). For a lower energy $E = 2$ eV and more pronounced unequal sharings ($E_1 = 0.25$ eV, $E_2 = 1.75$ eV and vice versa) figure 6 shows (at $\theta_1 = 90^\circ$) the triple DCS compared to that with $E_1 = E_2 = 1$ eV. These three curves are very similar and such a result, which also holds for other values of θ_1 , is a strong confirmation of Wannier theory validity. On the other hand the Coulomb dipole theory (6), (7) which would apply when $E_1 < E/5$ does not predict (29) a tight angular correlation and therefore disagrees with the present results, unless taking place at an incredibly low energy (7).

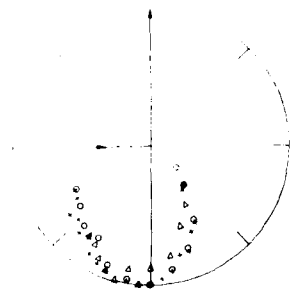


Figure 6

$\theta_1 = 90^\circ$
 + $E_1 = E_2 = 1$ eV
 o $E_1 = 1.75$ eV $E_2 = 0.25$ eV
 Δ $E_1 = 0.25$ eV $E_2 = 1.75$ eV

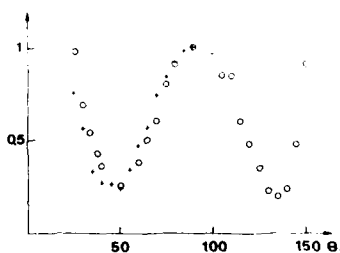


Figure 7

$\theta_{12} = \pi$
 + $E_1 = E_2 = 1$ eV
 o $E_1 = 1.75$ eV $E_2 = 0.25$ eV

Similarly figure 7 shows that in the Wannier geometry the curve for $E_1 = 0.25$ eV, $E_2 = 1.75$ eV is very close to that with $E_1 = E_2 = 1$ eV. Now dealing with the symmetry with respect to $\theta_1 = 90^\circ$, this is automatic when $E_1 = E_2$ (see §4.2.1.) ; when $E_1 = E_2$ any asymmetry could only appear by the contribution of terms such as the $^1P^a (\cos \theta_1 - \cos \theta_2)$ component of the $^1P^0$ state. Therefore the solely experimental observation that the $E_1 = 0.25$ eV, $E_2 = 1.75$ eV curve is symmetric directly supports the near threshold cancellation of the radially antisymmetric terms predicted by the Wannier theory.

5. CONCLUSION

The results presented in this report constitute the first direct experimental proof that a few (LSII) states definitely contribute to the near threshold ionization cross section. The Wannier Peterkop Rau theory is an useful tool to their understanding and a more precise determination of the angular correlation width is still needed. It has been shown that the values of the a_{LSII} coefficients can be extracted from the observations. These are physically interesting quantities as they are directly related to the probability of forming Wannier ridge riding states above the double escape threshold, and considerable theoretical effort is presently in progress to investigate such states.

Acknowledgments

The authors are indebted to Dr. ARP Rau for many helpful discussions and to Dr DSF Crothers for communicating his results prior to publication.

References :

1. G.H. Wannier, Phys. Rev. 90 (1953) 817.
2. S. Cvejanovic and F.H. Read, J. Phys. B : At. Mol. Phys. 7 (1974) 1841.
3. F. Pichou, A. Huetz, G. Joyez and M. Landau, J. Phys. B : At. Mol. Phys. 11 (1978) 3683.
4. G.A. Keenan, I.C. Walker and D.F. Dance, J. Phys. B : At. Mol. Phys. 15 (1982) 2509.
5. Vinkalns I. and Gailitis M., Proc. 5th Int. Conf. on the Physics of Electronic and Atomic Collisions, (Nauka, Leningrad 1967) Abstract pp.648-50.
6. Temkin A., J. Phys. B : At. Mol. Phys. 7 (1974) L 450.
7. Temkin A. Electronic and Atomic Collisions J. Eichler, I.V. Hertel, N. Stolterfoht Elsevier Science Publishers B.V. 1984, pp.755-765.
8. Read F.H., J. Phys. B : At. Mol. Phys. 17 (1984) 3965.
9. P. Hammond, F.H. Read, S. Cvejanovic and G.C. King, J. Phys. B : At. Mol. Phys. 18 (1985) L 141.
10. E. Schubert, K. Jung and H. Ehrhardt, J. Phys. B : At. Mol. Phys. 14 (1981) 3267.
11. C.H. Greene and A.R.P. RAU, Phys. Rev. Lett. 48 (1982) 533.
12. P. Fournier-Lagarde, J. Mazeau and A. Huetz, J. Phys. B : At. Mol. Phys. 17 (1984) L 591 and 18 (1985) 379.
13. F. Gresteau, R.I. Hall, A. Huetz, D. Vichon and J. Mazeau, J. Phys. B : At. Mol. Phys. 12 (1979) 2925.
14. A.D. Stauffer, Phys. Lett. 91A (1982) 114.
15. G. Breit, Phys. Rev. 35 (1930) 569.
16. P.M. Morse and H. Feshbach, Methods of Theoretical Physics vol 2 (Mc Graw Hill, New-york 1957) pp.1719-28.
17. P.L. Altick, J. Phys. B : At. Mol. Phys. 18 (1985) 1841.
18. P. Selles, A. Huetz and J. Mazeau to be published.
19. R. Peterkop, J. Phys. B : At. Mol. Phys. 4 (1971) 513.
20. A.R.P. Rau, Phys. Rev. A 4 (1971) 207.
21. A.R.P. Rau, Phys. Report : 110 (1984) 369.
22. A.R.P. Rau, J. Phys. B : At. Mol. Phys. 9 (1976) L 283.
23. C.H. Greene and A.R.P. Rau, J. Phys. B : At. Mol. Phys. 16 (1983) 99.
24. R. Peterkop, J. Phys. B : At. Mol. Phys. 16 (1983) L 587.
25. J.M. Feagin, J. Phys B : At. Mol. Phys. 17 (1984) 2433.
26. T.A. Roth, Phys. Rev. A 5 (1972) 476.
27. H. Klar and W. Schlecht, J. Phys. B : At. Mol. Phys. 9 (1976) 1699.
28. D.S.F. Crothers, to be published.
29. C. Bottcher, J. Phys. B : At. Mol. Phys. 15 (1982) L 463.

ELECTRON ATTACHMENT TO VAN DER WAALS MOLECULES

Y. HATANO

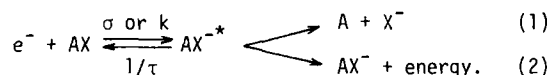
Department of Chemistry, Tokyo Institute of Technology
Meguro-ku, Tokyo 152, Japan

A survey is given of recent experimental studies of low-energy electron attachment to O₂, N₂O and other molecules in dense gases and in sonic nozzle beams with emphasis on the important role of pre-existing van der Waals molecules in the attachment mechanism. The experimental results particularly for O₂ are compared with recent theories. A survey is also given briefly of recent studies on electron solvation and localization in the condensed phase from the viewpoint of the studies on electron interaction with van der Waals molecules.

1. INTRODUCTION

Electron attachment is a process in which electrons are captured by atoms or molecules to form negative ions. Electron attachment or negative-ion formation processes are of great importance not only in atomic collision research itself, but also in related research fields such as radiation physics and chemistry, electrical discharge physics, plasma chemistry, new laser research and development, the space and upper-atmosphere sciences, etc.

Electron attachment processes are classified into two types; dissociative and non-dissociative processes as shown in the following reaction scheme,



Interaction of low-energy electrons with molecules, AX, produces unstable negative ions, AX^{-*}, with a cross section σ or a rate constant k . The autodetachment of electrons from AX^{-*} with a lifetime τ may compete with the dissociation of AX^{-*} or with the formation of stable molecular negative ion, AX⁻, which requires the release of excess energies from AX^{-*}. The lifetime τ is related to the electron-energy width of the attachment resonance. The value of $1/\tau$ is a rate constant for the autodetachment process. In the presence of third-body molecules, AX^{-*} is collisionally stabilized to form stable AX⁻. The branching ratios among the unimolecular processes of decaying AX^{-*} depend on the interrelationship of the potential energy curves between AX and AX⁻, and also on electron energies. The relative importance of the collisional stabilization process in the overall decaying processes of electrons depends largely on these unimolecular processes particularly the lifetime τ and of course on the number-density and character of third-body molecules, in which one may expect some *environmental effects* on the over-all scheme of electron attachment processes. In addition to the determination of cross sections or rate constants for electron attachment or negative-ion formation and their electron energy dependences, it has been of prime importance to clarify the attachment mechanism, not only the overall mechanism but how environmental conditions affect the mechanism.

Electron attachment processes have been extensively studied both theoretically and experimentally, and these are comprehensively summarized in recent review papers.[1-9]

Various types of *electron scattering experiments* at low energies less than several eV have given cross sections of electron attachment and information on the initial interaction potential between an electron and a molecule, and thus provided an efficient knowledge of the structure of formed negative ions. Since it has been very difficult, in general, to make electron attachment experiments using beam methods at extremely low energies particularly near thermal energies [10,11], heavy particle collisions such as those using Rydberg atoms[3,12,13] or alkali metal atoms[14] as low energy electron sources have been a good substitute giving an important information on electron attachment processes. Electron scattering experiments using beam methods at such low energies including even thermal energies are certainly one of the important subjects not only in collision physics itself but also as a bridge between beam experiments and swarm experiments.

Electron-swarm or drift tube techniques have played a major role in those investigations and accumulated data on attachment rate constants, their electron energy dependences, formed negative ions, etc[2,7]. Most electron swarm studies monitor the rate of removal of electrons in the swarm drifting in a tube, in most cases, under DC electric field in the presence of a buffer gas. Christophorou and his coworkers[2,7,15-18] have extensively studied electron attachment in dense gases as quasi-liquids by using his swarm technique and obtained interesting data also from the viewpoint of this review. The data will be carefully compared later in this review with those obtained by the present author's group[19]. In addition to usual swarm techniques an interesting approach of measuring cyclotron resonance signals due to free electrons in gases has been carried out for the study of electron attachment to various molecules as a function of electron energy in the range of 1 to 10 kT[20]. Another interesting approach to electron attachment studies is highly sensitive monitoring of electron density in the swarm by the Cavalleri method[21,22]. The pulse sampling technique[23] is simple but capable of yielding precise data particularly on energetics of negative-ion formation. A microwave technique for monitoring the rate of removal of electrons in the swarm has been combined with static or flowing afterglows produced by electrical discharges[24,25]. This technique has been recently combined also with the pulse radiolysis method in order to eliminate essential limitations including in the above-mentioned microwave technique[19,26-43]. The response time of the detection system for electrons has been highly improved and the effect of the presence of various species in afterglows on electron attachment processes has been eliminated. This combination, therefore, has given a reasonably good selectivity of measuring electron attachment processes even in multiple collision systems[19,31].

In the following one may find an unique standpoint of *the microwave technique combined with the pulse radiolysis method* in electron attachment experiments. For the study of electron attachment mechanism, ordinary swarm techniques may have some essential limitations in the experiment as they are almost unavoidable to use only a few environmental buffer gases for which the swarm parameters, electron energy distributions, etc., are well known. Therefore, in cases where the attachment mechanism is strongly dependent on the particular nature of environmental gases, the technique may not give enough information to evaluate adequately the mechanism in detail. Usual beam techniques are evidently not suitable for the study of environmental effects on the attachment mechanism. On the other hand, the microwave technique has been used as an alternative means for such studies with the main advantage of the technique allowing to observe the behavior of *thermal* electrons, thus excluding any factor dependent on the electron-energy distribution. For usual swarm and beam techniques it has been difficult to study electron collision processes at very low energies such as thermal, whereas such studies are obviously of great importance in understanding of not only a two-body problem such as electron interaction

with molecules, but also various phenomena in ionized gases.

The microwave technique combined with the pulse radiolysis method has shown recently a distinct advantage in studying thermal electron attachment to molecules [19,26-43]. By employing the pulse radiolysis method it is possible to perform time-resolved observation of decaying electrons with very fast response in a very wide range of the pressure of an environmental gas which is chosen with virtually no limitation. Thus, the mechanism of low-energy electron attachment to molecules has been discussed primarily in terms of the interaction of electrons with molecules.

Recent studies of thermal electron attachment to O_2 , N_2O and other molecules have revealed that the electron attachment to pre-existing van der Waals (vdW) molecules or neutral clusters plays a significant role in the overall mechanism [19,29-43]. The idea of electron attachment to dimer or cluster molecules was suggested and discussed to some extent in earlier studies [44-46] where electron attachment to O_2 was investigated at low temperature, but no definite conclusion on the mechanism could be drawn because of the insufficient experimental data. A significant development in such studies has been started in electron attachment studies using experimental techniques which were originated from radiation chemistry; one is the microwave technique combined with pulse radiolysis [19,32,33,35-37,40-43], the other is the competition kinetics of steady-state γ -radiolysis [47-49]. Evidently the existence of electron attachment to vdW molecules compels us more or less to re-interpret various experimental data obtained previously. Furthermore, since such process must be more important in dense gases or in the condensed phase, the studies of those processes will provide insight as to the effect of the density on the reactions involving electrons or generally on the electron-molecule interaction processes.

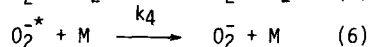
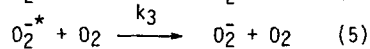
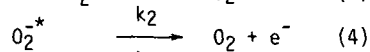
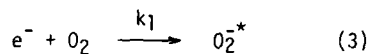
There have been remarkable advances in the investigation of electron dynamics in dense gases. The obtained experimental results and theoretical aspects of electron attachment, recombination and transport in dense gases have been summarized in recent review articles [2,15-19,83,89,141-143,158-160].

In this review, therefore, discussions are focused on the recent development in the experimental studies of electron attachment in dense gases giving evidence for an important role of pre-existing vdW molecules in the attachment mechanism, and on the essential features of electron attachment to vdW molecules in comparison with those of ordinary electron attachment to isolated molecules. Important results on electron attachment to ordinary isolated molecules have been also obtained in this experiment and they are compared with recent theories and experiments. A comparison between the results on electron attachment to vdW molecules and those on electron attachment to ordinary isolated molecules has clarified characteristic features of the former attachment mechanism, in which the substantial effect of the presence of vdW potentials on the electron attachment resonance has been indicated. The rate constant for the former attachment process is much larger than that for the latter process. The main emphasis of the argument is on the electron attachment to O_2 , but the attachment processes involving N_2O and some other molecules are also discussed. A survey is also given of recent related topics such as electron attachment to cold clusters in nozzle beams, Rydberg atom collisions with clusters to form negative ions, electron collisions with thin-layer condensed molecules, and electron solvation and localization in condensed molecular media.

2. THERMAL ELECTRON ATTACHMENT TO O_2 AND VAN DER WAALS MOLECULES CONTAINING O_2

Oxygen is probably the most extensively studied molecule in the investigation of low-energy (<1 eV) electron attachment, mainly because this molecule is a main constituent of atmospheric gases and therefore practically important in various viewpoints. A number of studies [2,5,16,19] have been devoted to elucidate the electron attachment mechanism since most experimental results have

shown that the rates of disappearance of electrons are proportional to the square of gas pressure. The well, and only, accepted mechanism has been the overall two-step three-body mechanism which was originally suggested by Bloch and Bradbury[50] and was later modified by Herzberg[46] to be consistent with modern experimental data; the mechanism for O_2 -M mixture, where M is a molecule other than O_2 , is expressed as follows,



The vibrational characteristics of the negative ion O_2^- are established from electron impact and scattering experiments[51-55] and the electron affinity of O_2 is 0.44 eV[56]. For convenience, the potential energy diagrams[19] for $O_2(X^3\Sigma_g^-)$ and $O_2^-(X^2\Pi_g)$ are shown in Fig.1. It can be seen that the lowest resonance involves the vibrational levels, O_2 ($v=0$) and O_2^- ($v'=4$), at low electron energies (especially for thermal electrons), and the resonance energy is about 0.08 eV. (See a detailed discussion in ref.[35])

Since all electron-decays for O_2 -M mixtures in the above-mentioned experimental condition show pseudo-first order behavior, each decay curve gives an electron lifetime τ_0 which is ascribed to the following thermal electron attachment process [31].



where k_{eff} is the effective two-body rate constant and is related to τ_0 as

$$k_{eff} = \frac{1}{\tau_0[O_2]} = \frac{k_1(k_3[O_2] + k_4[M])}{k_2 + k_3[O_2] + k_4[M]} \quad (8)$$

where the bracket [] means the density of each molecule. The key feature to which one should pay attention when one evaluates the validity of the Bloch-Bradbury (BB) mechanism is the saturation of electron attachment rate with increasing the pressure of M. This is due to the fact that the overall attachment rate can not exceed the value of k_1 , which can be understood from Eq. 8. Equation 8 can be reduced to

$$k_{eff} = \frac{k_1 k_4 [M]}{k_2 + k_4 [M]} \quad \text{or} \quad \tau_0[O_2] = \frac{1}{k_1} + \frac{1}{k_4 [M]} \quad (9)$$

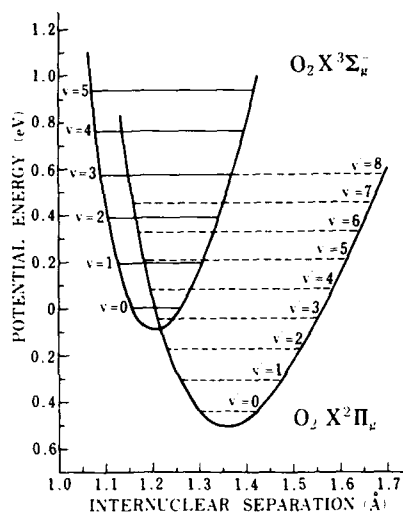


FIGURE 1
Potential-energy curves for O_2 and O_2^- [19].

when $[O_2]$ is much smaller than $[M]$, where $k_M (=k_1k_4/k_2)$ is the overall three body rate constant. Based on Eqs. 8 and 9, Shimamori and Hatano[31] confirmed the validity of the BB mechanism in many O_2 -M binary gas mixtures. From the plot of $\tau_0[O_2]$ against $1/[M]$ which is based on Eq. 9, they determined the value of $k_1=4.8 \times 10^{-11}$ cm³/sec and the value of k_M for each stabilization partner, which is listed in Table 1 with the values obtained by other workers. The auto-ionization lifetime of O_2^+ , i.e., the value of $1/k_2$, was also estimated to be $\sim 10^{-10}$ sec which was comparable to the predictions of some theoretical treatments[46,57-60] (see Table 2). On the other hand, however, there existed some inconsistencies between these results and other data. Christophorou and co-workers[15,17,61-63] investigated electron attachment in O_2 - C_2H_4 , O_2 - C_2H_6 and O_2 - N_2 mixtures at very high gas pressures (≤ 30 atm), and observed that the attachment rate in O_2 - C_2H_4 system showed a saturation at very high pressures, but the rates in O_2 - C_2H_6 and O_2 - N_2 mixtures continued to increase steeply with increasing the pressures of C_2H_6 and N_2 respectively. They reported the value of k_1 much larger than that obtained by Shimamori and Hatano[31] and correspondingly a considerably shorter lifetime of O_2^+ (see Table 2). A similar difficulty was encountered when the earlier work by Pack and Phelps[64,65] on O_2 - CO_2 mixtures was examined. Their result showed no saturation behavior up to 1 atm of CO_2 pressures, whereas according to the results of Shimamori and Hatano[31] the saturation could be expected at CO_2 pressures around several hundreds Torr. Such difficulties have been demonstrated more clearly and analyzed by recent work of Kokaku and coworkers [32,33].

Kokaku and coworkers in the joint research between Tokyo and Notre Dame have studied using the microwave technique combined with the pulse radiolysis method O_2 - CO_2 and several O_2 -hydrocarbon systems at pressures from less than 100 Torr to 1000 Torr and found that the BB mechanism can account for the data in the low pressure range but fails to explain the result at higher pressures. The data for O_2 - C_2H_4 mixtures are shown in Fig. 2 as an example, where the high density part of the data agrees well with the data obtained by Goans and Christophorou[62] using a swarm technique. This research[32,33] has clarified a significant discrepancy between the values of k_1 and $1/k_2$ obtained by the pulse radiolysis-microwave technique[31] and those obtained by the swarm technique[62]. A deviation from the three-body pressure dependence of attachment rates was also observed by Grünberg[77,78] for pure O_2 and O_2 - CO_2 mixtures and by Bartels for O_2 -He mixtures[79]. Thus it has become obvious that a consistent interpretation in terms

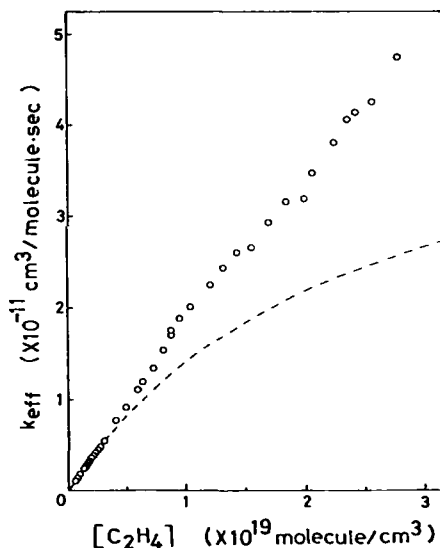


FIGURE 2
Dependence on C_2H_4 density of the effective two-body rate constant of thermal electron attachment in O_2 - C_2H_4 mixtures at room temperature. The dashed curve represents the expected contribution from the BB mechanism[32].

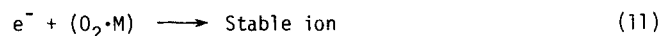
TABLE 1 Three-body Attachment Rate Constants, k_M , for the Reaction,
 $e^- + O_2 + M \rightarrow O_2^- + M$, at Room Temperature.

M	$k_M(10^{-30} \text{ cm}^6/\text{sec})$	Ref.	M	$k_M(10^{-30} \text{ cm}^6/\text{sec})$	Ref.
He	0.033	31	C ₂ H ₆	1.3	33
	0.03	44		1.5	62
	0.07	66		1.7	31
Ne	0.023	31		0.9	35
Ar	0.05	31	C ₃ H ₈	3.2	33
Kr	0.05	31		3.3	31
Xe	0.085	31	n-C ₄ H ₁₀	4.2	41
H ₂	0.48	29		4.5	33
D ₂	0.14	29		5	31
N ₂	0.06	44	n-C ₅ H ₁₂	7.9	31
	0.085	30	neo-C ₅ H ₁₂	7	32
	0.09	41		8.0	31
	0.1	67	n-C ₆ H ₁₄	8.1	31
	0.11	22,66	C ₆ H ₆	8.5	74
	0.15	62,63,68		18	73
	0.26	69	CO	1.31	41
	0.10	37	CO ₂	3	65,71,73
	1.7	69			74,76
	2.0	65		3.2	32
O ₂	2.1	45,66,70		3.23	67
	2.15	67		3.5	22
	2.2	29,41,71	H ₂ O	14	65,74,75
	2.3	30,68		15.2	73
	2.6	72	H ₂ S	9	74
	2.8	44		10	73
	2.2	22	NH ₃	6.8	74
	0.34	31		7.5	73
CH ₄	1.5	62	CH ₃ OH	8.8	74
C ₂ H ₄	1.7	73		9.6	73
	2.0	32		11	31
	2.3	72	C ₂ H ₅ OH	18	31
	2.5	74	CH ₃ COCH ₃	27	74
	3	31		35	73
	3.1	75			
	3.4	75			
	1.3	36			

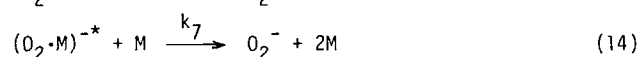
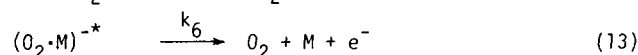
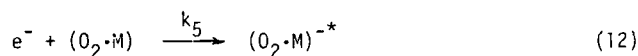
 TABLE 2 Lifetime of O_2^{-*} ($X^2\Pi_g$, $v'=4$)

Lifetime (10^{-12} sec)	Ref.	Author(s)
Theory		
300	46	Herzenberg (1969)
170	59	Koike and Watanabe (1973)
72	57,58	Koike (1973, 1975)
88	60	Parlant and Fiquet-Fayard (1976)
Experiment		
100	31	Shimamori and Hatano (1977)
63	41	Shimamori and Fessenden (1981)
2	61-63	Christophorou et al. (1972, 1972, 1974)
91	35	Toriumi and Hatano (1983)
66	37	Toriumi and Hatano (1985)

of only the BB mechanism is not possible in a wide range of the pressures of M and additional mechanism must be considered to explain the high-pressure data. One of the strong candidates for such a mechanism is *electron attachment to vdW molecules* as was indicated by Kokaku and coworkers[32,33].



where K_{eq} is the equilibrium constant for vdW molecule formation. One should note here that the density of vdW molecules is determined by $K_{eq}[\text{O}_2][\text{M}]$, and the value of K_{eq} can be estimated by Stogryn and Hirschfelder's theoretical treatment[80]. Several experiments have provided evidence for the existence of vdW molecules in the gas phase[81-83]. The analysis of experimental data for several O_2 -M mixtures[32,33] has shown that process 11 may not be a single step but a BB type mechanism involving an intermediate $(\text{O}_2 \cdot \text{M})^{-*}$;



In the treatment made by Kokaku and coworkers[32,33] k_{eff} is expressed as

$$k_{eff} = k_{eff}^{BB} + \frac{k_{eq} k_5 k_7 [\text{M}]^2}{k_6 + k_7 [\text{M}]} \quad (15)$$

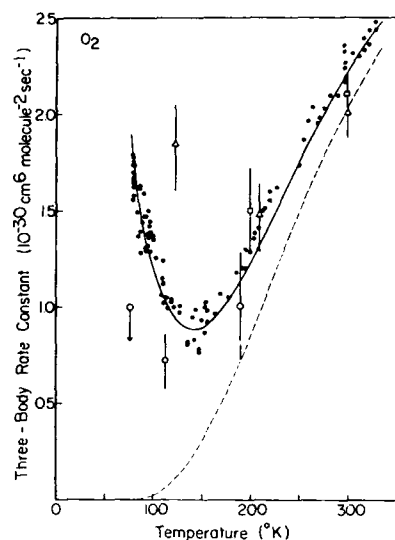
where k_{eff}^{BB} is equivalent to Eq. 8. The estimated values of k_5 are $(2-20) \times 10^{-9}$ cm³/sec depending on M, where it is highly attractive that all the values for k_5 are much larger than the value of k_1 ($=4.8 \times 10^{-11}$ cm³/sec). This result suggests that in the case of vdW molecules the initial electron capture mechanism differs substantially from the case of isolated molecules. There was some doubt in the proposed vdW mechanism in a sense that the introduction of such mechanism resulted from the procedure of data analysis in order to elucidate the additional mechanism of electron attachment at higher pressures of M. A recent study by Shimamori and Fessenden[41], however, has wiped out this doubt and verified the presence of the vdW mechanism. They have measured the temperature dependence of three-body rate constants in pure O_2 ($^{16}\text{O}_2$ and $^{18}\text{O}_2$), O_2 - N_2 , and O_2 -CO mixtures. The $^{18}\text{O}_2$ molecule has been used in order to understand the effect of a change in the resonance energy of the electron attachment. It has been found in the above system that when temperature is lowered from room temperature down to liquid nitrogen temperature the rate constants show marked increases. The result for $^{16}\text{O}_2$ is shown in Fig. 3. According to Herzenberg's theory[46], which is based on the Breit-Wigner formalism for the resonance capture, the three-body rate constant, as denoted here by k^{BB} which corresponds to the experimentally obtained k_M , can be expressed as

$$k^{BB} = \frac{2}{3} \left(\frac{h^2}{2\pi mk} \right)^{3/2} \epsilon \cdot k_L \cdot \left(\frac{1}{T} \right)^{3/2} \exp(-E_0/kT) \quad (16)$$

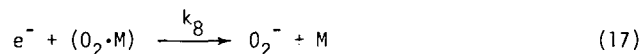
where h , m , and k have their usual meanings, k_L the Langevin's rate constant, ϵ the stabilization efficiency, T the absolute temperature, and E_0 the resonance energy. Equation 16 predicts a simple decrease in rate constant with reduced

FIGURE 3

The temperature dependence of the three-body rate constant of O_2 [41]. The broken line shows the temperature dependence of the rate constant calculated from Herzenberg's theory[46]. The solid line shows a calculated curve which involves both the contributions from the broken line and the rate constant due to electron attachment to van der Waals molecule $(O_2)_2$.



temperature. The expected curve for $^{16}O_2$ calculated from Eq. 16 assuming ξ to be unity is drawn in Fig. 3. Since an extra contribution which increases with lowered temperature is evident, electron attachment to the vdW molecule $(^{16}O_2)_2$ has been proposed to account for this. Similarly the importance of electron attachment to $(O_2 \cdot N_2)$ and $(O_2 \cdot CO)$ has also been demonstrated. Consequently the proposed mechanism responsible for the extra increase in attachment rates at low temperatures is written as



where M is not only a foreign molecule, but can be O_2 itself in the case of pure O_2 . Thus the total effective rate constant can be expressed as

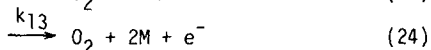
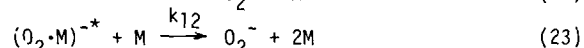
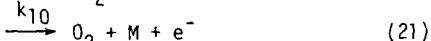
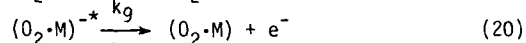
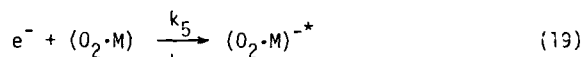
$$k_{\text{eff}} = k_M[M] + K_{\text{eq}}k_8[M] \quad (18)$$

where the first-term means a contribution from the BB mechanism in the low-pressure region. As the dependence of the excess portion of the rate constant on temperature follows rather closely the density of vdW molecules calculated on the basis of Stogryn and Hirschfelder's theory[80], the rate constant for electron attachment to vdW molecules is only weakly dependent on temperature. The estimated rate constants for this attachment are of the same order of magnitude as those obtained from high pressure data.

It is evident that not only at low temperatures but even at room temperature there are definite contributions from electron attachment to vdW molecules. In the case of pure oxygen approximately 10% of the attachment may be due to the vdW molecules at around room temperature. Quite remarkable is the result of O_2 - N_2 mixtures. The three-body rate constant for N_2 increases monotonically with reduced temperature, which implies that most of the electron attachment is resulting from a vdW mechanism at all temperatures studied (79-300 K). Therefore previous analyses and the interpretation of the experimental data for O_2 - N_2 system may need to be changed somewhat as far as the detailed mechanism is concerned.

Both pressure dependent[32,33] and temperature dependent[41] experiments, therefore, have given the evidence for an important role of pre-existing vdW molecules in the mechanism of thermal electron attachment in pure O_2 and O_2 -M mixtures. In the pressure dependent experiments, however, the obtained data have been analyzed, assuming the vdW mechanism as an overall two stage mechanism involving a collisional stabilization of $(O_2 \cdot M)^{-*}$, while in the temperature dependent experiments assuming the mechanism as a single-step process without collisional stabilization of $(O_2 \cdot M)^{-*}$. In order to get quantitative information about the vdW mechanism, it has been necessary to make experiments in the wide range of both pressure and temperature and to analyze the obtained data without these assumptions[35-37].

To analyze the experimental data of O_2 - C_2H_6 , O_2 - C_2H_4 and O_2 - N_2 mixtures, a general vdW mechanism has been presented[35-37] as follows;



The observed electron attachment rate constant, k_{eff} , is divided into two components.

$$k_{eff} = k_{eff}^{BB} + k_{eff}^{vdW} \quad (25)$$

The former component corresponds to electron attachment to isolated oxygen molecule or the BB mechanism, while the latter component to electron attachment to vdW molecule or the mechanism as listed above. The both components can be expressed as,

$$k_{eff} = \frac{k_1 k_M^{BB} [M]}{k_1 + k_M^{BB} [M]} + K_{eq} \frac{k_5 (k_{11} + k_{12} [M]) [M]}{k_9 + k_{10} + k_{11} + (k_{12} + k_{13} [M]) [M]} \quad (26)$$

This is a general expression for the pressure dependence of the observed attachment rate. The temperature dependence of the process 19 is given by,

$$k_5 = \frac{2}{3} \frac{2\pi h^2}{(2\pi mk)^{3/2}} \Gamma_5 \left(\frac{1}{\tau}\right)^{3/2} \exp(-E_r/kT) \quad (27)$$

where E_r and Γ_5 are, respectively, the energy and the width for the resonance attachment process 19. The observed electron attachment rates in the wide ranges of both pressure and temperature have been analyzed using Eqs. 16, 26 and 27 by the least-square fitting. Important rate parameters for the BB mechanism such as the rate constant for the initial electron attachment to O_2 (k_1), the lifetime τ of O_2^{-*} (χ^2/ν , $\nu=4$); i.e., the resonance width, and the overall three body attachment rate constants have been obtained from the experiments on O_2 - C_2H_6 , O_2 - C_2H_4 , and O_2 - N_2 mixtures. The values of τ are again in good agreement with those obtained by theories (See Table 2). Each three body rate constant is, respectively, smaller than that obtained previously without taking

TABLE 3 Rate Constant k_5 , Resonance Energy E_r , Resonance Width Γ_5 , Electron Density $v_r f_r$ and Cross Section σ_h

(O ₂ -M)	E_r (meV)	Γ_5 (μ eV)	$v_r f_r$	σ_h (\AA^2)	k_5 (10^{-11} cm ³ /sec)
(O ₂ -N ₂)	20	800	0.71	2500	3000
(O ₂ -C ₂ H ₆)	30	450	0.89	1700	1100
(O ₂ -C ₂ H ₄)	45	270	0.92	1100	380
O ₂	88(E_0)	10(Γ_1)	0.47	570	3(k_1)

into consideration of the vdW mechanism (See Table 1). The value of k_1 obtained from O₂-N₂ system[37], which is selected as a convenient system to determine the value of k_1 , is about 3×10^{-11} cm³/sec. This value agrees within experimental errors with those obtained from O₂-C₂H₆[35] and O₂-C₂H₄[36] systems, and with the value, 4.8×10^{-11} cm³/sec, which was obtained previously by Shimamori and Hatano[31]. This value is also consistent with qualitative results of k_1 obtained by other groups[66,69,71] except for the value obtained by the extremely high pressure swarm technique[62]. It should be noted here that the value, 3×10^{-11} cm³/sec, is in good agreement with the theoretical values, 2.5×10^{-11} [57-59] and 2.1×10^{-11} [60] cm³/sec.

The important rate parameters for the vdW mechanism such as the rate constant for the initial electron attachment to (O₂-M) where M=C₂H₆, C₂H₄ and N₂, and the lifetime τ of (O₂-M)^{-*}, i.e., the resonance width, have been also obtained from this experiment[35-37]. The rate constants for the initial electron attachment to (O₂-M) which are summarized in Table 3 are larger than those obtained from either pressure- or temperature-dependent experiment with an assumed mechanism.

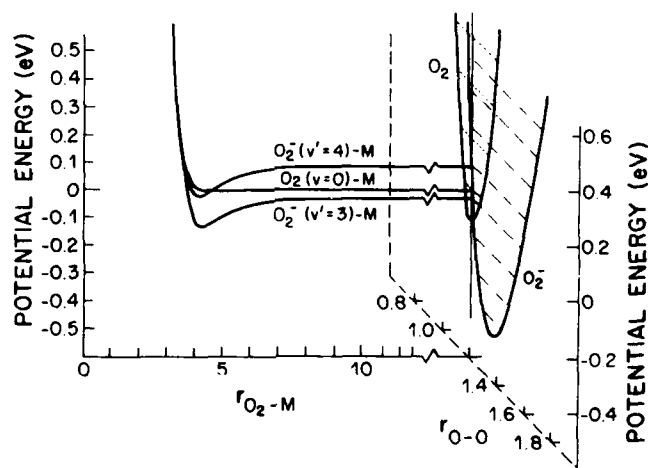


FIGURE 4

A model of variation of potential energies for O₂(v=0)-M and O₂(v'=4)-M systems as a function of intermolecular distance[19].

The values of k_5 in Table 3 are again much larger than the above-mentioned k_1 values. The values of the resonance energy and width are also summarized in Table 3. The resonance energy for $e^- + (O_2 \cdot M) \rightarrow (O_2 \cdot M)^{-*}$ is much smaller than that for $e^- + O_2 \rightarrow O_2^{-*}$, while its width for the former process is much larger than that for the latter process. The large enhancement in the attachment rate constant from k_1 to k_5 has been discussed qualitatively as related to the decrease in the resonance energy and the increase in the resonance width [37]. The reason for the decrease in the resonance energy has been ascribed to the fact that the resonance state is much stabilized by the polarization interaction between O_2 and M [19,35,41]. Such situation is depicted in Fig. 4 where schematic potential energy curves are shown for $O_2 \cdot M$ and $O_2^{-*} \cdot M$ systems [19]. Figure 4 shows that near to the equilibrium intermolecular distance the effective resonance energy of $O_2^{-*} \cdot M$ system is much reduced and even superimposed on the $O_2 \cdot M$ curve. The existence of a number of vibrational states in both ion complex and neutral systems may be another major factor of the large transition probabilities.

When the resonance width is narrower than the energy distribution of thermal electrons, the attachment rate constant is expressed as,

$$k_5 = \int v f_r dv = v_r f_r \int dv \quad (28)$$

where v is electron velocity, f is a Maxwell distribution function of electrons, σ is attachment cross section, the suffix r means a value at resonance energy E_r . The factor $v_r f_r$ in this equation means the density of electrons with velocity v_r to attach to vdW molecules. The value of $v_r f_r$ is given in Table 3, which shows that $v_r f_r$ increases with decreasing resonance energy. The number of electrons which can attach to vdW molecules increases as compared with those to isolated O_2 .

Since the cross section of a resonance process is expressed by the Breit-Wigner formula [46,84,85], the energy-integrated cross section is written as follows;

$$\int \sigma dE = \frac{4\pi^2}{3k^2} \Gamma_5 \quad (29)$$

where k is the wave number of incident electron, E_r and Γ_5 are assumed to be independent of energy, and σ_h means the effective magnitude of electron attachment cross section, which equals to $\sigma_h = \sigma / \sigma_0$, where σ_0 is the maximum value of σ . σ_h is also listed in Table 3. At extremely low energy electron collision such as electron attachment to vdW molecule, a "small" vdW molecule is supposed to collide with "large" electron clouds, of which cross section is determined by a size of the de Broglie wave length of incident electrons. With decreasing the resonance energy, therefore, the attachment cross section should increase. It should be noted that the maximum value of empirically obtained cross section values for dissociative attachment processes at low energy are reasonably explained by the de Broglie wavelength of incident electron [86,87].

The resonance width Γ_5 is expressed by Wigner's threshold rule [57-59]

$$\Gamma_5 \propto k^{2l+1} |F|^2 \quad (30)$$

where F is the Franck-Condon factor and l is an angular momentum of resonant electronic partial wave. In the case of isolated O_2 the resonance state $O_2^{-*}(X^1\Sigma_g, v'=4)$ can couple with only one electronic partial wave with an angular momentum $l=2$ [46,57-59]. In the case of vdW molecules intermolecular interaction may couple with additional partial waves such as p wave and s wave with

low energy. If the orbital of $O_2^-(\Pi_g)$ is distorted by a third-body molecule, new attachment channels can open with lower angular momentum of electrons and the resonance width may increase.

It has been necessary to make a quantitative calculation of these effects using precise wave functions of O_2 -M system. Very recently, Huo et al.[88] have made such calculations on O_2 - N_2 system and compared their result with experiments. They have been successful in explaining the large enhancement in the attachment rate constant for vdW molecules using SCF wave functions corresponding to two geometries, T-shape and linear, for $(O_2 \cdot N_2)$ vdW molecules. The large enhancement in the attachment rate constant has been clearly elucidated quantitatively in this theoretical calculation by the effect of additional vibrational structures of the vdW molecule on the attachment process, the symmetry breaking which allows the molecule to attach a p wave electron, and the lowering of resonance energy due to a deeper O_2 - N_2 potential in comparison with O_2 - N_2 potential as shown schematically in Fig. 4.

Very recently an interesting approach to this problem[42,43], the use of $^{18}O_2$ instead of $^{16}O_2$, has substantiated further the electron attachment to vdW molecules. For the BB mechanism, the isotope effect may be expected to appear as change in rates of the initial attachment and autoionization channels, which are caused by the decrease of the resonance energy for $^{18}O_2$ in comparison with $^{16}O_2$. Such an effect brings about the increase of the three-body rate constant for $^{18}O_2$ by a factor of about 2.4 which is obtained from the isotope effect of Eq. 16. In the case of the BB mechanism, therefore, the ratio of the three-body rate constant for $^{18}O_2$ system to that for $^{16}O_2$ system at the same temperature should be 2.4, while in the case of the vdW mechanism the ratio is expected to be unity. The experimental ratios for rare gases as third bodies are almost equal to or even less than unity, which strongly indicates that the BB mechanism is not important and therefore the vdW mechanism dominates in these systems. In contrast with rare gases the ratios for hydrocarbons are rather close to the theoretically estimated value 2.4.

As mentioned in the introduction of this review, electron swarm data[62] were reported in O_2 - C_2H_6 , O_2 - C_2H_4 and O_2 - N_2 systems up to about 10^{21} molecules/cm³ (3×10^4 Torr) and simply elucidated only by the BB mechanism. An attempt has been made[33,35,36], therefore, to elucidate the high-density region data by the combination of the BB mechanism and the vdW mechanism. The electron swarm data for O_2 - C_2H_6 and O_2 - C_2H_4 systems are well explained up to about 4×10^{20} molecules/cm³ by the combination of both mechanisms. It is obvious that the contribution from the vdW molecule is dominant in these density ranges. The large deviations in the data from the combination of the two mechanisms at the higher densities than 4×10^{20} molecules/cm³ may indicate the electron attachment to large vdW molecules such as $O_2(C_2H_6)_2$, or may require to introduce additionally some collective properties of these hydrocarbon molecules to explain the density effect of electron attachment in this region.

An attempt has been made to explain theoretically such density effects in the whole density ranges by using the polarization model[89,90], in which the electron attachment rate to an O_2 molecule depends on the number of hydrocarbon molecules inside an effective volume over which the electron attachment rate is significantly perturbed. The least-squares fit of the theoretically obtained equation to the data has given various rate parameters corresponding to the contribution from the larger clusters.

Electron attachment to O_2 has been investigated in various hydrocarbon fluids at densities up to about 10^{22} molecules/cm³ using the pulsed electric conductivity technique[91], and the results have been explained in terms of the effect of the change in the electron potential energy and the polarization energy of O_2^- in the medium fluids. In general electron attachment to O_2 is considered to be a convenient probe to explore electron dynamics in the con-

densified phase.

It must be pointed out finally that, since in many O_2 -M systems the BB mechanism has been found to be unsatisfactory especially in dense gases or at low temperatures and even at ordinary experimental condition such as at room temperature at low pressures an evidence for electron attachment to pre-existing vdW molecules has been obtained, then the magnitudes of the values of three body rate constants listed in Table 1 may not reflect the magnitudes of collisional stabilization efficiencies of O_2^* by third bodies.

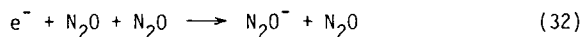
3. THERMAL ELECTRON ATTACHMENT TO VAN DER WAALS MOLECULES CONTAINING N_2O AND OTHER MOLECULES, AND A GENERAL DISCUSSION OF THE ATTACHMENT MECHANISM

There have been a number of studies of low-energy electron attachment to N_2O . The proposed mechanism was a dissociative electron attachment,



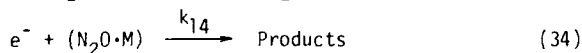
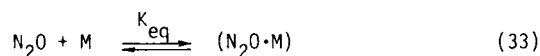
This process is known to be 0.21 eV endothermic, but early electron impact studies[92,93] indicated the process to have a threshold close to 0 eV, which was explained by attachment to internally excited N_2O molecules[94]. In fact a strong temperature dependence of O^- formation was found at electron energies near 0 eV[95].

On the other hand, quite interesting was the observation of an apparent three-body pressure dependence of attachment rates in pure N_2O even at electron energies below 0.2 eV[96,97]. This effect was ascribed to a three-body reaction



although there has been no evidence for N_2O^- formation by direct electron capture.

Most significant results obtained in recent studies[38-40], however, are the appearance of upward deviation from the saturation curve as expected from the two-step three-body processes for attachment rate in N_2O -hydrocarbon and N_2O - CO_2 mixtures in the high pressure regions. This behavior has been explained by the appearance of electron attachment to vdW molecules.



The estimated values of k_{14} are $(2-10) \times 10^{-11} \text{ cm}^3/\text{sec}$ depending on the third body M . These are about two orders of magnitudes larger than that for $e^- + N_2O \rightarrow N_2O^*$. It has also been found that the excess portion of the attachment rates shows almost no temperature dependence thus suggesting that process 34 has quite a small activation energy.

All these characteristics are quite similar to the case of oxygen. Therefore essentially the same effects as discussed in the case of O_2 may be responsible in the mechanism of electron attachment to the vdW complex ($N_2O \cdot M$). It may be plausible to extract from the results of O_2 and N_2O systems some general conditions under which one can predict the existence of electron attachment to vdW molecules. The common feature to both O_2 and N_2O is that the rate constants of electron attachment to those isolated molecules are relatively small (10^{-11} - $10^{-13} \text{ cm}^3/\text{sec}$) on an absolute scale. This is due to the presence of activation energy, i.e., the resonance energy, for electron attachment (0.08 eV for O_2 and 0.23 eV for N_2O). In contrast there is virtually no activation energy in the

electron attachment to vdW molecules containing O_2 or N_2O , thus yielding much larger rate constants for this process. The formation of vdW complexes appears to act just like it has an effect of lowering the activation energy or the resonance energy. Consequently one may expect to observe the contribution of vdW molecules only for compounds which have activation energies for electron attachment, or for the molecules of which attachment cross section for electron energies near thermal increases with increasing electron energy.

Independently of the experiments on O_2 and N_2O systems, however, electron attachment to hydrogen halide dimer, $(HX)_2$, has been observed by Nagra and Armstrong[47-49]. Although there are similarities between the vdW mechanisms for O_2 and N_2O systems and HX system, there are some significant differences. The rate constant for $e^- + HX$ is already close to the maximum value and the large enhancement in the rate constant can not be expected for $e^- + (HX)_2$. The mechanism of this type of electron attachment to vdW molecules may be largely different from that of O_2 or N_2O system.

Recent preliminary studies[98] of thermal electron attachment to CH_2Cl_2 in pure CH_2Cl_2 and CH_2Cl_2 -hydrocarbon mixtures may be interesting from the point of view discussed above. In order to confirm the above viewpoint the pressure dependence of thermal electron attachment rates have been examined in SF_6 -hydrocarbon and $n-C_4F_{10}$ -hydrocarbon mixtures[98]. The observation of the pressure dependent electron attachment to SO_2 , C_2H_5Br and C_6H_6 at very high pressures of N_2 , C_2H_4 , and Ar as environmental gases[62,99,100] is also quite attractive.

One may expect generally that even in the case of molecules with negative electron affinities or with high threshold electron energies for attachment some environmental effects or the effect of the vdW molecule formation bring about the large enhancement in the cross sections or the rate constants for the lower energy electron attachment to these molecules. Based on the discussions presented in the preceding chapters in this review, the reasons for this expectation are summarized as follows:

- 1) *The lowering of the resonance energy*, due to a deeper ion-neutral potential in comparison with neutral-neutral potential of the vdW molecule.
- 2) *The additional vibrational structures* of the vdW molecule.
- 3) *The symmetry breaking* due to the vdW interaction which allows the molecule to attach electron with additional partial waves.
- 4) *The deformation of the molecular structure* or the change of the vibrational modes due to the surrounding molecules.
- 5) *The additional vibrational relaxation* of the formed negative ion with excess energies due to the presence of a bath of third body molecules in the vdW molecule.

Further investigation from different approaches is greatly needed to solve these problems and thus to substantiate more an important role of vdW molecules in the mechanism of electron attachment.

4. ELECTRON ATTACHMENT TO VAN DER WALLS MOLECULES IN SONIC NOZZLE BEAMS

Electron attachment to vdW molecules has been observed also in electron impact experiments using sonic nozzle beams.

Increasing interest has been shown recently in the static and dynamic behavior of neutral and ionic clusters[101]. In the case of ionic clusters there have been already extensive studies on their stability and reaction dynamics, while in the case of neutral clusters or vdW molecules which are relatively new subjects of research there has been just a dramatic growth of interest in such studies during the past several years. Various properties of vdW molecules, e.g., their structure and size, have been investigated using optical spectrosc-

copy and electron-impact or photoionization mass-spectrometry of vdW molecules which are produced in sonic nozzle beams. Recently, however, special attention has been paid further to *the interactions or collisions of vdW molecules* [83,101]. This is an important subject of research in the future from the viewpoint of both collision research and cluster research.

Klots and Compton [102-106] have studied electron attachment to vdW polymers of CO_2 , N_2O and H_2O which are produced in sonic expansions and found various new features of electron attachment processes. In the case of CO_2 which has a negative electron affinity and can not form stable linear CO_2^- , they have detected $(\text{CO}_2)_n^-$ with $2 \leq n \leq 6$ and ascribed this result to stable bent CO_2 surrounded with linear CO_2 molecules. In the case of N_2O which one may expect a similar conclusion to the case of CO_2 , however, they have not detected $(\text{N}_2\text{O})_n^-$ but $\text{O}^-(\text{N}_2\text{O})_n$ and explained the difference between the two cases in terms of energetics of the fragmentation of the initially formed polymer ions. The observation of $(\text{CCl}_4)(\text{CO}_2)$ is particularly interesting because thermal electron attachment to CCl_4 yields almost entirely Cl^- . The detection of the parent ion, such as those in the case of CO_2 and CCl_4 surrounded with neutral molecules is a good example of *the collisional stabilization by a built-in third body*. Experimental evidence for the thermal electron attachment to CO_2 to form CO_2^- was already obtained in the condensed phase radiation chemistry [107-109]. In collisions between fast potassium and CCl_4 the production of CCl_4^- has been reported [110]. In the case of alkyl halides and aromatic halides in certain matrices experimental evidence has been obtained using optical or electron spin resonance spectroscopy technique also for the formation of their parent molecular negative ions [111,112]. These experimental results show obviously that some environmental conditions enable the molecule, which undergoes a dissociative electron attachment, to form the stable parent negative ion.

Based on the experimental results on the collisional stabilization of negative ions with excess energies by built-in third body molecules Klots and Compton [103] have discussed the implication of their results to the mechanism of the overall two-stage three-body electron attachment processes like the BB mechanism. Their investigation have spurred much our experiments [32,33,41] on electron attachment to O_2 using the microwave technique.

Observation of *the hydrated electron*; $(\text{H}_2\text{O})_n^-$, in beam-experiments has been a changing subject in terms of electron attachment studies of vdW molecules. Measurements of the hydrated or solvated electron has been extensively carried out [113-116] in radiation chemistry and its related fields and almost conclusive experimental evidence has been obtained for its formation not only in the condensed phase but also in the gas phase [117,118]. Theoretical investigations have been also successful in describing its electronic properties and structures [119]. Cluster-beam experiments have been recently attempted [104,120] to substantiate more the microscopic structure of the hydrated or solvated electron; to detect $(\text{H}_2\text{O})_n^-$ as a function of n , because the single H_2O molecule has a negative electron affinity and does not form a stable negative ion while some stable structures of negatively charged water clusters in the isolated system and also some microscopic structures of the hydrated electron in the condensed-phase dielectric media have been theoretically proposed [121-124]. Haberland et al. [125,126] have been recently successful in the detection of $(\text{H}_2\text{O})_n^-$ where $n=2,3$ and $n \geq 5$ in the mass spectrometry of negative ions in an expanding supersonic beam of water clusters mixed with electrons; i.e., β -rays from ^{63}Ni or photoelectrons produced by the irradiation of UV photons upon a metal surface.

5. NEGATIVE ION FORMATION IN HEAVY PARTICLE COLLISIONS WITH VAN DER WAALS MOLECULES

Ion-pair formation by collisional charge transfer between neutral heavy particles has been an effective source of information on the energetics and dynamics of negative ion formation in electron attachment to neutral particles

as well as an effective source of negative ion itself.[14]
Collisional electron transfer between neutrals, A and B;



has been extensively studied particularly for the combination of alkali atoms (A) and electron-attaching molecules (B). Other species than alkali atoms, such as various accelerated atoms in the ground state[127] or electronically excited rare gas atoms[128], have been also used as an electron donor A.

Herschbach et al.[129,130] have used the collisional charge transfer from fast Rb atoms to molecular clusters in sonic beams of Cl₂, SO₂, or hydrogen halides in order to study electron attachment to these clusters and observed mass-spectrometrically various stable cluster ions such as those including n-mer ions; i.e., (Cl₂)_n⁻ and (SO₂)_n⁻. In the case of hydrogen halides the solvated halide ions have been predominant and no evidence has been found for any intact n-mer ions. It is particularly interesting from a similar point of view that the Rydberg electron in a high-Rydberg state can be viewed as almost free and slow. This has been demonstrated both theoretically and experimentally in a variety of the combination of A and B[3,12,13]. In terms of the titled subject here in this review there have been very recently interesting experimental results on the negative ion formation by collision of Rydberg atoms with cluster molecules[131,132].

6. ELECTRON SOLVATION AND LOCALIZATION IN THE CONDENSED PHASE

This problem has been one of the central subjects in radiation chemistry and now this is relevant to a variety of chemical areas, and even biological or physical areas. Experimental evidence for the *solvated electron* has been obtained using the radiolysis-product analysis, photoconductivity and optical or electron spin resonance spectroscopy techniques[113-116,119]. Solvated electrons have been observed in a variety of polar solvents including water, alcohols, ammonia, amines, and ethers, and even in nonpolar solvents such as hydrocarbons[133]. Optical absorption spectra of the solvated electron in various solvents are characterized by a broad, structureless, and asymmetric band, and are positioned at wavelength regions from visible to near-infrared depending on the solvent.

Theoretical investigation of the solvated electron has been also extensively carried out to explain the above-mentioned experimental results and therefore to obtain information on electron solvent-molecule interaction or the structure of the solvated electron[119]. Very recently the stability of negatively charged water clusters have been theoretically investigated in terms of the modeling of the hydrated electron[123,124].

Electrons are localized or trapped also in low temperature glassy or amorphous matrices of these solvent-molecules and observed by optical or electron spin resonance spectroscopy techniques[134,135]. Electron localization and reactivities in various condensed media particularly in nonpolar media have been investigated also by measuring electrical conductivities due to the excess electrons in the media[136]; the measurements of electron mobilities[137], and potential-energies[138], which are largely dependent on the molecular structure of medium molecules. These values, and their temperature and density dependences have been measured in a variety of liquids[139]. Electron attachment to solute molecules and electron-ion recombination have been also investigated in these media[140]. In order to clarify systematically the static and dynamic behavior of the electrons in the condensed phase, these values have been measured also in dense gases and molecular crystals [141-143,158-162].

Although there have been a variety of experimental and theoretical investi-

gations as to electron solvation, localization, trapping, and reactivities in the condensed phase, further investigations from different approaches; one is from gas-phase science, the other is from solid-state science, are greatly needed to solve remaining important problems and thus to substantiate more the electrons in the condensed phase. One of the strong candidates among the former approaches to solve this problem is the investigation of electron interaction with vdW molecules, while that among the latter approaches is the investigation of electron interaction with thin-layer molecular solids[144-150].

7. CONCLUSIONS

Electron attachment to van der Waals molecules has been observed in both dense gases and sonic nozzle beams. The large enhancement in the attachment rate constants in comparison with those for the ordinary attachment to isolated single molecules has been ascribed to essentially important several factors (See Section 3) which change the electron attachment resonance mechanism due to the presence of the vdW interaction between the host molecule such as O₂, N₂O, CO₂, H₂O, etc. and the surrounding molecules. It is also interesting to observe negative ion formation in the collision of vdW molecules with alkali metal atoms or high Rydberg atoms. Based on these experimental results, one may expect generally that even in the case of molecules with negative electron affinities or with high threshold electron energies for attachment some environmental effects or the effect of vdW molecule formation bring about the large enhancement in the cross sections or the rate constants for the electron attachment at the lower energies.

The distinct features of the electron attachment to vdW molecules as summarized above may become a substantial clue to understand the fundamental nature of electron attachment not only in dense gases but also in the condensed phase. It is also apparent that most of the electron attachment in bulk system is no longer a simple process as consisted of the interaction of electron with isolated molecules. A definitely important role of pre-existing vdW molecules formed by weak intermolecular forces must be admitted. From this point of view, interesting phenomena in ionized gases such as the attachment cooling effect[151-155] and the response-time of the air-filled fast-response ionization chamber[156,157] should be analyzed by taking into account the important role of vdW molecules in the electron attachment mechanism.

In order to further substantiate the detailed situation of vdW molecules in the electron attachment mechanism more elaborate work will be required both experimentally and theoretically.

ACKNOWLEDGEMENT

The author wishes to thank Prof. R.W. Fessenden and Dr. H. Shimamori for helpful discussions. He is grateful also to Dr. A.V. Phelps, Prof. R.W. Crompton, Prof. M.A. Biondi, Prof. I. Ogawa and Dr. F. Koike for many helpful discussions, and to Y. Kokaku and M. Toriumi for their excellent co-operation. Our research described herein has been supported financially by the Ministry of Education, the Mitsubishi Foundation, and the Kurata Foundation.

REFERENCES

- 1] R.N. Compton, Negative-ion states, in: Photophysics and Photochemistry in the Vacuum Ultraviolet, eds. S.P. McGlynn, G.L. Findley and R.H. Huebner (D. Reidel Publ. Co., 1985) p.261.
- 2] L.G. Christophorou, D.L. McCorkle and A.A. Christodoulides, Electron attachment processes, in: Electron-Molecule Interactions and Their Applications,

- Vol.1, ed. L.G. Christophorou (Academic Press, 1984) p.477.
- 3] R.N. Compton, Electron attachment to molecules, in: Electronic and Atomic Collisions, eds. N. Oda and K. Takayanagi (North-Holland, 1980) p.251.
 - 4] H.S.W. Massey, Negative Ions (Cambridge Univ. Press, 1976).
 - 5] G.E. Caledonia, Chem. Rev., 75 (1975) 333.
 - 6] G.J. Schulz, Rev. Mod. Phys., 45 (1973) 423.
 - 7] L.G. Christophorou, Atomic and Molecular Radiation Physics (Wiley Interscience, 1971).
 - 8] R.N. Compton and R.H. Huebner, Adv. Radiat. Chem., 2 (1970) 281.
 - 9] J.N. Bardsley and F. Mandl, Rept. Prog. Phys., 31 (1968) 471.
 - 10] A. Chutjian and S.H. Alajajian, Phys. Rev., A31 (1985) 2885.
 - 11] D. Field, J.P. Ziesel, P.M. Guyon and T.R. Govers, J. Phys. B17 (1984) 4565.
 - 12] M. Matsuzawa, J. Phys. Soc. Jpn. 32 (1972) 1088, 1108.
 - 13] M. Matsuzawa, Theory of thermal collisions between high-Rydberg atoms and neutral species, in: Electronic and Atomic Collisions, eds. N. Oda and K. Takayanagi (North-Holland, 1980) p.493.
 - 14] K. Lacmann, Adv. Chem. Phys., 42 (1980) 513.
 - 15] L.G. Christophorou, Chem. Rev., 76 (1976) 409.
 - 16] L.G. Christophorou, Radiat. Phys. Chem., 12 (1978) 19.
 - 17] L.G. Christophorou, Adv. Elect. Electron Phys., 46 (1978) 55.
 - 18] L.G. Christophorou and S.R. Hunter, Electrons in dense gases, in: Swarms of Ions and Electrons in Gases, eds. W. Lindinger, T.D. Märk and F. Howorka (Springer-Verlag, 1984) p.241.
 - 19] Y. Hatano and H. Shimamori, Electron attachment in dense gases, in: Electron and Ion Swarms, ed. L.G. Christophorou (Pergamon Press, 1981) p.103.
 - 20] K.G. Mothes, E. Schultes and R.N. Schindler, J. Phys. Chem., 76 (1972) 3758.
 - 21] G. Cavalleri, Phys. Rev., 179 (1969) 186.
 - 22] R. Hegerberg and R.W. Crompton, Aust. J. Phys., 36 (1983) 831.
 - 23] W.E. Wentworth and J.C. Steelhammer, Adv. Chem. Ser., 82 (1968) 75.
 - 24] M.A. Biondi, Rev. Sci. Instr., 22 (1951) 500.
 - 25] M.A. Biondi, Adv. Elect. Electron Phys., 16 (1963) 67.
 - 26] R.W. Fessenden and J.M. Warman, Adv. Chem. Ser., 82 (1968) 222.
 - 27] M.C. Sauer, Jr., The use of pulse radiolysis to study transient species in the gas phase, in: The Study of Fast Processes and Transient Species by Electron pulse Radiolysis, eds. J.H. Baxendale and F. Busi (D. Reidel Publ. Co., 1982) p.601.
 - 28] J.M. Warman, R.W. Fessenden and G. Bakale, J. Chem. Phys., 57 (1972) 2702.
 - 29] H. Shimamori and Y. Hatano, Chem. Phys. Lett., 38 (1976) 242.
 - 30] H. Shimamori and Y. Hatano, Chem. Phys., 12 (1976) 439.
 - 31] H. Shimamori and Y. Hatano, Chem. Phys., 21 (1977) 187.
 - 32] Y. Kokaku, Y. Hatano, H. Shimamori and R.W. Fessenden, J. Chem. Phys. 71 (1979) 4883.
 - 33] Y. Kokaku, M. Toriumi and Y. Hatano, J. Chem. Phys., 73 (1980) 6167.
 - 34] Y. Hatano, Y. Kimizuka and H. Shimamori, Radiat. Phys. Chem., 19 (1982) 255.
 - 35] M. Toriumi and Y. Hatano, J. Chem. Phys., 79 (1983) 3749.
 - 36] M. Toriumi and Y. Hatano, J. Chem. Phys., 81 (1984) 3748.
 - 37] M. Toriumi and Y. Hatano, J. Chem. Phys., 82 (1985) 254.
 - 38] H. Shimamori and R.W. Fessenden, J. Chem. Phys., 68 (1978) 2757.
 - 39] H. Shimamori and R.W. Fessenden, J. Chem. Phys., 69 (1978) 4732.
 - 40] H. Shimamori and R.W. Fessenden, J. Chem. Phys., 71 (1979) 3009.
 - 41] H. Shimamori and R.W. Fessenden, J. Chem. Phys., 74 (1981) 453.
 - 42] H. Shimamori and H. Hotta, J. Chem. Phys., 78 (1983) 1318.
 - 43] H. Shimamori and H. Hotta, J. Chem. Phys., 81 (1984) 1271.
 - 44] L.M. Chanin, A.V. Phelps and M.A. Biondi, Phys. Rev., 128 (1962) 219.
 - 45] F.K. Truby, Phys. Rev., A6 (1972) 671.
 - 46] A. Herzenberg, J. Chem. Phys., 51 (1969) 4942.
 - 47] S.S. Nagra and D.A. Armstrong, Can. J. Chem., 54 (1976) 3580.
 - 48] S.S. Nagra and D.A. Armstrong, J. Phys. Chem., 81 (1977) 599.
 - 49] S.S. Nagra and D.A. Armstrong, Radiat. Phys. Chem., 11 (1978) 305.

- 50] F. Bloch and N.E. Bradbury, *Phys. Rev.*, **48** (1935) 689.
51] M.J.W. Boness and G.J. Schulz, *Phys. Rev.*, **A2** (1970) 1802.
52] F. Linder and H. Schmidt, *Z. Naturforsch.*, **A26** (1971) 1617.
53] J.E. Land and W. Raith, *Phys. Rev.*, **A9** (1974) 1592.
54] D. Spence and G.J. Schulz, *Phys. Rev.*, **A2** (1970) 1802.
55] D. Spence and G.J. Schulz, *Phys. Rev.*, **A2** (1972) 724.
56] R.J. Celotta, R.A. Bennett, J.L. Hall, M.W. Siegel and J. Levin, *Phys. Rev.*, **A6** (1972) 631.
57] F. Koike, *J. Phys. Soc. Jpn.*, **35** (1973) 1166.
58] F. Koike, *J. Phys. Soc. Jpn.*, **39** (1975) 1590.
59] F. Koike and T. Watanabe, *J. Phys. Soc. Jpn.*, **34** (1973) 1022.
60] G. Parlant and F. Fiquet-Fayard, *J. Phys.* **B9** (1976) 1617.
61] L.G. Christophorou, *J. Phys. Chem.*, **76** (1972) 3730.
62] R.E. Goans and L.G. Christophorou, *J. Chem. Phys.*, **60** (1974) 1036.
63] D.L. McCorkle, L.G. Christophorou and V.E. Anderson, *J. Phys.* **B5** (1972) 1211.
64] J.L. Pack and A.V. Phelps, *J. Chem. Phys.*, **44** (1966) 1870.
65] J.L. Pack and A.V. Phelps, *J. Chem. Phys.*, **45** (1966) 4316.
66] V.A.J. van Lind, E.G. Wikner and D.L. Trueblood, *Bull. Am. Phys. Soc.*, **5** (1960) 122.
67] R.W. Crompton, R. Hegerberg and H.R. Skullerud, *Proc. Int. Seminar on Swarm Experiments in Atomic Collision Research* (Tokyo), ed. I. Ogawa (1979) p.18.
68] R. Hackam and J.J. Lennon, *Proc. Phys. Soc.*, **86** (1965) 123.
69] B.G. Young, A.W. Johnson and J.A. Garruthors, *Can. J. Phys.*, **41** (1963) 625.
70] D.R. Nelson and F.J. Davis, *Bull. Am. Phys. Soc.*, **16** (1971) 217.
71] J.M. Warman, K.M. Bansal and R.W. Fessenden, *Chem. Phys. Lett.*, **12** (1971) 211.
72] G.S. Hurst and T.E. Bortner, *Phys. Rev.*, **114** (1959) 166.
73] L. Bouby and H. Abgrall, *Proc. 5th ICPEAC (Leningrad)* (1967) p.584.
74] L. Bouby, F. Fiquet-Fayard and Y. LeCoat, *Int. J. Mass Spect. Ion Phys.*, **3** (1970) 439.
75] J.A. Stockdale, L.G. Christophorou and G.S. Hurst, *J. Chem. Phys.*, **47** (1967) 3267.
76] A. Zastawny, *Acta. Phys. Polonica*, **A46** (1974) 39.
77] R. Grünberg, *Z. Naturforsch.*, **A24** (1969) 1039.
78] R. Grünberg, *Z. Naturforsch.*, **A33** (1978) 1346.
79] A. Bartels, *Phys. Lett.*, **45A** (1973) 491.
80] D.E. Stogryn and J.O. Hirschfelder, *J. Chem. Phys.*, **31** (1959) 1531.
81] B.L. Blaney and G.W. Ewing, *Ann. Rev. Phys. Chem.*, **27** (1976) 553.
82] G.E. Ewing, *Angew. Chem. Int. Ed. Engl.*, **11** (1972) 486.
83] B.M. Smirnov, *Sov. Phys. Usp.*, **27** (1984) 1.
84] G. Breit and E. Wigner, *Phys. Rev.*, **49** (1936) 519.
85] H.S.W. Massey and E.H.S. Burhop, *Electronic and Ionic Impact Phenomena* (Clarendon, 1969).
86] L.G. Christophorou and J.A. Stockdale, *J. Chem. Phys.*, **48** (1968) 1956.
87] L.G. Christophorou, *Environmental Health Perspectives*, **36** (1980) 3.
88] W.M. Huo, R.W. Fessenden and C.W. Bauschlicher, Jr., *J. Chem. Phys.*, **81** (1984) 5811.
89] D.R.A. McMahon, Theoretical aspects of environmental effects on the electron attachment rate to O₂ molecules, in: *Electron and Ion Swarms*, ed. L.G. Christophorou (Pergamon Press, 1981), p.117.
90] D.R.A. McMahon, *Chem. Phys.*, **66** (1982) 67.
91] M. Nishikawa and R.A. Holroyd, *J. Chem. Phys.*, **79** (1983) 3754.
92] G.J. Schulz, *J. Chem. Phys.*, **34** (1961) 1778.
93] R.K. Curran and R.E. Fox, *J. Chem. Phys.*, **34** (1961) 1590.
94] F. Kaufman, *J. Chem. Phys.*, **46** (1967) 2449.
95] P.J. Chantry, *J. Chem. Phys.*, **51** (1969) 3369.
96] A.V. Phelps and R.E. Voshall, *J. Chem. Phys.*, **49** (1968) 3246.
97] J.M. Warman and R.W. Fessenden, *J. Chem. Phys.*, **49** (1968) 4718.

- 98] H. Shimamori and R.W. Fessenden, to be published.
- 99] R.E. Goans and L.G. Christophorou, *J. Chem. Phys.*, **63** (1975) 2821.
- 100] J. Rademacher, L.G. Christophorou and R.P. Blaunstein, *J. Chem. Soc., Faraday Trans. II*, **71** (1975) 1212.
- 101] A.W. Castleman, Jr. et al., in "Symposium on Clusters", in: *Electronic and Atomic Collisions*, eds. J. Eichler, I.V. Hertel and N. Stolterfoht (North-Holland, 1984) p.579, and references cited therein.
- 102] C.E. Klots and R.N. Compton, *J. Chem. Phys.*, **67** (1977) 1779.
- 103] C.E. Klots and R.N. Compton, *J. Chem. Phys.*, **69** (1978) 1636.
- 104] C.E. Klots and R.N. Compton, *J. Chem. Phys.*, **69** (1978) 1644.
- 105] C.E. Klots, *J. Chem. Phys.*, **71** (1979) 4172.
- 106] C.E. Klots, *Radiat. Phys. Chem.*, **20** (1982) 51.
- 107] J.P. Keene, Y. Reaf and A.J. Swallow, Pulse radiolysis studies of carboxyl and related radicals, in: *Pulse Radiolysis*, eds. M. Ebert, J.P. Keene, A. J. Swallow and J.H. Baxendale (Academic Press, 1965) p.99.
- 108] J.M. Warman, K.D. Asmus and R.H. Schuler, *Adv. Chem. Ser.*, **82** (1968) 25.
- 109] R.W. Fessenden and R.H. Schuler, *Adv. Radiat. Chem.*, **2** (1970) 1.
- 110] H. Dispert and K. Lacmann, *Int. J. Mass Spect. Ion Phys.*, **28** (1978) 49.
- 111] M.C.R. Symons, Some electron-gain and electron-loss reactions of molecules and ions in condensed phases, in: *Radiat. Res., Proc. 6th ICRR*, 1979, Tokyo, eds. S. Okada, M. Imamura, T. Terashima and H. Yamaguchi (JARR, 1979) p.238.
- 112] T. Shida, private communication (1985).
- 113] Colloque Weyl VI, *J. Phys. Chem.*, **88** (1984) 3699.
- 114] G.A. Kenny-Wallace, *Acc. Chem. Res.*, **11** (1978) 433.
- 115] J. Jortner and N.R. Kestner, eds., *Electrons in Fluids* (Springer-Verlag, 1973).
- 116] E.J. Hart and M. Anber, *The Hydrated Electron* (Wiley-Interscience, 1970)
- 117] A. Gaathon, G. Czapski and J. Jortner, *J. Chem. Phys.*, **58** (1973) 2648.
- 118] J. Jortner and A. Gaathon, *Can. J. Chem.*, **55** (1977) 1801.
- 119] a) D. Feng and L. Kevan, *Chem. Rev.*, **80** (1980) 1, and references cited therein;
b) K. Fueki, private communication (1985).
- 120] M. Armbruster, H.G. Schindler and H. Haberland, *Phys. Rev. Lett.*, **47** (1981) 423.
- 121] M. Newton, *J. Chem. Phys.*, **58** (1973) 5833.
- 122] D.M. Chipman, *J. Phys. Chem.*, **83** (1979) 1657.
- 123] N.R. Kestner and J. Jortner, *J. Phys. Chem.*, **88** (1984) 3818.
- 124] B.K. Rao and N.R. Kestner, *J. Chem. Phys.*, **80** (1984) 1587.
- 125] H. Haberland, H. Langosch, H.G. Schindler and D.R. Worsnop, *J. Phys. Chem.*, **88** (1984) 3903.
- 126] H. Haberland, C. Ludewigt, H.G. Schindler and D.R. Worsnop, *J. Chem. Phys.*, **81** (1984) 3742.
- 127] R.B. Cohen, C.E. Young and S. Wexler, *Chem. Phys. Lett.*, **19** (1973) 99.
- 128] K.T. Gillen, T.D. Gaily and D.C. Lorents, *Chem. Phys. Lett.*, **57** (1978) 192.
- 129] K.H. Bowen, G.W. Liesegang, R.A. Sanders and D.R. Herschbach, *J. Phys. Chem.*, **87** (1983) 557.
- 130] E.L. Quitevis, K.H. Bowen, G.W. Liesegang and D.R. Herschbach, *J. Phys. Chem.*, **87** (1983) 2076.
- 131] T. Kondow, Negative ion formation by collision of Rydberg atoms with clusters, this volume.
- 132] T. Kondow and K. Mitsuke, *J. Chem. Phys.*, in press.
- 133] L.M. Dorfman and F.Y. Jou, Optical absorption spectrum of the solvated electron in ethers and in binary liquid systems, in: *Electrons in Fluids*, eds. J. Jortner and N.R. Kestner (Springer-Verlag, 1973) p.447.
- 134] K. Funabashi, *Adv. Radiat. Chem.*, **4** (1974) 103.
- 135] L. Kevan, *Adv. Radiat. Chem.*, **4** (1974) 181.
- 136] W.F. Schmidt, *IEEE Trans. EI-19* (1984) 389.
- 137] G.R. Freeman, Measured mobilities of electrons, in: *Radiat. Res., Proc.*

- 5th ICRR, 1974, Seattle, eds. O.F. Nygaard, H.I. Adler and W.K. Sinclair (Academic Press, 1975) p.367.
- 138] R.A. Holroyd, Energies of conduction bands in dielectric liquids, in: Radiat. Res., Proc. 5th ICRR, 1974, Seattle, eds. O.F. Nygaard, H.I. Adler and W.K. Sinclair (Academic Press, 1975) p.378.
- 139] A.O. Allen, NSRDS-NBS-58 (1976).
- 140] J.M. Warman, The dynamics of electrons and ions in nonpolar liquids, in: The Study of Fast Processes and Transient Species by Electron Pulse Radio-lysis, eds. J.H. Baxendale and F. Busi (D. Reidel Publ. Co., 1982) p.433.
- 141] G.R. Freeman, Electron transport in dense gases and low density liquids, in: Electron and Ion Swarms, ed. L.G. Christophorou (Pergamon Press, 1981) p.93.
- 142] R.A. Holroyd and N.E. Cipollini, Dependence of conduction band energy and electron mobility on fluid density, in: Radiat. Res., Proc. 6th ICRR, 1979, Tokyo, eds. S. Okada, M. Imamura, T. Terashima and H. Yamaguchi (JARR, 1979) p.228.
- 143] L.G. Christophorou and K. Siomos, Interphase physics: linking knowledge on electron-molecule interactions in gases to knowledge on such processes in condensed matter, in: Electron-Molecule Interactions and Their Applications, Vol.2, ed. L.G. Christophorou (Academic Press, 1984) p.221.
- 144] L. Sanche and M. Michaud, Vibrational-librational excitation and shape resonances in electron scattering from condensed N₂, CO, O₂, and NO, in: Resonances in Electron-Molecule Scattering, van der Waals Complexes, and Reactive Chemical Dynamics, ed. D.G. Truhler (ACS, 1984) p.212.
- 145] L. Sanche and M. Michaud, J. Chem. Phys., 81 (1984) 257.
- 146] L. Sanche and M. Michaud, Phys. Rev., B27 (1983) 3856.
- 147] L. Sanche, Phys. Rev. Lett., 53 (1984) T638.
- 148] K. Hiraoka, J. Phys. Chem., 85 4008 (1981).
- 149] K. Hiraoka, M. Nara and Y. Iijima, J. Phys. Chem., 87 (1983) 3959.
- 150] K. Hiraoka and M. Nara, Bull. Chem. Soc. Jpn., 57 (1984) 2243.
- 151] R.W. Crompton, R. Hegerberg and H.R. Skullerud, J. Phys. B 13 (1980) L455.
- 152] K. Koura, J. Chem. Phys., 76 (1982) 390.
- 153] D.R.A. McMahon and R.W. Crompton, J. Chem. Phys., 78 (1983) 603.
- 154] K. Koura, J. Chem. Phys., 78 (1983) 604.
- 155] H.R. Skullerud, Aus. J. Phys., 36 (1983) 845.
- 156] J.W. Boag, private communication (1984).
- 157] R.W. Fessenden, private communication (1985).
- 158] S.R. Hunter and L.G. Christophorou, Electron motion in low- and high-pressure gases, in: Electron-Molecule Interactions and Their Applications, Vol.2, ed. L.G. Christophorou (Academic Press, 1984) p.90.
- 159] G.L. Braglia and V. Dallacasa, Multiple scattering theory of electron mobility in dense gases, in: Electron and Ion Swarms, ed. L.G. Christophorou (Pergamon Press, 1981) p.83.
- 160] D.A. Armstrong, Radiat. Phys. Chem., 20, 75 (1982).
- 161] T. Tezuka, H. Namba, Y. Nakamura, M. Chiba, K. Shinsaka and Y. Hatano, Radiat. Phys. Chem., 21, 197 (1983).
- 162] Y. Nakamura, K. Shinsaka and Y. Hatano, J. Chem. Phys., 78, 5820 (1983).

ASPECTS OF ELECTRON DETACHMENT IN NEGATIVE ION COLLISIONS

V.A. ESAULOV

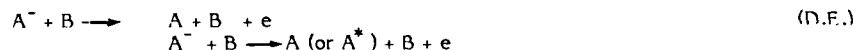
Laboratoire des Collisions Atomiques et Moléculaires, Bâtiment 351, Université Paris Sud,
91405 Orsay, France

1. INTRODUCTION

Electron detachment in negative ion collisions has attracted much attention over past years. Study of this process provides a "simple" means of investigating interactions between discrete states and continua. Indeed negative ions possess no singly excited states (e.g. $1snl$ for H^-) and hence direct detachment is the process



is the first energetically accessible electronically inelastic channel
Other processes, like target or projectile excitation



may also be important.

Numerous experimental and some theoretical studies of a few of the simplest negative ions like H^- and some halogen negative ions have been performed in a wide collision energy range and in some cases have led to a fair understanding of the main detachment channels. More recently collisions with molecular targets have attracted considerable interest and some insight into some peculiarities of these collisions has now been gained.

In this review I shall limit myself to a discussion of low keV negative ion collisions where in most cases a molecular description of the collision should be valid. I shall also limit the discussion to the presentation of mainly results concerning the most extensively studied negative ion i.e. H^- . The conclusions that can be drawn from the following discussion are quite general however, and will illustrate the main aspects of electron detachment in negative ion collisions known to date. More complete reviews of various aspects of this subject may be found elsewhere (1-4).

2. EXPERIMENTAL ASPECTS

To date the available experimental data on electron detachment in negative ion collisions has come from three types of experiments.

The first type concerns total detachment cross section (TDCS) measurements. These have been mainly performed either by electron collection (5) or by monitoring incident beam attenuation (6). The latter type of measurements may suffer serious drawbacks at low energies due to large angle elastic scattering, and in both cases one can not distinguish between single ($Q_{-1,0}$) and double ($Q_{-1,1}$) electron loss. Neutral particle detection has also been used at high energies (7) but here some arbitrary assumptions about their detection efficiencies are usually made.

TDCS measurements give a global information about detachment giving the importance of this process as a function of energy. In certain cases, as will be seen below, some information about the dynamics of this process may also be obtained.

Further information may be gained from the measurement of detached electron

energy spectra (DEES). These yield high resolution information about (i) the spectrum of detached electrons in the detachment process (ii) decay channels of unstable states, and (iii) the characteristics of the spatial distribution of the electrons. To date DEES measurements have not been performed in coincidence with the scattered neutrals and hence they correspond to a sum over all detachment channels and also all impact parameters.

One should mention a serious problem in DEES measurements related to the correct determination of the transmission function (variation of the transmitted electron intensity as a function of electron energy). This effect was not taken into account in early measurements of e.g. Risley (8), but is taken into account in more recent studies (9-11).

The transmission function is determined by studying ionisation (for $\epsilon_e < 2$ eV) and elastic scattering ($\epsilon_e > 2$ eV) in electron He collisions. At low energies the method is based on the knowledge of the Wannier threshold law and at high energy on the elastic scattering measurements (9).

To date the most in depth information about detachment has come from differential TOF neutral energy loss studies 12-14. These allow the separate study of the various detachment channels, the determination of the differential cross sections, (DCS), which in turn upon integration can yield data about the relative contribution of the various channels to the TDCS. A particularly interesting aspect of TOF studies is that in certain cases they can give information about the impact parameter dependence of DEES, since by energy conservation the neutral particle energy loss spectrum reproduces it:

$$A^- + B \longrightarrow A(-f(\epsilon)) + B + e^-(+f(\epsilon))$$

TOF studies are however limited to a small energy range (0.1 to 2 keV) on the present setups. The low energy limit is due to low detection efficiency of neutrals of the detectors (usually multichannel plates) used. Also the energy resolution is limited. Indeed the best resolution obtained to date is of about 0.3 eV.

Finally some information about detachment has come from a study of the elastic DCS (12, 13, 15, 16). Here the study of the absorption of this DCS due to detachment as a function of collision energy can provide useful information about the detachment dynamics.

3. ELECTRON DETACHMENT IN COLLISIONS WITH ATOMIC TARGETS

Let us now consider some results pertaining to collisions with some of the most frequently used targets, i.e. the inert gases (I.G.). We shall first consider TDCS. These usually increase more or less sharply from a threshold which is somewhat higher than the electron affinity (e.g. about 6 eV for Cl^- Ar collisions and around 1 eV for H^- He collisions) and then reach a broad maximum which extends over tens of keV (for H^-) before decreasing slowly at higher energies. Fig 1 illustrates the TDCS for $H^-(D^-)$ collisions with He (17) and Ne (18) plotted as a function of center of mass energy (E_{cm}). Such a plot corresponds to the fact that for the same E_{cm} the ions will follow the same trajectory but with different radial velocities. It can be seen that in the case of He, the heavier and hence slower isotope has the greater TDCS. In the case of Ne the TDCS is greater for the lighter and hence faster isotope. The study of the isotope effects in $H^-(D^-)$ I.G. collisions thus reveals two apparently distinct behaviours of the detachment process. A further difference between the He and Ne case should be noted. For He the TDCS rises sharply from threshold. Whereas for Ne a slowly increasing cross section is obtained which is also significantly smaller than in the He case. At higher energies the TDCS are found to increase slowly till energies of the order of some tens of keV.

How can one account for these features? One of the first attempts to describe detachment in H^- He collisions was made by Lam et al (5) using the local complex potential (LCP) description, which is well known in electron molecule collisions and has been used in treatments of Penning Ionisation. In this model one assumes that the energy level associated with the initial AB^- state (fig 2a) crosses the level of the continuum

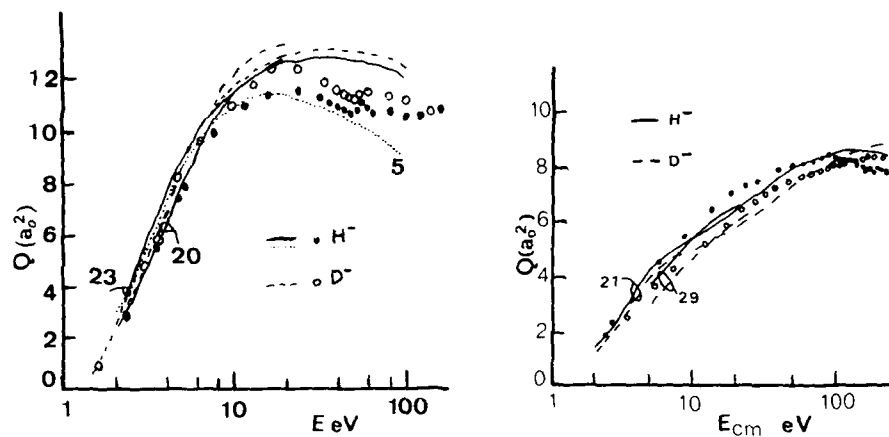


Fig 1. Total detachment cross sections versus relative energy for (a) H^-/D^-He collisions. Experiment (17), theory (5), (23) (20). (b) H^-/D^-Ne collisions. Experiment (18), theory (21) and (29).

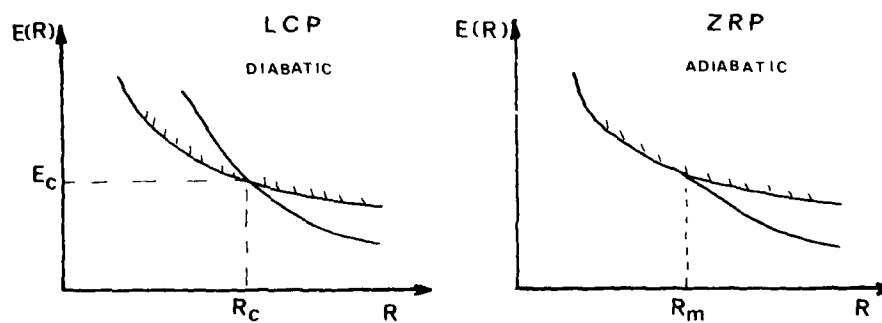


Fig 2. Schematic diagram of the AB^- and AB states. (a) LCP descriptions and (b) ZRP descriptions.

state corresponding to the quasimolecule AB. One then speaks of a quasistationary state which corresponds to a resonance in the inverse process of electron molecule collisions. Under certain conditions one can show (19) that the detachment problem reduces to the consideration of the decay of this quasistationary state whose energy is given by the local complex potential

$$E(R) = V(R) - i/2 \Gamma(R), \quad \Gamma(R) = 0 \text{ for } R > R_C$$

In this description one neglects all dynamic effects, i.e. the effects of nuclear motion (radial or rotational couplings) on the detachment probability, which is given by

$$P_d = 1 - \exp(-\int \Gamma dt) = 1 - \exp(-\int_{R_{\min}}^{\infty} dR \Gamma(R)/v(R))$$

where R_{\min} is the distance of closest approach and $v(R)$ is the radial velocity. Thus here the product $\int \Gamma dt$ determines the detachment probability and the energy spectrum of detached electrons. One can therefore expect that the TDCS will increase rapidly from a threshold energy given by $E(R_C)$. As the collision energy increases the time spent in the continuum will decrease and the TDCS will then decrease with increasing energy. This behaviour may be seen on the example of the H^- He TDCS calculated by Lam et al (5) (fig. 1). In the LCP model the D^- TDCS will obviously be larger than that for H^- for the same E_{cm} . Lam et al's fit reproduces the low energy behaviour of the TDCS but fails at high energies. Also it is clear, that though the isotope effect predicted in this model is consistent with the experimental findings for H^- He collisions, this is certainly not true for H^- Ne collisions.

Thus it appears that the applicability of this model may be very limited. This is further confirmed by the study of detachment in other negative ion systems like e.g. Cl^- I.G. collisions where fits in the LCP model gave reasonable results only in a limited energy range (13). In some systems (15) the absorption of the elastic DCS due to detachment was found to increase with increasing energy - an effect opposite to the one expected in the LCP model.

The failure of the LCP model is clearly associated with the neglect of dynamic, nuclear motion induced effects (radial or rotational couplings). One is thus led to consider treatments in which these are taken into account. Efforts have been made in the past few years to develop what some authors call a "dynamical complex potential" treatment (20) and some of these theories are presented in the poster sessions of this meeting. As an example of such a treatment one can mention the semi classical close coupling description of Delos and coworkers (20, 21) in which promisingly good agreement with the TDCS and isotope effects for the H^- He and H^- Ne cases has been achieved (fig 1). It should be noted however that the coupling elements are not evaluated ab initio but some modeling assumptions are made.

I will not go any further into these descriptions but turn to a somewhat (22) different model proposed in 1964 by Demkov, i.e. the zero range potential (Z R P) model.

The situation considered is shown in fig 2b where for distances smaller than R_m (the merging point of the AB^- and AB curves) there is no quasistationary state but the electron is essentially free (formally speaking this corresponds to the existence of a virtual state).

As the negative ion and atom approach the ionisation potential of the system will be small and the wave function of the weakly bound outer electron will have dimensions that are appreciably greater than the region where the potential is significantly different from zero. One can then divide the space into an outer region where the electron is essentially free and an inner region corresponding to the neutral core and whose effect on the outer electron may be defined by specifying a boundary condition on the logarithmic derivative of the wave function. In the limit the dimensions of the inner region may be neglected and the boundary condition specified at the origin. The effect of the changes in internuclear distance in time may be modelled by specifying a time dependant boundary condition. The problem thus reduces to solving the Schrödinger equation for a free particle (s waves)

$$(2^{-1} \cdot d^2/dr^2 + i d/dt) \psi(r, t) = 0 \quad (1)$$

with the boundary condition

$$(r\psi)^{-1}(d\psi/dr)|_{r=0} = f(t) \quad (2)$$

When $f(t)$ is negative there exists a bound state of energy $-f^2/2$. Positive values of $f(t)$ corresponding to a negative eigenvalue $-f^2/2$ are physically unacceptable with a wavefunction ($\exp(f.r)$) exponentially increasing for large r . The boundary condition (2) in principle contains all the information relevant to the problem in particular information about low energy scattering of electrons off the AB molecule. Indeed the continuum wavefunction for a wavenumber k is

$$\psi = \sin(kr + \delta)/r \quad (3)$$

and the phase is determined from the relation (2)

$$k \cdot \text{ctg}(\delta) = -f \quad (4)$$

Comparison of (4) with the expression for the expansion of the phaseshift on a short range potential for small k ,

$$k \text{ ctg}(\delta) = -1/a + q \cdot k^2/2 \quad (5)$$

where q is the effective range, and 'a' the scattering length shows that for a zero range potential

$$f = 1/a$$

The zero range potential thus provides a unified treatment of both bound and continuum states.

The $f(t)$ function that models negative ion atom collision is shown schematically in fig 3. For $t \rightarrow -\infty$ there is a bound state of energy $--- \epsilon_a = -\alpha^2/2$ where ϵ_a is the electron affinity. As the negative ion and atom approach the binding energy decreases becoming eventually zero and then again increases tending to ϵ_a as $t \rightarrow +\infty$.

Integration of (1) under the condition (2) and the initial condition

$$\psi(r,t) = 2\sqrt{\alpha} \exp(-\alpha \cdot r + i\alpha^2 \cdot t/2) \quad \text{as } t \rightarrow -\infty$$

yields as $t \rightarrow +\infty$ (Demkov 1964)

$$\psi(r,t) = C\sqrt{2\alpha} \cdot \exp(-\alpha r + i\alpha^2 t/2) + R(r,t)$$

the square of the modulus of the coefficient C determines the probability W that detachment will not occur. The residual term $R(r,t)$ represents a spreading wave packet. For large t this packet characterises a free electron and expansion of $R(r,t)$ into a Fourier integral gives the momentum distribution of the detached electron.

In order to apply the above model knowledge of the negative ion atom and atom-atom states are necessary. These determine the binding energy $\epsilon(R)$ and therefore a R dependent boundary condition $f(R) = -\sqrt{2\epsilon(R)}$, which for a given collision energy and knowing the potentials gives $f(t)$. Once $f(t)$ is known the problem may be solved numerically to give the detachment probability and the detached electron spectrum. This procedure allows in particular to visualise the detachment process since the wavefunction is known at all instants of time. Fig 3b represents the instantaneous probability of finding the outer electron at a distance r , ie $|\psi(r)|^2$ (23). The initial distribution (at $t = -53$ a.u) is a straight line in a logarithmic plot. If the system were to evolve adiabatically this distribution would remain a straight line with its slope decreasing during the collision as the atoms approach, until it would eventually correspond to an electron uniformly distributed in space. However as can be seen in fig

3b. this is not the case. At a certain time the variation of the boundary condition is not followed adiabatically and $\log |\psi(r)|^2$ changes only in a small region around the origin. When the system enters the continuum, for positive t this results in a hump in the $\log |\psi(r)|^2$ plot and the electron moves out from the origin. As the atoms separate and f becomes negative again, only that part of the wavepacket that remains in the central region can be recaptured whereas the rest spreads out in space. The hump in the figure that moves out as t increases (corresponding to $R(r, t)$ above) represents the escaping electron, while the linear part at the origin corresponds to the recaptured electron.

We thus see that as the atoms approach the system first follows adiabatically the changes at the origin, but then at some time the change is too rapid leading to the nonadiabatic behaviour of the system and resulting detachment of the outer electron.

It is clear from qualitative considerations that the greater the collision velocity, the sooner will be felt the changes in the binding energy, leading to the nonadiabatic behaviour of the system. In other words with increasing velocity the internuclear distance corresponding to the onset of the nonadiabatic behaviour should increase. It is also clear that at high velocities the wavepacket found at small internuclear distances will have less time to spread out and therefore the recapture probability (P_s) should increase with energy for small R . Clearly rather different behaviours of the detachment cross sections can therefore be expected depending upon the relative importance of these opposite effects.

The above image of a too rapid variation of the binding energy suggests a way to a solution of the problem in the sudden approximation, where the actual $f(t)$ function is replaced by a step function (fig 3) located in the region of the beginning (time, $-T_f$) and end (time $+T_f$) of the sudden variation. The solution of the problem is thus obtained by projecting the bound state function at $-T_f$ onto the eigenfunction corresponding to $t=0$ and then at $+T_f$ back onto the bound state function. This is the approach followed by Bronfin and Ermolaev (24) and later by Gauyacq (25) using different definitions of T_f . A conceptually similar model was also proposed by Herzenberg and Ojha (26). In these models depending upon the definition of the "forgetting" point is the moment when the system ceases to evolve adiabatically TDCS which decrease (24) or increase (25, 26) with increasing collision energy are obtained.

To illustrate further these effects let us look at the expression of the detachment probability (P_d) in one of the early analytical models due to Devdariani (27) in which a parabolic form for $f(t)$ was assumed

$$f(t) = -\alpha t^2 + \beta$$

$$P_d = 0.62 + 0.42(1 - R_{\min}^2/R_M^2) \cdot |f'(R_M)|^{0.8} \cdot R_M^{1.2} \cdot M^{0.2} / 2 \cdot E_c^{0.2}$$

where R_M is the merging point, R_{\min} the distance of closest approach, E_c the collision energy, M the projectile mass and $f'(R_M)$ derivative of $f(R)$ at R_M .

As can be seen P_d is finite for $R > R_{\min}$. For a given $R_{\min} < R_M$, P_d increases as the energy decreases (just as in the LCP model). On the other hand for $R_{\min} > R_M$, P_d increases as the energy increases. Thus in this model an important role is played by direct transitions from the discrete state into the continuum. The range of internuclear distances leading to detachment increases with increasing energy and the TDCS increases with energy due to the dominant role played by "tunnelling" transitions.

Devdariani's model was quite successful in describing most of the features of H^- I.G. collisions (12). However some, like the H^- Ne isotope effect could not be described. Also the applicability of the parabolic approximation is rather limited (23, 27). Numerical solutions of the real problem have therefore to be envisaged. This was made possible by a calculation of the states of the $(H\ He)^-$, and $(H\ Ne)^-$ systems by Gauyacq (23) and Olson and Liu (28). These calculations reveal an interesting difference between the two systems. The $(H\ Ne)^-$ state was found to be bound for all internuclear distances whereas the energy level of the $(H\ He)^-$ system was found to merge with that of the continuum of states corresponding to $H\ He$ and a free electron. Rather different behaviours of detachment follow from this as illustrated by Gauyacq's calculation (23, 29) of $P_d(R)$ for

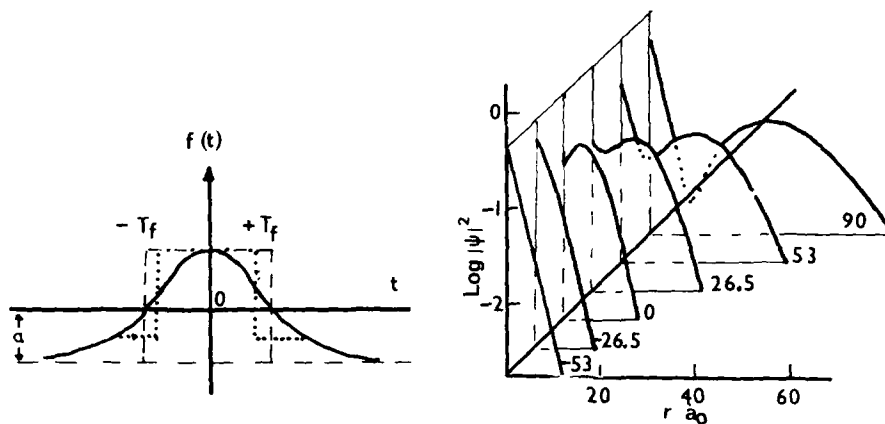


Fig 3. (a) Schematic diagram of the $f(t)$ function and various approximations of it. Numbers correspond to references.
 (b) Time dependence of the instantaneous probability of finding the outer electron at a distance r in a 250 eV H^- He collision (impact parameter $b = 1a_0$).

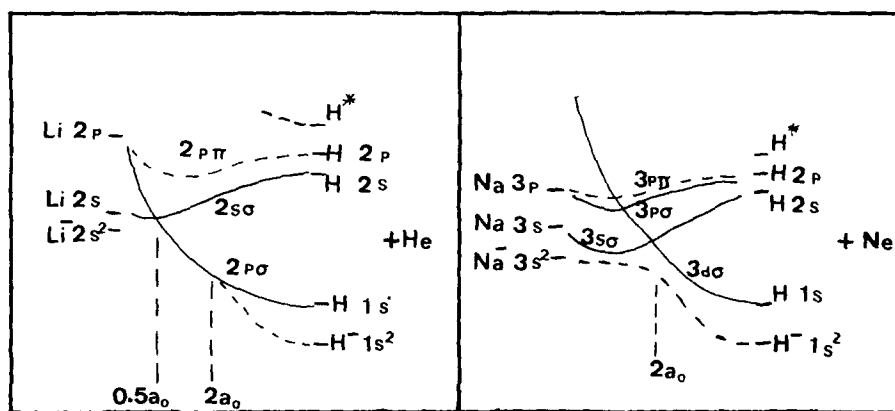


Fig 4. Schematic MO diagram for the H^-He and H^-Ne systems.

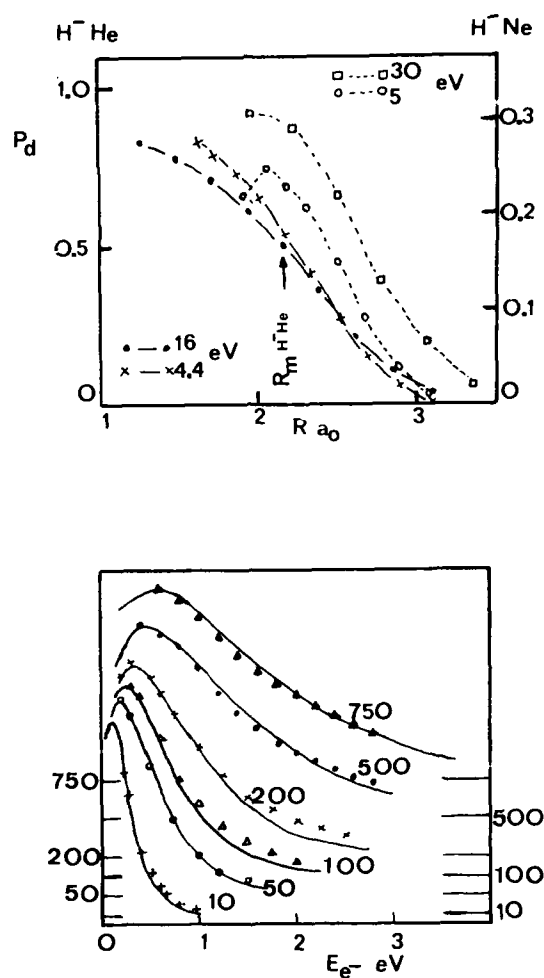


Fig 5. (a) Detachment probability P_d (b) for the $H^- He$ and $H^- Ne$ systems for several collision energies.
 (b) Detached electron energy spectra for $H^- He$ collisions for some collision energies. Points : experiment (9) Lines : theory (23).

these systems (fig 5). For the H^-He collisions for small R P_d is smaller for the higher energies and for large R , P_d increases with increasing energy. It turns out that intra continuum transitions dominate in collisions with He and hence the D^- cross section is greater for the same relative energy than that for H^- . In the case of Ne only "tunnelling" transitions exist resulting in an ill defined detachment threshold and slowly increasing TDCS as well as an inverted isotope effect.

The origin of the differences between the H^-He and H^-Ne systems lies in the changes of certain characteristics of the parent neutral H I.G. systems i.e. in the changes of the wavefunction of the ground 2Σ state near the first diabatic MO crossing (fig. 4). In the case of H Ne the $3d\sigma - 3s\sigma$ MO crossing occurs at relatively large internuclear distances (2) resulting in the $(HNe)^-$ state remaining bound. In the HHe case the corresponding $2p\sigma - 2s\sigma$ crossing occurs at much smaller distances 0.5 and has no effect on the $(HHe)^-$ ground state at large internuclear distances (2) where merging with the continuum occurs. It may be noted in passing that in the HAr case the corresponding $3d\sigma - 4s\sigma$ crossing also occurs at large distances (see Sidis (57) for the H^+Ar problem) and a situation similar to the H^-Ne one, of a bound $(HAr)^-$ state and a similar isotope effect may be anticipated and is indeed observed (39).

Fig. 5b shows the H^-He DEES measured by Montmagnon et al (9). These are found to be structureless and broaden slowly as the collision energy increases. Theoretical results of Gauyacq (23) are found to be in excellent agreement with these spectra. As stated previously this DEES represents a sum over all detachment channels and all impact parameters. A more stringent test of theory would be provided by comparison with the impact parameter dependence of these spectra for the direct detachment process. These were made available by the TOF studies of Esaulov et al (12) and Tuan et al (30).

Fig. 6a shows a typical TOF spectrum obtained in H^-He collisions. The first peak here corresponds to the direct detachment (DD) process and the higher energy peak to various excitation processes. The angular dependence of the DD peak is shown in fig. 6b along with the theoretical predictions of Gauyacq. Excellent agreement is found and the theory correctly describes the broadening of the spectrum for decreasing impact parameters.

The broadening and shifting to higher energy losses of the DD peak should be noted carefully since in certain cases it may lead to ambiguities in the identification of peaks in energy loss spectra.

Esaulov et al (12) have reported measurements of differential cross sections (DCS) of the various processes observed. These DCS (fig. 8) show that excitation processes in H^-He collisions make a small contribution to the TDCS (about 10% at 0.5 keV). The DEES reported by Montmagnon et al should therefore not be significantly perturbed by these and hence the above comparison with ZRP theory which does not take these into account, is deemed to be meaningful.

The problem of the treatment of excitation processes comes up when trying to calculate the DCS. A simple "hybrid" model was proposed by Esaulov et al (12) to include excitation processes. As pointed out above in the ZRP model the outer electron is assumed to be essentially free. This assumption can be extended (12) and it may be assumed that the outer electron is unperturbed by inelastic processes in the core collision and vice versa. The DCS can then be obtained as products of the survival or detachment probability and the elastic and inelastic DCS of the core H He collision. The latter may be treated in a usual quasimolecular model.

$$\sigma_{EL}(H^-He) = P_s \cdot \sigma_{EL}(HHe)$$

$$\sigma_d(H^-He) = P_d \cdot \sigma_{EL}(HHe)$$

$$\sigma_d^*(H^-He) = P_d \cdot \sigma^*(HHe)$$

$$\text{and also } \sigma^+(H^-He) = P_s \cdot \sigma^*(HHe)$$

Here $\sigma^*(HHe)$ corresponds to the DCS for excitation processes. The last equation describes the formation of autodetaching states by recapture of the outer electrons. Note that ionisation in the core will also produce excited states in a

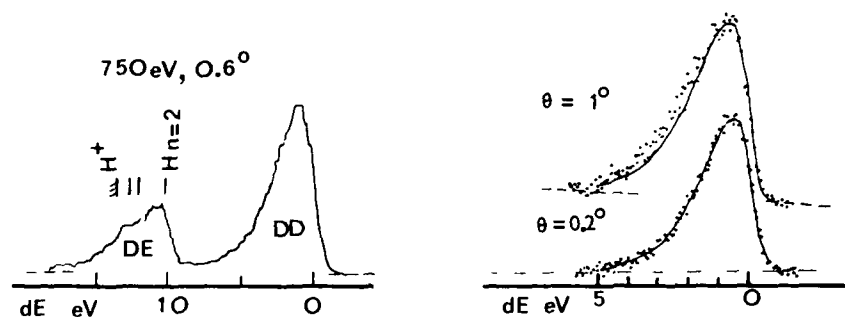


Fig 6. (a) TOF spectrum for H^-He collisions. The zero of the energy scale is taken at an energy loss of -0.75eV from the elastic peak, so as to coincide with the ground state of H .
(b) Angular (impact parameter) dependence of the TOF spectra for a 500eV collision energy (30). Points : experiment. Lines : theory.

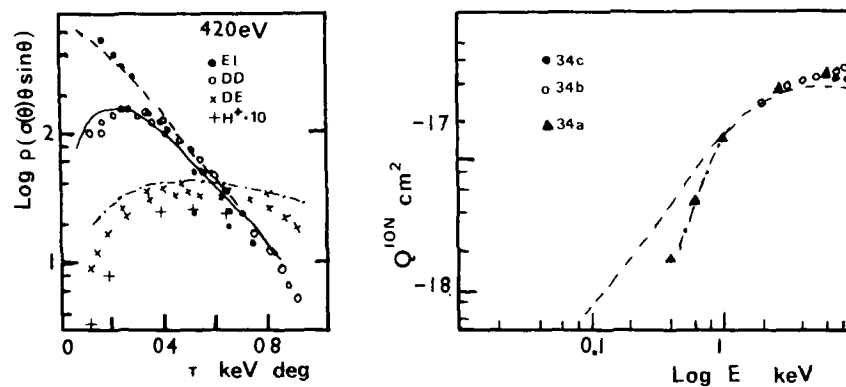


Fig 7. (a) Elastic and inelastic DCS for H^-He collisions. Points : experiment (12), lines : theory (23).
(b) H^+ production cross section. Points : experiment (34), lines : theory based on data of -- (32) and --- (33).

mechanism similar to the one proposed by Drukarev (31) in high energy H^- collisions.

$$\sigma^+(H^- He) = P_d \cdot \sigma^+(H He)$$

$$\sigma^*(H^- He) = P_s \cdot \sigma^+(H He)$$

In describing the $H^- He$ DCS Esaulov et al assumed that ionisation in the core was not significant at low energies as confirmed by existing measurements (32). Also because autodetaching states are observed in the neutral channel in TOF studies one gets

$$\sigma^*(H^- He) = \sigma^*(H He)$$

The results of these calculations of H^- I.G. DCS are in excellent agreement with experiment (fig. 7a).

In the above description the H I.G. DCS were taken from the experimental work of Benoit (35) and the calculations (for $H He$) of Benoit and Gauyacq (36). The latter also give some justification for the model employed since they show that excitations in the core occur at R at which the outer electron wavepacket is already spreading out from the core. Note that this situation may not always occur and a priori the above model's applicability could turn out to be limited.

The "hybrid" model also allows for a correction of the ZRP TDCS to include effects due to excitation.

$$Q_{-1,0} = Q_{-1,0}^{ZRP} + \Delta Q_{-1,0}^{EXC} + \Delta Q_{-1,0}^{ION}$$

$$\text{where } \Delta Q_{-1,0}^{EXC} = 2\pi \int P_s(b) \cdot P_{exc}(b) \cdot b \cdot db$$

$$\Delta Q_{-1,0}^{ION} = 2\pi \int P_s(b) \cdot P_{ion}(b) \cdot b \cdot db$$

Inclusion of these effects leads to an increase of the TDCS which in $H^- He$ collisions amounts to 25% at 1 keV (23). This model also allows calculation of the H^+ production cross section. Noting that excitation processes occur at small R , where the detachment probability is slowly varying one gets (56),

$$Q^{ION}(H^- He) = \langle P_d \rangle \cdot Q^{ION}(H He)$$

The result of such a calculation of Q^{ION} is compared with the data of Risley and Tennyson (34) in fig. 7b. The two calculations correspond to two sets of $H He$ data (32, 33). The better agreement with data of (33) is presumably due to an underestimation of large angle scattering in (33) and (34a).

Summarizing one sees that reasonably good general understanding of electron detachment in H^- collisions was possible using the zero range potential model. This is successful because it correctly accounts for dynamical nuclear motion induced (radial coupling) effects. Study of other negative systems e.g. studies of halogen negative ion I.G. collisions (15, 37) also reveals the existence of such effects which are thus quite a general phenomenon.

4. DETACHMENT IN COLLISIONS WITH MOLECULAR TARGETS

Collisions of negative ions with molecular targets have attracted much attention recently. One of the characteristics of these systems is that at low collision energies (in the c.m. frame) there often exists the possibility of nuclear rearrangement channels and we are thus confronted with the fascinating realm of reactive scattering. Thus for e.g. F^- collisions with H_2 :



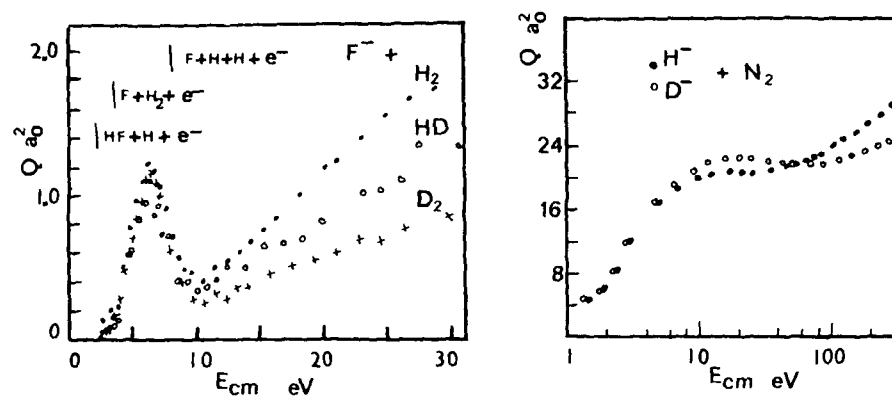


Fig. 8. Total detachment cross section for (a) F^- , H_2 , D_2 , HD collisions and (b) H^-/D^- N_2 collisions.

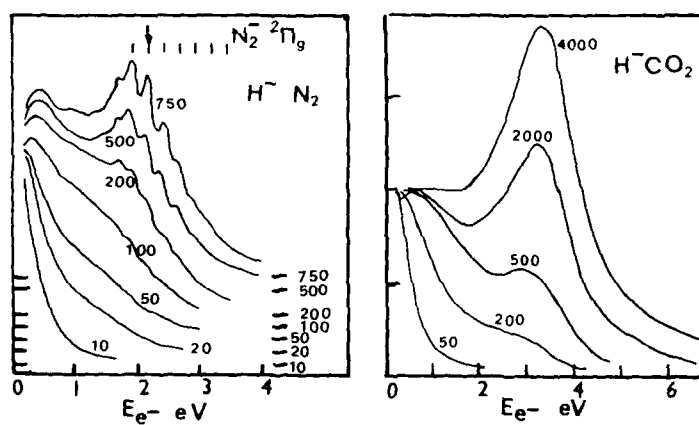


Fig. 9. (a) Detached electron energy spectra for $H^- N_2$ collisions (9,10) (b) D E E S for $H^- CO_2$ collisions (10).



This may be accompanied by electron detachment :



We also have the possibility of direct detachment :



We shall not consider reactive scattering here, but rather turn to the characteristics of the detachment processes. It should be noted that often isotope effects in reactive scattering will render interpretation of isotope effects in accompanying detachment processes rather difficult.

The first question that we shall ask ourselves concerns the importance of dynamic effects. Measurements of the TDCS for the specific case mentioned above, clearly illustrate their existence. Fig.8a shows the TDCS for F^-H_2 (D_2 and HD) collisions measured by Huq et al (38). As can be seen for energies above about 10eV in the c.m. frame the TDCS depends on the collision velocity and not on the c.m. energy as at the lower energies. Huq et al attribute detachment in this region to the direct detachment channel (g), and explain the behaviour of the TDCS as being due to the fact that the $(\text{F}^- + \text{H}_2)$ surface lies below that for $(\text{F} + \text{H}_2)$ and hence as in $\text{H}^- \text{Ne}$, detachment is purely dynamic and has a small cross section. For $E < 10\text{eV}$ detachment was attributed to channels (f) and (e). At these energies it was assumed that the corresponding trajectories lie within the continuum and an LCP model could be applicable since dynamic effects do not seem important. Note however that the isotope effect observed is not attributable to detachment alone but is strongly affected by the reactive scattering isotope effects also seen in the ionic channels.

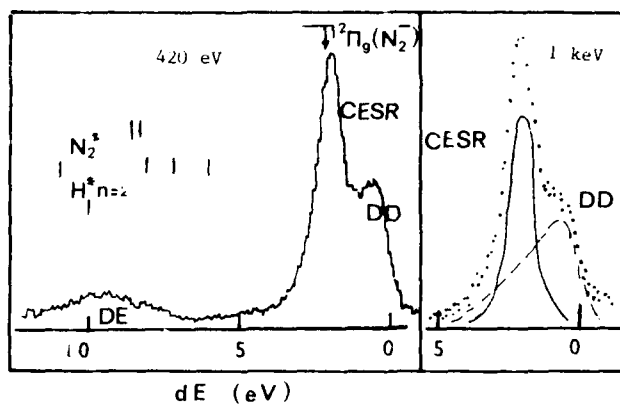
Recently another peculiar dual isotope effect was observed in the case of H^-N_2 collisions (39, 40) 8b. At low energies the isotope effect is consistent with what one might expect of detachment occurring primarily in the continuum (as for $\text{H}^- \text{He}$). Whereas at high energies detachment appears to be dominated by some channel whose importance increases as the collision velocity increases.

In order to identify this channel let us consider the DEES (8, 9, 10). Fig. 9a shows the (DEES) for different collision energies obtained by Esaulov et al (10). At low energies the DEES is fairly narrow, presents no structure and is attributable to the DD and DE channels. As the energy increases a series of structures appear at about 2eV for energies above 50eV. These are attributed to the onset of charge exchange to the shape resonances (CESR) of N_2^- ($^2\Pi_g$). This process populates the various 'vibrational levels' of N_2^- . These can decay into the ground and excited vibrational levels resulting in a series of lines lying around 2eV. The slight difference in the vibrational spacings of N_2 (0.3 eV) and N_2^- (0.25eV) results in a slight broadening of the lines. From this result it appears that charge exchange onsets at about 50eV and it appears plausible that the reversal of the isotope effect in the H^-N_2 TDCS (fig 8b) is due to CESR.

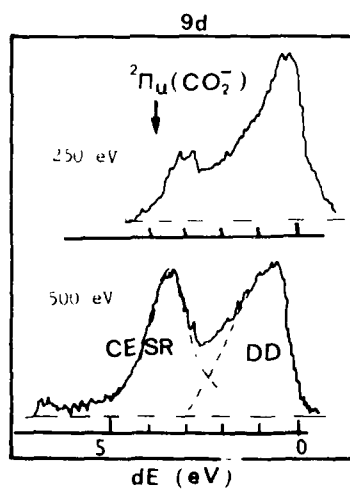
Further evidence for the existence of this process is provided by TOF studies (41, 42). Fig 9c shows a typical energy loss spectrum for a 420eV H^-N_2 collision. The spectrum displays two sets of peaks :

a) Peak B : corresponds to a series of excitation processes corresponding to N_2 and H excitation.

and b) Peak A corresponds to direct detachment and to CESR to N_2^- ($^2\Pi_g$). An interesting feature of this peak is that the CESR peak does not lie at the Franck Condon position of the resonance but somewhat lower. The same effect is also observed in the DEES, but there an additional shift due to summation over entry and exit channels may also be present. This non Franck Condon behaviour is rather surprising given the high velocity of H^- which would lead us to expect vertical transitions since the "collision time" is shorter than the "vibrational time" of N_2^- .



9c



9d

Fig 9. (c) T OF spectra for H^+N_2 collisions for 420 eV and 1 keV impact energies.
 (d) T OF spectra for H^+CO_2 collisions.

The above observations are true also in the case of other molecular targets with the exception of H_2 for which the very broad ($\Gamma(R_0) \approx 8\text{eV}$) $^2\Sigma^+ u^+$ resonance does not appear to play any role. As an example fig 9d shows some TOF spectra for CO_2 (42). CCSR to the $CO_2^- (^2\Pi_u)$ resonance lying at 3.8 eV is observed to onset for energies above about 150eV. This can also be seen in the DEES of Esaulov et al (34) (fig 9c). No oscillations are apparent in the DEES because of the greater number of vibrational modes and also because of the summation over exit channels. The 'non Franck-Condon' behaviour of CCSR at small energies is particularly visible in this case. Indeed at 250eV the CCSR peak in the TOF spectrum appears at about 3eV rather than at 3.8 eV. This can also be seen in the DEES, though here the summation over entry and exit channels may also provoke a further shift to smaller energies as discussed above. The shift from the F.C. position is found to decrease with increasing collision energy ($\Delta E \approx 0.2\text{ eV}$ at 1 keV).

At present no molecular model for CCSR has yet been proposed. Problems of this kind i.e. charge exchange and problems concerning spin-orbit coupling involving states lying within a continuum have been treated theoretically by e.g. Devdariani et al. (43) who have proposed a generalization of models of Demkov (44) and Nikitin (45) (in this context see also Hazi (46) with reference to the $e^- HBr$ problem), but a quantitative treatment of a specific system has not been made. Note however that given the low binding energy of the outer H^- electron (0.75 eV) for collision energies of the order of 1.5 keV, the orbital velocity of the outer electron becomes equal to the collision velocity and one can attempt to describe detachment in an independent electron scattering model. In simple classical terms one will say that the total detachment cross section (TDCS) is given by the total electron scattering cross section of the outer loosely bound electron on the target with a collision energy given by the translational energy and the binding energy; the latter on addition of velocities determines the 'incident energy spread'. This 'spread' results in a broadening out of any sharp features in the electron scattering cross section. At very high collision energies the binding energy is often neglected. Thus the free collision models (see 47 and references therein) which solve the problem either by classical mechanics or in the Born approximation are valid at very high energies ($E \approx 1.5\text{keV}$ for H^-). More recently Vu Ngoc Tuan et al (42) and Kazanskii (48) proposed treatments which take the binding energy of the outer electron into account and should be valid down to somewhat lower energies.

In the model proposed by Vu Ngoc Tuan et al (42) nuclear motion is treated classically. A frame transformation is performed on the outer H^- electron wavefunction to bring it from the projectile frame to the target N_2 frame. It is then expanded over both energy and spherical harmonics around the target. Knowing the electron-target scattering amplitude one gets the flux scattered by the target. After integration over time and energy the detachment probability is obtained in a first order perturbation theory. The energy spectrum of detached electrons is given by:

$$S(\epsilon) = |f_a(\epsilon)|^2 A_a(\epsilon) \int dt \phi_{H^-}(R(t)) \cdot \exp(-i(E_{H^-} + v^2/2 - \epsilon)t) G_a(t)^2$$

where

$f_a(\epsilon)$ is the electron target scattering amplitude for mode 'a',

$A_a(\epsilon)$ is a flux normalization factor,

ϕ_{H^-} is the H^- outer electron wavefunction evaluated at a distance $R(t)$ from the center,

$R(t)$ is the time dependence of the straight line trajectory,

E_{H^-} is the electron binding energy,

v is the collision velocity,

and $G_a(t)$ is a geometric factor depending on the trajectory-molecular axis relative orientation.

For N_2 a Breit-Wigner formula gave the resonant amplitude f :

$$|f(r)|^2 = \frac{(2\ell+1)}{k^2} \frac{\Gamma^2/4}{(\epsilon - \epsilon_R)^2 + \Gamma^2/4}$$

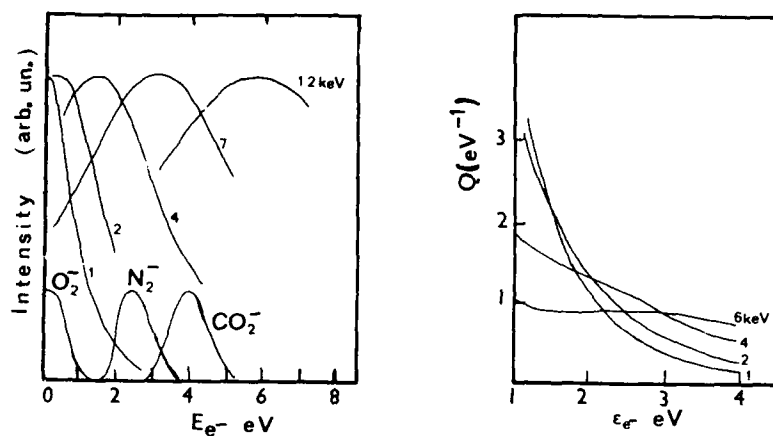


Fig 10. (a) Energy distribution in the electron wavepacket for several collision energies. The Franck Condon envelope of some shape resonances is also shown. (b) $Q(\epsilon, \nu)$ function in Kazanskii's (48) treatment for the indicated H^- collision energies.

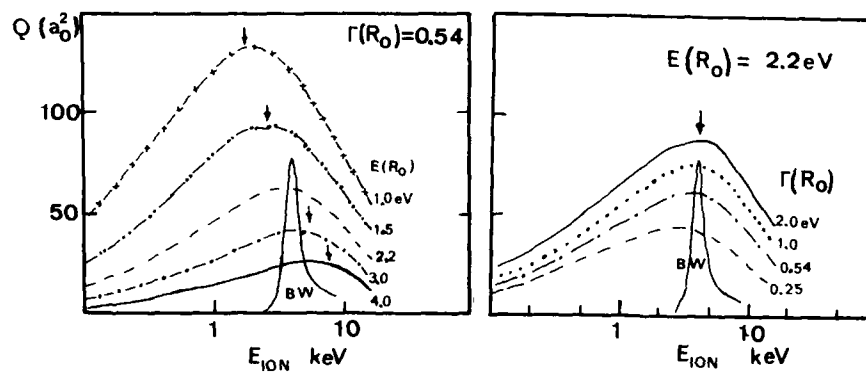


Fig 11. Dependence of the C E S R cross section on the (a) Energy $E(R_0)$ and (b) width $\Gamma(R_0)$ of a resonance for a fictitious target. The form of a Breit-Wigner (BW) resonance is also shown.

The integral over time contains a phase factor $\exp(-i E \cdot t)$ and if the time dependences of σ_{ij} and $G_i(t)$ are small compared with this phase factor, the integral does not vanish only for energies around $E_H + v^2/2$ i.e. the electron behaves almost like a free electron whose energy is given by the translational energy and the binding energy.

The calculated energy distribution of the 'equivalent electron packet' are shown in fig. 10a. Also shown schematically is the position and the spread of the shape resonance of O_2 , N_2 and CO_2 in the FC region. From this figure one can deduce that

(a) the $H^- N_2$ TDCS will reach its maximum for energies over 4 keV and for CO_2 above 7 keV.

and (b) that even when in a fast collision one treats the target molecule nuclei as fixed and assumes vertical transitions, if the incident wavepacket is not broad enough a Franck-Condon distribution of vibrational levels will not be obtained.

Similar conclusions should be valid in Kazanskii's (48) impulse approximation treatment, where the energy spectrum of detached electrons is given by

$$d\sigma = \sum_{n=0}^{\infty} Q(\epsilon_i^{(n)}, v_0) \cdot \sigma_{n \rightarrow n}(\epsilon_i^{(n)}) d\epsilon_f$$

where $\epsilon_i^{(n)} = \epsilon_f + E - E_{n0}$, ϵ_f is the ejected electron energy, E_{n0} is the initial and E_n the final vibrational states of the target molecule, $\sigma_{n \rightarrow n}$ is the total cross sections for vibrational excitation. The function Q is illustrated in fig. 10b for several collision energies for the case when an H^- wave functions of the type $\psi(r) = A \exp(-\alpha \cdot r) + \exp(-\beta \cdot r)/r$ is used.

Using their model and assuming vertical transitions Vu Ngoc Tuan et al calculated the shape of the TOF peaks corresponding to CESR. The theoretical curve, convoluted by the apparatus function, is compared in Fig. 9d with experiment. Note that the shift from the FC position is correctly described. The 'deconvolution' used was simply subtraction assuming a smooth curve for the DD process. This deconvolution was performed for other scattering angles and collision energies and thus allows the separation of the DCS for peak A into components due to DD and CESR. Integration over angles then shows that at 1keV CESR contributes about 40% to the TDCS for $H^- N_2$ collisions and 25% for $H^- CO_2$ collisions.

At present no attempt has yet been made to calculate the DEES. One of the reasons is that it represents a sum of distributions of all possible detachment channels.

Vu Ngoc Tuan et al have also investigated the behaviour of the CESR cross section in H^- collisions as a function of $E(R_0)$ and $\Gamma(R_0)$, i.e. the position and width of the resonance using a fictitious target with varying characteristics.

A Breit-Wigner formula for the scattering amplitude was used. Their results are summarised in fig. 11. For a given width and varying $E(R_0)$, the maximum of the CESR cross section is reached when the electron translational energy is close to the resonance energy (indicated by arrows). The maxima are however much broader than the corresponding electron scattering cross section as may be seen by comparing them to the electron scattering cross section shown in fig. 11a (marked BW) for the case $E(R_0) = 2.2\text{eV}$ and $\Gamma(R_0) = 0.54\text{eV}$.

When studied as a function of Γ , CESR is shown (fig. 11b) to be more important for larger Γ . This may be understood if one remembers that since in this model the incident wave packet has a broad energy distribution, the shape resonance only selects in it a slit equal to its width. Hence a broader resonance scatters a larger part of the incident wavepacket. It should be noted here that in the case of H_2 both experiment and theory show that the broad ($\Gamma(R_0) \approx 8\text{eV}$) H_2^- ($^2\Sigma_u^+$) resonance does not play any role and detachment may be described in a non resonant electron scattering formalism.

CESR has also been observed in collisions of other negative ion with various molecular targets (18, 49, 50). Contrary to the lighter and hence faster H^- the onset energy of CESR in e.g. halogen negative ion collisions is found to lie at higher energies. Thus in $F^- N_2$ collisions CESR onsets at energies around 1keV. The earlier made claim (14, 49) that this process is important in low energy ($E \approx 200\text{eV}$) $Cl^- N_2$ etc. collisions thus appears unfounded on the basis of existing data (50). As for the H^- case no indication of CESR to the broad $^2\Sigma_u^+$ H_2^- resonance is found in F^- collisions (50). Note that contrary to the deductions of Cheung and Datz (58) on the basis of low resolution

data, no CCSR was observed in more recent studies of $\text{Cl}^- \text{H}_2$ collisions for relative energies above 25 eV (59).

The above studies of negative ion molecule collisions lead to another question: can shape resonance play a role in collisions with atoms? For inert gases these do not exist, but recent experiments of Johnston and Burrow (39) show the existence of low lying shape resonances for alkali atoms. A TOF study of $\text{H}^- \text{Na}$ collisions by Esaulov and Vu Ngoc Tuan (52) suggests that the answer is affirmative. Indeed as may be seen in fig. 12 the TOF energy loss peak corresponding to detachment reaches a maximum at the resonance position.

5. CONCLUDING REMARKS

The above studies of negative ion collisions show that detachment can proceed via a variety of channels.

In low keV collisions with atoms the main channel is direct detachment. Dynamic effects i.e. nuclear motion induced transitions (e.g. radial coupling) play an important role here. The actual behaviour of detachment cross sections is determined by the relative importance of "intra-" and "extra-" continuum transitions for a given collision energy. Knowledge of the characteristics of the parent neutral quasimolecular system is important for the understanding of some of these features. To date the most successful description of detachment appears to be the zero range potential formalism. This is however applicable a priori to negative ions with an outer s electron, though some attempts have been made to use it to calculate total cross sections in the case of halogen negative ions. A generalisation of the ZRP model to include $l \neq 0$ cases has been proposed (53), but no applications exist. Alternatively a finite range model (54) could be useful here. Recently other descriptions have been proposed and some give rather good agreement with experiment (20, 21).

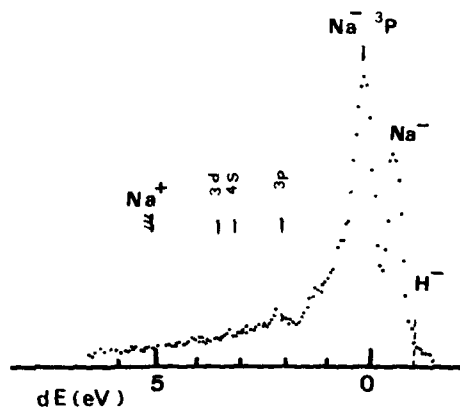


Fig 12. TOF spectrum for a 500 eV $\text{H}^- \text{Na}$ collision (52) for a 0.3 deg scattering angle.

Excitation processes have not yet been very extensively investigated. In collisions with atoms they are not very important representing some 10% in low keV H^- and F^- collisions (12, 37). In the case of molecular targets they can be the dominant channel: thus in F^-CO_2 collisions at 2keV (50) they represent 62% of the TDCS. Excitation of autodetaching states appears to be quite small (50, 55) representing about 2% of the TDCS in 1keV H^- collisions (55). Contrary to statements made in existing literature (18, 49) on the basis of existing data it seems doubtful that these resonance states make significant contributions to TDCS. Detailed theoretical descriptions of these processes have not yet been proposed, though some simple models exist (12, 31).

Study of collisions with molecules has revealed the existence of charge exchange to shape resonances. This process is important in fast collisions (42, 55). The maximum of the CESR cross section is reached for energies such that the translational energy of the outer electron is equal to the resonance energy. Its magnitude is found to increase with the resonance width (42).

The study of CESR has revealed the existence of non-Franck Condon effects in fast collisions when the target nuclei can be considered to be frozen during the collision time. This is because CESR is determined by both Franck Condon factors and an energy defect dependent charge exchange probability.

ACKNOWLEDGEMENTS

The author wishes to thank M. Barat, R.L. Champion, L.D. Doverspike, D. Dhucq, J.P. Gauiacq, J.P. Grouard, R.I. Hall, M.S. Huq, J.L. Montmagnon, V. Sidis and Vu Ngoc Tuan, for stimulating collaboration and many useful discussions.

REFERENCES

1. Champion R.L. Adv. Electron. Electron Physics 58, 143, (1982).
2. Massey H.S. Negative Ions, (Cambridge Univ. Press, 1976).
3. Hall R.I. and Esaulov V.A. Invited Papers, Symp. Physics of Ionized Gases, ed. Popovic M. (Institute of Physics, University of Belgrade, 1985).
4. Smirnov B.M. Negative Ions, (Mc GrawHill, New York, 1982).
5. Lam S.K., Champion R.L., Doverspike L.D., Phys. Rev. A9, 1828, (1974).
6. Risley J.S. and Geballe R. Phys. Rev. A9, 2485 (1974).
7. Geddes J., Hill J., Shah M.B., Goffe T.V. and Gilbody H.B. J. Phys. B13, 319 (1980).
8. Risley J.S. Phys. Rev. A16, 2346 (1977).
9. Montmagnon J.L., Esaulov V.A., Grouard J.P., Hall R.I., Landau M., Pichou F. and Schermann C. J. Phys. B 16, 393, (1975).
10. Esaulov V.A., Grouard J.P., Hall R.I., Landau M., Montmagnon J.L., Pichou F. and Schermann C. J. Phys. B 17, 1855 (1984).
11. Okamoto T., Sato Y., and Inouye H., Phys. Rev. Lett. 52, 184, (1984).
12. Esaulov V.A., Dhucq D., Gauiacq J.P., J. Phys. B 11, 1049, (1978).
13. Fayeton J., Dhucq D., Barat M. J. Phys. B 11, 1267 (1978).
14. Annis B.K., Datz S, "Electronic and Atomic collisions" XIIth ICPEAC, ed. S. Datz (North Holland, Amsterdam) p. 115.
15. Esaulov V.A., J. Phys. B 14, 1303 (1980).
16. De Vreugd C., Wijnaendts Van Resandt R.W., Delos J.B. and Los J. Chem Phys. 68, 261 (1982).
17. Huq M.S., Doverspike L.D., Champion R.L. and Esaulov V.A. J. Phys. B 15, 951, (1982).
18. Champion R.L. and Doverspike L.D., Electron Molecule Collisions and Their Applications, ed. Christophorou L.G., (Academic Press, 1984), p. 619.
19. Soloviev. E.A., Sov. Phys. JETP 43, 453, (1976).
20. Taylor R. and Delos J.B., Proc. Roy. Soc. A379, 209 (1982).
21. Wang T.S. and Delos J.B., J. Chem. Phys. 79, 4306 (1983).
22. (a) Demkov Yu. N. Sov. Phys. JETP, 19, 762, (1964).

- (b) Demkov Yu. N. and Ostrovskii V.N. "Zero Range Potential Methods in Atomic Physics" (Leningrad University Press, Leningrad 1975).
23. Gauyacq J.P., J. Phys. B 13, 4417 (1980).
 24. Bronfin F.B. and Ermolaev A.M., (Leningrad University Bulletin) Vestnik LGU 22, 29, (1971).
 25. Gauyacq J.P., J. Phys. B 13, L387 (1979).
 26. Herzenberg A. and Ojha P. Phys. Rev. A20, 1905, (1979).
 27. Devdariani A.Z. Sov. Phys. Tech. Phys. 18, 255, (1973).
 28. Olson R.E. and Liu B. Phys. Rev. A22, 1389, (1980).
 29. Gauyacq J.P., J. Phys. B 13, L 501 (1980).
 30. Vu Ngoc Tuan, Gauyacq J.P. and Esaulov V.A., J. Phys. B 16, L 95 (1983).
 31. Drukarev G.F. Sov. Phys. JETP 31, 1193, (1970).
 32. Fleishmann H.H. and Young R.A., Phys. Rev. 178, 254 (1969).
 33. Roussel F. Thesis, Univ. Paris VI, (1978).
 34. a Risley J.S. and Tennyson P., Abstracts XIth ICPEAC, (1979).
 b Fogel J.M. Sov. Phys. JETP 34, 400, (1958).
 c Williams J.F. Phys. Rev. 154, 9, (1967).
 35. Benoit C. Thesis, Univ. Paris XI, Orsay, (1976).
 36. Benoit C. and Gauyacq J.P. J. Phys. B 9, L 391, (1976).
 37. Grouard J.P., Esaulov V.A., Hall R.I., Montmagnon J.L., and Vu Ngoc Tuan submitted to J. Phys. B (1985).
 38. Huq M.S., Fraedrich D.S., Doverspike L.D., Champion R.L. and Esaulov V.A., J. Chem. Phys. 76, 4952, (1982).
 39. Champion R.L., Doverspike L.D., and Lam S.K., Phys. Rev A 13, 617 (1976).
 40. Huq M.S., Champion R.L. and Doverspike L.D. Phys. Rev. A 27, 785 (1983).
 41. Vu Ngoc Tuan and Esaulov V.A., J. Phys. B 15, L 95 (1982).
 42. Vu Ngoc Tuan, Esaulov V.A., Gauyacq J.P. and Herzenberg A., J. Phys. B 18, 721 (1985).
 43. Devdariani A.Z., Ostrovskii V.N., Sebyakin Yu. N. Zh. Eksp i Teor. Fiz 76, 529 (1979).
 44. Demkov Yu. N. Zh. Eksp i Teor Fiz 45, 195 (1963).
 45. Nikitin E.E. Disc Faraday Soc. 33, 14 (1962).
 46. Hazi A.V., J. Phys. B 16, L29 (1983).
 47. Dewangan D.P. and Walters H.R.J., J. Phys. B 11, 3983 (1978).
 48. Kazanskii A.K. Sov. Phys. JETP 59, 1160, (1984).
 49. Annis B.K., Datz S., Champion R.L. and Doverspike L.D., Phys. Rev. Let. 45, 1554, (1980).
 50. Vu Ngoc Tuan, Esaulov V.A., Grouard J.P., Hall R.I., Montmagnon J.L. J. Phys. B 17, 2897 (1984).
 51. Hall R.I., Grouard J.P., Montmagnon J.L. and Esaulov V.A. To be published.
 52. Vu Ngoc Tuan and Esaulov V.A., Phys. Rev. A 32 (1985) 883.
 53. Borodin V.M. Leningrad University Vestnik 16, 18, (1978).
 54. Drukarev G.F. Sov. Phys. JETP 53, 271, (1981).
 55. Risley J.S. Proc 4th ICAP, Invited Papers, ed. G. Zu Putlitz, E.W. Weber and Winnacker A. (Plenum Press, 1975) p. 487.
 56. Gauyacq J.P. and Esaulov V.A., Invited Papers, XIth ICPEAC ed. Oda N and Takayanagi.
 57. Sidis V. J. Phys. B6, 1517, (1972).
 58. Cheung J.T. and Datz S. J. Chem. Phys. 73, 3159, (1980).
 59. Esaulov V.A. and Vu Ngoc Tuan To be published.

COLLISION DYNAMICS WITH NONLOCAL POTENTIALS

W. DOMCKE and C. MÜNDEL

Theoretische Chemie, Physikalisch-Chemisches Institut, Universität
Heidelberg, D-6900 Heidelberg, West Germany

The nonlocal complex potential theory of nuclear motion in short-lived electronic states is reviewed with particular emphasis on resonant electron-molecule scattering and dissociative attachment.

1. INTRODUCTION

Short-lived autodetaching (or autoionizing) electronic states of molecular negative ions (or neutral molecules) occur as intermediates in a variety of collision processes such as electron-molecule scattering, dissociative attachment (or recombination), associative detachment (or associative ionization) and collisional detachment (or Penning ionization). It can be shown that the nuclear motion in these intermediate states is governed by an effective electronic potential which is (i) complex and (ii) energy-dependent and nonlocal. Property (i) accounts for the loss of flux by autodetachment (autoionization). The energy-dependence and nonlocality is a general property of effective potentials obtained by the projection of the Schrödinger equation on a certain subspace (in this case the onedimensional Hilbert space corresponding to the electronic resonance state). The general theoretical description of molecular dynamics in short-lived electronic states is based on the projection-operator formalism of Feshbach [1] or Fano's theory of configuration interaction in the continuum [2] and has been worked out, among others, by Chen [3], O'Malley [4], Bardsley [5] and Nakamura [6].

Since the nonlocality of the effective potential complicates considerably the solution of the dynamical problem, the approximation of a local and energy-independent complex potential has been introduced in most practical applications, see, e.g. [7-9]. Recent progress in the *ab initio* calculation of projected electronic resonance states and the energy-dependent width and level-shift functions [10,11] has made possible the calculation of electron-molecule scattering and dissociative attachment cross sections without recourse to the local approximation, at least for simple diatomic systems [12-14]. Here we review briefly the theoretical methods and discuss recent results which shed light on the importance of nonlocal effects in negative-ion dynamics.

2. PROJECTION-OPERATOR FORMALISM

Assuming, for simplicity, that we are dealing with a single isolated resonance decaying into a single continuum, we introduce a closed-channel (for Feshbach resonances) or localized (for shape resonances) discrete electronic state $|\phi_d\rangle$ and an orthogonal continuum $|\phi_k^{(+)}\rangle$. In the case of superexcited autoionizing states of neutrals, the Rydberg series converging to the ionization threshold under consideration is considered as a continuation of the continuum to negative energies. In the dissociation limit $R \rightarrow \infty$ (we assume a diatomic system for simplicity) $|\phi_d\rangle$ is a stable bound state of the fragments, but it moves into the continuum when the internuclear distance R decreases. The construction of $|\phi_d\rangle$ is a relatively simple task for Feshbach resonances:

it represents an excited discrete configuration lying in the ionization or detachment continuum. The construction of $|\phi_d\rangle$ is less obvious for shape resonances which are often very short-lived. Here the relevant criterion is the diabaticity [15] of $|\phi_d\rangle$ and $|\phi_k^{(+)}\rangle$. The discrete state is constructed such as to extract the resonance from the scattering continuum, yielding usually a structureless background continuum to which the simple adiabatic-nuclei approximation is applicable, see, e.g., ref. [16].

Given the diabatic discrete state $|\phi_d\rangle$ and background continuum $|\phi_k^{(+)}\rangle$, we introduce the potential energy function of the discrete state

$$V_d(R) = \langle \phi_d | H_e | \phi_d \rangle \quad (1)$$

where H_e is the fixed-nuclei electronic Hamiltonian, and the width and level-shift functions

$$\Gamma(R, E) = 2\pi \int d\Omega_k |V_k(R)|^2 \quad (2)$$

$$\Delta(R, E) = (2\pi)^{-1} P \int dE' \Gamma(R, E') / (E - E') \quad (3)$$

where $V_k(R)$ is the discrete-continuum coupling element

$$V_k(R) = \langle \phi_k^{(+)} | H_e | \phi_d \rangle. \quad (4)$$

The transition matrix elements for low-energy inelastic and reactive collision processes such as vibrational excitation, dissociative attachment or associative detachment can formally be expressed in terms of the fixed-nuclei quantities (1-4). The T-matrix element for $v \rightarrow v'$ vibrational excitation, for example, reads

$$T_{v'v}^{(\text{res})}(k_f, k_i) = \langle v' | V_{kf}(E - \mathcal{H})^{-1} V_{ki}^* | v \rangle \quad (5)$$

where k_i and k_f are the initial and final momenta of the electron. The superscript "res" indicates that (5) is the resonant contribution to the process; in principle, there is also a background contribution, which is usually negligible, however, for inelastic processes. The central quantity of the formalism is the effective Hamiltonian \mathcal{H} whose resolvent appears in equation (5). It is defined as [17]

$$\mathcal{H} = T_N + V_{\text{opt}} \quad (6)$$

$$V_{\text{opt}} = V_d(R) + \Delta(R, E - H_0) - \frac{i}{2} \Gamma(R, E - H_0) \quad (7)$$

$$H_0 = T_N + V_0(R) \quad (8)$$

Here T_N is the kinetic-energy operator of the nuclear motion and $V_0(R)$ the potential-energy function of the target molecule. H_0 is the target vibrational Hamiltonian with eigenstates $|v\rangle$ and eigenvalues ϵ_v . V_{opt} is the effective or "optical" potential for the nuclear motion in the resonance state and is seen to be complex, energy-dependent and - owing to its dependence on the operator H_0 - nonlocal. Explicitly, the nonlocal parts Δ and Γ , which depend on the non-commuting operators R and H_0 , are given by (we suppress here the rotational motion for simplicity)

$$\Gamma(R, E - H_0) = 2\pi \sum_m V_{E-\epsilon_m}^*(R) |m\rangle \langle m| V_{E-\epsilon_m}(R) \quad (9)$$

$$\Delta(R, E - H_0) = \sum_m P \int dE' V_{E'}^*(R) |m\rangle \langle m| V_{E'}(R) / (E - E' - \epsilon_m) \quad (10)$$

where the sum over m includes integration over the dissociation continuum. The $V_E(R)$ are defined as

$$|V_E(R)|^2 = \int d\Omega_k |V_k(R)|^2 \quad (11)$$

with $E = k^2/2$.

The effective Hamiltonian \mathcal{H} governs the time-evolution of the nuclear

motion in the resonance state. It determines, therefore, also the T-matrix elements for the other processes mentioned in the Introduction. The T-matrix element for dissociative attachment of an electron with momentum k_i to a molecule in the vibrational level v , for example, can be written as

$$T(K; k_i, v) = \langle \hat{K}(-) | V_{k_i}^* | v \rangle \quad (12)$$

$$| \hat{K}(+) \rangle = | K \rangle + G_0^{(+)} V_{\text{opt}} | \hat{K}(+) \rangle \quad (13)$$

where $| K \rangle$ denotes the plane-wave state of dissociating fragments and $G_0^{(+)}$ is the corresponding free Green's function. By detailed balance, the T matrix element (12) determines also the cross section for the reverse process, associative detachment. The corresponding processes involving short-lived electronic states of neutral molecules, namely dissociative recombination and associative ionization, are included in the above description, provided the Rydberg series converging to the ionization threshold is taken into account in the definition of the nonlocal level-shift operator Δ [18].

The widely used local-complex-potential approximation [7-9] consists in the replacement of the nonlocal operators Γ and Δ of equations (9,10) by the local functions

$$\Gamma(R) = \Gamma(R, E_{\text{res}}(R)) \quad (14)$$

$$\Delta(R) = \Delta(R, E_{\text{res}}(R)) \quad (15)$$

where $E_{\text{res}}(R)$ is the fixed-nuclei resonance energy defined via

$$E_{\text{res}}(R) = V_d(R) - V_0(R) + \Delta(R, E_{\text{res}}(R)) \quad (16)$$

With this approximation the effective potential for the nuclear motion becomes an energy-independent and local function of R

$$V_{\text{opt}}^L(R) = V_d(R) + \Delta(R) - \frac{i}{2} \Gamma(R) \quad (17)$$

We have to replace, furthermore, the energy-dependent entrance and exit amplitudes in equations (5,12) by local amplitudes, see, e.g., [13,19].

The derivation of the local-complex-potential model as a limiting case of the nonlocal resonance theory has been discussed, for example, in references [5,19-21]. The derivation of locality requires the assumption of closure for the sum over vibrational states in equations (9,10). Therefore, the local approximation for the width must break down for resonances near the detachment (or ionization) threshold, where few vibrational decay channels are open. More generally, the local approximation can be expected to fail when either $\Gamma(R, E)$ or $\Delta(R, E)$ defined in (2,3) are large and strongly energy-dependent [18,22].

In conclusion of this Section we mention that there are alternative formulations of the problem which do not invoke the concept of a diabatic discrete resonance state. Among these approaches are the R-matrix theory for dissociative attachment [23] and theories based on the zero-range-potential approximation [24] or Faddeev's equations [25].

3. SOLUTION OF THE DYNAMICAL PROBLEM

The solution of equation (13) for the scattering states of nuclear motion in the nonlocal and complex potential (7) is not a trivial problem and has been circumvented in most applications of the theory by resorting to the local-complex-potential approximation. In recent model calculations [26,27] we have learned, however, that separable expansions [28] of the nonlocal potential may yield rapidly convergent and numerically manageable approxi-

mation schemes.

Since the generally strongly repulsive local part $V_d(R)$ of V_{opt} is not well approximated by separable expansions, we rewrite equation (13) as

$$|\hat{K}^{(+)}\rangle = |K_d^{(+)}\rangle + G_d^{(+)} F |\hat{K}^{(+)}\rangle \quad (18)$$

where

$$F = \Delta(R, E-H_0) - \frac{i}{2} \Gamma(R, E-H_0) \quad (19)$$

is the nonlocal part of the optical potential and $|K_d^{(+)}\rangle$ and $G_d^{(+)}$ are the scattering states and the Green's function for the local potential $V_d(R)$, which can be determined by standard numerical methods.

To generate the separable expansion of F , we introduce a suitable complete set of orthonormal square-integrable basis functions $\chi_n(R)$ and diagonalize the representation of H_0 in a large, but finite, subset of these functions. This procedure yields approximate eigenstates $|\bar{n}\rangle$ and eigenvalues $\bar{\epsilon}_n$ of H_0 . For an appropriate choice of the basis functions $\chi_n(R)$, the Hilbert space spanned by the $|\bar{n}\rangle$ comprises the finite-dimensional space of bound states of H_0 and includes, furthermore, a discretized representation of the dissociation continuum. Approximating the nonlocal operator F by

$$F(s) = \sum_{n,m=1}^N F|\bar{n}\rangle (F^{-1})_{nm} \langle \bar{m}|, \quad (20)$$

$$F_{nm} = \langle \bar{n}|F|\bar{m}\rangle,$$

the kernel of the integral equation (18) becomes separable and (18) reduces to a finite set of linear algebraic equations, see, e.g., [28]. Calculations for a variety of examples have shown that this procedure converges reasonably fast with respect to the number of basis functions $\chi_n(R)$, even for large and possibly singular level-shift functions $\Delta(E)$ [14,26,27]. It is in general essential, however, to include the contribution of the continuum of H_0 in equation (10) to obtain converged results.

In the application of the theory to the $^2\Sigma_u^+$ resonance in electron- H_2 scattering to be discussed below we have parametrized $V_d(R)$ by a generalized Morse potential, which allows us to obtain $\langle R|K_d^{(+)}\rangle$ and $\langle R|G_d^{(+)}|R'\rangle$ analytically. For the basis functions $\chi_n(R)$ the Lanczos basis [29] of the Morse Hamiltonian $H_d = T_N + V_d(R)$ has been adopted. This has the particular advantage that matrix elements of $G_d^{(+)}$ can be evaluated by three-term recursion relations, which leads to great savings in computing time. Details of this method are given in reference [26].

4. EXAMPLES

We have applied the above-discussed methods to vibrational excitation of N_2 via the $^2\Pi_g$ shape resonance (the prototype of a resonance of intermediate width) and to vibrational excitation and dissociative attachment in H_2 and D_2 via the $^2\Sigma_u^+$ resonance (the prototype of a very short-lived shape resonance) with particular emphasis on the quantitative assessment of the accuracy of the local approximation [13,14].

The $^2\Pi_g$ resonance in electron- N_2 scattering has been extensively studied both experimentally and theoretically and represents the most spectacular success of the local-complex-potential or boomerang model [7,30]. Ab initio calculations yielding vibrational excitation cross sections in good agreement with experiment have been performed by Schneider et al. [31] and Hazi et al. [19]. The width function $\Gamma(R, E)$ for the $^2\Pi_g$ resonance has been calculated by Hazi [10] and with different methods by Berman and Domcke [11]. Based on the

fixed-nuclei ab initio data of Hazi [10] a fully nonlocal treatment of the nuclear dynamics in the $^2\Pi_g$ resonance state has been achieved by Berman et al. [13]. The results show that the local-complex-potential approximation is of excellent quantitative accuracy for the inelastic channels $v = 0 \rightarrow 1$ up to $v = 0 \rightarrow 5$ or 6. There are, however, significant deviations of the local model from the exact non-local theory for the elastic channel which dominates the total cross section. These deviations also lead to noticeable effects in the electron transmission spectrum [13]. Interestingly, simple model calculations [22] predict that the local approximation fails severely for deeply inelastic channels where the electron in the final state is slow. Recently, Allan [32] has measured vibrational excitation functions in N_2 up to $v = 17$ with excellent signal-to-noise ratio. The experimental results agree well with the predictions of the nonlocal model calculation [22]. In summary, the local-complex-potential-approximation is clearly a useful and physically appealing concept to rationalize the nuclear dynamics in the $^2\Pi_g$ shape resonance of N_2 , but significant deviations from the more exact nonlocal theory occur for the elastic channel as well as in deeply inelastic channels.

Dissociative electron attachment in F_2 via the $^2\Sigma_u^+$ shape resonance has been considered by Hazi et al. [12] and Bardsley and Wadehra [33] using a nonlocal description of the width Γ and a local approximation to the level-shift Δ . Since the level-shift is rather small and a smooth function of energy for this particular resonance, the latter approximation is justified, as has been confirmed by explicit calculations [34]. The nonlocal treatment of Γ is important, however, since dissociative attachment in F_2 occurs at low electron impact energies and few vibrational decay channels are available for the auto-detachment process.

The $^2\Sigma_u^+$ shape resonance in electron- H_2 scattering represents an interesting borderline case where resonant and non-resonant formulations of electron-molecule scattering, dissociative attachment and associative detachment meet. It is not possible to cover here the extensive amount of literature on this system and we refer the reader to the review article [35] and to the references given in recent papers on electron scattering and dissociative attachment in H_2 [14,24].

The discrete-state potential energy $V_d(R)$ and the width and level-shift functions for this resonance have recently been obtained by Berman et al. [16] and we refer to this paper for the details of the calculation. The width and level-shift functions $\Gamma(R,E)$, $\Delta(R,E)$ of the $^2\Sigma_u^+$ resonance state of H_2^- are large (of the order of several eV) and strongly energy-dependent. Correspondingly, the real part of the local complex potential (see equation (17)) deviates strongly from the discrete-state potential $V_d(R)$. While the latter is purely repulsive for the $^2\Sigma_u^+$ resonance, the former exhibits an attractive well which is deep enough to support many vibrational levels [14].

Integral cross sections for vibrational excitation and dissociative attachment in H_2 obtained with these ab initio data by Mündel et al. [14] are shown in figure 1 (full lines) together with absolute experimental data [36,37] (crosses). There is good agreement between theory and experiment for $0 \rightarrow 1$ and $0 \rightarrow 2$ vibrational excitation, although the deviations become larger for the $0 \rightarrow 3$ channel [14]. The dissociative attachment cross section is overestimated by the calculation, but its energy dependence seems to be in good agreement with experiment. The results obtained with the local approximation using the same ab initio input data are included as the full line with circles in figure 1. These cross sections are off by factors up to 10 and could be included in figure 2 only after rescaling them by appropriate factors as indicated in the figure. The cross sections obtained in the local approximation are generally much too large, in particular for dissociative attachment. We observe thus a complete breakdown of the local-complex-potential approximation for the

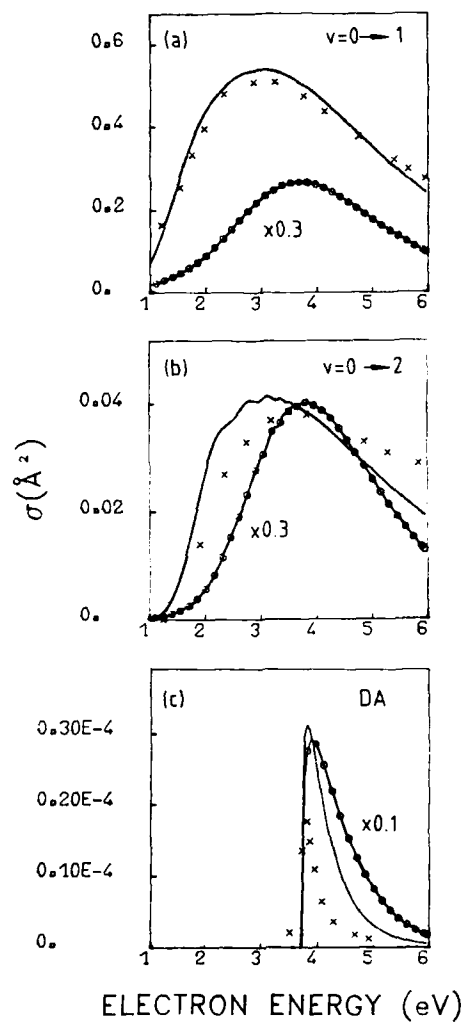


FIGURE 1

Integral cross sections for vibrational excitation (a,b) and dissociative attachment (c) in H_2 . Full line: non-local resonance theory; full line with circles: local-complex-potential approximation, rescaled by the indicated factors; crosses: experimental data [36,37].

nuclear dynamics in the $^2\Sigma_u^+$ state of H_2^- . The origin of the breakdown is the large size and the strong energy-dependence of the width and level-shift functions of the resonance. Our findings are in accord with the observation of Bieniek [20] who pointed out inconsistencies in local calculations of the $H^- + H$ associative detachment reaction, indicating a severe breakdown of the local model.

An interesting prediction of the calculations [14] is the appearance of vibrational fine structure in the $0 \rightarrow v$ vibrational excitation functions for $v \geq 4$ in H_2 . The results of the calculations for $0 \rightarrow 4$, $0 \rightarrow 5$ and $0 \rightarrow 6$ vibrational excitation of H_2 are shown in figure 2. Qualitatively, this fine structure is associated with vibrational levels of the local potential energy curve of H_2^- which converge towards the dissociation limit of H_2^- at 3.725 eV. The observation of fine structure is intuitively unexpected for this very short-lived resonance ($\tau \approx 4$ eV at the equilibrium geometry of H_2), but can be rationalized as a vibration-induced narrowing effect [38]. The fine structure is reproduced qualitatively, but not quantitatively, by the local-complex-potential model, i.e., the positions and intensities of the fine-structure peaks are not identical to those found in the nonlocal calculation.

The predicted fine structure has recently been confirmed experimentally by Allan [39] who has been able to measure the $0 \rightarrow v$ vibrational excitation functions of H_2 up to $v = 6$. Distinct fine structure is first observed for $v = 4$ and becomes progressively more pronounced for larger v . As expected, the theoretical cross sections are not in quantitative agreement with the experimental data, owing to limitations in the accuracy in the *ab initio* calculation. The experimental observation of this fine structure has established the $^2\Sigma_u^+$ resonance of H_2 as a very interesting new prototype system to study the nuclear dynamics in a strongly nonlocal complex potential with high precision.

5. CONCLUSIONS

We have sketched the general theoretical description of inelastic and reactive electron-molecule collisions and detachment processes based on the projection-operator formalism. In this formulation the calculation of cross sections reduces to the treatment of the nuclear dynamics in the nonlocal complex potential of the electronic resonance state formed during the collision. Recent work in this field has resulted in the quantitative assessment of the importance of nonlocal effects in resonant electron-molecule scattering and dissociative electron attachment. The specific cases studied so far on an *ab initio* level ($e + F_2$ [12], $e + N_2$ [13], $e + H_2$ [14]) indicate that nonlocal effects are generally important for broad resonances and for resonances which cross the threshold in the vicinity of the equilibrium geometry of the target molecule.

It is hoped that the quantitative results available now for electron-molecule scattering and dissociative attachment will stimulate the application of these methods to the related processes associative detachment, collisional detachment and associative and Penning ionization, which involve the dynamics in the same nonlocal potential, but under different kinematical conditions (collision energy and angular momentum). The treatment of the multidimensional dynamics in short-lived electronic states of polyatomic anions (e.g. electron attachment to CCl_4 and SF_6) is also a challenging problem for future theoretical work.

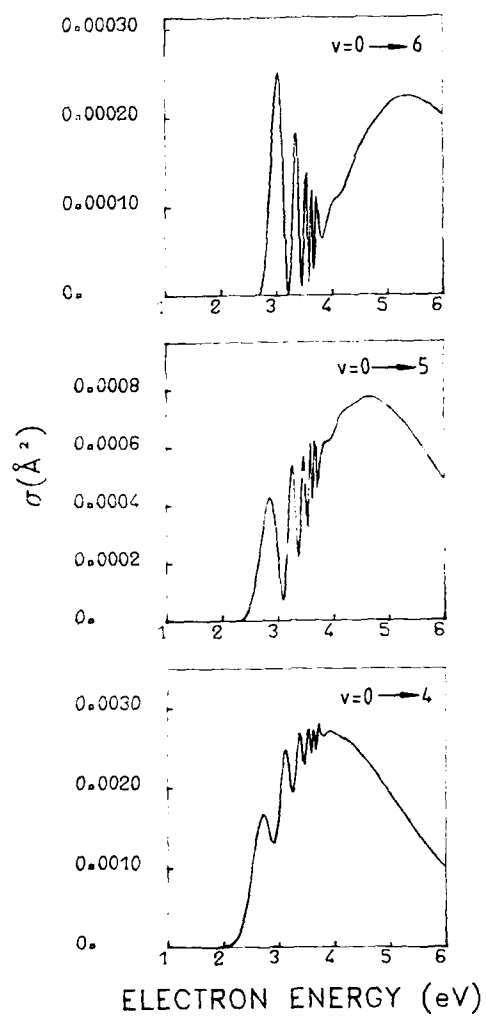


FIGURE 2

Integral excitation functions for $0 \rightarrow 4$, $0 \rightarrow 5$, $0 \rightarrow 6$ vibrational excitation in H_2 , calculated with the nonlocal resonance theory.

REFERENCES

- 1) H. Feshbach, *Ann. Phys. (N.Y.)* 19 (1962) 287.
- 2) U. Fano, *Phys. Rev.* 124 (1961) 1866.
- 3) J.C.Y. Chen, *Phys. Rev.* 148 (1966) 66; 156 (1967) 12.
- 4) T.F. O'Malley, *Phys. Rev.* 150 (1966) 14.
- 5) J.N. Bardsley, *J. Phys.* B1 (1968) 349, 365.
- 6) H. Nakamura, *J. Phys. Soc. Jpn.* 26 (1969) 1473.
- 7) D.T. Birtwistle and A. Herzenberg, *J. Phys.* B4 (1971) 53.
- 8) W.H. Miller, *J. Chem. Phys.* 52 (1970) 3563.
- 9) R.J. Bienieck and A. Dalgarno, *Astrophys. J.* 228 (1979) C35.
- 10) A.U. Hazi, *Molecular Resonance Phenomena*, in: *Electron-Atom and Electron-Molecule Collisions*, ed. J. Hinze (Plenum, New York, 1983) p. 103.
- 11) M. Berman and W. Domcke, *Phys. Rev. A* 29 (1984) 2485.
- 12) A.U. Hazi, A.E. Orel and T.N. Rescigno, *Phys. Rev. Lett.* 46 (1981) 918.
- 13) M. Berman, H. Estrada, L.S. Cederbaum and W. Domcke, *Phys. Rev. A* 28 (1983) 1363; *Chem. Phys. Lett.* 97 (1983) 352.
- 14) C. Mündel, M. Berman and W. Domcke, *Phys. Rev. A*, in press.
- 15) J.B. Delos and W.R. Thorson, *J. Chem. Phys.* 70 (1979) 1774.
- 16) M. Berman, C. Mündel and W. Domcke, *Phys. Rev. A* 31 (1985) 641.
- 17) W. Domcke and L.S. Cederbaum, *Phys. Rev. A* 16 (1977) 1465.
- 18) W. Domcke, *J. Phys. B* 14 (1981) 4889; 16 (1983) 359.
- 19) A.U. Hazi, T.N. Rescigno and M. Kurilla, *Phys. Rev. A* 23 (1981) 1089.
- 20) R.J. Bienieck, *J. Phys. B* 13 (1980) 4405; *Phys. Rev. A* 18 (1978) 392.
- 21) K.-S. Lam and T.F. George, *Phys. Rev. A* 29 (1984) 492.
- 22) L.S. Cederbaum and W. Domcke, *J. Phys. B* 14 (1981) 4665.
- 23) B.I. Schneider, M. Le Dourneuf and P.G. Burke, *J. Phys. B* 12 (1979) L 365.
- 24) J.P. Gauyacq, *J. Phys. B* 13 (1980) 4417; 18 (1985) 1859.
- 25) G. Drukarev and S. Pozdnev, *J. Phys. B* 13 (1980) 2611.
- 26) C. Mündel and W. Domcke, *J. Phys. B* 17 (1984) 3593.
- 27) W. Domcke and C. Mündel, *J. Phys. B*, in press.
- 28) S.K. Adhikari and I.H. Sloan, *Phys. Rev. C* 11 (1975) 1133.
- 29) C. Lanczos, *J. Res. Natl. Bur. Stand.* 45 (1950) 367.
- 30) L. Dubé and A. Herzenberg, *Phys. Rev. A* 20 (1979) 194.
- 31) B.I. Schneider, M. Le Dourneuf and V.K. Lan, *Phys. Rev. Lett.* 43 (1979) 1926.
- 32) M. Allan, *J. Phys. B*, in press.
- 33) J.N. Bardsley and J.M. Wadehra, *J. Chem. Phys.* 78 (1983) 7227.
- 34) C. Mündel, Thesis, University of Heidelberg, 1985, unpublished.
- 35) N.F. Lane, *Rev. Mod. Phys.* 52 (1980) 29.
- 36) H. Ehrhardt, L. Langhans, F. Linder and H.S. Taylor, *Phys. Rev.* 173 (1968) 222.
- 37) G.J. Schulz and R.K. Asundi, *Phys. Rev.* 158 (1967) 25.
- 38) W. Domcke and L.S. Cederbaum, *J. Phys. B* 13 (1980) 2829.
- 39) M. Allan, *J. Phys. B*, in press.

THE ROLE OF INDIRECT PROCESSES IN ELECTRON-IMPACT IONIZATION OF
MULTICHARGED IONS*

D.C. GREGORY

Physics Division, Oak Ridge National Laboratory, Oak Ridge, TN 37831 USA

Recent studies of electron impact ionization in this laboratory are discussed with emphasis on the role of indirect processes. Examples are used to illustrate the importance of excitation-autoionization (Ti^{2+} and Al^{2+}), autoionizing metastable ions in the Na isoelectronic sequence, multiple ionization (triple ionization of Xe^{6+}), the relative importance of indirect ionization with increasing charge in the Mg isoelectronic sequence, and the extension of ionization measurements to higher-charged target ions (Fe^{9+}).

1. INTRODUCTION

Electron impact ionization is of primary importance to the understanding of laboratory plasmas through power balance calculations, analysis of diagnostics, edge plasma studies, and other interpretative research (1). In addition, there is basic interest in the varied physical processes which result in ionization. One of the principal aims of our laboratory has been the measurement and interpretation of cross sections for electron impact ionization of multicharged ions. A large number of cross sections have been measured to test existing theories (or to provide a base for comparison with planned calculations). Our measurements have concentrated on systematic studies of isoelectronic (same number of electrons with varying elements in appropriate charge states), isonuclear (same element with varying charge states), and isoionic (ions with similar outer electron configurations) target ion groups (2).

The crossed beams apparatus currently in use for electron impact ionization measurements at ORNL is shown in Figure 1. In the main interaction chamber, the incident ion beam is focussed and then bent by 90° by the charge purifier. It then passes through the interaction region, where it is intersected at right angles by a magnetically-confined electron beam (3). The ion beam is then separated into charge-state components in the post-collision analyzing magnet. Incident ion beam current is measured by collection in one of two Faraday cups while signal (further ionized) ions are counted in a channeltron electron multiplier.

The new analyzing magnet extends our potential range of measurements of single ionization to ions with incident charge states up to +14. This extended range was intended to match the capabilities of the new ORNL-ECR ion source which has recently been commissioned for full-time use on atomic physics experiments (4); the source has in fact already surpassed its expected ultimate performance criteria for beam intensity and charge state output. Details of the previous ion source and other experimental details are available in previous publications (5,6).

A number of indirect processes must be considered to fully understand observed ionization cross sections (7). In addition to direct ionization of an outer shell electron, e.g.,

*Research sponsored by the Office of Fusion Energy, U.S. Department of Energy, under contract DE-AC05-84OR21400 with Martin Marietta Energy Systems, Inc.

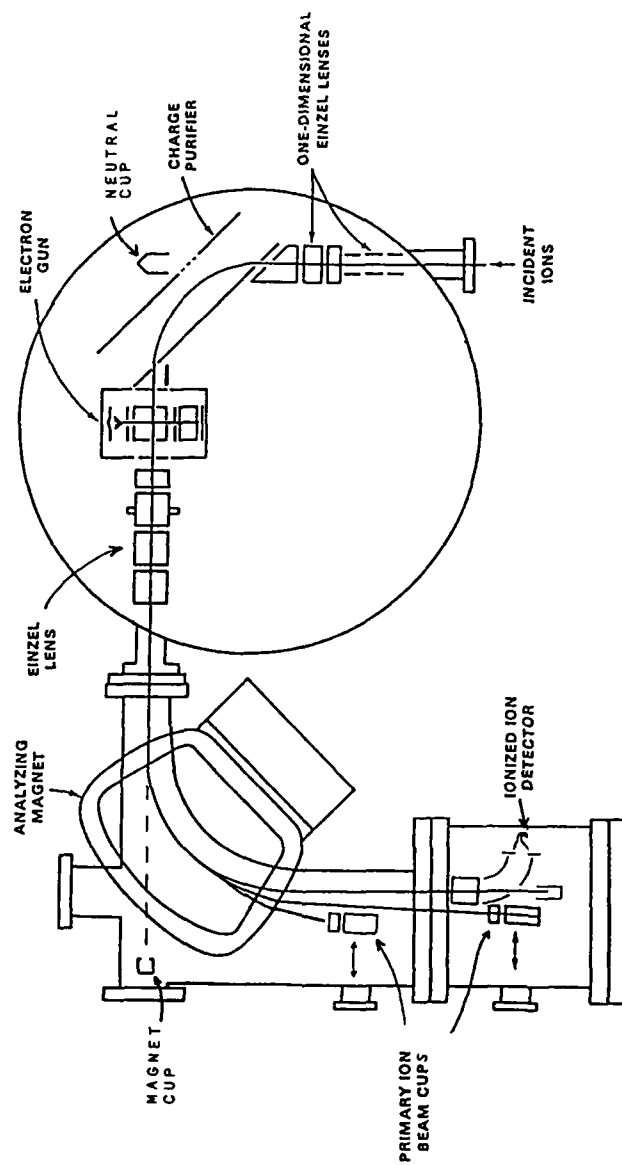
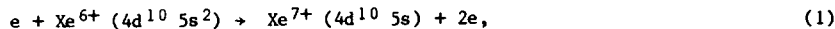
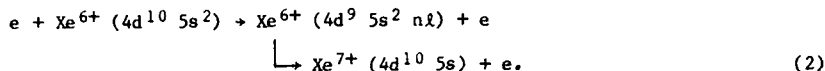


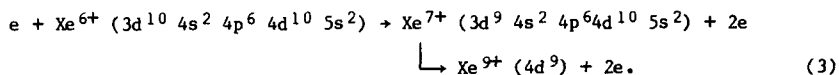
FIGURE 1
ORNL Crossed Electron-Ion Beams Apparatus.



removal of an electron from the target ion may occur through excitation of an inner-subshell electron followed by autoionization, as in



Detailed knowledge of the energy level scheme for the target ion is generally necessary in order to make an accurate evaluation of which excited states will autoionize and which are trapped in the incident ion charge state, but rough guesses can often be made based on available inner-subshell ionization energies (8). Net multiple ionization may also result from excitation or ionization of an inner-shell electron:



In this example, direct ionization of a 3d electron leads eventually to triple ionization. Careful accounting of possible branching paths for ions with inner-shell holes must be used to optimize the usefulness of any theory, whether it is a detailed distorted-wave or close-coupling calculation or the simple Lotz formula.

Two examples of indirect ionization due to excitation-autoionization will be discussed followed by an example of multiple ionization. Recent preliminary cross section measurements on a highly-charged ion will be presented along with a discussion of our future plans.

2. EXCITATION-AUTOIONIZATION

The effects of excitation-autoionization may range from negligible to dominant, and we are still learning how to make intelligent guesses of its importance to total ionization in a given case. For this reason, a large number of comparisons between experiment and theory seems the only way to develop an understanding of the "rules" that govern which transitions and processes are important. In cases where the transitions leading to autoionizing states are well-separated in energy, the experimental data may provide an indirect measure of the excitation cross sections to compare with detailed calculations.

One of the measurements which drew our attention to the importance of excitation-autoionization was the cross section for single ionization of Ti^{3+} (9). Indirect ionization dominates over the direct process by a factor of up to ten over the entire energy range from threshold to high energies. A subsequent study (10) of the cross section for single ionization of Ti^{2+} is shown in Figure 2 along with direct ionization calculations from Pindzola et. al. (11) and the three-parameter Lotz formula (12). It is obvious that total ionization is almost uniformly twice the direct cross section, so that the direct and indirect contributions must be approximately equal. In such cases where widely used formulas (like the Lotz semiempirical formula) underestimate total ionization by a large factor for several successive charge states of an important element, any plasma modeling or diagnostic analysis based on these formulas will be very misleading and may lead to conclusions which are seriously in error.

Ionization of Al^{2+} , shown in Figure 3, has been the subject of controversy for several years (13). Detailed calculations (14) of the expected contributions of excitation-autoionization (upper solid curve) appear to overestimate

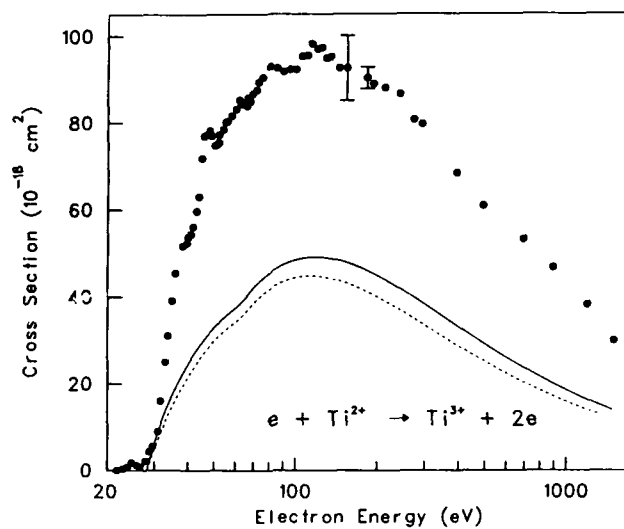


FIGURE 2

Electron impact ionization of Ti^{2+} (from Ref. 10). The solid and dashed curves are thought to be reasonable estimates of direct ionization; direct and indirect ionization contribute approximately equally to the total cross section.

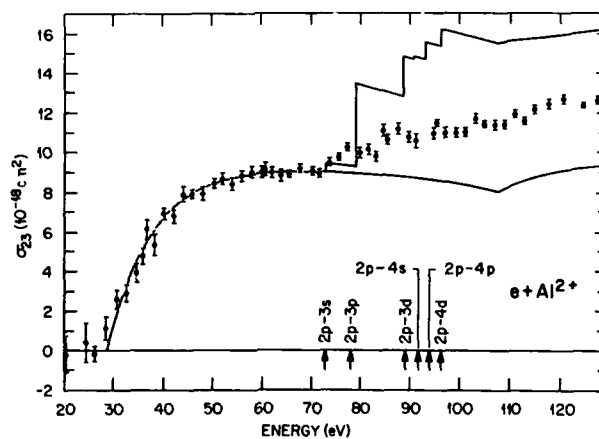


FIGURE 3

Electron impact ionization of Al^{2+} in the threshold energy region (from Ref. 13). It is now thought that the predicted 2p-3p excitation-autoionization feature does not contribute to the measured cross section because the excited ion is trapped in a metastable autoionizing state.

the indirect contribution by almost a factor of two, and although the overall disagreement is not large, this is an excellent test case for comparison between theory and experiment. Al^{2+} is also a member of the Na isoelectronic sequence which is critical to plasma diagnostics and X-ray laser development. The transitions expected to lead to single ionization are listed on the figure along with arrows indicating the excitation onset energies. A number of effects may lead to a "washing-out" of the sharp onsets indicated in the theory curve, but some fairly sharp rise should be observed at least in the case of the strongest transition (2p-3p). It should also be noted that elimination of this one transition would bring experiment and theory into good agreement.

Recent measurements and calculations of ionization in the neighboring Mg isoelectronic sequence (15,16) have led to reasoning which explains the results of both sequences; without this explanation neither sequence can currently be explained. If the excitation of a 2p electron from the ground state of Al^{2+} leaves the resulting excited Al^{2+} ($2p^5 3s3p$) ion in one of the metastable states of this configuration, the subsequent autoionization event might not occur for several microseconds; this delay is long enough to eliminate that ion from our signal channel and probably long enough in a plasma to allow other collisions which will alter the ion configuration once again. Thus the "missing" transition may only be trapped in an unexpected metastable state. In the Mg sequence, ionization from metastable target ions leave a similar metastable ion; this ionization event is detected in our signal channel even though it should autoionize and result in net double ionization. These cases provide an excellent example not only of cooperation between experiment and theory, but also of seemingly unrelated discrepancies leading to a single unified explanation.

The relative importance of indirect ionization with increasing charge along an isoelectronic sequence is illustrated in Table 1 where the peak direct and estimated peak indirect cross sections for some members of the Mg isoelectronic sequence are compared. While the peak direct cross section decreases rapidly with increasing charge, the peak indirect cross section remains almost constant over the range studied. This only means that the energy required and probability of exciting (or ionizing, for that matter) an inner-shell electron is not very sensitive to the exact number of outer-shell electrons. As the charge state increases, however, competing processes (such as radiative stabilization in the case of excitation-autoionization) will eventually change the relative importance of the various indirect processes. We may discover new processes or new significance for processes thought to be negligible as ionization measurements are extended to significantly higher charge states.

TABLE 1
Direct and indirect ionization peak cross sections in Mg-like ions (Ref. 15).

	Direct Peak (10^{-18} cm^2)	Indirect Peak (10^{-18} cm^2)	Indirect/Direct Ratio
Al^{1+}	75	3.0	0.04
S^{4+}	5.0	2.5	0.5
Cl^{5+}	2.5	2.5	1.0
Ar^{6+}	2.0	2.2	1.1

3. AUTOIONIZING ION BEAMS

Attempts to extend measurements in the Na isoelectronic sequence to higher charge states, however, encountered unexpected difficulties. Figure 4 shows the background measured for a number of Na-like ions. This background is generally dominated by ions in the target beam which have lost one electron in a collision with the residual gas in the main chamber. In order to minimize this effect, the ion beam is charge-analyzed just before the interaction volume; the normal background rate is then 1-10 counts/sec/particle nA. The dramatic increase in background seen in Figure 4 with increasing charge state has been determined to be due to target ions which leave the ion source in one or more autoionizing metastable state(s) of the $2p^5 3s3p$ configuration. A crude measurement in our apparatus indicates a mean lifetime in the 1-10 micro-sec. range for S^{5+} ; a lifetime very much longer would result in few autoionizing events in our interaction region, while states with much shorter lifetimes would have almost all decayed before reaching our charge-state purifier. Since the lifetimes of these states are predicted to become shorter with increasing charge, it is hoped that ionization of even higher-charged Na-like ions will again be manageable. Similar spontaneous autoionizing ion beams have been observed in a similar apparatus in Belgium (17) and they confirm that their background count rate is lower for Ar^{7+} . Our laboratory is also considering experiments which could take advantage of these unusual autoionizing ion beams.

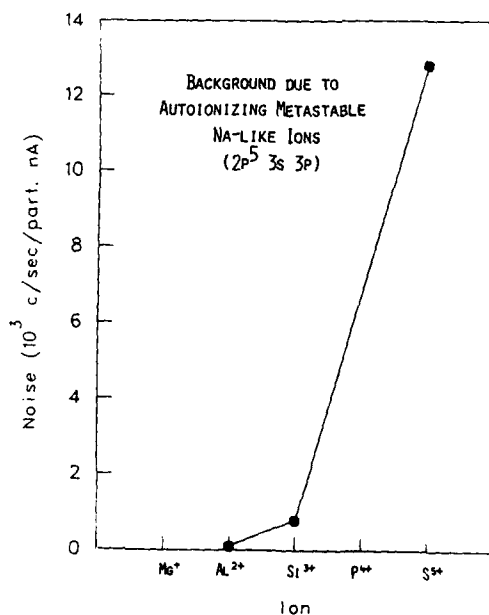


FIGURE 4

Background in ionization measurements on Na-like ions. Autoionizing metastable ions in the target ion beam are responsible for the high background at higher charge states.

4. MULTIPLE IONIZATION

The number of physical events that can result in multiple ionization is much greater than for single ionization. Excitation or removal of a single inner electron will often lead to multiple ionization as the resulting highly excited ion relaxes. In addition, multiple electron processes from a single collision can also lead to further autoionization or result in an ion trapped in its original charge state. The large number of possibilities means that considerable care must be given to studying energy levels and decay paths in order to predict which processes will be important for a given multiple ionization. The relative lack of experimental data and the difficulties involved in calculating multielectron processes has left us with considerably less data (both theoretical and experimental) to compare. The only readily available theory (18) which can be applied by the casual user is based on binary encounter approximation (BEA), and it is not immediately clear how to apply even this theory if the user wishes to take subshells into account.

As an example of recent measurements of multiple ionization, the cross section for triple ionization of Xe^{6+} is shown in Figure 5. This measurement (19) presents a rare opportunity to observe a two-electron process. In almost every previous multiple ionization study, the complete cross section curve could be explained in terms of single electron processes which result in final multiple ionization. Since such first-order processes are expected to strongly dominate over multiple-electron contributions, it is difficult to compare or isolate the two effects. Triple ionization of Xe^{6+} , however, can only occur

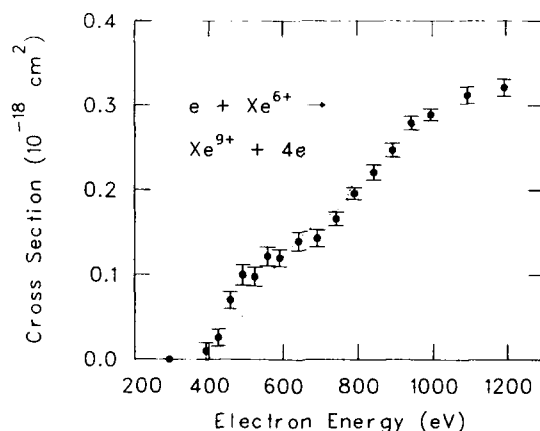


FIGURE 5

Triple ionization of Xe^{6+} (from Ref. 19). Ionization in the energy range from 374 to 670 eV can only be due to multiple-electron excitation or ionization in a single collision. The dashed curve is the sum of contributions from direct double ionization (Ref. 18) and direct ionization of a single, inner-shell electron (Ref. 12) followed by autoionization.

due to a one-electron process above 670 eV, while removal of three electrons only requires 374 eV. The dominant contribution to triple ionization is expected to come from direct ionization of a single 3d inner-shell electron which onsets at 762 eV. As can be seen from Figure 5, the cross section onsets near 374 eV (the lowest allowed energy), and a break in the slope of the data can be seen where the expected direct inner-shell ionization onsets. If the trend of the low-energy data is extended, it can be seen that the peak contributions from the multiple-electron and single-electron processes are approximately equal. This is a surprising result since single ionization is expected to be dominant. The dashed curve is the summed result of double direct ionization calculations based on Gryzinski's BEA model (18) and Lotz (12) calculations for direct ionization of a single 3d electron. Direct double ionization (followed by autoionization) is expected to be the dominant contribution in the multiple-electron region, but the good agreement between BEA calculations and experiment are considered fortuitous since a number of approximations were necessary to adapt the BEA theory to this situation.

Although only a few multiple ionization systems have been studied in our laboratory, the new ion source and experimental apparatus will make such measurements much easier and systematic studies possible in the future. Multiple ionization should be considered an important part of total ionization as well as an interesting physical process, and we intend to carry out additional studies in the future.

5. FUTURE PLANS

In recent years we have measured numerous cross section curves for ions of initial charge +2 through +6, almost all as part of systematic studies. We plan to extend measurements to higher charge states using the new capabilities of the ORNL-ECR ion source and the improved experimental apparatus. As an example of the possibilities presented by this combination, Figure 6 shows preliminary measurements of single ionization of Fe^{9+} which were collected in a

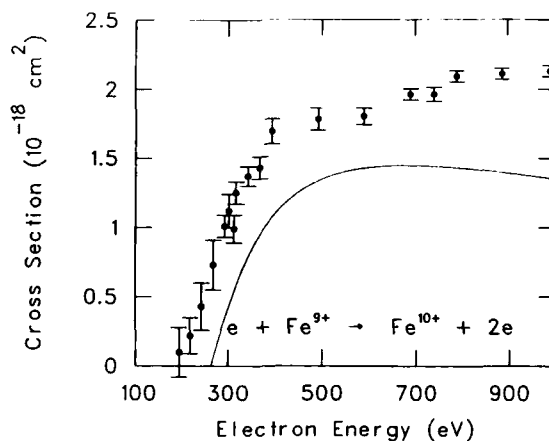


FIGURE 6

Preliminary measurements of electron impact ionization of Fe^{9+} (Ref. 20). The solid curve is distorted-wave theory from Younger (Ref. 21). Most of the target ion beam is apparently in a metastable state about 100 eV above the ground state.

few hours recently (20). Although the data are not final and complete diagnostics were not performed as is customary, it appears that the incident ion beam is mainly trapped in a metastable level approximately 100 eV above the ground state. This measurement typifies the new capabilities of such experiments, since no crossed beams data has been published for ions of initial charge state greater than +6. The ECR ion source produced a 500 nA beam of Fe^{15+} in a recent test, so that it appears that we are limited in charge state only by the current experimental apparatus, which was designed for incident ion beams up to charge +14.

In order to answer the needs of the fusion community, our measurements will concentrate in the near future on metallic ions, particularly on Fe and other likely plasma contaminants. Some multiple ionization studies will be used to complement our understanding of single and total ionization. Long range plans could involve analysis of the direction and/or energy of scattered (or ejected) electrons. Experiments on state-selected incident ion beams (or state-analysis of the signal ionized ions) are also exciting long-range possibilities. We intend to continue our coordination and cooperation with other laboratories involved in similar research, and we will continue to address the needs of the physics community in general and of the fusion community in particular.

ACKNOWLEDGEMENT

A number of people at ORNL have participated in these experiments in recent years. D.H. Crandall and R.A. Phaneuf have been leaders of the research effort, and J.W. Hale has kept all of the apparatus in working condition. A.M. Howald led a number of the measurements during his two years of postdoctoral research, and F.W. Meyer was responsible for the development of the ECR ion source. A long and fruitful collaboration with the research group led by G.H. Dunn at JILA is acknowledged.

REFERENCES

- 1) David H. Crandall, Nucl. Instrum. Methods 214 (1983) 129.
- 2) D. C. Gregory, D. H. Crandall, R. A. Phaneuf, A. M. Howald, G. H. Dunn, R. A. Falk, D. W. Mueller, and T. J. Morgan, "Electron Impact Ionization of Multicharged Ions at ORNL: 1980-1984," Oak Ridge National Laboratory Report ORNL/TM-9501 (May 1985).
- 3) P. O. Taylor, K. T. Dolder, W. E. Kauppila, and G. H. Dunn, Rev. Sci. Instrum. 45 (1975) 588.
- 4) F. W. Meyer, "The ORNL-ECR Multicharged Ion Source," Nucl. Instrum. Methods Phys. Res. (in print).
- 5) M. L. Mallory and D. H. Crandall, IEEE Trans. Nucl. Sci. NS-23 (1976) 1069.
- 6) D. C. Gregory, P. F. Dittner, and D. H. Crandall, Phys. Rev. A 27 (1983) 724.
- 7) See, for example: C. Bottcher, D. C. Griffin, M. S. Pindzola, and R. A. Phaneuf, "Indirect Processes in Electron-Ion Scattering," Oak Ridge National Laboratory Report ORNL/TM-8868 (October 1983).
- 8) Available for many ions from: Enrico Clementi and Carlo Roetti, Atomic Data and Nuclear Data Tables 14 (1974) 177.
- 9) R. A. Falk, G. H. Dunn, D. C. Gregory, and D. H. Crandall, Phys. Rev. A 27 (1983) 762.
- 10) D. W. Mueller, T. J. Morgan, G. H. Dunn, D. C. Gregory, and D. H. Crandall, Phys. Rev. A 31 (1985) 1905.
- 11) M. S. Pindzola, D. C. Griffin, C. Bottcher, D. C. Gregory, A. M. Howald, R. A. Phaneuf, D. H. Crandall, G. H. Dunn, D. W. Mueller, and T. J. Morgan, "Survey of Experimental and Theoretical Electron-Impact Ionization Cross Sections for Transition Metal Ions in Low Stages of Ionization," Oak Ridge National Laboratory Report ORNL/TM-9436 (March 1985).

- 12) Wolfgang Lotz, *Z. Physik* 206 (1967) 205; *Z. Physik* 216 (1968) 241; *Z. Physik* 220 (1969) 466.
- 13) D. H. Crandall, R. A. Phaneuf, R. A. Falk, D. S. Belic, and G. H. Dunn, *Phys. Rev. A* 25 (1982) 143.
- 14) D. C. Griffin, C. Bottcher, and M. S. Pindzola, *Phys. Rev. A* 25 (1982) 154.
- 15) A. M. Howald, D. C. Gregory, F. W. Meyer, R. A. Phaneuf, A. Müller, N. Djuric, and G. H. Dunn, "Electron-Impact Ionization of Mg-Like Ions: S^{4+} , Cl^{5+} , and Ar^{6+} ," submitted to *Phys. Rev. A*.
- 16) M. S. Pindzola, D. C. Griffin, and C. Bottcher, "Electron-Impact Ionization in the Magnesium Isoelectronic Sequence," submitted to *Phys. Rev. A*.
- 17) P. Defrance, private communication (1985).
- 18) M. Gryzinski, *Phys. Rev.* 138 (1965) A336.
- 19) A. M. Howald, D. C. Gregory, R. A. Phaneuf, D. H. Crandall, and M. S. Pindzola, "Observation of Multiple-Electron Processes in Ionization of Xe^{6+} by Electron Impact," submitted to *Phys. Rev. Lett.*
- 20) D. C. Gregory, F. W. Meyer, A. Müller, and P. Defrance, preliminary data (1985).
- 21) S. M. Younger, *J. Quant. Spectrosc. Radiat. Transfer* 29 (1983) 61.

INNER SHELL EXCITATION IN ATOMS AND MOLECULES BY HIGH RESOLUTION ELECTRON
IMPACT

George C. KING

Department of Physics, Schuster Laboratory, Manchester University,
Manchester M13 9PL, England.

1. INTRODUCTION

Inner-shell excited states of atoms and molecules are formed when an inner-shell electron is promoted to an unoccupied valence or Rydberg orbital, for example the excitation of a 2p electron in argon or a 1s atomic electron in N_2 . This excitation can be induced by photoabsorption or by charged particle impact. The first observation of a molecular inner-shell excitation (1) used a bremsstrahlung continuum source to investigate x-ray absorption in N_2 and other gases. In N_2 , a strong absorption peak was observed to occur at an energy of approximately 40 eV, 9 eV below that of the K-shell ionisation energy, and this was correctly attributed to excitation of an atomic K-shell electron to the first unfilled 2p π orbital of the molecule, giving the configuration $(1s)^{-1}(2p\pi)^{1\pi}$. More recently, for example (2), synchrotron radiation has been used in these photoabsorption studies. These inner-shell transitions can also be studied by electron energy-loss spectroscopy and, as we shall see, this technique can have important advantages over photoabsorption measurements. Van der Wiel et al (3), used the electron energy-loss technique and observed inner-shell transitions in N_2 and CO. This work was followed by a systematic and comprehensive study of inner-shell transitions in molecules by Brion and co-workers using the electron energy-loss technique at an energy resolution of approximately 0.5 eV (for a recent review see (4)). This resolution was comparable to or better than that obtainable in photoabsorption measurements using synchrotron radiation and was adequate for observing the more prominent energy-loss peaks and for studying the gross features associated with centrifugal and other barriers. Subsequently a significant improvement in resolution was obtained by the Manchester group, for example (5,6), who obtained a resolution of 0.07 eV in electron energy-loss measurements in a number of atoms and molecules. These latter studies illustrated one of the important advantages of the technique, namely its superior resolution to photoabsorption measurements for state excitation energies of above about 200 eV. This allowed a full investigation of the parameters of inner-shell states including their energies, natural widths, and in the case of molecules, their vibrational spacings and equilibrium internuclear separations. An example of what can be observed with the electron energy-loss technique at high resolution (75 meV) is shown in figure 1, King et al (7). The vibrational structure of the $(1s)^{-1}(2p\pi)^{1\pi}$ state of N_2 is clearly visible. The energy resolution is less than the natural line widths of the peaks which was deduced to be 0.123 ± 0.01 eV (8). To obtain the same resolution in a conventional absorption spectrum would require a spectral resolution of 0.0006 nm at 3.1 nm which appears to be unobtainable at the present time.

A second and perhaps more important advantage of electron impact excitation is its ability to induce electric-dipole-forbidden transitions. This can occur when the value of the incident electron energy is reduced to a value close to the excitation energy of the state, when optical selection rules are considerably relaxed. Recently the electron energy-loss technique has been applied for the first time to the study of these electric-dipole-forbidden transitions,

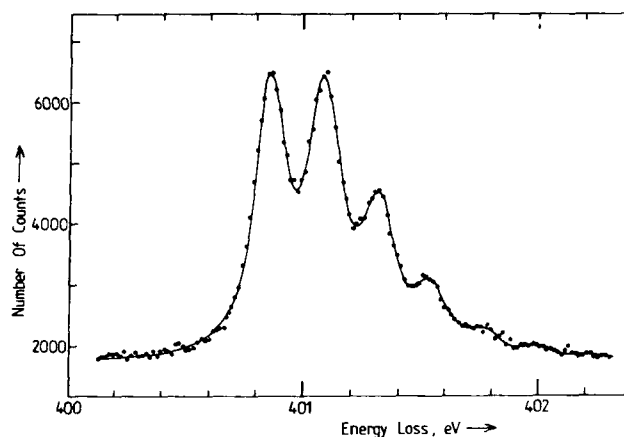


FIGURE 1

Vibrational structure of the electronic state of N_2 formed by the promotion of an atomic $1s$ electron to the first unoccupied valence orbital ($2p\pi$). After (7).

Shaw et al (8). In this work an inner-shell spin-forbidden transition in N_2 and a parity-forbidden transition in Ar were studied. These transitions were observed by using incident electron energies as low as 1.15 times the excitation energy of the inner-shell states. Yet another advantage of electron impact excitation is that energy-loss scales can be accurately calibrated by direct voltage measurement. This, for example, enables accurate ionisation energies to be established by observation and analysis of Rydberg series. Values of inner-shell ionisation energies obtained from high-resolution energy-loss studies have been summarized by King and Read (9). A comprehensive bibliography of all the experimental (electron energy-loss and photoabsorption) and theoretical studies of inner-shell excitations of free atoms and molecules has been given by Hitchcock (10).

2. THE TECHNIQUE OF ELECTRON ENERGY LOSS SPECTROSCOPY

In this technique an electron beam is produced and energy selected to provide a well defined beam with an energy spread of typically 0.03 to 0.05 eV and with an adjustable energy. This ability to change the energy of the incident electron is very powerful and is a degree of freedom not available in photo-absorption measurements. The electron beam is passed through a gas cell or beam of the target atoms and molecules, and those electrons that are inelastically scattered through a small angular range, usually in the forward direction, are analysed in energy, again with a resolution of typically 0.03 to 0.05 eV. A spectrum is thus obtained of inelastically scattered electrons versus the amount of energy they have lost. The peaks in the energy-loss spectrum correspond directly to the energy levels of the target gas.

An apparatus used in some recent inner-shell studies (11) is shown in figure 2. It consists of an electron spectrometer and utilises 180° hemispherical electrostatic deflectors to select and analyse the electron energy. Of note is the use of two hemispherical deflectors placed in tandem in the electron energy analyser. This arrangement provides very efficient rejection of

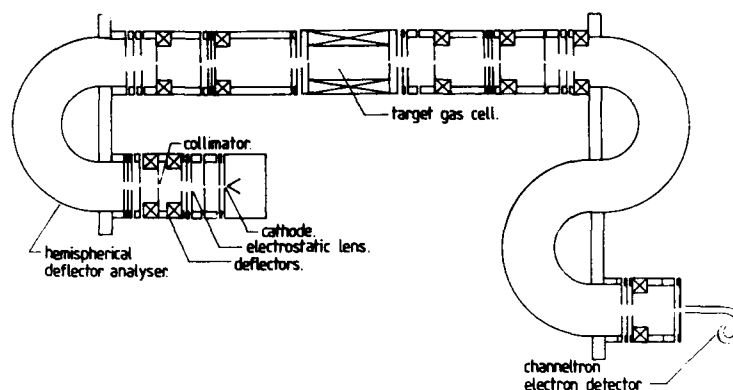


FIGURE 2
Schematic diagram of a high resolution electron energy-loss spectrometer.

unwanted scattered electrons which is an important consideration since the cross sections for exciting inner-shell electrons are low. Combinations of triple-aperture electrostatic lenses are used to transport and focus the electron beam from the electron source, a directly heated tungsten filament, to the energy selector and from the selector to the target region and similarly through the analyser section of the spectrometer. These lenses also enable the incident energy of the electrons to be varied over the range 50 to 1500eV.

The inner-shell states that can be studied most usefully with an energy resolution of 0.05eV are those having natural decay widths, Γ , that are in the range from approximately 0.05 to 0.2eV. Many states having a vacancy in the sub-shell immediately below the valence sub-shell (for example a vacancy in the 3s sub-shell of Ar) have values of Γ in this range as do most states having vacancies in the next lower lying sub-shell or full shell (for example a 2p vacancy in Ar). Their excitation energies are typically in the range from 50 to 500eV. States with deeper lying vacancies tend to have natural widths greater than 0.2eV and are therefore better studied with lower-resolution techniques.

3. COMPARISON BETWEEN ELECTRON IMPACT AND PHOTOABSORPTION MEASUREMENTS

At high values of incident electron energy electron impact excitation is analogous to photoabsorption. This analogy was first established by Bethe (12) who showed that for fast electrons there is a quantitative relationship between the differential electron scattering cross section and the generalised oscillator strength $f_n(K)$ (see also Inokuti (13)).

$$\frac{d\sigma}{d\Omega} = \frac{4k_n R f_n(K)}{E_n k_0 K^2} \quad (1)$$

Here $\hbar k_0$, $\hbar k_n$ are the momenta of the incident and scattered electrons respectively, $\hbar k$ is the momentum transferred to the target atom or molecule, R is the Rydberg energy and E_n is the excitation energy. When k_n is small compared with

a_0^{-1} (where a_0 is the Bohr radius) the generalised oscillator strength can be expanded in powers of K (see also (14)).

$$f(K) = f^{\text{opt}} + Kf^{(1)} + K^2f^{(2)} + \dots \quad (2)$$

where f^{opt} is the familiar optical oscillator strength. The second and higher terms of the expansion become negligible when E_0 is much smaller than the incident electron energy and when the angle of scattering is small. Then the electron scattering cross section is directly related to the optical oscillator strength, and an electron energy-loss spectrum then effectively simulates the photoabsorption spectrum. In inner-shell excitation experiments E_0 is usually large enough that linear and quadratic terms in equation (2) cannot be ignored, and then the electron energy-loss spectrum contains peaks due to non-electric-dipole transitions. This was first exploited by King et al (6) who observed electric-quadrupole transitions in Ar, Kr and Xe. The effect can be enhanced by a judicious use of incident electron energy and the scattering angle. Thus electron impact excitation can excite transitions that cannot be seen with photoabsorption.

A further process that is possible with electron impact excitation and not photoabsorption is electron exchange. Thus as the incident electron energy approaches the excitation energy of the state it becomes possible for the incident electron and the target electron to exchange places. Singlet-to-triplet transitions otherwise electric-dipole-forbidden, can thus be excited.

4. HIGH RESOLUTION STUDIES OF ATOMS

Early studies of the absorption of soft x-rays by atoms, in particular the rare gases, revealed the existence of structures near the inner-shell ionisation potentials, arising from the promotion of one of the inner-shell electrons

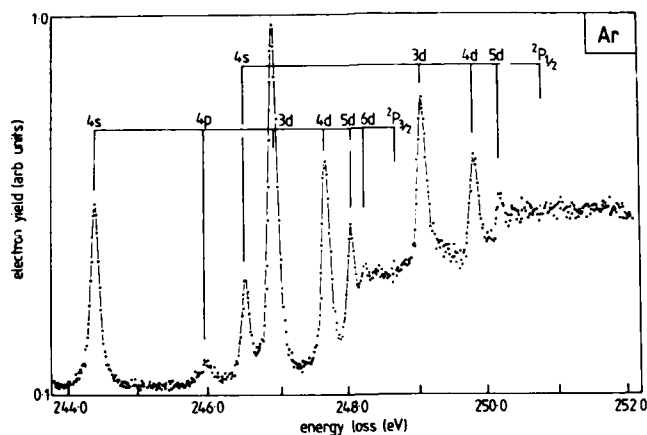


FIGURE 3
Energy-loss spectrum of Ar obtained at an incident electron energy of 1.5keV and with a resolution of 65meV.

to an unfilled orbital. More recently King et al (6) studied inner-shell excitation in Ar, Kr and Xe using electron impact excitation at high resolution. Figure 3 shows such an energy-loss spectrum in Ar obtained at an incident electron energy of 1.5keV and with a resolution of 65meV. The ground state configuration of Ar is $1s^2 2s^2 2p^6 3s^2 3p^6$ and optically allowed transitions of a 2p electron to one of the orbitals $ns(n>4)$ and $nd(n>3)$ are observed. A weaker, parity-forbidden transition to the 4p orbital is also seen and occurs because the selection rules are sufficiently relaxed at the relatively low value of incident electron energy used.

The 2p hole can have $j = 3/2$ or $1/2$ and consequently two Rydberg series are observed each converging to one of these two states of the ion. The ratio of the intensities of the corresponding peaks in the two series is observed to be approximately equal to the ratio of statistical weights, $2j+1$. An analysis of the energies of the Rydberg series can be made to provide very accurate values of the $^2P_{3/2,1/2}$ ionisation potentials. (The energy scale of the spectrum can be directly calibrated against the $4s^3P_1$ and $4s^1P_1$ states of neutral Ar using a digital voltmeter, with an estimated uncertainty of 0.01eV.)

Another important result of these studies is that the accurate measurement of energies of optically allowed and forbidden transitions in Ar (and also Kr and Xe) allowed the equivalent core model to be tested much more thoroughly than was previously possible. (In the equivalent core model an inner-shell electron in a neutral atom of nuclear charge Z which has been promoted to an outer orbital nl , has an effective quantum number n^* which is expected to be similar to the effective quantum number of an excited nl electron in the neutral atom of nuclear charge $Z+1$.) The result of the test is that the model provides, for these three atoms at least, an accurate and reliable means of estimating the energies of inner-shell excited states.

Another result of the work is the accurate measurement of the widths and lifetimes of the inner-shell excited states; that for argon represents the first accurate measurement of any atomic lifetime in this range of excitation energy. In fact very little experimental data of any kind exist on the lifetime of x-ray levels in this range.

5. HIGH RESOLUTION STUDIES OF MOLECULES

High resolution studies of inner-shell excitation in molecules provide information similar to that obtained in atoms plus further information that is characteristic of molecules only, such as vibrational spacings and intensities. Thus as well as being able to obtain excitation energies, relative intensities and natural decay widths, potential curves can be deduced. Another difference concerns the equivalent-core model; for inner-shell excitation of atoms the relevant properties of the equivalent-core atom are invariably already known, whereas for inner-shell excitation of molecules the equivalent-core molecule usually has an odd number of electrons and does not exist as a free molecule. Simulating this molecule by inner-shell excitation can therefore provide useful information that is difficult or impossible to obtain by other means. In this way Shaw et al (15) were able to obtain valuable information about $ArCl$.

The experimental work of Brion and co-workers (see for example Wight et al (16)) shows clearly that much can be learned about the fields that exist within molecules from studies of the promotion of atomic inner-shell electrons to unfilled outer molecular orbitals or to continuum states close to the ionisation threshold. The relative probabilities with which the available bound or continuum states can be reached, either by photoabsorption or by electron impact excitation, depend partly on the probability with which an electron can be ejected with the necessary energy from its atomic inner-shell, but more importantly on the "focusing" effect of the molecular field. Dehmer and Dill (17) have discussed these points in full, and have given references to the earlier experimental and theoretical work, in connection with their calculations of the

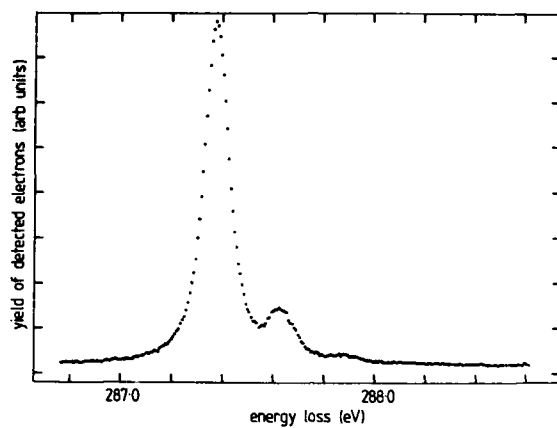


FIGURE 4
Energy-loss spectrum of CO, obtained at an incident electron energy of 1.5keV and with a resolution of 55meV. The peaks correspond to the $(1s_C)^{-1}(2p\pi)^{1\pi}$ state of CO.

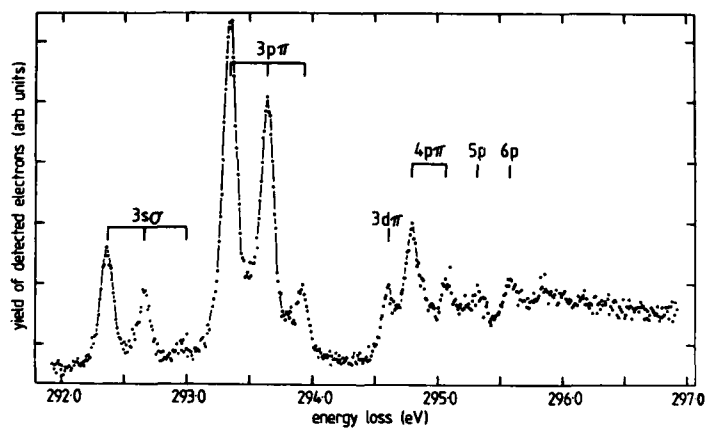


FIGURE 5
Energy-loss spectrum of CO obtained at an incident electron energy of 1.5keV and with a resolution of 65meV. The peaks correspond to transitions of a $1s_C$ carbon electron to Rydberg orbitals.

cross section for photoabsorption by the atomic K shell electrons of N_2 .

The vibrational structure of the $(1s)^{-1}(2p\pi)^1\Pi$ state of N_2 was first revealed by the high-resolution electron energy-loss studies of King et al (7). Their spectrum is shown in figure 1. An analysis of the spectrum reveals firstly the vibrational parameters ω and ωx . Information about the mean internuclear separation R_0 in the inner-shell excited molecule is obtained from the relative areas of the vibrational peaks by assuming that these areas are proportional to the Franck-Condon overlap integrals $q_{v'v}$ between the vibrational wavefunction of the ground vibrational state ($v=0$) of the target molecule and the vibrational wavefunctions of inner-shell excited states (v'). Recently Barth and Schirmer (18) have calculated the energies and oscillator strengths for inner-shell transitions in N_2 and have obtained good agreement with the results of King et al (7). The high resolution of the measurements again allows the natural line width of the state to be measured (123 ± 10 meV) and hence the mean lifetime to be deduced. The fact that the lifetime ($\approx \hbar/\Gamma = 5.10^{-15}$ s) of the state is approximately one third as long as the classical vibrational period ($= \hbar/\omega = 1.8 \times 10^{-14}$ s) of the molecule means that the vibrational wavefunctions are not those of stationary states, cf. the analysis and interpretation of the vibrational structure of short lived negative ion resonances (Schulz(19)).

As discussed above the high resolution studies by King et al (6) of inner-shell excited states of Ar, Kr and Xe have demonstrated the usefulness of the equivalent-core model for these states. In the case of inner-shell excited states of homonuclear diatomic molecules however an ambiguity exists in the definition of the equivalent-core molecule, depending on whether the inner-shell hole is regarded as being localised or delocalised (e.g. Cederbaum and Domcke (20), Lozes et al (21), Dutta and Huang (22)). For example, if the inner-shell hole of N_2^{K*} is delocalised (having the configuration $1s\sigma_g^{-1}$ or $1s\sigma_u^{-1}$) the "core" can be taken to be the two nitrogen nuclei and the three accompanying $1s$ electrons, which is thus approximately equivalent to two separated charges of magnitude 5.5 each, but if the inner-shell hole is localised in the vicinity of one of the nuclei (having the configuration $1s^{-1}$) then this nucleus and its single $1s$ electron has a total charge of 6 while the core charge at the other centre is 5. Thus for a localised hole the outer electrons of the molecule move in a mean electrostatic potential similar to that of the outer electrons of the neutral NO molecule, which is thus the "equivalent-core molecule". Assuming complete localisation and ignoring the effects of exchange interaction, the values of ω , ωx and R_0 deduced for the $N_2(1s)^{-1}(2p\pi)$ state should be similar to those of the ground electronic state of NO. King et al (7) found that there is indeed a close similarity between the two sets of parameters. This similarity also extends, despite the existence of the singlet-triplet splitting, to the binding energies of the states with respect to their ionisation limits, as noted by Wight et al (16). It is interesting to note that although the lifetime appears to be short enough for the vacancy to remain localised and for the NO equivalent-core model to have some validity, it is nevertheless long enough to support a discrete vibrational structure for the N_2^{K*} molecule.

Inner-shell excitation has been studied in a number of other molecules, including diatomics and polyatomics, see for example (9) and references therein. Both the low lying and usually intense valence states have been studied as well as the higher lying Rydberg states. Energy-loss spectra of CO corresponding to the excitation of a $1s\sigma$ carbon electron are shown in figures 4 and 5. Figure 4 shows the vibrational structure observed when the $1s\sigma$ carbon electron is promoted to the first unfilled valence orbital $2p\pi$ and exhibits a resolution of 55 meV. The oscillator strength for this transition is exceptionally high due to the fact that the $2p\pi$ orbital is highly localised since it is confined to the vicinity of the molecular core by a centrifugal barrier in its d-wave component, (17). Figure 5 shows excitation of a $1s\sigma$ carbon electron into Rydberg orbitals of CO below the $1s\sigma$ ionisation potential and illustrates the high

sensitivity of the technique.

6. THE OBSERVATION OF ELECTRIC-DIPOLE-FORBIDDEN INNER-SHELL TRANSITIONS

At sufficiently high values of incident energy, electron-impact excitation is analogous to photoabsorption and so optical selection rules apply. However at low values of incident electron energy (comparable to the excitation energy of the target state), these selection rules are considerably relaxed, and then electron-impact excitation has the great advantage that it is able to induce electric-dipole-forbidden transitions. This advantage is potentially more powerful than that of having superior resolution at high values of state excitation energies, but it has only recently been exploited, when inner-shell electric-dipole transitions were observed in the rare gases by King et al (6). More recently Shaw et al (8) have made a systematic study of the parity-forbidden $2p \rightarrow 4p$ transitions in Ar and of an inner-shell spin-forbidden transition in N_2 . The results of Shaw et al in Ar are shown in figure 6. The peaks

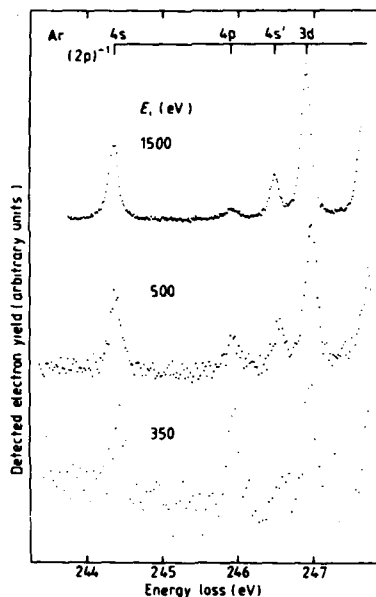


FIGURE 6
Energy-loss spectra of Ar, obtained at the indicated values of incident electron energy, and with an energy resolution of 65meV.

in the spectra correspond to the promotion of a $2p_{3/2}$ or $2p_{1/2}$ electron to an unoccupied Rydberg orbital. The features observed in the 1500eV incident energy spectrum are similar to those described by King et al (6). The major point of note is the dramatic rise in the intensity of the electric-dipole-forbidden $2p \rightarrow 4p$ transition relative to the optically-allowed transitions as the incident electron energy is reduced. The observed peak will correspond to several different J values that will be separated by spin orbit and electrostatic terms

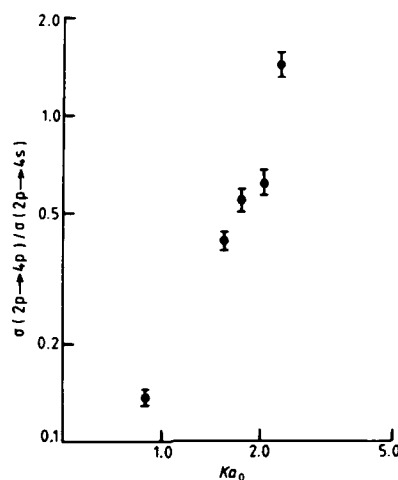


FIGURE 7

The dependence of the ratio of intensities of the observed peaks corresponding to the transitions $2p \rightarrow 4p$ (parity-forbidden) and $2p \rightarrow 4s$ (electric-dipole allowed) on the dimensionless quantity Ka_0 , when $\hbar K$ is the momentum transfer and a_0 is the Bohr radius.

but Shaw et al (8) estimated that these splittings are small compared to the natural line widths of the states and the finite resolution of the experiments.

The ratio of the observed intensities of the $2p_{3/2} \rightarrow 4p$ and $2p_{3/2} \rightarrow 4s$ transitions is displayed in figure 7 as a function of the dimensionless quantity Ka_0 , where $\hbar K$ is the momentum transferred to the atom by an electron scattered in the forward direction and a_0 is the Bohr radius. From the figure it may be seen that the intensity ratio is approximately proportional to K^2 . From the Born approximation which gives the leading power of K in an expansion of the differential cross section it may be found that the $J=0$ and $J=2$ levels of the $(2p_{3/2})^{-1}4p$ configuration have differential cross sections proportional to K^0 corresponding to electric-quadrupole transitions. Further, the ratio of the cross section to that of the $(2p_{3/2})^{-1}4s$ level should be proportional to K^2 at sufficiently high energies. This is in fact approximately the observed dependence although the Born approximation may apply only poorly at the incident energies used in the work of Shaw et al. Recently Shaw et al (23) have investigated inner-shell transitions near the N-edge of Xe and have been able to resolve individual J levels and measure their relative cross sections as a function of incident electron energy.

Electron energy-loss spectra obtained in N_2 (Shaw et al (8)) are shown in figure 8. The high energy feature corresponds to excitation of the $(1s)^{-1}(2p\pi)^1\pi$ state of N_2 and at incident energies above about 1000eV it is the only structure observed in this region. As the incident energy is reduced, however, a low energy structure becomes evident and at the lowest values of incident energy used, becomes dominant. This structure corresponds to the promotion of a $1s$ nitrogen electron to the $2p\pi$ orbital to give the $(1s)^{-1}(2p\pi)^3\pi$ state of N_2 . The spectra are the first observation of an inner-shell singlet-to-triplet transition.

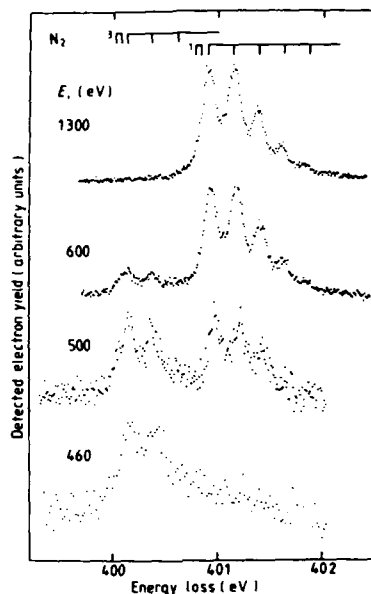


FIGURE 8
Energy-loss spectra of N_2 , obtained at the indicated values of incident electron energy, and with a resolution of 65 meV. The lower- and higher-energy vibrational structures correspond to excitation of the $(1s)^{-1}(\pi 2p)^3\Pi$ and $(1s)^{-1}(\pi 2p)^1\Pi$ states of N_2 respectively.

The work of Shaw et al (8) also gives information about whether the $1s$ hole is localised at the site of one of the nitrogen nuclei. If the hole is delocalised then $u-g$ symmetry is appropriate and a $u-g$ splitting in energy would be expected. Rescigno and Orel (24), for example, have calculated this splitting to be 0.06 eV. The $1s\sigma_u \rightarrow 2p\pi_g$ transition would be electric-dipole allowed while the $1s\sigma_g \rightarrow 2p\pi_g$ transition would be electric-dipole forbidden. In the earlier work on the $(1s)^{-1}(2p\pi)^1\Pi$ state of N_2 King et al (7) did not see any evidence of the occurrence of two closely lying states, although the predicted splitting is smaller than the natural widths of the states (123 meV) and the finite resolution of the measurements (75 meV) would have made such a splitting difficult to discern. In the work of Shaw et al (8) however, an enhancement of electric-dipole-forbidden transitions (as predicted by Rescigno and Orel) might be expected since it was possible to achieve a large value of momentum transfer, increasing from 1.65 au at 1300 eV incident electron energy to 3.73 au at 460 eV. This enhancement might lead, for example, to a change in the relative areas of the vibrational levels, or to changes in the peak energies or widths. However, within the limited statistical accuracy of the measurements it was not possible to detect any changes of this type.

Shaw et al have observed electric-dipole-forbidden transitions in a number of other molecules, including CO (11). Here they found a $(1s\sigma_c)^{-1}(2p\pi)^1\pi$

singlet-triplet splitting which has a value of 1.46eV. Firstly this is quite different to the singlet-triplet splitting of the analogous inner-shell states of N_2 , which is isoelectronic with CO and which has the same equivalent core molecule. Presumably this occurs because the 1s hole has a smaller radius in the nitrogen atom than it has in the carbon atom. Consequently the overlap between the hole and the excited $2p\pi$ orbital, the latter being the same in both cases, will differ, resulting in a smaller exchange interaction in N_2 . Secondly the splitting gives a direct measure of K , the exchange integral for the inner-shell 1s hole orbital and the $2p\pi$ orbital since K is equal to half the singlet-triplet splitting. The measured value of 1.46eV compares with the theoretical value of 1.29eV (18).

The energies of the singlet and triplet $(1s)^{-1}(2p\pi)$ states of N_2 and CO can be used to calculate the weighted mean energy of the $(1s)^{-1}(2p\pi)$ configuration of each molecule, and hence to calculate the mean binding energy of this configuration with respect to the ion core configuration $(1s)^{-1}$. This mean binding energy is found to be the same, 9.69eV, for both molecules. This appears to indicate that the ion core N_2^{K+} and CK^0 provide the same environment for the $2p\pi$ electron, as they would in the equivalent-core model since they are then both equivalent to NO^+ .

REFERENCES

- 1) M.J.-A. Prins, *Physica* 1 (1934) 1174.
- 2) M. Nakamura et al, *Phys. Rev. A* 178 (1969) 80.
- 3) M.J. Van der Wiel, Th.M.El. Sherbini and C.E. Brion, *Chem. Phys. Letts* 7 (1970) 161.
- 4) C.E. Brion, in: *Physics of Electronic and Atomic Collisions*, ed. S. Datz (North Holland, Amsterdam, 1982) 579.
- 5) M. Tronc, G.C. King, R.C. Bradford and F.H. Read, *J. Phys. B: Atom. Molec. Phys.* 9 (1976) L555.
- 6) G.C. King, M. Tronc, F.H. Read and R.C. Bradford, *J. Phys. B: Atom. Molec. Phys.* 10 (1977) 2479.
- 7) G.C. King, F.H. Read and M. Tronc, *Chem. Phys. Letts.* 52 (1977) 50.
- 8) D.A. Shaw, G.C. King, F.H. Read and D. Cvejanović, *J. Phys. B: Atom. Molec. Phys.* 15 (1982) 1785.
- 9) G.C. King and F.H. Read, *Investigations of inner-shell states by the electron energy-loss technique at high resolution in: Atomic Inner-Shell Physics* ed. B. Crasemann (Plenum Press New York 1985, in print).
- 10) A.P. Hitchcock, *J. Electron Spec.* 25 (1982) 245.
- 11) D.A. Shaw, G.C. King, D. Cvejanović and F.H. Read, *J. Phys. B: Atom. Molec. Phys.* 17 (1984) 2091.
- 12) H. Bethe, *Ann. Phys. (Leipzig)* 5(5) (1930) 325.
- 13) M. Inokuti, *Rev. Mod. Phys.* 43 (1971) 297.
- 14) W.M. Huo, *J. Chem. Phys.* 71 (1979) 1593.
- 15) D.A. Shaw, G.C. King and F.H. Read, *J. Phys. B: Atom. Molec. Phys.* 13 (1980) L723.
- 16) G.R. Wight, C.E. Brion and M.J. Van der Wiel, *J. Elec. Spec.* 1 (1972/3) 457.
- 17) J.L. Dehmer and D. Dill, *J. Chem. Phys.* 70 (1976) 3390.
- 18) A. Barth and J. Schirmer, *J. Phys. B: Atom. Molec. Phys.* 18 (1985) 867.
- 19) G.J. Schulz, *Rev. Mod. Phys.* 45 (1973) 378.
- 20) L.S. Cederbaum and W. Domcke, *J. Chem. Phys.* 66 (1977) 5084.
- 21) R.L. Lozes, O. Goscinski and U.I. Wahlgren, *Chem. Phys. Lett.* 63 (1979) 77.
- 22) C.M. Dutta and H.W. Huang, *Phys. Rev. Lett.* 44 (1980) 643.
- 23) D.A. Shaw, G.C. King and F.H. Read, *J. Phys. B: Atom. Molec. Phys.* (1986) to be published.
- 24) T.N. Rescigno and A.E. Ore1, *J. Chem. Phys.* 70 (1979) 3390.

DESCRIPTION OF THE INTENSE, LOW ENERGY, MONOENERGETIC POSITRON BEAM AT
BROOKHAVEN

K. G. LYNN
Brookhaven National Laboratory, Upton, NY 11973

A. P. MILLS, JR.
A.T.&T. Bell Laboratories, Murray, NJ 07974

L. O. ROELLIG and M. WEBER
City College of New York, New York, NY 10031

An intense ($4 \times 10^7 \text{ s}^{-1}$), low energy ($\approx 1.0 \text{ eV}$), monoenergetic ($\Delta E \approx 75 \text{ meV}$) beam of positrons has been built at the Brookhaven National Laboratory. This flux is more than 10 times greater than any existing beam from radioactive sources. Plans are underway to increase further the flux by more than an order of magnitude. The intense low energy positron beam is made by utilizing the High Flux Beam Reactor at Brookhaven to produce the isotope ^{64}Cu with an activity of 40 curies of positrons. Source moderation techniques are utilized to produce the low energy positron beam from the high energy positrons emitted from ^{64}Cu .

1. INTRODUCTION

Since the discovery of the positron almost half a century ago, the number of experiments using these particles has expanded at an ever increasing rate. Very few studies using low energy positrons were possible at first, but after the early 1950's a number of interesting and promising measurements in this energy range were made.(1) The discovery of positronium (Ps) opened a new regime of atomic physics in which purely leptonic systems could be studied; many of the measurements made in the decade thereafter were of the properties of this atom.(2) Not long to follow, however, were the first of many studies of the properties of solids using positrons as probes.(3) By measuring the shift in energy or angle of the gamma rays produced by positron annihilation (with respect to those produced in the center of momentum frame of the positron and electron), or by measuring the lifetime prior to annihilation of positrons in materials, many characteristics of the solids could be obtained. A particular advance in this field came when positrons were shown to be sensitive to the presence of many types of lattice defects in solids.(4-5)

While many varied studies were performed during this period, the full capabilities of positrons remained to be realized. The necessary key was the discovery of the reemission of positrons from certain materials at energies of only a few electron volts.(6) This was the discovery necessary to permit the construction of relatively intense, narrow energy width, variable energy positron beams. Many of the essential ideas behind reemission were described as early as 1950 (1) and reemission was first seen in 1958,(7) but it was not until the mid-1970's that the first practical slow positron beams began to be constructed.(8-10) To this day, much work continues to be done to improve both the beam optical designs and the energy moderation efficiencies.

The beams currently in use can be classified based both on the source of the positrons and the type of moderator employed, and on the method used to trans-

port the slow positrons thus produced. Common positron sources are the isotopes ^{58}Co , ^{22}Na , and ^{11}C , the former two being obtained commercially in purified form and the latter being produced directly from ^{11}B irradiated by protons.(10) Very promising results have also been reported in producing slow positrons from the positron-electron showers produced by the beams of electron linacs.(11) A beam has been constructed at BNL using the isotope ^{64}Cu which can be produced in large quantities from ^{63}Cu by thermal neutron capture in the BNL High Flux Beam Reactor. The design of this beam has been discussed in Ref. 12.

Many different materials and designs have been employed as positron moderators. Successful B and Au moderators were described several years ago (6,7,10) and considerable success was reported using various metal foils coated with a layer of MgO powder.(8,9,13,14) To date, however, the best moderators in common use have been clean single crystal samples of Cu and Ni as well as such crystals with submonolayer S coatings.(15,16) Polycrystalline W has also been used as a moderator, especially in low vacuum environments where clean surfaces are not possible,(17-18) and there are new results indicating that clean single crystal W or W with a thin epitaxial layer of Cu at the surface may be the best yet.(19) In the high flux beam, we make use of the abilities of Cu as a moderator to produce a self-moderating single crystal ^{64}Cu source.

2. CHARACTERISTICS OF THE BEAM

The self-moderator ^{64}Cu source consists of ^{63}Cu and ^{64}Cu atoms, and it should be a single crystal to prevent positrons from being trapped in voids or defects and hence not diffusing back to the surface of the copper. Typically a 250mg high purity copper pellet in an aluminum container is placed in the core of the High Flux Beam Reactor for a period of two days where it attains an activity of 200 curies, 19% of the disintegrations are in the positron emission channel. It is then removed from the container, and by means of an airlock it is brought from atmospheric pressure to a pressure of 10^{-10} Torr, and guided through a tube into a wire basket with an alumina insert. The pellet is then evaporated onto a W(110) crystal substrate where Cu(111) is grown epitaxially.(20) The copper crystal on the tungsten substrate is annealed and treated with H_2S to improve the moderator efficiency. Annealing improves the moderator efficiency by one order of magnitude and putting sulfur on the surface improves it another 20%. The copper coated tungsten then is rotated so that its face is perpendicular to the beam line. The positrons emanating from the copper crystal are energy analyzed by two ExB plates and guided magnetically down a beam tube into the target chamber. Figure 1 shows the interior of the source chamber. The source chamber and the first ExB analyzer are located inside an 88 ton block house which is capable of providing radiation shielding for a 10,000 Ci gamma ray source. The second ExB analyzer and target chamber are located outside the blockhouse.

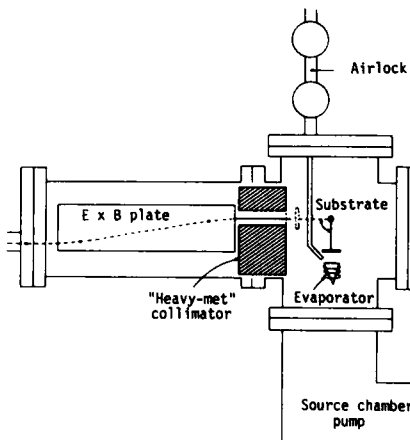


Fig. 1 Schematic representation of source chamber (not to scale).

3. CHARACTERISTICS OF THE SOURCE

The amount of positron activity from the copper pellet as a function of the time the pellet is in the core of the reactor is shown in Fig. 2. An advantage of the production of the source by the reactor is that it does not interrupt or disturb any work performed by other reactor users who mainly use it for neutron scattering. It is a completely parasitic operation. Another advantage is that the half life of ^{64}Cu is 12.8 hours, thus after several half lives the radiation level in the block house is low enough for a person to enter it, and provide maintenance work on the source preparation chamber. Due to the high radiation level when the copper pellet is first put into the blockhouse from the reactor all operations must be remote controlled outside of it, e.g. radiation sensors, video cameras, valves, and the removal of the pellet from its container.

Figure 3 shows the large number of interactions which can occur when a beam of high energy positrons impinges on a metal surface. The positrons which

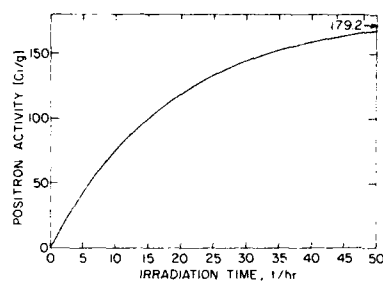


Fig. 2 The calculated dependence of the positron activity of the source on the time the copper pellet is in the reactor core.

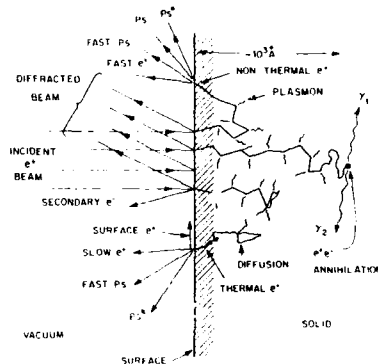


Fig. 3 Various interactions resulting from a positron beam striking a surface (from Ref. 21).

penetrate the surface rapidly thermalize in 10^{-12} sec by undergoing inelastic scattering with core electrons, and then with plasmons and phonons in the metal. Approximately 10^{-3} - 10^{-4} of the fast positrons which impinge upon the surface are emitted as moderated positrons with about an eV of energy and with an energy spread of 75 meV at room temperature or 24 meV at 23°K.(22) This result which appears to hold for all metals which emit slow positrons is shown in Figure 4 for Ni(100). The slow positrons also are emitted essentially normal to the surface. For example, for clean Cu(111) the angular spread is $\Delta\theta_{FWHM} = 24^\circ$ at a temperature of 300K and $\Delta\theta_{FWHM} = 18^\circ$ at 23K.(22)

In Figure 5 the calculated efficiency of the copper moderator is plotted as a function of its thickness. It is evident from this figure that one should use thin moderators. However, this reduces the source activity and hence the number of slow positrons. A more useful quantity is the product of efficiency and thickness vs. thickness. This is shown in Figure 6. The lower curve shows the contribution due to backscattering of the positrons from the tungsten substrate and the upper curve shows the contribution due to both backscattering and forward scattering of the positrons in the moderator.

We have recently installed a 10,000Å thick W(100) film in front of the copper crystal to provide transmission moderation of the high energy positrons emanating from the copper.(23) The tungsten film can be rotated either into

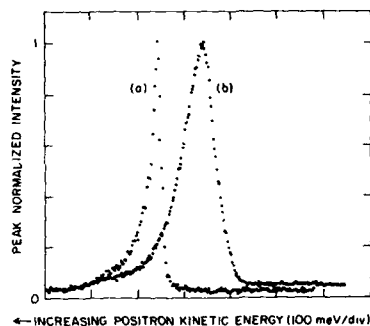


Fig. 4 Peak normalized reemitted positron intensity versus positron kinetic energy. Curve (b) is the elastic peak for Ni(100) at a temperature of 300K, curve (a) is at 23K. Taken from Ref. 22.

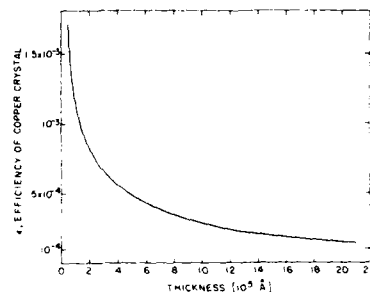


Fig. 5 Calculated efficiency of the copper moderator versus its thickness.

the beam line or out of it by remote control. However, preliminary tests indicate there was a 20% reduction in the number of slow positrons from the number obtained by using the copper crystal as a source and moderator.

4. POSSIBLE IMPROVEMENTS OF THE PERFORMANCE OF THE BEAM

One of the obvious improvements is to employ the concept of brightness enhancement first proposed by Mills.(24-26) This would reduce the beam size from its present size, one cm^2 to a very small cross sectional area, depending upon the number of remoderation stages. Another would be to evaporate the copper on a tungsten substrate of much larger area, thereby producing many more positrons and then use brightness enhancement to reduce the beam size. A third would not use the moderating properties of copper and instead use a tungsten film as a transmission moderator and thereby eliminate the need to grow a copper crystal. A fourth would be to enrich the copper crystal with ^{64}Cu relative to ^{63}Cu by means of a mass analyzer, thereby achieving as much as three orders of magnitude improvement in beam intensity. Lastly to make a better copper crystal to increase its efficiency as a moderator.

5. AN EXAMPLE OF THE INITIAL RESEARCH PERFORMED WITH THE BEAM

The beam was first used by K. G. Lynn, A. P. Mills, Jr., R. N. West, S. Berko, K. F. Canter, and L. O. Roellig to obtain a measurement of the two-dimensional angular correlation of the 2γ annihilation radiation from a clean Al(100) surface.(27) It showed there was a significant difference in the angular correlation of annihilation radiation between positrons annihilating in the bulk of the sample and on its surface. (See Fig. 7.) The data also did not support two prevailing models of positrons annihilating on the surface of a metal: the model of a positron bound in its "image-correlation-potential" well(28) and the picture of a weakly bound positronium atom (Ps) where the parallel motion would be thermal and the perpendicular motion would be associated with the 0.5 eV Ps binding energy to the surface.(29)

6. APPLICATIONS TO ATOMIC PHYSICS

It is obvious that an intense monoenergetic beam is useful for certain types of experiments, e.g. measurement of differential scattering cross sections,

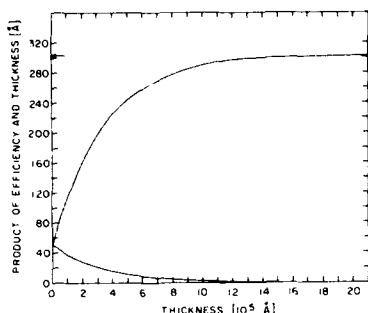


Fig. 6 Calculated product of efficiency and thickness of the copper moderator versus its thickness. The lower curve shows the contribution due to backscattering and the upper curve shows the contribution due to both backscattering and forward scattering.

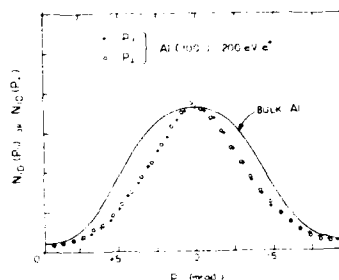


Fig. 7 One-dimensional projections of the angular correlation of annihilation radiation spectra for momentum parallel and perpendicular to the surface. The three spectra for positrons annihilation on the surface and in the bulk have been normalized to equal peak heights. See Ref. 27.

measurement of positron-atom cross sections which may be small, or for those experiments requiring a narrow energy width, e.g. measuring the ionization threshold cross section for atoms.

Presently at Brookhaven a Ps beam line is under construction by S. Berko, B. L. Brown, K. F. Canter, K. G. Lynn, A. P. Mills, Jr., L. O. Roellig, and M. Weber, for the purpose of observing Ps diffraction, but will also be used for measuring Ps-atom scattering cross-sections.⁽³⁰⁾ The positron beam will be transmitted through a relatively high density He cell (10^{-3} Torr) which is differentially pumped at both ends. Positronium is formed by the positron capturing an electron from the helium atom. This method has been calculated to yield a monoenergetic positronium beam with an angular spread of $\approx 20^\circ$ FWHM and an efficiency for a 5° cone of Ps of 1.3% for 50 eV positrons and 0.7% for 80 eV positrons.⁽³¹⁾

7. ACKNOWLEDGEMENTS

The intense positron beam has been developed as part of a collaborative program involving S. Berko, K. F. Canter, K. G. Lynn, A. P. Mills, Jr., and L. O. Roellig. We wish to acknowledge useful contributions and technical discussions with W. E. Frieze. This work is supported in part by the Division of Materials Sciences, U.S. Dept. of Energy, under Contract No. DE-AC02-76CH00016, and in part by the National Science Foundation through Grant No. DMR-8315691.

REFERENCES

- 1) L. Madanski and F. Rasetti, Phys. Rev. **79**, 397 (1950).
- 2) M. Deutsch, Phys. Rev. **82**, 455 (1951).
- 3) S. DeBenedetti and H. Corben, Ann. Rev. Nucl. Sci. **4**, 191 (1954).
- 4) I. K. MacKenzie, T. L. Khoo, A. B. McDonald, and B. T. A. McKee, Phys. Rev. Lett. **19**, 946 (1967).
- 5) S. Berko, and J. C. Erskine, Phys. Rev. Lett. **19**, 307 (1967).
- 6) D. G. Costello, D. E. Groce, D. F. Herring and J. W. McGowan, Phys. Rev. **B5**, 1433 (1972).

- 7) W. Cherry, Ph.D. dissertation (Princeton University, 1958), available from University Microfilms Inc., Ann Arbor, Mich.
- 8) K. F. Canter, P. G. Coleman, T. C. Griffith and G. R. Heyland, *J. Phys. B: Atom. and Mol. Phys.* **5**, L167 (1972).
- 9) K. F. Canter, A. P. Mills, Jr., and S. Berko, *Phys. Rev. Lett.* **33**, 7 (1974).
- 10) T. S. Stein, W. E. Kauppila and L. O. Roellig, *Phys. Lett.* **51A**, 327 (1975).
- 11) R. H. Howell, R. A. Alvarez, and M. Staneh, in *Positron Annihilation*, edited by P. G. Coleman, S. C. Sharma, and L. M. Diana (North-Holland, Amsterdam, 1982), p. 860.
- 12) K. G. Lynn and W. E. Frieze, in *Positron Scattering in Gases*, edited by John W. Humberston and M. R. C. McDowell (Plenum Press, New York, 1984), p. 165.
- 13) K. G. Lynn and B. T. A. McKee, *Appl. Phys.* **19**, 247 (1979).
- 14) P. G. Coleman, J. D. McNutt, J. T. Hutton, L. M. Diana and J. L. Fry, *Rev. Sci. Instrum.* **51**, 935 (1980).
- 15) A. P. Mills, Jr., *Appl. Phys. Lett.* **35**, 427 (1979).
- 16) A. P. Mills, Jr., *Appl. Phys. Lett.* **37**, 667 (1980).
- 17) J. M. Dale, L. D. Hulet, and S. Pendyala, *Surface and Interface Analysis* **2**, 199 (1980).
- 18) L. D. Hulet, J. M. Dale, and S. Pendyala, *Surface and Interface Analysis* **2**, 204 (1980).
- 19) K. G. Lynn and H. Lutz, *Rev. Sci. Instrum.* **51**, 977 (1980).
- 20) Norman J. Taylor, *Surf. Sci.* **4**, 161 (1966).
- 21) A. P. Mills, Jr. in *Positron Annihilation*, edited by P. G. Coleman, S. C. Sharma, and L. M. Diana (North-Holland, Amsterdam, 1982), p. 121.
- 22) D. A. Fischer, Ph.D. dissertation (State University of New York at Stony Brook, 1984); D. A. Fischer, K. G. Lynn, and D. W. Gidley (submitted to *Phys. Rev. B*).
- 23) K. G. Lynn, B. Nielsen, and J. H. Quateman, *Appl. Phys. Lett.*, Aug. 1985 (in press).
- 24) A. P. Mills, Jr., *Appl. Phys.* **23**, 189 (1980).
- 25) K. F. Canter and A. P. Mills, Jr. *Can. J. Phys.* **60**, 551 (1982).
- 26) W. E. Frieze, D. W. Gidley, and K. G. Lynn, *Phys. Rev. B* **31**, 5628 (1985).
- 27) K. G. Lynn, A. P. Mills, Jr., R. N. West, S. Berko, K. F. Canter, and L. O. Roellig, *Phys. Rev. Lett.* **54**, 1702 (1985).
- 28) R. Nieminen and M. Manninen, *Solid State Commun.* **15**, 403 (1974).
- 29) P. M. Platzman and N. Tzoar, to be published.
- 30) K. F. Canter, in *Positron Scattering in Gases*, J. W. Humberston and M. R. C. McDowell, eds. Plenum Press, p. 219 (1984).
- 31) B. L. Brown, to be published in Proceedings of the VII International Conference on Positron Annihilation, New Delhi, India (World Scientific Publishing, Singapore, 1985).

IONIZATION OF HELIUM BY POSITRON IMPACT

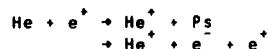
Dieter FROMME, Wilhelm RAITH and Günther SINAPIUS

Universität Bielefeld, Fakultät für Physik, D-4800 Bielefeld, F.R.G.

Positrons ionize helium atoms either by charge exchange leading to positronium (Ps) or by impact ionization. From a gas target in form of a long thin tube with longitudinal magnetic guiding and electric extraction fields positrons and ions are extracted, mass separated and detected. Relative cross sections, normalized at high energies to the electron-impact ionization cross section, are obtained for the sum of positronium-formation and impact-ionization cross section by detecting all extracted ions and for the ionization cross section σ_{Ion}^+ without Ps formation by detecting only those ions which are time-correlated to a positron. The Ps-formation cross section σ_{Ps} is then given by the difference of the two measurements. Our results for σ_{Ps} confirm the measurements made at the University of Texas, Arlington. The three partial cross sections σ_{Ps} , σ_{Ion}^+ and σ_{Ion}^- (for electron-impact ionization) peak at 35, 95 and 130 eV, respectively, and have respective cross section maxima of 0.39, 0.45 and $0.37 \times 10^{-16} \text{ cm}^2$.

1. INTRODUCTION

The positron-impact ionization proceeds via two reaction channels, the positronium formation (cross section σ_{Ps}) and the ionization with three outgoing particles (σ_{Ion}^+):



The threshold for Ps formation lies at 17.8 eV, 6.8 eV below the ionization energy, of 24.6 eV. Recently, several methods were developed for measuring σ_{Ps} and σ_{Ion}^+ . The results obtained thus far are controversial, in particular in case of σ_{Ps} in which the results of a 3 γ -coincidence experiment (1) are substantially smaller than those of a positron transmission experiment (2,3). The latter one was extended for measuring σ_{Ion}^+ by employing electron detection; the ionization cross sections obtained in this way (4) are larger than σ_{Ion}^+ , whereas those measured by means of a time-of-flight retarding-potential method (5) are very close to σ_{Ion}^+ .

We developed an apparatus in which the positrons and the ions are extracted from the gas target and, after mass separation, detected separately. This method yields relative values of $\sigma_{\text{Ps}} + \sigma_{\text{Ion}}^+$ which can be normalized to literature values of σ_{Ion}^- (6) at high energies. In addition, the measurement of ions in time correlation with positrons yields relative values of σ_{Ion}^+ which can be normalized in the same way. The difference of both measurements gives σ_{Ps} .

2. METHOD OF MEASUREMENT

The layout of the experiment is shown in Fig. 1.

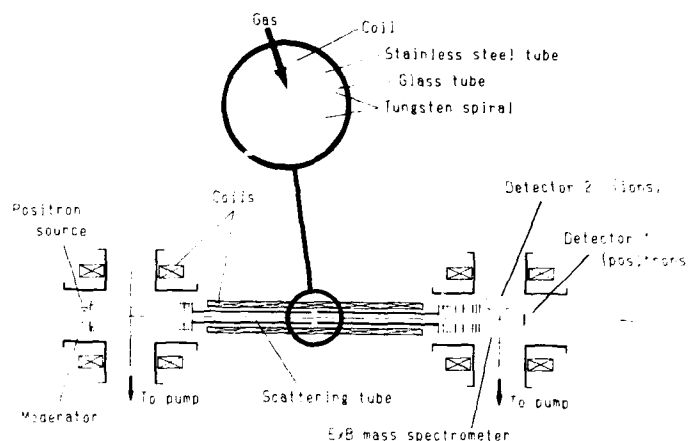


FIGURE 1
Apparatus for measuring relative positronium
formation and ionization cross sections

2.1. Gas target

The target cell consists of a long thin glass tube (length 50 cm, inside diameter 1 cm) with gas inlet in the middle and differential pumping at both ends. The tube's large flow resistance makes it possible to have a high gas pressure of close to 10^{-3} Torr in the middle together with a small gas flow of only about 10^{-4} Torr l/s, convenient for differential pumping. For background measurements the gas flow is directed to both tube ends. Because of the unknown ion-extraction efficiency the apparatus is not yet suitable for absolute cross-section measurements. Instead, the high-energy behavior of the cross sections is used for normalization:

$$\sigma_{ps}(E) \rightarrow 0 \quad \text{and} \quad \sigma_{ion}^+(E) \rightarrow \sigma_{ion}^-(E) \quad \text{for } E \rightarrow \infty$$

Positronium formation is a rearrangement process for which the cross section is expected to peak near threshold and to vanish at high energies. The equality of σ_{ion}^+ and σ_{ion}^- is expected at energies at which the first Born approximation is valid. Total cross section measurements on Helium show a merging of electron and positron data already at $E = 200$ eV (7).

2.2 Positron beam

The sodium-22 positron source is located on the side of the beam-transport system such that there is no line of sight to the channelplate detectors (Fig.1). The moderator is an annealed tungsten plate mounted at 45° with respect to the beam axis. Several coils produce a longitudinal magnetic field of about 350 G in the target region and with lower field strengths elsewhere,

adjusted for best focusing properties. The tungsten spiral inside the glass tube (enlargement of Fig.1) provides a wall of well defined electric potential. By drawing a current through the tungsten wire a longitudinal electric extraction field (10 V potential difference between tube ends) is generated.

The tube entrance aperture of 5 mm diameter insures that primary positrons do not hit the inside wall. The scattered positrons are radially confined by the magnetic field and (except a few scattered backwards at full energy) extracted from the target unless they disappear by forming positronium with subsequent annihilation. After leaving the target the positrons are accelerated to 500 eV plus collision energy and traverse the region of the ExB mass spectrometer (8) on trajectories whose projections onto a plane perpendicular to the beam axis are trochoids with several periods. This results in a horizontal offset of less than 0.6 cm. The positron counting rate of detector 1 is about 1000/s.

2.3 Ion beam

The He^+ ions, produced by Ps formation or ionization are accelerated in axial direction by the electric extraction field. The present magnetic guiding field of 350 G is not strong enough for complete radial confinement. Ions with transverse velocities corresponding to the tail of the thermal distribution can hit the wall. In addition, ions already accelerated in the extraction field can be deflected toward the wall in a He^+-He collision. Estimates indicate that less than 10% of the produced ions are extracted. After leaving the target they are accelerated to 500 eV and deflected in the ExB mass spectrometer toward the mesh in front of detector 2. Before reaching the mesh the ions go through 1/30 of a trochoid period. The trochoid amplitude, however, is m_{He}/m_e times larger than that for the positrons. The result is a nearly vertical ion deflection. The ion counting rates lie mostly between 1 and 10/s.

2.4 Data acquisition

Without gas in the target the counting rate of detector 1 is a measure of the primary positron intensity. The ratio of the counting rates of detectors 2 (with gas) and 1 (without gas) is a relative measure of $\sigma_{\text{e}} + \sigma_{\text{ion}}$. In addition to accumulating the counts of detectors 1 and 2 a TAC-MCPHA combination is employed in the following way: A positron-detection event starts the TAC and the next ion-detection event stops it; if none occurs within 100 μs the TAC is reset. The time distribution accumulated by the MCPHA shows a flat background, mainly resulting from He^+ ions whose correlated positrons were not detected or disappeared by forming positronium, and a distinct peak centered at about 35 μs (depending on the extraction and acceleration voltages) due to the He^+ ions originating from ionization by the positrons which provided the corresponding TAC start pulses. The ratio of the number of events in the peak on top of the background to the number of TAC starts is a relative measure of σ_{ion} , as long as pile-up corrections are negligible.

2.5 Data evaluation

For measuring the energy dependence of the cross sections the energy of the primary positrons is varied by changing the potential difference between moderator and target entrance. Not varied are the extraction field across the tube, the ion energy in the ExB mass separator, the potentials of detectors 1 and 2, and all magnetic fields. This raises the question about energy dependent systematic errors, for example due to changes in the ion-extraction efficiency. In order to check how serious these errors are, an electron-impact ionization experiment was performed using the secondary electrons from the moderator as primary beam. By putting detector 1 at a positive potential for counting the electrons without gas in the target it was found that the intensity of secondary electrons is proportional to the intensity of positrons at all energies. With gas in the target, however, the potentials between target exit

and detectors were chosen the same as in the positron experiment, repelling the electrons but detecting the He^+ ions. The curve of relative values of $\sigma_{\text{Ion}}(E)$ was then compared with the literature values of $\sigma_{\text{Ion}}(E)$ of Montague et al. (6), matching the curves at low energies. This comparison shows a rather good agreement. Only at higher energies our values are slightly lower, by about 8% at 400 eV. The deviation is interpreted as a slight decrease of the extraction efficiency because the effect is more serious when a weaker magnetic guiding field is used. The positron data are corrected for this decrease in extraction efficiency with increasing energy. Both the sets of relative cross-section values are normalized to σ_{Ion} in the energy interval of 200 - 400 eV.

3. RESULTS

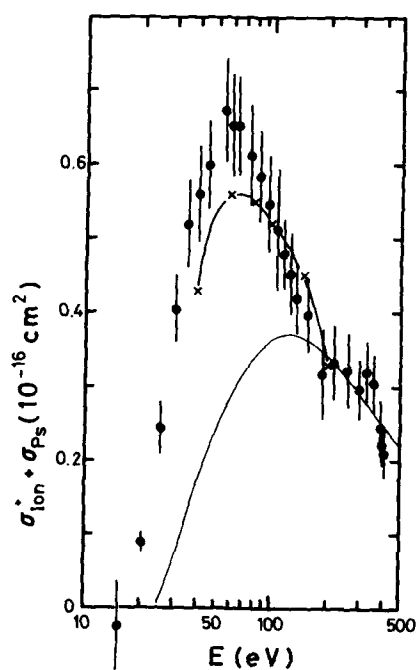


FIGURE 2

The sum of Ps-formation and ionization cross sections for positron impact on helium, versus energy. Dots - this work, line with crosses - Willis and McDowell (9). For comparison: solid line - electron-impact ionization cross section σ_{Ion} of Montague et al. (6).

The results for $\sigma_{Ps}(E) + \sigma_{Ion}^+(E)$ are displayed in Fig. 2 together with the estimates of Willis and McDowell obtained from measured total cross sections and five-state close-coupling calculations for elastic scattering and excitation. For comparison the curve of $\sigma_{Ion}^-(E)$ is also shown. The error bars of our data points in Figures 2-4 are the sum of statistical one-standard deviation error and an 8% systematic error due to normalization.

Our data on $\sigma_{Ion}^-(E)$, measured with the time-correlation method and normalized to σ_{Ion}^+ are shown in Fig. 3 together with other experimental and theoretical results. The experimental results of Sueoka (5) which are nearly equal with $\sigma_{Ion}^-(E)$ are contradicted by our results. The trend $\sigma_{Ion}^- > \sigma_{Ion}^+$ indicated by the theoretical result of Basu et al. obtained with a distorted wave for the incoming positron and complete screening in the final state, is now substantiated. The measurements of Diana et al. (4) agree only partially with our results. The differences of our data plotted in Fig. 2 and Fig. 3 represent our results for $\sigma_{Ps}(E)$ plotted in Fig. 4. They agree very well with those of the Arlington group (2,3) and the distorted-wave polarized-orbital calculations of Khan and Ghosh. There is a significant disagreement with the results of the London group (1).

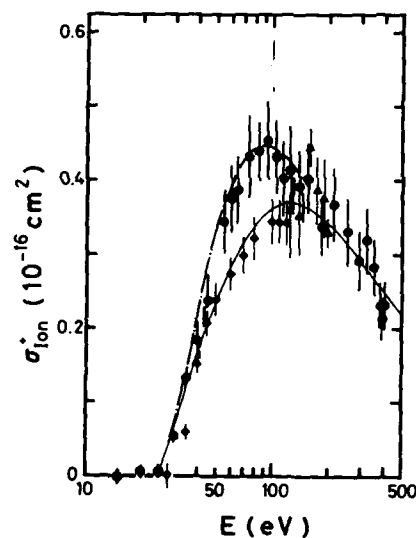


FIGURE 3

Ionization cross section for positron impact on helium vs. energy. Dots - this work, triangles - Diana et al. (4), diamonds - Sueoka (5), dash-dotted line - Basu et al. (10), solid line - $\sigma_{Ion}^-(E)$ as in Fig. 2.

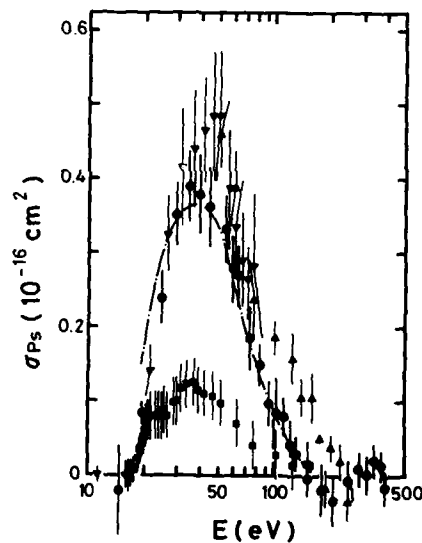


FIGURE 4

Positronium formation cross section for helium vs. energy. Circles - this work, triangles - Fornari et al. (2) and Diana et al. (3), squares - Charlton et al. (1), dash-dotted line - Khan and Ghosh (11).

The energy width of our data points is about 4 eV FWHM as estimated from the width of the He^+ ion peak in the MCPHA spectrum and the potential gradient in the target.

4. FUTURE DEVELOPMENTS

The deviations of our σ_{Ion}^+ data points from σ_{Ion}^- in the energy range of 300-400 eV, believed to be caused by a systematic error related to electron optics, will be further investigated. With a four times stronger magnetic field we will increase the extraction efficiency and thus reduce any related systematic errors (e.g. different transverse velocity distributions for ions from the two reaction channels). The energy resolution will be increased by reducing the extraction field for the measurement of $\sigma_{\text{Ps}} + \sigma_{\text{Ion}}^+$ and by pulsing the extraction field for the σ_{Ion}^+ measurements. A long-range goal is the test of threshold laws for positron-impact ionization.

ACKNOWLEDGEMENTS

This work has been supported by the Deutsche Forschungsgemeinschaft and the University of Bielefeld.

REFERENCES

- 1) M. Charlton, G. Clark, T.C. Griffith and G.R. Heyland, J. Phys. B: At. Mol. Phys. 16 (1983) 1465.
- 2) L.S. Fornari, L.M. Diana and P.G. Coleman, Phys. Rev. Lett. 51 (1983) 2276.
- 3) L.M. Diana, S.C. Sharma, L.S. Fornari, P.G. Coleman, P.K. Pendleton D.L. Brooks and B.E. Seay, Total positronium formation cross sections for helium from low to intermediate energies, in: Positron Annihilation, eds. P.C. Jain, R.M. Singru and K.P. Gopinathan (World Scientific, Singapore 1985) in print.
- 4) L.M. Diana, L.S. Fornari, S.C. Sharma, P.K. Pendleton and P.G. Coleman, Measurement of total ionization cross sections for positrons, in: Positron Annihilation, eds. P.C. Jain, R.M. Singru and K.P. Gopinathan (World Scientific, Singapore 1985) in print.
- 5) O. Sueoka, J. Phys. Soc. Jpn. 51 (1982) 3757.
- 6) R.G. Montague, M.F.A. Harrison and A.C.H. Smith, J. Phys. B: At. Mol. Phys. 17 (1984) 3295.
- 7) W.E. Kauppila, T.S. Stein, J.H. Smart, M.S. Oababneh, Y.K. Ho, J.P. Downing and V. Pol, Phys. Rev. A24 (1981) 725.
- 8) W. Bleakney and J.A. Hipple, Jr., Phys. Rev. 53 (1938) 521; L.E. Bailey, Rev. Sci. Instr. 31 (1960), 1147.
- 9) S.L. Willis and M.R.C. McDowell, J. Phys. B: At. Mol. Phys. 15 (1982) L31.
- 10) M. Basu, P.S. Mazumdar and A.S. Ghosh, J. Phys. B: At. Mol. Phys. 18 (1985) 369.
- 11) P. Khan and A.S. Ghosh, Phys. Rev. A28 (1983) 2181.

OBSERVATIONS OF SPIN DEPENDENCE IN SUPERELASTIC SCATTERING OF POLARIZED
ELECTRONS FROM Na(3P)

J. J. McCLELLAND, M. H. KELLEY, and R. J. CELOTTA

Radiation Physics Division, National Bureau of Standards,
Gaithersburg, MD 20899 USA

Measurements are presented of spin asymmetries observed in the superelastic scattering of 10 eV electrons from laser excited Na(3P). Asymmetries as large as 16% are seen, despite the fact that the target is not spin-polarized. Data are presented both as a function of scattering angle and laser polarization angle. An interpretation of the effect is given in qualitative terms.

1. INTRODUCTION

In the study of inelastic electron-atom collisions at low energies, the investigation of alignment and orientation introduced in the excited atomic state has provided a significant avenue for detailed comparison of theory with experiment. Such experiments can be done either with coincidence techniques, or with the inverse, superelastic process(1). By measuring not only cross sections, but also the probability of creating a particular angular momentum state in the excited atom, one is able to compare a larger set of experimental variables with theoretical predictions. Different theoretical approaches which do not significantly disagree in the cross section can give quite different alignment or orientation parameters. Thus decisions can be made as to the applicability of a theory in situations where knowledge of a cross section is of little value.

The natural extension of this type of experiment is to include spin in the list of experimentally resolved parameters. When spin-dependent cross sections are measured as a function of alignment and orientation of the target, the major new information that can be gained is the role played by exchange, or spin-orbit coupling, if any, in the creation of a particular angular momentum state of the target. Thus the scattering process can be broken down into its most basic elements. Not only are the scattering amplitudes for the various magnetic sublevels of the excited state probed, but these are also separated into their spin-dependent contributions.

It is with this in mind that the current experiments were performed(2). We have measured the spin dependence of the cross section for superelastic scattering of 10 eV electrons from laser-excited Na(3P) as a function of scattering angle and laser polarization angle. These results represent the first measurements of spin dependence in superelastic scattering from an aligned target. As such they provide the first direct experimental probe of the role played by exchange in the excitation (or de-excitation, as it were) of an aligned excited state.

2. EXPERIMENT

A complete description of the experimental apparatus will be presented in a forthcoming publication. Briefly, it consists of a spin-polarized electron beam, produced in a negative electron affinity GaAs source(3), incident on a beam of Na atoms originating from an effusive oven. The scattering volume is illuminated from a direction perpendicular to the scattering plane by a linearly polarized laser beam with frequency corresponding to the $3S_{1/2}(F=2) \rightarrow 3P_{3/2}(F=3)$ transition in Na. Figure 1 shows a schematic of the scattering geometry. The laser is a single-mode frequency-stabilized ring dye laser (linewidth approximately 1 MHz). It is frequency locked to the desired transition by imaging the fluorescence onto a split photodetector whose difference signal provides feedback to the dye laser frequency control(4). Superelastically scattered electrons are detected with a channel electron multiplier equipped with a retarding field analyzer to reject elastically and inelastically scattered electrons. This detector is mounted on a rotatable turntable to allow measurement of the angular dependence of the scattering.

A typical measurement protocol involves modulating the electron spin direction at a rate of 100 Hz while two scalars, gated with reference to this modulation, collect counts for the two different spin orientations. The two scalar readings are averaged over several (typically 10) runs of 200 seconds each, and then combined to form the spin asymmetry $A = P_e^{-1}(N_+ - N_-)/(N_+ + N_-)$, where P_e is the electron beam polarization (0.26) and N is the number of counts for spin up (+) or spin down (-) incident electrons. One standard deviation error bars are obtained from the reproducibility of the 10 measurements, and these typically agree very well with those predicted from counting statistics. Not included in the error bars shown in the present results is an overall scale factor uncertainty in the asymmetry measurement due to an uncertainty in the measurement of P_e . This is estimated to be $\pm 6\%$ (1 σ) of the asymmetry value(5).

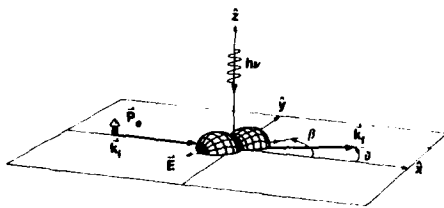


FIGURE 1. Schematic of the scattering geometry, showing a representation of the charge density of the prepared 3P state. Electrons with spin polarization P_e perpendicular to the scattering plane are incident with momentum \vec{k}_i , and scatter into an angle θ with momentum \vec{k}_f . The initial atomic state is prepared with linearly polarized laser light incident perpendicular to the scattering plane. The electric vector \vec{E} of the light makes an angle β with the incident electron direction.

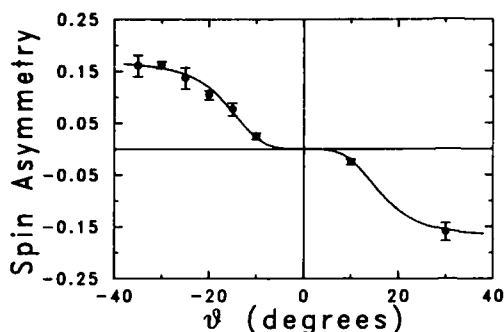


FIGURE 2. Spin asymmetry in superelastic scattering as a function of scattering angle θ . The laser is linearly polarized parallel to the incident electron direction ($\beta=0$). An antisymmetric curve is drawn to guide the eye.

3. DISCUSSION

The antisymmetric spin asymmetry results shown in Figure 2 are quite surprising when one considers them from the point of view of the usual presumptions made in discussing spin-dependent effects in low energy electron-atom collisions(6). Firstly, considering the fact that the target is not spin-polarized, it is surprising that there should be any spin asymmetry in the cross section at all. Spin-orbit coupling is generally the only type of interaction which can cause left-right antisymmetric spin-dependent effects with an unpolarized target, but it should be negligible when incident electron energies are low, the target Z is small and scattering angles are small. One is thus left with exchange as the only possible source of the spin asymmetry, but this also leads to contradictory conclusions. Exchange usually produces asymmetries only when the target is spin-polarized, and these asymmetries do not change sign when one goes from positive to negative scattering angles. Hence we are faced with the following dilemma: an explanation of the observations in terms of spin-orbit coupling seems reasonable in view of the unpolarized target and the left-right sign change of the asymmetry, but seems unreasonable in terms of energy, target Z , and scattering angle. Similarly, exchange seems reasonable in terms of the latter considerations, but appears to fall short in predicting the scattering angle antisymmetry or, indeed, even the existence of the effect.

A qualitative resolution of the apparent paradoxes presented by the data is obtained by considering the roles played, in the presence of exchange, by the four angular momenta in the problem: the incident electron's spin, its orbital angular momentum, the target electron's spin, and its orbital angular momentum. In order to understand how these come into play, we must first consider the state of the target as prepared by the linearly polarized laser beam. For convenience in describing the scattering dynamics, we choose to discuss the atomic state in terms of the coordinate system in which the quantization axis is antiparallel to the incident light direction(7). Neglecting for the purposes of this discussion the fact that the atom is in a single hyperfine state, simple transition probabilities for linearly polarized light predict that the excited state atoms are in a superposition of M_J levels of the $3P_{3/2}$ state, the $M_J = \pm 3/2$ having $3/8$ of the population each and $M_J = \pm 1/2$ having $1/8$ each.

The next step is to recognize, as demonstrated by Hermann et al.(1), that when an electron superelastically scatters to the left side of the atom, the cross section for deexciting positive M_L states is much larger than for negative M_L states. Thus if one has a superposition of M_L states in the target, one would expect the majority of electrons scattered to one side to be those which have deexcited positive M_L states, while those scattered to the other side have, for the most part, deexcited negative M_L states.

An explanation of the spin-dependent effect is now apparent, when one considers the fact that the $M_J = +3/2$ state consists of an $M_L = +1$ coupled with an $M_S = +1/2$ state, while $M_J = -3/2$ has $M_L = -1$ coupled with $M_S = -1/2$. Since most of the excited state population is in the $M_J = +3/2$ and $-3/2$ states, it can be said that in detecting electrons scattered to one side, we have not only selected those electrons which have mostly deexcited a specific M_L state, but also those which have mostly deexcited a specific M_S state. Thus we have, in effect, selected those electrons which have scattered from a spin-polarized subset of the excited atoms. This removes the above-mentioned objections to attributing the observed spin-asymmetries to exchange. Spin polarization of the target is achieved by selection of a spin-polarized subset, while left-right scattering antisymmetry arises from the selection of the opposite sign of target polarization when the scattering angle sign is switched.

The data shown in Figure 3 also, at first consideration, present a somewhat unforeseen result. These data show the effect on the spin asymmetry of changing the angle which the polarization vector of the linearly polarized laser light makes with the incident electron direction. The observed variation in the spin asymmetry is somewhat difficult to understand in light of the fact that a rotation of the electric vector does not change the relative populations of the M_J sublevels in the excited state, but rather only changes the relative quantum phases. Hence the spin-polarization of any subset of the excited state remains constant, suggesting that the observed spin asymmetry in the scattering shouldn't change.

Qualitative understanding of this phenomenon can be achieved when one considers the fact that while the majority of the scattering to one side is from $M_J = +3/2$ states, there is also some contribution from the other M_J levels. In particular, the contribution from $M_J = -1/2$ is coherent with that from $M_J = +3/2$ since the atomic state contains a coherent superposition of these two states. Because the $M_J = -1/2$ state is a mixture containing some $M_L = 0$, $M_S = -1/2$, there is some scattering from $M_S = -1/2$ coherently combined with the scattering from $M_S = +1/2$. One would thus expect an interference term in the resulting scattering intensity and also in the spin asymmetry, the size of which depends on the angle β .

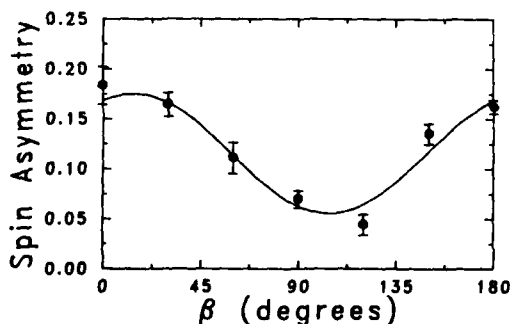


FIGURE 3. Spin asymmetry in superelastic scattering vs. laser polarization angle β . The scattering angle is -30° . The curve is a least-squares fit of the function $A+B\cos(2\beta+C)$. The parameters A, B and C have the values 0.115 ± 0.006 , 0.060 ± 0.008 and $-28^\circ \pm 9^\circ$.

4. CONCLUSION

We have presented first measurements of spin-dependent effects in superelastic scattering from laser excited Na. In the process of probing this new area of experimental investigation, we have uncovered some surprising effects which stress the necessity of carefully considering the assumptions made in the description of spin effects in electron-atom collisions. We have presented explanations of the apparent paradoxes posed by our measurements in physical terms, in the hopes that greater physical understanding can be achieved this way.

Clearly, although progress has been made in this direction(8), a complete theoretical description of these phenomena is required before it can be said that they are fully understood. Once such an analysis is carried out, the comparison with experiment should yield new information which will, in combination with cross section measurements and alignment and orientation parameter determinations, provide the ultimate test of *ab initio* calculations of complex scattering factors.

The results shown here are only the beginning of a large series of measurements which can be made. Work is currently underway to measure spin asymmetries with circularly polarized excitation, which should provide information more directly comparable with theory, since optical pumping allows the atom to be prepared in a pure $M_L = \pm 1$, $M_S = \pm 1/2$ state. In addition, the incident energy dependence of the spin asymmetries is certainly of interest and is also being investigated. With the completion of these measurements, it is hoped that a large improvement in the understanding of the role played by electron spin in inelastic collisions can be realized.

ACKNOWLEDGEMENT

This work is supported in part by U. S. Dept. of Energy, Office of Basic Energy Sciences, Division of Chemical Science.

REFERENCES

- 1) See, e.g., H. W. Hermann, I. V. Hertel, W. Reiland, A. Stamatovic and W. Stoll, J. Phys. B10 (1977) 251, H. W. Hermann, I. V. Hertel and M. H. Kelley, J. Phys. B13 (1980) 3465, or P. J. O. Teuhner, J. L. Riley, J. E. Furst and S. J. Buckman, J. Phys. B18 (1985) 351.
- 2) J. J. McClelland, M. H. Kelley, and R. J. Celotta, Phys. Rev. Lett., in print.
- 3) D. T. Pierce, R. J. Celotta, G.-C. Wang, W. N. Unertl, A. Galejs, C. E. Kuyatt and S. R. Mielczarek, Rev. Sci. Instrum. 51 (1980) 471.
- 4) J. J. McClelland and M. H. Kelley, Phys. Rev. A31 (1985) 3704.
- 5) L. G. Gray, M. W. Hart, F. B. Dunning and G. K. Walters, Rev. Sci. Instrum. 55 (1984) 866.
- 6) J. Kessler, Polarized Electrons (Springer-Verlag, Berlin, 1976).
- 7) H. W. Hermann and I. V. Hertel, Comments At. Mol. Phys. 12 (1982) 61, and Comments At. Mol. Phys. 12 (1982) 127.
- 8) G. F. Hanne, Phys. Rep. 95 (1983) 95.

THIS BEAM IS YOUR BEAM

By M. J. Coggiola

Tune: This Land is Your Land

This beam is your beam
This beam is my beam, from early morning to the next day ev'ning
From the ion sources to the down stream magnets;

This beam was made for you and me.

As I was tuning my beam of protons
I accidentally lost all my muons
By now my vacuum is just a mem'ry

This beam was made for you and me.

I've begged and pleaded for longer run time
But NSF has spent their last dime
While all around me are users waiting

This beam was made for you and me.

When will we ever get higher count rates
Enough to burn up our fancy channel plates
As all was working my shift was over

This beam was made for you and me.

RELATIVISTIC ATOMIC COLLISIONS

R. ANHOLT

Department of Physics, Stanford University, Stanford California 94305*

X-ray and charge-state studies of relativistic heavy-ion-atom collisions have been made at the Lawrence Berkeley Laboratory's BEVALAC accelerator. This paper reviews studies of ionization processes, radiative electron capture, and bremsstrahlung x-ray emission in solid targets.

1. INTRODUCTION

The coupling of Lawrence Berkeley Laboratory's heavy ion linear accelerator (SuperHILAC) with its relativistic synchrocyclotron (BEVATRON) has opened up new frontiers in atomic-collision physics. The BEVALAC is capable of accelerating U ions to energies of ~ 1 -GeV/amu (total energy 238 GeV), which makes possible for the first time the study of collisions and interactions of the heaviest few-electron ions.

From the point of view of atomic collision physics, the relativistic ion velocity is less important than the relative velocity. Most fundamental processes in atomic-collision physics scale with the ratio of the ion velocity v to the velocity of the active electron (v_e for processes involving the 1s electron). With relativistic projectiles one can obtain velocities that are high with respect to the fastest electron in the heaviest atom, the Uranium K electron. This allows the ion to be stripped, so that one can study one- or two-electron, high- Z ions where the atomic structure problem is greatly simplified. Most theories of scattering processes are greatly simplified also. While theories at low relative velocities are becoming increasingly refined only by employing numerically intensive coupled-channel calculations including ten, fifty, perhaps hundreds of basis states (1), at high relative velocities we can still make use of high-velocity theories like the first Born approximation for ionization and excitation processes (2,3) and second-Born (4), eikonal (5,6), strong-potential-Born (7), or impulse approximations (8) for capture processes.

This is not to imply that scattering processes at high velocities are well understood, else their study would not be worthwhile. In this paper, we examine distortion effects (9) on ionization processes which reduce projectile ionization cross sections by factors as small as 0.2 in some cases. We also examine radiative electron capture processes (REC), which are negligible in low-velocity collisions, but account for most of the observed capture cross sections for relativistic ions incident on low- Z targets (10). Nonradiative electron capture (NRC) is discussed elsewhere in this volume (11). Lastly, we discuss radiative continuum processes which have been observed in measurements of x-ray production by relativistic heavy ions.

*Supported in part by the National Science Foundation grant No. PHY-83-13676.

2. EXPERIMENTS

Until now two different kinds of atomic-collision measurements have been made: measurements of x-ray production (12) and of charge changing cross sections (13). Both employed many solid targets ranging from Be to U, and several different ions and beam energies were used. The methods used are, except for a few cases, standard in atomic collision physics, and are discussed elsewhere (12,13).

Figure 1 illustrates the type of x-ray processes observed when 4.2-MeV/amu U ions bombard Be and U targets. The most prominent features in the U + U spectrum are the K x-rays coming from the target atom (U) and projectile ions. The target K x-rays are sharp since the target atom is initially stationary and does not recoil significantly when a projectile ion passes by sufficiently close to create a K vacancy. The target K x-rays mainly come from ionization by the projectile nucleus, but uncertain contributions due to target K electron capture by the projectile are present. The projectile x-rays in U + U and U + Be collisions are broad due to the Doppler shift over the range of angles subtended by the x-ray detector. They mainly come from $1s+2p$ excitation followed by radiative decay in one- and two-electron projectiles, and give information about the state of the ion inside the solid target, which is discussed elsewhere (14).

The peak at approximately 270 keV is due to the radiative capture of target K electrons into the K shell of the projectile. The peak in U + Be collisions is very broad due to Doppler broadening, and is not observable in U+U collisions due to intense continuum x-ray emission. The REC photon cross section gives a direct measure of the radiative contribution to the total capture cross sections and indirect information about the state of the projectile inside the target (10,14).

Below the K REC peak in U+Be collisions, L REC (radiative capture into the L and higher projectile states) is expected. Also a continuum spectrum we call primary bremsstrahlung (15-17) is seen. We discuss primary bremsstrahlung and secondary-electron bremsstrahlung (18,19), which is dominant in U + U collisions, in Section 5.

Measurements of charge-changing cross sections using incident zero-, one-, and two-electron ions on thin targets give direct information about projectile $1s$ ionization and capture. For example, when Xe^{53+} ions are used, the yield of Xe^{54+} is proportional to the $1s$ ionization cross section, and the yield of Xe^{52+} ions is proportional to the electron capture cross section, if the target is sufficiently thin (13). Figure 2 shows typical results. The projectile ionization cross sections increase roughly as Z_t^2 , which measures the strength of the perturbing interaction between the target nucleus and projectile electron. The electron capture cross sections increase linearly with Z_t at low Z_t where REC is dominant, then begin to increase faster with Z_t than the ionization cross sections, due to NRC. This qualitative Z_t -behavior has been seen in collisions with projectiles ranging from Carbon to Uranium. The point where NRC overwhelms REC varies with the ion energy and the atomic number of the projectile.

3. IONIZATION PROCESSES

Charge-state measurements of projectile ionization using relativistic heavy ions is an unambiguous method for studying ionization processes as one varies the strength of the perturbing potential. When one measures target ionization, contributions due to K electron capture by the projectile are present, which despite the advanced state of our knowledge of electron capture

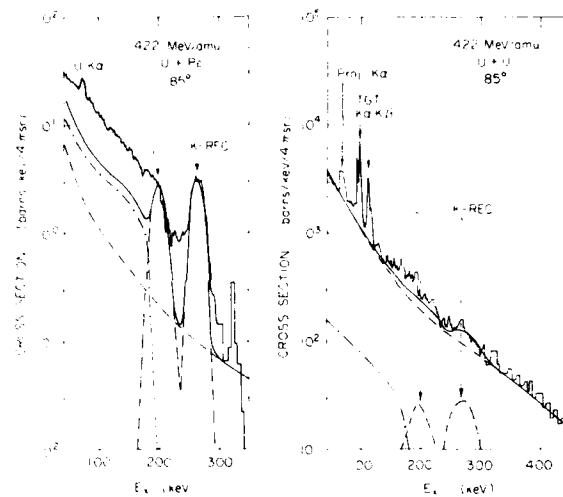


FIGURE 1

X-ray cross section spectra for 422-MeV/amu U+Be and U+U collisions at $\theta' = 85^\circ$. In addition to target $K\alpha$ and $K\beta$, projectile $K\alpha$, $K\beta$ and L-REC x-ray lines, primary bremsstrahlung (chain curve) and secondary electron bremsstrahlung (dashed lines) are shown. The solid line shows the total calculated continuum x-ray intensity.

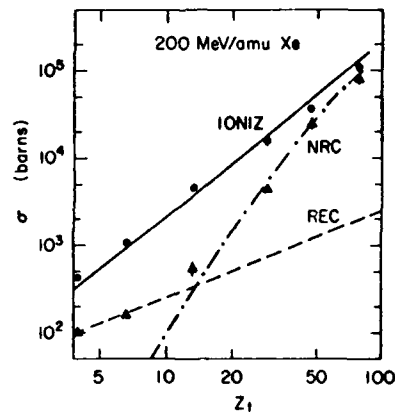


FIGURE 2

Cross sections for Xe^{33+} 1s ionization (solid line and closed circles) and Xe^{34+} electron capture (triangles). The calculated radiative electron capture (dashed lines) and nonradiative capture (chain curve) cross sections are shown.

by relativistic projectiles (5,6), can still not be calculated accurately within a factor of two. These contributions are absent when projectile ionization is measured, since the neutral target atoms cannot capture projectile electrons.

The screening of the perturbing target nucleus by the target electrons must be considered when projectile ionization is studied (20). In the plane-wave Born approximation, the projectile ionization cross section per electron is given by (21)

$$\sigma_{1s} = 4\pi \left(\frac{a_0 \alpha}{\beta}\right)^2 \int_0^\infty d\epsilon \int_{q_0}^\infty \frac{dq}{q^3} |\langle \epsilon | \exp(i\mathbf{q} \cdot \mathbf{r}) | 1s \rangle|^2 S(q), \quad (1)$$

where ϵ is the kinetic energy of the ionized electron, $q_0 = (E_K + \epsilon)/\beta c$ is the minimum momentum transfer needed to excite the K electron with binding energy E_K , βc is the ion velocity, a_0 is the Bohr radius, $\alpha = 1/137.037$, the target screening factor is given by

$$S(q) = \left[Z_t - \sum_i |\langle \psi_i | \exp(i\mathbf{q} \cdot \mathbf{r}) | \psi_i \rangle|^2 \right]^2 + Z_t - \sum_i |\langle \psi_i | \exp(i\mathbf{q} \cdot \mathbf{r}) | \psi_i \rangle|^2, \quad (2)$$

Z_t is the target nuclear charge, and the sum includes all occupied target orbitals ψ_i . The first two terms in this expression represent the interaction with a screened target nucleus. At very high velocities, $q = q_0$ is nearly zero, and this term vanishes. Excitation, which would normally occur at large impact parameters, is not present because the projectile electron sees a neutral atom. The second two terms represent the excitation of projectile electrons by Z_t separate electron-electron interactions. This term also vanishes as q_0 approaches zero. In collisions with very heavy ions like Xe and U, the momentum transfer is large, so that the target form factors, $\langle \psi_i | \exp(i\mathbf{q} \cdot \mathbf{r}) | \psi_i \rangle$, are small, and the ionization cross sections vary as $(Z_t^2 + Z_t) \sigma_B$, where σ_B is the plane-wave Born approximation cross section for protons.

Equations (1) and (2) do not incorporate threshold effects on the electron excitation contribution. In 82-MeV/amu Xe collisions, the target electron kinetic energy in the projectile frame is 45 keV, which is barely energetic enough to ionize a Xe K electron with a binding energy of 40 keV. To account for the electron ionization contribution, we therefore subtracted $Z_t \sigma_e$ from the measured cross sections, where σ_e is the calculated electron ionization cross section of Rudge and Schwartz (22) which is reasonably accurate near the ionization threshold.

With relativistic projectiles one must include not only the Coulomb interaction between the projectile electron and target nucleus, but also the current-current interaction in the projectile frame (23). This gives an additional transverse ionization cross section, which is dominant at energies exceeding about 10 GeV/amu, but is negligible for 82 to 200 MeV/amu.

Figure 3 shows reduced ionization cross sections

$$\sigma_{\text{red}} = (\sigma_{\text{meas}} - Z_t \sigma_e) Z_t^{-2} \quad (3)$$

for 82- to 200-MeV/amu Xe ions plotted against the atomic number of the perturbing nucleus. Studies of target inner-shell ionization by light ions have explored the region of small perturbing charges. At low velocities where the electrons form diatomic molecular orbitals around the projectile and target nuclei and become more tightly bound, the electrons are more difficult to ionize, hence smaller ionization cross sections are found (9). At high velocities, the distortion of the electron clouds redistributes the electron density toward the perturbing nucleus, thus bringing the electron and perturber closer together, and increasing the probability of excitation (9). Basbas et al. (9) formulated a theory relevant to the present intermediate velocities ($v-v_K$) that interpolates between the two regimes. However, this theory generally predicts that the present projectile ionization cross sections

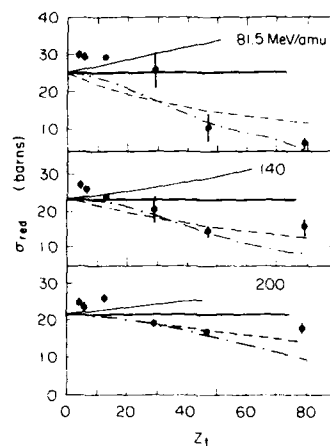


FIGURE 3

Reduced single ionization cross sections for 81.5-, 140-, and 200-MeV/amu Xe projectiles. The data points are compared with the plane-wave Born approximation (thick solid line), the theory of Basbas et al (9) incorporating distortion effects (thin solid line), a semiempirical modification of the Basbas theory (dashed line), and the Glauber approximation (chain curve).

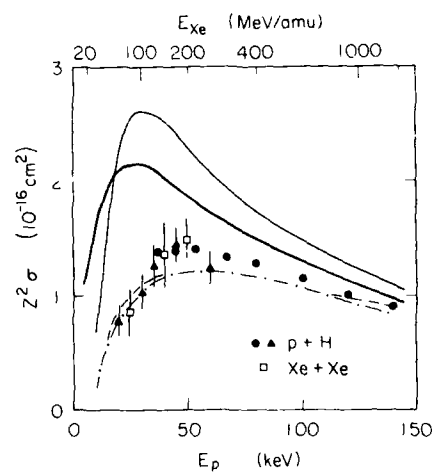


FIGURE 4

Scaled p+H and Xe+Xe 1s ionization cross sections plotted against proton kinetic energy. The p+H data points are from Park (24; triangles) and Shah and Gilbody (25; closed circles). The curves are the same as in Fig.3.

should be larger than the plane-wave Born calculations, but most of the data for $Z_t > 20$ lie below the Born ones. To estimate the ionization cross sections for other applications, we semiempirically modified the Basbas calculation by increasing the relative weight of the binding effect. The resulting cross sections, shown in Fig. 3, are in reasonable agreement with experiment at large Z_t .

We noted that scaled $p + H$ ionization cross sections (24,25) for the same ratio of v to v_k agree well with interpolated $Xe+Xe$ ionization cross sections for symmetric collisions (Fig. 4). This led us to apply theories like the Glauber approximation (26) that have normally been used exclusively for near symmetric collisions in the present highly asymmetric ones. The Glauber ionization cross sections are always below the Born cross sections, which possibly indicates the lack of elements in the theory that can be physically connected with the polarization effect. At large Z_t , the Glauber calculations agree well with experiment, but at small Z_t , the measured cross sections lie above the Born and Basbas theories. The low Z_t data points are significantly affected by target antiscreening where we do not have a definite theory incorporating threshold effects.

4. RADIATIVE ELECTRON CAPTURE

Radiative electron capture is the inverse of the photoelectric process. In the projectile frame, an incident bound target electron is captured with the emission of a photon whose energy is equal to the sum of the electron kinetic energy, $(\gamma-1)mc^2$ where $\gamma^2=(1-\beta^2)^{-1}$, and the final electron binding energy. Raisbeck and Yiou (27) noted that REC was needed to explain observed total electron capture cross sections for >300 MeV/amu protons incident on low- Z target atoms. The REC photon was observed at nonrelativistic velocities by Kienle et al. (28) and others.

The cross section for REC into the projectile shell i is calculated using photoelectric cross sections σ_{PEi} :

$$\sigma_{RECi} = Z_t \left(\frac{k}{\gamma\beta}\right)^2 \sigma_{PEi} (kmc^2), \quad (4)$$

where $k = E_i/mc^2 + \gamma - 1$, and the factor of Z_t is present because there are Z_t target electrons per atom that can be captured with equal likelihood.

There are two ways of measuring the REC cross section. Charge-changing cross-section measurements give the sum of the REC and NRC cross sections. At low- Z_t , REC dominates (Fig.2), so one directly measures the REC cross section, but at high- Z_t , this is not possible. The K REC photon cross section is given by (10)

$$\sigma_{RECY} = \frac{1}{2} N_{Kv} \sigma_{RECK}, \quad (5)$$

where N_{Kv} (≤ 2) is the average number of K vacancies carried by the projectile inside the solid target. Therefore, the measured REC photon cross sections depend on two unknowns: the number of projectile vacancies and the K REC cross section. From our parallel studies of the states of ions in solid targets (14), we have evidence that for the present high- Z ions, the equilibrium charge states of projectiles inside the target are equal to those measured downstream using a magnetic spectrometer. While this may not be the case for low- Z , low-velocity ions in solid targets where projectiles in highly excited states can Auger decay after leaving the target, giving larger post-target charge states (29), it is the case for the present high- Z ions where the high radiative decay

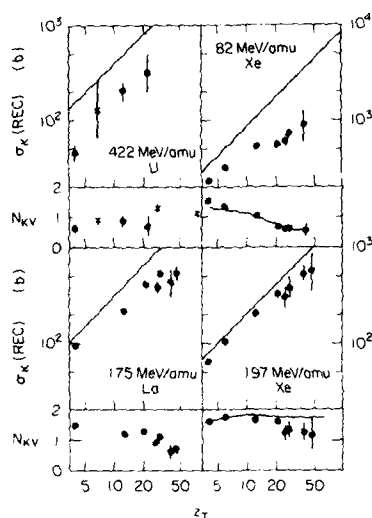


FIGURE 5

Measured and calculated KREC photon cross sections and the derived number of projectile K vacancies, obtained from Eq.(5). The crosses for 422-MeV/amu U and the solid lines for the Xe collisions show N_{KV} values obtained from post-target charge-state measurements. The REC photon cross sections become uncertain for $Z_T > 20$ and impossible to measure for $Z_T > 50$ where secondary electron bremsstrahlung overwhelms the REC cross sections.

rates keep excited-state populations small. This is shown in Fig.5 where equal values of N_{KV} have been obtained from measured photon cross sections and measured post-target charges states for U and Xe ions. This also verifies that we can calculate REC cross sections accurately. Therefore, we conclude that the theory of REC is well understood.

5. RADIATIVE CONTINUUM PROCESSES

Radiative electron capture is the capture of target electrons into bound states of the projectile. An analogous process is the capture into continuum states of the projectile, which we call primary bremsstrahlung (PB, 15-17). Viewed differently: in the projectile frame, the projectile nucleus is bombarded by target electrons with mean kinetic energy $(\gamma-1)mc^2$. These electrons may emit bremsstrahlung photons with energy E_x as large as the electron kinetic energy in the projectile frame. In the laboratory frame, the end-point x-ray energy is given by

$$E_x' = (\gamma-1)mc^2 \gamma^{-1} (1-\beta \cos \theta')^{-1}, \quad (6)$$

where θ' is the laboratory photon emission angle. For 422-MeV/amu U collisions viewed at 85° , the PB spectrum endpoint is near 170 keV.

As a first approximation, the PB cross section is just the bremsstrahlung cross section for Z_T electrons with kinetic energy $T = (\gamma-1)mc^2$ bombarding the

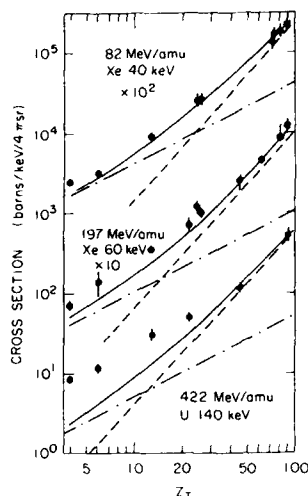


FIGURE 6

Continuum x-ray cross sections in 82-MeV/amu Xe collisions at an x-ray energy of 40 keV, 197-MeV/amu Xe at 60 keV, and 422-MeV/amu U at 140 keV. The measured data points are compared with calculations of primary bremsstrahlung (chain curve) and secondary-electron bremsstrahlung (dashed line), and the total continuum yield (solid line).

projectile nucleus Lorentz transformed into the laboratory (30):

$$\frac{d^2\sigma_{PB}(E_X', \theta')}{dE_X' d\Omega'} = Z_t \frac{d^2\sigma_{brem}(E_X, \theta, Z_p, T)}{dE_X d\Omega} \frac{dE_X}{dE_X'} \frac{d\Omega}{d\Omega'}, \quad (7)$$

where

$$\cos \theta = \frac{\beta - \cos \theta'}{1 - \beta \cos \theta'}, \quad \frac{d\Omega}{d\Omega'} = \frac{1 - \beta^2}{(1 - \beta \cos \theta')^2},$$

and

$$\frac{dE_X}{dE_X'} = \frac{1 - \beta \cos \theta'}{(1 - \beta^2)^{1/2}}. \quad (8)$$

Here the unprimed quantities are projectile-frame quantities (center-of-mass for projectile-electron collisions), and the primed ones are laboratory quantities. For the bremsstrahlung cross section we used the Bethe-Heitler formula [Eq.(3BN) of ref.31] including the Elwert Coulomb correction factor.

For the calculations shown in Fig. 1, we folded in the target electron Compton distribution to take into account the motion of the bound target electrons in the target frame, and we averaged over the laboratory angles subtended by the x-ray detector. These folding procedures have no effect on the PB cross section for x-ray energies well below the end point. The electron momentum folding causes the spectrum to drop off more slowly above the end point; the Doppler folding shifts the position of the end point to slightly higher energies, due to the inclusion of smaller laboratory angles, and rounds off the continuum shape near the end point.

The calculated PB cross sections are generally lower than experiment, as discussed in more detail below. However, the shape of the continua agree well with experiment, especially where PB is dominant, as in the Be collisions. The

measured photon angular distribution in 197-MeV/amu Xe+Be collisions is in good agreement with Eq.(7) when normalized near 90°.

Secondary electron bremsstrahlung (SEB; 18,19) is dominant in the U+U collisions, as shown in Fig.1. In a binary collision between a 422-MeV/amu heavy ion and a nearly free electron, ionized electron kinetic energies up to $E_{\max} = 1140$ keV are possible. These electrons can collide with other nearby target nuclei in solid targets, emitting bremsstrahlung photons with energies up to ~1140 keV. To calculate the cross section for SEB, we assume (i) that Z_t target electrons per atom are free and scatter elastically from the projectile nucleus, and (ii) the ionized electrons follow a tortuous path inside the solid target so electrons never leave the target material, and the angle between the bremsstrahlung photon direction and the projectile direction is random. The latter assumption follows from a calculation of the mean multiple scattering angle for 100- to 400-keV electrons in the targets used. The mean angle is of the order of several radians, so one cannot assume the electrons travel in a straight line after being emitted. With these assumptions, the cross section is given by

$$\frac{d\sigma_{\text{SEB}}(E_x')}{dE_x'} = Z_t \int_{E_x'}^{E_{\max}} dE_e' \frac{d\sigma_{\text{elas}}}{dE_e'} \int_{E_e'}^{E_x'} \frac{dE_e'}{S(E_e')} n_2 \frac{d\sigma_{\text{brem}}(E_x')}{dE_x'}, \quad (9)$$

where $d\sigma_{\text{elas}}(E_e)/dE_e$ is the elastic electron scattering cross section, $E_{\max} = 2\gamma^2\beta^2 mc^2$, n_2 is the target-atom density, $S(E_e)$ is the electron stopping power in the target material, and $d\sigma_{\text{brem}}/dE_x$ is the angle-integrated bremsstrahlung cross section calculated using the Bethe-Heitler-Elwert formula (31). The calculated SEB cross sections are in good agreement with the measured U+U spectrum in Fig.1.

Figure 6 shows the Z_t -dependence of continuum x-ray production in 82-,197-, and 422-MeV/amu Xe and U collisions. The x-ray energy chosen falls within the region where both PB and SEB are present. Given the good agreement between the shape of the calculated and measured x-ray spectra, identical qualitative results are expected at other x-ray energies. The x-ray energies were partly chosen to avoid, as much as possible, interference with characteristic x-rays and REC photons (though cross sections for continua falling beneath target x-ray lines could not be obtained at some Z_t values).

The fully logarithmic plot in Fig. 6 demonstrates that PB increases linearly with Z_t and SEB increases quadratically with Z_t . Good agreement between the SEB calculations and experiment is found at high- Z_t , but there is a systematic discrepancy at low- Z_t where PB dominates. If one subtracts the calculated SEB contribution from the measured cross sections, the resulting cross sections increase linearly with Z_t , as predicted by the PB theory, but are factors of 1.7 (197-MeV/amu Xe) to 2.9 (422-MeV/amu U) too high.

We have double checked every assumption made to determine PB and believe the calculated cross sections are accurate to within $\pm 30\%$. We conclude that the disagreement between the theory of PB and experiment is fundamental. The shape of the PB spectrum and the angular distribution of the radiation agree with theory, but the magnitudes of the measured and calculated cross sections differ. Given the reasonably good agreement between measured atomic electron bremsstrahlung cross sections (32) for similar electron energies and Z values and our Bethe-Heitler-Elwert calculations, it is unlikely that the origin of the disagreement between the PB calculations and experiment lies in the electron bremsstrahlung cross sections. It should be emphasized, however, that electron bremsstrahlung cross sections have never been measured on nearly bare, high- Z ions, but all Dirac-many-electron bremsstrahlung cross-section comparisons suggest that little difference should exist. The discrepancy may indicate a failure of the impulse approximation to describe

electron bremsstrahlung for incident projectiles on bound target electrons, but the good agreement between experiment and REC cross sections calculated with the same theory limits the options one has for modifying the impulse approximation. Possibly, high- Z projectiles polarize the target atoms to such an extent that the density of target electrons increases near the projectile nucleus, but this should also affect the PB and REC cross sections equally. Wake or bound electrons traveling with the projectile bombard target nuclei giving bremsstrahlung up to the PB endpoint, but given the lower bremsstrahlung cross sections on target nuclei like Be, it is unlikely that that wake electron-bremsstrahlung can compete with target-electron-projectile nucleus bremsstrahlung.

6. CONCLUSIONS

In conclusion, we would like to emphasize areas requiring further study. The Glauber theory of ionization adequately explains projectile ionization cross sections at large perturbing charge, but the measured points are about 25% higher than the Glauber calculations at small Z_t . This may be due to the dominance of polarization effects at low- Z_t or due to target electron antiscreening effects. The development of a theory of target screening incorporating threshold effects on the electron ionization contribution is important.

Radiative electron capture cross sections can be calculated accurately using photoelectric cross sections, and NRC cross sections can be calculated with the eikonal approximation (11). The calculated NRC cross sections still differ by up to a factor of two from experiment in some cases.

The disagreement between calculations of PB and continuum x-ray measurements in Xe+Be and U+Be collisions is a mystery which we have not resolved. Experimentally, it is desirable to determine whether this discrepancy is a projectile Z -dependent or velocity-dependent effect. The present measurements with Xe ions and higher-energy, higher- Z U ones can not decide this. We plan further studies with U ions at different energies in the near future.

ACKNOWLEDGMENTS

The author would like to thank many people who participated in the x-ray and charge-state measurements: H. Gould, C. Munger, J. Alonso, J.O. Rasmussen, and H. Bowman (LBL), Z.-Z. Xu and J.-S. Xu (Fudan Univ.), H.E. Wegner and P. Thieberger (Brookhaven National Laboratories), W.E. Meyerhof, C. Stoller, D. Spooner, and J.D. Molitoris (Stanford), D.H.H. Hoffmann (GSI-Darmstadt), S.A. Andriamonje (Univ. Bordeaux), and E. Morenzoni (ETH-Zurich). J.H. McGuire (Kansas State Univ.), W.E. Meyerhof and J. Eichler participated in developing the theory of relativistic heavy-ion-atom collisions.

REFERENCES

- 1) R. Shakeshaft, Phys. Rev. A18 (1978) 1930.
- 2) E. Merzbacher and H.W. Lewis, Encyclopedia of Physics, vol 34, ed. by S. Flügge (Springer, Berlin, 1958).
- 3) M.R.C. McDowell and J.P. Coleman, Introduction to Ion-Atom Collisions (Amsterdam, North-Holland, 1970).

- 4) W.J. Humphries and B.L. Moiseiwitsch, *J. Phys.* B17 (1984) 2655.
- 5) R. Anholt and J. Eichler, *Phys. Rev.* A31 (1985) 3505.
- 6) J. Eichler, *Phys. Rev.* A32 (1985) 112.
- 7) J. Macek and S. Alston, *Phys. Rev.* A26 (1982) 250.
- 8) J.S. Briggs, *Phys.* B10 (1977) 3075.
- 9) G. Basbas, W. Brandt, and R. Laubert, *Phys. Rev.* A17 (1978) 1655.
- 10) R. Anholt, S. A. Andriamonje, E. Morenzoni, Ch. Stoller, J. D. Molitoris, W. E. Meyerhof, H. Bowman, J.-S. Xu, Z.-Z. Xu, J. O. Rasmussen, and D. H. H. Hoffmann, *Phys. Rev. Lett.* 53 (1984) 234.
- 11) J. Eichler, Relativistic Eikonal Theory of Electron Capture, this volume.
- 12) R. Anholt, W.E. Meyerhof, Ch. Stoller, E. Morenzoni, S.A. Andriamonje, J.D. Molitoris, O.K. Baker, D.H.H. Hoffmann, H. Bowman, J.-S. Xu, Z.Z. Xu, K. Frankel, D. Murphy, K. Crowe, and J.O. Rasmussen, *Phys. Rev.* A30 (1984) 2234.
- 13) W. E. Meyerhof, R. Anholt, J. Eichler, H. Gould, Ch. Munger, J. Alonso, P. Thieberger, and H. E. Wegner, ms. submitted to *Phys. Rev. A*.
- 14) R. Anholt and W.E. Meyerhof, ms. in preparation.
- 15) H. W. Schnopper, J. P. Delvaille, K. Kalata, A. R. Sohval, M. Abdulwahab, K. W. Jones and H. E. Wegner, *Phys. Lett.* 47A (1974) 61.
- 16) D.H. Jakubassa and M. Kleber, *Z. Physik* A273 (1975) 23.
- 17) A. Yamadera, K. Ishii, K. Sera, M. Sebata, and S. Morita, *Phys. Rev.* A23 (1981) 24.
- 18) F. Folkmann, C. Gaarde, T. Huus, and K. Kemp, *Nucl. Inst. Meth.* 116 (1973) 487.
- 19) K. Ishii, M. Kamiya, K. Sera, S. Morita, and H. Tawara, *Phys. Rev.* A15 (1977) 2126.
- 20) J.H. McGuire, N. Stohterfont and P. Simony, *Phys. Rev.* A24 (1981) 97.
- 21) R. Anholt, *Phys. Rev.* A31 (1985) 3579.
- 22) M.R.H. Rudge and S.D. Schwartz, *Proc. Phys. Soc. London* 88 (1966) 563.
- 23) R. Anholt, *Phys. Rev.* A19 (1979) 1009.
- 24) J.T. Park, *Ad. At. and Mol. Physics* 19 (1983) 67.
- 25) M.B. Shah and H.B. Gilbody, *J. Phys.* B14 (1981) 2361.
- 26) J.H. McGuire, *Phys. Rev.* A26 (1982) 143.
- 27) G. Raisbeck and F. Yiou, *Phys. Rev. Lett.* 4 (1971) 1858.
- 28) P. Kienle et al., *Phys. Rev. Lett.* 31 (1973) 1099.
- 29) H.D. Betz, *Rev. Mod. Physics* 44 (1972) 465.
- 30) E. Spindler, H.-D. Betz, and F. Bell, *Phys. Rev. Lett.* 42 (1979) 832.
- 31) H. W. Koch and J. W. Motz, *Rev. Mod. Phys.* 31 (1959) 920.
- 32) C.A. Quarles and D.B. Heroy, *Phys. Rev.* A24 (1981) 48.

RELATIVISTIC EIKONAL THEORY OF ELECTRON CAPTURE

Jörg EICHLER[†]

Department of Physics, Stanford University, Stanford, California 94305
and Molecular Physics Department,
SRI International, Menlo Park, California 94025

The recently developed eikonal theory for electron capture by relativistic projectiles is briefly reviewed. Special attention is given to the proper choice of the post or prior version of the theory for transitions between arbitrary principal shells and to a simple analytical formula for $1s-1s$ transitions. The results from eikonal calculations including contributions from higher principal shells are in good agreement with experimental data.

1. INTRODUCTION

The recent emergence of experimental data (1,2) for electron capture at relativistic projectile velocities requires an extension of capture theory to the relativistic regime. Previous work on relativistic capture (3-5) has been confined to the Oppenheimer-Brinkman-Kramers (OBK) (3,4) and the second Born (5) approximation. The failure of these theories to account for the experimental cross sections suggests that a multiple-scattering capture theory is needed to explain the data in the range of 100-1000 MeV/amu projectile energy. We have developed a relativistic eikonal theory (6,7) which in its prior (post) form treats the electron-projectile (electron-target) interaction in first order while the electron-target (electron-projectile) interaction is treated in all orders of perturbation theory, albeit in an approximate way. The conceptual basis of the approach has been discussed in some detail (8,9), and it has been shown that, physically, the prior (post) version of the theory describes a hard collision of the electron with the projectile (target) nucleus followed (preceded) by multiple soft collisions with the target (projectile) nucleus. The nonrelativistic eikonal approximation renders good agreement with experimental data for total (10) and differential (11) cross sections close to the forward direction.

2. OUTLINE OF THE THEORY

For a bare projectile (charge Z_p) impinging on a one-electron target (charge Z_T) with velocity v , the impact parameter dependent amplitude in the prior form can be written (6), using atomic units, as

[†]Permanent address: Bereich Kern- und Strahlenphysik, Hahn-Meitner-Institut für Kernforschung Berlin, and Fachbereich Physik, Freie Universität Berlin, D-1000 Berlin 39, West Germany.

$$A_{fi} = i \int dt \int d^3r [\psi_f'(\vec{r}_p, t')]^\dagger S \frac{Z_p}{r_p} \psi_i(\vec{r}_T, t) \quad (1)$$

where primed (unprimed) quantities refer to the projectile (target) rest systems. The spinor transform S , represented by a 4×4 matrix, transforms a spinor ψ from the target frame to the projectile frame. Within the prior form of the eikonal approximation the initial and final wave functions are

$$\psi_i = \phi_i(\vec{r}_T) e^{-iE_i t}$$

and

$$\psi_f' = \phi_f'(\vec{r}_p') e^{-iE_f t'} \exp \left(-iZ_T' \int_{t'}^{\infty} \frac{dt''}{r_T} \right), \quad (2)$$

where ϕ_i and ϕ_f are relativistic target and projectile eigenfunctions and E_i and E_f the corresponding eigenenergies including the electron rest mass. The final-state wave function contains a phase distortion caused by the electron-target interaction integrated from the time of capture to infinity. The associated target charge is denoted by Z_T' so that, by letting $Z_T'=0$ in Eq.(2), one may retrieve the OBK approximation (3,4).

From Eq.(1) one derives the cross section per electron averaged over the initial and summed over the final angular momentum projections as (6)

$$\sigma_{fi} = \frac{(2\pi)^4}{2j+1} \frac{\eta^2}{2} Z_p^2 \int \text{Tr}(S P_g S P_h) d^2 p_b \quad (3)$$

where $\eta=1/v$, $\gamma=(1-v^2/c^2)^{-1/2}$ and the integration extends over the transverse momentum \vec{p}_b . The integrand is expressed as the trace of four 4×4 matrices that are built from simple 2×2 Pauli matrices. The density matrices P_g and P_h characterize final and initial states, respectively. The density matrix formulation introduced in Ref.(6) renders it unnecessary to separately calculate (currently unobservable) non-spin-flip and spin-flip transitions (3-5) and thus greatly facilitates the calculations. At the same time, target and projectile properties factor in a simple way, so that the P_g and P_h matrices can be easily specified (6) for arbitrary initial and final states.

Explicit calculations have been performed (7,2) for initial K,L,M shells and final shells up to $n=10$. It turned out (2) that only the K-shell had to be treated relativistically, whereas for higher shells nonrelativistic electron motion yields sufficiently accurate results.

3. THE POST AND THE PRIOR FORM OF THE THEORY

The formulation in Eqs.(1)-(3) has been based on the prior form of the theory, the post form being simply obtained by interchanging target and projectile, i.e. $Z_p \leftrightarrow Z_T$, $Z_T' \leftrightarrow Z_p'$, $Z_T' \leftrightarrow Z_p'$ and initial and final states. In an asymmetric theory like the eikonal approximation, one has to treat the stronger one of the two electron-nucleus interactions non-perturbatively and the weaker one in first order. Therefore, if $Z_p < Z_T$ one uses the prior form, and the post form is used in the opposite case. However, while this prescription is indisputable for transitions between equal principal shells, one has to take into consideration the weighting of the Coulomb wave functions at different electron-nucleus separations if the initial and final principal quantum numbers n_T

and n_p are different. Since the expectation value of the Coulomb potential is equal to $\langle Z/r \rangle_n = (Z/n)^2$ irrespective of the subshell, the effective strength of the potential should be measured by Z/n rather than by Z . This leads to the prescription (2):

if $Z_p/n_p < Z_T/n_T$, then use the prior form,

if $Z_T/n_T < Z_p/n_p$, then use the post form. (4)

This rule may entail different choices for different combinations of initial and final states in the same collision system. It is presumably due to this rule together with the dominance of capture into higher projectile shells, that for nonrelativistic reactions $A^{Z+} + H(1s) \rightarrow H^+ + \sum_n A^{(Z-1)+}(n)$ the prior and not the post form of the eikonal theory (10) gives total cross sections in good agreement with experiment for $Z=1,2,3$.

4. A SIMPLE ANALYTICAL FORMULA AND ITS APPLICATION

For the special case of relativistic $1s-1s$ transitions a simple closed formula has been derived (6) from Eq.(3) using an αZ expansion ($\alpha=1/137.036$ is the fine-structure constant) of the electronic energies and wave functions. With $\delta=[(\gamma-1)/(\gamma+1)]^{1/2}$ and $p_-=\eta(E_f/\gamma-E_i)$ the formula can be written as

$$\begin{aligned} \sigma_{1s-1s}^{eik} &= \frac{2^8 \pi Z_p^5 Z_T^5}{5v^2(Z_T^2 + p_-^2)^5} \frac{\gamma+1}{2\gamma^2} \frac{\pi \eta Z_T'}{\sinh(\pi \eta Z_T')} e^{-2\eta Z_T' \tan^{-1}(-p_-/Z_T')} [S_{eik} + S_{mag} + S_{orb}] \\ S_{eik} &= 1 + \frac{5}{4} \eta \frac{Z_T'}{Z_T} p_- + \frac{5}{12} \eta^2 \frac{Z_T'^2}{Z_T^2} p_-^2 + \frac{1}{6} \eta^2 \frac{Z_T'^2}{Z_T^2} \\ S_{mag} &= -\delta^2 + \frac{5}{16} \delta^4 + \frac{5}{8} \delta^2 \frac{\gamma}{\gamma+1} \frac{Z_T'}{Z_T} + \frac{1}{4} \delta^2 \eta^2 \frac{Z_T'^2}{Z_T^2} + \frac{5}{48} \delta^4 \eta^2 \frac{Z_T'^2}{Z_T^2} \\ S_{orb} &= \frac{5\pi}{18} \delta \alpha (Z_p + Z_T) - \frac{5\pi}{36} \delta^3 \alpha (Z_p + Z_T) - \frac{5}{8} \delta \alpha Z_T \eta \frac{Z_T'}{Z_T} (1 - \frac{1}{2} \delta^2) \\ &\quad - \frac{5\pi}{18} \delta \frac{\gamma}{\gamma+1} \alpha Z_p \frac{Z_T'}{Z_T} + \frac{5\pi}{28} \delta (\frac{\gamma}{\gamma+1})^2 \alpha Z_p \frac{Z_T'^2}{Z_T^2} - \frac{5\pi}{28} \delta \frac{\gamma}{\gamma+1} \alpha (Z_p + Z_T - \delta^2 Z_p) \frac{Z_T'}{Z_T} \end{aligned} \quad (5)$$

In connection with the approximate result Eq.(5) we wish to point out a number of observations: (a) If we ignore the eikonal phase distortion and put $Z_T'=0$, we retrieve the approximate relativistic OBK (3,4) result (summed over non-spin-flip and spin-flip contributions). (b) In the nonrelativistic limit ($\gamma \rightarrow 1$, $\delta \rightarrow 0$), we recover the exact nonrelativistic eikonal cross section. (c) The term S_{mag} does not depend on the binding nuclear charges and hence is interpreted as a magnetic contribution to capture mediated by the interaction between the relativistically induced magnetic field and the Dirac magnetic moment of the electron. (d) S_{orb} is composed of terms that explicitly include

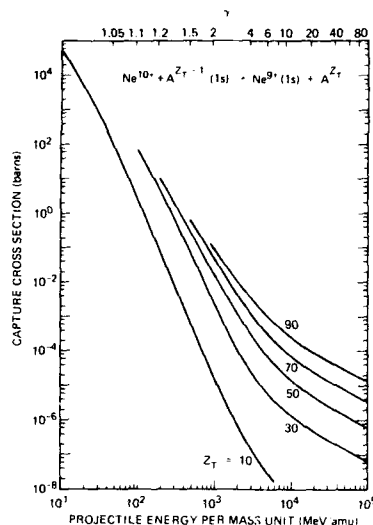


FIGURE 1

Cross sections for electron capture from a hydrogenic Dirac $1s$ orbital of a target with nuclear charge Z_T into a hydrogenic Dirac $1s$ orbital of a projectile with nuclear charge $Z_P=10$. On the upper edge of the figure the relativistic parameter γ is also shown. Each curve starts at projectile velocities that are about twice the K-shell electron velocity in the target.

αZ_P or αZ_T and hence is interpreted as a correction arising from a relativistic modification of the electron orbitals.

A comparison with the results of an exact numerical evaluation of Eq.(3) shows that Eq.(5) is very accurate at not too large $\alpha Z_P, T$ (7). As has been observed for the OBK and second Born approximation (3-5), the cross section given by Eq.(3) or (5) has an asymptotic energy dependence as E^{-1} . This behavior is shown in figure 1 which reveals that after a steep E^{-6} fall-off the cross-section curves start to decline less rapidly (as E^{-1}) around $\gamma = 6$ to 10. Compared to the OBK cross section (4) the eikonal cross section is, however, reduced (6,7) by a factor of 5 to 15. It is a factor of this order that is needed to bring theory into agreement with experimental data.

Equation (5) may also be used as an approximation (2) to obtain prior cross sections (averaged over initial and final orbital states) for higher initial or final principal shells by replacing Z_P with Z_P/n_P and Z_T with Z_T/n_T . In the post form, the role of target and projectile and of initial and final state is interchanged. This scaling rule (2) can be partially justified (2) by the observation that, nonrelativistically, (a) the first and second-order terms of the transition amplitude rigorously scale with Z_P/n_P and Z_T/n_T , and (b) for high velocity only these single and double scattering terms contribute to the nonrelativistic eikonal cross section (9). In fact, numerical application of the scaled version of Eq.(5) to initial and final K,L,M shells shows

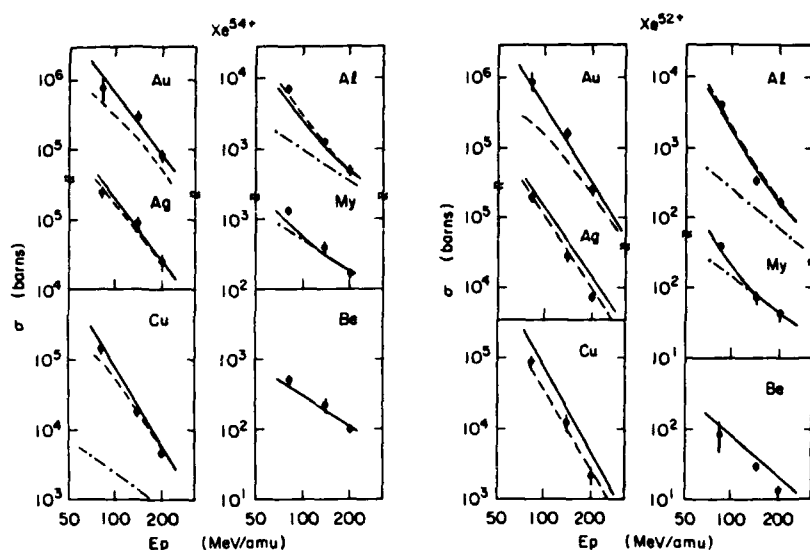


FIGURE 2

Total (nonradiative plus radiative) capture cross sections (2) for Xe^{54+} and Xe^{52+} impinging on various targets (My denotes mylar foils). Solid lines represent eikonal calculations using the Z/n criterion Eq.(4), dashed lines are based on the conventional Z criterion for selecting between the post and prior form; see text. For low- Z targets such as Be and mylar, the radiative electron capture (dash-dot lines) is dominant.

(2) that one may get total cross sections that are in surprisingly good agreement with a large body of experimental data.

5. RESULTS AND DISCUSSION

The exact eikonal cross section, Eq.(3), has been worked out and applied (2) to a number of target and projectile combinations for which capture cross sections have recently been measured (2) at the BEVALAC in Berkeley. It was found that for low- Z projectiles with energies of about 1000 MeV/amu, K-K transitions give the main contribution to the total cross section (although K-L, L-K is not negligible), but that for high- Z ions of comparatively low energy (100-200 MeV/amu), the contributions of initial and final K,L,M shells are all of comparable magnitude. Since for the eikonal approximation to be valid, the projectile velocity has to be somewhat (in principle: much) larger than the electron velocity in the relevant shell, the dominance of higher shells at lower projectile velocities renders the approximation applicable to the calculation of total cross sections in a range where, for K-K transitions alone, the criterion is no longer fulfilled.

Figure 2 displays a comparison between measured and calculated (2) capture cross sections for Xe^{52+} and Xe^{54+} projectiles. The difference between the

two sets of curves can be ascribed to capture into $1s$ states. It is seen that in most cases the Z/n criterion of Eq.(4) (solid line) for choosing the post or prior form is in better accord with the data. But, since Eq.(4) is based on an estimate using a diagonal matrix element, the effect of the shell size on the effective interaction strength tends to be overestimated. Therefore, in some cases, the conventional Z criterion (dashed line) appears to yield better agreement with the data.

It is concluded that on the whole, multiple-scattering effects approximately embodied in the relativistic eikonal approximation (6) are crucial for obtaining good agreement with measured capture cross sections. Clearly, it is to be expected that in order to reproduce detailed cross-section features in the lower velocity range one will eventually need more detailed calculations, such as coupled-channel calculations.

ACKNOWLEDGEMENTS

I would like to thank W. E. Meyerhof and R. Anholt for inspiring and helpful discussions. For the warm hospitality extended to me during my sabbatical year I want to express my gratitude to D. C. Lorents and J. R. Peterson and their colleagues at the Molecular Physics Department, SRI International, and to W. E. Meyerhof at the Department of Physics, Stanford University.

REFERENCES

- 1) H. J. Crawford, Ph.D. Thesis, University of California, Lawrence Berkeley Laboratory Report No. LBL-8807, 1979 (unpublished); H. J. Crawford, L. Wilson, D. Greiner, P. J. Lindstrom, and H. Heckman (unpublished); R. Anholt, Phys. Rev. A 31 (1985) 3579.
- 2) W. E. Meyerhof, R. Anholt, J. Eichler, H. Gould, Ch. Munger, J. Alonso, P. Thieberger, and H. E. Wegner, submitted to Phys. Rev. A.
- 3) M. H. Mittleman, Proc. Phys. Soc. London 84 (1964) 453; R. Shakeshaft, Phys. Rev. A 20 (1979) 729.
- 4) B. L. Moiseiwitsch and S. G. Stockman, J. Phys B 13 (1980) 2975.
- 5) W. J. Humphries and B. L. Moiseiwitsch, J. Phys B 17 (1984) 2655.
- 6) J. Eichler, Phys. Rev. A 32 (1985) 112.
- 7) R. Anholt and J. Eichler, Phys. Rev. A 31 (1985) 3505.
- 8) J. Eichler and H. Narumi, Z. Phys. A 295 (1980) 209.
- 9) L. J. Dube and J. Eichler, J. Phys B 18 (1985) 2467.
- 10) J. Eichler and F. T. Chan, Phys. Rev. A 20 (1979) 104; J. Eichler, Phys. Rev. A 23 (1981) 498.
- 11) K. Kobayashi, N. Toshima, and T. Ishihara, submitted to Phys. Rev. A and private communication.

ATOMIC COLLISIONS IN THE TIME-DEPENDENT HARTREE-FOCK APPROACH

K. R. Sandhya DEVI
Shell Bellaire Research Center, Houston, TX 77001, USA

J. D. GARCIA and N. H. KWONG
Physics Department, University of Arizona, Tucson, AZ 85721, USA

Application of Time-dependent Hartree-Fock approximation to atomic collisions is reviewed. Merits and defects of the approach, progress to date and possible extension to new areas like muon capture by atoms are discussed.

1. INTRODUCTION

The study of many-body collision dynamics is of importance both in nuclear and atomic physics. Exchange of ideas and techniques from one field to another can therefore prove to be very useful. Further, as quantum systems with well known interactions, atomic systems provide testing grounds for various approximations developed for many-body problems. Over the past few years, collisions of nuclei have been studied extensively in the framework of time-dependent Hartree-Fock (TDHF) approximation (1). It has been shown that this approximation gives a good description of the inclusive aspects of the collision dynamics. It is therefore of interest to see to what extent this method can be applied to colliding atomic systems. Of particular interest is the ion-atom or atom-atom collision. In these cases, the bulk of the mean field arises from the electron-nucleus interaction. The Hartree-Fock or the mean field approximation to electron-electron interactions can therefore be expected to be a good approximation - the truncation effects arising from the residual correlations being perturbative. Several groups have now been actively engaged in studying atomic collisions in the TDHF approximation (2-5). Extension of the method to new areas like muon capture by atoms is also currently being explored (6).

Large amplitude changes from equilibrium and rapidly varying couplings during atomic collisions pose a number of problems in a theoretical treatment of the dynamics. Traditional basis expansion methods, when extended to study collision phenomena, have to face a number of problems like 1) appropriate choice of basis 2) proper handling of translational factors arising from the nuclear motion 3) inclusion of intermediate continuum

states. An alternative approach which bypasses these difficulties is the direct integration of dynamical equations on a space-time mesh. Pioneering calculations in this regard were carried out by Maruhn-Rezwani et.al. (4), for one electron system (p+H), using finite difference techniques and by Bottcher (5) with finite element techniques. With the present day computational capabilities extension of direct integration technique to many electron colliding systems appears feasible in the TDHF approximation (2-3).

2. THEORY

For the range of colliding energies of interest, an impact parameter treatment would be assumed adequate. The nuclear positions are determined by a Coulomb trajectory corresponding to the motion of two point charges. With this decoupling of nuclear motion, the evolution of the many electron system is governed by the Schroedinger equation

$$H\Psi(r_1, r_2, \dots, R, t) = i\hbar \dot{\Psi} \quad (1)$$

H is the total many electron Hamiltonian and R is the relative nuclear coordinate. In the TDHF approximation, the many-body wave function is approximated by a variational solution determined by the least action principle

$$\delta \int dt \{ \langle \Psi | H - i\hbar \partial/\partial t | \Psi \rangle \} = 0 \quad (2)$$

with the constraint

$$\Psi = \det(\psi_\lambda) \quad (3)$$

at all t . This variation results in a set of non-linear, time dependent, single particle equations

$$\mathcal{H}\psi_\lambda = i\hbar \dot{\psi}_\lambda \quad (4)$$

where,

$$\begin{aligned} \mathcal{H} = & \delta_{\sigma\sigma'} \delta(r-r') \{ -(h^2/2m) \nabla^2 \\ & + Z_1 e^2 / |r-R_1| + Z_2 e^2 / |r-R_2| \\ & + e^2 \int dr'' \rho(r, r'') / |r-r''| \} \\ & + \text{exchange terms} . \end{aligned} \quad (5)$$

Here ρ is the one-body density given by

$$\rho = \sum \psi_\lambda^* \psi_\lambda \quad (6)$$

and σ is the spin coordinate. R_1 and R_2 are the target and projectile nuclear coordinates respectively.

Since the nuclear motion is decoupled from the electronic motion, the most appropriate coordinate system to work with is the cylindrical coordinate system with the z -axis along the inter-nuclear axis. However, for non-zero impact parameter collisions, effects arising from the rotation of the nuclear axis have to be considered. In this rotating coordinate system, the single particle wave function can be written as

$$\psi_{\lambda} = \sum \phi_{\lambda m}(\rho, z) e^{im\phi} . \quad (7)$$

For incident velocities less than the characteristic velocities of the electrons in the atom, the electrons have time to follow nuclear motion. Therefore an axial symmetry about the inter-nuclear axis can be assumed. This simplifies the computational efforts considerably, since only one term in the expansion in eqn. 7 need to be considered. As the velocity increases, however, the axial symmetry assumption breaks down due to the inability of the electrons to follow the nuclei. More and more terms have therefore to be taken into account in the expansion.

3. RESULTS AND DISCUSSIONS

One of the advantages of solving the dynamical equations on a space-time mesh is that one can take snap shots of single particle density distributions (representative of the most probable process at any instant for a given set of initial conditions) at various times as the collision proceeds. Fig. 1 shows these snap shots for $\text{He}^{++} + \text{He}$ collision at 30 KeV. This energy corresponds to a velocity much smaller than the characteristic velocity of the electrons in He atom. Note the molecular type orbital formation at close distances. A measure of assymetry about the inter-nuclear axis is the contribution to the norm of the single particle orbital, from $m=m_{\lambda} \pm 1$ components in eqn. 7. This quantity, which is also a measure of the population of $2p\pi_U$ orbital through rotational coupling to $2p\sigma_U$ orbital, reaches a maximum of 12% at closest distance of approach and falls off to 3% asymptotically. Fig. 2 shows the density evolution for a high energy collision (250 KeV). Note the development of considerable assymetry as the ion and atom approach each other. Very little charge is transferred due to the inability of the electron to follow nuclear motion. Imposing axial symmetry can therefore result in large spurious charge transfer probabilities.

Final transition amplitudes can be obtained by projecting the TDHF state on to a final single determinantal state. The cross sections are obtained by integrating the corresponding transition probabilities over all impact parameters. In general, construction of final channel wave functions for many-body collisions is extremely complicated. However, if the final states are assumed to be single determinantal atomic states with proper traslation factors, the transition probabilities involve only single particle overlaps which can easily be calculated (3).

At this stage, however, it should be noted that the truncation of a full many-body Hamiltonian to an effective one-body, non-linear Hamiltonian in the TDHF approximation introduces spurious fluctuations in the transition amplitudes which persist even asymptotically (7). Since correlation effects are expected to be small for ion-atom collisions, these fluctuations can also be expected to be small. Therefore meaningful cross sections can be extracted for dominant processes for a give energy or for inclusive processes like total single, double charge exchange. This is borne out by numerical calculations as well (3). There exists a rigorous formulation of one-body approximation to a many-body S-matrix wherein these fluctuations are exactly removed (8). This formulation involves suitable averaging over many forward and backward going TDHF trajectories. As expected, numerical calculations for $p + \text{He}$ collisions indicate that, the inclusive probabilities obtained from the S-matrix formulation differ from those obtained from TDHF calculations by only about 6% (9).

Inclusive single and double charge transfer probabilities as functions of impact parameter are shown in Fig. 3 for $\text{He}^{++} + \text{He}$ collision at 30 KeV. The oscillations which arise from the interference of many channels available for electrons during collision, have long been predicted by Lichten (10) in a

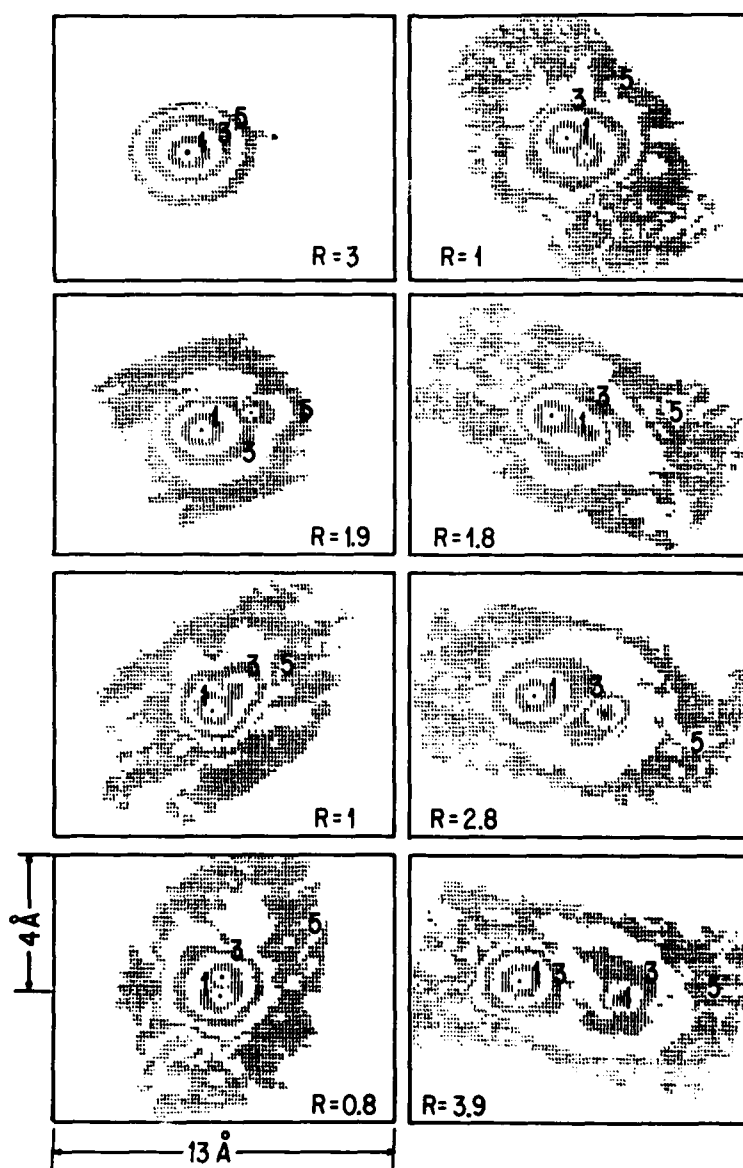


FIG. 1 Evolution of one-body density for $\text{He}^{++} + \text{He}$ collision at 30 KeV and $b = .8 \text{ \AA}$. The numbers 1, 3, 5 ... indicate the negative powers of 10, times the central density. The relative distances (R) are in \AA .

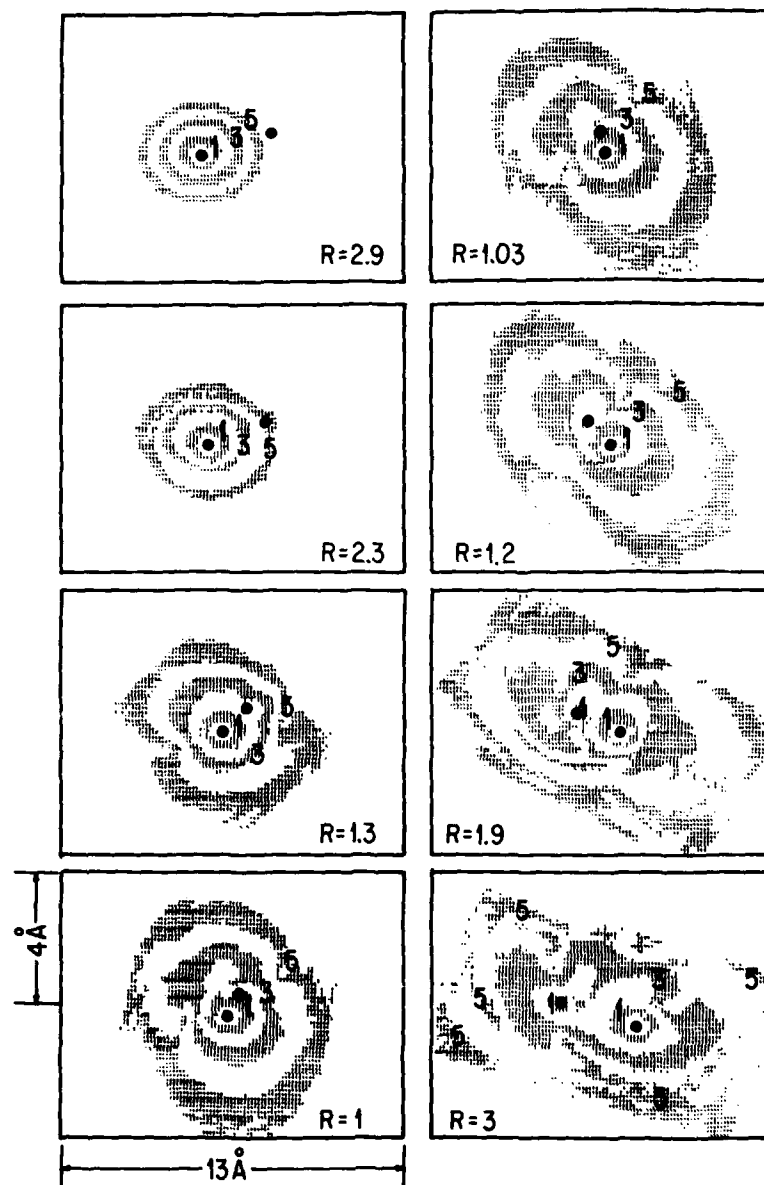


Fig. 2 Same as Fig. 1 for 250 KeV.

single particle, adiabatic, molecular orbital formulation of the problem. This model also predicts that the number of oscillations in single charge transfer probability is twice those in double charge transfer probability. This is borne out in the present calculations as well. Note that the peaks are shifted when rotation coupling is included. This can be understood in terms of molecular single particle model as due to the removal of degeneracy between $2p\pi_u$ and $2p\sigma_u$ levels by Coriolis coupling. This splitting changes the difference $E_{\sigma u} - E_{\pi u}$ by $\hbar\omega$ (ω is the angular velocity of rotation), introducing a shift in the peaks of charge transfer probability curves.

Total double charge transfer cross sections from TDHF calculations are shown in Fig. 4 and compared with the experimental data (11). Results of molecular orbital calculations of Harel and Salin (12) and those from the atomic state expansion calculations of Mukherjee et. al. (13) are also plotted for comparison. At high energies TDHF calculations give completely spurious results when Coriolis coupling is not included. When this coupling is included reasonable agreement with the data are obtained over a wide range of energies.

The TDHF approximation and direct integration techniques are currently being extended to the study of muon capture process by atoms (6). Some preliminary results are shown in Fig. 5. These are muon and electron densities at the beginning and around the middle of the collision for the case of muon collision with hydrogen atom at .26 eV (cm). Initially muon is represented by a wave packet. As the evolution continues, at the end of about 1500 time steps (time required for a free muon to traverse twice the initial separation distance), the r.m.s radius of muon decreases from 1.44 Å to 1.26 Å where as that of electron increases from .92 Å to 1.70 Å indicating the electron is being ionised due to the shielding of proton by muon. Integration of muon density around the proton within a radius of about 2 Å yields a rough value of .8 for capture probability at this energy.

4. CONCLUSIONS

Summarizing, the studies to date indicate that the TDHF approximation gives a reasonably accurate description of dominant collision processes in atomic collisions over a wide energy range. Extensions to areas like muon capture are currently being explored both in terms of feasibility and accuracy. The method is best suited for determining inclusive probabilities. Non-dominant collision processes, however, may not be represented very accurately due to the effects of spurious fluctuations arising from the truncation of the Hamiltonian. More studies are needed in this regard. Another disadvantage is the total absence of certain channels in the time evolved wave function due to the single determinant restriction. An example of this is the triplet state of He. Initially electrons are started off in a singlet state (ground state of He). This symmetry is frozen in at all times since there is no term in the TDHF Hamiltonian that breaks this symmetry. Extension of the TDHF approximation to include linear combination of determinants have to be considered in this regard.

This work is supported in part by National Science Foundation (PHY-8406194).

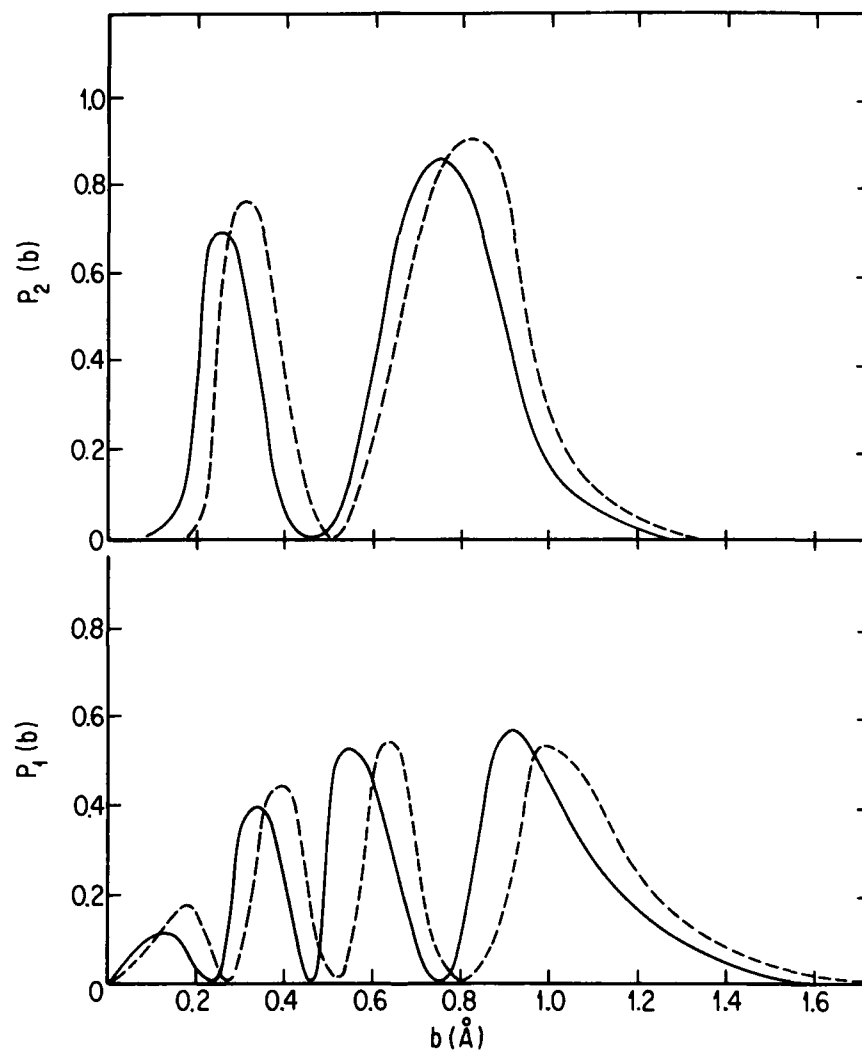


Fig. 3 a) Double charge transfer probability as a function of impact parameter for $E(\text{He}^{++}) = 30$ KeV. The solid curves are from axial symmetric calculations and the dashed curves are from those including the Coriolis coupling.
b) Corresponding single charge transfer probabilities.

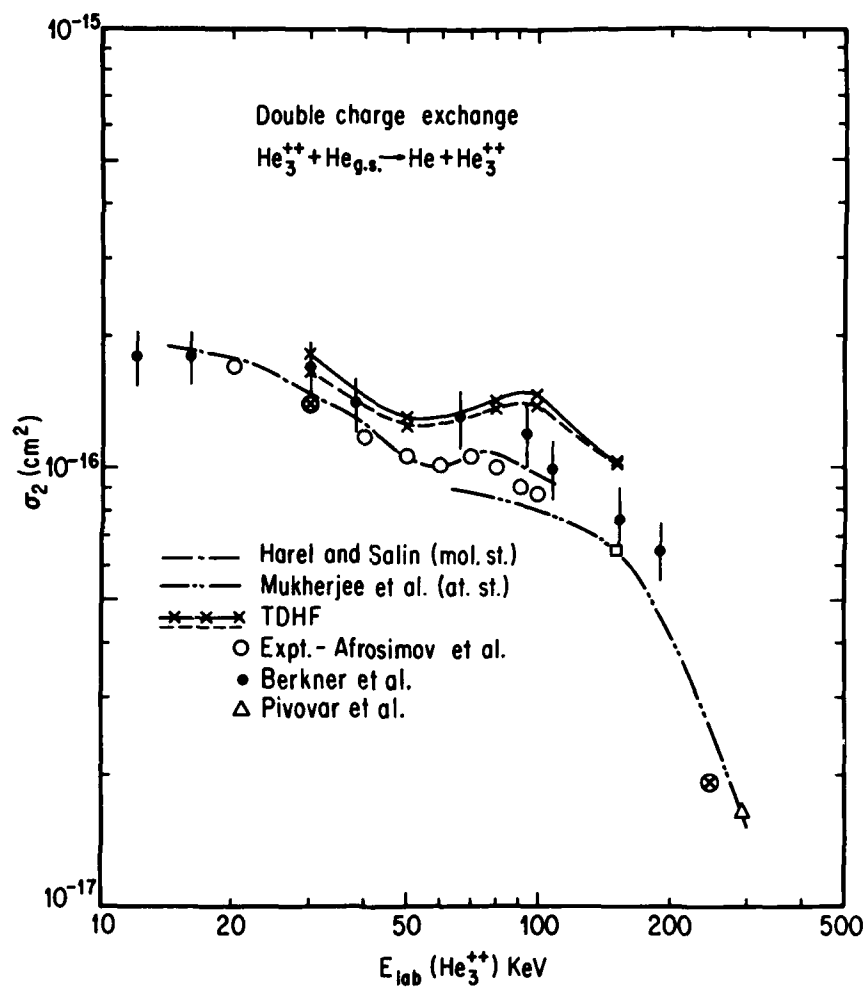


Fig. 4. Total double charge transfer cross sections vs. incident energy for $\text{He}^{++} + \text{He}$ collisions. The x's connected by solid line correspond to total capture in TDHF calculations and those connected by dashed lines are for capture into ground state only. Circled crosses: Coriolis coupling included.

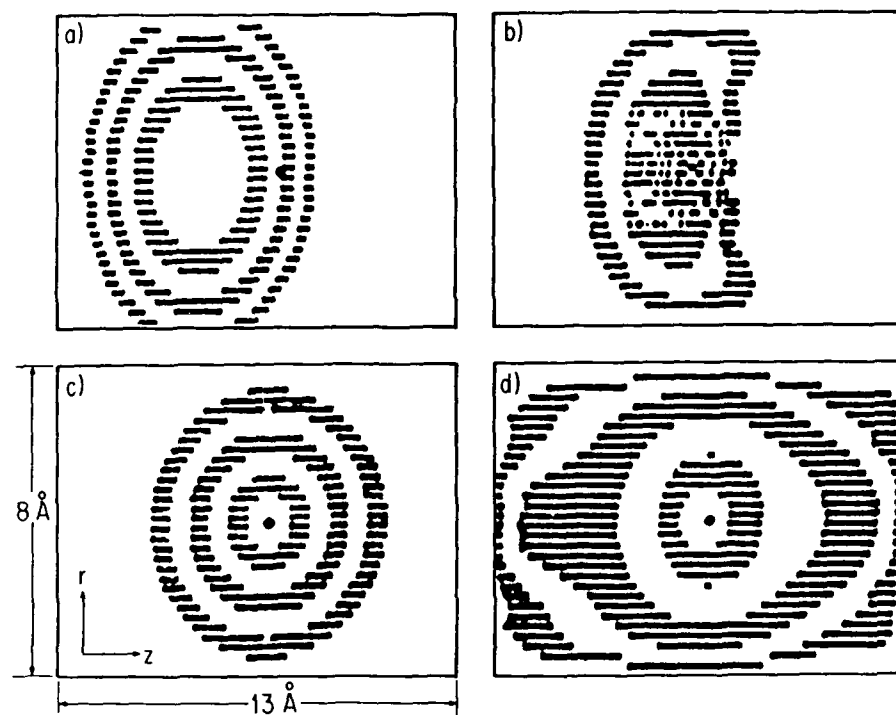


Fig. 5 Density distributions of muon and electron in muon-hydrogen collision at $E_{cm} = 0.27 \text{ eV}$. a) muon at $t=0$ b) muon at $t=35000 \text{ Å}/c$ c) electron at $t=0$. d) electron at $t=35000 \text{ Å}/c$.

REFERENCES

- 1) K. T. R. Davies, K. R. Sandhya Devi, S. E. Koonin and M. R. Strayer, 'Treatise on Heavy-Ion Science', Ed. by D. Allan Bromley, Plenum Press, Vol. 3 (1985) 1.
- 2) K. C. Kulander, K. R. S. Devi and S. E. Koonin, Phys. Rev. A25 (1982) 2968.
- 3) K. R. Sandhya Devi and J. D. Garcia, J. Phys. B16 (1983) 2837;
K.R. Sandhya Devi and J. D. Garcia, Phys. Rev. A30 (1984) 600.
- 4) V. Maruhn-Rezwani, N. Gruen and W. Scheid, Phys. Rev. Letts. 43 (1979) 43.
- 5) C. Bottcher, Phys. Rev. Letts. 48 (1982) 85.
- 6) N. H. Kwong and J. D. Garcia, contributed paper, XIV ICPEAC (1985).
- 7) J. J. Griffin, P. C. Lichtner and M. Dworzecka, Phys. Rev. C23 (1980) 1351.
- 8) Y. Alhassid and S. E. Koonin, Phys. Rev. C23 (1981) 1590.
- 9) K. R. Sandhya Devi and S. E. Koonin, Phys. Rev. Letts. 47 (1981) 27.
- 10) W. Lichten, Phys. Rev. 131 (1963) 229.
- 11) K. H. Berkner, R. V. Pyle, J.W. Stearns and J. C. Warren, Phys. Rev. 166 (1968) 44; V. V. Afrosimov, G. A. Leiko, A. Yu Mamaev and M. N. Panov, JETP 40 (1975) 661; L. J. Pivovar, V. M. Tubaev and M. T. Novikov, JETP 15 (1962) 1035.
- 12) C. Harel and A. Salin, J. Phys. B13 (1980) 785.
- 13) S. C. Mukherjee, K. Roy and N. C. Sil, J. Phys. B6 (1973) 467.

INNER-SHELL EXCITATION IN SLOW ION-ATOM COLLISIONS

Ilse WILLE

Bereich Kern- und Strahlenphysik, Hahn-Meitner-Institut für Kernforschung
Berlin, and Fachbereich Physik, Freie Universität Berlin, Postfach 390128,
D-1000 Berlin 39, West Germany

Recent progress in the field of inner-shell excitation in slow ion-atom collisions is reviewed. The theoretical description of inner-shell excitation in terms of the molecular-orbital model is summarized. Experimental results as well as the results of theoretical studies which aim at unravelling the excitation mechanisms are surveyed. Particular emphasis is placed on the mechanisms of L-shell and M-shell vacancy production.

1. INTRODUCTION

The field of inner-shell excitation in slow ion-atom collisions, i.e., collisions characterized by impact velocities much smaller than the orbital velocities of inner-shell electrons, has evolved in the past two decades into one of the most active areas of research in atomic-collision physics. The incentive to study inner-shell processes in slow collisions has arisen mainly from the intuitively attractive idea [1-4] that such collisions may proceed via the formation of a di-atomic, quasimolecular collision complex. The picture of a transient quasimolecule implies the assumption that electronic transitions between individual quasimolecular states are the basic excitation mechanisms in slow ion-atom collisions. Since the motion of inner-shell electrons in the collision complex is largely determined by the nuclear Coulomb fields, the quasimolecular states are expected to be well described by an independent-electron molecular-orbital (MO) approximation [3,4]. The identification of individual MO transitions in the transient quasimolecule constitutes the ultimate goal of inner-shell studies in slow ion-atom collisions.

The development of the field until about 1975 was characterized by a rapid accumulation of experimental data from (differential) inelastic-energy-loss measurements [5] and from spectroscopic (x-ray and Auger-electron) measurements [5-8]. The spectroscopic investigations of inner-shell excitation in slow ion-atom collisions were mainly concerned with total cross sections for K-shell vacancy production [7], and only a few studies of the impact parameter dependence of inner-shell vacancy production based on ion-x-ray and ion-Auger-electron coincidence measurements were reported [8]. These early experimental investigations were accompanied by the first successful attempts [9,10] to quantitatively interpret the data in terms of the MO model of atomic collisions. An important result of these analyses was the disclosure of $2p\pi-2p\sigma$ MO transitions induced by the rapid rotation of the internuclear axis at small distances of the collision partners as the principal mechanism of K-shell vacancy production in collision systems involving first-row ions and atoms.

The past decade has witnessed a tremendous expansion of the field with respect to the number and the degree of sophistication of experimental and theoretical studies. Much interest has been devoted to the investigation of heavy collision systems, in particular of systems for which the sum of the charge numbers of the collision partners exceeds the charge number of the heaviest known element ("superheavy quasimolecules"). The extension to heavier systems has led in a natural way to systematic studies of vacancy production in the

L-shell and in higher shells. In many of these investigations, detailed information on the excitation mechanisms has been derived by determining the impact parameter dependence of inner-shell vacancy production from ion-x-ray or ion-Auger-electron coincidence measurements. The availability of beams of slow ions in well-defined, high charge states has enabled one to study the dependence of inner-shell vacancy production on projectile charge state. In addition to the information gained from the spectroscopy of characteristic x-rays and Auger electrons, insight into the mechanisms of inner-shell vacancy production in slow ion-atom collisions has been obtained from the study of continuum x-ray and Auger-electron emission ("quasimolecular x-rays", "quasimolecular Auger electrons"). On the theoretical side, particular attention has been paid to the construction of quasimolecular single-electron potentials suitable for dynamical MO calculations.

In the present report, a survey will be given of recent progress in the field of inner-shell excitation in slow ion-atom collisions. After summarizing the MO description of inner-shell excitation, we compile and discuss recent experimental results as well as the results of theoretical analyses which, in one way or the other, have contributed to the understanding of the basic excitation mechanisms. Particular emphasis will be placed on L-shell and M-shell vacancy production. K-shell vacancy production has been reviewed at the 1981 ICPEAC conference [11], and selected new results in this subfield will be presented in another review at this conference [12]. No consideration will be given in this report to studies of continuum x-ray and Auger-electron emission and of super-heavy systems. Specific aspects of these topics will be surveyed in reviews presented elsewhere at this conference [12,13].

2. MOLECULAR-ORBITAL DESCRIPTION OF INNER-SHELL EXCITATION

We begin with a summary and discussion of the theoretical description of inner-shell excitation in terms of the MO model of atomic collisions. We assume throughout the validity of a classical description of the internuclear motion in the collision system ("impact parameter method") [10]. Accordingly, we have to deal with an explicitly time-dependent quantum-mechanical problem for the electronic motion in the collision complex. Further, we consider the many-electron scattering problem in the one-hole approximation, which corresponds to describing inner-shell vacancy production in terms of the "migration" of vacancies initially present at the Fermi surface of the collision complex down to inner-shell MOs deeply embedded in the Fermi sea. Cross sections calculated in the one-hole approximation must be interpreted as inclusive cross sections for vacancy production, i.e., cross sections for vacancy production in a specific atomic shell regardless of the final state of excitation of the other shells [14-16]. Experimental cross sections for inner-shell vacancy production are usually inclusive cross sections which comprise contributions from many final configurations carrying a vacancy in the inner shell under consideration.

In the one-hole approximation, the time-dependent scattering wavefunction describing the "active" vacancy is expanded as

$$\psi(\vec{r};t) = \sum_{k=1}^K a_k(t) \phi_k(\vec{r};\vec{R}(t)) \quad (1)$$

where the functions $\phi_k(\vec{r};\vec{R}(t))$ are basis functions depending parametrically on the time-dependent internuclear vector $\vec{R}(t)$, and the position vector \vec{r} is referred to a space-fixed frame of coordinates (spin degrees of freedom are suppressed throughout). In terms of MO wavefunctions $\phi_k(\vec{r};\vec{R}(t))$ referred to body-fixed (molecular) coordinates \vec{r}' , the functions ϕ_k may be expressed [10] as

$$\begin{aligned}\phi_k(\vec{r}; R(t), \theta(t)) &\equiv \tilde{\phi}_k(\vec{r}'; R(t)) \\ &= \exp(-i \theta(t) l_y) \tilde{\phi}_k(\vec{r}; R(t))\end{aligned}\quad (2)$$

where l_y is the electronic angular momentum perpendicular to the scattering plane (taken as the x-z plane) and $\theta(t)$ denotes the angle between z-axis and internuclear line. If inserted into the Schrödinger equation (atomic units are used throughout)

$$\{h(t) - i \frac{\partial}{\partial t}\} \psi(\vec{r}; t) = 0, \quad (3)$$

the expansion (1) leads to the system of coupled equations

$$i \underline{N} \dot{\underline{a}} = \underline{M} \underline{a} \quad (4)$$

for the expansion coefficients a_k comprising the column vector \underline{a} . The matrix \underline{N} is the overlap matrix with elements $N_{kk'}(t) = \langle \phi_k(t) | \phi_{k'}(t) \rangle$, and the elements of the coupling matrix \underline{M} are given by

$$M_{kk'}(t) = \langle \phi_k(t) | h(t) - i \frac{\partial}{\partial t} | \phi_{k'}(t) \rangle. \quad (5)$$

The (static) single-electron Hamiltonian $h(t)$ is assumed to have the form

$$h(t) = -\frac{1}{2} \nabla^2 + v^{\text{eff}}(\vec{r}; \vec{R}(t)) \quad (6)$$

where the effective, quasimolecular potential v^{eff} includes the interaction with the nuclear charges as well as screening corrections reflecting the presence of more than one electron in the collision complex. Inserting the representation (2) for the basis functions ϕ_k into eq. (5) and recognizing that the time derivative $\partial/\partial t$ is to be performed with the space-fixed coordinates \vec{r} kept fixed, one may decompose the coupling matrix \underline{M} as

$$\underline{M} = \underline{M}^{\text{pot}} + \underline{M}^{\text{dyn}}, \quad (7)$$

with the matrix elements of the potential-coupling part $\underline{M}^{\text{pot}}$ given by

$$M_{kk'}^{\text{pot}}(t) = \langle \tilde{\phi}_k(t) | h(t) | \tilde{\phi}_{k'}(t) \rangle \quad (8)$$

and those of the dynamic-coupling part $\underline{M}^{\text{dyn}}$ given by

$$M_{kk'}^{\text{dyn}}(t) = M_{kk'}^{\text{rad}}(t) + M_{kk'}^{\text{rot}}(t), \quad (9)$$

where

$$M_{kk'}^{\text{rad}}(t) = -i \dot{R} \langle \tilde{\phi}_k(t) | \frac{\partial}{\partial R} | \tilde{\phi}_{k'}(t) \rangle \quad (10)$$

and

$$M_{kk}^{\text{rot}}(t) = -\partial \langle \tilde{\phi}_k(t) | l_y | \tilde{\phi}_k(t) \rangle \quad (11)$$

are the matrix elements of radial and rotational (Coriolis) coupling, respectively.

The actual solution of system (4) requires three questions to be decided which have been the subject of substantial controversy in the past:

- (i) What is the appropriate choice for the effective potential v^{eff} ?
- (ii) What is the optimum choice for the basis functions ϕ_k ?
- (iii) In which way are the functions ϕ_k to be modified in order that the total wavefunction $\psi(\vec{r};t)$ fulfils correct scattering boundary conditions at $t = \pm \infty$?

Regarding question (i), the most sophisticated choice for the effective potential v^{eff} is certainly given by the self-consistent (two-center) Hartree-Fock (HF) potential. The difficulties arising in the solution of the HF problem at arbitrary, fixed internuclear distance R are essentially those encountered by quantum chemists when solving the (di-atomic) molecular-structure problem at a given equilibrium distance. The necessity in scattering calculations to obtain HF solutions for a large number of R -values, however, makes self-consistent calculations of v^{eff} a laborious and expensive task. Nevertheless, HF calculations have been performed for a variety of quasimolecular systems [10], in recent years particularly also in a relativistic framework [17]. The properties of the HF potentials form the standard to which the properties of other effective potentials are to be compared.

Effective quasimolecular potentials simpler than the HF potential can be calculated numerically within the framework of Thomas-Fermi (TF) theory [18,19] or can be constructed, in a completely analytic manner, from analytic atomic potentials [20-22]. The latter method of constructing the quasimolecular single-electron potential, which is referred to as the variable-screening model (VSM), employs a smooth interpolation of the atomic screening parameters between the united-atom and the separated-atom limits. The computing time required to obtain the energies and wavefunctions of the VSM Hamiltonian at fixed R is much less than the time spent for the solution of the corresponding HF problem, in particular for heavy collision systems involving a large number of electrons. Comparisons of the HF, TF and VSM energies and wavefunctions for truly inner-shell MO have shown that the different methods give results which agree within the accuracy required for dynamical MO calculations. This explains why in recent years mainly the VSM as by far the simplest method has been applied in such calculations.

When selecting the basis functions ϕ_k (or $\tilde{\phi}_k$) used in the expansion of the total scattering wavefunction for a particular excitation process (question (ii) above), one may optimize these functions in such a way that the effort spent in their construction and in the computation of coupling matrix elements becomes minimum and/or that the number of functions to be used in the expansion becomes as small as possible. The most straightforward choice for the orbitals $\tilde{\phi}_k$, which, however, does not necessarily meet one of the latter criteria, is that of adiabatic orbitals $\tilde{\phi}_k^{\text{ad}}$, i.e., orbitals which exactly diagonalize the Hamiltonian $h(R)$ at fixed R :

$$h(R) \tilde{\phi}_k^{\text{ad}} = \epsilon_k^{\text{ad}}(R) \tilde{\phi}_k^{\text{ad}} \quad (12)$$

The orbitals $\tilde{\phi}_k^{\text{ad}}$ form an orthogonal set and diagonalize the potential coupling matrix M^{pot} . After a trivial phase transformation, the coupled system (4) reduces in the adiabatic basis to

$$i \dot{\tilde{a}} = \tilde{M}^{\text{dyn}} \tilde{a} \quad (13)$$

with M^{dyn} given by eqs. (9) to (11).

The search for optimum basis sets in MO calculations has led to the construction of diabatic orbitals which depart from the strictly adiabatic MO. The objective in defining diabatic MO is [23,24] that these orbitals should diagonalize, at least partly, the dynamic-coupling matrix M^{dyn} . The elaboration of this concept has met, however, with considerable conceptual and practical difficulties [25]. Most interesting among the different approaches to construct diabatic MO appears to be the so-called "dynamical-state representation" [26] in which the rotational-coupling part of M^{dyn} is diagonalized along with the potential coupling M^{pot} . It must be realized, however, that the dynamical-state basis depends on both impact parameter and collision velocity. In general, it appears that the notion of diabatic MO is most useful in the context of a qualitative discussion of inner-shell excitation, in which "diabatic correlations" [27-29] are constructed to connect the separated-atom and united-atom orbitals of a collision system. In recent years, MO calculations using the coupled-state approach have been performed almost exclusively in the adiabatic basis.

Adiabatic MO (or any diabatic MO which merge in the adiabatic MO at large internuclear distances), if used in the expansion of the total scattering wavefunction $\psi(\mathbf{r};t)$, fail to properly take into account the translational motion along with one or the other nucleus, which the electron (or vacancy) experiences at large internuclear distances. Accordingly, the wavefunction $\psi(\mathbf{r};t)$ does not fulfil the correct scattering boundary conditions at $t = \pm \infty$ (we assume the time-zero to correspond to the minimum internuclear distance reached during the collision). It was realized early [30] that the latter deficiency of the adiabatic basis can be removed (question (iii) above) by multiplying the adiabatic MO by plane-wave factors ("translational factors") corresponding to the electronic translational motion at $R = \infty$. With decreasing internuclear distance, the modified MO basis including the asymptotic plane-wave factors becomes progressively inadequate since the electrons tend to increasingly "forget" to which nucleus they had been attached at large distances. In the united-atom limit no net translational motion should be left in the electronic basis functions. This aspect can be taken into account by introducing [31] into the plane-wave translational factors a "switching function" which smoothly interpolates between zero translational velocity in the united-atom limit and the full, asymptotic velocity at infinite internuclear distances. While many attempts have been made towards ab initio calculations of the switching function [25], it appears that in actual MO calculations on inner-shell excitation one must rely on phenomenological (parametrized) forms for this function. Usually, present-day calculations employ a common translational factor for all MO under consideration, thereby preserving the orthogonality of the adiabatic basis. It should be noted that the primary quasimolecular processes leading to inner-shell vacancy production essentially take place at fairly small internuclear distances (see below) and that, accordingly, their description is expected to be largely independent of the particular form chosen for the switching function. Only specific MO transitions at large internuclear distances, which decide whether an electron or vacancy eventually ends up in one or the other collision partner (and which therefore are associated with large momentum transfers), will be sensitive to the specific choice of translational factors.

In order to visualize the mechanisms of inner-shell vacancy production in slow ion-atom collisions, one usually uses MO correlation diagrams, i.e., diagrams in which the energies $\epsilon_k(R)$ of quasimolecular orbitals ϕ_k are plotted as function of internuclear distance R . MO correlation diagrams allow those orbitals to be selected which actively participate in a certain type of excitation process and which therefore should be included in a dynamical calculation pertaining to this process. As an example for an MO correlation diagram, we show in Fig. 1 the adiabatic diagram for the Kr-Kr collision system [32], calculated from the variable-screening model.

An important feature of MO correlation diagrams, which becomes apparent from

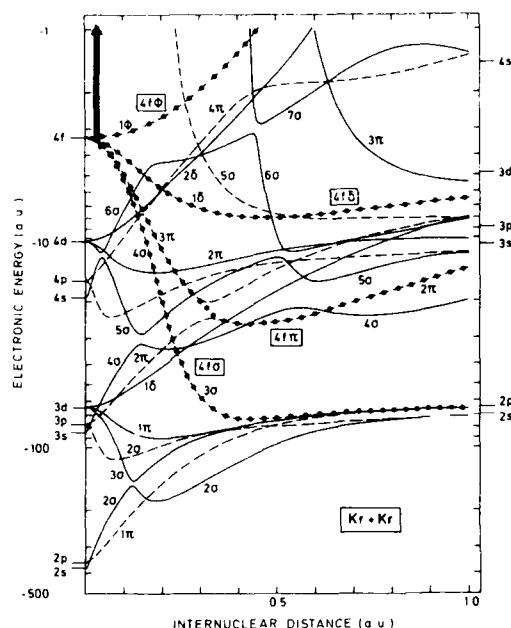


FIGURE 1
Adiabatic MO correlation diagram for the Kr-Kr system, calculated from the variable-screening model [21]. Full (broken) curves denote "gerade" ("ungerade") orbitals. The diabatic $4f\sigma$, $4f\pi$, $4f\delta$ and $4f\phi$ energy curves have been obtained from the adiabatic curves by ignoring the screening gaps at close avoided crossings. The heavy arrow indicates the possibility of direct $4f\sigma$ ionization. (From Ref. [32].)

Fig. 1, is the occurrence of energetically promoted MO, i.e., of MO whose binding energy decreases rapidly in a narrow R -range when small internuclear distances R are approached. If promoted MO become near-degenerate to unoccupied MO, electronic transitions are likely to occur. In the diagram of Fig. 1, the promoted $4f\sigma$ MO (in diabatic notation) is, at small R -values, near-degenerate to the other MO emerging from the united-atom $4f$ shell. Vacancies initially present in the (asymptotically empty) $4f\phi$ MO may then be transferred into the $4f\sigma$ MO via $4f\phi$ - $4f\delta$ - $4f\pi$ - $4f\sigma$ rotational coupling and eventually give rise to Kr L-shell vacancy production. As indicated by the heavy arrow in Fig. 1, $4f\sigma$ excitation in the Kr-Kr system may be accomplished also by direct coupling to the continuum ("direct MO ionization") at very small internuclear distances. In lighter collision systems, for example in the Ar-Ar system, the $4f\sigma$ MO is not bound at $R = 0$, but effectively merges in the continuum at a fairly large, "critical" internuclear distance R_c . In this case, it is appropriate to assume [33] that the $4f\sigma$ electrons are excited virtually with unit probability into the continuum if the internuclear distance falls below R_c . The impact parameter dependence of the excitation probability associated with this "promotion into the continuum" is expected to be well approximated by a unit step function.

The analysis of correlation diagrams like the one shown in Fig. 1 leads to distinguish three types of mechanisms which may be responsible for primary vacancy production in the quasimolecular collision complex:

- (i) electron promotion into the continuum (example: $4f\sigma$ promotion in Ar-Ar);
- (ii) rotationally induced transitions in the vicinity of the united-atom (n,l) shells (examples: $2p\sigma$ excitation via $2p\pi$ - $2p\sigma$ rotational coupling, $3d\sigma$ excitation via $3d\delta$ - $3d\pi$ - $3d\sigma$ rotational coupling, $4f\sigma$ excitation via $4f\phi$ - $4f\delta$ - $4f\pi$ - $4f\sigma$ rotational coupling);

(iii) direct MO ionization at very small internuclear distances (examples: $2p\sigma$, $3d\sigma$, $4f\sigma$ ionization).

The relative importance of these mechanisms depends on the charge numbers of the collision partners (particularly on the asymmetry of the system) and on collision velocity and impact parameter (particularly on the minimum internuclear distance reached in the collision) as well as on the availability of vacancies in specific incoming MO. The final distribution of vacancies over the various separated-atom shells is not only decided by the primary vacancy production processes at small internuclear distances, but also by "vacancy sharing processes" at large distances on the outgoing branch of the collision, which are mainly effected by radial couplings. An example for such type of process is provided by $2p\sigma$ - $1s\sigma$ vacancy sharing in slightly asymmetric collision systems.

The theoretical treatment of rotationally induced excitation as well as of vacancy sharing processes is usually possible within coupled-state calculations involving a fairly small number of rotationally or radially coupled, bound MO. Electron promotion into the continuum involves a large number of loosely bound MO as well as the continuum. An explicit coupled-state treatment of this mechanism is prohibitively complicated, but fortunately one may resort to the simple description in terms of the "critical" promotion distance R_c , which has been alluded to above. Direct MO ionization in the sense defined above is also hardly accessible to a full coupled-state solution. A first-order solution of this problem has been obtained [34] in the strict united-atom limit. In this limit, direct MO ionization can be viewed as being caused by the perturbation of the united-atom orbital due to the "coherent" motion of projectile and target nucleus.

A detailed qualitative survey of the mechanisms of inner-shell vacancy production in slow ion-atom collisions can be found in Ref. [25].

3. K-SHELL VACANCY PRODUCTION

Recent investigations of K-shell vacancy production in slow ion-atom collisions have mainly aimed at a detailed understanding of the role played in this type of process by rotationally induced transfer of vacancies out of the $2p\pi$ MO into the $2p\sigma$ MO at small internuclear distances. Simple theoretical considerations [10,25] lead to the prediction that the impact parameter dependence of the excitation probability associated with $2p\pi$ - $2p\sigma$ rotational coupling exhibits, at not too low collision velocity, a double-hump structure. The "kinematic" maximum at small impact parameters b (corresponding to center-of mass ion scattering angles $\theta_{CM} = 90^\circ$) is of purely geometric origin, and its shape is determined in the sudden approximation [25] by $P(\theta_{CM}) = \sin^2 \theta_{CM}$, if one vacancy is assumed to be initially present in the $2p\pi_x$ MO. The "adiabatic" maximum shows up at larger b -values, and its position and height depend on the $2p\pi$ - $2p\sigma$ energy splitting $\Delta_{2p\pi-2p\sigma}(R)$. The b -dependence of the $2p\pi$ - $2p\sigma$ excitation probability for an arbitrary combination of collision partners can be approximately obtained, over the full b -range, by scaling [35] the coupled-state solution for a particular system. If a description of the internuclear motion in terms of a straight-line trajectory is employed (which usually is appropriate for b -values in the range of the adiabatic maximum), the scaling law predicts the $2p\pi$ - $2p\sigma$ excitation probabilities for different collision systems and collision velocities to fall on a universal curve if the probabilities are plotted as function of the reduced impact parameter $b' = (\alpha/v_0)^{1/3} b$, where α is the coefficient in a quadratic approximation to the $2p\pi$ - $2p\sigma$ energy splitting ($\Delta_{2p\pi-2p\sigma} = \alpha R^2$) and v_0 is the collision velocity.

In Fig. 2, the experimental K-shell vacancy production for various near-symmetric collisions involving gas targets [36] is plotted as function of the reduced impact parameter b' . The full curve is the universal curve given by the $2p\pi$ - $2p\sigma$ scaling law, normalized to one incoming $2p\pi_x$ vacancy. The peak values

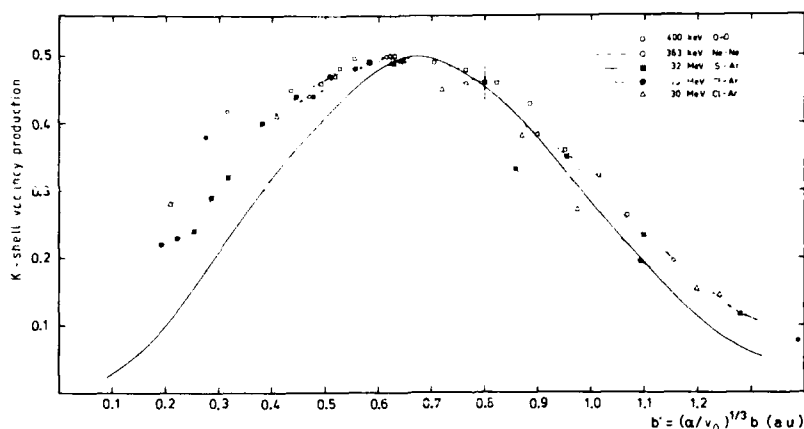


FIGURE 2

Impact parameter dependence of K-shell vacancy production in near-symmetric collisions involving gas targets. The abscissa is defined in terms of the reduced impact parameter b' explained in the text. (From Ref. [36].)

of the experimental data sets have been normalized to the peak value of the theoretical curve. The good overall agreement between theory and experiment suggests that the maximum seen in the data indeed reflects the adiabatic maximum of $2p\pi$ - $2p\sigma$ rotational coupling. Notably enough, the agreement not only holds for systems involving first-row ions and atoms, in which $2p\pi$ vacancies are carried into the collision, but also for heavier systems in which outer-shell interactions at an early stage of the collision are responsible for $2p\pi$ vacancy production. The fact that at small b' -values the experimental data are somewhat larger than the calculated vacancy production can be partly ascribed to the use of straight-line internuclear trajectories in the calculation of the theoretical curve of Fig. 2. Use of curved trajectories makes the theoretical vacancy production at small impact parameters rise towards the kinematic maximum. Closer inspection shows, however, that the data systematically tend to stay above the theoretical vacancy production in the range between kinematic and adiabatic maximum ("filling of the valley" [37]). Explanations for this filling can be sought for in an inadequacy of the scaling law for $2p\pi$ - $2p\sigma$ rotational coupling and/or in a breakdown of the two-state approximation, particularly in direct coupling of the $2p\sigma$ MO to the continuum. No conclusive answer has been found, however, to this question.

The detailed shape of the kinematic maximum of $2p\pi$ - $2p\sigma$ rotational coupling has been explored in a number of measurements extending to $\theta_{CM} = 180^\circ$. Figure 3 shows results for the I-Aq system at 60 MeV collision energy [38] in comparison to theoretical curves corresponding to the sudden approximation and to the $2p\pi$ - $2p\sigma$ scaling law based on curved internuclear trajectories. Good agreement between experiment and theory is observed. A similar agreement has been achieved for the Ca-Ti system at 30 MeV collision energy [39].

The agreement between theory and the gas-target data in Fig. 2 does not fully extend to collisions involving solid targets. Figure 4 shows solid-target data for different collision systems, plotted as function of the reduced impact parameter b' (the normalization of the data is the same as in Fig. 2). While

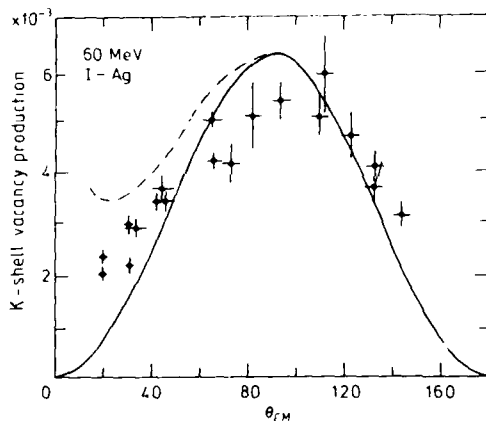


FIGURE 3
K-shell vacancy production in 60 MeV I-Ag collisions, plotted as function of the center-of-mass ion scattering angle θ_{CM} . Full curve: prediction of the sudden approximation; broken curve: prediction of the $2p\pi$ - $2p\sigma$ scaling law. The theoretical curves have been arbitrarily normalized to the experimental data. (From Ref. [38].)

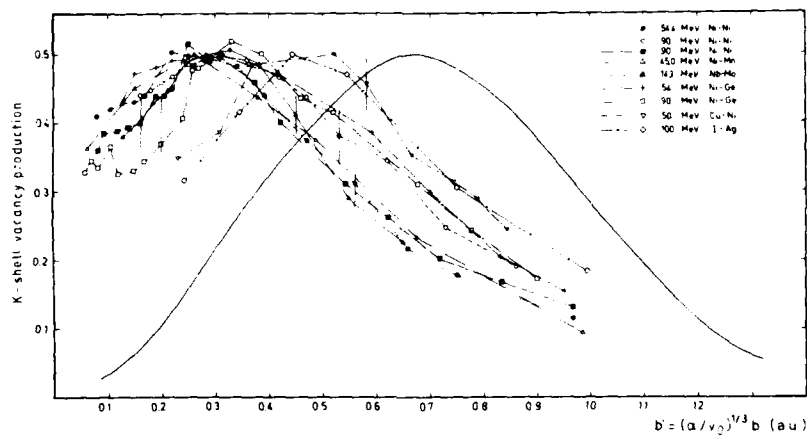


FIGURE 4
Same as Fig. 2, for near-symmetric collisions involving solid targets. (From Ref. [36].)

the different data sets in Fig. 4 exhibit a broad maximum, the b' -values about which the experimental maxima are centered are roughly by a factor of two smaller than the corresponding value for the theoretical maximum. This "shift of the adiabatic maximum" is not understood hitherto. The basic difference between collisions in (thin) gas targets and in solid targets lies in the possibility of multiple collisions in solid targets. Multiple collisions are expected to influence K-shell vacancy production mainly in two ways. First, due to previous collisions with target atoms, the charge state of projectile ions which undergo K-vacancy-producing collisions may differ from the initial charge state. In collision systems in which the L-shells of the collision partners are initially occupied, L-shell vacancies may be created in collisions prior to the K-vacancy-producing collision and may enhance the number of $2p\pi$ vacancies available in the latter collision. Such an enhancement possibly provides an explanation for

the fact that the observed K-shell vacancy production [11] in (solid-target) Br-Se and Br-Rh collisions is much larger than the vacancy production in the (gas-target) Br-Kr system. Regarding the impact parameter dependence of K-shell vacancy production, this dependence will certainly be influenced to some extent by the mechanisms of L-shell vacancy production in previous collisions, but there are no conclusive arguments that these mechanisms conspire in such a way that the adiabatic maximum of $2p\pi$ - $2p\sigma$ rotational coupling is systematically shifted to smaller impact parameters. Second, multiple collisions in solid targets may in principle prohibit the unambiguous assignment of an impact parameter to a specific ion scattering angle because the ion may undergo, after the close collision in which a K-vacancy has been produced, further (elastic or inelastic) collisions. Since, however, successive close collisions are rather unlikely, one may expect the impact parameter dependence of K-shell vacancy production in solid targets to be a well-defined concept.

Much information on the mechanisms of K-shell vacancy production in slow ion-atom collisions has been gained in recent years by studying the dependence of this type of process on projectile charge state. Of particular interest is the use of highly charged, heavy projectiles carrying L-shell vacancies. Variation of the number of L-shell vacancies provides a test of the $2p\pi$ - $2p\sigma$ rotational-coupling theory which predicts K-shell vacancy production to be proportional to the number of projectile $2p$ vacancies. Studies of K-shell vacancy production using highly charged, slow ions will be discussed in detail in the review given by Schuch [12] at this conference. Therefore, we confine ourselves here to presenting two examples which seem particularly instructive.

In Fig. 5, total cross sections for Xe K-shell vacancy production in Sm^{q+} -Xe collisions [40] are shown as function of projectile charge state q . A rapid (linear) increase of the cross section is seen to set in at $q = 53$, i.e., when the projectile starts to carry $2p$ vacancies into the collision. The analysis of the cross section increase for $q > 52$ has shown [40] that the data are compatible with the prediction of a relativistically corrected [41] $2p\pi$ - $2p\sigma$ rotational-coupling model. The slow increase of the Xe K-shell cross section setting in already at $q = 45$, i.e., when the Sm $3p$ shell starts to carry vacancies into the collision, cannot be easily understood because a large number of individual MO transitions may contribute to vacancy transfer from the Sm M-shell into the Xe K-shell.

Figure 6 displays the impact parameter dependence of K-shell vacancy production in 3.6 MeV/nucleon Xe^{q+} -Xe collisions [42] for projectile charge states $q = 43, 45, 47$. The increase in the vacancy production with increasing q reflects the fact that for $q = 45$ and 47 one and three L-shell vacancies, respectively, are present in the projectile ion. For $q = 45$, the experimental data are compared to theoretical curves corresponding to non-relativistic [35] and relativistic [41] $2p\pi$ - $2p\sigma$ rotational coupling. The relativistic calculation appears to be in better agreement with the data than the non-relativistic result.

The relative distribution of vacancies over the K-shells of the lighter and heavier partner in near-symmetric collision systems is determined by $2p\sigma$ - $1s\sigma$ vacancy sharing processes. Extensive studies have shown that the observed sharing ratios in heavy collision systems [43] can be explained quite well in terms of the analytic Nemkov-Meyerhof model [44]. Substantial discrepancies between the predictions of this model and the experimental data have been found for light collision systems, in particular for systems with united-atom charge number smaller than 15. In the latter case, a better description of $2p\sigma$ - $1s\sigma$ vacancy sharing can be achieved [45] by applying the two-state model of Nikitin [46] with parameter values determined from fits to realistic MO energy differences. Interesting effects have recently been disclosed in studies of "double-passage" $2p\sigma$ - $1s\sigma$ vacancy sharing using hydrogen-like projectile ions which serve to carry one $1s\sigma$ vacancy into the collision complex. Pertinent results will be discussed in the review presented by Schuch [12] at this conference.

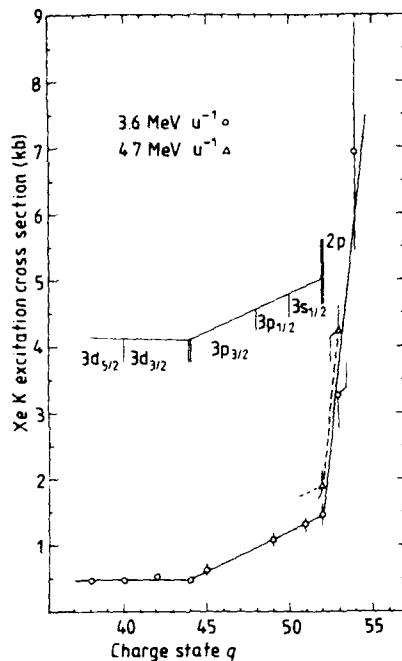


FIGURE 5
Dependence of the total cross section for Xe K-shell vacancy production in 3.6 MeV/nucleon and 4.7 MeV/nucleon Sm^{q+} -Xe collisions on projectile charge state q . Full and broken curves are drawn to guide the eye only. The vertical bars labelled by subshell quantum numbers mark those q -values at which the corresponding subshells start to carry vacancies into the collision. (From Ref. [40].)

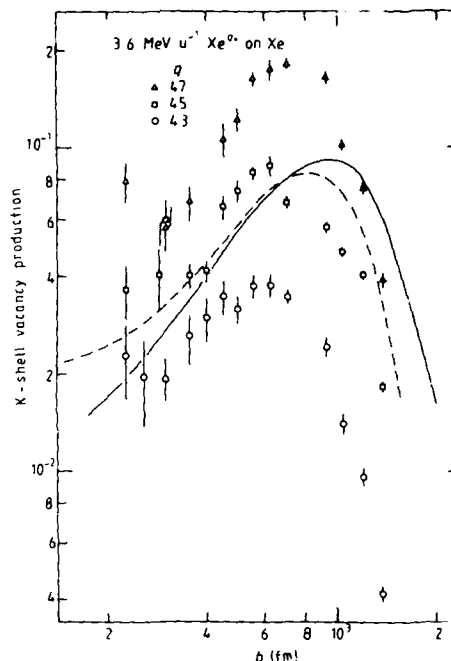


FIGURE 6
Impact parameter dependence of K-shell vacancy production in Xe^{q+} -Xe collisions for different charge states q . Full (broken) curve: prediction of non-relativistic (relativistic) $2p\pi$ - $2p\sigma$ rotational-coupling theory. (From Ref. [42].)

In strongly asymmetric collision systems, direct iso ionization may prevail as the dominant mechanism of K-shell vacancy production in the heavier partner. The study of iso vacancy production is of particular relevance in very heavy collision systems leading to the formation of superheavy quasimolecules. We shall not go into details here because these matters will be discussed in another review at this conference [13].

4. L-SHELL VACANCY PRODUCTION

The process of L-shell vacancy production in slow ion-atom collisions has been of basic importance in the conceptual development of the MO model of atomic collisions [3]. However, systematic investigations exploring the details of the quasimolecular mechanisms of L-shell vacancy production have been undertaken only in the past few years. In the following, we describe the progress made in this subfield by first considering light collision systems including the prototype system Ar-Ar as well as near-symmetric systems involving argon as one of the collision partners. Subsequently, heavy collision systems will be discussed, with particular consideration of the prototype case Kr-Kr.

4.1. Light collision systems

Experiments relevant to L-shell vacancy production in Ar-Ar collisions were first performed by Everhart and coworkers [47,48] and by Afrosimov et al. [49], who observed step-like rises in the inelastic energy loss as function of minimum internuclear distance R_0 when R_0 dropped below about 0.5 and 0.2 a.u., respectively. These results were linked to Ar L-shell vacancy production by Fano and Lichten [3,4] who associated peak structures in the inelastic-energy-loss spectra to the excitation of a definite number of Ar L-shell electrons, in addition to a certain number of M-shell excitations. More specifically, Fano and Lichten ascribed the steep rise in the inelastic energy loss at $R_0 \approx 0.5$ a.u. to electron promotion along the diabatic $4f\sigma$ MO in the quasimolecular collision complex. The early spectroscopic measurements of total cross sections in light collision systems [33,50-53] essentially confirmed $4f\sigma$ promotion as the dominant mechanism of L-shell vacancy production in the lighter collision partner.

Finer details of the quasimolecular mechanisms of L-shell vacancy production have been disclosed by performing ion-Auger-electron and ion-x-ray coincidence measurements. Thomson et al. [54,55], who measured ion-Auger-electron coincidences in the Ar-Ar collision system for a single projectile scattering angle and a variety of collision energies, observed a step in the Auger-electron production when R_0 dropped below about 0.2 a.u. At this position, also the inelastic-energy-loss measurements had revealed a step-like rise. Thomson [55] ascribed the rise in the Ar-L Auger-electron production to the onset of rotationally induced excitation of $3d\pi$ and $3d\sigma$ electrons into the initially empty $3d\delta$ MO. Schmid and Garcia [56] approximately solved the $3d\delta$ - $3d\pi$ - $3d\sigma$ rotational-coupling problem and obtained, by superimposing the contribution of this excitation mechanism and of $4f\sigma$ promotion, satisfactory agreement between their calculations and the experimental data of Thomson et al.

The impact parameter dependence of L-shell vacancy production in Ar-Ar collisions at 300, 500 and 700 keV collision energy has been investigated both experimentally and theoretically by Shanker et al. [57]. In the experimental part of this study, Ar-L Auger electrons were detected in coincidence with scattered projectile ions. The theoretical analysis of the experimental data of Shanker et al. assumed $4f\sigma$ promotion and $3d\delta$ - $3d\pi$ - $3d\sigma$ rotational coupling to be the relevant excitation mechanisms. The $3d\delta$ - $3d\pi$ - $3d\sigma$ rotational-coupling problem was numerically solved by using united-atom values for the coupling matrix elements as well as (diabatized) MO energies computed from the variable-screening model. The number of incoming $3d\delta$ vacancies, $N_{3d\delta}$, was used as a fitting parameter whose value was determined separately at each collision energy by adjusting the total theoretical vacancy production to the experimental data in the range of impact parameters $b < 0.25$ a.u.

Figure 7 displays the results of Shanker et al. At 300 keV collision energy, the experimental vacancy production at large impact parameters exhibits a steep rise towards a value of two, which sets in at $b \approx 0.5$ a.u. and which obviously corresponds to the rise seen at $R_0 \approx 0.5$ a.u. in the inelastic-energy-loss data and in the coincidence data of Thomson et al. For all collision energies, a further rise in the measured impact parameter dependence of Ar L-shell vacancy production sets in at $b \approx 0.25$ a.u. The shapes of the experimental data are

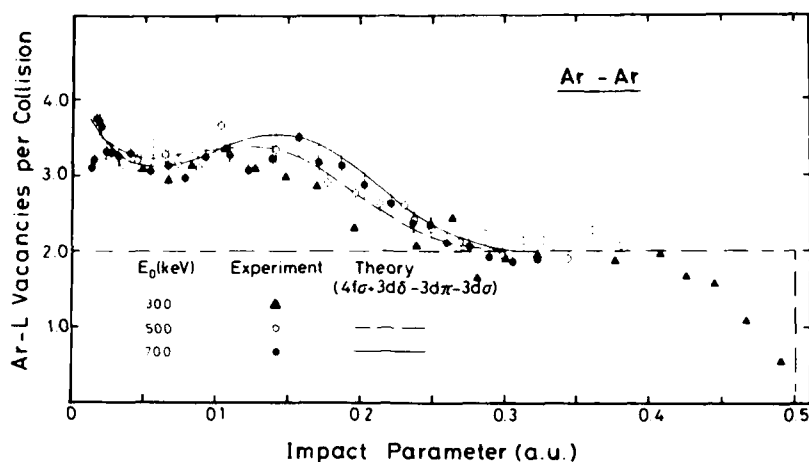


FIGURE 7
Impact parameter dependence of L-shell vacancy production in Ar-Ar collisions at different collision energies E_0 . The broken curve gives the theoretical prediction corresponding to $4f\sigma$ promotion. (From Ref. [57].)

quite well reproduced by the theoretical results for $4f\sigma$ promotion plus $3d\sigma$ - $3d\pi$ - $3d\sigma$ rotational coupling, with fitted values of $N_{3d\delta}$ ranging between 1.5 and 2.0. The enhancement of the measured vacancy production in the range $b < 0.25$ a.u. is interpreted as the contribution of the adiabatic maximum of $3d\delta$ - $3d\pi$ - $3d\sigma$ rotational coupling. In the 700 keV data, some indication is found for the appearance of a kinematic maximum which, according to the sudden approximation [25], is predicted to occur at an impact parameter corresponding to $\theta_{CM} = 90^\circ$.

A number of recent investigations have considered the role of $3d\delta$ - $3d\pi$ - $3d\sigma$ rotational coupling in near-symmetric, light collision systems. In near-symmetric systems, $3d\pi$ excitation is expected to contribute to L-shell vacancy production in the lighter collision partner, while $3d\sigma$ excitation should give rise to L-shell vacancy production in the heavier partner.

In the study of Schneider et al. [58], total cross sections for Si-L and Ar-L vacancy production in slow Si-Ar collisions were determined from Auger-electron measurements and were analyzed within the framework used by Shanker et al. [57] in their analysis of the Ar-Ar collision system. While the contribution of rotationally induced $3d\pi$ excitation to Si L-shell vacancy production turns out to be too small to be discriminated from the $4f\sigma$ contribution, rotationally induced $3d\sigma$ excitation accounts fairly well for the cross section of Ar L-shell vacancy production for collision energies up to 200 keV if a value of two is chosen for the vacancy occupation number $N_{3d\delta}$.

Shanker et al. [59] have measured and analyzed the impact parameter dependence of Ar L-shell vacancy production in 200, 400 and 700 Ne-Ar collisions. The analysis of the data in terms of rotationally induced $3d\sigma$ excitation showed that the shape of the observed b -dependence agrees with the calculated shape only for b -values in the range of the adiabatic maximum and beyond. Values of about 2.5, i.e., values slightly larger than in the Ar-Ar and Si-Ar cases, have

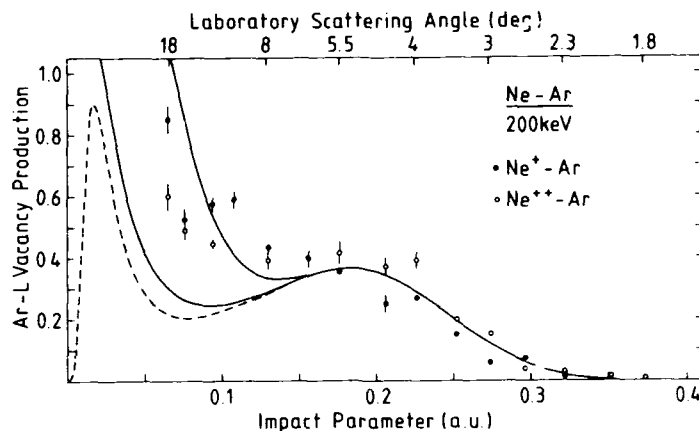


FIGURE 8

Impact parameter dependence of Ar L-shell vacancy production in 200 keV Ne-Ar collisions. Broken curve: theoretical prediction for rotationally induced 3d excitation; lower (upper) full curve: sum of theoretical predictions for rotationally induced 3d excitation and for direct 3d ionization, calculated with a united-atom 3d binding energy corresponding to the doubly ionized (neutral) system. (From Ref. [59].)

been determined for N3d δ by fitting the theoretical curves to the data in that range. In the small- b range, the measured vacancy production is substantially larger than the theoretical result for rotationally induced 3d excitation (cf. the 200 keV case shown in Fig. 8). The discrepancy between experiment and the rotational-coupling theory may be qualitatively explained by the onset of direct ionization of the loosely bound 3d MO at small internuclear distances. The contribution of this mechanism to Ar L-shell vacancy production has been evaluated by Shanker et al. [59] within a non-perturbative generalization [60] of the united-atom ionization model of Briggs [34]. Figure 8 shows theoretical results including the contribution of direct 3d ionization for two different choices of the effective binding energy of the united-atom 3d orbital. The strong dependence of the ionization probability upon the latter quantity renders difficult a conclusive assessment of the results.

Bilau et al. [61] have studied the impact parameter dependence of Kr L-shell vacancy production in Ar-Kr collisions for energies ranging between 0.97 and 10 MeV by measuring ion-x-ray coincidences. The Ar-Kr system has about the same ratio of projectile to target charge number as has the Ne-Ar system. While, however, the 3d δ MO in the Ne-Ar system is empty prior to the collision, in the Ar-Kr system all MO correlating to the united-atom 3d shell are initially occupied with electrons. Hence, Kr L-shell vacancy production in Ar-Kr collisions is expected to reflect the "dynamical" creation of vacancies in the 3d δ and 3d π MO at an early stage of the collision. Bilau et al. have analyzed their experimental data by solving the 3d δ -3d π -3d σ rotational-coupling problem separately for one incoming 3d δ vacancy and one incoming 3d π vacancy, respectively (this procedure corresponds to assuming incoherent vacancy production in the latter MO). By fitting the calculated 3d δ vacancy production to the experimental data,

values of the vacancy occupation numbers $N_{3d\delta}$ and $N_{3d\pi}$ were determined separately at each collision energy. While the sum $N_{3d\delta} + N_{3d\pi}$ rises monotonically with increasing collision energy, the ratio $N_{3d\delta}/N_{3d\pi}$ decreases more or less monotonically from a very large value at the lowest energy to values considerably smaller than unity at the highest energies. This tendency is hard to understand because the $3d\pi$ MO is, at large internuclear distances, much stronger bound than the $3d\delta$ MO. Accordingly, excitation of $3d\pi$ electrons into empty bound or into continuum orbitals is expected to be much less likely than excitation of $3d\delta$ electrons.

4.2. Heavy collision systems

In the realm of L-shell vacancy production in heavy collision systems, the Kr-Kr system plays a similar prototype role as does the Ar-Ar system for light collision systems. While measurements of the inelastic energy loss in Kr-Kr collisions did not allow specific conclusions regarding the mechanisms of L-shell vacancy production to be drawn, much progress in the understanding of these mechanisms has been achieved recently by measuring and analyzing Kr-L x-ray production.

Woerlee et al. [62] have measured total cross sections for Kr-L x-ray production in Kr-Kr collisions for collision energies ranging between 0.175 and 1.6 MeV. The corresponding vacancy production cross sections (deduced by using the single-vacancy value for the Kr-L fluorescence yield) showed, as function of collision energy, a behavior similar to the cross sections for L-shell vacancy production in Ar-Ar collisions [33]. Therefore, Woerlee et al. assumed 4f_o promotion to be the dominant excitation mechanism and extracted a value of 0.19 a.u. for the promotion distance R_C . Such a large value for R_C is clearly at variance with the calculated behavior of the 4f_o MO in the Kr-Kr system. Figure 1 shows that the united-atom 4f orbital has a fairly large binding energy.

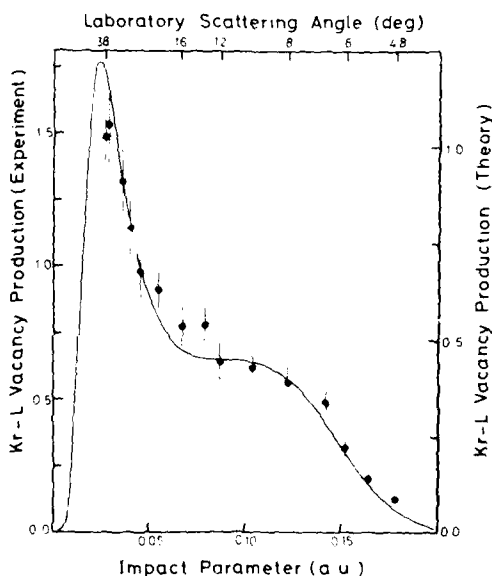


FIGURE 9
Impact parameter dependence of L-shell vacancy production in 1.4 MeV Kr-Kr collisions. Full curve: theoretical prediction for rotationally induced 4f_o excitation. The right-hand scale has been expanded in such a way that the theoretical curve fits the experimental data. (From Ref. [32].)

The impact parameter dependence of L-shell vacancy production in Kr-Kr collisions as well as total cross sections have been measured by Shanker et al. [63,62] for collision energies ranging from 0.7 to 3.0 MeV. The total cross sections are considerably smaller than those measured by Woerlee et al. [62] (on average by a factor of 2.5). The shapes of the b -dependent data of Shanker et al. grossly deviate from the step-functional form typical of $4f\sigma$ promotion. As an example, Fig. 9 displays the b -dependence of Kr L-shell vacancy production at 1.4 MeV collision energy. The behavior of the measured b -dependence is reminiscent of a developing double-hump structure. Shanker et al. have associated this behavior with $4f\sigma$ excitation via $4f\phi$ - $4f\delta$ - $4f\pi$ - $4f\sigma$ rotational coupling. For quantitative analysis of their data, they assumed vacancies to be initially present in the $4f\phi$ MO and solved the $4f\phi$ - $4f\delta$ - $4f\pi$ - $4f\sigma$ rotational coupling problem within a framework similar to the one employed in the solution of the $3d\delta$ - $3d\pi$ - $3d\sigma$ problem in Ar-Ar and Ne-Ar collisions [57,59]. As exemplified by Fig. 9, the shape of the measured b -dependence of Kr L-shell vacancy production is well reproduced by the calculations for collision energies up to 1.75 MeV. For higher energies, the data at small impact parameters exhibit an enhancement of the vacancy production over the rotational-coupling contribution. Theoretical estimates support the assumption that direct $4f\sigma$ ionization is responsible for this enhancement. The absolute magnitude of Kr L-shell vacancy production as measured by Shanker et al. is somewhat underestimated by the rotational-coupling calculations even if the maximum (asymptotic) value of four is assumed for the initial vacancy occupation number $N_{4f\phi}$. The theoretical results corresponding to $N_{4f\phi} = 4$ can be adjusted to the data by multiplying them

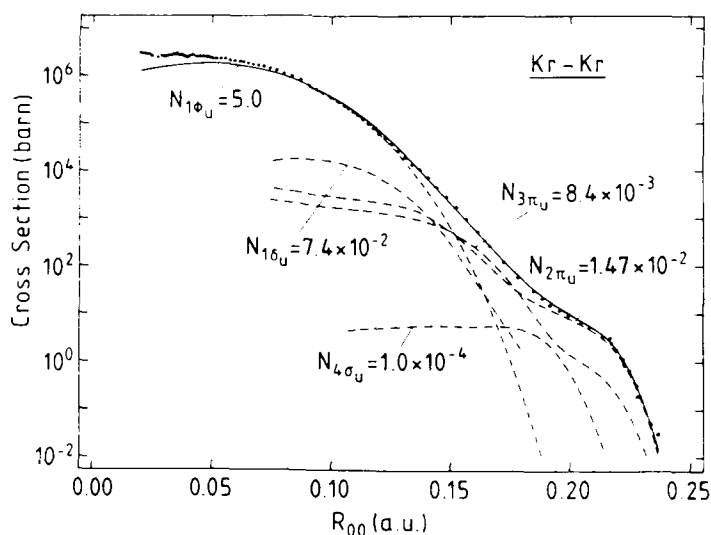


FIGURE 10

Total cross sections for L-shell vacancy production in Kr-Kr collisions, plotted as function of the minimum internuclear distance at zero impact parameter. Broken curves: calculated partial cross sections corresponding to the indicated number of vacancies in the incoming MO; full curve: sum of partial cross sections. (From Refs. [64,65].)

by a "normalization factor" with average value of about 1.5 (note the different scales for experimental and theoretical results in Fig. 9, which reflect the normalization factor). The occurrence of this factor is not yet understood.

Total cross sections for Kr L-shell vacancy production in slow Kr-Kr collisions have been measured recently by Cleff et al. [64] down to collision energies as low as 90 keV. In the plateau region of the cross section, the values of Cleff et al. are larger than those of Shanker et al. [32] by about 30%. If plotted (cf. Fig. 10) against the minimum internuclear distance at zero impact parameter, R_{00} , the cross sections of Cleff et al. reveal a shoulder-like structure at $R_{00} \approx 0.2$ a.u. (or, correspondingly, at a collision energy of about 140 keV). This feature points to the presence of new excitation mechanisms prevailing at very low collision energies. Cleff et al. have analyzed [65] their experimental results by assuming vacancy production in the $4f\sigma$ MO to be effected not only by $4f\sigma-4f\delta-4f\pi-4f\sigma$ rotational coupling, but also by radial and rotational couplings with the MO which emerge from the separated-atom M- and N-shells and which form real or avoided crossings with the $4f\sigma$ MO at non-zero internuclear distances (cf. the Kr-Kr correlation diagram shown in Fig. 1). These MO are expected to carry with non-zero (albeit small) probability "dynamically created" vacancies into the coupling region. By performing coupled-state calculations within the space of the adiabatic $3\sigma_u$, $4\sigma_u$, $2\pi_u$, $3\pi_u$, $4\pi_u$, $1\delta_u$ and $1\phi_u$ MO, Cleff et al. obtained "partial" cross sections for the different incoming MO, which are shown as broken curves in Fig. 10 (the initial vacancy occupation numbers for the incoming MO have been used as fit parameters; the value $N_{4f\sigma} = 5.0$ may be interpreted to include a "normalization factor" of 1.25). The comparison between the experimental data and the calculated total cross section for $4f\sigma$ excitation (full curve in Fig. 10) suggests that the structure seen in the data at $R_{00} \approx 0.2$ a.u. corresponds to rotationally induced transfer of vacancies out of the $2\pi_u$ MO into the $3\sigma_u$ MO (cf. Fig. 1).

Similar structure as in the Kr-Kr case has been observed by Cleff et al. [64] in the threshold region of the L-shell cross sections in the (symmetric) Ge-Ge, Mo-Mo, In-In and Xe-Xe collision systems. The results await further analysis. Very recently, Cleff et al. have also measured [66] the impact parameter dependence of L-shell vacancy production in Kr-Kr collisions and have found that their results essentially confirm those of Shanker et al. [32].

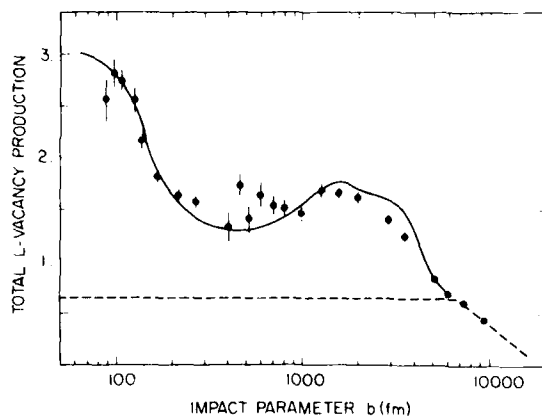


FIGURE 11
Impact parameter dependence of L-shell vacancy production in 63 MeV I-Aq collisions. Full circles: experimental results of Ref. [68]; broken curve: estimated contribution of $4f\sigma$ excitation [68]; full curve: sum of estimated $4f\sigma$ contribution and of calculated contributions of $3d\delta-3d\pi-3d\sigma$ and $3p\pi-3p\sigma$ rotational coupling [69]. (From Ref. [68].)

The impact parameter dependence of L-shell vacancy production in collisions involving solid targets has been systematically investigated by Presser et al. [67] for 17 to 40 MeV Ag-Ag and Ag-Cs collisions and by Morenzoni et al. [68] for 40 and 63 MeV I-Ag collisions. One may expect that multiple-collision effects in solid targets enhance the contributions of rotational-coupling processes in the vicinity of the united-atom 3d and 3p shells. The analyses of Presser et al. and Morenzoni et al. indeed have shown that the experimental data at small impact parameters can be essentially explained in terms of a superposition of contributions from 3d δ -3d π -3d σ and 3p π -3p σ rotational coupling. By adjusting the theoretical results to the data, a value of about two was determined for the ratio $N_{3p\pi}/N_{3d\delta}$ of the numbers of incoming vacancies in the 3p π and 3d δ MO. Figure 11 shows the experimental results of Morenzoni et al. for 63 MeV I-Ag collisions together with a theoretical curve obtained by superimposing the calculated contributions of 3d δ -3d π -3d σ and 3p π -3p σ rotational coupling [69] onto an estimated contribution of 4f σ excitation.

Vacancy sharing processes between MO correlating to the L-shells of the lighter and the heavier partner, respectively, in near-symmetric, heavy collision systems have been studied by Meyerhof et al. [70]. The experimental sharing ratios can be quantitatively understood in terms of the Nemkov-Meyerhof vacancy sharing model [44] if one assumes that L-L vacancy sharing takes place predominantly between those MO whose energy separation is smallest, i.e., between the MO correlating to the L₃-subshell of the heavier partner and the L₁-subshell of the lighter partner. In their analysis of L-subshell cross section, Meyerhof et al. [70] have investigated the relevance of diabatic correlation rules [27,28]. They found that the correlation of the 4f σ MO tends to change from "minimum promotion" (as expressed by the Barat-Lichten correlation rule [27]) in symmetric systems towards "maximum promotion" (as expressed by the correlation rule of Eichler et al. [28]) in asymmetric systems.

In strongly asymmetric, heavy collision systems, vacancy sharing processes may occur between the MO correlating to the K-shell of the lighter partner and the L-shell of the heavier partner ("K-L level matching"). A satisfactory theoretical description of these processes has been achieved [71] by applying the two-state model of Nikitin [46] to separately calculate the vacancy sharing between the K-shell and the L₁-, L₂- and L₃-subshells, respectively. Meyerhof [72] has considered the summed cross section for L-shell vacancy production in the heavier partner and K-shell vacancy production in the lighter partner and has found this quantity to depend mainly on the united-atom charge number and not so much on the individual charge numbers of projectile ion and target atom. This finding led Meyerhof to identify the summed cross section with the cross section for vacancy production in the 3d σ MO and to analyze experimental data within a simplified version of the united-atom ionization model of Briggs [34].

The impact parameter dependence of inner-shell vacancy production in the region of K-L level matching has been measured by Warczak et al. [73,74] for various collision systems. The data exhibit structure in the small b-range, which so far is not fully understood.

5. M-SHELL VACANCY PRODUCTION

Not much information has been gained so far on the quasimolecular mechanisms of M-shell vacancy production.

The measurements of Kessel and coworkers [75-77] on Kr-Kr, Kr-Xe and Xe-Xe collisions have shown rises in the final charge state and in the inelastic energy loss already at R_0 -values much larger than those values at which the L-shells of the collision partners start to interpenetrate. Antark and Kessel [77] associate the rise seen in the Kr-Kr system at $R_0 \approx 0.75$ a.u. to the onset of M-shell vacancy production due to promotion of two Kr 3d electrons along the diabatic 6h σ MO. This assignment had been proposed earlier by Kessel and

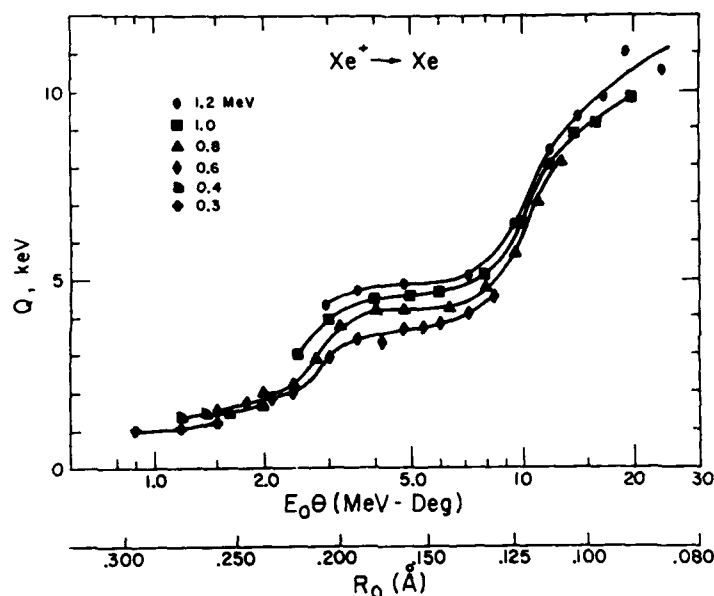


FIGURE 12
Inelastic energy loss in Xe-Xe collisions, plotted as function of reduced scattering angle $E_0\theta$ and of distance of closest approach R_0 . Full curves serve to guide the eye only. (From Ref. [76].)

Fastru, [5] on the basis of measurements of Fastrup and Hermann [78], which had revealed a triple-peak structure in the energy loss spectrum for $R_0 = 0.75$ a.u. Further rises in the Kr-Kr data setting in at $R_0 = 0.6$ a.u. and $R_0 = 0.4$ a.u. are ascribed by Antar and Kessel to promotion of 3d electrons along the $5q\pi$ MO and of 3s or 3p electrons along the $5q\sigma$ MO, respectively. In the asymmetric Kr-Xe system, Antar and Kessel observed rises in the R_0 -dependence of the final charge state and the inelastic energy loss, which may be associated with Kr M-shell vacancy production via $6h\sigma$ promotion (and presumably also via $5q\pi$ promotion) and with Xe M-shell vacancy production via $5q\sigma$ promotion.

The Xe-Xe data of Kessel and coworkers [75,76] (cf. Figure 12) exhibit rises which can be attributed to M-shell vacancy production via $6h\sigma$ promotion and via $5q\pi$ promotion (and possibly $5q\sigma$ promotion), respectively. In addition, the magnitude of the inelastic energy loss at large R_0 -values suggests the occurrence of multiple-vacancy production in the Xe N-shell (and presumably also in the Xe O-shell). However, no analysis of the data in terms of electron promotion out of these shells has been possible.

Shanker et al. [79] have studied the impact parameter dependence of M-shell vacancy production in 1.05 MeV Xe-Xe collisions by performing both ion-x-ray and ion-Auger-electron coincidence measurements. Figure 13 displays the b-dependence of the Auger-electron production (which, in view of the very small Xe-M fluorescence yield, directly gives the b-dependence of the vacancy production) as well as of the x-ray production. The steep rise of the x-ray production for $b < 0.25$ a.u. reflects a strong impact parameter dependence of the

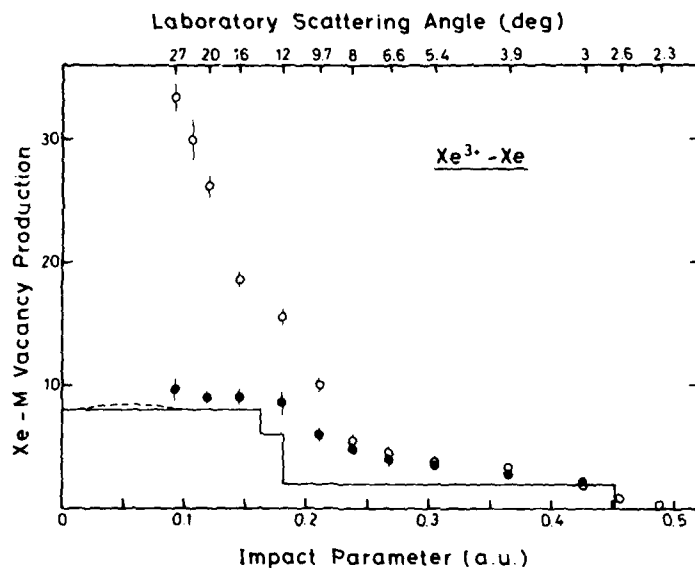


FIGURE 13
Impact parameter dependence of M-shell vacancy production in 1.05 MeV Xe^{3+} -Xe collisions. Full circles: Auger-electron data; open circles: x-ray data, normalized to the Auger data at large impact parameters. The theoretical curves are explained in the text. (From Ref. [79].)

Xe-M fluorescence yield. The full curve in Fig. 13 gives the vacancy production calculated by assuming the maximum possible number of electrons to be promoted along the $6h\sigma$, $5q\pi$ and $5q\sigma$ MO. The promotion distances R_C were read from the relevant MO correlation diagram [79] and the corresponding "critical" impact parameters b_C were obtained from the R_C -values by using internuclear trajectories generated from the Molière potential [79]. The broken curve in Fig. 13 gives the calculated contribution of rotational-coupling processes in the vicinity of the united-atom 4f and 5f shells, superimposed on the contribution of $6h\sigma$, $5q\pi$ and $5q\sigma$ promotion. It is seen that the Xe-M vacancy production measured by Shanker et al. is in fairly good agreement with the theoretical prediction, although the step-like rises predicted by the promotion model are scarcely exhibited by the data.

6. CONCLUDING REMARKS

The analyses of a large body of experimental data, which have been performed in recent years, have shown that inner-shell vacancy production in slow ion-atom collisions can be understood in rather fine detail in terms of simple quasi-molecular excitation mechanisms.

In the case of K-shell vacancy production, $2p\pi$ - $2p\sigma$ rotational coupling has been firmly established as the dominant excitation mechanism. However, a fully quantitative description of K-shell excitation by means of universal scaling laws for $2p\pi$ - $2p\sigma$ rotational coupling seems not to be possible. In this situation, detailed model calculations for individual collision systems will be most helpful.

Considerable progress has been achieved in the past years in the understanding of the mechanisms of L-shell vacancy production. Apart from $4f\sigma$ promotion, which is the dominant excitation mechanism in light collision systems, various united atom rotational coupling processes have been found to contribute to L-shell vacancy production. In order to disentangle the different excitation mechanisms, the dependence of L-shell vacancy production on the charge numbers of projectile ion and target atom and, in particular, on the asymmetry of the collision system should be systematically studied.

The understanding of the mechanisms of M-shell vacancy production is still at a rudimentary stage, and much experimental and theoretical work will be necessary in order to make progress in this field.

A remarkable feature that has emerged from the studies of inner-shell vacancy production in slow ion-atom collisions is the outstanding role played by united-atom rotational coupling as a mechanism for primary vacancy production in promoted MO. Because of its weak dependence upon details of the quasimolecular potential and upon other ingredients of the MO model, united-atom rotational coupling is a particularly simple excitation mechanism. The dominance of such mechanisms in a seemingly complicated many-body scattering situation should provide further stimulus for studying inner-shell excitation in slow ion-atom collisions.

ACKNOWLEDGMENTS

The author wishes to acknowledge the fruitful collaboration on topics covered in this review, which he has enjoyed over the past years with many colleagues. He is indebted to M. Ahmed and I. Lang for their efficient help in the preparation of this manuscript.

REFERENCES

1. W. Weizel and O. Beeck, *Z. Phys.* 76 (1932) 250.
2. W.M. Coates, *Phys. Rev.* 46 (1934) 542.
3. U. Fano and W. Lichten, *Phys. Rev. Lett.* 14 (1965) 627.
4. W. Lichten, *Phys. Rev.* 164 (1967) 131.
5. Q.C. Kessel and B. Fastrup, *Case Stud. At. Phys.* 3 (1973) 137.
6. *The Physics of Electronic and Atomic Collisions*, eds. J.S. Risley and R. Geballe (University of Washington Press, Seattle, 1976).
7. B. Fastrup, in Ref. [6], p. 361.
8. H.O. Lutz, in Ref. [6], p. 432.
9. J.S. Briggs, in Ref. [6], p. 384.
10. J.S. Briggs, *Rep. Prog. Phys.* 39 (1976) 217.
11. R. Schuch, in: *Physics of Electronic and Atomic Collisions*, ed. S. Datz (North-Holland, Amsterdam, 1982) p. 151.
12. R. Schuch, this volume.
13. J. Reinhardt, this volume.
14. W. Fritsch and U. Wille, *J. Phys. B: At. Mol. Phys.* 11 (1978) 4019.
15. R.L. Becker, A.L. Ford and J.F. Reading, *Phys. Rev. A* 29 (1984) 3111.
16. H.J. Lüdde and R.M. Dreizler, *J. Phys. B: At. Mol. Phys.* 18 (1985) 107.
17. B. Fricke and W.-D. Sepp, *J. Phys. B: At. Mol. Phys.* 14 (1981) L549.
18. E. Gross and R.M. Dreizler, *Phys. Lett.* 57A (1976) 131.
19. A. Toepfer, E.K.U. Gross and R.M. Dreizler, *Z. Phys. A - Atoms and Nuclei* 299 (1980) 167.
20. J. Eichler and U. Wille, *Phys. Rev. Lett.* 33 (1974) 56.
21. J. Eichler and U. Wille, *Phys. Rev. A* 11 (1975) 1973.
22. P. Kaufmann and U. Wille, *Z. Phys. A - Atoms and Nuclei* 279 (1976) 259.
23. F.T. Smith, *Phys. Rev.* 179 (1969) 111.
24. T.G. Heil and A. Dalgarno, *J. Phys. B: At. Mol. Phys.* 12 (1979) L557.
25. U. Wille and R. Hippler, *Phys. Rep.*, to be published.
26. H. Nakamura, *J. Phys. Chem.* 88 (1984) 4812.
27. M. Barat and W. Lichten, *Phys. Rev. A* 6 (1972) 211.
28. J. Eichler, U. Wille, B. Fastrup and K. Taulbjerg, *Phys. Rev. A* 14 (1976) 707.
29. J. Eichler and U. Wille, in: *Electronic and Atomic Collisions*, ed. G. Watel (North-Holland, Amsterdam, 1978) p. 331.
30. D.R. Bates and R. McCarroll, *Proc. Roy. Soc. (London)* A245 (1958) 175.
31. S.B. Schneiderman and A. Russek, *Phys.* 181 (1969) 311.
32. R. Shanker, U. Wille, R. Bilau, R. Hippler, W.R. McMurray and H.O. Lutz, *J. Phys. B: At. Mol. Phys.* 17 (1984) 1353.
33. R.K. Cacak, Q.C. Kessel and M.E. Rudd, *Phys. Rev. A* 2 (1970) 1327.
34. J.S. Briggs, *J. Phys. B: At. Mol. Phys.* 8 (1975) L485.
35. K. Taulbjerg, J.S. Briggs and J. Vaaben, *J. Phys. B: At. Mol. Phys.* 9 (1976) 1351.
36. R. Schuch, G. Nolte and H. Schmidt-Böcking, *Phys. Rev. A* 22 (1980) 1447.
37. N. Luz, S. Sackmann and H.O. Lutz, *J. Phys. B: At. Mol. Phys.* 12 (1979) 1973.
38. R. Anholt, Ch. Stoller and W.E. Meyerhof, *J. Phys. B: At. Mol. Phys.* 13 (1980) 3807.
39. R. Schuch, R. Hoffmann, K. Müller, E. Pflanz, H. Schmidt-Böcking and H.J. Specht, *Z. Phys. A - Atoms and Nuclei* 316 (1984) 5.
40. P.H. Mokler, D.H.H. Hoffmann, W.A. Schönfeldt, D. Maor, Z. Stachura and A. Warczak, *J. Phys. B: At. Mol. Phys.* 17 (1984) 4499.
41. D.H. Jakubassa and K. Taulbjerg, *J. Phys. B: At. Mol. Phys.* 13 (1980) 757.
42. R. Schuch, E. Justiniano, R. Hoffmann, W. Schadt, H. Schmidt-Böcking, P.H. Mokler, F. Bosch, W.A. Schönfeldt and Z. Stachura, *J. Phys. B: At. Mol. Phys.* 16 (1983) 2029.
43. W.E. Meyerhof, R. Anholt and T.K. Saylor, *Phys. Rev. A* 16 (1977) 169.

44. W.E. Meyerhof, Phys. Rev. Lett. 31 (1973) 1341.
45. E. Bøving, J. Phys. B: At. Mol. Phys. 10 (1977) L63.
46. E.E. Nikitin, in: Advances in Quantum Chemistry (Academic Press, New York, 1970) Vol. 5, p. 135.
47. G.H. Morgan and E. Everhart, Phys. Rev. 128 (1962) 667.
48. Q.C. Kessel and E. Everhart, Phys. Rev. 146 (1966) 16.
49. V.V. Afrosimov, Yu. S. Gordeev, M.N. Panov and N.V. Fedorenko, Zh. Tekhn. Fiz. 34 (1964) 1613, 1624, 1637.
50. B. Fastrup, G. Hermann and K.J. Smith, Phys. Rev. A3 (1971) 1591.
51. F.W. Saris, Physica 52 (1971) 290.
52. K.-H. Scharfner, H. Schäfer and R. Hippler, J. Phys. B: At. Mol. Phys. 7 (1974) L111.
53. R.J. Fortner, Phys. Rev. A10 (1974) 2218.
54. G.M. Thomson, P.C. Laudieri and E. Everhart, Phys. Rev. A1 (1970) 1439.
55. G.M. Thomson, Phys. Rev. A15 (1977) 865.
56. G.B. Schmid and J.D. Garcia, Phys. Rev. A15 (1977) 85.
57. R. Shanker, R. Bilau, R. Hippler, U. Wille and H.O. Lutz, J. Phys. B: At. Mol. Phys. 14 (1981) 997.
58. D. Schneider, G. Nolte, U. Wille and N. Stolterfoht, Phys. Rev. A28 (1983) 161.
59. R. Shanker, R. Hippler, U. Wille, R. Bilau and H.O. Lutz, Z. Phys. A - Atoms and Nuclei 313 (1983) 281.
60. U. Wille, J. Phys. B: At. Mol. Phys. 16 (1983) L275.
61. R. Bilau, W.R. McMurray, U. Wille, R. Shanker, R. Hippler and H.O. Lutz, submitted for publication.
62. P.H. Woerlee, R.J. Fortner and F.W. Saris, J. Phys. B: At. Mol. Phys. 14 (1981) 3173.
63. R. Shanker, R. Hippler, U. Wille, R. Bilau and H.O. Lutz, J. Phys. B: At. Mol. Phys. 15 (1982) L495.
64. B. Cleff, R. Frekers and H. Schulze, to be published.
65. B. Cleff, R. Frekers, H. Schulze and U. Wille, to be published.
66. B. Cleff, R. Frekers and H. Schulze, private communication.
67. G. Presser, J. Stähler, R. Werner and U. Wille, J. Phys. B: At. Mol. Phys. 16 (1983) 197.
68. E. Morenzoni, M. Nessi, P. Bürgy, Ch. Stoller and W. Wölfl, Z. Phys. A - Atoms and Nuclei 311 (1983) 7.
69. U. Wille, private communication to E. Morenzoni.
70. W.E. Meyerhof, A. Rüetschi, Ch. Stoller, M. Stöckli and W. Wölfl, Phys. Rev. A20 (1979) 154.
71. W.E. Meyerhof, R. Anholt, J. Eichler and A. Salop, Phys. Rev. A17 (1978) 108.
72. W.E. Meyerhof, Phys. Rev. A18 (1978) 414.
73. A. Warczak, D. Liesen, D. Maor, P.H. Mokler and W.A. Schönfeldt, J. Phys. B: At. Mol. Phys. 16 (1983) 1575.
74. A. Warczak, D.H. Dohmann, D. Liesen and B. Liu, in: Electronic and Atomic Collisions (Abstracts of ICPEAC XIII), eds. J. Eichler et al. (North-Holland, Amsterdam, 1983) p. 445.
75. R.A. Spicuzza and Q.C. Kessel, Phys. Rev. A14 (1976) 630.
76. R.A. Spicuzza, A.A. Antar and Q.C. Kessel, Phys. Rev. A18 (1978) 776.
77. A.A. Antar and Q.C. Kessel, Phys. Rev. A29 (1984) 1070.
78. B. Fastrup and G. Hermann, Phys. Rev. A3 (1971) 1955.
79. R. Shanker, R. Hippler, U. Wille and H.O. Lutz, J. Phys. B: At. Mol. Phys. 15 (1982) 2041.

COLLISION PHYSICS WITH HIGHLY STRIPPED SLOW IONS

Reinhold SCHUCH

Physikalisches Institut der Universität Heidelberg, 6900 Heidelberg, FRG

A review about recent studies with highly stripped heavy ions is given. Its scope is limited to mainly inner shell processes and slow collisions compared to the Bohr velocity of electrons in these shells. The processes discussed are: population of excited states by electron capture in asymmetric collision systems; electron capture and excitation in symmetric collisions with an emphasis on the impact parameter dependence of K- to L-shell and K- to K-shell vacancy transfer; the interference structure in the quasi-molecular X-rays from slow hydrogenlike ion-atom collisions which is used for direct spectroscopy of quasimolecular energies.

1. INTRODUCTION

The number of papers submitted to the ICPEAC on the subject of collision physics with highly charged ions has increased steadily in recent years. The growing activity in this field has mainly two origins: Sources of highly stripped heavy ions have become available, and the interest in data from such collision experiments has strongly increased.

From the point of view of pure atomic collision physics the interest in highly charged heavy ions arises because electronic states on the incoming part of the collision can be emptied. This makes a more selective study of the reaction mechanism possible. Shell effects can be seen and channels leading to specific couplings isolated. This will be the main subject of this paper. Another important advantage that one can explore is that after the collision of a highly charged ion with a light target atom the number of electrons is reduced to a very few which mostly populate an excited state. This provides an excellent environment for high resolution spectroscopic studies. For applications, the availability of highly charged slow ions makes the study of processes possible which were up to recently only observed in astrophysical and fusion plasmas.

In this review, recent developments in collision physics with slow highly stripped ions are presented. The meaning of slow is specified by the condition that the kinetic energy E of the ion Z_1 should be much smaller than the ionization potential multiplied by M/m_e of the most strongly bound electron which is stripped. M and m_e are the ion and electron rest masses, respectively. Very low collision energies are not discussed, however, partly because a special symposium is dedicated to collisions at very low velocities of highly charged ions, but also because one needs kinetic energy in order to reach small enough internuclear distances for inner shell studies. The production of such ions by e.g. acceleration, poststripping and deceleration is explained in part 2.

In the third part, electron capture of highly charged ions in asymmetric and symmetric collisions is treated. This process is of considerable purely scientific interest because it represents quantum mechanically a very complex collision problem. At low and intermediate velocities many strongly interacting electronic states are involved to form the final states occupied in the projectile and target ion after the collision. For practical purposes, it is important that at low velocities the electron capture cross-section is very large (of the order of 10^{-15} cm^2) and the transferred electrons occupy preferentially excited states both in projectile and target ion after the collision. This leads to high inten-

sity radiation sources and therefore also to important energy transport phenomena in e.g. astrophysical and fusion plasmas. A determination of the states with n and l quantum numbers occupied by electron capture is therefore actively pursued. This aspect is reviewed especially for very low E , by other articles in this volume.

Examples of state selective charge transfer processes between inner shells in nearly symmetric collision systems are given in the third and fourth parts of this article. There the dependence of the K X ray cross section on the projectile charge state is considered and two regions are distinguished: one where the projectile bears L-vacancies which can be transferred into the target K shell by 2p π -2p σ rotational coupling (see also previous article by U. Wille) and the other where the projectile is hydrogenlike or bare and the process of K-shell to K-shell vacancy transfer can be observed. In both cases the dependence of the K vacancy probability on impact parameter $P_K(b)$ is most informative about the couplings, in particular for the K-K transfer process where oscillations in the $P_K(b)$ reflect an interference of the transfer amplitude.

Essential to the descriptions of slow ion atom collision processes are the quasimolecular electronic states formed during the collision. Questions like this arise: are the states of a united atom system really formed in a close ion-atom encounter? This is of particular interest for very heavy quasimolecules ($Z_1+Z_2 > 130$). There the binding energy of an electron in the 1s state (for $Z_1+Z_2 > 175$) could exceed even double its rest mass. A spectroscopy of such superheavy quasimolecular states has been the goal of active studies during recent years. It was achieved in the analysis of measured inner shell ionization probabilities, and of positron and δ -electron emission, but in an indirect model dependent way. A direct spectroscopy of the quasimolecular states was tried in measurements of quasimolecular X-rays. In part 5 of this review measurements of interference structures in quasimolecular X ray spectra are presented. Utilizing these structures a direct spectroscopic determination of quasimolecular transition energies has been achieved.

2. PRODUCTION OF HIGHLY STRIPPED SLOW IONS

One of the main experimental difficulties in the studies discussed here is the preparation of the highly charged slow ions. Normally, if accelerators deliver beams of ions with $Z_1 > 10$, these have a fully occupied L shell. If one is interested in inner-shell processes it is therefore mandatory to poststrip such a beam to a very high charge state, usually with a thin foil. For this poststripping to be effective, a general rule is that the projectile velocity v_p must be comparable to the Bohr electron velocity, $\langle v_e \rangle_n$, of the n^{th} shell that one seeks to strip (Bohr criterion). In fig.1 plots of the mean charge states \bar{q} for different Z_1 as function of the ion energy are shown. The stripping occurs in C-foils, thick enough to produce equilibrium charge state distributions. For this plot, the semiempirical formula of ref.(1) and the experimental results given in ref.(1-4) were used. The dashed line on the high-energy side shows the energies obtained from the Bohr criterion for stripping up to the K-shell. The dashed line at the left side shows the energies where the mean charge state enters the K-shell. The same is plotted for the L-shell as dashed dotted lines. These lines give only a rough overview of the charge states produced by stripping in C-foils. As always a distribution of charge states is obtained after the foil (as for example in the insert in fig.1). Therefore high charge states with low beam intensities can already be obtained at a lower beam energy in the wing of the q distribution. This technique is indeed used very frequently. One manages to obtain significant results for the couplings between inner shell states by operating with beam velocities reasonably below the relevant electron orbiting velocity. In this way systematic studies of e.g. the L- to K-shell vacancy transfer by 2p π -2p σ rotational coupling (5-10) and of the K- to K-shell vacancy transfer process have been made (e.g.11-14). For investigations at

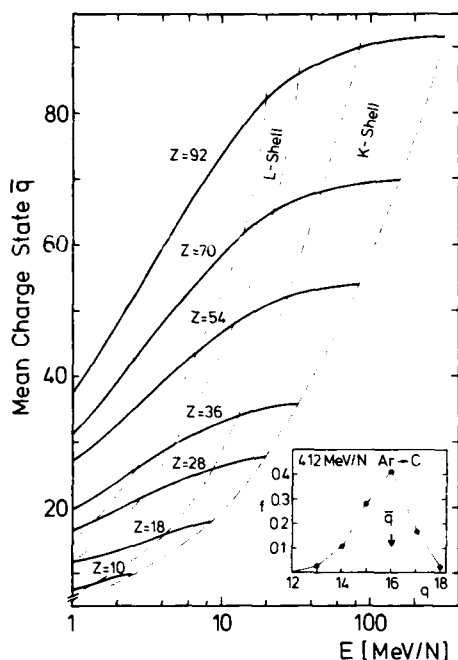


FIGURE 1 Mean charge state by stripping in a C-foil for different ions Z as function of their kinetic energy. Insert shows a charge state distribution from ref(1).

lower velocities or heavier collision systems, but still with very high charge states, beams where the charge state can be varied independently of the velocity are highly desirable. There are three main ways in which, at least in principle, such ion beams can at present be produced:

- From novel ion sources such as the Electron Cyclotron Resonance and the Electron Beam Ion Source.
- The Secondary Ion Recoil Source where atoms in a tenuous gas target are pumped to a high charge state by collisions of heavy ions of high charge state and high energy.
- The accel-decel method where after a first acceleration the ion is poststripped and then decelerated to low energies ($v_p \ll \langle v_e \rangle_n$).

In the first two methods ECR and EBIS, and SIRS the intensities of hydrogenlike or fully stripped ion beams in the region of $Z > 18$ is still very low. Nevertheless, a large number of interesting experiments with these sources employing lighter ions or lower charge states are currently in progress, and they are the subject of a separate symposium in this conference. Even with the expected large improvement in beam currents the ions so produced would still have to be accelerated to higher energies than provided by these ion sources to be of use for inner-shell processes. This is because the kinetic energy must be large enough to compensate the Coulomb repulsion at minimum distance of approach R_{min} , inside the K shell radius of the united atom r_{ua} (u.a. is the atom of Z_1+Z_2 nuclear charge). The criterion obtained for the lower limit of the collision energy is therefore

$$r_{ua} = r_0 / (Z_1 + Z_2) > R_{min} = a \left(1 + \frac{1}{\sin \theta_{cm}/2} \right)$$

($a = R_{min}/2$ for head-on collision, θ_{cm} is the center of mass scattering angle)

of the projectile).

If for impact parameter definition in a coincidence experiment the scattered ion is to be detected, a reasonable maximum scattering angle is required for practical purposes. One obtains from the above relation for symmetrical collisions ($Z = Z_1 = Z_2$): $E(\text{a.u.}) > 2 Z^3(1 + 1/\sin\theta)$ or for e.g. Ar^{q+} on Ar with a laboratory scattering angle of $\theta = 20^\circ$ a lower boundary for the kinetic energy of $E > 1.3 \text{ MeV}$.

These energies for, and reasonable beam currents of highly charged ions can be reached with the accel-decel method. In fig.2 schematic drawings of the three different structures presently available for accelerating, poststripping and decelerating heavy ion beams are shown. In general, one needs two independent accelerators with a stripper foil in between, and the second accelerator has to be converted into a decelerator. At Pittsburgh University (15), and at the Brookhaven National Laboratory, two tandems are coupled (16). The first tandem accelerates with a positive terminal voltage. The second tandem is on negative voltage thus accelerating up to the terminal where the poststripper foil generates high charge states, and decelerating in its second stage. The energies, beam currents and charge states obtained in Brookhaven for experiments which are reported here are listed in table 1. At GSI Darmstadt the positive ions were accelerated in the Linacs "Wideroe" and "Alvarez" to high energies, then poststripped and decelerated to low energies with single resonators. In Heidelberg a 12 MV tandem for accelerating and an rf Linac were used for decelerating (17). The beam parameters reached there for the reported experiments are also listed in table 1.

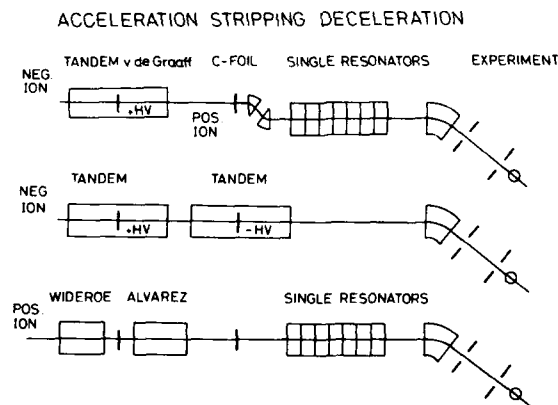


FIGURE 2 Structures for accelerating, poststripping and decelerating.

3. ELECTRON CAPTURE AND EXCITATION: TOTAL CROSS SECTIONS

A general overview of the cross section for single electron capture in Helium and Argon as function of the ion kinetic energy is given in fig.3. The data is taken from a collection by Knudson et al. (18) in reduced cross section and energy scale. Roughly speaking, two different regimes in the energy scale can be distinguished: Very low energies, where the cross section is almost constant. There a molecular orbital picture is generally used for the description of the capture process. Intermediate and high energies; here the cross section starts to decrease strongly with the ion energy. In this regime of intermediate velocities and asymmetric collision systems e.g. a classical Monte Carlo method (19) and an atomic state close-coupling method (20) has been developed. The

TABLE 1 Beam parameters for the accel-decel method

Facility	Ion	Poststripped at:	Final q	Final E	Electric current
Brookhaven Nat. Lab.	^{16}S	4 MeV/N	16+	130 keV/N	2 nA
	^{17}Cl	4.6 MeV/N	16+	70 keV/N	
G S I UNILAC	^{32}Ge	8.6 MeV/N	31+	2.6 MeV/N	2 nA
	^{36}Kr	8.6 MeV/N	33+	2.4 MeV/n	2 nA
		11.5 MeV/N	35+	4.6 MeV/N	3 nA
		"	36+	4.6 MeV/N	100 pA
	^{54}Xe	"	47+	4.5 MeV/N	1 nA
MPI Heidelberg	^{16}S	3.5 MeV/N	15+	150 keV/N	1 nA
	^{17}Cl	"	16+	500 keV/N	2 nA
		3.7 MeV/N	17+	600 keV/N	1 nA

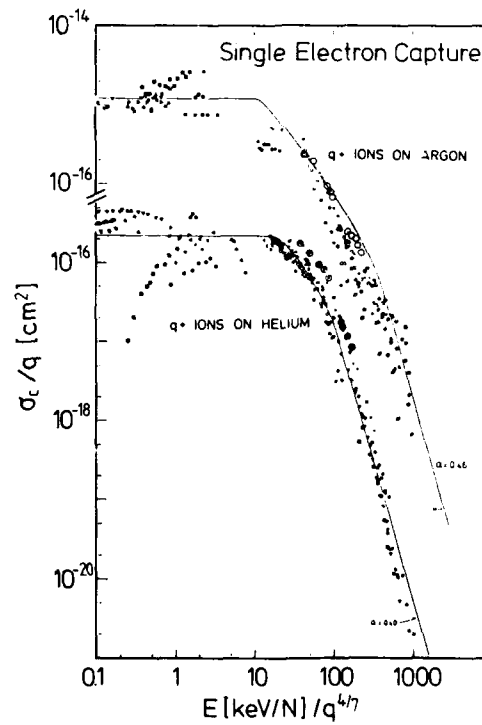


FIGURE 3 Reduced single electron capture cross sections for different ions (see ref 25) and for S^{16-16} (ref 27, big circles) in He and Ar as function of the reduced energy.

situation is here more complex than in the regime of very slow collisions, because a large number of strongly coupled states are involved in the capture of highly charged ions. In ref. 18 this complexity was exploited by introducing the simplifying assumption that there is a quasicontinuum of states to which coupling can occur. With this condition a scaling law for single electron capture has been derived (18) from the simplifying classical model of Bohr and Lindhard (21) that the single electron capture cross section for a fixed target divided by q should form a universal curve as function of $E \cdot q^{-4/7}$.

The regime of energies which can be covered by the accel-decel technique is indicated in fig. 3 by large circles. These represent new sets of data for S^{q+} ions obtained with the accel-decel technique at Brookhaven (22). There the charge state has been varied between $6+$ and $16+$ and the energy between 6 and 20 MeV. These data show in the general trend agreement with the scaling, only the He data are somewhat higher than the universal curve.

For a more rigorous test of the theoretical models for charge transfer, state selective measurements are needed. Much data is available in particular for electron capture in the low velocity regime where the molecular picture applies. These data are obtained with beams from SIRS, EBIS and ECR ion sources. The state of the art in such measurements is the spectroscopy of the translational energy gain of the projectile during the capture process (e.g. 23-25), the spectroscopy of autoionization electrons (e.g. 26-28) and characteristic X-rays. We want to consider here only processes of charge transfer and excitation leading to projectile and target characteristic X-ray emission after collisions of slow highly ionized ions with atoms.

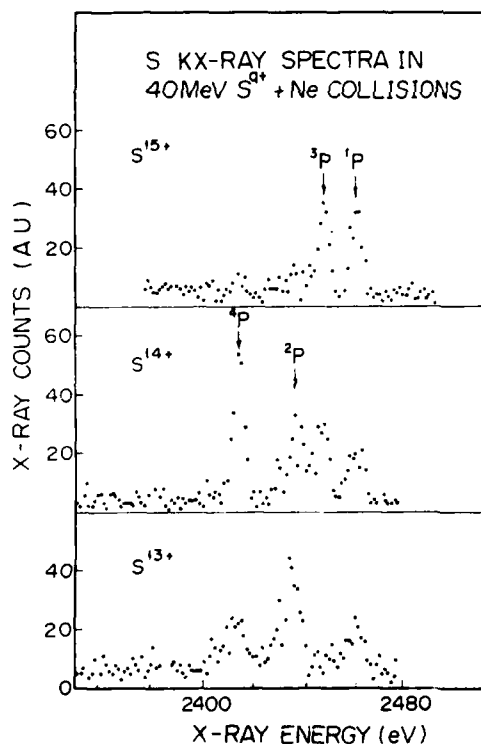


FIGURE 4 K-satellite lines for different initial charge states of the S-ions (ref 30).

Two classes of X-ray measurements can be distinguished: one which is done with high resolution crystal spectrometers ($\Delta E_x/E_x < 10^{-3}$); the other with Si(Li) or Ge detectors ($\Delta E_x/E_x \approx 10^{-2}$), where sometimes also coincidences with scattered particles are required to define the impact parameter of the scattering event. In the regime of slow highly stripped ions few experiments with crystal spectrometers have been performed. For the measurements with recoil ions we refer to the article of H. Beyer et al. (29). Poststripping of tandem beams has been used by a group at KSU to measure state selective capture with a crystal spectrometer (30). An example of X-ray spectra from such measurements with 40 MeV S^{q+} , $q = 13, 14, 15$ on a Ne target is shown in fig. 4. The X-ray lines with S^{15+} and S^{14+} are from electron capture into excited states (S^{14+} has the well known $1s1/2s1/2$ 1S metastable component), whereas the lines in S^{13+} are from excitation. Although in that paper no strong conclusions are drawn from these spectra one can clearly see the potential power of this method for identifying the states populated by electron capture.

In a development in this line, single electron capture can be used to create the excited states which are interesting for precision spectroscopy. Recently an experiment was performed (31) where bare Cl^{17+} nuclei were decelerated at the Heidelberg Linac and then allowed to capture a single electron into an excited state. The Lyman α lines (fig. 5) observed with a Johann type bent crystal spectrometer were free of spectator electrons and background distortion. In combination with a reduction and control of Doppler effects this technique can be used in the future to reach a very high accuracy in the determination of e.g. the 1s Lamb-shift.

Many studies of X-ray emission in near symmetric highly charged ion atom collisions were performed with the goal of determining the mechanisms for inner shell charge transfer and excitation.

The two mechanisms which could be isolated in these studies to be most important for K-vacancy production in slow symmetrical collision systems are 2p π -2p σ rotational coupling and 1s σ -2p σ radial coupling (see e.g. 32). Fig. 6 shows an example of a SCF relativistic many electron correlation diagram for the Ar+Cl

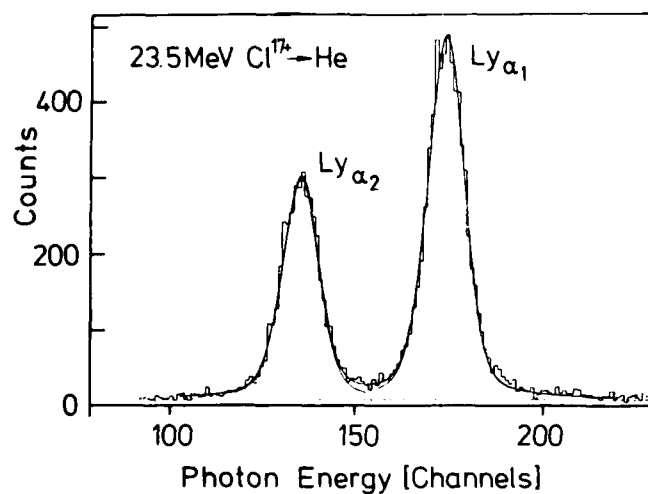


FIGURE 5 Lyman α lines in H-like Cl after electron capture of Cl^{17+} in a He gas target.

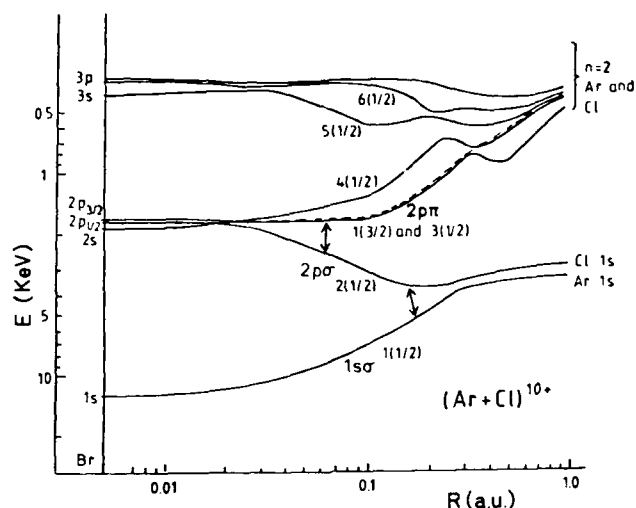


FIGURE 6 SCF relativistic many electron correlation diagram for a Ar+Cl quasimolecule (ref 33).

quasimolecule (33). It was calculated for a 10 times ionized collision system. For the levels most important for this discussion relativistic as well as non-relativistic descriptions are given. The two coupling channels mentioned above are indicated by arrows. The operation of one of these channels depends on the probability for having a vacancy in the incoming quasimolecular state. In order to verify this model, the dependence of the K X ray cross section on the projectile charge state has been measured (9,10,13).

Recently, by utilizing the accel-decel method, large variations of the charge states at a rather low collision velocity have been achieved. One result for Sn-Xe is displayed in the previous article (34). In fig.7 the total cross sections for 2 MeV/N Kr⁹⁺ → Kr and 3.6 MeV/N Xe⁹⁺-Xe are plotted as functions of the number of electrons in the ion. These experiments were performed with decelerated beams at GSI. The open circles are from a direct measurement of the total K X ray cross section for Xe on Xe (35). The open squares and full dots for Kr on Kr were obtained from the impact parameter dependent K-vacancy probabilities (ref.(36) and next paragraph) using $\sigma_K = 2\pi \int b \cdot P_K(b) db$. Within the systematic error bars of about 30% which usually exist in such measurements the two methods agree.

The total cross section is about constant for projectile charge states lower than Ne-like. This behaviour is explained as being due to excitation into higher states and ionization. The strong increase of the cross section with the number of projectile L-shell vacancies was seen as an indication for the operation of the 2p π -2p σ rotational coupling mechanism. The increase which is predicted (37) by the 2p π -2p σ rotational coupling model is shown by the full line for Xe-Xe and by the dashed line for Kr-Kr. The increase in the data points is somewhat weaker than predicted by 2p π -2p σ rotational coupling and the additional assumption of statistically distributed projectile L-vacancies between the almost degenerate L-shell states of projectile and target. This deviation could be due to a nonstatistical distribution of the L-vacancies among the L shell states caused by couplings to higher (e.g. M shell) states.

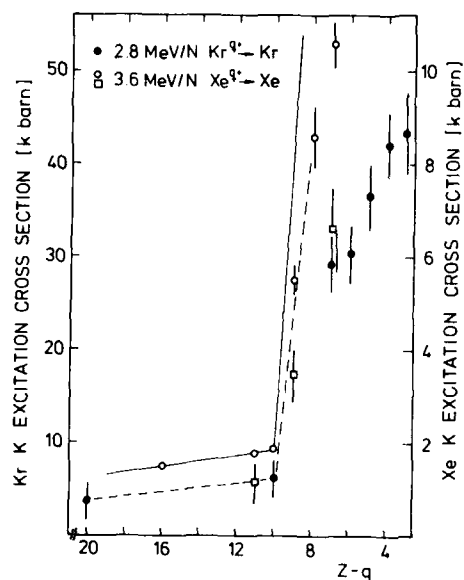


FIGURE 7 Total K-shell excitation cross section as function of the number of electrons in the projectile, open circles from ref (35), squares and full dots from ref (36).

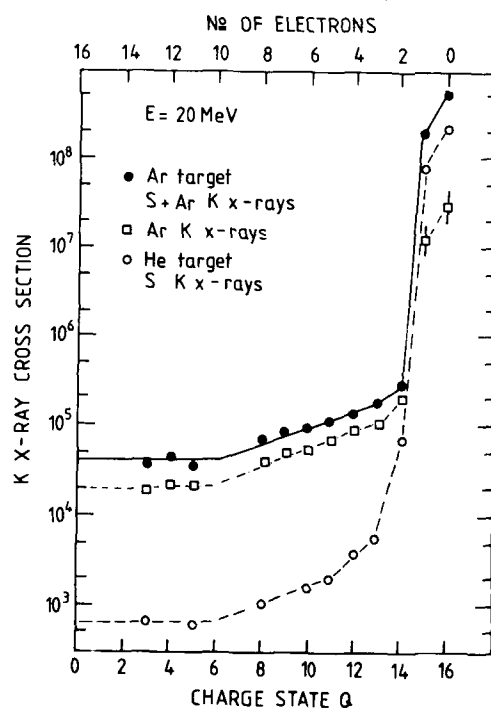


FIGURE 8 K X ray cross sections for 20 MeV S^{q+} ions in He and Ar gas target as function of the charge state q (open and full circles are from ref (39)).

As pointed out in the literature (e.g. 38,39) this charge state dependence alone cannot be seen as a proof for the operation of the $2\pi\pi$ - $2p\sigma$ rotational coupling mechanism. This is demonstrated in an obvious way by K X ray cross sections measured in a symmetric and a very asymmetric collision system. An example of a recent measurement (39) using decelerated 20 MeV Sq^+ beams in Brookhaven is given in fig.8. The K X ray cross sections increase with an Ar target in the same way for $q \geq 6$ as with a He target. In the very asymmetric collision system S on He, however, the $2\pi\pi$ - $2p\sigma$ rotational coupling cannot effectively operate. Therefore excitation into bound states might show the same projectile charge state dependence as $2\pi\pi$ - $2p\sigma$ rotational coupling, as it is seen in fig 8. A much better tool to identify these channels is the impact parameter dependence of the K vacancy probability. In part 4 this subject will be briefly discussed.

The very large increase in the projectile K X ray cross section for H-like and bare ions in fig 8 is due to electron capture into excited states of the He-like and H-like ions. The strong increase in the cross section for Ar K X rays is caused by the quasis resonant K-K transfer process which will also be discussed in the following paragraph.

4. INNER SHELL ELECTRON TRANSFER AND EXCITATION: IMPACT PARAMETER DEPENDENCES

The impact parameter dependence of inner shell vacancy production is usually determined by measuring characteristic X ray-particle coincidences. The scattering angles are converted into impact parameters (b) by use of a screened Coulomb-potential. The probability is obtained by correcting the true coincident X rays with fluorescence yield and detection efficiency, and normalizing this to the number of detected particles at b . Examples for the K vacancy probability $P_K(b)$ in slow symmetric collision systems was already given in the review by U. Wille (34) and in refs(5-8,10-12,36,40,41).

Here we want to show the $P_K(b)$ measured from collisions with highly ionized and decelerated Kr and Xe projectiles with Kr and Xe gas targets, respectively (35). These are the probabilities from which the total cross sections in fig.7 were obtained. For a comparison (in fig.9) with $P_K(b)$ from lighter collision systems (Ne^+ on Ne (40) and Cl^{11+} on Ar (5)) we use the reduced impact parameter scale $b' = (\alpha/v)^{1/3}b$ in atomic units, where $\alpha(Z_1, Z_2)$ is the coefficient in a quadratic expansion of the $2\pi\pi$ - $2p\sigma$ energy difference.

The Ne-Ne and Cl-Ar data is normalized at the maximum to the same value of 0.5, because the fluorescence yield in these light systems has a large uncertainty. In the heavier systems Kr-Kr and Xe-Xe the fluorescence yield correction does not cause a large error in the probabilities. They are therefore plotted in absolute values with respect to one vacancy in $2\pi\pi_x$, the state which couples to the $2p\sigma$. The normalization constant is obtained from the number of L-vacancies in the projectile and their statistical distribution among the L-shell states. These probabilities $P(b')$ in fig.9 for Kr-Kr agree reasonably well with those of Xe-Xe in absolute value, but at maximum they are both clearly below the theoretically expected values. This behaviour was already found in the total cross sections of fig.7 and a possible reason was given there.

Comparing the shape of the $P(b')$ curves for the very different collision systems one finds in all of them a similar behaviour with a maximum, the so called adiabatic maximum, at about the same position. The adiabatic maximum in Xe-Xe could be shifted to somewhat smaller b' values which might be explained by a relativistic effect. The fine structure splitting (see fig.6) between $1(3/2)$, $3(1/2)$ ($2\pi\pi$) and $2(1/2)$ ($2p\sigma$) has in Xe-Xe already reached 30% of the L-binding energies. The dashed line in fig.9 considers this relativistic effect (43) in the reduced impact parameter representation.

In the following part we report investigations of K-shell to K-shell charge transfer processes with H-like decelerated beams which causes e.g. the drastic rise of the Ar K X ray cross section seen in fig.7. The first observation of

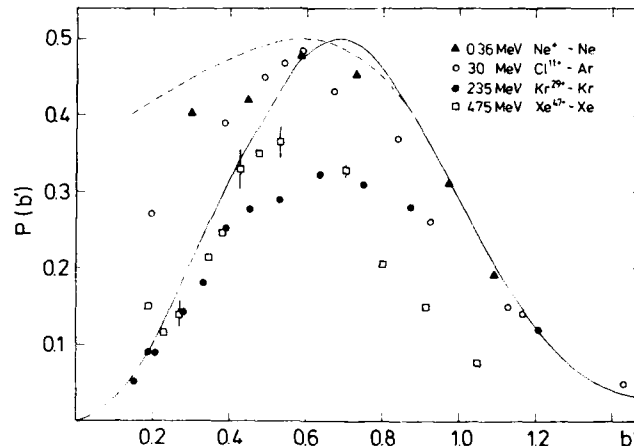


FIGURE 9 Normalized K-vacancy probabilities as function of the reduced impact parameter b' (for ref., normalization and lines see text)

this process was achieved with H^+ and He^+ beams obtained directly from an ion source and a H or He gas target (44-46). The oscillating structure seen in the capture probability as function of the collision energy was correctly interpreted (47) as the quantum mechanical interference of the transition amplitude for in- and outgoing parts of the collision trajectory.

First experiments with heavy ions were performed (11) with S poststripped at 32 MeV to charge state 15+ by observing characteristic X-ray particle coincidences from collisions with Ar. Here we report similar experiments (see also ref (48)) for the same collision system which, by exploiting the accel-decel technique, reached much higher precision and lower collision energies. Similar studies of this effect were performed for the F^{8+} -He collision system by Ne K Auger-electron-particle coincidences. Those were reported at the previous ICPEAC (49) and in ref (12). Total cross sections for single and double K-K transfer were measured at somewhat higher energies for a large variety of collision systems by Hall et al. (14) and Chetoui et al. (13).

In the experiment at the Heidelberg Linac performed with decelerated S^{15+} ions colliding with Ar, K X rays of projectile and target were measured in coincidence with scattered particles. The target (Ar) K vacancy probabilities $P_K^{Ar}(b)$ are plotted for 4.7, 7.9, 16, 32, and 90 MeV collision energy in fig.10. The data reveal clear oscillations as a function of b with an increasing "frequency" with decreasing collision velocity. The $P_K^{Ar}(b)$ extend with a considerable probability to very large b , more than three times the K-shell radius. This is the reason for the strongly enhanced target K-X-ray emission cross section as soon as the projectile bears a K-vacancy, as observed e.g. in 20 MeV $S^{9+} + Ar$ (fig.7).

The probabilities for K-vacancy production by 2pπ-2pσ rotational coupling and ionization have been measured for 32 MeV $S^{5,11}$ on Ar as function of b by Nolte et al. (6). The Ar K-vacancy probability extracted from these data is represented in fig.10 by the dashed line. We see that it only has a considerable probability at small b relative to the b -range of K- to K-shell transfer and it only has a comparable probability with those of S^{15+} at values of b where the K-K charge transfer probability has a minimum. If the 2pπ-2pσ rotational coupling channel is included coherently it could, however, have a dramatic effect on the K- to K-shell charge transfer probabilities, as will be discussed below.

Various models for the coupling between the two states $2p\sigma$ and $1s\sigma$ corresponding to the K-shell states of the two collision partners have been proposed (see e.g. ref(50-57)) to describe the oscillating structure found in K- to K-shell charge transfer. Most of these calculations have taken into account only the coupling between the two quasimolecular states $1s\sigma$ and $2p\sigma$, neglecting couplings to higher orbitals (see fig.6). Within such two-state models of a long range coupling, oscillations in the vacancy transfer probability can be understood as follows. It is known (see e.g. in refs. given above) that nonadiabatic transitions between the two interacting states take place over a range of internuclear distances around some coupling distance R_c far outside the K-shell radius of either of the collision partners. The $1s\sigma$ and $2p\sigma$ wave functions evolve adiabatically during the collision, changing their phases according to their energy values $E_{1s\sigma}$ and $E_{2p\sigma}$. This phase difference integrated along the trajectory is then:

$$\phi = \frac{1}{\hbar} \int_0^{t(+R_c)} \Delta E(R(t)) dt \approx \frac{1}{\hbar v} \int_b^R \Delta E \frac{RdR}{\sqrt{R^2 - b^2}} \quad [1]$$

The interference between the two wave functions produces the oscillations in the transfer probability according to this phase difference. This means that an experiment accurately determining the interference pattern allows a spectro-

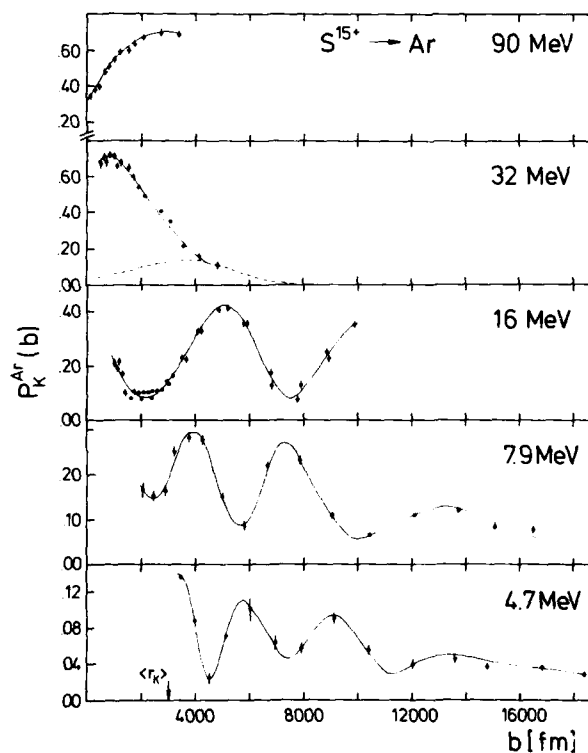


FIGURE 10 Target K vacancy probability as function of impact parameter from collisions with H-like S ions at different energies (full lines are drawn to guide the eye, dashed line see text).

scopy of the quasimolecular $1s\sigma-2p\sigma$ energy difference $\Delta E(R)$ in such a collision system. An analysis of the $S^{15+}-Ar$ data in this respect was performed in ref (48). If the LCAO for the wavefunctions is used one obtains (50,47):

$$P_2 = 4P_1(1-P_1) \sin^2 \phi$$

where P_2 is the transfer probability for double passage through the coupling region at R_c , P_1 is the probability for a single passage of R_c .

With relation (2) one gets extrema for $\phi = (n - 1/2)\pi$ where the maxima are at $n=1,2,\dots$ and the minima at $n=3/2,5/2,\dots$. The different maxima and minima can be identified in fig.10 according to their respective n -values, so that the phase difference is known for the b -values corresponding the maxima and minima. According to [1] these phase differences multiplied by v should define a common curve. In Fig.11a the values of $\hbar v \phi = \hbar v(n-1/2)\pi$ are plotted as function of the impact parameter, and indeed all data points fall within the error bars on a common curve.

The $2p\sigma-1s\sigma$ energy difference $\Delta E(R)$ in the $S-Ar$ quasimolecule obtained from HF calculations (57) for neutral projectile and target atoms is shown in fig.11b and the corresponding phase integral in fig.11a by the full line. A fit of the phase integral to the data points (fig.11a dashed line) with a parametrization of ΔE gives the dashed line in fig.11b as an energy curve.

Furthermore, sensitive tests of the dynamical couplings between the innermost quasimolecular states can be performed using the interference structure. Comparisons with calculations of this kind have been made in ref (48). The agreement with a two state molecular approximation (57) improves with decreasing velocity. However, also at low velocities, a large deviation in phase remains at small impact parameters which will be discussed with the following example. There we want to point out an influence of the coherent inclusion of the $2p\pi-2p\sigma$ rotational coupling channel on the phase of the $2p\sigma-1s\sigma$ radial coupling probability. This effect has been discussed already by McCarroll and Piacentini (58) for low energy proton-hydrogen collisions. In that work it was shown that for decreasing collision velocities at a fixed laboratory projectile scattering angle,

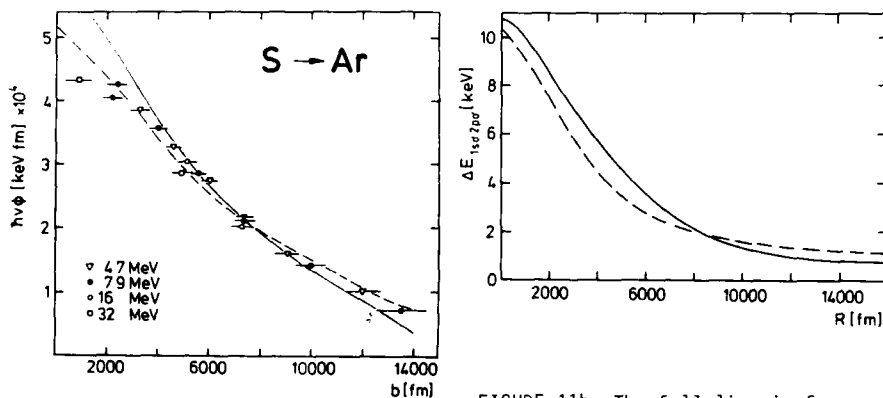


FIGURE 11a The product of phase and velocity as function of impact parameter b . The full and dashed lines are results of the phase integrals of the $2p\sigma-1s\sigma$ energy difference

FIGURE 11b The full line is from a HF calculation (57), the dashed is from a fit to $\hbar v \phi$.

the charge exchange probability is out of phase by a factor of π with the experimental results of Helbig and Everhart (46) if the $2p\pi-2p\sigma$ rotational coupling is not taken into account. This effect is also indicated in the present results as exemplified in a comparison of the dashed and dotted curves with the 16 MeV and 32 MeV S^{15+} -Ar data in figs. 12 and 13. Both curves were calculated with one-electron diatomic-molecule wavefunctions and coupling matrix elements, and using the routine TANGO (59) for an integration of the coupled state equations.

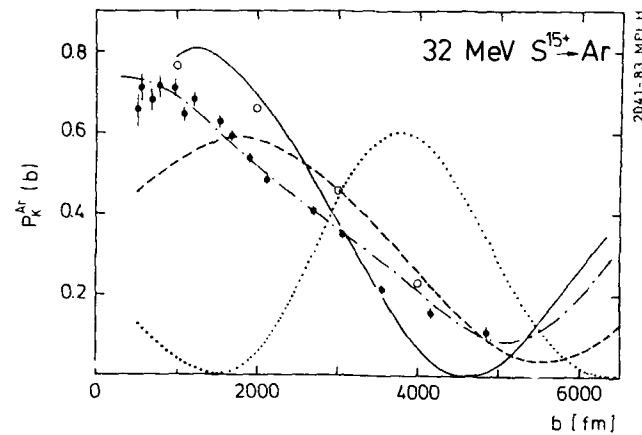


FIGURE 12 $P_K^{Ar}(b)$ for 32 MeV S^{15+} in comparison with results of Lin (54) (full line), of Fritsch (55) (dash-dot line). Two state (dotted line) and three state (dashed line) MO calculation.

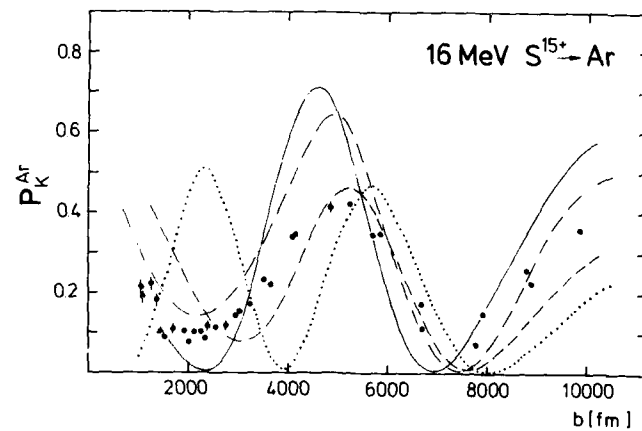


FIGURE 13 Same as fig. 12 for 16 MeV.

The dotted curve in figs.12 and 13 presents the results of a two-state calculation where only the $2p\sigma$ and $1s\sigma$ states were included. At 16 MeV we find the minimum in P_K^{Ar} at around 2300 fm whereas by this two-state calculation a maximum is predicted to occur at this impact parameter. The predictions of this calculation are, however, not so bad for larger impact parameters ($b > 6000$ fm) showing there a relatively good agreement with our data. A second calculation involving the $2p\pi$, $2p\sigma$ and $1s\sigma$ states is shown in figs.12 and 13 as dashed curves. We see that the inclusion of the $2p\pi$ state (and therefore of the $2p\pi$ - $2p\sigma$ rotational coupling) has two obvious effects. Not only does it provide a much better prediction of the position of maxima and minima, but it also raises the absolute value of the charge exchange probability in the minimum bringing it into good agreement with the measured value.

The two state atomic expansion (A0) (54) agrees quite well at higher velocities where molecular effects are not important. A comparison of this calculation (54) with the data is shown in figs.12 and 13 by the full line. A calculation (55) in such an atomic basis (A0+) which includes more states as well as united atom orbitals placed at the two charge centers is shown by the dashed dotted line in figs.12, 13 and for 7.9 MeV S^{15+} on Ar in fig.14. The agreement with the data is substantially improved. The numerical integration of the time dependent Schrödinger equation (60) for the collision system S^{16+} on Ar^{17+} is in good accordance with the data at all collision energies (see ref (48)). In figs.12 and 14 an example of these calculations is given by the open circles. Also shown there by the dashed line are the results of an MO approximation of Stolterfoht (57). In ref (48) a semiempirical formula was also derived which showed reasonable agreement with the S-Ar data and the data of ref (12) and is rather useful to estimate K- to K-shell transfer probabilities.

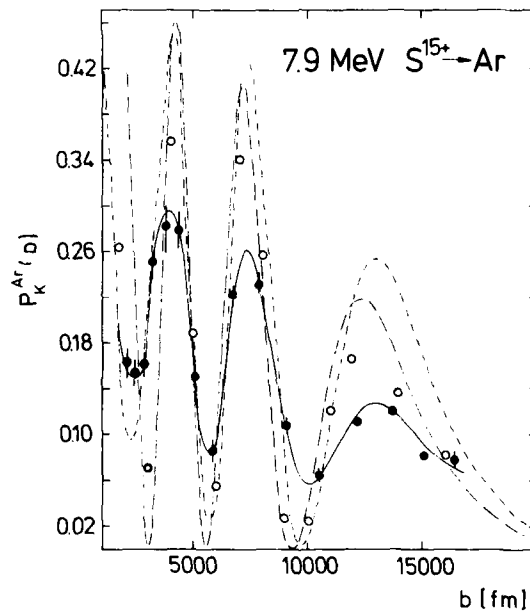


FIGURE 14 Comparison of P_K^{Ar} with results of Fritsch (55) (A0+, dashed dotted), of Stolterfoht (57) (dashed), and of Grün (60) (circles).

5. QUASIMOLECULAR X RAYS FROM COLLISIONS WITH H-LIKE DECELERATED PROJECTILES

The direct spectroscopy of the quasimolecular states formed transiently during a collision was the main goal of measuring quasimolecular X rays in recent years. These X rays are emitted by radiative transitions during the collision thus resulting in a broad continuum above and below the characteristic lines of projectile and target atom. Here we want to consider again only transitions into the innermost quasimolecular (1s) state, and collisions of H-like projectiles. These provide the 1s vacancy which is necessary for the decay.

In previous studies (see e.g. 61,62), with projectiles in lower charge states (as they are usually obtained from the accelerator) the spectroscopic information was not clearly visible. The method of finding end points or structures in the quasimolecular spectra failed mainly for two reasons: The Heisenberg broadening of the transition makes an end point of the spectrum at the united atom transition energy to vanish. Structures like those expected from an interference of transition amplitudes on the incoming and outgoing part of the collision cannot appear when the 1s vacancy needs first to be created in the collision. Also investigations in a different line, such as measuring the anisotropy were not successful although they were very helpful for the understanding of the radiation process. Anisotropies with a maximum at about the united atom transition energy were indeed observed (62). However, it was found that the

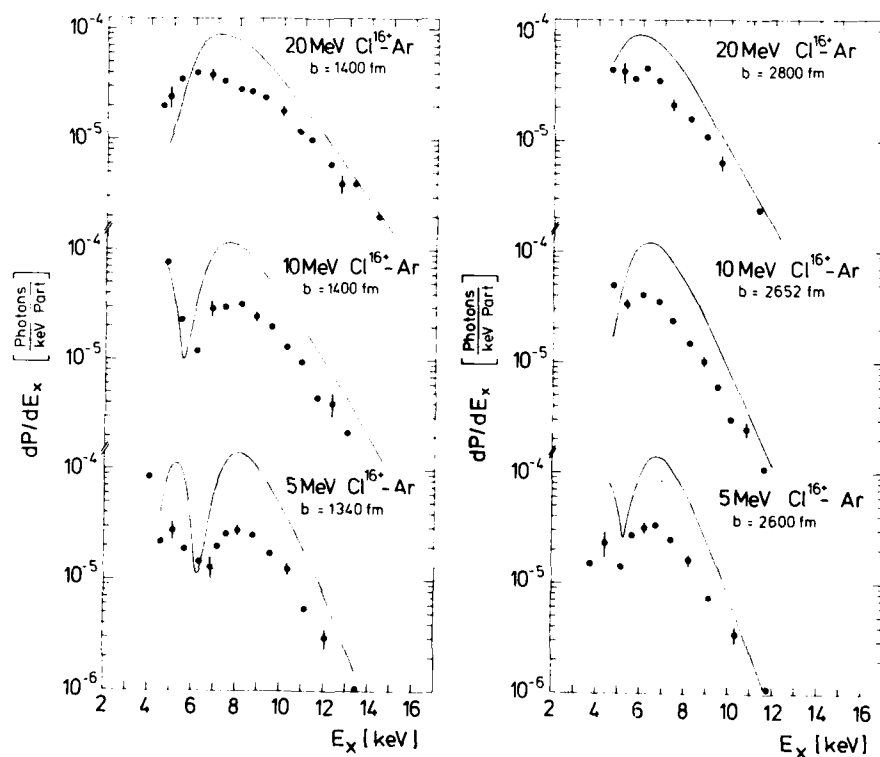


FIGURE 15 Quasimolecular X ray emission probabilities for different collision energies and impact parameters. The full line represents a dynamical calculation by Anholt (67) in absolute scale.

physical reason leading to this anisotropy is too complex to be of any use for spectroscopic purposes.

Taking advantage of decelerated highly charged ions, these problems could be circumvented. With H-like ions the 1st vacancy can be present already in the incoming part of the collision, and at low collision velocity the Heisenberg broadening is reduced. One could then expect to find interference structure in the quasimolecular X ray spectra as predicted by Lichten, Macek and Briggs (63, 64). This observation was indeed made with Cl^{16+} ions decelerated to 2.5, 5, 10 and 20 MeV, which have single collisions with atoms in an Ar gas target (65,66).

Some examples of the X ray spectra at different impact parameters of the scattering event and different collision energies are shown in fig.15 and 16. The structure appears clearly at lower collision energies and small impact parameters. A shift of the maxima and minima with both b and E can be observed.

The curves in fig.15 are from a dynamical electron stop calculation done by Anholt (67). The quasimolecular energy levels used there are scaled from the many electron u.a. K_{α} energy. A good agreement in the shape is obtained. However, the level of disagreement in absolute value is not very clear. Possible experimental uncertainties which could lead to lower probabilities are discussed in ref (68).

The curve in fig.16 represents a uniform approximation of the phase (69). A quadratic expansion of the transition energy ΔE in the collision time around the turning point ($t=0$) $\Delta E(t) = \Delta E_0 - ct^2$ leads to a closed form for the Fourier

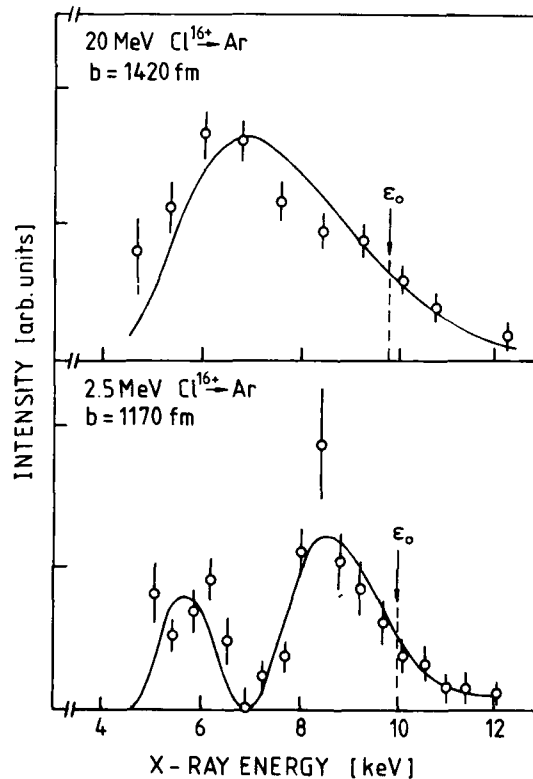


FIGURE 16 Quasimolecular X ray spectra in comparison with Airy functions from ref (69).

integral (64):

$$I(E_x) \approx \left| \int_{-\infty}^{+\infty} dt D_{if}(R(t)) \exp i/\hbar (E_x t - \int_0^t \Delta E d\tau) \right|^2$$

($D_{if}(R)$ is the dipole transition matrix element) in the form of an Airy function (69):

$$I(E_x) \sim |Ai((E_x - \Delta E_0)/c^{1/3})|^2$$

In ref (69) the two free parameters ΔE_0 and c were chosen so that $I(E_x)$ fits the 2.5 MeV measurement and with these the spectrum of 20 MeV was calculated. One can therefore apply this formula to fit the spectra at different b and E in order to construct the quasimolecular $1s\sigma$ - $2p\pi$ transition energy ΔE as function of R . Such an analysis was done in ref (70) and these results are shown in fig. 17 by the full dots. These are the transition energies at the turning point for different b and they are therefore restricted to small b .

For extracting the $\Delta E(R)$ at larger R from the interference structure a linear expansion of $\Delta E(t)$ in small intervals around a stationary point ($t_0 > 0$) should be a good approximation. The stationary point is defined by $E_x = \Delta E(t_0)$ and this so called stationary phase approximation (66) gives a $\cos^2 \phi(E_x)$ dependence of the spectral shape from a phase:

$$\phi(E_x) = \frac{1}{2\hbar} (E_x t_0 - \int_0^{t_0} \Delta E dt) . \quad [2]$$

The analysis of the interference structure in this way was made in ref (66). It uses only the E_x values of the maxima and minima which give the mean collision time

$$\bar{t} = \frac{\hbar \pi}{2|E_{\max} - E_{\min}|} \quad [3]$$

corresponding to a mean transition energy $\Delta E = \frac{(E_{\max} - E_{\min})}{\hbar}$.

The $\Delta E(R)$ so obtained are plotted as open dots in fig. 17. It is obvious that all energy points from different collision energies, impact parameters, and from the quadratic or linear expansion fall together within the error bars on a common curve. These points should represent mainly the $2p\pi$ - $1s\sigma$ transition energy at large R (there $D_{2p\sigma-1s\sigma} \rightarrow 0$) and a superposition of $2p\pi$ - $1s\sigma$ and $2p\sigma$ - $1s\sigma$ at small R , where the $2p\pi$ and $2p\sigma$ binding energies are anyhow nearly degenerate.

In fig. 17 two theoretical predictions for the $2p\pi$, $2p\sigma \rightarrow 1s\sigma$ transition energies are plotted. The full curve and dashed curve are scaled from the very frequently used H^+H energy curves (71) for $2p\sigma \rightarrow 1s\sigma$ and $2p\pi \rightarrow 1s\sigma$ transitions, respectively. A correction for the screening is done following Heinig et al. (72) by adjusting Z_{eff} to the neutral separated atom and u.a. transition energies. There is a clear discrepancy both in value and shape.

Very good agreement is obtained with $2p\pi$ - $1s\sigma$ energies from a Dirac Fock Slater calculation for a 10 times ionized $Cl \rightarrow Ar$ quasimolecule (33) (dashed dotted line). The energy curves of this calculation are displayed in fig. 6.

Similar studies were performed for the $S^{15+} \rightarrow Ar$ collision system (73). Here also the anisotropy of the quasimolecular X rays was investigated. We found a small shift of the interference structure at different observation angles with respect to the beam axis. Such anisotropy measurements with H-like ions could distinguish the energy curves of transitions from $2p\pi$ and $2p\sigma$ states (74).

One main goal in the studies of such interference structures is the spectroscopy of superheavy quasimolecular states. One very important condition which needs to be fulfilled is to have very heavy hydrogen-like projectiles. With the new generation of heavy ion accelerators (synchrotron and storage ring (75))

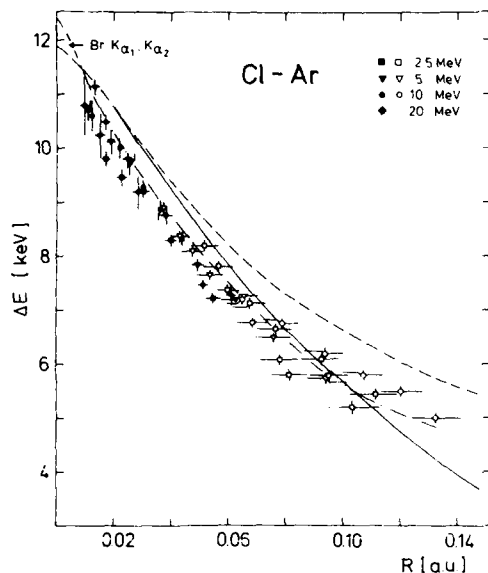


FIGURE 17 Experimentally determined $2p\pi-1s$ transition energies in the Cl-Ar quasimolecule as function of the internuclear distance R (for lines see text).

it should be possible to obtain even bare U-nuclei decelerated down to below the Coulomb barrier (6 MeV/N).

Still one needs to fulfill the condition of single collisions for K-shell processes, which seems to require thin gaseous targets. Here recently an important result was obtained (76) by bombarding a Mo solid target with Kr^{35+} decelerated to 4.5 MeV/N. With a careful selection of this target foil the interference structures both in the K-K transfer and the quasimolecular X rays were again found. Such studies can therefore be performed with solid targets which is important for heavier systems where gas targets are not available.

Also for the following application of interference effects, solid targets would be essential. Here the sensitivity of the interference structure to a small change in the collision time is exploited. In an inelastic nuclear reaction the two nuclei stick together for some time exchanging mass, energy and charge. The sticking time is calculated from models for this transfer to be in the order of $\Delta t > 10^{-21}$ s. Observing e.g. the quasimolecular X rays from collisions of H-like projectiles producing such a sticking event a shift of the interference structure, which depends on the sticking time should be observable. For an estimate of the sensitivity of this method we use relation [3] from the stationary phase approximation which gives:

$$\Delta E_x \approx 2\Delta t(E_{\max} - E_{\min})^2 / \hbar\pi$$

So that $\Delta t \approx 10^{-21}$ s corresponds to a change in the E_x difference between maxima and minima of about 1 keV in an intermediate heavy system like 5 MeV/N Zr^{39+} on Mo. This shift should be detectable. The "atomic clock" for nuclear sticking could further be calibrated with sub-Coulomb collisions in the way described above, so that a clock for times of $> 10^{-21}$ s could be available in the future.

6. SUMMARY

In this review atomic collisions of highly stripped ions at low and intermediate velocities with respect to the inner-shell electron orbiting velocity

were treated. In most of the experiments discussed, the ions were produced by poststripping at high velocities and decelerating with the second stage of an accelerator.

Electron capture processes of such ions in dilute gas targets were found to populate predominantly excited states, which can be studied by high resolution X ray spectroscopy. It has been indicated that precision spectroscopy of such states prepared by electron capture could reach a high accuracy in determining QED and electron-electron interaction effects.

K shell processes in close symmetrical collisions of highly stripped ions revealed two main coupling channels, $2p\pi$ - $2p\sigma$ rotational coupling as long as there are only L-vacancies in the projectile, and K-shell to K-shell vacancy transfer if the projectile bears a K vacancy. The impact parameter dependence gives in both cases very detailed informations about the coupling processes, especially in K-K transfer where an interference structure in the K vacancy probability is observed.

With hydrogenlike projectiles the quasimolecular X rays show an interference structure in near symmetric collisions at fixed impact parameter. This can be utilized for a direct spectroscopy of the $2p\pi$ - $2p\sigma$ quasimolecular energies as function of the internuclear distance.

In short, it could be said, that highly stripped slow ions can give very clear and detailed information about atomic collision processes and they open new ways for accurate X ray and electron spectroscopy. This is in particular fascinating in view of the new generation of ion sources, heavy ion accelerators and storage rings.

ACKNOWLEDGEMENTS

The author is indebted for the fruitful collaboration with many colleagues he has enjoyed, in particular with S. Hagmann, B.M. Johnson, K.W. Jones, E. Justiniano, J. Konrad, M. Meron, P.H. Mokler, A. Oppenländer, H.G. Reiter, H. Schmidt-Böcking, M. Schulz, W. Schwab, I. Tserruya and H. Vogt. I also wish to thank R.E. White for his critical remarks to the manuscript and Brigitte Wieland for her patient and expert typing of it.

REFERENCES

- 1) Y. Baudinet-Robinet, Nucl. Instr. Meth. 190 (1981) 197 and Phys. Rev. A26 (1982) 62
- 2) H.D. Betz, Rev. Mod. Phys. 44 (1972) 465
- 3) H. Gould, Phys. Rev. Lett. 52 (1984) 180
- 4) B. Franzke private communication
- 5) C.L. Cocke, R.R. Randall, S.L. Varghese, B. Curnutte, Phys. Rev. A14 (1976) 2026
- 6) G. Nolte, J. Volpp, R. Schuch, H.J. Specht, W. Lichtenberg, H. Schmidt-Böcking, J. Phys. B13 (1980) 4599
- 7) H. Schmidt-Böcking, H. Baumann, K. Bethge, A. Gruppe, W. Schadt, R. Schuch, K.E. Stiebing, Z. Physik A304 (1982) 177
- 8) R. Schuch, R. Hoffmann, K. Müller, E. Pflanz, H. Schmidt-Böcking and H.J. Specht, Z. Phys. A316 (1984) 5
- 9) A. Warczak, D. Liesen, J.R. Macdonald, P.H. Mokler, Z. Phys. A285 (1978) 235
- 10) W.N. Lennard, I.V. Mitchell, G.C. Ball, P.H. Mokler, Phys. Rev. A23 (1981) 2260
- 11) R. Schuch, G. Nolte, H. Schmidt-Böcking, W. Lichtenberg, Phys. Rev. Lett. 43 (1979) 1104
- 12) S. Hagmann, C.L. Cocke, J.R. Macdonald, P. Richard, H. Schmidt-Böcking, R. Schuch, Phys. Rev. A25 (1982) 1918
- 13) A. Chetoui, J.P. Rozet, J.P. Briand and C. Stephan, J. Phys. B14 (1981)

- 625 and A. Chetoui in X Ray and Atomic Inner Shell Physics, ed. B. Crasemann, 291, 1982
- 14) J. Hall, P. Richard, T.J. Gray, J. Newcomb, P. Pepmiller, C.D. Lin, K. Jones, B. Johnson, D. Gregory, Phys. Rev. A28 (1983) 99
 - 15) J.E. Bayfield, L.D. Gardner, J.Z. Gutkok, T.K. Saylor and S.D. Sharma Rev. Sci. Instr. 51 (1980) 651
 - 16) P. Thieberger, J. Barrette, B.M. Johnson, K.W. Jones, M. Meron and H.E. Wegner, IEEE Trans. Nucl. Sci., NS-30 (1983) 1431
 - 17) H. Ingwersen, E. Jaeschke, and R. Repnow, Nucl. Instr. Meth. 215 (1983) 55
 - 18) H. Knudson, H.K. Haugen and P. Hvelplund, Phys. Rev. A23 (1981) 597
 - 19) R.E. Olson and A. Salop, Phys. Rev. A16 (1977) 531
 - 20) H. Ryufuku and T. Watanabe, Phys. Rev. A19 (1978) 1538
 - 21) N. Bohr and J. Lindhard, K. Dan Vidensk. Selsk. Mat. Fys. Medd. 28 (1954) No.7
 - 22) J. Barrette, B.M. Johnson, K.W. Jones, R. Schuch, I. Tserruya, T.H. Kruse, in Electronic and Atomic Collisions (Abstracts ICPEAC XII) p.716, 1981
 - 23) C. Schmeissner, C.L. Cocke, R. Mann and W. Meyerhof, Phys. Rev. A30 (1984) 1661
 - 24) S. Tsurubucki, T. Iwai, Y. Kaneko, M. Kirmra, N. Kobayashi, A. Matsumoto, S. Ohtani, K. Okuno, S. Takagi and H. Tawara, J. Phys. B15 (1982) L733
 - 25) J.J. Bonnet, A. Fleury, M. Bonnefoy, M.F. Politis, M. Chassevent, S. Bliman, S. Dousson, D. Hitz, J. Phys. B (1985) in print
 - 26) R. Mack, A.G. Drentje and A. Niehaus, Abstr. of Contr. Pap. XIV ICPEAC, Palo Alto 1985, p.466
 - 27) A. Gleizes, P. Benoit-Catin, A. Bordenave-Montesquieu, S. Dousson, D. Hitz, Abstr. of Contr. Pap. XIV ICPEAC, Palo Alto 1985, p.464
 - 28) R. Mann, private communication
 - 29) H.F. Beyer, R. Mann, F. Folkmann in X Ray and Atomic Inner-Shell Physics, ed. B. Crasemann, p. 253, 1982
 - 30) K. Kawatsura, P. Richard, P.L. Pepmiller in print
 - 31) R.D. Deslattes, R. Schuch, E. Justiniano, Phys. Rev. A, in print
 - 32) J.S. Briggs, Rep. Prog. Phys. 39 (1976) 217
 - 33) B. Fricke, W.-D. Sepp, and T. Morovic, Z. Phys. A318 (1984) 369
 - 34) U. Wille, this volume
 - 35) P.H. Mokler, D.H.H. Hoffmann, W.A. Schönfeldt, D. Maor, Z. Stachura, and A. Warczak, J. Phys. B17 (1984) 4499
 - 36) R. Schuch, E. Justiniano, R. Hoffmann, W. Schadt, H. Schmidt-Böcking, P.H. Mokler, F. Bosch, W.A. Schönfeldt, and Z. Stachura, J. Phys. B16 (1983) 2029
 - 37) J.S. Briggs and J. Marcek, J. Phys. B5 (1972) 579 and K. Taulbjerg, J.S. Briggs and J. Vaaben, J. Phys. B9 (1976) 1351
 - 38) I. Tserruya, B.M. Johnson, and K.W. Jones, Phys. Rev. Lett. 45 (1980) 894
 - 39) B.M. Johnson, J. Barrette, Wang Da-Hai, K.W. Jones, I. Tserruya, R. Schuch, T.H. Kruse, Phys. Rev. A31 (1985) 1154
 - 40) S. Sackmann, H.O. Lutz, and J. Briggs, Phys. Rev. Lett. 32 (1974) 805
 - 41) R. Schuch, G. Nolte, and H. Schmidt-Böcking, Phys. Rev. A22 (1980) 1447
 - 42) E. Morenzoni, M. Nessi, P. Burgy, Ch. Stoller, W. Wölflin in X Ray and Atomic Inner Shell Physics, ed. B. Crasemann (1982) p. 133
 - 43) R. Anholt, W.E. Meyerhof and A. Salin, Phys. Rev. A16 (1977) 951
 - 44) C. Lockwood, H. Helbig, E. Everhart, Phys. Rev. 132 (1963) 2078
 - 45) F.P. Ziemba, G.J. Lockwood, G.H. Morgan, and E. Everhart, Phys. Rev. 118 (1960) 1552
 - 46) H.F. Helbig and E. Everhart, Phys. Rev. 140 (1965) 715
 - 47) W. Lichten, Phys. Rev. 139 (1965) 27
 - 48) R. Schuch, H. Ingwersen, E. Justiniano, H. Schmidt-Böcking, M. Schulz, F. Ziegler, J. Phys. B (1984) 2319
 - 49) S. Hagmann, C.L. Cocke, P. Richard, A. Stucklartz, S. Kelbch, H. Schmidt-Böcking, R. Schuch in Electronic and Atomic Collisions, eds. J. Eichler et al. (North Holland, Amsterdam 1983)

- 50) D.R. Bates and R. McCarroll, Proc. R. Soc. A 245 (1958) 175
- 51) Y.N. Demkov, Sov. Phys. JETP 18 (1964) 138
- 52) K. Taulbjerg, J. Vaaben, B. Fastrup, Phys. Rev. A12 (1975) 2325
- 53) A. Macias, A. Riera and A. Salin, J. Phys. B12 (1979) 447
- 54) C.D. Lin and L. N. Tunnell, Phys. Rev. A22 (1980) 76
- 55) C.D. Lin, T.G. Winter and W. Fritsch, Phys. Rev. A25 (1982) 2395,
W. Fritsch and C.D. Lin, J. Phys. B, in print and W. Fritsch private
communication
- 56) H.J. Lüdde, R.M. Dreizler, J. Phys. B13 (1981) 2119
- 57) N. Stolterfoht, J. Phys. B16 (1983) 2385 and private communication
- 58) R. McCarroll and R.D. Piacentini, J. Phys. B3 (1970) 1336
- 59) R.D. Piacentini and A. Salin, Comp. Phys. Comm. 12 (1976) 199
- 60) N.D. Grün, A. Mühlhaus and W. Scheid, J. Phys. B15 (1982) 4043
- 61) W.E. Meyerhof in Science 193 (1976) 839
- 62) P. Vincent in X Ray and Atomic Inner Shell Physics, eds. Fabian et al.,
Plenum Press, New York, London (1981) 117, or R. Anholt, Rev. Mod. Phys.
to be published
- 63) W. Lichten, Phys. Rev. A9 (1974) 1498
- 64) J. Macek and J.S. Briggs, J. Phys. B7 (1974) 1312
- 65) I. Tserruya, R. Schuch, H. Schmidt-Böcking, J. Barrette, Wang Da-Hai,
B.M. Johnson, K.W. Jones, and M. Meron, Phys. Rev. Lett. 50 (1983) 30
- 66) R. Schuch, H. Schmidt-Böcking, I. Tserruya, B.M. Johnson, K.W. Jones,
M. Meron, Z. Phys. A (1985)
- 67) R. Anholt, Z. Phys. A288 (1978) 257
- 68) R. Schuch, R. Hoffmann, I. Tserruya, H. Schmidt-Böcking, B.M. Johnson,
K.W. Jones and M. Meron in preparation
- 69) A.Z. Devdariani, U.N. Ostirowskii, and A. Niehaus, J. Phys. B in print
- 70) M. Meron, B.M. Johnson, K.W. Jones, R. Schuch, H. Schmidt-Böcking,
I. Tserruya, NIM B10/11 (1985) 64
- 71) D.R. Bates and R.H. Reid, Adv. Atom. Mol. Phys. 4 (1968) 13
- 72) K.H. Heinig, H.U. Jäger, H. Richter, H. Woittenek, W. Frank, P. Gippner,
K.-H. Kaun, P. Manfrass, J. Phys. B10 (1977) 1321
- 73) R. Hoffmann, Diss. Univ. of Heidelberg 1983
- 74) J.S. Briggs, J. Macek and K. Taulbjerg, J. Phys. B12 (1979) 1457
- 75) Die Ausbaupläne der GSI, March 1985 and Workshop on Heavy Ion Cooler Rings,
Heidelberg (1984)
- 76) A. Oppenländer, E. Justiniano, J. Vonrad, P.H. Mokler, W. Schad, H. Schmidt-
Böcking, M. Schulz, R. Schuch in preparation

LASER-INDUCED CHARGE EXCHANGE IN ION-ATOM COLLISIONS

A. RIERA

Departamento de Química Física y Química Cuántica.
Universidad Autónoma de Madrid. Cantoblanco.
28049 MADRID. (Spain)

The theory of laser-induced charge transfer (LICT) in ion-atom collisions is presented for the range of impact energies in which a quasimolecular description is appropriate. For each relative orientation of the AC field, LICT cross sections can be obtained with trivial modifications of standard programs. Simpler, perturbative expressions for the orientation-averaged cross sections are accurate for $I \nu^{-1} < 10^6 \text{ W s cm}^{-3}$, and the analytical Landau-Zener perturbative expression often provides good estimates for these cross sections. The practical advantages of the dressed state formalism as an alternative approach are critically examined, and the general characteristics of LICT cross sections in multicharged ion-atom collisions are shown with the help of an example.

1. INTRODUCTION

In the last decade, the ability of intense optical fields to modify charge exchange ion-atom reaction cross sections has stimulated considerable interest (1-11). In particular, attention has been drawn (3)(6)(7)(11) to the possibility of using laser induced charge transfer (LICT) processes to provide information on the impurity content of magnetically confined fusion plasmas, and to the relevance of LICT reactions to the development of short wavelength lasers. From the theoretical point of view, the basic characteristics of laser induced processes in ion-atom reactions are known. More importantly, existing computer programs that calculate field-free charge exchange cross sections can be easily modified to include the radiation-matter interaction, and simple and fast procedures can often be employed to estimate the cross sections for a given process. A summary of existing theoretical approaches to calculate LICT cross sections is presented in this report. I shall start by setting up the basic equations of the standard quasimolecular picture of the collision process, and the approximations that can be used to estimate the orientation averaged LICT cross section. For ultraintense laser fields, a dressed quasimolecular picture of collision processes is often advocated as being better adapted to describe these processes; the practical advantages of this alternative approach for LICT in ion-atom collisions will be briefly, and critically, examined. Finally, the general characteristics of the cross sections as functions of laser wavelength and nuclear velocity will be described. Atomic units will be used unless otherwise specified.

2. MOLECULAR FORMALISM

We consider an ion-atom collision taking place in the presence of an intense laser radiation. Because of the very larger number of photons in the laser mode, it can be accurately described (12) as a classical electromagnetic field:

$$\underline{\epsilon}(t) = \underline{\epsilon}_0 \cos(\omega t + \eta) \quad /1/$$

where ϵ_0 (a.u.) = $5.338 \times 10^{-9} (I \text{ W cm}^{-2})^{1/2}$ and I is the laser intensity. Although not strictly necessary in our treatment, the theoretical formalism to describe the collision process is simplified when a semiclassical description is employed. This description is adequate when the collision energy exceeds the binding energy of the active electrons (usually above a few tens of eV amu⁻¹). In it, the nuclei are assumed to follow a trajectory $\underline{R}(t)$, where \underline{R} is the internuclear distance, while the electronic motion is represented by a wavefunction ψ that fulfills the Schroedinger equation:

$$i \frac{\partial \psi}{\partial t} = (H_{el} + H_{int}) \psi \quad /2/$$

where H_{el} is the fixed-nuclei Born-Oppenheimer Hamiltonian, and H_{int} the radiation-matter interaction. As is well known (12,13), several forms for H_{int} (in the usual dipole approximation), differing by a gauge transformation, are equally meaningful and give identical results in an accurate treatment; for the present application the simplest and most convenient form (14) is given by the $\underline{\epsilon} \cdot \underline{\mu}$ gauge, with $\underline{\epsilon}_0$ in /1/ a vector of polar coordinates $(\epsilon_0, \theta, \phi)$ in a laboratory-fixed frame with the Z axis in the \underline{v} direction, $\underline{\mu}$ the electric operator.

Because of the large disparity between the electronic and nuclear masses, a molecular description of the process is adequate up to collision energies of the order of tens of KeV amu⁻¹, the relative nuclear velocity being smaller than the classical velocity of the active electrons. In that description, the electronic wavefunction ψ is expanded in terms of the set of eigenfunctions of H_{el}

$$\psi = \sum_n a_n(t) \chi_n(\underline{r}, \underline{R}) \exp \left\{ -i \int_0^t E_n[\underline{R}(t')] dt' \right\} \quad /3/$$

and this ansatz is introduced in /2/, yielding a system of coupled differential equations for the coefficients:

$$i \frac{da_n}{dt} = \sum_m a_m(t) \langle \chi_n | H_{int} - i \frac{\partial}{\partial t} | \chi_m \rangle \times \exp \left\{ -i \int_0^t (E_m - E_n) dt' \right\} \quad /4/$$

In this picture, charge transfer and excitation processes are interpreted as taking place through dipole (H_{int}) and dynamical ($\partial/\partial t$) couplings between the molecular channels. In the vicinity of sharp pseudocrossings between two molecular energies it is often useful to replace these eigenfunctions of H_{el} by linear combinations of them, called diabatic (15)(16) functions, whose character does not change in the avoided crossing region and which present, therefore, a negligible small dynamical coupling in this region. Also, in the intermediate range of nuclear velocities ($0.1 \lesssim v \lesssim 1$ a.u.) it becomes indispensable to introduce translation factors (17)(16) in the molecular wavefunctions, so as to ensure Galilean invariance of the results.

In practice, computer programs that are routinely used (18) to calculate the cross sections for the field-free case can be implemented with little modification in order to calculate the coupling matrix elements and to solve the set of differential equations /4/. Integration of each transition probability over all impact parameters b (i.e., over all nuclear trajectories) and average over all initial phases η in /1/ yields the corresponding laser and collision induced cross section $\sigma(\theta, \phi)$. Averaging over all initial (quasi)molecular orientations,

or equivalently over all directions of \mathbf{e} , gives the orientation-averaged cross section $\bar{\sigma}$.

3. APPROXIMATE MOLECULAR TREATMENTS

As pointed out above, solving the system /4/ poses no difficulty. However, angle and phase averaging can render this procedure unnecessarily cumbersome when orientation-averaged cross sections $\bar{\sigma}$ are required. Fortunately, several approximations can often be employed (1)(7) to drastically reduce the computational effort. Usually, the rotating wave approximation applies, and photon-induced transitions occur between two molecular channels x_1 and x_2 which are coupled by the operator H_{int} . Provided that $I \nu^{-1} < 10^6 \text{ W s cm}^{-3}$ (7) (11), one can employ perturbation theory to treat the photon-induced process and set:

$$i \frac{da_2}{dt} = a_1(t) \epsilon_0 \mu_{12} \exp \left\{ -i \left[\pm n + \int_0^t (E_1 - E_2 \pm \omega) dt' \right] \right\} \quad /5/$$

where $a_1(t)$ is the coefficient of x_1 in the field-free collision; this is set $a_1 \equiv 1$ when dynamical couplings to other molecular channels are ineffective in the energy range considered; otherwise, it has to be evaluated by solving eq. /4/ for the field-free case. Except for very high intensities or transitions taking place at very large internuclear distances (11) (quasimolecular dipole moments increase linearly with R) AC Stark shift and broadening of the molecular energies E_1, E_2 can be neglected in /5/. We notice that the phase n of eq. /1/ does not appear in the expression of the LIC transition probability $|a_2(\infty)|^2$ and therefore need not be considered. Furthermore, orientation averaging of the transition probability can be performed directly so that closed-form expressions for $\bar{\sigma}$ are obtained in the following way. Consider for example photon-induced transitions between two sigma states, and let $V(R)$ be the effective potential defining a nuclear trajectory $R(t)$ with azimuthal angle θ (19)

$$\theta = \pi \int_R^\infty \frac{b}{R^2} \left[1 - \frac{V}{E} - \frac{b^2}{R^2} \right]^{-1/2} dR \quad /6/$$

$$\epsilon_0 \mu_{12} = \epsilon_0 \mu_{12} (\sin \theta \cos \phi \sin \theta + \cos \theta \cos \theta) \quad /7/$$

$$\bar{\sigma} = \frac{1}{4\pi} \int d\Omega \int_0^\infty |a_2(\infty)|^2 b db = \frac{2\pi}{3} \epsilon_0^2 \int_0^\infty db b (|A|^2 + |B|^2) \quad /8/$$

where A and B are given by:

$$\int_{-\infty}^{+\infty} a_1(t) f(t) \mu_{12}[R(t)] \exp \left[-i \int_0^t (E_1 - E_2 \pm \omega) dt' \right] dt \quad /9/$$

and $f \equiv \sin \theta, \cos \theta$ for A, B , respectively. The corresponding expression for $\pi - \theta$ transitions is

$$\sigma = \frac{2\pi}{3} \epsilon_0^2 \int_0^\infty db b (|A|^2 + |B|^2 + |C|^2) \quad /10/$$

where C is also given by /9/ with $f \equiv 1$. For the special case of straight line trajectories (7) $V \equiv 0$ and $\sin \theta = b/R$; $\cos \theta = vt/R$.

It is clear that calculation of $\bar{\sigma}$ through eqs. /8/ and /10/ is a trivial problem, even if, at small nuclear velocities, the integrands in these equations strongly oscillate as functions of the impact parameter b . When collision-induced transitions can be neglected, and photon-induced ones are completely localized at the point of zero detuning $E_1 - E_2 = \pm \omega$ (where the phase in /9/ is stationary), a further simplification of the theory is still possible (1,7) and pro-

vides a very useful procedure to estimate $\bar{\sigma}$. Taking $a = 1$ in /9/ and evaluating this integral by the method of stationary phase (20) one obtains, for $b < b_{\max} = R_0 (1 - V(R_0)/E)^{1/2}$ where R_0 is the point of stationary phase:

$$A = \frac{2 \sin \theta(R_0) \mu_{12}(R_0)}{v} \left[\frac{2 \pi v}{F_1 - F_2 \left(1 - \frac{V(R_0)}{E} - \frac{b^2}{R_0^2} \right)} \right]^{1/2} \times \quad /11/$$

$$\times \cos^2 \left[\frac{1}{v} \int_{R_{\min}}^{R_0} \frac{E_1 - E_2 \pm \omega}{\left(1 - \frac{V}{E} - \frac{b^2}{R^2} \right)^{1/2}} dR' \right]$$

with $F_n = dE_n/dR$, and $A = 0(v^{-1})$ for $b > b_{\max}$. The corresponding expression for the B integral is similar, with $\cos \theta$ instead of $\sin \theta$. An illustration of the result of using this stationary phase approximation is presented in Fig. 1, for 200-300 laser induced transitions in $\text{He}^{2+} + \text{H}$ collisions (7). We plot the values of $\epsilon_0^2 |A|^2 b$ (----) and $\epsilon_0^2 |B|^2 b$ (-----) for a laser wavelength $\lambda = 3000 \text{ \AA}$, an intensity $I = 10^{11} \text{ Wcm}^{-2}$ and nuclear velocity $v = 1.55 \times 10^7 \text{ cm s}^{-1}$ (for smaller velocities the oscillations make the drawing unclear). To avoid cramming the figure with curves, only the non-oscillatory factors of the stationary phase approximations for A(....) and B(-----) are drawn. The accuracy of these approximations worsens as we approach the point of stationary phase R_0 ; notice in particular the divergence of the approximation for the A integral at $b = R_0$.

Reducing the integration domain in /8/ to $[0, b_{\max}]$, and taking the average value 1/2 for the oscillatory factor in /11/, one then obtains from this equation the perturbative Landau-Zener expression for the orientation averaged cross section (21):

$$\bar{\sigma}_{\text{LZ}} = \frac{8\pi^2 \epsilon_0^2 \mu(R_0)^2 R_0^2}{3 v |F_2 - F_1|} \left[1 - \frac{V(R_0)}{E} \right]^{1/2} \quad /12/$$

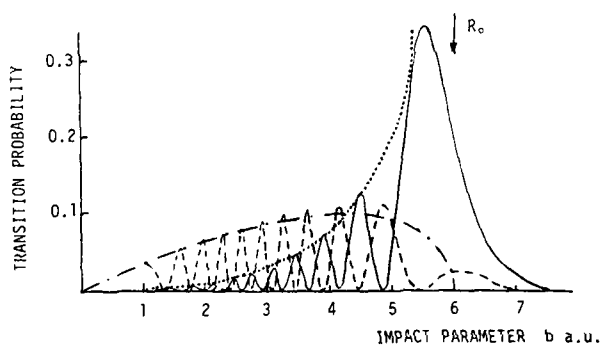


Fig. 1.

for $\lambda - \pi$ transitions, and twice this value for $\pi - \pi$ transitions. The general conditions of validity for the Landau-Zener approach are known (22)(23), and the simple formula /12/ often yields accurate values for $\bar{\sigma}$ provided that the value of $|F_1 - F_2|$ is carefully evaluated. Furthermore, it permits drawing general conclusions as to the most favourable conditions to obtain sizeable LICT cross sections with moderately high laser intensities. Transitions involving almost parallel energy curves and a non-negligible dipole matrix element at large internuclear distances are obviously to be favoured. Large cross sections can also be obtained (11) for photon-induced transitions between field-free energies that either avoid crossing or present a double crossing; in both these cases, however, the value of the integral /9/ is often not solely determined by the points of stationary phase, and the basic assumptions of the Landau-Zener theory are not fulfilled. Even then, eq. /12/ can often be used to obtain a rough estimate of the LICT cross sections, and the accurateness of this estimate can be predicted from consideration of the values of the molecular energies and transition dipole moments as functions of the internuclear distance.

4. DRESSED STATE FORMALISM

It is well known that, in the very strong laser intensity régime, an appropriate physical basis in the theory of laser-atom(molecule) interactions is provided by the so-called dressed states, or molecular quasistationary states modified by coupling to the external AC field. These states can be determined by using a quantized field approach, or equivalently in the semiclassical Floquet theory (24-28). To be consistent with our semiclassical formalism, I shall adopt here this latter theory, and I shall attempt an assessment of the usefulness of this alternative approach over the more "conventional" one presented in the previous sections. Before exposing the theory, two differences between LICT and laser-atom interactions are worth pointing out: i) the time interval when H_{int} is effective is usually much longer in the latter processes; ii) H_{el} exhibits an explicit time dependence, via the nuclear trajectory $R(t)$, in the former case. A rigorous theory of LICT processes in the dressed state formalism has been recently put forward by Ho et al (8). These authors show that, in order to construct dressed states ϕ_α for each value of the internuclear distance, one is led to consider first R and t as two independent variables, and look for solutions of

$$[H_{el}(r, R) + H_{int} - i \frac{\partial}{\partial t}] \phi_\alpha(r, R, t) = \epsilon_\alpha(R) \phi_\alpha(r, R, t) \quad /13/$$

where ϵ_α are the quasi-energies; ϕ_α fulfills the periodicity equation:

$$\phi_\alpha(r, R, t + \frac{2\pi}{\omega}) = \phi_\alpha(r, R, t) \quad /14/$$

The standard procedure (24) is to expand ϕ_α in a Fourier series and in the complete set of eigenfunctions of H_{el} :

$$\phi_\alpha = \sum_{in} C_{\alpha in} x_i e^{in\omega t} \quad /15/$$

Assuming the total photon number to be sufficiently large, the dressed wavefunctions ϕ_α can be interpreted (24) as linear combinations of states consisting of a definite photon occupation number n and a given electronic structure represented by x_i . Substitution of /15/ into /13/ and /2/ leads to a secular equation for the Floquet Hamiltonian:

$$[H^F(R) - \epsilon_\alpha(R) I] C_\alpha(R) = 0 \quad /16/$$

where H^F is an infinite dimensional block diagonal four-index matrix:

$$H_{ijnm}^F = [E_i(R) + n\omega] \delta_{ij} \delta_{mn} + \frac{1}{2} \epsilon_0 \cdot \mu_{ij}(R) [\delta_{m,n+1} + \delta_{m,n-1}] \quad /17/$$

where indices i, j refer to electronic states and n, m to photon occupation numbers. The sought-for solution of eq./2/ is then expanded, for each value of R , in terms of the complete set of dressed wavefunctions:

$$\psi = \sum_{\alpha} a_{\alpha}(t) \phi_{\alpha} [r, R(t), t] \exp \left\{ -i \int_0^t \epsilon_{\alpha}[R(t')] dt' \right\} \quad /18/$$

yielding an alternative approach to the usual molecular expansion /3/. In rigour, the quasi-energy spectrum $\{\epsilon_{\alpha}\}$ of the Floquet Hamiltonian forms a continuum (29-31), and expansion /15/ is only useful when its first coefficients decrease sufficiently rapidly so that it can be truncated to yield approximations $\{\epsilon_{\alpha}, \phi_{\alpha}\}$ to the quasi-energy resonances. It can then be shown (32) that this truncation requires the frequency ω to be much larger than the difference between AC Stark shifts. Since for LICT processes, heteronuclear molecular electronic states have permanent dipole moments that increase with R , the usefulness of the formalism is limited, for a given intensity, to high enough frequencies, and for a given ω , (rather paradoxically for an ultrahigh intensity method) to low enough I . When these conditions are met, one can restrict the secular equation /16/ to that of a small block of the Floquet matrix. For example, single photon processes can be treated by considering a 2×2 submatrix:

$$\begin{bmatrix} E_1 & \epsilon_0 \cdot \mu_{12} \\ \epsilon_0 \cdot \mu_{12} & E_2 \pm \omega \end{bmatrix} \quad /19/$$

and successive bordering of /19/ permits to treat multiphoton absorption or emission. Substitution of /18/ in /2/ yields a system of coupled differential equations for the coefficients, and in the dressed state picture the LICT process is visualized as occurring through transitions caused by radial couplings at avoided crossings between the quasi-energies, which are situated at the points of zero detuning in the previous molecular formalism. Since new radial couplings $\langle \phi_{\alpha} | \partial/\partial R | \phi_{\beta} \rangle$ need to be calculated, the practical advantages of this dressed state formalism over the standard approach are not obvious. Moreover, even within the two-state approximation /19/, when the radial coupling $\langle \chi_1 | \partial/\partial R | \chi_2 \rangle$ is effective in causing transitions, the dressed states arising from the eigensolutions of the infinite set of submatrices:

$$\dots \begin{bmatrix} E_1 \mp \omega & \epsilon_0 \cdot \mu_{12} \\ \epsilon_0 \cdot \mu_{12} & E_2 \end{bmatrix}; \begin{bmatrix} E_1 & \epsilon_0 \cdot \mu_{12} \\ \epsilon_0 \cdot \mu_{12} & E_2 \pm \omega \end{bmatrix}; \begin{bmatrix} E_1 \pm \omega & \epsilon_0 \cdot \mu_{12} \\ \epsilon_0 \cdot \mu_{12} & E_2 \pm 2\omega \end{bmatrix}; \dots \quad /20/$$

are, in general, all radially coupled, and the computational effort is thereby enormously increased.

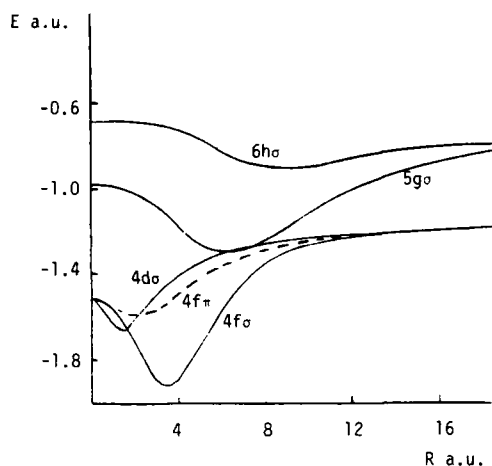


Fig. 2

5. CROSS SECTIONS

Calculated values of cross sections for laser induced charge transfer in multicharged ion-atom collisions are reported in refs. (7)(9)(10)(11). To show the basic characteristics of the cross sections as functions of wavelength and nuclear velocity, I shall take the specific case of $C^{6+} + H(1s) + h\nu$ collisions (11), and present the results (calculated using eqs. /8/ and /10/) for the orientation-averaged cross sections.

The energy correlation diagram for the CH_6^+ quasimolecule is presented in Fig. 2. For $R < 20$ a.u. the entrance channel is described by the $5g\sigma$ molecular orbital, whose energy diabatically correlates to $C^{6+} H(1s)$ at infinite internuclear separation. The values of the transition dipole moments between this channel and other molecular states are shown in Fig. 3. For two nuclear velocities: (1) 0.5×10^7 cm s $^{-1}$ and (2) 10^7 cm s $^{-1}$, the orientation-averaged LICT cross section is plotted in Fig. 4 as a function of the laser wavelength, for several processes with different characteristics. It will be noticed that LICT cross sections have a common, and useful, feature, which is their relative insensitivity to the precise wavelength employed within a wide interval of λ . This favours the use of powerful (Nd,CO $_2$) lasers, and solid state frequency multipliers when the wavelength should be in the visible or ultraviolet. We also notice that the final output of the reaction, i.e. the resulting radiation from the C^{5+} ions, corresponds to soft X-ray photons, and this feature might be of relevance in the development of short wavelength lasers.

Fig. 4a corresponds to $5g\sigma$ - $6h\sigma$ transitions, and the maximum cross sections, for a wavelength range 2600-3600 Å are accurately given by the Landau-Zener formula /12/ and a straight line trajectory ($V \neq 0$). It is worth pointing out that the range of frequencies that yield a maximum σ corresponds to a range of R_0 (the point of stationary phase) from 10.65 a.u. to 12.2, while the $5g\sigma$ - $6h\sigma$ transition dipole matrix element peaks for $R = 7$ a.u.. This shows that it is not optimal to use a laser frequency equal to $E_1 - E_2$ at the distance where μ_{12} presents a maximum value, as might be thought at first sight. The reason may be seen from eq. /12/: a larger value $R_0 > 7$ a.u. means that the magnitude of the transition

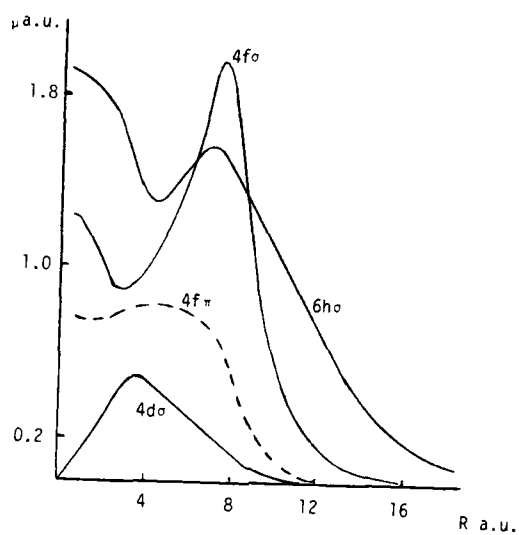


Fig. 3

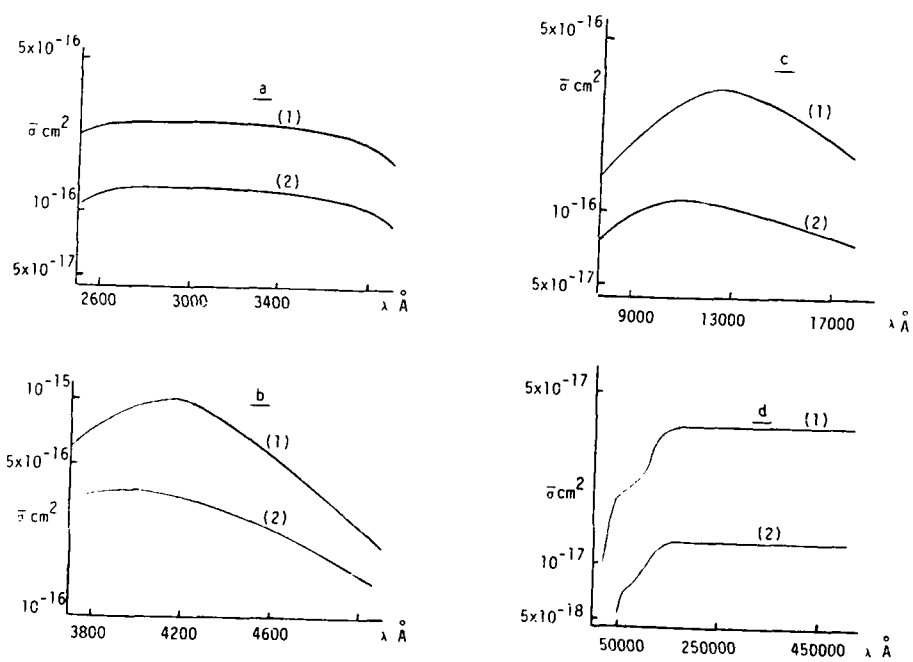


Fig. 4

dipole is decreased, but this is overcompensated by an increase of the range of impact parameters contributing to LIC (R₀ is larger in eq. /12/) and an enhancement of the effectiveness of the transition because the angle of intersection of the electron + field energy curves $E_1 + \omega$ and E_2 is smaller ($|F_1 - F_2|$ is smaller in eq. /12/).

The cross section of Fig. 4b, corresponding to $5g\sigma \rightarrow 4f\sigma$ induced photon emission, peaks for a values of $\lambda \approx 4000 \text{ \AA}$. For these wavelengths, laser induced transitions occur within the avoided crossing region between the field free energy curves; then, as pointed out above, the Landau-Zener prediction /12/ is not accurate. The same holds for the results of Fig. 4c, corresponding to $5g\sigma \rightarrow 4f\pi$ transitions, except that the reason is (obviously) not that the energy curves pseudocross, but that they are quasiparallel for the region of internuclear distances ($6 < R < 8 \text{ a.u.}$) where LIC takes place. Fig. 4d presents a further instance where, precisely in the wavelength region where the cross section is largest, the Landau-Zener estimate /12/ is least accurate in this case because of double crossing of the field free energy curves; in spite of the smallness of the $5g\sigma \rightarrow 4d\sigma$ transition dipole (Fig. 3), this last case is an interesting one because of the fact that in the double crossing region the energy curves are very close to one another (their maximum separation is 0.0038 hartree). When this happens, at long wavelengths ($\lambda > 120000 \text{ \AA}$ in this example) the contributions to the cross section of absorption and induced emission processes are practically identical, and $\bar{\sigma}$ is independent of laser wavelength. Then lasers operating in the infrared region of the spectrum can be directly used: e.g. a CO_2 laser could be employed either directly or to optically pump a NH_3 laser ($\lambda = 120000\text{--}160000 \text{ \AA}$) so that high intensities could be used.

In the calculation of the previous results, dynamical couplings were assumed to be either totally effective (as in the $5g\sigma \rightarrow 6h\sigma$ avoided crossing which is crossed diabatically) or totally ineffective, so that in either case they could be neglected in the treatment of the LIC process. We compare in Fig. 5 the values of the orientation averaged $\bar{\sigma}$ (—) for a laser intensity $I = 10^{11} \text{ W cm}^{-2}$ and wavelengths approximately corresponding to the maxima of $\bar{\sigma}$ in Fig. 4, with the values of the collision induced (33) cross sections for $\text{C}^{6+} + \text{H}(1s) \rightarrow \text{C}^{5+}(n=4) + \text{H}^+$ (-----) and $\text{C}^{6+} + \text{H} \rightarrow \text{C}^{5+}(n=5) + \text{H}^+$ (-----). Because of the shape of the cross sections, one can expect that competition between d/dR and dipole couplings will only be important for the narrow range of nuclear velocities where laser and collision induced cross sections are of comparable magnitude; then, to a reasonable approximation the total charge exchange cross section will be given by the sum of the two separate contributions, calculated independently. This assumption has been seen to be correct (10) in a calculation carried out for $\text{K}^+ + \text{Ca}$ collisions, for a given relative orientation of the electric field (fixed values of θ and ϕ in eq. /7/). Of course, there is no a priori reason to expect it to be valid when the collision induced cross section does not diminish rapidly with decreasing v .

6. CONCLUSION

In this report I have presented the theory of laser-induced charge transfer (LIC) in ion-atom collisions for the range of impact energies in which a quasi-molecular description of the colliding system is appropriate. Trivial modifications of the standard programs that calculate unassisted excitation and charge exchange cross sections permit to obtain the LIC σ for a given orientation of the electric field with respect to the incident beam direction. To calculate orientation-averaged cross sections $\bar{\sigma}$ a perturbative approach is accurate for $I v^{-1} < 10^6 \text{ W s cm}^{-3}$, and yields expressions /8/, /10/ which are much less time consuming than the general approach. Often, the Landau-Zener expression /12/ provides reasonable estimates for $\bar{\sigma}$. The conclusions on an alternative formulation which is often used in qualitative treatments of laser induced processes -the so-called dressed state approach-, are rather disappointing to treat

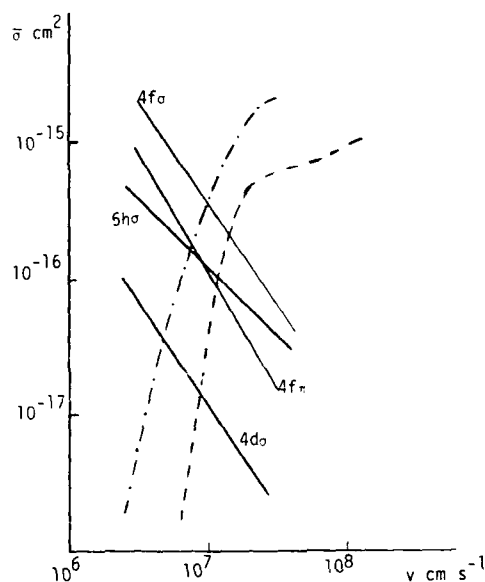


Fig. 5

LICT ion-atom collisions; this point is further developed in ref. (32). Firstly, new (sharp) radial couplings need to be evaluated in this alternative approach. Secondly, when radial couplings between "undressed" molecular states cannot be neglected in the impact energy range considered, one needs to include so many dressed states in the expansion /18/ that the new formalism becomes in practice exceedingly time consuming. Finally, because of the existence of diagonal matrix elements of the radiation-matter interaction Hamiltonian, dressed states can only be defined, for a given wavelength, for low enough laser intensities, which is a disturbing feature for a high intensity approach.

In the last section, the general characteristics of LICT cross sections of multicharged ion-atom collisions have been exposed with the help of an example. LICT cross sections are in general rather insensitive to the precise value of the wavelength employed, which is a desirable feature, especially when frequency multiplying devices must be employed. The intensities used in the example are of the order of 10^{11} W cm $^{-2}$, which is high, though within present day technology; for $\nu < 10^6$ cm s $^{-1}$, smaller intensities can be employed since the orientation averaged cross sections $\bar{\sigma}$ roughly vary like $I \nu^{-1}$ (eq./12/). Further advances in the study of LICT processes await the appearance in the literature of experimental counterparts to the theory.

REFERENCES

- 1) D.A. Copeland and C.L. Tang, J. Chem. Phys., 65 (1976) 3161.
- 2) M.H. Mittleman, Phys. Rev. A. 14 (1975) 586.
- 3) S.I. Yakovlenko, Sov. J. Quantum Electr. 8 (1978) 151.

- 4) J. Weiner, Proc. Summer School on Chemical Photophysics, Les Houches (1979)
- 5) G. Ferrante, L. Lo Cascio and B. Spagnolo, J. Phys. B 14 (1981) 3961.
- 6) J.F. Seely, J. Chem. Phys. 75 (1981) 3321.
- 7) L.F. Errea, L. Méndez and A. Riera, J. Chem. Phys. 79 (1983); Proc. XIII ICPEAC(1983) p. 691; Chem. Phys. Lett, 104 (1984) 401.
- 8) T.S. Ho, S.I. Chu and C. Laughlin, J. Chem. Phys. 81 (1984) 788.
- 9) S. Ganguly, K. Rai Dastidar and T.K. Rai Dastidar, Phys. Rev. A 31 (1985) 1171.
- 10) Y.P. Hsu, M. Kimura and R.E. Olson, Phys. Rev. A 31 (1985) 576.
- 11) L.F. Errea, L. Méndez and A. Riera, J. Chem. Phys. 82 (1985) 4536. J. Phys. B. (submitted for publication).
- 12) M.H. Mittleman, Theory of Laser-atom interaction (Plenum, New York, 1982)
- 13) C. Cohen-Tannoudji, B. Diu and F. Laloe, Mécanique Quantique (Hermann, Paris, 1977)
- 14) M. Sargent III, M.D. Scully and W.E. Lamb Jr., Laser Physics (Addison-Wesley, Reading, 1974); W.J. Meath and E.A. Power, J. Phys. B., 17 (1984) 763.
- 15) W. Lichten, Phys. Rev. 131 (1963) 229; F.J. Smith, Phys. Rev., 179 (1969) 111.
- 16) For a discussion on this concept see A. Macías and A. Riera, Phys. Rep. 90 (1982) 299.
- 17) D.R. Bates and R. McCarroll, Proc. Roy Soc A 245 (1958) 175.
- 18) e.g. C. Gaussorgues, R.D. Piacentini and A. Salin, Comput. Phys. Comm. 10 (1975) 223; A. Salin and R.D. Piacentini, Comp. Phys. Comm 12 (1976) 199.
- 19) H. Goldstein, Classical Mechanics (Addison-Wesley, Reading, 1950).
- 20) H. Jeffreys and B. Swirles, Methods of Mathematical Physics (Cambridge, University Press, 1962); F.W.J. Olver, Introduction to Asymptotics and Special Functions (Academic, New York, 1974).
- 21) L.D. Landau and E.M. Lifshitz, Quantum Mechanics (Pergamon, Oxford, 1965) p. 330.
- 22) D.R. Bates, Proc. Roy Soc. London A 257 (1960) 22.
- 23) F. Borondo, A. Macías and A. Riera, J. Chem. Phys., 74 (1981) 6125. Chem. Phys. 81 (1983) 303.
- 24) J.H. Shirley, Phys. Rev. 138 (1965) B 979.
- 25) C. Cohen-Tannoudji and S. Haroche, J. de Physique 30 (1969) 153.
- 26) M. Allegrini and E. Arimondo, J. Phys. B. 4 (1971) 1008.
- 27) D.T. Pegg, J. Phys. B 6 (1973) 246.
- 28) J.V. Moloney and W.J. Meath, Mol. Phys. 31 (1976) 1537.
- 29) Ya B. Zel'dovich, Sov. Phys. JETP 24 (1976) 1006.
- 30) R.H. Young, W.J. Deal Jr., and N.R. Kestner, Mol. Phys., 17 (1969) 369.
- 31) A.G. Fainshtein, N.L. Manakov and C.P. Rappoport, J. Phys. B, 11 (1978) 2561
- 32) L.F. Errea, L. Méndez and A. Riera, J. Chem. Phys. (submitted for publication).
- 33) T.A. Green, E.J. Shipsey and J.C. Browne, Phys. Rev. A 25 (1982) 1364.

DOUBLY DIFFERENTIAL CROSS SECTIONS OF COLLISION-PRODUCED FORWARD ELECTRON EMISSION

Stuart B. ELSTON

Department of Physics and Astronomy, University of Tennessee, Knoxville,
TN 37996-1200, and Physics Division, Oak Ridge National Laboratory, Oak
Ridge TN 37831

The velocity space distribution of electrons emitted near the forward direction from collisions involving fast, highly stripped oxygen ions with gaseous and solid targets is presented and described in terms of multipole moments of the ejected charge distribution, which permits direct comparison with recent theory. The results are from a novel apparatus permitting rapid and efficient data acquisition by employing position-sensitive electron detection to combine emission angle definition with conventional electrostatic spectrometry. Excellent agreement is obtained between distributions observed for electron loss to projectile continuum processes and recent theory in the case of argon targets; less favorable results for simpler helium targets may indicate the need for theoretical study of higher order inelastic processes in that case. The multipole content observed with a solid target is consistent with a conceptual model of convoy electron production dominated by electron loss from the projectile within the bulk of the target and may signify the importance of steady-state production of excited states within the bulk solid.

1. INTRODUCTION

1.1. Overview

The spectrum of electrons emitted near zero degrees in ion-atom and ion-solid collisions is dominated by a strong 'cusp'-shaped peak corresponding to electrons nearly matched in vector velocity to that of the projectile ion. Recent advances in experimental technique and theory permit new insights which simplify resolution of early puzzles over the spectrum of such electrons and suggest new approaches to long-standing questions about the importance of excited states of ions traversing condensed matter. In short, the signature of cusp electrons produced by capture processes is now seen as the result of a strong dipole moment in the emitted charge distribution, explainable in second Born approximation; that produced by projectile ionization processes is a transversely emitted charge distribution characterized by even-order multipole moments (monopole, quadrupole, hexadecapole, etc.) and maximum multipolarity $k = 2n$ determined by the principal quantum number n of the contributing projectile orbital; the cusp produced by swift charged particles passing through solid materials possesses the transverse signature of the projectile loss mechanism and becomes enriched in high-order multipoles with increasing projectile speed, suggesting steady-state excitation of high n -states during passage of the bulk material.

1.2. Background

Because of various experimental difficulties associated with performing electron spectrometry in the direction of a fast, intense ion beam, the mere existence of this prominent forward peak went unnoticed until the 1970 letter of Crooks and Rudd (1), who observed it in proton collisions with helium targets, and the only slightly later work with solid targets performed

by Harrison and Lucas (2). Since then, two fundamental processes have been identified as contributing to the forward peak: projectile capture of target electrons into low continuum states in the projectile rest frame, often referred to as Electron Capture to the Continuum (ECC); and loss of projectile electrons due to collisions with the target, or Electron Loss to the Continuum (ELC). Production of electrons in the forward peak in ion-solid collisions is more complex, and must involve some combination of at least these two processes and may involve others as well (3,4); in solid collisions, the forward peak electrons are named convoy electrons. The generic phenomenon is frequently called Electron Transfer to the Continuum (ETC). Several reviews of relevant experimental work have appeared (5-7).

Early theoretical work (8) showed the existence of the forward peak to be the consequence of the population of final states in the low-lying continuum of the projectile, i.e. states having velocities \vec{v} in the projectile rest frame (PRF) approaching zero. Under these circumstances the normalization factor associated with the Coulomb waves needed to describe emitted electrons interacting with a charged projectile leads to a cross section $d\sigma/d\vec{v}$ which diverges as $1/v$. This singularity is integrable and is integrated by any detection apparatus with finite solid angle, giving rise to a cusped peak in the laboratory frame (LF) cross-section. Further, there exists an intimate connection between the divergence of the ETC amplitude and the density of high Rydberg states; this connection is the result of the expectation that the probability per unit energy interval for finding an electron in a particular state is constant or continuous as the ionization limit is crossed.

Although the existence of the ETC cusp is merely a consequence of the Coulomb final state interaction, the details of the shape of the cusp reflect the entire history of the collision: anisotropies arise in the doubly differential cross section (DDCS) which are collision mechanism-dependent. In a recent theoretical paper, Burgdörfer (9) has developed a density matrix description of the ELC process which exploits smooth continuation of projectile excitation across the ionization limit to show that a set of dynamical multipoles originally introduced to describe bound-state coherences are suited for the description of continuum-state coherences as well. Consequently, the anisotropies in the DDCS for ELC can be expressed as expectation values of the dynamical multipoles. These dynamical multipoles contain the orientation and alignment parameters introduced by Fano and Macek (10) as a subset. In the Rydberg limit they reduce to multipoles of a constant of the motion, the Runge-Lenz vector \vec{A} , which in a classical picture points from the heavy particle to the electron perihelion, is proportional to orbital eccentricity, and defines the principal axis of the electronic orbit. Burgdörfer has since shown the method to be extensible to other ETC processes and to collisionally excited Rydberg manifolds (11). A unified approach thus emerges in which the same fundamental parameters describe the populations of cusp (ETC) and Rydberg electrons.

In the framework of the method advanced by Burgdörfer, the DDCS for ETC processes is expanded in the zero-velocity limit as

$$\frac{d\sigma}{d\vec{v}} = \left(\frac{a}{v}\right) \sum_{k=0}^{\infty} P_k(\cos\theta) \beta_k \quad [1]$$

where \vec{v} is the electron PRF emission velocity, P_k are the Legendre polynomials, and β_k are the asymmetry parameters derivable from the theory. Contact can also be made with the double-series expansion of the DDCS introduced by Meckbach, Garibotti, and co-workers (12) and employed in previous work in our laboratory (13) by expanding the β_k to account for finite-velocity

corrections to the cross section:

$$\frac{d\sigma}{dv} = \left(\frac{a}{v}\right) \sum_{k,j=0}^{\infty} B_{kj} v^j P_k(\cos\theta) . \quad [2]$$

Most experimental data on ETC processes to date, as typified by measurements presented in references (1),(2),(6),(12), and (13) for example, have been singly differential (in electron energy or longitudinal velocity component), even though in most cases a small range of collection angles have been employed. As a result, much of the collision-dependent information contained in the above DDCS expansions is lost in apparatus-dependent averaging over emission angles interior to the spectrometer collection cone. At the end of this paper, I will describe in more detail an apparatus and method developed in our laboratory which subdivides a forward-oriented collection cone of about 5 degrees half-angle into differential angular elements of about one-third degree full angle. These elements are sized so that the effective angular resolution in the PRF corresponds to a differential slice in transverse electron emission velocity v_t of a size comparable to that of the slice in longitudinal emission velocity v_L determined by the electron spectrometer employed. The apparatus collects data simultaneously from all elements within this forward cone by means of position-sensitive detection techniques and thereby permits efficient data acquisition, eliminates mechanical scanning linkages, and automatically determines the zero-degree direction. Sample emission distributions will be presented and interpreted in the framework of the multipolar expansion described above and related to specific theoretical results.

2. PROJECTILE ELECTRON LOSS (ELC)

2.1. Previous theory and experiment

ELC is most conveniently described in the projectile rest frame and in terms of projectile ionization to low-lying continuum states by means of collisions with the target nucleus and target electrons. From previous experiments measuring ELC from heavy ion projectiles in single collisions (6) it is known that the singly differential ELC cusp has a full-width-at-half-maximum (FWHM) which is smaller than expected and does not scale with projectile velocity as predicted by the earliest theories (14) of the process. While later theories (15) explicitly provided for anisotropic emission which in principle could account for this behavior, detailed agreement was not obtained for two reasons. First, the theory applied to loss of 1s projectile electrons, requiring a fully stripped L-shell (e.g. O^{7+} or O^{6+}); competition from ECC capture processes produces roughly an equal contribution to the cusp (6) under these circumstances with heavy ions. As we shall see later, the ECC process is anisotropic also, but with a strikingly different distribution than ELC.

It is possible to generate ETC cusps which are dominated (by roughly 10 to 1) by ELC by employing projectiles which carry more loosely-bound $n=2$ electrons (e.g. O^{5+}). The density matrix description of ELC developed by Burgdörfer (9) addresses the role of L- as well as K-shell electrons, thus permitting comparison with non-coincidence experiments, but more importantly provides a previously unnoted signature of ELC in the context of the first Born and hydrogenic projectile wave function approximation: in the cross-section expansions presented in Eqs [2] and [3], all odd-order multipoles vanish, and only those even order multipoles beginning with $k = 0$ and extending through $k = 2n$ occur, where n is the principal quantum number labelling the orbital from which the electron is lost. Thus for ELC from projectiles having L-shell electrons, one expects only monopole (β_0), quadrupole (β_2), and hexadecapole (β_4) moment terms in the DDCS expansion.

This leads to a distribution in \vec{v} -space which is transversely enhanced and thin-waisted longitudinally, and produces a singly-differential cusp, integrated over a small, fixed range of θ and all ϕ , which has a FWHM that is relatively narrow and relatively independent of projectile velocity.

ECC has received much detailed experimental and theoretical attention in the case of fast, heavy projectiles, most of which has centered about explaining the strong skewing of the singly-differential cross section (SDCS) toward emission of electrons slower than the projectile. References to most of the work pertinent to the present discussion, including theoretical approaches, can be found in the recent experimental paper by Berry et al. (13). The observed asymmetries of the ECC SDCS cusp are shown in that paper to be the result of a strong dipole moment in the emitted electron distribution. As discussed by Macek et al. (16), the presence of a dipole moment of this nature implies the necessity of second Born approximation terms in the cross section, as originally pointed out by Shakeshaft and Spruch (17). While instrumental in advancing our understanding of ECC, most of these treatments are of only qualitative use, as they are restricted to one-electron targets. A notable exception is the work by Jakubassa-Amundsen (18) based on expansion of the Faddeev equations in an impulse approximation, which obtains good agreement with the ECC cusp shapes observed with He targets and $v_p \sim 17$ au neon and oxygen projectiles.

2.2. Present observations and multipole content

Doubly differential distributions obtained in our laboratory with the apparatus described in Section 4 are shown in Figure 1 for the specific instance of 82 MeV O^{5+} in single collisions with Ar. The isometric display

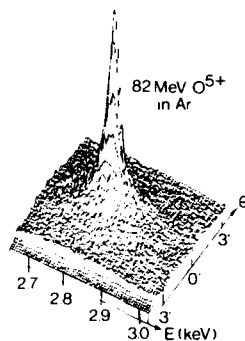


FIGURE 1

Doubly differential emission distribution observed for the forward peak in collisions of $v_p = 14.3$ au O^{5+} ions traversing a thin argon gas target.

format used in that figure is of limited utility in discussing emission distributions; a better display is obtained by showing only contours of equal emission intensity, with the longitudinal (emission energy) and transverse (emission angle) axes scaled so that equal intervals in either direction represent approximately equal intervals in longitudinal projectile frame emission velocity v_{\parallel} and transverse projectile frame emission velocity v_{\perp} . Such contoured data, corresponding least-squares fits (described later), and theoretical predictions are shown in summary form in Figure 2. The data shown are contours of equal intensity of electron emission in the emission-

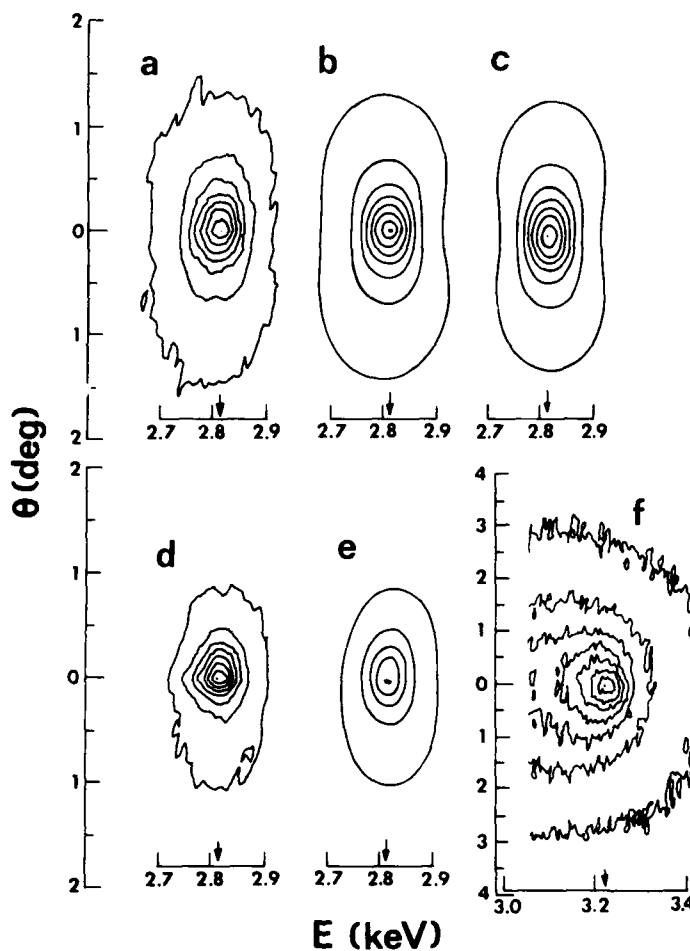


FIGURE 2

Contour plots for ELC by O^{5+} in Ar and He at $v_p = 14.3$ au, and ECC by O^{8+} in Ne at 15.4 au. Contours shown represent multiples of 12.5% of the peak height. Horizontal scale represents lab frame electron energy; vertical scale represents polar electron ejection angle. Scaling is chosen so that isotropic emission would produce essentially circular contours. (a) Measured distribution for Ar target. (b) Corresponding best fit to (a), normalized to peak height of data. (c) Theoretical distribution (Ref. 11) after convolution with spectrometer acceptance, also normalized to peak of (a). (d) Measured distribution for He target. (e) Corresponding He target fit, normalized to peak of (d). (f) Measured ECC distribution for 15.4 au O^{8+} in Ne.

energy and polar-emission-angle plane for single collisions of $v_p = 10.1$, 14.3 , and 16.2 au O^{5+} ions with He and Ar targets. As expected from the preceeding, the distributions are dominated by ELC from the loosely bound $n = 2$ levels by an order of magnitude over ECC and ELC from $n = 1$. The immediate appearance of these data are of strongly transverse emission, as predicted by Burgdörfer's calculation (9,11), and in striking contrast to the strong dipole character of the ECC distribution obtained from a $v_p = 15.4$ au collision in Ne. Also shown is the theoretical angular distribution calculated by Burgdörfer, convoluted with the spectrometer acceptance function $S(v_e, \Omega_e)$ (discussed in section 4.2).

Table I presents a comparison of experimentally extracted (by means of a fitting procedure discussed in section 4.2) and theoretical values for the asymmetry parameters β_2 and β_4 (with $\beta_0 \equiv 1$) as defined in Eq. [1]. Also shown in the table are ELC cross sections extracted from the DDCS data by integrating over the velocity interval $v_p \pm 0.5$ au and over a forward collection cone of half-angle $\theta_0 = 1.8$ deg. Agreement of the Ar target cross section with the value published previously (6) for $v_p = 10.1$ au is satisfactory, and with theory is at the factor-of-two level.

TABLE I. Comparison of experimental fit results with theoretical results of Burgdörfer (Ref. 9 and 11). Where multiple data sets were available, the fitted values represent the mean, and the statistical standard deviation of these averages (expressed as a percentage of the value) appears beneath the coefficients in parentheses.

v_p (au)	Gas	σ_{ELC} (kb)	β_2		β_4		χ^2 ^a
			Exp.	Th.	Exp.	Th.	
16.2	Ar	220	-0.68 (0.0)	-0.70	0.13 (0.0)	0.18	1.74 (8.1)
	He	5	-0.23	-0.66	-0.07	0.15	2.4
14.3	Ar	230	-0.62 (3.2)	-0.67	0.12 (16.7)	0.16	1.64 (17.2)
	He	8	-0.43	-0.64	0.06	0.14	1.83
10.1	Ar	330	-0.26	-0.56	0.05	0.10	1.55
	He	3	-0.23	-0.51	-0.04	0.07	1.85

^aReduced χ^2 as defined in Reference 26.

Excellent agreement is obtained for fitted values of the multipole strengths β_k of the argon data at the higher two velocities; the lesser agreement at 10 au is not of concern because the first Born approximation is suspected to be less accurate at lower v_p (9,11). The lack of agreement between helium target data and theory is of much greater concern. The simpler structure of this target and the use of more accurate scattering functions (9) than were available for argon would at first suggest a more accurate description for helium. An experimental source of a difference between these targets is unlikely because the data sets were alternately acquired for He and Ar targets by merely switching between target gas bottles on a time scale of minutes, while the accelerator operators were instructed

to leave all beam conditions (i.e. focusing and steering) unchanged. Further, although pixel-by-pixel 'gas-dump' background subtractions (see section 5) contribute more heavily to statistical and systematic errors with helium targets, the ELC to background ratio at the cusp peak was $\geq 11:1$ in the worse case (at $v_p = 16.2$ au where γ -Ray induced photoelectron background flux at the detector is most serious).

Lacking a known, sufficiently large source of experimental error that would selectively affect the helium data, we speculate that doubly inelastic collisions between the active projectile electron and target electrons may be responsible for the difference. In particular, Burgdörfer takes target-inelastic processes into account within the framework of a closure approximation and discusses it as a potential source of inaccuracy (9,11). Since the contribution of target-inelastic processes is fractionally more important for He because of its much smaller nuclear charge, study of the adequacy of the approximation seems to be indicated. It is also possible, of course, that an as yet unidentified excitation or ionization process is occurring either in addition to, or in combination with simple electron loss to the forward peak.

Applications of this confirmation of the even-order multipole nature of ELC processes to a more detailed study of ELC itself, especially with the addition of coincident-measurement of the post-collision charge state, or to the study of the convoy production process as described in section 4, are obvious. In addition, the method is applicable to the interesting experiment of Andersen et al. (19) who studied coincident double electron capture by 20 MeV Au^{15+} ions in He, one to a continuum state and one to a bound state. They find that the measured cusp shape (singly differential) is much more suggestive of ELC in its forward-backward symmetry than of the asymmetric shape they measure for ECC. In explaining how a captured electron can display the signature of a loss process, they conjecture the formation of a two-electron (quasi-bound) capture event involving a tightly space-correlated, two-electron wave function that rapidly autoionizes, producing a continuous energy spectrum characteristic of loss and having 'forgotten' its original capture origin. If so, the details of the angular distribution of this released electron could reveal much about the hypothetical correlated intermediate state. The methods presented here are ideally suited to confirmation and further study of this potentially important observation.

3. CONVOY ELECTRONS FROM SOLID TARGETS

3.1. Previous theory and experiment

The question of the extent to which charge and excitation states of ions are well-defined during passage through condensed matter targets and the relationship those states bear to measured charge and excitation states after passage is a long-standing one (20) which has gained much attention (21). It is often argued that high states of excitation have no meaning in a solid, especially when the characteristic orbital size $\sim n^2 a_0 / Z_p$ exceeds interatomic spacings. In models that take this approach, it is necessary that the processes which determine the exit charge and excitation state of the projectile occur in the last one or few atomic layers or in the electron 'selvage' that penetrates into the vacuum beyond the last layer. In the context of the production of convoy electrons, Yamazaki and Oda (3) have presented data that appear to favor such a last-layer mechanism.

On the other hand, the (singly differential) shape of previously reported convoy electron spectra produced by heavy ion passage through thin amorphous foil targets and channeled through single crystals have been most easily interpreted in terms of an electron loss (ELC) process occurring in the bulk medium, accompanied by elastic and inelastic scattering of the liberated

electron (6). The channeling data indicated a precursor electron capture inside the solid, probably to an excited n -state, followed almost immediately by loss to convoy states, since to a first approximation low- n electrons of well-channeled projectiles interact with neighboring lattice sites (and become ionized) only when the characteristic projectile size exceeds the channel dimensions. In these measurements, performed in coincidence with the emergent projectile charge state, little or no correlation was observed between convoy production yield and emergent charge state, at the projectile velocities (8 - 10 au) studied. This left a puzzle, as mean free paths for free electrons at the velocities in question were known to be ~ 20 Å, whereas the mean free paths for projectile charge changing was ~ 200 Å. It therefore seemed unlikely that a projectile responsible for convoy production would subsequently change charge state and should therefore be associated with the convoy in a coincidence measurement. Z (or Q) dependence of the capture and subsequent loss processes was then expected to produce convoy production noticeably stronger for some emergent charge state. Such was not found to be the case. Even if an additional process acting at the exit surface contributed to the final charge state, one would not expect the association between projectile and convoy electron to be completely broken.

Additional, although indirect, evidence that a bulk ELC process is involved in the production of high Rydberg states of foil-excited ions has been recently reported by Betz (4). Further, a study (22) of the target-thickness dependence of convoy production shows a gradual increase in production over thickness ranges of many hundreds of atomic layers, suggesting anomalously long mean free paths for convoy electron scattering (compared to free electron values) as well as bulk production.

Our recent measurements of the multipole moments of the emitted charge distribution, while limited in scope, are intriguing in that they suggest the feasibility of applying knowledge gained from ELC studies such as those in the previous section and extensions of theoretical studies like those of Burgdörfer (9) to probe the processes leading to convoy emission from condensed matter targets. They reveal multipole content of order well beyond the quadrupole and hexadecapole moments obtained for ELC from $n = 2$ orbitals and offer an opportunity to perform unique, new measurements sensitive to excitations of swift projectiles that occur while immersed in bulk material.

3.2 Present observations and multipole content

Figure 3 presents contoured emission distributions we have observed for convoy electron production together with corresponding data for ELC from equal velocity O^{5+} in argon. The targets employed ($15 \mu\text{g}/\text{cm}^2$) were substantially below equilibrium thickness. The resemblance between the convoy cusps and those for ELC is striking - both are strongly transverse - and the convoy data displays no evidence of the strong dipolarity which is the hallmark of ECC (see Figure 2f). We interpret this feature of the data to signify a prominent role for ELC in the convoy production process. The displayed ELC and convoy distributions differ in one important respect, however: attempts to fit multipole moments to the convoy distributions in the same manner as was done with the ELC data produced poor results until multipoles of order up to $k \sim 10$ were included in the fitting procedure. The resulting fitted values of β_k are given in Table II for the three impact velocities studied. As can be seen from a close examination of the β_k values, the enhanced multipolarity of convoy emission skews toward higher multipoles with increasing projectile velocity. Recalling that the maximum predicted multipolarity P_k of ELC from a given n level is $k = 2n$, the data then suggests convoy production which behaves as loss from highly excited states formed by capture or capture plus excitation within the bulk material of the target. Also shown in the table are values of $B_k \equiv \beta_k(\text{convoy})/\beta_k(\text{ELC})$ for $k = 2, 4$, which reflects the extent to which high k values for the convoy distributions rise beyond those for ELC at larger projectile velocities.

The observation of high n, l excitation within the target agrees with

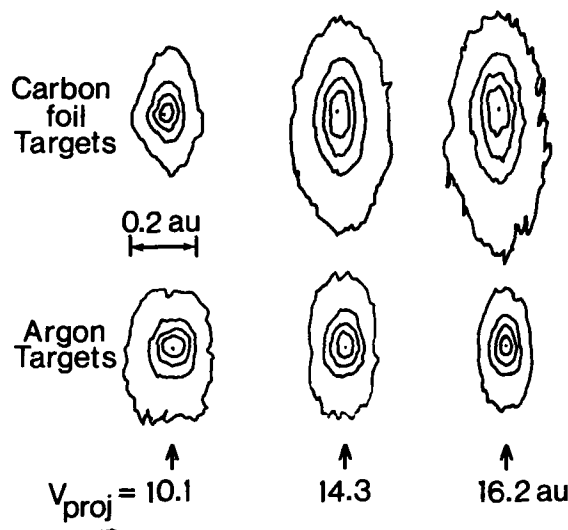


FIGURE 3

Contour plots of emission distributions for convoy electrons produced in thin carbon targets compared with those for ELC in argon. Contour levels shown represent intervals of 20% of each peak height. The horizontal dimension of each plot represents longitudinal velocity components; the vertical dimension is transverse to the projectile direction. Equal velocity scales are shown in each direction, with the bar indicating an interval of 0.2 au. Isotropic angular distributions would have circular contours.

recent assertions made by Betz, et al. (4) that such high states, produced within the bulk, are required to explain long-lived cascade tails of foil-excited S^{15+} Ly α .

The power and speed with which our method can determine high-order multipole content of ejected electron distributions and the inferred connection with high n, l excitation make several follow-up measurements of interest. Perhaps most obvious is a measurement of the target thickness dependence of the multipole content of convoy emission; addition of coincident detection of emergent ion charge state would permit measurement and comparison, in the same apparatus and under the same conditions, of mean free paths for convoy electron production and extinction and for projectile charge-changing. While it is expected that elastic and inelastic electron scattering processes which occur after convoy production and prior to or during exit from the foil surface (including the effect of the exit potential 'step') must be taken into account in any detailed examination of convoy multipole distributions, the strong Coulomb 'focusing' (23) provided by the nearby projectile ion may make these effects smaller than they would appear to free electrons of the same speed, at least for the highly charged ions studied here.

TABLE II. Comparison of β_k values for convoy distributions with those for ELC. Also shown are the even order coefficient ratios B_k defined in the text.

v_p (au)	Target	β_2	β_4	β_6	β_8	β_{10}
16.2	Carbon	-0.78	0.25	-0.32	0.19	-0.16
	Ar ^a	-0.68	0.13			
	Ar ^b	-0.70	0.18			
	B_k	1.1	1.9			
14.3	Carbon	-0.82	0.29	-0.26	0.07	-0.03
	Ar ^a	-0.62	0.12			
	Ar ^b	-0.67	0.16			
	B_k	1.3	2.4			
10.1	Carbon	-0.48	0.11	-0.18	0.09	-0.05
	Ar ^a	-0.26	0.05			
	Ar ^b	-0.56	0.10			
	B_k	1.8	2.2			

^aExperimental values from Reference 6.

^bTheoretical values from References 9 and 11.

4. METHOD

4.1. Apparatus

The electron spectrometric apparatus used in this work closely resembles that used in earlier experiments (6) on ECC, ELC, and convoy production, but differs in that electrons which have been energy-analysed are detected in a manner that recovers emission angle information. The major elements of the apparatus are diagrammed in Figure 4. The target region, which is a ~0.5 cm thick cell for gaseous targets and a self-supporting foil for solid target measurements, is viewed by a spherical sector electrostatic spectrometer having a mean deflection radius of 5.5 cm and a deflection angle of 160 deg. As is nearly universal in ETC apparatus, the primary ion beam exits the spectrometer through a hole in the outer spherical sector. Apart from small aberrations and in the absence of extraneous fields, the focusing properties of the spectrometer reestablish, with unit magnification at the exit aperture, the in-beam angular distribution of electrons having energies within the spectrometer pass-band. Collision region emission angles thus correspond one-to-one with arrival angles at the exit aperture. A drift region 15 cm in length following the exit aperture permits the preserved emission angles to develop into transverse position coordinates at the location of a position-sensitive detector (PSD).

The PSD consists of a tandem chevronned pair of microchannel plate electron multipliers, which preserve the primary event position information during the amplification process, followed by a circular-arc-terminated resistive anode of the kind first described by Lampton and Carlson (24). Four charge pulse outputs at the corners of the anode are independently amplified and then decoded using a simple ratiometric method to recover the primary event position and thus the emission angles or, more fundamentally, the transverse velocity components as a digital quantity that, in combination with the spectrometer pass energy, determines the emission coordinates of the

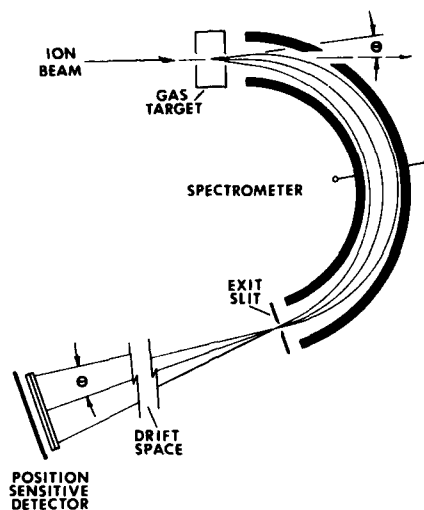


FIGURE 4

Schematic diagram of the spectrometric apparatus, equipped with position-sensitive detection to achieve resolution of emission angles.

detected electron. By acquiring such data for a sequence of pass-band energies (by scanning the deflection field), the entire three-dimensional \vec{v} -distribution of the ETC cusp can be obtained (in velocity space the projectile and laboratory frame distributions are related through the simple translation $v_{PRF} = v_{LF} - v_p$, where v_p is the projectile velocity). While the intrinsic position resolution of the PSD alone is 100 to 150 μm , the corresponding angular resolution of ~ 0.05 deg is broadened by the size of the 1 mm diameter spectrometer exit aperture (1.5 mm for ECC data) to ~ 0.35 deg (0.5 deg). The latter figure is improvable at the expense of counting rate. The spectrometer energy resolution is 0.9% FWHM (1.4% FWHM for the ECC data).

Not shown in Figure 4 are a pair of parallel mesh grids (80% transparent) oriented perpendicular to the axis of the drift space, spaced 3 mm apart, and located immediately prior to the microchannel detector entrance. The grids are biased to reject stray, low energy electrons. Also not shown are a pair of transverse deflection plates in the drift space which can be used both to compensate for deflection of energy-analyzed electrons induced by residual magnetic fields. The local magnetic field in the region of the spectrometer is nulled by a triplet of coils external to the vacuum system. Target gas pressure is controlled by a piezoelectric valve and monitored by a capacitance manometer. Beams of Oq^+ ions, $q = 5, 8$, having $v_p = 10.1, 14.3$, and 16.2 au were collimated and stripped of convoy electrons produced upstream of the apparatus by a pair of shielded electrostatic deflector plates.

4.2. Analysis of multipole content

The three-dimensional (differential in emission energy and polar and azimuthal angles) distributions produced by the apparatus are assessed for multipole content by means of a fitting procedure (25) based on the multipole expansions discussed in the introduction. The method is a straightforward

extension of that used for previous data published by our laboratory (13). In brief a trial function based on the double-series expansion in Eq. [2] and trial values of the parameters B_{kj} is convoluted with the spectrometer sensitivity function $S(E_e, \Omega_e)$, which in turn is assumed to be separable:

$$S(E_e, \Omega_e) = R(E_e) G(\theta_e, \phi_e). \quad [3]$$

$R(E_e)$ describes the spectrometer resolution and is approximated by a trapezoidal function characterized by a top width (TW) and a full-width-half-maximum (FWHM), whereas $G(\theta_e, \phi_e)$ describes the angular resolution and is approximated by a 'pillbox' function which is unity within an angle $\delta Y = (\text{angular resolution})/2$ of the central direction (θ_e, ϕ_e) . The integration implied by the convolution is done numerically. The fitting algorithm is based on the method of linearizing the trial function in the chi-square space formed by the variable (fitted) parameters, combined with a gradient-least-squares procedure as formulated in Bevington (26). The fitting routine permitted variation of an arbitrary subset of the above parameters while keeping the remainder fixed, to assess the importance of particular terms in the expansion with regard to the quality of the fit. Background subtraction was also incorporated into the fitting procedure using background emission distributions acquired specifically for that purpose. Because of the essential singularity of the DDCS for ETC processes at $\bar{v} = 0$, the cusp distributions are almost entirely determined by the spectrometer sensitivity function S at the peak of the cusp. To examine the sensitivity of the fitted parameters to the assumptions made in the spectrometer convolution, the fitting procedure also permitted the exclusion of data within one spectrometer sensitivity 'volume' of the cusp peak.

5. SUMMARY

Electron capture and loss to projectile-centered continuum states both produce a cusp-shaped electron emission spectrum centered at \bar{v}_p in velocity space and possessing a measured shape which is directly interpretable through multipole moments of the ejected electron charge distribution. Observed moments range from monopole to hexadecapole and beyond. For high projectile velocities, capture cusps typically differ from loss cusps by exhibiting larger longitudinal spread and large dipole moments parallel to \bar{v}_p . Loss cusps at similar velocities display larger transverse spread characterized by only even-order multipoles. By applying the principle of continuity of population amplitudes across the ionization limit, these multipole distributions are predicted for similar collisions which populate high Rydberg states and experiments testing this conjecture are indicated for the future.

Comparison of ELC cusp moment distributions with those for cusps produced by passage of ions through solids implies a dominant role for bulk ELC processes in the formation of the convoy peak. In addition, the presence of high-order moments indicates the possible importance of steady-state excitation of high n -states as projectiles traverse the bulk, and suggest a variety of further measurements that may shed light on the interesting problem of the state of ionic projectiles traversing condensed media.

ACKNOWLEDGEMENTS

I am especially grateful to J. Burgdörfer for providing the results of calculations from his theory for parameters specifically relevant to the electron loss measurements reported, and for helpful discussions. Other colleagues who have materially contributed to this work include I. A. Sellin, M. Breinig, R. DeSerio, C. Gonzalez Lepera, and J. Berry from the University of Tennessee and Oak Ridge National Laboratory, L. Liljeby of Atomfysik,

Sweden, K.-O. Groeneveld, D. Hofmann, and P. Koschar from U. Frankfurt/M., West Germany; and I. Nemirovsky of Centro Atomico Bariloche, Argentina. The work on electron loss is the subject of the Ph.D. thesis of S. Berry. I am also grateful for the cooperation and support of the Holifield Heavy Ion Research Facility staff in making the reported measurements. This research was supported by the U.S. National Science Foundation, Physics Division and Division of International Programs, and by the U.S. Department of Energy, under contract no. DE-AC05-84OR21400 with Martin Marietta Energy Systems, Inc.

REFERENCES

- 1) C.B. Crooks and M.E. Rudd, *Phys. Rev. Lett.* **25**, 1599 (1970).
- 2) K.G. Harrison and M.W. Lucas, *Phys. Lett.* **33A**, 142 (1970).
- 3) Y. Yamazaki and N. Oda, *Phys. Rev. Lett.* **52**, 29 (1984), and references therein.
- 4) H.-D. Betz, D. Röschenhaler, and J. Rothermel, *Phys. Rev. Lett.* **50**, 34 (1983).
- 5) V. Ponce and W. Meckbach, *Comments At. Mol. Phys.* **10**, 231 (1981).
- 6) M. Breinig, S. Elston, S. Hultdt, L. Liljeby, C. Vane, S. Berry, G. Glass, M. Schauer, I. Sellin, G. Alton, S. Datz, S. Overbury, R. Laubert, M. Suter, *Phys. Rev.* **A25**, 3015 (1982).
- 7) K.O. Groeneveld, W. Meckbach, I.A. Sellin, J. Burgdörfer, *Comments At. Mol. Phys.* **14**, 187 (1984).
- 8) J. Macek, *Phys. Rev.* **A1**, 235 (1970); M.E. Rudd and J. Macek, *Case Stud. At. Mol. Phys.* **3**, 47 (1972).
- 9) J. Burgdörfer, *Phys. Rev. Lett.* **51**, 374 (1983); J. Burgdörfer, M. Breinig, S.B. Elston, and I.A. Sellin, *Phys. Rev.* **A28**, 3277 (1983).
- 10) U. Fano and J. Macek, *Rev. Mod. Phys.* **43**, 553 (1973).
- 11) J. Burgdörfer, Density matrix description of collisional electron transfer into the continuum of ionic projectiles, in: *Lecture Notes in Physics; Forward Electron Ejection in Ion Collisions*, eds. K.O. Groeneveld, W. Meckbach, and I.A. Sellin (Springer-Verlag, Berlin, 1984) pp. 32-51; J. Burgdörfer, private communication.
- 12) W. Meckbach, I.B. Nemirovsky, C. Garibotti, *Phys. Rev.* **A24**, 1793 (1981); C.R. Garibotti and J. Miraglia, *J. Phys.* **B14**, 863 (1981).
- 13) S.D. Berry, G.A. Glass, I.A. Sellin, K.O. Groeneveld, D. Hofmann, L.H. Anderson, M. Breinig, S.B. Elston, P. Engar, M.M. Schauer, N. Stolterfoht, H. Schmidt-Böcking, G. Nolte, and G. Schiwietz, *Phys. Rev.* **A31**, 1392 (1985).
- 14) F. Drepper and J.S. Briggs, *J. Phys.* **B9**, 2063 (1976).
- 15) J.S. Briggs and F. Drepper, *J. Phys.* **B11**, 4033 (1978); J.S. Briggs and M.H. Day, *J. Phys.* **B13**, 4797 (1980); M.H. Day, *J. Phys.* **B13**, L65 (1980); M.H. Day, *J. Phys.* **B14**, 231 (1981).
- 16) J. Macek, J.E. Potter, M.M. Duncan, M.G. Menendez, M.W. Lucas, and W. Steckelmacher, *Phys. Rev. Lett.* **46**, 1571 (1981).
- 17) R. Shakeshaft and L. Spruch, *Phys. Rev. Lett.* **41**, 1037 (1978).
- 18) D.H. Jakubassa-Amundsen, *J. Phys.* **B. 16**, 1767 (1983).
- 19) L.H. Andersen, et al. *Phys. Rev. Lett.* **52**, 29 (1984).
- 20) N. Bohr and J. Lindhard, *K. Dan. Vidensk. Selsk. Mat. Fys. Medd.* **28**, No. 7 (1954).
- 21) See contributions to the proceedings of the 1981 and 1983 international conferences on atomic collisions in solids, *Nucl. Inst. and Meth.* **194**, pp. 1-514 (1982) and *Nucl. Inst. and Meth.* **B2**, pp. 1-279 (1984); H.-D. Betz, *Rev. Mod. Phys.* **44**, 465 (1972).

- 22) I.A. Sellin, S.D. Berry, M. Breinig, C. Bottcher, R. Latz, M. Burkhard, H. Folger, H.J. Frischkorn, K.O. Groeneveld, D. Hofmann, and P. Koschar, Anomalous mean free paths for scattering of convoy electrons generated by fast, highly ionized ions in thin solid targets, in: *Lecture Notes in Physics; Forward Electron Ejection in Ion Collisions*, eds. K.O. Groeneveld, W. Mehbach, and I.A. Sellin (Springer-Verlag, Berlin, 1984) pp. 109-114.
- 23) C. Bottcher, *J. Phys. B.* 11, 3887 (1978).
- 24) M. Lampton and C.W. Carlson, *Rev. Sci. Instr.* 50, 1093 (1979).
- 25) S.D. Berry, Ph. D. Dissertation, Univ. of Tennessee (unpublished, 1985).
- 26) P.R. Bevington, *Data Reduction and Error Analysis in the Physical Sciences*, (McGraw-Hill, New York, 1969).

MULTIPLE SCATTERING CONTRIBUTIONS IN ELECTRON CAPTURE THEORIES

Louis J. DUBÉ

Fakultät für Physik, Universität Freiburg
D-7800 Freiburg, West Germany

Recent advances in the inclusion of multiple scattering contributions in perturbation approaches to the electron capture process are reviewed. Special attention is given to the structural and asymptotic properties of existing theoretical models, as well as to the search for possible experimental evidences of multiple scattering effects in charge exchange collisions.

1. INTRODUCTION

The well-documented deficiencies of the single scattering approximation (hereafter referred to as the first Born (B1) or Oppenheimer-Brinkman-Kramers (OBK) approximation) in ion-atom collisions have led theorists over the years to look for more adequate alternatives (1). The unescapable necessity of including higher order (*multiple scattering*) terms in the description of the collision mechanism is particularly acute in electron capture collisions where the double and not the single scattering contribution is known (2) to dominate the total cross section at high (but non-relativistic) scattering energies, in distinction to the processes of excitation and ionization. The inclusion of multiple scattering contributions in perturbation approaches to the electron capture process provides the leit-motif of the entire discussion which now follows and is the central theme of this presentation.

Because of the special rôle played by the second order term in charge exchange, I devote Section 2 to the comparison of the single versus double scattering mechanism and present some perhaps unfamiliar aspects of the second Born (B2) approximation. Section 3 tells the saga of the birth and rise of multiple scattering approximations which have recently been proposed. The accent is placed not so much on a detailed discussion of the various scattering models but more so on their structural content resulting from successive approximations of the exact expression. New results concerning the high energy behaviour of the respective approximations are also briefly discussed. The penultimate Section 4 addresses itself to the comparison theory/experiment in two cases where the B1 approximation fails miserably. This provides a unique experimental and theoretical "measure" of multiple scattering effects. Finally, I conclude and summarize in Section 5.

Atomic units are used throughout.

2. SINGLE AND DOUBLE SCATTERING CONTRIBUTIONS

2.1 Some Notation

Let us consider for simplicity the collision of a fully stripped projectile (P) on an hydrogenic target (T). The capture process is characterized by the charges Z_T , Z_P and masses M_T , M_P of the target and projectile respectively, as well as by the initial and final bound state quantum numbers which I denote succinctly by $i = (Z_T, n'l'm')$ and $f = (Z_P, nlm)$.

The exact transition amplitude is then expressed as

$$t_{fi} = \langle \psi_f | V_{T,P} + V_T G^+ V_P | \psi_i \rangle \quad (2.1)$$

where the notation $V_{T,P}$ means that the *prior*, V_P , or the *post*, V_T , interaction of the electron with the projectile or target can be used interchangeably. G^+ is the full Green's operator associated with the complete Hamiltonian, H , which reads in terms of the initial and final unperturbed Hamiltonians, H_T and H_P ,

$$H = H_O + V_T + V_P \equiv H_T + V_P \equiv H_P + V_T \quad (2.2)$$

where H_O is the kinetic energy term. The corresponding wavefunctions, ψ_i and ψ_f , satisfy the equations

$$H_T | \psi_i \rangle = E | \psi_i \rangle, \quad H_P | \psi_f \rangle = E | \psi_f \rangle \quad (2.3)$$

at the same total energy E . Remark that I disregard from the onset the inter-nuclear interaction, V_{PT} , consistent with a formulation accurate to $O(m/M_{T,P})$. This is permissible at forward scattering angles where the dominant contributions to the total capture cross section arise.

By using the formal expansion

$$G = G_O \sum_n \{ (V_T + V_P) G_O \}^n \quad (2.4)$$

in terms of the *free* Green's function G_O , and inserting in (2.1), one obtains the *Born series*. In particular, retaining only the first term in (2.4), we arrive at the second Born amplitude

$$t_{B2} = \langle \psi_f | V_{T,P} + V_T G_O^+ V_P | \psi_i \rangle \\ \equiv t^{(1)} + t^{(2)}, \quad (2.5)$$

$t^{(1)}$ being the single and $t^{(2)}$ the double scattering contribution to the B2 amplitude.

2.2 Two capture mechanisms

The mechanisms underlying the single and double scattering contributions are perhaps best understood from the high velocity behaviour of the first, $\hat{\sigma}_{B1}$, and second, $\hat{\sigma}_{B2}$, Born cross sections. High velocity means $v \gg \max(v_T, v_P)$ where v_T and v_P are the characteristic orbital velocities in the initial and final states. The analysis for $\hat{\sigma}_{B1}$ is elementary and leads to the following velocity dependence

$$\hat{\sigma}_{B1} \propto v^{-12-2\ell'-2\ell} \quad (2.6)$$

which is easily understood as follows.

Since a free electron cannot be captured in a single binary collision, one is faced with a full three-body problem. Furthermore, that the electron does not change velocity during capture in the first-order approximation implies, therefore, that the single scattering mechanism (at high velocity) must operate with recourse to the high momentum components of the Fourier transforms of the wavefunctions in the initial and final state. These components fall off rapidly with increasing momentum as $v^{-4-\ell}$, explaining the strong velocity dependence of the single scattering mechanism.

In contrast, the double scattering amplitude gives rise to a v^{-11} dependence independent of the initial and final orbital momenta, reflecting the fact that the initial electron can be considered as free, or alternatively, that no high momentum components are needed to mediate capture. This result was first deri-

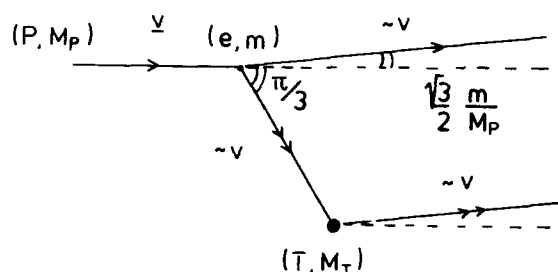


FIGURE 1

The classical Thomas scattering for electron capture ($m \ll M_P, M_T$).

ved by Drisko (3) whose analysis demonstrates that the quantum mechanical amplitude contains a dominant part which corresponds to two separate binary collisions, thereby reconciling the *quantum mechanical* calculation with the *classical* model of electron capture proposed by Thomas (4), a model which also predicts a v^{-1} fall-off of the cross section.

The classical description breaks up the three-body collision into two successive binary collisions where the electron first scatters off the projectile ion through 60° with respect to the beam direction and then through 60° off the target nucleus in such a way as to leave the electron with almost zero momentum with respect to the projectile nucleus (Fig. 1). In this picture, the v^{-1} originates from the product of two Coulomb scattering cross sections ($\propto v^{-4}$) and a geometrical factor $\propto v^{-2}$ (2).

One notices that in the process the projectile is scattered by a small but finite angle θ_T (called Thomas angle or more generally "critical angle" (2, 5, 6)) which in our case, i.e. $m \ll M_P, M_T$, is given by

$$\theta_T \approx \frac{m}{M_P} \sin 60^\circ = \frac{m}{M_P} \frac{\sqrt{3}}{2} \quad (2.7)$$

For proton impact, $\theta_T \approx 0.475 \text{ mrad} \approx 0.0272^\circ$. This prediction together with the equivalence of the Thomas scattering and the second Born approximation leads one to speculate (2) on the possible observation of the double scattering contribution in a differential scattering experiment. Although the search for the "Thomas peak" must have resembled at times the search for the Holy Grail, a recent experiment performed by Horsdal-Pedersen, Cocke and Stöckli (7) has succeeded to isolate the manifestation of the double scattering mechanism (Fig. 2). Instead of a single peak at the Thomas angle, they observe at high but non-asymptotic velocity a shoulder (around θ_T) in the differential cross section superimposed on a fast decreasing background, where the width of the structure reflects the finite momentum distribution of the captured electron.

A few remarks are worth mentioning. First, the success of this experiment has sparked renewed interest (6) in the appearance of critical angles in the general three-body collision where collision partners and hence mass ratios are taken arbitrary. Second, second order effects are not necessarily a particularity of rearrangement process, but are also present in break-up collision as predicted and measured (8) in the triple differential cross section of electron impact ionization, (e, 2e) process. Third, the experiment of Ref. 7 has taught us

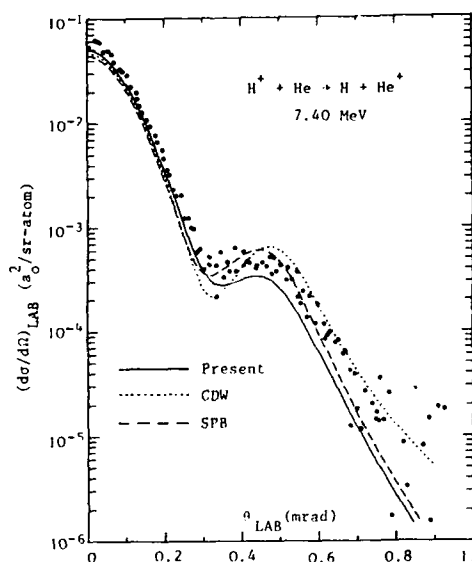


FIGURE 2

Experimental observation of the Thomas peak (7) compared with various theoretical models. From Ref. 10.

that although a second Born calculation reproduces qualitatively the data, it is however necessary to resort to multiple scattering theories (Section 3) in order to obtain quantitative agreement (9,10).

The asymptotic second Born cross section obtained by Drisko (3) for $1s + 1s$ capture is given by

$$\hat{\sigma}_{B2} = \hat{\sigma}_{B1} \left(0.295 + \frac{5\pi}{2^{11}} \frac{v}{Z_T + Z_P} \right) \quad (2.8)$$

which is the special case of a more general formula (11), namely

$$\hat{\sigma}_{B2} = \hat{\sigma}_{B1} (a_0 + a_1 v + \dots + a_{2\ell'+2\ell+1} v^{2\ell'+2\ell+1}) \quad (2.9)$$

valid for arbitrary initial and final states. Inspection of (2.8) indicates that in the integrated cross section the second term does not become equal to the first before $v \approx 80$ a.u. (for $Z_T = Z_P = 1$) although the presence of the double scattering is perceptible already at $v \approx 10$ a.u. (7). Since the dominance of the double scattering (v^{-11}) versus the single scattering ($v^{-12-2\ell'-2\ell}$) mechanism is strongly dependent on the orbital quantum numbers ℓ close this Section by displaying results obtained by considering capture from and to excited states.

Figure 3 shows the individual contributions to the B2 differential cross section, i.e.

$$d\sigma_{B1}/d\Omega \propto |t^{(1)}|^2, \quad d\sigma_2/d\Omega \propto |t^{(2)}|^2, \quad d\sigma_{B2}/d\Omega \propto |t^{(1)} + t^{(2)}|^2 \quad (2.10)$$

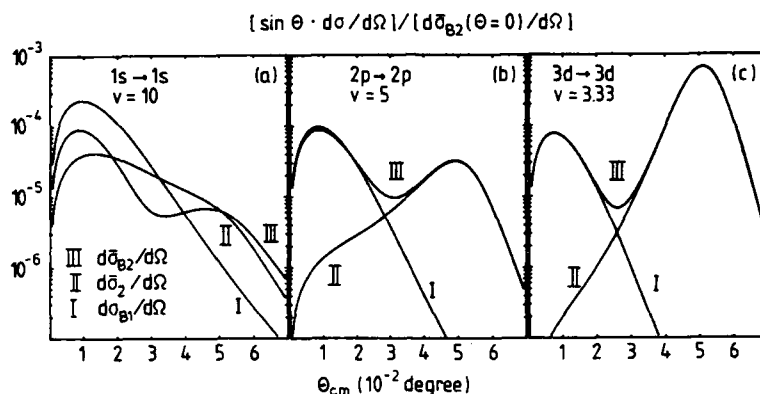


FIGURE 3

Separate contributions to the quantum mechanical second Born approximation ($Z_T = Z_P = 1$).

The cross sections are multiplied by $\sin\theta$ to make the area under the curves directly proportional to the integrated cross section. In order to facilitate the comparison, the velocity v and the states are chosen to give approximately equal integrated cross section in all three cases. As l' and l increase, the relative importance of the double scattering mechanism increase enormously for fixed reduced velocity $v/v_T = 10$ and the two mechanisms "separate" in their respective angular regions. Notice that the absence of interference between the first and second Born contribution for all but $s \rightarrow s$ states is a general result which is also reflected in the asymptotic behaviour (2.9) and in particular in the size of a_0 . Indeed a_0 can be shown to arise mainly from $\text{Re}(t_{11}^* t_{22})$ in (2.10). Whereas $a_0 = 0.295$ for all $s \rightarrow s$ states, a_0 approaches rapidly unity for higher orbital states, e.g. $a_0 = 0.811$ for $s \rightarrow p$ states and $a_0 = 0.997$ for $s \rightarrow d$ states (11).

Pursuing the task of mapping the regions where the differences between the single and double scattering mechanisms are most likely to appear, I show in Fig. 4 the final state distributions following electron capture from a Rydberg state ($n'=10, l'=6$). One sees that for all but the smallest velocity, the contribution of the double scattering mechanism, σ_2 , dominates clearly the final state distribution: σ_2 favours the larger n final states and for a fixed n (Fig. 4b) the largest possible l in strong contrast to σ_{B1} . That is to say that a signature of the double scattering mechanism is expressed in the fact that if one is to start from a Rydberg state, one is most likely to end up in a Rydberg state.

These results are consistent with the derivation of Spruch (12) who further points out that for systems involving electron transfer from one Rydberg state to another, the classical double scattering cross section is not only equivalent to the quantum mechanical one but becomes identical to it in the limit of large quantum numbers. In other words, classical and quantum mechanics agree that the double scattering process is the simplest mechanism that will mediate charge transfer at high velocity.

Having dwelt so far with only the first term beyond the single scattering approximation and leaving the processes of Fig. 3 and 4 as a challenge to the experimentalist, I now turn to consider the recent advances made in formulating multiple scattering approximations in charge exchange collisions.

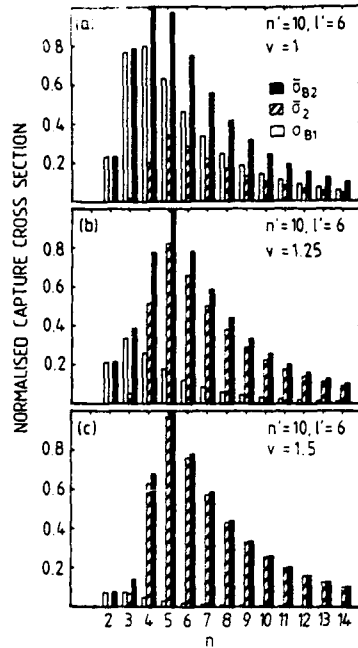


FIGURE 4a

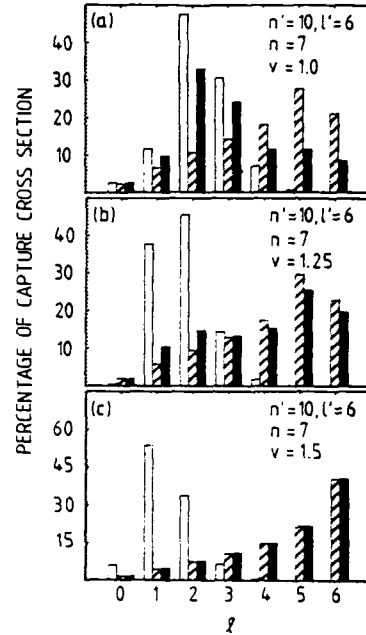


FIGURE 4b

Electron capture from an initial Rydberg state $(n'=10, l'=6)$. Individual contributions to the second Born approximation. a: $p + H(n'=10, l'=6) \rightarrow H(n) + p$, $\sigma(n'l' \rightarrow nl)$ normalised to unity at the maximum of the n -distribution; b: $p + H(n'=10, l'=6) \rightarrow H(n=7, l) + p$, $(\sigma(n'l' \rightarrow nl)/\sigma(n'l' \rightarrow n))\%$.

3. MULTIPLE SCATTERING APPROXIMATIONS

3.1 Formal expansions

To bring the concept of multiple scattering into sharper focus, let me start with the exact transition amplitude (2.1). On the energy shell, one can rewrite (2.1) in two equivalent forms, viz.

$$\begin{aligned} t_{fi}^+ &= \langle \psi_f | V_T | \psi_i^+ \rangle \\ t_{fi}^- &= \langle \psi_f^- | V_P | \psi_i \rangle \end{aligned} \quad (3.1)$$

where t_{fi}^+ and t_{fi}^- are referred to as the *post* and *prior* forms respectively. The corresponding transition operators, T^\pm , are then obtained by using in (3.1) the Lippmann-Schwinger equations for the scattering waves,

$$\begin{aligned} \psi_i^+ &= \psi_i + G_T^+ V_P \psi_i^+ = \psi_i + G_T^+ V_P \psi_i \\ \psi_f^- &= \psi_f + G_P^- V_T \psi_f^- = \psi_f + G_P^- V_T \psi_f \end{aligned} \quad (3.2)$$

to give $t_{fi}^{\pm} = \langle \psi_f | T^{\pm} | \psi_i \rangle$ where

$$\begin{aligned} T^{+} &= V_T + V_T G^{+} V_P \\ T^{-} &= V_P + V_T G^{+} V_P \end{aligned} \quad (3.3)$$

The Green's operators associated with H , H_T , H_P and H_0 are denoted by G , G_T , G_P and G_0 and defined as

$$G_X^{\pm} = \{E - H_X \pm i\eta\}^{-1} \quad (3.4)$$

where η is a positive infinitesimal.

Approximations of the transition operators (3.3) (or alternatively of the scattering waves (3.2)) are most easily obtained by truncating a series expansion of the full Green's operator. We have already encountered in Section 2 such an approximation in the truncation of the Born series (2.4). In fact insertion of (2.4) in (3.3) makes particularly clear the interpretation of the Born expansion as a *multiple scattering series* in which the electron interacts repeatedly with the potential V_P or V_T and propagates according to the free propagator, G_0 , between two such interactions. Explicitly, the individual multiple scattering terms, $T_B^{(j\pm)}$, of the Born expansion for the transition operator T^{\pm} read

$$\begin{aligned} T_B^{(1+)} &= V_T, \quad T_B^{(1-)} = V_P \\ T_B^{(j\pm)} &= V_T G_0^{+} \{(V_T + V_P) G_0^{+}\}^{j-2} V_P \end{aligned} \quad (3.5)$$

with the n th-order approximation given by

$$T_{Bn}^{(\pm)} = \sum_{j=1}^n T_B^{(j\pm)} \quad (3.6)$$

The appearance of the full interaction, $V_T + V_P$, in (3.5) shows that for each multiple scattering term, $T_B^{(j\pm)}$, there exist 2^{j-2} different sequences of scattering events corresponding to distinct ordering of the individual interactions. For example, for $j=4$, one has the four possible combinations (classified for short by the appropriate sequence of interactions): $V_T V_T V_P V_P$, $V_T V_T V_P V_P$, $V_T V_P V_T V_P$

$V_T V_P V_P V_P$. That is to say that the n th Born approximation contains all powers of the potentials V_T and V_P up to the order $n-1$, i.e. the Born approximation provides no ordering, as one could expect from a perturbation expansion, in powers of one or the other interactions. Although this remark applies to direct as well rearrangement collisions, one sees moreover that for the rearrangement process the first Born approximation is never a consistent first order approximation. This flaw of the Born series for charge exchange and, in particular for asymmetric collision partners ($Z_P \gg Z_T$ or $Z_T \gg Z_P$) where the strength of one interaction is markedly larger than the other, has been recently stressed and has led to a resummation of the Born series (13,14). For reasons which will become clear shortly, the expansion is called the strong potential Born (SPB) series.

Since the difficulty clearly arises from the use of the *free* Green's function in (2.4), one considers as alternative the following operator identities:

$$\begin{aligned} G &= G_P + G_P V_T G = G_P \sum_n (V_T G_P)^n \\ G &= G_T + G_T V_P G = G_T \sum_n (V_P G_T)^n \end{aligned} \quad (3.7)$$

involving the Coulomb Green's operators G_P , G_T . These expansions in turn lead in (3.3) to a series characterized by multiple scattering terms of the form

$$T_{SPB}^{(1+)} = V_T + V_T G_P^+ V_P, \quad T_{SPB}^{(1-)} = V_P + V_T G_T^+ V_P \quad (3.8a)$$

$$\begin{aligned} T_{SPB}^{(j+)} &= V_T G_P^+ \{V_T G_P^+\}^{j-1} V_P \\ T_{SPB}^{(j-)} &= V_T \{G_T^+ V_P\}^{j-1} G_T^+ V_P \end{aligned} \quad (3.8b)$$

In distinction to (3.5), these expansions are well-ordered in powers of V_P or V_T and possess a consistent first order approximation in (3.8a).

Let me consider in more details these first order approximations. First, an infinite subset of terms of the full Born series is now summed explicitly in

$T_{SPB}^{(1\pm)}$. These terms have the following structure: either $V_T V_T \dots V_T V_P$ in $T_{SPB}^{(1-)}$

or $V_P V_P \dots V_P V_P$ in $T_{SPB}^{(1+)}$. One potential is therefore retained to first order only whereas multiple scatterings with the other potential are built in to all orders through the Coulomb Green's operators. This makes plausible, in the context of asymmetric collisions for which $Z_P \gg Z_T$ ($Z_T \gg Z_P$) and where in some sense one can speak of a strong V_P (V_T) and a weak potential V_T (V_P), the name SPB approximation. Second, since the approximation is by construction *asymmetric* in the way it treats both interactions, the two forms of the SPB transition amplitudes

$$t_{SPB}^{\pm} = \langle \psi_f | T_{SPB}^{(1\pm)} | \psi_i \rangle \quad (3.9)$$

are obviously no longer equivalent in contrast to (3.1), although they still possess the important property of containing to lowest order (i.e. $G_T \approx G_P \approx G$) the second Born approximation guarantying thereby the correct high energy behaviour. Third, as far as the transition operator is concerned, there exists only one proper *physical* form of the approximation dictated by the ratio Z_T/Z_P : the post form for Z_T/Z_P small and the prior form for Z_T/Z_P large. However since ψ_f and ψ_i are also functions of Z_P and Z_T the situation is not so clear-cut for the amplitudes (3.9) because they are not analytic functions of Z_T/Z_P (14). One should then probably consider in addition other collision parameters such as v_P and v_T , in selecting the appropriate approximate amplitude in a given physical situation. This point is currently under investigation.

Fourth, the expressions (3.9) can also take the form

$$t_{SPB}^+ = \langle \psi_f | V_T | \chi_i^+ \rangle \quad \text{and} \quad t_{SPB}^- = \langle \chi_f^- | V_P | \psi_i \rangle \quad (3.10)$$

where I have introduced the "distorted" waves

$$|\chi_i^+\rangle = (1 + G_P^+ V_P) |\psi_i\rangle \quad |\chi_f^-\rangle = (1 + G_T^- V_T) |\psi_f\rangle, \quad (3.11)$$

displacing simply the approximations from the transition operators to the scattering wavefunctions.

3.2 Structural (genealogical) information

Having introduced the fundamentals of some formal multiple scattering expansions, I now want to turn to the classification of existing multiple scattering approaches. Two groups can be distinguished: one in which a partial summation of subsets of the Born series is sought for, and one where a distorted wave formalism attempts to incorporate an adequate description of the distortion caused by the projectile and target ions in the entrance and exit channel respectively. The members of the first class emerge in the particular choice of *continuum*

intermediate states, whereas the members of the second class are obtained by successive approximations of the channel distortions. It is evident that this separation is somewhat artificial since both points of view often provide complementary information on the approximation. Other characteristics are also necessary to qualify the different approaches, such as i. their *symmetry properties* in the treatment of the target and projectile fields, ii. their *asymptotic behaviours* (Section 3.3), and iii. their *region of applicability* in terms of the various collision parameters (Z_T/Z_P , v_T , v_P and the relative velocity v). Two possible classification schemes are shown in Fig.5. The reader is urged to take these orderings with the necessary grain of salt.

Starting from the top in Fig.5a, one encounters the newly derived (15) distorted-wave Born (DWB) approximation. The approach is meant to extend the regime of applicability of the SPB approximations to *symmetric* collision partners ($Z_T=Z_P$) by removing the blatant asymmetric introduced in the SPB amplitudes: to this effect, the DWB amplitudes do not have any post-prior discrepancy, i.e. $t_{DWB}^+ = t_{DWB}^-$. Their connection to the SPB theory is best illustrated by defining the two-body transition operators

$$T_P = V_P + V_P G_P V_P, \quad T_T = V_T + V_T G_T V_T \quad (3.12)$$

in terms of which the DWB amplitudes take the form (10)

$$t_{DWB}^\pm = t^{(1\pm)} + \langle \psi_f | T_T G_T^+ T_P | \psi_i \rangle = t^{(1\pm)} + \langle \chi_f^- | V_T G_O^+ V_P | \chi_i^+ \rangle \quad (3.13)$$

followed by the chain of approximations

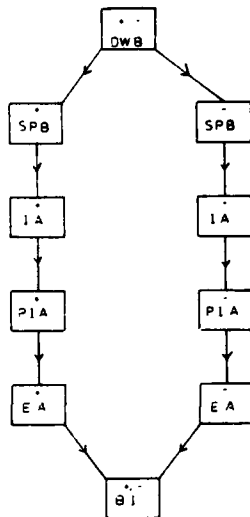


FIGURE 5a

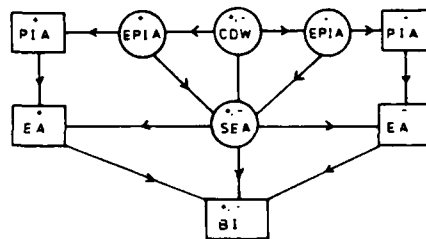


FIGURE 5b

Classification of multiple scattering approaches according primarily (a) to their treatment of the intermediate continuum state and (b) to the inclusion of channel distortions.

$$\begin{aligned}
t_{\text{SPB}}^+ &= t^{(1+)} + \langle \psi_f | V_T G_O^+ T_P | \psi_i \rangle = t^{(1+)} + \langle \psi_f | V_T G_O^+ V_P | \chi_i^+ \rangle \\
t_{\text{SPB}}^- &= t^{(1-)} + \langle \psi_f | T_P G_O^+ V_P | \psi_i \rangle = t^{(1-)} + \langle \chi_f^- | V_T G_O^+ V_P | \psi_i \rangle
\end{aligned}$$

One observes the close structural similarity of (3.13) with the B2 approximation. The DWB theory incorporates a much broader subset of the Born series as the SPB approach does, in that all terms of the form $V_T V_T \dots V_T V_P V_P \dots V_P V_P$ are summed up. It is perhaps interesting in the present context to mention that the DWB approximation can also be derived from the Schwinger variational principle (15, 16) in which the SPB amplitudes emerge as the lowest order approximation (17) (i.e. when ψ_i and ψ_f are chosen as trial wavefunctions). The connection with the Faddeev-Watson scattering formalism (16) has also been made (10, 15).

On the practical side, the SPB amplitude has been evaluated to date only for low quantum numbers and with the help of various analytic approximations (13, 18) and a single approximate calculation of t_{DWB} has been reported (10, curve labelled "present" in Fig. 2). It is not clear to what extent the approximations destroy the physics one has built into these theories and one badly needs reference calculations to answer this question. At present, little is known about the exact evaluation of t_{SPB} and t_{DWB} except that one would be faced with unsuspected difficulties, in form of divergences, in trying to do so (19). It is fair to say that the initial excitement over the SPB and DWB has now given way in some circles to wary skepticism. However, suggestions for the removal of these singular behaviours (19, 20) are already paving the way to an anomaly-free theory.

Ignoring for the moment these controversial aspects, let me concentrate on the strength of the SPB approach. This is most easily done by performing the Fourier analysis of (3.9) to get (for conciseness only the prior form is presented)

$$t_{\text{SPB}}^-(K) = (2\pi)^{3/2} \int d\underline{k} \, \tilde{\phi}_f^*(\underline{k}) \tilde{V}_P(\underline{k}') \langle \psi_{\underline{k}+\underline{v}, \epsilon_-}^-(Z_T; \underline{r}) | \exp(i\underline{k}' \cdot \underline{r}) | \phi_i \rangle \quad (3.14)$$

with $\underline{k}' = \underline{k} + \underline{K}$. \underline{K} is the momentum transfer, ϕ_i, ϕ_f are initial/final bound state wavefunctions with binding energies ϵ_i, ϵ_f and \tilde{f}_- represents the Fourier transform of the function f_- . The intermediate state $\psi_{\underline{k}+\underline{v}, \epsilon_-}^-(Z_T; \underline{r})$ is in general an off-shell (i.e. $\epsilon_- \neq (\underline{k}+\underline{v})^2/2$) continuum wavefunction in the field of the target with the off-shell energy given by

$$\epsilon_- = v^2/2 + \underline{k} \cdot \underline{v} + \epsilon_f \quad (3.15)$$

The amount by which this energy differs from its on-shell value can easily be estimated as

$$|\epsilon_f| \equiv v_P^2/2 \lesssim (\underline{k}+\underline{v})^2/2 - \epsilon_- \lesssim v_P^2 \equiv 2|\epsilon_f|. \quad (3.16)$$

This follows from the observation that the momentum wavefunction $\tilde{\phi}_f(\underline{k})$ has a sharp maximum at $\underline{k} = 0$ with half width of the order $|\underline{k}| < v_P$. Although the relative deviation from the on-shell energy can be made small for $v^2 \gg v_P^2$, the approach to the shell is non-uniform and lead to sizeable corrections with respect to the pure on-shell wavefunction. The essential and novel features of the SPB theory follow from allowing for a proper account of the off-shell nature of the intermediate continuum state. A comprehensive mathematical discussion of this point is to be found in Refs. (13, 14, 18).

For our purpose, the important result lies in the increased region of validity of the SPB amplitudes to the intermediate energy regime. Roughly, they are expected to be applicable for velocities

$$\begin{array}{lll}
 v^2 \gg v_p^2 & v^2 = v_T^2 & \text{in the prior SPB with } Z_T \gg Z_P \\
 v^2 \gg v_T^2 & v^2 = v_p^2 & \text{in the post SPB with } Z_P \gg Z_T
 \end{array} \quad (3.17)$$

This should be compared with the criterion $v^2 \gg \max(v_p^2, v_T^2)$ which applies to all other approaches (except DWB) listed in Fig.5. The absence of complete and reliable error analysis and the scarcity of experimental data over a wide range of collision parameters make it difficult however to delineate the regions of validity of each approximation in any definitive manner.

Inspection of Eqn.(3.14) reveals a simple physical interpretation of the capture process. The mechanism consists of first "ionizing" the active electron from its initial state to a continuum state centred on the target by absorption of a momentum \underline{k}' from the heavy particle motion. This transfer of momentum is mediated by the single scattering in the (weak) field V_P whose strength is given by $\tilde{V}_P(\underline{k}')$. The capture is then completed by projecting this ionization matrix element onto the momentum distribution $\tilde{\phi}_f(\underline{k})$ of the final state. This close resemblance with the ionization process (13,14,21) gives further support to the statement that the SPB approximation is to charge exchange what the first Born approximation is to ionization.

In connection with the classification of Fig.5a, one has yet to indicate the relationship among the other members of the hierarchy. They all emerge from successive simplifications in the way the target continuum is treated. The necessary mathematical steps are spelled out in Refs.(21,22) and the interested reader is to look there for the technical details. The impulse approximation (IA,23) is obtained by replacing the off-shell wavefunction $\psi_{\underline{k}+\underline{v},\epsilon_-}$ by its on-shell counterpart $\psi_{\underline{k}+\underline{v}}$,

$$t_{IA}^-(\underline{K}) = (2\pi)^{3/2} \int d\underline{k} \tilde{\phi}_f^*(\underline{k}) \tilde{V}_P(\underline{k}') \langle \psi_{\underline{k}+\underline{v}}^-(Z_T; \underline{r}) | \exp(i\underline{k}' \cdot \underline{r}) | \phi_i \rangle. \quad (3.18)$$

A peaking form of the IA (PIA,24) eliminates further the \underline{k} dependence of the matrix element appearing in (3.18), recognizing that $\tilde{\phi}_f(\underline{k})$ experiences a strong maximum at $\underline{k} \approx 0$,

$$t_{PIA}^-(\underline{K}) = (2\pi)^{3/2} \langle \psi_{\underline{v}}^-(Z_T; \underline{r}) | \exp(i\underline{K} \cdot \underline{r}) | \phi_i \rangle \int d\underline{k} \tilde{\phi}_f^*(\underline{k}) \tilde{V}_P(\underline{k}') \quad (3.19)$$

This apparently innocuous approximation has the virtue of making (3.19) analytically tractable for arbitrary initial and final states (22) but affects its asymptotic behaviour (Section 3.3) in such a way as to decrease enormously its applicability (25). Another akin method is the eikonal approximation (EA,26) which was the first multiple scattering approach to appear going beyond the BI approximation and for which amplitude and cross sections are available in closed form and for a wide range of quantum numbers. One obtains the EA amplitude from expression (3.19) by using instead of $\psi_{\underline{v}}^-(Z_T; \underline{r})$ its asymptotic form for large argument ($v r + \underline{v} \cdot \underline{r}$), viz.

$$\psi_{\underline{v}}^-(Z_T; \underline{r}) \rightarrow (2\pi)^{-3/2} \exp(i\underline{v} \cdot \underline{r}) \exp(i v_T \ln(v r + \underline{v} \cdot \underline{r})) \quad (3.20)$$

with $v_T = Z_T/v$. In view of the success that the EA has enjoyed in comparison with experiment, the present way of "deriving" it as a mathematical infant of the PIA probably obscures its merits. Finally, the BI approximation is recovered by replacing the continuum state by an undistorted free wave.

Of the many multiple scattering methods which have appeared over the years, the continuum distorted wave (CDW) approximation has received constant attention (27) since its conception in the mid-sixties by Cheshire (28). The method is the central element of the classification shown in Fig.5b. Its major characteristics are i. a symmetric (albeit approximate) treatment of channel distortions

ii. a particular attention to satisfy the proper boundary conditions and iii. the possible reduction of its transition amplitude to an analytic closed-form expression. The recent developments are many and comprise the implementation of t_{CDW} to cover arbitrary initial and final states (22,29,30), the proposal for various refinements (31), the extension of CDW to second-order (CDW2,32), the discussion (33) and derivation (34) of its asymptotic velocity dependence and to emphasize its versatility its successful application to ionization (35).

Once again I confine myself to an operational derivation of the approximations appearing in Fig.5b. Let me consider for this purpose the functional (36)

$$t(\psi_{tf}^-, \psi_{ti}^+) = \langle \psi_{tf}^- | (H - E) | \psi_{ti}^+ \rangle \quad (3.21)$$

where the functions ψ_{tf}^- , ψ_{ti}^+ are still to be chosen. One can easily convince oneself that the on-shell limit (i.e. E_f of ψ_{tf}^- and E_i of ψ_{ti}^+ both equal to E) of $t(\psi_{tf}^-, \psi_{ti}^+)$ is identical to the exact transition amplitude (3.1) when ψ_f^- and ψ_i^+ are the exact scattering wavefunctions given by (3.2). The choice of distorted waves appropriate to the methods of Fig.5b can then be shown to be of the form

$$\begin{aligned} |\xi_i^+\rangle &= |\psi_i\rangle L_i^+ & |\hat{\xi}_i^+\rangle &= |\psi_i\rangle \hat{L}_i^+ \\ |\xi_f^-\rangle &= |\psi_f\rangle L_f^- & |\hat{\xi}_f^-\rangle &= |\psi_f\rangle \hat{L}_f^- \end{aligned} \quad (3.22)$$

where the coordinate representation of the distortion operators $L_{i,f}$ and $\hat{L}_{i,f}$ reads

$$\begin{aligned} L_i^+ &= N(v_p) |F_1(i v_p, l; i(v r_p + v \cdot r_p)) \\ L_f^- &= N(v_T)^* |F_1(i v_T, l; -i(v r_T + v \cdot r_T)) \\ L_i^+ &= \exp(-i v_p \ln(v r_p + v \cdot r_p)) \quad , \quad \hat{L}_f^- = \exp(i v_T \ln(v r_T + v \cdot r_T)) \end{aligned} \quad (3.23)$$

where $N(v) = \exp(\pi v/2) \Gamma(1-iv)$ and r_p , r_T are the position vectors of the electron with respect to the projectile and target respectively. The symmetric CDW approximation and its asymmetric partners PIA \pm correspond to the insertion of (3.22) in the functional (3.21) to give

$$t_{CDW}^+ = \langle \xi_f^- | (H - E) | \xi_i^+ \rangle \quad (3.24a)$$

$$t_{PIA}^+ = \langle \psi_f^- | (H - E) | \xi_i^+ \rangle = \langle \psi_f^- | V_T | \xi_i^+ \rangle \quad (3.24b)$$

$$t_{PIA}^- = \langle \xi_f^- | \{(H - F) | \psi_i^+\} \rangle = \langle \xi_f^- | V_P | \psi_i^+ \rangle \quad (3.24c)$$

where the asymmetric nature of the PIA \pm is once again reemphasized. If one is then to use the eikonal phases, $\hat{L}_{i,f}^{\pm}$, as distortions, one obtains, in the same spirit as in the CDW, a symmettization of the eikonal approximation. This newly proposed method, called the symmetric EA (SEA, 37), again with its asymmetric versions EA \pm , is explicitly

$$t_{SEA}^+ = \langle \hat{\xi}_f^- | (H - E) | \hat{\xi}_i^+ \rangle \quad (3.25a)$$

$$t_{EA}^+ = \langle \psi_f^- | (H - E) | \hat{\xi}_i^+ \rangle = \langle \psi_f^- | V_T | \hat{\xi}_i^+ \rangle \quad (3.25b)$$

$$t_{EA}^- = \langle \hat{\xi}_f^- | \{(H - E) | \psi_i^+\} \rangle = \langle \hat{\xi}_f^- | V_P | \psi_i^+ \rangle \quad (3.25c)$$

The SEA has already been shown to be quite successful in comparison with experiment (37) and possesses the advantage that the distorted waves used are always

properly normalized in distinction to the CDW approximation where the lack of normalisation leads to difficulties (too large cross sections) at small velocities. The last two members of the present family which I denote by EPIA \pm are some sort of hybrid where distortions are included in both channels, using the eikonal distortion \hat{L}_f^- (\hat{L}_i^+) in the final (initial) channel and L_i^+ (L_f^-) in the initial (final) channel for EPIA $+$ (EPIA $-$). The incentive and predictions of such an hybridization are discussed in Ref.38. Remark finally that the SPB amplitudes can be obtained formally by replacing $|\xi_i^+\rangle$ and $|\xi_f^+\rangle$ in (3.24 b-c) by $|\chi_i^+\rangle$ and $|\chi_f^+\rangle$ of Eqn.(3.11).

A common feature of the members of this second hierarchy is that, once the choice of distorted waves has been made, the transition amplitude can be reduced in all cases without any further approximation to a closed-form expression for arbitrary initial and final states. This will allow in the future for a test of the consistency of the various approximations.

The methodology I have adopted in this Section to expose the connections between a variety of multiple scattering theories can not pay full credit to the formal and mathematical developments of the last few years. However, the simple vehicles of continuum intermediate states and channel distortions serve well the purpose of displaying and classifying the common and complementary facets of the rapidly growing classes of multiple scattering methods.

3.3 Asymptotic information

The asymptotic velocity dependence of charge exchange theories is still another way to classify the various approximations. Many new results have appeared lately and we will see that few of the methods discussed so far have the desirable property of behaving asymptotically as the double scattering term.

In order to simplify the analysis, I have proposed recently (39) to extract the leading velocity dependence (i.e. the equivalent last term in an expansion of the type (2.9)) of higher order theories from a study of the double scattering term. The strategy is that under the assumption that the leading velocity dependence is given solely by the double scattering term, the problem of finding this dependence for a full multiple scattering expansion is reduced to that of examining the asymptotic behaviour of the corresponding double scattering amplitude included (implicitly or explicitly) in the expansion. This procedure has been applied with success to the PIA \pm (39) and the EA \pm (40) and the reader is referred to Refs(39,40) for more details.

Since the DWB, SPB and IA theories contain explicitly the double scattering term $V_i^+ G_0^+ V_f$ in its multiple scattering expansion (Sections 3.1, 3.2), the method of Ref.39 makes it plausible in the absence of a rigorous mathematical derivation that the asymptotic velocity dependence of these theories is given by

$$\delta_{DWB}^+ = \delta_{SPB}^+ = \delta_{IA}^+ = \delta_{B2}^+ \propto v^{-11} \quad (3.26)$$

to leading order only and for arbitrary states. This statement is valid only for the leading coefficient and much more care is necessary to extract the lower terms in the complete asymptotic expansion.

On the other hand, the PIA \pm as a result of the peaking approximation have lost part of their Thomas scattering contribution and display a velocity dependence at variance with that of the IA from which it is derived, viz.

$$\delta_{PIA}^+ \propto v^{-11-2\ell}, \quad \delta_{PIA}^- \propto v^{-11-2\ell} \quad (3.27)$$

This discrepancy can be traced directly to the use of the peaking approximation and sheds some light on the application of this high energy approximation. Table 1 and Fig.6 displays rather eloquently the effects of the peaking on the IA: for example, for $Z_T=Z_P=1$, $1s \rightarrow 3d$, the ratio $R_{PIA} = \delta_{PIA}^+ / \delta_{B2}^+ = 4^5 = 1024$! That is to say that while peaking approximations are frequently valuable, their

TABLE 1. Asymptotic ratios $\hat{R}_x = \hat{\sigma}_x / \hat{\sigma}_{B2}$ ($v_T = \gamma v_p$).

	1s \rightarrow 1s	1s \rightarrow 2p	1s \rightarrow 3d
\hat{R}_{PIA}^+	$(1+\gamma)$	$(1+\gamma)^3$	$(1+\gamma)^5$
\hat{R}_{PIA}^-	$(1+\gamma)/\gamma$	$(1+\gamma)^3 2^3 (v_p/v)^2 / \gamma$	$(1+\gamma)^5 2^7 (v_p/v)^4 / 3\gamma$
\hat{R}_{CDW}	1	$(1+\gamma)$	$(1+\gamma)^2 (1+\gamma/3)$

use in obtaining quantitative estimates of cross sections must be regarded with suspicion.

The EA cross sections behave asymptotically as in the B1 approximation

$$\hat{\sigma}_{EA}^{\pm}(i|f;Z') = \hat{\sigma}_{B1} (1 + \hat{a}_E^{(1\pm)} (Z'/Z) + \hat{a}_E^{(2\pm)} (Z'/Z)^2) \quad (3.28)$$

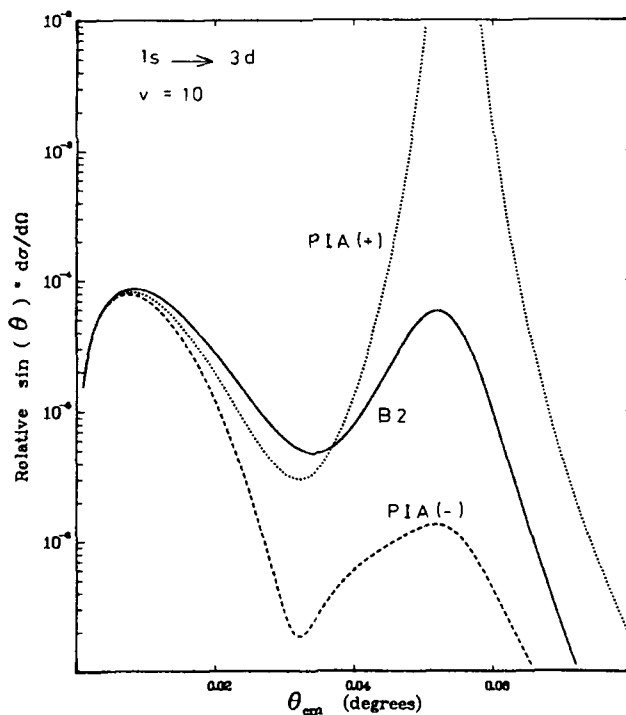


FIGURE 6

Differential cross section (normalised to $d\sigma(\theta=0)/d\Omega$) in $p + H(1s) \rightarrow H(3d) + p$. The discrepancies with respect to the second Born calculation result from the use of the peaking approximation.

where the full asymptotic expansion is solely due to the corresponding single and double scattering term of the eikonal expansion (40), i.e. the first two terms in the series expansion of the eikonal phases (3.23) in the amplitudes (3.25 b,c). Z' is used to allow freedom in the choice of the Coulomb distortion. The absence of v^{-1} (or remnants thereof as in (3.27)) dependence reflects the fact that the eikonal multiple scattering approximation allows only for forward propagation between two successive collisions eliminating from the onset the presence of a Thomas-type scattering.

For the CDW approximation, the complete transition amplitude must be analysed directly without any further simplification. One can show (41) that for $1s \rightarrow 1s$, $\hat{\sigma}_{CDW}$ coincides with $\hat{\sigma}_{B2}$ completely (not only to leading order) and some analytic and numerical studies (22,33) indicate that $\hat{\sigma}_{CDW} \propto v^{-1}$ for all states but with a forefactor which differs from that of $\hat{\sigma}_{B2}$ (Table I). These results are substantiated by the analysis of Crothers (34) where he derives the leading coefficient for $1s \rightarrow nlm$. He also shows that by going to second order in the distorted wave expansion one alleviates this discrepancy and recovers asymptotically (to leading order) the correct asymptotic behaviour (34).

As for the SEA, only $1s \rightarrow 1s$ transition has been examined in details (37) but one can conclude from the structure of the theory that $\hat{\sigma}_{SEA}$ can be written as in (3.28) with however slightly different coefficients \hat{a}_E . Remarkably, the derivation of a second order (SE2, 42) brings again (at least for $1s \rightarrow 1s$) the asymptotic dependence in agreement with that of the second Born.

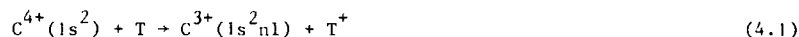
Finally, one may be concerned about the relevance of the asymptotic results to calculations at less than asymptotic velocities. This question is not completely elucidated. My point of view is that the significance of an asymptotic study does not lie in a particular application but rather in what it teaches us about the structure of the theories.

4. EVIDENCES OF MULTIPLE SCATTERING EFFECTS

The experimentalists have increasingly confronted the theorists in the last few years with new generations of experiments where finer details of the collision dynamics are examined: such as differential cross sections, state to state cross sections (43-45) and coherence effects (46). In some sense, the theoretical response to this stimulus forms the most part of Section 3. I have chosen two examples where the need to include higher order contributions in the description of the charge exchange mechanism is particularly apparent.

4.1 Final state distribution

The first experiment consists of the following capture reaction



where T is either H_2 or He (44). The high-resolution spectroscopy of the subsequent photon emission is used to extract selective information about the final state (n,l) population produced during the capture process. The impact energies ($E = 2, 3, 4$ and 5 MeV or $v = 2.58, 3.16, 3.65$ and 4.08 a.u.) were selected such that the relative velocities are large enough for perturbative charge transfer theories to be applicable but small enough for the cross sections to remain sizeable. A common feature of all experiments (44,45) performed at those velocities, is that, in contrast to similar investigations at lower velocity (43) ($v \lesssim 1$ a.u.), where the electron is preferentially captured into one or two well defined principal shells, several prominent lines can be identified as transitions from Rydberg states (nl) with $n \lesssim 10$.

One recalls that it is often assumed that even the simplest capture approximation (i.e. B1), although overestimating the magnitude of the experimental cross sections, should nevertheless describe the relative capture cross sections. This is a fallacy and the comparison shown in Fig.7 provides the necessary

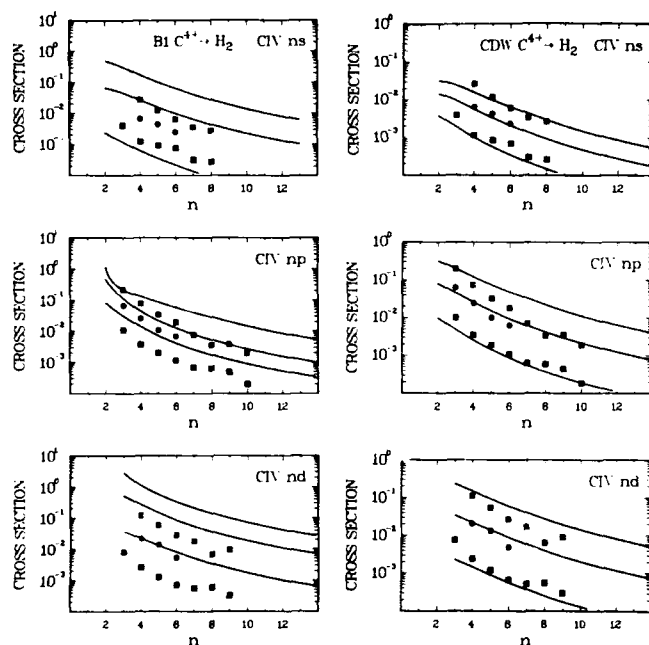


FIGURE 7

Final state distribution in $C^{4+}(1s^2) + H_2 \rightarrow C^{3+}(1s^2 ns, p, d) + H_2(?)$, ($E = 2$ MeV, \square), ($E = 3$ MeV, \bullet), ($E = 5$ MeV, \blacksquare) from Ref.46, compared to the first Born approximation (left) and to the CDW approximation (right). The data are normalized to the corresponding theoretical result at 2 MeV for the final state $nl = 3d$.

theoretical and experimental evidences that contradict the essence of this ad hoc assumption.

In Fig.7, the experimental signal is normalized to theory at 2 MeV for the final state $nl = 3d$. One notices immediately some spectacular differences between the single scattering (BI) and the multiple scattering (CDW) calculations. Whereas the first Born approximation is clearly inadequate to represent the data, and this, independent of the normalisation point, the CDW cross sections reproduce (at least qualitatively) the systematic trends and velocity dependence of the s, p, and d series. This in turn gives further evidence of the inadequacy of the former theory and provides a direct measure of the importance of the multiple scattering effects in the capture process.

Other experimental studies (45) have reached the same conclusions and confirm the superiority of a multiple scattering description of the capture mechanism over the single scattering approximation. The comparison of the CDW and BI calculations also indicates that multiple scattering effects are responsible not only for a change in the magnitudes of the cross sections but also for a redistribution of the final state population. Although the CDW predictions show a dramatic improvement over the BI results and are in this respect encouraging, the agreement with experiment is still not fully satisfactory.

4.2 Coherent excitation in electron capture collisions

The second type of experiment consists of the complete determination by Havener et al. (46) of the $n=3$ density matrix formed by electron capture in $H^+ + He \rightarrow H(n=3) + He^+$. One remembers that the density matrix is the fundamental quantity to describe final-state coherences and contains the maximum quantum mechanical information on the scattering amplitudes in an ion-atom collision process.

The investigation of Havener et al. (46) shows clear evidence of a large, positive dipole moment of the excited electron, $\langle d \rangle > 0$, along the beam axis in contrast to the predictions of the BI approximation which predicts a vanishing expectation value. Therefore, the observation of a nonvanishing dipole moment clearly indicates the failure of the first Born approximation and points to the necessity of including multiple scattering contributions in a calculation of the density matrix.

To quantify this deviation, we have calculated (47) with different approximations the axially symmetric $n=3$ density matrix defined as

$$\sigma_{lm, l'm'} = \frac{\delta_{m,m'}}{(2\pi)^2 v} \int dK t_{lm}(K) t_{l'm'}^*(K) \delta(K \cdot v - v^2/2 - \Delta\epsilon) \quad (4.2)$$

where $t_{lm}(K)$ denotes the transition matrix element from a $1s$ initial state to an hydrogenic final projectile state ($n=3, lm$) as a function of the momentum transfer K . The difference in the binding energies is written $\Delta\epsilon = \epsilon_f - \epsilon_i$. The diagonal elements correspond to the usual substate cross sections and the off-diagonal elements provide detailed information on the relative phases of the scattering amplitudes not accessible in conventional determinations of the cross sections.

The density matrix elements can be further parametrized in terms of expectation values of the angular momentum operator L , the Runge-Lenz vector A and the perihelion vector $(L \times A)$ (48). In particular, the z -component of A is related to the elements of $\sigma_{lm, l'm'}$ by

$$\langle A_z \rangle = \frac{4}{3} \text{Re} \left\{ \frac{1}{2} \sigma_{00} + \frac{1}{3} \sigma_{00} + \frac{1}{3} \sigma_{11} \right\} / \text{Tr} \quad (4.3)$$

The importance of A_z stems from the observation that its matrix elements are directly related to those of the dipole moment for each n subspace by

$$\underline{d} = \frac{3}{2} n \underline{A} \quad (4.4)$$

The calculation of $\langle A_z \rangle$ shown in Fig.8 together with the experimental data of Havener et al. (46).² As mentioned already, in the BI (in Fig.8 denoted OBK) approximation, $\langle A_z \rangle$ vanishes at all energies. A simple analysis (49) shows further that this behaviour would also be found in the prior form of the EA, PIA, and the peaking near-shell approximation to the SPB (13). The CDW method yields a nonvanishing $\langle A_z \rangle$ (or dipole moment). The direction of displacement as well as the energy dependence agrees reasonably well with the data. The captured electron lags behind the projectile, i.e. $\langle A_z \rangle > 0$. The absolute magnitude however is too small although the experimental trend suggests that agreement should improve at higher velocities. It is no surprise that only a qualitative agreement is obtained since the CDW approximation is intrinsically a high-energy approximation. Nevertheless, one sees that a finite value of $\langle A_z \rangle$ is a unique measure of the presence of second- and higher-order terms in a perturbation expansion of the capture amplitude. More of these delicate experiments would be welcome to provide a sensitive test of our various scattering models.

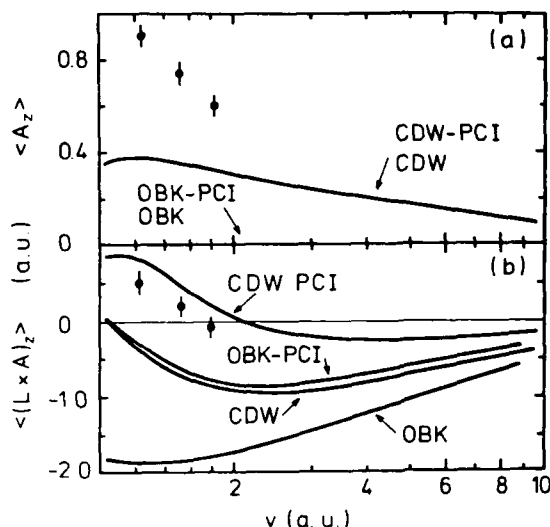


FIGURE 8

Expectation value of the z component of (a) the Runge-Lenz vector $\langle A_z \rangle$ and of (b) the perihelion vector $\langle (L \times A)_z \rangle$ following charge transfer $p + He \rightarrow H(n=3) + He^+$ as a function of the projectile velocity (47). Dots with error bars, experimental data of Havener et al. (46).

5. SUMMARY

I have reviewed the recent theoretical progress achieved in formulating and implementing multiple scattering approximations to the electron capture process. In classifying them in related families, I have tried to extract and display their main characteristic features. Despite their deficiencies, the strength of the perturbation expansions is to isolate dominant mechanisms for charge transfer and I have exposed some of them in the discussion. Although much progress has been made, we are still far from a definitive answer to the rather elusive problem of electron capture. For the next future, I suspect that a satisfactory compromise between realism and tractability would have to be considered in improving the accuracy of existing approximations.

ACKNOWLEDGEMENT

It is a pleasure to thank several colleagues who have contributed to this work through their diverse suggestions and discussions. They are S. Alston (Freiburg), H.-D. Betz (München), J.S. Briggs (Freiburg), E. Bruch (Keno), J. Burdicker (Oak Ridge), B.S.F. Crothers (Belfast) and J. Eichler (Berlin). I am also grateful to the Deutsche Forschungsgemeinschaft for financial support.

REFERENCES

- 1) M.R.C. McDowell and J.P. Coleman, Introduction to the Theory of Ion-Atom Collisions (North-Holland, Amsterdam, 1970).
- 2) R. Shakeshaft and L. Spruch, Rev.Mod.Phys. 51 (1979) 369.
- 3) R.M. Drisko, Thesis, unpublished (Carnegie Institute of Technology, 1955).
- 4) L.H. Thomas, Proc.R.Soc. A114 (1927) 561.
- 5) K. Dettmann and G. Leibfried, Z.Phys. 218 (1969) 1; R. Shakeshaft and J. Wadhera, Phys.Rev. A22 (1980) 968.
- 6) J.S. Briggs, submitted to J.Phys. B.
- 7) E. Horsdal-Pedersen, C.L. Cocke and M. Stöckli, Phys.Rev.Lett. 50 (1983) 1910.
- 8) F.W. Byron, C.J. Joachain and B. Piraux, J.Phys. B16 (1983) L769; A. Pochat, R.J. Tweed, J. Persse, C.J. Joachain, B. Piraux and F.W. Byron, J.Phys. B16 (1983) L775.
- 9) J. McGuire, M. Stöckli, C.L. Cocke, E. Horsdal-Pedersen and N.C. Sil, Phys.Rev. A30 (1984) 89; R.D. Rivarola, A. Salin and M. Stöckli, J.Phys.Lett. 45 (1984) L259.
- 10) S. Alston, Abstracts of Contributed Papers, XIV. ICPEAC, Stanford University 1985.
- 11) J.S. Briggs and L.J. Dubé, J.Phys. B13 (1980) 771; L.J. Dubé and J.S. Briggs J.Phys. B14 (1981) 4595.
- 12) L. Spruch, Phys.Rev. A18 (1978) 2016.
- 13) J.H. Macek and K. Taulbjerg, Phys.Rev.Lett. 46 (1981) 170; J.H. Macek and S. Alston, Phys.Rev. A26 (1982) 250.
- 14) K. Taulbjerg, Electron Capture in Ion-Atom Collisions in: Fundamental Processes in Energetic Atomic Collisions, eds H.O. Lutz, J.S. Briggs and H. Kleinpoppen (New York, Plenum, 1983) pp. 349-388.
- 15) K. Taulbjerg and J.S. Briggs, J.Phys. B16 (1983) 3811.
- 16) C.J. Joachain, Quantum Collision Theory (North-Holland, Amsterdam, 1979).
- 17) L.J. Dubé, J.Phys. B16 (1983) L47.
- 18) S. Alston, Phys.Rev. A27 (1983) 2342; J.H. McGuire and N.C. Sil, Phys.Rev. A28 (1983) 3679; D.H. Jakubassa-Amundsen, Z.Phys. A316 (1984) 161.
- 19) D.P. Dewangan and J. Eichler, J.Phys. B18 (1985) L65.
- 20) J. Macek, J.Phys. B18 (1985) L71; J.H. McGuire, J.Phys. B18 (1985) L75.
- 21) J. Briggs, J. Macek and K. Taulbjerg, Comm.At.Mol.Phys. 12 (1982) 1.
- 22) L.J. Dubé, J.Phys. B17 (1984) 641.
- 23) M.R.C. McDowell, Proc.R.Soc. A264 (1961) 277; J.S. Briggs, J.Phys. B10 (1977) 3075.
- 24) B.H. Bransden and I.M. Cheshire, Proc.Phys.Soc. 81 (1963) 820; Dz. Belkic, J.Phys. B10 (1977) 3491.
- 25) L.J. Dubé and J. Eichler, in preparation.
- 26) F.T. Chan and J. Eichler, Phys.Rev.Lett. 42 (1979) 58; J. Eichler, Phys.Rev. A23 (1981) 498; T.S. Ho, D. Umberger, R.L. Day, M. Lieber and F.T. Chan, Phys.Rev. A24 (1981) 705.
- 27) Dz. Belkic, R. Gayet and A. Salin, Phys.Rep. 56 (1979) 279 and references therein.
- 28) I.M. Cheshire, Proc.Phys.Soc. 84 (1964) 89.
- 29) D.S.F. Crothers, J.Phys. B14 (1981) 1035; D.S.F. Crothers and J.F. McCann, Phys.Lett. 92A (1982) 170.
- 30) Dz. Belkic, R. Gayet and A. Salin, C.P.C. 30 (1983) 193; C.P.C. 32 (1984) 387.
- 31) D.S.F. Crothers, J.Phys. B15 (1982) 2061; Phys.Scr. T3 (1983) 236.
- 32) D.S.F. Crothers and J.F. McCann, J.Phys. B17 (1984) L177.
- 33) J. Burgdörfer and L.J. Dubé, Phys.Rev. A31 (1985) 634.
- 34) D.S.F. Crothers, CDW1: J.Phys. Bxx (1985) in press; CDW2: J.Phys. Bxx (1985) in press.
- 35) D.S.F. Crothers and J.F. McCann, J.Phys. B16 (1983) 3229.
- 36) J.E. Miraglia, J.Phys. B15 (1982) 4205.

- 37) J.M. Maidagan and R.D. Rivarola, J.Phys. B17 (1984) 2477; G.R. Deco, J.M. Maidagan and R.D. Rivarola, J.Phys. B17 (1984) L707.
- 38) J.E. Miraglia, Phys.Rev. A30 (1984) 1721.
- 39) L.J. Dubé, J.Phys. B16 (1983) 1783.
- 40) L.J. Dubé and J. Eichler, J.Phys. B18 (1985) 2467.
- 41) R.D. Rivarola and J.E. Miraglia, J.Phys. B15 (1982) 2221.
- 42) G.R. Deco and R.D. Rivarola, J.Phys. B18 (1985) 2283.
- 43) R.K. Janev and H.F. Winter, Phys.Rep. 117 (1985) 265 and references therein.
- 44) R. Bruch, L.J. Dubé, E. Träbert, P.H. Heckmann, B. Raith and K. Brand, J.Phys. B15 (1982) L857; L.J. Dubé, U. Will, R. Bruch, E. Träbert and P.H. Heckmann, Nucl.Instr. and Meth. B9 (1985) 408.
- 45) A. Chetoui, K. Wohrer, J.P. Rozet, A. Jolly, C. Stephan, Dz. Belkic, R. Gayet and A. Salin, J.Phys. B16 (1983) 3993; J.P. Rozet, P. Chevallier, P. Legagneux-Piquemal, A. Chetoui and C. Stephan, J.Phys. B18 (1985) 943; H.D. Betz and R. Höppler, Abstracts of Contributed Papers, XIV. ICPEAC, Stanford University 1985.
- 46) C. Havener, W. Westerveld, J. Risley, N. Tolk and J.C. Tully, Phys.Rev.Lett. 48 (1982) 926; C.C. Havener, N. Rouze, W.B. Westerveld and J.S. Risley, Phys.Rev.Lett. 53 (1984) 1049.
- 47) J. Burgdörfer and L.J. Dubé, Phys.Rev.Lett. 52 (1984) 2225.
- 48) J. Burgdörfer, Z.Phys. A309 (1983) 285.
- 49) J. Burgdörfer and L.J. Dubé, Nucl.Instr. and Meth. B10/11 (1985) 198.

CORRELATED ELECTRON EFFECTS IN ELECTRON-TRANSFER PROCESSES FOR
HIGHLY CHARGED ION-ATOM COLLISIONS

Lars H. ANDERSEN

Institute of Physics, University of Aarhus, DK-8000 Aarhus C, Denmark

Zero-degree electron spectroscopy has been applied to collisions between highly charged gold ions and helium. Experimental evidence for the necessity of taking into account correlated motion of two electrons in double-electron-transfer processes is presented. Models are suggested that might explain the experimental findings.

1. INTRODUCTION.

The understanding of collisional processes involving more than one active electron has not reached the same level as that of single-electron transitions. Since the study of escape of two electrons from an atom by electron impact just above threshold¹, the interest in two-electron correlations has been increasing. One of the main result of Wannier's work was the realization of the necessity of taking into account correlated motion. Wannier showed that double escape near threshold requires the two electrons to emerge from the ion in opposite directions. Further, during the escape process, r_1 must be approximately equal to r_2 , where r_i ($i=1,2$) is the distance from the nucleus to the i 'th electron. The argument is as follows: If r_1 and r_2 differ substantially, then the closer electron tends to screen the outer one. This results in exchange of energy which, in turn, increases the difference between r_1 and r_2 . For sufficiently small total energies, one electron will eventually be captured, and only one will escape. The problem of correlated two-electron motion at low energy has been successfully treated by using the hyperspherical-coordinate method².

The present paper deals with collisions between highly charged gold ions (charge q) and helium. The velocity of the projectile V is comparable to or slightly greater than the orbital velocity of a $1s$ electron in He. Focus will be put on collisional processes where more than one electron is involved, in particular two-electron transfer and transfer plus ionization. We find that transfer plus ionization (TI) for $q > 10$ can be accounted for by double-electron transfer followed by loss of one electron to the continuum of the highly charged ion. We believe that transfer of two electrons creates a strongly correlated two-electron state, the decay of which causes one electron to be emitted into the continuum³. The necessity of taking into account the correlated

motion of the two active electrons will be discussed.

Throughout this work, the term transfer ionization (TI) is used for such collisional processes where the number of electrons released from the target exceeds the number captured by the projectile. Thus TI relates to the final charge states of the projectile and the target long after the collision. We consider the following TI reaction:



where a multiply charged ion A^{q+} has captured one electron, but the target has lost two electrons. ΔE is the energy gain from the electronic rearrangement. Note that in the definition of TI, nothing is stated about the mechanism responsible for the TI-reaction.

It turns out that the collision dynamics depends critically upon the impact velocity of the projectile. At low velocity, the charge-transfer process is expected to proceed via couplings between the entrance molecular orbital for the initially neutral target and the charged projectile and orbitals relating to the finally charged particles. In principle, TI may take place even at vanishing collision energy. In this limit, the additional ionization of the target takes place at the expense of ΔE . At high impact velocity, the TI contribution may be very important compared to that for capture without additional ionization⁴. In the limit of high-impact velocity, only few attempts have been made to describe TI theoretically. The basic idea has been to apply the independent-particle assumption^{4,5}.

Generally speaking, the difficulty of treating the problem of transfer and ionization is closely connected to the importance of correlation effects which can play a dominant role in the dynamics of these processes. Further, the mere existence of two active electrons introduces a large variety of collisional processes which are absent in the one-electron case.

2. EXPERIMENTAL UNCOVERING OF TI

To determine the total transfer-ionization cross section, it is necessary to measure simultaneously the amount of both ionization and capture that takes place in a collision. This can be done by analyzing the final charge state of the projectile in coincidence with the final ionization stage of the target. Our knowledge about TI has increased substantially with the development of such coincidence techniques. An experimental arrangement is shown schematically in Fig. 1. The technique has been applied by several groups (see, e.g., Ref. 4,6).

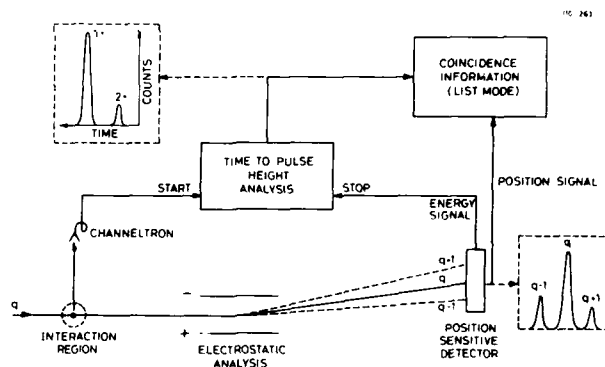


Fig. 1. Schematic drawing of the experimental setup used to measure partial cross sections.

The results of charge-state coincidence measurements are normally expressed through the partial cross sections $\sigma_{q,q'}^{on}$. We consider here the collision between 20-MeV Au^{q+} and He. The cross-section notation then refers to the reaction

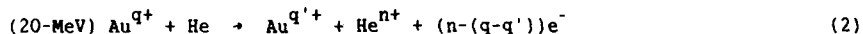


Figure 2 shows the partial cross sections as measured by Damsgaard et al.⁶. The dominating cross section is $\sigma_{q,q-1}^{01}$ which is the single-electron-transfer cross section. At high values of the projectile charge q , it is seen that the transfer-ionization cross section $\sigma_{q,q-1}^{02}$ becomes of crucial importance. In particular, we note that the other cross sections for loss of both He electrons $\sigma_{q,q}^{02}$ and $\sigma_{q,q-2}^{02}$ are lower than $\sigma_{q,q-1}^{02}$ by more than an order of magnitude for $q > 15$.

From data like those displayed in Fig. 2, the importance of TI is accentuated. Further, information such as the q and velocity dependence of TI can be obtained. However, it is important to note that the very nature of TI is not revealed, i.e., no direct information about the mechanisms that lead to transfer ionization is obtained.

A main characteristic of TI is the production of free electrons. Since the different mechanisms leading to transfer ionization result in different energy spectra of emitted electrons, useful information can be obtained from such spectra. If the released electrons move with a small velocity relative to the high-speed projectile, the electrons are most conveniently detected in the for-

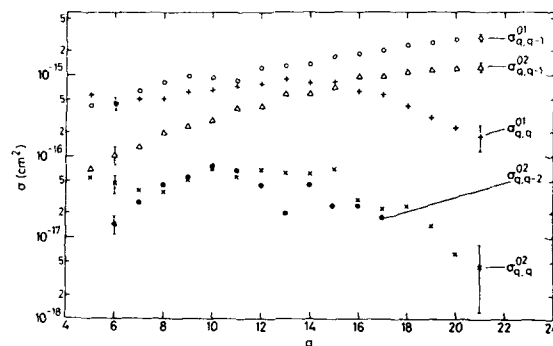


Fig. 2. Partial cross sections as a function of q for 20-MeV $\text{Au}^{q+} + \text{He}^6$.
ward direction ($\theta=0^\circ$) due to the small laboratory scattering angle. To distinguish between electrons created in an ionization event and those created via transfer ionization, the electrons were recorded in coincidence with the final charge state of the projectile.

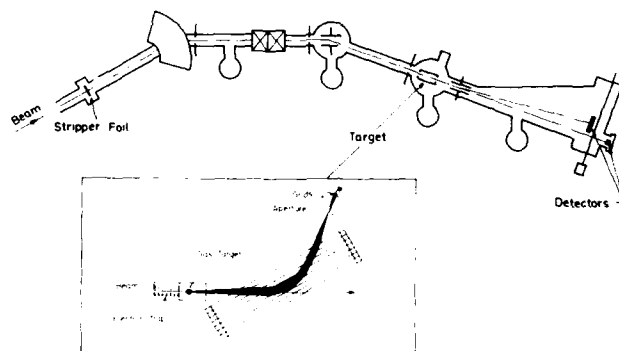


Fig. 3. Schematic drawing of the beam line together with the target region and the spectrometer.

Figure 3 shows a schematic drawing of the experimental set-up used in the present work. The beams were provided by the Aarhus EN-tandem accelerator. The energy-analyzed beam from the accelerator was post-stripped by a thin carbon foil, and the desired charge-state component was selected by the bending magnet and directed toward the target arrangement. The beam was cleaned of undesired charge-state components created through collisions with the rest gas in the

beam line by a 3° deflection immediately before the interaction with the target. Having passed through the target-gas cell, the beam could either be measured in a Faraday cup or it could be charge-state-analyzed and detected by a channel-electron multiplier. An electrostatic trap was used in front of the collision cell to strip off any electrons which might travel along with the ion beam. The acceptance angle of the spectrometer was 3.4° . The spectrometer was a 30° parallel-plate analyzer⁷. In front of the channeltron, by which the electrons were detected, two high-transmission grids were located. To prevent slow electrons from reaching the detector, the first grid was held at a small negative potential. The second grid was held at the same potential as the detector cone, ensuring a field-free detection. This latter potential was then adjusted in such a way that the electrons had a constant impact energy of about 300 eV on the detector; this ensured a constant detection efficiency.

In the coincidence measurements, the electrons produced the start pulses, and the charge-state-analyzed ions produced the stop pulses for a time-to-amplitude converter (TAC). The TAC pulse-height spectrum was recorded, and three spectra were recorded as a function of laboratory kinetic energy: (i) The "totals" spectrum with no coincidence requirements, (ii) the "reals" spectrum which registered TAC/SCA counts, and (iii) the "accidentals" TAC/SCA spectrum. In all the coincidence measurements, the number of accidental coincidences was extremely small.

3. RESULTS AND DISCUSSION.

Electron energy spectra were measured in the forward direction for 20-MeV Au^{9+} ($5 < q < 19$) on He, for 20-MeV Au^{15+} on H_2 and Ar, and for 45-MeV and 72-MeV Au^{11+} on He. The noncoincident spectra are dominated by a cusp which is due to different electron transfer to the continuum processes⁸. In addition to the cusp, some autoionization lines may be observed on the wings of the cusp.

Coincidence measurements were performed in order to single out the different contributions to the totals spectrum. In Fig. 4 are shown the experimental results for 20-MeV Au^{17+} on He. The autoionization lines are seen in the $17+ \rightarrow 17+$ coincidence channel. Therefore the lines are due to the reaction



which is transfer and excitation (TE). The positions of the autoionization lines vary with Au charge state, but they are independent of the target⁸. The identification of the origin of the doubly excited states could be obscured by a possible presence of metastable ions in the beam because single capture

(without excitation) by such ions might lead to autoionization. Since the flight time from the poststripper foil to the target is more than 2 μsec for 20-MeV gold ions, only a small fraction of metastables is expected, if any. To

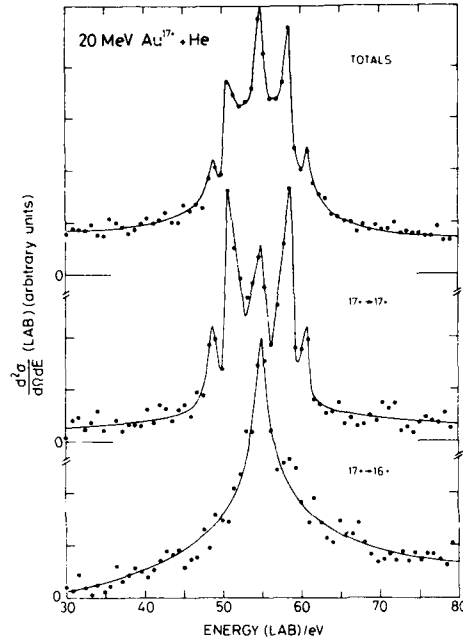


Fig. 4. Double-differential cross sections in the laboratory frame as a function of electron energy for 20-MeV Au^{17+} on He. Lines are drawn to guide the eye.

reveal the possible presence of metastables, the beam was prepared in two ways: by foil stripping from 5+ to 15+ and by foil stripping to 16+, followed by capture in the beam-line rest gas to 15+. Both beams gave the same result, and it is believed that metastable contributions are insignificant. For details about the TE process, see Ref. 8.

We now turn to the continuous part of the electron-energy spectra. Evidently the cusp from a noncoincidence measurement may be composed of several contributions. To characterize the cusps observed in the two coincidence channels $q^{+}q^{+}$ and $q^{+}(q-1)^{+}$, we have applied an expansion method in which the general scattering amplitude of the transfer to the continuum process is partial-wave expanded. The method has been used to characterize cusp shapes for a number of collision systems^{9,10}. In the rest frame of the projectile, we obtain

$$\left(\frac{d^2\sigma}{d\Omega dE}\right)_P = \sum_l B_l(v_P) P_l(\cos\theta') = B_0^0 + B_0^1 v_P + (B_1^0 + B_1^1 v_P) \cos\theta' \quad (4)$$

and in the laboratory frame

$$\left(\frac{d^2\sigma}{d\Omega dE}\right)_L = v_L \left(\frac{B_0^O}{v_P} + \frac{B_1^O}{v_P} \cos\theta' + B_0^1 + B_1^1 \cos\theta' \right) . \quad (5)$$

In Eq. (4), two Legendre polynomials and two terms in the Taylors expansion of

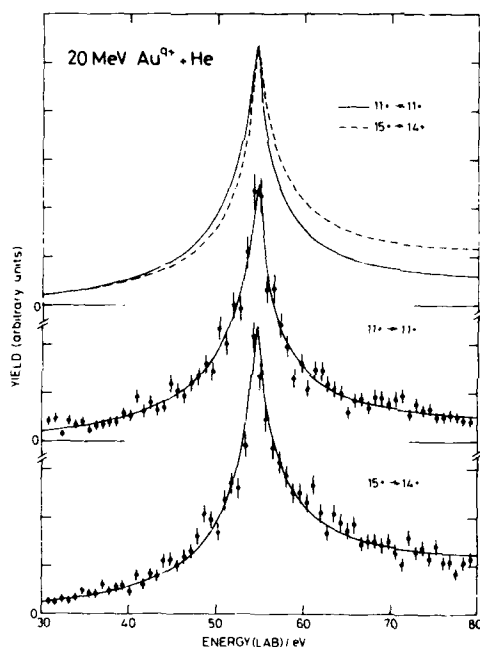


Fig. 5. The two spectra 11+ to 11+ (ECC) and 15+ to 14+ (TI) are shown together with the best fit obtained with the expansion (4). At the top of the figure, the two fits are compared.

B_1 are included (v_L and v_P are the laboratory and the projectile-frame velocities in au, respectively, B_1 are the expansion coefficients, and θ' is the scattering angle in the rest frame of the projectile). The singular character of the cross section is represented by the terms B_0^O and B_1^O . The terms containing B_0^O and B_1^O have an s-wave character, while the two terms $B_1^O \cos\theta'$ and $B_1^1 \cos\theta'$ are characteristic of a p wave. By integrating the differential cross section Eq. (5), including the spectrometer transmission function, over the experimental acceptances in velocity and angle, an expression is obtained, which can be fitted to the experimental data. Thus the cusp can be characterized by the expansion coefficients $B_1^{(j)}$ independent of the experimental apparatus used.

The continuous emission observed in the $q+q$ coincidence spectrum is due to electron capture to the continuum (ECC). The continuous emission in the $q+(q-1)+$ coincidence spectrum is due to transfer plus ionization (TI) since in this case, two electrons have been released from the target of which one ends up in a projectile bound state and one in a projectile continuum state.

Information about the collision dynamics can be obtained from an analysis of the cusp shape. To examine the ECC cusp shape, we performed a fit to the 20-MeV $Au^{11+}+He+Au^{11+}$ coincidence spectrum since in that case, no autoionization lines were observed. We found that to get a satisfactory fit, "p waves" had to be included in the expansion, Eq. (5). This is in agreement with general findings for ECC^{10,11}. When fitting to the TI cusp, only the "s-wave" component of the expansion (Eq. (5)) is required to obtain a satisfactory fit to the experimental data. Fits to an ECC cusp ($11++11+$) and a TI cusp ($15++14+$) are shown in Fig. 5. In the upper part of the figure, the two fits are compared; the yield is set equal at the cusp center. The difference between the ECC cusp and the TI cusp becomes more pronounced when the data are transformed into the rest frame of the projectile. This is demonstrated in Fig. 6. Also the expression (Eq. (4)) is shown for the two fits considered. The TI cusp is found to be sym-

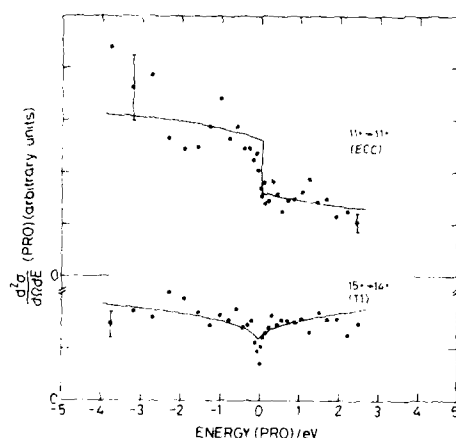


Fig. 6. Double-differential cross sections in the rest frame of the projectile as a function of electron energy. The experimental data for $11++11+$ and $15++14+$ are shown. Curves calculated from the expression (4) are also shown.

metric with respect to zero energy. This is characteristic for the "s-wave" contribution (see Eq. (4)). The ECC cusp, on the other hand, shows a strong asymmetric behaviour with a discontinuity at zero energy¹².

The shape of the TI cusp measured in the coincidence channel $q \leftrightarrow (q-1)^+$ has been studied for q equal to 7, 11, 15, and 17 for 20 MeV Au^{q+} on He. Figure 7 shows B_1^0/B_0^0 obtained from fits to the data as a function of q . B_1^0/B_0^0 is a measure of the step in the cross section at $v_p=0$ and is related to the asymmetry of the cusp. B_1^0/B_0^0 is found to be very close to zero for the values of q considered.

In Fig. 6 is seen the variation of B_1^0/B_0^0 on energy of the projectile for Au^{11+} on He. It is clearly seen that the TI cusp and the ECC cusp are characterized by different values of B_1^0/B_0^0 , reflecting the different cusp shapes.

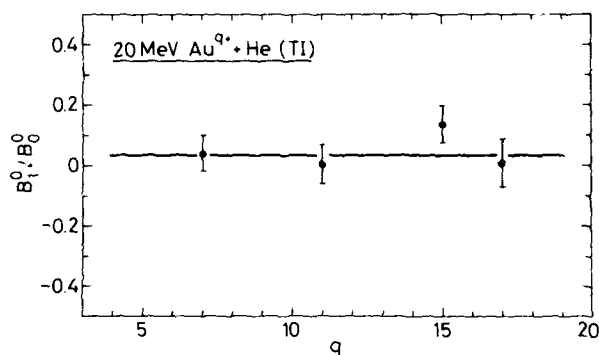


Fig. 7. B_1^0/B_0^0 as a function of q for 20-MeV Au^{q+} on He. A line is drawn to guide the eye.

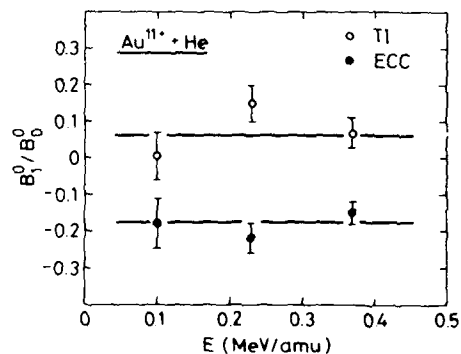


Fig. 8. B_1^0/B_0^0 as a function of energy for Au^{11+} on He. Lines are drawn to guide the eye.

Two possibilities exist for the origin of cusp electrons. The electrons may be captured from the target, in which case the cusp is due to electron capture to the continuum (ECC). Alternatively, the electrons may be emitted from the projectile, in which case one is dealing with electron loss to the continuum (ELC). ECC gives rise to an asymmetric cusp with an enhanced yield on the low-

energy side of the peak¹¹. This corresponds to a negative value of B_1^0 (see Figs. 6 and 8). ELC, however gives rise to an almost symmetric peak¹¹. The obtained values of B_1^0 as well as the observed symmetry of the electron distribution of the TI cusp (Fig. 6) favour the idea that the TI process is closely related to an ELC process.

To convert the yield of cusp electrons into absolute cross sections, we applied the procedure previously used by Vane et al.¹³. We measured the yield of ELC electrons for (20-MeV) $\text{Au}^{7+} + \text{He} \rightarrow \text{Au}^{8+} + \text{He} + e^-$. In this particular case, the total-loss cross section had been measured. Comparing the yield of TI and ELC electrons and assuming similar cusp shapes enable us to calculate the cross section for TI with continuous emission of low-energy electrons. We find that to first order, the entire TI cross section can be accounted for by the TI-cusp yield.

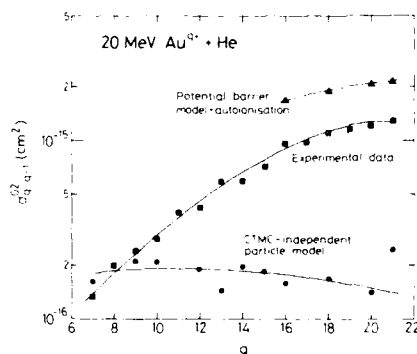


Fig. 9. Transfer ionization cross sections as a function of q . The experimental data are shown⁶ and two theoretical approaches of McDowell and Janev⁵. Lines are drawn to guide the eye.

The total TI cross section for 20 MeV $\text{Au}^{q+} + \text{He}$ has recently been calculated by McDowell and Janev⁵. They used the independent-particle model, and total cross sections were obtained by using the classical-trajectory Monte-Carlo method. In this model, no correlation effects were taken into account. In Fig. 9, the results of these calculations are compared with the experimental transfer-ionization cross sections⁶. For $q < 10$, the predictions of the independent-particle model are in good agreement with the experimental data. For higher charge states of the projectile, however, the calculated cross sections are much too small. In Fig. 9 are also shown the results of a "potential-barrier model"⁵. In this model, TI is accounted for in terms of transfer of two electrons to a doubly excited state which autoionizes with a probability w . For w we use the ratio $\sigma_{q,q-1}^{02} / (\sigma_{q,q-1}^{02} + \sigma_{q,q-2}^{02})$ from the experimental data⁶. For the high charge states, $w \approx 95\%$. Evidently, these simple calculations support the double-transfer + autoionization mechanism for higher values of q .

The experimental findings may be summarized as follows: (i) The TI process has as its final electron state one projectile-bound state and one projectile-continuum state. (ii) For the high values of q , the TI cusp is similar to an ELC cusp. (iii) The energy distribution of the emitted electrons is flat. Further, one must take into account the fact the total TI cross section is much larger than the double-capture cross section. Also, it must be emphasized that no autoionization lines are observed as a result of double-electron transfer.

The mechanism for TI clearly involves two electrons. Based on the shape analysis, we suggest that both electrons are transferred to the rest frame of the projectile, whereupon one is lost to the continuum and one is left in a bound state. We present two models in which two different loss mechanisms are considered. In the first, the two electrons enter a highly correlated state, the size of which resembles that of the He atom. The spatial extension of the two-electron wave packet is much smaller than the extension of the wave function for two corresponding but uncorrelated electrons on the projectile. Therefore one of the two electrons is immediately emitted into the continuum (see Fig. 10). Due to the short lifetime of such a highly excited and correlated state, the energy spectrum of the emitted electrons is continuous. The high probability for electron emission after double-electron transfer causes the very small double-capture cross section.

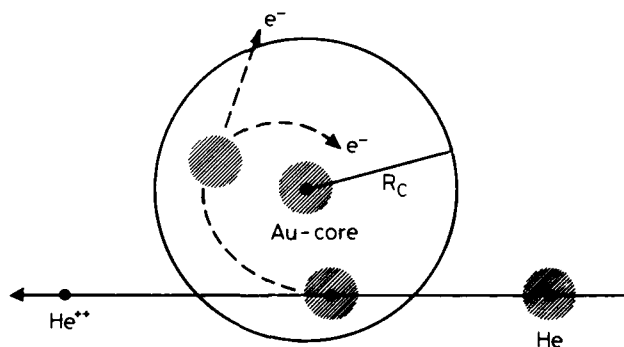


Fig. 10. Schematic drawing of a proposed model for TI (see text).

Inspired by the flatness of the electron distribution, another model is suggested. In this model, it is emphasized that the flatness of the distribution suggests that the release process is similar to the so-called "Wannier" ionization process near threshold². The electrons share the total available energy in the Wannier state (see Fig. 11). In this picture, the electron correlation results in a state where the electrons are located at opposite sides of the gold

core and move apart along a line. Since both electrons cannot be ionized, finally one electron moves toward the nucleus, transferring energy to the other one, which becomes ionized. Numerical calculations on this problem have recently been performed¹⁴.

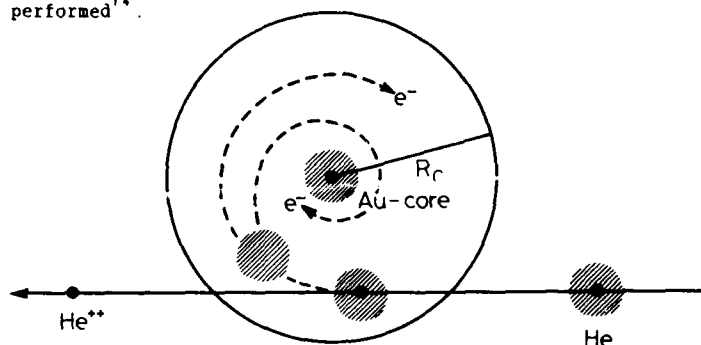


Fig. 11. Schematic drawing of a proposed model for TI (see text).

In both models suggested, the electron correlation plays a crucial role. However, it should be emphasized that theoretical calculations are very much needed in order to uncover the underlying physics.

ACKNOWLEDGEMENTS

I am thankful for the close cooperation with S. Datz, H. Knudsen, and P. Hvelplund.

REFERENCES.

- 1) G.H. Wannier, Phys. Rev. **90**(1953)817
- 2) J. Macek, J.Phys.B:Atom.Mol.Phys. **2**(1968)832
- 3) L.H. Andersen, M. Frost, P. Hvelplund, H. Knudsen, and S. Datz, Phys.Rev. Lett. **52**(1984)518
- 4) T.J. Gray, C.L. Cocke, and E. Justiniano, Phys.Rev.A **22**(1980)849
- 5) M.R.C. McDowell and R.K. Janev, J.Phys.B:Atom.Mol.Phys. **17**(1984)2295
- 6) H. Damsgaard, H.K. Haugen, P. Hvelplund, and H. Knudsen, Phys.Rev.A **27**(1983)112
- 7) W. Steckelmacher and M.W. Lucas, J.Phys.E:Sci.Instrum. **12**(1979)961
- 8) L.H. Andersen, M. Frost, P. Hvelplund and H. Knudsen J.Phys.B:Atom.Mol.Phys. **17**(1984)4701
- 9) W. Meckbach, I.B. Nemirovsky, and C.R. Garibotti Phys.Rev.A **24**(1981)1793
- 10) S.D. Berry et al., Phys.Rev.A **31**(1985)1392
- 11) M. Breinig et al., Phys.Rev.A **25**(1982)3015
- 12) J. Macek, J.E. Potter, M.M. Duncan, M.G. Menendez, M.W. Lucas, and W. Steckelmacher, Phys.Rev.Lett. **46**(1981)1571
- 13) C.R. Vane, I.A. Sellin, S.B. Elston, M. Suter, R.S. Thoe, G.D. Alton, S.D. Berry, and G. Glass, Phys.Rev.Lett. **43**(1979)1388
- 14) S. Datz, C. Bottcher, L.H. Andersen, P.Hvelplund, and H. Knudsen, to appear in Nucl.Instr.and Methods (1985).

UNITED ATOM X-RAYS FROM NUCLEAR FUSION REACTIONS

J.F. CHEMIN, S. ANDRIAMONJE, D. GUEZET, J.N. SCHEURER
IN₂P₃, Centre d'Etudes Nucleaires de Bordeaux-Gradignan,
Le Haut-Vigneau, 33170 Gradignan, France

J.P. THIBAUD, P. AGUER, F. HANNACHI
IN₂P₃, Centre Spectroscopie Nucleaire et Spectrometrie de Masse,
Bat. 104, 91400 Orsay, France

J.F. BRUANDET
IN₂P₃, Institut des Sciences Nucleaires, 38026 Grenoble, France

1. INTRODUCTION

In the last few years a growing interest has been shown for atomic processes occurring during a nuclear reaction in connection with the possibility of measuring very short nuclear lifetimes(1). The observation of Compound nucleus x-rays has been evidenced in reactions induced by protons on medium weight targets ¹⁰⁶Cd (2), ¹¹²Sn (3). In these experiments, the decay of a vacancy created by the Coulomb interaction between the charged projectile and a K-shell electron of the target is observed during the short, but finite lifetime of the Compound nucleus (CN) formed in the reaction.

Compound nucleus x-rays emitted in heavy ion induced nuclear reactions have been searched for in the last few years (4-6). In this case two difficulties must be faced. First, the lifetime of the CN becomes very short due to the large excitation energy of the system. In order to reduce the excitation energy of the CN, while keeping a significant fusion reaction cross-section, symmetric collision systems appear to be more appropriate. Then, the second difficulty arises to evaluate the probability for creating a vacancy in the K-shell of the CN. In symmetric collisions between medium weight atoms, the main part of the excitation of the K-shell partners at the end of the collision is due to 2p π -2p σ rotational-coupling combined with a sharing of the vacancies between the nearly degenerate 1s σ and 2p σ molecular orbitals in the second half of the collision. In the case of a fusion evaporation nuclear reaction, the rotational-coupling matrix element vanishes, and the second part of the collision does not exist, since the united atom is also the final state of the system (except for the evaporation of a few nucleons). The only active mechanism which can create a vacancy in the K-shell of the CN is then a direct excitation (ionization) of the 1s σ molecular orbital formed on the way into the nuclear reaction. Evidently, in Coulombic collisions, both mechanisms contribute to the vacancy formation at the end of the collision but the molecular 2p σ mechanism dominates so much over the direct 1s σ process that even in accurate measurements of the dependence of the vacancy production on the scattering angle, the contribution of the latter cannot be extracted.

As a consequence, for heavy ion induced reactions, the comparison between the probability for making a vacancy in a pure Coulombic collision and the value of the excitation probability of the 1s σ MO on the way into the nuclear reaction $P_{1s\sigma}^{1/2}$ is meaningless.

We show in this paper that the observation of the x-rays emitted in nuclear fusion reactions gives a unique opportunity to measure the probability

for creating a vacancy in the 1st molecular orbital by a direct mechanism. It also gives the contribution of the direct process to the vacancy production in the K-shell of the collision partners.

In the first part of the paper we outline the basic principles of the experiment. The experimental details are given in the second part. Then we compare the experimental results to theoretical predictions.

2. PRINCIPLE OF THE EXPERIMENT

We have chosen to investigate the $^{58}\text{Ni} + ^{56}\text{Fe}$ collision system. The energy of the beam was 238 MeV in the laboratory system. At this energy, the Ni beam may induce complete fusion nuclear reactions, leading to a highly excited Compound Nucleus (CN) of ^{112}Xe . The CN will subsequently decay by emission of light particles. During the approach of the collision partners, the time varying Coulomb field may also produce ionization of the inner shells of the projectile and/or target. In the following we will only select the collisions in which nuclear and atomic excitations take place simultaneously. This is achieved by observing the x-rays emitted in the collision in coincidence with a reaction product. The x-rays have two different origins. They may come from the filling of K-vacancies created on the way into the nuclear reaction. We call these atomic x-rays (AT x-rays) in the following. Emission of x-rays may also follow the decay by internal conversion of the evaporation residues. We call those nuclear x-rays (IC x-rays). In order to understand how we separate these two x-ray components we successively investigate the collision $\text{Ni} + \text{Fe}$, from a nuclear and an atomic point of view.

2.1. Nuclear Aspects of the Collision.

The CN is formed at a mean excitation energy of 54 MeV, in different spin states up to a maximum value $J_{\text{CR}} = 53\hbar$.

Due to the very neutron deficient structure of the ^{112}Xe , the CN will decay essentially by emission of protons and alpha particles (7) which will be followed by emission of γ rays. The evolution of excitation energy and angular momentum of the system during the de-excitation of the CN is illustrated in Figure 1 for a particular de-excitation channel: $^{112}\text{Xe} \rightarrow 4p + ^{108}\text{Sn}$. Particles are evaporated first, down to a point in the $E^* - J$ plane for

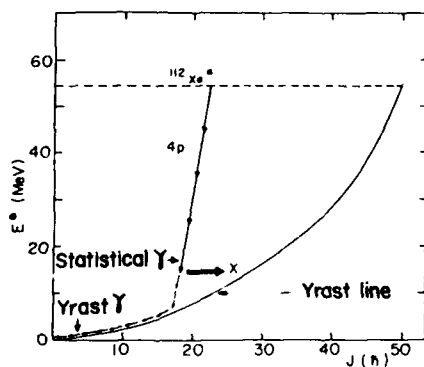


FIGURE 1

Schematic representation of the de-excitation of ^{112}Xe in the $4p$ channel. The variation of the excitation energy E^* of the system is given versus the spin J during the decay of the CN. The dashed line corresponds to the different states of the CN formation. The Yrast line corresponds to the state of minimum E^* for a given spin J . The heavy and light arrows show the evolution of the system by particle emission and γ -ray emission down the ground state of the final nucleus ^{108}Sn .

which the remaining excitation energy above the yrast line is smaller than the energy required by the next particle to be evaporated. The residual nucleus will then continue to de-excite by emission of statistical γ rays, followed by a cascade of stretched E2 transitions(8). A particular reaction channel leading to a given evaporation residue (ER), can be identified by the detection of a few γ rays emitted in the last transitions before reaching the ER ground state.

The formation of a ^{100}Sn residual nucleus formed in the collision can be signaled by the observation of one of the γ rays at 1206 keV, 1196 keV, 905 keV, 254 keV (7). Nevertheless, a transition between two states of the ^{100}Sn excited nucleus may also occur by an internal conversion process (IC). In this process, a vacancy is created in an atomic shell of the ^{100}Sn . This vacancy will decay subsequently with the emission of an x-ray characteristic of the nuclear charge of the ER. For a given transition, the ratio between the number of vacancies created in a given shell and the number of emitted γ rays defines the internal conversion coefficient for the corresponding atomic shell. The value of the IC coefficient varies strongly with the multipolarity and the energy of the transition. For example, the IC coefficients in the K-shell of Sn are respectively equal to 5.6×10^{-2} for the 254 keV and 7×10^{-4} for the 1206 keV γ ray. Such characteristic IC x-rays are in coincidence with the other γ rays used to sign the formation of one given ER.

2.2. Atomic Aspects of the Collision

From an atomic point of view, the ratio of the projectile velocity v to the K-shell electron velocity in the collision partners v_K , places the collision in the molecular regime $v/v_K = 0.48$. In this condition the binding energy of the inner most electrons of the target and projectile will evolve during the collision from the binding energy in the separated atoms up to the binding energy of a K-shell electron in the united atom of Xe. The main difference between collisions inducing nuclear reactions and usual atomic collisions at the same energy is that the united atom is actually formed in fusion reactions while it is only a transient situation in the atomic collisions.

Once formed, the CN decays by emission of a few light particles, which, from the electronic point of view, is only a small perturbation, so that the atomic system appears to be fixed after the formation of the united atom. The

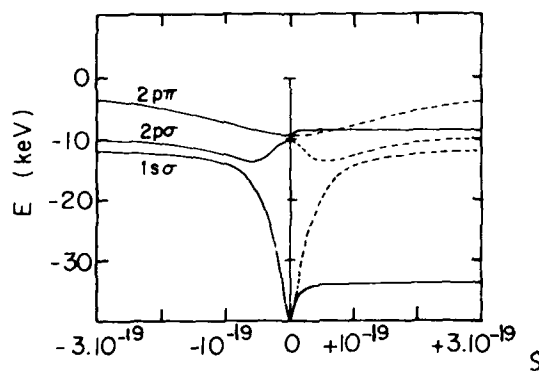


FIGURE 2

Correlation diagram of the collision $^{58}\text{Ni} + ^{58}\text{Fe}$. The dashed line represents the evolution of the binding energy of the inner electrons in the case of a Coulombic collision, and the solid lines represent a collision where a compound nucleus is formed that subsequently emits 4 protons.

correlation diagram of the collision, shown in Fig. 2, illustrates the comparison between an atomic collision in which the system will continue to evolve from the UA atom to the separated atoms in the second half of the collision and a fusion-evaporation nuclear collision. This correlation diagram corresponds to the 4p channel. The orbital energies have been calculated with hydrogenic wave functions (9). The atomic collision, $\text{Ni} + \text{Fe}$, at the energy of 230 MeV, has been investigated in detail by Chetoui and Rozet (10). The authors have measured a cross section for the production of K x-rays equal to $0.9 \times 10^{-19} \text{cm}^2$. They also measured an equilibrium thickness for projectile L vacancies equal to $20 \mu\text{g}/\text{cm}^2$. From the observed shift in the energy of the $K\alpha$ x-rays of Ni, they have deduced a mean number of vacancies in the L-shell, \bar{m}_{2p} , equal to 3.9. Assuming a statistical sharing of the Ni L vacancies in the collision between the $2p\pi$ and $3d\sigma$ MO, they found good agreement between the experimental K x-ray emission cross section and the theoretical x-ray cross section calculated in the framework of the rotational coupling between the $2p\pi$ and $2p\sigma$ MO followed by vacancy sharing between the $2p\sigma$ and the $1s\sigma$ MO.

From Figures 1 and 2, it is clear that a vacancy which has been created in the approach of the nuclear reaction may decay at different stages of the CN de-excitation. The actual atomic number of the nuclear reaction product at the moment of the filling of the vacancy depends on the relative lifetimes of the nuclear states and on the mean lifetime of the vacancy (1),(2). For a Xe atom, the mean lifetime of a K-shell vacancy is of the order of $\tau_K = 5 \times 10^{-15} \text{s}$. Consequently, in coincidence with a particular γ -ray transition, we can, in principle, observe the characteristic x-rays of the CN or the characteristic x-rays of all the intermediate states formed in the sequential decay or the characteristic x-rays of the final evaporation residue. If we assume that τ_K is larger than the mean lifetimes of the CN and of the intermediate states involved in the de-excitation of the CN by charged particles, it is seen that the vacancy will mainly decay in the final state. For example, if we follow the 4p channel, in coincidence with one of the ^{108}Sn γ rays, we will mainly observe Sn AT x-rays. Nevertheless, we remark, that these AT x-rays are emitted within a very short time after CN formation so that the ER nucleus is still moving in the target with the full recoil velocity. The energy of the AT x-rays will be affected by a strong Doppler effect. The resulting Doppler shift energy will be maximum if the x-rays are observed along the direction of the recoiling nucleus which is zero degree with respect to the beam direction. This Doppler shift energy difference can be used to discriminate between IC x-rays and AT x-rays emitted in the same final state of the nuclear reaction (12).

As mentioned above, IC x-rays are emitted in competition with γ rays in the ultimate state of de-excitation of the ER formed in the nuclear reaction. The decay rate of an electromagnetic E2 transition can be evaluated from (11)

$$\lambda = 7.4 \times 10^7 \alpha A^{1.33} E_\gamma^5 \quad (1)$$

where A is the mass in AMU of the ER, E_γ is the energy of the transition, and α is an enhancement factor which is introduced to account for the strongly collective character of the stretched E2 transitions emitted in the gamma cascade(8). The parameter α is very dependent of the nuclear structure.

Since the IC coefficient becomes larger as the energy of the transition becomes smaller, it is seen from relation 1, that strongly converted transitions are also long delayed transitions. A consequence is that the ER's formed have enough time to be completely (or partially) slowed down before the emission of the radiation. The energy of the characteristic x-rays following the IC process will not be affected by a Doppler effect.

The principle of the experiment can be summarized as follows. We shall identify a particular ER formed in the reaction $\text{Ni} + \text{Fe}$ by one discrete γ -ray corresponding to a particular transition in a particular nucleus. The x-rays will be detected in coincidence with the γ rays in the direction of the recoil

of the ER, which corresponds to the incident direction of the beam. The difference in the energy of the x-rays, due to different Doppler effects, will enable the discrimination between IC x-rays and AT x-rays in the same final nucleus. A similar method based on the Doppler shift to discriminate between IC and AT x-rays has also been used by Bosch et al.¹² to discriminate between Cm AT x-rays and Cm IC x-rays following Coulomb excitation of ^{240}Cm in the collision $^{208}\text{Pb} + ^{240}\text{Cm}$.

3. EXPERIMENTAL RESULTS

The experimental set up is schematically drawn in Fig. 3. The γ rays emitted in the reaction are detected by six 20%-efficient, intrinsic-Ge γ ray detectors surrounding the target. The resolution of the detectors was of the order of 2 keV. The use of several Ge detectors was necessary to increase the detection efficient of the system. The x-rays were detected by a 200-mm² Si(Li) detector at 0°. The active thickness of the detector was 5 mm. The detector was mounted as shown in Fig. 3, in the direction of the beam.

Coincident events between the Si(Li) detector and each Ge detector were detected within a 250 ns time window by a fast coincidence module. The time difference between the fast x-rays and fast γ -ray signals was also analyzed separately by 6 time to digital converters (TDC). In addition, a time spectrum between the Ge detectors and the high frequency signal of the cyclotron, called THF in the following, was also recorded in order to make the difference between prompt and delayed events. The FWHM of the THF spectrum was 30 ns. For each coincident event, the linear signals and the timing information were stored on magnetic tape and subsequently analyzed off-line. The dead time of the acquisition system was measured with a pulse generator. The direct spectrum of one of the 6 Ge detectors was also recorded on tape.

The target was 1 mg/cm², 99% enriched ^{54}Fe mounted on a 12-mg/cm² Ta backing. The beam was stopped behind the target in a 7-mg/cm² Ti foil. This mounting enables the beam to be stopped avoiding nuclear reactions except for nuclear Coulomb excitation in the beam catcher. It also allows us to mount the Si(Li) detector 1 cm away from the target. The Fe and Ni K x-rays and the Ta L x-rays were absorbed by Al and Ni foils placed in front of the Si(Li)

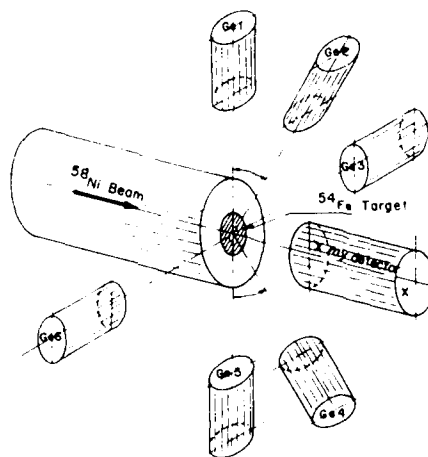


FIGURE 3

detector.

We kept the counting rate in the x-ray detector below 3000 counts per second. A higher counting rate destroys the resolution in the x-ray spectrum. In such conditions the FWHM resolution of the $K\alpha$ x-ray lines was equal to 400 eV.

Figure 4 shows the x-ray spectrum coincident with all γ -rays detected in one Ge detector. Part of the radioactive events have been eliminated. We noticed the presence of $K\alpha$ and $K\beta$ x-ray lines corresponding to the following nuclei: Cd, In, Sn, Sb. It is seen that the resolution of the detector enables a clean separation between the different x-ray energies. The different transitions correspond to different decay channels of the CN. Nevertheless, a given x-ray energy, may be connected to:

- ~ an IC process in one ER whose atomic number is equal to Z
- ~ a fully Doppler shifted AT x-ray decaying in a $(Z-1)$ final state ($v/c = 0.043$)
- ~ a $K\beta$ transition following IC taking place in a $(Z-3)$ ER.

This ambiguity can be resolved if we select one particular evaporation residue. The selection is achieved by gating the x-ray spectrum by some gamma transitions in a particular product nucleus.

The γ -ray spectrum shown in Fig. 5 corresponds to coincident events recorded in one Ge detector during the active part of the source cycle. All but some γ -rays have been attributed to some final nucleus. We will focus our attention on the following lines corresponding to the de-excitation of ^{100}Sn : 1206 keV, 906 keV, 1196 keV, 254 keV. Other transitions at 616 keV, 1141 keV in ^{100}Sn have also been identified. Gamma rays corresponding to the de-excitation of Sb isotopes are also seen in the spectrum.

For each γ -ray the following x-ray spectra have been sorted:

a) A spectrum of prompt x-rays in coincidence with γ -rays whose energy corresponds to one of the above mentioned transitions. The energy windows selected on the γ -ray energy spectrum were set as narrow as possible. Prompt events are selected by a gating condition placed on the peak in the THF spectrum. A condition was also set on the peak in the TDC spectrum.

b) The spectrum of prompt x-rays defined by the same gating conditions on the γ spectrum and THF spectrum but corresponding to a window

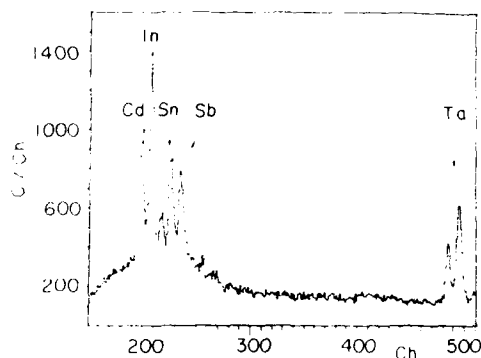


FIGURE 4

X-ray spectrum recorded in coincidence with γ -rays. Ta $K\alpha$ x rays are in coincidence with the Ta γ rays produced by Coulomb excitation.

set on the flat part (random) of the TDC spectrum. The spectrum b) was then subtracted from the spectrum a) to give a true coincidence x-ray spectrum. In this spectrum part of the counts are due to Compton events in the γ -ray detector arising from nuclear transitions whose energy is larger than the considered transition. Such Compton events are not necessarily connected with the same final state as the analyzed transitions.

c) An x-ray spectrum corresponding to prompt events in coincidence with γ -ray background taken separately on the left side and the right side of the photopeak. The windows used to define the background have the same width as the peak window. The same gating condition on the TDC spectrum as the one defined in spectrum a) was set to obtain a true plus random coincidence spectrum.

d) A random coincidence spectrum, as defined in b), but for the γ background. The difference between spectra c) and d) gives a spectrum of true events associated to the γ background. In order to check the procedure we systematically verified that the difference between the left side background and the right side background was in the TDC spectrum flat and free of structure.

Finally, a net coincidence spectrum was obtained by taking the difference between the true coincidence spectra associated respectively to the photopeak window and the background window.

4. RESULTS AND INTERPRETATION

The x-ray spectrum in coincidence with the 905 keV, 1196 keV and 1206 keV γ -rays following the de-excitation of the ^{106}Sn residual nuclei is shown in Fig. 6.

Two peaks are clearly seen in this spectrum which are labelled A and B. The energy of peak A, which is exactly 25.3 keV, corresponds to the energy of the Sn $K\alpha$ transition when emitted by an atom at rest. From the discussion above this line is associated with the de-excitation by Internal Conversion of the ^{106}Sn ER.

The measured energy of the second is equal to 26.3 keV. This energy corresponds exactly to the energy of a Sn $K\alpha$ x-ray emitted by a Sn atom

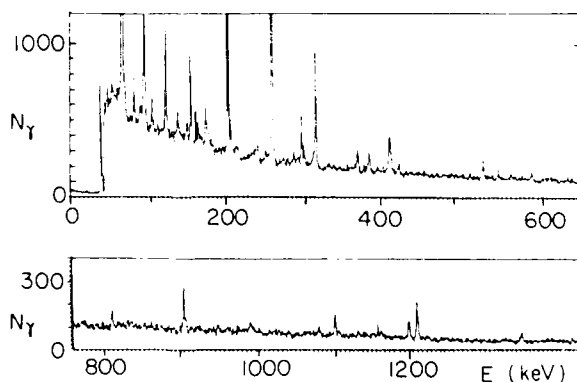


FIGURE 5

Coincident γ -ray spectrum. The large intensity peaks at low energy are due to Coulomb excitation of the Ta backing.

having the full recoil velocity $v/c = 0.043$. We demonstrated above that the decay of an atomic vacancy made on the way into the nuclear reaction should have such an energy. The same shape was found for the x-ray spectra in coincidence with each of the three γ -rays. This rules out the possibility that the second peak is caused by the IC of a transition which has the same energy as one of the three analyzed transitions in ^{108}Sn but in some Sb isotope.

The number of $\text{AT}_{1s0}^{1/2}$ x-rays detected in coincidence with the γ -rays is given as a function of $P_{1s0}^{1/2}$ by:

$$N_{\text{AT}} = N_{\gamma} P_{1s0}^{1/2} \omega_K \epsilon \Omega R T_m / 4\pi \quad (2)$$

where N_{γ} is the number of detected γ -rays, $\Omega/4\pi$ is the relative solid angle subtended by the x-ray detector, ϵ is the detection efficiency of the x-ray detector at the energy of $\text{AT}_{1s0}^{1/2}$ x-rays, R is the ratio of $K\alpha$ to $(K\alpha + K\beta)$ x-rays, T_m is the live time of the acquisition system and ω_K is the fluorescence yield. The number N_{γ} is deduced from the intensity of the analysed γ transitions in the spectrum of single events. The absolute values of $\epsilon \Omega$ have been measured with radioactive sources. We have taken for R and ω_K the usual values corresponding to a Sn atom.

The number of Doppler shifted x-rays deduced by a curve fitting analysis of the spectrum in Fig. 6 leads to a value of the number of vacancies made per nuclear reaction in the $1s_0$ molecular orbital: $P_{1s0}^{1/2} = (2.9 \pm 0.8) \times 10^{-2}$. Another method to deduce the value of $P_{1s0}^{1/2}$ based on the relative intensities of the $\text{IC}_{1s0}^{1/2}$ x-ray peak and the $\text{AT}_{1s0}^{1/2}$ x-ray peak is given elsewhere (22) leading to a value: $P_{1s0}^{1/2} = (3.1 \pm 0.6) \times 10^{-2}$.

Within the statistical fluctuations attached to the data points in Fig. 6, the assumption that all the atomic vacancies are filled after the emission of the 4 protons appears justified. Nevertheless, experiments with better statistics and including a selection on the spin of the ER may slightly modify this picture. We believe that the error on the $1s_0$ value accounts for this effect.

The value of $P_{1s0}^{1/2}$ can be compared with theoretical predictions given by different atomic models.

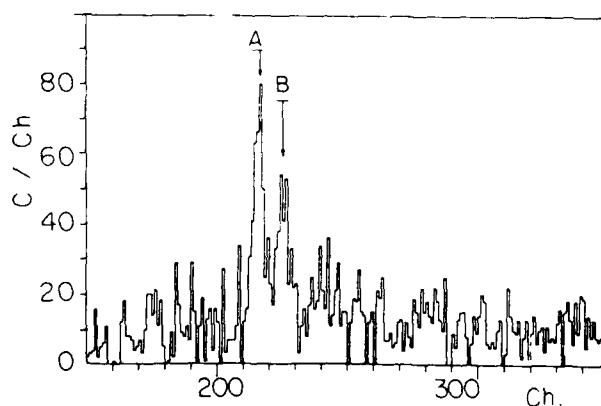


FIGURE 6

Net x-ray spectrum in coincidence with 905 keV + 1196 keV + 1206 keV transitions in ^{108}Sn .

We will first consider a double collision mechanism. In a first collision a projectile K-shell vacancy is formed. The dominant mechanism for the creation of this vacancy is by excitation of electrons from the $2p_0$ MO which is later transferred by radial coupling to the $1s_0$ MO on the way out of the collision. Such interactions take place at large internuclear distances so that the projectile motion is only slightly disturbed. Some of the vacancies created in the first collision may survive to enter the $1s_0$ MO in a second collision at zero impact parameter inducing the nuclear reaction. The number of surviving vacancies, N_K has the same interpretation as the $P_{1s_0}^{1/2}$ measured in this experiment: N_K is given by (13)

$$N_K = \frac{\sigma_{2p_0} n v W}{\lambda_p} \quad (13)$$

where σ_{2p_0} is the $2p_0$ vacancy production cross section, n is the target atomic density, v is the projectile velocity, λ_p is the decay rate of projectile K-shell vacancies and W is the probability that the $2p_0$ vacancy will be transferred to the projectile K-shell at the end of the first collision, and into the $1s_0$ in the second.

To evaluate N_K , we can use the values of σ_{2p_0} measured by Chetoui et al (10) in the system Fe + Ni at 200 MeV and the sharing probability, $W = 0.33$, found in good agreement with theoretical calculations. The lifetime of a Ni vacancy in an unperturbed atom is equal to 2×10^{-16} s. Introducing these values in Eq.3 leads to a number $N_K = 1.5 \times 10^{-3}$.

The value of λ_p given above can be affected by the presence of vacancies in the L and M shells of the projectile at the end of the collision. Chetoui et al have measured a mean number of $2p$ vacancies in the projectile equal to 4. Statistical considerations show that the mean lifetime of a K-shell vacancy can be double so that the above value of λ_p may also be enhanced by a factor of two. Nevertheless, a very large discrepancy, of the order of one order of magnitude, remains between the estimated N_K value and the measured value of $P_{1s_0}^{1/2}$. Consequently, we must conclude that, at this energy, the double mechanism cannot explain by itself the number of vacancies found in the $1s_0$ MO.

In the investigation of the number of vacancies made in a single collision, two different processes must be considered. We will first analyze the excitation of the K-shell of the CN and of the subsequent ER by the sequential evaporation of charged particles. Secondly, we will investigate the direct excitation of the $1s_0$ MO on the way into the nuclear reaction.

In the Ni + Fe system, the calculated mean energy of the evaporated protons is equal to 6 MeV and the particle energy ranges between 2 MeV and 20 MeV. Using a straight line, nonrelativistic version of the SCA code (14), we have calculated the probability for making a vacancy in the K-shell of a Xe atom in a zero impact parameter collision induced by protons with energies ranging between 2 MeV and 20 MeV. The ionization probability for each proton energy was then folded with the energy distribution of the particles to obtain a mean ionization probability by emitted proton I_0 . The result was then multiplied by four to account for the particle multiplicity in the considered reaction channel. This procedure leads to a result $I_0 = 10^{-3}$, which is one order of magnitude smaller than the measured value of $P_{1s_0}^{1/2}$.

The calculation of $P_{1s_0}^{1/2}$ corresponding to the ionization of the $1s_0$ MO on the way into the collision can be made in the framework of a semiclassical approximation since in heavy-ion induced collisions, the relative motion of the nuclei can be treated classically. In a one collision process, P_{1s_0} is obtained from the time dependent amplitude $a_{1s_0}(t)$ for exciting the $1s_0$ electron to a continuum state with energy ϵ and angular quantum number l_m (15).

$$a_{1s0} = \int_{-\infty}^t dt' \dot{R} T_{\epsilon\ell m}(R) \exp[i \int (E_{1s0}(t') + \epsilon) dt' / \hbar] \quad (4)$$

where $T_{\epsilon\ell m}(R)$ is the radial coupling matrix element between the $1s$ and the continuum state, R is the radial velocity, $E_{1s0}(t)$ is the time dependent electron binding energy of the electron, and ϵ is the energy of the electron in the continuum.

The probability for making a vacancy in the $1s$ MO is given by:

$$P_{1s0} = \int_0^\infty d\epsilon \sum_{\ell m} |a_{\epsilon\ell m}|^2 \quad (5)$$

Different approximations have been made to connect the direct excitation process in heavy-ion collisions to semiclassical perturbation theories used to describe the direct Coulomb ionization in asymmetric collisions induced by light ions. One remarks, that in adiabatic collisions, the dominant internuclear distance for ionization is much smaller than the K-shell radius of the target atoms (16). Several authors have proposed replacing the continuously evolving wavefunctions of the MO states by the atomic wavefunctions of the UA (17-19). Within this assumption, Briggs suggests that for a symmetric system, the ionization of the $1s$ can be described as the ionization of the K-shell UA, fixed at the center of mass of the collision. One electron of this fictitious UA, at rest in the collisions system, will feel a potential perturbation caused by the Coulomb fields of the projectile and of the target colliding with this UA atom with a relative velocity equal to $v/2$ (20).

In this model, Eq.(4) can be written:

$$a_{\epsilon\ell m}(0) = -i \int_{-\infty}^0 dt \langle \phi_{\epsilon\ell m} | \frac{Z_P}{|\mathbf{r}-\mathbf{v}t/2|} + \frac{Z_T}{|\mathbf{r}+\mathbf{v}t/2|} | \phi_{1s} \rangle e^{i\Delta\epsilon t} \quad (6)$$

where ϕ_{1s} and $\phi_{\epsilon\ell m}$ are respectively the $1s$ state and continuum states of the UA, \mathbf{r} are the electronic coordinants of the UA relative to the CM of the collision, Z_P and Z_T are respectively the atomic numbers of projectile and target, and \mathbf{v} is the velocity of the projectile in the laboratory system. The projectile and target masses are assumed to be equal, and $\Delta\epsilon$ is the energy transferred to the electron.

In this model the projectile and the target are treated on completely equal footing. The ionization amplitudes with respect to projectile and target are added coherently. In the case of a completely symmetric system, the relative target and projectile ionization amplitudes are equal to:

$$a_{\epsilon\ell m} = -i(1+p_f p_o) \int_{-\infty}^0 dt \langle \phi_{\epsilon\ell m} | \frac{Z}{|\mathbf{r}-\mathbf{v}t/2|} | \phi_{1s} \rangle e^{i\Delta\epsilon t}, \quad (7)$$

where p_o and p_f are the parities of the UA wave functions ϕ_{1s} and $\phi_{\epsilon\ell m}$. An evaluation of P_{1s0} , in the framework of the Briggs model by Trautmann (21) leads to the following result for a pure atomic collision involving the way into and the way out of the collision:

$$P_{1s0}^{\text{Briggs}} = 2.6 \cdot 10^{-2}$$

The theoretical evaluation of P_{1s0} is comparable to the presently measured value of the half-collision probability. From this comparison we may conclude that the essential part of the mechanism for creating a K-shell vacancy in the UA comes from the direct ionization of the $1s_0$ electron at small internuclear distances. Nevertheless the experimental data refers to the way into the collision while the calculated value refers to an entire collision in which the internuclear distances evolve continuously from minus infinity to plus infinity. A calculation of P_{1s0} on the way into the collision made in the framework of the Briggs model is highly desirable. A detailed comparison with the experimental value may bring a new insight to the phase relation of the atomic amplitudes (1,22)

5. CONCLUSION AND FURTHER DEVELOPMENTS

We have measured for the first time the ionization probability on the way into a nuclear reaction. Furthermore, this measurement shows clearly the part of the direct excitation process on the creation of K-shell vacancies in symmetric collisions in the adiabatic regime. We clearly demonstrate the feasibility of separating the x-rays following atomic excitation from the x-rays having a nuclear origin. It is shown that a correct understanding the x-ray emission in nuclear reactions can only be achieved if the reaction channels are clearly identified.

ACKNOWLEDGMENTS

We would like to thank the ALICE accelerator crew for their technical assistance during the experiment, and R. Anholt and Ch. Stoller for correcting the manuscript.

REFERENCES

- 1) W.E. Meyerhof and J.F. Chemin, *Advances in Atomic and Molecular Physics*, Vol. 20, eds. D. Bates and B. Bederson (Academic Press, 1985), p. 173-234.
- 2) J.F. Chemin, S. Andriamonje, J. Roturier, B. Saboya, J.P. Thibaud, S. Joly, S. Plattard, J. Uzureau, H. Laurent, J.M. Maison, and J.P. Schapira, *Nucl. Phys. A331* (1979) 407.
- 3) S. Rohl, S. Hoppenau, M. Dost, *Phys. Rev. Lett.* 43 (1979) 1300.
- 4) W.E. Meyerhof, R. Anholt, and W. Wolfli, *Phys. Lett.* 84B (1979) 59.
- 5) R. Bock, Y. Chu, M. Dakowski, A. Gobbi, E. Grosse, A. Olmi, H. Sann, D. Schwalm, U. Lenzen, W. Muller, S. Bjornholm, M. Esbensen, W. Wolfli and E. Morenzoni, *Nucl. Phys. A388* (1982) 334.
- 6) W.E. Meyerhof, J.F. Chemin, R. Anholt and Ch. Stoller, *Trans. Nucl. Sci. (N.Y.)* 40 (1980) 134.
- 7) G. Auger, G. Albouy, C. Roulet, H. Sergolle, A. Kered, and T.H. Lindblad, *Z. Phys.* 296 (1980) 319.
- 8) R.M. Diamond and F.S. Stephens, *Am. Rev. Nucl. Part. Sci.* 30 (1980) 85.
- 9) A. Salin and R. Gayet, Private Communication.
- 10) A. Chetoui, J.P. Rozet, J.P. Briand and C. Stephan, *J. Phys.* B14 (1981) 1625.
- 11) J.M. Blatt and V.F. Weisskopf, *Theoretical Nuclear Physics* (John Wiley and Sons, New York, 1951), 627.
- 12) F. Bosch, in *Quantum Electrodynamics of Strong Fields*, ed. W. Greiner (Plenum Publishing Corporation, 1983) pp. 155-178.
- 13) R. Anholt, *Z. Physik A292* (1979) 123.
- 14) J.M. Hansen, O.M. Johnsen, and L. Kocbach, *Atomic and Nuclear Tables*, 15 (1975) 205.

- 15) B. Muller, G. Soff, W. Greiner and V. Ceauscu, Z. Phys. A285 (1978) 27.
- 16) J.U. Andersen, E. Laegsgaard, M. Lund and C. Moak, Nucl. Inst. Meth. 132 (1976) 507.
- 17) J.S. Briggs, Rep. Prog. Phys. 39 (1976), 217.
- 18) W.E. Meyerhof, Phys. Rev A18 (1978) 414.
- 19) P. Amundsen, J. Phys. B11 (1978) L 737.
- 20) J.S. Briggs, J. Phys. B8 (1975) L485.
- 21) D. Trautmann, Private Communication.
- 22) J.F. Chemin et al, in print.
- 23) M. Dost, R. Loreck, S. Rohl, J. Seidel and W. Koenig, in print.

POSITRON CREATION IN SUPERCRITICAL HEAVY ION COLLISIONS

J. REINHARDT¹, T. DE REUS¹, W. GREINER¹, B. MÜLLER¹, U. MÜLLER², A. SCHÄFER¹,
P. SCHLÜTER², S. SCHRAMM¹, and G. SOFF²

¹Institut für Theoretische Physik der Johann Wolfgang Goethe-Universität
Robert-Mayer-Straße 8-10, Postfach 11 19 32
D-6000 Frankfurt am Main 11, West-Germany

²Gesellschaft für Schwerionenforschung mbH
Planckstraße 1, Postfach 11 05 41
D-6100 Darmstadt 11, West-Germany

Two recent experiments have discovered monoenergetic line structures in the collision of high-Z heavy ion collisions. We discuss this phenomenon using the concept of a change of the QED vacuum in supercritical electromagnetic fields. As an alternative the hypothesis is reviewed, that the positron lines are caused by the creation of a previously unknown elementary particle.

1. QED OF STRONG FIELDS

The theory of quantum electrodynamics (QED) without doubt is among the best understood and most successful domains of modern physics. Starting from Dirac's pioneering work on relativistic quantum mechanics and culminating in the completion of the renormalization programme, today QED is able to predict the properties of atoms and other leptonic systems with an accuracy unrivaled by any other theory. Nevertheless, until about a decade ago, one important question [1] of principal interest has lain rather dormant, mainly due to the lack of interaction with the experiment. This topic is related to the external field problem of QED. Already very early an apparent inconsistency of the theory was noticed (Klein's paradox) if a strong external field is present. Phrased in today's language this is due to an *instability of the vacuum* of the theory. In the absence of interactions, or if the external field is very weak, a vacuum state $|0\rangle$ can be defined which is characterized by the absence of real particles.

If the strength of the external potential exceeds a critical value (which is $2m$ in the case of a potential step) the positive and negative frequency solutions of the Dirac equation become intermixed. Now a new type of wavefunctions can be found which tunnel through the 'forbidden' energy gap of the Dirac equation, defined by $-m < E - V < +m$. In terms of physical observables this has to be interpreted as a pair production process being most easily visualized in Dirac's hole picture where all the states of the lower continuum are occupied. Normally invisible vacuum electrons now can escape to a region of space where they are observable, leaving behind positively charged holes, i.e. positrons. Since this is a quantum process it is required that the potential difference is localized within a few Compton wavelengths.

The only systems where one can hope to find this situation realized in nature are atomic nuclei. Unfortunately, while the Coulomb potential well produced by stable nuclei is very deep it is too narrow to support sufficiently deeply lying electronic states. In a gedankenexperiment, however, the charge Z of a nucleus may be increased beyond the limits set by nuclear stability. Then the atomic bound states rapidly descend in energy, cf. Fig. 1. At a critical charge $Z_{cr} = 173$ (taking into account the finite nuclear extension) the binding energy of the

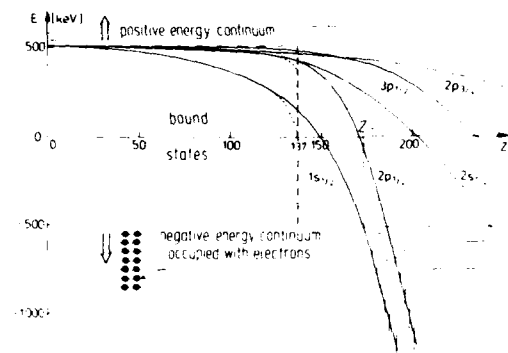


Figure 1: Lowest bound states of the Dirac equation for nuclei with charge Z . While the Sommerfeld fine-structure energies (dotted lines) for $\kappa = -1$ end at $Z = 137$, the solutions for extended Coulomb potentials (full curves) can be traced down to the negative energy continuum which is reached at the critical charge Z_{cr} . The bound states entering the continuum obtain a spreading width.

lowest state ($1s$) reaches the threshold for pair creation, $2m$. Beyond that limit the $1s$ -state enters the negative energy continuum as a resonance. Within about 10^{-18} s a hole prepared in the $1s$ -state will be emitted spontaneously and escapes to infinity. The K -shell of the remaining atom now is filled with electrons, which, when removed by external forces, will be replaced almost immediately through the process of pair creation. The new stable groundstate of the system (electron positron field + external potential) contains real electrons, i.e. a transition to a *charged vacuum* has taken place.

Although the problem of the critical coupling strength still is the subject of theoretical investigations [2], the concept of the charged vacuum has been worked out in detail and is believed to be well understood [1].

The question remains, however, whether this new and interesting phenomenon can be made the subject of experimental investigation. Perhaps by an accident of nature, the critical charge Z_{cr} has a value slightly below twice the charge of the most heavy stable elements. Thus it should be possible to produce a supercritical field at least transiently in a heavy ion collision. So, formulating the problem somewhat more broadly, we have to study the question to what extent the electronic properties of an atom with nuclear charge $Z = Z_1 + Z_2$ can be deduced from the outcome of a collision experiment using two separate atoms.

2. ATOMIC EXCITATION PROCESSES IN HEAVY ION COLLISIONS

A complete solution of the quantum mechanical relativistic many particle inelastic scattering problem clearly cannot be found. Due to the large mass of heavy nuclei, however, the semiclassical method may be used to describe the electron dynamics during the collision. Furthermore, electron correlation interactions should be of minor importance for the processes of interest. Therefore the problem reduces to the solution of the *time dependent two center Dirac equation* ($\hbar=c=1$)

$$i\partial/\partial t \psi_i(t) = H_{TCD}(\vec{R}(t)) \psi_i(t), \quad (1)$$

where

$$H_{TCD} = \vec{\alpha} \cdot \vec{p} + \beta m + V_1(\vec{r}, \vec{R}_1(t)) + V_2(\vec{r}, \vec{R}_2(t)). \quad (2)$$

Electron screening may be included in the Hamiltonian by a mean screening potential, also the magnetic interaction with the nuclear current may be added. The index i denotes the initial conditions at $t \rightarrow -\infty$ from which the state ψ_i evolves in time. Within the independent particle approximation, the one-electron wavefunctions ψ_i may be used to extract the full information on the excitation of the many-particle system. The number of particles in the asymptotic eigenstate $\psi_p =$

$\phi_p(t \rightarrow \infty)$ simply is

$$N_p = \sum_{k < F} |\langle \phi_p(t \rightarrow \infty) | \phi_k(t \rightarrow \infty) \rangle|^2, \quad (3)$$

where the summation extends over all states initially occupied, i.e. lying below the 'Fermi level' F . Using the language of second quantization, expressions for multiparticle states are easily derived [3].

To find the wavefunctions $\phi_k(t \rightarrow \infty)$, the four dimensional partial differential equation (1) may be integrated directly by numerical methods [4], which is particularly useful at high collision energies. As an alternative method we employ a basis expansion of the time dependent wavefunction

$$\phi_k(t) = \sum_j a_{ij}(t) \phi_j(\vec{R}(t)) \exp(-ix_j(t)), \quad (4)$$

where the sum includes integration over continuum states of positive and negative frequency.

We are mostly interested in collisions close to the nuclear Coulomb barrier where the nuclear velocity is slow compared to the relativistic motion of inner shell electrons. Thus an expansion in terms of adiabatic solutions ϕ_j of the two center Dirac equation (*quasimolecular basis*) is best suited. This leads to the well-known set of coupled differential equations for the amplitudes $a_{ij}(t)$

$$\dot{a}_{ij}(t) = - \sum_{k \neq j} a_{ik}(t) \langle \phi_j | \partial/\partial t | \phi_k \rangle \exp(i(x_j - x_k)), \quad (5)$$

with the initial condition $a_{ij}(-\infty) = \delta_{ij}$. The phase factors $x_j(t)$ are chosen to eliminate the diagonal coupling matrix element.

Using the bound state solutions of the two center Dirac equation [5] it is found that the matrix elements of the radial coupling operator $\vec{R} \partial/\partial \vec{R}$ involving $ns_{1/2}$ and $np_{1/2}$ states are strongly peaked at small internuclear distances R . This stands in contrast to the nonrelativistic case and is due to the relativistic 'collapse of the wavefunctions'. In the relevant region of small R the two center potential can be approximated by its spherically symmetric monopole part. Only quite recently the two center Dirac continuum problem was attacked. Using a specially tailored representation of the Dirac spinors, K.H. Wietschorke and P. Schlüter devised a method to construct continuum wavefunctions which in the spherical limit become eigenstates of the Dirac angular momentum operator K . Their results substantiate the validity of the monopole approximation, which, of course, can be handled with much greater ease.

The model which we have briefly sketched in eqs. (1) to (5) leads to predictions on a variety of electronic excitation phenomena in heavy ion collisions.

Let us just mention some key results without going into any detail.

(1) Remarkably large *K-shell excitation rates* are predicted for close collisions (small impact parameters). This can be understood from the relativistic contraction of the wavefunctions.

(2) The spectrum of δ -electrons extends up to energies of several MeV with reasonable intensity. This reflects the presence of high momentum components in the quasimolecular relativistic wavefunctions.

(3) High energy *quasimolecular X-ray radiation* is emitted.

All of these predictions are in good, sometimes excellent agreement with experimental data. Therefore it is justified to conclude that the dynamics of inner shell electrons in collisions of very heavy ions can be well understood using the language of superheavy quasimolecules. The effects of the strong external field in such systems lead to characteristic properties quite foreign to ordinary atomic physics.

Attempts to go beyond these statements, however, and to detect a signal from the decay of the neutral vacuum seemed to prove rather futile. Obviously one wants to look for the *emission of positrons*. To describe this process in the case of supercritical collisions it is necessary to amend the formalism [3] to take proper account of the resonance properties of the 'dived' $1s$ -state which has vanished

from the bound state spectrum of the adiabatic Hamiltonian. To incorporate the resonance into the formalism of eqs. (1) - (5) a projection operator technique borrowed from nuclear physics has been used.

The formalism naturally leads to the emergence of 'induced' and 'spontaneous' positron creation, the latter resulting from the presence of an unstable state ϕ_R in the expansion basis. In practice, however, this does not result in a marked threshold behaviour at the border of the supercritical region. The rapid variation of the quasimolecular potential causes significant contributions from the dynamical coupling, whereas the period of time for which the internuclear distance $R(t)$ is less than R_{cr} is usually very short ($\sim 10^{-21}$ s) as compared with the decay time of the $1s$ resonance ($\sim 10^{-19}$ s).

Therefore, the predicted production rates and energy spectra of positrons continue smoothly from the subcritical to the supercritical region. Nevertheless the remarkably steep increase of positron emission intensity (roughly given by a power law $p^{e+} \approx Z^{22}$) in itself bears witness that the electron-positron field is subject to extreme conditions in heavy ion collisions with $Z = Z_{cr}$.

3. POSITRON CREATION AND NUCLEAR REACTIONS

Qualitative deviations of the positron production rate in supercritical collision systems are expected only under favourable conditions: Since the 'spontaneous' and 'dynamical' couplings exhibit a different functional dependence on the nuclear motion, an increase in collision time can be expected to provide a clear signature for supercritical collisions. Therefore Rafelski, Müller, and Greiner [6] suggested the study of positron emission in heavy ion reactions at bombarding energies above the Coulomb barrier, where the formation of a di-nuclear system or of a compound nucleus would eventually lead to a time delay within the bounds of the critical distance R_{cr} . During this sticking time T the spontaneous decay of the $1s$ resonance, by filling dynamically created K-shell holes under emission of positrons, will be strongly enhanced.

Thus one is led to the general question, how to describe atomic excitations in the presence of a nuclear reaction. This interesting field of research at the borderline between two domains of physics usually separated has received much attention during recent years. Here we will concentrate on the aspect of positron creation, for a recent review cf. [7].

In a simple, schematic formulation a nuclear reaction, as far as the electrons are concerned, is just characterized by a standstill of the nuclear motion for some time interval T . This is easily incorporated into our semiclassical theory [8]. The asymptotic excitation amplitude

$$a_{fi}(\infty) = \sum_{qq'} a_{iq}(-\infty, 0) C_{qq'}(T) a_{q'f}(T, \infty) \quad (7)$$

is determined by the solutions of the coupled channel equations (5) in the incoming and outgoing parts of the trajectory, joined by the expectation value of the time development operator

$$C_{qq'}(T) = \langle \phi_{q'}(R_0) | e^{-iH(R_0)T} | \phi_q(R_0) \rangle. \quad (8)$$

In the eigenstate basis this matrix just reduces to a phase factor $\delta_{qq'} \exp(-iE_q T)$. When inserted into (7) this factor will lead to interference effects observable in the energy spectra of the emitted electrons and positrons [9]. Furthermore a significant reduction of K-hole production rates is predicted for which experimental indications have been found [7] recently.

In supercritical collision systems the factor (8) gains special significance. Due to the presence of a quasi-bound state in the basis, a nondiagonal coupling term $C_{1s,e+}$ will arise, which grows with time T . The effect of this term is demon-

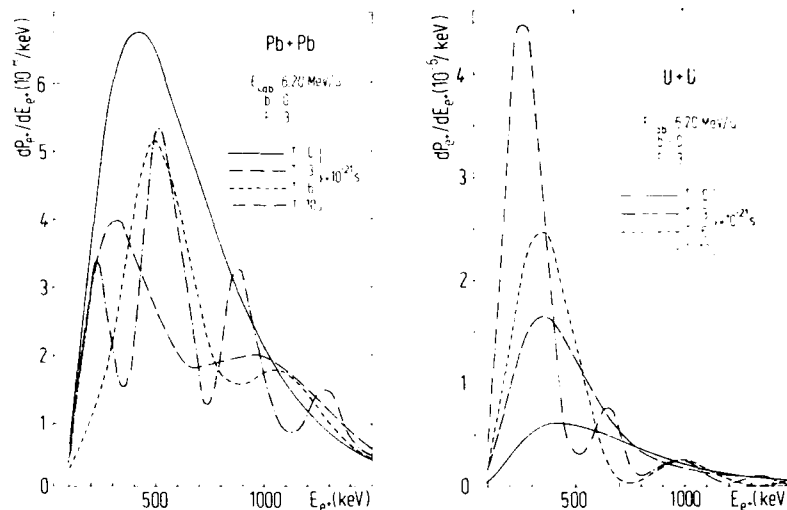


Figure 2: Spectra of positrons created in subcritical (part a) and supercritical heavy ion collisions (part b) assuming almost grazing Coulomb trajectories (full lines) and nuclear reactions leading to delay times $3 \times$, $6 \times$, and 10×10^{-21} sec, respectively, using a schematic model for the trajectory [8].

strated in figure 2, where coupled channel calculations for a subcritical ($Z=164$) and a supercritical ($Z=184$) system are compared.

In addition to the interference patterns an *enhancement of positron production in time-delayed supercritical collisions* is observed, where the binding energy of the lowest bound states exceeds the value $2m$. For long delay times a *distinct peak in the positron spectrum* is found at the location of the supercritical bound state resonance (binding energy minus $2m$) due to the spontaneous pair creation process.

4. EXPERIMENTAL EVIDENCE FOR POSITRON LINE STRUCTURES

Several generations of experiments investigating positron creation in high- Z heavy ion collisions have been performed at the Gesellschaft für Schwerionenforschung (GSI) in Darmstadt.

During the past six years three different collaborations concentrated their efforts on the investigation of the energy spectrum of positrons, measured in collisions with well defined scattering kinematics. The groups make use of three different experimental set-ups:

- The *ORANGE* spectrometer [10,11] (P. Kienle, Ch. Kozhuharov, and collaborators);
- the *EPOS* detection system [12,13] (J.S. Greenberg, H. Bokemeyer, J. Schweppe, P. Vincent, D. Schwalm, and coworkers);
- the *TORI* spectrometer [14] (headed by E. Kankaleit).

Most of the measurements were performed on the systems Th+Th, U+Th, U+U, Th+Cm, and U+Cm at bombarding energies in the vicinity of the nuclear Coulomb barrier. In their gross structure, the experimental findings seem to be well understood. For all the heavy ion systems, bombarding energies, and impact parameters that were studied, the measured positron production is in good agreement with the results of coupled channel calculations based on the quasimolecular model.

Looked upon more closely, however, the measured energy spectra reveal remarkable deviations from the predicted smooth shape. This is true for the results of both the EPOS and the ORANGE group. The TORI experiments, dedicated mostly to the study of e^+ and e^- emission in deep inelastic nuclear collisions, have observed less clear indications for this effect [15].

Let us discuss the experimental discovery in detail. Figure 3 shows some of the most recent data obtained by the ORANGE spectrometer. Kienle's group measured positron spectra in U+U collisions at 5.9 MeV/u in coincidence with the heavy ions scattered into various angular windows. The broad curve (a) shows the theoretical predictions for dynamical positron production, calculated under the assumption that the nuclei move on Rutherford trajectories. The theoretical values have been reduced by a common normalization factor 0.75 to give an optimal fit at high positron energies. In all the spectra displayed in the figure, prominent structures are found. The 'positron lines' are centered at an energy $E_{e^+} = 280$ keV, having a width of $\Delta E = 80$ keV. The total production cross section is $\sigma_{e^+} \approx 100 \mu\text{b}$.

The angular dependence is consistent with a fit $\sim 1/\sin\theta$, which would correspond to a distribution of the emitted nuclei which is isotropic in the reaction plane. Very similar results also have been reported for the collision system U+Th, except that here the cross section is smaller by a factor of 2.

Figure 4 shows the results of the EPOS group [13] for a variety of collision systems in the range between Th+Th ($Z=180$) and U+Cm ($Z=188$). Striking line structures with a width $\Delta E \leq 80$ keV have been observed in all the systems. (Note that in preparing the data particular 'kinematic cuts' have been chosen for the

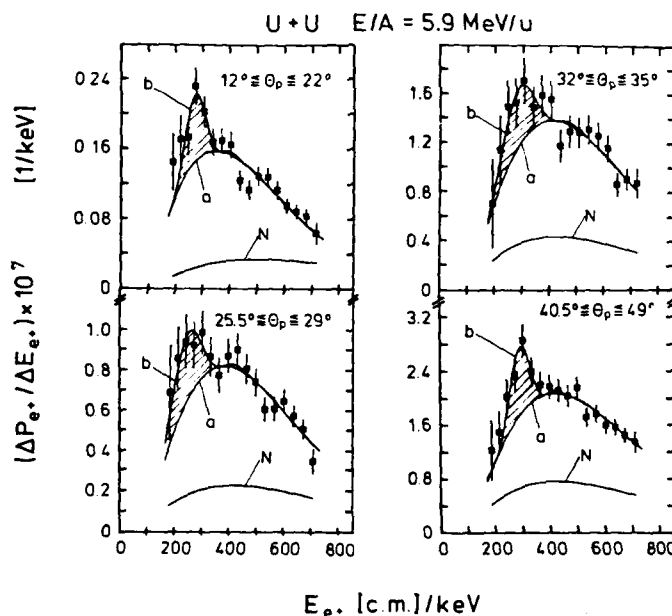


Figure 3: Positron spectra measured with the ORANGE spectrometer for U+U collisions at the Coulomb barrier [11]. For various scattering angles a structure is observed. N: Nuclear conversion background, which has been subtracted, a: Dynamical positron creation from Rutherford scattering. b: Line-fit assuming spontaneous positron production from a long-lived nuclear quasimolecule.

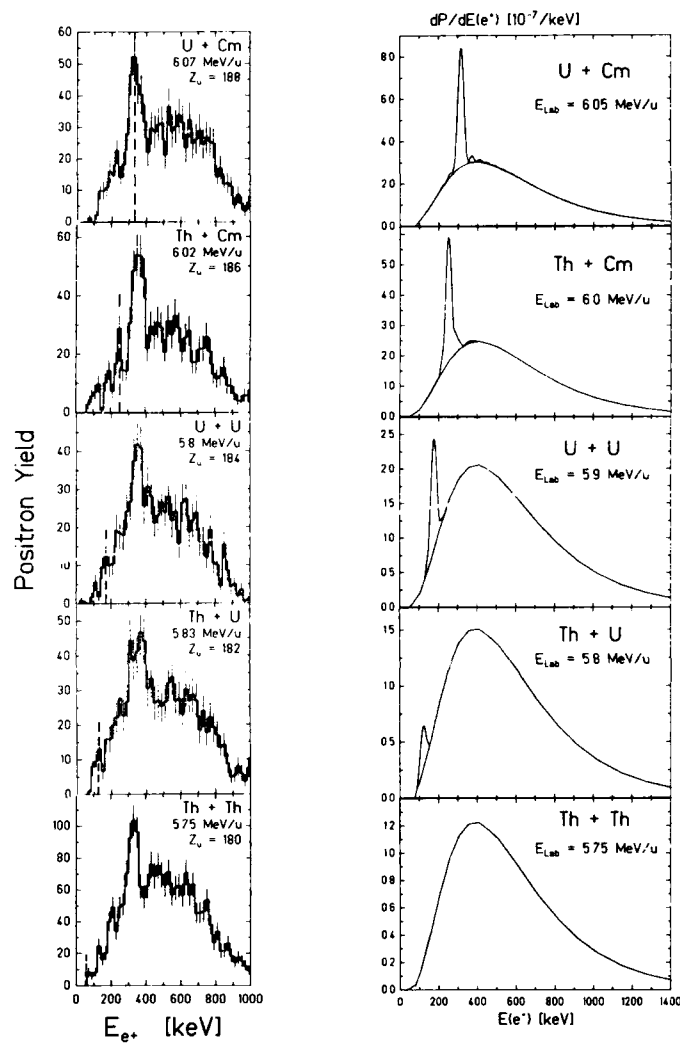


Figure 4a: Positron energy spectra for the collision systems U+Cm ($Z_U = 188$), Th+Cm (186), U+U (184), Th+U (182), and Th+Th (180) at bombarding energies close to the Coulomb barrier measured by the EPOS group at GSI [13]. Positron lines at $E_{e^+} \sim 330$ keV nearly independent of Z_U , are clearly visible.

Figure 4b: Positron spectra corresponding to part a calculated under the assumption that in all systems elongated giant nuclear molecules of similar type are formed. The fraction of delayed collisions and the lifetime have been taken over from the U+Cm system.

scattering angles. This was used to enhance the line structure with respect to the broad background.)

Before drawing far reaching conclusions on the origin of the new structures depicted in figures 3 and 4, any explanation in terms of 'trivial' effects have to be ruled out. Here one has to think of *pair conversion* processes from nuclear levels excited by the Coulomb and nuclear force or through transfer reactions. Pair conversion is known to be responsible for a quasi-continuous 'background' to the observed positron spectra. In principle a very strongly excited state undergoing conversion could lead to structures in the spectrum, although it is hard to understand why various nuclei with different structure used in the experiments should produce the same effect. Fortunately, nuclear conversion coefficients can be calculated reliably [16]. The resulting positron spectrum has a triangular shape and the width of the spectra should be twice as large as the observed value.

Further experimental conclusions can be drawn from the energy distribution of emitted γ -rays and δ -electrons: Nuclear transitions of, e.g., multipolarity E1 or E2 should also be observable in the spectra of *photons* with an intensity that can be predicted. If the observed positron lines are caused by nuclear E0 transitions, one should also observe a distinct peak in the δ -electron distribution. No such structures have been found in the experiments of the EPOS and the ORANGE group [18,12]. From these arguments we can conclude that the sharp positron line structure does not originate from a trivial conversion in the separated collision partners.

These conclusions are substantiated by two other experimental facts: The Orange group [18] has measured the emission probability in the positron line as a function of the azimuthal angle relative to the scattering plane. If positrons are emitted from a system moving with the velocity of the center of mass, the emission probability for a given positron energy can not depend on the azimuthal

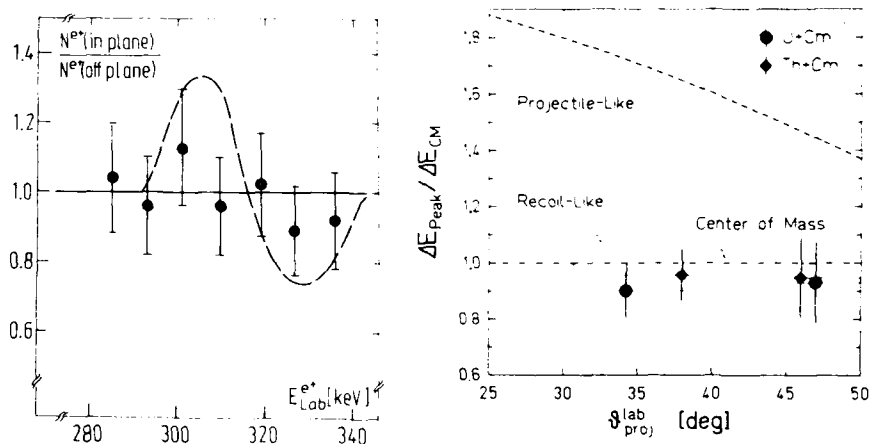


Figure 5a: Ratio of positrons emitted in the scattering plane ($0^\circ \leq \phi \leq 45^\circ$) to those emitted off-plane ($45^\circ \leq \phi \leq 90^\circ$), as a function of positron energy. For emission from the combined system moving into the beam direction this ratio should be constant (=1.), whereas for an emission from the separated collision partners the ratio should follow the dashed line [18].

Figure 5b: Doppler broadening of the positron line expected from projectile, target, and centre-of-momentum emission in binary scattering events from 6.05 MeV/u U+Cm and 6.02 MeV/u Th+Cm collisions plotted as a function of the laboratory projectile scattering angle. Broadening is expressed as a fraction of the calculated width for c.m. emission. The independence of the scattering angle indicates that the emitting system travels with c.m. velocity. From [13].

angle between the scattering plane and the positron detector. Thus, the ratio $N(\text{in-plane}) / N(\text{off-plane})$ should be constant. For positron emission from the separated collision partners, however, the ratio should follow the curve displayed in figure 5a. A preliminary analysis of these data indicates that the emitting system moves in the direction of the beam (i.e., the center of mass).

The EPOS group [13] used the widths of the peaks to determine the emitter velocity. They appear to be independent of the scattering angle for all collision systems investigated. Moreover, it was found that the observed width corresponds to the value expected from Doppler broadening, assuming that the source moves with center of momentum velocity, cf. Figure 5b.

Thus the experimental evidence presently available seems to exclude the hypothesis that the positron line is emitted by the separating nuclei. Instead, the emitting source seems to be correlated with the center of mass motion of the heavy ion system.

5. PRODUCTION OF A NEW ELEMENTARY PARTICLE?

Looking at the experimental spectra one might be led to the conclusion that all the observed positron lines have a single common origin. One mechanism which in a natural way would lead to exactly the same positron energy in all systems is the creation of a new light particle X decaying under positron emission [19,20]. Although such an explanation is highly speculative it seems worth while to investigate its consequences and check its consistency with the experimental facts.

We will concentrate on the hypothesis that the new particle is a neutral boson decaying into an electron-positron pair, $X \rightarrow e^+e^-$. The mass required to explain a positron energy of $E_{e^+} = 330$ keV is $m_X = 2(m_e + E_{e^+}) \approx 1.68$ MeV. One candidate for the new particle is the pseudoscalar *axion* which has been postulated on theoretical grounds in order to explain the absence of CP violating terms in the theory of strong interaction [21]. However, since at least the standard axion model is in conflict with experiment we will leave open the type of coupling of the particle, only assuming that it couples linearly to the lepton fields, with the interaction Lagrangian $L = g \bar{\psi} \Gamma \psi \phi$ where $\Gamma_S=1$, $\Gamma_P=i\gamma^5$, $\Gamma_V=\gamma^\mu$, and $\Gamma_A=\gamma^5\gamma^\mu$ for scalar, pseudoscalar, vector and axial vector coupling.

Let us discuss the *kinematical aspects* of the hypothesis that in heavy ion collisions new particles of mass m_X are created which decay into electron-positron pairs. The energy distribution of positrons (or electrons) will be broadened since: (1) the distribution of the created bosons will have a finite energy spread in the heavy ion center of mass system; (2) the proper momentum of the moving particles adds up to the momentum of the decay products depending on a varying relative angle. Therefore the mere fact that particles with an appropriate mass m_X are created does not automatically guarantee the emergence of a line in the positron spectrum having the observed narrow width $\Gamma \leq 80$ keV.

If the particles are radiated dynamically during the course of the heavy ion collision, their energy distribution must be rather broad, reflecting the available 'Fourier frequencies' of the nuclear motion. The possible emergence of a line structure in the spectrum of the decay products depends sensitively not only on the fall-off constant of the particle spectrum but even more so on its behaviour at small kinetic energies. In Figure 6 we show the expected positron spectra in the laboratory for two different assumptions on the energy distribution of created X -particles. If the latter is an exponential function dw/dE with respect to energy, the line width comes nowhere near the required value. This situation would change if the low-velocity component of the particle spectrum were enhanced. If we assume an exponential decrease of dw/dp with respect to momentum, sufficiently narrow line spectra can be produced, cf. Figure 6b. However, explicit models for the production mechanism lead to just the opposite effect: The low

momentum emission is suppressed. Thus, the particle creation hypothesis from the outset suffers from the shortcoming, not to predict the correct positron line-width.

Further severe problems are encountered if we try to explain the required production cross section of the order 100 μb . For the *coupling constant* strict upper limits can be found by looking at the effects, virtual X-creation would have on well understood high-precision data. The coupling to the electron will influence the electronic *anomalous magnetic moment*. The contribution to the electron anomaly $a = \frac{1}{2}(g-2)$ is proportional to the squared coupling constant, $\Delta a = (\alpha^e/2\pi) \cdot K(m_X/m_e)$ where K is a slowly varying function of the mass ratio. From the high level of agreement between theory and experiment for the g-factor of the electron an upper limit for the coupling strength $\alpha^e < 10^{-8}$ is found, quite independent of the Lorentz coupling type (S, P, V, A).

An estimate of the dynamical particle creation cross section in heavy ion collision at the Coulomb barrier using this coupling constant falls short of experiment by about five orders of magnitude. Therefore the hypothesis that a light boson created via coupling to the electron field is responsible for the observed positron line seems not to be tenable.

Similar arguments apply also if we assume that the particle is *created from the nuclear current*. Since a light boson creates an additional short range potential competing with the electromagnetic interaction, atomic physics data are sensitive to its presence. From the Lamb-shift, in hydrogen, e.g., we find an upper limit for the product of coupling constants $g^e g^p/4\pi < 10^{-7}$ (except for a pseudoscalar particle, which has vanishing coupling to the nucleon in the nonrelativistic limit).

The particle creation mechanism can be calculated in the semiclassical approximation, in close analogy to the semiclassical approach to electromagnetic bremsstrahlung. Results of a calculation [22] of scalar and pseudoscalar parti-

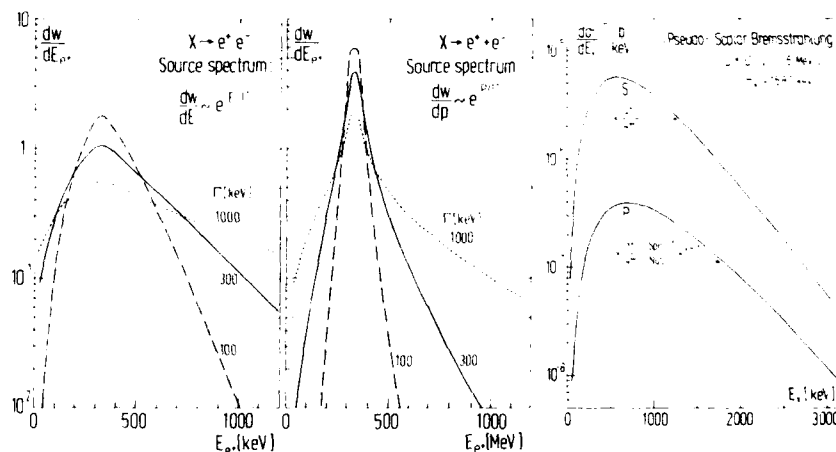


Figure 6a,b: Positron spectrum in the lab. system following the two-body decay of a light boson of ~ 1.7 MeV mass. If the production spectrum with respect to kinetic energy falls off exponentially, no sharp line can be produced (a). The assumption of an exponential source spectrum with respect to momentum could explain a narrow positron line (b).

Figure 7: The predicted spectrum of scalar or pseudoscalar particles emitted in a U+U collision by a nuclear bremsstrahlung mechanism.

cle emission are shown in Figure 7 for a collision of U+U at 6 MeV/nucleon bombarding energy. The spectra exhibit broad maxima at $E_x = 600$ keV and decay exponentially at high energies. At low kinetic energy the intensity is suppressed. This argument alone is sufficient to rule out the bremsstrahlung creation of a new particle, since the decay can not lead to narrow positron spectra. Furthermore, the intensity is much too low, in view of the limit on the coupling constant.

From these arguments we conclude that the creation of a new particle with linear coupling to other fields is not able to explain the positron lines on quantitative reasons. Only if one is willing to accept nonlinear interactions with matter fields, the 'particle scenario' for the origin of the positron lines cannot be ruled out absolutely.

6. FORMATION OF GIANT NUCLEAR SYSTEMS?

6.1 Analysis of the Positron Line

According to the experimental investigations summarized in Sect. 4 it seems very unlikely that a trivial explanation for the observed positron line structures can be found. Therefore we come back to the theoretical concept which originally had stimulated the experimental searches and ask the questions: Are the observed positron lines related to the strong Coulomb field? Do they signal the decay of the vacuum?

From the arguments of Sect. 3 it is obvious that calculations based on nuclear Rutherford scattering do not support such an interpretation. In fact, by the time-energy uncertainty relation the small width $\Delta E \leq 80$ keV of the positron lines calls for a life-time of the emitting system larger than several times 10^{-22} s. This is more than an order of magnitude larger than the 'diving time interval' defined by $R(t) < R_{cr}$. To explain the experiment we have to assume that

a rather long lived superheavy nuclear complex is formed. Then the experimental spectra can be described by a superposition of Rutherford collisions (giving the broad basis spectrum) and a small fraction of delayed collisions, since positron production is very strongly enhanced for reaction times larger than 10^{-22} s.

Position, width, and strength of the spontaneous positron line are determined by the nuclear reaction process: The kinetic energy of spontaneously created positrons by the shape of the giant nuclear molecule and by the (partly screened) nuclear charge, the line width by the nuclear reaction time T for not too short nuclear reactions (for very long reaction times $T \gg \hbar/\Gamma$ by the spontaneous decay width Γ); and the relative strength by the life time of the nuclear composite system and by the ratio q defining the number of nuclear molecule residues per elastically scattered ion in the angular window considered.

To explain the U+Cm measurement at 6.05 MeV/u [12] an elongated, molecular configuration of the two nuclei has to be assumed (two center distance $R = 16.3$ fm if the screened electronic energy is used). The reaction time used for the fit is 10^{-21} s and the fraction of delayed collisions required is $q = 1.3 \times 10^{-3}$. This corresponds to a reaction cross section of roughly 20 mb assuming isotropic breakup of the nuclear composite system.

6.2 Nuclear Physics Aspects

The analysis presented so far has been phenomenological, deducing nuclear physics properties from the experimental data on positron line production. Ultimately, however, it should be possible to understand the results in terms of a theoretical model and to make predictions. Due to the complexity of the problem, this goal has been reached only partly up to now.

According to the conventional lore of nuclear physics, the collision of very heavy ions should be dominated by the strong Coulomb repulsion. However, Seiwert, Oberacker and collaborators have shown that the attractive force between the touching nuclear surfaces even in such systems may be strong enough to overcome the Coulomb force. Using a double folding model which successfully describes

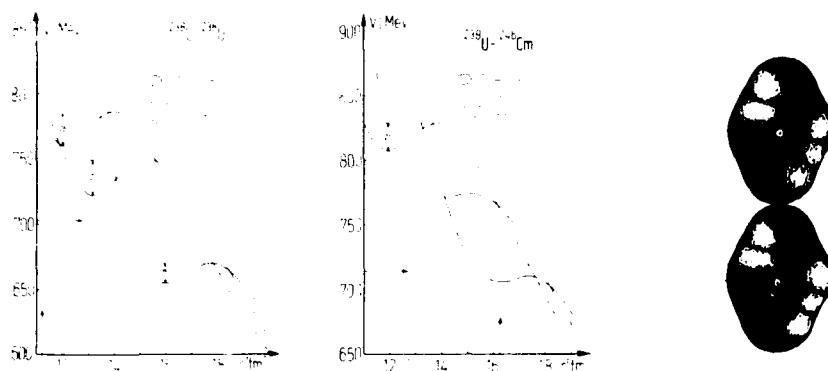


Figure 8: Nucleus-nucleus potentials for the systems $^{238}\text{U}+^{238}\text{U}$ and $^{238}\text{U}+^{246}\text{Cm}$ with surface thickness corrections for various orientations of the colliding nuclei show attractive potential pockets [23]. The arrows designate the values required to explain the positron lines. Part c gives an impression of the nuclear shapes involved in the collision of two uranium nuclei.

elastic scattering of medium heavy nuclei, the internuclear potential was found to bend down as the nuclear atmospheres start to overlap [23]. In the case of strong overlap, spurious volume and surface terms had to be renormalized, so that the detailed results can be only indicative. Nevertheless, it is encouraging that the calculation is able to predict pockets in the internuclear potential. Two examples are shown in Figure 8 for several orientations of the two strongly deformed actinide nuclei. The energetically most favourable situation is found for the head on head orientation, since here the Coulomb repulsion is smallest. It is remarkable that in the U+Cm system the potential pocket exactly corresponds to the bombarding energy and nuclear elongation required to explain the positron peak.

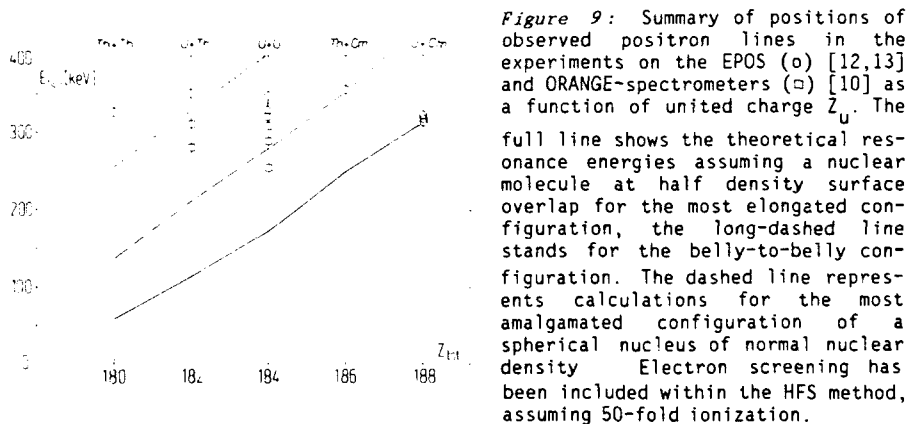
To improve the schematic method (frozen-in nuclear motion) by which the nuclear reaction has been described up to now, U. Heinz et al. extended the theory towards a quantum mechanical treatment of the nuclear relative motion [24]. This in principle allows to calculate the mechanism responsible for nuclear delayed reactions. If the atomic and nuclear excitations can be localized in different spatial regions, a formula for atomic excitation amplitudes completely analogous to eq. (7) can be deduced. But now the time development matrix $C_{qq'}(T)$ is replaced by the nuclear scattering matrix [25]. From this it can be shown that the schematic classical model of Sect. 3 in fact is equivalent to the quantal formulation if the result is averaged over a life-time distribution function $f(T)$. This function is given by the Fourier transform of the nuclear autocorrelation function. Under the assumption that the potential pocket supports a large number of closely spaced collective rotational bands, the emergence of a reaction component with long life-time was deduced within this framework. The model up to now is too crude to give quantitative predictions of the positron lines. In particular, it will be important to include inelastic channels which should increase the formation probability, while, on the other hand, preference of nuclear alignment at $\beta=90^\circ$ [26] will have the reverse effect. Despite its shortcomings the model makes an important prediction on the excitation function of the process: At energies far below the potential barrier, resonances are too narrow to be excited, and the cross section for long delayed scattering events is negligible. Far above the

barrier, the beam can only hit the high-lying short lived resonances. Therefore the excitation function of the positron line should be narrow.

6.3 Problems and Speculations

The hypothesis of giant nuclear molecule formation has been quite successful to explain the monoenergetic positron emission in the U+Cm system. There is, however, a serious problem with this model: It does not in a natural way, predict the energetic position of the positron line for different heavy ion systems. This is demonstrated in Figure 4b, where we have assumed that in all cases the same type of nuclear reaction takes place. The extension of the nuclear molecule was determined by the requirement of half density overlap of the nuclear surfaces. Within the Hartree-Fock-Slater (HFS) formalism, assuming 50-fold ionisation of the quasimolecules, the binding energies of the molecular 1s_o states are 1080 keV for Th+Th, 1135 keV for U+Th, 1195 keV for U+U, 1270 keV for Th+Cm, and 1340 keV for U+Cm. Assuming equal conditions for the nuclear reaction process and the parameters used to explain the U+Cm spectrum, the model of spontaneous positron production from a giant nuclear molecule predicts a shift of the positron line and a distinct reduction in intensity (due to the smaller spontaneous decay width Γ) if Z is decreased. [This reduction in intensity could be avoided if the life-time of the nuclear system were very large, so that in all cases a large fraction of the K-holes present ($P_{1s_0}(t=0) \approx 5\%$) were emitted as positrons, irrespective of the spontaneous decay width.]

The expected relation between the positron line energy and the total nuclear charge is shown in Figure 9 for three different assumptions on the nuclear configuration. (In the absence of electron screening, the curves would be shifted by about 100 keV towards higher energy.) Obviously the expected trend is not in



accordance with the experimental data. The sets of data points from the EPOS and the ORANGE group essentially are Z-independent, while they show systematic deviations from each other.

Presently only speculations on the reason for the observed systematics of line energies can be given.

1. It is possible that the shape of the giant nuclear complex strongly depends on the nucleon number and is more spherical for smaller nuclei. The nuclear matter properties in the region $A \approx 480$ could be radically different from that known from ordinary nuclei. In particular, the compressibility may be strongly altered due to the quark degree of freedom [27].

2. It is conceivable that in all collisions the same nucleus is formed (probably by fast α -emission), followed by spontaneous positron production characterized by

the charge of the residual nucleus.

3. Part of the positron lines may be of different origin. If we want to stay in accordance with the evidence for emission from the center of mass system (cf. Sect. 4) one possible supplementary mechanism is *conversion in the nuclear compound system*. Due to the relativistic shrinkage of the wavefunctions, such a mechanism can be very fast, contrary to what we are used to in ordinary nuclei. Figure 10 shows results of an illustrative quantum mechanical calculation [28] of such a process. Energy is transferred from a transition between two states in a nuclear potential pocket to the positron producing a second peak of appreciable intensity. In this way the spontaneous positron emission can be accompanied by 'satellite peaks' at higher or lower energy (if energy is absorbed by the nucleus), quite analogous to the Stokes and Anti-Stokes lines known from molecular physics. Note that the process of conversion in the compound system does not depend on the presence of spontaneous positron creation and can be present also in subcritical systems.

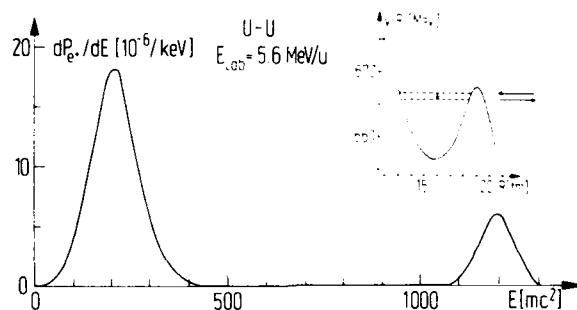


Figure 10: Scattering potential of a U+U collision system and resulting positron spectrum showing two line structures which originate from different processes. The first peak at $E_{e+} = 200$ keV originates from the spontaneous decay of a hole in the supercritical $1s$ state. The second peak at $E_{e+} = 1200$ keV emerges due to conversion: the energy set free in a transition between two states in a potential pocket is transferred to the positron [28].

None of these speculations up to now has been put on a firm basis. In part this is due to the incompleteness of the presently available experimental data. Let us mention some of the problems: (1) A slowly varying excitation function was found by the ORANGE group, while it seems to be very sharply peaked at the Coulomb barrier according to the EPOS experiment. (2) The energetic positions show systematic deviations between both groups. (3) It is not clear whether there are significant line structures in subcritical collision systems. (4) The dependence on the heavy ion scattering angle and the role played by the 'kinematic cuts' in the EPOS experiment is not fully understood.

7 SUMMARY

The gross features of positron creation in heavy ion collisions can be well understood within the quasimolecular model. They reflect the action of the strong nuclear Coulomb field and are dominated by relativistic effects. In addition to these features two experimental groups have discovered striking narrow structures in the positron spectra at bombarding energies close to the Coulomb

barrier. All the experimental evidence collected up to now strongly suggests that the effect does not have a trivial explanation in terms of pair conversion in the separating excited nuclei. On the basis of this experimental evidence, we are compelled to search for nonconventional explanations. Only two mechanisms have been found which in principle are able to explain the positron line, both having quite radical consequences.

The hypothesis that a *new elementary particle* of mass 1.68 MeV has been found (Sect. 5) is highly improbable since the coupling constants required to explain the measured positron cross section are much too large to be reconciled with established high precision data. If one does not take recourse to the assumption of a nonlinear coupling to other matter fields, the hypothesis can be ruled out.

We are left with the explanation that the observed effect originates from a *giant nuclear complex* with a lifetime $T \approx 10^{-19}$ s (Sect. 6). The decay of the QED vacuum in supercritical fields then provides a natural mechanism for monochromatic positron emission. This interpretation of the data, however, is beset with the problem that it does not in a natural way predict the observed nearly constant line energy. Unusual and presently not understood properties of the giant nucleus have to be invoked. Particularly in view of several discrepancies between the results of the different experiments, we have to conclude that a fully consistent picture of positron creation in heavy ion collisions which can explain all the experimental data has not yet emerged.

REFERENCES

- [1] Instead of quoting the original works on this field we refer the reader to W. Greiner, B. Müller, J. Rafelski, *Quantum Electrodynamics of Strong Fields*, (Springer, Berlin, 1985); *Quantum Electrodynamics of Strong Fields*, NASI series B80 W. Greiner, ed., (Plenum, New York, 1983)
- [2] G. Hardekopf and J. Sucher, *Phys. Rev. A* **31**, 2020 (1985)
- [3] J. Reinhardt, B. Müller, and W. Greiner, *Phys. Rev. A* **24**, 103 (1981)
- [4] C. Bottcher and M.R. Strayer, *Phys. Rev. Lett.* **54**, 669 (1985)
- [5] B. Müller and W. Greiner, *Z. Naturforsch.* **31a**, 1 (1976)
- [6] J. Rafelski, B. Müller, and W. Greiner, *Z. Physik* **A285**, 49 (1978)
- [7] W.E. Meyerhof and J.F. Chemin in *Advances in Atomic and Molecular Physics*, vol. 20, D.R. Bates and B. Bedersen, eds. (Academic Press, New York, 1985)
- [8] J. Reinhardt, U. Müller, B. Müller, and W. Greiner, *Z. Physik* **A303**, 173 (1981)
- [9] G. Soff, J. Reinhardt, B. Müller, and W. Greiner, *Phys. Rev. Lett.* **43**, 1981 (1979)
- [10] M. Clemente, E. Berdermann, P. Kienle, H. Tsertos, W. Wagner, C. Kozhuharov, F. Bosch, and W. Koenig, *Phys. Lett.* **137B**, 41 (1984)
- [11] H. Tsertos, E. Berdermann, F. Bosch, M. Clemente, P. Kienle, W. Koenig, C. Kozhuharov, and W. Wagner, 'On the Scattering Angle Dependence of the Monochromatic Positron Emission from U+U and U+Th Collisions', submitted to *Phys. Lett.*
- [12] J. Schweppe, A. Gruppe, K. Bethge, H. Bokemeyer, T. Cowan, H. Folger, J.S. Greenberg, H. Grein, S. Ito, R. Schulé, D. Schwalm, K.E. Stiebing, N. Trautmann, P. Vincent, and M. Waldschmidt, *Phys. Rev. Lett.* **51**, 2261 (1983)
- [13] T. Cowan, H. Backe, M. Begemann, K. Bethge, H. Bokemeyer, H. Folger, J.S. Greenberg, H. Grein, A. Gruppe, Y. Kido, M. Klüver, D. Schwalm, J. Schweppe, K.E. Stiebing, N. Trautmann, and P. Vincent, *Phys. Rev. Lett.* **54**, 1761 (1985)

- [14] H. Backe, P. Senger, W. Bonin, E. Kankleit, M. Krämer, R. Krieg, V. Metag, N. Trautmann, and J.B. Wilhelmy, *Phys. Rev. Lett.* **50**, 1838 (1983)
- [15] R. Krieg, Ph.D. thesis, TH Darmstadt (1985)
- [17] H. Bokemeyer, GSI-84-43 preprint (1984)
- [16] G. Soff, P. Schlüter, and W. Greiner, *Z. Physik A303*, 139 (1981)
- [16] P. Schlüter, T. de Reus, J. Reinhardt, B. Müller, and G. Soff, *Z. Physik A314*, 297 (1983)
- [18] P. Kienle, in: *Fundamental Problems in Heavy Ion Collisions*, eds. N. Cindro, W. Greiner, and R. Caplar. World Sc. Publ. Co., 1984, p. 429
- [19] A. Schäfer, J. Reinhardt, B. Müller, W. Greiner, and G. Soff, *J. Phys. G11*, L69 (1985)
- [20] A.B. Balantekin, C. Bottcher, M.R. Strayer, and S.J. Lee, 'Axion Production in heavy-ion collisions', preprint (1985)
- [21] R.D. Peccei and H. Quinn, *Phys. Rev. Lett.* **38**, 1440 (1977); S. Weinberg, *Phys. Rev. Lett.* **40**, 223 (1978); F. Wilczek *Phys. Rev. Lett.* **40**, 279 (1978)
- [22] J. Reinhardt, A. Schäfer, B. Müller, and W. Greiner, 'Phenomenological consequences of a hypothetical light neutral particle in heavy ion collisions', preprint (1985)
- [23] M. Seiwert, W. Greiner, and W.T. Pinkston, *J. Phys. G11*, L21 (1985)
- [24] U. Heinz, J. Reinhardt, B. Müller, W. Greiner, and U. Müller, *Z. Physik A314*, 125 (1983)
- [24] U. Heinz, U. Müller, J. Reinhardt, B. Müller, and W. Greiner, *Ann. Phys.* **158**, 476 (1984)
- [25] T. Tomoda and H.A. Weidenmüller, *Phys. Rev. C28*, 739 (1983)
- [26] V.E. Oberacker, 'Influence of nuclear alignment on subbarrier fusion and spontaneous positron production', preprint (1985)
- [27] C. Derreth, Q. Zhang, et al., to be published
- [28] S. Schramm, diploma thesis, Frankfurt (1985)

ANOMALOUS POSITRON PEAKS FROM SUPERHEAVY COLLISION SYSTEMS

John SCHWEPPE

Yale University, A. W. Wright Nuclear Structure Laboratory, P.O. Box 6666,
New Haven, CT 06511, USA

Narrow peaks are observed in the positron energy distributions of five supercritical collision systems with combined nuclear charge $180 \leq Z_U \leq 188$. The peaks appear to be produced in a narrow range of projectile energies near the Coulomb barrier. Several observations exclude nuclear internal pair conversion as a source of the peaks. A particularly notable feature is an apparent independence of the peak energy on Z_U . A similar peak is observed in a subcritical collision system. These observations are discussed in the context of the spontaneous decay of the QED vacuum and other new potential sources of line positron spectra.

1. INTRODUCTION

We have conducted a series of experiments (1) in the last years to systematically study the production of anomalous peak structures in the energy distribution of positrons emitted in superheavy collision systems. The experiments were undertaken to determine the origin of the peaks, with particular emphasis on their possible connection to spontaneous positron production. This process is predicted (2) to occur when a vacant electronic state becomes supercritically bound to a nuclear charge distribution with a binding energy greater than $2mc^2$. An unstable electron-positron vacuum state is then created which decays spontaneously by positron emission if the supercritically bound state is unoccupied.

The motivation for this study was particularly the discovery (3) of a narrow peak in the energy distribution of positrons emitted from the U+Cm collision system associated with a particular particle scattering-angle region, as shown in Figure 1, part (a). (Peak structures have also been reported in another investigation (4).) The region has been empirically chosen to enhance the peak relative to the underlying smooth continuum of positrons dynamically produced during the collision, and takes advantage of an apparent shift in the kinematic correlations of the scattering events associated with the peak relative to the dominant Rutherford-scattering events. Part (b) shows a neighboring angular region where the peak is absent, demonstrating that the peak is not a trivial apparatus effect. The peak appears at a positron kinetic energy of 316 ± 10 keV with a measured width of about 80 keV. Calculations (5,6) of the binding energy of the innermost electron for a di-nuclear complex consisting of an uranium and a curium nucleus side by side reproduced this energy. The width of the peak implies a source living $\geq 10^{-20}$ s, or more than 10 times longer than the Rutherford-scattering collision time. At the same time, the width is consistent with the Doppler broadening expected for a source moving with the velocity of the center of mass of the two colliding nuclei. In addition, the appearance of the peak in a narrow range of bombarding energies near the Coulomb barrier, its apparent association with scattering events differing in their particle scattering-angle dependence from the dominant Rutherford-scattering events, and the absence of lines in the simultaneously measured gamma-ray and electron spectra had prompted the suggestion (5) that the line could be due to spontaneous positron emission enhanced (7) by the formation of long-lived, di-nuclear molecular complexes in these collisions near the Coulomb barrier.

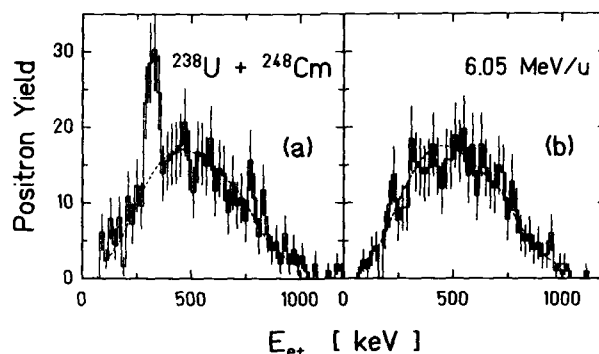


FIGURE 1

Positron energy distribution observed for the U+Cm collision system at a projectile energy of 6.05 MeV/u. Parts (a) and (b) are associated with two neighboring regions of particle scattering angles, as described in the text. The dashed lines represent a fitted sum of the nuclear positron background deduced from γ -ray spectra and a theoretical calculation (16) of the dynamic positron production.

The experimental study that we have undertaken concentrated on two aspects that have a direct bearing on the hypothesis of spontaneous positron production. Spontaneous positron emission would clearly imply emission from the center of mass of the colliding nuclei as opposed to either of the two collision partners. In addition, theoretical calculations (5) predict a strong, Z_U^2 dependence on the combined nuclear charge for the energy of the peak, a change in energy that would be readily observable even with the restricted range of available targets and heavy-ion beams.

The experiments were carried out with the UNILAC heavy-ion accelerator at GSI Darmstadt and the EPOS spectrometer (8) depicted in Figure 2. The positron spectrometer uses the axial focussing property of a solenoidal magnetic field for charged particles together with a baffle system and an annihilation radiation detector to provide a large detection efficiency for positrons while suppressing the huge gamma-ray and electron backgrounds. Two position-sensitive, parallel-plate, avalanche particle detectors determine the kinematic parameters for each collision, allowing the isolation of interesting scattering events. The background of positrons from the internal pair conversion of excited nuclear states is calculated from the gamma-ray flux monitored in NaI(Tl) detectors. The possibility of structure in the positron energy spectrum from the internal pair conversion of strong, isolated, nuclear transitions is checked with the gamma-ray measurement and the detection of electrons in a planar Si(Li) detector axially mounted behind the magnetic mirror field on the opposite arm of the solenoid as the positron detector.

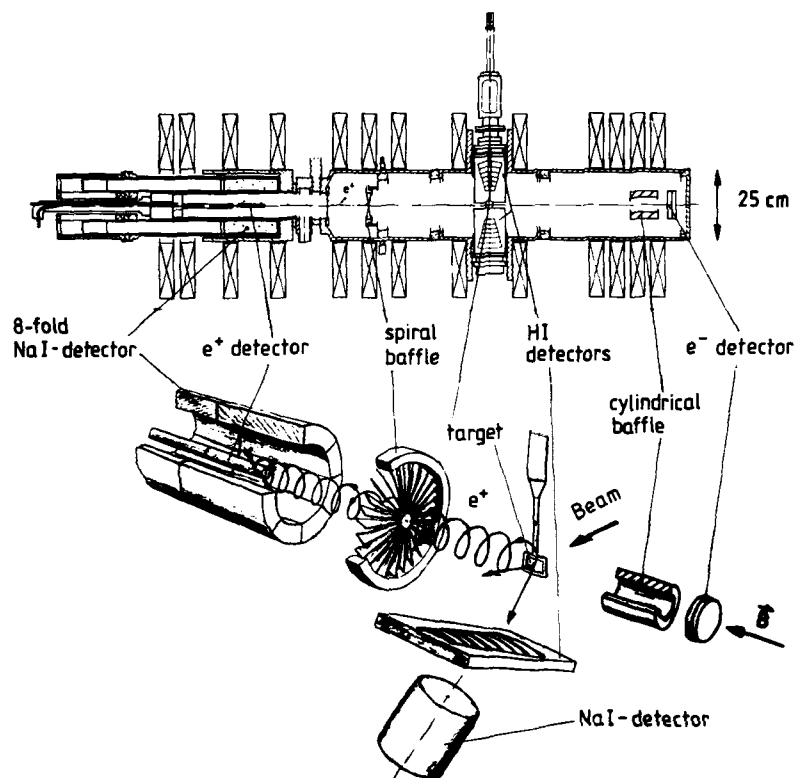


FIGURE 2

Schematic view of the EPOS spectrometer (upper panel) and a perspective drawing of the main components (lower panel).

2. POSITRON PEAKS IN SUPERCRITICAL SYSTEMS

2.1. Similar Peaks Observed in All Measured Supercritical Systems

The positron production was measured in five different collision systems that span the supercritical range of combined nuclear charge $Z_U \equiv Z_P + Z_T$ from 188 down to 180. The systems studied were $^{238}\text{U} + ^{248}\text{Cm}$ ($Z_U = 188$), $^{232}\text{Th} + ^{248}\text{Cm}$ (186), $^{238}\text{U} + ^{238}\text{U}$ (184), $^{232}\text{Th} + ^{238}\text{U}$ (182), and $^{232}\text{Th} + ^{232}\text{Th}$ (180). In each case the projectile kinetic energy was scaled from the original U+Cm measurement to produce the same partial overlap of the deformed nuclear-density distributions in a head-on, end-to-end collision. The measured positron energy distributions are shown in Figure 3. (Part (a) repeats the plot of Figure 1 and part (b) shows a remeasurement of the same system with improved detection efficiency.) In each plot a prominent peak is visible above the dynamic continuum. Again, kinematic constraints similar to those described above have been applied to enhance the peak relative to the dynamic background. As is apparent, the energy and width of the peak is nearly the same in all systems.

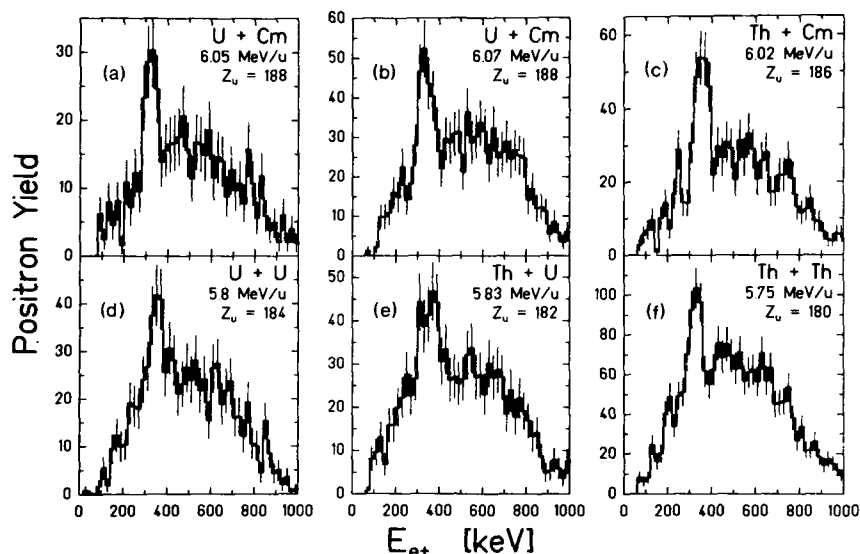


FIGURE 3

Positron energy distributions for the five collision systems and projectile energies indicated. Kinematic constraints have been chosen as discussed in the text.

2.2. Nuclear Internal Pair Conversion

Since an obvious trivial source of positrons in heavy-ion collisions is the internal pair conversion of nuclear states excited during the collision, we have investigated this possibility by a study of the lineshape of the positron peak and of the simultaneously measured gamma-ray and electron distributions. Both normal internal pair conversion (IPC) and the rare monoenergetic internal pair conversion (MIPC) process have been considered. In the second case, the electron is captured into a vacant electron orbital (predominantly the close-lying K-shell) leaving the positron in a state of well-defined energy. In both cases, however, the experimental data speak against a nuclear origin for the positron peaks.

To begin with, the narrow width alone of the peaks of ~ 70 keV effectively excludes normal IPC in either of the two colliding nuclei, since this process produces a triangular-shaped positron energy distribution with a width (FWHM) of ~ 150 keV at the peak energy of ~ 340 keV.

Moreover, IPC would compete with the internal conversion of an electron for an E0 nuclear transition or with gamma-ray emission for all higher multipolarity transitions. Electron and gamma-ray spectra measured simultaneously with the positron distributions shown above in Figure 3, however, show no structure consistent with an explanation of the positron peak if due to IPC. Figure 4 shows the electron spectrum (histogram) measured for the U+Cm collision system simultaneously and under the same kinematic constraints as the positron spectrum in Figure 3(b) above. The solid line indicates the structure which must be present to account for the intensity of the peak in the positron spectrum by IPC of an E0 transition (9). Figure 5(a) shows the same calculation for the measured gamma-ray spectrum for E1 (dashed line) and E2 (solid line) (10). Higher multi-

polarity transitions have smaller IPC coefficients and would require even larger structures in the gamma-ray spectrum.

The same calculation for the case of monoenergetic internal pair conversion is shown for E0 transitions as the dotted line in Figure 4 and for E1 and E2 transitions in Figure 5(b) (11). Since in this case the capture of the electron of the internally converted pair requires a vacancy, some assumption about the vacancy production is necessary. The very fact that the typical lifetime of a K-shell vacancy in heavy ions of $\sim 10^{-17}$ s (12) is about four or five orders of magnitude shorter than the typical conversion time of $\sim 10^{-13}$ to 10^{-12} s implies that this process must be strongly suppressed. The calculations shown in Figures 4 and 5(b) assume one K-shell vacancy on the average still present at the time of the conversion, even though the considerations above imply that $\leq 10^{-4}$ is more realistic. A more detailed calculation shows that on the average nearly two vacancies must live for $\geq 10^4$ the normal K-shell vacancy lifetime to account for the positron peak by MIPC. The absence of large enough structure in either the electron or the gamma-ray spectrum seems to rule out a nuclear origin for the positron peak.

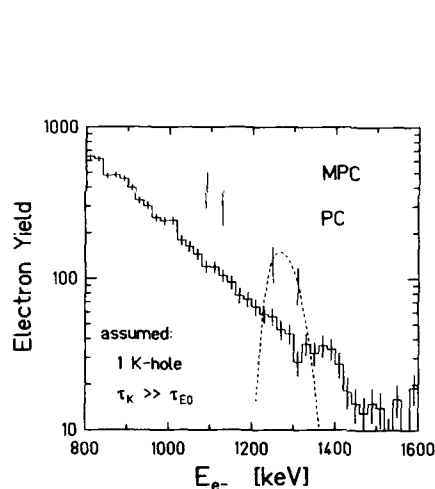


FIGURE 4

Electron energy distribution for the U+Cm collision system at a projectile energy of 6.05 MeV/u. The kinematic constraints match those of Figure 3(b). The dashed line is a calculation of the needed intensity to explain the positron peak in Figure 3(b) by IPC, the dotted line that by MIPC.

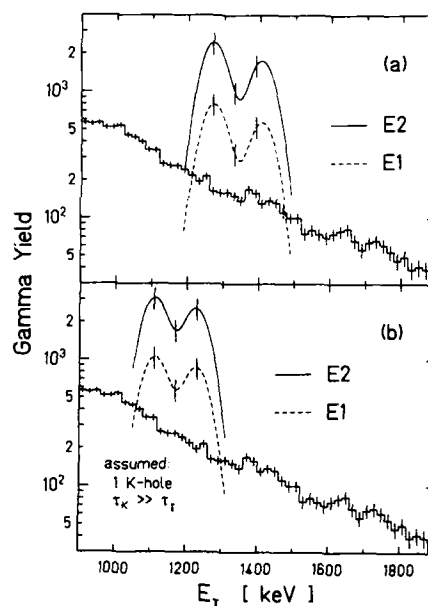


FIGURE 5

Gamma-ray energy distribution for the U+Cm collision system at a projectile energy of 6.05 MeV/u. The kinematic constraints match those of Figure 3(b). The lines in part (a) are a calculation of the needed intensity to explain the positron peak in Figure 3(b) by IPC of an E1 (dashed) or E2 (solid) transition. A similar calculation is shown in part (b) for MIPC.

2.3. Velocity of the Emitting System

The Doppler-broadened width of the positron peak also provides information on the velocity of the positron emitter system. If the positron production is roughly isotropic in the coordinate system of an emitter which is moving along the beam direction, and since the solenoidal positron transport system lies perpendicular to the beam axis, the main Doppler effect is a broadening $\Delta E = 2\beta\gamma p_{e+}$ of the positron line shape proportional to the emitter velocity, with only a small Doppler shift $\delta E = (\gamma-1)(E_{e+}+mc^2)$. As an example, the line shape measured in the laboratory for monoenergetic positron emission with $E_{e+} = 315$ keV in the center of mass (CM) of the U+Cm collision system at a bombarding energy of 6.05 MeV/u (cf. Figure 3(a) above) is shown as the solid line in Figure 6. The dotted line shows the expected lineshape including the effects of the positron detection system. (The dip in the middle of the line shape is due to reduced detection efficiency for positrons emitted along the solenoid axis which pass through the mirror field or strike the center of the electron baffle system. Note that this line shape must also be folded with the response function of the Si(Li) positron detector.) The main effect on the 315 keV line is clearly a Doppler broadening of 73 keV, with a shift of only 1.3 keV.

To confirm these calculations, the line shape has been measured by observing the internal conversion electron lines from short-lived states of ^{126}Ba formed in the nuclear reaction $^{12}\text{C}(^{118}\text{Sn}, 4n)^{126}\text{Ba}^*$. The results of the measurement made with a beam of ^{118}Sn on carbon foils at a bombarding energy of 5.86 MeV/u ($B_{\text{cm}} = 0.101$ for ^{126}Ba) is shown in Figure 7. The solid and dashed lines show the results of a ray-tracing calculation of the expected electron line shape in the laboratory. As can be seen, the overall agreement is very good. The calculated width of 109 keV for the most prominent structure (K-conversion of the $2^+ \rightarrow 0^+$ transition in ^{126}Ba) is in excellent agreement with the measured value of 107 ± 5 keV.

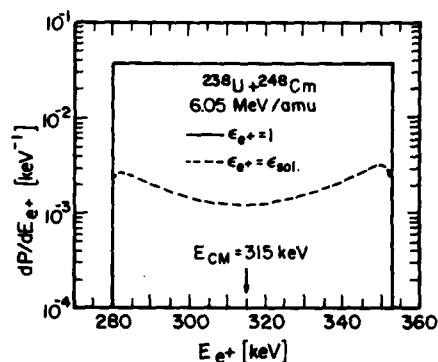


FIGURE 6

The laboratory lineshape (solid line) of monoenergetic positron emission with $E_{e+} = 315$ keV in the CM of the U+Cm collision system at a projectile energy of 6.05 MeV/u. The dashed line shows the lineshape measured by the EPOS spectrometer.

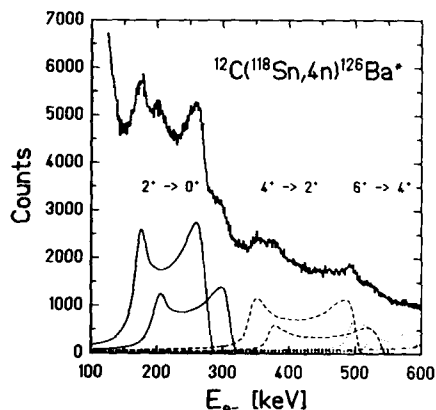


FIGURE 7

Electron energy distribution for the $^{118}\text{Sn} + ^{12}\text{C}$ collision system at a projectile energy of 5.86 MeV/u. The observed structures are electron conversion lines in ^{126}Ba . The lines are Monte Carlo calculations of the expected laboratory electron lineshape.

If we assume for the sake of illustration that the positron emission comes from either the center of mass of the collision system or from one of the scattering nuclei, the Doppler-broadened width of the positron peak can be used to distinguish between these two cases by measuring the width as a function of the scattering angle of one of the nuclei. (The minimum Doppler-broadening, for emission from the CM, of ~ 70 keV, dominates the ~ 12 keV intrinsic resolution of the Si(Li) positron detector.) The dash-dot line in Fig. 8 shows the constant width as a function of scattering angle expected for emission from the CM while the dashed lines show the angular dependence for emission from the projectile or the target nucleus, respectively (depicted as the ratio to the constant CM width). The measured data points are from the two collision systems U+Cm (circles) and Th+Cm (squares), which are sufficiently asymmetric in mass to allow an unambiguous kinematic determination of the nuclear scattering angles. The measured width of the positron line is nearly constant as a function of angle and consistent in magnitude with emission from an object moving with the CM velocity rather than from either of the separate nuclei.

It must be stressed that the conclusions reached above follow only under the assumption that the positron emission comes from either the CM of the collision system or from one of the detected scattered nuclei. Other possibilities to produce a narrow positron line involving the isotropic creation of a positron source in the CM with a broad distribution of velocities including low velocity components will be discussed below.

2.4. Z-dependence of the Peak Energy

Probably the most notable feature of the data assembled in Figure 3, however, is the apparent constancy of the energy of the main peak observed in all collision systems. This is summarized in Figure 9, where the peak energy is plotted

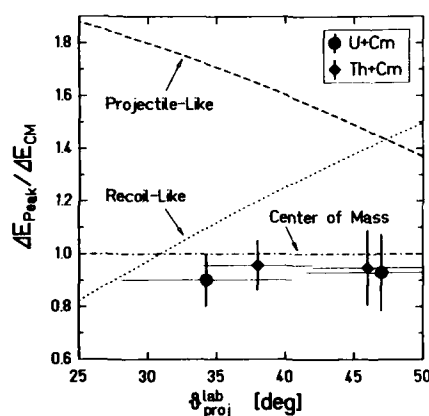


FIGURE 8

The measured, Doppler-broadened width of the positron peak in the 6.05 MeV/u U+Cm (circles) and the 6.02 MeV/u Th+Cm (squares) collision systems is plotted against the projectile scattering angle. The lines show the calculated width for emission from the projectile, recoil, and CM system, as indicated, expressed as a fraction of the CM width.

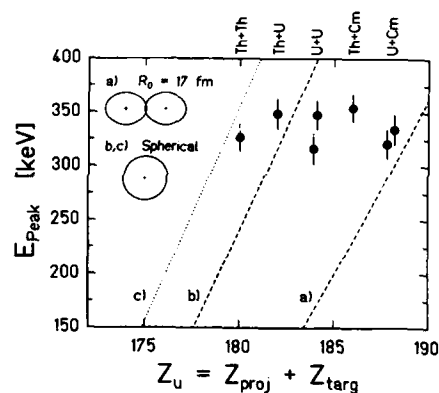


FIGURE 9

The mean energies of the positron peaks in FIGURE 3 are plotted as a function of Z_U . The calculated (5) lines are described in the text.

against the combined nuclear charge, Z_U . A simple average of the peak energies is 336 ± 10 keV. Also shown are the theoretical predictions (5) for spontaneous positron production from a nuclear complex living long enough ($\geq 10^{-19}$ s) to account for the narrow width of the peak. The three different calculated lines demonstrate not only the strong dependence of the peak energy on Z_U , but also show its dependence on the nuclear configuration and the screening effects of atomic ionization. Lines (a) and (b) give the limiting cases of nuclear configuration for the expected ionization of about 50^+ . Line (a) shows the Z_U -dependence for two deformed nuclei sticking together end-to-end, separated by 17 fm, while line (b) shows the dependence assuming the two nuclei have coalesced into a spherical form. Line (c) demonstrates the additional effect of screening under the assumption that all electrons are stripped away from the spherical nuclear configuration.

Clearly the observed peaks can be accommodated within a scenario based on spontaneous positron production only if the nuclear configuration and the atomic ionization should track with Z_U in such a way as to produce a nearly constant binding energy for the $1s_0$ electron state that should be responsible for the positron peak. In addition, the colliding nuclei must somehow coalesce into a spherical form and re-emerge in a way that reproduces the two-body kinematics of Rutherford scattering in order to satisfy our kinematic constraints. The alternate possibility of forming the same, particularly stable, spherical nuclear complex in all these collision systems is excluded by the requirement that $Z_U \leq 180$, in which case enough nucleons must be ejected from the heavier collision systems to fall outside the kinematic constraints applied to produce the spectra in Figure 3 (unless the ejected nucleons have highly asymmetric angular distributions). The possibility (13) of forming a narrow positron peak from the fast ($\sim 10^{-19}$ s) internal pair conversion of a transition in a composite nuclear complex formed during the collision suffers from the need for a dominating transition of nearly the same energy in all the different collision systems.

3. POSITRON PEAKS IN SUBCRITICAL SYSTEMS

Because of these difficulties with an explanation for the peak based on spontaneous positron production, we have recently extended our measurements to the subcritical system $^{232}\text{Th} + ^{181}\text{Ta}$ with $Z_U = 163$, well below the spontaneous threshold of $Z_{\text{crit}} = 173$ (14) predicted for normal nuclear density. Scaling the beam energy as described above and using similar kinematic constraints produces the positron energy distribution shown in Figure 10. A peak structure with approximately the same energy and width as those seen in the supercritical systems described above is evident.

A more careful analysis is necessary here because, contrary to all the supercritical collision systems considered above, in this case structure is found in the gamma-ray spectrum which allows a possible contribution to the positron peak from the internal pair conversion of a nuclear transition. The structure in the gamma-ray spectra, which appears most prominently for particle scattering angles associated with far collisions, does not seem to be correlated in scattering angle, however, to the prominent peak in the positron distribution. Indeed, the structure is barely visible in Figure 11 in the gamma-ray distribution with the same kinematic constraints as the positron spectrum of Figure 10. An analysis similar to that described above for the U+Cm collision system in Figure 5 is shown by the dashed and dotted lines in Figure 11 (which, as above, give the required *absolute* gamma-ray intensity). It can be seen that also in this subcritical collision system, there is not enough intensity evident in the gamma-ray spectrum to account consistently for all of the positron peak by nuclear processes.

In addition, the reverse analysis of calculating from the intensity of the gamma-ray line the corresponding contribution through internal pair conversion to the positron emission, indicates that IPC of an E1 transition can account for no more than $25 \pm 10\%$ of the positron peak intensity, as well as requiring much

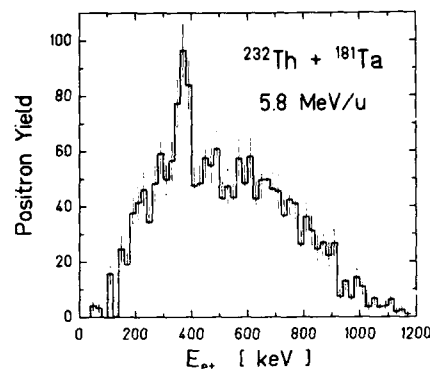


FIGURE 10

Positron energy distribution for the Th+Ta collision system at a projectile energy of 5.8 MeV/u. Kinematic constraints have been chosen as described in the text.

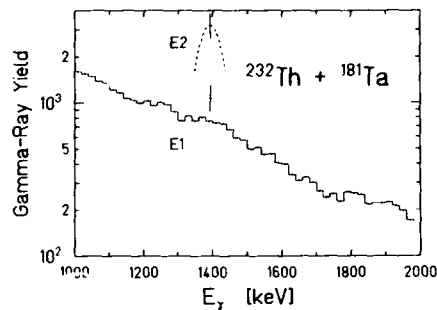


FIGURE 11

Gamma-ray energy distribution for the Th+Ta collision system at a projectile energy of 5.8 MeV/u. Kinematic constraints match those of Figure 10. The lines are a calculation of the needed intensity to explain the positron peak in Figure 10 by IPC of an E1 (dotted) or E2 (dashed) transition.

too broad a structure in the positron spectrum. Higher multiplicities, of course, can account for even less. As above for the supercritical systems, the electron spectrum shows no structure, and the internal conversion of an E0 transition can also be excluded as a source of the positron peak.

There is thus strong evidence that the same positron peak seen in the supercritical collision systems is also present in a subcritical system. This would effectively rule out spontaneous positron production as a possible source of *all* the peaks and point to the necessity of another explanation.

4. POSITRON LINE SHAPE FOR A TWO-BODY DECAY

The similar energy of the positron emission in all the different collision systems certainly suggests a common source. A ready explanation for the apparently constant, nearly monoenergetic positron emission would be the two-body decay of an undetected source produced during the heavy-ion collisions or in the decay of an excited nuclear state. Two obvious possibilities are a neutral particle which decays into an electron-positron pair, $X^0 \rightarrow e^+e^-$, or a pair of charged particles (15) which decay into a lepton pair, $X^+ \rightarrow e^+\nu$ and $X^- \rightarrow e^-\bar{\nu}$.

In either case, one would anticipate a range of velocities for the undetected source, as opposed to the constant source velocities discussed above. As the following calculations demonstrate, however, this does not preclude the appearance of a narrow peak in the positron energy distribution. Under the very general conditions that the velocity distribution of the source contain substantial low velocity components, a well-pronounced peak can be produced.

In the following schematic calculation it is assumed that a source of monoenergetic positrons with $E_{e^+} = 340$ keV is produced in the center of mass of the Th+Cm collision system at a bombarding energy of 6.0 MeV/u. In the CM system, the positron source is taken to have a constant distribution of velocities in velocity-phase space. The distribution of source velocities seen in the laboratory

system is shown in Figure 12(a). The transformation of the constant velocity distribution to the laboratory produces a Jacobian peak at $\beta = \beta_{cm} = 0.055$ in the laboratory source-velocity distribution due to the effective boost of slower velocity components up to the CM velocity. The Doppler-shifted lineshape measured in the laboratory of the isotropically emitted, monoenergetic positrons is shown in Figure 12(b). The preponderance of laboratory velocity components at $\beta = \beta_{cm}$ leads to a width of the positron peak which is only $\sim 10\%$ greater than that due to emission directly out of the CM system. The difference in widths and the higher energy tail would be difficult to discern in the present data with any statistical significance.

The exact width and the shape of the high energy tail depend on the details of the velocity distribution of the positron source. In general, though, a significant contribution of low velocity components is enough to guarantee a narrow line similar in width and shape to that of CM emission. Moreover, high velocity components can be further suppressed if the lifetime of the undetected source is long enough ($\geq 10^{-8}$ s) so that only the slower moving sources remain within the ~ 1 cm sensitive region of the positron detection system.

5. POSITRON-ELECTRON COINCIDENCE MEASUREMENT

These considerations suggest the possibility of a new approach to explaining the observed positron peaks. The experimental verification of the two-body decay of a source produced in superheavy collisions has been the focus of our most recent efforts.

The signature of the two-body decay of a neutral particle $X^0 \rightarrow e^+e^-$ would be, for example, the production of monoenergetic electrons in coincidence with the peak positrons. To this end we have recently modified our experimental apparatus to measure electrons in coincidence with positrons in superheavy collision sys-

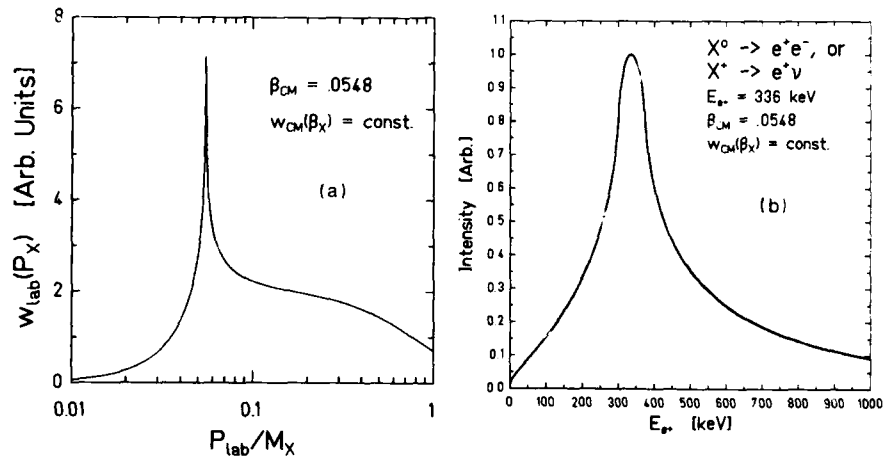


FIGURE 12

Part (a) shows the laboratory velocity distribution of a positron source emitted with a constant distribution in velocity-phase space in the CM of the Th+cm collision system at a projectile energy of 6.0 MeV/u. Part (b) shows the resulting laboratory line shape for monoenergetic positron emission from the source with $E_{e^+} = 340$ keV.

tems. To measure electrons with greater efficiency, two planar Si(Li) detectors have been mounted off-axis in the arm of the solenoid opposite the positron detector. This detector arrangement combines high detection efficiency for the interesting range of electron energies just above 250 keV with a very sharp fall-off in detection efficiency below this energy to suppress the high counting rate of low-energy delta electrons copiously produced in heavy-ion collisions. In addition, the solenoidal magnetic field has been rearranged to provide more balanced transport of positrons and electrons to the respective arms of the solenoid. Experiments are presently underway to look for monoenergetic electron emission in coincidence with the peak positrons produced in superheavy collision systems.

6. SUMMARY

The present experimental situation is as follows. Narrow, well-defined peaks are observed in the energy distribution of positrons emitted in several superheavy collision systems above, and in one probable case, well below the critical combined nuclear charge for spontaneous positron production. The peak energy of ~ 340 keV is essentially independent of Z_U . The peak width of ~ 70 keV both implies a source living $\geq 10^{-20}$ s and is consistent in size with the Doppler broadening of a source moving with a velocity similar to that of the CM of the collision systems. The peak appears to be produced in a narrow range of bombarding energies near the Coulomb barrier. Nuclear conversions in the separated nuclei are convincingly excluded as a possible source of the peaks. Spontaneous positron production similarly has difficulties providing a consistent picture of the peak production. Experiments are underway to investigate new suggestions that the peaks might be due to the two-body decay of an undetected source produced during heavy-ion collisions.

ACKNOWLEDGEMENT

The experiments described here were carried out by the EPOS collaboration at GSI Darmstadt and reflect the combined efforts of its many members: Hartmut Backe, Klaus Bethge, Helmut Bokemeyer, Tom Cowan, Helmut Folger, Jack S. Greenberg, Kiyo Sakaguchi, Dirk Schwalm, Kurt Stiebing, and Paul Vincent. I would particularly like to single out Tom Cowan, who did a large part of the work described in this report, and Jack S. Greenberg, who has continually provided the guidance and inspiration for these experiments.

This work was supported in part by the U.S. Department of Energy Contract No. DE-AC02-76ER03074 and by the Bundesministerium für Forschung und Technologie of the Federal Republic of Germany.

REFERENCES

- 1) T. Cowan, H. Backe, M. Begemann, K. Bethge, H. Bokemeyer, H. Folger, J.S. Greenberg, H. Grein, A. Gruppe, Y. Kido, M. Klüver, D. Schwalm, J. Schweppe, K.E. Stiebing, N. Trautmann, and P. Vincent, *Phys. Rev. Lett.* **54** (1985) 1761.
- 2) W. Pieper and W. Greiner, *Z. Physik* **218** (1969) 327.
B. Müller, J. Rafelski, and W. Greiner, *Z. Physik* **257** (1972) 62, 183.
S.S. Gershtein and Ya.B. Zel'dovich, *Zh.ETF* **57** (1969) 654 (*Sov. Phys. JETP* **30** (1969) 358); *Lett. Nuovo Cim.* **1** (1969) 835.
- 3) J. Schweppe, A. Gruppe, K. Bethge, H. Bokemeyer, T. Cowan, H. Folger, J.S. Greenberg, H. Grein, S. Ito, R. Schüle, D. Schwalm, K.E. Stiebing, N. Trautmann, P. Vincent, and M. Waldschmidt, *Phys. Rev. Lett.* **51** (1983) 2261.
- 4) M. Clemente, E. Berdermann, P. Kienle, H. Tsertos, W. Wagner, C. Kozhuharov, F. Bosch, and W. Koenig, *Phys. Lett.* **137B** (1984) 41.

- 5) J. Reinhardt, U. Müller, B. Müller, and W. Greiner, *Z. Physik A* 303 (1981) 173.
- 6) U. Müller, G. Soff, T. de Reus, J. Reinhardt, B. Müller, and W. Greiner, *Z. Physik A* 313 (1983) 263.
- 7) J. Rafelski, B. Müller, and W. Greiner, *Z. Physik A* 285 (1978) 49.
- 8) J.S. Greenberg and P. Vincent, High-Energy Atomic Physics - Experimental, in: *Treatise on Heavy-Ion Science*, ed. D.A. Bromley (Plenum Press, New York, 1985) pp. 139-421.
- 9) G. Soff, P. Schlüter, and W. Greiner, *Z. Physik A* 303 (1981) 189.
- 10) P. Schlüter and G. Soff, *ADNDT* 24 (1979) 509.
- 11) P. Schlüter, T. de Reus, J. Reinhardt, B. Müller, and G. Soff, *Z. Physik A* 314 (1983) 297.
- 12) R. Anholt and J.O. Rasmussen, *Phys. Rev. A* 9 (1974) 585.
- 13) W. Greiner, The Decay of the Vacuum in Supercritical Fields of Giant Nuclear Systems, in: *Proceedings of the International Conference on Nuclear Physics, Florence, 1983, Vol. II*, eds. P. Blasi and R.A. Ricci (Tipografia Compositori, Bologna, 1984) pp. 635-687.
G. Soff, Private communication.
- 14) B. Fricke and G. Soff, *ADNDT* 19 (1977) 83.
- 15) A. Schäfer, B. Müller, and W. Greiner, *Phys. Lett.* 149B (1984) 455.
- 16) U. Müller, Private communication (1983).

PRODUCTION OF MULTIPLY CHARGED IONS FROM MOLECULAR TARGETS IN
HEAVY ION IMPACT

H. TAWARA

Institute of Plasma Physics, Nagoya University, Nagoya 464, Japan
and

T. TONUMA, S.H. BE, H. SHIBATA, M. KASE, T. KAMBARA, H. KUMAGAI and I. KOHNO
Institute of Physical and Chemical Research, Wako-shi 351 Japan

In 1.05 MeV/amu Ar^{q+} ($q=4,12$) + N_2 collisions, multiply charged secondary ions, N^{6+} and possibly N^{7+} , have been observed. These multiply charged atomic ions are believed to originate from multiply charged molecular ions such as N_2^{12+} , N_2^{13+} or N_2^{14+} ions which in turn dissociate into two atomic ions with fairly symmetric charge. Slight shifts of peak positions in the charge/mass spectra toward high energy side for N^{i+} ions, compared with those for C^{i+} ions from CH_4 targets and Ar^{i+} ions from Ar targets, indicate that the product N^{i+} ions have the relatively large initial kinetic energies which are thought to be due to the Coulomb explosions of multiply charged molecular ions.

Since Cocke measured the cross sections for multiply charged secondary ions by heavy ion impact¹⁾, a number of the investigations on production mechanism of multiply charged recoil ions in energetic, heavy ion impact have been reported²⁾. We have also reported some results on the partial ionization cross sections of Ar^{i+} ion production in 1.05 MeV/amu Ne^{q+} ($q=2-10$) and Ar^{q+} ($q=4-14$) ion impact³⁾. These results strongly indicate, in addition to the direct multiple ionization due to strong Coulomb interaction, a significant contribution of electron capture processes to production of such multiply charged recoil ions when the innershell vacancies of the projectile ions are brought into collisions⁴⁾. Up to now, the rare gas atoms have exclusively been used as targets. No systematic investigations on molecular gas targets have been reported.

There should be some significant difference in production mechanisms of multiply charged secondary ions among atomic targets and molecular targets in charged particle impact such as electrons and heavy ions. In fact, though in electron impact the cross sections for production of singly charged ions (N_2^+) from nitrogen molecules are nearly the same as those of singly charged Ar^{+2} ions, both having similar ionization potentials of the outershell electrons, it is found that those of doubly charged N_2^{2+} ions observed are only of the order

of one percent of those of N_2^+ ions, whereas those of Ar^{2+} ions are of the order of 10 percent of those of Ar^+ ions⁵⁾. This is easily understood from the fact that a part of the doubly charged N_2^{2+} ions produced in collisions can not reach a detector because they break up with finite life times during flight to the detector⁶⁾. It is expected that the life times of such multiply charged molecular ions should become short significantly with increasing the multiplicity of ions and these molecular ions quickly dissociate into atomic ions after collisions. In reality, up to now, no trace of the triply charged ions, for example N_2^{3+} ions, has been found experimentally. Daly and Powell looked for the triply charged N_2^{3+} ions in electron impact with the sensitivity corresponding to as low as 10^{-24} cm² but found no evidence for them⁷⁾. There is no information on characteristics, such as the energy levels or life times, of multiply charged molecular ions except for those of doubly charged ions like N_2^{2+} and O_2^{2+} ⁸⁾.

Also only a limited number of informations on multiply charged atomic ions produced from molecular targets are available. For instance, the highest charge state ions directly observed in charged particle impact on N_2 targets are N^{3+} ions. Daly and Powell claimed to determine the cross sections for production of N^{3+} ions by electron impact on N_2 with a maximum value of 2.5×10^{-23} cm² at 240 eV. Edwards et al. observed N^{3+} ions in 1 MeV He^+ + N_2 collisions and determined their energy distribution which showed a maximum at 25 eV and was extended up to 50 eV⁹⁾. They did not discuss the detailed mechanism for production of N^{3+} ions.

Some dissociative ionization processes resulting in production of multiply charged atomic ions from molecular targets have been investigated by Mann et al.¹⁰⁾ who observed the broadening of the Auger electron spectra emitted from the metastable Li-like $(1s2s2p)^4P$ N^{4+} ions from N_2 target in 1.40 MeV/amu Ar^{12+} ion impact. This broadening in N_2 targets, much significant compared with that in NH_3 targets, has been explained by the Doppler broadening due to the kinetic energy of the emitting ions. This kinetic energy is provided by the Coulomb interaction between the two dissociating ions and is found to be in good agreement with the ab initio self-consistent field calculation by Hartung et al.¹¹⁾. These experiments and calculations have confirmed that two dissociating atomic ions have the same or nearly the same ionicities, indicating that the dissociation of multiply charged (diatomic) molecular ions results in nearly symmetric charge distribution.

Most recently Edwards et al. reported the cross sections for production of the fully stripped hydrogen molecular ions (H_2^{2+}) in ~ 1 MeV/amu H^+ and D^+ ion impact by observing two protons in coincidence with two detectors placed 180°

relative to each other¹²⁾ ($5 \times 10^{-19} \text{ cm}^2$ at 100 keV/amu H^+ ion impact, decreasing with increasing the impact energy). Their results indicate a fairly symmetric production of H^+ ions from H_2^{2+} ions, each ion emitted into the opposite direction, with respect to the projectile direction.

Bearing the above discussion in mind, we have investigated the charge distribution of ions produced in 1.05 MeV/amu Ar^{q+} ($q=4, 12$) ion impact on molecular targets. The experimental apparatus used has already been described in detail³⁾. Typical examples of the charge spectra of ions from N_2 molecular targets are shown in Fig.1(a). In these spectra are seen a number of peaks corresponding to multiply charged nitrogen atomic ions including a weak peak of N^{6+} ions in addition to a dominant peak of the singly charged molecular N_2^+ ions. The doubly charged molecular N_2^{2+} ion peak is overlapped on the singly charged atomic N^+ ion peak. From these spectra it is clearly seen that, with increasing the projectile charge q , the relative production of multiply charged atomic ions is strongly enhanced, as observed in atomic gas target experiments^{1,3)}.

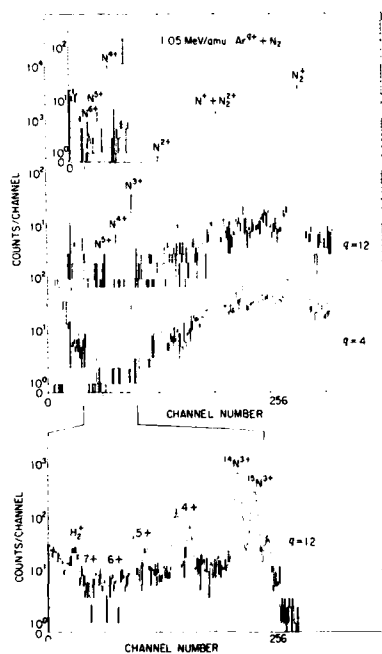


Fig. 1

(a) Charge spectra of nitrogen ions produced in 1.05 MeV/amu Ar^{q+} ($q=4, 12$) ion impact on N_2 targets. An arrow indicates a position corresponding to N_2^{3+} ions with $M/e=9.33$.
(b) Expanded charge spectrum of nitrogen ions produced in 1.05 MeV/amu Ar^{12+} ion impact on ($^{14}\text{N}_2 + ^{15}\text{N}_2$) mixed targets.

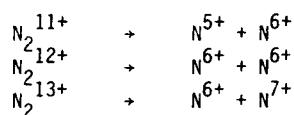
As mentioned already, in the present charge spectra is found no trace at $M/e=9.33$ corresponding to N_2^{3+} ions (shown by an arrow in Fig. 1(a)), an indication that N_2^{3+} ions could not reach the detector. More detailed charge/mass spectrum taken with a mixture of $^{15}N_2$ and $^{14}N_2$ gases is shown in Fig. 1(b). Clearly peaks corresponding to N^{6+} ions can be seen. Though less clear due to background of H_2^+ , a peak originated probably from the fully ionized atomic $^{15}N^{7+}$ ions is seen.

As will be discussed later on, the atomic ions produced from molecular targets might have relatively large kinetic energies due to the Coulomb explosion. Therefore, no complete collection of atomic ions by the present extraction system with low fields could be expected. Hence, no absolute cross sections for production of multiply charged atomic ions have been determined in the present work. It is found, however, that the production of multiply charged atomic ions, relative to N_2^+ ions, in heavy ion impact is enhanced, compared with that in electron impact observed by Daly and Powell⁷⁾. By extrapolation of our previous measurement of total ionization cross sections combined with the present spectra, production cross section for N^{6+} ions in 1.05 MeV/amu Ar^{12+} ion impact is estimated to be of the order of 10^{-18} cm^2 .

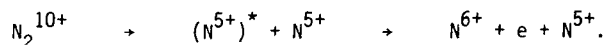
Mechanisms responsible for production of multiply charged secondary atomic ions from molecular targets are expected to be different from those in single atom targets. The question in molecular targets is whether these multiply charged atom ions are produced in ionization processes followed by the dissociation or they are produced in dissociation processes followed by the ionization. In this respect, the collision time and dissociation time seem to be the important factors. The collision time in the present system (projectile velocity = $1.4 \times 10^9 \text{ cm/s}$, molecular bond length = 1.0 Å) is estimated to be of the order of 10^{-17} s , whereas the dissociation time of molecular ions which should be strongly dependent upon their ionicity, is $10^{-14} \sim 10^{-15} \text{ s}$ though no direct measurements of the dissociation time of nitrogen molecular ions have been reported yet. These numbers indicate that the dissociation processes are slow, compared with the ionization processes. Therefore, the dissociation into atoms followed by the ionization is unlikely to be dominant in production of multiply charged atomic ions. Instead, these multiply charged atomic ions are believed to be produced through production of multiply charged molecular ions followed by the dissociation into two or more multiply charged atomic ions. As discussed above, with increasing the ionicity of ions, such multiply charged molecular ions are quickly dissociated into multiply charged atomic ions. As already confirmed by Mann et al.¹⁰⁾, these multiply charged molecular

ions are thought to be less likely to dissociate into ions with very asymmetric charge and, then, it is unlikely that a low charged molecular ion dissociates into a multiply charged atomic ion, the other ion being at lower charge state (see the following discussion).

From the above discussion, the multiply charged atomic ions, for example N^{6+} ions observed in Fig. 1, are probably produced via one of the following dissociations of multiply charged molecular ions:



or via the dissociation into multiply charged ions in highly excited state followed by the electron emission (i.e., autoionization):



One of other possible processes which should be taken into consideration is based upon the fact that, at high energy collisions, the (diatomic) molecules can often be assumed to consist of (two) independent atoms. Under this assumption, the projectiles collide with one of them, which is ionized to, for example N^{7+} , the other(s) being a spectator which has no interaction with the projectiles. If so, the product N^{7+} ions should have only small recoil energy. This is in contrast to the observation by Edwards et al.⁹⁾ and Mann et al.¹⁰⁾. Both groups reported that the product atomic ions from molecular targets have usually large kinetic energies which increase with increasing the product ion charge. Also, as the relaxation time (rearrangement time: $\sim 10^{-17}$ s) of electrons in the collision product, for example $(N \cdot N^{7+})$, is much shorter than the dissociation time, this collision product becomes rearranged to N_2^{7+} before the dissociation into neutral N atom and N^{7+} ions. Instead, the product N_2^{7+} would probably result in dissociation into $N^{3+} + N^{4+}$ ions, a similar process to that observed by Mann et al.¹⁰⁾. Therefore, this process is less likely to produce the atomic ions with higher charge.

Of course these proposed processes are a few examples for possible production mechanisms of such ions. If these multiply charged atomic ions are assumed to be produced through the dissociation (Coulomb explosion) of multiply charged molecular ions, the product atomic ions should have some kinetic energies due to the Coulomb force between the dissociated atomic ions. Based upon a simple Coulomb force between two equally charged ions at a bond length,

their kinetic energies after the Coulomb explosion can be calculated. If the bond length before explosion is assumed to be 1.0 Å, each N^{6+} ion, for example, produced from N_2 target through the above processes could have the kinetic energy of ~ 230 eV. In fact, in our preliminary measurements, the atomic nitrogen ions have been observed even with relatively large retarding field applied in the collision region, whereas no molecular ions such as N_2^+ could reach the detector with very weak retarding field, because their recoil energy is small¹⁾.

Similar charge spectra for 1.05 MeV/amu $Ar^{12+} + CH_4$ collisions are shown in Fig. 2. Carbon ions up to C^{5+} as well as hydro-carbon ions and hydrogen ions are clearly observed.

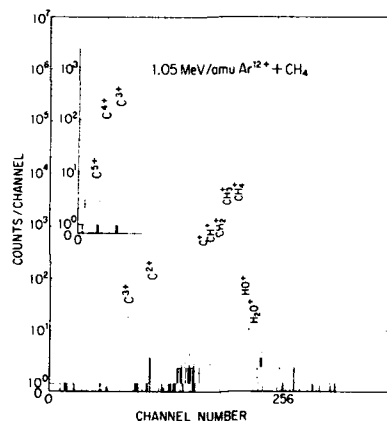


Fig. 2

Charge spectra of ions produced in 1.05 MeV/amu $Ar^{12+} + CH_4$ collisions

Through careful comparison of the charge/mass spectra, slight shifts toward high energy side in the peak position for $^{15}N^{5+}$ ions, compared with that for C^{4+} ions (both having $M/e = 3.00$), and for $^{15}N^{3+}$ ions, compared with that for Ar^{8+} ions ($M/e = 5.00$), are observed, whereas no apparent shift could be seen between C^{3+} and Ar^{10+} ions ($M/e = 4.00$). This fact indicates that the product N^{i+} ions should have the relatively large initial kinetic energies, compared with those for monatomic Ar^{i+} ions and for product C^{i+} ions. The C^{i+} ions originated from $(CH_4)^{P+}$ ions should have small kinetic energies because C^{i+} ions sit at a fairly symmetric center and, then, most of the kinetic energies due to the Coulomb explosion are partitioned to H^{i+} ions.

To clarify the mechanisms for production of highly charged secondary atomic

ions from molecular targets mentioned above, measurements of the kinetic energies of these atomic ions and of the angular correlation of the dissociating atomic ions are planned in our laboratory. Information such as the energy levels and their life times of multiply charged molecular ions such as N_2^{13+} or N_2^{14+} ions would be useful toward further understanding production mechanism of multiply charged atomic ions from molecular targets in ion impact.

The authors would like to thank Dr. T. Watanabe and Dr. Y. Awaya for their encouragement and support to the present work.

REFERENCES

- 1) C. L. Cocke, Phys. Rev. A 20 (1979) 749.
- 2) T. J. Gray, C. L. Cocke and E. Justiniano, Phys. Rev. A 22 (1980) 849; A. S. Schlachter, W. Groh, A. Muller, H. F. Beyer, R. Mann and R. E. Olson, Phys. Rev. A 26 (1982) 1373; S. Kelbch, J. Ullrich, R. Mann, P. Richard and H. Schmidt-Bocking, J. Phys. B 18 (1985) 323.
- 3) T. Tonuma, H. Shibata, S. H. Be, H. Kumagai, M. Kase, T. Kambara, I. Kohno and H. Tawara, to be published.
- 4) T. Tonuma, M. Kase, T. Kambara, H. Kumagai, T. Matsuo, J. Urakawa, H. Shibata, J. Takahashi, S. Ozkok, S. H. Be, I. Kohno and H. Tawara, J. Phys. B 17 (1984) L317.
- 5) H. Tawara, T. Kato and M. Ohnishi, IPPJ-AM-37 (Inst. Plasma Phys., Nagoya Univ., 1985).
- 6) T. D. Mark, J. Chem. Phys. 63 (1975) 3731.
- 7) N. R. Daly and R. E. Powell, Proc. Phys. Soc. 89 (1966) 273.
- 8) E. W. Thulstrup and A. Anderson, J. Phys. B 8 (1975) 965.
- 9) A. K. Edwards, R. M. Wood and M. F. Steuer, Phys. Rev. A 15 (1977) 48.
- 10) R. Mann, F. Folkmann, R. S. Peterson, Gy. Szabo and K. O. Groeneveld, J. Phys. B 11 (1978) 3045.
- 11) H. Hartung, B. Fricke, T. Morovic, W. D. Sepp and A. Rosen, Phys. Letters 69A (1978) 87.
- 12) A. K. Edwards, R. M. Wood and R. L. Ezell, Phys. Rev. A 31 (1985) 99.
- 13) S. H. Be, T. Tonuma, H. Kumagai, H. Shibata, M. Kase, T. Kambara, I. Kohno and H. Tawara, J. Phys. B (to be published, 1985).

CORRELATED ELECTRON CAPTURE AND INNER-SHELL EXCITATION MEASUREMENTS IN
ION-ATOM COLLISIONS

J. A. TANIS*, E. M. BERNSTEIN*, M. W. CLARK*, W. G. GRAHAM#, R. H.
MCFARLAND\$, T. J. MORGAN†, A. MULLER‡, M. P. STOCKLI¶, K. H. BERKNER†,
P. GOHIL†, A. S. SCHLACHTER†, J. W. STEARNS†, E. M. JOHNSON§,
K. W. JONES§, M. MERON§, J. NASON§

* Dept. of Physics, Western Michigan University, Kalamazoo, Michigan
49008 USA

Physics Dept., Univ. of Ulster, Coleraine, Northern Ireland

\$ Dept. of Physics, Univ. of Missouri, Rolla, Missouri USA

† Dept. of Physics, Wesleyan Univ., Middletown, Connecticut USA

‡ University of Giessen, Giessen, Federal Republic of Germany

¶ Dept. of Physics, Kansas State University, Manhattan, Kansas. USA

† Lawrence Berkeley Laboratory, Berkeley, California USA

§ Brookhaven National Laboratory, Upton, New York USA

In an ion-atom collision projectile excitation and charge transfer (electron capture) may occur together in a single encounter. If the excitation and capture are correlated then the process is called resonant transfer and excitation (RTE); if they are uncorrelated then the process is termed non-resonant transfer and excitation (NTE). Experimental work to date has shown the existence of RTE and provided strong evidence for NTE. Results presented here provide information on the relative magnitudes of RTE and NTE, the charge state dependence of RTE, the effect of the target momentum distribution on RTE, the magnitude of L-shell RTE compared to K-shell RTE, and the target Z dependences of RTE and NTE.

1. INTRODUCTION

In single collisions between ions and atoms vacancies may be created by one of three mechanisms: excitation, ionization, and charge transfer. Recent experimental studies (1,2,3) have shown that two of these processes, excitation and charge transfer, can occur together in a single encounter with a target atom resulting in the formation of an intermediate excited state. This capture and excitation can be either a correlated or an uncorrelated process.

If the combined process is correlated then the mechanism involved is an electron-electron interaction between a projectile electron and a (weakly bound) target electron similar to the inverse of an Auger transition. Resonant formation of intermediate states occurs for incident ion energies such that the target electron energy, in the rest frame of the ion, equals one of the Auger electron energies. This process of correlated electron capture and projectile excitation followed by photon emission is called resonant-transfer-and-excitation (RTE). RTE is analogous to dielectronic recombination (DR) (4), except that for DR the captured electron is initially free instead of bound.

If the electron capture and projectile excitation are uncorrelated then the mechanisms involved are electron-nucleus interactions between the projectile nucleus and a target electron resulting in electron capture, and between the target nucleus and a projectile electron resulting in excitation. Such a combination of excitation and capture events is a two-step process which does not depend resonantly on the incident projectile velocity and hence has been given the name non-resonant-transfer-and-excitation (NTE).

A formal theoretical treatment of simultaneous charge transfer and excitation in single collisions has recently been developed by Feagin, Briggs, and Reeves (5). In this work separate amplitudes for the correlated and uncorrelated contributions to the capture plus excitation process are formulated. The calculations indicate that NTE and RTE can occur with comparable probabilities. Furthermore, it is predicted that the NTE probability exhibits a maximum in its energy dependence, but at a lower projectile energy than the RTE maximum. Qualitatively, this NTE maximum may be viewed as the result of the product of an increasing excitation cross section and a decreasing single electron capture cross section.

Our recent experimental work with highly stripped sulfur, calcium, and vanadium ions colliding with helium (1,2,3) has shown the existence of RTE and provided evidence for NTE. The RTE results are in good agreement with calculations (6) using the method of Brandt (7) based on theoretical dielectronic recombination cross sections (8). In addition, RTE and NTE have been investigated by other groups for hydrogenlike fluorine ions (9) incident on helium, neon, and argon targets and lithiumlike silicon ions (10) colliding with these same targets.

New results presented here are for (1) $^{20}\text{Ca}^{12,16,17,18,19+} + \text{H}_2$ collisions, (2) $^{57}\text{La}^{40+} + \text{H}_2$ collisions, and (3) $^{16}\text{S}^{13+} + \text{Ne}$ collisions. These results provide information on the charge state dependence of RTE and the effect of the target momentum distribution on RTE, the magnitude of L-shell RTE compared to K-shell RTE, and the target Z dependence of RTE.

2. EXPERIMENTAL PROCEDURE

The experimental measurements were carried out at Lawrence Berkeley Laboratory using the SuperHILAC and at Brookhaven National Laboratory using the coupled MP tandem Van de Graaffs. The experimental technique consists of measuring x rays associated with electron capture events. Projectiles in a given charge state pass through a differentially pumped gas cell. After emerging from the cell, the beam is magnetically or electrostatically analyzed into its charge state components. Ions which undergo capture in the target gas are detected in a solid state particle detector while the x rays are detected with a Si(Li) detector mounted at 90° to the beam. Coincidences between projectile ions and x rays are measured with a time-to-amplitude converter. The non-charge-changed-component of the emerging beam is collected in a Faraday cup. Coincidence yields were measured as a function of gas pressure to check for linearity thereby ensuring that single collision conditions prevailed.

3. RESULTS AND DISCUSSION

A sample of previous experimental studies (1,2,3), taken from Ref. 3, is shown in Fig. 1 for 15-200 MeV $^{16}\text{S}^{13+} + \text{He}$ collisions. This figure shows the cross section for total projectile K x-ray emission, $\sigma_{\text{K}\alpha\beta}$, and the cross section for projectile K x rays coincident with single electron capture, $\sigma_{\text{K}\alpha\beta}^{g-1}$. It is seen that $\sigma_{\text{K}\alpha\beta}^{g-1}$ exhibits a maximum near 130 MeV due to RTE and a maximum near 30 MeV attributed to NTE. The dashed curve is the calculated (7) RTE cross section (multiplied by 0.85) and the solid curve is a calculated NTE cross section obtained from the product of the K-shell excitation cross section and the probability for capture to the L-shell (11). This product has been normalized to the data near 30 MeV.

Fig. 1b shows the calculations of Reeves and Feagin (12), for the $1s^2 2s \rightarrow 1s 2s^2 2p$ and $1s^2 2s \rightarrow 1s 2s 2p^2$ transitions only, which include both the uncorrelated (NTE) and correlated (RTE) contributions to charge transfer and excitation. These calculations, in which the lower energy maximum arises from

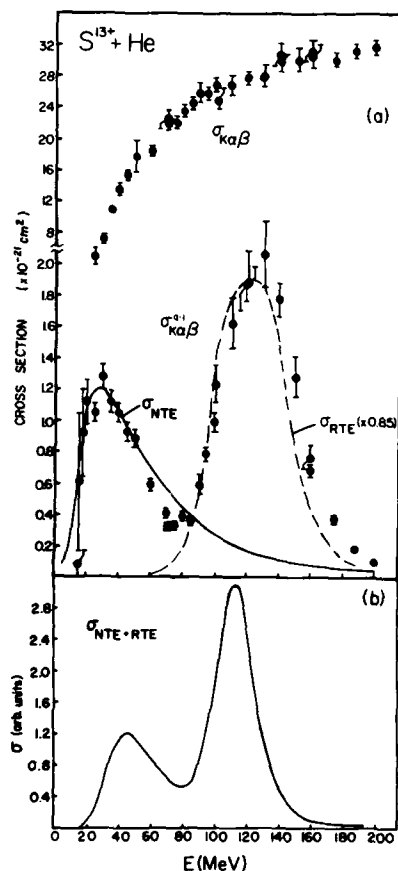


FIGURE 1

(a) Projectile K x-ray cross sections for $16S^{13+} + He$ collisions; $\sigma_{K\alpha\beta}$ is the cross section for the total sulfur K x ray production and $\sigma_{K\alpha\beta}^{q-1}$ is the cross section for sulfur K x rays coincident with single electron capture. The dashed curve is the calculated (Ref. 7) RTE cross section multiplied by 0.85. The solid curve is the calculated (Ref. 11) NTE cross section normalized to the data. (b) Theoretical cross section (Ref. 12) for charge transfer accompanying K-shell excitation in single collisions of $S^{13+} + He$.

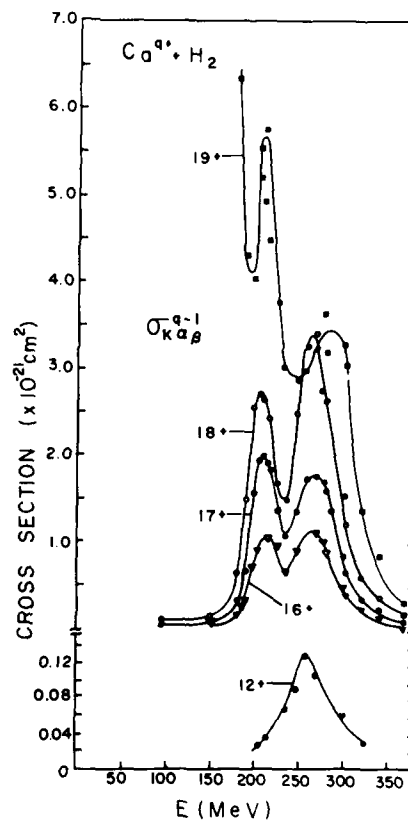


FIGURE 2

Cross sections for projectile K x rays coincident with single electron capture, $\sigma_{K\alpha\beta}^{q-1}$, for $20Ca^{q+} + H_2$ with $q=12, 16, 17, 18$, and 19 . The solid curves are drawn to guide the eye.

the uncorrelated amplitude (NTE) and the higher energy maximum arises from the correlated amplitude (RTE), provide substantial qualitative agreement with the measured energy dependence of $\sigma_{K\alpha\beta}^{q-1}$. The narrower RTE width in Fig. 1b compared to the corresponding $\sigma_{K\alpha\beta}^{q-1}$ width in Fig. 1a is due to the fact that only the two transitions mentioned above have been included in the calculations.

In more recent work at LBL, RTE was investigated for 100-370 MeV $^{20}\text{Ca}^{12,16,17,18,19+} + \text{H}_2$ collisions. The results, shown in Fig. 2, are consistent with previous measurements (2) for $^{20}\text{Ca}^{9+}$ and $^{23}\text{V}^{9+} + \text{He}$ in which two maxima were also observed in the energy dependence of $\sigma_{K\alpha\beta}^{q-1}$. These maxima correspond to groups of intermediate resonance states in the RTE process for which both the excited and the captured electrons occupy energy levels with quantum numbers $n=2,2$ and $n=2, \geq 3$ (see Fig. 1b of Ref. 2). The present results for Ca^{9+} are the first observation of RTE for a hydrogenlike ion. The large rise in $\sigma_{K\alpha\beta}^{q-1}$ as the beam energy is decreased below 200 MeV is due to electron capture, without accompanying excitation, to an excited state ($n \geq 2$) followed by deexcitation via photon emission. For Ca^{12+} the transitions giving rise to the first maximum, i.e. those involving quantum numbers $n=2,2$, apparently occur with a small probability compared to the transitions with $n=2, \geq 3$ and so only the second maximum is observed. Calculations (13) which have just become available indicate that these results for Ca^{12+} are consistent with theory.

The measurements for $\text{Ca}^{16,17,18+} + \text{H}_2$ provide a direct comparison with earlier results (2) for these same ions incident on He. Due to the smaller electron momentum distribution for H_2 compared to He, it is expected that the widths of the RTE maxima will be less for H_2 . The results indicate that this is the case as shown in Fig. 3 for Ca^{17+} . It is noted that the discrepancy between theory and experiment for energies ≥ 260 MeV is similar for H_2 and He targets. This same discrepancy has been observed in RTE measurements for $^{16}\text{S}^{13+} + \text{He}$ collisions (3). The origin of the discrepancy is not understood at present.

We have also conducted a preliminary investigation of RTE involving excitation of the projectile L-shell for 455-710 MeV $^{57}\text{La}^{40+}$ ions colliding with H_2 as shown in Fig. 4. Although there are no theoretical calculations at present with which to compare these results, the position of the observed maximum in $\sigma_{L\alpha\beta}^{q-1}$ is consistent with the calculated energies of three of the most probable Auger transitions as shown. Evidence for L-shell RTE has also been obtained in the observation of anomalous variations in the L x-ray production cross sections as a function of charge state for $\text{Sm}^{9+} + \text{Xe}$ collisions (14). In a future study we plan to examine the L-shell RTE resonance region more closely to look for structure (as observed for the K-shell) in $\sigma_{L\alpha\beta}^{q-1}$ and to determine the relative participation of the L subshells (i.e. L_1 , L_2 , or L_3) in the RTE process.

The target Z dependence of RTE has not been established. The only published result in which the measurements span the resonance region for a target other than H_2 or He is that for $\text{S}^{13+} + \text{Ar}$ reported in Ref. 1. In our most recent BNL work we have measured projectile K x rays coincident with single capture for 40-160 MeV $^{16}\text{S}^{13+} + \text{Ne}$ collisions as shown in Fig. 5. Since the RTE maximum occurs near 120 MeV for sulfur ions, it is seen that there is no measureable evidence for RTE in these data while there may be a considerable contribution due to NTE as evidenced by the apparent peak near 60 MeV. These results are similar to results previously obtained for $\text{Ar}^{13+} + \text{Ne}$ collisions (15). At present we have no explanation for these results with neon targets.

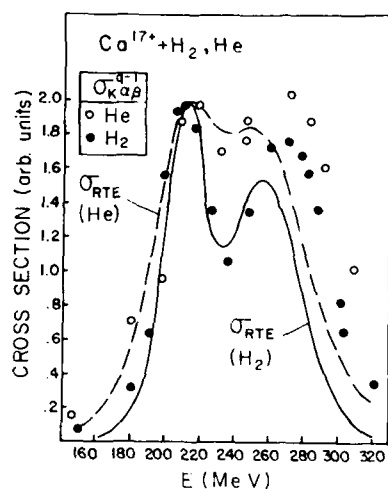


FIGURE 3
Comparison between the measured $\sigma_{K\alpha\beta}^{q-1}$ for Ca^{17+} ions on H_2 and He. Also shown are the predicted RTE cross sections (Ref. 6) for these collision systems. The lower energy maximum has been normalized to the same value in each case.

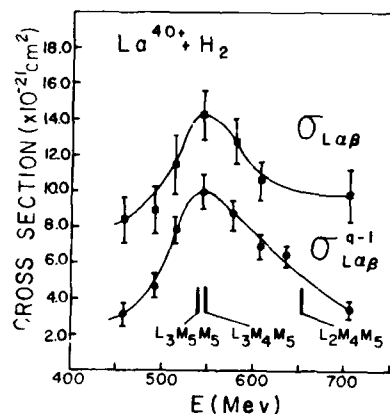


FIGURE 4
L x-ray cross sections for $^{57}\text{La}^{40+} + \text{H}_2$ collisions; $\sigma_{L\alpha\beta}$ is the cross section for total projectile L x-ray emission and $\sigma_{L\alpha\beta}^{q-1}$ is the cross section for projectile L x rays coincident with single electron capture. The solid curves are drawn to guide the eye. The vertical lines denoted by $L_3M_5M_5$, etc. give the energy positions of selected Auger transitions.

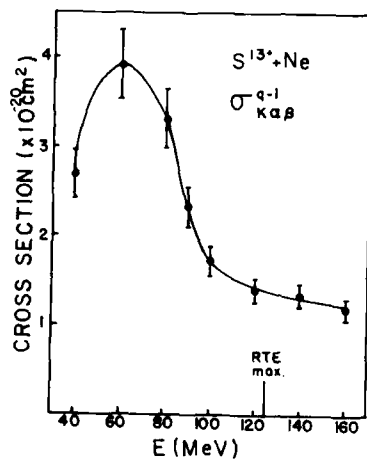


FIGURE 5
Cross sections for projectile K x rays coincident with single electron capture, $\sigma_{K\alpha\beta}^{q-1}$, for $^{13}\text{S}^{13+} + \text{Ne}$ collisions. The solid curve is drawn to guide the eye.

4. CONCLUSIONS

New measurements of projectile x-ray emission coincident with single electron capture have provided significant new information on (a) the charge state dependence of RTE, (b) the effect of the target momentum distribution on RTE, (c) the magnitude and width of L-shell RTE compared to K-shell RTE, and (d) the target Z dependence of RTE and NTE (neon target compared to H₂ and He). Preliminary results indicate that the charge state dependence of RTE and the effect of the target momentum distribution on RTE are consistent with theory. For L-shell RTE, no calculations yet exist to compare with the measurements. The neon target results are anomalous in that the expected RTE maximum is not observed; no NTE calculations for neon are currently available.

ACKNOWLEDGEMENTS

This work was supported in part by the U. S. Department of Energy, Division of Chemical Sciences. W.G.G. was supported in part by the Science and Engineering Research Council, Great Britain. R.H.M. and T.J.M. were supported in part by the U.S. DOE, Office of Magnetic Fusion Energy. The authors wish to thank W.E. Meyerhof for the use of his Si(Li) detector and Y. Hahn for providing calculations prior to publication.

REFERENCES

- 1) J.A. Tanis, E.M. Bernstein, W.G. Graham, M. Clark, S.M. Shafroth, B.M. Johnson, K.W. Jones and M. Meron, *Phys. Rev. Lett.* **49** (1982) 1325.
- 2) J.A. Tanis, E.M. Bernstein, W.G. Graham, M.P. Stockli, M. Clark, R.H. McFarland, T.J. Morgan, K.H. Berkner, A.S. Schlachter and J.W. Stearns, *Phys. Rev. Lett.* **53** (1984) 2551.
- 3) J.A. Tanis, E.M. Bernstein, M.W. Clark, W.G. Graham, R.H. McFarland, T.J. Morgan, B.M. Johnson, K.W. Jones and M. Meron, *Phys. Rev.* **A31** (1985) 4040.
- 4) J.B.A. Mitchell, et al., *Phys. Rev. Lett.* **50** (1983) 335; D.S. Belic et al., *Phys. Rev. Lett.* **50** (1983) 339; P.F. Dittner et al., *Phys. Rev. Lett.* **51** (1983) 31.
- 5) J.M. Feagin, J.S. Briggs and T.M. Reeves, *J. Phys.* **B17** (1984) 1057.
- 6) C.S. Oglesby, E.M. Bernstein, J.A. Tanis, *Bull. Am. Phys. Soc.* **29** (1984) 743.
- 7) D. Brandt, *Phys. Rev.* **A27** (1983) 1314.
- 8) D.J. McLaughlin and Y. Hahn, *Phys. Lett.* **88A** (1982) 394; I. Nasser and Y. Hahn, *JQSRT* **29** (1983) 1.
- 9) P.L. Pepmiller, P. Richard, J. Newcomb, J. Hall and T.R. Dillingham, *Phys. Rev.* **A31** (1985) 734.
- 10) M. Clark, D. Brandt, J.K. Swenson and S.M. Shafroth, *Phys. Rev. Lett.* **54** (1985) 544.
- 11) T.L. McAbee, *Nucl. Instr. Meth.* **214** (1983) 89; D. Brandt, *Nucl. Instr. Meth.* **214** (1983) 93.
- 12) T.M. Reeves and J.M. Feagin, private communication.
- 13) Y. Hahn, private communication.
- 14) W.A. Schonfeldt, P.H. Mokler, D.H.H. Hoffmann, A. Warczak, GSI Annual Report, (1984) unpublished.
- 15) J.A. Tanis, E.M. Bernstein, C.S. Oglesby, W.G. Graham, M. Clark, R.H. McFarland, T.J. Morgan, M.P. Stockli, K.H. Berkner, A.S. Schlachter, J.W. Stearns, B.M. Johnson, K.W. Jones and M. Meron, New evidence for resonant transfer and excitation for ¹⁶S, ²⁰Ca and ²³V ions colliding with helium, in: *X-Ray and Inner-Shell Processes in Atoms, Molecules and Solids*, X84 Conference Proceedings, eds. A. Meisel and J. Finster, (Karl-Marx-Universität, Leipzig, 1984), pp. 125-134.

THEORETICAL TREATMENT OF ELECTRON CAPTURE AND EXCITATION IN TWO-ELECTRON
SYSTEM ION-ATOM, ATOM-ATOM COLLISIONS AT LOW TO INTERMEDIATE ENERGY

M. KIMURA

Joint Institute for Laboratory Astrophysics, University of Colorado and
National Bureau of Standards, Boulder, Colorado 80309 USA

A review of various theoretical treatments which have been used to study electron-capture and excitation processes in two-electron-system ion-atom, atom-atom collisions at low to intermediate energy is presented. Advantages as well as limitations associated with these theoretical models in application to practical many-electron ion-atom, atom-atom collisions are specifically pointed out. Although a rigorous theoretical study of many-electron systems has just begun so that reports of theoretical calculations are scarce to date in comparison to flourishing experimental activities, some theoretical results are of great interest and provide important information for understanding collision dynamics of the system which contains many electrons. Selected examples are given for electron capture in a multiply charged ion-He collision, ion-pair formation in an atom-atom collision and alignment and orientation in a $\text{Li}^+ + \text{He}$ collision.

1. INTRODUCTION

Much theoretical progress toward understanding the dynamics of inelastic processes in ion-atom or atom-atom collisions in various energy regimes has been achieved in the last decade. This can be clearly realized by noting the sequential series of invited progress talks in the past several ICPEAC meetings (1-3). Although the electron capture process, for instance, has been considered to be qualitatively well understood, precise theoretical prediction of the electron capture cross section is still an extremely difficult task for theorists. Moreover, due in part to recent technological advances, new details from already known findings, as well as new phenomena in ion-atom collisions, have been observed experimentally. Accurate theoretical models which can be compared with experimental findings have only recently become possible in conjunction with the development of fast computers. Some of these new experimental findings, however, are as yet unexplained, even qualitatively, and they provide new challenges for theorists.

The theoretical investigation of electron-capture in one-electron and pseudo one-electron systems in the keV energy region has been one of the most prominent subjects in atomic physics since late 1970. Among models used, the finite basis function expansion method is considered to be the main stream for this study. The molecular orbital (MO) (4-8), the atomic orbital (AO) (including pseudo states) (9-11), the Sturmian (12), the Hylleraas (13) and combinations (14,15) of these functions are among those most commonly employed. However, other approaches including direct numerical integration of a time-dependent Schrödinger equation (TDSF) (16) might not only open up the possibility of a new subfield in collision theory, but also provide different perspectives on this field.

Excellent agreement between different approaches in various one-electron systems is so frequently seen in the literature it may be regarded as routine and without surprise now (10). The long-standing problem of the electron

translation factor (ETF) in the MO expansion method is now well recognized both formally and practically. Although the question of what form of the ETF should be used is still open, it has become standard technique to include the ETF effect somehow in the MO close-coupling calculation. Hence, the ETF-corrected MO method satisfies Galilean invariance and therefore, observable physical quantities can be extracted uniquely from calculations. Fairly accurate molecular wave functions and their eigenvalues for collision systems are now easily accessible with support from molecular structure studies by quantum chemists. These MO studies clearly confirm the concept of close and distant collisions in ion-atom collisions. This has led not only to a revival of the AO expansion method (3), but also to a more aggressive role for the AO expansion method itself in ion-atom collision theory. It is widely believed that to account properly for the electron distribution when a projectile and target approach within the molecular regime, inclusion of a third-center orbital in addition to the conventional two-center expansion is indispensable to represent the collision dynamics correctly (particularly in close collisions). This "three-center" AO expansion method is now considered to be an alternative to the MO expansion method.

Although certain aspects observed in various types of ion-atom collisions are common to all, apparently there are fundamental differences between one- (or pseudo one)-electron systems and two- (or pseudo two) or many-electron systems, which can be traced back to electron correlation effects in many-electron systems. Because of the presence of this additional electron, theoretical models, though formally the same, should be modified to interpret these effects in applications to many-electron systems, and this requires enormous effort for theorists. Stimulated by extremely active and precise measurements in a multiply-charged ion-He collision and an alignment and orientation study of the electron cloud in pseudo-two-electron ion-atom collisions, theorists have applied various models to interpret observed phenomena. Unfortunately, however, rigorous theoretical attempts for many-electron systems are still few, and agreement among existing theories, and between theory and experiment, is far from satisfactory either qualitatively or quantitatively. This is in contrast to the impressive harmony among theories and measurements on one-electron systems. More effort is required for theorists to develop more concrete models for understanding the collision dynamics in many-electron systems. Keeping the current status in mind, it is worthwhile to take a critical look at various theoretical approaches.

In the following, theories that have been used to investigate ion-atom collisions in the 0.1 to 25 keV/amu energy region are briefly reviewed with special emphasis on their applicability. Some representative results are given for two-electron systems. Atomic units are used throughout.

2. THEORETICAL TREATMENT

Unfortunately, in the 0.1-25 keV/amu energy range in which we are interested, cross sections for the various inelastic channels including electron-capture, excitation and ionization in ion-atom collisions are usually known to have the same order of magnitude because they couple to each other rather strongly (see Fig. 1). This suggests that the electrons are strongly perturbed in the collision and nonperturbative methods, such as close coupling, are certainly preferable for the study of ion-atom collisions. In Fig. 2 several approaches commonly used for low to intermediate energy collisions are listed.

The basis function expansion method is commonly used in the form of coupled equations and is always truncated after a limited number of bound states have been included. Also without exception, explicit inclusion of continuum states is always avoided in the expansion, although some attempts have been made to build in the "flavor" of the ionization channel into the expansion through the

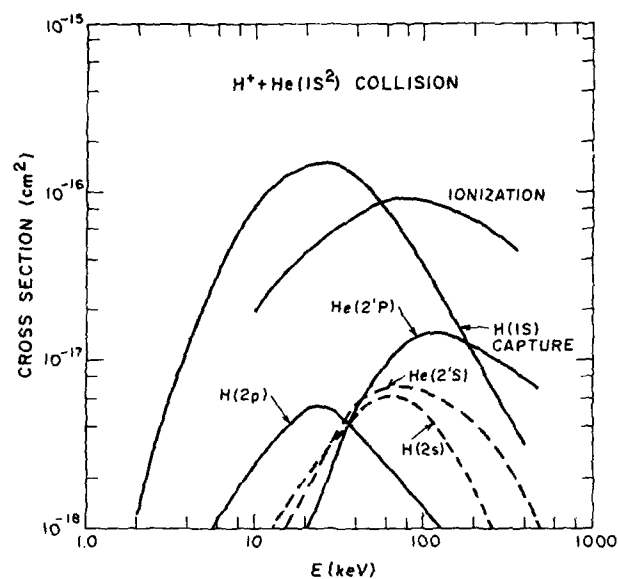


FIGURE 1
Cross sections for various inelastic events in $\text{H}^+ + \text{He}$ collisions.

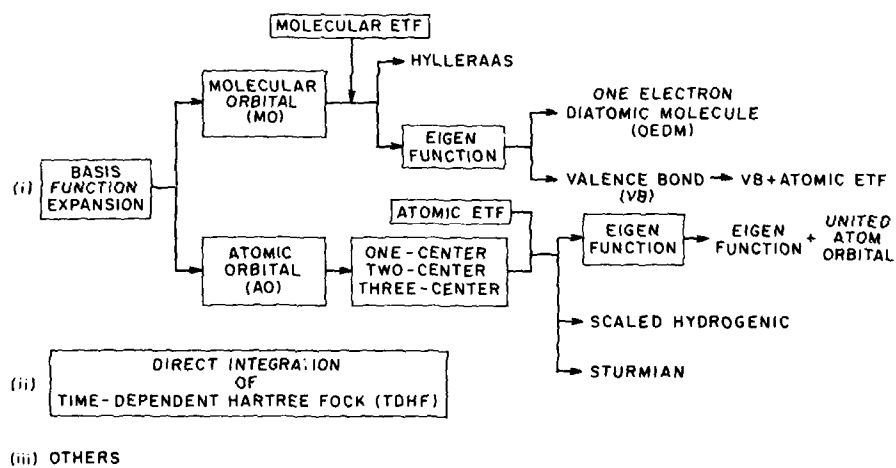


FIGURE 2
Theoretical methods frequently used to investigate ion-atom, atom-atom collisions at low to intermediate energies.

pseudostate approach. Sometimes, however, the physical meaning of the pseudostates is not clear at all, and hence, care is needed to apply it.

In the following, the basis function expansion method is mainly reviewed, and some comments on other methods are made.

3. BASIS FUNCTION EXPANSION METHOD

In the 0.1 to 25 keV/amu energy range, the energy transfer is usually much smaller than the collision energy so that the semiclassical formulation of inelastic processes in ion-atom collisions is considered to be quite accurate and convenient to solve. In this approximation, the electron moves in the time-dependent field created by the motion of the projectile relative to the target. This heavy particle motion is treated semiclassically, while the electron motion is solved quantum mechanically. Defining the collective electron coordinates as $\vec{r} = (r_1 \dots r_n)$ measured from the origin of some inertial frame, the wave function for the electronic system is the solution of the time-dependent Schrödinger equation

$$H_{el} \psi(\vec{r}, t) = \left[\sum_{i=1}^N \left(-\frac{1}{2} \nabla_{r_i}^2 - \frac{Z_p}{r_{p_i}} - \frac{Z_T}{r_{T_i}} \right) + \sum_{i>j}^N \frac{1}{|\vec{r}_i - \vec{r}_j|} \right] \psi(\vec{r}, t) = i \frac{\partial}{\partial t} \psi(\vec{r}, t) \quad (1)$$

where the first term in the bracket on the LHS is the kinetic energy of the electron, Z_p is the charge of the projectile, Z_T is the charge of the target, r_{p_i} , r_{T_i} , r_i are the distances of the electron measured from the projectile, target, and chosen origin, respectively, and the last term in the bracket denotes the electron-electron interaction.

If the wave function $\psi(\vec{r}, t)$ is expanded in terms of some basis functions $U_i(\vec{r}, t)$

$$\psi(\vec{r}, t) = \sum_i a_i(t) U_i(\vec{r}, t) \quad (2)$$

then, following standard procedures, Eq. (1) can be reduced to a set of linear coupled equations,

$$i \dot{\underline{S}} \underline{A} = \underline{M} \underline{A} \quad (3)$$

where the column matrix \underline{A} is formed from the time-dependent expansion coefficients a_i , \underline{S} is the overlap matrix with elements $S_{ij} = \langle U_i | U_j \rangle$, and \underline{M} is the coupling matrix with elements $M_{ij} = \langle U_i | H_{el} - i \frac{\partial}{\partial t} | U_j \rangle$. Equation (3) is usually solved numerically subject to appropriate conditions, i.e., $a_k(-\infty) = \delta_{ik}$.

The probability for finding the electronic system in the j th state after the collision can be written as a function of the collision energy and impact parameter b ,

$$P_j(E, b) = |a_j(+\infty)|^2. \quad (4)$$

The cross section for the j th electronic state is obtained by integration over the impact parameter, b

$$\sigma_j(E) = 2\pi \int db b P_j(E, b). \quad (5)$$

Up to this point, we have discussed the semiclassical collision theory without specifying the basis set, $\{U(\vec{r}, t)\}$. An adequate choice of the basis set is extremely important to describe the collision system properly. As for determining the criteria for the choice of the basis set, collision parameters such as the charge ratio Z_p/Z_T or the ratio of relative velocity to the velocity of the orbital electron, V/V_e , are often employed as indicators. The magnitudes of these parameters suggest whether the molecular orbital or atomic orbital

representation should be used. However, as we shall discuss later, recent progress on the basis function expansion method relaxes the intrinsic limitation imposed on individual basis set and broadens the region of validity of each approach in terms of the collision energies being overlapped. This was not apparently true in basis function expansion studies a decade ago. This remarkable new feature in basis function expansion methods is evidence of recent progress.

3.1. Molecular orbital (MO) basis

Customarily, the MO expansion method is considered to be appropriate when the parameter $V/V_e < 1$, where the colliding partners are thought to form a quasi-molecule during the collision. Then, the basis set $\{\phi_i(\vec{r}, t)\}$ is constructed from the adiabatic molecular (the Born-Oppenheimer) wave function $\phi_i^{MO}(\vec{r}, R)$ defined by

$$H_{el} \phi_i^{MO}(\vec{r}, R) = E_i(R) \phi_i^{MO}(\vec{r}, R) \quad (6)$$

Expansion of the scattering wave function using the molecular orbitals yields

$$\psi(\vec{r}, t) = \sum_i a_i \phi_i^{MO}(\vec{r}, R) F_i(\vec{r}, R) \quad (7)$$

where F_i represents the molecular electron translation factor (ETF) which has the form

$$F_i(\vec{r}, R) = \exp[i \sum_k \{(1/2) f_i(\vec{r}_k, R) \vec{V} \cdot \vec{r}_k - (1/8) \int^t v^2 dt'\}] \quad (8)$$

In Eq. (8), \vec{V} is the relative velocity of the heavy particles and f_i is, in general, a state-dependent switching function employed to represent a local propagation velocity, $f_i \vec{V}$, of the electron in the quasimolecule formed during the collision. Various forms of the switching function have been proposed (17), but each form has disadvantages as well as advantages; arguments for the proper choice of the switching function have not been settled yet. It is clear, however, that neglect of the ETF in the scattering wave function [Eq. (7)], this method, which has been termed the perturbed-stationary-state (PSS) method, results in a wave function that does not satisfy Galilean invariance and hence, introduces several fatal problems into the coupling.

In the MO representation, the electronic Hamiltonian is diagonalized as in Eq. (6), hence the perturbation which causes the transition in the system arises from the nuclear motion of the heavy particles, i.e. nonadiabatic coupling. For slow collisions, a reasonable approximation is obtained by expanding the ETF in powers of \vec{V} and retaining the first few order terms of V . This approximation simplifies the form of the ETF corrected nonadiabatic coupling significantly.

This ETF corrected MO expansion method has been applied successfully to the investigation of excitation and electron capture processes in one-electron ion-atom, atom-atom collisions (5-7, 18-20). In particular, it appears that extensive studies on the multiply charged ion and H-atom collisions explicitly disclose most of the fundamental dynamics in these systems. However, few applications of the ETF corrected MO method to many-electron systems have been reported (21-24). Two main problems arise from many-electron systems:

1. It is quite difficult to obtain accurate wave functions and eigenvalues for many-electron systems.
2. The molecular ETF for these systems has not been sufficiently well investigated so that we do not have enough practical experience with them.

For problem 1, only recently, several methods including the *ab initio* and semiempirical, have become available to solve the nonrelativistic stationary electronic Schrödinger equation for molecular systems, owing to impressive recent progress in theoretical quantum chemistry. Among those, probably the

pseudopotential or model potential method is one of the most popular for obtaining the molecular wave function as well as its eigenvalue. This approach skillfully adopts the concept of difference between valence-electron and core-electron orbitals which leads to significant simplicity in the construction of molecular wave functions. By replacing all interactions which involve core electrons by pseudopotentials or model potentials and including explicitly only valence electrons in the electronic Hamiltonian, many-electron problems can be reduced to the simpler one- or two-electron problem. Commonly, the molecular wave function is constructed in the same manner as in the valence-bond (VB) method. Although this approach to obtaining approximate electronic states apparently fails when the core electron actively takes a role in the collision dynamics, its simplicity and high accuracy in a practical application provide a good remedy for some of the weaknesses of this method.

The one-electron in diatomic molecule (OEDM) method belongs to a category of MO method (25). The OEDM method employs the molecular orbital from the one-electron two-nuclei system (26) as a basis function to construct the molecular wave function. Wave functions and eigenvalues of a one-electron two-nuclei system can be obtained exactly by solving the nonrelativistic electronic Hamiltonian with the utilization of prolate spheroidal coordinates. Thus evidently, this method involves a more lengthy calculation when it is extended to the many-electron system as in the case of the usual *ab initio* approach to molecular structure calculations. Some results from using the OEDM method with the He atom have been reported recently. However, the study in Ref. 25 neglects the ETF completely, and its result does not satisfy Galilean invariance.

Another basis which has also been used in the MO category is the Hylleraas function (13). This function has been employed in large scale close coupling calculations for the study of one-electron ion-atom collisions, but no report has been published for many-electron systems yet.

Although several different approaches to determining the molecular-ETF have been proposed for problem 2, few results of practical tests of these forms within the MO approach have been reported for the study of many-electron ion-atom collision to date. Therefore, assessments of usefulness or effectiveness of each proposed molecular-ETF are still premature and extensive work on this subject is really needed. Instead, we would like to point out that some pioneering work on these systems is now under way in several groups (27,28). Due to inclusion of the ETF, i.e. the velocity-dependent term, it has been verified that the ETF corrected MO method is legitimate for use up to a fairly high energy region, say ~50 keV/amu, depending on the character of the system. This new feature has not been seen in the PSS theory in which the energy range of validity of the theory is quite limited, although the PSS theory is known now, in principle, to be wrong.

3.2 Atomic orbital (AO) basis

Contrary to the MO expansion method, the AO expansion method is considered an appropriate representation when $V/V_e \gtrsim 1$. Since the collision velocity is so fast compared to the orbital velocity of the bound electron, the colliding partners retain atomic character (i.e. diabatic) throughout the collision event. In this representation, the basis $U_i(\vec{r}, t)$ in Eq. (2) is well described by traveling atomic orbital and the scattering wave function is expanded in terms of these traveling atomic orbitals with

$$\psi(\vec{r}, t) = \sum_i b_i \phi_i^{AO}(\vec{r}_{C_i}) \exp(i\vec{V}_{C_i} \cdot \vec{r}_i - (1/8) \int^t v_C^2(t') dt') \quad (9)$$

The last term of Eq. (9) represents the atomic ETF (29) (or plane-wave ETF) where the electronic coordinate r_c is measured from nucleus C (C=P or T), which can be determined uniquely and without ambiguity, in contrast to the MO case. The ϕ_i^{AO} satisfies the atomic Hamiltonian, $H_C = [-(1/2) \nabla_{r_c}^2 + (Z_C/r_c)]$

$$H_C \phi_i^{AO}(\vec{r}_C) = \epsilon_i^{AO} \phi_i^{AO}(\vec{r}_C) \quad (10)$$

where ϵ_i^{AO} is the atomic eigenvalue.

The ϕ_i^{AO} does not diagonalize the full electronic Hamiltonian, and the interaction term is a purely potential interaction. In addition, a rotational coupling similar to the MO case plays a role in the rotating coordinate system.

The original formulation of the AO expansion is due to Bates (30) using a two-center expansion method in the late 50's. Since then, various expansion techniques, namely one-center and three-center in addition to the two-center expansion, have been developed and applied to study the collision dynamics, mostly for the one-electron system. Despite the fact that in some cases, the two-center AO expansion approximation explains the experimental findings remarkably well both qualitatively and quantitatively, it unfortunately fails miserably in others. The reason is that for some collision systems, the dominant contribution to, for instance, electron capture probability occurs at large impact parameter, larger than the radius of the electron orbital, i.e. distant collisions, while for others, it comes from small impact parameters, smaller than the radius of the electron orbital, i.e. close collisions. For a distant collision, distortion of the initial and final electronic states is well described by the two-center AO. Actually, this is the philosophy underlying the linear combination of the atomic-orbital-molecular-orbital (LCAO-MO) method to express approximate molecular wave functions frequently used in quantum chemistry. However, this is not the case for a close collision. A conventional two-center AO can not represent the electron distribution correctly when the particle approaches within the molecular region. To remedy these deficiencies in the AO expansion method, various ideas have been introduced and have converged mainly to a pseudostate approximation, in which the pseudostate that has the largest overlap with the united atom orbital is included in the expansion. However, trials of the pseudostate approximation have not been entirely successful in terms of convergence of the calculated cross section with respect to the size of the basis set used and comparison with experiment.

Along this line, but of course with a different philosophy, another pseudostate approximation has been proposed (the so-called AO+) (31), which is augmented by some of the system's united atom orbitals in addition to the conventional two-center AO's and applied to various one-electron systems with much success. The pseudopotential technique is also commonly used to reduce the problem to a quasi-one-electron system. In fact, the only difference between the ETF-corrected MO method and the AO+ method is in the manner of representing the ETF's attached to each expansion. In this view, excellent agreement seen in the ETF-corrected MO result and the AO+ result for various one-electron systems is not entirely surprising, but rather expected. In this connection, the three-center AO expansion method (11,32) can be regarded as a general extension of the AO+ method. The third center atomic state, which is normally placed on the center of nuclear charge of the system, is augmented to the conventional two-center AO expansion. The third center atomic state is taken to be a bound atomic state of a fictitious atom having nuclear charge which is the sum of the charges of the projectile and target's nucleus. The atomic-ETF is normally attached to the third center atomic state. Although a single application of the three-center AO expansion method to study the symmetric proton and hydrogen system revealed an interesting feature of this approximation as well as good agreement with the MO and AO+ results, this method is extremely time-consuming even for the simplest system, such as the proton-hydrogen collision system. At any rate, this new pseudostates method, like the AO+ and three-center AO expansion methods has proved that its validity is far wider in collision energy range than was usually thought for the AO expansion method, which completely overlaps with that of the ETF-corrected MO method in the lower energy region as we can speculate from the discussion

above. Thus, this pseudostate method is considered to have established its position as a subfield of collision theory.

Attempts to extend the successful pseudostate method beyond one-electron systems, have immediately run into practical difficulties. As the number of electrons increases from one to two in a collision system, the number of configurations needed to describe the electronic states included also increases dramatically. Moreover, the third-center state (united-atom orbital in the AU^+ or the "third-center" orbital in the three-center expansion) has to be included to represent the electron relaxation correctly. This inclusion of the additional state at the third-center makes the numerical calculation almost impossible at present. However, there has been one attempt using the AU^+ -type pseudostate method, which includes a small number of united atom orbitals in the expansion, for the multiply charged ion-He collisions (33).

3.3 Others

As a completely new theoretical probe, the time-dependent Hartree-Fock (TDHF) (34,35) procedure has been developed to study collision processes which involve many-electron systems. The TDHF is the natural successor to the direct numerical solution of the time-dependent Schrödinger equation, which has been used to investigate one-electron systems (36,37). Although the TDHF approach for many-electron systems has several advantages over the basis function expansion method, e.g., no MO-ETF problem and automatic inclusion of the continuum state, this method is based on the independent electron model and hence there is clear evidence of the break down of the TDHF method (36).

4. THEORETICAL RESULTS AND DISCUSSION

Some recently obtained representative results for two-electron systems will be presented. Our aim is not to review all theoretical and experimental findings of this flourishing field, but rather to limit the discussion to selected characteristic cases of two-electron ion-atom collision-like one-electron capture in multiply charged ion-He collisions, ion-pair formation in atom-atom collisions, and alignment and orientation in ion-atom collisions.

4.1. Electron capture in multiply charged ion-He collisions

With the rapid development of ion sources for slow ions, new important physical insights into inelastic processes in multiply charged ion-He collisions have been revealed recently (38,39). Stimulated by the excitement on the experimental side, theorists have also reported attempts at understanding the collision dynamics in a single electron capture process. In a highly asymmetric system one-electron capture usually proceeds mainly into the specific one or two high n -levels of the projectile ion preferentially. The observed shape of the total cross section is almost independent of collision energy except for the projectile is in a low charge state, since many sub- ℓ levels contribute to the determination of the total cross section. Hence, unless all these ℓ -levels are considered in the theory, precise calculations are not possible in multiply charged ion-atom collisions.

$O^{8+} + He$. There have been fairly extensive experimental as well as theoretical studies on electron capture in the $O^{8+} + He$ collisions. However, unfortunately, the marked disagreement among various experiments and also theories remains unresolved. All experimental and theoretical data are plotted in Fig. 3. The MO results obtained by a ten-state close-coupling calculation (40) are in good accord with measurements by Iwai *et al.* (41), Kaneko *et al.* (42), and Afrosimov *et al.* (43) in the energy region from 0.5 to 10 keV/amu. The MO theory predicts that electron capture proceeds to the $n = 4$ manifold of the projectile oxygen ion, which is also confirmed experimentally. Note that the total one-electron capture cross section shows a structureless shape which is rather flat and apparently independent of the impact energy.

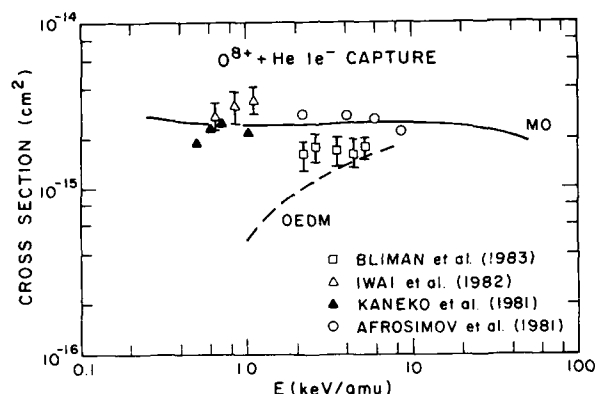


FIGURE 3

One electron capture cross section in the $O^{8+} + He$ collision. Theory: Solid line MU (Ref. 40); broken line OEDM (Ref. 45). Experiment; \square , Bliman *et al.* (Ref. 45); Δ , Iwai *et al.* (Ref. 41); \triangle , Kaneko *et al.* (Ref. 42); \circ , Afrosimov *et al.* (Ref. 43).

One theoretical result obtained by the unitarized distorted wave approximation (UDWA) (44) demonstrates good accord with the MO result as well as with the measurements. The measurement by Bliman *et al.* (45) displays an energy dependence similar to the others, but their values lie approximately 40% below all other measurements and the MO and UDWA theoretical results. The theoretical results by Bliman *et al.* (45), who used the OEDM method, display remarkable disagreement with other theories and all experiments except their own. Their theoretical results drop sharply as the energy decreases and differs by about a factor of 4 from the MO result at 1 keV/amu. Probably this large discrepancy between two MO approaches can be traced back to the fact that Bliman *et al.* only included one channel in their calculation which correlates the dominant one-electron capture channels, $O^{7+}(n=4) + He^+$ levels; they neglected the ETF completely. Since the many ℓ, m -sublevels in the given higher n -manifold are closely packed, it is surely necessary to include effects arising from all these ℓ, m -sublevels in the calculation.

$C^{6+} + He$. Although electron-capture in collisions of various carbon ions with hydrogen atoms has been extensively studied both theoretically and experimentally, studies of electron capture in $C^{9+} + He$ collisions are scarce.

Among $C^{9+} + He$ systems, experiments have concentrated on the $C^{6+} + He$ collision. In particular, workers at the FOM (46) and Institute of Plasma Physics in Nagoya (41) have been analyzing the electron capture mechanism by translational energy spectroscopy and have offered extremely important information for understanding the collision dynamics. Their experimental data are plotted along with two recent theoretical results in Fig. 4. As predicted by two different experiments, two theories have proved that electron-capture proceeds preferentially to the $n = 3$ manifold of the C^{5+} ion at least below 10 keV/amu. The MO result (47) shown in Fig. 4 was obtained by a seven-state close-coupling calculation, while a semi-AO+ result (48) was calculated by using a two-center AO plus the inclusion of a limited number of united atom orbitals.

Agreement of the two theories is sufficiently good within 20% above 1 keV/amu. Below 1 keV/amu, the AO+ results drop rather sharply in contrast to the

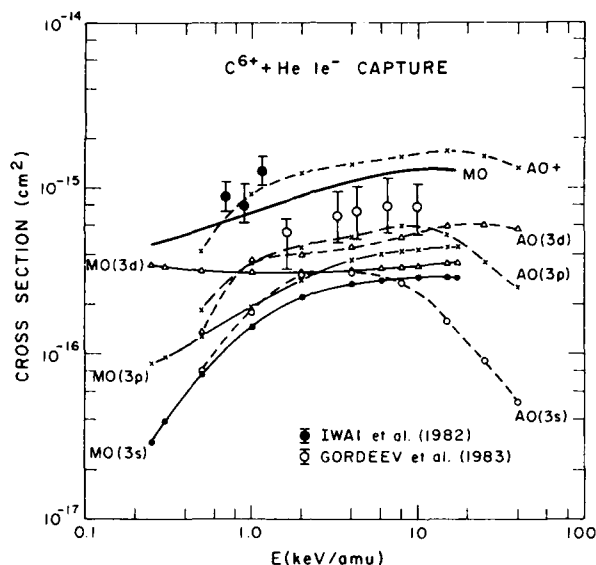


FIGURE 4
One-electron capture cross section in the $C^{6+} + He$ collision. Theory: solid line MO (Ref. 47); broken line AO+ (Ref. 48). Experiment: \circ , Gordeev *et al.* (Ref. 46); \bullet , Iwai *et al.* (Ref. 41).

slow decrease of the cross section in the MO results. The origin of this discrepancy between the two theories in the lower energy regime is not yet clear. Agreement of these theories with the two experiments by Gordeev *et al.* and Iwai *et al.* is reasonable. Measurements by Gordeev *et al.* lie consistently lower by about 15% than the MO result, although the energy dependence of their cross section seems to be in good accord with both MO and AO+ results above 1.5 keV/amu. In spite of the fair agreement of the total one-electron capture cross section between the two theories, agreement of partial cross sections (ℓ -distribution) is not as satisfactory, as can be seen in Fig. 4. Qualitatively, the general trend of each calculated partial cross section, however, is similar in the two theories as the 3p cross section is the dominant one in the energy range from ~1.5 keV to 10 keV, while the 3s cross section has the smallest contribution at all energies studied. At lower energy, below ~2 keV/amu, the 3d cross section contributes the most in the MO calculation.

4.2. Electron capture in atom-atom collisions

$H + Na$. The mechanism of ion-pair formation in atom-atom (in particular the alkali and halogen system) collisions has long been known as the "harpoon mechanism" in the study of ion-pair formation. This process has been studied experimentally for hydrogen-alkali collisions because of the practical application.

Calculated adiabatic potential curves show a series of avoided crossings between Σ states from the ground state to high lying Rydberg states. Strong radial couplings at these avoided crossings are responsible for the main flux promotion mechanism and this mechanism finally brings flux to the ion-pair formation channel. The MO result (49) for the $H + Na$ system is illustrated along with the multichannel Landau-Zener (MCLZ) (50) result and experiments in Fig.

5. The MO calculation has been performed by using six states in a close-coupling method. Marked disagreement between the MO and MCLZ is found. The origin of this large discrepancy can be traced to the assumptions in the MCLZ method. The assumed conditions are very specific and thus limit the applicability of the theory. Apparently the conditions are not satisfied in the present case.

The MO result is more favorable to the measurements by Howald et al. (51) in the 1.0 to 5.0 keV/amu energy range. Experimental data by Nagata (52) seem to drop too drastically in the lower energy side.

4.3. Alignment and orientation study of the electron cloud

Li⁺ + He. In recent years, very precise experimental coherence and correlation analysis techniques have been developed and utilized to study the alignment and orientation of the electron cloud of colliding particles (53). Among those beautiful experiments carried out within the last year, the experiment performed for alignment and orientation of Li(2²P) and He(2¹P) excited states in Li⁺ + He collisions by Andersen et al. (54) is most attractive to theorists. The main feature in this experiment is the finding that at energies below ~5 keV the shape of the electron clouds in the Li(2²P) and He(2¹P) excited states is very nearly that of a p-orbital, aligned perpendicular to the asymptotic internuclear axis, independent of impact parameters and of whether the electron stays on the He-core or is transferred to the Li-center during the collision. At energies above 5 keV, the shape changes from that of a pure p-orbital, the alignment angle deviating from the perpendicular direction with a larger angle for Li and a smaller angle for He. From the theoretical point of view, this problem is extremely difficult to tackle, since the important dynamics takes place at small impact parameter, $b < 1$ a.u.

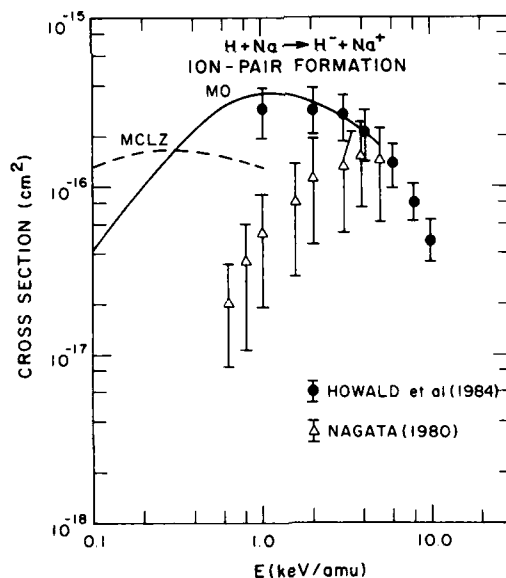


FIGURE 5

Ion-pair formation cross section in H + Na collisions. Theory: solid line MO (Ref. 49); broken line MCLZ (Ref. 50). Experiment: ●, Howald et al. (Ref. 51); △, Nagata (Ref. 52).

Thus, to represent the collision system accurately in either the MO or the AU approach in such a small R region requires a calculation of extremely high precision. Also, in the MO representation, a "good" molecular ETF is needed to describe the two-center character of the ETF properly at small R . Although one theoretical attempt has been reported on this system (55), it was not completely successful due in part to the lack of Galilean invariance of the treatment. In the $\text{Li}^+ + \text{He}$ system the MO diagram tells us that the ground state $\text{Li}^+(1s^2) + \text{He}(1s^2)$ is degenerate with the $2p\pi$ state, $\text{Li}(1s^2 2p_1) + \text{He}^+(1s)$, at the united atom limit. Although there is an avoided crossing at small R between the ground state and the $2s\sigma$ state, $\text{Li}(1s^2 2s) + \text{He}^+(1s)$, the main source of the flux promotion to upper levels is considered to be this strong rotational coupling. The MO calculation (56) has been performed by using a seven-state close coupling method with MO ETF's. The MO calculation confirms that at energies below 5 keV, the flux is promoted to the $2p\pi$ state, $\text{Li}(2p_1) + \text{He}^+$, through strong $2p\sigma$ - $2p\pi$ rotational coupling initially at small R . However, in the later part of the collision, long range π - π radial coupling redistributes the flux between the electron-capture to the excited $\text{Li}(2^2P)$ state and the direct excitation channel to the $\text{He}(2^1P)$ state.

At energies above 5 keV, the stepwise flux promotion from the ground state through sequential radial couplings, as well as the flux mixture between $p\sigma$ and $p\pi$ states of the $\text{Li}(2^2P)$ and $\text{He}(2^1P)$ atoms start playing an important role in the mechanism.

The results clearly support the experimental findings and give a theoretical rationale. Figure 6 displays both experimental and theoretical results for the alignment angle, γ , at an impact parameter $b = 0.55$ a.u. Very good agreement between theory and experiment is noticeable. Also it is worth pointing out that γ_{Li} and γ_{He} show nearly out-of-phase oscillation. This phenomenon can be understood from the fact that the large electron cloud is shared by the two colliding nuclei before the electron settles in the final state. If most of the electron cloud moves with the projectile in an electron capture event, then the electron cloud at the target is minimum, and vice versa [57]. This simple picture explains qualitatively the out-of-phase phenomena.

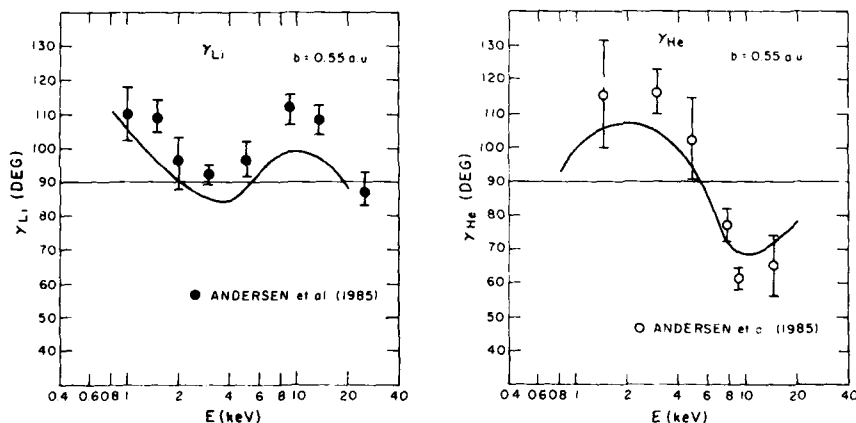


FIGURE 6

Alignment angle for $\text{Li}(2^2P)$, left panel, and $\text{He}(2^1P)$, right panel. Points are from experiment (Ref. 54); solid lines are theory, MO + MOETF (Ref. 56).

5. FURTHER REMARKS

We have been looking at the validity of various theoretical approaches commonly used to investigate different inelastic events observed in ion-atom, atom-atom collisions in the low to intermediate energy regime. In contrast to the study of one-electron (or pseudo one-electron) systems where impressive agreement between the MO and AO results is not viewed with surprise any more, the appropriateness and effectiveness of various theoretical approaches for the more than one-electron systems have not been established yet. Indeed, the application of these theoretical models has just begun. Within the next few years, it will become clear that only some of the theoretical approaches mentioned above can survive and be successful with many-electron systems. Although the molecular ETF may remain a major problem in the MO representation, it will become known that certain types of MO ETF's are useful and effective in specific cases.

Although the time is not yet ripe to discuss the new approach to ion-atom collision theory, namely the R-matrix method (14,15,57), more practical applications will be reported for many-electron systems as well as ion-molecule collision systems in the next few years.

Measurements other than cross sections, for example the study of alignment and orientation in the collision, will become more feasible and these new measurements will definitely provide more detailed insight into collision dynamics. These studies will certainly feed back to, and require rigorous theoretical models, from theorists.

ACKNOWLEDGMENTS

The author wishes to thank R. E. Olson for his collaborations. This work was supported by the U. S. Department of Energy, Magnetic Fusion Division and Division of Basic Energy Science.

REFERENCES

- 1) R. E. Olson, XI ICPEAC in Kyoto 1979, invited papers, eds., N. Oda and K. Takayanagi (North Holland, Amsterdam, 1980), p. 391.
- 2) A. Salin, XII ICPEAC in Gatlinberg 1981, invited papers, ed. S. Datz (North Holland, Amsterdam, 1982), p. 485.
- 3) W. Fritsch and C. D. Lin, XIII ICPEAC in Berlin 1983, invited papers, eds. J. Eichler, I. V. Hertel and N. Stolterfoht (North Holland, Amsterdam, 1984), p. 331.
- 4) R. D. Piacentini and A. Salin, J. Phys. B 7 (1974) 1666.
- 5) T. G. Winter and N. R. Lane, Phys. Rev. A 17 (1978) 66.
- 6) M. Kimura and W. R. Thorson, Phys. Rev. A 24 (1981) 3014.
- 7) M. Kimura, R. E. Olson and J. Pascal, Phys. Rev. A 26 (1982) 3113.
- 8) R. McCarroll and P. Valiron, Phys. Scr. T3 (1983) 226.
- 9) B. H. Bransden and C. J. Noble, J. Phys. B 14 (1981) 1849.
- 10) W. Fritsch and C. D. Lin, Phys. Rev. A 29 (1984) 3039.
- 11) T. G. Winter and C. D. Lin, Phys. Rev. A 29 (1984) 567.
- 12) T. G. Winter, Phys. Rev. A 25 (1982) 697.
- 13) H. J. Lüdde and R. M. Dreizler, J. Phys. B 15 (1982) 2713.
- 14) M. Kimura and C. D. Lin, Phys. Rev. A 31 (1985) 590.
- 15) T. G. Winter and N. F. Lane, Phys. Rev. A 31 (1985) 2698.
- 16) a) V. Maruhn-Rezwani, N. Grün and W. Scheid, Phys. Rev. Lett. 43 (1979) 512; b) C. Bottcher, Phys. Rev. Lett. 48 (1982) 85.
- 17) J. B. Delos, Rev. Mod. Phys. 53 (1981) 287.
- 18) T. A. Green, E. J. Shipsey and J. C. Browne, Phys. Rev. A 25 (1982) 1364.
- 19) M. Kimura and W. R. Thorson, J. Phys. B 16 (1983) 1471.
- 20) H. Sato and M. Kimura, Phys. Lett. 96A (1983) 286.

- 21) M. Kimura, H. Sato and R. E. Olson, *Phys. Rev. A* 28 (1983) 2085.
- 22) M. Kimura and R. E. Olson, *J. Phys. B* 17 (1984) L713.
- 23) R. E. Olson, M. Kimura and H. Sato, *Phys. Rev. A* 30 (1984) 1692.
- 24) M. Kimura, *Phys. Rev. A* 31 (1985) 2153.
- 25) C. Harel and A. Salin, *J. Phys. B* 13 (1980) 85; *ibid.* 16 (1983) 55.
- 26) D. R. Bates and T. R. Carson, *Proc. R. Soc. London Ser. A* 234 (1956) 207.
- 27) M. Kimura, in preparation.
- 28) N. Shimakura and T. Watanabe, in preparation.
- 29) D. R. Bates and R. McCarroll, *Proc. R. Soc. London Ser. A* 245 (1958) 175.
- 30) D. R. Bates, *Proc. R. Soc. London Ser. A* 247 (1958) 294.
- 31) W. Fritsch and C. D. Lin, *J. Phys. B* 15 (1982) 1255.
- 32) D. G. M. Anderson, M. J. Antal and M. B. McElroy, *J. Phys. B* 7 (1974) L118.
- 33) W. Fritsch and C. D. Lin, private communication.
- 34) K. C. Kulander, K. R. Sandhya Devi and S. E. Koonim, *Phys. Rev. A* 21 (1982) 2968.
- 35) W. Stich, H. J. Lüdde and R. M. Dreizler, *J. Phys. B* 18 (1985) 1195.
- 36) H. J. Lüdde and R. M. Dreizler, *J. Phys. B* 14 (1981) 2968; *ibid.* 15 (1982) 2703.
- 37) C. Bottcher, XIII ICPEAC in Berlin 1983, invited papers, eds. J. Eichler, I. V. Hertel and N. Stolterfoht (North Holland, Amsterdam, 1984), p. 187; also, see references therein.
- 38) E. Salzborn and A. Müller, XI ICPEAC in Kyoto 1979, invited papers, eds., N. Oda and K. Takayanagi, (North Holland, Amsterdam, 1980), p. 407.
- 39) S. Ohtani, XIII ICPEAC in Berlin 1983, invited papers, eds. J. Eichler, I. V. Hertel and N. Stolterfoht (North Holland, Amsterdam, 1984), p. 353.
- 40) M. Kimura and R. E. Olson, *J. Phys. B* 18 (1985) 2729.
- 41) T. Iwai, Y. Kaneko, M. Kimura, N. Kobayashi, S. Ohtani, K. Okuno, S. Takagi, H. Tawara and S. Tsurubuchi, *Phys. Rev. A* 26 (1982) 105.
- 42) Y. Kaneko, T. Iwai, S. Ohtani, K. Okuno, N. Kobayashi, S. Tsurubuchi, M. Kimura, H. Tawara and S. Takagi, XIII ICPEAC in Berlin 1983, abstract, eds. J. Eichler, I. V. Hertel and N. Stolterfoht (North Holland, Amsterdam, 1984), Vol. 2, p. 696.
- 43) V. V. Afrosimov, A. A. Basalaev, E. D. Doret, K. O. Lozhlein, and M. N. Panov, XII ICPEAC in Gatlinberg 1981, abstract, ed. S. Datz (North Holland, Amsterdam, 1982), Vol. 2, p. 690.
- 44) H. Suzuki, Y. Kajikawa, N. Toshima, H. Ryofuku and T. Watanabe, *Phys. Rev. A* 29 (1984) 525.
- 45) S. Bliman, D. Hinz, B. Jacquot, C. Harel and A. Salin, *J. Phys. B* 16 (1983) 2849.
- 46) Y. S. Gordeev, D. Dijkkamp, A. G. Drehtje and F. J. de Heer, *Phys. Rev. Lett.* 50 (1983) 1842.
- 47) M. Kimura and R. E. Olson, *J. Phys. B* 17 (1984) L713.
- 48) W. Fritsch and C. D. Lin, private communication.
- 49) R. E. Olson and M. Kimura, *Phys. Rev. A*, in press.
- 50) R. K. Janev and Z. M. Radulovic, *Phys. Rev. A* 17 (1978) 889.
- 51) A. M. Howald, R. E. Miers, J. S. Allen, L. W. Anderson and C. C. Lin, *Phys. Rev. A* 29 (1984) 1083.
- 52) T. Nagata, *J. Phys. Soc. Japan* 48 (1980) 2068.
- 53) See for example, T. Andersen and H.-P. Neitzke, XII ICPEAC in Berlin 1983, invited papers, eds. J. Eichler, I. V. Hertel and N. Stolterfoht (North Holland, Amsterdam, 1984), p. 667.
- 54) N. Andersen, T. Andersen, H.-P. Neitzke and E. Horsdal Petersen, *J. Phys. B* 18 (1985) 2247.
- 55) S. Gala, C. Duro, P. Wahnnon, C. Courbin-Gaussorgues and V. Sidis, XV QUITEL, abstract (1984).
- 56) M. Kimura, to be published.
- 57) M. Kimura and C. D. Lin, *Phys. Rev. A*, in press.

STATE-RESOLVED SINGLE ELECTRON CAPTURE IN SLOW COLLISIONS OF MULTI-CHARGED IONS WITH ONE- AND TWO-ELECTRON ATOMS

D. DIJKAMP*, D. ĆIRIĆ[†] and F.J. DE HEER

FOM-Institute for Atomic and Molecular Physics, Kruislaan 407,
1098 SJ Amsterdam, The Netherlands

We discuss recent experimental results on state-selective single electron capture by slow multi-charged ions from one- and two-electron targets, with emphasis on the *l*-distribution as a function of the collision velocity, in the range 0.1–0.5 au. Some of the results for atomic hydrogen and helium as target are compared with detailed calculations.

During the last decade, electron capture by slow multi-charged ions (MCI) has been the subject of many experimental and theoretical studies. At first, the emphasis was on the study of the behaviour of the total capture cross section, σ_t , as a function of relevant parameters, such as the charge state *q* of the projectile, the target binding energy I_T and the collision velocity *v*. However, for a more stringent test of theoretical calculations, as well as for applications in fields like plasma diagnostics and astrophysics, one desires information on the final state distribution of the captured electron. A recent review of theoretical and experimental progress in this field has been given by Janev and Winter (1). At present, two experimental methods are widely used to obtain such information: Energy Change Spectroscopy (ECS), in which one determines the energy gain (loss) of the projectiles, and Photon Spectroscopy (PS), in which one observes the photon emission of the excited projectiles. ECS has the advantages of giving direct information on the population of the various energy levels, with a detection efficiency of the order unity. PS gives only indirect information; to obtain population distributions the relevant transition probabilities should be known. The sensitivity of PS is very low, typically of the order 10^{-7} , and in addition wavelength dependent. However, the resolution of PS is far superior to that of ECS, which is a decisive advantage if one wants to study *l*-distributions resulting from collisions with, e.g., helium-like ions, since the different *l*-subshells within one *n*-shell are very close in energy for the resulting lithium-like final states.

We have used PS to study *n**l*-distributions in slow collisions of fully stripped (He^{2+} , C^{6+} , N^{7+}), helium-like (C^{4+} , N^{5+} , O^{6+}) and lithium-like (C^{3+}) ions

*Present address: Bell Communications Research, Murray Hill, NJ 07974, USA.

[†]Boris Kidric Institute, P.O. Box 522, Belgrade, Yugoslavia.

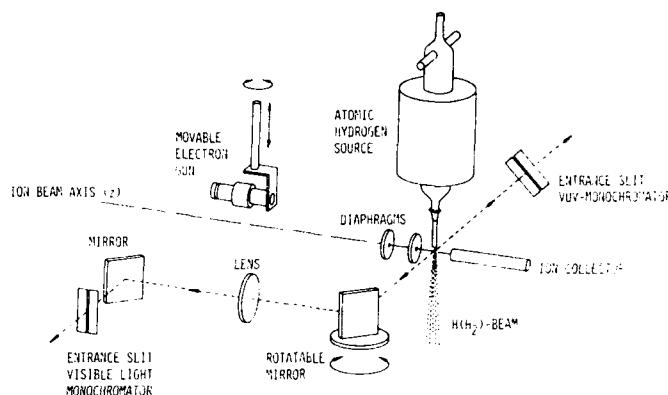


FIGURE 1

Schematic view of the collision region with the atomic hydrogen source and the optical system which is used for the calibration of target density and composition, by means of electron impact excitation (cf. ref. 5).

with lithium, helium, molecular and atomic hydrogen (2)-(9). The experimental set-up (cf. fig. 1) has been described in several publications (2,3,5) and will not be discussed in detail here. To compensate for the low sensitivity, intense ion beams are needed which were produced by an ECR ion source of the MINIMAFIOS type (10) installed at the KVI, Groningen, The Netherlands (11). Light emission in the wavelength range 10-600 nm was measured by means of several monochromators, absolutely calibrated on sensitivity. From the measured line emission cross sections, $\sigma_{em}(\lambda)$, we deduced absolute subshell-selective cross sections, σ_{n1} . The experiments were done in a crossed beam configuration; atomic hydrogen was produced by means of a radiofrequency discharge, similar to that described by Slevin and Stirling (12). The target density and composition were measured by electron impact excitation, as described in ref. 4. In the following we will discuss a few representative results, with special attention to the behaviour of the l -distributions as a function of velocity.

Figs. 2a,b show σ_{31} for $C^{4+}-H, H_2$, figs. 3a,b show σ_{41} for $O^{6+}-H, H_2$. For atomic hydrogen the results of extended AO-calculations by Fritsch and Lin (13) are also shown. The agreement between theory and experiment is quite satisfactory. It is clear that the σ_{n1} data for the same ion on atomic or molecular hydrogen exhibit a rather different velocity dependence, even though $\sigma_n = \sum_l \sigma_{n1}$ is quite similar for both targets and is almost independent of velocity in all cases. In fact, both the dominance of one particular n -shell as well as the weak velocity dependence of σ_n are consistent with the well known classical barrier model (CBM) for electron capture, as we have shown in refs. 6,8.

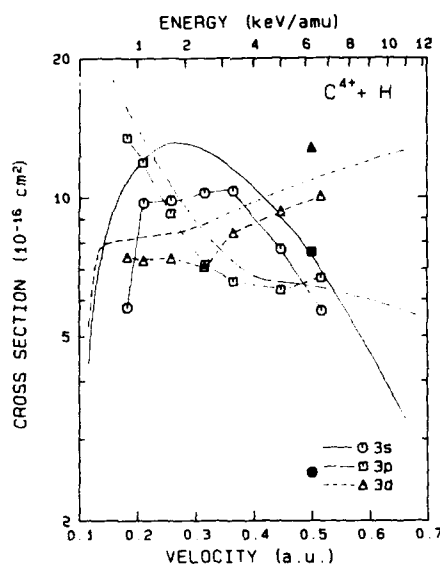


FIGURE 2a

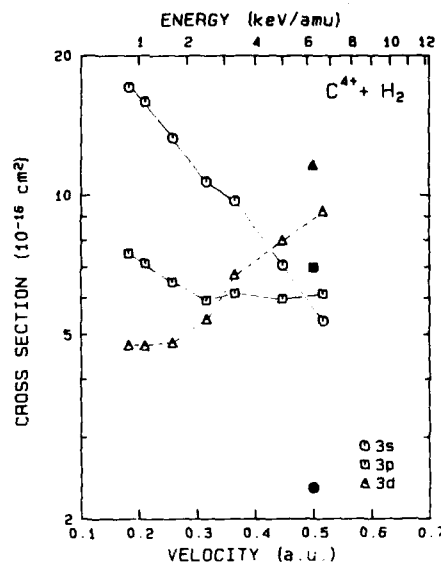


FIGURE 2b

σ_{3l} as a function of velocity for C^{4+} colliding with a) atomic and b) molecular hydrogen. Smooth curves in a) - AO-calculation by Fritsch and Lin (13). Full symbols - normalized statistical distribution at $v = 0.5 \text{ au}$.

Also shown in figs. 2,3 are normalized statistical l-distribution at $v = 0.5 \text{ au}$ (full symbols), which fit the data reasonably well, except for some of the s-states. This feature is in agreement with the so-called rotational mixing model for the l-distribution, developed by Abramov et al. (14) (see also ref. 1). In this model, the l-distribution is strongly influenced by long range rotational mixing, induced by the electric field of the receding target ion, after the electron capture has taken place. The strength of this mixing decreases with decreasing collision velocity. At very low velocities ($v \ll 0.1 \text{ au}$) the model predicts that the l-distribution is determined by the geometrical overlap between the initially populated Stark state and the various spherical final states, leading to dominant population of p- or d-subshells, depending on the initial coupling mechanism. However, this model was developed for collisions involving fully stripped ions, which are subject to a linear Stark effect. In our case, the degeneracy between the final states is removed, which should reduce the strength of rotational mixing. This might explain why we already observe strong changes in the l-distributions if the velocity is reduced from 0.5 to 0.1 au. This explanation is corroborated by comparing detailed AO-calculations by Fritsch and Lin (15) for $\text{Be}^{4+} - \text{H}$ with their results for $\text{C}^{4+} - \text{H}$ (13). At

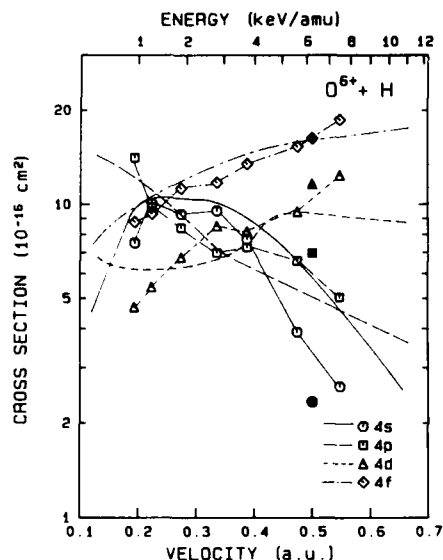


FIGURE 3a

σ_{4l} for O^{6+} colliding with a) atomic and b) molecular hydrogen. Smooth curves in a) - AO-calculation by Fritsch and Lin (13). Full symbols - normalized statistical distribution at $v=0.5$ au.

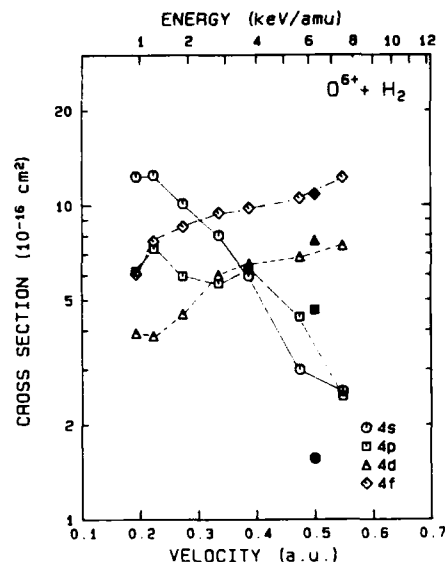


FIGURE 3b

$v \approx 0.5$ au the 3l-distributions are almost identical (and close to statistical), but the distribution for Be^{4+} changes only slightly when decreasing the velocity to 0.1 au, in contrast to the result for C^{4+} . A similar behaviour is observed when comparing the calculated 4l-distributions for $C^{6+}-H$ with those for $O^{6+}-H$.

Summarizing, we have found that the l-distribution at $v \approx 0.5$ au is qualitatively statistical for all systems involving helium-like ions, whereas towards lower velocity the distribution behaves differently for each system. Elsewhere (6,8) we show that the l-distributions at $v \approx 0.1$ au can be qualitatively understood from simple diabatic potential diagrams, by comparing the position of the various crossings with the crossing radius R_c as predicted by the CMB. It turns out that the most favourable crossing is always the first one inside R_c . For $v > 0.5$ au, the distribution becomes overstatistical, which can be most clearly seen in our results for $C^{4+}-Li$ (2). (In that system the effective velocity is higher, because of the low target binding energy). This trend is in agreement with the results of AO-calculations by Fritsch and Lin (13), and was also seen in the Monte-Carlo calculations by Olson (16) and the UDWA calculations by Ryufuku (17).

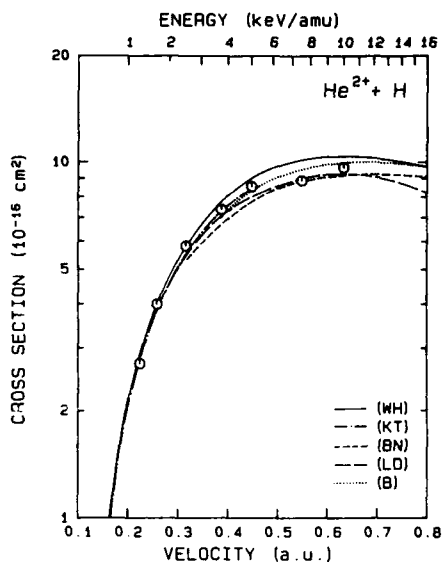


FIGURE 4
 σ_{2p} for He^{2+} -H collisions. Circles - our experimental results. Theoretical results are represented by smooth curves: (WH) - Winter and Hatton (18), (KT) - Kimura and Thorson (19), (BN) - Bransden and Noble (20), (LD) - Lüdde and Dreizler (21), (B) - Bransden et al. (22)

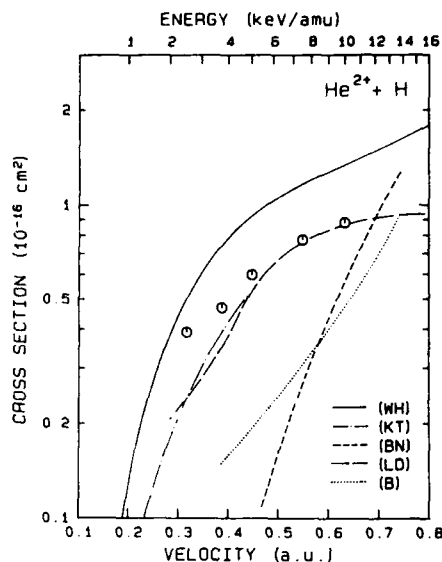


FIGURE 5
 σ_3 for He^{2+} -H collisions. For the meaning of the symbols see the previous figure.

Of course, pure one-electron systems are the starting point for any theoretical approach to the charge transfer problem. Thus, it is not surprising that many calculations have been reported for the system He^{2+} -H. In fig. 4 we show as an example the comparison between our experimental result (4,5) for σ_{2p} and several theoretical results (references are given in the figure caption). For this dominant channel, the agreement is quite good, but for non-dominant channels, such as capture into the $n=3$ states, deviations occur, as show in fig. 5. The results of Kimura and Thorson (19) and Lüdde and Dreizler (21) are closest to our experimental data; the result of Winter and Hatton (18) also includes capture into higher states which explains why their data rise more strongly with increasing velocity. The AO-calculations by Bransden and Noble (20) and Bransden et al. (22) do not agree very well with the experimental results.

For fully stripped ions with higher charge, the degeneracy between the various l-subshells prevents a determination of σ_{n1} from optical measurements

alone. One can then only compare the measured emission cross sections with those calculated from the theoretical state-selective capture cross sections. Such a comparison is made in fig. 6 for the system C^{6+} -H (7). The theoretical results shown are the MO-calculations of Green et al. (23) and of Salin (24). However, it should be remarked that the AO calculation of Fritsch and Lin (15) gives results identical to those of Green et al. Also shown are experimental results for the total capture cross section σ_t , obtained by means of charge state analysis, both by our own group (7) and by Phaneuf et al. (25).

This way of comparing state-selective cross sections is rather indirect, because one averages over several states. For these one-electron systems, ECS would give direct information on the n -distribution. Combining such data with the optical data would make it possible to determine the separate σ_{n1} , which illustrates the complementary nature of the ECS and PS methods. In this connection, it should be remarked that until now the only system involving atomic hydrogen which has been studied by both methods is C^{3+} -H. In a forthcoming publication (9) we compare our results for this system with data obtained by the Belfast group (26). Although the results are in good agreement with regard to the dominant channels, PS is able to identify ten different final channels, whereas in the ECS measurements only four channels could be discriminated.

The rotational mixing model mentioned above, as well as the work of Salin (24), indicates that important information about the physical nature of the charge exchange process is contained in the m -distribution. Baptist et al. (27) have measured the m -distribution from the polarization of the emitted photons, for the system C^{4+} -H₂. Their results for the ratio $\sigma_{3p0}/\sigma_{3p1}$ show that the $m=0$ state is predominantly populated which implies that for this system charge exchange occurs mainly via radial coupling.

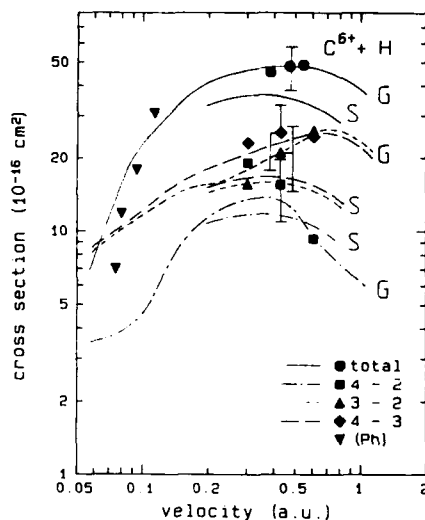


FIGURE 6
Total capture cross section σ_t and line emission cross sections $\sigma_{em}(n-n')$ for C^{6+} -H as a function of velocity. Error bars indicate total uncertainties. (Ph) - σ_t by Phaneuf et al. (25), long curves indicated with G - theory by Green et al. (23), short curves indicated with S - theory by Salin (24).

Very recently, several theoretical groups have attempted to calculate state-selective cross sections for two-electron systems, in particular for collisions with helium. Fig. 7 shows our experimental results for C^{4+} -He, compared with a MO-calculation by Kimura and Olson (28). Also shown are σ_t data from the Nagoya (29) and Oak Ridge groups (30). The agreement for the dominant channel, σ_{2p} , is quite good, however, we observe a noticeable amount of capture into the $n=3$ shell, at variance with the theoretical prediction. Fritsch and Lin obtained theoretical results for O^{6+} -He, reported at this conference (31), which compare well with our experimental results, at least for the dominant 31-channels.

We may conclude that theoretical and experimental efforts have rapidly converged in the last two years: As we have shown there are now several systems for which theoretical and ex-

perimental results on state-selective cross sections can be directly compared. The overall agreement is quite satisfactory, but the energy range over which a comparison can be made is still rather limited.

We may expect that in the future more efforts will be made to obtain a deeper insight into the charge transfer mechanism. In particular, more complex (multi-electron) systems should be studied, and more information on the m-distributions would be desirable. Finally, our own group will attempt to extend some of the state-selective measurements discussed above to lower velocities, possibly down to 0.02 au.

ACKNOWLEDGEMENTS

We would like to thank Dr. W. Fritsch for providing some of his results prior to publication. The hospitality of the KVI during the measurements is gratefully acknowledged. This work is part of the research program of the Stichting voor Fundamenteel Onderzoek der Materie and was made possible by financial support from the Nederlandse Organisatie voor Zuiver Wetenschappelijk Onderzoek.

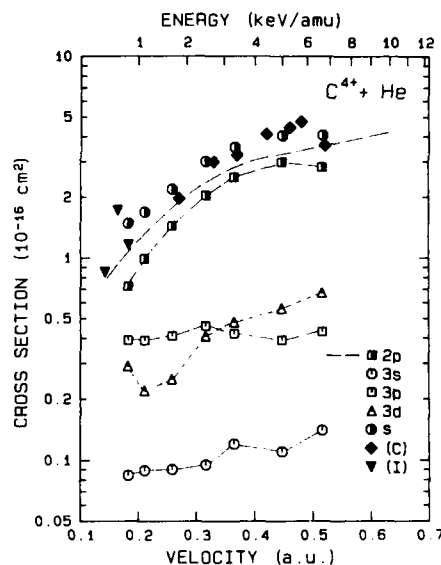


FIGURE 7
 σ_{2p} , $\sigma_{3\ell}$ and $\sigma_s = \sigma_{2p} + \sum_{\ell} \sigma_{3\ell}$ for C^{4+} -He.
 Also shown are experimental σ_t data by Iwai et al. (29) - (I) and by Crandall (30) - (C). The smooth curve is the theoretical result for $\sigma_{2p} = \sigma_t$ by Kimura and Olson (28).

REFERENCES

- 1) R.K. Janev and H. Winter, Phys.Reports 117 (1985) 257.
- 2) D. Dijkkamp, A. Brazuk, A.G. Drentje, F.J. de Heer and H. Winter, J.Phys.B: At.Mol.Phys. 17 (1984) 4371.
- 3) D. Dijkkamp, Yu.S. Gordeev, A. Brazuk, A.G. Drentje and F.J. de Heer, J. Phys.B: At.Mol.Phys. 18 (1985) 737.
- 4) D. Ćirić, D. Dijkkamp, E. Vlieg and F.J. de Heer, J.Phys.B: At.Mol.Phys. 18 (1985) L17.
- 5) D. Ćirić, D. Dijkkamp, E. Vlieg and F.J. de Heer, J.Phys.B: At.Mol.Phys. (1985) accepted for publication.
- 6) D. Dijkkamp, D. Ćirić, E. Vlieg, A. de Boer and F.J. de Heer, J.Phys.B: At. Mol.Phys. (1985) accepted for publication.
- 7) D. Dijkkamp, D. Ćirić and F.J. de Heer, Phys.Rev.Lett. 54 (1985) 1004.
- 8) D. Dijkkamp, Thesis (1985) State University of Utrecht, The Netherlands.
- 9) D. Ćirić, A. Brazuk, D. Dijkkamp, F.J. de Heer and H. Winter, J.Phys.B: At. Mol.Phys. (1985) accepted for publication.
- 10) R. Geller and B. Jacquot, Physica Scripta T3 (1983) 19.
- 11) A.G. Drentje, Physica Scripta T3 (1983) 45.
- 12) J. Slevin and W. Stirling, Rev.Sci.Instrum. 52 (1981) 1780.
- 13) W. Fritsch and C.D. Lin, J.Phys.B: At.Mol.Phys. 17 (1984) 3271 and private communication.
- 14) V.A. Abramov, F.F. Baryshnikov and V.S. Lisitsa, JETP Letters 27 (1978) 464.
- 15) W. Fritsch and C.D. Lin, Phys.Rev. A 29 (1984) 3039.
- 16) R.E. Olson, Phys.Rev. A 24 (1981) 1726.
- 17) H. Ryufuku, Rep. JAERI-M-82-031 (1982).
- 18) T.G. Winter and G.J. Hatton, Phys.Rev. A 21 (1980) 793.
- 19) M. Kimura and W.R. Thorson, Phys.Rev. A 24 (1981) 3019.
- 20) B.H. Bransden and C.J. Noble, J.Phys.B: At.Mol.Phys. 14 (1981) 1849.
- 21) H.J. Lüdde and R.M. Dreizler, J.Phys.B: At.Mol.Phys. 15 (1982) 2713.
- 22) B.H. Bransden, C.J. Noble and J. Chandler, J.Phys.B: At.Mol.Phys. 16 (1983) 4191.
- 23) T.A. Green, E.J. Shipsey and J.C. Browne, Phys.Rev. A 25 (1982) 1364.
- 24) A. Salin, J.Physique 45 (1984) 671.
- 25) R.A. Phaneuf, I. Alvarez, F.W. Meyer and D.H. Crandall, Phys.Rev. A 26 (1982) 1892.
- 26) R.W. McCullough, F.G. Wilkie and H.B. Gilbody, J.Phys.B: At.Mol.Phys. 17 (1984) 1373.
- 27) R. Baptist, J.J. Bonnet, G. Chauvet, J.P. Desclaux, S. Edusson and D. Hitz, J.Phys.B: At.Mol.Phys. 17 (1984) L417.
- 28) M. Kimura and R.E. Olson, J.Phys.B: At.Mol.Phys. 17 (1984) L713.
- 29) T. Iwai, Y. Kaneko, M. Kimura, N. Kobayashi, S. Ohtani, K. Okuno, S. Tagaki, H. Tawara and S. Tsurubuchi, Phys.Rev. A 26 (1982) 105.
- 30) D.H. Crandall, Phys.Rev. A 16 (1977) 958.
- 31) W. Fritsch and C.D. Lin, Contr.Papers of this conference.

TRANSLATIONAL ENERGY SPECTROSCOPY AND ANGULAR DISTRIBUTIONS FOR LOW ENERGY CAPTURE BY MULTIPLY CHARGED C, Ne AND Ar FROM He, D₂, AND D TARGETS

C. L. COCKE, J. P. GIESE, L. N. TUNNELL, W. WAGGONER, and S. L. VARGHESE*

J. R. Macdonald Laboratory, Physics Dept., Kansas State University,
Manhattan, KS 66506, USA

Translational energy spectra for multiply charged Ar, Ne and C projectiles at 400-5000 eV capturing electrons from targets of atomic and molecular deuterium have been measured. Direct capture can be explained in terms of simple reaction window arguments, but structure and location of transfer ionization groups is not well understood. Angular distributions for capture by Ne and C from He targets have been measured. Oscillatory structure for double capture by C⁴⁺ on He is qualitatively explained, but structure for Ne⁶⁺ and Ne⁷⁺ on He is poorly described by simple two-state models.

1. INTRODUCTION

The capture of electrons from neutral targets by multiply charged projectiles has been the subject of intense study in recent years. At low velocities the capture is well known to populate quite selectively states of high excitation on the projectile core, nearly always with positive energy balance. In a curve crossing picture, the transfer at crossings of the incoming channel with the Coulomb promoted final channels, strongly favoring crossings which occur within a "reaction window" centered on an optimum value of internuclear distance (R_c). For multielectron targets, capture of more than one electron or transfer ionization (T.I.), usually in the form of capture to unbound doubly excited states, is important. (See fig. 1.) The long range nature of the transfer has led to the development of several quite successful theoretical descriptions of the process which have the advantage of broad applicability to a wide range of target and projectile species.^{2,3} For systems with a small number of active electrons, detailed theoretical treatments of specific systems are increasingly available.⁴ On the experimental side, total cross section measurements abound, although data for true one electron systems is still available only through the first row elements.⁵ State selective measurements,

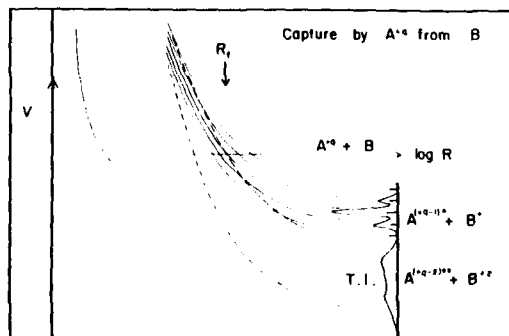


Fig. 1: Schematic of potential curves for capture by A^{q+} from B.

through translational energy spectroscopy and electron and photon spectroscopy, are necessary in many cases to advance our understanding of the capture process further. Little angular distribution data for such systems have been reported for more than doubly charged projectiles.

Considerable recent work has been reported on energy gain spectroscopy for such collisions. In this paper we present some of our recent energy gain results on single and double capture from light targets by multiply charged Ne and Ar projectiles. We have chosen targets with no more than two electrons in the hope that such systems will ultimately prove more tractable theoretically. This choice carries with it one experimental cost: the kinematic spread in projectile energies which results from low energy capture increases rapidly with increasing projectile to target mass ratio. This effect can limit the final state spectral resolution in energy gain experiments. It points to the fact that the energy and angular distributions in the laboratory are inextricably connected, and originally led to our investigations of the angular distributions of the capturing projectiles. Ion source limitations restrict us to the use of less than fully stripped projectiles. Although the theoretical treatment of the capture is eased for the case of a bare projectile, resolution of final l values is not possible in such a case due to the degeneracy of the final states. To this extent, there is even some advantage to the use of less than fully stripped ions for which this degeneracy is removed.

2. ENERGY-GAIN SPECTROSCOPY

The apparatus which we have used for energy gain spectroscopy is shown in fig. 2.¹⁴ The ions are produced from a recoil ion source pumped by 20-25 MeV F beams. The recoil ions are extracted with an energy of 35 to 60 eV \cdot q, where q is the ion charge state. After momentum analysis they enter a resistively heated atomic hydrogen oven which also serves as a normal gas cell for other targets. The entire oven can be maintained at a voltage which is varied in order to change the collision energy. Thereafter the ions pass into a hemispherical electrostatic analyzer for charge and energy analysis. The best energy resolution we have obtained is 0.24 eV \cdot q, which is less than the resolution of the magnetic momentum analyzer, and thus greater than or equal to the intrinsic energy spread in the recoil source. The atomic deuterium target is obtained by heating the oven to a temperature between 2000°K and 2100°K, for which a dissociation fraction of approximately 0.8 is obtained.

The kinetic energy given to the target, and thus lost to the projectile, increases rapidly with the scattering angle of the projectile, θ , with a coefficient which increases with projectile to target mass ratio. The projectile reaction products are distributed near a characteristic scattering angle θ_c which we define as that angle which corresponds to capture at an impact parameter equal to the crossing radius. In the absence of polarization effects on the potential curves, it can be shown that, for small angles, $\theta_c = Q/2E$, where Q is the energy released in the reaction and E the laboratory bombarding energy. This remarkably simple result is independent of the masses involved and of the number of electrons captured. Table 1 shows values of ΔE , defined as the difference between the energy gain at θ_c and that at $\theta=0^\circ$, for selected cases, and shows the advantage of using higher bombarding energies and heavier target masses. For this reason we have used deuterium rather than normal hydrogen as a target. Large shifts are to be associated with large spreads in energy gain as well, due to the finite angular distribution of the reaction products.

In fig. 3 we show energy spectra for 3955 eV Ne⁺⁷ on Ar, D₂ and atomic deuterium targets. All events shown correspond to Ne⁺⁶ final ions. Several features of this spectrum are common to nearly all cases we have studied. Normal single capture to identifiable states on the Ne⁺⁷ core appear at lower energy gains, with a broad band of population occurring at higher energy gains

Fig. 2: Apparatus used for energy gain measurements with molecular and atomic deuterium and hydrogen.

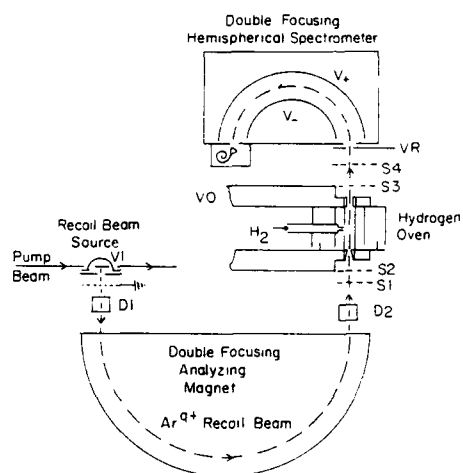
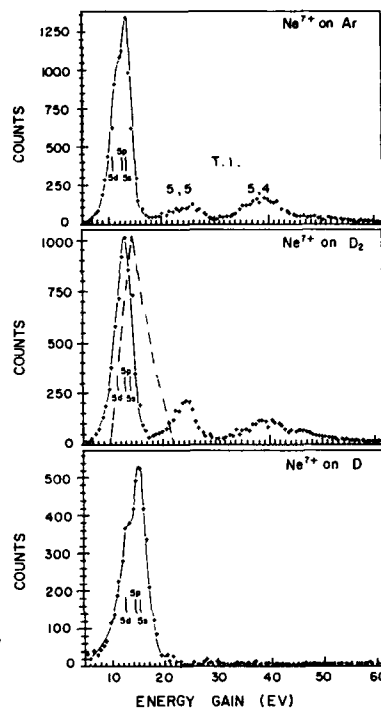


Fig. 3: Energy gain spectra for 3955 eV Ne^{+7} on Ar, D_2 and D.



for the multi-electron targets. In this case, the normal capture is to unresolved k values with $n=5$. A Q-value window, calculated on the basis of a two-level Landau-Zener model with the coupling matrix element given by Olson *et al.*, is shown for the Ne^{+7} on D_2 case. It would favor population of even higher Q, but the $5k$ levels are the only nearby candidates. The higher energy group might be attributed to population of lower n , but it is much more likely that it is due instead to transfer ionization (T.I.), presumably in the form of double capture to unresolved doubly excited states which autoionize back to the Ne^{+6} channel before detection. Such an interpretation is strongly supported by the disappearance of this group for the one-electron target. Similar interpretations of T.I. groups have been made previously by other workers.^{7,15} The energies of the densely distributed doubly excited states involved here are not known but may be estimated on the basis of the binding energies of single electrons to a Ne^{+7} core. In this way we tentatively identify the two T.I. groups near 25 and 38 eV as due to capture to $n,n'=5,5$ and $5,4$ respectively.

The similarity between the Ar target spectrum (which is in good agreement with that of Nielsen *et al.*) and the D_2 spectrum is striking. The first binding energy for argon (15.76 eV) is nearly equal to that for molecular deuterium (15.24), and the spectral comparison shows dramatically that the energy balance rather than the molecular or atomic structure is the major factor which determines the final state populations in the reaction. The process seems not to know that D_2 is a molecule rather than an atom. It is surprising, however, that the T.I. spectra are so similar, since the ionization potentials for Ar and D_2 by 11 eV. This suggests that the structure in the T.I. may be characteristic of the location of reaction windows for population of doubly excited states as well as the density of such levels. The effective crossing radii for the direct and two T.I. groups in fig. 3 are at approxi-

mately 13.6, 11.3 and 7.19 a.u., respectively, indicating that the doubly excited levels are populated at smaller internuclear distances than are singly excited levels. Since both sequential one-electron transfer and two-electron transfer can occur, it is possible that two reaction windows can occur for T.I. Similar structure occurs for Ne^{+5} projectiles.

In fig. 4 we show energy gain spectra for Ar^{+6} on atomic and molecular deuterium targets, as well as on Ar and H_2 . A comparison of the D_2 and H_2 targets shows the resolution advantage of having the heavier target mass.

The density of final states is sufficiently high in this case that the population distribution is thought to reflect directly the reaction window in Q value. We have used a Landau-Zener multi-level model to calculate the shape of such a window, following the procedure given by Olson. We have assumed a uniform spacing in Q value of the many possible final states. Two parameters enter this model: the level density and the strength of the coupling matrix element H_{12} which couples the incident channel with each crossing reaction channel. We have used Olson's universal expression¹⁵

$$H_{12} = C \cdot 9.13/\sqrt{q} \exp[-1.324 R a/\sqrt{q}]$$

but have introduced C as an adjustable parameter which we use to investigate the effect of the strength of H_{12} on the window placement and width. The windows shown in fig. 4 were calculated from this model using the parameters given in Table 2. Also given are total cross sections from both the model and experiment. We have included the T.I. in the experimental cross sections because we suspect that these channels only serve to take flux out of the single capture channel, although no T.I. is treated by the model. The cross sections are in fairly good agreement with the model, but are quite insensitive to C . The location of the reaction window is quite sensitive to C . We find it surprising that a value of C so near unity is found when the coupling strength of the sigma state for which the universal expression of Olson was developed, must be shared among so many different ℓ states for any given n . The shift in reaction window between Ar and D_2 and between D_2 and D cannot be explained in terms only of ionization potential differences, but must be due to differences in the coupling matrix elements as well.

3. ANGULAR DISTRIBUTIONS

In fig. 5 is shown the apparatus we have used for measuring angular distributions for Ne and C projectiles on He. Charge state selection is done with a retarding grid located in front of the detector. A one-dimensional position sensitive channel plate detector assembly, collimated with a bow-tie shaped collimator to convert a radial distribution into approximately (within 3° FWHM) a linear one, records $d\sigma/d\theta$ directly. The effective angular resolution of the system, limited by aperture sizes, is between 0.2 and 0.35 degrees (FWHM). Even with such a modest resolution count rates are rarely above a hundred Hz in the charge exchange group.

The collision schematic of fig. 6 illustrates the qualitative features one might expect for the trajectories and deflection functions for systems considered here. The picture we use is semi-classical, although the validity of this picture is open to debate. The deflection function for a two level case is expected to be characterized by two branches corresponding to transfer at the crossing region on the incoming and outgoing parts of the trajectory. The two branches meet at 0° . For such a deflection function, a rainbow is expected at an angle θ_R . Oscillatory behavior due to interference between scatterings from different b leading to the same θ is expected with the separation between peaks calculable from the deflection function, as discussed by Ford and Wheeler.¹⁶ In a region where the branches of the deflection function are nearly parallel, the separation between peaks is given by $\Delta\theta = 2\pi/\Delta l$ ($l = mv\hbar/h$).

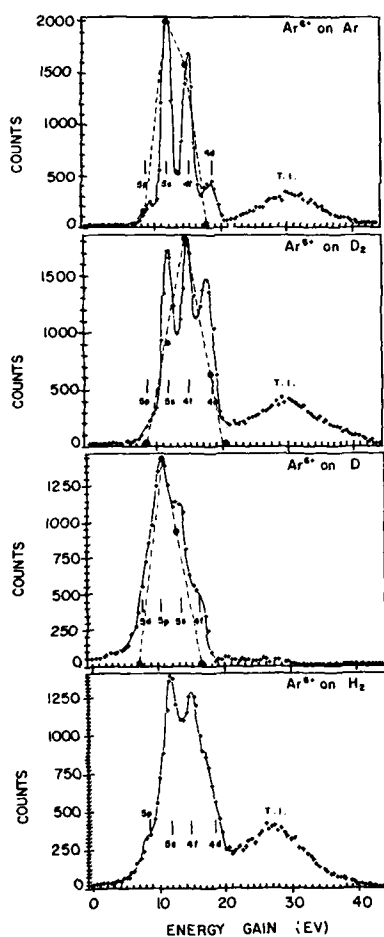


Fig. 4: Energy gain spectra for 3390 eV Ar^{+6} on Ar, D_2 , D and H_2 . The dashed lines are reaction windows calculated using the parameters in Table 2.

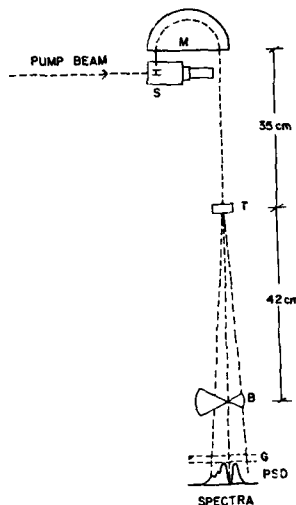


Fig. 5: Apparatus used for angular distribution measurements.

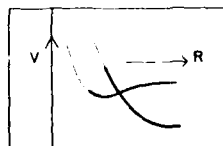


Fig. 6: Two-potential curve schematic showing two paths for capture.

In fig. 7 is shown the angular distribution for double capture from He by C^{+4} , which shows clear oscillations of this type. For this case double capture via crossing with the E_3 state is stronger than single capture to the E_2 state, as discussed by Crandall *et al.*¹⁷ and by Shipsey *et al.*¹⁸ Strong interaction between these channels still exists, however, and interference between transitions to the E_3 state on incoming and outgoing branches gives rise to the oscillations. Oscillatory behavior in the energy gain spectra, caused by the oscillation in the angular distribution, was seen earlier by Cedequist *et al.*¹⁹ and a theoretical interpretation is reported by Barany *et al.*²⁰ at this conference. The present data are in excellent qualitative agreement with these results.

Fig. 8 shows the experimental angular distribution for Ne^{+6} on He. The distribution centers in the neighborhood of θ_c , although much of the distribution lies outside this angle and indeed there is substantial cross section beyond the range of our detector. As shown in the energy gain spectrum in the insert, the main population is to a 3d state on the Ne^+ core at this energy.

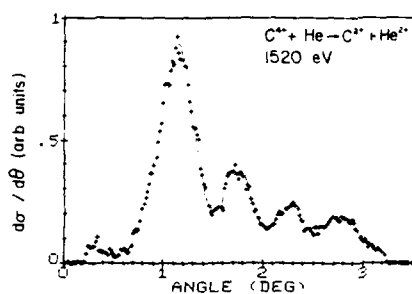


Fig. 7: Angular distribution for double capture by 1520 eV C^{+4} from He.

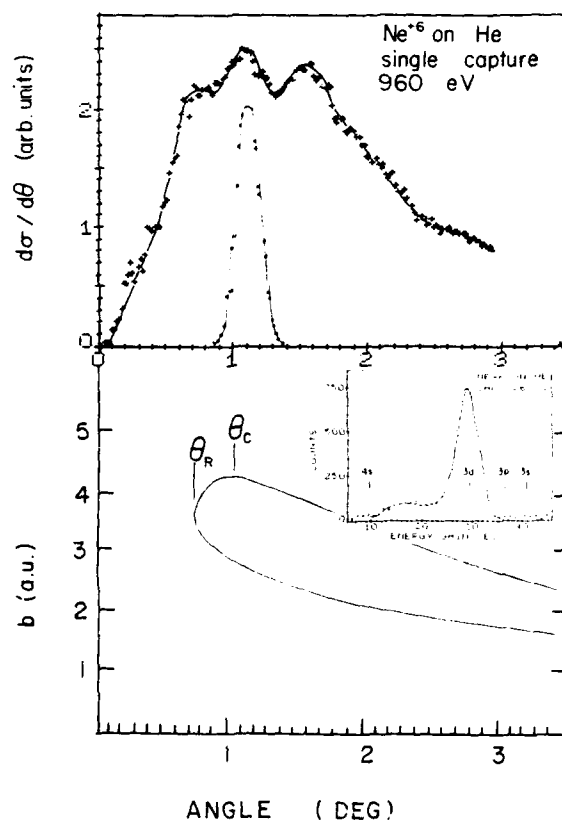


Fig. 8: Angular distribution for capture by Ne^{+6} from He. The deflection function is from a simple two-state model with screened Coulomb potentials. The filled circles show the angular resolution function.

The deflection function shown comes from a simple two state model in which the Ne^{+6} is taken to be a point charge and screened Coulomb potentials are taken for both potential curves. The rainbow angle thus predicted is in reasonable agreement with the data but the oscillation frequency, barely resolvable with the present resolution, is a factor of three lower than that found by the expression for $\Delta\theta$ given above. The data indicate that a much smaller separation between the two branches of the deflection is needed. It is possible that such a result could come from interaction with double capture channels not included in the model potential, even if such channels are not ultimately populated in the reaction. There are many such crossings in the region of the reaction window.

An even more puzzling result is shown in fig. 9 for Ne^{+4} on He. A similar potential model results in the deflecting function shown, and again predicts an oscillation frequency which is about a factor of four higher than the separation of the two main structures at 1.2 and 1.8 degrees. In addition there is a strong forward peak which is well inside the calculated rainbow angle and for which we have no explanation. This peak sharpens with improvement in experimental resolution and its true width is not shown by the experiment. It is

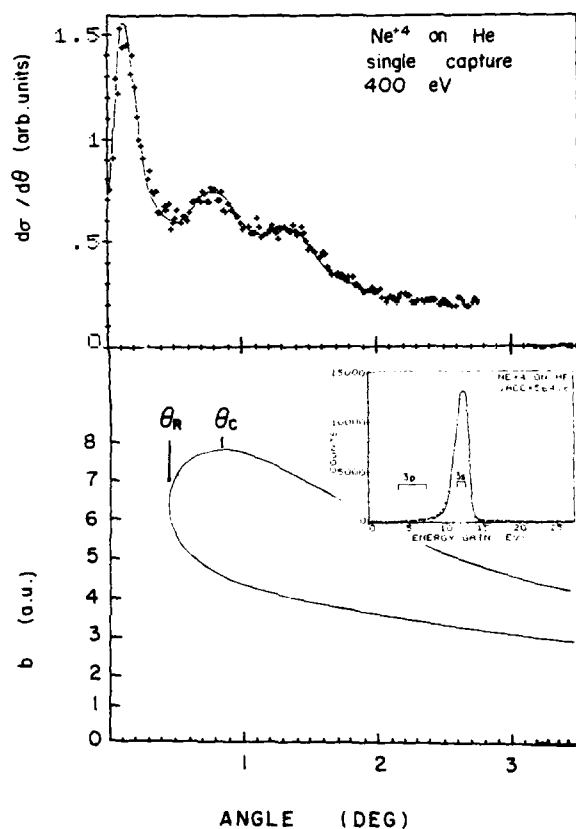


Fig. 9: Similar to Fig. 7, but for Ne^{+4} on He.

possible that a true quantal treatment of the process will be necessary for understanding of these distributions.

4. ACKNOWLEDGMENTS

We thank P. Hvelplund and A. Bárány for sharing with us their results on C^{+4} on He prior to publication. This work is supported by the Division of Chemical Sciences, U. S. Department of Energy.

TABLE 1: KINEMATIC ENERGY SHIFTS ΔE FOR Ar PROJECTILES

TARGET	$E(eV)$	$\theta_c(^{\circ})$	$Q(eV)$	$\Delta E(eV)$
D	3590	0.180	20	1.19
H	3390	0.188	20	2.37
H	3390	0.090	10	0.59
H	800	0.425	10	2.47

TABLE 2: PARAMETERS USED FOR Q-WINDOW CALCULATION

PROJECTILE	TARGET	LEVELS/eV	C	σ_{MODEL}	$\sigma_{EXPT.} (10^{16} cm^2)$
Ar ⁺⁶	Ar	0.33	1.2	51.1	71.4 ^a
Ar ⁺⁶	D ₂	0.33	0.65	48.8	49 ^b
Ar ⁺⁶	D	0.33	1.42	55.1	48 ^b
Ne ⁺⁷	D ₂	one only	1.0	--	--

^a Ref. 7	^b Ref. 21				

REFERENCES

- * Permanent address: Physics Dept., Univ. of South Alabama, Mobile, AL 36688.
1. See for example, *Electronic and Atomic Collisions*, ed. I. V. Hertel and N. Stolterfoht, p. 317 (1984) (North-Holland, Amsterdam).
 2. R. Olson and A. Salop, Phys. Rev. A **14** (1976) 579.
 3. H. Ryufuku, K. Sasaki and T. Watanabe, Phys. Rev. A **21** (1980) 746.
 4. e.g., see W. Fritsch and C. D. Lin, J. Phys. B **17** (1984) 3271.
 5. F. R. Meyer, A. M. Howard, C. C. Havener and R. A. Phaneuf, Phys. Rev. Lett. **54** (1985) 1663.
 6. E. L. Kamber and J. B. Hasted, J. Phys. B **16** (1983) 3025.
 7. E. H. Nielsen, L. H. Andersen, A. Bárány, H. Cederquist, J. Heinemeier, P. Hvelplund, H. Knudsen, K. B. MacAdam and J. Sørensen, J. Phys. B **18** (1985) 1789.
 8. B. A. Huber and H.-J. Kahlert, J. Phys. B **16** (1983) 4655.
 9. E. L. Kamber, A. G. Brenton, J. H. Begnon and J. B. Hasted, J. Phys. B **18** (1985) 933.
 10. P. Roman, M. Barat, H. Laurent, J. Pommier, S. Dousson and D. Hitz, J. Phys. B **17** (1984) 1521.

11. R. W. McCullough, F. G. Wilke and H. B. Gilbody, *J. Phys. B* 17 (1984) 1373.
12. R. Mann, C. L. Cocke, A. S. Schlachter, M. Prior and R. Marrus, *Phys. Rev. Lett.* 49 (1982) 1329.
13. S. Ohtani, *Electronic and Atomic Collisions*, ed. I. V. Hertel and N. Stolterfoht (Amsterdam: North Holland) (1983) p. 353.
14. C. L. Cocke, R. DuBois, T. J. Gray, E. Justiniano and C. Can, *Phys. Rev. Lett.* 46 (1981) 1671.
15. R. E. Olson and A. Salop, *Phys. Rev. A* 14 (1976) f579.
16. K. W. Ford and J. A. Wheeler, *Ann. Physics* 7 (1959) 259.
17. D. H. Grandall, R. E. Olson, E. J. Shipsey and J. C. Browne, *Phys. Rev. Lett.* 36 (1976) 858.
18. E. J. Shipsey, J. C. Browne and R. E. Olson, *Phys. Rev. A* 15 (1977) 2166.
19. H. Cederquist, L. H. Andersen, A. Bárány, P. Hvelplund, H. Knudsen, E. H. Nielsen, J. O. K. Pedersen and J. Sørensen (to be published, 1985).
20. A. Bárány and H. Danared, XIV ICPEAC Contributed Abstracts (1985) 468.
21. C. Can, T. J. Gray, S. L. Varghese, J. M. Hall and L. N. Tunnell, *Phys. Rev. A* 31 (1985) 72.

STATE-SELECTIVE ELECTRON CAPTURE BY SLOW MULTIPLY CHARGED IONS IN ATOMIC HYDROGEN USING TRANSLATIONAL ENERGY SPECTROSCOPY

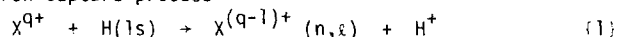
R. W. McCULLOUGH

Department of Pure and Applied Physics, The Queen's University of Belfast, Belfast, UK

The application of the technique of translational energy spectroscopy in a furnace target arrangement to provide the first state-selective measurements of one electron capture by slow ($v < 1$ a.u.) multiply charged ions in atomic hydrogen is described. Results for C^{q+} and N^{q+} ($q = 2, 3$) are presented and the influence of metastable primary ions discussed. State selective one electron capture cross sections for N^{2+} and C^{3+} in H are compared with theory and in the case of C^{3+} with the recent data from the complementary technique of photon emission spectroscopy.

1. INTRODUCTION

The electron capture process



involving multiply charged ions and hydrogen atoms resulting in the production of specific states n, ℓ of the $X^{(q-1)+}$ product ion plays an important role in both astrophysical and fusion plasmas. At low collision velocities ($v < 1$ a.u. or 25 keV amu⁻¹) a quasi-molecular description of the collision system is appropriate and the electron capture process (1) can be considered as the result of transitions between the adiabatic potential energy curves of the initial and final molecular states. Selective capture into a limited number of product ion states occurs with maximum probability via pseudo-crossings of these curves which, for exothermic reaction channels with energy defects ΔE , occur at internuclear separations $R_c = (q-1)/\Delta E$ a.u. (neglecting polarisation).

The first experimental studies of (1) were carried out in our laboratory (1) where the feasibility of using translational energy spectroscopy TES in conjunction with a tungsten tube furnace to provide a target of highly dissociated hydrogen was demonstrated. In this method the primary ion beam X^{q+} of well defined energy T_1 is passed through the target. If the kinetic energy of the forward scattered $X^{(q-1)+}$ ions formed as products of single one electron capture collisions is measured as T_2 then the energy change

$$\Delta T = T_2 - T_1 = \Delta E - \Delta K \quad (2)$$

where ΔE is the energy defect of a particular collision channel in (1) characterised by the initial and final states of both the target and projectile, and ΔK is the recoil energy of the target. Provided $\Delta E/T_1 \ll 1$ and scattering angles are small then the observed change in translational energy $\Delta T \approx \Delta E$. This technique requiring only very low primary beam intensities of $\sim 10^4$ counts/s is capable of providing an unambiguous indication of the presence and influence of any metastable species present in the primary beam. Moreover, with a knowledge of the total one electron capture cross sections, state-selective cross sections can be determined in a direct manner enabling the first detailed comparisons with theory to be made.

This method has now been successfully applied in this laboratory (McCullough

et al (2), Wilkie et al (3), (4)) for collisions involving 0.6-18 keV C^{q+} and N^{q+} ($q = 2, 3$) ions in atomic hydrogen.

Recently, the Amsterdam/Groningen group (Ciric et al (5), (6) and Dijkkamp et al (7), have used photon emission spectroscopy (PES) for state-selective electron capture studies of 7-120 keV multiply charged ions of C, N and O in atomic hydrogen. In the PES method, data is obtained from an analysis of emission cross sections for spectral lines emitted in the spontaneous decay of the excited products of single collisions. This method which is capable of much higher energy resolution than TES requires primary beam intensities several orders of magnitude larger and requires data on energy levels, transition probabilities together with absolute photon detection efficiency calibrations of several spectrometers. In contrast to TES, capture processes resulting in the formation of either ground state or long lived excited states of the product ion cannot be studied by the PES method. The two methods are therefore complementary.

2. EXPERIMENTAL APPROACH

The basic apparatus and method of measurement was the same as that described in our previous work (Lennon et al (8), Wilkie et al (3) so that only the essential features and recent improvements need be summarised here.

A beam of primary ions X^{q+} derived directly from an oscillating electron type ion source, was momentum analysed by magnetic deflection. The ions were then focussed and decelerated in passage through an electrostatic lens to an energy typically between 20 q and 120 q eV before passing through two electrostatic hemispherical analysers to select ions with an energy spread down to 0.17 q eV FWHM. After acceleration the ions passed through two diametrically opposed apertures midway along a tungsten tube furnace into which hydrogen gas flowed at a constant rate. The furnace tube was heated by passing a.c. directly through it and was maintained at collision potential while the surrounding heat shield and walls of the vacuum chamber housing were biased negatively with respect to the furnace to prevent ions formed by electron capture in the residual gas outside the furnace from contributing to the measured signals.

The furnace was operated either at room temperature as a simple gas cell containing H_2 or at a temperature of about 2400 K to provide a target of highly dissociated hydrogen with an estimated degree of dissociation of at least 92 compared to the ~75% achieved in our earlier work (1). The hydrogen flow rate to the furnace was at all times low enough to ensure single collision conditions.

Forward scattered $X^{(q-1)+}$ ions formed as products of single collisions were focussed and decelerated by an electrostatic lens and energy analysed by a third hemispherical electrostatic analyser which was operated with a FWHM energy resolution down to 0.17 (q-1) eV. The geometry of the furnace tube, product ion analyser and detector was such that ions $X^{(q-1)+}$ scattered within a mean half angle of 0.5° were detected.

In all our previous work the energy analysed $X^{(q-1)+}$ product ions passed through a 1 mm diameter aperture at the exit of the final analyser and were detected by a multiplier operating as a single particle counter. The energy change spectrum was thus seen as a linearly dispersed image of which only a small fraction could be sampled by voltage scanning at any instant. Recently, we have used a position sensitive detection system PSD similar to that described by Hicks et al (9) which simultaneously records the intensity and position of the dispersed image to obtain a considerable increase in the effective product ion detection efficiency.

An energy change spectrum which previously required an accumulation time of approximately 2 hours could be obtained in 90 seconds with the same statistical accuracy. This has enabled higher resolution measurements to be made which were previously precluded by the need for very long counting times. This improved experimental arrangement has enabled measurements of higher statistical accuracy combined with a factor of ~2 increase in energy resolution to be carried out.

Also the higher dissociation fractions resulted in a negligible contribution from channels involving undissociated hydrogen to our observed energy change spectrum for atomic hydrogen.

3. RESULTS AND DISCUSSION

3.1 Measurements for C^{2+} and N^{2+} in H

Energy change spectra for one electron capture by C^{2+} ions in H were obtained in the energy range 2-8 keV and for N^{2+} in H in the energy range 0.6-8 keV. Figure 1 shows a measured energy change spectrum for C^{2+} in H at 4 keV with vertical lines indicating the energy changes $\Delta T = \Delta E$ corresponding to each reaction channel and labelled according to the C^+ state formed.

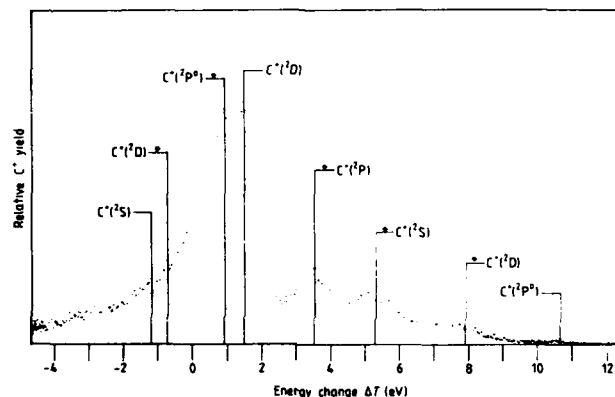


FIGURE 1

Energy change spectrum for one electron capture by 4 keV C^{2+} ions in H. An asterisk indicates channels involving metastable $C^{2+}(^3P^0)$ primary ions (see text).

Channels involving metastable $C^{2+}(^3P^0)$ ions (labelled with an asterisk) are clearly identified. Our results within the energy range 2-8 keV, indicate that between 60 and 65% of the total C^+ product yield arises from exothermic channels associated with $C^{2+}(^3P^0)$ metastable ions in the primary beam. The presence of this unknown metastable fraction precludes a determination of the individual cross sections for one electron capture by either C^{2+} metastable or ground state ions. However, theoretical studies of charge transfer in thermal energy $C^{2+}(^1S) - H(^1S)$ collisions by McCarroll and Valiron (10) and by Heil et al (11) predict that $C^{2+}(^2D)$ formation with an energy defect $\Delta E = 1.48$ eV provides the main contribution to the C^+ product yield. This is in accord with our observations for the ground state primary ions. This example clearly illustrates the experimental problems incurred when the primary ion beam contains an unknown fraction of metastables. It is possible to overcome these problems using the technique of Double Translational Spectroscopy as illustrated by Huber and Kahlert (12) for the case of $Ar^{2+}-He$ collisions.

Figure 2 shows typical energy change spectra for 2 and 6 keV N^{2+} ions in H together with a typical primary ion beam energy profile (FWHM 1.0 eV). Measurements in a subsidiary experiment using a beam attenuation technique indicated

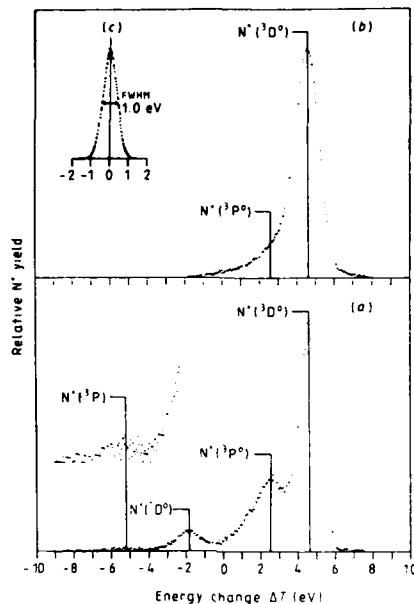
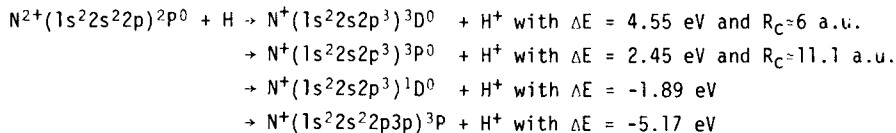


FIGURE 2

Energy change spectra for one electron capture by (a) 6 keV and (b) 2 keV N^{2+} ions in H. Inset (c) shows energy profile of primary N^{2+} ions.

that the N^{2+} primary ion beams were almost entirely in the $N^{2+}(^2P^0)$ ground state with only a few percent in the metastable $N^{2+}(^4P)$ state. Moreover, channels involving $N^{2+}(^4P)$ primary ions have similar energy defects to those for $N^{2+}(^2P^0)$ ground state primary ions and are thus expected to have similar cross sections. As a result our observed energy change spectra for N^{2+} ions in H can be treated as though the primary ion beam was entirely in the $N^{2+}(^2P^0)$ ground state.

The main reaction channels indicated by the vertical lines at $\Delta T \approx \Delta E$ in Fig. 2 are:-



A simple deconvolution technique (McCullough et al (2)) was used to determine the relative contributions of these four main collision channels to the total N^+ yield. Separate cross sections for capture into $^3D^0$, $^3P^0$, $^1D^0$ and 3P states of N^+ were obtained by reference to our measured total cross sections σ_{21} .

Figure 3 shows the state-selective cross sections and the measured total cross section σ_{21} together with the theoretical prediction by Dalgarno et al (13) using a molecular approach (Heil et al (14)). Theory predicts that capture into $N^+(^3D^0)$ provides the main contribution to σ_{21} . For low impact energies up to about 3 keV the agreement between theory and experiment is good. However, above 3 keV our measured values for the $N^+(^3D^0)$ product channel fall increasingly

below theory. Other reaction channels not accounted for by theory are seen to provide increasing contributions to the total cross section above about 3 keV.

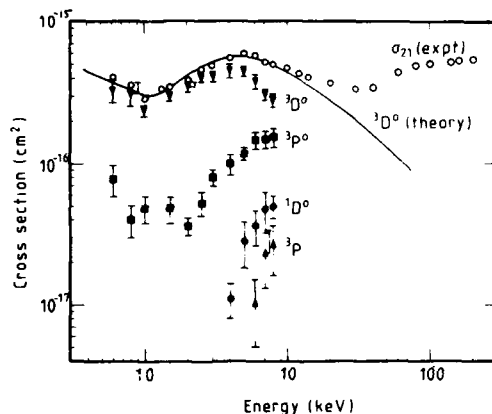


FIGURE 3

Cross sections for electron capture by N^{2+} ions in H. Present data: Open circles σ_{21} total one electron capture cross sections. Solid symbols cross sections for capture into states indicated. Theory: cross sections for capture into $N^*(^3D^0)$ from reference (13).

3.2 Measurements for C^{3+} and N^{3+} in H

Measurements for C^{3+} ions in H have been carried out for impact energies in the range 1.5-18 keV with an energy resolution of about 1.7 eV FWHM which is almost a factor of 2 better than our previous measurements (2). Figure 4 shows a comparison between the present and previous energy change spectrum for 15 keV C^{3+} in H, while the main features are in good agreement, the present measurements show clear evidence of additional channels in the energy change region below 2.15 eV previously attributed to a single collision channel involving $C^{2+}(2s3p)^3P^0$ production. As in our previous work the contribution to the observed energy spectrum from channels involving undissociated H_2 was negligible. C^{2+} product channels which may contribute to the observed energy change spectra (see Fig. 4) are:-

- (A) $C^{2+}(1s^22s3d)^1D - 0.02$ eV
- (B) $C^{2+}(1s^22s3d)^3D + 0.78$ eV with $R_C = 67.7$ a.u.
- (C) $C^{2+}(1s^22s3p)^3P^0 + 2.05$ eV with $R_C = 26.5$ a.u.
- (D) $C^{2+}(1s^22s3p)^1P^0 + 2.15$ eV with $R_C = 25.3$ a.u.
- (E) $C^{2+}(1s^22s3s)^1S + 3.61$ eV with $R_C = 15.1$ a.u.
- (F) $C^{2+}(1s^22s3s)^3S + 4.72$ eV with $R_C = 11.5$ a.u.
- (G) $C^{2+}(1s^22p^2)^1S + 11.63$ eV with $R_C = 4.7$ a.u.
- (H) $C^{2+}(1s^22p^2)^1D + 16.17$ eV with $R_C = 3.4$ a.u.

A simple deconvolution technique (2) was used to obtain relative cross sections for the resolvable channels. The separate contributions from G and H were determined together with the combined contributions from E + F, C + D and

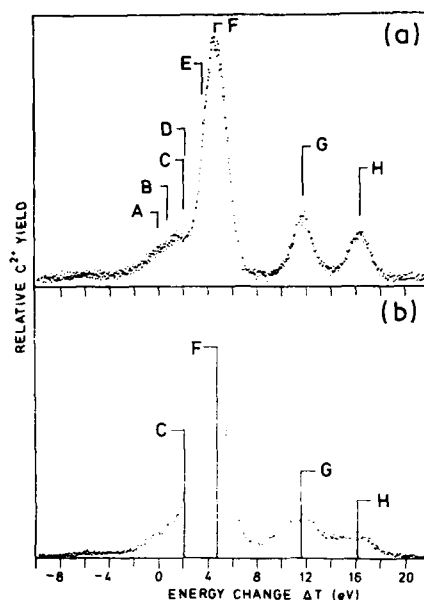


FIGURE 4

Energy change spectra for one electron capture by 15 keV C^{3+} in H using (a) position sensitive detector (b) particle multiplier from McCullough et al (2).

A + E. The symmetry of the peak centred on 4.72 eV indicates that the contribution from channel E is negligible. Cross sections for the formation of these channels were then determined (as in our previous work) by reference to the total one electron capture cross sections σ_{32} calculated by Bienstock et al (15) which agree well with experimental values over a wide range (see figure 5d).

Figure 5 shows the cross sections for channels F, G, H, (C + D) and (A + B) determined in this way. These can be seen to be in good agreement with our previous experimental values (2). Within the limits of the combined experimental uncertainties it can also be seen that, while there are some differences, there is a reasonable overall degree of accord in the energy range of overlap with the 9-60 keV cross sections measured recently by Ciric et al (5) using the PES technique. In our data uncertainties associated with the deconvolution procedure are shown where significant. Ciric et al (5) estimate uncertainties (not shown in figure 5) of approximately 30% due to systematic errors and approximately 10% due to random errors for the major channels with larger unspecified uncertainties for the minor channels.

Calculations by Bienstock et al (15) which are based on a full quantal quasi-molecular description predict strong adiabatic coupling for the collision channels F, G, C and H. Cross sections calculated for these channels are included in figure 5. For channels F and G, our measured cross sections are in good accord with the theoretical predictions but, beyond our energy limit, the PES cross sections fall increasingly below the theoretical values.

Our cross sections for channels C + D can be seen to be in reasonable agreement at the lower impact energies with the theoretical estimates for channel C

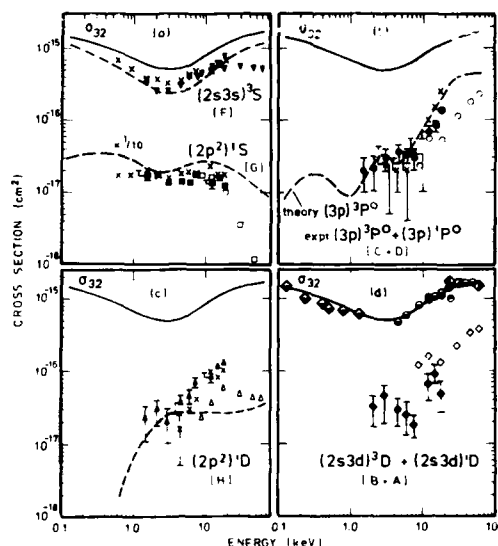


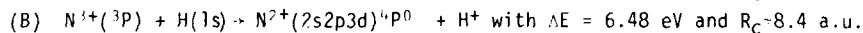
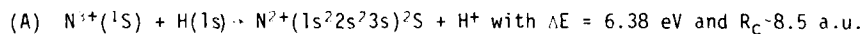
FIGURE 5

Cross sections for one electron capture by C^{+} ions in H leading to C^{2+} in specified states (channel A-H in text). Experiment: Solid symbols present results (4). Crosses, previous results (2). Open symbols PES results (5). Half shaded symbols experimental total cross sections (see ref (2)). Theory from ref (15): Solid curves σ_C , dashed curves cross sections for capture into states indicated.

alone. This suggests that the contribution from channel D is small. This is confirmed by the PES measurements which have a resolution high enough to separate the contributions from C and D. Their measurements show that below 12 keV the contribution from D is small, but becomes comparable with that from C at higher energies. Nevertheless, the PES cross sections for C + D at the higher impact energies can be seen to fall below the theoretical values for C alone.

In the case of N^{3+} -H collisions we have obtained energy change spectra for collision energies of 2.1-15 keV. The main peak corresponding to an energy change of 6.4 eV accounts for 90% of the N^{2+} at 2.1 keV and 62% at 15 keV. The smaller peak at about 3.3 eV contributes about 3% of the N^{2+} yield at 2.1 keV rising to about 16% at 15 keV. There are smaller contributions from numerous unresolved channels.

The interpretation of the energy change spectra in this case is complicated by the presence in the primary beam of an unknown fraction of metastable $N^{2+}(1s^2 2s 2p)^3P$ as well as ground state $N^{2+}(1s^2 2s^2)^1S$ ions for which there are numerous closely spaced collision channels. The main peak in the energy change spectra can be correlated with the two unresolved channels:-



Provided the cross sections for channels A and B (for which ΔE differs by only 0.1 eV) do not differ greatly, we might expect the N^{2+} yield associated with this peak to be approximately the same as if the N^{3+} ions were entirely in the ground state.

The smaller peak at about 3.3 eV seems likely to contain a significant contribution from the ground state primary ion channel.

(C) $N^{3+}(1S) + H(1s) \rightarrow N^{2+}(2s^2 3p)^2P^0 + H^+$ with $\Delta E = 3.35$ eV and $R_C \approx 16.2$ a.u.

but may also contain contributions from as many as eight channels involving metastable 3P primary ions.

Quantal calculations for electron capture by $N^{3+}(1S)$ ground state ions carried out by Bienstock et al (16) and by Gargaud and McCarroll (17) predict that channel A should account for at least 94% of the total N^{2+} yield over the present energy range. Our measurements, while confirming the dominance of channel A, indicate that channel C (not accounted for by theory) and other minor channels with energy defects in the range 8-22 eV, become increasingly important as the energy is increased from 2.1 to 15 keV.

CONCLUSIONS

Translational energy spectroscopy together with a furnace target arrangement has been successfully applied to state-selective studies of one electron capture processes for slow multiply charged ions in atomic hydrogen. Together with the PES technique, detailed experimental checks on theory can now be carried out to provide a better understanding of the nature of these processes. Work is now in progress to extend these measurements to higher charge states and other primary ion species of astrophysical and fusion interest.

ACKNOWLEDGEMENTS

This work was supported by an SERC grant. The author gratefully acknowledges the contributions of Professor H B Gilbody and F G Wilkie throughout these studies.

REFERENCES

- 1) R.W. McCullough, M. Lennon, F.G. Wilkie and H.B. Gilbody, J.Phys.B.16 (1983) L173.
- 2) R.W. McCullough, F.G. Wilkie and H.B. Gilbody, J.Phys.B.17 (1984) 1373.
- 3) F.G. Wilkie, F.B. Yousif, R.W. McCullough, J. Geddes and H.B. Gilbody, J. Phys. B.18 (1985), 475.
- 4) F.G. Wilkie, R.W. McCullough and H.B. Gilbody, J. Phys. B. submitted for publication.
- 5) D. Ciric, A. Brazuk, D. Dijkkamp, F.J. de Heer and H. Winter, J. Phys. B. (1985a) submitted for publication.
- 6) D. Ciric, D. Dijkkamp, E. Vlieg and F.J. de Heer, J. Phys. B.18 (1985b) L17.
- 7) D. Dijkkamp, D. Ciric and F.J. de Heer, Phys. Rev. Lett. 54 (1985) 1004.
- 8) M. Lennon, R.W. McCullough and H.B. Gilbody, J. Phys. B.16 (1983) 2191.
- 9) P.J. Hicks, S. Daviel, B. Wallbank and J. Comer, J. Phys. B.13 (1980) 713.
- 10) R. McCarroll and r. Valiron, Astro. Astrophys. 44 (1975) 465.
- 11) T.G. Heil, S.E. Butler and A. Dalgarno, Harvard Smithsonian Center for Astrophysics (1983) Preprint Series 1732.
- 12) B.A. Huber, H.J. Kahlert and K. Wiesemann, J. Phys. B.17 (1984) 2883.
- 13) A. Dalgarno (1984) Private communication.
- 14) T.G. Heil, D.E. Bulter and A. Dalgarno, Phys. Rev. A23 (1981) 1100.
- 15) S. Bienstock, T.G. Heil, C. Bottcher and A. Dalgarno, Phys. Rev. A25 (1982). 2850
- 16) S. Bienstock, T.G. Heil and A. Dalgarno, Phys. Rev. A29 (1984) 2239.
- 17) M. Gargaud and R. McCarroll, J. Phys. B.18 (1985) 463.

ELECTRON CAPTURE BY SLOW AND HIGHLY STRIPPED IODINE IONS FROM HELIUM ATOMS

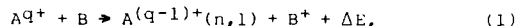
Masahiro KIMURA

Department of Physics, Osaka University Toyonaka, Osaka 560, Japan

One-electron capture by very highly stripped iodine ions, $Iq^+(q=10-41)$ from He atoms have been investigated at the collision energies of $0.75q - 2.25q$ keV. In contrast to low- q ions ($q < 10$), the total cross sections observed have shown no oscillatory behavior with q , but increase monotonously with the increase of q . Population distributions among electron capturing states in product ions have been also measured by translational energy spectroscopy, and it was found that the electrons are transferred into a few selective high Rydberg states. These experimental results have been compared with the multi-channel Landau-Zener (MCLZ) calculations.

1. INTRODUCTION

Final-state analysis has been one of the interesting and important subjects in the study of the electron capture by slow ($v < 1$ a.u.) and highly stripped ions from neutral atoms, and has been reviewed recently by several authors [1-3]. So far we, the NICE group in IPP Nagoya, have measured systematically final-state distributions by using energy spectroscopy as well as total cross sections for one electron capture processes in the slow collisions of highly stripped $Cq^+(3 \leq q \leq 6)$, $Nq^+(4 \leq q \leq 7)$, $Oq^+(5 \leq q \leq 8)$, $Fq^+(6 \leq q \leq 8)$, $Neq^+(7 \leq q \leq 9)$, $Sq^+(q=11,13)$ and $Krq^+(7 \leq q \leq 25)$ with He atoms;



where B is He atom, ΔE is the reaction energy, and n and l are the principal and the azimuthal quantum numbers, respectively. The results have been published in a series of our previous papers [4-15] and reviewed by Ohtani in XIII ICPEAC in Berlin together with related work made by other groups [1]. The main results obtained for the process (1) are summarized as follows.

1) When Aq^+ is highly stripped and q is less than 10, electron capture processes show very similar behavior for the same charge state q irrespectively of element species; for the same q -ions the electron is captured selectively into the same single n -state. The total cross sections oscillate with q particularly for low q -ions, and gradually increase with q . The classical one-electron model [16] predicts almost satisfactorily the capturing levels and explains the oscillatory behavior in the q -dependence of cross sections qualitatively, but fails in reproducing the total cross sections and in explaining the capture into more than two n -states as observed when $q > 9$.

2) In the system $Aq^+ + B$ several potential curves of the product states cross with that of the initial state. As for $q < 10$, the crossing distance leading to the observed final states, R_c , is limited to rather a narrow region called "reaction window" which is centered at around 3.5 \AA [11,17].

3) In the cases of partially but highly stripped $Krq^+(7 \leq q \leq 25)$, S^{11+} and S^{13+} ions, there always exist several crossings within the reaction window. The window seems to shift toward larger R_c in collisions of higher q -ions, and the total cross section increases monotonously with the increase of q .

In order to get better understanding of the process (1) over a wide range of q we have then applied to those systems a simpler and more straightforward method, which is based on the multichannel Landau-Zener model and obtained fairly good agreement with our measurements [13]. In the present work we extend our study to very highly stripped iodine ions to confirm the picture we have hitherto obtained for the process (1). This is a measurement with the highest primary charge states so far involved.

2. EXPERIMENTAL PROCEDURES AND RESULTS

The ion source NICE-1 employed in the present study is of EBIS (Electron Beam Ion Source) type. Successive ionizations by strongly confined electron beam of 2.4 keV produce highly stripped iodine ions. As shown in Fig.1, ions up to I^{42+} are clearly observed. Target He gas was introduced into a cell of 2 cm in length and the pressure inside the cell was less than 10^{-2} Pa. Total cross sections for charge state $q \leq 41$ have been determined from the initial growth rate of product ions. On the other hand, the energy gain spectra of the product ions were recorded through a 127°-electrostatic energy analyzer for charge state $q \leq 38$ in order to determine the final state distributions. Detailed descriptions of these methods have been given in Refs. 10 and 15.

The total cross sections were nearly independent of collision energies studied, and the cross sections obtained at 1.25q keV are shown in Fig.6 together with data for Kr^{q+} ions. Though collision energy and ionic species are different between them, all the data are smoothly connected with each other, and the total cross sections increase monotonously with the increase of q . Some typical energy gain spectra are shown in Figs. 3 and 4; the position of the main peak shifts toward large R_0 with the increase of q .

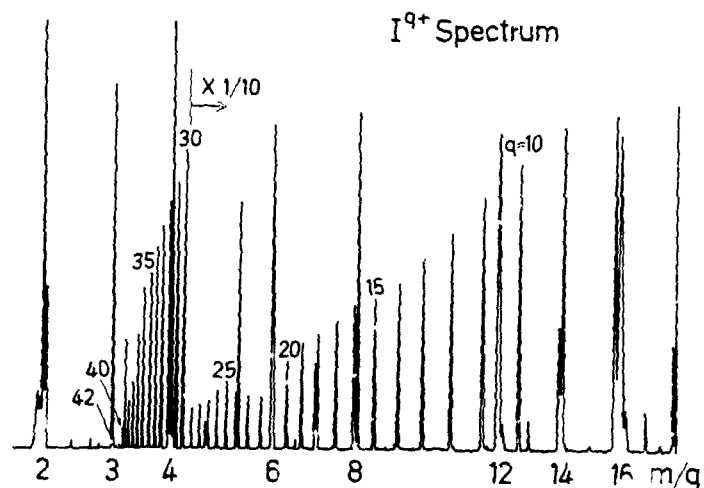


Fig.1 Charge state distribution of I^{q+} ions produced in NICE-1.

3. MULTICHANNEL LANDAU-ZENER (MCLZ) MODEL

As stated in Section 1 potential curves of several final channels cross with the initial channel. If we assume Coulomb interaction only in the product channels, the crossing distance R_C of the potential curves is expressed by

$$R_C(\text{\AA}) = 14.4(q-1)/\Delta E(\text{eV}). \quad (2)$$

Here ΔE is the difference between the ionization potentials of the excited product $A^{(q-1)+}$ ion and that of the B atom; different excited states of $A^{(q-1)+}(n,l)$ correspond to different R_C values. At these curve crossings strong coupling occurs, leading to the electron transfer.

When the cross section is calculated according to the Landau-Zener model, the important problem is to estimate the coupling matrix element H_{12} at the R_C . Analytical forms of H_{12} for one-electron capture processes by multicharged ions were proposed by several authors. After some trials, we have found that H_{12} , derived by Olson and Salop[18] shows a good agreement with a series of our previous measurements after reducing their expression by 40%. Thus the expression we adopted in the present calculation is

$$H_{12} = 0.6 \times 9.13q^{-1/2} \exp(-1.324\alpha q^{-1/2}R_C), \quad (\text{all in a.u.}) \quad (3)$$

where $\alpha = (2I_C)^{1/2}$ and I_C is the ionization potential of the target atom.

As far as a single potential curve crossing is concerned, the Landau-Zener cross section is fairly large only when the coupling matrix element H_{12} has a suitable value, i.e. neither too large nor too small value. As seen in Eq.(3), the H_{12} is sharply dependent on $R_C/q^{1/2}$. Therefore, when the charge state q becomes higher, the reaction proceeds with a large probability even at large internuclear distance. This is consistent with the trend found in our observations that for higher- q ions the favorable crossing distance shifts toward a larger value. Since the H_{12} depends very sensitively on R_C , the reaction proceeds through crossings located only in a rather narrow and restricted region; this situation leads to the existence of the reaction window. It should be noted, however, that such a reaction window has a definite meaning for collision systems with the similar q and the similar collision velocity. Having determined the coupling matrix element H_{12} at the crossing, one can calculate transition probability and then the partial cross section of a specified exit channel $A^{(q-1)+}(n,l) + \text{He}^+$. The general expression of the probability for a particular product ionic level when there are N possible reaction channels is given by Salop and Olson [19], assuming that the interference effect between the possible exit channels can be neglected. In the following sections, we calculate individual cross sections according to the multichannel Landau-Zener (MCLZ) model and compare them with the experimental results.

4. HIGHLY STRIPPED IONS OF C,N,O,F AND Ne

In Fig.2 are compared one-electron capture cross sections measured previously with MCLZ calculations for ions with relatively small atomic number as a function of crossing distance R_C [13]. For the widely split distribution of the capturing levels in the observed spectra, the cross sections are divided according to the observed peak intensity in the energy-gain ΔE spectra, and only data for stronger peaks are shown. The two dotted curves represent πR_C^2 and $1/2\pi R_C^2$, classical cross section. Most cross sections are less than $1/2\pi R_C^2$ because there exist no crossings very near to the center of the reaction window. In cases where several l states in a single n -state are degenerate as for H-like products, n level-crossings have been assumed in our MCLZ calculations. As seen, the agreement between our measured data and calculations is satisfactory except for $q=4$ and $q=6$ ions, which have the crossings at the left wing of the reaction

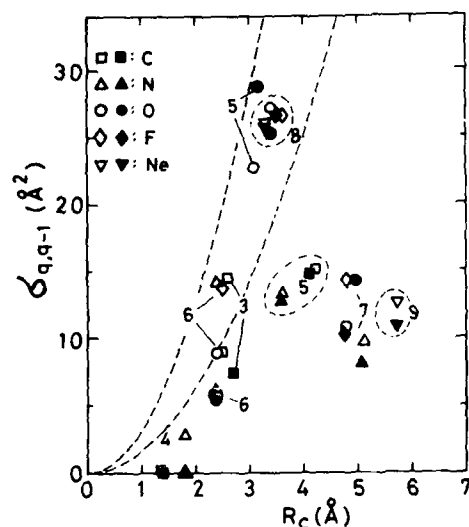


Fig.2
One-electron capture cross sections versus crossing distance R_c in $Aq^+ + \text{He}$ collisions at the energy of 600 eV/amu. Experimental data in Ref.5 (open symbols) are compared with the MCLZ calculations (black symbols). Projectile charge q is written beside the symbols. The upper and lower broken lines represent πR_c^2 and $1/2\pi R_c^2$, respectively.

window. In such small distances our simple assumption on the potential curves does not hold any more and also the scaled coupling matrix element H_{12} becomes inaccurate.

Another technique, photon spectroscopy, is also used to investigate the final-state analysis by de Heer and coworkers [20] for the collisions of highly stripped C, N, O and Ne ions with He. Their observations are consistent with ours.

5. IONS IN VERY HIGH CHARGE STATE: Kr^{q+} ($7 \leq q \leq 25$) AND I^{q+} ($10 \leq q \leq 41$)

We have no accurate knowledge about the energy levels of $\text{Kr}^{(q-1)+}$ and $\text{I}^{(q-1)+}$ observed in the present study. However, quite a large number of product channels should cross with the initial channel. Thus we make a further assumption; these ions have the hydrogen-like energy levels. This seems to be reasonable because an electron is captured predominantly into high Rydberg states for very high q -ions. Then they are assumed to have ionization potentials of $13.6q^2/n^{*2}$ (eV), where n^* is the effective principal quantum number. For simplicity we assume that each n^* -state consist of n^* sublevels, and that the coupling with the initial state is given by the expression (3). In Fig.3(a) are shown, as a typical example, the relevant potential curves and the observed translational energy spectrum of I^{29+} ions produced in $\text{I}^{30+} + \text{He}$ collision. For comparison is also shown in (b) the predicted spectrum, which was obtained from the convolution of the n^* -distributions calculated by using MCLZ model. It is noted here that states with the crossing distance R_c in the interval from 5 to 10 Å are populated; this R_c interval corresponds to $n^*=10-14$, and the window is far outside of those seen in collisions of ions with lower charge state $q < 10$. The MCLZ can well reproduce the spectrum except for the observed small peak at the wing of higher energy gain. The latter peak is perhaps due to the transfer

ionization, i.e. the collisional Auger process after double electron capture from He atom. Such a process is always observed when q is large enough and the targets are multielectron atoms [21].

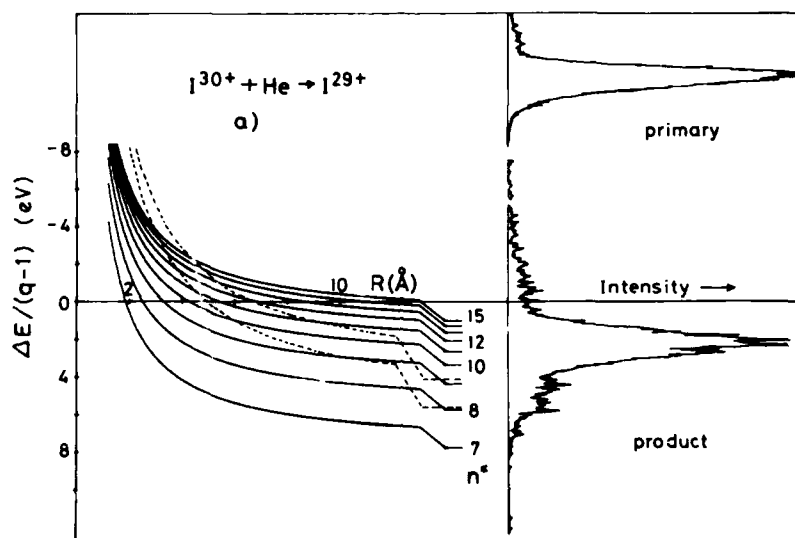
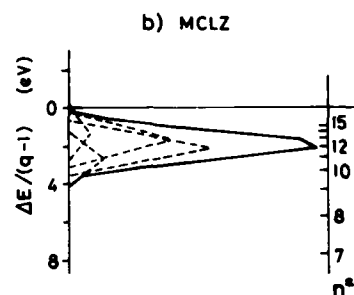


Fig.3

(a) Translational energy spectrum of I^{29+} and potential energy curves in the $I^{30+}+He$ system. The energy curves corresponding to double electron capture processes are shown by dotted curves. (b) Energy spectrum (solid curve) convoluted from the calculated partial cross sections (broken curves).



In Fig.4 are shown the observed(a) and calculated(b) translational energy spectra for $q=15, 25$ and 35 . The quantity $\Delta E/(q-1)$, where ΔE (in eV) is the energy gain observed at the main peak, becomes small when q increases. This means that the crossing distance $R_C=14.4(q-1)/\Delta E$ becomes large with the increase of q , reflecting that the coupling H_{12} is still strong enough for higher q even at larger internuclear distances. The relative shapes of the MCLZ spectra obtained by the same procedure as for the case of $q=30$ are again in satisfactory agreement with the present observations.

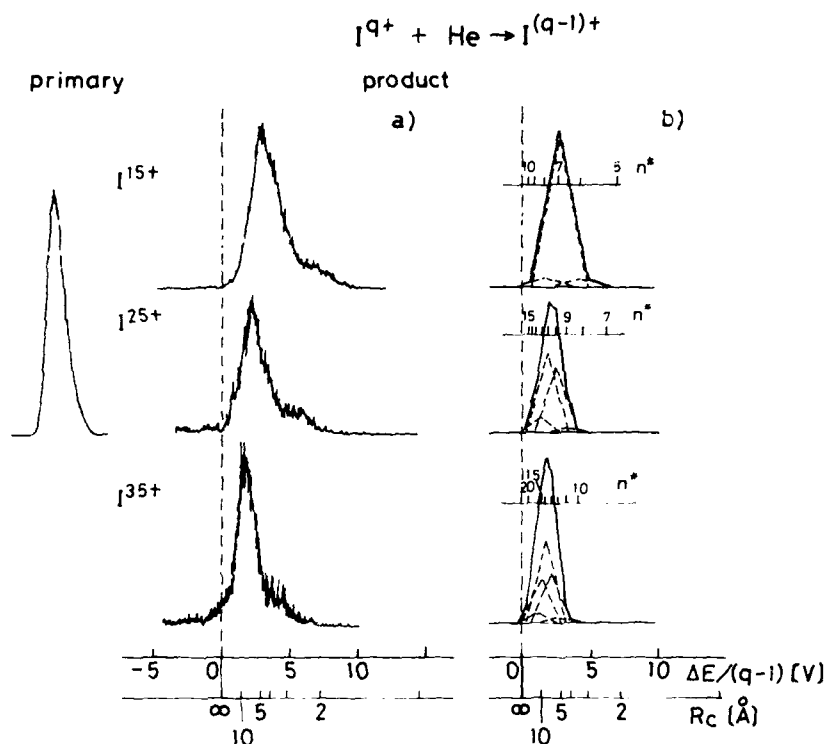


Fig.4 Translational energy spectra of $I^{(q-1)+}$ ions in the $I^{q+}+He$ systems at the collision energy of $1.25q$ keV are compared to the MCLZ predictions for a) $q=15$, b) $q=25$ and c) $q=35$.

{ n -distributions}

From the peak positions in energy gain spectra we have determined the capturing level n^* through

$$\Delta E = 13.6q^2/n^{*2} - I_t, \quad (4)$$

where I_t is the ionization potential of target atom. On the other hand, the MCLZ calculation gives the n^* -distribution; from this distribution we have also determined the weighted average of the capturing level n^* , which is compared with the experimental n^* in Fig.5. According to the classical model, the most probably populated final state energy level should asymptotically show $0.885q^{3/4}$ dependence for the He-target when q is very large[2]. Both our observations and calculations for n^* -distributions seem to follow this scaling. [Total cross sections]

Measured and calculated total cross sections for one-electron capture are shown in Fig.6 together with the data for Kr^{q+} . They agree well with the scaled form of $q^{1.17}$, which was derived by Müller and Salzborn [22] and shown in broken straight line. The MCLZ somewhat overestimates the cross sections for higher q ions; this is caused probably by the present simple assumptions.

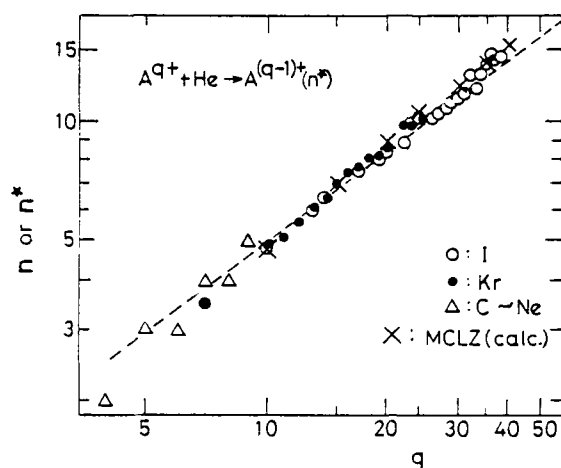


Fig.5

Effective principal quantum number n^* of the electron capturing level as a function of q . \circ , experimental and \times , calculated results in $\text{I}^{q+} + \text{He}$ collisions. \bullet , $\text{Kr}^{q+} + \text{He}$ [12]; Δ , $\text{C}^{q+} + \text{Ne}$ [6,8,10 and 11] collisions. The broken line represents the asymptotic form derived from the classical model.

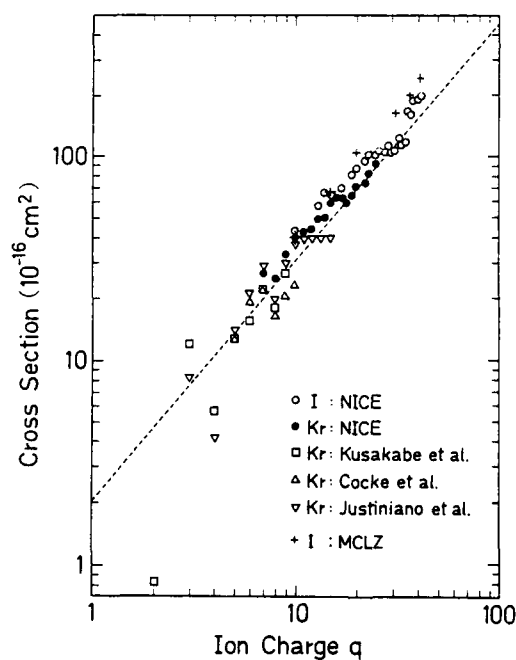


Fig.6

Observed and calculated total one-electron capture cross sections as a function of charge q in I^{q+} and $\text{Kr}^{q+} + \text{He}$ collisions. \circ , in $\text{I}^{q+} + \text{He}$ at the energy of $1.25q \text{ keV}$; $+$, the MCLZ calculation; ---, empirical formula [22]. Symbols \bullet [12], Δ [23], ∇ [24] and \square [25] show $\text{Kr}^{q+} + \text{He}$ data.

6. CONCLUSIONS

In the present work we have investigated one-electron capture processes in slow collisions of very highly charged ions with He atoms. The measured total cross sections and the distributions over the excited energy states of product ions have been compared with the calculations of the multichannel Landau-Zener (MCLZ) model. It is found that the present MCLZ calculation reproduces the observations fairly well in spite of its simplicity and rather crude assumptions. Both total cross sections and dominantly populated ionic levels can be well fitted by simple scaling expressions as a function of the initial charge q . These conclusions should be applicable if the projectiles are highly charged ions of any elements. When H-atoms are used as target, however, the cross sections will become larger than the corresponding ones with He target owing to the lower ionization potential of H than He.

ACKNOWLEDGMENT

I would like to thank all the members of NICE group for giving me the opportunity to participate in this collaboration work. I deeply appreciate Professor Iwai's careful reading of this manuscript.

REFERENCES

- 1) S. Ohtani, in "Electronic and Atomic Collisions" eds. J. Eichler, I.V. Hertel and N. Stolterfoht (North Holland, Amsterdam, 1984) p.353.
- 2) R.K. Janev and H. Winter, Phys. Reports 117 (1985) 265.
- 3) F.J. de Heer, in "Atomic and Molecular Physics of Controlled Thermonuclear Fusion" eds. C.J. Joachain and D.E. Post (Plenum Press, 1982) p.265.
- 4) Y. Kaneko et al., in "Physics of Electronic and Atomic Collisions" ed. S. Datz (North Holland, 1982) p.697.
- 5) T. Iwai et al., Phys. Rev. A 26 (1982) 105.
- 6) S. Ohtani et al., J. Phys. B 15 (1982) L533.
- 7) S. Tsurubuchi et al., J. Phys. B 15 (1982) L733.
- 8) M. Kimura et al., J. Phys. B 15 (1982) L851.
- 9) A. Matsumoto et al., J. Phys. Soc. Japan, 52 (1983) 329.
- 10) K. Okuno et al., Phys. Rev. A28 (1983) 127.
- 11) H. Tawara et al., Phys. Rev. A29 (1984) 1529.
- 12) T. Iwai et al., J. Phys. B17 (1984) L95.
- 13) M. Kimura et al., J. Phys. Soc. Japan, 53 (1984) 2224.
- 14) N. Kobayashi et al., J. Phys. Soc. Japan, 53 (1984) 3736.
- 15) H. Tawara et al., J. Phys. B18 (1985) 337.
- 16) H. Ryufuku, K. Sasaki and T. Watanabe, Phys. Rev. A21 (1980) 745.
- 17) B.A. Huber, Phys. Scr. T3 (1983) 96.
- 18) R.E. Olson and A. Salop, Phys. Rev. A14 (1976) 579.
- 19) A. Salop and R.E. Olson, Phys. Rev. A13 (1976) 1312.
- 20) D. Dijkkamp, doctoral thesis (1985) and references therein.
- 21) A. Müller, W. Groh and E. Salzborn, in "Electronic and Atomic Collisions" eds. J. Eichler, I.V. Hertel and N. Stolterfoht (North Holland, Amsterdam, 1984) p.371.
- 22) A. Müller and E. Salzborn, Phys. Lett. 62A (1977) 391.
- 23) C.L. Cocke, R. Du Bois, T.J. Gray and E. Justiano, IEEE Trans. Nucl. Sci. NS-28 (1981) 1032.
- 24) E. Justiano, C.L. Cocke, T.J. Gray, R. Du Bois, C. Can and W. Waggoner, Phys. Rev. A29 (1984) 1088.
- 25) T. Kusakabe, T. Hanaki, N. Nagai, T. Horiguchi, I. Konomi and M. Sakisaka, Phys. Scr. T3 (1983) 191.

EXPANDING OVERCOOLED LASER PLASMA AS A PROMISING MEDIUM FOR ATOMIC COLLISION STUDIES

S. V. BOBASHEV and L. A. SHMAENOK

A. F. Ioffe Physico-technical Institute, Academy of Sciences of the USSR,
Leningrad 194021, USSR

1. INTRODUCTION

The advent of high power lasers has initiated a new branch of modern physics, namely, the physics of the laser-produced plasma. By focussing pulsed laser radiation onto the surface of a solid one succeeds in creating power densities in the range 10^{10} - 10^{18} W/cm² which corresponds to an energy release for target atoms considerably in excess of the ionization potential. Under these conditions a hot high density plasma possessing unique properties is formed at the target surface.

The laser-produced plasma (LPP) has become a subject of numerous theoretical and experimental studies.

A strong impetus to LPP studies has been given primarily by the inertial fusion program, more specifically by the development and production of pulsed high-power laser systems for the heating and confinement of fusion targets (1).

Present-day machines for the experimental investigation of LPPs operate over a wide range of major parameters, such as laser frequency, laser pulse duration, and power density focussed onto the target. The plasma is produced by the radiation at the fundamental frequency or its harmonics of pulsed Nd lasers (wavelength $\lambda = 1.06 \mu\text{m}$), CO₂ lasers ($\lambda = 10.3 \mu\text{m}$), and iodine lasers ($\lambda = 1.3 \mu\text{m}$). Such machines are capable of producing radiation in pulses with a duration τ ranging from 10^{-11} to 10^{-7} s and a power density $q \sim 10^{10} - 10^{18}$ W/cm² when focussed onto a spot with diameter $d \sim 10 - 1000 \mu\text{m}$.

High temperature plasma with a density on the order or that of a solid persists during the action of the laser pulse. During this stage of its existence the LPP is an intense source of multicharged ions and emission in the X-ray, soft X-ray and VUV regions (2,3,4).

The heating stage is followed by the expansion of the LPP in vacuum driven by gas kinetic pressure. This stage produces favorable conditions for stimulated emission in the X-ray and VUV regions (5,6,7,8,9).

In the present report we are going to confine ourselves to discussing a limited range of problems related to the possibility of using LPPs in atomic collision experiments.

2. PARAMETERS OF THE LPP EXPANDING IN VACUUM

Consider the major stages in the expansion in vacuum of a plasma produced on the surface of a solid by laser radiation of moderate characteristics: $q \sim 10^{10} - 10^{14}$ W/cm², $\tau \sim 1 - 100$ ns, $d \sim 10 - 500 \mu\text{m}$. We have at present a

satisfactory consistent picture of the physical processes and phenomena controlling the behavior of such an LPP in different stages of its evolution.

One may conveniently isolate three stages in the evolution of an LPP as it expands in vacuum. The first stage, or the hot core includes the formation of the plasma and its development during the laser pulse; the corona where the various relaxation processes occur after the termination of the laser pulse with comparable rates; and, finally, the distant zone where the plasma cloud expands freely.

The hot core is formed and exists during the action of the laser pulse (τ). In the initial stage of the radiation interaction with matter a high-frequency breakdown of the target vapor occurs producing a plasma at the target surface. The heating radiation is strongly absorbed by the plasma electrons via the inverse Bremsstrahlung effect in the region of critical electron density N_{ec} where the frequency of Langmuir oscillations is close to that of the laser emission (for the Nd laser frequency, $N_{ec} \approx 10^{21} \text{ cm}^{-3}$, for CO_2 laser $N_{ec} = 10^{19} \text{ cm}^{-3}$). The energy absorbed in time penetrates into the target to a depth on the order of the focal spot d by electronic heat conduction. The hot core plasma of size $R_0 \sim d$ is characterized by a high electron and ion density $N_e \sim N_i \sim 10^{21} - 10^{22} \text{ cm}^{-3}$, high temperature $T_e \sim 1 \text{ keV}$, and high mean ionic charge $\bar{Z} \gg 1$.

While the processes of ionization and excitation responsible for the ion composition of the LPP core depend essentially on the incident radiation wavelength, target material and power density, the overall features of the plasma core formation remain largely the same within a broad range of initial conditions.

In the hot core region the plasma is overheated with the ionization not in equilibrium since the rates of excitation and ionization exceed by far those of the recombination processes.

Internal gas kinetic pressure and electrostatic acceleration drive the plasma to expand in vacuum with the result that the electron density drops dramatically, the thermal energy of the electrons becoming converted into the translational energy of the plasma cloud. In the corona region, at a distance of R_c from the target ($R_c \gg R_0$), the plasma is transparent to the laser radiation, with recombination processes playing the major role. The corona plasma has a high particle density, $N_c \sim 10^{20} - 10^{19} \text{ cm}^{-3}$, and a comparatively low temperature, $T_e \sim 100 - 10 \text{ eV}$. The plasma corona region is studied intensively both from the standpoint of diagnostics of the fusion target heating and compression and with a view of attaining stimulated emission on transitions of multicharged ions.

The relaxation processes in a rapidly expanding plasma differ essentially in behavior from those in the quasisteady state. One of the effects specific for the LPP is the freezing of the ionization state of expanding plasma. This phenomenon manifests itself in an anomalously high content of multicharged ions observed in the plasma at large distances from the target ($R \gg R_c$). The freezing originates from the fact that part of the ions undergoing collective acceleration in the hot core pass through the region of intense relaxation processes in the corona too fast for a noticeable recombination to occur. This conclusion is reinforced by numerous experiments which revealed strong fluxes of multicharged ions of the target material at distances $R \gtrsim 1 \text{ m}$ from the target.

The distant zone of LPP expansion covering the distances from the target $R_c \ll R \gtrsim 1 \text{ cm}$ has not until recently attracted much interest on the part of experiments. Estimates suggest that in this region of space the expanding LPP

should have a low temperature, $T_e < 1$ eV, density $N_e \sim 10^{11} - 10^{13} \text{ cm}^{-3}$, and a comparatively high concentration of ions of different ionization state. Spectroscopic studies (10) have confirmed the idea that the LPP reaches the distant zone in a highly ionized state far from recombination equilibrium. The major relaxation process here is three-particle recombination of ions with slow electrons. This results in a heating of the electron component which reduces the recombination rate, and in decreasing ionization state of the expanding plasma.

In our opinion, this combination of parameters makes the LPP in the distant zone a promising tool for beam-plasma experiments aimed at studying the fundamental processes of electron and photon interaction with multicharged ions.

3. STUDIES OF LPP IN THE DISTANT ZONE

The available information on the physical processes occurring in the distant zone of LPP expansion draws upon experimental data on the energy and charge state spectra of ions at large distances from the target ($R > 1$ m) obtained by time-of-flight mass spectrometry, as well as on theoretical calculations performed to simulate the experimentally measured spectra.

In some studies (11-14) the plasma was produced with a Nd laser with pulses $\tau \sim 10 - 30$ ns long, focussed power density $q \sim 10^{10} - 10^{13} \text{ W/cm}^2$ and spot diameter $d \sim 100 - 150 \mu\text{m}$. In other experiments (15-18) pulsed CO_2 laser radiation was used with 100 ns, power density $q \sim 10^{10} - 10^{12} \text{ W/cm}^2$ and spot diameter $d \sim 150 - 1000 \mu\text{m}$. Despite the marked differences in the experimental conditions, the major qualitative features in the behavior of the ion component were found to be close.

1. The angular distribution of the ions is symmetric with respect to the normal to the target plane. For a fixed value of q the ion expansion cone angle decreases with increasing charge Z becoming $20 - 30^\circ$ for $Z = Z_{\text{max}}$ (Fig. 1).

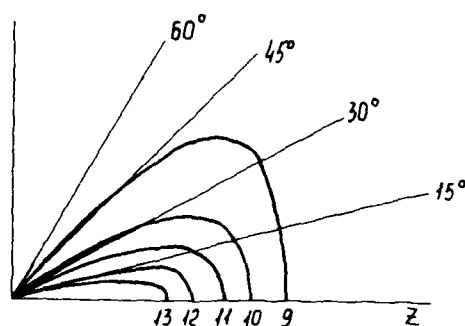


FIGURE 1

Angular distribution of Al ions with different Z for $q \sim 3 \times 10^{13} \text{ W/cm}^2$ (Nd laser).

2. The maximum charge state of the LPP ions was universally observed to grow with increasing q . Figs. 2 and 3 display the experimental and theoretical values of power density at which ions of given charge state appear for targets of carbon and tungsten.

The observed features are usually explained in the context of the coronal model of ionization equilibrium which can obtain in the core at $T_e \sim 100$ eV. The theoretical estimates of the threshold values of q presented in Fig. 3 were derived for the case of coronal equilibrium taking into account dielectronic recombination.

3. Another common feature of the expanding LPPs is the shape of the ion energy spectra. Fig. 4 shows a typical energy spectrum of cobalt ions moving perpendicular to the target plane. All energy spectra reveal a growth of mean ion energy with increasing charge state and a dramatic drop in the number of

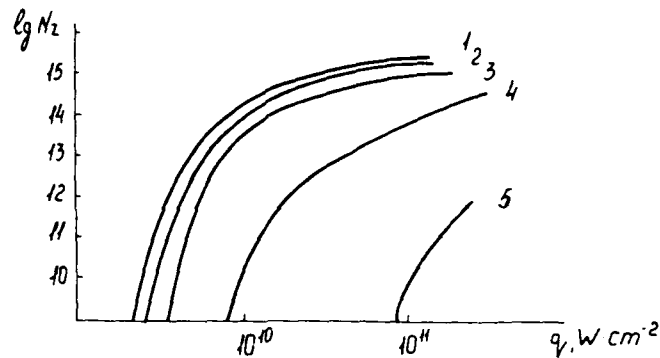


FIGURE 2

Total number of C ions ($Z=1-5$) vs. q for Nd laser

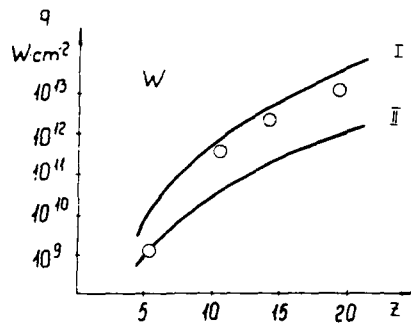


FIGURE 3

Threshold value of q vs. Z for W.
I: calculation including dielectronic recombination; II: coronal model calculation; O: experiment with Nd laser.

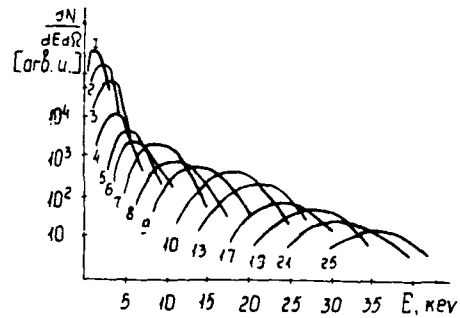


FIGURE 4

Co ion energy distribution for Z from 1 to 25. Nd laser, $q \sim 10^{13}$ W/cm².

ions with increasing Z . For the Nd laser the ratio of highly- to low-charged ions varies within 10^{-2} - 10^{-5} , a typical relation being shown in Fig. 5 in an example of cobalt ions (12). For the CO_2 laser the fraction of highly charged ions is somewhat greater, 10^{-1} to 10^{-2} .

Such a shape of the energy spectrum is accounted for in the context of the hydrodynamic model of acceleration by recombination in the course of plasma expansion (19). The ions at the front of the plasma cloud are accelerated most efficiently and travel with the highest velocities which favors efficient freezing. On the other hand, the ions that were initially in the interior of the plasma are accelerated to a much lesser extent, reside for a longer time within the hot core and recombine at a higher rate. In the context of this model, the highly charged ions observed in the distant zone were initially of dominant charge state, propagated at the front of the plasma cloud and escaped practically without recombination. The hydrodynamic model of plasma cloud expansion including possible mechanisms of recombination in the hot core (20) was used to evaluate the corresponding number of highly charged ions (21). Experimental data were shown to be in a good agreement with the calculations taking into account dielectronic recombination in the hot core and corona as well as photo- and three-particle recombination.

Studies of the energy and charge state spectra of the LPP ions at large distances from the target were analyzed (21-25) assuming three-particle recombination to be predominant in the relaxation kinetics of the plasma in the distant zone. Three-particle recombination of a highly ionized plasma consists in the ion's capturing a free electron, the corresponding binding energy being imparted to another free electron. The mean change of the electron energy in a three-body collision is comparable with the electron temperature

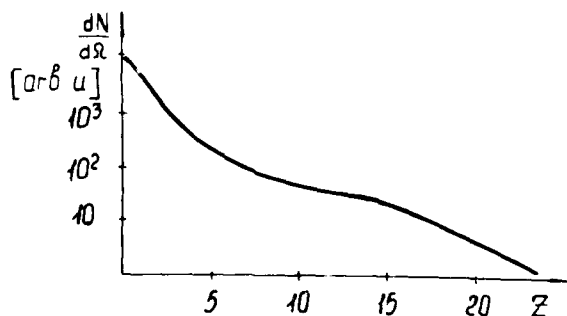


FIGURE 5

Co ion distribution in charge state Z . Nd laser, $q \sim 10^{13}$ W/cm².

$$n_0 = Z \left(\frac{10^{18}}{N_e} \right)^{1/7} \left(\frac{r_e}{Z R_v} \right)^{1/14}, \quad (1)$$

$$e \cdot e + Z \rightarrow (Z-1) + e$$

Diagram illustrating the energy levels and transitions for a hydrogen atom. The energy levels are labeled $n=1, 2, 3, 4$. Transitions from $n=4$ to $n=1, 2, 3$ are shown, with corresponding photon energies $\hbar\omega_1, \hbar\omega_2, \hbar\omega_3, \hbar\omega_4$. The total energy of the electron is indicated as T_e (eV).

FIGURE 6
Schematic diagram of three-particle recombination.

The transfer of electrons over excited ion states may be considered (27) as diffusion in a quantum number space. Solving the problem of electron flow towards negative energies yields the following expression for the three-particle recombination coefficient α :

$$\alpha = N_e \frac{4\sqrt{2}\pi^{3/2}}{g} \cdot \frac{e^{10} Z^3 \Lambda}{m^{1/2} (T_e)^{9/2}}, \quad (2)$$

where $\Lambda = \ln Z^2 + 1$, Z is the ionic charge m is the electron mass, T_e is the electron temperature. As a result of a strong temperature dependence, this recombination mechanism in a cooling expanding plasma becomes predominant and remains essential throughout the expansion stage, thereby governing, in particular, the charge state composition of LPP in the distant zone. The LPP temperature in the distant zone, in its turn, should depend markedly on the heating involved in recombination. Therefore the theoretically calculated charge state spectra of the LPP should depend substantially on the correct inclusion of the recombination heating. The energy E^* transferred to plasma electrons in each recombination event may be calculated by the expression (25)

$$E^* = 1.6 \cdot 10^{-14} \cdot Z^{2/3} \cdot N_e^{1/6} \cdot T_e^{1/12}. \quad (3)$$

Eq. (3) was derived assuming a gradual electron transfer down the excited states which does not take into account transitions to deep levels. This results in an overevaluation of the heating. Inclusion of transitions to all levels in accordance with the cascade decay matrix of an excited state with a given n yields the following expression for E^* (28):

$$E^* = 7 \cdot 10^{-22} \cdot N_e^{2/3} \cdot Z^{-2/3} \cdot T_e^{-1}. \quad (4)$$

To compare calculations by Eq. (4) with observations, energy and charge state spectra of LPP ions in the distant zone were calculated in the hydrodynamic approximation for the typical experimental conditions (1,29,30). One of the studies (29) involved a plasma produced by heating with a CO_2 laser beam of supersonic gas jets with a thickness about equal to the focal spot diameter $d \sim 1$ mm. Fig. 7 presents the calculations (28) and collector current measurements performed at a distance of 325 cm from the target (29) as a plot of mean plasma ion charge vs. expansion velocity. The width of the shaded bands reflects the dependence of the numerical solution on the choice of initial experimental conditions. The best fit was found when using Eq. (4) for the recombination heating.

Similar data are displayed in Fig. 8 for spherical targets heated by a Nd laser in the conditions typical for the Kalmar machine (1,30) with polystyrene targets. The plasma temperature in these experiments was $0.5 \text{ keV} \pm 20\%$. The LPP charge state composition was studied with an electrostatic mass spectrometer, the time-of-flight base being 3 m. In the calculations, the charge state of the carbon ions in the initial stage of expansion was varied from 5 to 6, and the initial temperature in the hot core, from 0.4 to 0.6 keV.

As seen in Figs. 7 and 8, evaluation of the recombination heating by Eq. (4) yields a satisfactory agreement with experiment.

The first direct measurements of LPP parameters in the distant zone were carried out spectroscopically (10). Direct and reliable determination of the major parameters and radiative characteristics of the LPP in this zone is a necessary prerequisite when preparing a collision experiment.

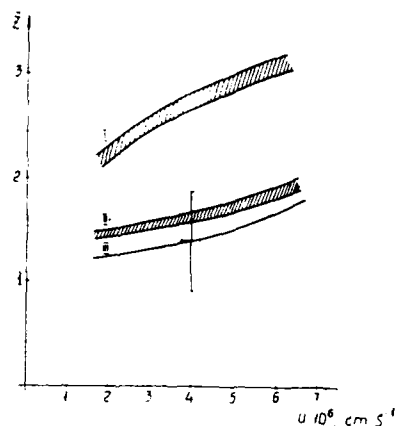


FIGURE 7

Mean ion charge state Z for nitrogen target vs. ion velocity. I-calculation by Eq. (3); II-calculation by Eq. (4); III-experiment (29).

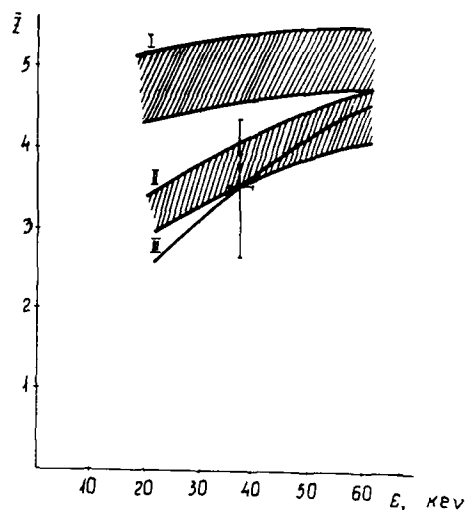


FIGURE 8

Mean charge state Z for carbon ions. I-calculation by Eq. (3); II-calculation by Eq. (4); III-experiment (1,30).

A study was made (10) of VUV emission from a laser-produced beryllium plasma far from the target ($R > 1$ cm). This study provided a means for developing VUV spectroscopy of plasmas in the spatial region which is still little explored by experimentalists.

The VUV emission spectra of the LPP were investigated on an installation shown schematically in Fig. 9. The radiation of a Nd laser was focussed onto a plane Be target in a vacuum chamber. At a laser pulse energy $Q = 10 - 50$ J and pulse duration of 50 ns the power density in the focal spot on the target was $q \sim 10^{12} - 10^{13}$ W/cm². The pressure in the chamber did not exceed 2×10^{-6} mm Hg. The geometry of plasma expansion in the vacuum chamber was controlled by a collimator system which defined a clear boundary of the plasma cloud and determined the expansion angle (45°) in the horizontal plane. The ion density in the plasma was measured by means of two adjustable collectors set at different distances from the target.

The emission spectra of the LPP were measured at distances $R_1 = 5$ cm, $R_2 = 10$ cm, and $R_3 = 20$ cm from the target with an axial spatial resolution not worse than 4%. The most detailed spectra were obtained at R_1 and R_2 , while the strongest lines could be reliably detected at R_3 as well. Within the range $R = 5 - 10$ cm the pattern of the spectrum was found to be practically independent of R , the relative line intensities remaining within the measurement precision (30%).

Fig. 10 presents a 25-80 nm plasma emission spectrum typical for the region $R = 5 - 10$ cm. The spectrum contains singlet and triplet lines of helium-like

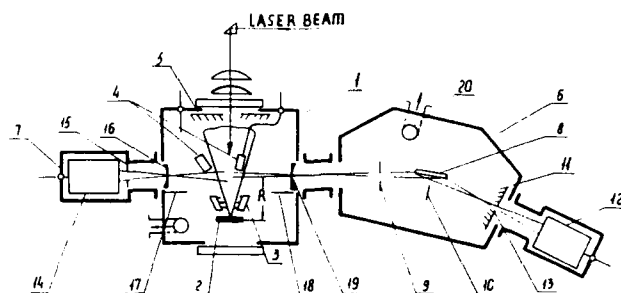


FIGURE 9

Schematic of experimental installation (10). 1. LLP expansion chamber; 2. Target; 3. Plasma collimators; 4. Ion collectors; 5. Ion trap; 6. Monochromator; 7. Soft X-ray monitor; 8. Diffraction grating; 9. Aperture diaphragm; 10. Screen; 11. Radiation trap; 12, 14. SEM's; 13. Exit slit; 15. Diaphragm with filter; 16. Entrance slit; 17, 18. Screens against scattered ions; 19. Monochromator entrance slit; 20. Pumping.

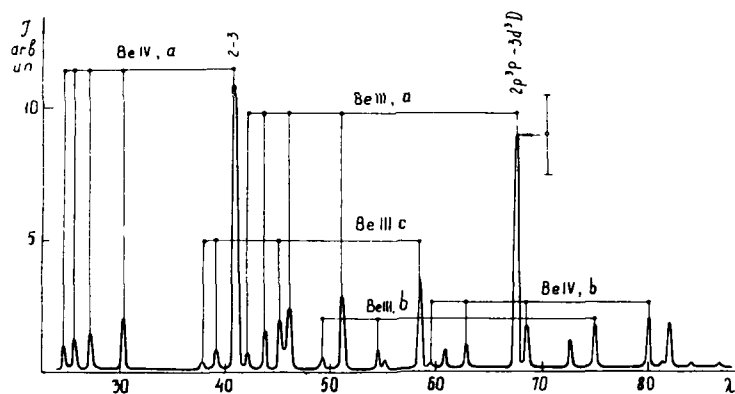


FIGURE 10

LLP emission spectrum in the distant zone for Be plasma.

Be IV, a - n	2 transitions (n = 3 - 7)
Be IV, b - n	3 transitions (n = 5 - 8)
Be III, a - nd^3D	$2p^3P$ transitions (n = 3 - 7)
Be III, b - nd^1D	$2p^1P$ transitions (n = 3 - 5)
Be III, c - np^3P	$2s^3S$ transitions (n = 3, 4, 6, 7).

Be ions (Be III) produced in transitions between the levels with $n = 3 - 7$ and $n = 2$, and lines of the hydrogen-like Be ions (Be IV) corresponding to the hydrogen series $n - 2$ ($n = 3 - 7$) and $n - 3$ ($n = 4 - 6$). Since within the measurement accuracy (30%) the relative intensities do not depend on R, the

spectrum and Tables 1 and 2 contain values for the ions Be^{3+} and Be^{2+} averaged over the region 5-10 cm and normalized to the intensity of the strongest line of the corresponding ions.

The plasma ion density in the region of interest was measured by means of ion collectors permitting separation of the ionic and electronic components of the plasma. The time resolved collector measurements revealed that in the region $R=5-10$ cm the peak densities vary within $10^{12} - 10^{13} \text{ cm}^{-3}$.

A series of control experiments demonstrated that the detected emission does indeed appear in the plasma and is not connected with the excitation involved in the scattering of plasma ions from the walls of the installation or in the interaction of these ions with residual gas.

The relative intensities $I_{nn'}$ were used to calculate the population of the Be^{3+} excited states with principal quantum numbers $n = 3 - 7$. In these calculations the available radiative transition probabilities for hydrogen-like ions were employed (26). The relative populations N_n/N_3 for Be^{3+} are presented in Table 3 whence it is seen that they differ strongly from Boltzmann's values for $T_e < 1 \text{ eV}$.

To evaluate the mean excited ion density in the region of observation, absolute intensities $J \text{ (cm}^{-3} \text{ s}^{-1}\text{)}$ of the strongest Be^{2+} and Be^{3+} lines were measured as functions of R . The results are shown in Table 4, the absolute values of J being estimated by us to within a factor of five.

TABLE 1

Be IV	$I_{nn'}$	λ
transition	arb. u.	nm
2-3	100	41.0
2-4	23	30.3
2-5	14	27.1
2-6	15	25.6
2-7	11	24.8
3-5	18	80.1
3-6	16	68.3
3-7	8	62.7
3-8	3	59.6

TABLE 2

Be III	$I_{nn'}$	λ
transition	arb. u.	nm
$2p^3p^0 - 3d^30$	100	67.5
2p - 4d	32	50.9
2p - 5d	28	45.7
2p - 6d	18	43.4
2p - 7d	8	42.0
$2s^3s - 3p^3p^0$	39	58.2
2s - 4p	22	45.1
2s - 6p	11	38.8
2s - 7p	8	37.7
$2p^3p^0 - 3s^3s$	13	72.5
$2p^1p^0 - 3d^1D$	20	74.6
2p - 4d	6	54.6
2p - 5d	6	48.9

TABLE 3

n	N_n/N_3	
	exper	theor
3	1.0	1.0
4	1.8	2.2
5	3.1	4.3
6	8.0	7.6
7	11.0	12.3

TABLE 4

R cm	$J, \text{cm}^{-3} \cdot \text{s}^{-1}$	
	Be III, $2p^3p - 3d^3D$	Be IV, 2-3
5	$1.3 \cdot 10^{18}$	$1.5 \cdot 10^{18}$
10	$1.1 \cdot 10^{17}$	$1.5 \cdot 10^{17}$
20	$1.1 \cdot 10^{15}$	$2.2 \cdot 10^{15}$

The analysis of the experimental data consisted primarily in considering the fundamental atomic processes which, in principle could produce, in an LPP at sufficiently large distances from the target, excited Be^{2+} and Be^{3+} ions with populations differing essentially from the Boltzmann distribution. These processes included three-particle and photorecombination and ion-ion collisions. The absence of any contribution from the latter processes in the distant zone becomes evident from an evaluation of the maximum energy of interaction E_{ij} between two ions, one of which escaping from the acceleration zone near the target ($R_0 \sim 100 \mu\text{m}$) and trailing behind the other by the time of the laser pulse duration τ overtakes it at a distance R . At the velocities v and laser pulse duration τ typical for the experiment ($v \sim 10^7 \text{ cm/s}$, $R \sim 10 \text{ cm}$, $\tau \sim 10^{-7} \text{ s}$), E_{ij} does not exceed a few eV which is far from being sufficient to produce excitation of the Be ions in inelastic collisions.

Turning now to a discussion of the recombination processes, we note that the rate of radiative recombination becomes noticeably less than that of three-particle recombination for $T_e \sim 10^{-14} Z N_e$ (6) which in our conditions is equivalent to $T_e \sim 0.5 \text{ eV}$. It is also known (26) that photorecombination occurs predominantly to the ground state, its rate dropping drastically with increasing principal quantum number n , which does not agree with the experimentally observed growth of population with increasing n (see Table 3).

Assuming three particle recombination to provide a major contribution to the observed plasma spectrum, we have calculated the populations of Be^{3+} excited states by the expression

$$N_n = I_c W_n^{-1} C(n_0, n), \quad (5)$$

where W_n is the radiative decay probability of a level with principal quantum number n , $C(n_0, n)$ is the element of the cascade matrix equal to the total relative probability of radiative decay from level n_0 to level n ($n_0 > n$), and $I_c = \alpha N_Z N_e^2$ is the rate of three-particle recombination for an ion of charge Z with the formation of an ion of charge $Z-1$, N_Z is the density of ions of charge Z , N_e is the electron density.

The calculations have revealed that variation of n_0 from 15 to $n_0 \rightarrow \infty$ does not produce any noticeable effect on the relative populations, the calculated values of N_n in Table 3 having been obtained for $n_0 \rightarrow \infty$. The good agreement between the calculated and measured values of N_n argues for the assumption of

the detected emission resulting from three-particle recombination via highly excited levels.

The absolute measurements of the LPP emission intensity (Table 4) offered a possibility to evaluate the electron temperature T_e in the region of the glow due to a favorable relation between T_e and the three-particle recombination rate in Eq. (2). It was found that in the plasma expansion zone in question, T_e decreases by about a factor 1.5 within $R = 5 - 10$ cm and constitutes $T_e = (0.1 \pm 0.05)$ eV. We believe the slow falloff of T_e accompanying the substantial increase of LPP volume to be due to the recombination heating of the electron gas.

Estimates show the beryllium plasma with such a temperature and density $N_e \sim 10^{13} \text{ cm}^{-3}$ to be weakly nonideal (6) which validates our use of Eq. (2).

The totality of the above experimental and calculated data implies that the LPP in the distant zone is dominated by one fundamental collisional process only, namely, the three-particle recombination with electrons. This process governs completely the radiative characteristics of the LPP in the distant zone and the evaluation of its charge state composition.

4. CONCLUSION

The unique properties of the LPP are used intensively in atomic collision studies. The fundamental collision processes involving multicharged ions in dense layers of LPP are investigated spectroscopically due to the high intensity of emission typical for the LPP in the earlier stages of its evolution (31).

The LPP is employed also as a source of multicharged ions in charge exchange experiments (32,33,36).

Experiments on the photoionization of the He atom from short lived excited states (34,35) made use of the fact that the LPP produced on the surface of a high Z target emits strong VUV continuum.

A possibility was demonstrated (36) to employ the LPP as a VUV source in photoabsorption studies.

Our review was aimed at focusing attention on the properties of LPP in the distant zone of expansion, i.e., at distances $R > 1$ cm from the target.

According to the available experimental and theoretical data, in this region the plasma is characterized by an electron temperature $T_e \sim 0.1$ eV, a high mean charge Z , electron and ion densities $N_e \sim ZN_i \sim 10^{13} - 10^{14} \text{ cm}^{-3}$. The only fundamental process occurring here with a noticeable rate is three-particle recombination of slow electrons and ions via highly excited states.

The plasma in the distant zone may be considered as a promising medium for studies of fundamental collision processes involving multicharged ions. In this region the plasma contains a noticeable density of multicharged ions which can be reliably detected by spectroscopic means.

ACKNOWLEDGEMENT

The authors are grateful to D. M. Simanovskii and S. V. Latyshev for fruitful discussions.

REFERENCES

- 1) N. G. Basov et al. Heating and compression of thermonuclear targets irradiated by laser, (In Russian), Itogi nauki i tekhniki, Radiotekhnika, 26 (1982) 1, Moscow.
- 2) Yu. V. Afanasiev et al. Interaction of powerful laser radiation with plasma (In Russian), Itogi nauki i tekhniki, Radiotekhnika, 17 (1978) Moscow.
- 3) V. A. Boiko et al. X-ray spectroscopy of laser-produced plasma, Itogi nauki i tekhniki, Radiotekhnika, 27 (1980) Moscow.
- 4) V. V. Afrosimov et al., Pis'ma Zh. Tekh. Fiz. 1 (1975) 851.
- 5) V. A. Boiko et al., Izv. AN SSSR, s. Fiz. 47 10 (1983) 1880.
- 6) L. I. Gudzenko and S. I. Yakovlenko, Plasma Lasers. (Atomizdat, Moscow, 1978).
- 7) L. Wood and G. Chapline. X-ray lasers, Phys. Today, 28 (1978) 40.
- 8) V. A. Boiko et al. IEEE Journ. of Quantum Electr. QE-20 3 (1984) 206.
- 9) A. L. Robinson, Science. 226 4676 (1984) 821.
- 10) V. V. Afrosimov et al. Pis'ma Zh. Tekh. Fiz. 10 16 (1984) 1017.
- 11) V. V. Apollov et al. Zh. Eksp. Teor. Fiz. 11 8 (1970) 377.
- 12) Yu. A. Bykovskii et al. Zh. Eksp. Teor. Fiz. 60 4 (1971) 1306.
- 13) O. B. Anan'in et al., Pis'ma Zh. Eksp. Teor. Fiz. 16 10 (1972) 543.
- 14) A. Perez, B.I.S.T., Commis. Energ. Atom. (1971) 160.
- 15) Yu. A. Bykovskii et al. Pis'ma Zh. Tekhn. Fiz., 5 1 (1979) 46.
- 16) V. V. Berezovskii et al. Pis'ma Zh. Tekhn. Fiz., 3 7 (1977) 310.
- 17) L. Z. Barabash et al., Laser and Particle Beams, 2 1 (1984) 49.
- 18) S. Denyz et al., J. Tech. Phys., 19 4 (1978) 503.
- 19) Yu. V. Afanasiev and V. B. Rozanov, Zh. Eksp. Teor. Fiz. 62 1 (1972) 247.
- 20) Ya. B. Zel'dovich and Yu. P. Raizer, Physics of Shock Waves and High-Temperature Hydrodynamic Phenomena, ed. by W. D. Hayes and R. F. Probstein (Academic, New York, 1967).
- 21) S. V. Latyshev, Preprint ITEF (1982) 54.
- 22) M. Mattioli, Plasma Physics 13 (1971) 19.
- 23) G. L. Payne et al., J. Appl. Phys. 49 9 (1978) 4688.
- 24) R. R. Goforth and P. Hamneiling, J. Appl. Phys. 47 (1976) 9.
- 25) N. M. Kuznetsov and Yu. P. Raizer, Zh. Priklad. Mekhan. Tekh. Fiz. (1965) 10.
- 26) L. A. Vainstein, I. I. Sobelman, E. A. Yukov. Excitation of atom and spectral line broadening (In Russian). (Nauka, Moscow 1979).
- 27) A. V. Gurevich and L. P. Pitaevskii, Soviet Physics JETP 19 (1964) 870.
- 28) S. V. Latyshev and I. V. Rudskoi, Preprint ITEF (1985) 33.
- 29) A. A. Golubev et al., Preprint ITEF (1983) 175.
- 30) E. Volokhovskii et al. Trudy FIAN. 149 (1984).
- 31) M. A. Mazing and A. P. Shevelko, Berlin, 143; Invited Papers of XIII ICPEAC (North-Holland, Amsterdam, 1983).
- 32) R. A. Phaneuf et al. Phys. Rev. A 26 4 (1982) 1892.
- 33) R. A. Phaneuf, IEEE Trans. Nucl. Sci. NS-28 2 (1981) 1182.
- 34) V. P. Belik et al. Pis'ma Zh. Eksp. Teor. Fiz. 25 (1977) 527.
- 35) M. Ya. Amusia et al., Zh. Eksp. Teor. Fiz. 76 (1979) 873.
- 36) C. G. Mahajan et al. Opt. Lett. 4 9 (1979) 283.

ELECTRON SPECTRA AND ION ANALYSIS IN LASER- EXCITED METALLIC VAPORS*

B. CARRÉ

Service de Physique des Atomes et des Surfaces, CEA, CEN-Saclay,
91191 Gif-sur-Yvette, France.

and

J.M. BIZAU⁺, P. BREGER[§], D. CUBAYNES⁺, P. GÉRARD⁺, J.L. PICQUE⁰, F. ROUSSEL[§],
G. SPIESS[§] and F.J. WUILLEUMIER⁺.

⁺ Laboratoire de Spectroscopie Atomique et Ionique and Laboratoire pour
l'Utilisation du Rayonnement Electromagnétique, Université Paris-Sud,
91405, Orsay, France.

[§] Service de Physique des Atomes et des Surfaces, CEA, CEN-Saclay,
91191 Gif-sur-Yvette, France

⁰ Laboratoire Aimé Cotton, Université Paris-Sud, 91405 Orsay, France.

Ionization processes are investigated in Na and Ba vapors of density
 $n_0 < 10^{13} \text{ cm}^{-3}$, excited by c.w. or pulsed laser sources. In the resonantly
excited vapor, collisional ionization of excited atoms is a dominant type
of process, which is unambiguously observed using electron spectrometry. The
results also demonstrate the importance of collisional energy transfer
between electrons and excited atoms. In Na vapor laser-excited off-resonance,
 Na_2 dimers are responsible for the ionization observed : multiphoton ioniza-
tion and alternative processes are supported by the results of, respectively,
a short pulse and a long pulse experiment.

INTRODUCTION

The study of the ionization processes which take place in a laser-excited
metallic vapor (or an effusive medium) has expanded within the past few years
into a wide domain of investigation. Numerous ion measurements in Li, Na
/ 1-6 /, K, Rb, Cs / 3, 7 /, Ca, Sr / 8 / and Ba / 9, 10 / vapors, and a few
electron measurements in Na and Ba vapors / 11, 12 /, excited by discharge
lamp, c.w. or pulsed laser light have been reported previously.

For a resonant, c.w. or pulsed excitation of the vapor, that is a laser light
tuned to a particular ground-excited state atomic transition, it has been
demonstrated through the different experiments that two ionization regimes 1)
in high density vapor ($n_0 > 10^{14} \text{ cm}^{-3}$), and 2) in low density vapor ($n_0 < 10^{13}$
 cm^{-3}), should be considered :

1) In high density vapor, high fractional ionization (10 % to 100 %) occurs
within short time periods ($\sim 1 \mu\text{s}$) as the result of sequential processes / 1,
2, 8-10 / : i) a seeding process produces the first free electrons in the
medium ; ii) the free electrons are "heated" by collisional energy transfer
from the excited atoms (superelastic collisions) / 13, 14 / ; iii) the "hot"
electrons initiate the electron-impact ionization of the vapor which combines
with step ii) to give rise to a cascade regime of ionization.

2) In low density vapor, or effusive beam ($n_0 < 10^{13} \text{ cm}^{-3}$), ionization
occurs mainly in atom-atom collisions : either associative ionization during
the collision of an excited atom with a ground or excited state atom, e.g. in
Na and Rb / 3, 15, 16 / (the energy of the colliding system may be inferior

or superior to the dissociative ionization threshold), or non associative (for simplicity, "Penning") ionization during the collision of two excited atoms, e.g. in Na / 11, 12, 17 / Rb / 7 / and Ba / 10, 12 /, is dominant in the medium.

Photoionization of excited atoms becomes a major process for laser intensities larger than 10^6 W.cm^{-2} .

Apart from the optical excitation (by laser or via further radiative decay) which produces the main population of excited atoms in one particular "optically-excited" state, energy pooling collisions of two "optically-excited" atoms can populate highly excited states / 18, 19 /, and the atoms in such highly excited states may be further involved in the ionization mechanisms. The important role of energy pooling collisions as an intermediate step in the observed ionization has been outlined in Na and Ba vapors / 11, 12, 17 /. The above mentioned processes serve as the "seeding" processes in the sequential ionization of high density vapor.

Ionization is still observed in the vapor (Na) when a pulsed laser excitation source is used "off-resonance", that is detuned from any atomic transition / 20-23 /. In sodium vapor, photoionization (dissociative or not) of laser-excited dimers is now commonly accepted as a major off-resonance process. The analysis of the yields of Na_2^+ and Na^+ ions measured as a function of the laser wavelength demonstrates the role of two-photon pumped $^1\Sigma_g$ and/or $^1\Pi_g$ intermediate states of Na_2 . In addition to photoionization other processes have received experimental support and will be briefly discussed.

In the series of experiments reported here we have investigated some of the above processes which take place in on- or off-resonance laser-excited, low density vapor. We will consider in the following sections :

- the electron spectrometry study of associative ionization (AI), Penning ionization (PI) and collisional energy transfer between electrons and excited atoms, in Na and Ba vapors laser-excited to the first optical resonance, respectively, Na ($3s \rightarrow 3p$) and Ba ($6s^2 \rightarrow 6s6p$).
- the ionization of sodium vapor laser-excited off-resonance : ion yield measurements and electron spectrometry provide contrasted but complementary results in two different experimental situations, a short pulse and a long pulse excitation of the vapor.

1. ON- AND OFF-RESONANCE IONIZATION IN LASER-EXCITED SODIUM VAPOR

1.1. On-resonance ionization : electron spectrometry studies

The electron spectrometry technique, which has already been used for a very accurate analysis of collisional ionization in rare gases or rare gas-alkali systems / 24 /, allows in our experiment i) to resolve and to observe simultaneously the different ionization processes which are characterized by the energy of the ejected electrons and ii) to observe the collisional energy transfers (superelastic or inelastic collisions) between atoms and electrons. Experimental results obtained with a c.w. and with a pulsed laser excitation source are successively presented. Penning ionization between excited alkali atoms is briefly discussed using the electron energy spectra and the extended cross section measurements of Chéret and Barbier in Rb / 7 /.

1.1.1. The experiment

An effusive beam of Na ($n_0 = 10^{12} - 10^{13} \text{ cm}^{-3}$) is excited by a perpendicular laser beam in the source volume of a cylindrical mirror analyzer (CMA) / 11, 12, 17 /. The laser excitation sources are successively i) a c.w. single mode laser source tuned to the $3s \ ^2S_{1/2} (F=2) \rightarrow 3p \ ^2P_{3/2} (F'=3)$ transition, which pumps up to 30 % of the atoms in the excited state for typical intensities of

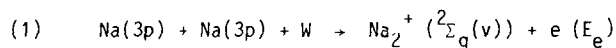
a few W.cm^{-2} , and ii) a long pulse (1 μs) laser source tuned to the $3s\ ^2S_{1/2} \rightarrow 3p\ ^2P_{1/2}$ or $3/2$ transition, for which an intensity between 10^4 and $10^6\ \text{W.cm}^{-2}$ saturates the $3s\text{-}3p$ transition. The transmitted electrons are energy-analyzed in the CMA with a resolution $\Delta E/E$ of about 10^{-2} . Accelerating grids can be used at the entrance of the spectrometer to compensate the retarding potentials which exist in the system, that is a plasma potential $V_p \sim .1\text{--}.5\ \text{V}$ in the excited medium, and a contact potential $V_c \sim 2\ \text{V}$ at the entrance of the CMA.

The experiment (and the similar one on Ba vapor) was associated with the study of photoionization of Na atoms in the ground state or in laser-excited states, by synchrotron radiation (SR) / 25 /. We have used the measurements from these parallel studies in the context of our experiment for calibration purposes : first, the absolute electron energy scale is determined from the observed photoelectron lines of known energy produced by the SR ; second, the absolute densities of atoms in the ground state and in the laser-excited state(s) are deduced from the intensities of the photoelectron peaks. Photoionization produced by SR has provided a useful technique of calibration ; it probes the medium within the interaction volume, simultaneously with the measurement of electrons produced by collisional ionization, and causing by itself a negligible fractional ionization.

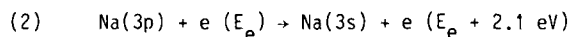
1.1.2. Results

Spectra a) and b) in Fig. 1 have been measured, respectively, in the range (0, 2.5 eV) (with accelerating grids) and (2, 6.5 eV) (without accelerating grids). In spectrum b), the cut-off energy of the spectrometer is approximately 2 eV. The two spectra display the main structures observed, the energy position of which characterize unambiguously the mechanisms responsible for their production.

- Associative ionization of excited atoms and superelastic collisions between electrons and excited atoms : Peak labelled a at energy $0.05 \pm 0.03\ \text{eV}$ corresponds to electrons produced by associative ionization in the collision of two Na(3p) atoms :



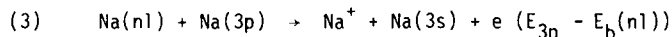
where W is the kinetic energy of the colliding atoms and v a particular vibrational level in which Na_2^+ is formed. The electrons produced in (1) may undergo $p = 1, 2, 3$ subsequent superelastic collisions with Na(3p) atoms, each of which boosts their energy by 2.1 eV :



The corresponding peaks a + p primes are observed in spectra a) and b). For a pulsed laser excitation of the $3s\text{-}3p$ transition, structures similar to peaks a and a' are observed as shown in the spectrum in Fig. 2.

- Penning ionization of excited atoms :

In spectrum a) in Fig. 1, peaks b, c, d, and e correspond to the electrons produced by Penning ionization in the collision of Na(nl) and Na(3p) atoms with, respectively, $nl = 3d, 4p, 5s$ and $4d/4f$:



where $E_b(nl)$ is the binding energy of the electron in the nl state. The primary electrons which have been superelastically heated in process (2) are also observed after $p = 1, 2$ superelastic collisions. These electrons appear on a larger scale (for $p = 1\ \text{SEC}$) and with a better resolution in Fig. 3 at temperature $T_0 = 520\ \text{K}$.

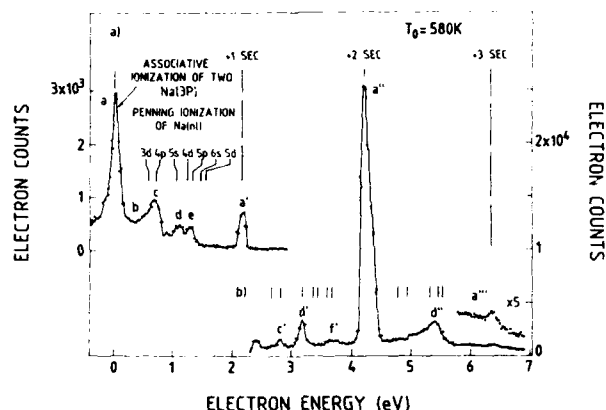
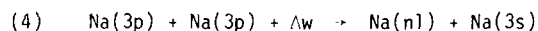


FIGURE 1

Electron energy spectra measured at a temperature $T_0 = 580$ K in a sodium vapor excited with a c.w. laser tuned to the $3S_{1/2} (F=2) \rightarrow 3P_{3/2} (F'=3)$ transition. Spectrum a) (0, 2.5 eV) is obtained using accelerating grids, whereas in spectrum b) the contact potential repels the electrons of energy < 2 eV. Both spectra characterize simultaneously i) associative ionization (peak a) and Penning ionization (peaks b, c, d and e) in the collision of excited atoms ii) superelastic energy transfer between electrons and Na(3p) atoms; peaks labelled with $p = 1, 2, 3$ primes correspond to p superelastic collisions (SEC). The spectra in Figs. 1, 2, 3, 5 and 7 are not corrected for the transmission of the system.

The $nl = 5s$ and $4d/4f$ states are populated in the energy pooling collisions of two Na(3p) atoms:



where Δw is the energy defect of the reaction. Process (4) was first observed from fluorescence measurements by M. Allegrini et al. / 18 /; the role of this process in the ionization is now clearly demonstrated from the electron energy spectra. Instead of a direct population by process (4), the 3d and 4p states are populated by radiative decay from upper-lying 5s and 4d/4f states.

- Photoionization of excited atoms by the laser

The spectrum in Fig. 2 (pulsed laser excitation) reproduces the same structure pattern (peaks b, c, d, and e) as in the spectra in Fig. 1. However, we have measured that the intensities of peaks b, c and e vary faster with the laser intensity I_L ($10^4 - 10^6 \text{ W.cm}^{-2}$) than the one of peak d. This demonstrates that peaks b, c and e are mainly produced by photoionization of Na(nl), $nl = 3d, 4p$ and $4d/4f$, respectively. Photoionization cross sections for the above nl states are between 2 and 5 Mb at the given wavelength / 26 /. The photoionization cross section for the 5s state is much smaller than the others (0.05 Mb) and peak d is still produced by Penning ionization of Na(5s) in collision (3).

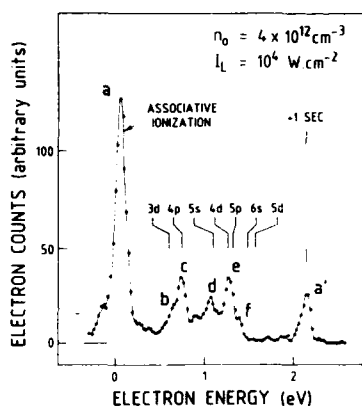


FIGURE 2

Electron energy spectrum measured between 0 and 2.5 eV in Na vapor ($T_0 \approx 550$ K) excited with a pulsed laser tuned to the $3S_{1/2} \rightarrow 3P_{3/2}$ transition. The labelling of the peaks is the same as in spectrum a) in Fig. 1. However notice that peak b, c, d and f are mainly produced by photoionization of Na(nl).

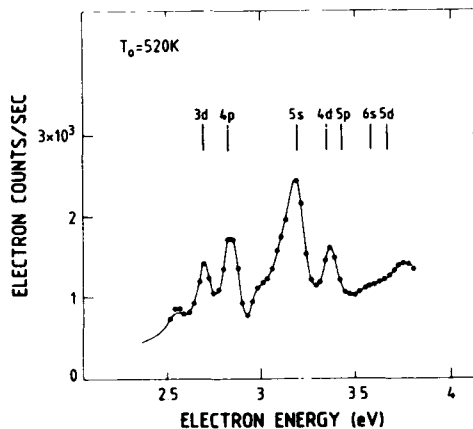


FIGURE 3

Electron energy spectrum in Na vapor at temperature $T_0 = 520$ K excited with a c.w. laser to the $3S_{1/2} (F=2) \rightarrow 3P_{3/2} (F'=3)$ transition. Peaks b', c', d', e' and f' correspond to the electrons produced by Penning ionization in the collision of Na(nl) and Na(3p) atoms, and superelastically heated in 1 SEC with Na(3p).

1.1.3. Interpretation

- Associative ionization of two Na(3p) atoms

The energy distribution of the electrons produced in (1) (peak a) is centered at a mean energy $E_e^0 \approx 0.05 \pm 0.03$ eV and its width δE_e deduced from the spectra is about .1 eV; δE_e should be roughly representative of the energy distribution of the ejected electrons in (1). We note that it is larger than the vibrational spacing in the final state of Na_2^+ ($\approx 109 \text{ cm}^{-1}$); rather it is of the order of the thermal width of the relative kinetic energy distribution for the colliding atoms. This suggests that Na_2^+ ions are produced in a few vibrational levels, namely between $v \approx 3$ and 10, and that the observed electron energy distribution corresponds to the relative kinetic energy distribution in the initial system. However, our results are not sufficiently accurate to support a definite conclusion. Since the kinetic energy distribution in the colliding system is large with respect to the vibrational spacing, electron spectrometry does not permit the resolution of the v-level distribution in the final state. Using a well-collimated atomic beam at low temperature / 15 /, or a crossed beam configuration / 5 /, would significantly improve the information supplied by electron spectrometry. In any case, L.I.F. would be also an appropriate technique as a probe of the v-level distribution in the Na_2^+ ion. Very recent calculations of a large set of energy potential curves for the Na(3p) - Na(3p) system should encourage further experimental investigation of process (1) / 27 /.

From a quantitative analysis of peaks a, a + p primes (and thus of the superelastic heating of the primary electrons, see further in the text), we deduce estimates of the cross sections for associative ionization (1),

$$^1\text{Al}(3/2, 3/2) \simeq 4 \times 10^{-16} \text{ cm}^2 \quad \text{and} \quad ^1\text{Al}(1,2, 1/2) \simeq 2 \times 10^{-16} \text{ cm}^2$$

(within a factor of 3). The values obtained are in reasonable agreement with previously measured values / 3, 16 /.

- Penning ionization of excited atoms

The observed structures b, c, d, and e in spectrum a) in Fig. 1 and with prime in Fig. 3 show that Penning ionization (3) is dominant over associative ionization which can also occur in the course of the $\text{Na}(n1) + \text{Na}(3p)$ collision at small internuclear distances ($R < 5 \text{ \AA}$). In effect one expects to see in the latter a broad energy distribution of the ejected electrons between 1 and 2 eV, which is not observed in the spectra. Rather ionization (3) occurs at large internuclear distances ($R > 5 \text{ \AA}$) for which the potential energy difference between the initial and the final state (i.e. the energy of the ejected electron) has reached its asymptotic value. This is confirmed by the high order of magnitude ($10^{-13} - 10^{-12} \text{ cm}^2$) of the cross sections for process (3) that we estimate from the spectra; they are larger than the geometrical cross sections by a factor of about 10, showing that long range dipole-dipole interaction induces the main coupling with the continuum in process (3). This was clearly demonstrated first by the extended measurements carried out by Chéret and Barbier / 7 / of the cross sections for Penning and associative ionization in the $\text{Rb}(n1) + \text{Rb}(5p)$ system. These authors have measured cross sections for Penning ionization between 10^{-13} and 10^{-12} cm^2 for the $n1 = 7s$ to $11s$ and $5d$ to $9d$ series. They are at least 100 times larger than the measured cross sections of associative ionization in the same system. Theoretical calculations confirm the order of magnitude of the experimental values / 28 /.

- Superelastic heating of the electrons

The characteristic time of superelastic collisions (2) for electrons of energy $E_0^0 = 0.05 \text{ eV}$ is between $4 \cdot 10^{-6} \text{ s}$ and $4 \cdot 10^{-7} \text{ s}$ for $n_{3p} = 10^{12}$ to 10^{13} cm^{-3} / 29 /. Thus, it is much longer than the free diffusion time for the electrons ($\sim 10^{-8} \text{ s}$). However, the plasma potential $V_p \sim .1 \text{ eV}$ can confine the low energy electrons within the excited medium for a long time, "infinite" for the c.w. laser excitation, and of about $1 \mu\text{s}$ for the pulsed laser excitation. Superelastic heating in the collision (2) thus becomes efficient and can be observed in spectra a) and b) in Fig. 1 as well as in the spectrum in Fig. 2.

Similarly, for the same conditions as those of spectrum b) in Fig. 1 (no accelerating grids), the electrons produced by Penning ionization (3) with a kinetic energy in the range (0.7 - 1.2 eV) were confined within the interaction chamber by the contact potential (2 V). As a result, it has been possible observing them in spectrum b) after one or even two superelastic collisions.

1.2. Off-resonance ionization of Na vapor

The production of Na_2^+ and Na^+ ions in a sodium vapor ($n_0 = 10^{11} - 10^{13} \text{ cm}^{-3}$) irradiated out of any atomic resonance in the range 5800 - 6200 Å by a pulsed laser light of moderate intensity, $I = 10^5 - 10^7 \text{ W.cm}^{-2}$, has been reported by several groups / 20-33 /. We now present two experiments in which we investigated off-resonance ionization, using, respectively, short pulse (10 ns) and long pulse (1 μs) excitation of the Na vapor. These two experiments support two contrasting interpretations of the respective ionization observed, and thus, suggest that pulse duration should be taken into account in the analysis of the results.

1.2.1. Short pulse excitation of the vapor

A first experiment / 23 / has been performed in a cell ($T_0 = 500$ K, $n_0 \sim 10^{11}$ cm $^{-3}$) using a relatively short pulse (10 ns) of laser light ; laser wavelength was tuned to operate in the range 5800 - 6200 Å with a spectral width ~ 0.07 Å (~ 2 cm $^{-1}$), and an intensity $I_L = 10^6$ - 10^7 W.cm $^{-2}$. An ion mass analysis was performed and Na $_2^+$ and Na $^+$ ion yields were measured both as a function of the laser wavelength. Numerous and complex structures are observed in the Na $_2^+$ yield spectrum in Fig. 4, for which the resolution is limited by the laser bandwidth. However, the presently reported observations have a significantly greater resolution than those of Refs. / 20-22 /.

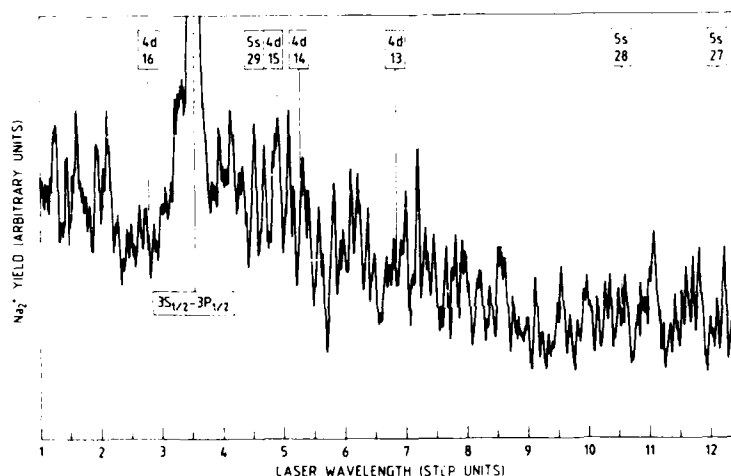


FIGURE 4

Na $_2^+$ ion yield measured in laser-excited sodium vapor ($n_0 \sim 1.2 \cdot 10^{13}$ cm $^{-3}$, 10 ns excitation pulse of intensity $\sim 10^6$ W.cm $^{-2}$) as a function of the laser wavelength between 5891 Å and 5910 Å. The wavelength origin is at the $3s_{1/2} - 3p_{3/2}$ resonance, $\lambda = 5889.94$ Å ; the wavelength step unit is equal to 1.6784 Å. The structures characterize three-photon ionization of Na $_2$ dimers enhanced by the resonant excitation of $1\Sigma_g^+$ or $1\Pi_g$ states of Na $_2$ - see text. Two-photon transitions, $(3s + 5s) 1\Sigma_g^+$ and $(3s + 4d) 1\Sigma_g^+ + X 1\Sigma_g^+$, to the highly excited states observed by Morgan et al. are labelled as in Ref. / 31 /.

Furthermore we have demonstrated that the Na $_2^+$ ion yield varies linearly with the density of Na $_2$ dimers for which the fractional value is approximately 10^{-3} - 10^{-4} in the vapor. Thus we attribute the production of Na $_2^+$ ions to the three-photon ionization of Na $_2$ dimers, enhanced by the resonant or quasi-resonant excitation of rovibrational levels in intermediate excited states of Na $_2$. More precisely we believe that the observed structures reflect the two-photon resonant transitions between rovibrational levels (v'', J'') and (v, J) of, respectively, the $X 1\Sigma_g^+$ ground state and $1\Sigma_g^+$ or $1\Pi_g$ excited states which lie in the two-photon energy range. The latter should be most likely the $(3s+5s) 1\Sigma_g^+$ and $1\Pi_g$ and the $(3s+4d) 1\Sigma_g^+$ and $1\Pi_g$ states observed by Carlson et

$$(5) \quad \text{Na}_2 (X \ 1_{\Sigma_g}^+) \xrightarrow{2 \ h\nu} \text{Na}_2^{**} (1_{\Sigma_g}^+, 1_{\Sigma_g}^+) \xrightarrow{h\nu} \text{Na}_2^+ + e \quad (5a)$$

The Na^+ ion yield which was measured simultaneously presents some of the same structures as for Na_2^+ . We attribute the production of Na^+ mainly to the three-photon dissociative ionization (5b) which occurs via resonant excitation (5) of Na_2 . Then, different Franck-Condon factors in (5a) and (5b) account for the difference between the observed structures in Na_2^+ and Na^+ ion yield spectra.

The experiment described in section 1.1 using a long pulse laser excitation source (1 μ s pulse duration, 70 GHz bandwidth, $I_L = 10^4$ - 10^6 W.cm $^{-2}$) has been extended to the case of off-resonance excitation of the effusive medium. In Fig. 5, we compare two spectra, a) and b), which have been measured at two different wavelengths :

- Spectrum b : the wavelength $\lambda = 6040 \text{ \AA}$ does not correspond to any atomic transition. Nevertheless, one notices that the γ and δ peaks remain the dominant structures in the spectrum. Processes (5a-b) produce electrons of energy between 0.0 and $\sim 1.4 \text{ eV}$. However, it would be a striking coincidence if these electrons were produced precisely at the energies which characterize the photoionization of atoms in the $n\ell = 4p, 5s$ and $4d$ states. Thus, we conclude that the above $n\ell$ states are populated off-resonance in the vapor. The possibility that they are excited directly by the laser or by its fluorescence background is excluded. Rather we propose either the photodissociation of the laser-excited dimers into excited atoms / 32 / :

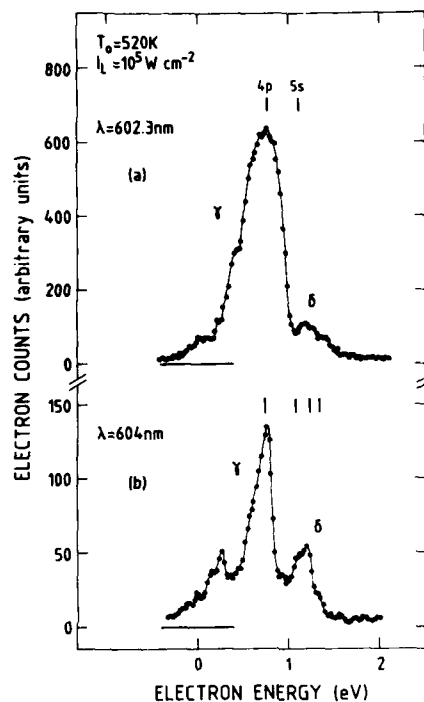
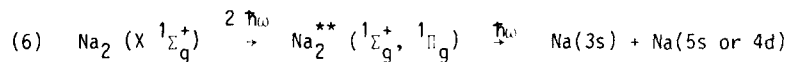
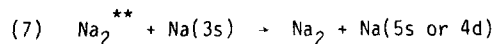


FIGURE 5

Electron energy spectra measured in Na vapor at temperature $T_0 = 520 \text{ K}$ excited with a long pulse laser ($1 \mu\text{s}$, $I_L \sim 10^5 \text{ W cm}^{-2}$). a) : $\lambda = 602.3 \text{ nm}$ corresponds to the two-photon $3s \rightarrow 5s$ transition. The γ and δ peaks are produced by photoionization of, respectively, $\text{Na}(5s)$ and $\text{Na}(4p)$ at the given wavelength, the $4p$ state being populated from the $5s$ by radiative decay. b) : $\lambda = 604 \text{ nm}$. From a comparison with spectrum a), one still attributes peaks γ and δ to the photoionization of, respectively, $\text{Na}(5s/4d)$ and $\text{Na}(4p/3d)$ atoms : a pool of excited atoms is produced off-resonance in the vapor by photodissociation of - or collisional energy transfer from dimers in two-photon excited $1\Sigma_g^+$ or $1\Pi_g$ states.



or the collisional energy transfer between laser-excited dimers and atoms
/ 33 / :



as two mechanisms capable of producing a pool of excited atoms in the vapor. The excited atoms are then photoionized as in the resonant cases. In the

present long pulse experiment, this process seems to be dominant over the three-photon direct ionization (5a,b) of Na_2 : the steady-state population in the 4p state is a reservoir of excited atoms which are photoionized with a relatively high cross section (which may be higher than the photoionization cross section of Na_2 in the $^1\Sigma_g$ and $^1\Pi_g$ states in 5a,b). Such a reservoir does not exist in the previous short pulse experiment ($\gamma_{5s-4p}^1 > \text{pulse duration}$). Thus we propose that processes (6) or (7) may explain the particular features of the electron energy spectra measured off-resonance. In Ref. / 21 / reporting the results of a long pulse experiment, we attributed the production of Na_2^+ ions to three-photon ionization (5a) of Na_2 ; Na^+ ion yield was not measured. Our present interpretation of the Na^+ production does not contradict the conclusions of Ref. / 21 /.

2. ELECTRON SPECTROMETRY STUDY OF ON-RESONANCE IONIZATION IN Ba VAPOR

In this experiment we have studied the energy distribution of the electrons produced in a resonantly excited Ba vapor using the experimental set-up of section 1.1 / 12 /. $\text{Ba}(6s^2 \ ^1S_0)$ atoms in the effusive beam were excited by a c.w. laser source to the $6s6p \ ^1P_1$ excited state (see Fig. 6); the $6s6p \ ^3P$ state could be populated from the $6s6p \ ^1P_1$ by collisional quenching / 10 /. However, the dominant populations of excited atoms are produced in the metastable states $6s5d \ ^1D$ and $6s5d \ ^3D$ which are populated by either radiative decay or collisional quenching from the upper-lying states.

2.1. Probe of atomic populations in the excited states - Absolute energy scale

As for Na (see § 1.1.1) parallel study of the photoionization of Ba in the ground state and in excited states by SR / 34 / has provided a useful method for calibrating the absolute energy and for probing the atomic population in the different states. A typical electron energy spectrum produced by collisional ionization of excited Ba atoms and by simultaneous photoionization of Ba atoms in ground and excited states is presented in Fig. 7. In spectrum b) in Fig. 7, the electron lines above 10 eV of kinetic energy are due to the ionization of Ba atoms by the synchrotron radiation. The peaks labelled G_1 and G_2 are produced by photoionization in the 6s outer-shell of the ground state atom by 18.49 eV photons (SR). The lines labelled M_1 , M_1' and M_2 , M_2' are produced by photoionization of the atoms in, respectively, the 6s and the 5d subshells of the $6s5d \ ^1D$ and $6s5d \ ^3D$ (peaks labelled with a prime) metastable states, this photoionization being resonantly enhanced at the given photon energy via the excitation of autoionizing states. A weak signal E is produced by photoionization in the 6p shell of the $6s6p \ ^1P$ laser-excited state.

As in the case of Na, the absolute energy scale can be determined from the known energy position of the observed photoelectron lines. In the low energy range of the spectra (0, 6 eV), we have used, as an additional reference, the photoelectron lines Xe_1 and Xe_2 produced by photoionization of Xe in the 5p shell (respectively, $\text{Xe}(5p^6) + h\nu \rightarrow \text{Xe}(5p^5 \ ^2p_{1/2} \text{ and } ^2p_{3/2}) + e$) by 18.49 eV photons. The choice of these energy references reduces the uncertainty due to slight differences in the diffusion conditions between low energy and high energy ($E_e > 6$ eV) electrons. Absolute energies of the peaks in the low energy range of spectra a) and b) are then determined within an uncertainty of 0.02 eV.

Photoelectron lines from Ba atoms give direct evidence that excited states (especially the metastable states) were populated in the vapor. Furthermore, it is possible, in principle, to determine the densities in the different states (ground and excited states) from the intensities of the corresponding peaks. One notes for instance that the relative decrease of the intensity of peak G_1 (from the ground state) when the laser is turned on is equal to the

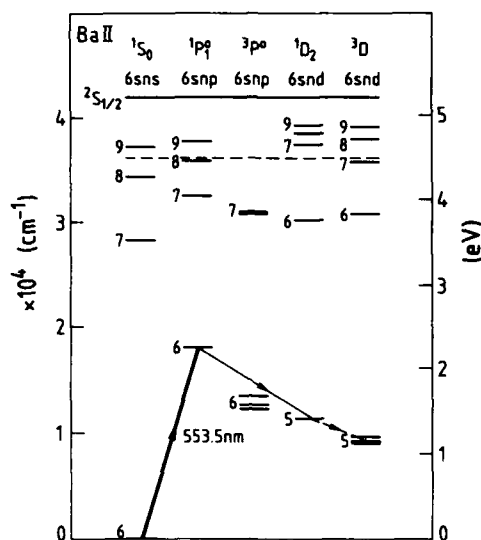


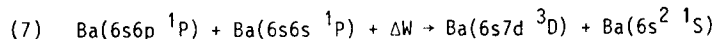
FIGURE 6

Energy diagram of Ba atomic states illustrating the laser-excited $6s^2 1S_0 \rightarrow 6s6p 1P_1$ transition and the way of populating the metastable $6s5d 1D$ and $3D$ states by either radiative decay or collisional quenching (also from collisionally populated $6s6p 3P$). The dashed line corresponds to the energy of the $Ba(6s6p 1P) + Ba(6s6p 1P)$ colliding system and shows that $6s8s 1S$ and $3S$ (the latter is not represented on the energy diagram), $6s8p 1P$ and $6s7d 3D$ can be populated in the above energy pooling collision.

total relative density of atoms in the excited states. By this method, we were able to determine that up to 90% of the atoms were transferred to the excited states, that are mainly in the metastable $1D$ and $3D$ states. However absolute photoionization cross sections or autoionization rates for the different excited states have not been yet either measured or calculated. Thus, an accurate determination of the different densities cannot yet be carried out. A tentative analysis of the spectra indicates that the densities in the two metastable states should be of the same order of magnitude, the $1D$ state being favoured, whereas the density in the $6s6p 1P$ and $6s6p 3P$ remains relatively weak.

2.2. Collisional, ionization and multiple superelastic processes

The spectra a) and b) in Fig. 7, in which $E_e > 1.5$ eV, are obtained without accelerating grids for two different laser powers: in spectrum a) the densities in the $1D$ and $3D$ metastable states are approximately 5 times smaller than in spectrum b). The spectra demonstrate the existence of hot electrons in the medium in the range 1.5 - 4 eV, produced by collisional ionization of excited atoms, and then further heated in superelastic collisions with excited atoms. One can interpret the different structures in spectra a) and b) ($E_e < 5$ eV) by assuming that one dominant electron population of either energy E_e



whereas the $6s8p \ ^1P$ cannot be produced in dipole-dipole interaction and should be less populated in the collision (7). From the spectra, the contribution to ionization via (I) and (I') of the $6s8s \ ^1S$ and 3S states (~ 4.26 eV) which can be populated in the collision (7) is much smaller (and not observed) than that of the $6s7d \ ^3D$ state.

Further studies of the primary electrons between 0 and 2 eV using accelerating grids are in progress. These experiments will provide us with a verification of the present interpretation of the spectra.

CONCLUSION

We have investigated the ionization processes which take place in laser-excited metallic vapors of Na and Ba.

For a resonant population of excited states by either a c.w. or a pulsed excitation source one observes first the subsequent population of highly excited states in energy pooling collisions of optically (laser)-excited atoms. From this latter, the dominant ionization processes are associative and Penning ionization in the collisions of optically-excited or collisionally excited atoms. Photoionization of excited atoms becomes significant in the case of a pulsed laser excitation source. Electron spectrometry allows simultaneous resolution and observation of the different ionization channels. In addition we used this technique to study superelastic energy transfer between electrons and excited atoms. This process can produce a complex energy distribution of the electrons in the Ba vapor case, for at least two different excited states ($6s5d \ ^1D$ and 3D) give rise to an efficient superelastic heating.

The off-resonance pulsed excitation of the vapor (Na) involves laser-excited dimers. However experimental results outline the difference between short pulse and long pulse experiments. In the short pulse experiment, Na_2^+ ion yield measurements characterize the three-photon ionization of Na_2 , resonantly enhanced by the excitation of intermediate states. In the long pulse experiment we conclude rather that a population of highly excited atoms is produced by photo-dissociation or collisional quenching of laser-excited dimers, these excited atoms being further efficiently photoionized.

REFERENCES

- 1) T.B. Lucatorto and T.J. McIlrath, Phys. Rev. Lett. 37 (1976) 428.
- 2) T.J. McIlrath and T.B. Lucatorto, Phys. Rev. Lett. 38 (1977) 1390.
- 3) A.N. Klucharev, A.Z. Devdariani, V. Yu. Sepman and V. Vujnovic, X ICPEAC, Paris (1977) Abstracts of papers, 1150.
- 4) G.H. Bearman and J.J. Leventhal, Phys. Rev. Lett. 41 (1978) 1227.
- 5) J. Weiner and P. Polak-Dingels, J. Chem. Phys. 74 (1981) 508.
- 6) B. Carré, F. Roussel, P. Breger and G. Spiess, J. Phys. B : At. Mol. Phys. 14 (1981) 4271.
- 7) M. Chéret and L. Barbier, Proc. of the Colloque International du CNRS "Collisions in a laser field", J. Phys., série des Colloques, 46 (1985) C1-193.
- 8) C.H. Skinner, J. Phys. B : At. Mol. Phys. 13 (1980) 55.
- 9) I.-A. Bachor and M. Kock, J. Phys. B 14 (1981) 2793.

* A large part of the experiments reported in this work was carried out at the french synchrotron radiation facility LURE-ACO, in Orsay. The constant support of Y. Pétrouff and C. Manus, and of the technical staff operating the ACO storage ring is gratefully acknowledged.

- 10) L. Jahreiss and M.C.E. Huber, *Phys. Rev. A* 28 (1983) 3382.
- 11) J.L. Le Gouët, J.L. Picqué, F. Wuilleumier, J.M. Bizau, P. Dhez, P.M. Koch and D.L. Ederer, *Phys. Rev. Lett.* 48 (1982) 600.
- 12) B. Carré et al., *Proc. of the Colloque International du CNRS "Collisions in a laser field"*, *J. Physique, Série des Colloques*, 46 (1985) C1-163.
- 13) H.W. Hermann, I.V. Hertel, W. Reiland, A. Stamatovic and W. Stoll, *J. Phys. B : At. Mol. Phys.* 10 (1977) 251.
- 14) R.M. Measures, *J. Appl. Phys.* 48 (1977) 2847.
- 15) A. de Jong and F. van der Valk, *J. Phys. B : At. Mol. Phys.* 12 (1979) L561.
- 16) J. Huennekens and A. Gallagher, *Phys. Rev. A* 28 (1983) 1276.
- 17) B. Carré, J.M. Bizau, P. Dhez, D.L. Ederer, P. Gérard, J.C. Keller, P.M. Koch, J.L. Le Gouët, J.L. Picqué, G. Spiess and F. Wuilleumier, *Optics Comm.* 52 (1984) 29.
- 18) M. Allegrini, G. Alzetta, A. Kopystynska, L. Moi and G. Orriols, *Optics Comm.* 19 (1976) 96.
- 19) L. Barbier and M. Chéret, *J. Phys. B : At. Mol. Phys.* 16 (1983) 3213.
- 20) J. Boulmer and J. Weiner, *Phys. Rev. A* 27 (1983) 2817.
- 21) C.Y.R. Wu, F. Roussel, B. Carré, P. Breger and G. Spiess, *J. Phys. B : At. Mol. Phys.* 18 (1985) 239.
- 22) C.E. Burkhardt, W.P. Garver and J.J. Leventhal, *Phys. Rev. A* 31 (1985) 505.
- 23) F. Roussel, P. Breger and G. Spiess, *J. Phys. B : At. Mol. Phys.* (1985) in press.
- 24) J. Lorenzen, H. Hotop, M.W. Ruf and H. Morgner, *Z. Physik A - Atoms and Nuclei* 297 (1980) 19.
- 25) J.M. Bizau, F. Wuilleumier, P. Dhez, D.L. Ederer, J.L. Picqué, J.L. Gouët, and P.M. Koch, in "Laser techniques for UV spectroscopy" ed. T.J. Mc Ilrath and R.J. Freeman, *AIP Proc. Series 90* (1982) New York, 331-343.
- 26) M. Aymar, *J. Phys. B : At. Mol. Phys.* 11 (1978) 1413.
- 27) A. Henriët, F. Masnou-Seeuws and C. Le Sech, *Chem. Phys. Lett.* (1985) in press.
- 28) L. Barbier, *Thèse de Doctorat, Université Paris-Sud, Orsay* (1984)
- 29) D.L. Moores, D.W. Norcross and V.B. Sheorey, *J. Phys. B : At. Mol. Phys.* 7 (1974) 371.
- 30) N.W. Carlson, A.J. Taylor, K.M. Jones and A.L. Schawlow, *Phys. Rev. A* 24 (1981) 822.
- 31) G.P. Morgan, H.R. Xia and A.L. Schawlow, *J. Opt. Soc. Am.* 72 (1982) 315.
- 32) See for $\text{Na}_2^* + \text{H}_2 \rightarrow \text{Na}(3s) + \text{Na}(3p)$:
M.L. Janson and S.M. Papernov, *J. Phys. B : At. Mol. Phys.* 15 (1982) 4175.
- 33) M.L. Janson and J.P. Klavins, *Chem. Phys. Lett.* 86 (1982) 453.
- 34) D. Cubaynes et al., to be published.

EXCITED ATOM-MOLECULE COLLISIONS AT THERMAL AND SUPRATHERMAL ENERGIES

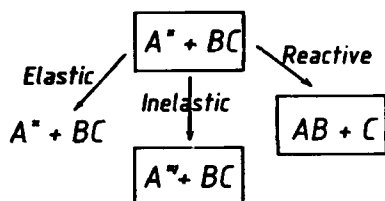
Jean-Michel MESTDAGH

Service de physique des atomes et des surfaces,
C.E.N. Saclay, 91191 Gif-sur-Yvette cedex France

1. INTRODUCTION

Collisions of excited atoms with molecules at thermal and suprathermal energies (0.01 eV to 1 eV) have attracted growing interest over the past few years. The excited atom studies mentioned in this report have focused on alkali atoms since they are easily optically pumped to n^2S , n^2P or n^2D excited levels using tunable dye lasers.

Collisions between an excited alkali atom A^* and a molecule BC can be divided into three classes (considering only neutral exit channels):



– First, A^* can be scattered elastically (same electronic excitation before and after the collision). In such a collision, the internal excitation (rotational or vibrational) of the molecular perturber can change. One question is how the excitation of the molecule BC is affected by the electronic

excitation of the collision partner A . Such processes are not reported here. The interested reader is referred to [1].

– The second possibility is that A is scattered inelastically from the excited level A^* to the level A' (A' may or may not be excited). Among these processes, the quenching of the first excited 2P doublet of alkali atoms has been recently extensively reviewed [2,3]. These quenching processes are fairly simple since only the initial state of A is excited. We will consider more complex situations in this report (see section 2) where both the initial and the final states of A are excited: we consider processes such as



where A is an alkali atom (Rb in this report), BC a molecule (diatomic here) and where nl ($n'l'$) are the principal and orbital quantum numbers describing the initial (final) state of A . When considering process (1), our purpose is to answer the following question: to what extent (and why?), is the inelastic transfer $A(nl) \longrightarrow A(n'l')$ modified when the perturber is a molecule BC instead of a rare gas atom?

– Finally, the collision $A^* + BC$ can be reactive. Recent reviews are available in this field [4,5,6]. A collision of this type is reported in section 3. It concerns the reaction



where the Na atoms are either in the ground state $3S$ or in the excited levels $3P, 5S$ or $4D$. This example is used to illustrate the dramatic effects that the electronic excitation of reactant atoms has on reactive scattering.

For both types of processes discussed in this report (inelastic and reactive scattering) the polarization of the excited atomic state can influence the collision (such phenomena are usually called polarization effects). The systematic observation of such effects in reactive collisions is fairly recent [6]. Since a symposium is devoted to collisions of polarized atoms during this conference we do not report on polarization effects here.

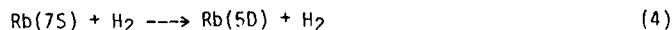
2 INELASTIC SCATTERING

For a general understanding of type (1) collision processes, it is often useful to investigate them, when they take place in collisions involving Rydberg atoms (i.e. highly excited atoms) [7]. In such collisions, fairly simple theoretical approaches are valid and give clear picture of the physical phenomena involved in the collision process under investigation. This can help us understand the collisional properties of less excited atoms where more complicated theories are required.

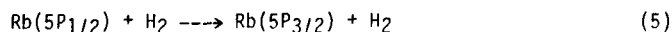
Following this idea, we first consider (section 2.1) the quenching of Rydberg atoms according to the scheme



where the principal quantum number n ranges from 25 to 45. Process (3) is a type (1) process. Studying process (3) will allow to identify one of the mechanisms by which molecular perturbers may have different behaviors from that of rare gases when inducing a type (1) inelastic transfer. This mechanism, a resonant transfer between electronic energy of Rb and rotational energy of the molecular perturber, is then studied in more detail in section 2.2 when considering the intermultiplet mixing



Finally, when considering in section 2.3 the process



we will see another way by which molecular perturbers differ from rare gas perturbers when inducing type (1) inelastic processes.

2.1 Quenching process of $\text{Rb}(nS)$ Rydberg atoms

The quenching of $\text{Rb}(nS)$ according to process (3) is fairly complicated since the final state of Rb is not specified. We only know it is different from the initial level nS . The depopulation process (3) thus includes several more elementary collisional processes. We must make clear what they are. The quenching of $\text{Rb}(25S)$ is taken as example in figure 1. The collisions called l -mixing transfer the excitation from the level $25S$ to levels such as $22F, 6...$ which have the same effective principal quantum number than the level $25S$. When the excitation is transferred to a level of different effective principal quantum number (upper or lower), the transfer is called n -changing (for example the transfers $25S$ to $26S$ or $25S$ to $24S$). Finally, the collision can ionize the Rydberg atom.

2.1.1 Experiment and results

Two pulsed lasers excite Rb atoms stepwise to a Rydberg nS state (first $5S-5P$ then $5P-nS$; the n value is varied by changing the wavelength of

the second laser). The depopulation of the nS state due to collisions with the perturber X is followed by field ionization in a cell experiment. This

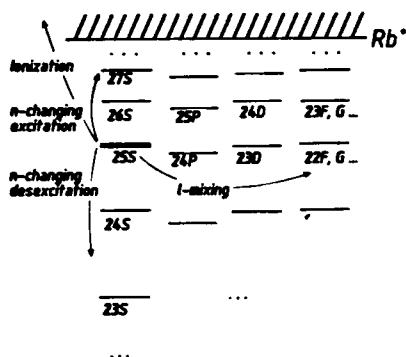


FIGURE 1
Energy levels of Rb (not to scale) and elementary processes included in process (3).

allows the measurement of the Maxwellian-averaged cross-section of process (3) as a function of the principal quantum number n over the range 25–45. The experimental methods and especially the field ionization technique are described extensively in references [8,9,10].

The cross-section of process (3) measured in references [8,10,11] are shown in figure 2. Two features can be distinguished: (i) cross-sections

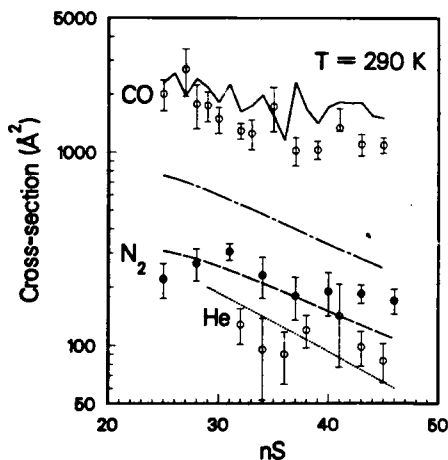


FIGURE 2
Cross-section of process (3) as a function of the principal quantum number n . Experiment (open and full circles with error bars). Theory: l-mixing cross section for He (dotted curve) N_2 (dashed curve) and CO (dotted dashed curve); total cross section for CO (full curve)

measured with the perturbers N_2 and He are almost identical (within a factor 2). (ii) Cross-sections measured with CO are one order of magnitude larger than those measured with N_2 .

2.1.2 Theoretical interpretation.

The interaction of the Rydberg electron with the perturber X is now recognized as being the dominant interaction responsible for quenching processes such as (3) [12,13]. Moreover, the impulse-approximation has proved very effective in predicting the corresponding cross-sections [14,15]. Simple analytical formulas are now available within this framework. They allow the calculation of the cross-sections of the elementary processes: l-mixing, n-changing and ionization [16,17]. When using these formulas explicitly for process (3), Petitjean et al give a quantitative interpretation of the experimental data of figure 2 [7,10,11]. Their results are plotted in figure 2. They give a clear picture of the three elementary processes l-mixing, n-changing and ionization.

L-mixing is induced by short range Rydberg electron-perturber forces. It is the dominant process when the perturber X is a rare gas. This is illustrated by the nice agreement observed in figure 2 between the calculated l-mixing cross-sections for He (dotted curve), and the corresponding experimental results. When calculating the l-mixing cross-section for N₂ (dashed curve), excellent agreement is also obtained. This means that for N₂ as for He, l-mixing is the dominant mechanism responsible for process (3).

Turning to CO, the calculated l-mixing cross-section (dotted-dashed curve in figure 2) underestimates the experimental results. Therefore l-mixing is no longer the only mechanism responsible for process (3) when the perturber is CO. This is confirmed when calculating the n-changing and ionization cross-sections (due to the long range Rydberg electron-CO dipolar moment interaction): n-changing collisions appear as the sum of near-resonant processes such as

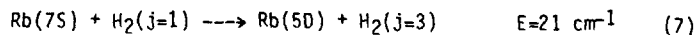


which have very large cross-sections (10940 Å² for process (6)). In comparison, ionization does not play an important role. When adding l-mixing, n-changing and ionization cross-sections, the solid curve of figure 2 is obtained. It is in excellent agreement with the CO experimental data.

The reason for the behavior differences between CO and N₂ in figure 2 is clear now. For CO near-resonant n-changing collisions have large cross sections because the rotational energy of CO is firmly coupled to the electronic energy of Rb. For N₂ which has no permanent dipolar moment, this coupling is much weaker. As a result, although near-resonant n-changing collisions exist for N₂, their contribution to process (3) is negligible. l-mixing thus appears as dominant for the perturber N₂ as if N₂ were a rare gas.

2.1 Intermultiplet mixing

To go deeper into the understanding of near-resonant processes such as that identified above, we must find a clean experimental situation where the resonant process is fairly well isolated. Process (4) is a satisfactory choice, since (i) a near resonant process exists when X=H₂



(the 7S-5D splitting is 608 cm⁻¹). In contrast, the rotational level splitting of D₂ mismatches this splitting, (ii) both the initial and the

final excited level of Rb can be characterized without ambiguity, (iii) process (4) can be studied using a crossed beam experiment, (iv) the initial rotational level population of the molecular perturber can be determined under our experimental conditions, (v) the absolute value of the cross-section of process (4) can be measured as a function of the relative velocity of the colliding partners. The experimental method is described in references [18,19,20].

The cross-section of process (4) as a function of relative velocity has been measured experimentally in reference [20] for the three perturbers H_2 , D_2 and He. The results are shown in figure 3. The velocity range covered in this figure corresponds to energies between 0.02 eV and 0.4 eV. The two important results are: (i) D_2 which cannot lead to resonant electronic-to-rotational energy transfers, acts very much like He, (ii) in contrast, H_2 at small velocities leads to much larger cross-sections than D_2 .

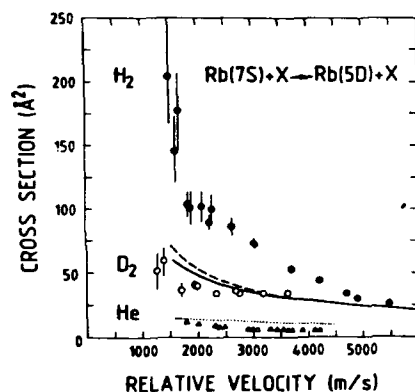


FIGURE 3
Process (4) cross-section as a function of the relative velocity of the colliding partners. Experiment (full and open circles open triangles). Landau Zener calculations for He (dotted curve), for D_2 (full curve) and for H_2 (dashed curve).

Following [20], avoided crossings between the potential curves appear to be the dominant coupling mechanisms for both perturbers D_2 and He (reliable potential curves for He and potential surfaces for D_2 are now available [21,22]). These avoided crossings have been treated by the simple Landau - Zener formula, and lead to nice agreement with the experimental results (see figure 3). In contrast, when such a model is used for H_2 , the calculated curve disagrees with experiment at small relative velocities. This strongly suggests that H_2 does not act as a rare gas. Its rotational levels play a direct role during the collision. They give rise to the near resonant process (7). Assuming that for relative velocities smaller than 4000 m/s, process (7) is dominant, it is possible to extract the cross-section of process (7) from the data of figure 3 as shown in figure 4 (arbitrary units). The cross-section of process (7) has been calculated using the impulse approximation already seen in section 2.1.2. The results are also plotted in figure 4. The main observation in this figure is the vanishing importance of the resonant process (7) as the relative velocity increases. The second important point is that the impulse approximation which is well established for the collision of Rydberg states is also fairly

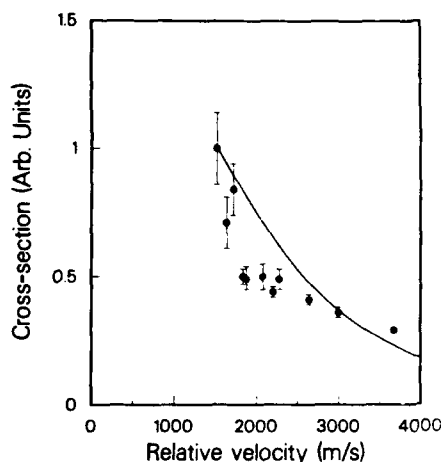


FIGURE 4
Velocity dependence of process (7) cross-section.
Experiment: full circles with error bars.
Theory: the full curve gives the results of the impulse approximation calculation.

accurate when dealing with low lying excited states of Rb (see the nice agreement between theory and experiment in figure 4). Note however that this theory overestimates the absolute value of the cross-section (measured but not shown in figure 4) by about a factor 3.

Near-resonant rotational-to-electronic energy transfers are thus associated with large cross-sections if two conditions, at least, are fulfilled. First, a strong coupling must exist between the molecular rotation and the atomic electronic energy (in process (3) an electron-dipole interaction is necessary to allow the resonant energy transfer to overcome the already large cross-section given by the non-resonant Λ -mixing mechanism while in process (4) a quadrupolar interaction is strong enough, because non-resonant processes have very small cross-sections). Secondly, small relative velocities of the colliding partners are required.

2.3 Fine structure transitions of Rb atoms

In both examples above, differences between molecular and rare gas behaviors are due to near-resonant rotational-to-electronic energy transfers. Of course, such resonances are not the only way for molecular perturbers to differ from rare gas perturbers. This is exemplified when considering process (5). The collision partners are the same as in the preceding example, but the inelastic process is different (a fine structure transition of Rb) and no near-resonances exist.

The cross-section of process (5) has been measured as a function of the collision energy with the same experimental device as that used in the preceding example [23]. The results are plotted in figure 5.

At small collision energies the cross-section is two orders of magnitude larger for H_2 than for He. This difference is not due to resonant energy transfers. Its origin has been identified by Hickman [24,25]. Figure 6 is a schematic plot of the potential curves describing the Rb(5P)-He interaction. The fine structure transition in Rb(5P) induced by He is due mainly to radial coupling between the $\Sigma_{1/2}$ and $\Pi_{1/2}$ curves which is localized at a Rb-He distance of about 12 a.u. (distance R1 in figure 6) [26]. When using this coupling in a simple semiclassical

calculation, the dashed curve of figure 5 is obtained [25]. Fair agreement

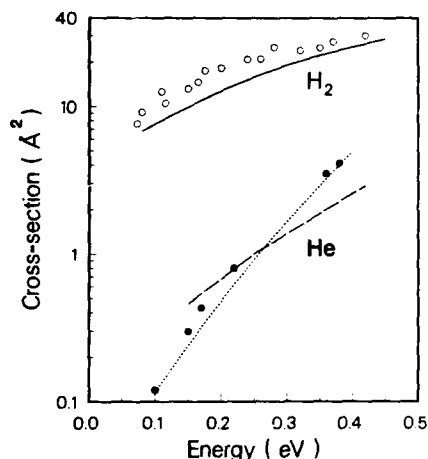


FIGURE 5

Absolute value of process (5) cross-section as a function of collision energy. Experimental data for He (full circles) and H₂ (open circles). Theoretical calculations for He (dashed and dotted curves) and H₂ (full curve). See text.

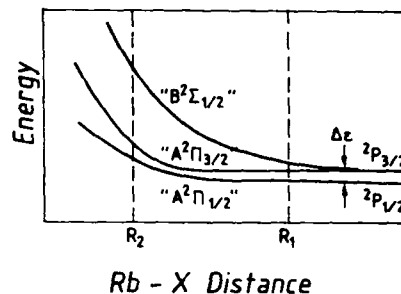


FIGURE 6

Scheme of the potential energy curves describing the Rb(5P)-He interaction. R₁ and R₂ are the distances where the first and second radial coupling are localized (see text).

with the He experimental data is observed. With He, because of its spherical symmetry, a selection rule prevents radial coupling between the $\Sigma_{1/2}$ and the $\Pi_{3/2}$ curves. This no longer the case with H₂ because it is not a spherical perturber. For this reason a second radial coupling occurs which couples the curves $\Sigma_{1/2}$ and $\Pi_{3/2}$ at closer distances than the first radial coupling (R₂ is roughly equal to 6 a.u.). When this second coupling is included in the above semiclassical calculation, the full curve of figure 6 is obtained. It is in good agreement with the H₂ data.

This example is important because it shows that resonances are not the only mechanism by which molecular perturbers are different from atomic perturbers.

Slightly outside the scope of this report, but nonetheless interesting is that the simple semiclassical model used above is not the only way to calculate the cross-section of fine structure transitions. Full quantum treatments are now available for both rare gas and molecular perturbers [27,28,29]. They are especially efficient for rare gas perturbers since very accurate potentials are available [21]. Process (5) for the perturber He is a typical example which shows how well these theories work. (see in figure 5 the excellent agreement between the dotted curve calculated by J. Pascale [private communication] and the He experimental data) [24,25].

3. REACTIVE SCATTERING

An important issue in chemical kinetics is understanding the role of reactant internal excitation on chemical reactivity. Growing interest concerns the reactivity of electronically excited atomic reactants (see for instance [4,5,6,30,31,32,33]). Within the necessarily limited frame of this report we will focus on one reactive process only: process (2) where the effect of electronic excitation in Na is particularly dramatic.

Process (2) is endothermic by 58 kcal/mole and 9.5 kcal/mole when Na is in the states 3S and 3P respectively. If Na is in either states 4D or 5S, the reaction is exothermic with about the same amount of excess energy (41 and 37 kcal/mole respectively).

A crossed beam apparatus, a rotatable detector (electron bombardment ionizer + mass spectrometer) and a two step laser excitation of the Na atoms are used to study process (2). The laboratory angular distribution of the product molecule NaO is measured as shown in figure 7 for various

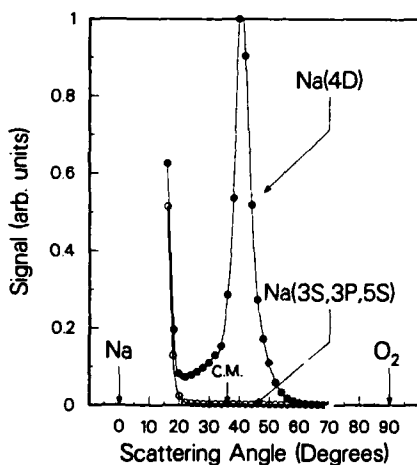


FIGURE 7
Laboratory angular distribution of NaO in process (2). Full circles correspond to the reaction of Na(4D). Open circles correspond to the reaction of Na(3²S, 3²P and 5²S). Lines are fits to the experimental points. Error bars are within the size of each experimental point.

electronic excitations of the Na atoms. These angular distributions have been recorded at a mass/charge ratio of 23 since most of the NaO molecules fragment into Na⁺ in the electron bombardment ionizer. Thus, the rising signal at small scattering angles is not related to the reaction product NaO, but to Na atoms scattered by non reactive processes. The signal due to the reactive process appears at larger scattering angles. Considering figure 7, we thus conclude that no reaction is observed when Na is in either states 3S, 3P or 5S. On the contrary a strong reactive signal is observed with Na(4D).

The most striking feature in figure 7 is the absence of reaction for the level Na(5S) since this level lies only 1350 cm⁻¹ below the reactive 4D level. This indicates that the symmetry of the excited state orbital severely controls the reaction.

The second striking feature in figure 7 is that the NaO product is backward scattered with respect to the Na atoms. This suggests that the reaction does not proceed via a long lived complex but through a direct mechanism with colinear approach. This is a very interesting and unexpected aspect in the dynamics of the reactive process (2): the collision $\text{Na} + \text{O}_2$ is expected to form the long lived complex $\text{Na}^+ - \text{O}_2^-$ very easily. If the reaction (2) were going through such a complex, the angular distribution of NaO would not be so much backward scattered than observed in figure 7. Therefore, the results of figure 7 imply that the long - lived complex $\text{Na}^+ - \text{O}_2^-$ does not lead to the reactive process (2), but to non - reactive processes (e.g. intermultiplet transitions and quenching). This point has been confirmed by a recent polarization measurement showing that the reactive process (2) is favoured when the 4D orbital of Na is aligned perpendicularly to the relative velocity of Na and O_2 (i.e. when the excited valence electron of Na is kept away from the O_2 molecule in order to prevent the electron transfer) [34].

The experimental observations of figure 7 do not yet receive a theoretical interpretation. We consider they are interesting enough to motivate such an investigation.

4. CONCLUSION

We hope that the examples reported here have been able to clarify the respective role played by the collision energy and by the rotational energy of the molecular perturber in inelastic collisions such as process (1). For instance, for collision energies larger than 0.2 eV (relative velocity $\text{Rb-H}_2 > 4000$ m/s), the rotation of the molecule plays no role in the intermultiplet transfer $\text{Rb}(7S - 5D)$. On the contrary, for lower energies, the molecular rotation can have a very important effect if near resonant conditions are fulfilled.

Concerning reactive scattering, we have seen that adding energy in the form of electronic excitation into the atomic partner affects the reaction in a way which is definitely not explained by simple energy balance considerations. The symmetry of the excited state orbital must be considered.

ACKNOWLEDGMENT

I acknowledge fruitful conversations with F. Gounand and L. Petitjean (collision of Rydberg states), J. Berlande, J. Cuvellier, F. Paillard and P. de Pujo (intermultiplet mixing and fine structure transitions), Y.T. Lee, P.S. Weiss, H.Schmidt and M. Covinsky (Reactive scattering).

REFERENCES

- [1] V. Bocvarski, J. Robert, I. Colomb de Daunant, M. Dumont, J. Reinhardt J. Baudon Abstract to the 2nd ECAMP Amsterdam (1985).
- [2] W.H. Breckenridge H. Umemoto Adv. Chem. Phys. 50, 325 (1982).
- [3] I.V. Hertel Adv. Chem. Phys. 50, 475 (1982).
- [4] W.H. Breckenridge in Reactions of small transient species M. Clyne and A. Fontijn eds. Academic Press, p 158 (1983).
- [5] J.C. Whitehead in Comprehensive Chemical Kinetics vol 24 Elsevier (1983)

- [6] P.S. Weiss, J.M. Mestdagh, H. Schmidt, M.F. Vernon, M.H. Covinsky, B.A. Balko, and Y.T. Lee Conference on Recent Advances in Molecular Reaction Dynamics, Aussois, France (1985)
See also the progress report given in this conference by H. Schmidt, I.V. Hertel and Y.T. Lee.
- [7] L. Petitjean These d'etat Paris (1985).
- [8] M. Hugon, B. Sayer, P.R. Fournier and F. Gounand J. Phys. B 15, 2391 (1982).
- [9] M. Ahrweiller, M. Hugon, P.R. Fournier and A. Hourdin J. Phys. Appl. 17, 349 (1982).
- [10] L. Petitjean, F. Gounand and P.R. Fournier Phys. Rev. A 30, 71 (1984).
- [11] L. Petitjean, F. Gounand and P.R. Fournier Phys. Rev. A 30, 736 (1984).
- [12] An extensive review of theoretical works is found in Rydberg States of Atoms and Molecules, R.F. Stebbings and F.B. Dunning eds. Cambridge university. Cambridge, NY, 1983).
- [13] F. Gounand and L. Petitjean Phys. Rev. A accepted for publication.
- [14] A.P. Hickman Phys. Rev. A 19, 994 (1979).
- [15] M. Matsuzawa J. Phys. B 12, 3743 (1979).
- [16] F. Gounand and L. Petitjean Phys. Rev. A 30, 2946 (1984).
- [17] L. Petitjean and F. Gounand Phys. Rev. A 30, 2946 (1984).
- [18] J. Cuveillier, J.M. Mestdagh, J. Berlande, P. de Pujo and A. Binet Revue Phys. Appl. 16, 679 (1981).
- [19] J.M. Mestdagh, J. Berlande, J. Cuveillier, P. de Pujo and A. Binet J. Phys. B 15, 439 (1982).
- [20] J. Cuveillier, L. Petitjean, J.M. Mestdagh, D. Paillard, P. de Pujo and J. Berlande Submitted to J. Chem. Phys.
- [21] J. Pascale Phys. Rev. A 28, 632 (1983).
- [22] F. Rossi and J. Pascale Submitted to Phys Rev A.
- [23] J.M. Mestdagh, P. de Pujo, J. Cuveillier, A. Binet, P.R. Fournier and J. Berlande J. Phys. B 15, 663 (1982).
- [24] A.P. Hickman Phys. Rev. Lett. 47, 1587 (1981).
- [25] A.P. Hickman J. Phys. B 15, 3005 (1982).
- [26] E.E. Nikitin Adv. Chem. Phys. 28, 317 (1975).
- [27] F. Rebentrost and W.A. Lester Jr J. Chem. Phys. 67, 3367 (1977).
- [28] R.E. Wyatt and R.B. Walker J. Chem. Phys. 70, 1501 (1979).
- [29] R.H.G. Reid J. Phys. B 6, 2018 (1973).
- [30] R.J. Buss, P. Casavecchia, T. Hirooka, S.J. Sibener and Y.T. Lee Chem. Phys. Lett. 82, 386 (1981).
- [31] J.W. Cox and P. Dagdigian J. Chem. Phys. 79, 5351 (1983).
- [32] Huoy-Jen and P. Dagdigian J. Chem. Phys. 81, 2375 (1984).
- [33] H. Schmidt, P.S. Weiss, J.M. Mestdagh, M.H. Covinsky and Y.T. Lee To appear in Chem. Phys. Lett.
- [34] P.S. Weiss, J.M. Mestdagh, M.H. Covinsky, H. Schmidt, M. F. Vernon and Y.T. Lee In preparation.

NEGATIVE ION FORMATION BY COLLISION OF RYDBERG ATOMS WITH CLUSTERS

Tamotsu KONDOW

Department of Chemistry, Faculty of Science,
The University of Tokyo, Bunkyo-ku, Tokyo 113
Japan

I. INTRODUCTION

In a collisional process involving a high-Rydberg rare gas atom, Rg^{**} , with a target molecule, M , the outermost electron (Rydberg electron) of Rg^{**} is readily liberated as a result of rotational or vibrational de-excitation of M (1). This collisional process can be treated as a scattering of a free electron by M ; here the electron is postulated to have a momentum and an energy distribution identical with those of the Rydberg electron bound to its core ion, Rg^+ . When M has a positive electron affinity, one expects collisional transfer of the Rydberg electron to M , that is,



The cross section for this process is governed by the interaction potential between the target molecule and the Rydberg electron. Typical systems such as SF_6-Rg^{**} (2) and CCl_4-Rg^{**} (3) have been studied in detail. When the target molecule, M , has a negative electron affinity, the cross section for process (1) is almost zero, partly because of the instability of M^- . Even in such a case, M^- is known to exist in the liquid phase and, therefore, M^- may be stabilized by charge-dipole and/or charge-induced dipole interactions in a van der Waals cluster of a certain size, $(M)_n$. In this case, one can expect that the electron-transfer cross section for



is sizable and increases with its size, n . Process (2) is probably composed of two major processes: (a) collisional electron transfer from Rg^{**} to an energy state of $(M)_n$ and (b) multiple inelastic collisions of the transferred electron inside $(M)_n$. The former process is similar to process (1) and is often encountered in atomic collisions, while the latter process resembles that of electron diffusion in the condensed phase. In other words, a collision process involving a cluster can be treated as a hybrid of those encountered in atomic physics and in solid state physics.

The kinetic energy of the Rydberg electron is very small (~ 10 meV), and the attachment cross section is expected to be on the order of 10^{-12} - 10^{-13} cm² (1). Therefore, collisional electron transfer (process (2)) can be used for gentle and efficient production of negative cluster ions from $(M)_n$. In mass spectroscopic studies of a van der Waals cluster, it is desirable to maintain the cluster essentially undisturbed in the process of ionization so as to obtain information on the parent neutral cluster. The cluster is always fragmented when it is ionized before detection by electron impact, which is used most commonly (4). This fragmentation occurring in the process of ionization tends to destroy information on the properties of the neutral cluster and on the relaxation processes taking place in the cluster during the ionization, and always introduces additional complexities in studies of clusters. In this connection, the collisional ionization with Rg^{**} appears to have a unique advantage.

We have studied collisional electron transfer from Rg^{**} to $(M)_n$ ($M=CO_2$, OCS , CS_2 , CH_3CN , SF_6 , NO , N_2O , C_5H_5N (pyridine) and $C_5H_5N+H_2O$ and detected a variety of negatively-charged cluster ions. Many cluster ions which can scarcely be generated by conventional techniques have been found to be produced with high efficiency. Analyses of the data have provided the vertical electron affinities of the clusters and information on the relaxations accompanied by the electron transfer. The experimental techniques and several typical examples are described in the following sections. The method of RAI is compared with several other methods for formation of negative cluster ions.

II. EXPERIMENTAL TECHNIQUES

A schematic diagram of the apparatus is shown in Fig.1. The apparatus consists of a supersonic beam source with four stages of differential pumping, a triple-grid ion source where neutral clusters are ionized, a quadrupole mass spectrometer with a negative ion detector and a CAMAC system based on an LSI-11/23 computer.

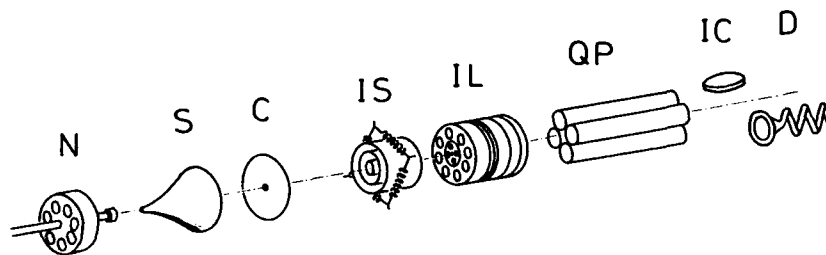


Fig. 1

A schematic diagram of the apparatus used.

N: nozzle, S: skimmer, C: collimator, IS: ionization source, IL: lens, QP: quadrupole mass spectrometer, IC: ion-conversion dynode, D: detector

1. Cluster Beam Source

The beam source consisted of a sonic nozzle having a thin platinum aperture and a Beam Dynamics skimmer with the smallest opening of 0.31 mm diameter; the nozzle-skimmer distance was externally adjusted to be typically 5 mm. The nozzle orifice had a diameter of 50 μm and a channel length of 0.2 mm. A sample gas was seeded in either H_2 or He gas with a stagnation pressure of 2000-2500 Torr, while the nozzle temperature was maintained at 293 K. A gas inlet system made of stainless steel was baked in vacuo before use. The seeded gas was expanded through the nozzle into a nozzle-exhaust chamber and a cluster beam was formed. The chamber pressure did not exceed 10^{-4} Torr when the beam was admitted. The partial pressure of the sample gas used was adjusted so as to maximize the intensity of the positive dimer ion produced by electron impact. The clusters in the supersonic jet were sampled through the skimmer into a collision chamber of 10^{-5} - 10^{-6} Torr, and then introduced into a reaction chamber where a concentric triple grid ion source was placed.

2. Ionization Source

The clusters were ionized in the triple-grid ion source. The source had a housing with 20 mm length and 60 mm diameter, in which three concentric

cylindrical grids and filaments were mounted as shown in Fig.2. The grids G_A , G_B and G_C were made of 50-mesh stainless steel. The central region surrounded by G_A was 20 mm in length and 10 mm in diameter. All grids were insulated by ruby balls of 3 mm diameter. The housing was isolated from the grids by steatite spacers. Four pieces of helical filaments made of thoriated tungsten wire of 0.15 mm diameter formed a regular square. A typical filament wattage was 5A x 7V. The cluster beam passing through the central region was ionized either by impact of Rg^{**} or by electron impact. Rare gas, Rg (Ar or Kr), with 99.95% purity was excited in the exterior of G_B by 50 eV-electrons. Ionic species and electrons were deflected back by application of appropriate potentials to the three grids so that only neutral species including Rg^{**} were allowed to enter the central region. The pressure in the ion source was evacuated to 1×10^{-6} Torr. When the rare gas was admitted, the pressure increased to 3×10^{-5} Torr. The principal quantum numbers, n_p , of Rg^{**} were estimated to range from 25 to 35: Rg^{**} with $n_p > 35$ were ionized by the field of 430 V/cm between G_A and G_B , and Rg^{**} with $n_p < 20$ could not reach the central region because of their short radiative lifetimes.

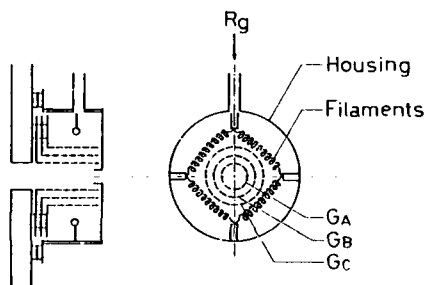


Fig. 2

A Schematic diagram of the ion source. The three concentric grids, G_A , G_B , and G_C are installed for preventing charged species from penetrating into the central collision region.

The following observations indicated that the observed negative ions originated from the electron transfer from Rg^{**} to the clusters by collision: (a) The signal intensity depended linearly on the pressure of Rg , (b) started to rise at the threshold energy of Rg^{**} , and (c) diminished almost completely by application of ~ 400 V between G_A and G_B ; this observation was interpreted as the field ionization of Rg^{**} at 1.3 kV/cm. Figure 3 shows that the negative ion spectrum obtained from the CH_3CN cluster by Ar^{**} impact is almost identical with that by Kr^{**} impact. By proper selection of the potentials applied to the three grids, electrons with an average energy of ~ 1 eV were admitted into the central region, where the cluster beam was bombarded by the electrons. ϕ was estimated from the difference between the potential of G_A and that of the filaments.

3. Mass Selection and Detection of Ions

The negative cluster ions thus produced were extracted through an entrance slit into a quadrupole mass spectrometer (Extranuclear, 162-8) installed in a detection chamber, where the pressure was approximately 5×10^{-7} Torr when the ion beam was admitted. The mass-selected ions were detected by a Ceratron (Murata) equipped with an ion conversion dynode made of a stainless-steel disk of 22 mm diameter placed perpendicularly to the beam axis. The time of flight between the ion source and the Ceratron was 20-100 μ s for the ions studied. The dynode, by which the negative ions were converted to positive ions before the detection, was found to improve the signal-to-noise ratio by three orders of magnitude. The maximum mass of the analyzed ions was m/z 1650, and the mass resolutions were about 10^2 at m/z 146 and about 300 at m/z 1460. The transmission and detection efficiencies of the mass spectrometer were calibrated by the known fragmentation patterns of the positive and negative ions produced from perfluorokerosene (PFK) by electron impact (5). The mass numbers were

calibrated by the fragment ions of PFK below m/z 800 and by the cluster ions of CO_2 above m/z 800. The measurement and the data acquisition were controlled by a Canberra #30 multichannel analyzer and a CAMAC-crate-mounted LSI-11/23 microcomputer. The intensity of a mass-selected ion was determined by the area of the peak in the calibrated mass spectrum. The reproducibility of the intensity was better than 10% over a period of several hours. Background noises were negligibly small in the spectrum obtained by electron impact while dark counts for Rg^{**} impact were 15-20 cpm.

III. EXPERIMENTAL CHARACTERISTICS OF NEGATIVE CLUSTER-ION FORMATION

When Rg^{**} or electrons are allowed to collide with a cluster with a size n , $(M)_n$ ($M=\text{CO}_2$, OCS , CS_2 , CH_3CN , SF_6 , NO , N_2O , $\text{C}_5\text{H}_5\text{N}$ and $\text{C}_5\text{H}_5\text{N}+\text{H}_2\text{O}$), negatively charged cluster ions are produced as summarized in Table 1.

Table 1

M	observed in (RAI)	m_L	observed ion (EI)	m_L
CO_2	$(\text{CO}_2)_m^-$	7	$(\text{CO}_2)_m^-$	3
OCS	$(\text{OCS})_m^-$	2	no data	
CS_2	$(\text{CS}_2)_m^-$	1	$(\text{CS}_2)_m^-$ $\text{S}(\text{CS}_2)_m^-$	1 0
CH_3CN	$(\text{CH}_3\text{CN})_m^-$	10	$(\text{CH}_3\text{CN})_m^-$ (very weak)	-
SF_6	$(\text{SF}_6)_m^-$	1	$(\text{SF}_6)_m^-$ SF_5^-	1
NO	$\text{NO}_2(\text{N}_2\text{O}_3)_m^-$	0	$\text{NO}_2(\text{N}_2\text{O}_3)_m^-$	0
	$\text{NO}_3(\text{N}_2\text{O}_3)_m^-$	0	$\text{NO}_3(\text{N}_2\text{O}_3)_m^-$	0
	$\text{N}_2\text{O}_4(\text{N}_2\text{O}_3)_m^-$	0	$\text{N}_2\text{O}_4(\text{N}_2\text{O}_3)_m^-$	0
N_2O	$(\text{N}_2\text{O})_m^-$	10		
	$\text{O}(\text{N}_2\text{O})_m^-$	6	$\text{O}(\text{N}_2\text{O})_m^-$	0
$\text{C}_5\text{H}_5\text{N}$	$(\text{C}_5\text{H}_5\text{N})_m^-$	4	$(\text{C}_5\text{H}_5\text{N})_m^-$	4
$\text{C}_5\text{H}_5\text{N}+\text{H}_2\text{O}$	$(\text{C}_5\text{H}_5\text{N})_m(\text{H}_2\text{O})_m^-$	$m+m'=4$	$(\text{C}_5\text{H}_5\text{N})_m(\text{H}_2\text{O})_m^-$	$m+m'=4$
	$(\text{C}_5\text{H}_5\text{N})_3(\text{H}_2\text{O})_k^-$		$(\text{C}_5\text{H}_5\text{N})_3(\text{H}_2\text{O})_k^-$	
	(the most abundant)		(the most abundant)	
	$1 \leq k \leq 4$		$1 \leq k \leq 4$	

1. Negative Ion Formation by Rydberg Atom Impact (RAI)

In all the clusters studied except for those of NO and N_2O , the dominant product ions are $(M)_m^-$, as exemplified in Figs.3 and 4. These spectra have the following common features: (a) The spectra obtained by use of different rare gases are almost identical (see Fig.3). (b) The intensity of $(M)_m^-$ rises at a threshold size, m_L , increases with increasing m , passes through a broad maximum at about m_L+10 and falls off gradually. (c) Several outstanding peaks are discernible at m_M (magic numbers). (d) A depletion region ($11 \leq m \leq 13$) is found in the spectrum of $(\text{CO}_2)_m^-$ (see Fig.4).

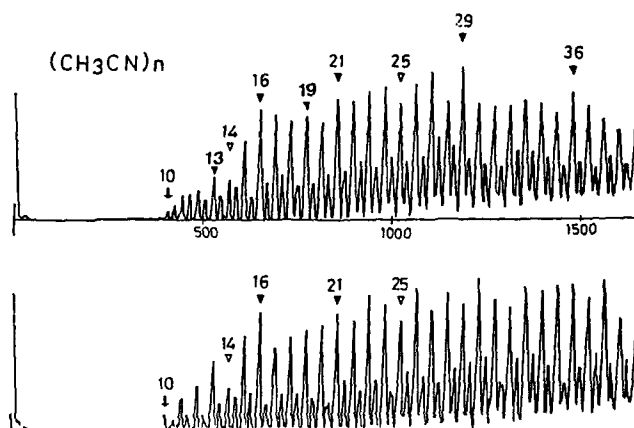


Fig. 3

The mass spectra of $(\text{CH}_3\text{CN})_n^-$ produced from $(\text{CH}_3\text{CN})_n$ in collision with Kr^{**} (upper panel) and Ar^{**} (lower panel).

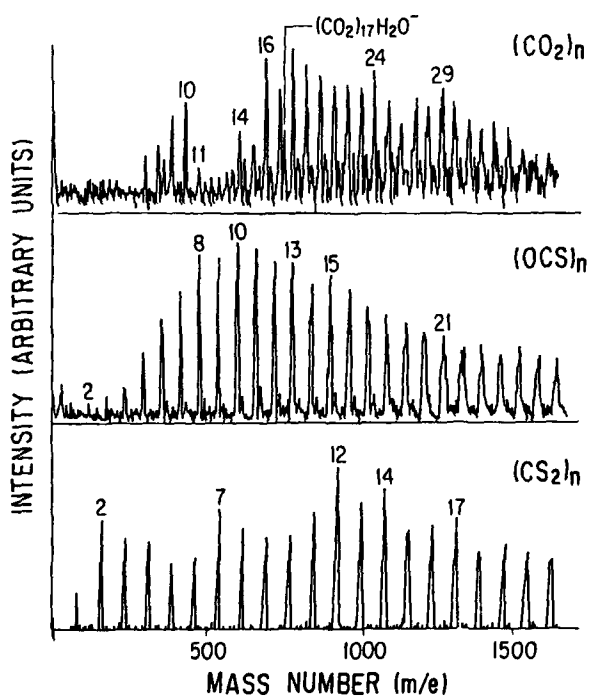


Fig. 4

The mass spectra of $(M)_n^-$ ($M = \text{CO}_2$, OCS and CS_2) from $(M)_n$ produced by Kr^{**} impact.

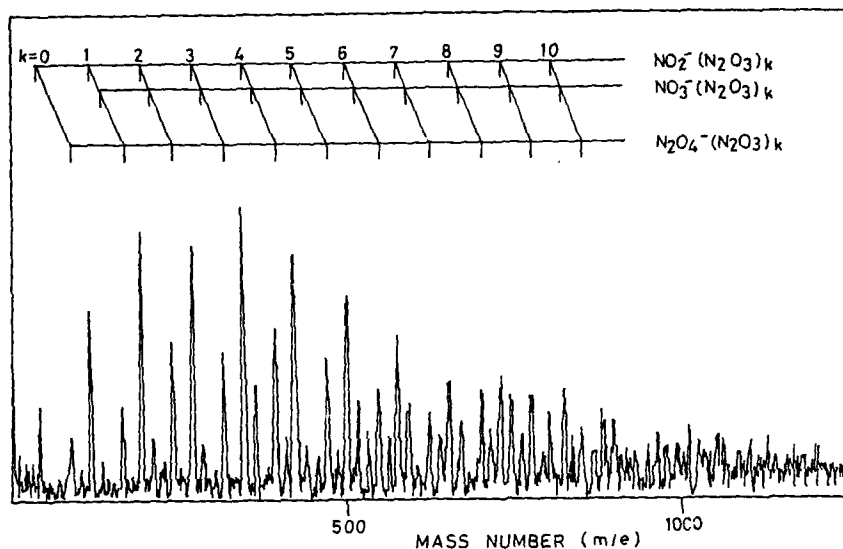


Fig. 5

The mass spectrum of the product ions from $(\text{NO})_n$ in collision with Kr^{**} .

On the other hand, the clusters of NO and N_2O are dissociatively ionized, and $[\text{NO}_2(\text{N}_2\text{O}_3)_m]^-$, $[\text{NO}_3(\text{N}_2\text{O}_3)_m]^-$ and $[\text{NO}_2\text{O}_4(\text{N}_2\text{O}_3)_m]^-$ are generated from $(\text{NO})_n$, while $[(\text{N}_2\text{O})_m\text{O}]^-$ in addition to a small amount of $(\text{N}_2\text{O})_m^-$ are generated from $(\text{N}_2\text{O})_n$. As an example, the spectrum for $(\text{NO})_n$ is shown in Fig. 5. The spectra for $(\text{NO})_n$ and $(\text{N}_2\text{O})_n$ both exhibit features similar to those mentioned above ((a)-(c)). Especially in the $\text{C}_5\text{H}_5\text{N}+\text{H}_2\text{O}$ cluster system, $[\text{C}_5\text{H}_5\text{N}(\text{H}_2\text{O})_m]^-$ are detected for $m+m'=4$. Furthermore, the intensity of the negative ions have a maximum value at $m'+m=5-7$, as shown in Fig. 6.

2. Negative Ion Formation by Electron Impact (EI)

In comparison with the ionization by RAI, the present EI ionization reveals the following properties common to all the cluster systems investigated: (e) The cross sections for the negative ion formation by EI are 10^{-3} - 10^{-4} of those by RAI. For example, $(\text{CH}_3\text{CN})_m^-$ is not efficiently produced by EI on $(\text{CH}_3\text{CN})_n$. (f) Fragmentation associated with bond rupture of the component molecule occurs extensively in the EI ionization, as is shown in Fig. 7. In the cases of CO_2 , OCS , CS_2 and SF_6 , (g) the size distributions given by EI are found to be significantly different from those by RAI. Figure 8 shows an example, where the size distributions of $(\text{CO}_2)_m^-$ for EI and RAI are given. Ions with smaller sizes tend to be more populated in the EI ionization and the magic numbers in the spectra for EI differ from those for RAI. (h) In the cases of NO, N_2O , $\text{C}_5\text{H}_5\text{N}$ and $\text{C}_5\text{H}_5\text{N}+\text{H}_2\text{O}$, on the other hand, the size distributions of the product ions given by EI are found to be almost identical in shape with those given by RAI.

IV. IONIZATION PROCESSES BY RYDBERG ATOM IMPACT

1. Two-Step Mechanism

The collisional ionization of a cluster with Rg^{**} can be accounted for in terms of a two-step mechanism, that is,

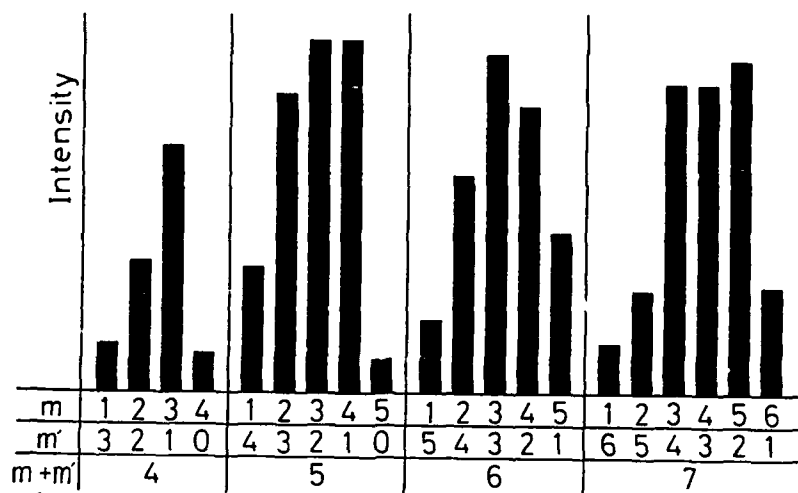


Fig. 6

The size-distribution of a hydrated pyridine cluster anion, $(C_5H_5N)_m(H_2O)_m^-$, produced from $(C_5H_5N)_n(H_2O)_n^+$ in collision with Kr^{**} .

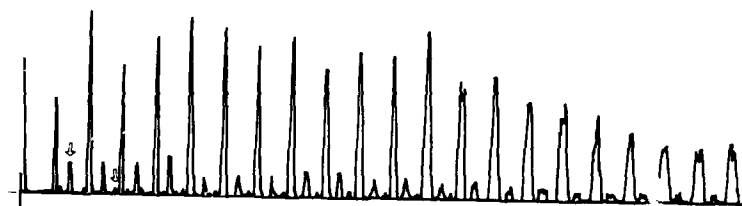
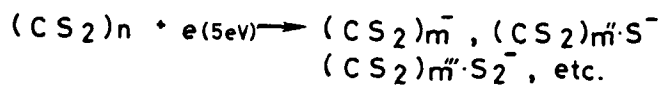
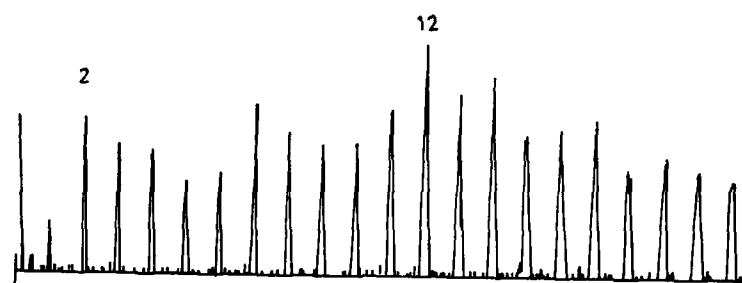
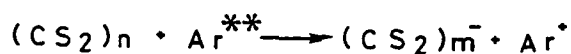


Fig. 7

Comparison of the mass spectrum of $(CS_2)_m^-$ produced by RAI with that by EI.

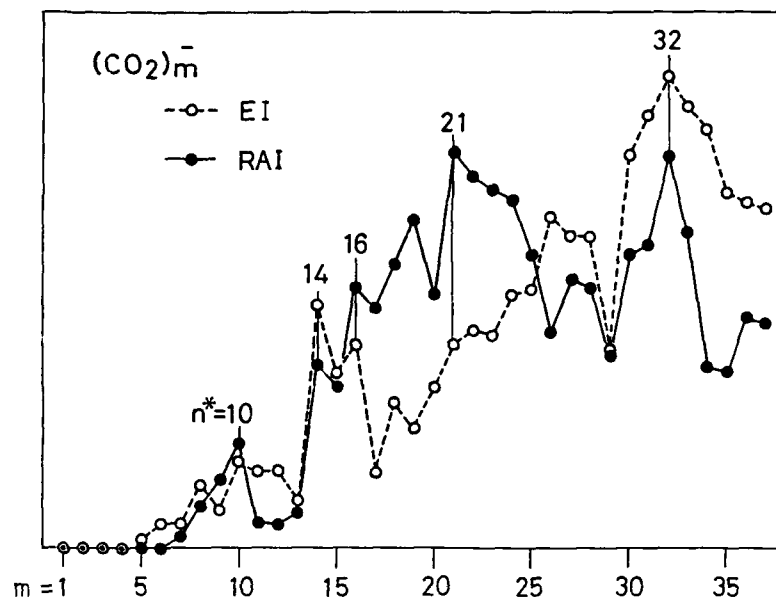


Fig. 8

The size-distribution of $(\text{CO}_2)_m$ produced by RAI in comparison with that by EI.



In process (3), the Rydberg electron of Rg^{**} having a kinetic energy of ~ 10 meV is transferred to an extended electron affinity state of $(\text{M})_n$ which retains its original geometry. The transferred electron in the extended state transmits its energy efficiently to the vibrational modes of the cluster (6) and is successively trapped into one component molecule. The energy released by the trapping is removed by evaporating $n-m$ ($\approx p$) molecules of M (process (4)). In some cases, the cluster ion, $(\text{M})_n^{*+}$, is excited in a repulsive state and fragmented into specific cluster ions (process (4)'). As argued in the following sections, the electron relaxation in the cluster varies cluster to cluster depending on the properties of the component molecule.

2. Non-Evaporative Ionization

In the case of the SF_6 cluster, $(\text{SF}_6)_n$, the excess energy released is estimated to be so insignificant that the cluster does not seem to evaporate sizably as argued below. When the Rydberg electron is attached to $(\text{SF}_6)_n$, the electron is trapped in a particular SF_6 molecule to form a vibrationally excited SF_6^* (1). Its vibrational energy is approximately 0.5 eV which is the electron affinity of SF_6 (7). This energy is transmitted to the intermolecular motions of the surrounding SF_6 , namely, the vibration of van der Waals bonds within 1 ns (8), and hence the effective temperature of the cluster ion is increased. In a typical case for $n=5$, the effective temperature rise, ΔT , amounts to about 180 K, because 15 intramolecular modes of SF_6 and 24 intermolecular modes of the cluster are expected to take part in the energy dissipation. This ΔT decreases with the size, n . Since the effective boiling temperature at which evaporation

becomes appreciable is estimated to be higher than 210 K, which is the sublimation temperature of solid SF_6 (9), it is unlikely that substantial evaporation participates in the ionization of $(\text{SF}_6)_n$ ($n=5$) by RAI. This argument is also valid in the case of $(\text{CH}_3\text{CN})_n$. The released energy is estimated to be about 1.5 eV, the sublimation energy of the monomer anion in the cluster, which is calculated on the assumption of the charge-dipole interaction between the anion and its solvated core. In this case, ΔT is at most 300 K for $n=13$ and is probably below the effective boiling temperature of $(\text{CH}_3\text{CN})_n^-$ expected from the well depth of the Lennard-Jones potential of CH_3CN (10). Accordingly, no significant evaporation takes place. The magic numbers at $m_M=13, 16, 19, 23, 26$ and 29 (see Fig.3) may be related to the stability of the neutral cluster. However, this conclusion is not definitive since even a small amount of evaporation possibly alters the size distribution. Similar arguments can be applied to $(\text{C}_5\text{H}_5\text{N})_n$ and again these clusters are considered to be non-evaporative in the ionization processes, since ΔT is about 300 K for $(\text{C}_5\text{H}_5\text{N})_5^-$ while the boiling point of $\text{C}_5\text{H}_5\text{N}$ is 388 K.

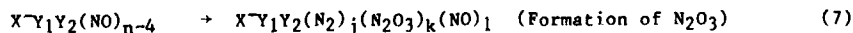
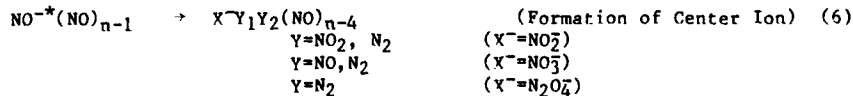
3. Evaporative Ionization

The depletion region observed in the $(\text{CO}_2)_m^-$ spectrum (see Fig.4) is ascribable to the evaporation of CO_2 from the initial cluster ion, $(\text{CO}_2)_n^-$, as described below. The energy released in process (4) could be as much as 3.5 eV, the difference in energy between CO_2^- in the linear and the bent configurations (11, 12). In a typical cluster with $n=13$, this energy difference corresponds to an effective temperature of about 900 K, which is well above the temperature range where the evaporation rate becomes appreciable (13). Therefore, evaporation is certain to occur. $p(=n-m)$ can be regarded as a constant value, p_0 , because the temperature rise is not strongly dependent on n . However, p becomes conspicuously small for $m_M < n - m_M + p_0$, since the evaporation ceases when a distinctly stable cluster ion, $(M)_{m_M}^-$, happens to be formed during the evaporation. This sudden decrease of p gives rise to a depletion region just below m_M having a width of $p_0 - 1$ in the spectrum: $(M)_n^-$ with $n=m_M$ boils off p_0 molecules of CO_2 . On the other hand, no ions are produced by dissociation from higher cluster ions in the depletion region because of the presence of $(M)_{m_M}^-$. Since $m_M=14$ and 16 and the size gap of the depletion region is 3 (finding (d)), one can conclude that at least 4 molecules of CO_2 are evaporated in process (4).

In the case of $(\text{CS}_2)_n$, our study on the dependence of the stagnation pressure of the ion signals shows that one molecule of CS_2 is eliminated in process (4) ($2 \leq n \leq 7$), that is, $p=1$ (4). On the other hand, $(\text{GCS})_n$ exhibits intermediate characteristics between those of the other clusters probably because of its intermediate nature between CO_2 and CS_2 ; $m_L=2$ and the evaporation of 2 or 3 molecules evidenced by a gentle rise of the intensity in the threshold region.

4. Dissociative Ionization

The ionization of the NO and N_2O clusters by RAI can be explained by a series of intracluster atomic rearrangements (process (4)'), where N_2 molecules are ejected from the initially formed cluster ion, $(M)_n^-$ ($M=\text{NO}$ and N_2O). In the case of NO, atomic rearrangements occur among NO molecules in the cluster when it is negatively charged by electron transfer from Rg^{**} . It is conceivable from the observed product ions (see section 2 of Chapter III) that the intracluster atomic rearrangements proceed via the following processes:





In the evaporation process (process (8)), the N_2O_3 ligands are left in the charged cluster probably because the dipole moment and polarizability of N_2O_3 are the largest among other species, N_2 , NO and NO_2 , so that N_2O_3 is held by its center anion most firmly.

In the case of N_2O , a dissociative ionization with an intramolecular bond rupture and a simple evaporative ionization seem to proceed simultaneously; the former and the latter give $[(N_2O)_mO]^-$ and $(N_2O)_m^-$, respectively. In the former case, the excess energy in the initial ion, $(N_2O)_n^+$, is carried away by the ejection of N_2 , and hence no significant evaporation of N_2O is conceivable. In other words, $(N_2O)_n$ is dissociatively ionized to be $[(N_2O)_{n-1}O]^-$. The latter process is similar to those of CO_2 etc. $(N_2O)_n^+$ is formed by vertical electron transfer from Rg^{**} and is then stabilized by trapping the Rydberg electron in a particular N_2O in a bent configuration (14). It is highly likely that evaporation is followed by the electron transfer.

5. Vertical Electron Affinities of the Clusters

In a cluster whose monomer unit has negative vertical electron affinity, the negatively charged cluster ion starts to appear at a threshold size below which no ion is formed (see Table 1). On the basis of the two-step mechanism, the cluster size n_L beyond which the vertical electron affinity of the cluster turns to be positive can be estimated from the observed m_L values and the $p(=n-m)$ values. That is, n_L is given by the sum of p and m_L . The n_L values thus obtained are listed in Table 2. Here, in the ionization of the N_2O cluster, it is postulated that $[(N_2O)_{n-1}O]^-$ is produced via $(N_2O)_n^+$.

V. Comparison with Other Ionization Processes

Thermal electrons also attach to the neutral clusters investigated (see

Table 2

M	m_L	$p(=n-m)$	n_L
CO_2	7	4	11
OCS	2	2-3	4-5
CS_2	1	1	2
SF_6	10	0	10
NO	-	-	-
N_2O	6	1	7
C_5H_5N	4	0	7
$C_5H_5N+H_2O$	4*	0	4

* $(C_5H_5N)_m(H_2O)_m$ starts to appear for $m+m' \geq 4$.

Chapter III). Similar studies are also reported by other groups (15). The two-step mechanism appears to operate in the EI ionization on the basis of the results given in Chapter III and the reported results. In the case of EI, the

kinetic energy of the incoming electron is so much larger that the attachment cross section (similar to process (3)) should be smaller and the relaxation (process (4) or (4)') should be more extensive. Indeed, the cross sections for the production of the negative ions are found to be three to four orders of magnitude smaller than those for RAI (see feature (e) in Chapter III). The size distributions given by EI differ from those by RAI (see feature (g) or Fig. 8), probably because of a larger amount of evaporation from the clusters owing to the collision with the energetic electrons. The extensive relaxation in the EI ionization is also evidenced in the mass spectra in which many fragmented ions are observed (see feature (f)).

It is reported recently that electron attachment to a weakly bound molecular cluster has been carried out by using endoergic electron transfer between an alkali metal and the cluster (16). In this collisional transfer, the electron jump occurs in the strong transient Coulombic field of the departing alkali cation and hence is proved to be adiabatic at least for the dimer. However, the adiabatic electron attachment is not permitted for clusters larger than dimers.

Low energy electrons emitted from a metal surface thermoionically or by photon impact are injected into a condensation zone of a supersonic expansion. Negative ions, $(\text{H}_2\text{O})_n^-$ and $(\text{NH}_3)_n^-$, are detected under conditions where neutral H_2O and NH_3 clusters are grown (17). This method is powerful for growing adiabatically negative cluster ions which are otherwise difficult to produce. The attachment proceeds under a multiple collision condition so that the cluster ions thus produced are relaxed and do not carry information on the corresponding neutral clusters. This ionization is particularly useful for the studies of thermodynamical properties of negative cluster ions. Swarm experiments can also be classified into multiple collision types of studies which are reviewed in the same proceeding (18).

In comparison with these techniques, the method of RAI is particularly suitable for dynamical studies of the electron capture processes to weakly-bound systems, such as van der Waals clusters. The Rydberg electron having a subthermal energy is expected to perturb the clusters in a much lesser amount, as argued in the previous sections.

VI. Future Prospects

The method of a gentle and efficient production of the negative cluster ions achieved in the present study provides an opportunity to study the dynamics of electron attachment processes to weakly bound systems such as van der Waals clusters. In order to gain further insight into the ionization processes, more elaborate experiments should be undertaken. First of all, the cross sections for the production of cluster ions should be measured as a function of the cluster size, n , and the principal quantum number, n_p . It is also essential to obtain internal-state distributions of the cluster and to determine more exact numbers of molecules evaporated in the ionization. A cluster beam with a narrow size distribution is necessary in any case.

From a theoretical point of view, the two-step model can be treated by a similar technique utilized in electron scattering by a solid surface, and a size-dependence of the attachment cross sections can be estimated (19).

ACKNOWLEDGEMENT

This work has been performed by collaboration with Professor K. Kuchitsu. Thanks are due to him and to Mr. K. Mitsuke and F. Misaizu who have assisted me to perform this work.

REFERENCES

- 1) Rydberg States of Atoms and Molecules, eds. R. F. Stebbings and F. B.

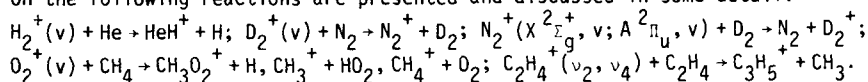
- Dunning (Cambridge Univ. Press, Cambridge, 1983).
- 2) I. Dimicoli and R. Botter, *J. Chem. Phys.* 74 (1981) 2355.
 - 3) I. Dimicoli and R. Botter, *J. Chem. Phys.* 74 (1981) 2346.
 - 4) T. Kondow, K. Mitsuke and K. Kuchitsu, *Rarefied Gas Dynamics*, vol 2, eds. H. Oguchi (Univ. Tokyo Press, Tokyo, 1984) pp.833.
 - 5) R. S. Gohlke and L. H. Thompson, *Anal. Chem.* 40 (1968) 1005.
 - 6) K. Mitsuke, T. Kondow and K. Kuchitsu, submitted to *J. Phys. Chem.*
 - 7) R. N. Compton, P. W. Reinhardt and C. D. Cooper, *J. Chem. Phys.* 68 (1979) 2023.
 - 8) J. Geraedts, S. Stotle and J. Reuss, *Z. Phys. A* 304 (1982) 167.
 - 9) G. H. Cady, *Advan. Inorg. Chem. Radio-chem.* 2 (1960) 105.
 - 10) J. Farges, M. F. de Feraudy, B. Raoult and G. Torchet, *Surface Science* 106 (1981) 95.
 - 11) R. N. Compton, P. W. Reinhardt and C. D. Cooper, *J. Chem. Phys.* 63 (1975) 3821.
 - 12) J. Pacansky, U. Wehlgren and P. S. Bayus, *J. Chem. Phys.* 62 (1975) 2740.
 - 13) R. D. Etters, K. Flurchick, R. P. Pan and V. Chandrasekharan, *J. Chem. Phys.* 75 (1981) 929.
 - 14) H. Shimamori and R. W. Fessenden, *J. Chem. Phys.* 71 (1979) 3009.
 - 15) for example, C. E. Klotz and R. N. Compton, *J. Chem. Phys.* 69 (1978) 1636.
 - 16) K. H. Bowen, G. W. Liesegang, R. A. Sanders and D. R. Herschbach, *J. Phys. Chem.* 87 (1983) 557.
 - 17) H. Haberland, C. Ludewigt, H-G. Schindler and D. R. Worsnop, *J. Chem. Phys.* 81 (1984) 3742.
 - 18) Y. Hatano, *Electron Attachment to van der Waals Molecules*, this volume.
 - 19) M. Tsukada, private communication.

STATE SELECTED ION-MOLECULE REACTIONS BY TESICO

Inosuke KOYANO, Kenichiro TANAKA, and Tatsuhisa KATO

Institute for Molecular Science, Myodaiji, Okazaki 444, Japan

Some recent results are reported for the state selected ion-molecule reactions obtained using the TESICO (Threshold Electron-Secondary Ion Coincidence) technique. Reactions studied include both charge transfer and rearrangement ones, and the states selected range over vibrational and vibronic states of diatomic ions, vibrational states of polyatomic ions, and spin-orbit states of rare gas atomic ions. As prototypal examples, the results on the following reactions are presented and discussed in some detail:



1. INTRODUCTION

It is more than ten years since the exciting new field known as state-to-state chemistry was opened up in chemical dynamics (1,2). This was evidently brought about with the advent of new chemical and tunable lasers which can prepare reagents in specific internal states (3,4) or identify internal states of nascent reaction products (3,5). However, the laser technique has severe limitations, especially when applied to the state selection of reagent molecules. The wavelength range covered by a single laser is highly limited and thus no single laser can excite molecules successively to a series of internal states of interest ranging over wide energies. Also, different lasers are needed for different molecules. Moreover, the laser technique is not a direct one. Information on a state selected process is usually deduced indirectly by subtracting a measured number from another, neither of them being a quantity belonging to the single state in question. Furthermore, these two numbers are usually obtained in two "experiments", i.e., these are not obtained from simultaneous measurements on the same system. Thus slight changes in experimental conditions between the two experiments often cause serious error in the final results obtained, since very small signal changes are dealt with in these experiments. For these and other reasons, the number of molecules or states studied with the laser technique has not been so many as expected at the beginning.

In ion-molecule reactions, selection of reagent internal states is possible based on a completely different principle. Ions, when produced from parent molecules by photoionization, generally populate all energetically accessible internal states and the emitted photoelectrons carry the information on the internal state of the corresponding ion. This very fact enables us to study reactions of ions in each of these populated states separately and directly. Namely, by measuring reactant and product ions in coincidence with photoelectrons of a particular kinetic energy, we can selectively detect only the reactant ions in a single internal state and the product ions produced from reactant ions in that state.

Seven years ago, we took this advantage to develop a technique named TESICO (Threshold Electron-Secondary Ion Coincidence) for the study of state selected ion-molecule reactions. Ever since the technique has successfully been applied to the selection of vibrational and vibronic states of diatomic ions, vibrational states of polyatomic ions (including multi-mode cases), and spin-

orbit states of rare gas atomic ions, thus proving to be very versatile. In the present paper, we present and discuss some recent representative results obtained with this technique.

2. EXPERIMENTAL

The apparatus which we constructed for these purposes is nicknamed TEPSICO and has been described in detail (6,7). It consists of six major parts, as shown schematically in Figure 1: a helium Hopfield continuum light source (LS), a 1 m Seya-Namioka vacuum monochromator (M), an ionization chamber (I), a reaction chamber (R), a hemispherical electrostatic electron energy analyzer (EA), and a quadrupole mass spectrometer (Q), these being assembled together via a six-stage differential pumping system.

The primary ions A and corresponding electrons are produced in the ionization chamber I by photoionization of parent molecule A by the monochromatic vacuum ultraviolet radiation from M. The ions and electrons are repelled out of the chamber in directions perpendicular to the incident photon beam and opposite to each other. The electrostatic electron energy analyzer EA, together with the straight section L₁ which serves as a steradiancy analyzer, selects threshold electrons from those having finite kinetic energies and allows them to pass to the channel multiplier. The ions, on the other hand, are extracted from the ionization chamber, formed into a beam of desired velocity by a lens system L₃, and focused into the reaction chamber R, where they react with neutral molecule B. Product ions C, as well as unreacted primary ions, are extracted from the reaction chamber in the same direction as the primary ion beam, mass-analyzed by a quadrupole mass spectrometer Q, and detected by another channel multiplier. These ion signals are then counted in coincidence with the threshold electron

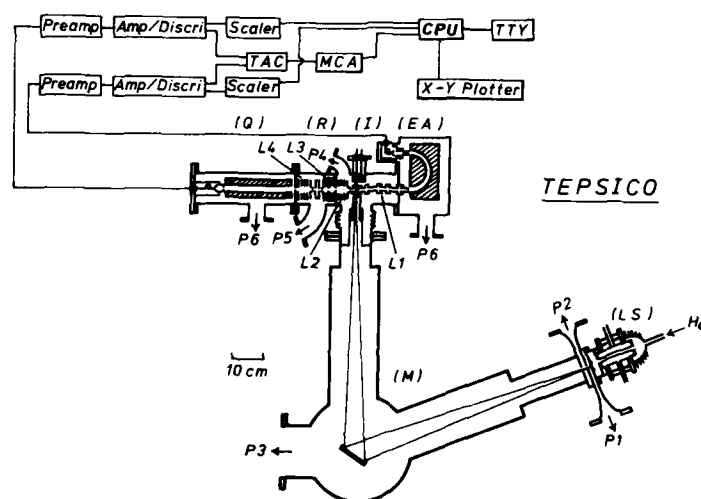


FIGURE 1
Schematic diagram of the TEPSICO apparatus. LS: light source; M: monochromator; I: ionization chamber; R: reaction chamber; Q: quadrupole mass spectrometer; EA: electron energy analyzer; P1-P6: pumping ports; L1-L4: lens systems for electrons and ions.

signals using a standard technique involving a time-to-pulse height converter and a multichannel analyzer.

In some of the studies, the above threshold electron analyzer was replaced by a non-line-of-sight steradiancy analyzer (8) of our own design. Its schematic is shown in Figure 2. This analyzer was found to give 4-5 times more intense threshold electron signals than the above one, although the resolution is somewhat lower. Some reactions with very small cross sections could be studied only with this analyzer.

In preparing and selecting a series of internal states successively, the threshold electron method with variable-wavelength light source as adopted here has several advantages over the method involving fixed-wavelength light (e.g. 584 Å) and analysis of energetic electrons. First, the collecting efficiency for threshold electrons is much higher than that for energetic electrons and, in addition, do not suffer the effect of different angular distributions for different photoelectrons. Second, we do not have to calibrate for the transmission coefficient of the analyzer, which is a function of energy of electrons to be transmitted. Third, in the threshold photoionization, we can often produce ions efficiently in those states that are not attainable in the fixed wavelength photoionization because of unfavorable Franck-Condon factors. This is possible through autoionization from near-resonant neutral excited states, which very often occur even with diatomic molecules. Such examples are given in the next section.

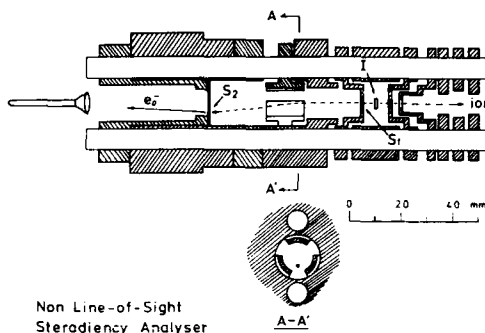


FIGURE 2
Schematic diagram of the non-line-of-sight steradiancy analyzer.

3. THRESHOLD ELECTRON SPECTRUM AND THE APPLICABILITY OF THE TECHNIQUE

The TESICO technique is versatile in the context that it is applicable to any state of any ion provided the state is resolved in the threshold electron spectrum (TES). Thus the TES characteristics are the most important factor in discussing the applicability of the technique to a particular internal state. In this section, we present some examples of threshold electron spectrum to show a variety of internal states that can be studied with this technique.

As an example of diatomic ions, we first show in Figure 3 a TES of N_2^+ , taken with energy resolution of the analyzer of ~ 14 meV (FWHM) and a photon bandwidth of 0.5 Å (FWHM) (9). As is usual with the moderate resolution photoelectron spectra of diatomic molecules, well-resolved vibrational progressions are clearly seen. However, a big difference of this spectrum from the HeI photoelectron spectrum (PES) of N_2 is the greatly enhanced intensities for the $v=1-4$ states of $N_2^+(X^2\Sigma_g^+)$. If one looks at a HeI PES of N_2 , it is seen that the $N_2^+(X^2\Sigma_g^+)$ ions are overwhelmingly dominated by $v=0$, with $v=1$ of less than 10% and essentially none of $v \geq 2$, in agreement with the Frank-Condon distribution. Thus, if one were to use a HeI photoionization, one could study reactions of $N_2^+(X^2\Sigma_g^+)$ only for $v=0$ and 1. In the threshold technique, the ions of all v up to $v=4$ are efficiently produced via autoionization through neutral states lying close to the individual vibrational states of the ion. All these ionic states could conveniently be studied in the reaction and this fact demonstrates the advantage of the threshold method mentioned in the preceding

Section.

The second progression corresponds to the vibrational states of $N_2^+(A^2\Pi_u)$ and exemplifies the feasibility of the technique to study reactions of *vibronic* states. There exists, however, another prerequisite in order for an electronically excited state to be studied with this technique. That is, the state in question must have a radiative lifetime which is at least comparable with and preferably longer than the flight time of the ion between the ionization and reaction chamber. The levels in the $N_2^+(A^2\Pi_u)$ state satisfy this condition, having a radiative lifetime longer than $10\mu s$ (10), although the transition $A^2\Pi_u \rightarrow X^2\Sigma_g^+$ is optically allowed. Thus, we could study several reactions of these vibronic states (11).

In the case of polyatomic molecules, PES or TES are usually broad and vibrational structures are not well resolved. In such a case (e.g. in CH_4), we can study reactions of corresponding ions only as a function of internal energy content and not in terms of selected *states*. However, there exist several favorable cases even with polyatomic molecules. As examples, we show in Figures 4 and 5 the TES of acetylene (12) and ethylene (13), respectively. Acetylene is a case in which progression of only one mode of ionic vibration appears in TES or PES in the threshold region. This progression is well resolved, as can be seen in Figure 4, and is assigned to the ν_2 (C-C stretching) mode. Thus we can study the roles of this mode of vibration in the reactions of $C_2H_2^+$ (12) just as in the case of diatomic ions.

In Figure 5, it is seen that the TES of ethylene is also structured, although peaks are broader than those in acetylene. Four major peaks are assigned (14) to the (0000), (0002), (0100), and (0102) states of the $C_2H_4^+$ ion (the numbers in the parenthesis represent quantum numbers of $\nu_1 - \nu_4$), although there seems to be considerable overlapping of the (0010) and (0012) states, respectively, on the third and fourth peaks. Thus the system involving ethylene provides a unique opportunity to investigate roles of vibrational energies in two different modes, i.e., *mode specificity* in bimolecular reactions.

Two *spin-orbit states* ($J=3/2$ and $1/2$) of rare gas ions in the 2P state constitute another important class of internal states that affect chemical reactions and can conveniently be selected by means of TESICO. The TES of rare gases, e.g., of Ar (not shown), consists of well-resolved simple two peaks corresponding to the $^2P_{3/2}$ and $^2P_{1/2}$ states of the ion, indicating that the reactions of these states are most easily studied by TESICO (15 - 17).

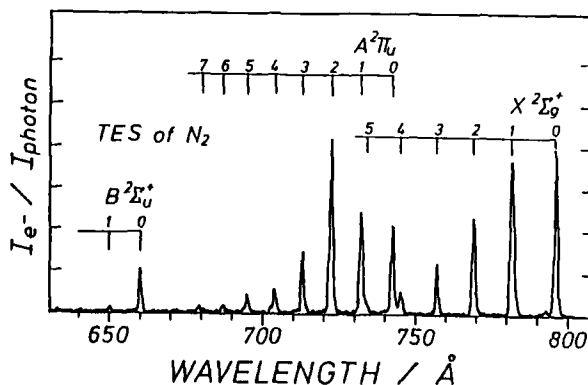


FIGURE 3
Threshold electron spectrum of nitrogen molecule.

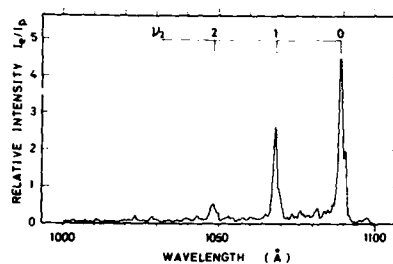


FIGURE 4
Threshold electron spectrum of
acetylene.

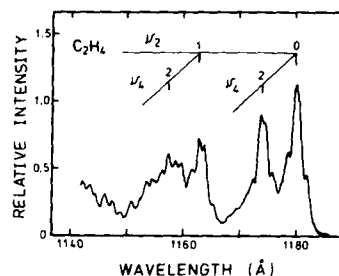


FIGURE 5
Threshold electron spectrum of
ethylene.

4. SOME RECENT RESULTS

4.1. Endoergic adiabatic reaction: $\text{H}_2^+ + \text{He} \rightarrow \text{HeH}^+ + \text{H}$
The reaction



is one of the simplest ion-molecule reactions for which exact calculation of potential energy surfaces is possible. Since the ionization potential of He (24.6 eV) is much higher than that of H_2 (15.4 eV), the excited and charge transferred states of this triatomic system lie far above the ground state so that the reaction at low collision energies is expected to take place on a single (ground) potential energy surface (so-called adiabatic reaction). The reaction is endoergic by 0.80 eV for H_2 ($v=0$) and becomes exoergic for $v=4$ and above. Thus a considerable part of the interest in this reaction centered on the problem of relative importance of vibrational and translational energies in promoting endoergic reactions.

For these reasons, the reaction has been extensively studied in the past, both experimentally and theoretically. Three experimental studies (18 - 20) concerned the vibrational state selection. In two of these (18, 19) the effects of both vibrational and translational energies were investigated, but the information on the reactants' vibrational states was derived indirectly relying on the propensities (21) in the autoionization of H_2 near the ionization threshold. However, the proportion of autoionization to direct ionization at a fixed wavelength is largely dependent on the bandwidth of photons used. Only a recent thermal energy study (20) utilizes a direct technique. We have applied our TESICO technique to investigate the state selected reaction of $\text{H}_2^+(v)$ for $v=0-4$ as a function of relative kinetic energy between 0.4 eV and 3.0 eV. Results are given in Figure 6, where relative cross sections are plotted versus total available energy (vibrational + relative translational). Solid lines connect data points of the same c.m. collision energy and the dotted lines connect those of the same vibrational quantum number.

From the figure, several important features of this reaction are clearly seen. First of all, remarkable vibrational enhancement of the reaction is immediately evident from the solid line curves. The gradients of these curves are sharper for lower collision energies, indicating that the vibrational energy enhances the reaction more effectively at lower collision energies than at higher collision energies. On the other hand, collision energy is seen to be quite ineffective in promoting this endoergic reaction, as evidenced from the $v=0$ and $v=1$ curves; with these low vibrational states, the cross sections are quite small even when the total energy exceeds the endoergicity considerably.

Relative effectiveness of the two forms of energy is readily obtained by

comparing cross sections for successive vibrational states at a fixed total energy, and is found to be a function of the total energy. Such a comparison is numerically given in Table I for three total energies, 1.4, 2.5, and 3.4 eV. It is seen that the replacement of a fixed amount of translational energy by the same amount of vibrational energy enhances the reaction considerably and that this effect is larger for smaller total energy. For instance, the replacement of 0.99 eV of translational energy by vibrational energy

(corresponding to the energy of $v=4$) enhances the reaction by a factor of 110 at 1.4 eV of total energy, while it is only by a factor of 11 at 3.4 eV.

When the cross section for each vibrational state is viewed as a function of collision energy, it is found that, in all the cases except for $v=0$, the cross section first rises sharply at an energy that exceeds the threshold by a certain amount, passes through a maximum, and then decreases sharply until it reaches a common, non-trivial value. The peak position is shifted to smaller energies as the vibrational quantum number is increased. All these features are consistent with the significant involvement of the spectator stripping mechanism (22) in these reactions of the vibrationally excited ions. The common, non-trivial value of the cross section that is reached by all reactions when the collision energy is increased seems to correspond to some other mechanism. The cross sections for $v=0$ rises much more slowly and peak is hardly discernible. The $v=0$ reaction seems to proceed via a non-spectator-stripping mechanism.

The essential features of the above results are in good agreement with previous studies (18, 19) and also with trajectory calculation (23) on a diatomic-molecules potential surface adjusted to fit *ab initio* points. However, there exist several quantitative discrepancies in finer detail between our and previous experimental studies. These discrepancies must originate from the different experimental conditions, such as the purity of the state selection, definition of the kinetic energies, and so on.

4.2 Charge transfer and rearrangement in the $(D_2 + N_2)^+$ system.

This is an example of four-atomic systems $(AB+CD)^+$ on which we have performed rather extensive studies over the last few years. In these systems,

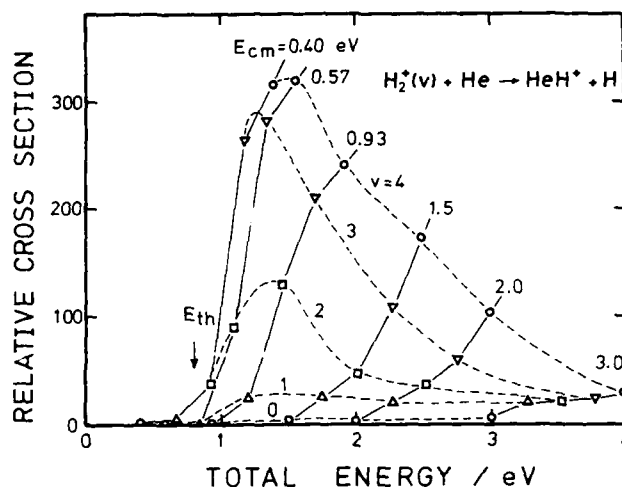


FIGURE 6

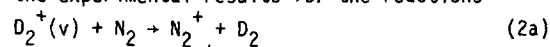
State selected cross sections for reaction (1) as a function of total energy.

Table I. Relative cross sections for the reaction $H_2^+(v) + He \rightarrow HeH^+ + H$ at fixed total energies.

v	E (eV)	Total Energy, E_{tot} (eV)		
		1.4	2.5	3.4
0	0.00	3 (1)	5 (1)	6 (1)
1	0.27	27 (9.0)	20 (4.0)	19 (3.2)
2	0.52	132 (44)	36 (7.2)	22 (3.7)
3	0.77	275 (92)	84 (16.8)	32 (5.3)
4	0.99	320 (107)	170 (34)	66 (11)

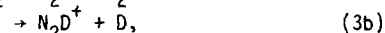
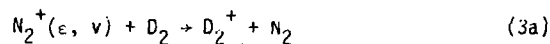
charge transfer and rearrangement reactions often compete, with the same rearrangement product ABC^+ being formed from both reactions $AB^+ + CD$ and $AB + CD^+$.

Figure 7 shows the experimental results for the reactions



obtained at 2.5 eV of collision energy. Here, vibrational states of D_2^+ was selected up to $v=7$. As can be seen from the figure, it has been found that the cross section of reaction (2a) shows a very interesting variation as the vibrational quantum number of D_2^+ changes: The cross section varies regularly, increasing at odd quantum numbers and decreasing at even quantum numbers (upper panel). In contrast, the cross section of reaction (2b) is found to be almost independent of the vibrational quantum number (lower panel). These trends are essentially the same for all collision energies studied (2.5, 6.0, and 9.0 eV).

On the other hand, the results for the reverse reaction, i.e., for the reactions



are shown in Figure 8. Here, ϵ denotes an electronic state, and the states selected are $v=0-3$ of $N_2^+(X^2\Sigma_g^+)$ and $v=0-3$ of $N_2^+(A^2\Pi_u)$. It is seen that, while the cross sections for both reactions (3a) and (3b) are almost independent of the vibrational state in the $X^2\Sigma_g^+$ electronic state, they exhibit interesting dependences on the vibrational state in the $A^2\Pi_u$ electronic state. Moreover, the effect of the electronic excitation to the $A^2\Pi_u$ state on the magnitude of the

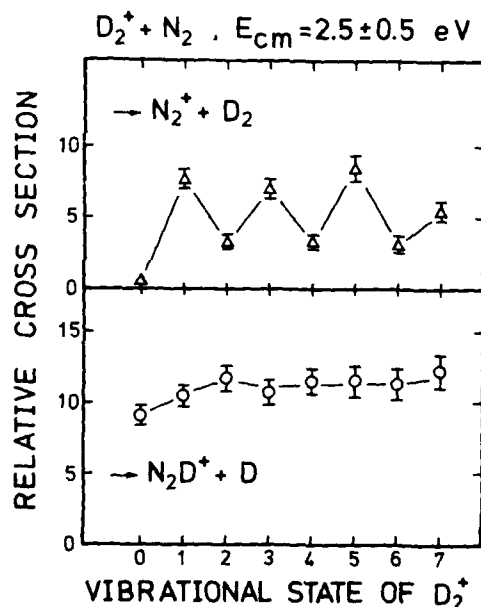


FIGURE 7
Vibrational state selected cross sections
for reactions (2a) and (2b).

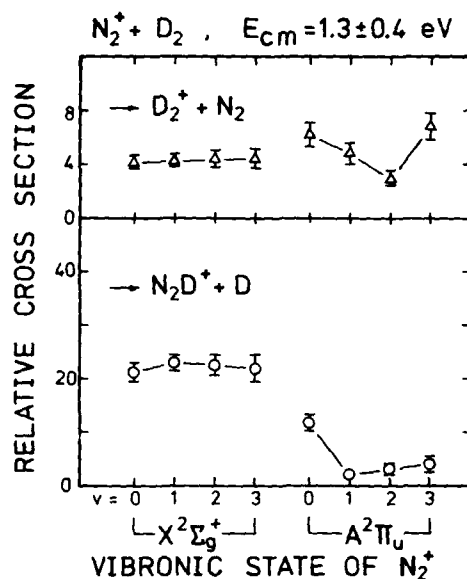


FIGURE 8
Vibrational and vibronic
state selected cross sections
for reactions (3a)
and (3b).

cross sections are found to be quite different between the two channels (3a) and (3b). This latter point is more conspicuous at lower collision energies.

The distinct vibrational state dependence of the cross sections for reaction channels (2a) and (2b) would suggest that the chemical reaction (2b) proceeds adiabatically on a potential energy surface correlating with $D_2^+ + N_2$ at infinite intermolecular separation (i.e., without hopping to the $D_2 + N_2^+$ surface). On the other hand, the similarity in the vibrational state dependence between reaction channels (3a) and (3b) with $N_2^+(X^2\Sigma_g^+)$ would indicate that the chemical reaction (3b) with this state proceeds via a nonadiabatic transition to the surface correlating with $D_2^+ + N_2$ at infinite intermolecular distance. Thus, the reactions from both reactant pairs consistently suggest that the rearrangement products $N_2D^+ + D$ correlate with the potential energy surface that correlates with the $D_2^+(X^2\Sigma_g^+) + N_2(X^1\Sigma_g^+)$ state, and not with the surface correlating with the $N_2^+(X^2\Sigma_g^+) + D_2(X^1\Sigma_g^+)$.

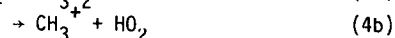
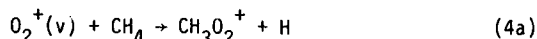
The above results might indicate that the probability of nonadiabatic transitions between these two surfaces strongly depends on the vibrational state of D_2^+ but not on that of N_2^+ . However, the origin of these dependences is not clear at present. From our previous studies on the $(Ar+BC)^+$ systems (9, 15 - 17, 24, 25), we have empirically found that, for the systems in which such a nonadiabatic transition takes place at fairly large intermolecular distances, the vibrational state dependences of charge transfer cross sections are well interpreted in terms of the energy defects and Franck-Condon factors between the reactant and product states. In the present system, the extension of the same consideration, including the Franck-Condon factors of both transitions $D_2(X^1\Sigma_g^+, v') \leftrightarrow D_2^+(X^2\Sigma_g^+, v)$ and $N_2(X^1\Sigma_g^+, v'') \leftrightarrow N_2^+(X^2\Sigma_g^+, v')$, is found hardly to explain the experimental results.

4.3. Reaction with multiple product channels: $O_2^+ + CH_4$

The reaction of O_2^+ with CH_4 has received considerable attention in recent years, since several experimental studies (26 - 29) revealed that its overall

rate constant varies in an interesting manner as a function of temperature or collision energy. In a drift or flow-drift experiments, it has been found that the extent of enhancement in the rate constant with increasing relative kinetic energy is largely dependent on the nature of the rare gas used as a buffer (26, 27). This fact has been ascribed to different extents of drift-induced internal (vibrational) excitation of the O_2^+ ion by collisions with different buffer gas, premising that the vibrationally excited ions have higher reactivity toward CH_4 . Furthermore, it has been customary to assume that this enhancement is due to the opening of endoergic channels forming $CH_3O_2^+$ or CH_4^+ (26, 27). However, there have been no direct information on the reactivities of the vibrationally excited O_2^+ ions with CH_4 .

We have determined the vibrational state selected (relative) reaction cross sections for $v=0-3$ for each of the following three product channels of the $O_2^+ + CH_4$ reaction.



The results obtained at 0.27 eV of relative kinetic energy are shown in Figure 9. As can be seen from the figure, the present results show, in a direct manner, that the vibrational excitation of the O_2^+ ions up to $v=3$ indeed enhances the overall reactivity of these ions with methane. In addition, our results clearly indicate that this enhancement for $v=1$ and 2 is primarily due to the enhancement of the exoergic channel producing $CH_3O_2^+$, and not due to the existence of endoergic channels that become accessible for these excited states, as was assumed in the previous studies. The enhanced overall reaction rate for the $v=3$ ions is seen indeed to be due to the opening of the endoergic channels, especially the charge transfer channel producing CH_4^+ . However, considering the relative populations of the $v=1-3$ ions in the drift or flow-drift tubes under usual conditions, it would obviously be incorrect to assume that the enhancement of the reactivity by possible vibrational excitation in drift experiments is due to the accessibility of the endoergic channels.

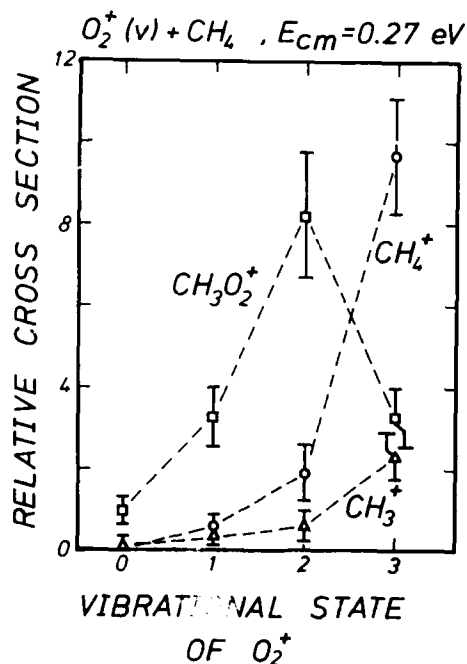
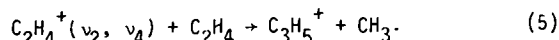


FIGURE 9
Vibrational state selected cross sections
for reactions (4a) - (4c).

4.4. Mode specificity in the reaction $C_2H_4^+ + C_2H_4 \rightarrow C_3H_5^+ + CH_3$.

Recently, there has been considerable interest in the mode specificity in chemical reactions (30 - 36). Most of the studies from this viewpoint utilize lasers to excite a molecule to specific states of different modes, and subsequent unimolecular processes of the excited molecule are compared. Obviously, it is of great interest to examine whether some mode specific behaviors are also observed in bimolecular reactions. We have performed such a study with the reaction



The possibility of selecting v_2 (C - C stretching) and v_4 (twisting) modes of the $C_2H_4^+$ ion by the TESICO technique has been discussed in Section 3.

Experimental results are shown in Figure 10, where relative reaction cross sections for the four states $(v_2, v_4) = (0, 0), (0, 2), (1, 0), (1, 2)$ are plotted as a function of the overall vibrational energy content of the reactant ion. The three curves correspond to the average collision energies of 0.1, 0.2 and 0.8 eV, as indicated.

As can be seen from Figure 10, the cross section at the lowest collision energy studied (0.1 eV) decreases linearly with increasing vibrational energy, regardless whether these energies are carried in by the v_2 or v_4 mode. When we go to a somewhat higher collision energy of 0.2 eV, however, it is found that the excitation of the v_4 vibration to $v=2$ becomes to have no effect on the reaction cross section [compare between the (0, 0) and (0, 2) states and between the (1, 0) and (1, 2) states], while the excitation of the v_2 vibration to $v=1$ still has an inhibiting effect on the cross section [compare between the (0, 0) and (1, 0) states and between the (0, 2) and (1, 2) states]. At still higher

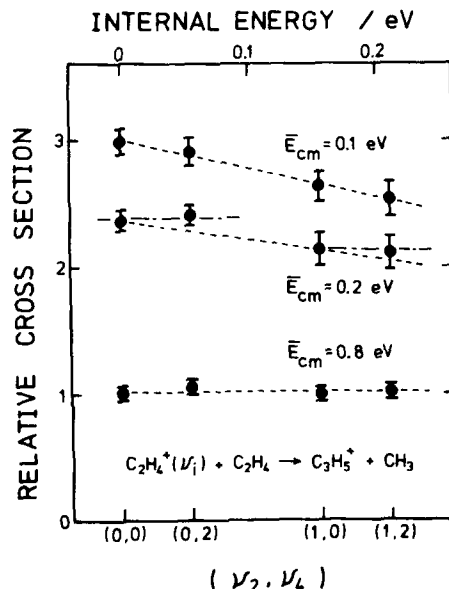


FIGURE 10
Relative cross sections of reaction (5)
for four different combinations of the
 v_2 and v_4 excitation.

collision energy of 0.8 eV, the cross section is completely independent of the vibrational energy of both modes.

Here, it should be emphasized that although the deviation of the (0, 2) and (1, 2) points from the dashed line (at $\bar{E}_{cm} = 0.2$ eV) is small, the repeated measurements with long data-collecting times gave always the same result and the error bar for the (0, 2) state never reached the dashed line. The somewhat longer error bar for the (1, 2) point is ascribed to the poorer resolution of this state in the threshold electron spectrum. Thus, we believe that we have observed a situation in which the two vibrational modes play different roles, i. e., mode specificity, in a bimolecular reaction. The experimental result indicates that this particular situation occurs only in a narrow, intermediate collision energy range.

Since reaction (5) is known to proceed via a long-lived intermediate complex at collision energies covered in the present study, the observed mode specificity must be considered to originate from the different behaviors of the ν_2 and ν_4 vibrations in this complex. Recent studies on infrared laser photodissociation of van der Waals molecules (35, 36) indicate that, although the energy flow through a low frequency intermolecular mode is a very fast process having a lifetime of the order of picosecond or even sub-picosecond, the rate of this flow does not necessarily represent the rate of complete randomization of the originally localized energy, but rather represents a rate for the very initial energy migration process which takes place only into a certain group of modes coupled strongly to the initially excited mode. Lifetimes for complete randomization or subsequent re-concentration of sufficient amount of energy on a particular bond to be ruptured (and hence the lifetimes for predissociation) are found to be much longer than that for the above-mentioned energy flow (i. e., the lifetime for the loss of identity of the initially excited state), often being as long as a few nanosecond or even a few hundreds nanoseconds. Moreover, the rates of these latter processes, as well as that of the initial energy flow, are found to be mode-specific.

Thus, at present we interpret the observed mode specificity as originating from the different rates of energy flow in the complex for the ν_2 and ν_4 vibrations of the reactant ion, which in turn lead to different lifetimes (with respect to back decomposition) for complexes formed from the ν_2 and ν_4 excited ions.

ACKNOWLEDGEMENTS

The authors would like to thank Dr. Kenji Honma and Mr. Shinzo Suzuki for their involvement in some part of the experiments reported here. Thanks are also due to Dr. Zdenek Herman for valuable discussions.

REFERENCES

- 1) P. R. Brooks and E. F. Hayes, State-to-State Chemistry (American Chemical Society, Washington, 1977).
- 2) R. N. Zare and R. B. Bernstein, Phys. Today 33 (1980) No. 11, 43.
- 3) R. B. Bernstein, Chemical Dynamics via Molecular Beam and Laser Techniques (Clarendon Press, Oxford, 1982).
- 4) M. Kneba and J. Wolfrum, Ann. Rev. Phys. Chem. 31 (1980) 47.
- 5) R. N. Zare and P. Dagdigian, Science 185 (1974) 739.
- 6) I. Koyano and K. Tanaka, J. Chem. Phys. 72 (1980) 4858; 69 (1978) 3422.
- 7) I. Koyano and K. Tanaka, State-selected reactive collisions of diatomic molecular ions by a coincidence technique, in: Electronic and Atomic Collisions, eds. N. Oda and K. Takayanagi (North-Holland, Amsterdam, 1980) pp. 547 - 556.
- 8) W. B. Peatman, G. B. Kasting, and D. J. Wilson, J. Electron Spectrosc. 7

- (1975) 233.
- 9) T. Kato, K. Tanaka, and I. Koyano, *J. Chem. Phys.* 77 (1982) 834.
 - 10) D. C. Cartwright, *J. Chem. Phys.* 58 (1973) 178.
 - 11) I. Koyano, K. Tanaka, and T. Kato, *Annual Review, Inst. for Molec. Sci., Okazaki, Japan* (1982) 73; K. Tanaka, T. Kato, and I. Koyano, *ibid.* (1984) 83.
 - 12) K. Honma, T. Kato, K. Tanaka, and I. Koyano, *J. Chem. Phys.* 81 (1984) 5666.
 - 13) K. Tanaka, T. Kato, and I. Koyano, to be published.
 - 14) J. E. Pollard, D. J. Trevor, J. E. Reutt, Y. T. Lee, and D. A. Shirley, *J. Chem. Phys.* 81 (1984) 5302.
 - 15) K. Tanaka, J. Durup, T. Kato, and I. Koyano, *J. Chem. Phys.* 73 (1980) 586; 74 (1981) 5561.
 - 16) T. Kato, K. Tanaka, and I. Koyano, *J. Chem. Phys.* 77 (1982) 337.
 - 17) T. Kato, *J. Chem. Phys.* 80 (1984) 6105.
 - 18) W. A. Chupka and M. E. Russell, *J. Chem. Phys.* 49 (1968) 5426; W. A. Chupka, *Ion-Molecule Reactions by Photoionization Technique*, in: *Ion-Molecule Reactions*, Volume 1, ed. J. L. Franklin (Plenum, New York, 1972) pp.33 - 76.
 - 19) T. Turner, O. Dutuit, and Y. T. Lee, *J. Chem. Phys.* 81 (1984) 3475.
 - 20) D. Van Pijkeren, E. Boltjet, S. van Eck, and A. Niehaus, *Chem. Phys.* 91 (1984) 293.
 - 21) J. Berkowitz and W. A. Chupka, *J. Chem. Phys.* 51 (1969) 2341; P. M. Dehmer and W. A. Chupka, *J. Chem. Phys.* 66 (1977) 1972.
 - 22) F. Schneider, U. Harvemann, L. Zulicke, V. Pacak, K. Birkinshaw, and Z. Herman, *Chem. Phys. Lett.* 49 (1977) 273.
 - 23) W. N. Whitton and P. J. Kunz, *J. Chem. Phys.* 64 (1976) 3624.
 - 24) K. Tanaka, T. Kato, and I. Koyano, *J. Chem. Phys.* 75 (1981) 4941.
 - 25) T. Kato, K. Tanaka, and I. Koyano, *J. Chem. Phys.* 79 (1983) 5969.
 - 26) I. Dotan, F. C. Fehsenfeld, and D. L. Albritton, *J. Chem. Phys.* 68 (1978) 5665.
 - 27) E. Alge, H. Villinger, and W. Lindinger, *Plasma Chem. Plasma Proc.* 1 (1981) 65.
 - 28) B. R. Rowe, G. Dupeyrat, J. B. Marquette, D. Smith, N. D. Adams, and E. E. Ferguson, *J. Chem. Phys.* 80 (1984) 241.
 - 29) M. Durup-Ferguson, H. Bohringer, D. W. Fahey, F. C. Fehsenfeld, and E. E. Ferguson, *J. Chem. Phys.* 81 (1984) 2657.
 - 30) I. Oref and B. S. Rabinovitch, *Acc. Chem. Res.* 12 (1979) 166.
 - 31) P. A. Schulz, Aa. S. Sudbo, D. J. Krajnovich, H. S. Kwok, Y. R. Shen, and Y. T. Lee, *Ann. Rev. Phys. Chem.* 30 (1979) 379.
 - 32) R. B. Hall and A. Kaldor, *J. Chem. Phys.* 70 (1979) 4027.
 - 33) X. de Hemptinne and D. de Keuster, *J. Chem. Phys.* 73 (1980) 3170.
 - 34) D. W. Chandler, W. E. Farneth, and R. N. Zare, *J. Chem. Phys.* 77 (1982) 4447.
 - 35) M. A. Hoffbauer, K. Liu, C. F. Giese, and W. R. Gentry, *J. Chem. Phys.* 78 (1983) 5567.
 - 36) I. Nishiyama and I. Hanazaki, *Annual Review, Inst. for Molec. Sci., Okazaki, Japan* (1983) 68.

LOW ENERGY ION REACTIONS MEASURED WITH GUIDED BEAMS

Dieter GERLICH

Fakultät für Physik der Universität Freiburg, D 7800 Freiburg, FRG

This report is concerned with recent advances in the application of the guided beam method and presents new results for some reactions and charge transfer processes ($C^+ + H_2$, $N^+ + CO$, $Ar^+ + O_2$ and CO , and $Ar^{++} + He$). Experimental progress involves the preparation of ion beams in the "sub - 0.1 eV range", the precise calibration of their kinetic energy and the determination of product velocities in an octopole. The successful combination of this technique with others (like photoionization or photon - ion coincidences) will be briefly mentioned. The above choice of reaction systems allows a comparison with other methods (SIFT, DRIFT, ICR, LIF and crossed beams).

1. INTRODUCTION

The goal of this report is to summarize the state of the art in the application of the "guided beam" technique (or more generally the use of inhomogeneous electrical radiofrequency fields) in studying ion-molecule reactions at very low energies. Therefore we will limit our discussion to collision energies below 1 eV, with emphasis on preparation and calibration of well defined translational and internal energy distributions.

RF ion optics (except for quadrupole filters and traps) has been used, so far, in a few laboratories only. In the first application (1), three elements (an RF storage ion source, a focussing RF mass filter, and an octopole beam guide) have been used to determine absolute values for integral cross sections (2-5). Subsequently, in an high resolution and low energy scattering experiment (also with a storage ion source), a long octopole was used to measure product ion energies by the time-of-flight technique. State-to-state differential cross sections have been obtained (6,7). In further developments combinations of the guided beam technique with different techniques have been applied. Photoionization has been used for the study of reactions with state selected ions (8-10). Photon - ion coincidences revealed specific features of chemiluminescent reactions (11).

A few other experiments using octopole beam guides, predominantly for the determination of integral cross sections have been reported recently (12 - 15). The preparation of an internally thermalized ion beam using the storage source has been demonstrated for several ionic species (2,17, and 18). In this summary, finally, it seems to be worthwhile to mention some unpublished work: Special RF-traps have been used in order to determine thermal rate coefficients or long lifetimes of metastable ions. In laser beam - ion beam interaction, it has been demonstrated that a long octopole allows one to collect slow photo induced products with high efficiency.

In this contribution, we want to discuss two improvements achieved with a new guided beam apparatus: 1. The production of extremely slow ion beams (in the meV range) and their use to measure effective cross sections down to thermal energies (16). 2. The determination of product velocity distributions in an energy range not accessible to other methods.

In the next paragraph we make a few remarks concerning the mathematical

treatment of RF ion optics, and we will give - more for practical applications - some formulas for the calculation of operating conditions for multipole arrangements. A brief description of the new "multi purpose" guided beam apparatus follows with emphasis on a few experimental details and measuring procedures.

Subsequently, experimental results are presented for several reactions and charge transfer processes. The selection of the systems has been partly motivated by recent experiments performed with other techniques. This gives the opportunity to discuss some advantages and disadvantages of the different methods, although it is out of the scope of this report to give a survey of the whole field of low energy ion reactions.

The following examples will be dealt with in this report:

For the endothermic reaction $C^+ + H_2 \rightarrow CH^+ + H$ the precise form of the integral cross section in the threshold region is still under discussion (15,19).

The internal energy of CO^+ , formed in the charge transfer reaction $N^+ + CO \rightarrow CO^+ + N$ has been determined by laser-induced fluorescence (20) and by an ICR technique in which the recoil translational energy distribution of the products is measured (21). The results will be analysed using recent crossed and guided beam data.

For $Ar^+ + O_2, CO$ results will be compared with recently published DRIFT tube data (22).

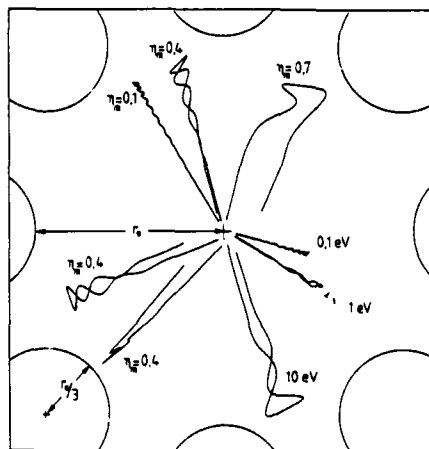
Some "differential" cross sections, measured with the guided beam apparatus for the charge transfer $Ar^{2+} + He \rightarrow Ar^+ + He^+$ will be compared to recent crossed beam experiments (23).

2. EXPERIMENTAL

2.1 Ions in RF fields

Ion optics using inhomogeneous oscillatory electrical fields (RF fields) offer a variety of applications in experiments with charged particles. The best known (but very special) examples are the quadrupole mass filter and ion trap. For the mathematical analysis of the ion motion in such fields, approximate solutions for high RF frequencies have been given (24,25). A more elaborate treatment has been developed by E. Teloy (1). The most important results are:

Fig. 1. Ion trajectories in an oscillatory octopole field. Sample ions all start in the middle, but in different directions and with different parameters. The examples with $\eta_m = 0.1$, 0.4, and 0.7 and with $(r/r_s)_m = 0.88$ illustrate, that the choice of $\eta_m = 0.3$ and $(r/r_s)_m = 0.8$ guarantees a safe operation (for $\eta_m = 0.7$, the energy is not conserved). For the three energies (0.1, 1, and 10 eV), E and V_0 are constant. In the two last examples only the starting angle has been changed, demonstrating the rotational symmetry of the effective potential: only the small oscillations are different.



The global ion motion (averaged over the fast oscillations, see fig.1) can be deduced from an effective potential V^* provided that the frequency is high enough. This condition is fulfilled if the stability parameter η is smaller than 0.3.

The general definitions for V^* and η are given in ref. (1) (formulas 7 and 10 respectively). Here we restrict the discussion to cylindrical multipoles ($2n$ -poles) which can be constructed out of $2n$ rods arranged symmetrically so that the diameter d of the rod and the inscribed circle fulfills the condition $r_0 = (n-1) \cdot d/2$. These boundary conditions define a potential which is in good approximation given by the first formula in tab. 1. For the calculation of the effective potential V^* and the stability parameter η it is useful to introduce the abbreviation \mathcal{E} . This term corresponds to the kinetic energy of an ion cycling in phase with the RF on a radius r_0 . The amplitude a of the fast motion (in first-order approximation, superimposed on the smooth trajectory) can be determined from the last equation in tab. 1.

$\Phi = (r/r_0)^n V_0 \cos(n\varphi)$ (1)	electrical potential	m, q mass and charge of the ion
$\mathcal{E} = \frac{1}{2n^2} m \omega^2 r_0^2$ (2)	characteristic energy	V_0 RF amplitude at the electrode
$V^* = \frac{1}{8} \frac{(qV_0)^2}{\mathcal{E}} (r/r_0)^{2n-2}$ (3)	effective potential	ω angular frequency ($\omega = 2\pi f$)
$\eta = \frac{n-1}{n} \frac{(qV_0)}{\mathcal{E}} (r/r_0)^{n-2}$ (4)	stability parameter	r_0 radius of the inscribed circle
$\frac{a}{r_0} = \frac{1}{2(n-1)} \eta (r/r_0)$ (5)	a : amplitude of the fast motion	E_m maximal transverse energy
		Numerical examples for an octopole: $n=4$ $(r/r_0)_m = 0.8$ $\eta_m = 0.3$ $q \cdot V_0 = 48.8 E_m$ $\mathcal{E} = 78.1 E_m$
		Units: μ , cm, MHz, e, V $\mathcal{E} = 1.03644 / 2n^2 m \omega^2 r_0^2$ $r_0 = 0.3$ $m \cdot f^2 = 679$ $E_m = 1$ $m = 1$ $f = 26$ $m = 679$ $f = 1$

Tab. 1 Formulas and numerical examples for multipoles.

For practical applications, two requirements must be met:

1. The maximum of the (r dependent) stability parameter is $\eta_m = 0.3$.

2. The trajectory in the large is limited by $(r/r_0)_m = 0.8$.

The first condition assures that the effective potential approximation remains good, the second guarantees that the ions don't hit the electrodes (there is enough space for the fast oscillation having an amplitude $a = 0.04 \cdot r_0$). These facts are illustrated in fig. 1. With these numbers one gets the simple result, that for a singly charged ion with a transversal energy of 1 eV a minimal amplitude of 48.8 V is needed (independent of the geometry and the mass) and \mathcal{E}/E_m has a fixed value of 78.1. It is evident that the choice of the frequency depends on r_0 and the mass, as demonstrated by the numerical examples (tab. 1).

2.2. Apparatus

The guided beam machine is in principle, the same as the apparatus previously described (1), consisting of a storage ion source, an RF quadrupole filter, an octopole beam guide with a scattering cell, a magnetic mass spectrometer, and a scintillation detector. An improved ion source and a long quadrupole (operating in a slightly different mode, see explanation in fig. 3) produces an (in most cases pulsed) intense ion beam with a very narrow energy distribution. The most important modification refers to the interaction region (see fig. 2).

In the present experiment the ions are injected into a first octopole (8a)

surrounded by a short scattering cell at the exit. Electrodes (9 a-c) surrounding the octopole can influence the potential in the interior. A second much longer octopole is coupled (electrically and mechanically) to the first one

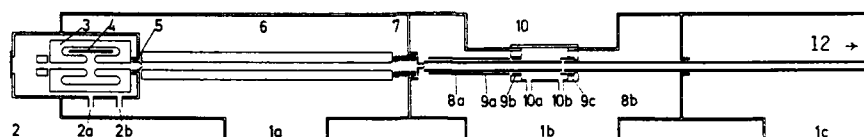


Fig. 2. Schematic diagram of the new guided beam apparatus (approximately to scale). 1a-c) The bakable UHV System is pumped separately by three turbomolecular pumps; 2ab) and 10ab) Gas inlet and capacitance manometer; 2) Storage ion source (transparent in the axial direction); 3) shape of the electrodes defining the storage volume; 4) cathode and electron beam; 5) Electrode (for pulsing the ion beam); 6) RF mass and velocity filter (rod diameter 1 cm, length 25cm); 7) Lens system for pulsing and focussing into the injection electrode; 8) Octopole I (14 cm) and II (46 cm); 9a-c) Correction electrodes; 10) Scattering cell with quartz window; 12) acceleration towards the magnetic mass spectrometer and scintillation detector (identical with 13) - 20) in fig. 1 of ref. 1).

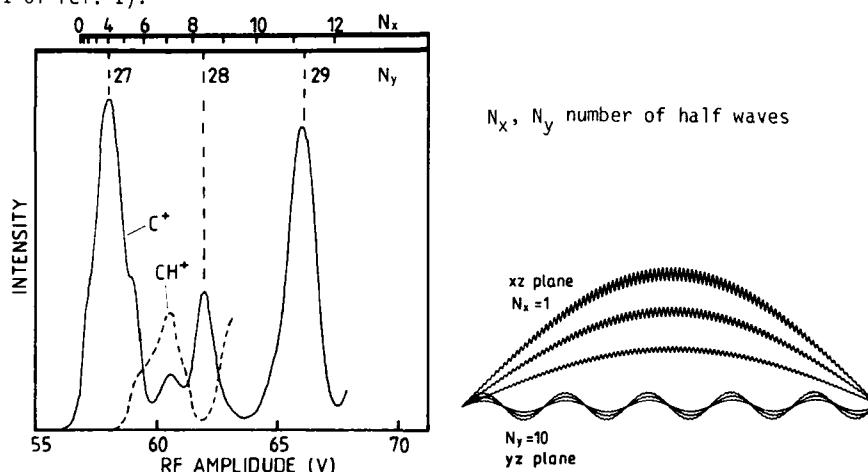


Fig. 3a,b. Measured transmission functions of the quadrupole mass and velocity filter as a function of the RF amplitude V_0 . ($f=12.25$ MHz, $r_0=.438$ cm, $U_0=.25$ V, longitudinal kinetic energy 0.25 eV, $a=0.00014$, $q=.016$, for the definition of a and q see (26)). The principle and purpose of the quadrupole has been described in detail in ref. (1) but the operational mode is slightly different in the present experiment. Instead of three holes, transposed radially with respect to the quadrupole axis (see fig. 3 of ref. (1)), the only boundary conditions for the ion trajectories are here the input and the exit hole, having primarily the advantage of axial symmetry. Adding a DC difference to the RF (both the DC potential and the effective potential are harmonic for a quadrupole, see. tab. 1) the focussing conditions are different in the xz and the yz plane as illustrated in fig. 3b. Transmission maxima occur at amplitudes (as can be seen easily in fig. 3a) were the number of half waves coincide. For the preparation of a C^+ beam, the (4/27) mode has been chosen where the xz motion of the CH^+ is still unstable.

in such a way that the RF field does not change in the joint, but the ions can be accelerated (or decelerated) by using different DC voltages. This long octopole, guiding the ions from the scattering region towards the detector, allows one to determine the axial velocity component of the products via the time of flight (TOF) method.

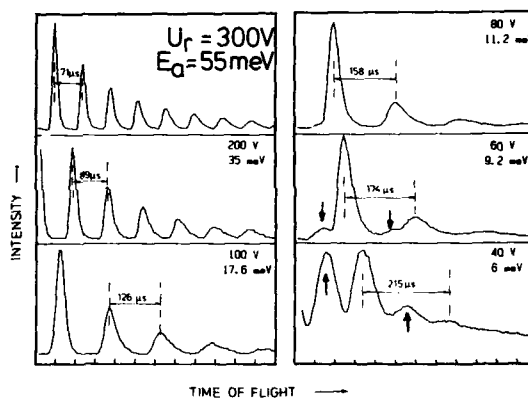
The lowest limit to the ion kinetic energy in an octopole is determined by surface potential variations. Although many different methods have been tested in the choice of materials and the preparation of electrode surfaces, long octopoles (~20 cm) have never guided ions with an average energy below 30 meV, in most cases the distortions have surpassed 50 meV. However it has been demonstrated (see fig. 3 and (16)) that the problem can be reduced using shorter octopoles (probably just because of statistical reasons).

For the determination of the kinetic energy distribution of the ion beam in the interaction region (between electrodes 9b and 9c), two measurements are routinely performed:

1. The test procedure, probing the potential inhomogeneities by slow ions, reflected on artificial potential barriers. It has been described in (16), some hints are given in the caption of fig. 4.

2. The actual energy distribution of the ion beam is extracted from a TOF calibration procedure (measuring the flight time for several DC voltages in octopole I and II). The accuracy is - depending on the energy spread - typically 10 meV.

Fig. 4. Determination of the largest (positive) potential distortion and the lowest energy transmitted through a short range of the octopole (scattering cell) by trapping ions between the two ring electrodes 9b and 9c. Electrode 9b is operated in a pulsed mode. After passage of the ions it closes with a high potential barrier this side of the octopole while a DC voltage U_r on 9c leads to a potential barrier, which works as an energy filter: Because the chance to surmount the barrier depends slightly on the angle of the trajectory, this region is semitransparent for ions in a very small energy band. This results in the plotted time dependence of the intensity (the main peak has been omitted). The average energy E_a of the semi-trapped ions is well defined by the time difference between the peaks and changes by only 0.18 meV per $U_r = 1$ V. The time width of the peak (at $U_r = 60$ V) corresponds to an energy spread of only 4.5 meV FWHM. The additional TOF peaks in the last two distributions (marked by arrows) are due to a potential distortion of about 6 meV, located approximately in the middle of the scattering cell.



3. RESULTS AND DISCUSSION

3.1 REACTION I $C^+ + H_2 \longrightarrow CH^+ + H$

Integral cross section for this reaction have been measured quite often and are illustrative examples for errors caused by an erroneous calibration of the energy scale, and for the need of very accurate absolute cross sections (e. g.

for kinetic models of interstellar cloud chemistry). Only recently, Ervin and Armentrout (15) have presented new results on that system obtained with an apparatus with an octopole beam guide. Their results are shown in fig. 5 and are in excellent agreement with former unpublished results from this laboratory (27).

Despite the improvement of the data relative to earlier experiments (cited in (15)) the cross section is not characterized well enough, especially near threshold. This becomes obvious in a recent reevaluation (19) of the rate constants (also for the reverse reaction) at interstellar cloud conditions. Chesnavich et al. show, that the experimental data are consistent with different cross sections leading to very different rate constants for the reverse channel of reaction I. As discussed in full detail in (15) and (19), the main difficulties arise from the energy spread, caused by the thermal motion of the target gas. Three various trial functions, that have been used (15,19) are plotted on the right hand side of fig. 6.

Due to the importance of reaction I, we have recently reinvestigated this process very carefully in the threshold region. The cross sections have been pinned down with constant statistical significance through three orders of magnitude. The center of mass energy half width of the primary beam is 7 meV (CM), calibration of the energy scale is better than 3 meV (CM). The largest error stems from the target gas temperature, which is mainly determined by that of the octopole. Due to the absorption of some RF power the rods are warmer ($T=380$ K) than the environment. In order to circumvent this problem, some measurements have been performed in an intermittent mode (switching the RF with a duty cycle of 1:30) resulting in $T=320$ K ± 10 K (total measuring time 5 h).

In order not to be restricted by a given analytical trial function for the deconvolution of the effective cross section, we have used a polygonal ansatz (see fig. 6 and table 2). In accordance with (15) we have assumed a threshold energy of 0.37 eV (accounting globally for the rotational excitation of the hydrogen molecule). The corresponding effective cross sections are shown (on a logarithmic scale) for three temperatures in fig. 6, they fit the experimental data quite well. The accuracy of the relative values of the deconvoluted cross section is smaller than the dotsize in fig. 6 (without taking into account the error due to the assumed threshold value). The absolute values, obtained with the three guided beam apparatuses are compared in fig. 5 (the solid line represents our 380 K data) and are in good agreement. Nevertheless an error of 20% is still possible, accounting for the uncertainty in the effective length of the scattering cell (especially with the short cell in the present experiment).

As can be seen from fig. 6, the present result rises slower than the other trial functions and stays below the function 2a (equ. 15 of ref. 19). As a consequence (comparing with fig. 3 of ref. 19) the cross section for the reverse reaction of I is decreasing at temperatures below 1000 K. Thermal rate constants (the change of the rotational excitation is not taken into account) are given in tab. 2.b. At 200, 500 and 1000K, these values are 100, 16, and 6 times higher than the currently accepted analytical expression (19) for the temperature dependence of reaction I.

$E(\text{eV})$	(\AA^2)	$E(\text{eV})$	(\AA^2)	$T(\text{K})$	$k(\text{cm}^3/\text{s})$	$T(\text{K})$	$k(\text{cm}^3/\text{s})$
0.37	0.000	0.55	1.480	200	3.6 -20	2000	2.3 -11
0.40	0.364	0.60	1.624	400	2.4 -15	3000	5.2 -11
0.43	0.707	0.65	1.723	600	1.0 -13	4000	8.1 -11
0.46	1.049	0.70	1.790	800	6.9 -13	5000	1.0 -10
0.50	1.292			1000	2.2 -12		

Tab. 2a. Points of the trial function, approximating the cross section in the threshold region.

Tab. 2b. Thermal rate coefficients, calculated with the cross section, given in tab. 2. a.

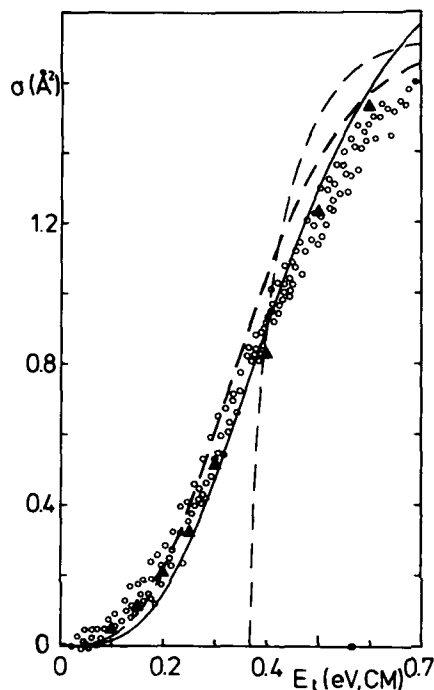


Fig. 5 Integral cross sections for reaction I. \circ : Ervin and Armentrout (15), \blacktriangle : Cahnbley (27), broken lines: trial function used in ref. (15) (number 1 in fig. 6) and corresponding effective cross section, solid line: effective cross section, fitting the 380 K data of the present work.

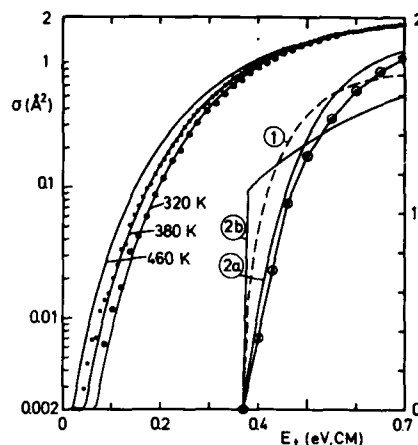


Fig. 6. Integral cross sections for the reaction $C^+ + H_2 \rightarrow CH^+ + H$. Left part (log. scale): This experiment (dots, 320 K and 380 K), and calculated effective cross sections (solid lines 320 K, 380 K, and 460 K), corresponding trial function see tab. 2. Right part (lin. scale): trial functions used by the different authors: 1: ref. (15), 2a and b: ref. (19) dots: this work, see table 2.

3.2. REACTION II $N^+ + CO \rightarrow CO^+ + N$

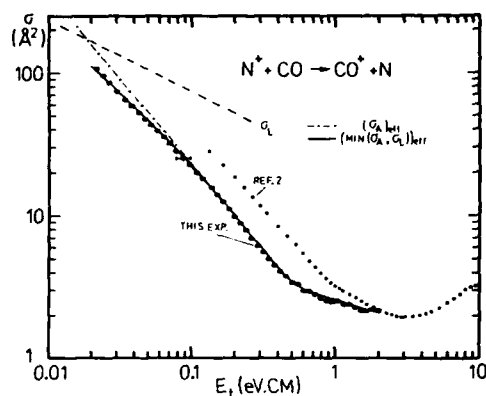
The charge transfer process II has been studied by several groups in the last two years in the sub-eV range. In a guided beam apparatus (fig. 7 and 16), the integral cross section has been measured between 2eV and 20meV beam energy closing the gap between thermal energies and a few eV with a beam experiment. Thermal rate coefficients, calculated with the deconvoluted cross section, the analytical expression for which is given in (16)) are compared with recently published values, obtained with a variable-temperature SIFT apparatus (28):

Temperature	88	146	196	245	296	371	454	k
Guided beam (16)	10.3	9.5	8.8	8.2	7.6	6.9	6.3	$10^{10} \text{ cm}^3/\text{s}$
SIFT (28)	9.7	7.2	6.7	6.3	5.9	5.3	4.6	
Guided Beam (76%)	7.8	7.2	6.7	6.2	5.8	5.3	4.8	

The SIFT results are in general about 25% lower which is within the combined uncertainties of the two experiments. But the decrease in k with rising temperature is in excellent agreement as can be seen on the last two lines of the table.

In order to get some information on the partitioning of the energy, several

Fig. 7. Integral cross sections for $N^+ + CO \rightarrow CO^+ + N$. Dots: ref. 2 and this experiment. Broken line: Langevin cross section, dash-dotted line: analytical trial function see ref. 16) Solid line (fitting the experimental points): calculated effective cross section.



methods have been applied. The laser-induced-fluorescence (20) studies, performed at a collision energy of 0.13 eV, resulted in a vibrational population favouring with 81% the $v=0$ state. In a crossed beam experiment (29) the translational energy of the CO^+ products has been measured at laboratory angles ranging from 0° to 70° (covering almost 80% of the accessible center of mass velocity range). Fig. 8. shows product translational distributions, derived from the scattering diagram in the usual way (23). As can be seen, the reaction has, even at the lowest energy of 0.54 eV, a strong tendency to convert most of the collision energy into internal excitation instead of channeling the exothermicity into translation as predicted by Franck-Condon factors or the LIF experiment.

The only method to extract some information on the translational energy of the secondary ion at thermal conditions is the kinetic energy ion cyclotron resonance spectroscopy (KEICR) developed by Mauclaire, Deraï, and Marx (30). This technique has recently been applied (21) to study the vibrational state distribution as a function of translational energy (0.025 to 0.1 eV). Unfortunately, the evaluation of the experimental data (85% in $v=0$ at thermal energies and a strong increase of the internal excitation with increasing translational energy) has been done without considering the averaging effects due to the thermal motion of the target gas and the influence of the angular and energy dependence of the cross section.

As a demonstration we have simulated numerically the ICR experiment for two different vibrational population: (a) $P(0)=1$ and (b) $P(0)=.75$, $P(1)=.21$, $P(2)=0.04$, assuming completely thermalized ions. It is evident from the example (fig. 9), that: 1. data of much higher quality are needed (especially at trapping potentials below 100 meV!) in order to deconvolute them, and 2. the extrapolation method used in the evaluation in ref. (21) is misleading.

It must be mentioned that this simulation holds only for a completely thermalized system (the ion velocity distribution must be a Maxwell-Boltzmann distribution with the same temperature as the neutrals!). For any deviation, e.g. for supra-thermal ions, the laboratory energy distribution depends strongly on the CM angular distribution. This can be easily seen on a Newton diagram, and is illustrated with the following numerical example (neutral temperature 300 K, N^+ lab. energy 0.1 eV, translational exoergicity 0.52 eV ($v=0$)). The mean value of the laboratory kinetic energy of the CO^+ ion ("nomi-

nal" value 0.17 eV) is 0.33 eV or 0.10 eV, respectively, if the product is scattered forward or backward with respect to the primary ion.

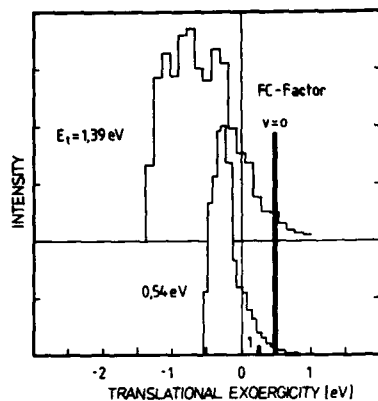


Fig. 8. Product translational distributions (29)

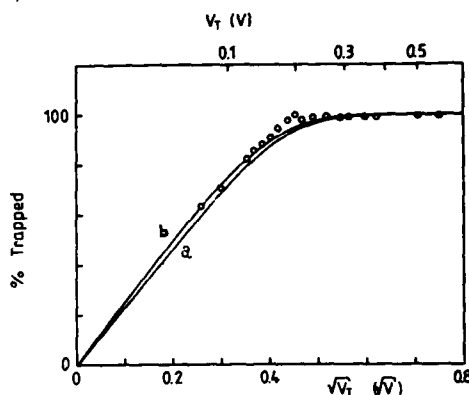


Fig. 9. ICR data ref. (21) and simulation (see text). V_T : trapping potential

Similar problems complicate the interpretation of the LIF results as discussed in (20, 31, and 16). For the determination of the state-to-state cross sections, the laboratory velocity distribution is needed to convert the measured densities into product fluxes. Due to these problems none of the experiments mentioned so far give conclusive evidence for the true internal state population. The LIF product distribution has been interpreted (20) to match fairly well the trend predicted by a Franck-Condon (vertical ionization) model, whereas the beam data are more indicative of a strongly interacting intermediate complex.

Supported by low resolution angular distributions (ref. (16)) a reaction mechanism has been proposed which is consistent with all experimental and theoretical information so far available.

Here, for clarity and simplicity, it will be explained exclusively with help of the potential curves of the $^3\Sigma^-$ states of the $(N..CO)^+$ isomer, (fig. 6 of ref. (32)).

1. The charge transfer occurs at an avoided crossing at large distances.

The SCF/CI calculations (32) predict from the leading configurations an avoided crossing between $r(NC) = 5$ and 7 bohr. The energy dependence of the integral cross section predicts (within a simple model (16)) $r(NC) = 7.2$ bohr and a transition probability proportional to $E^{0.7}$.

2. The system crosses the critical region twice, but the overall transition probability is not $2 \cdot P \cdot (1-P)$ as in atom atom collisions and can be as large as $P + P \cdot (1-P)$.

a) The transfer on the approach leads to the formation of a strongly bound (several eV) intermediate complex, where all the energy can be partitioned statistically (probably with some constraints favouring for example, the linear conformation). During the dissociation an electron retransfer may be hindered for energetic reasons.

b) If, on the other hand, the trajectory remains on the upper surface during the approach, the repulsive potential prevents the system from strong interaction, and it has therefore a second chance for the electron jump.

The mechanism 2a and 2b lead to different angular and energy distributions explaining the different experimental results (discussed in 16). The model is also consistent with the fact that the rate coefficient reaches the Langevin limit at low temperatures. Of course, due to different isomers and several potential surfaces in three dimensions the reality will be more complicated,

3.3. REACTION III a,b $\text{Ar}^+ + \text{CO} \rightarrow \text{CO}^+ + \text{Ar}$ and $\text{Ar}^+ + \text{O}_2 \rightarrow \text{O}_2^+ + \text{Ar}$

Reactions of Ar^+ ions have been studied thoroughly since the early days of ion molecule research (for a summary see (22)). In this report, these systems have been chosen for two reasons. First, we want to discuss the comparison between data measured with a FLOW-DRIFT and an ion beam apparatus, and secondly we want to give a first example for the determination of the kinetic energy of product ions in an octopole.

Fig. 10 shows the rate constant K for $\text{Ar}^+ + \text{CO}$ (22) as a function of the mean relative kinetic energy and (in the same coordinate system but with different meaning) the "effective rate" $K^*(V_1) = \sigma_{\text{eff}}(V_1)V_1$ as a function of the "nominal CM translational energy" $E_1 = \mu/2 V_1^2$ (μ being the reduced mass of the system, for a detailed discussion of this presentation of data see (1)).

For a comparison of the two sets of data a careful distinction must be made between the true cross section $\sigma(V)$, which is the desired result, and the actually measured quantities. In our beam experiment, the ion energy is much better defined (in this case within 25 meV) than the broadening due to the target motion. Unfolding of the measured effective cross sections with the

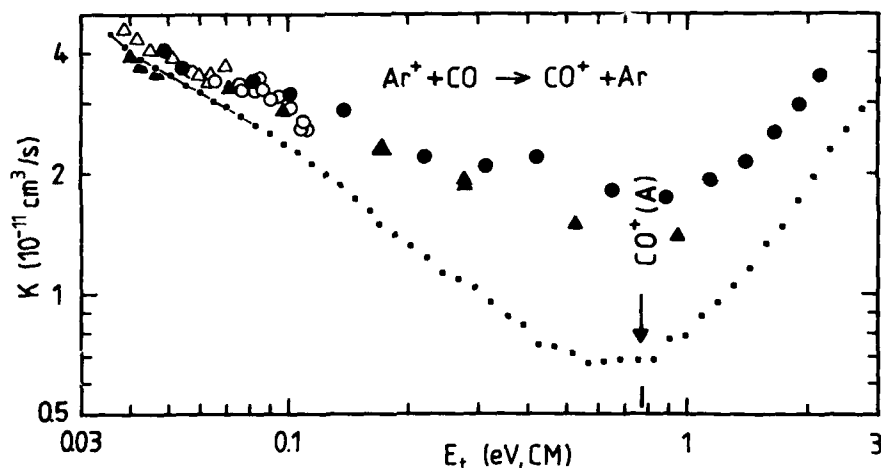


Fig. 10 Δ \circ Rate constants (Flow Drift (22)), \bullet effective rate coefficient, explanation see text.

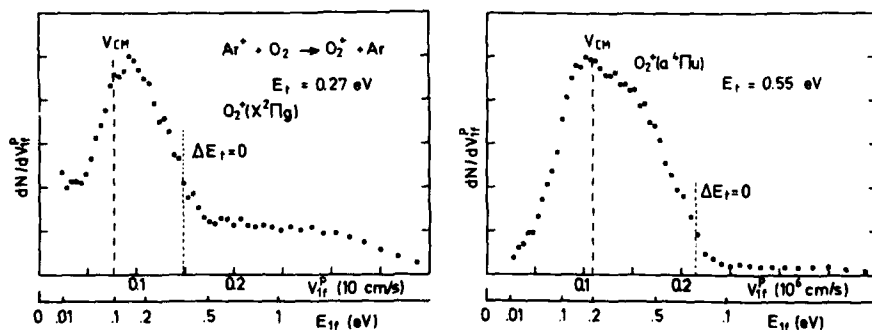


Fig. 11. Distribution of the axial velocity component of the O_2^+ products.

well defined generalized Maxwell-Boltzmann distribution is feasible with good data as demonstrated for the $C^+ + H_2$ reaction but has not yet been done for this system. With this cross section and with the (more or less well known) energy distribution of the ions in the drift tube, the latter data should be simulated for a precise comparison.

At low energies where both methods approach more or less the usual thermal rate coefficient, the agreement is gratifying.

The minimum in the rate constant at a few tenths of an eV and the strong increase above the threshold for the first electronically excited state (marked in fig. 10) have been observed and discussed in (22) for both O_2 and CO. In fig. 11 distributions of the axial velocity of O_2 products are plotted for two collision energies. At 0.27 eV there is still a remarkable amount of the exothermicity channeled into translation (ions at right of the second dashed line), but there is also a peak at the first dashed line, marking the center of mass velocity. At this velocity all the available energy is transferred into internal excitation. This peak gets even more dominant at 0.55 eV where the the channel $O_2^+(^2\Pi_u) + Ar - 0.35$ eV is energetically accessible. For a more quantitative analysis, the distribution of the transversal component of the product velocities has to be determined.

Experiments towards that goal are in progress, in this report the method will be demonstrated briefly in the next paragraph for a simple atom-atom charge transfer process.

3.4. REACTION IV $Ar^{++} + He \rightarrow Ar^+ + He^+$

Only recently have state resolved differential cross sections been measured for reaction IV at energies down to 0.5 eV in a crossed beam experiment (23). In order to obtain some more information in the interesting sub-eV range, we have investigated this charge transfer process in our guided beam apparatus. For the first time, not only integral cross sections (fig. 12) but also absolute values for differential cross sections have been measured with this technique.

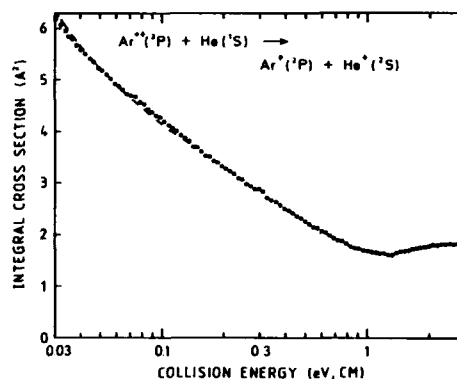


Fig. 12 Integral cross sections for reaction IV

The dependence of the integral cross section on the collision energy E_t can be represented by the formula

$$\sigma = P(E_t) \pi R_c^2 (1 - V_{pol}(R_c)/E_t)$$

where $R_c = 4.7$ Å is the crossing radius between the polarisation potential $V_{pol}(R)$ and the Coulomb potential, attracting the reactants and repelling the products. The (impact parameter averaged) probability for a charge transfer, $P(E_t)$, has a local minimum of less than .03 at about 1 eV. The rise of the cross section towards lower energies is only to a minor part due to the long range attraction. Therefore that change must be explained by the energy dependence of the coupling (Coriolis or radial coupling, fine structure).

More detailed information on this coupling can be extracted from the angular distribution of the products. For this simple process only one channel (ignoring fine structure), is energetically accessible. Under such conditions, as can be seen from the Newton diagram, the product velocity can be determined by only measuring their axial component (guiding all ions independent on their transversal component). One example (transformed from a TOF distribution, measured at 0.1 eV is shown in fig. 13. The distribution is obviously symmetric relative to the dashed line, marking the center of mass velocity.

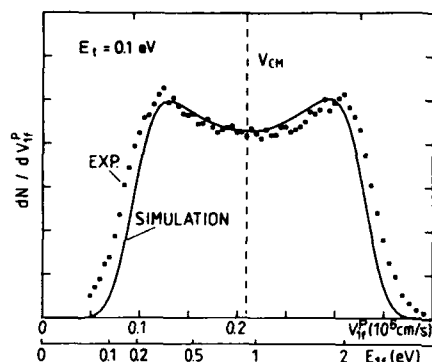


Fig. 13. Velocity distribution

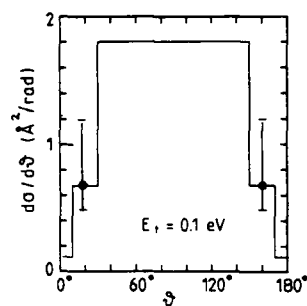


Fig. 14. Differential absolute cross section

The differential cross section shown in fig. 14 has been used to simulate these experimental values (taking into account exclusively the target motion). The overall agreement is gratifying, there are some discrepancies in the forward and backward direction, leading probably to a larger differential cross section at these angles.

The pronounced sideways peak in the scattering diagram of Friedrich and Herman (23) shows up also in our experiment. For a more quantitative analysis, some more development of the guided beam technique is needed, especially the determination of the transversal component of the velocity with the help of the guiding field. Experimental work is in progress.

CONCLUSION

It has been demonstrated with a few examples, that the guided beam technique is a very versatile method to reveal detailed information on low energy ion-molecule reaction dynamics.

Accurate absolute cross sections as a function of well defined translational energies can be obtained even at thermal energies. The high sensitivity allows the incorporation of other techniques like photoionisation, coincidence technique, or the use of a secondary beam instead of a scattering cell.

First steps have been made towards the determination of (low resolution) differential cross sections in an energy range not accessible to crossed ion beam experiments.

ACKNOWLEDGEMENT

The author is grateful to Prof. Ch. Schlier for stimulating discussions and generous support, to Dr. E. Teloy for many valuable suggestions, to R. Disch and S. Scherbarth, who helped to perform the experiments, and to U. Persson and I. Weber for technical assistance.

REFERENCES

- 1) E. Teloy, and D. Gerlich, Chem. Phys. 4 (1974) 417
- 2) W. Frobin, Ch. Schlier, K. Strein, and E. Teloy, J. Chem. Phys. 67 (1977) 5505
- 3) G. Ochs, and E. Teloy J. Chem. Phys. 61 (1974) 4930
- 4) Ch. Schlier, Some 'Simple' Ion-Molecule Reactions Measured with Guided Beams, in: Symposium on Atomic and Surface Physics, eds. W. Lindinger, F. Howorka, T. D. Märk, and F. Egger (Salzburg 1982) pp. 251-256
- 5) Ch. Schlier, Charge Transfer from He^+ to Ar and Xe at low Energies, in: Symposium on Atomic and Surface Physics, eds. F. Howorka, W. Lindinger, and T. D. Märk, (Salzburg 1984) pp. 122-126
- 6) E. Teloy, Proton-Hydrogen Differential inelastic and reactive Scattering at low Energies, in: Electronic and Atomic Collisions, ed. G. Watel (North-Holland, Amsterdam, 1978) pp. 591-604, and D. Gerlich, Thesis, Freiburg 1977
- 7) D. Gerlich and H. Bohli, Ortho - Para Transitions in slow $\text{H}^+ + \text{H}_2$ Collisions, in European Conference on Atomic Physics, eds. J. Kowalski, G. zu Putlitz and H. G. Weber (Heidelberg 1981) pp. 930-931
- 8) S. L. Anderson, F. A. Houle, D. Gerlich, and Y. T. Lee, J. Chem. Phys. 75 (1981) 2153
- 9) F. A. Houle, S. L. Anderson, D. Gerlich, T. Turner, and Y. T. Lee, Chem. Phys. Lett. 82 (1981) 392
- 10) F. A. Houle, S. L. Anderson, D. Gerlich, T. Turner, and Y. T. Lee, J. Chem. Phys. 77 (1982) 748
- 11) D. Gerlich, and G. Kaefer, Photon Ion Coincidences in low Energy Ion Reactions, in: Second European Conference on Atomic and Molecular Physics, eds. A. E. de Vries and M. J. van der Wiel (Amsterdam 1985) 396
- 12) K. Okuno, and Y. Kaneko, Low-Energy Electron-Capture in Ne^{++} -He, Ar^{++} -He and Kr^{++} -He Collisions in: Electronic and Atomic Collisions, eds. J. Eichler, I. V. Hertel, and N. Stolterfoth (Berlin 1983) p. 543
- 13) H. Villinger, J. H. Futrell, A. Saxer, R. Richter, and W. Lindinger, J. Chem. Phys. 80 (1984) 2543
- 14) K. M. Ervin, S. K. Loh, N. Aristow, and P. B. Armentrout, J. Phys. Chem. 87, (1983) 3593
- 15) K. M. Ervin and P. B. Armentrout, J. Chem. Phys. 80 (1984) 2978
- 16) D. Gerlich, Guided Beam Experiments on the low Energy Charge Transfer $\text{N}^+ + \text{CO} \rightarrow \text{CO}^+ + \text{N}$, in: Symposium on Atomic and Surface Physics, eds. F. Howorka, W. Lindinger, and T. D. Märk (Salzburg 1984), pp. 116-121
- 17) W. Beyer, Diplom Thesis Freiburg 1976
- 18) A. Sen, J. Wm. McGowan, J. B. A. Mitchell, Production of H_2^+ Ions in Low vibrational states Using a Radio Frequency Storage Ion Source, in: Electronic and Atomic Collisions (Stanford 1985), contributed paper F 131
- 19) W. J. Chesnavich, V. E. Akin and D. A. Webb, Ap. J. 287 (1984) 676
- 20) D. R. Guyer, L. Hüwel, and S. R. Leone J. Chem Phys. 79 (1983) 1259
- 21) A. O'Keefe, D. Parent, G. Mauclaire, and M. T. Bowers J. Chem Phys. 80 (1984) 4901
- 22) I. Dotan, and W. Lindinger, J. Chem. Phys. 76 (1982) 4972
- 23) B. Friedrich, and Z. Herman Chem. Phys. Lett. 107 (1984) 375
- 24) L. D. Landau and E. M. Lifschitz, Theoretical physics, Vol. 1 (Pergamon, Oxford, 1960) p. 93
- 25) H. G. Dehmelt, in: Advances in atomic and molecular physics, ed. D. R. Bates Vol. 3 (Academic Press, New York, 1967) pp. 53 - 72
- 26) P. H. Dawson, Quadrupole Mass Spectrometry, Elsevier Scientific Publishing, (Amsterdam 1976)
- 27) D. Cahnbley, Diplom thesis, Freiburg 1982
- 28) T. M. Miller, R. E. Wetterskog, and J. F. Paulson, J. Chem. Phys. 80 (1984) 4922
- 29) M. Wirth, Diplom thesis, Freiburg 1984
- 30) G. Mauclaire, R. Derai, S. Fenistein, and R. Marx, J. Chem. Phys. 70 (1979) 4017
- 31) L. Hüwel, D. R. Guyer, G. Lin, and S. R. Leone, J. Chem. Phys. 81 (1984) 3520
- 32) A. A. Wu and Ch. Schlier, Chem. Phys. 28 (1978) 73

ATOM CAPTURE AND LOSS IN ION MOLECULE COLLISIONS

Marianne BREINIG, Scott E. LASLEY, Carl C. GAITHER, III

University of Tennessee, Knoxville, TN 37996 and Oak Ridge National
Laboratory, P.O. Box X, Oak Ridge, TN 37831*

Progress is reported in measuring the energy and angular distribution of protons emerging with velocity close to the beam velocity from the target region when Ar^+ beams collide with a CH_4 target and ArH^+ beams collide with a He target at asymptotically high speeds. The protons result from the transfer of a target constituent to the projectile (atom capture) or from the dissociation of the projectile molecule in the collision (atom loss). For atom capture processes the Thomas peak is clearly observed.

1. INTRODUCTION

Ion-atom collisions at asymptotically high speeds involving electronic charge transfer, projectile ionization or target ionization are the subject of many recent theoretical investigations. In the asymptotic velocity regime, where the projectile speed v is substantially greater than the characteristic orbital speed of the electron in a target or projectile atom, a perturbation expansion is supposed to provide an increasingly accurate description of these processes. For charge transfer, interesting ties to classical descriptions exist.

In current electron capture and loss experiments, however, the asymptotic velocity regime can only be reached if the projectiles have velocities ≥ 10 au even for light targets. Furthermore, angular distributions measurements for electronic charge transfer and projectile ionization processes become increasingly difficult at projectile speeds over 10 au because of the small scattering angles involved.

A simple physical picture of such three-body scattering processes may emerge from alternative experiments, involving the capture of a whole atom from a molecule by a projectile ion or of the loss of an atom from a projectile molecular ion. Projectiles with kinetic energies on the order of 100 eV/u have asymptotically high speeds, substantially greater than the characteristic vibrational speeds of atoms in molecules, while the laboratory scattering angles for atom capture and atom loss events are measurably different from 0 deg. Doubly and triply differential cross section measurements become possible, promising to reveal completely new information about the associated scattering amplitudes.

We are investigating collisions at asymptotically high speeds between singly charged diatomic hydride ions (H_2^+ , HeH^+ , ArH^+ , KrH^+) and neutral atoms (He, Ne, Ar, Kr) and between singly charged atomic projectiles (Ar^+ , Kr^+) and neutral target molecules with one or more hydrogen atom constituents (H_2 , H_2O , CH_4). We focus on the dissociation of the projectile molecule into states in which the relative velocity of the fragments is small compared to the projectile velocity and on the transfer of target constituents into projectile centered continuum states, i.e. states in the vibrational continuum of the electronic ground state of the projectile hydride ion.

2. ATOM LOSS

In a collision between a diatomic hydride ion and a target atom, low lying states in the vibrational continuum of the projectile molecule can be excited. The molecule dissociates, most often into a neutral fragment and a proton. In the laboratory frame the velocity spectrum of protons produced in such atom loss events peaks at the projectile velocity v . We have observed this peak (1) by measuring the velocity distribution of protons emerging from the target into a cone of half angle θ_0 between 0.6 deg and 2.6 deg about the beam direction. However, at asymptotically high speeds excitation to low-lying states in the vibrational continuum of the ground states is not the only mechanism for collisional dissociation. Our spectra show prominent features in the wings of the proton loss peaks at the proton velocity $v_p = v$. Symmetric structure appears in both wings, growing more intense as the projectile energy increases. We observe peaks corresponding to proton velocities v_s , such that $|v_s - v|$ is constant, independent of projectile energy and target gas. The intensities of the features in the wings are, however, strongly dependent on the nature of the target atoms and are most intense for He targets. For ArH^+ projectiles at the higher projectile energies, we observe two well-resolved lines at $|v_s - v| = (7.2 \pm .3) \cdot 10^{-3}$ au ($1.3 \pm .1$ eV), and $(15.9 \pm .3) \cdot 10^{-3}$ au ($6.3 \pm .3$ eV), respectively; and one weak structure between these lines at $|v_s - v| = (11.9 \pm .4) \cdot 10^{-3}$ au ($3.5 \pm .3$ eV), as shown in Figure 1. We assume the observed lines

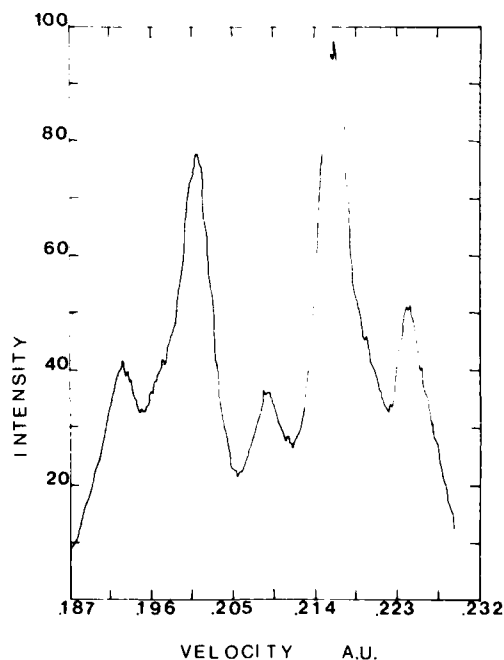


Figure 1. Velocity spectrum of protons emerging into a cone of half angle $\theta_0 = 1.6$ deg about the beam direction for 44.8 keV ArH^+ ions traversing a He target. The beam velocity is .209 au.

to be due to sudden electronic rearrangements of the molecular projectile in the collision, leaving its nuclear constituents relatively static (Frank-Condon transitions). The projectile undergoes a sudden vertical transition from the electronic ground state to some excited electronic state, which then dissociates, liberating a total CM kinetic energy $U(r) - U(\infty)$, where $U(r)$ is the potential energy corresponding to the internuclear separation r for the particular electronic state excited. The distribution of internuclear separations in the electronic ground state from which the excitation proceeds is of course determined by the populations of the various vibrational states present in the incident beam. In addition to measuring the proton velocity distribution along the beam direction we are now making detailed angular distribution measurements of energy-analyzed protons produced in atom loss events. This will allow us to map the complete velocity distribution of these protons in the projectile rest frame.

3. ATOM CAPTURE

In 1927 Thomas (2) gave a classical treatment of the transfer of a light target constituent to a heavy projectile valid in the asymptotic regime. Thomas scattering is a two step process. The light particle is first scattered by the projectile and then by a heavy target constituent in such a manner that projectile and captured particle emerge with almost the same velocity at a critical angle θ_c with respect to the incident beam direction. For electron capture by protons from He $\theta_c = \sqrt{3m/2M} = 0.47$ mrad. (m and M are the electron and proton mass respectively). It is now widely understood that any quantum treatment of capture and high energies must take this process into account (3). In a perturbation expansion, it corresponds to a second order Born process that dominates over the first order Born term in the limit of high projectile velocity. Only recently, the first observation of the Thomas peak in the differential cross section for high energy electron capture by protons from He has been reported (4), and experiments involving heavy ion projectiles would be even more difficult. For atom capture at asymptotically high velocities however we have observed the Thomas peak at $\theta_c = 1.3$ deg with Ar^+ projectiles and a CH_4 target (5). In two recent theoretical papers Shakeshaft and Spruch (6,7) have focussed attention on the connection between classical and quantum mechanical scattering descriptions, and atom capture experiments are among the most suitable to reveal such ties.

In our early measurements we have recorded the number of protons emerging into a cone of half angle θ_0 about the forward direction as a function of proton energy for 100-300 eV/u Ar^+ and Kr^+ projectiles incident on CH_4 . States in the vibrational continuum of ArH^+ and KrH^+ dissociate into $\text{Ar} + \text{H}^+$ and $\text{Kr} + \text{H}^+$, respectively (8). After a continuum capture event the electron follows the projectile ion and the proton emerges with velocity $v_p \approx v$. If atom capture proceeds via the double scattering mechanism, then the projectile and the captured atom emerge at a critical angle θ_c . For Ar^+ on CH_4 , $\theta_c \approx 1.3$ deg and for Kr^+ on CH_4 , $\theta_c = 0.6$ deg. For Ar^+ projectiles we have varied θ_0 from being smaller to being larger than the critical angle while still collecting protons emerging at all azimuthal angles. For acceptance angles $\theta_0 > \theta_c$ we observe a central peak in the proton spectra centered at a proton velocity $v_p = v'$ where v' is close to but slightly less than the beam velocity v . This peak vanishes for $\theta_0 < \theta_c$. We interpret this central peak as the atom capture to the continuum peak, produced via the double scattering mechanism. For 100-300 eV/u Ar^+ and Kr^+ projectiles on the CH_4 measured integrated cross sections are small, they lie between 5 and 100 barn.

In earlier experiments Cook et al (9) observed the Thomas peak in the formation of H_2^+ by fast proton impact on CH_4 . The position of the Thomas

peak can be predicted classically. The shape of the Thomas peak, however, depends on the detailed nature of the interaction. To extract this shape information we are now making the first doubly differential cross section measurements for atom capture to continuum states, differential in captured particle scattering angle and energy.

4. APPARATUS

Measurements differential in proton scattering angle and energy are made using a two dimensional position sensitive particle detection system which is described in detail in this volume (10).

Our beams pass through a 1 cm long target gas cell located at the entrance focus of a doubly focussing spherical sector electrostatic analyzer accepting protons emitted into a cone of half angle $\theta \leq 6$ deg about the beam direction. A 1 mm aperture in the exit focus of the analyzer sets the energy resolution to $\Delta E/E = 1\%$ FWHM. The position sensitive detector system is mounted 15 cm away from the exit aperture. We record an atom capture to the continuum or atom loss event by detecting a proton emerging from the collision with velocity v_p close to the beam velocity v . We measure the angular and energy distribution of the protons emerging from the collision, i.e., we measure $d^2\sigma/d\Omega_p dE_p$. The angular distribution of the protons with v_p close to v in the scattering region is imaged one to one into the detection region. The entire distribution in polar angle θ and azimuthal angle ϕ can be acquired simultaneously. A microchannel electron multiplier array of 25 mm diameter active area is the primary event detector. Output pulses are collected on a resistive anode, and position decoding utilizes the charge division method. Computer assisted data acquisition is implemented using the modular CAMAC standard and a multitasking control program.

5. RESULTS

Measurements using the position sensitive detector system have just begun and only preliminary results can be presented here.

Figure 2 shows the angular distribution of protons emerging from the target region with speed equal to the projectile speed v , for 7 keV Ar^+ projectiles on CH_4 . It can clearly be seen that the protons emerge preferentially at a nonzero angle $\theta \approx 1.4$ deg relative to the beam direction. This measured angle agrees well with $\theta_c = 1.3$ deg predicted for atom capture via Thomas double scattering. Figure 2 shows raw data, not yet corrected for slight distortions due to the imperfect focussing properties of the 160 deg spherical sector proton energy analyzer. Because atom capture cross sections are so small (on the order of barn) great care must be taken to eliminate background. Here we have not yet been completely successful and the ring structure in the angular distribution, which is the Thomas peak, does not have perfect symmetry. Background problems are now being corrected. The results presented in Figure 2 clearly show that atom capture to the continuum at asymptotically high speeds proceeds via the Thomas double scattering mechanism. To investigate the detailed shape of the Thomas peak, measurements are now being made of the angular distribution of the protons emerging from the target region as a function of proton energy. We will then be able to map the complete velocity distribution of the captured particles. The velocity of a detected proton along the beam direction is determined by the analyzer field and the velocity transverse to the beam direction from the measured position of arrival on the channel plate.

For atom loss processes complete velocity distributions will also be obtained from measurement of proton spectra differential in proton energy and scattering angle.

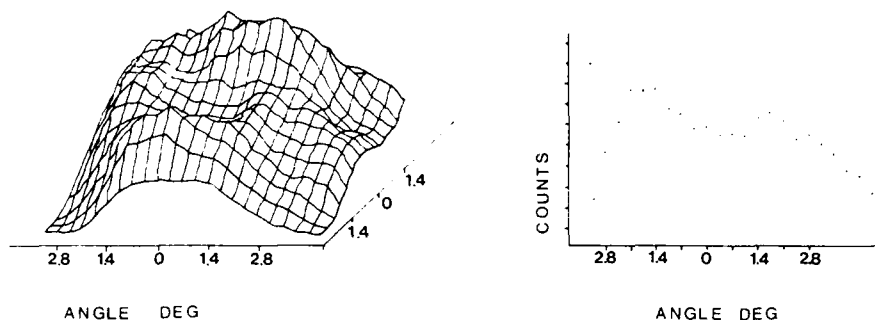


Figure 2. Angular distribution of protons emerging from the target region with speed equal to the projectile speed v for 7 keV Ar^+ projectiles on CH_4 . The protons emerge preferentially at a nonzero angle $\theta \approx 1.4$ deg relative to the beam direction as predicted for continuum capture proceeding via the Thomas double scattering mechanism. The right graph shows a cut through the channel plate image shown in the left graph.

Figure 3a shows a cut through a channel plate image measured with 40 keV ArH^+ projectiles on He. The proton velocity along the beam direction equals the projectile velocity $v = .1975$ au. We observe a peak at zero transverse velocity due to dissociation of ArH^+ after excitation to low lying states in the vibrational continuum of the ground state. Peaks at -7.5×10^{-3} au transverse velocity are due to protons being emitted in the projectile rest frame with this speed transverse to the beam direction.

In Figure 3b the proton velocity along the beam direction equals .1940 au. The central peak has disappeared and the peaks at -7×10^{-3} au are due to protons being emitted in the projectile rest frame with the speed -7.5×10^{-3} au as above but -25 deg backwards from the direction transverse to the beam. When angular distributions at proton velocities between $v \pm .02$ au have been measured, a map of the complete velocity distribution in the projectile rest frame can be assembled.

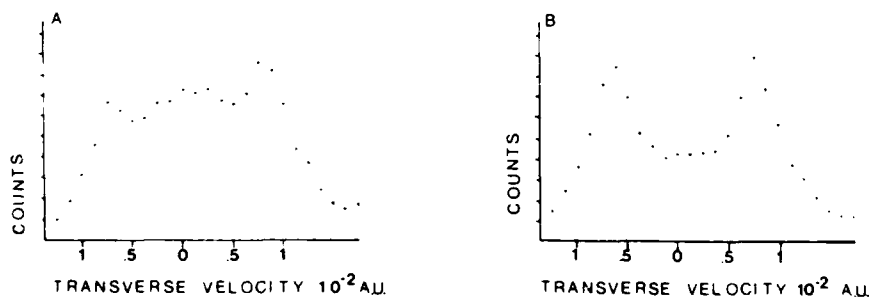


Figure 3. Cuts through channel plate images (angular distributions) measured for 40 keV ArH^+ on He. The protons result from the dissociation of the ArH^+ molecule in the collision. a) The proton velocity equals the beam velocity $v = .1975$ au b) The proton velocity is .1940 au

ACKNOWLEDGEMENT

This research was supported by the National Science Foundation, and by the U.S. Department of Energy, under contract no. DE-AC05-84OR21400 with Martin Marietta Energy Systems, Inc.

REFERENCES

- 1) S.D. Berry, M. Breinig and I.A. Sellin, Proton Loss to Projectile-Centered Continuum States for 7-57 keV ArH^+ Projectiles Traversing He, Ne, and Kr Targets, in Abstracts of Contributed Papers, XII International Conference on the Physics of Electronic and Atomic Collisions, ed. by Sheldon Datz (1981), pp. 996-997.
- 2) L.H. Thomas, Proc. R. Soc. London 114, (1927) 561.
- 3) J.S. Briggs, J.H. Macek, and K. Taulbjerg, Comment At. Mol. Phys. 12 (1983) 1.
- 4) E. Horsdal-Pedersen, C.L. Cocke, and M. Stockli, Phys. Rev. Lett. 50 (1983) 1910.
- 5) M. Breinig et al., Phys. Rev. Lett. 51 (1979), 1251.
- 6) R. Shakeshaft and L. Spruch, Rev. Mod. Phys. 51 (1979) 369.
- 7) R. Shakeshaft and L. Spruch, Phys. Rev. A 21 (1980), 1161.
- 8) P. Rosmus and E.A. Reinsch, Z. Naturforsch. 35a (1980) 1066.
- 9) C.J. Cook, N.R. A. Smyth, and O. Heinz, J. Chem. Phys. 63 (1975)
- 10) S.B. Elston, Doubly Differential Cross Sections of Collision-Produced Forward Electron Emission, this volume.

INELASTIC AND REACTIVE COLLISIONS WITH POLARIZED EXCITED
Na ATOMS

H. SCHMIDT, I.V. HERTEL

Institut für Molekülphysik, Freie Universität Berlin,
Arnimallee 14, D-1000 Berlin 33, Germany

and

Y.T. LEE

Materials and Molecular Research Division, Lawrence Berkeley
Laboratory, and Department of Chemistry, University of
California, Berkeley, CA 94720, U.S.A.

Polarization effects in inelastic collisions of laser state-prepared $\text{Na}(3^2\text{P}, M_J)$ with Na^+ leading to $\text{Na}(3^2\text{D})$ or $\text{Na}(3^2\text{S})$ are discussed for the energy range $E_{\text{cm}} = 5\text{--}47.5\text{eV}$. Studies with linearly polarized light can be explained with a simple "locking" model of the $\text{Na}(3\text{p})$ -orbital. The investigations employing circularly polarized light are a very sensitive test of the models describing the nonadiabatic angular momentum coupling between electronic and nuclear motion. The dynamical effects of the electronic spin on the angular momentum transfer are discussed. Recent crossed-beam experiments on the $\text{Na} + \text{O}_2 \rightarrow \text{NaO} + \text{O}$ reaction in the energy range $E_{\text{cm}} = 0.3\text{--}0.8\text{eV}$ show a pronounced dependence on the electronic symmetry of Na.

1. Introduction

Polarizing the electronical motion of a sodium atom prior to collision with another heavy particle serves as a powerful probe to test the fine details of the collisional event. A simple system like $\text{Na} + \text{Na}^+$ can be studied in a crossed beam experiment with state preparation before and state analysis after the scattering process. This permits to determine absolute value and phase of the scattering amplitudes (1). For the quasi-one-electron system Na accurate potential curves even for high excited states may be calculated (2). Semiclassical theory is well suited to treat the dynamics of the problem and to study the effect of approximations, e.g. a straight line trajectory for the nuclear motion. In the first part of this article we will discuss inelastic collisions excluding the influence of the electronic spin. The laser optical pumping of sodium allows in principle to analyse the effect of higher multipoles on the electronic motion e.g. the octopolemoment (3). This makes it superior to the particle-photon coincidence technique where from the complete polarization analysis of the emitted light the highest measurable quantity is the quadrupolemoment. The comparison between experiment and theory including dynamics of the electron spin will reveal the quality of the semiclassical methods employed. In the last part of this work the reaction dynamics of Na in the

3^2S , 3^2P , 4^2S , 4^2P , 4^2D and 5^2S state reacting with O_2 to $NaO + O$ are discussed. The large excitation energies associated with the higher states of Na are well above the threshold of the reaction. The dominant aspect of electronic excitation however is the drastically different chemical behaviour owing to the change of electronic orbital symmetry of the atom. This article will not deal with scattering experiments studying fine-structure transitions (4).

2. $Na^*(3^2P) + Na^+$ scattering experiments

2.1 Experimental geometry

The crossed beam apparatus has been described in detail before (1). Briefly, an energy selected Na^+ beam $\Delta E(\text{FWHM}) = 150\text{meV}$ was

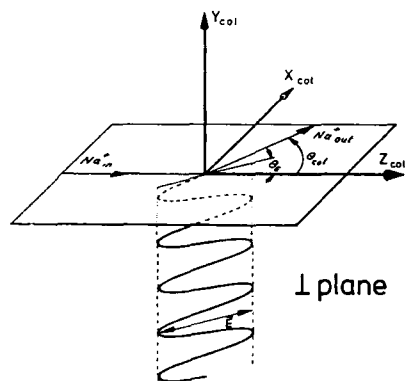


FIGURE 1
Preparation of the atomic p-orbital with linearly polarized light, showing excitation by a laser beam perpendicular to the collision plane. The polarization angle θ_E is measured with respect to the Z_{col} axis.

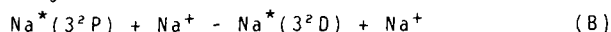
crossed at 90° to a sodium atom beam. The sodium atoms in the interaction region were optically pumped on the $Na(3^2S, F=2 \rightarrow 3^2P, F=3)$ hyperfine transition. In fig.1 the experimental geometry for the situation employing linearly polarized light travelling perpendicularly to the scattering plane is displayed. Fig. 1 shows that at large internuclear distances one prepared a $|p\pi\rangle$ or a $|p\sigma\rangle$ state for $\theta_E = 90^\circ$ or 0° respectively.

Owing to the fine- and hyperfine structure of sodium not a pure $3p$ orbital is prepared but an incoherent mixture of the orthogonal $|3p\pi^+\rangle$, $|3p\pi^-\rangle$ and $|3p\sigma\rangle$ states. The relative population of these states is determined for each polarization measurement from the detected fluorescence intensity of the $Na(3P)$ as a function of θ_E (5). For all studies with circularly polarized light the laser is directed perpendicularly to the scattering plane.

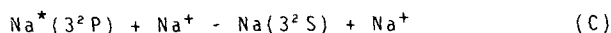
2.2.1 Potential energy curves

Only presently potential curves for the Na ion have been calculated which cover the energy range probed in the present experiment (2a), (2b). The computations included 12Σ , 10Π and 6Δ states, thus covering all asymptotic energies up to $Na + Na(5^2S)$. The relevant states of the quasimolecule formed transiently in

the collision are depicted in fig.2 (from ref (2a)). They relate to the processes of collisional excitation



and deexcitation



The potentials at large internuclear distances, where the dynamics of angular momentum recoupling occur are shown in fig.3.

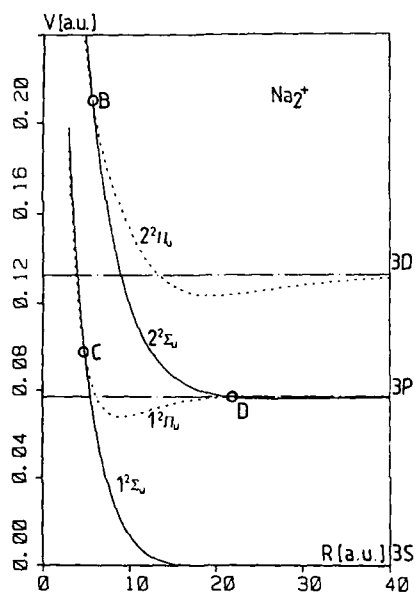


FIGURE 2
On scale plot of the four potential curves contributing to the processes (B) and (C). The positions of the relevant curve crossings are marked.

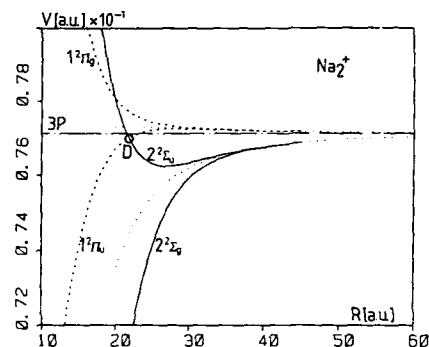


FIGURE 3
Long range dependence of the potentials where Na_2^+ is dissociating to $\text{Na}^+ + \text{Na}(3\text{P})$. The dotted curves give the long range potentials owing to quadrupole moment and polarizability of the 3p electron.

2.3 Linear polarization studies

From the calculated potential curves (fig.2) one can see that the inelastic process (B) is proceeding via the $2^2\Sigma_u - 2^2\Pi_u$ curve crossing (B) at $R_c = 5.6\text{a.u.}$ The polarization measurements displayed in fig.4 show indeed that the maximum scattering signal is observed close to $\theta_F = 180^\circ$ where $|p\sigma\rangle$ state is prepared asymptotically. Here and in the rest of the article σ and π will denote the preparation of molecular states at large internuclear distances (Hund's coupling case (e) (7)), whereas Σ and Π denote the states of the molecule at small distances (Hund's coupling case (a), (b)). The angular position γ of the maximum cross section for process (B) is clearly different from 180° .

This behaviour can be understood in terms of the "locking" model which is illustrated in fig.5. For convenience the Na^+ ion is shown at rest while the $\text{Na}(3\text{P})$ is moving

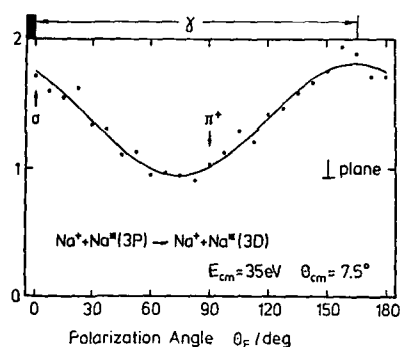


FIGURE 4
Polarization dependence of the scattering intensity as a function of the angle θ_E . In the upper half the laser beam is propagating perpendicular to the collision plane and in the lower half is in the collision plane.

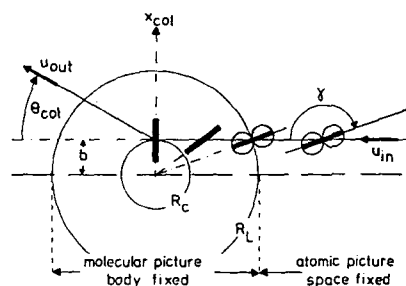


FIGURE 5
Schematic illustration of an effectively repulsive trajectory and its influence on the alignment angle γ of the p-charge cloud for maximum molecular state preparation at R_L (3P - 3D excitation process).

Since the polarization angle θ_E is measured with respect to the relative velocity the situation shown in fig.5 reproduces the experimental geometry. The calculations of Allan and Korsch (8) indicate that the inelastic transition of process (B) occur only over a small range of impact parameters. Thus it is well justified to display one specific impact parameter. Fig.5 shows that at large internuclear distances the p-orbital aligned under the angle γ stays space fixed. In the angular momentum coupling scheme this situation corresponds to Hund's coupling case (e). At internuclear distances close to R_L the electric field between the ion and the p-orbital is strong enough to gradually lock the orbital to the internuclear axis (Hund's coupling case (a), (b)).

Fig. 6 shows that the measurement of the energy dependence of the angle γ is in very good agreement with semiclassical calculations (9),(10). In these computations the time dependent Schrödinger equation for the electronic motion under the influence of a nuclear trajectory $R(t)$ dependent electronic potential $V(R(t))$ has been solved. These calculations (L-reference frame) did not include the couplings owing to the electron spin. The computations show that the transition from the space fixed to the body fixed behaviour is occurring in a "merging" region, where $\Sigma - \Pi$ transitions proceed. Thus one finds only a dominant population of the Σ -state rather than a pure one. The angle γ depends on the absolute value and the phase of the Σ and Π amplitudes (10) which may be visualized from the corresponding situation of the Lissajou figures.

In fig. 7 the "merging" process is displayed by a plot of the alignment angle $\bar{\gamma}$ as a function of the internuclear distance. $\bar{\gamma}$ is here the angle with respect to the internuclear axis. At small distances R $\bar{\gamma}$ is equal to 180° , gradually decreases for larger R and behaves geometrically $\bar{\gamma} = \bar{\gamma}_0 + \arcsin b/R_L$ at very large R .

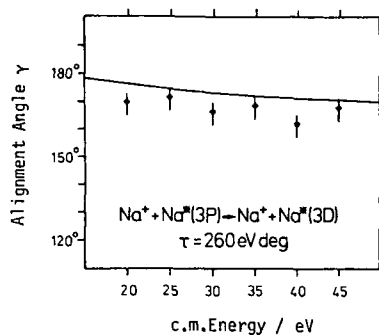


FIGURE 6
Alignment angle γ as a function of energy for constant reduced scattering angle τ ; excitation process $3P - 3D$. Dots give experimental points, the full line represents the semi-classical calculations.

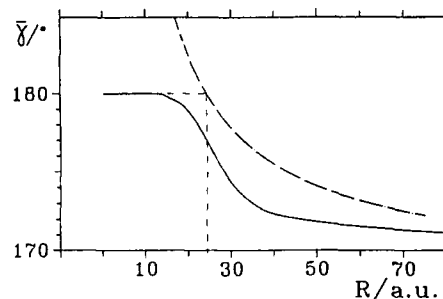


FIGURE 7
Alignment angle $\bar{\gamma}$ relative to the direction of the internuclear axis as a function of internuclear distance for Na collisional excitation.

2.4 Circular polarization studies

The transitions in the merging region lead to a change of the inherent angular momentum of the electronic charge cloud by non-adiabatic coupling to the nuclear motion. This can be measured by orienting the Na-target with RHC (right hand circularly) or LHC (left hand circularly) polarized laser light. The asymmetry parameter

$$S = (I_{RHC} - I_{LHC}) / (I_{RHC} + I_{LHC})$$

is closely related to the nonadiabatic angular momentum transfer between electronic and nuclear motion (11). In the polarization analysis of light the quantity S is dominated "Stokes Parameter P_3 ". In photon-particle coincidence measurements the highest extractable tensor quantity characterizing the angular momentum of the electron charge distribution is the quadrupole moment. Since in the laser optical pumping process of the $Na(3^2P)$ state many photons are absorbed, higher multipole moments e.g. the octopole (3) are prepared and may be studied in the scattering experiment. One can investigate the spin effects connected with the higher moment in measurements with circularly polarized light. Fig.8 and Fig.9 show a comparison between the measured asymmetry S for collisional excitation and deexcitation of Na and calculations in the L- and J-reference frame.

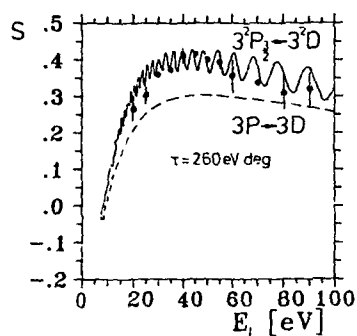


FIGURE 8
Circular asymmetry S as a function of laboratory energy. Full line J-frame, broken line L-frame.

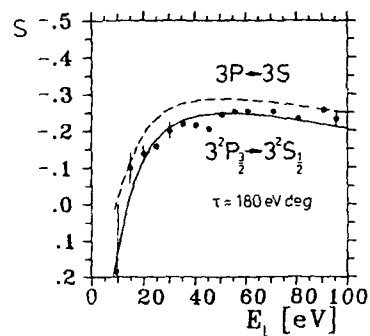


FIGURE 9
Same as fig.8 but $P \rightarrow S$ collisional deexcitation

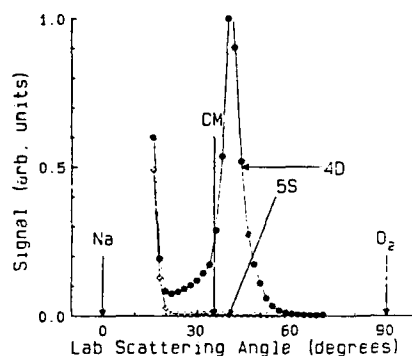
The agreement with the calculations in the J-frame where dynamical spin couplings are included is excellent, though the oscillations present in fig.8 yet have not been resolved in the experiment. The oscillations are equally spaced as function of $1/v_{rel}$ where v_{rel} is the relative velocity of the colliding particles. A comparison of the characteristic times in this system reveals that the oscillations are related to the orbit precession period calculated from the average $V_{\Sigma} - V_{\Pi}$ splitting in the region $R = 23-60a.u.$

3 Symmetry effects in the $Na^* + O_2$ reaction

The large energies associated with electronic excited atoms are often high above the energetic threshold of endothermic reactions. Experiments show however that the most important aspect of electronic excitation is the dramatic different reactivity owing to the change in the spin state or the orbital symmetry of the excited atom. This has been shown in the reaction of ground state $O(^3P)$ and excited $O(^1D)$ with H_2 or saturated hydrocarbons (12). Orbital alignment effects have been investigated in the chemiluminescent reaction of $Ca(^1P)$ with small halogenic molecules (13). The present study focusses on the reaction of $Na(3^2P, 4^2S, 4^2P, 4^2D, 5^2S)$ with molecular oxygen in the collision energy range $E_{cm} = 0.3-0.8eV$. This reaction is endothermic by 2.4eV for ground state sodium and zero relative energy of the reactants

3.1 Experimental setup

Details of the crossed beam experiment are described elsewhere (14). Briefly, seeded or neat supersonic beams of Na or O_2 are crossed under single collision conditions at right angles in a scattering chamber. Scattered product is detected by a rotatable mass spectrometer. The experimental technique to maintain a large stationary population in the $Na(3^2P)$, $Na(5^2S)$ and $Na(4^2D)$ states



by excitation with two c.w. dye lasers has been demonstrated before (15). One laser is tuned to the sodium D₂ line, while the other is tuned to the transition from the Na(3²P) level to the upper level. It is important to remember that preparation of the Na(5²S) or Na(4²D) state results also in considerable population of the Na(4²S), Na(4²P), Na(3²P) and Na(3²S) states.

FIGURE 10
Laboratory angular distribution of NaO at $E_{cm} = 0.78\text{eV}$.

3.2 Results and Discussion

The laboratory angular distributions of NaO were measured for three collision energies $E_{cm} = 0.3, 0.7, 0.78\text{eV}$ and for Na in the (5²S, 4²P, 4²S, 3²P, 3²S) or (4²D, 4²P, 4²S, 3²P, 3²S) states (16). Fig. 10 shows the result for $E_{cm} = 0.78\text{eV}$ with the mass spectrometer tuned to $q/m = 23$ because most of the NaO fragments to Na⁺ in the detector ionizer.

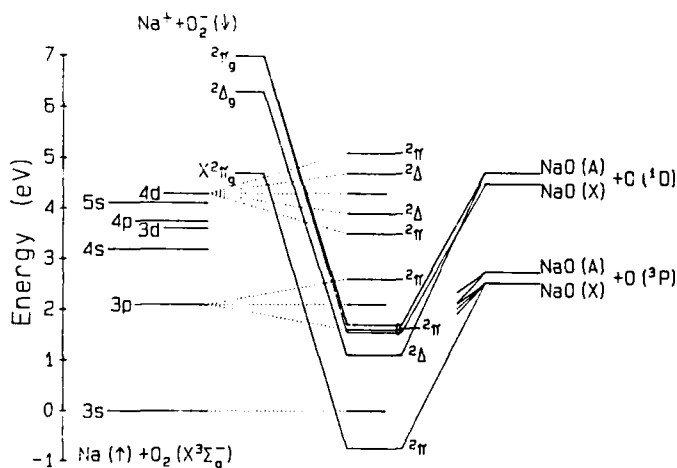


FIGURE 11
Diabatic correlation diagram for Na + O₂ in C_{∞v} symmetry

There are four remarkable features in the experimental study of this reaction:

- (i) Since no reaction is observed for optical pumping of the Na(5²S) state at either collision energy the Na²(4²D) state only leads to reaction
- (ii) The measurements with Na(4²D) at three different energies show that the reaction has an energy barrier of at least 0.3eV and less than 0.7eV

- (iii) The NaO is predominantly scattered backwards with respect to the incoming sodium atom in the c.m. reference frame.
- (iv) Kinematical considerations show that the limited angular range of the NaO product makes the production of $\text{NaO}(A^2\Sigma^+) + \text{O}(D)$ most likely.

The backward scattering suggests a collinear approach geometry of the reactants. The reaction only for $\text{Na}(4^2D)$ implies that a NaO_2 Δ -transition state in $C_{\infty v}$ symmetry leads to $\text{NaO} + \text{O}$, since this state is only accessible to the $\text{Na}^*(n^2D)$ state and not to the states $\text{Na}(n^2S)$ or $\text{Na}(n^2P)$. Fig. 11 displays a diabatic correlation diagram for $\text{Na} + \text{O}_2$ in $C_{\infty v}$ symmetry. Only the energy of the two lowest NaO_2 states is known from calculations (17), the other energy positions of NaO_2 are qualitative guesses.

Acknowledgements

H.S. and I.V.H. acknowledge financial support by the Sonderforschungsbereich 161 of the Deutsche Forschungsgemeinschaft. Y.T.L. acknowledges financial support by the U.S. Department of Energy under contract No. DE-AC-03-76SF00098

References

- 1) H. Schmidt, A. Bähring, E. Meyer and B. Miller, Phys. Rev. Lett. 48, 1008 (1982)
- 2) A. Bähring, I.V. Hertel, E. Meyer and H. Schmidt, Z. Phys. A 312, 293 (1983)
- 3) a) A. Bähring, I.V. Hertel, E. Meyer, W. Meyer, N. Spies and H. Schmidt, J. Phys. B 17, 2859 (1984)
b) A. Henriët and F. Masnou-Seeuws, Chem. Phys. Lett. 101, 535 (1983)
- 4) I.V. Hertel and W. Stoll, Adv. At. Mol. Phys. 13, 113 (1978)
- 5) J.M. Mestdagh, J. Berlande, P. de Pujo, J. Cuvellier and A. Binet, Z. Phys. A 304, 3 (1982)
- 6) A. Fischer, I.V. Hertel, Z. Phys. A 304, 103 (1982)
- 7) H. Schmidt, A. Bähring and R. Witte, Z. Phys. D, Atoms, Molecules, Clusters, submitted
- 8) H. Herzberg, Spectra of Diatomic Molecules, van Nostrand
- 9) R.J. Allan and H.J. Korsch, Z. Phys. A 320, 191 (1985)
- 10) A. Bähring, E. Meyer, I.V. Hertel and H. Schmidt, Z. Phys. A 320, 141 (1985)
- 11) I.V. Hertel, H. Schmidt, A. Bähring and E. Meyer, Rep. Prog. Phys. 48, 375 (1985)
- 12) H.W. Hermann and I.V. Hertel, Comm. At. Mol. Phys. XII, 61 and 127 (1982)
- 13) R.J. Buss, P. Casavecchia, T. Hirooka, S.J. Sibener and Y.T. Lee, Chem. Phys. Lett. 82, 386 (1981)
- 14) C. Rettner and D. Zare, J. Chem. Phys. 77, 2416 (1982)
- 15) M.F. Vernon, H. Schmidt, P.S. Weiss, M.H. Covinsky and Y.T. Lee, J. Chem. Phys. (1985) to be submitted
- 16) G. Jamieson, W. Reiland, C.P. Schulz, H.U. Tittes and I.V. Hertel, J. Chem. Phys. 81, 5805 (1984)
- 17) H. Schmidt, P.S. Weiss, J.M. Mestdagh, M.H. Covinsky and Y.T. Lee, Chem. Phys. Lett. (1985)
- 18) M.H. Alexander, J. Chem. Phys. 69, 3502 (1978)

POLARIZATION EFFECTS IN ASSOCIATIVE IONIZATION OF EXCITED SODIUM ATOMS

Gerard NIENHUIS

Fysisch Laboratorium, Rijksuniversiteit Utrecht, Postbus 80 000,
3508 TA Utrecht, The Netherlands

We discuss several recent experimental and theoretical results on the rate of associative ionization of two laser-excited Na atoms, as a function of the polarization direction of the exciting radiation.

1. INTRODUCTION

Illumination of an atomic vapor with nearly resonant light can induce a large degree of ionization, either by photoionization or by collisional ion production involving excited atoms (1). A detailed understanding of ionization processes is important both in astrophysics and laboratory physics.

In the present contribution we consider the collision of two excited Na atoms, leading to associative ionization, as indicated by the reaction equation



This reaction is of a simple type in the sense that it contains only two fragments both in the initial and the final state. The electronic transition in the collision complex may be looked upon as molecular autoionization. After the electron ejection, the remaining system has insufficient energy to separate in a ground state Na atom and a Na^+ ion, so that it is left as a bound molecular ion. The Na_2^+ production in a Na vapor illuminated with pulsed laser light has been observed by Roussel et al.(2).

An interesting possibility arises when this same process is studied in an atomic beam. When the polarization of the exciting light is rotated with respect to the beam axis, the distribution over the magnetic substates of the initial excited state is modified, and the variation of the ion production with the polarization direction contains information on the dependence of the rate of reaction (1.1) on the magnetic substates.

A first experimental study of this effect was performed in our laboratory (3). The experiment used a single atomic beam, which was crossed at right angles by a laser beam tuned to the $F=2 \rightarrow F=3$ hyperfine transition of the Na-D2 line. A scheme of the experiment is given in figure 1. Collisions between two excited Na atoms result from the velocity spreading in the beam, leading to typical values of the relative kinetic energy of 15 meV. The exoergicity of the reaction is about 50 meV. A strong polarization effect was observed. For a linear polarization direction parallel to the atomic beam, the production rate of Na_2^+ was about a factor 1.5 higher than for a polarization direction perpendicular to the beam. A more recent experiment by Rothe et al. (4) gave strikingly different results. The ion yield as a function of the angle θ between the atomic beam axis and the polarization direction displayed maxima both for $\theta=0^\circ$ and $\theta=90^\circ$, with a minimum at $\theta=45^\circ$.

We have given a theoretical analysis of the relation between the Fourier coefficient of the Na_2^+ yield as a function of θ , and the rate constants as a function of pairs of magnetic quantum numbers (5). A discussion of the relative contribution to the process from the various adiabatic potential curves has been given by Jones and Dahler (6). Here we review the present status of our understanding of the polarization effects of associative ionization.

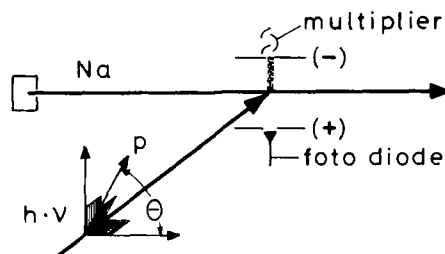


Figure 1. Scheme of the experiment. A laser beam crosses the atomic beam at right angles. Both ions and fluorescence photons can be detected.

2. SYMMETRY CONSIDERATIONS

We indicate the state of the two identical atoms before the collision by the density matrix

$$\rho = \rho_A \rho_B \quad (2.1)$$

Since both atoms A and B are excited by the same laser beam, we can assume that ρ_A and ρ_B are identical matrices. The scattering amplitude for associative ionization is denoted as $f(\gamma \vec{v}_f + \alpha \vec{v}_i)$, where α indicates the initial state of both collision partners, \vec{v}_i is the initial relative velocity, \vec{v}_f is the final relative velocity of the ejected electron with respect to the molecular ion, and γ denotes the final internal state of the ion. When ρ_A and ρ_B are normalized to the density n_e of excited atoms, the rate of ion production can be put in the form (5)

$$R = \sum_{\alpha} \sum_{\gamma} \langle \alpha' | G | \alpha \rangle \langle \alpha | \rho | \alpha' \rangle = \text{Tr} G \rho \quad (2.2)$$

where the detection operator G has matrix elements between internal states α of the pair of atoms defined by

$$\langle \alpha' | G | \alpha \rangle = \int d\vec{v}_f \int d\vec{v}_i (m \vec{v}_f / \mu) f(\gamma \vec{v}_f + \alpha \vec{v}_i) f^*(\gamma \vec{v}_f + \alpha' \vec{v}_i) \rho_{\alpha \alpha'} \quad (2.3)$$

The average is performed over the distribution of initial relative velocities \vec{v}_i . An integration is performed over the unobserved direction of the ejected electron, and likewise the internal states γ of the molecular ion are summed over. The reduced masses m and μ refer to the final and initial states.

If we expand ρ_A and ρ_B in spherical tensors t_{kq} , defined with the quantization axis in the polarization direction for linear polarization, or the propagation direction for circular polarization, then we may write (5)

$$\rho_A = \sum_k \sum_q c_k t_{kq}^+ \quad (2.4)$$

and likewise for ρ_B , since in this polarization frame the density matrices are diagonal in the magnetic quantum numbers, so that only components with $q=0$ arise. The tensors t_{kq} are related to the tensors T_{kq} with the beam axis as quantization axis, by a simple rotation over the angle θ between the polarization axis and the beam axis. We expand the detection operator G in the spherical tensors T_{kq} for both atoms, according to

$$G = \sum_{kq} \sum_{k'q'} g(kq; k'q') T_{kq}(A) T_{k'q'}(B) \quad (2.5)$$

From the axial symmetry of the distribution function of the initial relative velocity \vec{v}_i and the identity of the two atoms we obtain the following symmetry relations (5)

$$\begin{aligned}
 g(kq; k'q') &= 0 \quad \text{for } q + q' \neq 0 \\
 g(kq; k'q') &= (-)^{k-q+k'-q'} g(k-q; k'-q') \\
 g(kq; k'q') &= g(k'q'; kq) \\
 g(kq; k'q') &= (-)^{q+q'} g^*(k-q; k'-q')
 \end{aligned} \tag{2.6}$$

The ion production rate R is then found to be given by

$$R(\vartheta) = \sum_{kq} \sum_{k'q'} c_k c_{k'} g(kq; k'q') d_{q0}^k(\vartheta) d_{q'0}^{k'}(\vartheta) \tag{2.7}$$

in terms of the reduced rotation matrices d_{q0}^k . Equation (2.7) determines the dependence of the ion production rate on the angle ϑ between the atomic beam axis, and the polarization axis, which is the direction of polarization for π radiation, or the propagation direction for σ radiation.

Excitation of the atoms with radiation of a selected polarization fixes the expansion coefficients c_k . For linear polarization only terms with even k appear. Measurement of $R(\vartheta)$ at these known values of c_k then provides information on the coefficients g , which determine the detection operator G , and thereby the ionization rates for any combination of magnetic quantum numbers, as well as off-diagonal terms, which depend on the relative phases of the scattering amplitudes.

The rotation matrices d_{q0}^k obey the symmetry relations (7)

$$d_{q0}^k(\vartheta) = (-)^q d_{q0}^k(-\vartheta) = (-)^{k-q} d_{q0}^k(\pi-\vartheta) = (-)^q d_{-q0}^k(\vartheta) \tag{2.8}$$

This leads to the identities

$$R(\vartheta) = R(-\vartheta) = R(\pi-\vartheta) \tag{2.9}$$

for the ionization rate. Expansion of R as a Fourier series gives

$$R(\vartheta) = \sum_{n=0}^{2J} R_n \cos(2n\vartheta) \tag{2.10}$$

where the upper limit $2J$ follows from the expressions for d_{q0}^k , which cannot have a higher Fourier component than $\exp(\pm i k \vartheta)$. Note that $2J$ is the maximal value of k . In the present case of excitation of atomic states with $J = 3/2$, the maximum value for n is 3. For linear polarization only even k values can appear, so that n can only attain the values 0, 1, 2 for $J = 3/2$.

To be specific, we now give the explicit expression for the Fourier coefficients R_0 , R_1 and R_2 in the relevant case of excitation of the $F=2 \rightarrow F=3$ hyperfine component of the Na-D2 line with linearly polarized light. The coefficients c_k are then equal to

$$c_0 = \frac{1}{2} n_e \quad c_2 = -\frac{1}{3} n_e \tag{2.11}$$

which corresponds to the populations $n_M = \langle M | \rho_A | M \rangle = 1/12 n_e$ for $M = \pm 3/2$, and $n_M = 5/12 n_e$ for $|M| = 1/2$. The relevant multipole coefficients of G are

$$\begin{aligned}
 p &= g(00;00) = A+2B+C \\
 s &= g(20;00) = A-C \\
 t &= g(20;20) = A-2B+C
 \end{aligned} \tag{2.12}$$

with

$$\begin{aligned}
 A &= \frac{1}{2} [K(\frac{3}{2}, \frac{3}{2}) + K(\frac{3}{2}, -\frac{3}{2})] \\
 B &= \frac{1}{2} [K(\frac{3}{2}, \frac{1}{2}) + K(\frac{3}{2}, -\frac{1}{2})] \\
 C &= \frac{1}{2} [K(\frac{1}{2}, \frac{1}{2}) + K(\frac{1}{2}, -\frac{1}{2})]
 \end{aligned} \tag{2.13}$$

The factors $K(MM')$ are rate constants, which equal the diagonal terms of G

$$K(MM') = -MM' |G| MM' \quad (2.14)$$

Furthermore we need the off-diagonal terms

$$u = g(21;2-1) = \frac{1}{2} \langle \frac{3}{2} - \frac{3}{2} | G | \frac{1}{2} - \frac{1}{2} \rangle + \frac{1}{2} \langle \frac{3}{2} - \frac{1}{2} | G | \frac{3}{2} - \frac{3}{2} \rangle - \langle \frac{3}{2} - \frac{1}{2} | G | \frac{1}{2} - \frac{3}{2} \rangle \quad (2.15)$$

and

$$v = g(22;2-2) = \frac{1}{2} \langle \frac{3}{2} - \frac{3}{2} | G | \frac{1}{2} - \frac{1}{2} \rangle + \frac{1}{2} \langle \frac{3}{2} - \frac{1}{2} | G | \frac{3}{2} - \frac{3}{2} \rangle + \langle \frac{3}{2} - \frac{1}{2} | G | \frac{1}{2} - \frac{3}{2} \rangle \quad (2.16)$$

The Fourier coefficients for linear polarization are then (5)

$$\begin{aligned} R_0 &= \frac{1}{4} p - \frac{1}{12} s + (11t - 12u + 9v)/288 \\ R_1 &= -\frac{1}{4} s + (t-v)/24 \\ R_2 &= (9t + 12u + 3v)/288 \end{aligned} \quad (2.17)$$

Eqs. (2.17) relate the observed Fourier coefficients R_0 , R_1 and R_2 to the matrix elements of G . Only when the off-diagonal terms u and v are neglected can we determine the three coefficients p , q and r , or equivalently, A , B and C from the measurement with linear polarization. This was effectively done in the interpretation of the original experiment (3). With this assumption that u and v can be ignored, we derive an explicit inversion for A , B and C in terms of the Fourier coefficients, with the result

$$\begin{aligned} A &= R_0 - \frac{7}{3} R_1 + \frac{89}{9} R_2 \\ B &= R_0 - \frac{1}{3} R_1 - \frac{79}{9} R_2 \\ C &= R_0 + \frac{5}{3} R_1 + \frac{41}{9} R_2 \end{aligned} \quad (2.18)$$

We wish to emphasize that the results of this section up to eq. (2.17) are exact, provided that the distribution of relative velocities of the excited atoms is axially symmetric. In particular we did not adopt any restrictive assumption on the dynamics of the process. The sole approximation occurred when we neglected u and v , in order to derive eq. (2.18).

3. COMPARISON OF EXPERIMENTAL RESULTS

Three different groups have performed rather similar experiments on the polarization effect of associative ionization of two Na(3P) atoms, excited by linearly polarized light tuned to the same hyperfine transition $F=2 \rightarrow F=3$ of the D2-line in a single beam (3,4,8,9). In Table 1 we list the various values of $r_1 = R_1/R_0$ and $r_2 = R_2/R_0$ reported in these references. Furthermore we introduce the parameters

$$\begin{aligned} a &= A/(A+2B+C) \\ b &= B/(A+2B+C) \\ c &= C/(A+2B+C) \end{aligned} \quad (3.1)$$

Then a is the relative contribution to the total ion production from an initial state with both atoms in a state with $|M| = 3/2$ with the beam axis as quantization axis. Likewise $2b$ is the relative contribution from a combination of $|M| = \frac{1}{2}$ and $|M| = 3/2$, and c from the state with $|M| = \frac{1}{2}$ for both atoms. If we adopt the assumption that u and v can be ignored, then (2.18) is valid, and we can calculate a , b and c from the observed values of r_1 and r_2 . The parameters a , b and c (which obey the obvious identity $a+2b+c = 1$) determine the ratio of rate constants for ionization with values of $|M|$ as mentioned above. We list the resulting values also in Table 1.

Table 1. Values of r_1 , r_2 as observed in various experiments and values of a , b , c deduced from these observations

Ref.	r_1	r_2	a	b	c
3	0.27	0.10	0.41	0.01	0.57
4	- 0.01	0.38	1.69	- 0.82	0.96
8	0.18	0	0.15	0.25	0.35
9a	0.225	0.032	0.220	0.179	0.422
9b	0.304	0.066	0.278	0.094	0.533

The data under 9a are measured with a single atomic beam, just as the results from ref. 3, 4 and 8. The mean relative velocity is evaluated to amount to 500 ms^{-1} . The result 9b refers to collisions between two atoms from counter-running beams. The mean velocity in this case is about 1500 ms^{-1} . The results of ref. 9 are displayed in figure 2.

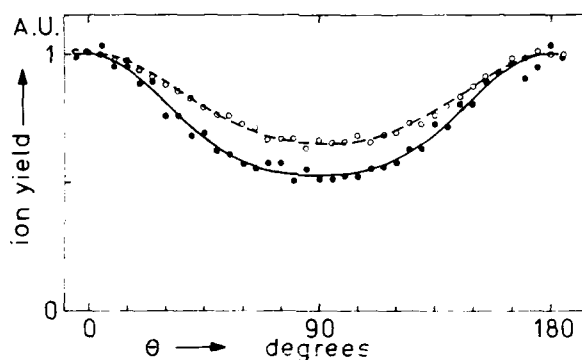


Figure 2. Polarization dependence of the ion production by collisions in a single beam (open circles) and from two counter-running beams (closed circles).

We may conclude that the results for a single beam from ref. 3, 8 and 9 are not in real conflict with each other, although the calculated values of a , b and c display marked differences. The differences in the observed values of r_1 and r_2 may well be explainable in terms of slightly different characteristics¹ of the atomic beams. On the other hand, the measurement of r_1 and r_2 as reported by Rothe et al. (4) is in obvious contradiction with the other observations. The calculated negative value of b in this case is clearly unphysical, since the detection matrix G is positive definite. It is true that this calculated value is based on the assumption of a negligible value of u and v , but some suspicion towards the result of ref. 4 seems warranted.

4. DISCUSSION OF POTENTIAL CURVES

We may gain some insight in the dynamics of the process of associative ionization by discussing the adiabatic potential curves which correlate to $\text{Na}(3P) + \text{Na}(3P)$ at large distances. Model potential calculations for this system have just been reported (10,11). The process of associative ionization can occur by population of the adiabatic states with an electronic energy above the $2p$ ground-state potential of Na_2^+ . Hence potential curves which do not cross this ionic curve cannot contribute to the process. This is the case for curve 1 in

figure 3, where a sketch of the various possibilities is given. On the other hand, when a potential curve crosses the ionic curve at too high an energy, the contribution of this curve to ionization must also be negligible small, at least at thermal or subthermal kinetic energy. Therefore, curve 3 in figure 3 cannot

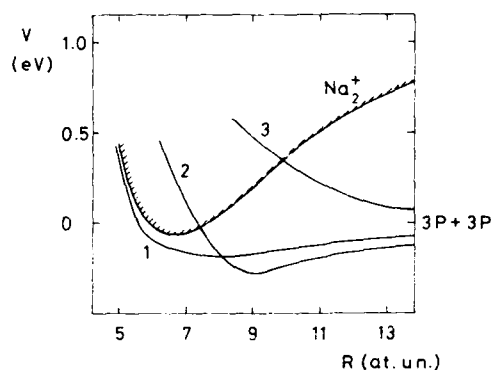


Figure 3. Scheme of potential curves for Na+Na. The ionic curve corresponds to calculations (ref. 11), the curves 1, 2 and 3 are merely illustrative.

appreciably contribute either. Only in the intermediate case of a crossing with the ionic curve not too far from its minimum is associative ionization possible as in curve 2.

In reality, there are twelve potential curves that correlate with the state Na(3P) + Na(3P) at large internuclear distance. In table 2 we give their spectroscopic notation as well as the atomic configurations corresponding to the adiabatic states for large interatomic distance. The gerade-ungerade symmetry of each configuration becomes apparent after proper symmetrization or anti-symmetrization for the orbital wavefunction in the singlet or triplet terms.

Table 2. Adiabatic molecular states originating from Na(3P) + Na(3P), and the atomic configurations for large internuclear distance. The singlet or triplet spin states of the two valence electrons are denoted as χ_s or χ_t . The indicated quantum numbers are the components of the electronic orbital angular momenta in the direction of the internuclear axis.

$\sigma^2 \ 1\Gamma_g^+$	$ 0\ 0\rangle_{\chi_s}$	$\sigma^2 \ 3\Sigma_u^+$	$ 0\ 0\rangle_{\chi_t}$
$\pi^2 \ 1\Sigma_g^+$	$[1\ -1\rangle + -1\ 1\rangle]_{\chi_s}/\sqrt{2}$	$\pi^2 \ 3\Sigma_u^+$	$[1\ -1\rangle + -1\ 1\rangle]_{\chi_t}/\sqrt{2}$
$\pi^2 \ 1\Sigma_u^-$	$[1\ -1\rangle - -1\ 1\rangle]_{\chi_s}/\sqrt{2}$	$\pi^2 \ 3\Sigma_u^-$	$[1\ -1\rangle - -1\ 1\rangle]_{\chi_t}/\sqrt{2}$
$\pi\sigma \ 1\Pi_g$	$[1\ 0\rangle + 0\ 1\rangle]_{\chi_s}/\sqrt{2}$	$\pi\sigma \ 3\Pi_u$	$[1\ 0\rangle + 0\ 1\rangle]_{\chi_t}/\sqrt{2}$
$\pi\sigma \ 1\Pi_u$	$[1\ 0\rangle - 0\ 1\rangle]_{\chi_s}/\sqrt{2}$	$\pi\sigma \ 3\Pi_g$	$[1\ 0\rangle - 0\ 1\rangle]_{\chi_t}/\sqrt{2}$
$\pi^2 \ 1\Delta_g$	$ 1\ 1\rangle_{\chi_s}$	$\pi^2 \ 3\Delta_u$	$ 1\ 1\rangle_{\chi_t}$

Model potential calculations (11,12) suggest that the potential curves which lead to electronic states within the autoionization region are the two $^2\Sigma_g^+$ states, the $^3\Delta_u$ state and possibly a $^1\Sigma_u^+$ state and the two $^3\Pi$ states. Since the final state of the molecular ion is a $^2\Sigma_g^+$ state, it seems reasonable to consider first the states which contain a σ electron, supposing that the one-electron quantum numbers have real significance. This would leave the $\sigma^2 \ 3\Sigma_u^+$ state

as the first candidate to contribute to the ionization process. If we adopt the rather drastic assumption that the collision process is fully adiabatic, then we can evaluate the population for each adiabatic state from the ratios in which the initial density matrix ρ branches into a distribution over the asymptotic configurations indicated in Table 2. For excitation with linearly polarized light with an angle θ between the polarization direction and the beam axis (which is taken as the direction of the internuclear axis before the collision), the density matrix of the excited atoms is

$$\rho_A = \rho_B = n_e \left[\frac{1}{2} T_{00} - \frac{1}{3} \frac{r_2}{q} T_{20} d_{q0}^2(\theta) \right]^+ \quad (4.1)$$

When $|\alpha\rangle$ is the asymptotic configuration of the state $\sigma^2 \ ^3\text{Z}_{\text{U}}^+$, then the population $\langle \alpha | \rho | \alpha \rangle$ as a function of θ is easily evaluated from (4.1), if we also use a Clebsch-Gordan expansion

$$|JM\rangle = \sum_{M_L M_S} \langle LM_L; SM_S | JM \rangle |LM_L; SM_S\rangle \quad (4.2)$$

for $J = 3/2$, $L = 1$, $S = \frac{1}{2}$. A straightforward calculation gives for the population of each one of the three α -substates of the term $\ ^3\text{Z}_{\text{U}}^+$ the value

$$\langle \alpha | \rho | \alpha \rangle = \left(\frac{2}{3} + \cos^2 \theta \right) / 36 \quad (4.3)$$

This population is entirely due to the state with $|M_A| = |M_B| = \frac{1}{2}$. The resulting values of r_1 and r_2 are $84/107 = 0.79$ and $9/107 = 0.08$, and the corresponding values of a , b and c are 0, 0 and 1.

A comparison with the observed values as listed in Table 1 shows that the deviations for r_1 are appreciable, and that the calculated value for r_2 corresponds reasonably well with the range of observations (except those of ref. 4). Although these calculated values for a , b and c do not agree well with the values determined from the observations, the calculated results are certainly not absurd. In particular, the observations indicate that c is the largest of the three, so that the dominant contribution to ionization is due to the initial state with $|M_A| = |M_B| = \frac{1}{2}$. The deviations could indicate that more than one potential curve contributes to ionization. In fact, this conclusion was drawn in a recent paper by Jones and Dahler (6). These authors performed a calculation of the θ -dependence of the contribution of some of the potential curves, assuming complete adiabaticity. They suggested the $\sigma^2 \ ^1\text{Z}_{\text{g}}^+$ state as the most reactive one, since its crossing with the ionic curve was favorable in the calculation of ref. 10. This is no longer true in the more extensive calculation of ref. 11. The θ -dependence for this curve is precisely the same as for the curve $\sigma^2 \ ^3\text{Z}_{\text{U}}^+$, which we suggest as the dominant contributor, on the basis of these new calculations. The conclusion of ref. 6 that at least two adiabatic states contribute to the process seems not to be necessary. The deviation of the observed θ -dependence of the ion signal from the calculated dependence (4.3) may well be due to non-adiabatic coupling, in particular rotational coupling at large distances, where the curve separation is not large enough to cause complete adiabatic reorientation. This coupling could lead to population of the $\sigma^2 \ ^3\text{Z}_{\text{U}}^+$ curve resulting from atom pairs with $|M_A|$ or $|M_B|$ equal to $3/2$ at large separation.

5. CONCLUSIONS

A comparison and evaluation of the observed polarization effects in the reaction (1.1) shows that the results of ref. 3, 8 and 9 are compatible with each other and with a simple interpretation in terms of a single or a few reactive Born-Oppenheimer states, with some non-adiabatic coupling on the incoming trajectory. The observation of (4) seems hard to explain in any model, since it produces a negative cross section for some combination of values of M_A and M_B , at least when the off-diagonal terms of the detection operator G are not excessively large.

The best candidate for the most reactive adiabatic state seems to be $\sigma^2 \ ^3\text{Z}_{\text{U}}^+$.

According to the calculations of ref. 11 this curve crosses the ionic curve $2\sigma_g^+$ at a favorable internuclear distance and energy, and its choice is in line with the observation of dominant values of c , which leads to a major contribution from asymptotic σ -states.

It is remarkable that the same observation at larger relative kinetic energy produced an enhanced polarization effect, with larger values of r_1 and r_2 , as listed in the last line of Table 1. Stronger non-adiabatic coupling would probably lead to a decrease of the polarization effect, since more asymptotic states would contribute to the reactive adiabatic states. This observation could indicate that the reaction probability is only partly due to a polarization-dependent mechanism as discussed above, which has a positive reaction energy, corresponding to the energy at the crossing of the dominant adiabatic curve and the ionic curve. A detailed study of the velocity dependence of the polarization effect and of the reaction rate would be worthwhile. Another extension of the measurements done so far could be the excitation with circularly or elliptically polarized light. This would allow a full determination of the detection operator G , including its off-diagonal terms (5).

REFERENCES

- 1) T.B. Lucatorto and T.J.M. McIlrath, Phys. Rev. Lett. 37 (1976) 428.
- 2) F. Roussel, B. Carré, P. Breger and G. Spiess, J.Phys. B14 (1981) L313.
- 3) J.G. Kircz, R. Morgenstern and G. Nienhuis, Phys. Rev. Lett. 48 (1982) 610.
- 4) E.W. Rothe, R. Theyunni, G.P. Reck and C.C. Tung, Phys. Rev. A31 (1985) 1362.
- 5) G. Nienhuis, Phys. Rev. A26 (1982) 3137.
- 6) D.M. Jones and J.S. Dahler, Phys. Rev. A31 (1985) 210.
- 7) D.M. Brink and G.R. Satchler, Angular momentum (Oxford University Press, 1962).
- 8) E. Meyer, H. Schmidt, R. Witte and I.V. Hertel, Abstracts XIV ICPEAC no. 377 (1985).
- 9) H.A.J. Meijer, H.P. v.d. Meulen, H.G.M. Heideman, G. Nienhuis and R. Morgenstern, Abstracts XIV ICPEAC no. 378 (1985).
- 10) R. Montagnani, P. Riani and O. Salvetti, Theor. Chim. Acta 64 (1984) 431.
- 11) A. Henriët, F. Masnou-Seeuws and C. Le Sech, Abstract XIV ICPEAC no. 372 (1985).
- 12) F. Masnou-Seeuws, private communication.

POLARIZATION EFFECTS IN IONIZING COLLISIONS OF EXCITED NEON ATOMS

T. BREGEL, W. BUßERT,* J. GANZ, H. HOTOP and M.-W. RUF

Fachbereich Physik der Universität Kaiserslautern, 6750 Kaiserslautern
Federal Republic of Germany

Using transverse excitation of a collimated metastable $\text{Ne}(3s\ ^3P_{2,0})$ atom beam with linearly polarized single mode dye lasers we have investigated ionizing thermal energy collisions of polarized $\text{Ne}(3s,3p,4s,4p,4d)$ atoms with Ar atoms. The resulting electrons have been energy analyzed with a high resolution, two-stage hemispherical condenser. The measured electron energy spectra reflect substantial differences between the interaction potentials for $\text{Ne}(3s)+\text{Ar}$, $\text{Ne}(3p)+\text{Ar}$ and $\text{Ne}(4s,4p,4d)+\text{Ar}$; for $\text{Ne}(3p\ ^1D_2)+\text{Ar}$, they reveal structure due to different Ω -components. The spectra exhibit a more or less strong dependence on the asymptotic polarization of the excited atoms (relative to the direction of relative velocity), as induced by the optical pumping process. Model calculations of the electron spectra and their polarization dependence have been carried out for $\text{Ne}(3s\ ^3P_{2,0})+\text{Ar}$ and $\text{Ne}(3p\ ^1D_2)+\text{Ar}$, using computed potentials for $\text{Ne}(3s,3p)+\text{Ar}$ and semiempirical $\text{Ne}+\text{Ar}^+$ potentials. Autoionization of the collision system is found to occur mainly by $\text{Ar}(3p\sigma)+\text{Ne}(2p\sigma)$ transfer along with ejection of the Ne^* valence electron.

1. INTRODUCTION

Tunable lasers, especially stabilized cw single mode dye laser, have been used by several groups to investigate collisions of laser-excited short-lived atoms with atoms and molecules (e.g. 1-3). A point of particular interest (4-18) is the search for polarization effects, i.e. for a dependence of observables on the polarization direction (relative to the collision axis, typically the direction of the relative velocity). Such polarization effects constitute sensitive probes of the dynamic behaviour of the collision system. Some time ago, we have started a program to investigate ionizing collisions of state selected heavy rare gas metastable atoms $X(\text{mp}^5(m+1)s\ ^3P_{2,0})$ ($X=\text{Ne},\text{Ar},\text{Kr}$) and of laser excited, short lived states $X(\text{mp}^5\text{nz})$ by high resolution electron spectrometry and mass spectrometry (4,14,15). It is our aim to gain insight into the ionization mechanism in collisions with states of medium to high excitation and to test potential curves for such multi-state systems. As a first example, we have reported results for $\text{Ne}(3p\ ^1D_2)+\text{Ar}$ (14,15). A substantial polarization effect was observed for $\text{Ne}(3p\ ^1D_2)+\text{Ar}$ and discussed in detail (14,15), whereas first investigations showed only a small, essentially negligible polarization effect for $\text{Ne}(3s\ ^3P_{2,0})+\text{Ar}$ (14,15). The potential curves for these two systems, shown in Fig. 1, are rather different and the Ω -splittings are very small for $\text{Ne}(3s\ ^3P_{2,0})$ (15, 19,20). Therefore, polarization effects for the $\text{Ne}(3s\ ^3P_{2,0})+\text{Ar}$ systems have to be associated with a selectivity of the autoionization probability due to the polarization of the $\text{Ne}(2p^5)$ core. Morgner (21) has shown in an analysis of the anomalous fine structure branching ratios found for $\text{Ne}(3s\ ^3P_{2,0})+\text{Ar}$ (22) that these data reflect the interference between the dominant electronic transition amplitude u_{00} involving $\text{Ar}(3p\sigma)$ to $\text{Ne}(2p\sigma)$ transfer and the non-negligible amplitude $u_{11}=-0.106\ u_{00}$ associated with $\text{Ar}(3p\pi)$ to $\text{Ne}(2p\pi)$ transfer. The more complicated

*Present address: Joint Institute for Laboratory Astrophysics, Boulder, Colo.
80309, USA

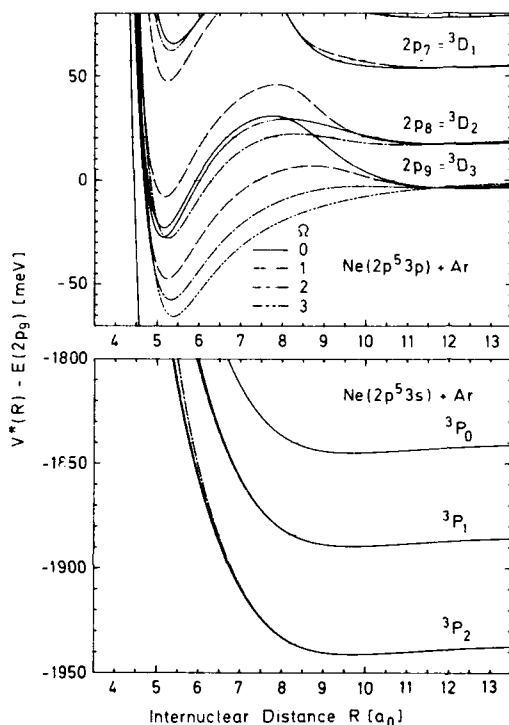


FIGURE 1

Potential energy curves for the excited molecular states $\text{Ne}(3s\ ^3P) + \text{Ar}$ and $\text{Ne}(3p\ ^3D) + \text{Ar}$, calculated by a perturbation method described in reference (14). The given potential energies are in meV and relative to the energy of the molecular $\text{Ne}(3p\ ^3D_3 = 2p_9) + \text{Ar}$ state.

Note the negligible Ω -splittings between the different Ω -components of $\text{Ne}(3s\ ^3P_2) + \text{Ar}$ for $R > 6\ a_0$.

analysis of the $\text{Ne}(3p) + \text{Ar}$ systems (15) has led to similar conclusions for the respective amplitudes; moreover, it was shown how the asymptotic polarization influences the effective population of the different Ω -states for $\text{Ne}(3p\ ^3D_3) + \text{Ar}$ at distances where autoionization occurs.

In the meantime, we have carried out further experiments under improved experimental conditions. For $\text{Ne}(3s\ ^3P_2)$, we have now been able to clearly detect a polarization dependence of the electron spectrum, both in shape and total intensity. Model calculations assuming a space-fixed core polarization along classical trajectories on the potentials of Fig. 1 and Ω -dependent autoionization widths based on the amplitudes u_{00} , u_{11} given above have been carried out and are found to reproduce the experimental findings in a satisfactory way. We compare the results with those for $\text{Ne}(3p\ ^3D_3) + \text{Ar}$, for which we present improved data at three collision energies, and briefly discuss new results obtained for $\text{Ne}(4s\ ^3P_2)$, $\text{Ne}(4p\ ^3D_3)$, $\text{Ne}(4d\ ^3F_4) + \text{Ar}$.

2. EXPERIMENTAL

Fig. 2 shows a semi-schematic drawing of the apparatus (15). A well-collimated, metastable $\text{Ne}(3s\ ^3P_{2,0})$ beam from a differentially-pumped dc discharge source (velocity spread about 30% of peak velocity) is state-selected by anti-collinear excitation and removal of either metastable component via a suitable $\text{Ne}(3p)$ state with a multimode dye laser (bandwidth around 10 GHz, mode spacing 63 MHz, power around 200 mW). Transverse excitation of $\text{Ne}(3s\ ^3P_2)$ atoms with

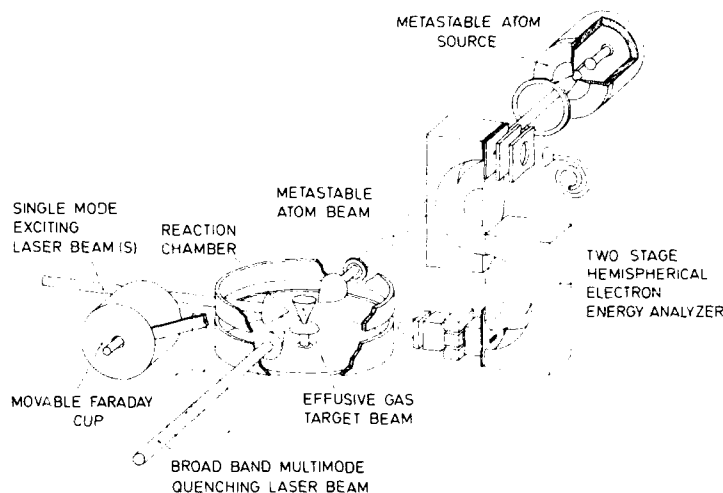


FIGURE 2

Semi-schematic drawing of apparatus

linearly-polarized, frequency-stabilized single mode dye lasers (640.2 nm, 576.6 nm) leads to substantial populations of the $\text{Ne}(3p \text{ } ^1D_2)$ and $\text{Ne}(4d \text{ } ^1F_3)$ states and - via spontaneous emission - of the $\text{Ne}(4p \text{ } ^1D_2)$ and $\text{Ne}(4s \text{ } ^1P_1)$ states in the reaction center, where an effusive target beam crosses the Ne^* beam. The ionization processes of the mentioned states with Ar are separated by energy analysis of the released electrons with a high resolution (10 meV), low back-ground two-stage hemispherical condenser.

In most cases, the direction of the electric vector \vec{E}_L of the transverse lasers was chosen parallel ($\vec{E}_L \parallel \vec{v}$, $\theta=0^\circ$) or perpendicular ($\vec{E}_L \perp \vec{v}$, $\theta=90^\circ$) to the direction of relative velocity. The polarization dependence of the signal is expected (9,14) to have the form $I(\theta) = \sum_{J=1}^{\infty} a_J \cos 2n\theta$, where J is the angular momentum of the excited Ne^* atom. Test measurements of $I(\theta)$ for the total electron intensity showed only small contributions from terms with $n \geq 1$. The $\text{Ne}(3s \text{ } ^1P_1)$ state may be polarized through optical pumping to the $\text{Ne}(3p \text{ } ^3D_2)$ state in a region upstream (≈ 8 mm) from the reaction center. With a sacrifice in signal, the $\text{Ne}(3s \text{ } ^1P_1)$ state can be prepared in a pure $|M_J|=0$ ($\vec{E}_L \parallel \vec{v}$) population by excitation to any of the $\text{Ne}(3p \text{ } J=2)$ states; the $|M_J|=1,2$ levels are removed, whereas the $\text{Ne}(3s \text{ } ^1P_1, M=0)$ level, which cannot be excited by linearly-polarized light for a $J=J'$ transition, even gains population through spontaneous decay from laser excited $\text{Ne}(3p \text{ } J=2, |M_J|=1)$. We have used the transition $\text{Ne}(3s \text{ } ^1P_1) \rightarrow \text{Ne}(3p \text{ } ^1D_2)$ at 633.4 nm, for which the final $\text{Ne}(3s \text{ } ^1P_1, M=0)$ population is calculated (23) to be 28.7% of the total initial $\text{Ne}(3s \text{ } ^1P_1)$ population. In the evaluation of the data, one has to correct for the signal due to the fraction of unpolarized, non-pumped $\text{Ne}(3s \text{ } ^1P_1)$ atoms, which amounts to 9.9% of the initial Ne population.

Table 1 summarizes the values for the alignment M_J (1,23,24) and the asymptotic $|M_J|$ populations $s(\infty)$, which result from the two mentioned optical pumping schemes; for $\vec{E}_L \parallel \vec{v}$, the collision frame and the photon frame coincide, whereas for $\vec{E}_L \perp \vec{v}$, the given values for $s(\infty)$ correspond to the diagonal elements of the $\rho_{JJ'}$ - density matrix after rotation through 90° . The influence of residual magnetic fields ($\sim 10^{-7}$ T) and depolarizing collisions (target density $5 \times 10^{12}/\text{cm}^3$) on

the π -distribution is negligible under our experimental conditions.

Table 1: Alignment M_2 and asymptotic populations $s(i)$... for $\text{Ne}(3s\ ^3P_2)$ and $\text{Ne}(3p\ ^3D_3)$ atoms polarized by laser optical pumping (see text).

Polarized Level	M_2	π_{\parallel}				π_{\perp}			
		$s(0)$	$s(1)$	$s(2)$	$s(3)$	$s(0)$	$s(1)$	$s(2)$	$s(3)$
$\text{Ne}(3s\ ^3P_2)$ via $\text{Ne}(3p\ J=2)$	-1.195	100	0	0	-	25	0	75	-
$\text{Ne}(3s\ ^3P_2)$ via $\text{Ne}(3p\ ^3D_3)$	-0.797	47.6	47.6	4.8	-	13.7	26.0	60.1	-
$\text{Ne}(3p\ ^3D_3)$ from $\text{Ne}(3s\ ^3P_2)$	-0.962	47.6	47.6	4.8	0	8.9	20.8	17.3	53

3. RESULTS AND DISCUSSION

Fig. 3 shows the electron energy spectra due to ionizing collisions of state-selected $\text{Ne}(3s\ ^3P_2)$ atoms with Ar atoms at two Ne velocities ($v_{\text{Ne}}=800$ m/s, 1200 m/s) and for the two polarizations π_{\parallel} and π_{\perp} , created by optical pumping via $\text{Ne}(3p\ ^3D_3)$, see Table 1. The total cross section $Q(\pi_{\parallel})$ (integrated spectral intensity) is found to exceed $Q(\pi_{\perp})$, and one recognizes a shift of the π_{\parallel} spectra towards higher electron energies. The fine structure branching ratio $F=Q(3/2)/Q(1/2)$ is slightly larger for π_{\perp} than for π_{\parallel} and in satisfactory agreement with the earlier unpolarized data of Hotop et al. (22); these authors have already given a qualitative discussion of the shape of the peaks, which signals a very small (0.5 meV) attraction in the entrance channel $V^*(R)$ (19,20) and an essentially monotonic difference potential $V^*(R)-V^+(R)$, increasing with decreasing R . These findings are in full accord with the behaviour of the potentials $V^*(R)$ in Fig. 1 and of the ionic potentials $V^+(R)$ for $\text{Ne}+\text{Ar}^+$ (15). We note that our calculated potentials $V^*(R)$ for $\text{Ne}(3s\ ^3P_2)+\text{Ar}$ (Fig. 1) deviate somewhat from the two potentials, which have been extracted from independent elastic differential scattering data (19,20); our potential is roughly an average between these

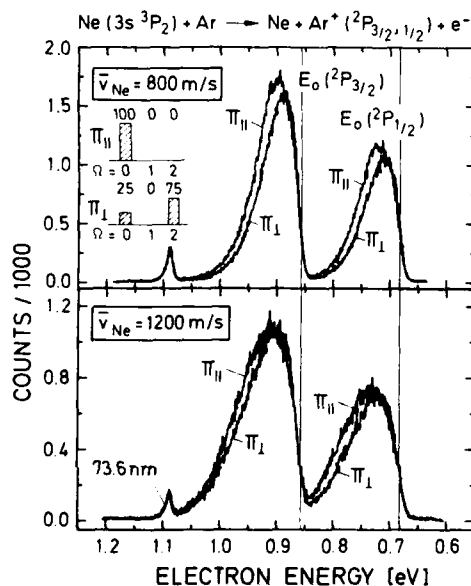


FIGURE 3

Electron energy spectra for ionizing collisions of state-selected, polarized metastable $\text{Ne}(3s\ ^3P_2)$ atoms with Ar atoms, measured with an electron energy resolution of about 10 meV (FWHM of 73.6 nm/ $\text{Ar}^+(^2P_{3/2})$ photoelectron peak; other photoelectron peaks have been subtracted). Polarization was achieved by optical pumping to the $\text{Ne}(3p\ ^3D_3)$ level. The vertical lines denote the nominal electron energies for $\text{Ne}(3s\ ^3P_2) / \text{Ar}^+(^2P_{3/2}, ^2P_{1/2})$ at 0.860 eV and 0.682 eV, respectively.

two potentials. Data for $\text{Ne}(3s^2P_1)+\text{Ar}$ were also obtained by polarization via the $\text{Ne}(3p^3D_3=2p_0)$ state; they show the same trend as in Fig. 3, but a smaller ratio $Q(\pi_{II})/Q(\pi_I)$, as expected for the less perfect asymptotic conditions (see Table 1).

Fig. 4 presents improved data for $\text{Ne}(3p^3D_3)+\text{Ar}$, measured - as the spectra in Fig. 3 - with 10 meV resolution (FWHM). Both fine structure components exhibit sub-structure due to the energy-split π -components of $V^*(R)$ (see Fig. 1). The velocity- and polarization-dependent peak at higher electron energies is due to the potential maximum in the $\Omega=0$ channel (15). The energy locations and widths of the spectra are compatible with the calculated potentials (Fig. 1) together with our semi-empirical ionic potentials $V^+(R)$ (15). The spectral shapes, total areas and fine structure branching ratios are all found to strongly depend on the asymptotic polarization (see Table 2).

A rather detailed analysis has been previously reported for $\text{Ne}(2p_1)+\text{Ar}$. A semiclassical close coupling method was applied to describe the evolution of the polarized collision system in the coupled entrance channels (including $\text{Ne}(2p_1)+\text{Ar}$). It was realized that the experimental polarization effects could not be reproduced with an Ω -independent local autoionization width $\Gamma(R)$, which leads to a calculated ratio $Q(\pi_{II})/Q(\pi_I)$ of 1.01 and $F=2$ independent of polarization. A dependence of the width on the initial and final state was therefore introduced and expressed in terms of a small number of reduced electronic transition matrix elements $u_{m+}m_Cm_V$ (m_+, m_C, m_V are the projection quantum numbers of the

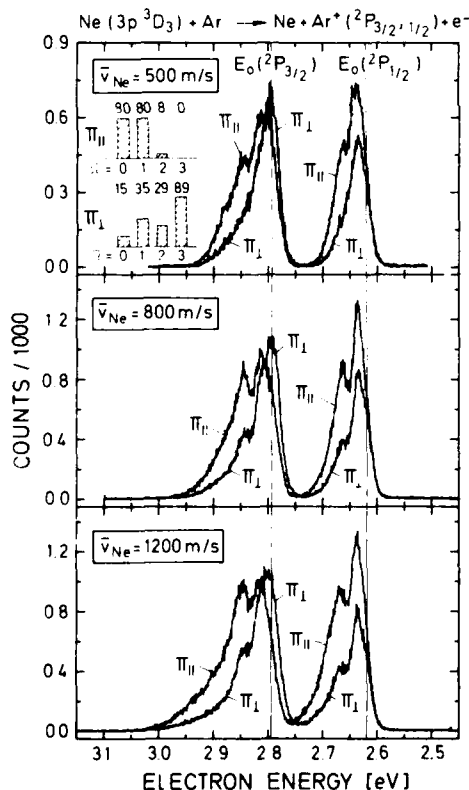


FIGURE 4

Electron energy spectra for ionizing collisions of laser-excited, polarized $\text{Ne}(3p^3D_3=2p_0)$ atoms with Ar atoms, measured with an electron energy resolution of about 10 meV. The vertical lines denote the nominal energies for E_0 $\text{Ne}(3p^3D_3)/\text{Ar}^*(^2P_{3/2,1/2})$ at 2.796 eV and 2.618 eV, respectively. The strongly polarization- and velocity-dependent high energy peaks at electron energies around $E_{el}(3/2) = E_0(3/2) + 52$ meV and $E_{el}(1/2) = E_0(1/2) + 44$ meV are due to the $\Omega=0$ entrance channel, see Fig. 1 and also the discussion in reference (15).

Table 2: Polarization dependence of total cross sections Q and fine structure branching ratios F for $\text{Ne}(3s^2\text{P}_2)+\text{Ar}$ and $\text{Ne}(3p^2\text{D}_2)+\text{Ar}$.

System	\bar{v}_{Ne} m/s	$Q(\pi_{\parallel})/Q(\pi_{\perp})$	$F(\pi_{\parallel})$	$F(\pi_{\perp})$
$\text{Ne}(3s^2\text{P}_2)+\text{Ar}$	800	1.26(6) ^a	1.56(6)	1.63(6)
polarized via $\text{Ne}(3p^2\text{D}_2)$	1,200	1.14(7) ^a	-	-
$\text{Ne}(3p^2\text{D}_2)+\text{Ar}$	500	1.41(5)	1.26(6)	1.68(7)
pumped from $\text{Ne}(3s^2\text{P}_2)$	800	1.42(4)	1.23(5)	1.69(6)
$\text{Ne}(3s^2\text{P}_2)$	1,200	1.48(4)	1.20(5)	1.73(12)

^aCorrected for contributions from unpolarized $21,22\text{Ne}(3s^2\text{P}_2)+\text{Ar}$ collisions to the experimental spectra (Fig. 3).

orbital angular momenta of the Ar^+ -ion, of the Ne^+ -core, and of the Ne^+ valence electron with respect to the internuclear axis). By comparison of measured and calculated values for Q and F for the eight $\text{Ne}(3p\text{J}=1,2,3)+\text{Ar}$ systems (14,15) the important $u_{m_1 m_2 m_3}$ were determined as (15): $u_{111}=1.76(+10\%)$; $u_{110}=1.26(+5\%)$; $u_{101}=-0.25(+12\%)$; $u_{100}=-0.33(+40\%)$, i.e. $\text{Ar}(3p)$ to $\text{Ne}(2p)$ transfer, accompanied by some $\text{Ar}(3d)$ to $\text{Ne}(2p)$ transfer, dominates the autoionization process.

For $\text{Ne}(3s^2\text{P}_2)+\text{Ar}$, we have taken the following approach in an attempt to rationalize the observed polarization effect: in view of the small energy splittings between the different π -components of $V^{\text{eff}}(R)$ (Fig. 1), we assume that the core polarization can be considered as space-fixed throughout the collision along classical trajectories, as illustrated in Fig. 5. Our model calculations of the total and partial cross sections consist of adding incoherently the sum of all autoionization contributions for all impact parameters along the respective curved trajectories with local R -dependent widths $\tau_{\parallel}(R)=w_{\parallel}\tau(R)$, which contain constant weights w_{\parallel} (as fixed by $u_{111}/u_{110}=-0.106$) and a reasonable choice for a common R -dependence. At each R for any trajectory the diagonal and non-diagonal elements of the system's density matrix lose flux by autoionization according to their appropriate coupling width, as will be described in detail elsewhere (25). The density matrix is propagated along the trajectory from the starting asymptotic density matrix by repeated infinitesimal rotations according to the rotation of the internuclear axis (body fixed frame) with respect to the space-fixed frame. So far, calculations have been carried out with the choice $\tau(R)=A \exp(-B(R-R_0))$ ($A=4$ meV, $B=1.5 a_0^{-1}$, $R_0=6 a_0$), which yields reasonable agreement of the computed cross sections with the experimental energy dependence of the total ionization cross section (19,27-29) and of the electron energy spectra (Fig. 3). The calculated $Q(\pi_{\parallel})/Q(\pi_{\perp})$ show a broad maximum in the range $E_{\text{rel}}=30-70$ meV with values around 1.27 and decrease at higher and lower energies (range 5-200 meV). Calculations of the electron spectra for π_{\parallel} - and π_{\perp} -conditions qualitatively reproduce the changes seen in Fig. 3. A more detailed description of the model and results will be given elsewhere (25).

We conclude our report with a brief discussion of the results (30) for the electron spectra of $\text{Ne}(4s\text{J}=2)+\text{Ar}$, $\text{Ne}(4p\text{J}=3)+\text{Ar}$, and $\text{Ne}(4d\text{J}=4)+\text{Ar}$. Since these systems are Rydberg states attached to the Ne^+-Ar ionic potentials, one expects well depths of comparable size, especially for non-penetrating Rydberg orbitals such as $\text{Ne}(4d)$. In agreement with recent results for Ne^+-Ar (31), the well depth for $\text{Ne}(4d)+\text{Ar}$ is found to be close to 160 meV as concluded from the location of the low-energy-edge of the spectra; those for $\text{Ne}(4s,4p)+\text{Ar}$ are about 30 meV smaller. These findings are in good qualitative agreement with the behaviour of the $\text{Ne}(4s,4d)+\text{Ar}$ potentials, calculated by Dürren et al. (32). Only the $\text{Ne}(4p)+\text{Ar}$ spectrum shows a significant polarization effect, again favouring π_{\parallel} -preparation

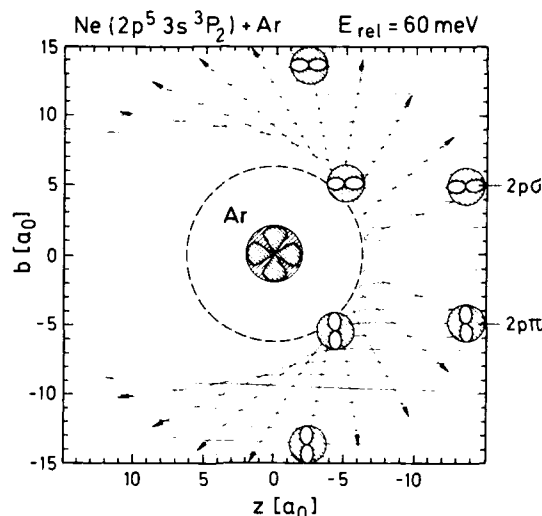


FIGURE 5

Illustration of the classical model used to explain the polarization dependence observed in ionizing $\text{Ne}(3s\ ^3P_2) + \text{Ar}$ collisions. The asymptotic atomic polarization, prepared by laser-optical pumping, is considered as space-fixed along the classical trajectories in view of the small Δ -splittings for this system.

and compatible with expectations on the basis of the $\text{Na}(4p) + \text{Ar}$ interactions (32).

From a comparison of the relative polarization-averaged electron intensities with the relative time-integrated excited state densities (30), one can determine the relative cross sections Q for the three systems. From data measured with the experimental setup shown in Fig. 2 and the electron detector positioned at 60° (relative to the Ne^* -beam), we have found with uncertainties of 10-20% (30) $Q(4d):Q(4p):Q(4s) = 0.14:0.86:1$, i.e. an unexpectedly small ionization cross section for $\text{Ne}(4d\ J=4) + \text{Ar}$.

In order to rule out electron angular distribution effects as a major source for the observed anomalous cross section ratio, we have repeated the experiment in a different apparatus; a cylindrical mirror analyzer with its axis perpendicular to the neon and laser beams samples all electrons ejected into a narrow cone, which encloses the "magic" angle (54.7°) with the symmetry axis. The target gas beam was directed along this axis. As before, the $\text{Ne}(4s,4d) + \text{Ar}$ spectra showed no significant polarization dependence, and the relative polarization-averaged cross sections came out as $Q(4d):Q(4p):Q(4s) = 0.16(2):0.87(4):1$ in good agreement with the earlier data (30).

In view of this result and the similarity of the electron spectral shapes and potentials $V^*(R)$ for these three systems, it is most likely that the comparatively small ionization cross section for $\text{Ne}(4d\ J=4) + \text{Ar}$ reflects a low autoionization width (we note that collisional mixing with the nearby $\text{Ne}(4f) + \text{Ar}$ states may also play a role (33)). Whether our results for $\text{Ne}(4s,4p,4d) + \text{Ar}$ indicate a general behaviour for Penning ionization of ground state atoms X in collisions with $A(n\ell)$ Rydberg states (which are not electric dipole-coupled to the ground state A) remains to be seen.

ACKNOWLEDGEMENTS

This work has been supported by the Deutsche Forschungsgemeinschaft (Sonderforschungsbereich 91). We thank K. Harth, M. Raab and A. Siegel for their valuable collaboration and acknowledge M. Müller for the careful construction and test of the cylindrical mirror analyzer.

REFERENCES

- 1) I.V. Hertel and W. Stoll, *Adv. At. Mol. Phys.* 13 (1978) 113
- 2) A. Kopystynska and L. Moi, *Phys. Rep.* 92 (1982) 135
- 3) J.L. Picqué, G. Spiess and F.J. Wuilleumier (Eds.) "Atomic and Molecular Collisions in a Laser Field", *J. de Physique* 46 (1985) Colloque C1
- 4) H. Hotop, in "Electronic and Atomic Collisions", N. Oda and K. Takayanagi (Eds.), p. 271f (North Holland Publ. Co., Amsterdam, 1980)
- 5) L. Hüwel, J. Maier and H. Pauly, *J. Chem. Phys.* 76 (1982) 4961
- 6) J.M. Mestdag, J. Berlande, P. de Pujo, J. Cuvelier and A. Binet, *Z. Phys.* A 304 (1982) 3
- 7) W. Reiland, G. Jamieson, U. Tittes and I.V. Hertel, *Z. Phys.* A 307 (1982) 51
- 8) C.T. Rettner and R.N. Zare, *J. Chem. Phys.* 77 (1982) 2416
- 9) J.G. Kircz, R. Murgestern and G. Nienhuis, *Phys. Rev. Lett.* 48 (1982) 610; G. Nienhuis, *Phys. Rev. A* 26 (1982) 3137
- 10) H. Schmidt, A. Bähring, E. Meyer, B. Miller, *Phys. Rev. Lett.* 48 (1982) 1008
- 11) R. Düren, E. Hasselbrink and H. Tischer, *Phys. Rev. Lett.* 50 (1983) 1983; R. Düren, *Comm. At. Mol. Phys.* 14 (1984) 127
- 12) M.O. Hale, I.V. Hertel and S.R. Leone, *Phys. Rev. Lett.* 53 (1984) 2296
- 13) Ch. Bender, W. Beyer, H. Haberland, D. Hausmann and H.P. Ludescher, *J. de Physique* 46 (1985) C1-75
- 14) W. Bußert, T. Bregel, J. Ganz, K. Harth, A. Siegel, M.-W. Ruf, H. Hotop and H. Morgner, *J. de Physique* 46 (1985) C1-199
- 15) W. Bußert, T. Bregel, R.J. Allan, M.-W. Ruf and H. Hotop, *Z. Phys.* A 320 (1985) 105
- 16) A. Bähring, E. Meyer, I.V. Hertel and H. Schmidt, *Z. Phys.* A 320 (1985) 141
- 17) I.V. Hertel, H. Schmidt, A. Bähring and E. Meyer, *Rep. Progr. Phys.* 48 (1985) 375
- 18) J.P.C. Kroon, H.C.W. Beijerinck, B.J. Verhaar and N.F. Verster, *Chem. Phys.* 90 (1984) 195; Manders et al., Abstracts 2nd ECAMP, p. 279, Amsterdam, 1985
- 19) R.W. Gregor and P.E. Siska, *J. Chem. Phys.* 74 (1981) 1078
- 20) W. Beyer, H. Haberland and D. Hausmann, Book of Abstracts, 9th Symposium on Mol. Beams, p. 229, Freiburg, 1983; D. Hausmann, Dissertation, Univ. Freiburg, 1985
- 21) H. Morgner, *J. Phys.* B 18 (1985) 251
- 22) H. Hotop, J. Lorenzen and A. Zastrow, *J. Electron. Spectrosc. Relat. Phenom.* 23 (1981) 347
- 23) W. Bußert, Dissertation, Univ. Kaiserslautern, 1985; *Z. Phys.* (to be publ.)
- 24) A. Fischer and I.V. Hertel, *Z. Phys.* A 304 (1982) 103
- 25) T. Bregel, W. Bußert, M.-W. Ruf and H. Hotop (to be publ.)
- 26) S.Y. Tang, A.B. Marcus and E.E. Muschlitz, Jr., *J. Chem. Phys.* 56 (1972) 566
- 27) R.H. Neynaber and G.D. Magnuson, *Phys. Rev. A* 11 (1975) 865
- 28) A. Aguilar-Navarro, B. Brunetti, S. Rosi, F. Vecchiocattivi and G.G. Volpi, *J. Chem. Phys.* 82 (1985) 773
- 29) M.J. Verheijen, PhD Thesis, Technische Hogeschool, Eindhoven, 1984
- 30) T. Bregel, W. Bußert, J. Ganz, K. Harth, M. Raab, M.-W. Ruf and H. Hotop 14th ICPEAC, Abstract No. 164, Palo Alto, Calif. USA, July 1985
- 31) D. Hausmann and H. Morgner, *Mol. Phys.* 54 (1985) 1085
- 32) R. Düren, E. Hasselbrink and G. Moritz, *Z. Phys.* A 307 (1982) 1
- 33) T.F. Gallagher, S.A. Edelstein and R.M. Hill, *Phys. Rev. Lett.* 35 (1975) 644

ENERGY TRANSFER PROCESSES OF ALIGNED EXCITED STATES OF Ca ATOMS

Dieter NEUSCHÄFER, Michael O. HALE,* Ingolf V. HERTEL,† and
 Stephen R. LEONE§

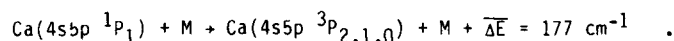
Joint Institute for Laboratory Astrophysics, National Bureau of Standards
 and University of Colorado, and Departments of Physics and Chemistry,
 University of Colorado, Boulder, Colorado 80309

Effects of orbital alignment on the near resonant energy transfer process from $\text{Ca}(4s5p\ ^1P_1)$ to $\text{Ca}(4s5p\ ^3P_J)$ induced by collisions with rare gases are studied in a crossed molecular beam. A linearly polarized, pulsed ultraviolet laser is used to introduce the initial orbital alignment, and the relative energy transfer cross sections as a function of alignment are monitored by time-gated fluorescence detection. Different results are observed with several rare gases; a rather large, ~50% enhancement in the rate is observed for the perpendicular vs. parallel approach with He and Ne. A smaller, but opposite effect is observed for Xe, and no effect of alignment occurs with Kr.

1. INTRODUCTION

Studies of the effects of alignment on inelastic collision phenomena are just beginning. In spite of the fact that there are very few direct measurements of the influence of atomic or molecular alignment on energy transfer probabilities, a number of recent experiments show promising new details concerning the effects of alignment and orientation on both reactivity and energy transfer (1-10). Such experiments have the capability to elucidate important geometry-dependent aspects of potential energy surfaces and the curve crossing mechanisms that occur during collisions.

In the experiments to be described here, a simple energy transfer system is considered between near resonant states of electronically excited calcium atoms induced by collisions with rare gas atoms. The particular process of interest is the near resonant spin-change:



Since the wave functions of the two electronically excited states in this case are mixed, the spin change is not rigorously forbidden. A facile transfer occurs even with weak perturbers such as rare gas atoms and has the appearance more like a fine structure-changing process.

This energy transfer system provides an almost ideal case for both experimental and theoretical studies of the effects of orbital alignment on a near

*Present address, Department of Chemistry, Mass. Inst. of Technology, Cambridge, MA 02139.

†Present address, Institut für Molekülphysik, Freie Universität Berlin, D1000 Berlin 3, West Germany.

§Staff Member, Quantum Physics Division, National Bureau of Standards.

resonant energy transfer process that involves a curve-crossing mechanism. Several experimental advantages can be noted. Because of the absence of nuclear spin hyperfine interactions, the $\text{Ca } ^1\text{P}_1$ state can be completely aligned via direct excitation from a linearly polarized, pulsed ultraviolet laser at 272 nm. These are the first experiments on alignment effects which employ pulsed laser excitation; the high signal-to-noise is encouraging for the future success of other studies requiring pulsed lasers to achieve wavelengths not available with cw lasers. The short 60 ns lifetime of the $^1\text{P}_1$ state minimizes the loss of the initial alignment by interaction with the Earth's magnetic field to about 5-10%. Fluorescence transitions from both the $^1\text{P}_1$ and $^3\text{P}_J$ states are readily monitored simultaneously in the visible region of the spectrum with time-gated detection to obtain the relative transition probabilities as a function of orbital alignment.

In consideration of the theoretical aspects of this problem, the $\text{Ca}^* + \text{rare gas}$ systems are relatively easy ones to obtain potential energy surfaces. It should be possible in the two-atom system to incorporate all the important aspects of angular momentum coupling from initial to final states and to calculate the dynamics of the energy transfer process.

2. EXPERIMENTAL

The experimental apparatus (Fig. 1) consists of crossed beams between Ca atoms and the rare gas, a pulsed, frequency-doubled, Nd:YAG-pumped dye laser, a polarization rotator (Pockels cell or Fresnel rhomb), photomultiplier tubes, and time-gated photon counting equipment (1). The Ca beam is an effusive beam from an oven at 850 K. The beam is skimmed by an orifice placed 0.75 cm away from the Ca nozzle to produce a ~0.3 mm diam. beam at a distance of 1.5 cm from the nozzle. The rare gas beam is a continuous, supersonic expansion from a 100 μm orifice which is placed 7 mm below the Ca beam. The rare gas beam is

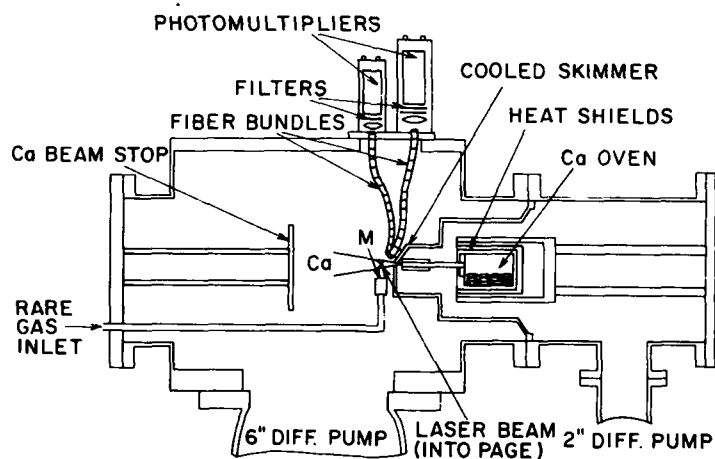


FIGURE 1

Schematic of the crossed beam apparatus for studies of energy transfer with aligned Ca^* .

established with a backing pressure of 1 atm behind the orifice. The fluxes of both atom beams and the required relative velocity vectors are calculated from the properties of the expansions and have been discussed in detail before (1). Under typical conditions, only one excited atom in 10^4 suffers a collision that results in transfer of the $1P_1$ state to the $3P_J$ states.

The pulsed dye laser is frequency doubled and tuned to the transition to excite the second $1P_1$ state at 272 nm (Fig. 2). The polarization is rotated manually with a Fresnel-rhomb retarder or electrically with a voltage on a UV transparent Pockels cell. The resultant polarization is checked for the degree of linearity with polarization analyzer sheets and is $\geq 90\%$. The Ca $1P_1$ state is excited with a 5 ns pulse, and fluorescent emissions from both the initially-excited $1P_1$ state at 672 nm and from the resulting collisional energy transfer state ($3P_J$) at 616 nm are collected with two fiber bundles and collimated onto separate photomultipliers. A typical gate time for the fluorescence detection is an open time of 200 ns beginning 100 ns after the laser pulse. High quality baffle arms reduce the scattered laser light reaching the photomultipliers to less than one count per laser pulse (laser power $\sim 600 \mu\text{J}$ per pulse).

The signal from the $1P_1$ state is large and is used to normalize for the amount of the initial excitation. The $3P_J$ signal is 10^4 times weaker and is

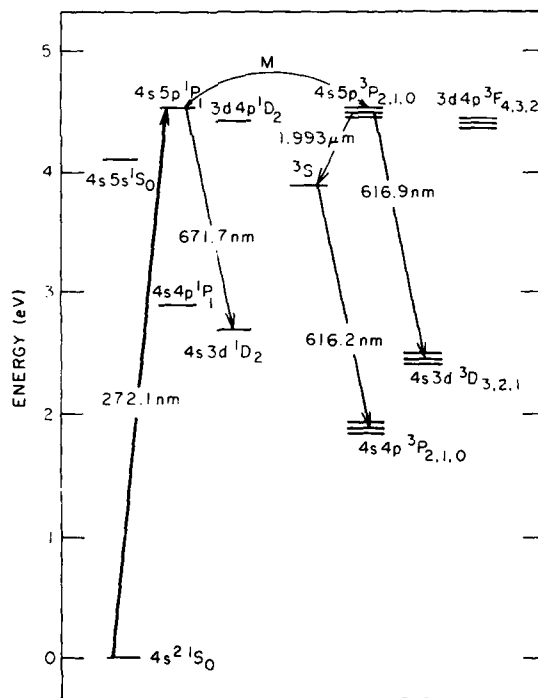


FIGURE 2

Energy level diagram of the relevant states for the collision-induced transfer between $\text{Ca}(4s5p 1P_1)$ and $\text{Ca}(4s5p 3P_J)$.

detected with time-gated photon counting equipment. Two filters which have a high rejection at 672 nm are required to prevent the much stronger $1P_1$ emission signal from reaching the photomultiplier. The counts from the $3P_J$ emission are integrated for 5000-8000 laser pulses at each angle of polarization. Both signals are monitored as a function of the angle of rotation of the polarization to obtain the relative cross sections as a function of orbital alignment. In addition, full time resolved signals are acquired with a fast transient digitizer/signal averager in order to verify the lifetimes of the emitting states (11).

3. RESULTS AND DISCUSSION

Figure 3 shows the relative probability for energy transfer from the $1P_1$ state to the $3P_J$ states as a function of the angle of polarization in the center-of-mass frame for four different collision partners, He, Ne, Kr and Xe. With Ar no fluorescence intensity from $3P_J$ could be detected because of the small cross section. It can be seen that for He and Ne the effect is large and the maximum comes at approximately a 90° angle with respect to the maximum effect for Xe. By the transformation from the laboratory to the center-of-mass frame, it is found that the maximum energy transfer cross section for He occurs when the Ca^* p-orbital is aligned essentially perpendicular to the relative velocity of approach (1). This establishes for the $Ca^* + He$ and Ne systems that the molecular π -state is the preferred geometry to bring about

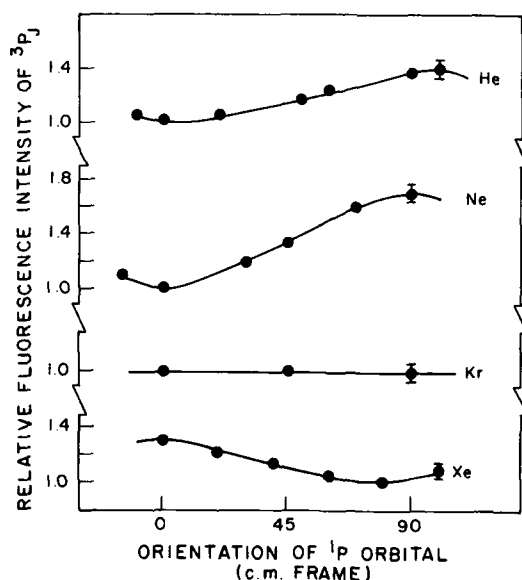


FIGURE 3

Data for the energy transfer probability from $1P_1$ to $3P_J$ with He, Ne, Kr, and Xe as a function of p-orbital alignment angle.

the curve crossing from the $1P_1$ to the $3P_J$ states. Although the effect is smaller for Xe, there is a clear preference for the molecular Σ -state. For Kr, no preferential alignment effect is observed.

The results for each of the different rare gases are summarized in Table I, along with the total cross section obtained in static cell experiments for the transfer from $1P_1$ to $3P_J$ (11).

Table I. Results of alignment experiments for energy transfer between $\text{Ca}(4s5p\ 1P_1)$ and $\text{Ca}(4s5p\ 3P_J)$ induced by collisions with rare gases.

Rare Gas	Total (\AA^2)	$I_{\text{max}}/I_{\text{min}}$	Angle of I_{max}	State
He	25	1.4 ± 0.2	$100 \pm 10^\circ$	π
Ne	5	1.7 ± 0.2	$90 \pm 10^\circ$	π
Ar	3	no signal	--	--
Kr	13	1.0 ± 0.1	constant	--
Xe	31	1.25 ± 0.2	$-5 \pm 10^\circ$	Σ

The qualitative trend in the total cross sections has been considered previously (11). It is explained by a competition between the effect of velocity on the Landau Zener curve-crossing probability and the effect of the rare gas polarizability on the potential energy surfaces. The heavier rare gas atoms have significantly greater attraction and typically are expected to involve curve crossings at longer range and with greater interaction strength. The lighter rare gases, especially He, are weaker perturbers, but the curve crossing probability can be enhanced by rapid passage through the crossing region.

The effects of alignment can be explained by consideration of a schematic set of potential energy curves for the quasimolecular states. Figure 4 shows two extremes, $\text{Ca}^* + \text{He}$ and $\text{Ca}^* + \text{Xe}$. The shallow potential well for interaction of the Ca p-orbital with He in the π molecular state leads to a substantial enhancement of the transfer cross section for the perpendicular alignment compared to the more repulsive Σ molecular state (parallel alignment). The laser preselects the collision system on either the π molecular state or the Σ molecular state via the initial polarization. Provided that the initial alignment is at least partially retained in the transition from the laboratory-fixed frame to the molecular-fixed frame (termed the locking radius), then the colliding system will follow through with some preferential character of one potential surface over the other. Hale et al. (1) have given a more rigorous discussion of these considerations of the locking radius and the maximum alignment effect that can be observed when averaged over all impact parameters.

The greater the retention of the initial alignment, the greater can be the effect due to the orbital alignment in the energy transfer. As shown in Fig. 4, the energy splitting between the π and Σ molecular states as a function of internuclear separation can become large well before the curve crossing region. The orbital then locks into the molecular frame early in the collision and can retain the memory of the initial alignment throughout the curve crossing region. A significant point to explain the observed behavior is that for He and Ne the curve crossing for the more repulsive Σ state occurs only at higher energies. Thus, the π -state because of its greater attraction leads to an efficient crossing between the $1P_1$ and $3P_J$ states at a longer distance than does the more repulsive Σ -state.

In contrast, the stronger attraction between Ca^* and Xe or Kr could cause the effect of the orbital alignment on the energy transfer to be both smaller and of opposite character to the results for He and Ne. One possible pictorial

view is offered in Fig. 4. The higher polarizability of Xe and Kr increases the well depths as well as the slope of the repulsive part of the potential curves, especially for the $\text{Ca}(^3\text{P}) + \text{rare gas complex}$. Thus a curve crossing between the two Σ states may be accessible for energies used in this experiment, leading to a contribution to the $^3\text{P}_J$ fluorescence via the Σ state.

An alternative possibility for the change from π to Σ on going from He to Xe has to do with the validity of the long-range locking model. For Xe and Kr, the curve crossing of the π state occurs at larger internuclear distances than with He and Ne. Therefore the ratio of the locking radius to the curve crossing radius may decrease. Thus the original alignment of the ^1P orbital defined by the laser can already be changed from π to Σ at the internuclear separation where the orbital is locked, i.e., the long-range π and Σ states are no longer good quantization frames in the collision system.

In order to test the hypothesis that the efficient transfer for He and Ne is from the π state out of $^1\text{P}_1$ to the Σ state in $^3\text{P}_J$, experiments are in progress to run the reaction in reverse. A clear prediction is that the transfer in the reverse process should be more efficient for initial excitation of the Σ state.

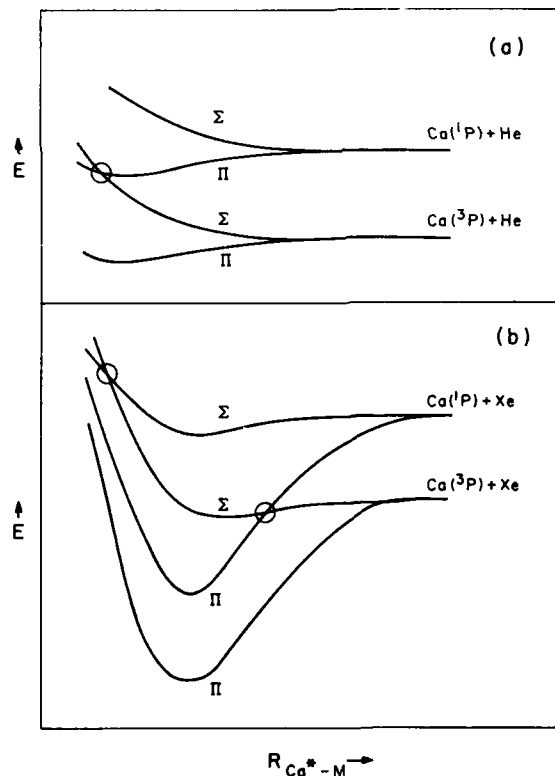


FIGURE 4

Hypothetical schematic of potential energy curves for Ca^*-He and Ca^*-Xe showing possible curve crossings.

4. CONCLUSION

Collisional energy transfer events between electronically excited states can show significant effects due to orbital alignment in the collision. These experiments are the first alignment-dependent studies carried out with pulsed laser excitation. The results can be interpreted in terms of simple curve crossing pictures and await more detailed dynamical calculations, which should be possible with accurate potential energy surfaces.

This work was supported by the Air Force Office of Scientific Research and the National Science Foundation.

REFERENCES

- 1) M. O. Hale, I. V. Hertel, and S. R. Leone, *Phys. Rev. Lett.* 53 (1984) 2296.
- 2) R. N. Zare, *Ber. Bunsenges. Phys. Chem.* 86 (1982) 422.
- 3) S. Stolte, *Ber. Bunsenges. Phys. Chem.* 86 (1982) 413.
- 4) C. T. Rettner and R. N. Zare, *J. Chem. Phys.* 75 (1981) 3630 and 77 (1982) 2417.
- 5) L. Huwel, J. Maier, R. K. B. Helbing, and H. Pauly, *Chem. Phys. Lett.* 74 (1980) 459.
- 6) J. G. Kircz, R. Morgenstern, and G. Nienhuis, *Phys. Rev. Lett.* 48 (1982) 610.
- 7) J. M. Mestdagh, J. Berlande, P. dePujo, J. Cuvellier, and A. Binet, *Z. Phys. A* 304 (1982) 3.
- 8) A. Bahrng, I. V. Hertel, E. Meyer, W. Meyer, N. Spies, and H. Schmidt, *J. Phys. B* 17 (1984) 2859.
- 9) I. V. Hertel, H. Schmidt, A. Bahrng, and E. Meyer, *Rep. Prog. Phys.* 48 (1985) 375.
- 10) R. J. Allan, A. Bahrng, J. Hanssen, R. Witte, and H. Schmidt, *Chem. Phys. Lett.* 117 (1985) 622.
- 11) M. O. Hale and S. R. Leone, *J. Chem. Phys.* 79 (1983) 3352.

ALKALINE

By M. J. Coggiola

Tune: My Darling Clementine

In a magnet, in a light trap, pumping on the hyperfine,
Dwelt a laser, standing-waver, and some atoms Alkaline.

Gettin colder, gettin colder, gettin colder Alkaline,
Till you can't skip less you spin flip, you're sub-Doppler, Alkaline.

H-new up, and h-new down then, so you're rambling will decline,
With no mode hop, you can all stop, and the record will be mine.

Gettin colder, gettin colder, gettin colder Alkaline,
Till you can't skip less you spin flip, you're sub-Doppler, Alkaline.

There's a substate got the wrong fate, with a moment can't align
Thermal spreading I was dreading, so I lost my Alkaline.

Gettin colder, gettin colder, gettin colder Alkaline,
Till you can't skip less you spin flip, you're sub-Doppler, Alkaline.

TRAPPING AND COOLING NEUTRAL ATOMS

David E. PRITCHARD

Department of Physics and Research Laboratory of Electronics,
Massachusetts Institute of Technology
Cambridge, Massachusetts 02139

This paper reviews a number of ideas for trapping neutral atoms, cooling them, and performing interesting experiments on them. Neutral atoms may be confined in traps consisting of static electric and magnetic fields if they are in quantum states whose energy increases with field strength. Traps with oscillating fields may trap atoms in any state. Radiative cooling schemes can cool particles to milli-Kelvin temperatures using the Doppler shift, and several proposed cooling schemes may ultimately attain micro-Kelvin temperatures. Trapped atoms will undergo collisions at ultra-low temperatures where pure s-wave scattering, resonances, and dipole-dipole depolarization may be studied. Atom traps afford opportunities for high resolution spectroscopy. Not only may such spectroscopy provide useful frequency standards but it may also permit study of quantum collective effects such as superradiance and Bose condensation.

1. INTRODUCTION

In the past decade electromagnetic traps for ions have been used to perform a tremendous number of seminal experiments in atomic and molecular physics and chemistry. It is now possible to trap a single elementary particle and measure its resonance frequencies to precisions of 10^{-11} (VSD84), to cool trapped ions using lasers to temperatures in the milli-Kelvin range (WTD84), to prepare multiply charged ions as a target in the study of atomic collisions (CHU84), and to monitor the temporal behavior of ionic reactants and reagents in multi-step chemical reactions.

Recent experiments (MPP85, CHB85) have demonstrated that it is now possible to trap and cool neutral atoms; we can now confidently predict that experiments with trapped neutral atoms (and possibly molecules) will become increasingly commonplace and will grow in sophistication and power. In this paper we shall review the physics of traps and speculate about some of the most interesting things to do with trapped neutral atoms, including dramatic cooling, collision studies, precision spectroscopy, and observation of collective effects.

2. TRAPPING

Colloquially the term trap means to "prevent from leaving", but as physicists we require a trap to have a definite force of confinement. We restrict our attention to neutral particle traps using only E-M fields generated by charges or currents external to the trapping volume. (Teflon walls, buffer gasses, superfluid He films, etc. are excluded.) Thus the ideal trap for neutral particles would have a static potential with a minimum at the center of the trap; we shall discuss these "static traps" first. Next we shall discuss "dynamic traps", which rely on time-varying trapping forces and/or the motion of the particles to prevent escape.

2.1. Static traps

The energies of interaction of an atom with electric and magnetic fields are well known:

$$U = -\frac{1}{2}\alpha E^2 \quad (\alpha \text{ is the polarizability})$$

$$\text{and } U = -\vec{\mu} \cdot \vec{B} = -g\mu_B m$$

where g is of order unity, m is the projection of the angular momentum along the B-field, and μ_B is the Bohr magnetron.

Two fundamental theorems interact to prevent us from trapping the lowest state of any system:

- a) the lowest energy level of any system is depressed by all perturbations - thus U of the lowest state will decrease with increasing E or B , consequently atoms in this state will feel a force toward higher E or B , and
- b) a static E or B field cannot possess a local maximum in free space (WIN84).

This is a serious restriction for an electric field trap, since in general only excited electronic states of opposite parity to the ground state will have $\alpha < 0$, permitting them to be trapped, but these states can decay radiatively. Nevertheless, several proposals have been advanced involving Rydberg atoms (WIN80, MET80) and the $j = 1, m_j = 0$ state of polar molecules offers a longer lived possibility (PRI83).

Being able to trap only particles which are drawn to weak fields is not so serious a limitation for magnetic traps since the spin up states of paramagnetic atoms (which have $U \propto |B| > 0$) have spontaneous decay rates to the ground magnetic sublevel of 10^{-10} s^{-1} . Traps one Kelvin deep for atoms with electron spin $s = 1/2$ are technically straightforward using superconducting technology.

The first static magnetic field trap for neutral atoms has recently been demonstrated. This is the simple spherical quadrupole trap of Migdall, Phillips, et. al. (MPP85), which consists of a pair of Helmholtz coils connected backwards so that zero field is produced at the center as shown in Fig. 1.

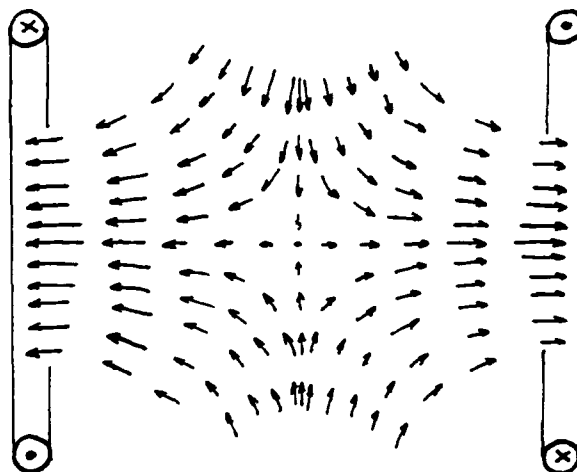


Figure 1

Cross sectional view of cylindrical quadrupole magnetic trap. Two loops with opposite currents produce a magnetic field which is zero in the center and increases linearly with radius in all directions. Roughly 10^5 atoms were confined in this trap for one second. A scheme for continuous filling of the trap and a cryo-vacuum of 10^{-12} torr should increase both numbers by 10^4 , producing an optically dense cloud of Na.

Our group at M.I.T. is working on a magnetic trap (PRI83) which has a uniform magnetic field at the center. This is a desirable property when using lasers to study or manipulate the trapped atoms because the magnetic field, and hence the quantization axis, does not reverse direction in the middle of the trap.

2.2. Dynamic traps

Even though a static field cannot possess a local maximum in free space, one must not conclude that it is impossible to trap atoms which are strong field seekers. It is well known that a charged particle cannot be trapped by static E-M fields because $\nabla \cdot \mathbf{E} = 0$ in charge-free space and hence the static force, $\mathbf{F} = q\mathbf{E}$, cannot be directed inwards over the entire surface of a sphere surrounding the center of the putative trap (Earnshaw's theorem). Nevertheless, two classes of dynamic traps for charged particles are widely used: the Penning trap in which the motion of the particle (in conjunction with $q\mathbf{v} \times \mathbf{B}$ forces) prevents its escape, and the RF trap (POF58) in which a rapid temporal variation of the sign of the electric fields leads to dynamic stability for the trapped particle. A third class of dynamic trap involves fields which oscillate rapidly enough that they must be regarded as radiation - we will call these "optical traps". We now present examples of all three types of dynamic traps which have been proposed for strong field seeking neutral particles.

A trap for non-stationary strong field seekers may be made by a current carrying loop like that shown in Fig. 2. Near the wire the magnetic field decreases inversely as the distance from the wire, so that particles in an orbit outside the loop will be attracted not only inwards towards the wire but also towards the plane of the loop. If the particles' angular momentum, L_z , and distance from the wire loop are appropriately chosen, then the centrifugal force (which decreases inversely as the cube of the distance from the center of the loop since L_z is conserved) will cancel the magnetic force, leading to a stable orbit. In practice it is helpful to space out several coils along z in order to optimize the field (KOP86).

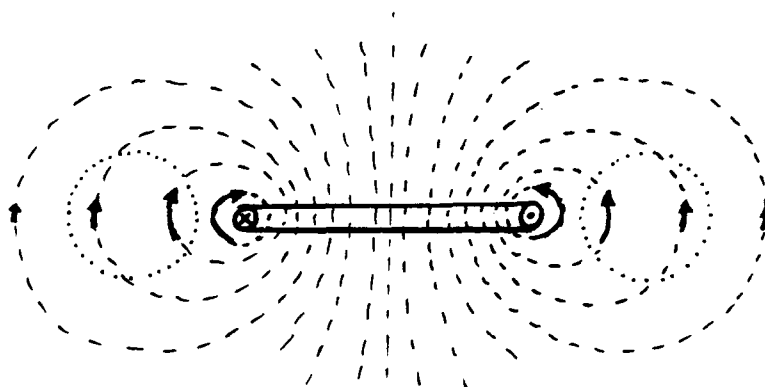


Figure 2

A single magnetic loop can trap strong field seeking atoms in stable circular orbits which pass through the regions indicated by dashed lines.

Recently an analog of the RF trap has been proposed for neutral hydrogen atoms (LMT85) which consists of a loop whose axis is parallel to a uniform magnetic field. Alternating current in the loop produces an alternating magnetic bottle which can confine either weak or strong field seekers.

The simplest optical trap relies on the fact that radiation can be focussed: the field has a local maximum at the center of this focus, so strong field seekers will be drawn to this center. (This does not violate the exclusionary theorem on local field maxima mentioned above since the optical fields are not static.) Unfortunately, optical frequency photons possess considerable momentum on an atomic scale (a Na atom recoils at 3 cm/sec from emission or absorption of a single D-line photon) and the resulting spontaneous forces can lead to sufficient heating of the trapped atoms to evaporate them from the trap. This interplay of trapping and heating has led to a wealth of theoretical literature on optical traps (PPM85). We now move on to discuss the converse of optical heating - optical cooling.

3. COOLING

The weakness of the neutral atom traps just described prevents trapping atoms with kinetic energies greater than 1 Kelvin or so; yet in the context of trapped atom physics these atoms are incredibly hot - nearly all of the interesting scientific applications of trapped atoms require atoms orders of magnitude cooler. Milli-Kelvin temperatures have already been obtained with trapped ions (WTD85), with untrapped atoms (CHB85), and in supersonic expansions of He. The likely prospects for obtaining much lower temperatures is one of the fascinations of trapped atom research.

The simplest cooling scheme involves the Doppler shift (HAS74): if the atoms are bathed in isotropic monochromatic radiation whose frequency is just below a resonance line, then photons whose momentum opposes the atomic velocity will be shifted closer to resonance and consequently preferentially absorbed, resulting in deceleration. Under proper conditions the velocity can be damped exponentially in ~ 10 μ s; hence this form of cooling is often referred to as "optical molasses". Recently S. Chu and coworkers have demonstrated this experimentally (CHB85), achieving cooling to $\sim 1/4$ mK. This is close to the limit expected theoretically (WII79, JAV80) due to the loss of preferential directionality of the absorbed photons when the velocity is too slow to produce a Doppler shift comparable to the natural width of the transition.

To get substantially below the milliKelvin limit imposed on Doppler cooling by the natural linewidth of strong resonance transitions, one can utilize transitions to long lived excited levels like the 5d level in Cs. Caution must be employed, however, to assure that the spontaneous decay processes back to the ground level do not change the magnetic sublevel (i.e. change trapped weak field seekers to untrapped strong field seekers).

An alternative way to circumvent linewidth limitations for Doppler processes is to utilize two photon stimulated Raman processes between sub-levels of the ground level. The Doppler shift for the two photon process is $(\mathbf{k}_2 - \mathbf{k}_1) \cdot \mathbf{v}$ which can easily be larger than the single photon shift. These have an essentially infinite lifetime so that there is virtually no limit imposed by the natural linewidth. However, the necessity to optically pump the atoms back to the original sublevel after the Raman cooling cycle necessarily involves spontaneous decay, whose photons will heat the atoms. One photon gives the atom a recoil energy of $(\hbar k)^2 / 2M$ - approximately 1 μ K for Na.

Still another way of cooling to microKelvin temperatures has been proposed (PRI83) in which RF transitions between sublevels of the ground level are made in a way which rapidly reduces the average potential energy of the trapped particles. As with stimulated Raman cooling, the cooling limit results from the spontaneous decay when the atom is optically pumped back to the original sub-level.

It should not be concluded that the photon recoil energy imposes an insurmountable limit to optically based cooling cycles - indeed it is possible to cool below this limit by velocity space optical pumping. The key idea is to set up conditions so that the atom may possibly have zero velocity after the terminal spontaneous decay and then to use some mechanism (either Doppler selective stimulated Raman or RF transitions will work) which will selectively cause atoms whose velocity is greater than some preselected fixed limit to be subject to another optical pumping cycle with another terminal spontaneous decay. Atoms whose velocities lie outside this limit will be recycled until their velocity lies inside it.

Two methods exist for cooling trapped particles further: evaporation (LMT85) and adiabatic cooling by slow (or cleverly rapid) weakening of the trap. These have the advantage that they are collective cooling effects and work well at high particle densities, in contrast to the optical methods described above which are basically single-particle and may therefore have degraded performance at high particle densities.

4. COLLISIONS

As soon as experimentalists solve the practical problems of trapping a sufficient number of atoms, a multitude of low energy collision processes will be opened to study. In addition to elastic atom-atom scattering, there will be spin depolarization processes (bad news for magnetic traps which confine only the spin up species), line broadening processes (anathema to resonance studies and Doppler cooling schemes), and three body recombination processes. In the following discussion of these collision processes, we shall compute cross sections for typical collisions involving Na and H.

4.1 Total ground state scattering cross sections

Since atoms interact at long range with the electrostatic potential CR^{-6} , the cross sections increase at lower velocity (SCH56).

$$Q(v) = 5.11 (C/vh)^{2/5} \lambda^2 \\ = 2\pi \left[\frac{5}{\pi} \sin \frac{\pi}{5} \Gamma(7/5) \right]^{-1} \left[\frac{3C}{8hv} \right]^{-2/5}$$

The values of C are (MAK69) $C_{H-H} = 6.2$ $C_{H-Na} = 70$ $C_{Na-Na} = 1512$ (all $\times 10^{-60}$ erg cm⁻⁶), and the corresponding cross sections are of the form (where T is the temperature in Kelvin)

$$Q(T) = Q_{X-Y} T^{-0.2}$$

with $Q_{H-H} = 120$ $Q_{H-Na} = 359$, and $Q_{Na-Na} = 2005$.

These expressions are invalid at sufficiently low temperatures because the semi-classical approximation (many partial waves contribute to the scattering) fails when the deBroglie wavelength becomes comparable to the range of the potential.

For very low temperatures only s-wave scattering contributes to the cross section

$$Q_s(T) = 4\pi a^2 \sin^2 \delta_s,$$

where δ_s is the s-wave phase shift (and μ is the reduced mass in nuclear mass units). In general, the phase shift will go as $\delta_s \sim ka$ at small enough energy ($k = [2\mu E]^{1/2}/\hbar$ with μ the reduced mass) a is the scattering length, which is related to the size of the potential. Then the cross section will asymptote to $Q = 4\pi a^2$. a is known to be 0.72 Å for H-H in the triplet state (KVS81), but the Na-H and Na₂ triplet potentials are not known well enough to find the scattering length. This raises the possibility that there may be a resonance ($\delta_s = \pi/2$) with associated cross section

$$Q_R(T) = 4\pi a^2 = 203 \text{ Å}^2 / \mu T, \quad (\mu \text{ in a.m.u.})$$

The total scattering cross sections above, multiplied by the relative velocity of the atoms, gives the scattering rate constant. Multiplied by the density, this determines the rate of the momentum transfer ring collisions - i.e. the rate of convergence toward thermal equilibrium. This is clearly an important rate, since it limits the cooling rate when collective cooling schemes such as evaporation are employed, or when single particle cooling schemes are leveraged to obtain lower ultimate temperatures by applying them to the hot tail of the distribution.

For reference, we give a typical numerical example. If $\sim 10^{10}$ Na atoms are confined to 1 cm³ at 10⁻⁴ K, the sample will be optically dense (transmission $\sim 10^{-4}$ at line center) and the velocity will be ~ 1 m/s. The ground state scattering cross section will be $\sim 10^{-12}$ cm², leading to a collision rate of ~ 1 per second.

4.2 Spin exchange depolarization

Unfortunately for atom trappers, some binary collisions are detrimental to the magnetic trapping of paramagnetic atoms. The most obvious such process is electron spin exchange. At first this might not seem to be a possible collision process between two spin up weak field seekers, and indeed this is the case if both atoms happen to have their nuclear spins up as well. However, weak field seeking atoms with $m_F < I+J$ will have a small component of electron spin down, and this can exchange with the electron spin up component of the wave function on another atom, leaving that atom in a spin down state which will be repelled from the trap. The reverse process for strong field seekers has been discussed (KVS81) and observations in spin polarized H (BHK86) agree with the predicted cross sections. Thus spin exchange should lead to a self-purification of the nuclear spin in weak-field seeker atoms: this poses no problem to experiments in which the atoms are optically pumped into a state with $m_F = F$ before being trapped, except that it represents a possible loss mechanism when making resonance transitions of these atoms.

4.3 Dipole-dipole depolarization

The most pernicious problem for trapped atoms is depolarization by the dipole-dipole interaction between electron spins. In this process two spin parallel atoms collide and one or both are flipped, the requisite angular momentum coming from the orbital angular momentum. This process has been observed in room temperature optical pumping experiments with cross sections $\sim 10^{-16} \text{cm}^2$ (for Cs-Cs collisions, BPC80) given by KVS81 (the atoms are left in a d-wave after the collision),

$$Q_{i,f}^d = \frac{8\pi}{5} \left(\frac{\mu_B^2}{\hbar^2} \right)^2 (k_f/k_i) \\ = 7\mu^2 (k_f/k_i) \times 10^{-20} \text{cm}^2$$

where the μ^2 comes from the density of final states in first order perturbation theory.

This expression overestimates the cross section when applied to trapped Na for two important reasons: the repulsive core of the Na-Na potential reduces the probability that the atoms are close together (where the dipole-dipole interaction is greatest), and the additional energy of $2\mu_B B$ per spin flipped reduces the overlap integral between initial and final states. We estimate from KVS81 that the latter effect reduces the cross sections for Na-Na in a 0.75 T field to approximately

$$Q_{\text{Na-Na}}^d \sim 5 \times 10^{-18} \text{cm}^2 (T^{-1/2}).$$

This gives a constant depolarization rate constant of $\sim 1.5 \times 10^{-14} \text{cm}^3 \text{s}^{-1}$, constant at all temperatures.

Spin depolarization and subsequent loss of the spin flipped atoms due to the dipole-dipole interaction may well present the most serious loss mechanism for magnetically trapped atoms, and a careful theoretical calculation for Na-Na would be very welcome (and should soon be testable experimentally). The fact that the cross section depends strongly on magnetic field adds interest to such a calculation: it may be possible to reduce the loss rate by judicious selection of the magnetic field!

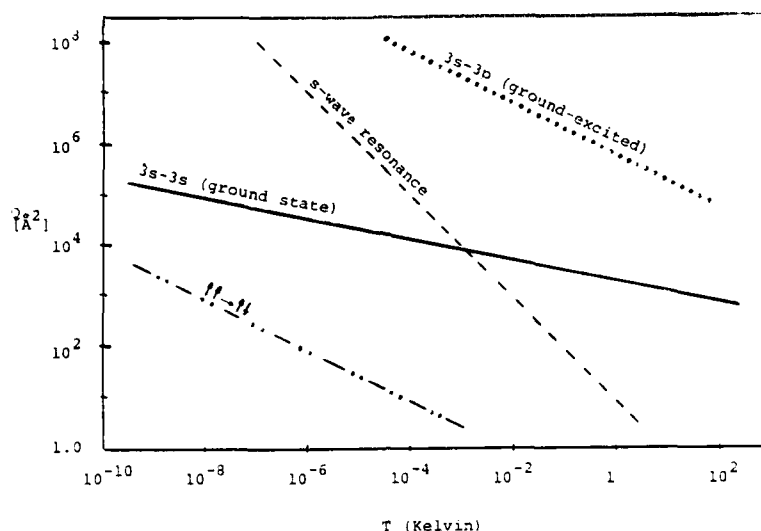


Figure 3

Cross sections for various collision processes involving trapped Na atoms. The ground state, s-wave resonance, and spin depolarization $\leftrightarrow\leftrightarrow\leftrightarrow$ cross sections are plotted. The large 3S-3P cross section results from the resonant $+C_3/R^3$ interaction between the excited state and ground state atoms of the same species.

4.4 Three-body recombination

At sufficient densities, three body collisions which lead to formation of bound dimers will cause loss of atoms both because of the energetic products and (worse) because of subsequent heating of other trapped atoms due to energy transfer from the hot internal excitation of any dimer which remains in the trap. One of the great attractions of hydrogen is that the triplet potential does not have a bound state - consequently three body recombination will happen in pure H only in three body collisions in which a spin depolarization occurs as well. This reduces the three body rate constant to $10^{-37} \text{ cm}^6 \text{ s}^{-1}$ (KVS81), a value confirmed experimentally (BHK86). For Na it is difficult to estimate the rate constant except by crude extrapolation of heated cell work (eg. SCG76) - fortunately simple models predict a weak temperature dependence, lending some confidence to our guess of $10^{-31 \pm 1} \text{ cm}^6 \text{ s}^{-1}$.

5. PRECISION SPECTROSCOPY AND FREQUENCY STANDARDS

One of the main motivations for neutral traps is the prospect of extremely precise spectroscopy. The cooling schemes mentioned previously are capable of reducing the second order Doppler shift to 10^{-20} or less, holding out the promise of unprecedented spectroscopic accuracy. Since neutral particles perturb each other far less than charged ones, neutral particle traps can maintain high spectroscopic precision at particle densities many orders of magnitude higher than the corresponding limit in ion traps (BPI85), suggesting that frequency standards of good short term precision may be possible.

There is, however, one obvious barrier for precise spectroscopy of trapped neutral atoms: the trap! This barrier arises because the energy of interaction of the trapped atoms with the (inhomogeneous) fields which constitute the trap generally depends on the internal quantum state of the atom, leading to inhomogeneous broadening (this is not the case for trapped ions).

Inhomogeneous broadening can be greatly reduced by selecting a field-independent transition such as the one between $F=0, m_F=0$ and $F=1, m_F=0$ at $B=0$ in Na. A more suitable choice is between " F "=2 $m_F=2$ and " F "=2 $m_F=1$ (the quotation marks indicate that F is a label only and not a good quantum number at finite magnetic fields) which for sodium has a fractional frequency shift of only

$$\frac{1}{\nu} \frac{M^2 \nu}{MB^2} = 3 \times 10^{-2} T^{-2}$$

at the magnetic field value where the first derivative vanishes. If the trap is adjusted so that its field minimum has this value, will not be affected by the thermal motion of the particles in first order. Particles with $T = 10^{-6}$ K will "ride up" the magnetic trap walls by an amount $\Delta B = kT/\mu_B = 1.4 \times 10^{-6}$ T (both states have equal magnetic moment, μ_B at this field). This will lead to a fractional shift of less than 10^{-13} , permitting high resolution spectroscopy ($\Delta\nu < 10^{-4}$ Hz). In fact, it is reasonable to contemplate the use of trapped atoms for a frequency standard since the temperature can be accurately measured by the broadenings or shifts of other (field-dependent) transitions, or may be reduced well below 10^{-6} K by various methods discussed previously.

6. COLLECTIVE EFFECTS

Perhaps the most interesting, and certainly the most speculative, possibility for trapped atom research, is to achieve conditions in which quantum collective effects may be observed and studied. Low temperature is a principle ally in this quest because the reduced deBroglie wavelength is

$$\lambda_d = h/p = \frac{h}{\sqrt{3mkT}} = 4\text{\AA}(\mu\text{T})^{-1/2}.$$

Thus Na at 10^{-6} K has $\lambda_d \sim 10^{-5}$ cm, the reduced wavelength of its resonance light. Cooling below this limit causes the quantum coherence length to exceed the light wavelength, raising the possibility of observing light scattering from collective excitations of the gas. Certainly one will reach a new regime in superradiance because Doppler broadening will be eliminated (the atoms move only $\sim 1\%$ of a wavelength in one spontaneous decay time).

A most interesting possibility is Bose condensation. This may occur when the particle density exceeds λ_d^{-3} - i.e. when the average interparticle spacing is less than one deBroglie wavelength. This is manifest as the condensation of a significant fraction of the particles into the lowest quantum momentum state, the 0, 0, 0 vibrational level of the trap. Bose condensation causes anomalies in the specific heat and other thermodynamic properties of the gas. More dramatically, it is manifest as a narrow spike in an otherwise inhomogeneously broadened resonance curve. It is not only the exact nature of the condensate which is of fundamental interest, but also the mechanism of its spontaneous growth in a sample cooled below the transition temperature.

These speculations, as well as our current attempts to do some of these things experimentally, are supported by ONR. I am also grateful for help with the figures from V. Bagnato.

REFERENCES

- BHK86 D.A. Bell, H.F. Hess, G.P. Kochanski et. al.,
submitted to Phys. Rev. B.
- BPC80 N.D. Bhaskar, J. Pietras, J. Camparo, and W. Happer,
Phys. Rev. Lett. **44**, 930 (1980).
- BPI85 J.J. Bollinger, J.D. Prestage, W.M. Itano, and D.J.
Wineland, Phys. Rev. Lett. **54**, 1000 (1985).
- BRM81 T. Breeden and H. Metcalf, Phys. Rev. Lett. **47**, 1726
(1981).
- CHB85 S. Chu, L. Hollberg, J.E. Bjorkholm, A. Cable, and
A. Ashkin, Phys. Rev. Lett. **55**, 48 (1985).
- CHU84 D. Church in Atomic Physics 9, eds. R.S. VanDyck and E.N.
Fortson (World Scientific, Singapore, 1984), pp. 137-153.
- HAS74 T.W. Hansch, A.H. Schawlow, Optics Comm. **13**, 68 (1974).
- JAV80 J. Javanainen, App. Phys. **23**, 175 (1980).
- KOP86 G. Kochanski and D.E. Pritchard, in preparation.
- KVS81 Yu. Kagan, I.A. Vartanyants and G.V. Shlyapnikov, Zh.
Eksp. & Teor. Fiz. (USSR) **81**, 1113 (1981).
- LMT85 R.V.E. Lovelace, C. Mehanian, J.J. Tommila, and D.M.
Lee, to be published Nature 1985.
- MAK69 H. Margenan and M.R. Kastner,
Theory of Intermolecular Forces,
Pergamon Press, New York, 1969.
- MET80 H.J. Metcalf, Phys. Rev. Lett.
- MPP85 L. Migdall, J.V. Prodan, W.D. Phillips, T.H. Bergman,
and H.J. Metcalf, Phys. Rev. Lett. **54**, 2596 (1985).
- POF58 W. Paul, O. Osberghaus, and E. Fischer, Forschungsher.
Wirtsch. Verkehrsministerium Nordrhein-Westfalen
No. 415 (1958).

- PPM85 W.D. Phillips, J.V. Prodan and H.J. Metcalf, *JOSA B*,
Nov. 1985.
- PRI83 D.E. Pritchard, *Phys. Rev. Lett.* 51, 1336 (1983).
- SCG76 R. Scheps and A. Gallagher, *J. Chem. Phys.* 65, 859
(1976).
- SCH56 L.I. Schiff, *Phys. Rev.* 103, 448 (1956).
- WII79 D.J. Wineland and W.M. Itano, *Phys. Rev. A* 20, 1521
(1979).
- WIN80 W.H. Wing, *Phys. Rev. Lett.* 45, 631 (1980).
- WIN84 W.H. Wing, *Progress in Quantum Electronics*, 8, 181
(1984).
- WTD85 For example, this has been accomplished by Wineland
et. al. at N.B.S., by Toschek et. al. at Heidelberg,
and by Nagourney et.al. at Seattle.
- VSD84 R.S. VanDyck, P.B. Schwinberg, and H.G. Dehmelt in
Atomic Physics 9, eds. R.S. VanDyck and E.N. Fortson
(World Scientific, Singapore, 1984), pp. 53-74.

THE ELECTRONIC AND MOLECULAR STRUCTURE OF FREE LIQUID SURFACES.
ELECTRON SPECTROSCOPY UNDER He(2³S) VERSUS HeI-PHOTON IMPACT

Wolfgang KELLER, Harald MORGNER, and Werner A. MÜLLER

Fakultät für Physik der Universität, Hermann Herder-Str. 3, D-7800 Freiburg

1. INTRODUCTION

Quite generally the information available on the detailed structure of liquids is much less abundant than our knowledge on isolated atoms and molecules on one side and on the crystallized state on the other side. This statement holds for both, the experimental and the theoretical approach to acquire information on liquids. The reason for this situation lies in the very complex nature of this state of matter which lends itself much less to a description by an idealized model. The concept of the molecular structure of liquids usually reduces to the pair correlation functions which can be evaluated from X-ray, neutron or electron diffraction data (1). For liquid formamide which will be the main subject of this paper this type of data has been taken by several authors (2,3). More detailed information on the relative orientation of pairs of formamide molecules within the liquid has been sought by means of *ab initio* calculations, but final conclusions are difficult to obtain (3).

The situation seems somewhat more favourable if one surveys the literature that deals with the electronic structure of liquids. Electromagnetic radiation provides the means to probe the electronic properties. Again with respect to formamide, several experiments have been performed: reflectivity from the visible to the VUV range and the yield of emitted electrons per absorbed photon (4,5). These measurements resulted in the determination of the complex dielectric function and the mean free path of electrons. Electron spectroscopy was applied with X-rays (6) and with photons of the HeI resonance line (7). It is interesting to note that studying the electronic properties of formamide resulted in one case in a strong suggestion with respect to the molecular structure. Siegbahn et al. (8) concluded from their data that the formamide molecules are arranged in chains within the liquid.

The studies reported above refer to the bulk properties of liquid formamide. To our knowledge no attempt has been made to clarify specifically the surface structure of liquids. In this paper we report a novel method to investigate surface properties in direct comparison to the bulk properties of a liquid. We use electron spectroscopy under impact of thermal metastable He* atoms versus HeI photons. We find remarkable differences between both modes of ionization. For (non-metallic) liquids they must be attributed to the well known fact that He* atoms can release their energy only to the topmost layer of the surface whereas photons penetrate several layers deep. Thus, He* atoms probe the electronic structure of the very surface whereas HeI photons make bulk properties visible. So far we have applied the method to formamide, N-methyl-formamide, dodekane, benzylalcohol, and mercury.

2. EXPERIMENTAL

To a molecular beam machine which was used so far to study the reaction of metastable He* atoms and HeI photons with atoms and molecules by electron spectroscopy we have added a liquid target. It is realized by a vertical liquid beam similar to the one described in (1).

It is an important feature of our measurements that He* atoms and HeI photons are produced in the very same He-discharge. The effect of the thermal He* atoms on the liquid target and that of the HeI photons is separated by means of a chopper wheel

and a time of flight method. Thus, we are able to distinguish both projectiles while performing the measurements under otherwise exactly the same conditions. Consequently, we can compare the data from UPS (ultraviolet photoelectron spectroscopy) and from MIES (metastable impact electron spectroscopy) down to details.

3. RESULTS

For liquid formamide we find in UPS that HeI photons populate all observed bands fairly evenly (fig.2). On the other hand He* metastables react predominantly with the π -orbitals rather than with the σ -orbitals of formamide (fig. 3). Considering the reaction mechanism of He* atoms we must conclude that the π -orbital of those molecules which form the outermost layer must protrude out of the surface whereas the σ -orbitals do not. This in turn requires the molecules to lie flat on the overall surface since the lobes of the π -orbital are oriented perpendicular to the molecular plane. Thus, metastable impact electron spectroscopy (MIES) contains information on molecular orientation. In combination with the known chainlike arrangement of formamide molecules in the liquid (8) we may conclude that the surfaces of liquid formamide is composed of chains of molecules which lie flat on the surface.

So far we have evaluated the relative band intensities of the MIES spectrum. However, there is more information contained in the data. Firstly, if we compare the widths of the two π -bands as obtained in MIES and in UPS we find that the former values are smaller. If we identify the MIES data with surface properties and the UPS result with bulk properties then we must state that the surface bandwidths amount to ca. 80% of the bulk bandwidths. This ratio is in good agreement with the results of a simple bandwidth calculation based on the tight binding model. It ascertains our assumption that UPS indeed probes bulk rather than surface properties. A further hint to this end consists in the fact that our UPS spectrum (fig.2) has almost zero intensity near 9.5 eV electron energy. This is in distinct contrast to the UPS spectrum from (7) which is shown in fig.1. According to (7) this is intensity due to electrons which have lost energy during their travel from within the bulk to the surface.

The authors evaluate their spectrum and conclude that only a small fraction of bulk electrons reaches the surface without loss of energy. This in turn would mean that the electrons within the band near 10 eV electron energy should originate from the surface and should not represent bulk properties. However, our own UPS spectrum (fig.2) which shows few electrons outside the bands (i.e. near 9.5 eV) indicates that the number electrons which experience energy loss in the liquid cannot be as high as assumed in (7). The lack of intensity near 9.8 eV cannot be an experimental artefact since the MIES spectrum - measured simultaneously - exhibits a peak at this energy (fig.3). We conclude that our UPS spectrum is composed dominantly of electrons released in the bulk.

In the light of the preceding discussion the last piece of information which we find in our spectra is noteworthy. It is known that going from gas to liquid phase the ionization energy is lowered. This is simply due to the electronic relaxation energy of the molecules which surround the formed ion in the liquid. It is obvious that the relaxation energy should be smaller at the surface than in the bulk. Still, we observe the same value $E_{\text{relax}} \approx 1.0 \pm 0.1$ eV for both spectra MIES and UPS. This means that the emitted electron leaves the ionized molecule in a surface position in both modes of ionization. In consequence we have to approach the question how an ion created within the bulk by HeI-photons can reach the surface during the short time the emitted electron is able to interact with the liquid. It is obvious that no true motion is possible. However, an ion at the surface can be produced by the motion of the electronic hole state rather than of the complete ion. Thus, one might speculate whether an electron hole pair created by a HeI photon carries out a correlated motion in liquid formamide. In case that this correlated motion of electron and hole is aimed at the surface then the hole will remain in a surface position while the electron reaches the vacuum (and the electron spectrometer).

Fig. 1

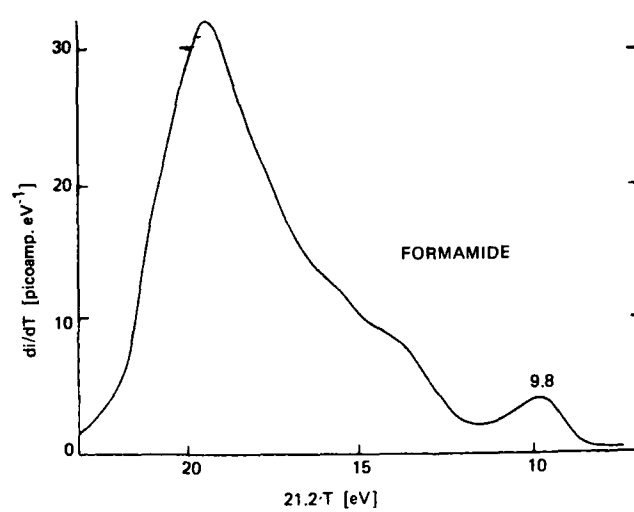


Fig. 2

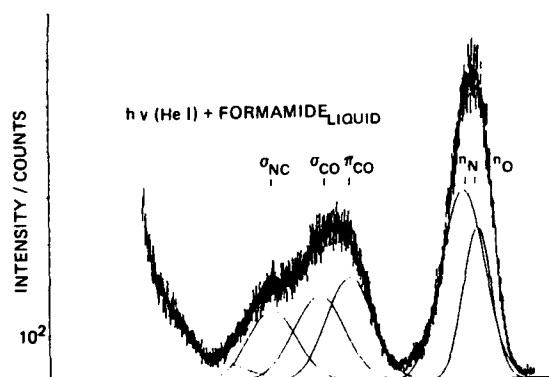
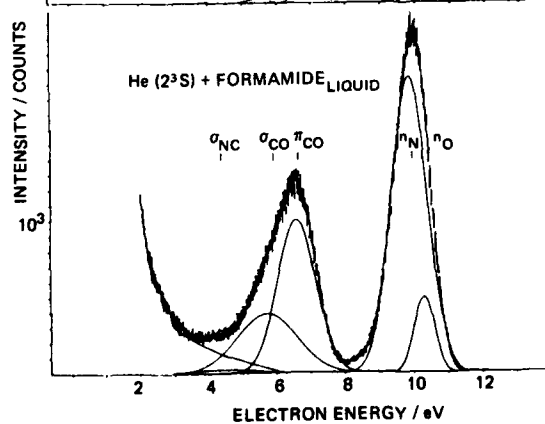


Fig. 3



In conclusion we state that taking electron energy spectra from MIES and UPS under otherwise identical conditions allows to derive interesting information on liquid surfaces. For formamide we have found clear evidence that the surface molecules lie flat on the surface. Further, the data lead us to interesting questions with respect to the motion of electrons within the liquid and the possible existence of exciton-like electron-hole motion.

REFERENCES

- 1) R.A. Egelstaff, *Adv.Chem.Phys.* **LIII** (1983)1, eds. I. Prigogine and S.A. Rice
- 2) E. Kálmán, I. Serke, G. Pálinkás, M.D. Zeidler, F.J. Wasmann, H. Bertagnolli and P. Chieux, *Z.Naturf.* **38a** (1983) 231
- 3) H. Ohtaki, A. Funaki, B.M. Rode and G. Reibnegger, *Bull.Chem.Soc.Jap.* **56** (1983) 2116
- 4) J.M. Heller Jr., H.H. Hubbel Jr., L.R. Painter and R.D. Birkhoff, *J.Chem.Phys.* **71** (1979) 4641
- 5) R.D. Birkhoff, J.M. Heller Jr., L.R. Painter, J.C. Ashley, and H.H. Hubbel Jr., *J.Chem.Phys.* **76** (1982) 5208
- 6) H. Siegbahn and K. Siegbahn, *J.Electr.Spectr.Rel.Phén.* **2** (1973) 319
- 7) L. Nemec, H.J. Gaehrs, L. Chia and P. Delahay, *J.Chem.Phys.* **66** (1977) 4450
- 8) H. Siegbahn, L. Asplund, P. Kelfve, K. Hamrin, L. Karlsson, and K. Siegbahn, *J.Electr.Spectr.Rel.Phén.* **5** (1974) 1059

DOUBLY EXCITED AUTOIONIZING STATES

T.F. GALLAGHER

Department of Physics, University of Virginia, Charlottesville, VA 22901

Using multistep laser excitation in which each of the two valence electrons of alkaline earth atoms are excited separately it is possible to excite only the doubly excited state, not the underlying continuum. This simplification allows inherently complex spectra of interacting autoionizing states to be unraveled.

1. INTRODUCTION

An interesting aspect of the spectra of multielectron atoms is the fact that they have autoionizing states, that is, states in which there is enough energy invested in two or more electrons to allow one electron to be removed from the atom. The apparently simplest case in which autoionization occurs is He, which has only two electrons. However due to the fact that He⁺ has degenerate energy levels for $n > 1$ there is appreciable correlation of the two electrons for all the autoionizing states.^{1,2} Consequently the alkaline earth atoms, with two valence electrons outside a closed shell core, are in many cases simpler.

As an example we shall consider Ba which has been studied extensively. In Figure 1 we show the energy levels of Ba up to the second ionization limit.³ The Ba⁺ levels are shown as bold lines. These are the levels for one of the two valence electrons added to the closed shell Ba⁺ core. Note that for $\ell < 4$ that the levels are energetically separated whereas for $\ell \geq 4$ they are degenerate. This is an important distinction. Adding the second electron to a low ℓ state of Ba⁺ produces a small shift in energy of the Ba⁺ state, at least small compared to the separation of the low Ba⁺ levels, and in this case adding the second electron produces a series of Ba states converging to the Ba⁺ state as shown by the shaded areas of Figure 1. The series converging to the Ba⁺ 6s state are the familiar bound states, but there are analogous autoionizing series converging to each of the low states of Ba⁺. This is of course an independent particle picture which has been shown to work well for low ℓ states $n\ell m\ell'$ for which $m-n \geq 2$. For $m=n$ however we would expect this picture to fail as the two electrons would be equivalent and therefore highly correlated.

Turning our attention to the high ℓ Ba⁺ states of Fig. 1, we see that they are degenerate and that there are no Rydberg states shown converging to them. The fact that the levels are degenerate means that the electric field of the second electron mixes and shifts the levels from the Ba⁺ level positions shown in Figure 1. As these two effects will depend upon the precise location of the second electron it is clear that the motions of the two electrons will be correlated. Thus these states can not be described as autoionizing states converging to specific high states of Ba⁺.

Here we shall focus on the Ba states converging to the low ℓ states of Ba⁺, primarily because these are the states which have been studied experimentally. If the two electrons were really independent, the only decay mechanism would be radiative decay. In fact though the coulomb interaction of the electrons couples the doubly excited states to the continua above lower lying Ba⁺ states, and the doubly excited states autoionize rapidly to the degenerate continua.

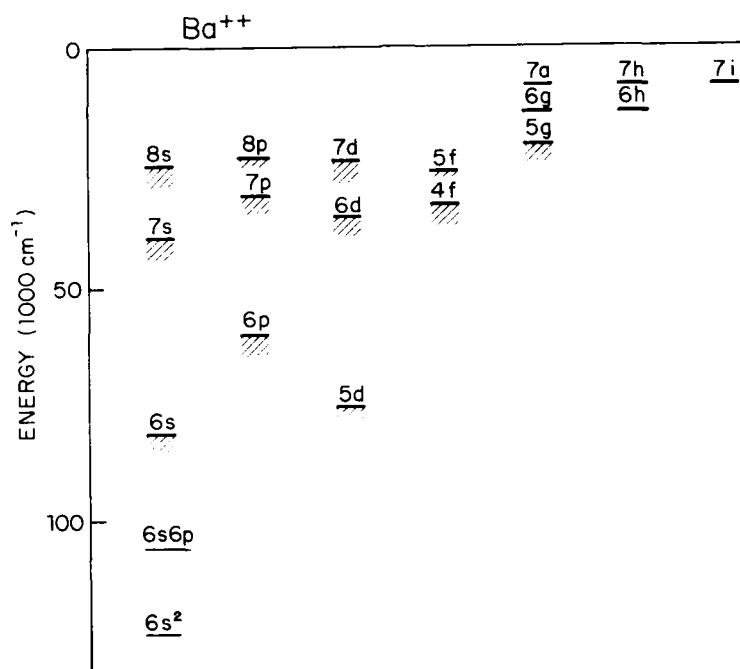


FIGURE 1

The energies of Ba and Ba⁺ up to the second ionization limit. The Ba⁺ states are shown as bold lines, and the Ba states converging to them are shown by the striped lines. This simple picture fails for the Ba states converging to the high Ba⁺ states, so no Ba states are indicated.

Although for many years⁴ autoionizing states may have been more of a curiosity than anything else, recently it has become increasingly clear that they have real practical significance. For example, the inverse of autoionization is dielectronic recombination,⁵ a two step process in which an ion captures an electron to form an autoionizing state which may either autoionize or radiatively decay to a state below the lowest ionization limit.

If radiative decay rather than autoionization occurs in the second step dielectronic recombination has occurred. This process is used as a temperature diagnostic for astrophysical plasmas⁶ and is an important factor in radiative power loss by impurity ions in tokamak plasmas because it lowers the charge state of these ions⁷. It is clear that to reach any sort of understanding of dielectronic recombination requires that the process of autoionization be well understood. In addition to its obvious role in plasmas, autoionizing states have mostly become the focus of several schemes to produce lasers at visible and shorter wavelengths.^{8,9} In fact a laser using a Ba⁺ transition has already been made by photoexciting Ba autoionizing states which rapidly decayed to the excited Ba⁺ state⁹ which was the upper laser level.

Autoionizing states are inherently more complex than their bound analogues due to the coupling to the degenerate continua. In traditional spectroscopy this situation has been further complicated by the fact that photoexcitation to the doubly excited states and the underlying continua are comparable in strength and interfere to produce the Beutler-Fano interference profiles

commonly associated with autoionizing states.¹⁰

Here we describe a multistep laser excitation approach with which it is possible to excite only the doubly excited state but not the degenerate continuum,¹¹ thus untangling the excitation from the study of the interaction of the doubly excited state with the continuum. The simplicity of this experimental approach allows the detailed study of inherently complex problems, such as interacting autoionizing series¹². Here we briefly review the experimental multistep excitation approach, and describe several applications of the method.

2. MULTISTEP EXCITATION

The multistep excitation scheme is perhaps unusual in that it is both conceptually and practically simple. The method was first used by Cooke et al.¹¹ to study the $5p\pi$ autoionizing states of strontium, which are analogous to the Ba $6p\pi$ states shown in Fig. 1. Since then the method has been applied and extended by several research groups to a variety of problems. Since we shall later consider the excitation of the Ba $6p\pi$ states, we shall use them to illustrate the method.^{12,13} In Fig. 2 we show the relevant energy levels for the excitation of the Ba $6p\pi$ levels.

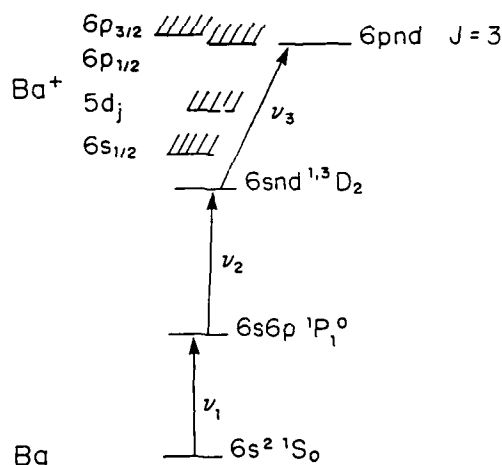


FIGURE 2
Ba energy levels showing the laser excitation

As shown by Fig. 2, there are three lasers involved in the excitation. The first and second lasers, at fixed wavelengths, excite the Ba atoms from the $6s6s$ level to the $6s6p$ level and then to a $6snd$ level, a bound Rydberg state. The third laser drives the transition $6snd \rightarrow 6pnd$, from the bound $6snd$ Rydberg state to the autoionizing Rydberg state, which autoionizes yielding an ion and an electron. As the third laser is swept through the $6pnd$ state, we observe an ionization signal proportional to its spectral density-- and essentially

nothing else. Why this method works so simply becomes clear if we consider what we are doing to the atom with each laser, as shown schematically in Fig. 3.

As shown by both Figs. 2 and 3, the first two lasers excite one of the electrons to a Rydberg state. From Fig. 3, though, it is clear that the outer

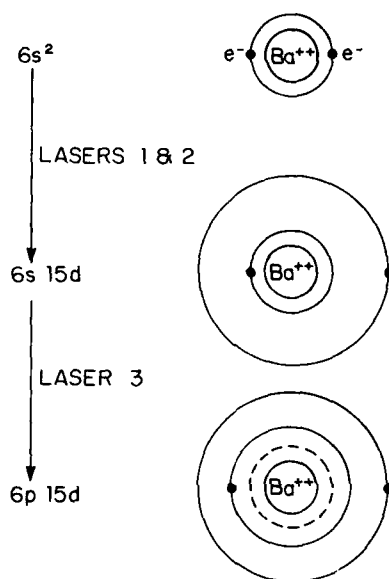


FIGURE 3

Sketch of the effort of the lasers in the Ba atom. The first two lasers excite one electron, and the third laser excites the second electron.

Rydberg electron spends most of its time far away from the ionic core near its classical turning point at large orbital radius. The third laser drives the inner electron transition $6s \rightarrow 6p$ while the outer electron remains a spectator, which makes small adjustments in its orbit as required by any difference in quantum defect of the $6s$ nd and $6p$ nd states. We note that this is the resonance line of Ba^+ , $f \sim 1.1$,¹⁴ and it is spread over the autoionization width of the $6s$ nd state, $\sim 10 \text{ cm}^{-1}$. This leads to peak optical absorption cross sections for the excitation of the $6s$ nd $\rightarrow 6p$ nd transitions of 10^{-14} cm^2 . This is to be compared with direct photoionization of the Rydberg state $6s$ nd ($6s$ nd $\rightarrow 6s\epsilon f$, for example) by a visible photon. Because of the gross mismatch between the slow spatial oscillations of the nd radial wavefunctions near the classical turning point where the nd electron is likely to be found and the rapid spatial oscillations of 2 eV continuum waves, the direct photoionization cross section is negligible, 10^{-20} cm^2 .¹⁵ Since photoionization is effectively absent, at any photon energy there is only one non zero transition amplitude, $6s$ nd- $6p$ nd. Thus, we observe directly, free of the usual Beutler-Fano interference,¹⁰ the $6p$ nd state. As we shall see shortly the $6p$ nd state appears as a nearly Lorentzian feature whose center gives the energy of the state and whose width gives the total autoionization rate.

The physical arguments used to describe the excitation of the autoionizing states can be put on a rigorous basis^{16,17} using quantum defect theory, and this understanding has been used to develop some novel techniques for the study of bound and autoionizing states,¹⁸⁻²⁰ for example better values of the

ionization limit.²⁰

The experiments are done in a laser-atomic beam apparatus shown in Fig. 4. Three pulsed dye lasers are all pumped by the same Nd:YAG pump laser. The dye

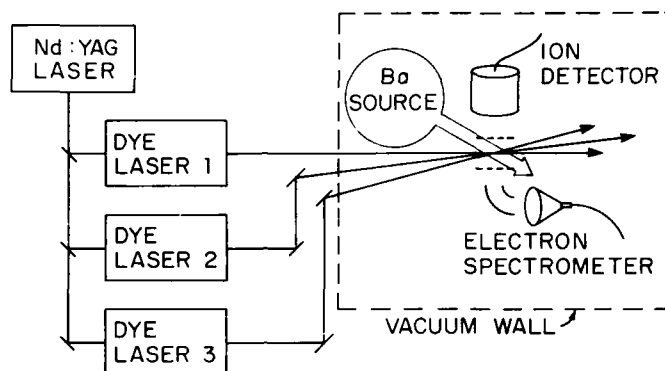


FIGURE 4
Schematic diagram of the apparatus.

lasers are modest by any standard, 100 μJ pulse energies, 1 cm^{-1} linewidths, and 5 ns pulse durations. The three dye laser beams are brought together at a small angle where they cross the atomic beam, and their optical path lengths are arranged so that the second and third laser pulses come about 5 ns and 10 ns, respectively, after the first pulse. The atomic beam apparatus is one 50-cm diameter vacuum chamber at a pressure of 10^{-6} torr. The atomic beam effuses from a resistively heated oven 10 cm from the interaction region and has a density from 10^8 cm^{-3} to 10^{10} cm^{-3} in the interaction region, which consists of a plate and a grid 1 cm apart. About 1 μs after the laser pulses, a positive voltage of 100 V is applied to the lower plate to drive the resulting ions through the grid in the upper plate to the particle multiplier. The multiplier signal is detected with a gated integrator and recorded as the y signal with an x-y recorder.

In practice an experiment consists of setting the first two lasers to excite a chosen 6snd Rydberg state, tuning the third laser through the 6pnd state, and recording the ion signal as a function of wavelength (the x signal for the recorder). An example is shown in Fig. 5, which is a recording of the $6s15d1D_2-6p_{3/2}15d_{J=3}$ transition. As shown by Figure 5 there is essentially one strong peak, corresponding to the $6p_{3/2}15d_{J=3}$ state, and its energy and spectral width, which is a direct measure of the autoionization rate, may be read directly from Figure 5.

3. APPLICATIONS OF THE METHOD

Using the multistep excitation method which is inherently simple it is possible to unravel complex problems. To illustrate this we shall consider two examples, the study of the Ba 6pnd_{J=3} states and the study of the higher lying nsms and nsmd states.

A. The Ba 6pnd Series

The Ba 6pnd series have been studied extensively using the multistep laser excitation scheme. In fact much of our understanding of how to treat the spectra theoretically has come from the study of the 6pnd series. There are

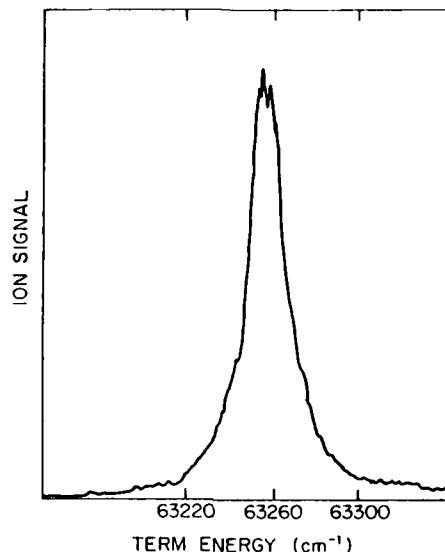


FIGURE 5

Recording of the $6.15d\ ^1D_2-6p_{3/2}\ 15d^+\ J=3$ transition which yields immediately the position and width of the $6p_{3/2}\ 15d^+$ level.

three $J=3$ $6pnd$ series, the $6p_{1/2}\ nd_{5/2}$ series converging to the $6p_{1/2}$ limit and two series converging to the $6p_{3/2}$ limit which are shown in Figure 6 as the $6p_{3/2}\ nd^\pm$ series. The $6p_{3/2}\ nd^\pm$ series are substantially overlapped as their widths are roughly equal to their separations.

By coincidence however the choice of the initial $6snd\ ^1D_2$ or 3D_2 state leads respectively to the predominant excitation of the $6p_{3/2}\ nd^+$ and $6p_{3/2}\ nd^-$ states. These labels are chosen merely to reflect the energy positions as no single coupling scheme seems to be appropriate.^{13,21} Although the selectivity in excitation is somewhat puzzling, as a consequence the three series of $6pnd\ J=3$ states can be excited separately, making their experimental study particularly straightforward. To begin, the positions and widths of these levels have been determined.^{12,13,21} The observed positions are the basis of Figure 6, and the widths are shown in Figure 7. The widths show clearly the effects of the interseries interactions which might have been anticipated from the energy level diagram of Fig. 6. As shown by Fig. 6 the $6p_{3/2}\ 10d$ states are degenerate with the $6p_{1/2}\ nd_{5/2}$ states for $n=20$. This interseries coupling leads to the large increase in the autoionization rates of the $6p_{1/2}\ nd_{5/2}$ states at $n^*=17$ as shown by Figure 7.

Careful scrutiny of Figure 7 reveals that the $6p_{3/2}\ 9nd^+$ and $6p_{3/2}\ 10d^+$ states are not shown on the graph because they are so wide that they overlap several $6p_{1/2}\ nd_{5/2}$ states and are highly structured due to the interseries interaction. We show in Figure 8 the $6s10d\ ^1D_2-6p_{3/2}\ 10d^+$ spectrum, as well as the quantum defect theory fit to the spectrum. This is to our knowledge the first synthetic spectrum calculated for interacting autoionizing atomic series. It was based upon the approach used by Fano²² which is ideal for photoexcitation from the ground state but slightly awkward for the multistep excitation method. More recently Cooke and Cromer²³ and Giusti Suzor and Fano²⁴ have developed formulations of quantum defect theory which are better matched to the multistep excitation method, and these approaches have been used to reproduce

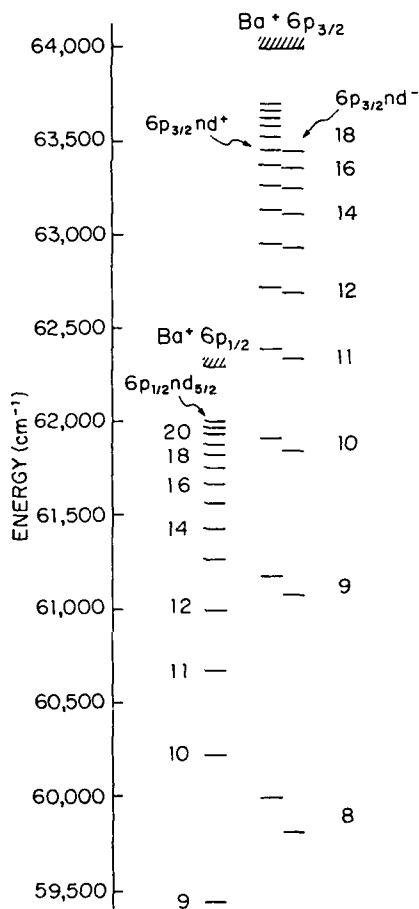


FIGURE 6

Ba energy levels near the Ba⁺ 6p_{1/2} and 6p_{3/2} limits. Note that the 10d and 9d states converging to the 6p_{3/2} limit fall below the 6p_{1/2} limit.

the spectrum of Figure 7 and similar spectra.^{23,25}

The spectrum from the 6s10d³D₂ state to the 6p_{3/2}10d⁻ state, shown in Figure 9 provides an interesting contrast. The 6p_{3/2}10d⁻ state is first of all much narrower, and second exhibits almost no interaction with the 6p_{1/2}nd_{5/2} states. Presumably the fact that the 6p_{3/2}nd⁻ states are generally narrower than the 6p_{3/2}nd⁺ states above the 6p_{1/2} limit is due to the analogous lack of interaction of the 6p_{3/2}nd⁻ states with the 6p_{1/2}nd_{5/2} continuum. Furthermore it is interesting to note that the 6p_{3/2}nd⁻ and 6p_{1/2}nd_{5/2} series have the same widths which indicates that their couplings to the 6sεf and 5dεl continua are the same, perturbations excepted.

B. Higher lying states

As was mentioned in the introduction the isolated electron picture which

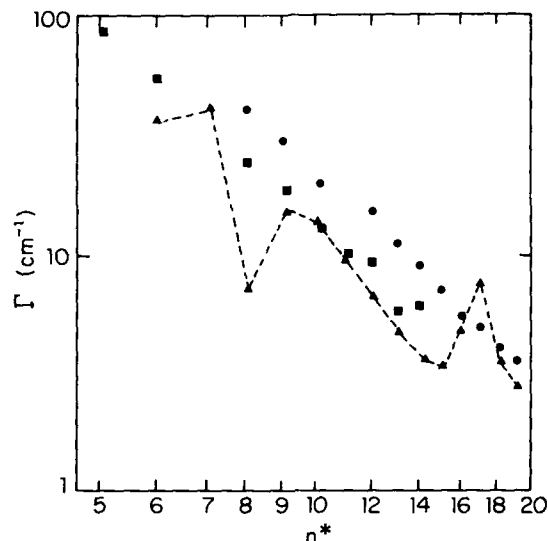


FIGURE 7

Autoionization rates of the three $6pnd$ $J=3$ series $6p_{1/2} nd_{5/2}$ (▲), $6p_{3/2} nd^+$ (●), and $6p_{3/2} nd^-$ (■). The perturbations in the $6p_{1/2} nd_{5/2}$ series are quite evident.

works so well for the low lying autoionizing states might be expected to collapse for Ba states converging to high states of the Ba^+ core or for $n m'$ states where $n = m$ irrespective of the values. As the latter states are accessible with photoexcitation they have been subject to experimental studies by several laboratories using a variety of ingenious techniques.^{18,19,26,27}

An impressive series of measurements has been done at Bell Laboratories by Freeman et al in which the bound Ba $6sns$ and $6snd$ states were excited as in Figure 2, but the final excitation was not a single photon transition as shown by Figure 1, but a two photon transition to the Ba states such as $10sns$ or $10snd$.²⁷ Since the transition is a two photon transition, it requires a high laser power density, and the nonresonant single photon excitation to a Ba^+ continuum provides a significant background signal which obscures and diminishes the two photon signal of interest. Thus to detect the two photon excitation by merely looking at the total ionization is not usually sufficient, and other techniques, such as monitoring very energetic electrons, Ba^+ fluorescence, or the production of Ba^{++} must be used. Using these techniques they have measured the positions and total autoionization rates of the $ndmd$ and $nsms$ states for n up to 11 and $m-n \leq 2$. In spite of the close approach of the quantum numbers no graphic evidence of strong electron correlations was observed. However the gradual increase of quantum defects was observed as well as an interesting variation of the scaled widths $m^{-1}\Gamma$ as the value of the inner electron is increased. In Figure 10 we show the variation in the scaled widths. For the $nsms$ states the widths are virtually constant while for the $nsmd$ states they increase with n . A qualitative explanation of this is the fact that in the $nsms$ states neither the ns or ms electrons experiences a centrifugal barrier and thus both electrons may be found close to the Ba^{++} core. Thus increasing the size of the inner electron's orbit does not substantially alter the overlap of the two electron's orbits or their interaction. On the other hand in the $nsmd$ states the outer md electron is forced out from the origin by the

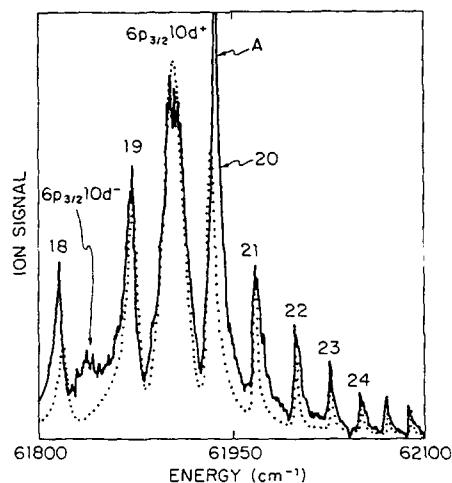


FIGURE 8
The $6s10d^3D_2 - 6p_{3/2}nd^+$ spectrum, observed (----), calculated by QDT (....)

centrifugal potential, and as the inner electron orbit is increased in size by increasing n the overlap and hence the interaction is increased. At this point no serious theoretical calculations have been undertaken to explain these observations although it would clearly be informative to do so.

4. CONCLUSION

Atomic autoionizing states are of both practical and intrinsic interest, and these atoms may be studied in extraordinary detail by multistep laser techniques. These techniques are attractive for two reasons. As with most laser

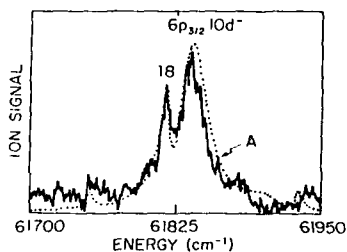


FIGURE 9
The $6s10d^3D_2 - 6p_{3/2}10dd^-$ spectrum observed (----), calculated by QDT (.....).

experiments, a small number of atoms is sufficient, allowing us to use atoms in an atomic beam and incorporate more sophisticated diagnostic tools such as electron energy analysis which are out of the question in an absorption cell. In addition they are conceptually and experimentally straightforward allowing one to unravel physically complex problems.

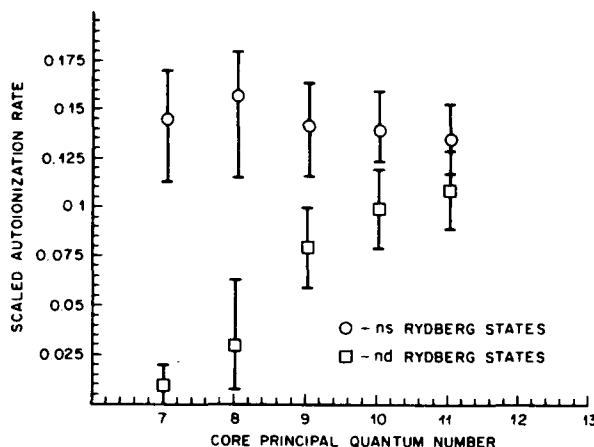


FIGURE 10
Scaled autoionization rates of the Ba msns (○) and msnd (◻) autoionizing states.

ACKNOWLEDGEMENTS

The notions presented here have been developed over a period of time and are the result of the efforts of many other people in the Molecular Physics Laboratory of SRI and recently at the University of Virginia, W.E. Cooke, F. Gounand, K.A. Safinya, W. Sandner, R. Kachru, N.H. Tran, O.C. Mullins, Y. Zhu, and E.Y. Xu. This work has been supported by the National Science Foundation.

REFERENCES

1. R.P. Madden and K. Codling, *Phys. Rev. Lett.* **10**, 516 (1963).
2. J.W. Cooper, U. Fano, and F. Prats, *Phys. Rev. Lett.*, **10**, 518 (1963).
3. C.E. Moore, *Atomic Energy Levels*, NBS Circular No. 467 (U.S. GPO, Washington, D.C., 1949).
4. E.U. Condon and G.H. Shortley, *The Theory of Atomic Spectra* (Cambridge University Press, London 1957).
5. A. Burgess, *Astrophysical J.*, **139**, 776 (1964).
6. B. Edlen and F. Tyren, *Nature* **143**, 940 (1939).
7. A.H. Gabriel and T. Paget, *J. Phys. B* **5**, 673 (1972).
8. S.E. Harris, *Opt. Lett.* **5**, 1 (1980).
9. J. Bokor, R.R. Freeman, and W.E. Cooke, *Phys. Rev. Lett.* **48**, 1242 (1982).
10. U. Fano, *Phys. Rev.* **124**, 1866 (1961).
11. W.E. Cooke, T.F. Gallagher, S.A. Edelstein, and R.M. Hill, *Phys. Rev. Lett.* **40**, 178 (1978).

12. F. Gounand, T.F. Gallagher, W. Sandner, K.A. Safinya, and R. Kachru, *Phys. Rev. A* **27**, 1925 (1983).
13. O.C. Mullins, Y. Zhu, E.Y. Xu, and T.F. Gallagher (to be published).
14. B.M. Miles and W.L. Wiese, Critically Evaluated Transition Probability for Ba I and Ba II, NBS Technical Note 474 (US GPO, Washington D.C., 1969).
15. D.C. Lorents, D.J. Eckstrom, and D.L. Huestis, SRI Report MP 73-2 (unpublished).
16. N.H. Tran, P. Pillet, R. Kachru, and T.F. Gallagher, *Phys. Rev. A* **29**, 2640 (1984).
17. S.A. Bhatti, C.L. Cromer, and W.E. Cooke, *Phys. Rev. A* **24**, 161 (1981).
18. T.F. Gallagher, R. Kachru, N.H. Tran, and H.B. van Linden van den Heuvell, *Phys. Rev. Lett.* **51**, 1753 (1983).
19. R.M. Jopson, R.R. Freeman, W.E. Cooke and J. Bokor, *Phys. Rev. Lett.* **51**, 1640 (1983).
20. W. Sandner (this volume)
21. L. Van Woerkom and W.E. Cooke (to be published).
22. U. Fano, *Phys. Rev. A* **2**, 353 (1970).
23. W.E. Cooke and C.L. Cromer (to be published).
24. A. Giusti-Suzor and U. Fano, *J. Phys. B* **17**, 215 (1984).
25. A. Giusti-Suzor and H. Lefebvre-Brim, *Phys. Rev. A* **30**, 3057 (1984).
26. P. Camus, P. Pillet and J. Boulmer, *J. Phys. B*.
27. L.A. Bloomfield, R.R. Freeman, W.E. Cooke and J. Bokor, *Phys. Rev. Lett.* **53**, 2234 (1984).

PROGRESS ON QUANTUM DEFECT THEORY—DYNAMICS OF EXCITED ATOMS AND MOLECULES

Jia-Ming Li*

Institute of Physics, Academia Sinica, Beijing, China

Multichannel Quantum Defect Theory provides a unified treatment of infinite Rydberg states, autoionizing states and their adjoining continua for atoms and molecules. The scope of applications has been reviewed. Our recent results on the correlations of the dynamics for excited atoms and molecules are presented. We also discuss further developments on Multichannel Quantum Defect Theory.

1. INTRODUCTION

Multichannel Quantum Defect Theory (1,2,3) provides a unified treatment of excited bound states and their adjoining continua for atoms and molecules. The level positions of the excited states forming perturbed Rydberg series and various cross sections of low-energy electron-ion collisions corresponding to adjoining continua can be quantitatively described in terms of the eigenchannel parameters (eigen quantum defects and transformation matrix). This compact set of parameters is related to the short-range scattering matrix and varies smoothly with excitation energies in the neighborhood of the thresholds. Formally, it can be regarded as a nice analytic property of the scattering matrix. Practically, it is very powerful in treating these complicated spectral phenomena and the related collision processes.

Before outlining the scope of applications, let us briefly review the physical picture in the theoretical treatment. A highly excited atom or molecule with the excitation energies below the double ionization threshold usually consists of an electron (bound or unbound) and a residual ion. The physical clue is following: Within a reaction zone in the configuration space, the electron and the ion will strongly couple together and form an excited complex. On the contrary, outside the reaction zone the interaction between the electron and the ion can be adequately described as the Coulomb potential. Thus, the wavefunction outside the reaction zone can be written rigorously in an analytic form. More specifically, wavefunctions with a specific total angular momentum J and parity π outside the reaction zone can be expressed as superpositions of Coulomb wavefunctions

$$\psi = \sum_i A \phi_i (f_i(r) e_i + g_i(r) d_i) \quad (1)$$

The index i indicates various couplings between the electron and the residual ion, and identifies the dissociation channels outside the reaction zone. The symbol A is an antisymmetrization operator. The ϕ_i is a combined wavefunction of the residual ion with the specific coupling. The regular radial Coulomb function $f(r)$ and the irregular radial Coulomb function $g(r)$ are continuous functions of energy across the threshold, and are normalized per unit energy range (2,3). The coefficients, e_i and d_i , are determined by the boundary conditions of the reaction zone and the asymptotic boundary conditions at infinity. To distinguish these two types of boundary conditions, equation (1)

*The previous name as C.M.Lee

can be recasted into

$$\begin{aligned}
 \Psi &= \sum_i A_i \Phi_i \left[f_i(r) \left(\sum_{\alpha} U_{i\alpha} \cos \pi \mu_{\alpha} A_{\alpha} \right) - g_i(r) \left(\sum_{\alpha} U_{i\alpha} \sin \pi \mu_{\alpha} A_{\alpha} \right) \right] \\
 &= \sum_{\alpha} \left[\sum_i A_i \Phi_i U_{i\alpha} (f_i(r) \cos \pi \mu_{\alpha} - g_i(r) \sin \pi \mu_{\alpha}) \right] A_{\alpha} \\
 &= \sum_{\alpha} \Psi_{\alpha} A_{\alpha}
 \end{aligned} \tag{2}$$

The parameters, $U_{i\alpha}$ and μ_{α} , lumping the dynamics within the reaction zone represent the boundary conditions of the reaction zone, and are related to the short-range scattering matrix (apart from analytically known Coulomb phase shifts), namely,

$$S_{ij} = \sum_{\alpha} U_{i\alpha} \exp(i\alpha\pi\mu_{\alpha}) U_{j\alpha} \tag{3}$$

The index α labels the eigenchannels which characterize the dynamics of the excited complex — diagonal representations of the short-range scattering matrix. The eigenchannel parameters, eigen quantum defects μ_{α} and transformation matrix $U_{i\alpha}$, vary smoothly with energy in the neighborhood of the thresholds. The eigenchannel wavefunctions Ψ_{α} and the relevant transition matrix elements are also continuous functions of excitation energy. Formally, it is the nice property of the scattering matrix. In practice, the smooth energy dependence is the reason why Multichannel Quantum Defect Theory is a very powerful method to treat the spectral phenomena and the relevant low-energy collision processes in a unified manner. Because of the smooth energy dependence, the eigenchannel parameters and the relevant transition matrix elements can be computed with minimum efforts by either first-principle theoretical calculations (4) or by semiempirical fitting to the spectroscopic data (5,6). Subsequently, the mixing coefficients A_{α} can be determined analytically by imposing the appropriate asymptotic boundary conditions at infinity (2,3,4,5). These boundary conditions differ for the different ranges of the spectra: the discrete spectrum, the autoionization spectrum and the continuum spectrum. In the discrete spectrum, the mixing coefficients A_{α} will provide a further characterization of the configurations for the perturbed Rydberg levels; they are important for the spectral analysis, for example, oscillator strength, g factor, hyperfine structure etc. (6,7,8,9,10,11). In the autoionization spectrum and the continuum, the mixing coefficients A_{α} pertain to the scattering matrix. The cross sections for the low-energy collisions can be calculated (12). In order to get more feeling about various applications of Multichannel Quantum Defect Theory, we will enumerate more examples: Rydberg spectral analysis (13,14,15,16), photoionization (17,18,19), photoelectron angular distribution (20,21), photoelectron spin polarization (21,22), connection between the tip bremsstrahlung and radiative recombination (23), resonant radiative recombination (dielectron recombination) (1,24,25), electron impact excitation (1,12), molecular photoionization (26), photodissociation (27) and dissociative recombination (28, 29). Here, I must apologize for presenting our interests only. Anyway, such a list suffices to show collective, international efforts and the scope of applications.

The key issue at present will be the determination of these vitally important eigenchannel parameters and the relevant matrix elements with an adequate accuracy. Although there have existed some computational programs for atoms such as variational eigenchannel method (4), R-matrix method (30,31), and relativistic random phase approximation (19), a flexible computational scheme directly aiming at the eigenchannel parameters is still not available. At the Institute of Physics, Academia Sinica, we have started a project to establish such flexible computation schemes for atoms and molecules. The details of the theory is beyond the scope of the article. We here will present

our preliminary results and our opinion on the developments of Quantum Defect Theory.

2. DYNAMICS OF EXCITED ATOMS

The energy spectra of the excited atoms or ions usually contain Rydberg series in which there are infinite number of excited bound states and auto-ionizing states converging to different ionization thresholds. As the compact set of eigenchannel parameters has been determined, the level positions of the perturbed Rydberg series can be calculated by imposing the asymptotic boundary conditions at infinity. We here present simple examples to illustrate how to correlate various dynamical properties of the excited atoms. Figure 1 shows our non-relativistic calculations of the eigenchannel parameters for the lithium isoelectronic sequence (the electron occupation number $N=3$ with the atomic number $Z \geq 3$). This is an one-channel problem. Extension to multichannel problems is merely appropriate superpositions of eigenchannels as discussed above. The eigen quantum defect for each partial wave is continuous function of the reduced energy $\tilde{\epsilon} = \epsilon/q^2$ where $q=Z-N+1$. Below the threshold, the orbital energy is expressed by the Rydberg formula (in atomic unit)

$$\epsilon_n = -\frac{q^2}{2(n-\mu)^2} \quad (4)$$

where n is the principle quantum

number. The quantum defect measures the degree of penetration of the excited radial wavefunction as a "phaseshift" in unit of π with respect to the corresponding radial Coulomb wavefunction. Thus, the μ is smoothly jointed to the short-range phase shift δ_s/π for the electron-ion collision in each partial wave. In this way, Figure 1 will concisely summarize all excited states of atoms or ions along the lithium

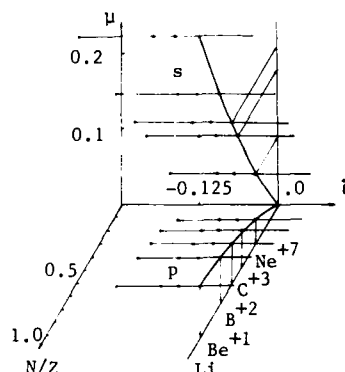


FIGURE 1

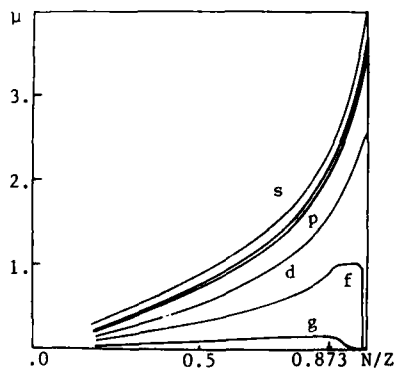


FIGURE 2

isoelectronic sequence. The quantum defect of the s wave is larger than that of the p wave, since the excited s orbitals have higher degree of penetration into the ionic core. Owing to the centrifugal potentials, the quantum defects for high partial waves $l \geq 2$ are almost zero and the excited orbitals with $l \geq 2$ are then hydrogenic in nature. As the atomic number Z increases, the quantum defects decrease. Because the nuclear attractive Coulomb potential becomes dominant, all excited orbitals become semi-hydrogenic. Figure 2 shows our relativistic calculations of the eigenchannel parameters at $\tilde{\epsilon}=0$ for the cesium isoelectronic sequence. There exist very interesting 6s-5d-4f-5p orbital competitions (32). The quantum defects of the penetrating

channels decrease as the atomic number Z increases. The quantum defect of the f channel jumps at $Z=56$ where the $4f$ orbital is collapsing from the outer valley into the inner valley. As the atomic number increases further, all quantum defects decrease and the excited orbitals become semi-hydrogenic. For $Z \geq 63$ ($N/Z \leq 0.873$), it becomes a multichannel problem since the samarium ion Sm VIII has the ground electronic configuration (core) $5p^4 4f^3$; the quantum defect of the (L_i) partial wave represents the statistical mean value of the eigen quantum defects involved with the (L_i) waves.

We now return to the dynamics of excitations into these infinite bound states by electron impacts. The differential cross section can be written as (in atomic unit)

$$\frac{d\sigma}{d\Omega} = \frac{2}{\Delta E} \cdot \left(\frac{k_f}{k_i} \right) \cdot \frac{f(\Delta E, Q, T)}{Q^2} \quad (5)$$

where $T = k_i^2/2$ is the incident kinetic energy, ΔE the excitation and $\vec{Q} = \vec{k}_f - \vec{k}_i$ the momentum transfer. The $f(\Delta E, Q, T)$ is the effective generalized oscillator strength. As the incident energy increases, the $f(\Delta E, Q, T)$ converges to the generalized oscillator strength $f(\Delta E, Q)$ which is independent of the incident kinetic energy (33,34). For excitations into infinite Rydberg states, the generalized oscillator strength density can be defined as the strength per unit reduced excitation energy (35,36)

$$\frac{d_f f(\Delta E, Q)}{d\bar{E}} = f_n(\Delta E, Q) \cdot N_n^2 \quad (6)$$

where the N_n^2 is the channel density of state. The N_n^2 is simply $(n-\mu)^3 d\mu/d\bar{E}$ for one-channel problems. In Figure 3, we present our theoretical results of the generalized oscillator strength density for the excitations from the lithium ground state into the s channel. The generalized oscillator strength density forms a smooth surface since the matrix elements between the initial state and the eigenchannel are continuous functions of excitation energy. Based on this smooth surface, we can conveniently correlate all high-energy excitation cross sections from the lithium ground state into infinite Rydberg states ns , $n \geq 3$. Furthermore, the generalized oscillator strength density has an interesting scaling relation along the isoelectronic sequence (36). For the optical allowed excitation from the lithium ground state, Figure 4 displays the generalized oscillator strength density for the p channel. At the first glance, the surface exhibits very interesting features. Since the generalized oscillator strength density is proportional to the square of the matrix elements, the nodal curve at which the matrix elements vanish as shown in Figure 5 gives rise to the behavior. The matrix elements themselves form a smooth surface.

As the momentum transfer Q approaches zero, the generalized oscillator strength density converges to the oscillator strength density which is proportional to the absorption cross section in the photon impact process.

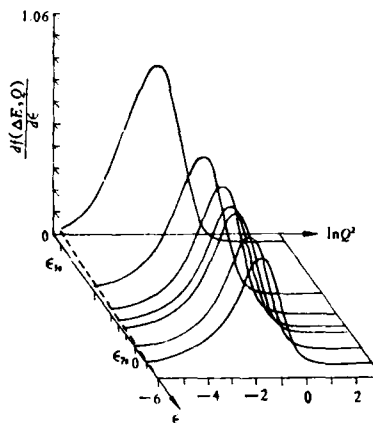


FIGURE 3

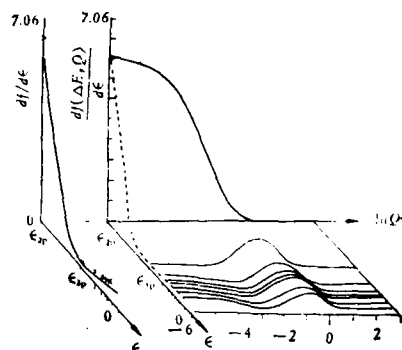


FIGURE 4

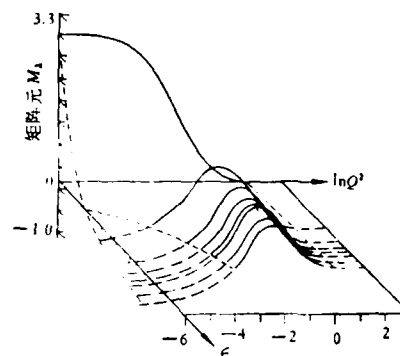


FIGURE 5

Because of the nodal surface, the oscillator strength density has a zero between the 2p state and the 3p state as shown in Figure 4. If a zero is located above the threshold, it is usually called the Cooper minimum (37). The excited atoms sometimes have more than two zeros (38). Here we will correlate the zeros for excited atoms (39). As illustrated above, all excited states forming the Rydberg series can be concisely summarized by a compact set of the smoothly energy-dependent eigenchannel parameters, in particular the quantum defects at the threshold. Owing to the dipole selection rule, photoabsorption will lead to the specific final channels which can be also represented by the corresponding quantum defects. In case of multichannel problems, the quantum defect is the statistical mean value of the relevant eigen quantum defects. The dipole matrix element is an integral involving the product of the initial and final wavefunctions which are Coulomb waves with the corresponding phase shifts $\pi\mu_i$ and $\pi\mu_f$ respectively. For an excited state with the principle quantum number n , the energy position $\delta(n)$ of the zero is related to the difference of the quantum defects, namely $\mu_f - \mu_i$. Since the $\delta(n)$ weakly depends on the principle quantum number (39,40), we can define $\delta = \lim_{n \rightarrow \infty} \delta(n)$. As $\delta = 0$, the zero of the oscillator strength density in the specific final channel is located below the threshold in the same way as shown in Figure 4. While $\delta > 0$, the zero is located above the threshold. Thus, we can correlate the number of the zeros of the oscillator strength densities for the excited atoms by examining the relation between δ and $\Delta\mu = \mu_f - \mu_i$ at the threshold. Figure 6 displays the relation.

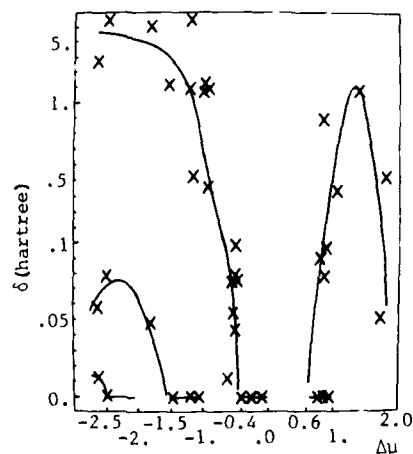


FIGURE 6

(A) For $\Delta\mu < 0$, it corresponds to the partial oscillator strength density for photoabsorption from the initial channel with l into the final channel with $l+1$.

(A-1) $-0.4 < \Delta\mu < 0$, there exists one zero below the threshold.

(A-2) $-1.0 < \Delta\mu < -0.4$, there exists one zero above the threshold.

(A-3) $-1.5 < \Delta\mu < -1.0$, there exist two zeros; one above the threshold.

Another one below the threshold disappears if

$$v_{nl} = n - \mu_l \leq l+1.$$

(A-4) $-0.2 < \Delta\mu < -1.5$, there exist two zeros above the threshold.

(A-5) $-2.5 < \Delta\mu < -2.0$, there exist three zeros; two of them above the threshold. The third one below the threshold disappears if $v_{nl} \leq l+1$.

(A-6) $-3.0 < \Delta\mu < -2.5$, there exist three zeros above the threshold.

(B) For $\Delta\mu \geq 0$, it corresponds to the partial oscillator strength density for photoabsorption from the l channel into the $l-1$ channel.

(B-1) $0.0 \leq \Delta\mu < 0.6$, no zeros.

(B-2) $0.6 < \Delta\mu < 1.0$, there exist two zeros; one above the threshold. Another one below the threshold disappears if $v_{nl} \geq v_{(n+1)}(l-1)$

(B-3) $1.0 < \Delta\mu < 2.0$, one zero above the threshold. Except for the g-f transition, as the final f channel exists the resonance due to the radial wavefunction moving from the outer valley into the inner valley, there will be some dynamically induced zeros.

Based on these relations, we can correlate the partial oscillator strength density minima for the excited atoms; for example, we expect that the excited Ne in the 3s states has a photoabsorption window above and near the threshold, and the excited Ar in the 4s states has a photoabsorption window little far above the threshold. These photoabsorption windows have been confirmed by the recent experiments (41).

3. DYNAMICS OF EXCITED MOLECULES

The highly excited states of molecules usually can be separated into two classes: (1) infinite Rydberg states with the electron configurations consisting of the molecular ion and the Rydberg molecular orbital, (2) some non-Rydberg states characterized by the electron configurations involved with excitations of the valence molecular orbitals. These states may be strongly perturbed. Such excited molecular complex produced by photon-impact, electron-impact or other excitation processes may be ionized or dissociated. Under the framework of Multichannel Quantum Defect Theory, these perturbed states can be treated in a unified manner. The infinite perturbed Rydberg states and autoionizing states can be concisely correlated by the smoothly energy-dependent eigenchannel parameters. The configuration mixings between the Rydberg and non-Rydberg states can be expressed in terms of the interaction matrix elements between the eigenchannels and the non-Rydberg states. The electronic parts of the matrix elements also vary smoothly with the energy (28). Perturbations of Rydberg states by the non-Rydberg states usually lead to predissociation.

In this report, we will present our theoretical calculations of the electronic parts of the eigenchannel parameters. A multiple-scattering-self-consistent-field method with a muffin-tin approximation (42) is adopted to calculate the multicenter self-consistent potentials for the molecules. Based on the molecular potential, the wavefunctions of the excited Rydberg states and the adjoining continua can be calculated (43,44). Figure 7 displays the quantum defects for the NO molecules. The internuclear distance is at the equilibrium position of the NO^+ ions. In each eigenchannel, the calculated quantum defect is smoothly jointed to the short-range phase shift at the threshold. Although the orbital angular momentum is not a good quantum number,

the orbital angular momentum l corresponding to the largest component in the eigenchannel is very useful to characterize the dynamics, namely $s\sigma$, $p\sigma$, $p\pi$,...etc. as shown in Figure 7. Owing to the quadratic field of the NO^+ ion, the $s\sigma$ channel has 66% s wave 32% d wave, while the $d\sigma$ channel has 31% s wave and 67% d wave. In other channels such as $p\sigma$, $p\pi$, $d\pi$, $d\delta$,...etc., the orbital angular momentum l is a quasi-good quantum number; for example, the $p\sigma$ eigenchannel has 97% p wave. The higher the l , the smaller the quantum defect because of the centrifugal potential. The quantum defect of the s channel is the largest. The quantum defects of the eigenchannels with $l \geq 3$ are almost zero except the resonance above the threshold in the $f\sigma$ eigenchannel. For the p and d waves, the components perpendicular to the molecular axis, namely $p\pi$ and $d\delta$ eigenchannels, have larger quantum defects. The corresponding radial wavefunctions penetrate more into the molecular ion core. In our previous theoretical studies (45), we adopted a single-center-expansion close-coupling method. We also calculated the eigenchannel parameters at the threshold by solving the problem of low-energy electron- NO^+ collision. Our present calculations are in good agreements with the experimental data and our previous theoretical results (45).

Figure 7 also shows some interesting features for the $f\sigma$ eigenchannel. There is a shape resonance above the threshold (46). Such a resonance pertains to the anti-bonding molecular orbital $(\sigma 2p)^*$ between the atoms in the second row of the Mendeleev Periodic Table (43). During the resonance, the enhancement of the p waves around the nucleus will occur. Thus, such a resonance is related to the fine structure above and near the X-ray absorption K edges (47,48). Figure 8 displays the relation between the resonance energy position and the internuclear distance. It clearly manifests the $f\sigma$ resonance with the $(\sigma 2p)^*$ anti-bonding nature. Very interestingly, the resonance energy decreases as the internuclear distance increases. Such relation has been utilized to diagnose the relevant bond length of the molecules chemisorbed on the surfaces (47,48).

4. DISCUSSION

We have shown some preliminary results of our theoretical calculations on the eigenchannels of atoms and molecules. Various dynamical properties of excited atoms and molecules can be correlated with a compact set of the

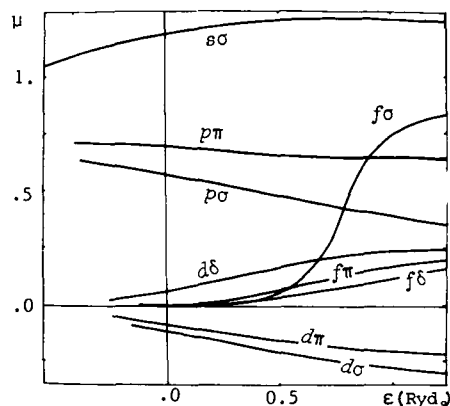


FIGURE 7

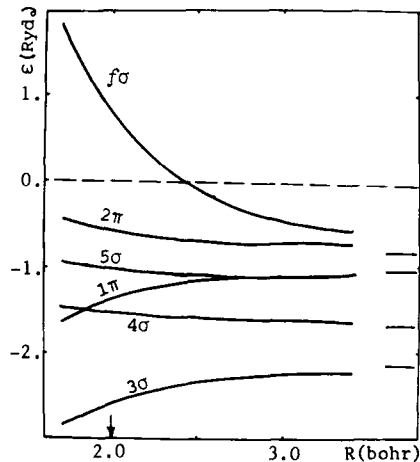


FIGURE 8

eigenchannel parameters. Now we will return to discuss the essence of our theoretical method. Our calculations begin with the exact Hamiltonians for atoms and molecules

$$H = H_0 + V_{\text{res}} \quad (7)$$

The H_0 is determined by self-consistent-field calculations. The residual interaction V_{res} is then the part of the exact Hamiltonian which has not been taken into account in the self-consistent-field calculations. As the V_{res} is not negligible, it can be treated successively as the intrachannel interactions and the interchannel interactions. Each channel consists of infinite configurations with the specific angular momentum coupling. Thus, traditional treatments via configurations and configuration mixings is extended to a novel treatment via channels and channel mixings. Our aim is to determine the smoothly energy-dependent eigenchannel parameters by comparatively minimum amount of computational efforts. Based on such physical meaningful parameters, dynamical properties of excited atoms and molecules can be correlated. Further researches along this direction are in progress.

In addition to the Coulomb potential outside the reaction zone, there have been some attempts to treat some other types of potentials outside the reaction zone, for example the free potential (49), the $1/r^2$ potential (50) and the Coulomb-Stark potential (51). All these approaches are based on the same physical clue. Outside the reaction zone, the wavefunctions can be written "rigorously" as linear combinations of the regular and irregular waves with the appropriate coefficients. Some of the coefficients are determined by matching the boundary conditions of the reaction zone. The rest of the coefficients can be treated analytically by imposing the appropriate asymptotic boundary conditions at infinity. Following this physical picture, one may ask how about the dynamics of two excited electrons outside the reaction zone — an outstanding problem in atomic physics. Near the double ionization threshold, it will involve infinite number of channels and become a formidable problem in practice. Further theoretical studies are required to elucidate the dynamics of this unsolved three-body quantum mechanical problem with long-range interactions. On the experimental side, there are some recent enlightening observations (52) which should stimulate more theoretical and experimental studies.

REFERENCES

- 1) M.J. Seaton, Phys. Soc. Lond. 88 (1966) 801, Rep. Prog. Phys. 46 (1983) 167
- 2) U. Fano, Phys. Rev. A2 (1970) 353, *ibid*, A15 (1977) 817, J. Opt. Soc. Am. 65 (1975) 979.
- 3) C.M. Lee and W.R. Johnson, Phys. Rev. A22 (1980) 979.
- 4) C.M. Lee Phys. Rev. A10 (1974) 584.
- 5) K.T. Lu, Phys. rev. A4 (1971) 579.
- 6) C.M. Lee and K.T. Lu, Phys. Rev. A8 (1973) 1241.
- 7) A.F. Starace, J. Phys. B: Atom. Molec. Phys. 6 (1973) 76.
- 8) J. Geiger J. Phys. B: Atom. Molec. Phys. 12 (1979) 2277.
- 9) P. Esherick, Phys. Rev. A15 (1977) 1920.
- 10) J.J. Wynn, J.A. Armstrong, P. Esherick, Phys. Rev. Lett. 39 (1977) 1520.
- 11) R. Beigand, E. Matthias, A. Timmermann, Phys. Rev. Lett. 47 (1981) 326.
- 12) Jia-Ming Li (C.M. Lee), Acta Physica Sinica 29 (1980) 419.
- 13) J.P. Connerade, M.W.S. Masfield, G.H. Newsom, D.H. Tracy, M.A. Baig, K. Thimm, Phil. Trans. Roy. Soc. A290 (1979) 327.
- 14) F. Gounand, T.F. Gallagher, W. Sandner, K.A. Safinya, R. Kachru, Phys. Rev. A27 (1983) 1925.
- 15) M. Aymar, O. Robaux, J. Phys. B: Atom. Molec. Phys. 12 (1979) 531.
- 16) J.A. Armstrong, J.J. Wynn, P. esherick, J. Opt. Soc. Am. 69 (1979) 211.
- 17) J. Dubau, J. Wells, J. Phys. B: Atom. Molec. Phys. 6 (1973) 1452.

- 18) M. Le Dourneuf, Vo Ky Lan, P.G. Burke, K.T. Taylor, *J. Phys. B: Atom. Molec. Phys.* 8 (1975) 2640.
- 19) W.R. Johnson, K.R. Cheng, K.N. Hwang, M. Le Dourneuf, *Phys. Rec. A22* (1980) 989.
- 20) D. Dill, *Phys. Rev. A7* (1973) 1976.
- 21) C.M. Lee, *Phys. Rev. A10* (1974) 1598.
- 22) U. Heinzmann, *J. Phys. B: Atom. Molec. Phys.* 13 (1980) 4353.
- 23) C.M. Lee, R.H. Pratt, *Phys. Rev. A12* (1975) 1825.
- 24) A.K. Pradhan, *Phys. Rev. Lett.* 32 (1983) 84. 47 (1981) 79.
- 25) Jia-Ming Li(C.M. Lee), *Acta Physica Sinica* 32 (1983) 84.
- 26) Ch. Jungen, D. Dill, *J. Chem. Phys.* 73 (1980) 3338.
- 27) Ch. Jungen, A. Giusti-Suzor, in: *Recent Developements in Electron-atom and Electron-molecule Collision Process*, ed. W. Eissner, (daresbury Laboratory Report DL/SC/R18, 1982).
- 28) C.M. Lee, *Phys. Rev. A16* (1977) 109.
- 29) A. Giusti, *J. Phys. B: Atom. Molec. Phys.* 13 (1980) 3867.
- 30) P.G. Burke, A. Hibbert, W.D. Robb, *J. Phys. B: Atom. Molec. Phys.* 4 (1971) 153.
- 31) K.A. Berington, P.G. Burke, J.J. Chang, A.T. Chiver, W.D. Robb, K.T. Taylor, *Comp. Phys. Comm.* 8 (1974) 149.
- 32) Zhong-Xin Zhao, Jia-Ming Li(C.M. Lee), *Chinese Phys. Lett.* 2 (1985) XXX.
- 33) H. Bethe, *Ann. Physik* 5(1930) 325.
- 34) M. Inokuti, *Rev. Mod. Phys.* 43 (1971) 279.
- 35) Bo-Gang Tian, Jia-Ming Li(C.M. Lee), *Acta Physica Sinica* 33 (1984) 1401.
- 36) Xiao-Chuan Pan, Jia-Ming Li(C.M. Lee), *Acta Physica Sinica* 34 (1985) XXXX.
- 37) U. Fano, J.W. Cooper, *Rev. Mod. Phys.* 40 (1968) 441.
- 38) A. Msezane, S.T. Manson, *Phys. Rev. Lett.* 35 (1975) 364, *ibid.* 48 (1982) 473.
- 39) Xiao-Ling Liang, Jia-Ming Li(C.M. Lee), *Acta Physica Sinica* 34 (1985) XXXX.
- 40) M.S. Wang, R.H. Pratt, *Phys. Rev. A29* (1984) 174.
- 41) N.S. Kopeika, R. Shuker, Y. Yerachmiel, Y. Gabai, C.S. Ih, *Phys. Rev. A28* (1983) 1517.
- 42) K.H. Johnson, *Scattered-wave Theory of the Chemical Bond*, in: *Advances in Quantum Chemistry*, Vol. 9, ed. P.O. Lowdin (academic Press, New York, 1973) 143.
- 43) Xiao-Ling Liang, Xiao-Chuan Pan, Jia-Ming Li(C.M. Lee), *Chinese Phys. Lett.* (to be published).
- 44) Xiao-Chuan Pan, Xiao-Ling Liang, Jia-Ming Li(C.M. Lee), *Acta Physics Sinica* (to be published).
- 45) Jia-Ming Li(C.M. Lee), Vo Ky Lan, *Commun. in Theo. Phys. (Beijing, China)* 2 (1983) 1175.
- 46) J.L. Dehmer, D. Dill, *Shape-resonance-enhanced Nuclear Motion Effects in Electron-molecule Scattering and Molecular Photoionization*, in: *Atomic and Molecular Collisions, Proceedings of the XIth International Conference on the Physics of Electronic and Atomic Collisions*, Kyoto, 1979, eds. N. Oda and K. Takayanagi (North-Holland, Amsterdam, 1980) 195-208.
- 47) J. Stohr, F. Sette, A.L. Johnson, *Phys. Rev. Lett.* 53 (1984) 1684.
- 48) F. Sette, J. Stohr, E.E. Kollin, D.J. Dwyer, J.L. Gland, J.L. Robbins, A.L. Johnson, *Phys. Rev. Lett.* 54 (1985) 935.
- 49) C.M. Lee, *Phys. Rev. A11* (1975) 1692.
- 50) C.H. Greene, A.R.P. Rau, U. Fano, *Phys. Rev. A26* (1982) 2441.
- 51) D.A. Harmin, *Phys. Rev. A30* (1984) 2413.
- 52) L.A. Bloomfield, R.R. Freeman, W.E. Cooke, J. Boker, *Phys. Rev. Lett.* 53 (1984) 2234.

MECHANISMS OF ATOMIC AND MOLECULAR AUTOIONIZATION

Joseph BERKOWITZ

Argonne National Laboratory, Physics Division, 9700 South
Cass Ave., Argonne, IL 60439 U.S.A.

I. AUTOIONIZATION IN ATOMS

It seems singularly appropriate that we should be discussing progress in our understanding of autoionization just 50 years since Beutler's⁽¹⁾ and Fano's⁽²⁾ first papers on this subject. This early work concerned the noble gases Ar, Kr and Xe. In each of these atoms, five optically allowed Rydberg series are observed, three converging to the ionic ground state $2p_{3/2}$, and two (one s-like and the other d-like) converging to the excited ionic state $2p_{1/2}$. These latter two, being degenerate with an ionization continuum, can and do autoionize, the s-like series giving rise to very sharp resonance structure and the d-like series to very diffuse autoionizing structure. When we examined Ne⁽³⁾, we found both s-like and d-like autoionizing series to have about the same width, which was in fact the instrumental resolution width. These experimental observations are summarized in Fig. 1.

The autoionization resonance structure in Ne was subsequently studied theoretically⁽⁴⁾ (using the relativistic random phase approximation, RRPA, and multichannel quantum defect theory, MQDT) and experimentally⁽⁵⁾, using a dye laser to excite the autoionizing states from pre-excited metastable levels. Both of these investigations concluded that the autoionization structure in Ne was sharp for the s-like and d-like resonances, the "d's" being even narrower than the "s's".

About this time, we began a series of experiments on the photoionization of open-shell atoms. We were motivated partly by two calculations of resonance structure in atomic Cl, one by the R-matrix method⁽⁶⁾ and the other by diagrammatic many-body perturbation theory (MBPT).⁽⁷⁾ We also felt that restricting our attention to the closed-shell atoms (which are much easier to handle both experimentally and theoretically) might limit our perspective, since at least 75% of the periodic chart involves open-shell atoms. Our experimental arrangement for studying atomic Cl is shown schematically in Fig. 2. In essence, it involves a microwave discharge in pure Cl₂, a fast flow system, a coating to retard recombination of the atomic Cl which is generated, and a sampling orifice. Our first results⁽⁸⁾ on atomic Cl are shown in Fig. 3.

The configuration of Cl⁺ (and in general, all the halogen species, X⁺) is ... np⁴, which gives rise to the states $3p_{2,1,0}$; $1d_{2,1,0}$; and $1s_0$. There are Rydberg series converging to each of these states, and those converging to the higher ionization potentials may autoionize.

Let us focus our attention on the series converging to $1d_{2,1,0}$. The one-electron optical selection rules allow for s-like and d-like Rydberg electrons which, when combined with the ion core, give rise to $2D$

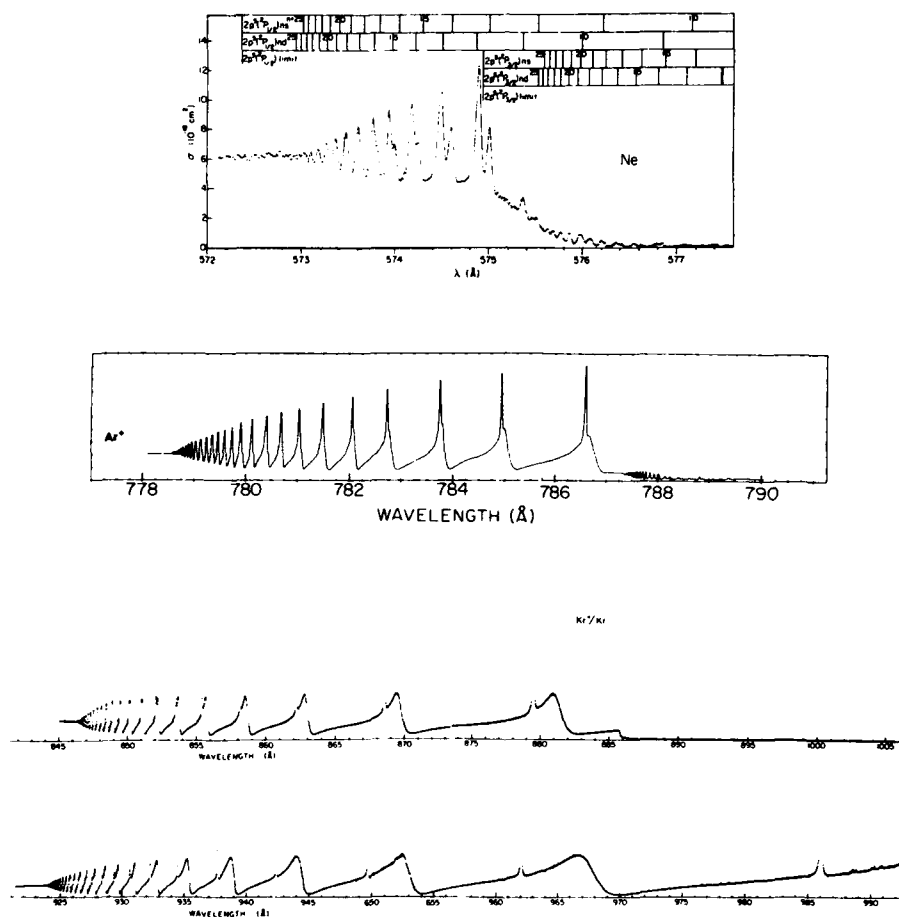


Figure 1

Autoionization in Ne, Ar, Kr and Xe between the $2P_{3/2}$ and $2P_{1/2}$ ionic states. Attributions to the individual spectra are given in ref. 18.

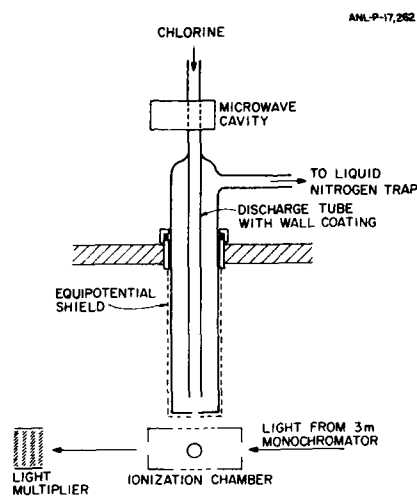
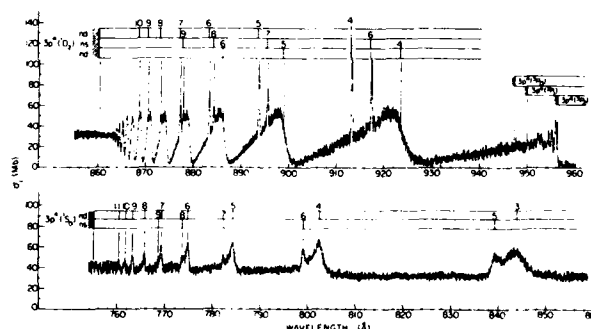


Figure 2

Schematic illustration of the atomic chlorine source and the photoionization region.



selection rule eliminates $2F$ and $2G$ from further consideration. Thus, we anticipate four autoionizing series in this energy region. Three are apparent - one broad and two narrow. By quantum defect continuation from the previously known discrete spectrum, we can identify one of the narrow series as "s" - like, the other two obviously being d-like.

In Fig. 4, we compare the experimental data with the diagrammatic MBPT calculations of Brown, et al.⁽⁷⁾ In general, the agreement is quite good, but one narrow series observed experimentally is absent in the calculated spectrum. We now know which series this is, and why it is absent. Autoionization is a process occurring in field-free space, and certain quantum properties, such as parity and total angular momentum, must be preserved. In addition, if Russell-Saunders coupling is rigorously obeyed, both orbital angular momentum and multiplicity must be preserved. It can be seen that the continuum between the $3p_2$ and $1d_2$ ionic states contains the P and D presentations but not an S representation. Hence, the $2S$ series should not autoionize if a rigorous L-S coupling scheme holds, but can achieve some probability as a result of spin-orbit coupling. Since the only competitive process is radiative emission, which is much slower, autoionization is experimentally observed for the $2S$ series. The diagrammatic MBPT calculations also reveal that the broad resonance is a composite of the d-like $2P$ and $2D$ series.

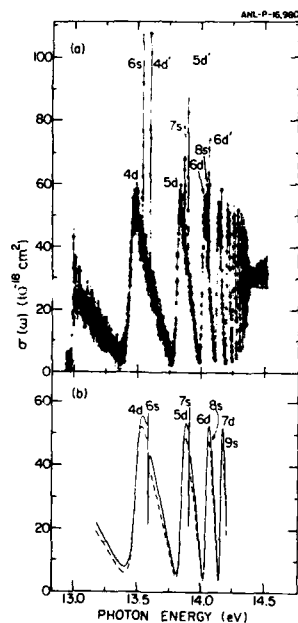
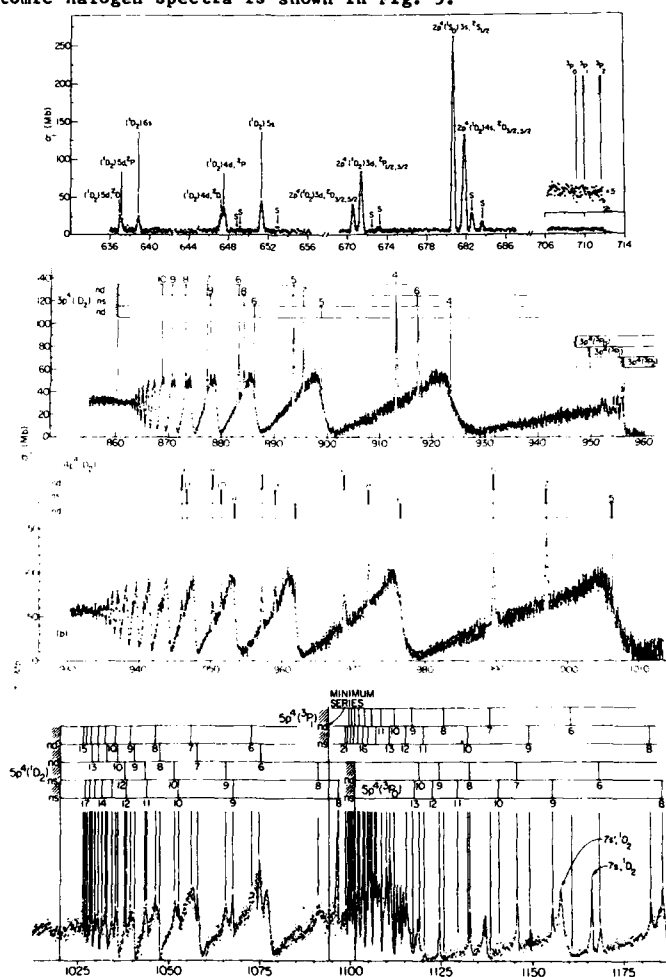


Figure 4

Comparison of experiment (top) and calculation (bottom) for autoionization of atomic chlorine. Experimental data from ref. 8, calculation from ref. 7.

In conclusion, all four series anticipated are observed. The s-like one is sharp, the d-like ones are broad except for one, which is itself forbidden in zeroth order.

Buoyed by our good fortune in obtaining the atomic chlorine photoionization spectrum, we decided to tackle the other halogens. Fluorine presented a formidable experimental problem, which I do not have time to detail here. We had previously generated and studied atomic iodine by a high temperature vaporization method.⁽⁹⁾ A corresponding portion of each of the atomic halogen spectra is shown in Fig. 5.



At this point, we began to examine what was already known in other columns of the periodic chart. Fig. 6 displays earlier work from our laboratory on atomic oxygen⁽¹⁰⁾ and atomic tellurium.⁽⁹⁾ Oxygen has only narrow resonances, tellurium broad as well as narrow ones. We wanted to obtain a spectrum of atomic sulfur, to test the generality of the apparent trend. We knew that vaporization of sulfur produces many polyatomic species, but not atomic sulfur. We have considered various schemes for generating atomic sulfur, and finally found one that produced the desired results. A viewgraph of our preliminary spectrum will be shown at the conference. The spectrum displays broad "d" and sharp "s" resonances.

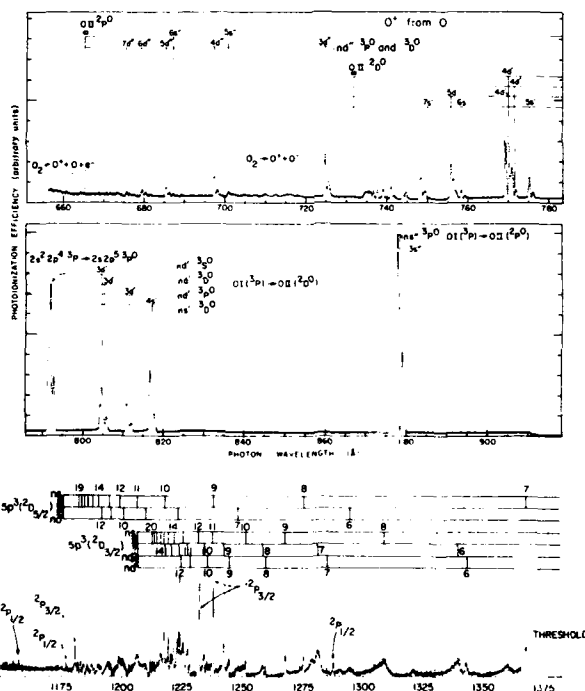


Figure 6

Autolization in atomic oxygen and atomic tellurium.
O from ref. 10;
Te from ref. 9

Column 1 of the periodic chart can give rise to autoionization structure by excitation from the inner $(n-1)$ p orbital. Photoabsorption studies of this region in atomic sodium⁽¹¹⁾ and atomic cesium⁽¹²⁾ are shown in Fig. 7. It appears that sodium has narrow resonances, and cesium broad resonances for the d-like features. Hence, there seems to be a clear demarcation in resonance behavior between light elements of the periodic chart (which we refer to for simplicity as "first row elements") and heavier elements of the same column.

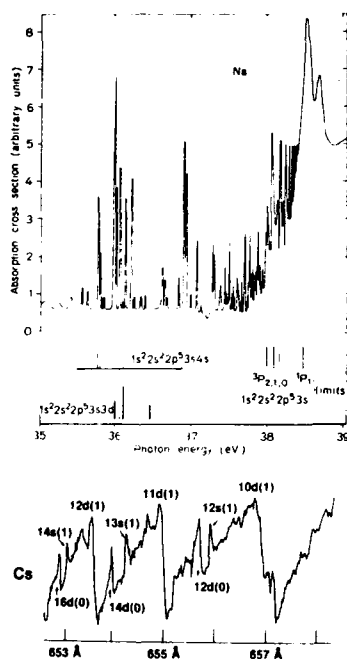


Figure 7

Photoabsorption spectra of atomic sodium (top) and atomic cesium (bottom) in the corresponding wavelength regions where inner p-shell absorption occurs. Na from ref. 11; Cs from ref. 12.

In an elegant series of experiments which bear on the present discussion, McIlrath, Lucatorto and collaborators⁽¹³⁾ have obtained the photoabsorption spectra of the isoelectronic species Xe, Cs^+ and Ba^{++} in wavelength regions corresponding to autoionization between the $5p^5\ ^2P_{3/2}$ and $5p^5\ ^2P_{1/2}$ limits. We have already seen the broad d-like resonance in Xe in this region. They find that the corresponding resonance in Cs^+ , though still much broader than the s-like resonance, is narrower than in Xe, and in Ba^{++} it is quite sharp. These two rather different sets of experiments appear to be telling us that a more compact ion core produces

narrow d-like resonances (as in Ba^{++} and the "first row elements") and a more diffuse ion core gives rise to broad d-like resonances. The matrix element responsible for the electronic autoionization,

$$V_E \sim \left\langle \psi_f \left| \frac{e^2}{r_{ij}} \right| \psi_i \right\rangle$$

and the width $\Gamma \sim |V_E|^2$ involve interaction between the Rydberg electron and the ion core, and hence it is not surprising that a more diffuse core will result in a larger interaction. There have been several attempts to parametrize this behavior. Our initial approach was to emphasize the proximity of the unoccupied d orbital in second row and heavier elements. If we wish to describe a polarizable ion core in perturbation theory, we can include low-lying excited states, and the nearby unfilled d-orbital is a particularly attractive candidate. For Ar^+ , Kr^+ and Xe^+ , this excitation energy is $\sim 132,000$, $\sim 120,000$ and $\sim 96,000 \text{ cm}^{-1}$, respectively whereas for Ne^+ it is $\sim 279,000 \text{ cm}^{-1}$. Similarly, for Ca^+ , Br^+ and I^+ , it is $\sim 110,000$, $\sim 112,000$ and $\sim 86,000 \text{ cm}^{-1}$, whereas for F^+ it is $\sim 231,000 \text{ cm}^{-1}$. One can see such an influence in the isoelectronic sequence Xe , Cs^+ and Ba^{++} as well - $\sim 96,000$, $\sim 130,000$, $\sim 160,000$ respectively - but this seems to be too crude a measure of the observed variation in resonance width. McIlrath, Lucatorto and collaborators⁽¹³⁾ have focussed their attention on the effective potential, the sum of the attractive Coulomb potential and the centrifugal potential. They note that the two effects nearly cancel in Xe , producing a long, very shallow potential plateau. In this circumstance, they argue that⁽¹³⁾ "a modest spin-orbit interaction has a large effect on the mixing of states and produces a strong autoionization rate." By contrast, in Cs^+ and Ba^{++} "the Coulomb attraction is significantly larger, eliminating the near cancellation with the centrifugal term, and the effect of the spin-orbit interaction is measurably reduced."

Both explanations are qualitatively in accord with the experimental observations, and both have modest quantitative predictability, but in this observer's judgment a more finely tuned parameter would be desirable to give a more quantitative measure of these resonance widths.

II. AUTOIONIZATION IN MOLECULES

1. At the 6th ICPEAC, 16 years ago, I had the opportunity to give an invited paper on some early studies of autoionization in molecules. In that paper, I noted the contrasting behavior in the decay of autoionizing peaks in N_2 and H_2 . For N_2 , the data in most cases seemed to be interpretable in terms of an electronic autoionization matrix element, (configuration interaction) as it is in atoms. This mechanism implies that relative transition probabilities connecting the quasi-discrete state and the final ionic state are dominated by Franck-Condon factors connecting these states. By contrast, the autoionization mechanism in H_2 (referred to as vibrational autoionization) involves a breakdown of the Born-Oppenheimer approximation, and transfer of vibrational energy in the molecular ion core to the Rydberg electron. For the latter case, a propensity rule was derived⁽¹⁴⁾ $\text{Prob}(\Delta v = -1 \text{ transitions}) \gg \text{Prob}(\Delta v = -2), \text{ etc.}$ Since that time, it has been observed that near zero energy electrons are produced in some autoionization processes which cannot readily be explained by either of the above mechanisms.⁽¹⁵⁾

More recently, White (16) has examined autoionization in $\text{HC}\lambda$, which is thought to be a good test case for electronic autoionization. The agreement between observed relative vibrational intensities and Franck-Condon factors is fair, and may be improved with better choices of internuclear distances for quasi-discrete states and better vibrational wave functions.

During this period, multichannel quantum defect theory has been applied to molecular autoionization. To explain some of the autoionization in NO , which appears to be vibrational autoionization but departs significantly from the $\Delta v = -1$ propensity rule, a satisfactory description was found (17) by including a predissociating state which couples to both the quasi-discrete Rydberg state and to the ionization continuum.

About one year ago, we chanced upon an autoionization process which does not seem to be explicable by any of the above theories. It involves the molecule PF_3 , which is pyramidal in its neutral ground state, like NH_3 , PH_3 and NF_3 . In each of these cases, the removal of the least bound electron has little effect on bond strengths, but opens up the pyramid. Thus, the ground state of NH_3^+ is planar, PH_3^+ has a very low barrier to inversion that supports one vibrational level, and NF_3^+ a somewhat higher barrier that is nevertheless surmounted in the Franck-Condon region. PF_3^+ has a lower barrier than neutral PF_3 , but the ion is still distinctly pyramidal.

The photoabsorption and photoionization spectra of NH_3 have been extensively investigated. (18) Prominent Rydberg progressions converging to the ionic ground state are observed in photoabsorption, but are largely absent in photoionization, implying that these quasi-discrete states decay predominantly by predissociation. We have examined the corresponding regions of PH_3 and NF_3 by photoionization, and there is very little evidence of resonance structure. Since the Rydberg-like quasi-discrete states are almost certainly present here as well, it seems fair to conclude that predissociation is the dominant mechanism in these molecules. Hence, we were surprised to find resonant autoionization structure when we examined the threshold region of PF_3 by photoionization mass spectrometry. (19) (See Fig. 8). In this long progression, stronger

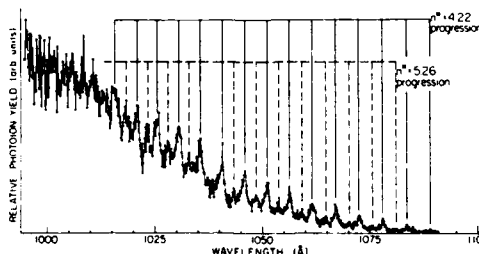


Figure 8

Photoionization yield curve of PF_3 in the threshold region. The autoionization peaks are assigned to vibrational components of two members of a Rydberg series.

and weaker peaks appear to alternate. The average spacing between stronger peaks is 474.7 cm^{-1} , that between weaker peaks, 478.4 cm^{-1} . In 1972, Maier and Turner⁽²⁰⁾ recorded the photoelectron spectrum of the first band of PF_3^+ , and reported $470 \pm 80\text{ cm}^{-1}$ as the average spacing of a long progression. Still earlier, Humphries, et al.⁽²¹⁾ had studied the absorption spectrum of PF_3 below the ionization threshold. They identified two progressions, one labelled "1405Å" with an average spacing of 460 cm^{-1} , the other labelled "1212Å" with an average spacing of 461 cm^{-1} .

The "1405Å" and "1212Å" bands, and the "strong" and "weak" autoionization resonances can be shown to be successive members of a Rydberg series converging to the ionic ground state of PF_3^+ . Each Rydberg member has an extended vibrational progression in the inversion bending mode. When a consistent quantum defect is obtained for each of these levels, we are drawn to the conclusion that Δv must be at least 13 in this autoionization process, which appears to be vibrational (i.e. the Rydberg series are converging to the ionic ground state).

Although we cannot be certain at this time that predissociation can occur and have a substantial unimolecular rate constant in this energy region of PF_3 , the circumstantial evidence points to this conclusion. We know that predissociation occurs at a rather rapid rate in NH_3 , PH_3 and NF_3 , and even in PF_3 the "1405Å" and "1212Å" bands are diffuse. Therefore, it does not seem likely that autoionization is observed in PF_3 because the competing rates are extremely slow. One way of stretching the propensity rule is to consider a sequence of transitions within the Rydberg manifold, each one of which adheres to the propensity rule, until finally a sufficient n^* is reached to permit ionization with $\Delta v = -1$. It seems unlikely that this multiplicative process would be able to compete with a strong predissociation.

The effective mechanism for promoting the autoionization in PF_3 could conceivably be the coupling of (pre)dissociation with autoionization, analogous to the description used to explain vibrational autoionization in NO. One might expect such a mechanism to be localized around the energy ranges and configurations where curve crossing occurs. The appearance of the autoionization structure in PF_3 is broad ranged, suggesting that it is occurring with almost equal facility over many vibrational levels and at least two Rydberg members.

It is not yet clear whether the PF_3 autoionization can be accommodated within the existing theories of autoionization or that a new formulation is required. Two views recently expressed by theorists at a Workshop on Autoionization at Argonne were:

1. That the propensity rule is more notorious in its violation than in its being obeyed.
2. That polyatomic molecules represent a special class, for which a new formulation is required.

ACKNOWLEDGEMENT

The experimental work from our laboratory presented here on the atomic halogens and sulfur involves the dedicated effort of my collaborators, Branko Rušćić, John Greene and Stephen Gibson.

This research was supported by the U.S. Department of Energy (Office of Basic Energy Sciences) under contract W-31-109-ENG-38.

REFERENCES

- 1) H. Beutler, *Z. Phys.* 93, 177 (1935).
- 2) U. Fano, *Nuovo Cimento* 12, 156 (1935).
- 3) K. Radler and J. Berkowitz, *J. Chem. Phys.* 70, 216 (1979).
- 4) W. R. Johnson and M. LeDourneuf, *J. Phys. B* 13, L13 (1980).
- 5) J. Ganz, A. Siegel, W. Bussert, K. Harth, M.-W. Ruf H. Hotop, J. Geiger and M. Fink, *J. Phys. B* 16, L569 (1983).
- 6) M. Lamoureux and F. Combet-Farnoux, *J. Phys. Paris* 40, 545 (1979).
- 7) E. R. Brown, S. L. Carter and H. P. Kelly, *Phys. Rev. A* 21, 1237 (1980).
- 8) B. Rušić and J. Berkowitz, *Phys. Rev. Lett.* 50, 675 (1983).
- 9) J. Berkowitz, C. H. Batson and G. L. Goodman, *Phys. Rev. A* 24, 149 (1981).
- 10) P. M. Dehmer, J. Berkowitz and W. A. Chupka, *J. Chem. Phys.* 59, 5777 (1973).
- 11) H. W. Wolff, K. Radler, B. Sonntag and R. Haensel, *Z. Phys.* 257, 353 (1972).
- 12) V. Kaufman, J. Sugar, C. W. Clark and W. T. Hill, III, *Phys. Rev. A* 28, 2876 (1983).
- 13) T. J. McIlrath and T. B. Lucatorto, "Techniques for Studying Autoionization in Isoelectronic and Isonuclear Sequences", in Workshop on Some Aspects of Autoionization in Atoms and Small Molecules held at Argonne National Laboratory on May 2-3, 1985. Proceedings to be published. See also W. T. Hill, III, K. T. Cheng, W. R. Johnson, T. B. Lucatorto, T. M. McIlrath and J. Sugar, *Phys. Rev. Lett.* 49, 1631 (1982).
- 14) R. S. Berry, *J. Chem. Phys.* 45, 1228 (1966).
- 15) T. Baer, P. M. Guyon, I. Nenner, A. Tabché-Fouhaillé, R. Botter, L. F. A. Ferreira and T. R. Govers, *J. Chem. Phys.* 70, 1585 (1979).
- 16) M. G. White and J. R. Grover, "Photoelectron Studies of Autoionizing Rydberg States in HC_2 ", presented at Workshop on Some Aspects of Autoionization in Atoms and Small Molecules at Argonne National Laboratory, May 2-3, 1985. Proceedings to be published.
- 17) A. Giusti and Ch. Jungen, Abstracts of the XII ICPEAC, Gatlinburg, Tenn. (1981), p. 71. See also A. Giusti-Suzor and Ch. Jungen, *J. Chem. Phys.* 80, 986 (1984).
- 18) See, for example, J. Berkowitz, "Photoabsorption, Photoionization and Photoelectron Spectroscopy", Academic Press, N.Y. (1979), pp. 128-130.

- 19) J. Berkowitz and J. P. Greene, *J. Chem. Phys.* 81, 4328 (1984).
- 20) J. P. Maier and D. W. Turner, *J. Chem. Soc. Faraday Trans. 2* 68, 711 (1972).
- 21) C. M. Humphries, A. D. Walsh and P. A. Warsop, *Discuss. Faraday Soc.* 35, 148 (1963).

CLASSIFICATION OF DOUBLY EXCITED STATES

C. D. LIN

Department of Physics, Kansas State University, Manhattan, Kansas, U.S.A.

Based upon the analysis of electron correlations in hyperspherical coordinates, a classification scheme for all doubly excited states of two-electron atoms is presented. A set of correlation quantum numbers, K , T , and A , is introduced. By projecting the two-electron wave functions onto the body-frame of the atom, the quantum numbers K , T and A can be related, respectively, to the vibrational, rotational and stretching modes of a triatomic molecule. The isomorphic correlations of states with identical correlation quantum numbers are shown to be the underlying reason for the existence of supermultiplet structure of doubly excited states.

1. INTRODUCTION

Microscopic many-body systems are often adequately described in the independent-particle approximation. In the case of atoms, the Hartree-Fock model or its equivalents are known to describe a wealth of atomic properties. Since the identification of doubly excited states of He in 1963^[1], it has been recognized that understanding of these states requires a careful examination of the correlation of two excited electrons and a drastic new approach different from the independent particle approximation is needed.

The conventional configuration-interaction (CI) method^[2] and its variants are adequate in predicting accurate position and width of individual doubly excited states, but it fails to provide any insight into the correlated motion of the two electrons. The results of the CI calculation are also often difficult to understand. As an example, consider the first few lowest $1p^o$ doubly excited states of He below the $\text{He}^+(N=3)$ threshold. According to the independent electron picture, one would expect that the wave functions of the first two lowest states are linear combinations of $3s3p$ and $3p3d$. This is the case for the lowest state. However, from a limited C.I. calculation, as shown in Table I, one can see that the second lowest state is mostly a linear combination of $3s4p, 3p4s, \dots$ etc., rather than a linear combination of $3s3p$ and $3p3d$. In fact, it is the third lowest state which is predominantly the linear combination of $3s3p$ and $3p3d$. This example illustrates that the results from

Table I. C.I. coefficients of the first three lowest doubly excited states of He^1P below the $\text{He}^+(N=3)$ threshold.

State	Energy (Ry)	3s3p	3p3d	3s4p	3p4s	3p4d	3d4p	3d4f
1	-0.667	0.683	0.616	-0.127	-0.172	-0.239	-0.203	-0.104
2	-0.563	-0.003	-0.005	0.630	-0.630	0.330	-0.304	0.068
3	-0.554	0.503	-0.557	-0.226	-0.317	-0.054	0.231	0.476

CI calculation is often unexpected, and it also exemplifies the limitation of the independent particle model where all information about correlation is contained awkwardly in the numerical coefficients.

Another important feature of doubly excited states has been revealed in the photoionization of He near the $N=3,4$ and 5 limits of He^+ . According to the simple counting, one would expect that there are 5, 7 and 9 series of doubly excited states leading to the respective $N=3,4$ and 5 thresholds. Experimental measurement by Woodruff and Samson^[3], as well as a recent calculation by Salomonson, Carter and Kelly^[4] clearly showed that there is only one channel which is predominately excited. The rest of the channels are not observed. Thus there is evidence of quasi-selection rules which forbid some classes of doubly excited states from being populated in a given collision condition. The quasi-selection rule then has to do with the dynamic aspect of the correlated electronic motion.

A complete classification scheme of doubly excited states should be capable of providing at least qualitative interpretation and prediction of the major properties of doubly excited states. The new set of quantum numbers pursued should also give qualitative pictures of the correlated motion of the two electrons. It is also desirable that this new scheme can incorporate the independent-electron model as the limiting case, and in the end, a computational procedure can be developed where these quantum numbers can be examined.

This report deals with the classification scheme of doubly excited states based on the analysis of electron correlations in hyperspherical coordinates.^[5,6] In developing this scheme, the understanding from the group-theoretical work of Herrick and co-workers^[7] and the model study of

Berry and co-workers^[8] has played an important role. I will report the classification scheme and present some new understanding of the correlation quantum numbers based on the analysis of the wave functions on the body-frame of the atom. This latter work is a collaboration with S. Watanabe.

II. CLASSIFICATION OF DOUBLY EXCITED STATES

(a) The classification scheme

In the present classification scheme a given state is designated by the notation ${}_N(K, T)_N^A 2S+1 L^\pi$, where L , S and π are the usual quantum numbers, N is the principal quantum number of the inner electron and n that of the outer electron. The correlation quantum numbers K and T , first introduced by Herrick and Sinanoglu,^[9] are used to describe the angular correlation. To incorporate the correlated radial motion between the two electrons, a radial correlation quantum number A was introduced.^[5,6] The allowable values of A are $+1$, -1 and 0 . All singly excited states have little radial correlation, and they have $A=0$.

The enumeration of possible K and T quantum numbers for a given N , L , and π has been given by Herrick and Sinanoglu. They are

$$\begin{aligned} T &= 0, 1, 2, \dots, \min(L, N-1) \\ K &= N-1-T, N-3-T, \dots, -(N-1-T) \end{aligned} \quad (1)$$

$T = 0$ is not allowed if $\pi=(-1)^{L+1}$. The radial correlation quantum number A is not independent of K . It is given by the following simple relations

$$\begin{aligned} A &= \pi(-1)^{S+T} = \pi(-1)^{S+N-K+1} & \text{if } K > L-N \\ A &= 0 & \text{if } K \leq L-N \end{aligned} \quad (2)$$

With the relations (1) and (2), all the correlation quantum numbers for states converging to a hydrogenic limit N can be assigned. The more precise definition of these quantum numbers will be described below. Roughly, a large positive K implies that the two electrons are almost 180 degrees from each other. If $K=0$, the two electrons are at about 90 degrees to each other. Negative K implies that the two electrons are on the same side of the nucleus. For the quantum number T , a nonzero T implies classically that the orbits of the two electrons are not coplanar, while $A=+1$ implies in-phase radial oscillation between the two electrons and $A=-1$ implies out-of-phase radial oscillation.

These correlation quantum numbers can be understood qualitatively from various approaches. In this talk, I will concentrate on the geometrical

representation of electronic correlations. To this end, it is most convenient to study the problem in hyperspherical coordinates.

(b) Analysis in hyperspherical coordinates

To examine the details of radial and angular correlations, we study the two-electron wave functions in hyperspherical coordinates. From the independent particle coordinates (r_1, ϕ_1) and (r_2, ϕ_2) , we replace r_1 and r_2 by a hyperradius R and a hyper-angle α :

$$R = (r_1^2 + r_2^2)^{1/2} \quad (3)$$

$$\alpha = \arctan(r_2/r_1)$$

In this coordinate system, there is only one radial coordinate R and the rest are the five angles, denoted collectively by $\Omega = \{\alpha, \phi_1, \phi_2\}$. Since correlation is a property of the relative motion between two electrons, the five angles can be further separated into three Euler angles describing the rotation of the whole atom plus two angles α and θ_{12} , the former describing radial correlation and the latter describing angular correlation.

One important underlying approximation in the hyperspherical approach is that as the atom expands or contracts, its correlation pattern changes only gradually. This leads to the quasi-separability of the two-electron wave functions in hyperspherical coordinates. (It has been shown that the conventional C.I. wave functions also exhibit approximate separability if the functions are expressed in hyperspherical coordinates, see Ref. 10)

In this coordinate system, the Schroedinger equation for the two-electron systems in reduced units is given by

$$\left[-\frac{d^2}{dR^2} + \frac{\Lambda^2 + 15/4}{R^2} + \frac{2C}{R} - 2E \right] (R^{5/2}\psi) = 0 \quad (4)$$

where Λ^2 is the grand angular momentum operator and C is an effective charge which includes electron-nucleus and electron-electron interactions,

$$C = -\frac{1}{\cos\alpha} - \frac{1}{\sin\alpha} + \frac{1/Z}{\sqrt{1-\sin^2\alpha} \cos\theta_{12}} \quad (5)$$

where Z is the charge of the nucleus.

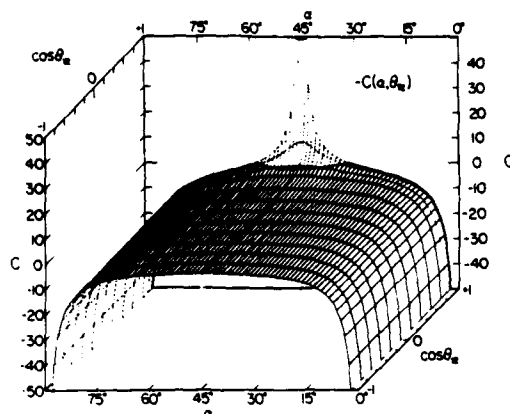


Fig. 1. Relief plot of the effective charge $C(\alpha, \theta_{12})$ with $Z=1$. The ordinates represent a potential surface in Rydberg units at $R=1$.

A surface plot of the effective charge on the two relative angles α and θ_{12} is shown in Fig.1 for H^- . We notice that the potential surface in the middle is quite flat. The two valleys near $\alpha=0^\circ$ or 90° correspond to the case when one electron is far away from the other, i.e., they correspond to the limit where the two electrons are nearly independent and where the independent particle approximation is quite adequate. The sharp spike near $\alpha=45^\circ$ and $\theta_{12}=0^\circ$ is due to the strong electron-electron repulsion when the two electrons are nearly on top of each other. In the middle part, we see there is a large flat region. The potential surface is symmetric with respect to $\alpha=45^\circ$. We will show that $A=+1$ states have an antinode at $\alpha=45^\circ$, and that $A=-1$ states have a node at $\alpha=45^\circ$. For $A=0$ states, the two particles hardly reach the plateau region and they are confined to the two valleys. Thus, states which have $A=+1$ or -1 are states lying on the top of the potential ridge, while the $A=0$ states, like singly excited states, are states confined in the valley region.

The results discussed above should come out directly from the solution of the two-electron Schrodinger equation (4). For this purpose, we solve eq. (4) in the quasi-separable approximation, i.e., we assume that the n -th state for channel μ is given by

$$\psi_\mu^n(R, \Omega) = F_\mu^n(R) \phi_\mu(R; \Omega) / R^{5/2} \sin \alpha \cos \alpha \quad (6)$$

where

$$\left[\frac{d^2}{d\alpha^2} + \frac{\tilde{I}_1^2}{\cos^2 \alpha} + \frac{\tilde{I}_2^2}{\sin^2 \alpha} + 2RC \right] \phi_\mu(R; \Omega) = R^2 U_\mu(R) \phi_\mu(R; \Omega) \quad (7)$$

and

$$\left(\frac{d^2}{dR^2} - U_\mu(R) + 2E_\mu^n\right) F_\mu^n(R) = 0 \quad (8)$$

This approach is similar to the Born-Oppenheimer approximation for diatomic molecules. Once the potential curve $U_\mu(R)$ for each channel μ is calculated, the states belonging to that channel can be easily obtained by solving the one-dimensional hyperradial equation (8).

The quasi-separability implied by eq(6) stresses the important fact that states belonging to the same channel μ have similar correlation properties. This is different from other approaches where correlation is usually examined for a single state a time. We note that the approximate selection rule for photoabsorption is a property of the whole channel, rather than that of individual states.

(c) Potential curves and correlation rules

In Fig. 2 the potential curves for the $1,3S^e$, $1,3P^o$ and $1,3D^e$ of He below the $He^+(N=3)$ are shown together with the $(K,T)^A$ labelling. Diabatic crossings

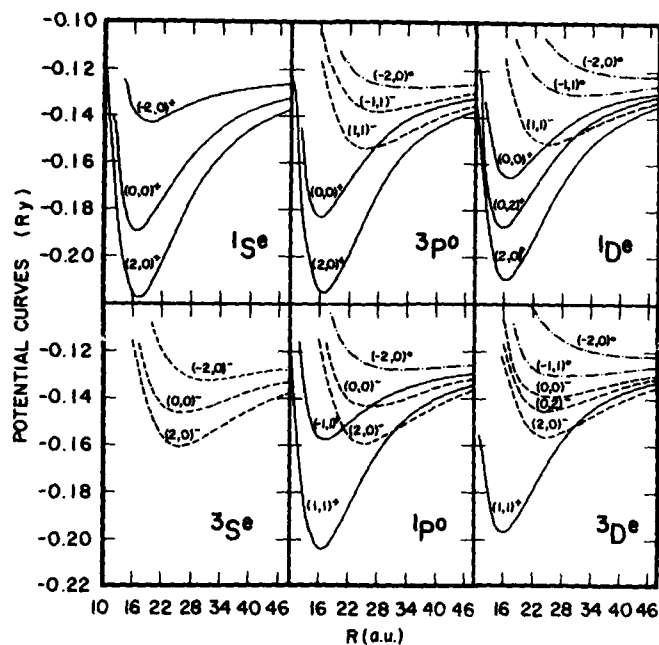


Fig. 2. Potential curves for He that converge to $He^+(N=3)$. Curves are labelled in terms of $(K,T)^A$ quantum numbers. Reduced units with $Z=1$ are used.

between different channels are evident. These crossings reflect the fact that the relative importance of radial and angular correlations changes with R . At small values of R , radial correlation is more important, thus the curves which are more attractive belong to $A=+1$, while the less attractive ones belong to $A=-1$ or 0 . For a given A , curves which have larger values of K are more attractive because of larger θ_{12} and thus less electron-electron repulsion. In the asymptotic region (large R), one electron stays inside and the other outside. In this case, radial correlation is not important and the relative asymptotic energy levels are determined by the values of K ; the larger the K is, the lower the asymptotic limit. For a given K , states with larger T are lower. Following this procedure, the quantum numbers K , T and A in the inner and asymptotic regions can be assigned. The curves shown in Fig. 2 are obtained by connecting the curves in the two regions.

We notice that the curves which are labelled by the same $(K,T)^A$ have nearly the same shape and values. This provides a first indication that the quantum numbers assigned have some physical significances. Since the quantum numbers we need are for the description of correlations, this information is implicitly contained in the angular functions $\Phi_\mu(R;Q)$.

(c) Isomorphism of electron correlations

To show that K, T and A indeed describe radial and angular correlations, we show in Fig. 3 surface charge density plots for the $(2,0)^+$ channel of $1S^e$, $3P^o$, $1D^e$ and $3F^o$ of $\text{He}(N=3)$ at $R=20$ a.u. For $L \neq 0$ channels, average over the rotations of the whole atom has been applied. We notice that all these channels have large densities near $\alpha=45^\circ$ and $\theta_{12}=180^\circ$. The surface plots show

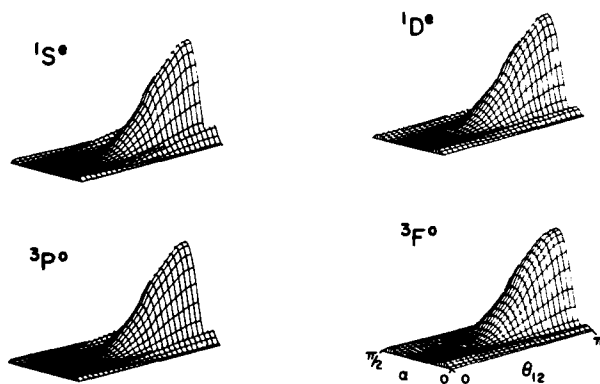


Fig. 3. Surface charge densities for the $(2,0)^+$ channels at $R=20$ for He.

little differences despite the fact that these channels have different L , S and π . The isomorphic correlations for all these channels illustrate that the correlation quantum numbers describe major features of correlations appropriately.

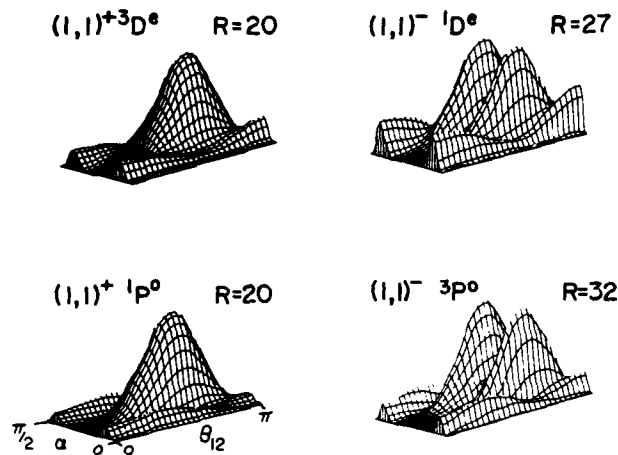


Fig. 4. Surface charge densities for the $(1,1)^+$ and $(1,1)^-$ channels at the values of R shown for He.

In another example, we show in Fig. 4 the correlation plots for the $(1,1)^+ 1P^o$, $(1,1)^+ 3D^e$, $(1,1)^- 3P^o$ and $(1,1)^- 1D^e$ of $\text{He}(N=3)$ at the values of R indicated. Notice that in this case the surface charge density peaks not at $\theta_{12}=180^\circ$ but approximately at $\theta_{12}=120^\circ$. We also notice that the '-' channels have an approximate node near $\alpha=45^\circ$. These plots illustrate the major features implied by the correlation quantum numbers K , T and A .

(d) Supermultiplet structure

One important spectral regularity from the present classification scheme is that channels which have identical (K,T) and $A=+1$ (or $A=-1$) exhibit supermultiplet structure. For intrashell states, this supermultiplet structure was pointed out by Herrick and Kellman as resembling the rotational spectra of a molecule. An example of this structure is shown in Fig. 5 for the doubly excited states of H^- below the $N=5$ threshold of H . Here only the '+' states are considered. The energy levels were obtained from the calculation of Ho and Callaway^[11]. Each state is assigned for the quantum numbers K and T following the prescription given in (1) and (2). We note that the spectra for a given (K,T) exhibit behavior similar to the rotational series of a molecule, particularly for the low-lying members.

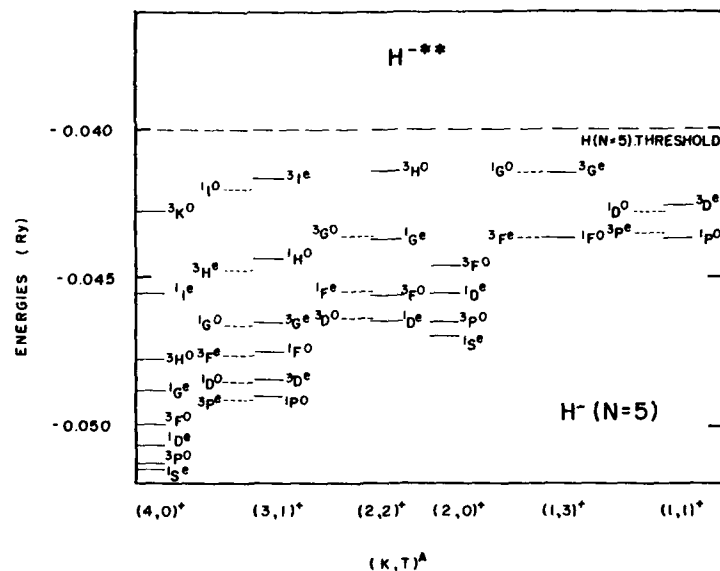


Fig. 5. Supermultiplet structure of H^- below the $H(N=5)$ limit. The energies are grouped accordingly to $(K,T)^A$. Data from Ref. 11.

The supermultiplet structure is not limited to intrashell states only. It is valid for the higher levels of each channel, as well as for the '-' channels. In Fig. 6 we show some portion of the supermultiplet structure for the doubly excited states of He below the $\text{He}^+(\text{N}=3)$ limits. The relative positions of intrashell states are repeated for the higher Rydberg states. There is also a repetition of $(\text{K},\text{T})^+$ and $(\text{K},\text{T})^-$ rotor structure. This is clearly seen in Fig. 6.

(e) Singly excited states

According to the present classification scheme, all singly excited states have $(K,T)=(0,0)$. The radial correlation quantum number is $A=+1$ for 1^1S^e , $A=-1$ for 3^1S^e and $A=0$ for all the others. Within the independent particle model the energy for $1snl\ 3^1L$ is always lower than the energy for $1snl\ 1^1L$. In terms of Pauli exchange correlations, it is easily understood that the two electrons in triplet states are kept away from each other because of identical

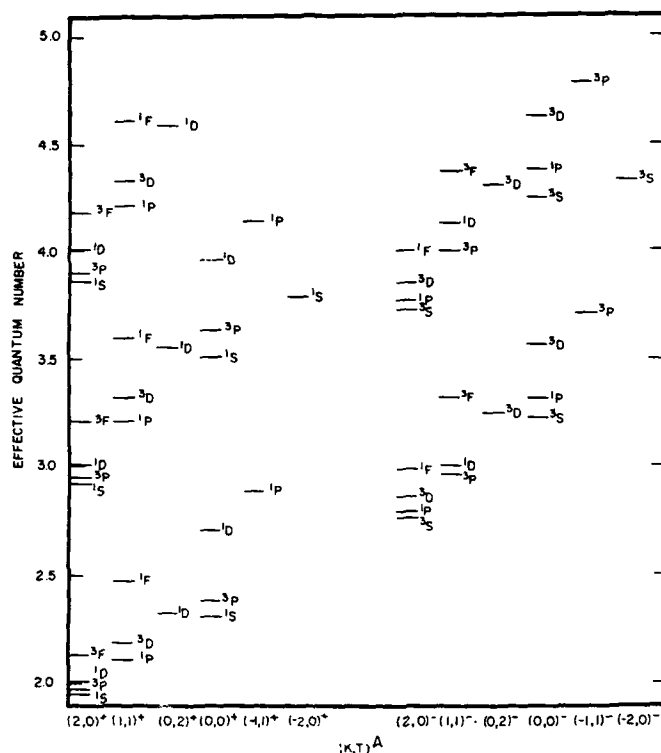


Fig. 6. Supermultiplet structure of He below the $\text{He}^+(N=3)$ limit. The energies are given in terms of effective quantum numbers N^* . Only states with parity $\pi=(-1)^L$ are given. Data from Ref. 2.

spin orientations, thus reducing the electron-electron repulsion. In hyperspherical analysis, all the $A=0$ states are confined in the two valley regions, and Pauli exchange correlations are reflected as angular correlations in that the two electrons in triplet states tend to stay away from $\theta_{12}=0^\circ$. Singlet states, because of the symmetry requirement, have larger amplitudes near $\theta_{12}=0^\circ$.

For doubly excited states that have been assigned for $A=0$, they also tend to stay in the valley region. These states do not exhibit supermultiplet structure. Instead, they behave more like singly excited states and the relative energy positions between singlet and triplet states is that triplet states are always lower. For a given N , L and parity, the number of channels with $A=0$ are the same for singlet states and for triplet states. Those with

identical (K,T) are nearly degenerate with triplet states lower than singlet states. This has been documented in Fig. 14 of Ref. 6.

III. Body-frame analysis of correlation quantum numbers and moleculelike normal modes^[12]

The quantum numbers K and T discussed above were derived originally from the group-theoretical analysis of approximate doubly excited state wave functions and later as labels for discussing the asymptotic dipole states.^[13] In the asymptotic region where one electron is far away from the other, the leading term which distinguishes the various channels of a given N manifold is the dipole interaction $2r_2 \cos \theta_{12} / r_1^2$ and the centrifugal potential l_1^2 / r_1^2 . If we neglect the latter term and diagonalize the first term in the hydrogenic basis, the new diagonal representation can be labelled by (K,T). This interpretation of K and T for labelling doubly excited states is unsatisfactory since correlation is a property of two electrons when they are close to each other. In the asymptotic region, there is also no radial correlation. To amend this situation, we introduce a radial correlation quantum number A. We also recognize that the potential surface, as shown in Fig. 1, is quite smooth along θ_{12} , and the potential is proportional to $1/R$. Thus in the quasi-separable approximation, the same quantum numbers describing angular correlations in the asymptotic region can be used to describe angular correlations in the inner region. This is the idea behind the (K,T)^A classification scheme.

The quantum numbers K, T and A used in the classification were treated as labels for correlations. We have shown that the quantum numbers do depict different correlation patterns as well as predicting several new regularities in the spectroscopy of doubly excited states. It is desirable to derive these quantum numbers directly. Since these quantum numbers are not exact, this is not straightforward. However, it is possible now to define T and A in a more rigorous way by analyzing the wave function in the body frame of the two electrons.

In the body-frame analysis, we take the interelectronic axis as the internal axis of rotation. The transformation of two-electron orbital angular momentum function from the laboratory frame to the body frame satisfies the following relationship,

$$Y_{1,1,2,LM}(\ell_1, \ell_2) = \sum_Q Y_{1,1,2,LQ}(\ell'_1, \ell'_2) D_{QM}^{(L)}(\hat{\omega}) \quad (9)$$

where (r_1, r_2) are defined in the laboratory frame and (r'_1, r'_2) in the body frame, and $D_{QM}^{(L)}$ is the rotation matrix. Suppose the wave function is known in the laboratory frame,

$$\Psi(\vec{r}_1, \vec{r}_2) = \sum_{l_1 l_2} \psi_{l_1 l_2}^L(r_1, r_2) Y_{l_1 l_2 LM}(r_1, r_2) \quad (10)$$

Using eq (9) we can rewrite (10) as

$$\Psi(\vec{r}_1, \vec{r}_2) = \sum_Q \psi_Q^L(R, \alpha, \theta_{12}) D_{QM}^{(L)}(\hat{\omega}) \quad (11)$$

where

$$\psi_Q^L(R, \alpha, \theta_{12}) = \sum_{l_1 l_2} \psi_{l_1 l_2}^L(R \cos \alpha, R \sin \alpha) Y_{l_1 l_2 LQ}(r'_1, r'_2) \quad (12)$$

and $-L \leq Q \leq L$.

From the symmetry property, one can show that under particle exchange

$$\psi_Q^L(R, \pi/2 - \alpha, \theta_{12}) = \pi(-1)^{S+Q} \psi_Q^L(R, \alpha, \theta_{12}) \quad (13)$$

We shall use a short hand notation for this phase factor:

$$A = \pi(-1)^{S+T} \quad (14)$$

where $T=|Q|$. The index A determines the reflection symmetry of the hyperradial wave function with respect to the $\alpha=\pi/4$ axis. Thus A serves as an index of radial correlation. In this analysis, it is clear that if there is only a single T component in eq(11), then A is a good quantum number. In other words, if T is a good quantum number, then A is a good quantum number.

To see how pure the quantum number T is, we display in Fig. 8 the projection of the $(1,1)_3^+ 1P^0$ channel of He onto the body-frame. The surface charge densities for each of the T=0 and T=1 component are displayed. Percentage represents the contribution to the normalization from each component. Notice that T=1 is the dominant component, and that the surface charge density for the T=1 component does exhibit an antinode at $\alpha=45^\circ$. This is consistent with the assignment of T and A quantum numbers for this channel. Admixture from T=0 represents a 10% effect here.

For a given T (and A), we can relate K to the number of nodes, n, in θ_{12} , or to the vibrational quantum number v. The detailed analysis is given elsewhere,^[12] but we can show that

$$\begin{aligned} K &= N - 2n - T - 1 \\ &= N - v - 1 \end{aligned} \quad (15)$$

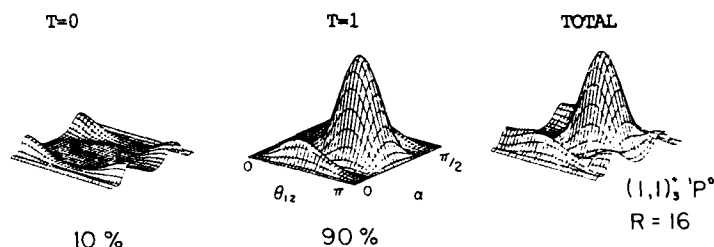


Fig. 7. Decomposition of the $(1,1)_3^+ 1P^\circ$ channel of He at $R=16$ into $T=0$ and $T=1$ components.

where v is the vibrational quantum number defined by

$$v=2n+T \quad (16)$$

When T is fixed, both K and v change in steps of 2. The vibrational quantum number (v or K) is used to label the vibrational motion in θ_{12} . In this way, we have derived the physical meaning of K, T and A quantum numbers. For a given state, if the projection of the total angular momentum onto the body frame axis has only a single T component, then T and A are good quantum numbers. The quantum number K , although it cannot be derived directly, has been shown to be related to the number of nodes in θ_{12} . It is also similarly related to the vibrational quantum number of a triatomic molecule. The rotor series arises from the breakdown of the (K, T) classification. If the states are arranged according to the number of vibrational nodes, or v , then a diamond structure, called d -supermultiplet by Herrick and Kellman, is obtained. The hierarchical order of radial (U_A), vibrational (U_K) and rotational (U_T) energies is such that

$$U_A > U_K > U_T. \quad (17)$$

The supermultiplet structure is a result of this hierarchical order. The moleculelike behavior of normal modes also are well respected if the above relation is true. This analysis allows us to unravel the different degree of the breakdown of the molecular rovibrational normal modes as well as to point out the situation where it works.

IV. Conclusions

The classification scheme presented here applies to pure two-electron atoms only. The correlation and designation of doubly excited states of other atoms are similar to what is discussed here qualitatively in the region where the two electrons are strongly correlated, but the channels are better described in the dissociated region by the independent electron picture.

The transition from the correlated limit at small R to the dissociated limit at large R , in certain circumstances, involves strong coupling between the channels. The hyperspherical method provides a well-defined computational procedure to study these problems. The structures of doubly excited states in several alkaline earth atoms and alkali negative ions have been studied in hyperspherical coordinates.^[14] Similar correlation patterns at small R have been documented. There are also studies of doubly excited states of He^- .^[15] Because the core is not spherically symmetric, the spin coupling scheme in different regions also differs. The recent study of Le Dourneuf and Watanabe^[16] on the doubly excited states of He^- showed similar classification schemes and moleculelike normal modes presented here.

Acknowledgement

Support for the work reported here has been provided by the U.S. Department of Energy, Division of Chemical Sciences. The author also acknowledges the contribution of Shinichi Watanabe on the body-frame analysis reported here.

References:

1. R.P. Madden and K. Codling, *Phys. Rev. Lett.* **10**, 516 (1963); *Astrophys. J.* **141**, 364 (1965).
2. L. Lipsky, R. Anania, and M.J. Conneely, *At. Data Nucl. Data Tables* **20**, 127 (1977). See also the references in P.G. Burke, *Advances Atomic and Mol. Phys.* **4**, pp. 173-249 ed. D.R. Bates and I. Esterman (Academic, New York, 1968).
3. Woodruff and J.A. Samson, *Phys. Rev.* **A25**, 848 (1982).
4. S. Salmonson, S.L. Carter and H.P. Kelly, *J. Phys.* **B18**, L149 (1985).
5. C.D. Lin, *Phys. Rev. Lett.* **51**, 1348 (1983).
6. C.D. Lin, *Phys. Rev.* **A29**, 1019 (1984).
7. D.R. Herrick and M.E. Kellman, *Phys. Rev.* **A21**, 418 (1980); D.R. Herrick, M.E. Kellman, and R.D. Poliak, *ibid.* **22**, 1517 (1980).
8. P. Rehmus and R.S. Berry, *Chem. Phys.*, **38**, 257 (1979); G.S. Ezra and R.S. Berry, *Phys. Rev.* **A25**, 1513 (1982).
9. D.R. Herrick and O. Sinanoglu, *Phys. Rev.* **A11**, 97 (1975).
10. C.D. Lin, *Phys. Rev.* **A27**, 22 (1983).
11. Y.K. Ho and J. Callaway, *Phys. Rev.* **A27**, 1887 (1983).
12. S. Watanabe and C.D. Lin, *Phys. Rev. A*, submitted 1985.
13. D.R. Herrick, *Phys. Rev.* **A12**, 413 (1975).
14. C.H. Greene, *Phys. Rev.* **A23**, 661 (1981); C.D. Lin, *J. Phys.* **B16**, 723 (1983).
15. S. Watanabe, *Phys. Rev.* **A25**, 2074 (1982).
16. M. Le Dourneuf and S. Watanabe (to be published).

COHERENCE EFFECTS IN ELECTRON EMISSION FROM ION-ATOM COLLISIONS

A. NIEHAUS

Fysisch Laboratorium, Rijksuniversiteit Utrecht, Princetonplein 5,
3584 CC Utrecht, The Netherlands

1. INTRODUCTION

Experimental information on a collision of microscopic particles can only be obtained indirectly, by observation of some asymptotic final state (f) for a collision system prepared in some asymptotic initial state (i). If we describe the unobserved state of the system during collision by assigning certain populations of intermediate substates (μ), (μ'), we may characterize an ion-atom collision leading to ionization by the scheme:



In cases where (i) and (f) represent complete sets of quantum numbers, the "multiple" differential cross sections $\sigma_{(f) \leftarrow (i)}$ are proportional to a coherent sum of amplitudes:

$$\sigma_{(f) \leftarrow (i)} \propto \left| \sum_{\mu} A_{f\mu i} e^{i\delta_{f\mu i}} \right|^2 \quad (b)$$

These cross sections represent the most detailed information we can possibly obtain on the transition (i) \rightarrow (f). By varying experimental conditions that define the prepared or observed state - in case of our collisions (a), for instance, the collision energy, the heavy particle scattering angle, or the electron ejection angle - there will usually arise interference effects of $\sigma_{(f) \leftarrow (i)}$, because of the well defined phase relations in the coherent sum (b) in connection with the dependence of the phases $\delta_{f\mu i}$ on the varied conditions. These interference effects then allow to obtain information on the amplitudes $A_{f\mu i}$, and on the phases $\delta_{f\mu i}$, i.e. on the collision itself. Incomplete experimental definition of states (i) and (f) leads to a partial masking of interference effects in the corresponding averaged cross sections $\bar{\sigma}_{(\bar{f}) \leftarrow (\bar{i})}$, which have to be represented by a relation

$$\bar{\sigma}_{(\bar{f}) \leftarrow (\bar{i})} = \sum_{(\bar{i})} \omega_{(\bar{i})} \sum_{(\bar{f})} \sigma_{(f) \leftarrow (i)} \quad (c)$$

where $\omega_{(\bar{i})}$ is the probability with which the state (i) is contained in the prepared mixture and where by (\bar{i}) and (\bar{f}) summation or integration over a certain regime of sets (i) and (f) is indicated. To the extent that interference effects are masked or completely averaged out, the information possibly obtainable on the collision is decreased. It is therefore the goal of experimental collision studies aimed at a clarification of collision mechanisms, to realize as complete a definition of initial and final state of the collision system as possible.

In case of collision process (a) a complete experimental definition of states (i) and (f) requires preparation and selection of well defined electronic states of the heavy particles, as well as a definition of the state of relative motion of all separated particles before and after the collision. The requirements regarding the relative motion of the particles can be met by directing a beam of ions (A^+) into a volume containing thermal target atoms

(B) at sufficiently low density to guarantee single collision conditions, and by detecting the scattered (A^+) at certain angles (θ, ϕ) in coincidence with the emitted electron at angles (ϑ, φ) . To select a certain electronic final states it is sometimes sufficient to measure the energy of the ejected electron (ϵ) or to determine the loss (or gain) Q of relative kinetic energy of the heavy particles by measuring the kinetic energy of (A^+). The situation is of course more complicated if A^+ and/or B, and/or B^+ are not in S-states, because then a complete determination requires the relative amplitudes and phases of the magnetic sublevels to be fixed.

We report here on recent progress that has been made in our group regarding measurements and interpretations of coherence effects occurring in multiple differential cross sections of the type (b)

$$\sigma_{(f)+(i)} = \sigma(\theta, \phi, \vartheta, \varphi, \epsilon, Q, E) \quad (d)$$

derived from coincidence measurements (sections 2 and 3), and of the partly averaged type (e), obtained from noncoincidence measurements (section 4 and 5).

2. EVALUATION OF M-COHERENCES FOR He^+-He -COLLISIONS

Multiple differential cross sections obtained by coincidence measurements between $\text{He}^+(1s)$ scattered into defined angles (θ, ϕ) , and electrons ejected after excitation by the target $\text{He}^{**}(2p^2)^1D$ into angles (ϑ, φ) have been reported earlier (1). Interference patterns arising as a function of (ϑ, φ) can be interpreted as representing the angular distribution of ejected electrons belonging to an excited 1D atom that has a well defined shape and orientation in space. This angular distribution is simply given by (2)

$$I(\vartheta, \varphi) = \left| \sum_M a_{LM} Y_{LM}(\vartheta, \varphi) \right|^2 \quad (e)$$

with a_{LM} the population amplitudes of the $(L = 2, M = -2, \dots, +2)$ -states of $(2p^2)^1D$. Because of the postulate of reflection symmetry, and because of the free choice of one phase of the complex amplitudes, the angular distribution is determined by the three moduli $|a_{LM}|$ and by the two relative phases $(\varphi_M - \varphi_0)$. These five quantities were determined, by fitting relation (e) to measured distributions, for several combinations of collision energy and scattering angle θ (3). The results are shown in Fig. 1: plotted are the three moduli $|D_M|$ and the two phases $(\varphi_M - \varphi_0)$, which are obtained from the $|a_{LM}|$ and the $(\varphi_M - \varphi_0)$ by rotating the quantization axis from the beam direction into the asymptotic direction of the internuclear axis after collision. As abscissa we chose the parameter (b/v) , where b is the impact parameter, obtained from the scattering angle θ , and v is the collision velocity. $(b/v)^{-1}$ may be considered as a "collision strength".

The experimental results are compared in Fig. 1 to theoretical results obtained on the basis of a rotational coupling model (3). The model is depicted in Fig. 2. The main features of the experimental data are explained by assuming a "complete" rotational coupling of the one electron molecular orbitals $2p\sigma_u$ and $2p\pi_u$ at the distance of closest approach. This leads to a two step two electron excitation sequence

$$(1s\sigma_g)(2p\sigma_u)^2 {}^2\Sigma_g \rightarrow (1s\sigma_g)(2p\sigma_u)(2p\pi_u)^2 {}^2\Pi_g \rightarrow (1s\sigma_g)(2p\pi_u)^2 {}^2\Delta_g, {}^2\Sigma_g, \quad (f)$$

and predicts for the $\text{He}(2p^2)^1D$ the values $|D_2| = 0.61$, $|D_0| = 0.5$, $|D_{\pm 1}| = 0$,

$(\varphi_2 - \varphi_0) = \pi$, $(\varphi_1 - \varphi_0) = 0$. It is seen from Fig. 1 that this prediction is approximately correct at the larger (b/v) -values. The remaining deviations are described in the model by additional couplings at large and small distances as indicated in Fig. 2.

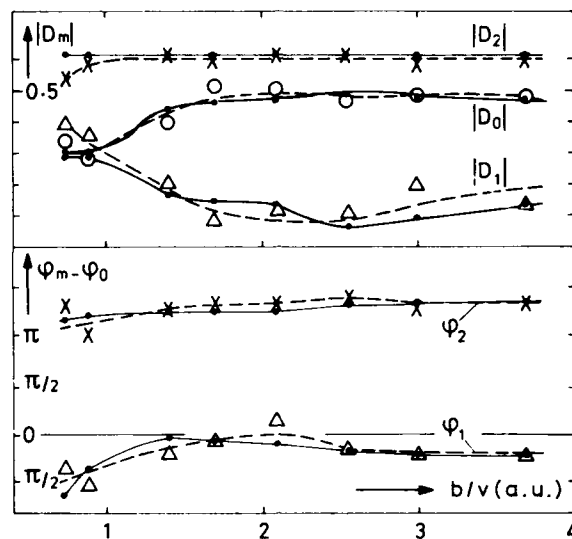


FIGURE 1

Moduli $|D_m|$ and relative phases $\varphi_m - \varphi_0$ as a function of (b/v) . Experimental data (\times Δ \circ) and calculation with model (—) (see Fig. 2). Numbers relate to coordinate frame with $z \parallel$ asymptotic internuclear axis, and $y \perp$ collision plane.

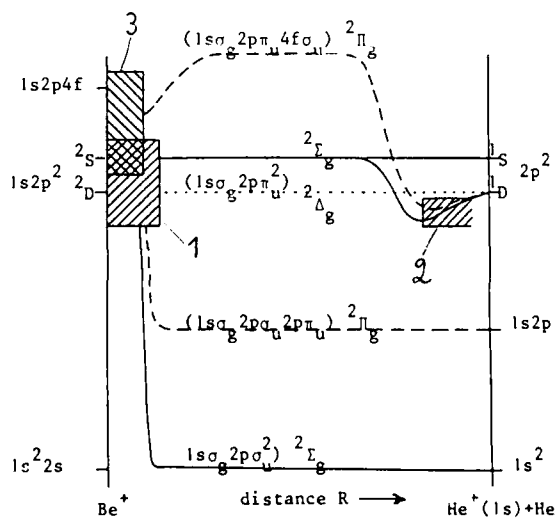


FIGURE 2

State correlation diagram depicting model used for calculations shown in Fig. 1. "Complete" rotational coupling (1) of one electron orbitals $2p\sigma_u$ and $2p\pi_u$ predicts $|D_2| = 0.61$; $|D_0| = 0.5$; $|D_1| = 0$; $\varphi_2 - \varphi_0 = \pi$.

As obvious from relation (e), the angular distribution of the ejected electron is closely connected to the "shape" and the "orientation" of the excited $(2p^2)^1D$ -atom. However, the angular distribution represents a one electron wave function with angular momentum $l = 2$, whereas the 1D -atom is represented by a two electron wave function of $L = 2$. In order to represent the shape of the 1D -atom, v.d. Straten and Morgenstern (4) have calculated its electron density, using independent $2p$ -atomic orbitals coupled to $L = 2$, for certain experimentally determined amplitudes a_{2M} . The angular part of this density is compared in Fig. 3 with the angular distribution corresponding to the same amplitudes a_{2M} . While the orientation of both, the atom and the angular distribution, is identical because it is directly determined by the a_{2M} , the shapes are different. The tilt angle γ may most conveniently be expressed in terms of moduli d_2 and d_{-2} and phases χ_2 and χ_{-2} of the $L = 2$ population amplitudes in a coordinate frame with z -axis perpendicular to the scattering plane and the x -axis parallel to the beam direction:

$$\gamma = \arctan \left\{ \frac{(d_{-2} \sin \chi_{-2} - d_2 \sin \chi_2)(d_{-2} \sin \chi_{-2} + d_2 \sin \chi_2)}{d_{-2} \sin \chi_{-2} + d_2 \sin \chi_2} \right\} \quad (g)$$

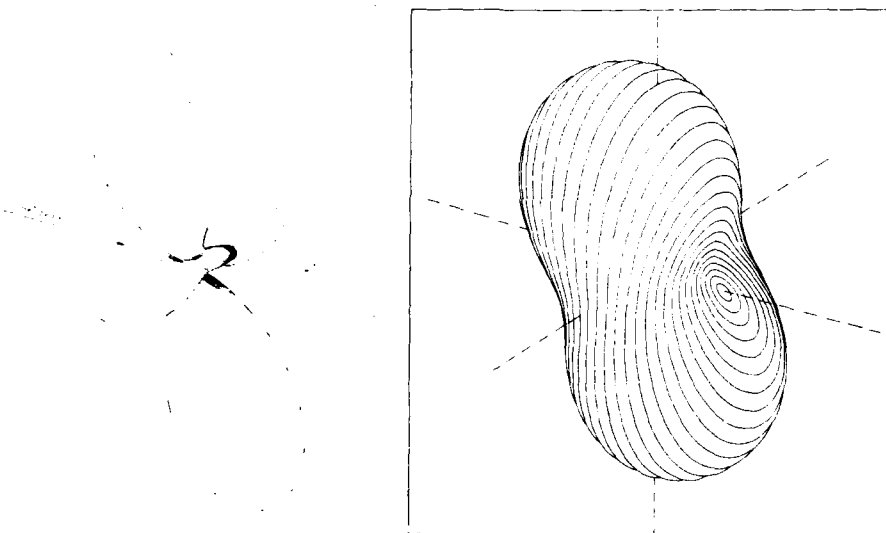


FIGURE 3

View in perspective of the angular intensity distribution of the electron emitted by $\text{He}^{**}(2p^2)^1D + \text{He}^+(1s) + e^-$ (left figure), and of the angular part of the electron density of $\text{He}^{**}(2p^2)^1D$ (right figure). Intensity and density, respectively, are given as distance from origin. Figures are calculated using the same set of experimentally determined values a_{2M} .

3. L-COHERENCES FOR Li^+ -He-COLLISIONS

The coherent superposition of M -states corresponds to certain shapes and orientations of stationary charge distributions of excited atoms, as we have seen in the previous section. Since different L -states belong to different energies E_L - except for hydrogen - the coherent superposition of L -states, describing the ensemble of atoms excited in a collision event with well de-

fixed initial state, corresponds to a nonstationary charge cloud. In case of two states L, L' there arise oscillations with frequency $\nu = \Delta E_{LL'}/2\pi$. Our general formula (b) shows that, in case of coincident observation of the emission of electron after collisional excitation, these oscillations will be observable if the time (t) elapsed between excitation and measurement is defined in state (f). In such a case (b) becomes

$$\sigma_{(f)+(i)} \propto \left| \sum_M A_{fMi} e^{i\delta_{fMi}} + \sum_{M'} A_{fM'i} e^{i\delta_{fM'i}} e^{i\Delta E_{LL'} \cdot t} \right|^2 \quad (h)$$

In a normal collision experiment (t) is not well enough defined to allow a resolution of the time oscillations. The time resolution necessary to resolve the beats for the He-states $(2s2p)^1P$ and $(2p^2)^1D$ - which are separated by .24 eV - corresponds to a precision of the order of 10^{-16} s, about six orders of magnitude higher than experimentally achievable. On the other hand, as we have pointed out earlier (5), the PCI-effect provides a kind of "clock" which measures the time point of electron emission after collision. This is so because the PCI-effect broadens an autoionization line of nominal energy ϵ_0 into a distribution of electron energies ϵ , with ϵ being related to the time point of emission (t) by the relation (in atomic units)

$$(\epsilon_0 - \epsilon) = (vt)^{-1}, \quad t = 1/(\epsilon_0 - \epsilon) \cdot v \quad (i)$$

The time resolution for this manner of measuring time by measuring ϵ , is limited by the uncertainty principle to

$$\Delta t/t \geq vt/\tau. \quad (j)$$

For velocities of the order of $v \sim 0.1$ a.u. used in our experiments Δt is thus smaller than 0.1τ for relevant times $t < \tau$.

If two PCI-broadened autoionization lines overlap, such as the lines belonging to autoionization of He in the states $(2p^2)^1D$ and $(2s2p)^1P$, the measurement of ejected electrons of energy ϵ in the overlap region defines a final state (f) that, according to relation (i), fixes well defined but different time points for the two states. These two different time points have to be used in the general formula for the multiple differential cross section (b), which leads to the relation

$$\sigma_{(f)+(i)}(\epsilon) \propto \left| \sum_M A_{fMi} e^{i\delta_{fMi}} + \sum_{M'} A_{fM'i} e^{i\delta_{fM'i}} e^{i\Delta E_{LL'} \Delta t_{LL'}(\epsilon)} \right|^2 \quad (k)$$

with $\Delta t_{LL'}(\epsilon) = t_L(\epsilon) - t_{L'}(\epsilon) = \Delta E_{LL'}/[(\epsilon_0^L - \epsilon)(\epsilon_0^{L'} - \epsilon) \cdot v]$. Formula (k) is given to show qualitatively in which way the time evolution of the system in a coherent superposition of L -states is reflected in the coincident electron spectra. A formula that describes quantitatively the shape and angular dependence of spectra arising from overlapping PCI-lines has been given earlier (5,6). In Fig. 4 we show two recently measured spectra belonging to the He states $(2p^2)^1D$ and $(2s2p)^1P$. The spectra are obtained with the electron detector in the collision plane but at opposite sides with respect to the direction of the impact parameter vector, as indicated. The solid lines are calculated using our earlier reported formula (5,6), and by taking into account our finite experimental energy resolution. The oscillations predicted by the qualitative relation (k) are clearly seen. These oscillations allow to derive one relative initial phase between the amplitudes of the different L -states. Angular distributions at specified ϵ allow to determine the complex amplitudes of the sublevels a_{1M} and $a_{2M'}$ of the 1P - and 1D -state, respectively, by fitting the theoretical formula. Calculated distributions of the emitted intensi-

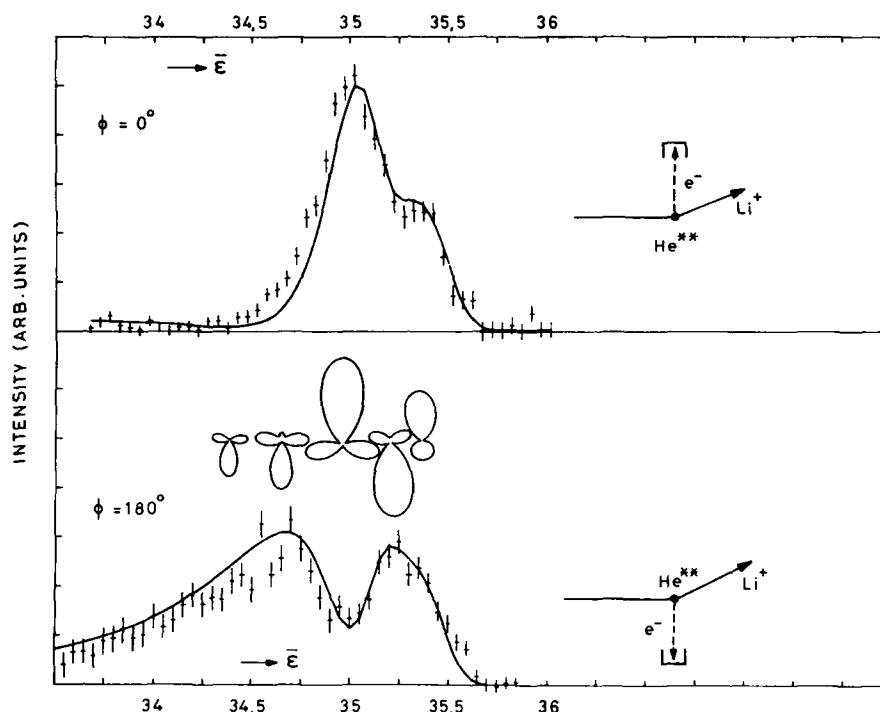


FIGURE 4
Electron energy spectra from He^{**} in a superposition of states $(2p^2)^1D$ and $(2s2p)^1P$. Upper- and lower spectra are measured in the collision plane and at opposite sides as indicated. (++) exp. data and (—) calculation are given in the frame of the emitting atom. The PCI-induced oscillations reflect the time evolution of the atom.

ty in the scattering plane at various energies are indicated in Fig. 4. The angular distribution of the, over energy (time) integrated, intensity is shown in Fig. 5, where the directly measured distribution is compared to the theoretical result obtained with amplitudes that also reproduce the energy spectra. One notices that the energy (time) integration has not averaged out the LL' -interference completely. The partial LL' -coherence reveals itself by the fact that the angular distribution does not have defined parity.

Since, by measurement, the amplitudes of the sublevels of the two states 1P and 1D are determined, as well as the relative phase between the 1P and the 1D population amplitudes, the time evolution of the charge cloud corresponding to the ensemble of He-atoms, excited in well defined collisions with Li^+ into a coherent superposition of the states $(2p^2)^1D$ and $(2s2p)^1P$, can be reconstructed. P. v.d. Straten and R. Morgenstern (4) have done this by calculating, for the two electron atom, the electron density in the independent electron approximation using the orbitals $|l_1 m_1\rangle$ and $|l_2 m_2\rangle$ coupled to LM and $L'M'$, respectively.

The electron density becomes

$$\rho(\Omega) = 2 \sum_{LL'} \sum_{MM'} \sum_{l_2 m_2} a_{LM} a_{L'M'}^* \langle l_1 m_1 l_2 m_2 | LM \rangle \times \langle l_1 m_1 l_2 m_2 | L'M' \rangle Y_{l_1 m_1}(\Omega) Y_{l_1 m_1}^*(\Omega) D_{l_1 l_1} \exp[i t \cdot \Delta E_{LL'}], \quad (1)$$

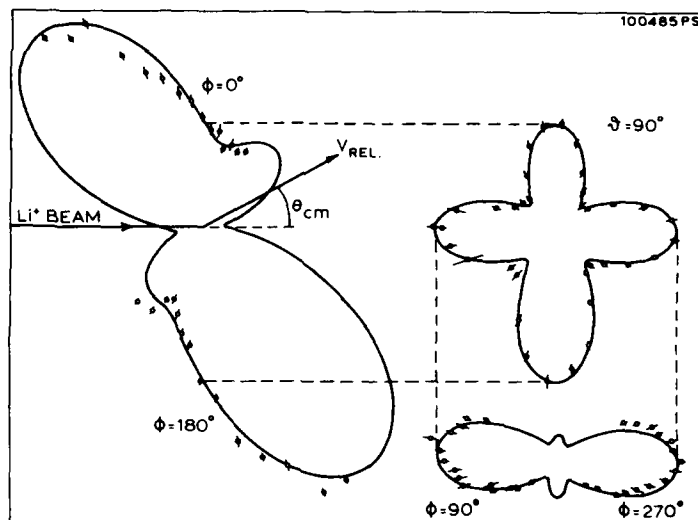


FIGURE 5
The angular distribution of electrons from He^{**} in a superposition of states $(2p^2)^1D$ and $(2s2p)^1P$. The three figures represent three cuts through the three dimensional distribution. (ϕ) exp. points with (statistical) error bars; and (—) calculation relate to Li^+ -energy of 2 keV and Li^+ -scattering angle of 10° .



FIGURE 6
View in perspective of the time evolution of the doubly excited He^{**} in a superposition of states $(2n^2)^1D$ and $(2s2p)^1P$. Left figure represents the time point of excitation by Li^+ ($t = 0$), and the other figures belong to $t = \frac{1}{4}T$, $t = \frac{3}{4}T$, and $t = T$, respectively, with $T = 1.74 \cdot 10^{-14}$ s the oscillation period.

where the brackets represent Clebsch-Gordan coefficients, and the $D_{\lambda\mu}$ are integrals of radial wave functions. Fig. 6 shows a three dimensional view of the atomic shape resulting for our example when the experimentally determined values a_{LM} , $a_{L'M'}$ are used. The oscillation period given by $\Delta E_{LL} = 8.8 \cdot 10^{-3} \text{ a.u.} \approx 0.24 \text{ eV}$ is $712 \text{ a.u.} \approx 1.7 \cdot 10^{-14} \text{ s}$. At $t = 0$, defined by the time point of excitation, which occurs close to the distance of closest approach (3), the charge cloud is apparently shifted towards the Li^+ -projectile, subsequently it starts to oscillate. This oscillation must be interpreted as a collective motion of the two participating electrons.

4. IMPROVEMENT OF PCI-DESCRIPTION FOR LARGE V

The theoretical formulation of PCI-broadening and PCI-induced interference of autoionizing lines in spectra arising from ion-atom collisions was originally derived (5) for cases where the relative velocity V of the heavy particles after the collision is small compared to the velocity of the ejected electron V_0 ($V \ll V_0$). In connection with recently measured He-autoionization spectra arising from collisions with He^+ at energies in the 100 keV region (7), where the condition ($V \sim V_0$) prevails, it seemed worth while to explore the possibilities to extend the original semiclassical description to the high velocity region. v.d. Straten and Morgenstern (8) found that in the original Ansatz for the PCI-transition amplitude (5,9) as a function of the detected electron energy ϵ_d ,

$$A(\epsilon_d) = (\Gamma/2\pi)^{\frac{1}{2}} \int_0^{\infty} \exp\left[-\frac{\Gamma}{2}t + i[(\epsilon_d - \epsilon_0)t + \int_0^t S(t')dt']\right] dt, \quad (m)$$

the shift $S(t') = (V \cdot t')^{-1} = \epsilon_0 - \epsilon(t')$ must be replaced by an expression which depends on the velocity of the electron, and on the angle of ejection (α) formed between the emission direction and the direction of the vector of relative velocity V . In the approximation that the width of the PCI-broadened line is small compared with the nominal energy ϵ_0 this expression simplifies to

$$S(t') = \frac{1}{Vt'} \frac{V_0(V_0 - V \cos \alpha)}{(V_0 - V \cos \alpha)^2 + V^2 \sin^2 \alpha} \quad (n)$$

The integral over $S(t')$ in relation (m) can be carried out. By introducing an effective velocity

$$\bar{V} = V \frac{[(V_0 - V \cos \alpha)^2 + V^2 \sin^2 \alpha]}{V_0(V_0 - V \cos \alpha)}$$

and the reduced quantities

$$\bar{\epsilon}_d = 2(\epsilon_d - \epsilon_0)/\Gamma; \quad \bar{t} = t \cdot \Gamma/2 \quad (p)$$

the amplitude (m) becomes

$$A(\epsilon_d) = (2/\Gamma\pi)^{\frac{1}{2}} \int_0^{\infty} \exp\left\{-\bar{t} + i[\bar{\epsilon}_d \bar{t} + \frac{1}{\bar{V}} \ln \bar{t}]\right\} dt \cdot \exp\left(\frac{1}{\bar{V}} \ln 2/\Gamma\right) \quad (q)$$

In the limit of infinite \bar{V} , (q) yields a Lorentzian line shape, and in the approximation $V \ll V_0$ the original analytic expression (5) is recovered if the stationary phase approximation is applied for the evaluation of the time integration. In the intermediate region ($V_0 \sim V$) the integration has to be performed numerically.

In case of two overlapping PCI-lines the energy dependent electron intensity in a direction (Ω) is obtained by coherently superimpose two amplitudes $A_1(\epsilon_d)$ and $A_2(\epsilon_d)$:

$$I(\epsilon_d, \Omega) \propto |f_1(\Omega)A_1(\epsilon_d) + f_2(\Omega)A_2(\epsilon_d)|^2 \quad (r)$$

To find out to what extent the PCI-effect influences autoionization spectra in the region ($V_0 \sim V$), the spectra arising from decay of $\text{He}(2p^2)^1D$ and $\text{He}(2s2p)^1P$ after excitation by He^+ in the collision energy range of 100 keV were calculated numerically using relations (q) and (r). An example for a collision energy of 100 keV and $\Omega = \alpha = 180^\circ$ is shown in Fig. 7. Although the collision velocity is $V = 1.00$ a.u. the spectrum deviates significantly from the sum of two Lorentzian profiles that correspond to the natural widths of $\Gamma(^1D) = 0.072$ eV and $\Gamma(^1P) = 0.042$ eV, respectively. Furthermore, when the relative initial phase between the two amplitudes is changed by π , the ratio of the peaks changes by almost a factor of two, showing that the effect of coherence is still important, although the peaks seem to be well separated.

These findings show that even at high collision velocities in the region $V \gtrsim 1$ the effect of PCI on autoionization electron spectra can be important. To demonstrate this, v.d. Straten and Morgenstern (8) have reanalyzed the He-autoionization spectra recently measured by Itoh et al (7) for He^+/He -collisions in the range from 100 keV to 500 keV. Part of their results are reproduced in Fig. 8. Plotted are the peak areas of the "upper" and the "lower"

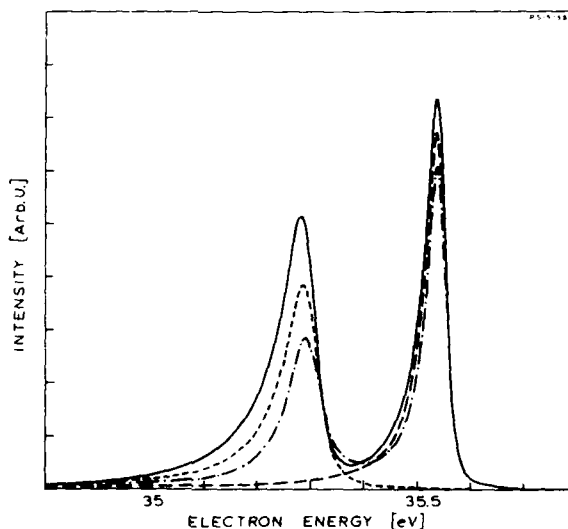


FIGURE 7

Calculated energy spectra resulting from autoionization of He^{**} in states $(2p^2)^1D$ and $(2s2p)^1P$, after excitation in 100 keV $\text{He}^+ + \text{He}$ collisions. The result of different assumptions regarding the relative phases are shown: (---) random phase, (—) phase zero, and (-.-) opposite phase.

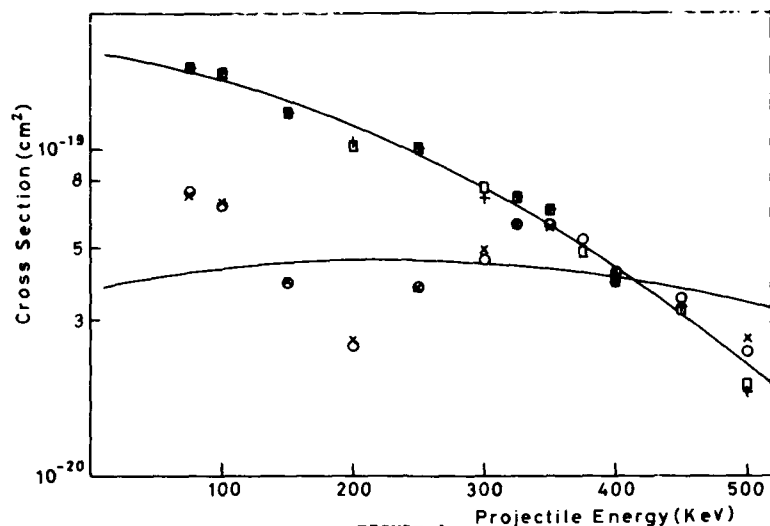


FIGURE 8

Intensities of the "upper" (\square), and of the "lower" peak (\circ) as determined by Itoh et al (7). Solid lines represent squares of the moduli for excitation of $(2s2p)^1P$, and $(2p^2)^1D$, respectively. (+++) and (xxx) are intensities for "upper" and "lower" peak, respectively, as calculated by adapting the relative phase and using the moduli shown.

peak of the spectrum belonging to decay of He in the states $(2s2p)^1P$ and $(2p^2)^1D$. Since Itoh et al (7) assumed that the "upper" peak is a measure for the excitation cross section of $(2s2p)^1P$, and the "lower" one for the excitation cross section of $(2p^2)^1D$, they ascribe the peculiar dip in the "lower" peak intensity to a minimum in the 1D -cross section, i.e. to a minimum of the moduli, of the 1D excitation amplitude. In contrast, the PCI-analysis shows (8), that the same experimental data may be explained by assuming smoothly varying moduli - the square of the moduli are represented by the solid lines in Fig. 8 - and by adapting the relative phase between the 1P - and the 1D -amplitudes. It should be noted that, although the electron spectra of Itoh et al (7) are non-coincident spectra for which neither the scattering angle nor the scattering plane are defined, the 1P - and 1D -contributions are expected to be coherent because (i) θ is confined to very low angles at the high collision energies, and (ii) at $\theta = 180^\circ$ integration over different orientations of the scattering plane does not have any effect regarding the coherence.

5. TURNING POINT RAINBOW FOR TRANSFER IONIZATION

The examples of coherence effects discussed so far pertained to electron emission after the collision. Other coherence effects in electron spectra arise when electron emission during the collision is important. This is the case for a whole class of collision systems, namely, collisions of multiply charged ions with atoms. Because of the high recombination energy of such ions, the combined ion-atom system is usually unstable with respect to spontaneous electron emission (10). A prototype system of this class is He^{++}/Xe which decays during a collision at very low energies (1 eV - 100 eV) to

$\text{He}^+/\text{Xe}^{++} + e^-(\epsilon)$ (11) with high probability. Different "paths" (μ), in the sense of the general formula (b), arise in such systems if the transition energy $V_i(R) - V_f(R) = \epsilon_{tr}(R)$ has an extremum in the region of distances where the transition probability is nonzero. If $\epsilon_{tr}(R)$ has a minimum at $\epsilon_{tr}(R_*)$, then for $\epsilon \gtrless \epsilon_{tr}(R_*)$ there are, classically, two distances, R_1 and R_2 , at which transitions leading to the final state with detected energy ϵ may occur. Semiclassically, this corresponds to two amplitudes in formula (b), and thus to interference effects in the electron spectrum. The effect itself is characterized by two conditions, (i) at R_* the phase difference between the two amplitudes vanishes, which leads to constructive interference at R_* , and (ii) at R_* there arises a classical singularity because the Jacobian $|d(\epsilon_{tr}(R))/dR| = 0$ at R_* . These characteristic features allow to approximate the spectrum $I(\epsilon)$ by the square of an Airy-function in the region $\epsilon \sim \epsilon_{tr}(R_*)$. Because of the mathematical similarity of this effect with the well known "rainbows" in differential scattering, we call this effect a "rainbow" in the electron energy spectrum. "Rainbows" of the described type have been discussed earlier (10,11) and they have been shown to arise for the He^{++}/Xe -system because of a minimum in the He^{++} -Xe-potential (11). Recently we have shown (12) that spectral features arising from spontaneous emission of an electron (or photon) close to the turning point of a heavy particle collision of well defined impact parameter can also be interpreted, and approximately described, as a "rainbow". Schematically the situation is depicted in Fig. 9: As a function of time, the transition energy $\epsilon_{tr}(t)$ for any system has an extremum at the turning point $R_0(t=0)$, and the two transition amplitudes for final states defined by $\epsilon \lesseqgtr \epsilon_{tr}(R_0) = \epsilon_0$ lead to the characteristic rainbow interference. By approximating, in the region $R \sim R_0$, the R -dependent initial potential $V_i(R)$, the R -dependent natural width $\Gamma(R)$, and $\epsilon_{tr}(R)$, as

$$\begin{aligned}\epsilon_{tr}(R) &= \epsilon_0 + \epsilon'_0(R - R_0) \\ \Gamma(R) &= \Gamma_0 + \Gamma'_0(R - R_0) \\ \sqrt{\Gamma(R)} &= \sqrt{\Gamma_0} + (\Gamma'_0/2\sqrt{\Gamma_0})(R - R_0) \\ V_i(R) &= V_{i0} + V'_{i0}(R - R_0),\end{aligned}\quad (s)$$

and by using an Ansatz equivalent to relation (m) for the spectral intensity $I(\epsilon)$, one obtains for a collision of impact energy E and impact parameter b the simple result (12)

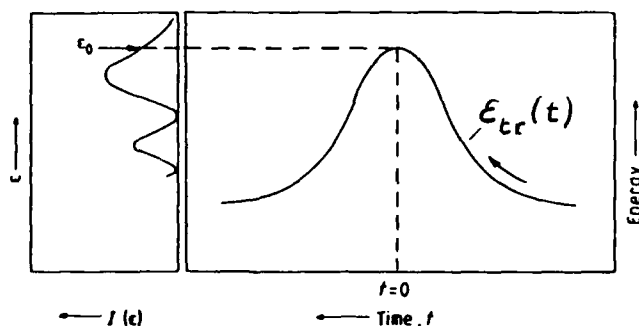


FIGURE 9

Schematic drawing showing the time variation of the transition energy $\epsilon_{tr}(t)$ in the neighbourhood of the turning point $R(t=0)$, and the resulting "rainbow"-feature in the emitted intensity $I(\epsilon)$.

$$I(\epsilon) \propto \left| 1 + \frac{\Gamma'_0}{2\Gamma_0} \cdot \frac{z \cdot c}{\alpha^{2/3}} \right|^2 |Ai(z)|^2 ; \quad z = \left(\epsilon - \epsilon_0 + \frac{i\Gamma_0}{2} \right) \alpha^{-1/3}$$

$$\alpha = -\left(v'_{10} + \frac{i\Gamma'_0}{2} \right) c$$

$$c = \frac{1}{2M} \left(\frac{2Eb^2}{R_0^3} - v'_{10} \right) \quad (t)$$

Since the transition energy at the turning point, ϵ_0 , sensitively depends on the impact parameter, "turning point rainbows" can only be observed if the impact parameter is well defined. A characteristic feature, which distinguishes the "turning point rainbow" from the "rainbow" caused by an extremum in $\epsilon_{tr}(R)$, is the fact that its energy position varies strongly with collision energy. An example of a recently measured "turning point rainbow" is shown in Fig. 10, where the doubly differential cross section $\sigma(\theta, Q)$ for the process

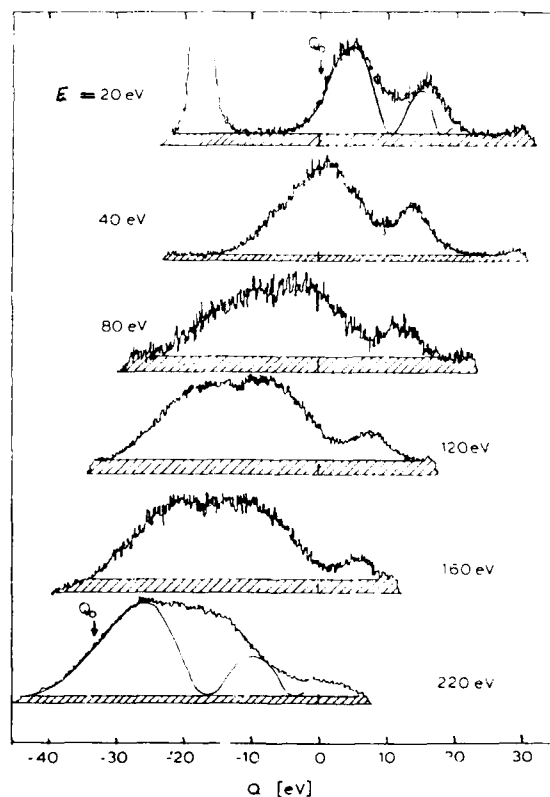
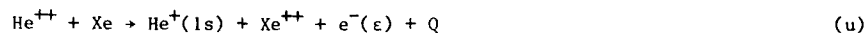


FIGURE 10
Measured "turning point rainbows" for $\text{He}^{++} + \text{Xe} + \text{He}^{+} + \text{Xe}^{+} + e^{-}(\epsilon) + Q$.
Shown are energy gain (loss) spectra for various collision energies E . Solid
lines show calculations using relation (t).



is reproduced for several impact energies E (13). For processes of well defined initial and final electronic states of the heavy particles, the angle integrated coincident electron spectrum and the spectrum of loss (or gain) of relative kinetic energy Q at defined angle ϑ are equivalent. The solid lines show a fit of formula (t) to the measurement.

As already pointed out, the "turning point rainbow" is a very general feature, which is not restricted to electron emission and not to a certain energy range. A fit of formula (t) to coincident MO-X-ray emission spectra from collisions of Cl^{16+} with Ar (14) is shown in Fig. 11. The value of the identification, and of the analysis, of such rainbows is, of course, that information of the quantities (s) is obtained.

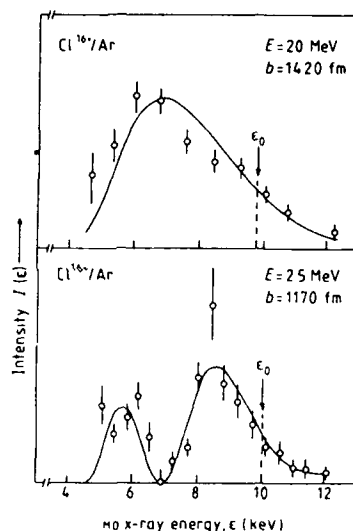


FIGURE 11
Measured MO-X-ray spectra (ϕ) from ref. (14), and calculations using relation (t). No parameter is varied to reproduce the dependence of the spectra on collision energy.

REFERENCES

- 1) E. Boskamp, R. Morgenstern and A. Niehaus, J. Phys. B 15 (1982) 4577.
- 2) Q.C. Kessel, R. Morgenstern, B. Müller and A. Niehaus, Phys. Rev. A 20 (1979) 804.
- 3) E. Boskamp, R. Morgenstern, P. v.d. Straten and A. Niehaus, J. Phys. B 17 (1984) 2823.
- 4) P. v.d. Straten and R. Morgenstern, submitted to Comments on Atom. Mol. Phys. (1985).
- 5) R. Morgenstern, A. Niehaus and U. Thielmann, J. Phys. B 10 (1977) 1039.
- 6) P. v.d. Straten, P.M. Koenraad, R. Morgenstern and A. Niehaus, Z. Phys. A 319 (1984).

- 7) A. Itoh, T.J.M. Zouros, D. Schneider, U. Stettner, W. Seitz and N. Stolterfoth (to be published J. Phys. B).
- 8) P. v.d. Straten and R. Morgenstern (to be published).
- 9) G. Gerber and A. Niehaus, J. Phys. B 9 (1976) 123.
- 10) A. Niehaus in: The Excited State in Chemical Physics, ed. J.Wm. McGowan (Wiley, 1981) pp. 399.
- 11) A. Niehaus, Comments Atom. Mol. Phys. 9 (1980) 153.
- 12) A.Z. Devdariani, U.N. Ostroskii and A. Niehaus, J. Phys.B 18 (1985) L161.
- 13) A.G. Kuiper and A. Niehaus, contrib. XIV ICPEAC, Palo Alto 1985.
- 14) R. Schuch, H. Schmidt-Böcking, I. Tserruya, B.M. Johnson, K.W. Jones and M. Meron, Z. Phys. Z 320 (1985) 185.

AUGER SPECTROSCOPY OF HIGHLY STRIPPED IONS

D. SCHNEIDER, N. STOLTERFOHT, A. ITOH**, T. SCHNEIDER, G. SCHIWIETZ,
W. ZEITZ, AND T. ZOUROS

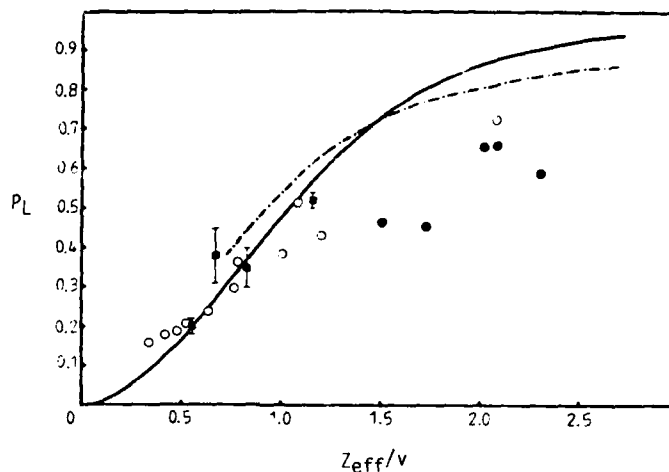
Hahn-Meitner-Institut für Kernforschung Berlin GmbH, D-1000 Berlin 39,
West Germany

1. INTRODUCTION

During the past two decades Auger-electron spectroscopy became a well-established spectroscopic tool for atomic structure studies of excited atoms as well as for studies regarding the excitation mechanisms themselves (1,2,3). Progress within the last 5 years is predominantly achieved for spectroscopic investigations of highly-ionized few-electron atoms (4-10). Because of fluorescence yield effects and the presently achievable detection efficiency the range of these investigations is limited to atoms ranging in atomic numbers up to about 18. The majority of the studies has been performed on collisionally excited target atoms. In the spectroscopy of target atoms neutral atoms are stripped to few-electron ions in a single collision event if high Z projectile ions are used (5,12). Here, line broadening effects can be greatly reduced if fast enough projectile ions are used to minimize the recoil momentum. Projectiles which ionize the outer shells less efficiently give rather complex spectra (8). Line assignments in those cases are complicated due to line blending. The projectile dependence of the multiple ionization has been studied over a wide range of projectile energies and species. It has been studied most extensively in the case of Ne where Ne K-Auger (and X-ray) spectra have been measured using projectile ions ranging from H^+ to U^{86+} (12), at projectile energies from a few keV up to a few hundred MeV. Average quantities like the centroid energy of the Ne KLL Auger spectra, the satellite to total line intensity ratios and the average number of L vacancies produced simultaneously with the K vacancy have been deduced. Fig. 1 shows experimental, fitted and theoretical values for the probability (P_L) of the removal of an L-shell electron simultaneous to that of a K-shell electron as a function of the effective nuclear charge versus the projectile velocity. The plotted data show that a universal scaling rule for P_L can be established to some extent; indicating a saturation effect for very high Z ions (9,10). In particular, the effect of electron capture in secondary collisions of slow-moving recoil ions with target atoms has been studied via Auger electron spectroscopy recently (6,12). Selective capture of electrons into the vacant shells of the highly-ionized recoil ions could be studied for specific mixtures of target gases. As an example, Figure 2 shows an Ne-K-Auger spectrum as produced with 1.4 MeV/amu Kr^{18+} incident on Ne. The spectrum shows a rather reduced number of Auger lines due to the high degree of multiple ionization. The inset in Fig. 2 demonstrates the effect of secondary collisions. The probability for the population of states at a few eV (recoil energy) is drastically increased as the target gas pressure is raised (see Ref. 5,6,11,12).

** University of Nebraska, Lincoln, Nebraska 68688, U.S.A.

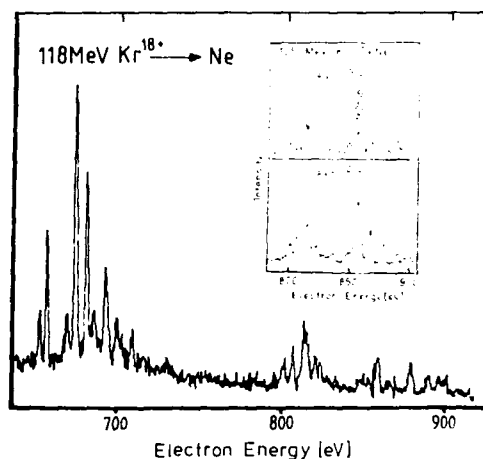
Fig. 1
Experimental P_L
values versus
 $Z_{eff}k/V$ from
Auger measure-
ments. Fig. from
Ref. (9); data
from Ref. (8,0);
(5,0); (10,m)
solid curve from
Sulik (10);
chain curve
Folkmann (7).



Spectroscopy of Auger electrons from fast gas or foil excited projectile ions has been performed to some extent. However, these measurements suffer, in general, from severe kinematic line broadening effects which cause limitations on the achievable spectroscopy resolution (13,14). Only in cases where sufficiently small forward angles have been used, these broadening effects could be reduced (15). Kinematic line broadening is in first order absent if the electron emission from the projectile is observed at 0° forward angle as will be discussed below (16-18).

Only recently systematic spectroscopy of Auger electrons emitted from excited projectile ions has been performed at 0° forward angle (16-19). The method reduces broadening effects such that high resolution as good as obtained in target electron spectroscopy can be achieved. This allows to take advantage of the spectroscopy of Auger electrons from excited projectile ions. The most striking advantage is that the electronic outer-shell configuration of the

Fig. 2 Ne-K Auger spectrum from 118 MeV Kr^{18+} impact on Ne. The inset shows the pressure dependence of the secondary electron capture (6,11,12).



projectile ions can be prepared. Subsequently, in a collision where only one inner-shell electron is removed a detailed study of atomic structures of selectively excited atoms can be performed via electron spectroscopy (17).

In the following, recent examples are described where the advantages of zero-degree electron spectroscopy are combined with the possibility of selective excitation of projectile ions (17-20).

2. EXPERIMENTAL SET-UP AND KINEMATICS

Only a few remarks regarding the experimental set-up and the kinematics of electrons emitted from fast projectiles are made here, a more detailed description is given in Ref. 19.

The experiments to measure Auger electrons in ion-atom collisions are generally performed using electrostatic spectrometers inside a magnetically shielded high-vacuum scattering chamber. Fig. 3 shows a schematic experimental set-up which is typically used for measurements of electrons from excited projectile ions at zero-degree observation angle. A collimated beam of ions from an accelerator is directed into the scattering chamber and collected in a Faraday cup. Excitation and decay of the projectile ions primarily takes place within a gas cell, after a foil target or at a collision region formed by a target gas (jet) and the ion beam.

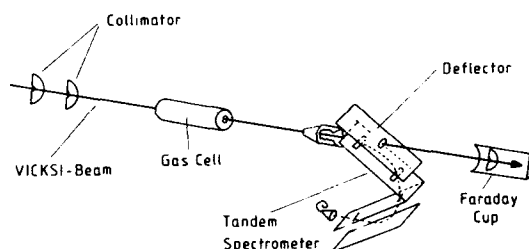


Fig. 3 Schematic of set-up for electron spectroscopy at zero-degree forward angle.

The Auger electrons ejected from the target region can be analyzed in energy by a tandem-type electrostatic electron spectrometer. This device consists of a deflector used to steer the electrons out of the ion beam and a parallel-plate analyzer used for the energy analysis of the electrons. High resolution is achieved by deceleration of the electrons between two grids in front of the analyzer. It should be noted that the analysis of the metastable components in an Auger spectrum can easily be achieved by deflecting electrons due to prompt transitions out of the viewing region of the spectrometer.

As demonstrated in a variety of experimental investigations projectile Auger electrons are influenced by kinematic (Doppler) effects since they are ejected from a moving emitter. For a straight-line trajectory of the projectile the energy E of the Auger electron in the laboratory frame at zero

degree (and 180°) observation angle is obtained from the corresponding energy E' in the projectile rest frame by

$$E = E' + t_p \pm 2(E' t_p)^{1/2} \quad (1)$$

where $t_p = T_p/M$ is equal to the projectile energy T_p reduced by the electron-projectile mass ratio; electrons are emitted in forward and backward direction ($t_p > E'$). The quantity t_p is equal to the energy of an electron moving with the velocity of the projectile. For fast projectiles ($t_p \gg E'$) the shift of the Auger lines follows primarily from the second term (t_p) on the right-hand side of Eq. (1). For $t_p > E'$ Auger lines can only be observed within a certain range of forward angles, there and at zero degree the Auger peak occurs twice in the spectrum. The width of the Auger line is changed according to the third term on the right-hand side of Eq.(1). The height of the Auger line is also changed, the corresponding double differential cross section transforms as

$$\frac{d^2\sigma}{d\Omega dE} = \left(\frac{E}{E'}\right)^{1/2} \frac{d^2\sigma'}{d\Omega' dE'} \quad (2)$$

The Auger line is broadened due to the non-zero acceptance angle of the spectrometer. The broadening effect cancels in first order when electrons are observed at zero degree.

Figure 4 shows an electron spectrum measured at 0° observation angle. The dominating peak (cusp) in this case ($\text{Ne}^{6+} + \text{He}$) is due to "electron loss to the continuum" (ELC). The peaks which are superimposed on the low and high energy tails of the cusp are due to autoionizing transitions in the excited Ne-ions. Similar results for different ion species have first been given in Ref. 16,18; recent data have been reported by T. Schneider (Ref. 21).

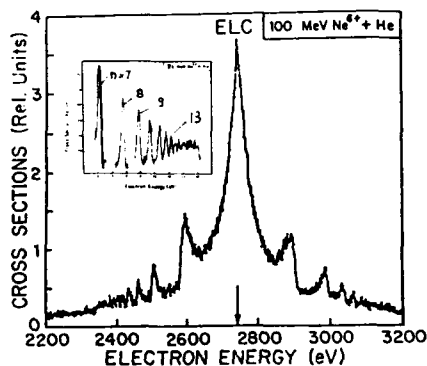


Fig. 4 Electron cusp and superimposed autoionization lines from 100 MeV Ne^{6+} impact on He (21).

The inset in Figure 4 shows these peaks after a transformation into the projectile system. The energy positions are very well described by the "Rydberg-formula" as pointed out in Ref. 21. It should be noted that it was possible to resolve structures in the line labelled $n=7$ which could be attributed to contributions involving higher ℓ -quantum numbers.

3. K-SHELL AUGER ELECTRON EMISSION FROM SELECTIVELY EXCITED FAST Ne-PROJECTILE IONS

Ne is the most extensively studied atom using Auger-electron spectroscopy. Most of these studies have been performed on collisionally excited target atoms. A few studies have been performed on excited Ne-projectile ions (4,22).

Recently new results (20) using the method of O^2 electron spectroscopy have been reported which are reviewed in the following. In Fig. 5 experimental results are shown for 70 MeV Ne^{5+} and 100 MeV Ne^{6+} incident on a He-gas target. The Auger peaks were fitted by a Lorentzian curve folded by a Gaussian-type spectrometer response function. The line identification was based on energy comparisons with previous experimental and theoretical studies. The Auger energies for B-like Ne are the first measurement of these lines with high resolution. (20,36).

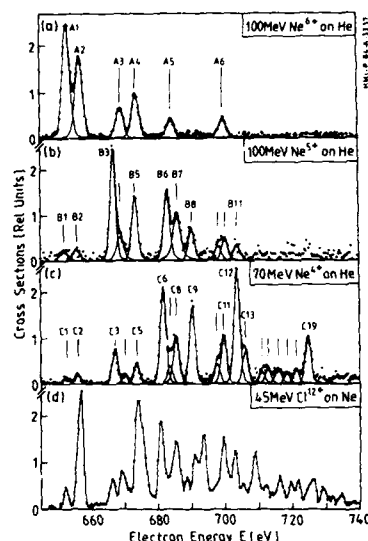


Fig. 5 Ne K Auger spectra from He excited Ne^{n+} ($n=4,5,6$) projectile ions in comparison with a heavy ion induced target spectrum

The study demonstrates the advantage of spectroscopy on projectile ions over the target atom. In previous measurements with the 45 MeV Cl^{12+} ions the strong Coulomb field induced by the highly charged Cl ion results in the removal of several electrons from the Ne L-shell whenever a vacancy is produced in the K-shell (36). This causes the simultaneous production of recoil atoms with different charge states which correspond to Li-, Be-, and C-like electron configurations. The decay of these states gives rise to the line blending (Fig. 5, target spectrum). In addition, the population of Rydberg states that can feed metastable Auger states by cascade transitions complicates the analysis of the Auger states of target spectra.

In the following different cases with different projectile charge states are considered (for more details see Ref. 20):

1. $Ne^{6+} + He$ (Fig. 5a): The spectrum obtained for Ne^{6+} impact shows relatively simple structure dominated by lines arising from three-electron (Li-like) states. The Auger state $1s2s^2\ ^2S$ gives rise to the strongest peak A1. Further prominent lines refer to the Li-like configuration $1s2s2p$. The peak A2 can be attributed to the metastable state $1s2s2p\ ^4P$. Peaks A3 and A4 refer to mixtures of the states $1s(2s2p\ ^3P)^2P$ and $1s(2s2p\ ^1P)^2P$. In principle the configuration $1s2s2p$ can be produced by different mechanisms. It may be created from the ground-state configuration $1s^22s^2\ ^4S$ by the removal of a 1s

electron and the simultaneous transfer of a 2s electron to the 2p orbital. The 2s-2p transition without spin flip could account for the excitation of the $1s(2s2p^1P)^2P$ state, while the transition with spin flip for the excitation of the $1s2s2p^4P$ and $1s(2s2p^3P)^2P$ states. In the present collision system the probability for such a 2s-2p transition is expected to be small.

The main indication that the 2s-2p transition is weak comes from the fact that no lines due to the configuration $1s2p^2$ could be identified on the basis of present energy calculations. In the spectra of Fig. 5 there are no peaks at Auger energies corresponding to the states $1s2p^2^1D$ and $1s2p^2^3S$. However, these states appear rather strongly in foil-excited Ne spectra or in recoil target spectra produced by high-energy heavy ions. Two-electron transition $2s^2-2p^2$ in addition to the removal of the 1s electron can be considered to be negligible in this collision system. Thus one may conclude that the probability for the 2s-2p transition is small. The configuration $1s2p^2P$ may also be formed from the incident metastable state $1s^22s2p^3P$ (the 3P_0 has a lifetime of mseconds) via ionization of a 1s electron. The excitation of the states $1s(2s2p^3P)^2P$ and $1s(2s2p^3P)^4P$ from the ground state $1s^22s^2^1S$ requires a spin-flip during the 2s-2p transition. In the excitation of projectiles by low Z target atoms such as He, spin-flip processes are expected to be negligible; therefore, the 2s-2p transition which requires a spin-flip in addition becomes even more improbable. Intensity comparison between lines A1-A4 in Fig. 5, based on the number of final spin states available indicate that the fraction of metastable particles in the Ne^{5+} beam could be as high as 10%. The Auger peaks A5 and A6 are tentatively assigned to the Be-like configuration $1s2s2p^2$. This state may be created from the incident metastable state $1s^22s2p^3P$ via a 1s-2p transition.

2. $Ne^{5+} + He$ (Fig. 5b): The most striking feature of this spectrum is the weakness of the first two Li-like lines B1 and B2 which are the most prominent peaks in Fig. 5a; this shows that the Li-like contributions are weak and can be neglected in the line analysis of this spectrum. In $Ne^{5+} + He$ collisions Be-like states are produced nearly exclusively, all Auger lines B3-B11 can be attributed to Be-like Ne. Thus, in conflicting cases where Li- and Be-like states are close in energy (within the experimental resolution), the corresponding line is attributed to a Be-like configuration. For example, the peak B5 is assigned to the Be-like state $1s2s^22p^1P$ (decaying to the $1s^22p^2P$). The most prominent lines such as B3, B5, B6 and B8 are found to originate from the configuration $1s2s^22p$ created by single ionization of a 1s electron from the initial state $1s^22s^22p$ of Ne^{5+} . The other Auger lines (B4, B7 and B9-11) are attributed to the configuration $1s2s2p^2$ created by the ionization of a 1s electron accompanied by the excitation of a 2s electron into a 2p hole. These peaks except for B4 are probably composed of at least two lines. It is seen that the intensities of these lines are much weaker in comparison with those which originate from the configuration $1s2s^22p$. Again this suggests that the probability for 2s-2p transitions is small. The absence of B-like lines indicates that the K vacancy is preferentially produced by ionization instead of excitation of a 1s electron.

3. $Ne^{4+} + He$ (Fig. 5c): The spectrum is again characterized by the initial charge state of the projectile. Most of the Auger lines observed at electron energies above 680 eV originate from the B-like initial configurations. The identification of each line is difficult, because in the present energy region there are many Auger lines expected from the B-like configuration. However, the line assignment is simplified, if one takes into consideration that the configuration of $1s2s^22p$ is expected to be predominantly produced. It is created via ionization of a single 1s electron in accordance with the results for Ne^{5+} and Ne^{6+} impact.

In Fig. 5c the Li-like C1 and C2 are also observed. The intensity of these lines is relatively small so that the influence of Li-like lines can be neglected in practice. Moreover, in Fig. 5c the Be-like lines C3-C5 are observed with noticeable intensity. Hence, the B-like Auger group especially in the energy range of 680-710 eV is probably mixed with some Be-like lines (contribution of the Be-lines is estimated to be less than 10%). The Be-like configuration $1s^2 2s^2 2p$ is probably created by simultaneous ionization of a 1s and 2p electron from the ground-state configuration $1s^2 2s^2 2p^2$ Ne^{4+} .

4. L-SHELL AUGER ELECTRON EMISSION FROM SELECTIVELY EXCITED FAST Ar PROJECTILE IONS

L-Augur electrons were measured with high resolution in collisions of 91.6 MeV Ar^{n+} ($n=5,6$) ions with He and Ar gas targets. Due to the projectile charge state the initial configurations $1s^2 2s^2 2p^5 3s^2 3p$ and $1s^2 2s^2 2p^5 3s^2$ are selectively excited (17).

Fig. 6 shows that the spectrum produced in 91.6 MeV $\text{Ar}^{6+} + \text{He}$ collisions is dominated by one peak at 102 eV. The data are compared with results acquired with Ar^{5+} . The corresponding Auger spectra are seen to be completely different. The peak at 102 eV is relatively weak in the Ar^{5+} spectrum. It exhibits additional structures which are dominated by the peak at about 112 eV.

Similarly as in the Ne-case, He only weakly effects the outer shell of the projectile during the L-shell excitation. Hence, it is expected that apart from the removal of the 2p electron the configuration of the incident projectile is essentially retained in the collisions. The groundstate configuration of Ar^{6+} is $1s^2 2s^2 2p^5 3s^2$, while Ar^{5+} has an additional 3p electron. Thus the most prominent peaks 2 and 3 are attributed to the configurations $1s^2 2s^2 2p^5 3s^2$ and $1s^2 2s^2 2p^5 3s^2 3p$, respectively. Also, peak 4 is attributed to the initial configuration $1s^2 2s^2 2p^5 3s^2 3p$, which, however, decays to a final state different from that for peak 3.

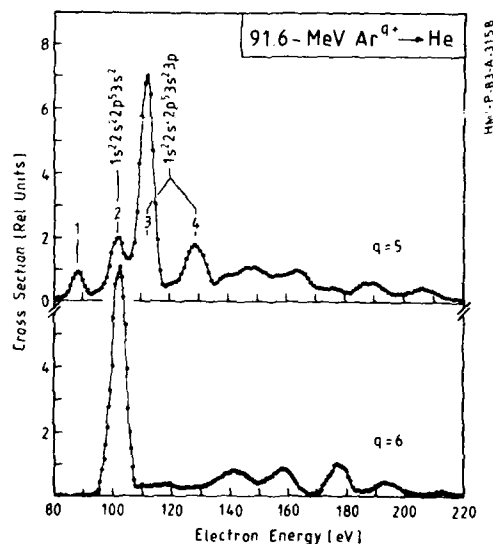


Fig. 6 Ar L Auger spectra from 91.6 MeV Ar^{n+} ($n=5$) impact on He (17).

The occurrence of the (weak) peak 2 in the Ar^{5+} spectrum shows that

there is a possibility of ionization of the 3p electron in addition to removal of the 2p electron. The corresponding probability is expected to increase when the nuclear charge of the target atom increases. This is shown in Ref. 17, where Ar Auger spectra are compared as a function target species. It was found that under the assumption that the 3p ionization is independent of the removal of the 2p electron, the relative intensity of the peak 2 in Fig. 6 is equal to the probability for 3p ionization by the target atom passing through the L-shell radius of the projectile. Theoretical ionization probabilities estimated using the scaling procedure of Hansteen et al. (37) are found to be consistent with the present results for H₂ and He. For Ne the perturbation theory is expected to lose significance for the ionization of Ar 3p electrons.

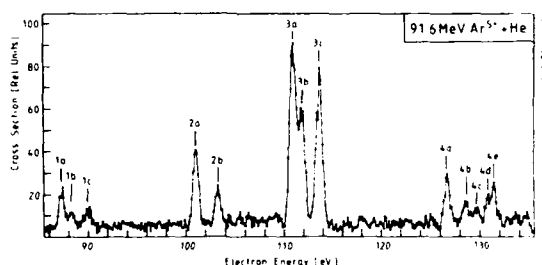


Fig. 7 High resolution L Auger spectrum from 91.6 MeV Ar⁵⁺ on He Collisions (17).

It is noted that each peak refers to a group of unresolved lines. For instance, doublets of 2.2 eV separation are expected following from the 2p_{1/2}-2p_{3/2} fine-structure splitting in the initial state. Individual lines are observed in the spectrum measured with the high-resolution with the tandem spectrometer. The spectrum is shown in Fig. 7; showing a part of the Ar⁵⁺ + He spectrum where the effective resolution is 0.5%.

To verify the spectral structures in Fig. 7, Ar-L Auger transition energies were calculated using a multi-configuration Dirac Fock (MCDF) program. For the cases studied, the term splitting and the fine structure splitting are of the same order so that the intermediate coupling schemes are suitable for the calculations. When the projectile is simply ionized in the 2p orbital in the collision, Ar⁶⁺ is created. When the 3p electron is removed in addition to the 3p ionization, Ar⁷⁺ is obtained.

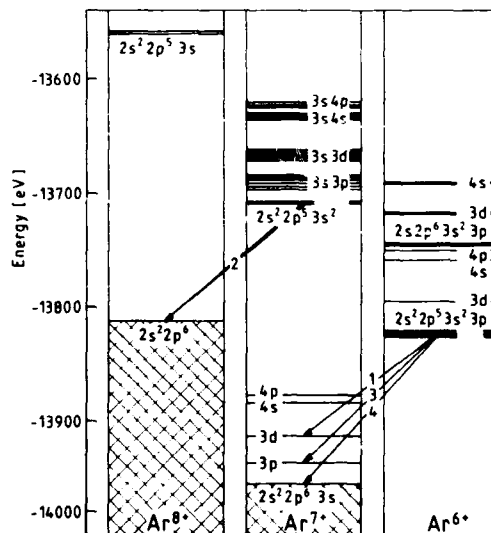


Fig. 8 Diagram for the decay of Auger states in Ar⁶⁺ and Ar⁷⁺ (23)

In Fig. 8 (23) the Auger transitions for Ar^{6+} and Ar^{7+} are indicated by arrows labelled in accordance with the notation of the peak groups (Fig. 1). The peaks 2a and 2b are attributed to the initial configuration $2s^2 2s^2 2p^5 3s^2$ forming the doublet $^2P_{1/2,3/2}$. The peak groups 1, 3, and 4 are due to a final configuration $1s^2 2s^2 2p^6$ with an additional 3d, 3p, and 3s electron, respectively.

The peak group 1 is particularly interesting, since it is produced by three-electron transition which cannot be initiated by the two-body Coulomb interaction operator in first order. Also, shake-up effects or configuration interaction in the final state of the residual ion should not be important. Here, higher order effects such as interchannel interaction have to be considered.

5. TRANSFER AND EXCITATION IN SLOW He^+ ON He COLLISIONS

High-resolution projectile Auger spectroscopy studies providing detailed information about each excited state have been performed previously for helium and lithium projectiles (25,26). However, studies with He projectiles have been limited to relatively low impact energies. This has been primarily due to the fact that electrons from fast projectiles are significantly influenced by kinematic line broadening effects produced by the finite acceptance angle of the spectrometer (19). Here measurements of autoionization electrons from helium projectiles in collisions of 50-500 keV He ions with He target atoms at 0° observation angle are reported (24).

Lines attributed to the states $(2s^2)^1S$, $(2s2p)^3P$, $(2p^2)^1D$ and $(2s2p)^1P$ were measured with high resolution (24).

An important advantage of using He ions is that the autoionizing states of the projectile can be created solely by transfer-excitation (TE) processes. Furthermore, it is of interest to note that the TE process may interfere with the electron capture-to-the-continuum (ECC) process, since both result in the same final state, i.e.

$\text{He}^+(1s^2S) + e(27)$. TE cross sections may reveal peak structures at some specific impact energy, since electron correlation effects are known to be relatively strong in He atoms. Clearly, these features may be different for different excited states as predicted by related theoretical calculations (28-30).

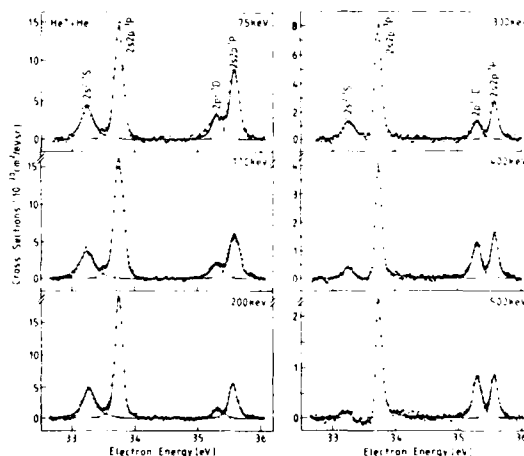


Fig. 9 Autoionization spectra from He projectile ions excited in collisions with He (CM energy) (24).

The autoionization spectra in the projectile rest frame are shown in Fig. 9 exhibiting the excited states $(2s^2)^1S$, $(2s2p)^3P$, $(2p^2)^1D$, and $(2s2p)^1P$. The line shapes of the singlet peaks are generally symmetric, while those of the state $(2s2p)^3P$ show increasing asymmetry (Fano profile) with increasing impact energy.

This Fano profile is caused by an interference between electrons ejected through the TE process and the electron capture-to-the-continuum (ECC) process. It is interesting to note that this mechanism is essentially different from that studied previously for the case of He as a target atom (31). In that case, interference takes place between autoionization following double electron excitation and direct ionization of a single electron.

The intensities of the spectral lines were obtained by a fitting procedure using a Lorentzian or a Fano line profile folded with the Gaussian-like spectrometer response function.

The TE cross sections for the four lines and the total of cross sections are shown in Fig. 10 as a function of the impact energy of the He^+ ions.

The cross sections of the 3P state have a maximum at about 150 keV and decrease monotonically as the impact energy increases. A similar monotonic decrease is observed for the singlet state 1P of the $2s2p$ configuration. The cross sections for the production of the $(2s^2)^1S$ state have a peak at around 150 keV and decrease more rapidly than those of the $(2s2p)^1,3P$ states with increasing impact energy.

The production behaviour of the $(2p^2)^1D$ state is found to be entirely different from that of the other states. The cross section decreases to a minimum value at 200 keV and then forms a broad peak between 300- and 400 keV. The origin of this peak structure is not clear at present. A possible interpretation may be given within the framework of the RTE model of Tanis et al. (30).

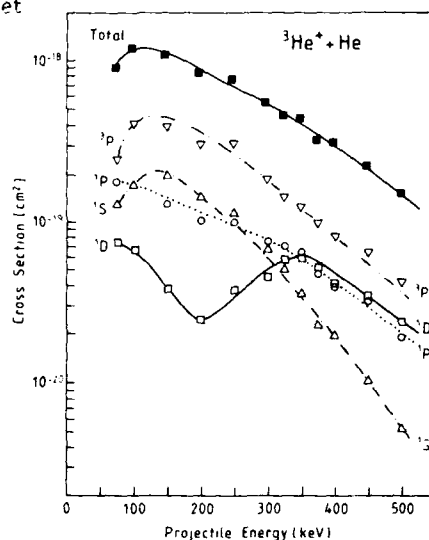


Fig. 10 Absolute excitation cross sections deduced from the lines in Fig. 9 (24).

The projectile electron is, in general, excited by the screened target nucleus while the target electron is captured by the projectile. This process is referred to as nonresonant transfer excitation (NTE). The electron capture and excitation are initiated by electron-nucleus interaction and they occur independently. Thus, the NTE probability is expected to be proportional to the product of the two related excitation probabilities (32). For $\text{He}^+ + \text{He}$ colli-

sions, it has been reported that the cross sections of electron capture into both the 2s and 2p states exhibit the same energy dependence in the present energy region (33, 34).

Transfer excitation may also occur resonantly (RTE) when the projectile electron is excited by the captured electron through electron-electron interaction and subsequently released by autoionization. This process is analogous to the well-known resonant electron scattering process forming doubly excited states. The peak position for such a correlated two-electron process is in principle higher than that of the noncorrelated NTE process. In the present collision systems the RTE peak is expected at the impact energy of about 300 keV (35), which is roughly in agreement with the present result observed for the $(2p)^2$ D state. The peak width of the RTE depends on the momentum distribution (Compton profile) of the initial target electron and is kinematically stretched in the laboratory frame. The width is estimated to be about 400 keV which is also in good agreement with the experimental results. Thus it can be assumed that the peak structure in the 1D excitation cross section is attributed to RTE, and that contributions from NTE are negligible for the production of the 1D state in this energy region. However, other processes like interference between the 1P and 1D states (38) may also cause a cross section maximum as observed.

6. LOW LYING AUTOIONIZING STATES IN Li- AND C-PROJECTILE IONS

As pointed out above zero-degree electron spectroscopy of projectile ions allows to study autoionizing transitions with very low transition energies from neutral or negative ions. Such ions are of fundamental importance in fusion research and reflect strong electron-electron correlation effects, which require and are testing many-body theoretical calculations. First, spectra of low energy electrons (<2 eV) following the decay of low-lying autoionizing states formed in gas (He, CH₄, Ne, Ar) or C-foil collisions with Li- and C-ions (100-500 keV) are shown in Fig. 11.

The inserted spectra indicate peaks in the vicinity of the high energy cusp tails after background subtraction and transformation into the center of mass system. In the Li spectrum three sharp lines occur below 1 eV which most likely stem from autoionizing transitions in neutral Li and possibly in $Li^--(1s^2 2s 2p)^1P$ and $(2s^2 2p^2)^1D$ and 1S initial states. We also note that the structures between one and two eV may arise from doubly excited states in Li^- such as $1s^2 n^2 n' 2'$ with n and $n' > 3$. Principally also high Rydberg states

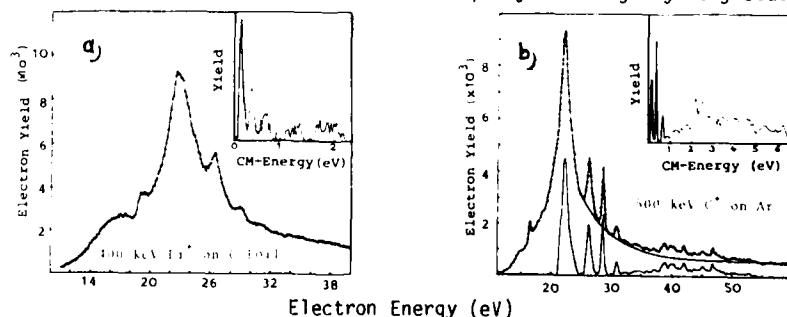


Fig. 11 Spectra of low-lying autoionization lines (<1 eV in C.M. system) from 400 keV excited Li(a) and C(b) ions (500 keV).

associated with doubly excited levels in Li^+ ($n\ell n'\ell'$), Li ($1s n\ell n'\ell'$) and triply excited Li ($n\ell n'\ell' n''\ell''$) states may contribute to the observed spectrum.

A similar tentative interpretation is assumed for the carbon autoionization structures (Fig. 11). A very intense line centered at 0.25 eV may result from $\text{C } 1s^2 2s^2 n\ell n'\ell'$ ($n, n' > 2$) or $\text{C}^- 1s^2 2s^2 2p n\ell n'\ell'$ ($n, n' > 2$) initial configurations. Theoretical transition energies are urgently needed for the data interpretation.

7. CONCLUSION

In conclusion, the method of zero-degree Auger spectroscopy for electrons from fast projectile ions was found to have various advantageous features. Line broadening effects are strongly reduced so that high-resolution spectroscopy is possible for electrons from fast projectiles. The transformation of the Auger spectra from the laboratory to the projectile rest frame yield energies of the projectile and the Auger electrons with relatively high accuracy. Moreover, the use of light target atoms allows the excitation of a few distinct states. Thus, problems are avoided concerning line blending which often inhibits the detailed analysis of Auger spectra produced in heavy ion-atom collisions. The observed peaks are characteristic for the projectile charge state which may readily be varied in the experiments. Consequently it is possible to obtain selective information about Auger transitions and individual excitation processes including electron-electron interaction in ion-atom collisions.

This report is dedicated to Markus, Christian and Christa.

REFERENCES

- (1) M.E. Rudd and J. Macek, Case Studies in Atomic physics, edited by E.W. McDaniel and M.C. McDowell, (North-Holland, Amsterdam, 1973), Vol. 3, p. 47.
- (2) N. Stolterfoht, IEEE Trans. Nucl. Sci. 9, 311 (1976).
- (3) R. Mann, H.F. Beyer, and F. Folkmann, in the Twelfth International Conference on the Physics of Electronic and Atomic Collisions, Invited Talks, Gatlinburg, Tennessee, 1981, edited by S. Datz (North-Holland, Amsterdam, 1981), p. 683.
- (4) S. Schumann, K.O. Groeneveld, G. Nolte, and B. Fricke, Z. Phys. A289, 245 (1979).
- (5) R. Mann, F. Folkmann, and H.F. Beyer, J. Phys. B 14, 1161 (1981).
- (6) R. Mann, H.F. Beyer, F. Folkmann, Phys. Rev. Lett. 46, 656 (1981).
- (7) F. Folkmann, R. Mann and H.F. Beyer, Phys. Scr. T3, 88-5 (1983).
- (8) D. Schneider, M. Prost, D. DuBois, and N. Stolterfoht, Phys. Rev. A25, 3102 (1982).
- (9) D. Berényi, G. Hock, J. Kádár, S. Ricz, V.A. Shchegolev, B. Sulik, D. Varga, J. Végh, Institute of Nucl. Research of Hungarian Academy of Sciences, M-4001 Debrecen Pf. 51, Hungary 1984).
- (10) I. Kádár, S. Ricz, V.A. Shchegolev, B. Sulik, D. Varga, J. Végh, D. Berényi, G. Hock, J. Phys. B18, 275 (1985; B. Sulik to be published).
- (11) N. Stolterfoht, D. Schneider, R. Mann, and F. Folkmann, J. Phys. B10, L281 (1977), N. Stolterfoht, D. Schneider, F. Folkmann, R. Mann, K. Graenereld, Hahn-Meitner-Institut Annual Report 1978, HMI ISSN 0440-0836, Berlin 1979, unpublished.
- (12) R. Mann, H.F. Beyer, F. Folkmann, Physics of Electronic and Atomic Collisions, ed. S. Datz, North-Holland Publ. Comp. Amsterdam, 683 (1982).

- (13) N. Stolterfoht, D. Schneider, D. Burch, B. Aagaard, E. Boving, and E. Fastrup, *Phys. Rev. A* **12**, 1313 (1975).
- (14) R. Bruch, D. Schneider, W.H.E. Schwarz, M. Mienhart, B.M. Johnson, and K. Taulbjerg, *Phys. Rev. A* **19**, 587 (1979).
- (15) R. Bruch, M. Rødbro, P. Bisgaard, and P. Dahl, *Phys. Rev. Lett.* **39**, 801 (1977).
- (16) M. Suter, C.R. Vane, S.R. Elston, G.D. Alton, P.M. Griffin, R.S. Thoe, L. Williams, I.A. Sellin, *Z. Physik* **289**, 433 (1979).
- (17) A. Itoh, T. Schneider, G. Schiwietz, Z. Roller, H. Platten, G. Nolte, D. Schneider, and N. Stolterfoht, *J. Phys. B* **16**, 3965 (1983).
- (18) L.H. Anderson, M. Frost, P. Hvelplund, H. Knudsen, and F. Datz, *Phys. Rev. Lett.* **52**, 518 (1984).
- (19) N. Stolterfoht, A. Itoh, D. Schneider, T. Schneider, G. Schiwietz, H. Platten, G. Nolte, R. Glodde, U. Stettner, W. Zeitz, T. Zouros, International Conference on X-Ray and Innershell Processes in Atoms, Molecules and Solids, Invited Lecture, August 1984, Leipzig, DDR.
- (20) A. Itoh, D. Schneider, T. Schneider, T. Zouros, G. Nolte, G. Schiwietz, W. Zeitz, and N. Stolterfoht, *Phys. Rev. A* **31**, 684 (1985).
- (21) T. Schneider, D. Schneider, W. Zeitz, G. Schiwietz, H. Platten, U. Stettner, N. Stolterfoht, 6. Arbeitsbericht EAS-6, ISSN 0724-4975, ed. by B. Fricke, D.H.H. Hoffmann, D. Kolb, H.O. Lutz, P.H. Mokler, Kassel, April 1985, p. 17.
- (22) T.R. Dillingham, J. Newcomb, J. Hall, P.L. Pepmiller, and P. Ricnard, *Phys. Rev. A* **29**, 3029 (1984).
- (23) N. Stolterfoht, T. Schneider, D. Schneider, Abstracts XIV ICPEAC (1985).
- (24) A. Itoh, T. Zouros, D. Schneider, U. Stettner, W. Zeitz, N. Stolterfoht (accepted, *J. Phys. B*, 1985).
- (25) P. Bisgaard, P. Dahl, B. Fastrup, and W. Mehlhorn, *J. Phys. B: At. Mol. Phys.* **14** (1981), pp. 2023-36.
- (26) A. Bordenave-Montesquieu, A. Gleizes, and P. Benoit-Gattin, *Phys. Rev. A* **25**, 345-67 (1982).
- (27) M. Breinig, S.B. Elston, S. Hultdt, L. Liljeby, C.R. Vane, S.D. Berry, G.A. Glass, M. Schauer, and S.A. Sellin, *Phys. Rev. A* **25**, 3015-48 (1982). P.G. Burke, *Advances in Atomic and Molecular Physics*, Vol. 4 ed. D.R. Bates and I. Eskermann (Academic Press, New York), pp. 173-219 (1968).
- (28) D. Brandt, *Phys. Rev. A* **27**, 1314-18 (1983).
- (29) T.M. Reeves, (1984), private communication.
- (30) J.A. Tanis, E.M. Bernstein, W.G. Graham, M. Clark, S.M. Sahfroth, B.M. Johnson, K.W. Jones, and M. Meron, *Phys. Rev. Lett.* **49**, 1325-8 (1982).
- (31) M. Prost, R. Morgenstern, D. Schneider, and N. Stolterfoht, Abstracts of the Tenth International Conference on the Physics of Electronic and Atomic Collisions, Paris, ed. M. Barat and J. Reinhardt, pp. 994-995 (1977).
- (32) P.L. Pepmiller, P. Richard, J. Newcomb, R. Dillingham, J.M. Hall, T.G. Gray, and M. Stockli, *IEEE Trans. Nucl. Sci.* **NS-30**, 1002-4 (1983).
- (33) T.G. Winter and C.C. Lin, *Phys. Rev. A* **12**, 434-43 (1975).
- (34) R. Shakeshaft, *Phys. Rev. A* **18**, 1930-34 (1978).
- (35) J.M. Feagin, J.S. Briggs, and T.M. Reeves, *J. Phys. B: At. Mol. Phys.* **17**, 1057-68 (1984).
- (36) D. Schneider, C. Moore, and B. Johnson, *J. Phys. B* **9**, L153 (1976).
- (37) J.M. Hanteen, O.M. Johnson, L. Kocbach, *At. Data Nucl. Data Tables* **15**, 305 (1975).
- (38) R. Morgenstern private communication.

SPECTROSCOPY OF HYDROGENLIKE AND HELIUMLIKE KRYPTON IONS

Jean Pierre BRIAND

Université P&M Curie*, Institut Curie Section de Physique et Chimie
11, rue Pierre et Marie Curie, F-75231 Paris Cedex 05

Hydrogenlike and heliumlike krypton ion beams have been prepared for the first time. The characteristic x rays emitted by these ions as well as the lifetimes of the excited levels have been precisely measured. These experiments have provided some checks on QED (Lamb shift, diamagnetic effect of spin-orbit), and on three-body relativistic theory in the heaviest ions available at present.

1. INTRODUCTION

We shall report in this talk on a series of experiments on hydrogenlike and heliumlike krypton ion beams. These beams have been produced with the two big heavy ion accelerators of the european community : the UNILAC at GSI Darmstadt (FRG) and the GANIL at Caen (France). The experiments have been carried out by the following international collaborations :

European community

P. Indelicato, P. Charles, M. Tavernier, V. San Vicente, O. Gorceix,
J.P. Briand (Université P&M Curie)
D. Liesen, H. Beyer, F. Bosch (GSI Darmstadt)
J.P. Desclaux (CEN Grenoble)

U.S.A.

R. Marrus (University of California Berkeley)
P. Richard (Kansas State University).

The aim of the experiments was the investigation on some QED or relativity effects in the strongest available fields, i.e. in the heaviest few electron ions.

Till 1982, the maximum energy delivered by the heavy ion accelerators was of the order of 10 MeV/amu. With such an energy, it was not possible to prepare fully stripped ion beams for elements of atomic numbers larger than $Z \approx 26$ (1). In the past few years, some new machines have been developed which have provided more energetic ions : the BEVALAC at Berkeley accelerating ions up to 1 GeV/amu, the UNILAC at Darmstadt whose energy has been upgraded to 20 MeV/amu, and the GANIL at energies up to 100 MeV/amu. It is now possible with the BEVALAC to prepare fully stripped uranium beams. These ion beams of relatively small intensity have been used, up to now, mainly for collision studies as reported in some talks in this conference. We shall mainly concentrate here on the ion beams delivered by the UNILAC and the GANIL which provided, for the first time, with a large intensity, fully stripped krypton ions (and very lately xenon ions), allowing accurate spectroscopic studies. We shall successively describe how to produce those ion beams and how to measure their unknown atomic properties such as energy losses, charge state distributions in thin foils, excitation mechanisms, and the experimental results on the decay of hydrogenlike and heliumlike ions. These experiments, being the first ones performed at the GANIL in the field of atomic physics, we shall begin with a brief description of this newly opened facility.

* Unité associée au CNRS 040771

Work supported by NATO Grant No.RG252.80

2. THE GANIL HEAVY ION FACILITY

The GANIL (Grand Accélérateur National d'Ions Lourds), located in the vicinity of Caen, delivered the first ion beam in the beginning of 1983. The machine has been operational since 1984. The first experiment in atomic physics using the GANIL, which is presented here, was carried out in June 1984. Originally the GANIL was built for the study of nuclear reactions, but 10% of the beam time could be used for solid state physics or atomic physics.

The GANIL is composed of two identical sector cyclotrons. The first one accelerates ions up to energies of 3 to 6 MeV/amu. The ions after being stripped and charge selected are injected into the second one, working with different harmonics, and reaccelerated up to energies ranging between 10 and 100 MeV/amu (Figure 1).

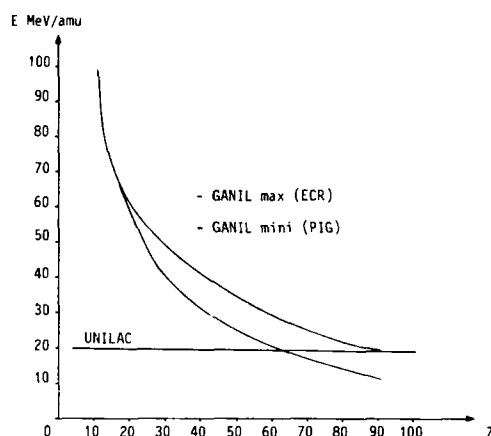


FIGURE 1
Maximum energies delivered by the UNILAC and the GANIL

After being accelerated, the ions are passed through a particle selector (the so-called α spectrometer) in order to be monochromatized up to a precision of 10^{-1} . The ions are then distributed into various dedicated caves of the experimental area. As seen in figure 1, the main characteristic of the GANIL is its ability to accelerate ions of medium mass elements up to energies of 10 to 40 MeV/amu depending on the ion source used. The heaviest ion beam prepared so far is a krypton beam of 36 MeV/amu, with typical intensities of the order of 100 nA. As discussed in the next section, this energy allows the production, with quite a large intensity, of fully stripped krypton ions.

The LISE (Ligne d'Ions Super Epluchés : beam line of highly stripped ions) is a specially dedicated cave for atomic physics studies (Figure 2).

The aim of this device is to provide the charge state separation of the most energetic ion beam. It is made of two identical dipole magnets and a series of quadrupoles. The ions after being stripped are dispersed in charge in the first magnet. A given charge state is then selected and sent into the second dipole magnet in order to tune a perfectly achromatic beam. The completely automatized spectrometer allows the preparation of very well defined ion beams of any charge

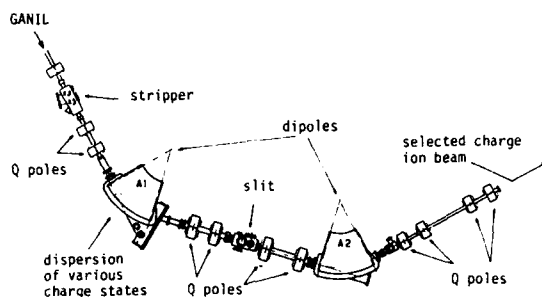


FIGURE 2
Schematic of the dedicated highly stripped ion beam facility
for atomic physics at the GANIL : LISE

state. It also allows an easy study of charge state distributions and energy losses as described in the next two sections.

3. CHARGE STATE DISTRIBUTIONS

The charge state distributions, even if predicted by semi empirical formulae, are not known for krypton ions at such high energies. At 18 MeV/amu, at the UNILAC, the charge state distribution observed after passing the beam through carbons foils of various thicknesses is presented in figure 3. As it can be seen only a very small fraction of the incident beam (less than 1%) is fully stripped. We observed the first hydrogenlike and heliumlike ions in these experimental conditions (2), but could not study the hydrogenlike ions for the production of which the GANIL energies were needed.

Some of the charge state distributions obtained at 36 MeV/amu are shown in figure 4. The observed distributions for foils of various natures and thicknesses are close from those predicted by Betz like formula (see arrows on the right side of figure 5).

In conclusion, the fully stripped fraction of the beam is only reached for very thick targets (6 mg/cm²). This will obviously constitute a serious limitation for the spectroscopic studies of krypton because of great angular and energy stragglings in such targets. This leads to pessimistic predictions for the study of xenon beams. In figure 5, the charge state of the beam for various foils of different thicknesses is compared to a semi empirical formula developed by San Vicente (3).

4. ENERGY LOSSES

As it will be pointed out in section 5, the energy of the ion beam for accurate x-ray measurements must be precisely known. This calibration is easily obtained at the GANIL with the use of the α spectrometer ($\Delta E/E \sim 10^{-4}$). In the experiments described in section 6, the beam is passed through two thick targets (stripping and dressing foils). This provides quite a large energy straggling and a change in the mean energy of the beam that cannot be predicted by extrapolations of the present data. We have made, using the LISE spectrometer, some measurements of these energy losses. The technique consists of looking with a

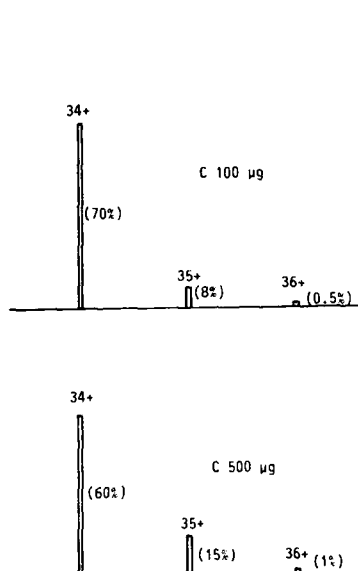


FIGURE 3
Charge state distributions of 18 MeV/
amu krypton ions (UNILAC)

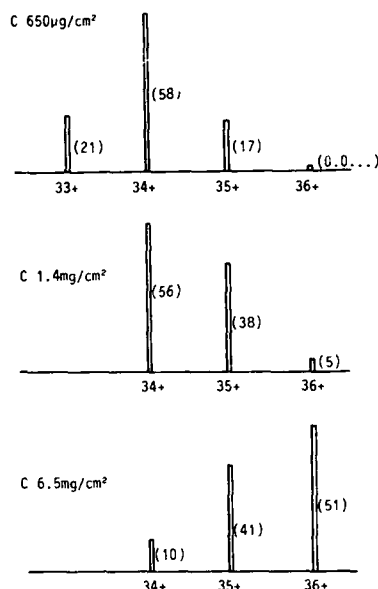


FIGURE 4
Charge state distributions of 35 MeV/
amu krypton ions (GANIL)

position sensitive detector at the angular dispersion of the ions in the first dipole of the LISE. We present in figure 6 some of the experimental results which are compared to the predictions of the Fleury's Table (4). The measured values do not differ, except perhaps in one of the cases, from the Fleury's predictions. The precision of the energy losses, reached in the experiments, is of the order of 10%, a point that will be discussed later.

5. EXCITATION MECHANISMS

The last point to discuss before starting an experiment is the excitation mechanisms. At energies of the order of 10 MeV/amu the excitation of the projectile is mainly due to electron capture via charge exchange with the target. The excitation of the hydrogenlike ions is, for instance, obtained when passing the beam of bare nucleus through a carbon foil (the dressing one) in which the ion picks up an electron in the $n=2$ or $n=3$ state. At energies of the order of 36 MeV/amu the charge exchange cross section, decreasing like $E^{-5.5}$, is very small and therefore it is difficult to excite the beam (1% of the ions is excited with a 36 MeV/amu krypton ion beam when 100% of an iron one can be excited at an energy of 10 MeV/amu). Another mechanism of importance at those high energies is the Coulomb excitation whose cross section, while small, scales only very slowly with the particle energy. Should the process be found important, we would have used, instead of bare ion beam to produce excited hydrogenlike ions, the

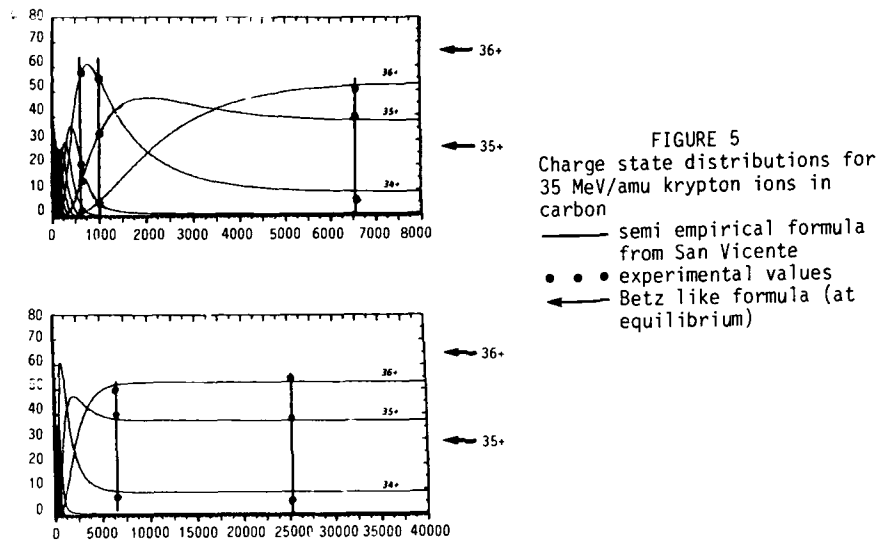
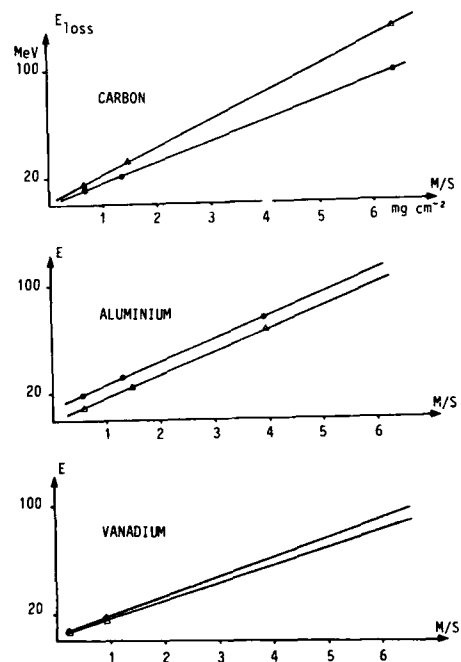
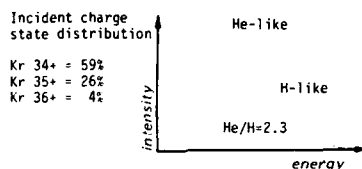


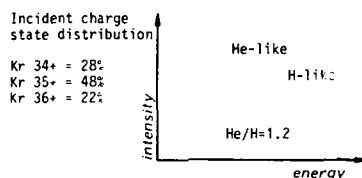
FIGURE 6
Energy loss of 35 MeV/amu krypton
ions in various foils
• • • experimental points (Indeli-
cato et al)
△ △ △ Fleury's Table (extrapolated
points)



Stripper Al 500 μ g/cm², target C 650 μ g/cm²



Stripper Al 1.5mg/cm², target C 650 μ g/cm²



Stripper C 6mg/cm², target C 650 μ g/cm²

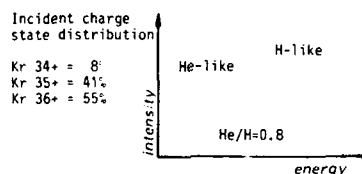


FIGURE 7
Excitation of hydrogenlike and heliumlike
krypton ions at 36 MeV/amu in different targets

hydrogenlike incident ions to be excited in the second foil. We have carried out a series of experiments looking, with a SiLi detector located just in front of the dressing foil, at the characteristic peaks of hydrogenlike and heliumlike ions. Some of the most typical results obtained are presented in figure 7.

The relative x-ray yields, in the same dressing foil, obtained with three different beams having different charge state distributions, are shown in the above figure. One can see the relative yields for hydrogenlike and heliumlike ions changing dramatically with the nature of the incident beam. A careful study of the quantitative data obtained in this experiment leads to the conclusion that at 36 MeV/amu the dominant process is still the capture but the excitation mechanism may not be neglected.

6. THE STUDY OF HYDROGENLIKE IONS

One of the main purposes of the experiments was to check fundamental theories in physics. The most precise check can, in principle, be made using two-body systems (hydrogenlike ions) for which exact calculations are possible. Because all relativistic and QED effects scale like Z^4 , it is interesting to study the hydrogenlike ions of the highest nuclear charge. The first one was studied in 1982 (1). So far the hydrogenlike chlorine and argon ions have been studied using different techniques. For the krypton ions, the technique used is similar to that described in (1). The principle of the experiment is to measure the energy of the characteristic x rays emitted in flight by the ions and to compare them to x-ray standards provided by a conventional x-ray tube linked to the ground (Figure 8).

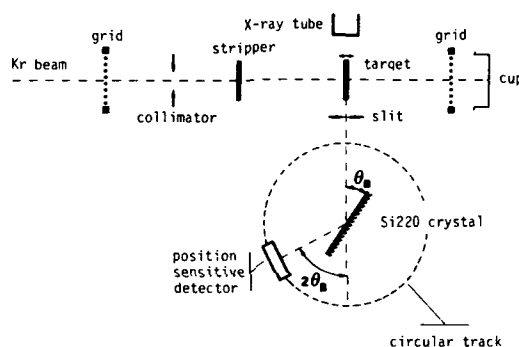
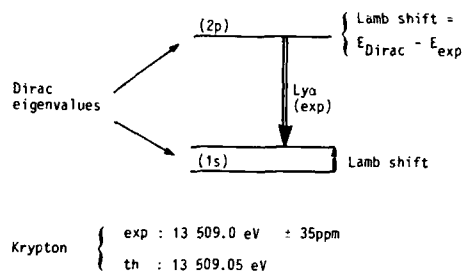


FIGURE 8
Schematic of the experimental set-up

The major difficulty in this kind of experiment is to get rid of the huge Doppler aberrations. Very precise angular measurements of the x-ray and ion beam directions ($\sim 10^{-4}$ rad) are necessary as well as accurate measurements of the ion velocity (technical information on the experimental procedure can be found in (5)). All previously described techniques have been improved in this experiment and a precision of 20 to 40 ppm on the absolute transition energy can be obtained. As seen in section 4, the main contribution to the experimental error bar is the uncertainty on the energy losses in the foils.

The first aim of the experiment was to measure the (1s) Lamb shift of the hydrogenlike krypton ion. The principle is simple and consists, as explained in figure 9, of comparing the experimental energy of the Lyman α ($n=2 \rightarrow n=1$ transition) with the value predicted by the Dirac equation. A typical spectrum of the Lyman α lines of hydrogenlike krypton is presented in figure 10. The experimental values (see Figure 9) have been found in very good agreement with theory (within a few ppm). It constitutes for the moment the most accurate measurement of the (1s) Lamb shift for the heaviest hydrogenlike ions.

The measurement of the spin-orbit splitting is another illustration of the interest of the study of hydrogenlike ions. The spin-orbit splitting is calculated in the text books from the perturbation theory using the well known formula of the spin-orbit energy in classical electrodynamics $w = -\vec{\mu} \cdot \vec{B}$, where $\vec{\mu}$ is the magnetic moment of the electron and \vec{B} the magnetic field induced by its rotation.



Compilation of present data

	H (Z=1)	Cl (Z=17)	Ar (Z=18)	Fe (Z=26)	Kr (Z=36)
precision of Lamb shift z^4		10	1.4	4.2	0.5
arbitrary unit	Hönsch 1981 (9)	Köllne / Richard 1984 (6)	Deslattes 1984 (7)(8)	our results 1982 (1)	June 1985

FIGURE 9
Measurement of the (1s) Lamb shift

Then using the correspondence principle and the perturbation theory, one can easily derive the formula

$$\Delta E = \frac{1}{32} \alpha^4 m_0 c^2.$$

This calculation is however an approximation, not only because it is a perturbative method, but also because the classical $w = -\frac{1}{r} \vec{B}$ formula neglects the diamagnetic effect, i.e. the reaction of the electron magnetic moment to its orbit.

In principle, the exact value of the spin-orbit coupling is, we believe, given by the Dirac equation which included all corrections at all orders. This assumption has however never been checked. In the case of hydrogenlike atoms, for which the spin-orbit energy has been measured with the greatest accuracy (10 ppm) this energy difference between the Dirac value and the corrected Schrödinger's one is much smaller ($\ll 1$ ppm) and cannot be measured. In the case of hydrogenlike ions, owing to the Z^4 scaling law for the spin-orbit energy, the energy now becomes measurable as it is shown in figure 11. Therefore it is now possible to observe the reaction effect of the Dirac relativistic theory and, for the first time, the diamagnetic effect of the spin-orbit.

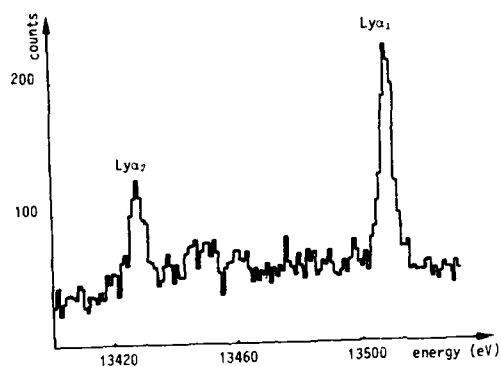


FIGURE 10
Hydrogenlike krypton spectrum

Spin-orbit splitting

magnetostatic
correction

$W = \vec{\mu} \cdot \vec{B}$

$$\Delta H = f(r) \mathbf{L} \cdot \mathbf{S} \Rightarrow \Delta E_{SO} = \frac{1}{32} \alpha^4 m_0 c^2$$

Spin-orbit splitting : hydrogen atom

$$SO(\text{Dirac}) - SO(\text{Schrödinger} + \text{correction}) \ll 1 \text{ ppm}$$

$$SO \text{ experimental value} : \approx 10 \text{ ppm}$$

Spin-orbit splitting : hydrogenlike krypton

spin-orbit		δ	precision exp
Schrödinger + correction	Dirac		
75.6 eV	79.55 eV	3.95 eV	1.4 eV

FIGURE 11
Spin-orbit splitting in hydrogenlike ions

7. THE HELIUMLIKE IONS

The major interest of the study of heliumlike ions is that of the most elementary three-body system in which the relativistic theory can be checked. In the non-relativistic case, the heliumlike ion energy is the sum of the Schrödinger eigenvalues for the electrons in the field of the nucleus plus the repulsive energy between the two electrons, i.e. the expectation value of $\langle \frac{1}{r} \rangle$. This term can be now calculated with a precision larger than that of experimental ones.

In the relativistic case, the electron energy in the field of the nucleus is given by the Dirac equation. In the calculation of the electron-electron interaction energy, all relativistic effects such as the spin-spin interaction retardation effect must be taken into consideration. It is the Breit term. In the calculation of this term, some of the contributions can be evaluated accurately and some others be neglected, but a few ones are absolutely unknown. A point that we would like to discuss.

Those terms scaling like Z^2 or Z^4 have, in the case of helium atoms, a negligible value, but play a great role for very heavy elements such uranium where they can reach 10 to 30 eV. Among the relativistic or QED corrections that have to be taken into account, two of them play an important part: the magnetic correlation effect and the three-body QED effect (all the others, as described in figure 12, are very small and can easily be calculated). The magnetic correlations effect, calculated for the first time by Desclaux (10), is the instantaneous effect in the magnetic spin-spin interaction between the two electrons (it is the relativistic counterpart of the *electrostatic* correlation effect). It has been calculated using the configuration interaction technique based on Dirac Fock results. This effect is, in the case of krypton as shown in figure 12, at present larger than the experimental error bar. The second term is the value of the (1s) Lamb shift in presence of a second (1s) electron. There is, so far, no method to calculate in a straightforward way this three-body effect. The "simplest" one, used at present, is the screening technique. As listed in figure 12 the correction is larger than the experimental error bar. The sum of both terms is found for the moment in reasonable agreement, at least for one of the two major components of the Lyman α spectrum of the heliumlike ion. Both terms scaling differently with Z , it is necessary to make some measurements on heavier systems to check completely the three-body relativistic theory.

Dirac-Fock	13 051.88 eV	
< Breit >	- 15.63	
retardation	- 0.39	
electrostatic correlation	+ 1.13	
magnetic correlation	+ 0.64	
(retard correlation)	(- 0.16)	omitted
	- 0.085	
Lamb shift	- 11.61	
3-body QED	+ 0.82	(+0.6)
total	13 026.75	
experiment (- 20 ppm)	13 026.80 \pm 0.25	

FIGURE 12
Energy of the $(1s)(2p) \ ^3P_1 \rightarrow (1s)^2 \ ^1S_0$ transition of heliumlike krypton ions

8. MEASUREMENTS OF THE LIFETIMES OF HELIUMLIKE IONS

The last point to be presented is the measurement of the lifetimes of most of the metastable levels of heliumlike ions. This experiment was first performed at the GANIL last year, and again two months ago at the UNILAC. The interest of this kind of experiment was to check, also for the first time, relativistic corrections (namely the relativistic part in the two-photon decay) for the oscillator strengths.

Figure 13 shows the typical energy scheme of the $(1s)(2\ell)$ state of a heliumlike ion. All levels can decay radiatively to the ground state, directly or by cascades. Some others are metastable. Among them are the $(1s)(2s)$ states. The $1S_0$ state can decay only to the ground state via a two-photon transition. This process was first observed in 1970 by Schmieder and Marrus (11).

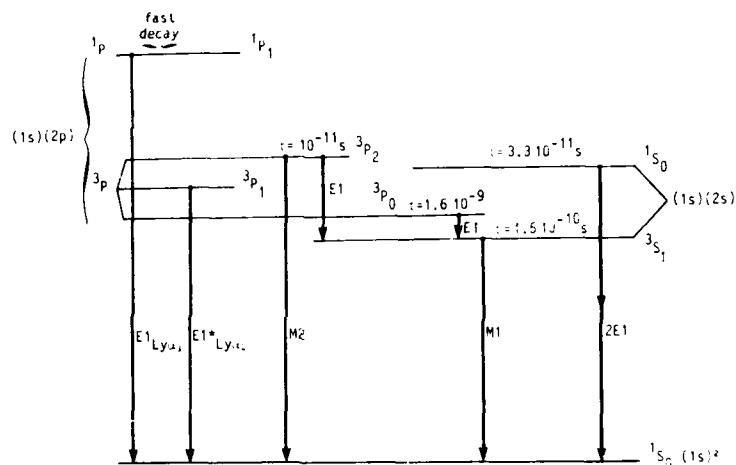


FIGURE 13
Decay scheme of heliumlike krypton ions

The $3S_1$ can also decay to the ground state via a $2E1$ transition but also via a $M1$ one. Due to correlation effects, this decay is slowed down with respect to the $1S_0$ one, but the $M1$ transition, whose contribution is negligible for light elements and scales like Z^{10} , is getting, for the first time, appreciable for krypton ions.

Among the $(1s)(2p)$ levels which are metastable are the $1P_1$ and $3P_0$ ones. The first level mainly decays to the $3P_1$ state for light elements. For heavy elements it chiefly decays directly to the ground state via a $M2$ transition. The $3P_0$ level decays only to the $3S_1$ and subsequently to the ground state (its lifetime is very long according to its small energy). These lifetimes have been measured using a conventional time-of-flight new device allowing the determination of lifetimes of the order of 10^{-11} s. The detector used to observe the two-photon continuous spectrum, the magnetic dipole ($M1$) or the magnetic quadrupole transition is a SiLi detector facing downstream after the foil. The main advantage of such an experiment was to become sensible, namely in the case of the two-

photon decay, to the relativistic effects. We present in figure 14 one of the most typical results obtained in this experiment for the lifetime by two-photon decay. The results, still under study, are in close agreement with recent theory. In the case of decays of two photons, it is then possible to check for the first time the validity of the relativistic theory (12).

non-relativistic theory	relativistic theory	experiment*
$3.19 \cdot 10^{-11} \text{s}$	$3.357 \cdot 10^{-11} \text{s}$	$3.4 \cdot 10^{-11} \text{s}$

FIGURE 14
Lifetime of the 1S_0 state (2E1 decay)
* preliminary result

REFERENCES

- 1) J.P. Briand, M. Tavernier, P. Indelicato, R. Marrus, H. Gould, Phys. Rev. Lett. 50 (1983) 832.
- 2) J.P. Briand, P. Indelicato, M. Tavernier, O. Gorceix, D. Liesen, H.F. Beyer, B. Liu, A. Warczak, J.P. Desclaux, Z. Phys. A 318 (1984) 1.
- 3) V. San Vicente et al, to be published.
- 4) F. Hubert, A. Fleury, R. Bimbot, D. Gardes, Ann. Phys. Fr. 5 (1980) 1.
- 5) J.P. Briand, International Conference on X-Ray and Atomic Inner-Shell Physics, Eugene, Oregon Aug.83, Book of invited papers Ed. B. Crasemann.
- 6) E. Källner, J. Källne, P. Richard, M. Stockli, J. Phys. B Atom. Molec. Phys. 17 (1984) 115.
- 7) P. Richard, M. Stockli, R. Deslattes, P. Cowan, R. LaVilla, B. Johnson, K. Jones, M. Merran, R. Mann, K. Scharfner, Phys. Rev. A 29 (1984) 2939.
- 8) H. Beyer, R. Deslattes, F. Folkmann, and R. LaVilla, J. Phys. B 18 (1985) 207.
- 9) C. Wieman, T. Hänsch, Phys. Rev. A 22 (1980) 192.
- 10) J.P. Briand, M. Tavernier, R. Marrus, J.P. Desclaux, Phys. Rev. A 29 (1984) 3143.
- 11) B. Schmieder, R. Marrus, Phys. Rev. Lett. 25 (1970) 1692.
- 12) G. Drake, to be published

DISSOCIATION OF H_2^+ PRODUCTS OF ELECTRON CAPTURE

D.P. de BRUIJN

FOM-Institute for Atomic and Molecular Physics, Kruislaan 407,
1098 SJ Amsterdam, The Netherlands

With the use of a position- and time-sensitive two-particle-detector it has become possible to perform detailed experiments on dissociations in a fast beam which produces two neutral fragments. In measurements of the dissociative charge exchange of H_2^+ with various target atoms the charge exchange process as well as the dissociative mechanisms in the H_2 molecule are investigated.

1. INTRODUCTION

In collisions of keV H_2^+ ions with atomic or molecular targets H_2 molecules as well as H^+ , H and H^- fragments are produced. The interest in these processes is fundamental and practical: because H_2^+ is the simplest molecule it is accessible for accurate collision theories and next to it empirical knowledge about collisions of hydrogen molecules is important in fusion research and astrophysics. It was already established in one of the earlier experiments (1) that in collisions of H_2^+ with H_2 , the production of H-H pairs through Dissociative Charge Exchange (DCE) is the dominant reaction in the keV range with cross sections exceeding 10^{-16} cm². Nevertheless this process has not yet been the subject of many detailed experiments because of the lack of an appropriate experimental technique, in contrast to dissociations which deliver a charged fragment.

1.1. Experiments

Many scattering experiments have been devoted to the measurement of the total and differential cross sections of the DCE of H_2^+ with various targets (1-4) (and references therein). Since the angular distribution of H-fragments is a convolution of the released kinetic energy (ϵ) and the center of mass recoil angle (θ) it is difficult to extract information on the H_2 states involved. McClure (1) concluded that probably the direct exchange into the repulsive $b^3\Sigma_u^+$ state (see fig. 2) is the dominant channel in the DCE of H_2^+ with H_2 . From other experiments (5-7), in which the appearance of excited H-atoms was observed, predissociations of highly excited H_2 molecules was inferred. Recently Gellene et al. (8) performed a combined study of "neutral beam profiles" and fluorescence after collisions of H_2^+ with several metal vapor targets. Radiative dissociation from the $a^3\Sigma_u$ state to the repulsive $b^3\Sigma_u$ state was identified through molecular $b \leftarrow a$ fluorescence.

The first experiments in which the released kinetic energy (ϵ) was directly measured were performed by Meierjohann and Vogler (9,10). They used two channel-trons to detect the Flight Time Difference (FTD) of correlated H-H pairs after charge exchange of H_2^+ with H_2 and noble gas targets. As a new channel the predissociation of the $c^3\Pi_u$ state, and tentatively also of the $e^3\Sigma_u^+$ state, was observed. Very recently another technique was used by Peterson and Bae (11) in which also ϵ is measured but with a low resolution. Neutral products of charge exchange collisions with Cs are converted into negative ions in a second collision and the kinetic energy distribution is measured with an electrostatic analyzer.

Our experimental method (12), described in section 2, can be seen as an extension of the FTD technique. Besides the FTD (τ) simultaneously the mutual dis-

tance (R) of the fragments is measured over the whole solid angle in which fragments are scattered. Measurements on the DCE of H_2^+ , differential in ϵ and θ and with a high resolution, are performed with a whole range of targets. From these experiments all important channels could be studied in detail.

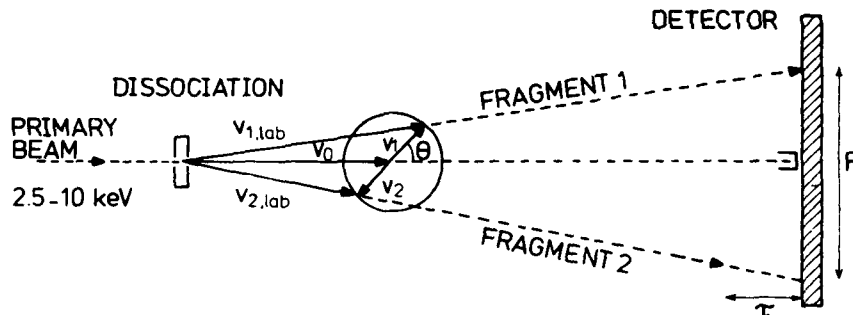


FIGURE 1
Experimental method for Translational Spectroscopy. Both fragments are detected in delayed coincidence on a channelplate detector.

2. EXPERIMENTAL METHOD

Figure 1 gives a schematic drawing of the experimental method (12). Both fragments are detected in delayed coincidence on a time- and position-sensitive double detector, based on micro channel plates. The released kinetic energy ϵ and the c.m. recoil angle θ can be calculated directly, for every event, from the measured mutual distance R and the flight time difference τ as:

$$\epsilon = (E_0/41^2)[(v_0\tau)^2 + R^2] \quad (m_1 = m_2) \quad (1)$$

$$\theta = \arctan(R/v_0\tau) \quad (2)$$

In (1) and (2) τ denotes the flight length from the dissociation to the detector, which has to be fixed, and E_0 and v_0 are respectively the energy and the velocity of the primary beam. The resolution in ϵ is typically 0.5%, the best absolute energy resolution observed so far is 3 meV. It will be clear that this method is very suitable to study DCE since the charge state of the fragments is of no importance. Because both fragments are detected even the scattering of the whole, dissociating, molecule in the charge exchange collision can be measured (13).

3. DISSOCIATIVE PROCESSES IN H_2 AFTER CHARGE EXCHANGE

In figure 2 the potential curves of the H_2 states which are found to be important in the DCE of H_2^+ are drawn. Four different channels ("a"-"d") are indicated in this figure as well as in the "typical" spectrum of figure 3. Among these are all three possible mechanisms for dissociation: i) direct dissociation - process "b", direct Charge Exchange (CE) to the repulsive b-state, ii) radiative dissociation - process "a", CE to the bound a-state which decays radiatively to the b-state and iii) predissociation - processes "c" and "d". In figure 2 also the ionization potentials of the different targets are indicated by vertical dashed arrows at the left.

Already from the realization that NRCE is the dominant mechanism and that the use of the Franck Condon principle is justified in the charge exchange processes

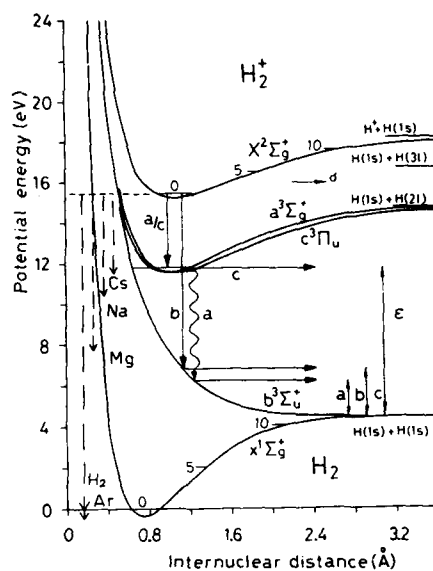


FIGURE 2
Four different mechanisms, denoted a-d, in the Dissociative Charge Exchange (DCE) of H_2^+ .

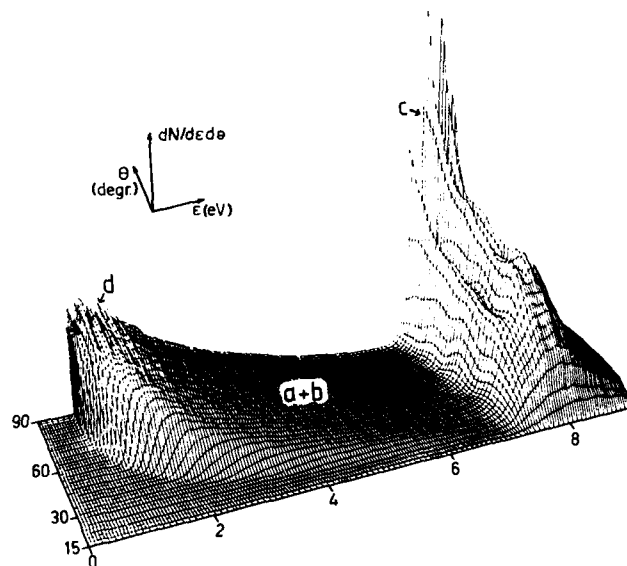


FIGURE 3
Experimental spectrum of the DCE of H_2^+ with a Cs target and a collision energy of 5 keV, differential to the released kinetic energy ϵ and the c.m. recoil angle θ . Different channels a-d (see fig. 2) are indicated.

discussed here, one gets a reasonable qualitative explanation of the results. Next to it the collision velocity v_{\max} where the maximum cross section for CE is reached can be found from the Demkov model (14,15). For the atom-atom case with a fixed resonance energy defect ΔI (fixed internuclear distance in a molecule) holds, with l being a parameter on the order of the dimension of the atoms:

$$(|\Delta I| \cdot l) / (h \cdot v_{\max}) \approx 1 \quad (3)$$

Summarizing this means that in the potential diagram of fig. 2 CE takes place vertically (FC principle) to states which are "chosen" by the target to give a low ΔI (NRCE). If ΔI is larger than 1-2 eV large cross sections will first be reached at a collision energy of roughly 10 keV (Demkov).

More detailed theoretical calculations on charge exchange of molecular ions are very scarce and mainly deal with non dissociative CE in symmetrical systems such as $H_2^+ + H_2$ (16,17). Sidis and de Bruijn (18) have recently published a semiclassical theory on NRCE of molecular ion+atom collisions, differential to the internal parameters of the molecule including its orientation. Calculations are presented for several (coupled) dissociative channels in the charge exchange of H_2^+ with Mg atoms. Good agreement was obtained with the experimental results of de Bruijn et al. (13).

3.1. Experimental results

Since NRCE is the dominant mechanism one observes with a Cs target (fig. 3) mainly processes "a" and "c" which are almost resonant for all vibrational levels. One expects roughly equal populations of the a- and c-states after the collision (18) as a result of the long range sharing process after these states have been mixed to $(2s\sigma_g \pm 2p\pi_u)$ hybrid states during the collision under the Stark effect of the target ion. Moreover processes "a" and "c" are enhanced for all targets because the resonance energy defect is reduced for the lowermost hybrid (18,19).

ϵ -spectra are given in fig. 4 for targets with ionization potentials ranging from 3.9 eV (Cs) to 15.8 eV (Ar) and several beam energies for a Mg target. For alkali targets it is indeed observed that processes "a" and "c" are roughly equally strong, presuming the continuum to consist mainly of process "a". This could be checked by measuring the deflection of the whole molecule, which is larger for the nonresonant process "b", and by experiments with vibrationally selected beams. The peaks at low ϵ of process "d" are only clearly observed with a Cs target, for Na the resonance energy defect ΔI is almost 4 eV (fig. 1) and the contribution has become very small. In general NRCE of H_2^+ is observed to give high cross sections until ΔI is about 2 eV. This means that for an Ar target NRCE to a dissociative state will be weak. The smallest ΔI 's are found for process "b" at large internuclear distances resulting in very low ϵ 's as observed. Neither for the alkali nor for an Ar target the ϵ -spectra changed very much over our energy range of 1.5 - 7 keV in agreement with the Demkov model.

With a Mg target a strong dependance of the ϵ -spectra for the DCE of H_2^+ on the beam energy is observed (fig. 4). For the lowest energy (1.5 keV) the spectrum is dominated by the resonant charge exchange from H_2^+ , $v=0$ to the b-state, calculated to have a cross section exceeding 10^{-14} cm^2 (18). Going to higher beam energies the cross section for $v=0$ decreases, according to eq.(3), while the cross section for higher vibrations increases resulting in a lowering and broadening of the observed continuum. At the same time the cross section for the processes "a" and "c" increases, NRCE is possible because the real ΔI is lower than the asymptotic value of 4 eV because of the Stark effect mentioned before. Process "a" manifests itself as a maximum around $\epsilon = 2 \text{ eV}$ for $E > 5 \text{ keV}$, the fluorescence is most likely around the outer turning point because the cross section increases with v^3 (20).

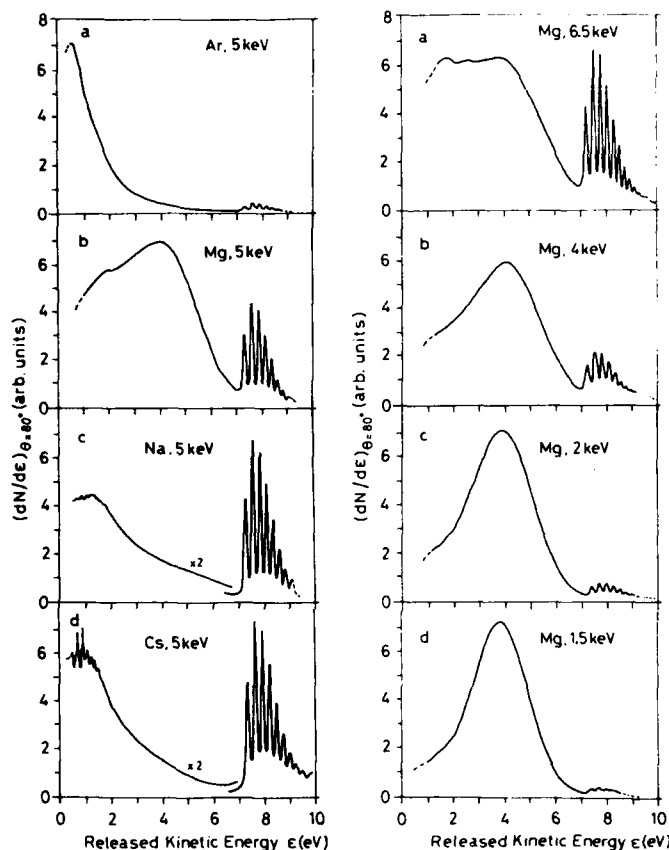


FIGURE 4
Experimental ϵ -spectra after DCE of H_2^+ for different target atoms (left row) and different collision energies (right row) for a Mg target.

4. PREDISSOCIATIONS IN H_2^+

4.1. Predissociations to the first dissociation limit $H(1s) + H(1s)$.

Predissociations producing two ground state H-atoms will have an ϵ larger than 6.5 eV because the first bound level lies this high above the first dissociation limit. For all targets the observed structure could be fully described as the vibrational series of the $c^3\Pi_u$ state (predissociating to the $b^3\Sigma_u^+$ state) (21), excluding other predissociations such as the $e^3\Sigma_u^+$ state. From a computer convolution procedure the populations and partially also the lifetimes of rovibrational levels could be deduced. The lifetime before predissociation produces an exponential tail towards lower ϵ 's because the flight length l is shortened. The lifetime of the $v=0$, $N=1$ level is found to be 6.2 ns, in good agreement with theoretical calculations (22). The most striking conclusion from the measured populations is the strong rotational excitation during the charge exchange collision, especially for higher vibrational levels and increasing con-

siderably with ΔI for different targets.

Knowledge on the behaviour of the $c^3\Pi_u$ state is important not only because it is a triplet state but also because it is the only metastable state in H_2 . Of every rotational level one of the Λ components, together forming the Π state, is metastable (23,24) while the other components (the Π^+ state) is allowed to predissociate. We have used the Π^- state, with all vibrations populated in CE, in photodissociation studies of higher lying triplet (gerade) states (25) as will be presented at this symposium by H. Helm.

4.2. Predissociations to higher dissociation limits.

The predissociative peaks at low e^+ 's, mainly observed with a Cs target, show a clear limit at 1.9 eV characteristic for dissociations into $H(1s) + H(21)$. Figure 5 shows a part of the rotationally resolved (!) spectrum with the assignments to three electronic states, indeed all dissociating into $H(1s) + H(21)$. No evidence was found for predissociations of higher lying Rydberg states, in agreement with the expectation that these states will be only very weakly populated in NRCE. The peaks below 0.35 eV which are unassigned in fig.5 are due to predissociations of quasibound levels of states with a potential barrier, converging to the second dissociation limit.

One of the remarkable results of these experiments is the predissociation of the $J^1\Delta_g$ state of which only the Δ^+ components are observed (by performing measurements with pure para hydrogen, see fig. 5). According to Kronigs selection rules a Δ state has to predissociate here to a Π state (the $I^1\Pi_g$ state) and this would be allowed also for the Δ^- components.

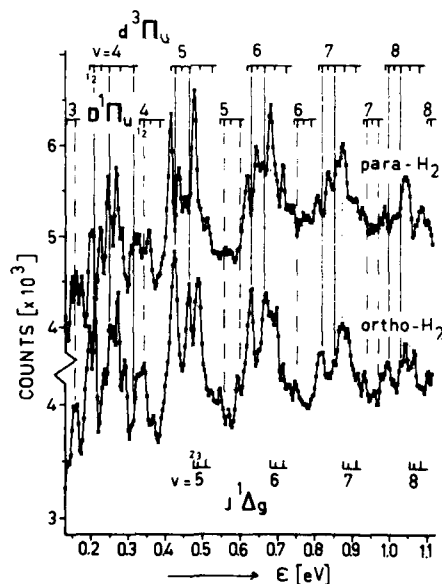


FIGURE 5

Predissociations to the second dissociation limit of H_2 after the DCE of H_2^+ with Cs at 2.5 keV. The upper spectrum is made with pure para hydrogen while the lower spectrum is obtained through subtraction of the para spectrum from a spectrum with natural hydrogen (75% ortho).

5. ORIENTATIONAL OSCILLATIONS

The measured anisotropy of the DCE (13) of H_2^+ will not be discussed in this progress report except for one extraordinary feature: the orientational oscillations, which are just visible in the overall spectrum of fig. 3, on the low energy tails of the vibrational peaks of process "c". These oscillations are not due to an experimental artifact, they differ with the target gas chosen and are best seen with a Cs target. As expected for an interference effect the frequency of the peaks is observed to depend on the collision velocity as $1/v$. It seems obvious to describe the oscillations to process "c", also because they appeared even stronger on the $v=0$ tail when the "background" of other processes around $\epsilon = 7$ eV was removed by using a vibrationally selected $v=0$ beam. In this explanation, however, one runs into a paradox.

As explained in section 4.1 the low energy tails of the vibrational peaks of process "c" are formed by predissociations occurring after the collision chamber of especially the lowest rotational level ($N=1$) which has the longest lifetime. Certainly these molecules will be in a well defined quantum mechanical eigenstate in which the orientational distribution of the internuclear axis is described by low order spherical harmonics. A distribution with at least 3 maxima (at 29, 50 and 66 degrees at 5 keV) as observed, is impossible in these eigenstates. If the charge exchange transition produces an oscillatory orientational distribution, the dissociation has to be immediate or very high rotational levels have to be populated in a predissociative state to make the distribution (or one of comparable complexity in the last case) observable.

ACKNOWLEDGEMENTS

This work is part of the research program of the Stichting voor Fundamenteel Onderzoek der Materie (Foundation for Fundamental Research on Matter) and was made possible by financial support from the Nederlandse Organisatie voor Zuiver Wetenschappelijk Onderzoek (Netherlands Organization for the Advancement of Pure Research).

REFERENCES

- 1) G.W. McClure, Phys.Rev. 140A (1965) 769.
- 2) M. Vogler and W. Seibt, Z.Phys. 210 (1968) 337.
- 3) F.W. Meyer and L.W. Anderson, Physics Letters 54A (1975) 333.
- 4) T.J. Morgan, K.H. Berkner, W.G. Graham, R.V. Pyle and J.W. Stearns, Phys. Rev. A 14 (1976) 664.
- 5) B. van Zyl, D. Jaecks, D. Pretzer and R. Geballe, Phys.Rev. 136A (1964) 1561.
- 6) R.C. Isler, Phys.Rev. A 9 (1974) 1865.
- 7) S. Solov'ev, R.N. Il'in, V.A. Oparin and N.V. Fedorenko, Sov.Phys. JETP 26 (1968) 1097.
- 8) G.I. Gellene, D.A. Cleary, R.F. Porter, C.E. Burkhardt and J.J. Leventhal, J.Chem.Phys. 77 (1982) 1354.
- 9) B. Meierjohann and M. Vogler, J.Phys. B 9 (1976) 1801.
- 10) B. Meierjohann and M. Vogler, Phys.Rev. A 17 (1978) 47.
- 11) J.R. Peterson and Y.K. Bae, Phys.Rev. A 30 (1984) 2807.
- 12) D.P. de Bruijn and J. Los, Rev.Sci.Instrum. 53 (1982) 1020.
- 13) D.P. de Bruijn, J. Neuteboom, V. Sidis and J. Los, Chem.Phys. 85 (1984) 215.
- 14) Y.N. Jemkov, Sov.Phys. JETP 18 (1964) 138.
- 15) R.E. Olson, Phys.Rev. A 6 (1972) 1822.
- 16) T.F. Moran, M.R. Flannery and D.L. Albritton, J.Chem.Phys. 62 (1975) 2869.
- 17) A.V. Evseev, A.A. Radtsig and B.M. Smirnov, Sov.Phys. JETP 50 (1979) 283.
- 18) V. Sidis and D.P. de Bruijn, Chem.Phys. 85 (1984) 201.
- 19) C. Kubach and V. Sidis, Phys.Rev. A 23 (1981) 110.

- 20) H.M. James and A.S. Coolidge, *Phys.Rev.* 53 (1939) 184.
- 21) D.P. de Bruijn, J. Neuteboom and J. Los, *Chem.Phys.* 85 (1984) 233.
- 22) G. Comtet and D.P. de Bruijn, *Chem.Phys.* 94 (1985) 365.
- 23) R.P. Freis and J.R. Hiskes, *Phys.Rev. A* 2 (1970) 573.
- 24) C.E. Johnson, *Phys.Rev. A* 5 (1972) 1026.
- 25) H. Helm, D.P. de Bruijn and J. Los, *Phys.Rev.Lett.* 53 (1984) 1642.

PHOTODISSOCIATION AND PHOTOIONIZATION IN TRIPLET MOLECULAR HYDROGEN

Hanspeter HELM

Molecular Physics Department
SRI International, Menlo Park, CA 94025

A progress report on recent studies of dissociation and ionization processes in triplet molecular hydrogen is given with specific emphasis on experiments in fast molecular beams of $\text{H}_2\text{c}^3\Pi_u^-$ using photofragment and photoionization spectroscopy.

INTRODUCTION

Using metastable molecular hydrogen as an example, we describe three novel experiments in which fast beams of neutral molecules have been employed to study interactions of excited molecules with their dissociation and autoionization continua. We discuss the background of metastable molecular hydrogen, its application to fast-beam experiments and excitation studies of high-lying dissociative, autoionized, and field-ionized states of triplet hydrogen.

METASTABLE MOLECULAR HYDROGEN

The partial metastability of $\text{H}_2\text{c}^3\Pi_u^-$ was first detected by Lichten¹ in a molecular beam magnetic resonance device using RF resonance spectroscopy. The decay mechanisms, lifetimes, fine structure, and hyperfine structure of the c-state have been subject of numerous experimental and theoretical investigations.¹⁻¹⁰ The bound c-state correlates to the first excited state dissociation limit and lies in the continuum of the repulsive $\text{b}^3\Sigma_u^+$ state, the lowest electronic triplet state of H_2 .

Rotational coupling connects the $2p\pi$ orbital of the c-state with the $2p\sigma$ orbital of the b-state, giving rise to predissociation. The doubly degenerate Π state consists of two components with parities $(-1)^N$ and $(-1)^{N+1}$ respectively, where N is the total orbital and rotational angular momentum quantum number.¹¹ The b-state on the other hand, being Σ^+ , has only levels with parity $(-1)^N$. In predissociation both N and parity are conserved. Hence, only the component of the Π state with parity $(-1)^N$ succumbs to rotational coupling to the b-state. This predissociation is observed⁹ and calculated¹⁰ to be rapid (6ns for $v=0$). The component of the Π state with parity $(-1)^{N+1}$ remains unaffected by this predissociation and is long lived.¹ With respect to reflection in a plane containing the rotating nuclei the electronic wavefunction of the metastable component of the Π state behaves antisymmetrically and may therefore be designated as Π^- .

The parity argument above is closely related to the nuclear exchange restrictions that appear in the homonuclear case. For the normal hydrogen isotope the $\text{c}^3\Pi_u^-$ rotational levels exist alternatively in either parahydrogen (even N) or orthohydrogen (odd N). The nuclear exchange operation on Π_u^- is equivalent to a parity operation (in the laboratory frame) followed by an

inversion of the electron coordinates in the molecule fixed frame. Due to the ungerade character of the c -state the latter is antisymmetric. Hence rotational levels of $c^3\Pi_u^-$ with even N are symmetric with respect to an exchange of the nuclei, while levels with N odd are antisymmetric. As a result the metastable $c^3\Pi_u^-$ state exists in orthohydrogen for only odd values of N and in parahydrogen for only even values of N .¹²

In its lowest vibrational level the $c^3\Pi_u^-$ state can only decay by magnetic dipole and electric quadrupole radiation with a calculated lifetime⁵ of 1.76 ms. However, vibrationally excited levels in the c -state lie energetically above the $v=0$ level of the $a^3\Sigma_g^+$ state and electric dipole transitions $c \rightarrow a$ which lie in the far infrared, lead to lifetimes⁶ of the order of 100 μ s for $v>0$ levels of $c^3\Pi_u^-$.

Owing to its long lifetime, high excitation energy (12eV) and ease of formation in near resonant charge transfer the $c^3\Pi_u^-$ state offers itself as a favorable lower state in excitation studies of high lying Rydberg states of H_2 as will be shown below.

FAST BEAM SPECTROSCOPY

The virtues of spectroscopy in fast beams of charged and neutral molecules are associated with the possibility of the precise definition of the molecular species under study and the reduction of inhomogeneous broadening.¹³ The former is related to the fact that a fast molecular ion beam can be mass selected and, if a neutral beam is required, neutralized in a suitable charge transfer gas. This seemingly complex way of preparing the sample molecule offers the possibility of selectively preparing molecules in states other than the ground electronic state, in non-statistical vibrational distributions, or radicals purified from their chemical precursors or reaction products. In what follows we describe how this scheme is accomplished for metastable molecular hydrogen in the triplet state using the apparatus shown in Figure 1.

Electron impact ionization of H_2 in a low pressure ion source forms H_2^+ , populated over a wide range of vibrational levels. This broad distribution reflects the unequal equilibrium internuclear separations of ground state H_2 and H_2^+ , since Franck-Condon arguments determine the ionization event. For spectroscopic studies of neutral molecular hydrogen this ion beam can be neutralized in a charge transfer cell. If alkalis are used⁹ as charge-transfer agent a dominant product in the charge transfer process is the near resonant formation of $H_2 c^3\Pi_u^-$. Again Franck-Condon factors influence the reaction and since H_2^+ is prepared in a wide range of vibrational levels by electron impact, so is the resultant neutral state. Also, since little momentum is transferred by the exchanged electron, a neutral beam with qualities comparable to the primary ion beam results particularly in the case of near resonance. This beam can now be purged of residual ions and apertured to suppress dissociative charge-transfer products which appear with a near isotropic angular distribution. In this manner a fast beam of typically 10^9 molecules per second travelling at speeds of the order of .1% of the speed of light can be prepared. Note that the density in this beam is equivalent to a pressure of 10^{-13} Torr. Nevertheless laser spectroscopy is readily performed with such beams.

An intrinsic second advantage of spectroscopy in a fast beam lies in the dramatic reduction in the inhomogeneous broadening of optical transitions. When an ion cloud is accelerated to high energy a compression of relative

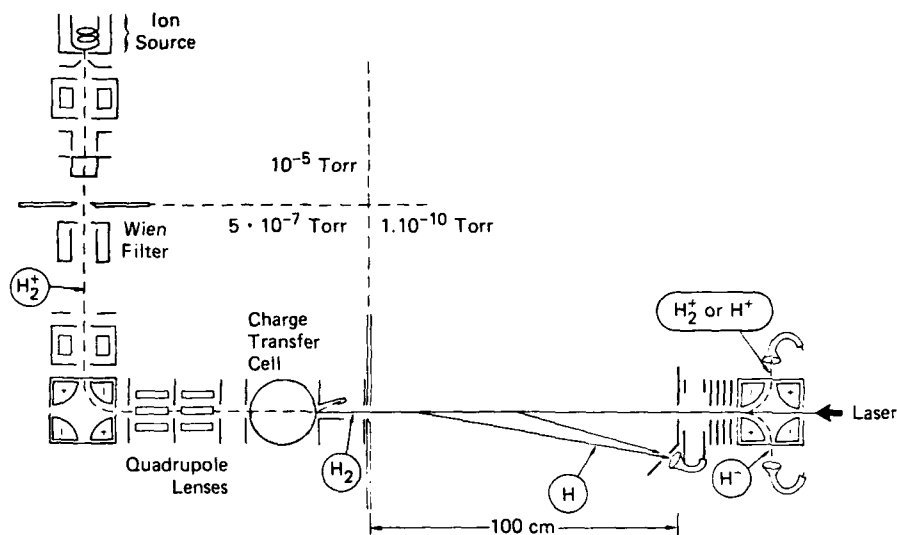


FIGURE 1 SRI Coaxial Laser-Neutral Beam Spectrometer.

velocities occurs when viewing the beam coaxially. If the angular spread of the ion beam is kept low by proper ion-optical focussing the residual spread of relative velocities in the beam is reduced to that of a gas sample at a few degrees Kelvin. For the metastable hydrogen beam formed in the apparatus shown in Figure 1 we have observed¹⁴ a residual Doppler spread, $\delta\lambda/\lambda < 2 \times 10^{-7}$. However, when viewing the beam coaxially, a significant coaxial Doppler shift arises which is readily calculated.

A third beneficial property of the fast beam can be employed in the study of dynamic processes of molecules that are induced by photoexcitation. This advantage derives from the fact that the center-of-mass of the products of a process such as dissociation, autoionization, ion-pair formation or detachment retains, but for a negligible photon recoil, the velocity of the parent. Since the parent is fast at keV energies, efficient single-particle detection techniques can be employed to monitor the reaction products and measure their translational energy, thus enabling to monitor single-molecule processes. The application of fast beams to photofragment spectroscopy and photoionization of neutral molecules is very recent, and is still in a developmental stage, but has high promise. In what follows we describe this new technique for the example of metastable hydrogen molecules.

PHOTODISSOCIATION

A novel approach to the study of dissociative processes in fast neutral beams has become possible with an ingenious time- and position-sensitive detector which has been developed at FOM.¹⁵ For photodissociation studies the

fast beam of excited neutral molecules is crossed with a tunable dye-laser in a crossed beam configuration and the resulting photofragments are detected with a time- and position-sensitive detector, which allows the measurement of the momentum distribution of fragment pairs arising from a single dissociation event.¹⁶ A schematic diagram of this experimental arrangement is shown in Figure 2. The fast neutral beam is crossed with the intracavity beam of a cw dye laser and then stopped in a V-shaped beam flag which shadows the inactive portion of the detector. The flight path from the photon interaction region to the detector is of the order of 150 cm.

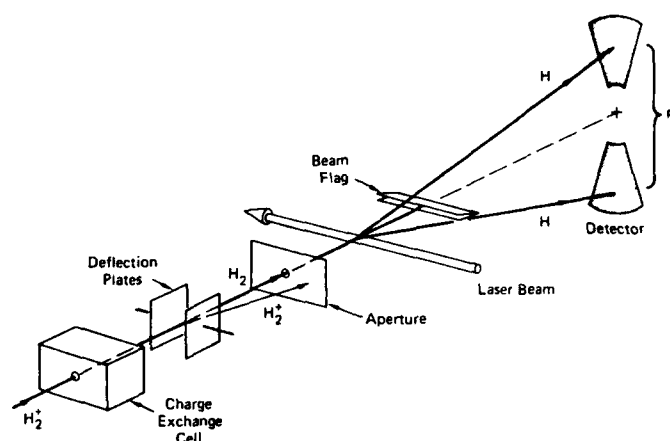


FIGURE 2 Schematic Diagram of the FOM Neutral-Beam Photofragment Spectrometer with Time- and Position-Sensitive Detector.

The multichannel plate detector consists of two opposing sectors of opening angle 2θ which allow separate detection of the two photofragments produced in a single photodissociation event. The detector and its associated electronics permit the measurement of the spatial separation, R , of the two fragments at the channel-plate surface with a precision of typically $70\text{ }\mu\text{m}$ by measurement of the center of charge of each electron cloud emitted by the channel plates with a multinode system using the charge division method.¹⁵ The flight-time difference between these two fragments can be measured with a precision of 500 ps with the fast current pulse induced in the supply lines to the output face of the channel plates when a particle is detected.

By tuning the laser and monitoring the coincidence count rate at the detector we may obtain absorption spectra of transitions in the neutral beam which lead to photodissociation. At an intracavity power of 20 W (multimode) counting rates of typically 10^4 fragment pairs/s are obtained on strong transitions in the $3d+2p$ systems of H_2 if a primary beam current of 10^{-10} A of H_2^+ is charge-exchanged in a 1 cm long cell of 10^{-3} Torr of Rb. Space- and time-resolved spectra of photofragments can then be recorded with the dye-laser set to an absorption transition. If the dissociation is instantaneous, on a time scale short compared to the flight time between the excitation region and the

detector, the time and spatial coordinates of the fragment pair carry all the information required to calculate the center-of-mass angle and energy under which the fragment pair emerges from the dissociation event.

Here we are primarily concerned with the energy release in the c.m. frame. It can be obtained from fragment pairs which appear coincident in time at the two detector halves. Such fragments are formed when dissociation occurs very nearly perpendicular to the molecular beam axis. Under these conditions the c.m. separation energy, W , is related to the measured spatial separation of photofragments, R , by the equation

$$W = E_0(R/L)^2,$$

where E_0 is the parent-beam energy and L is the distance from the photon interaction region to the detector.

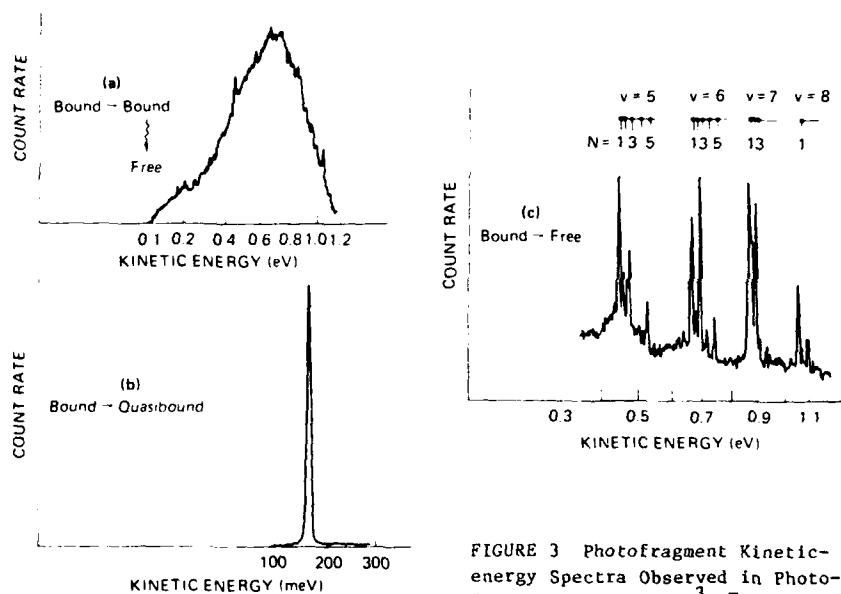


FIGURE 3 Photofragment Kinetic-energy Spectra Observed in Photodissociation of H_2 $c^3\Pi_u^-$

Figure 3 shows three spatial spectra of correlated fragment pairs, $H + H$, which illustrate three different mechanisms of photodissociation which we have observed for the H_2 $c^3\Pi_u^-$ state.¹⁶

(1) Bound-bound excitation followed by radiative dissociation.

The excitation of bound triplet gerade states from $c^3\Pi_u$ gives rise to radiation¹⁷ into the continuum of the $b^3\Sigma_u^+$ state. As an example, excitation of a single rovibrational level in the $g^3\Sigma_g^+$ state will give rise to a continuum distribution of photofragment energies which reflects the overlap of the bound-state vibrational wave function with the continuum wavefunction of the $b^3\Sigma_u^+$ state (see Figure 4).

A number of such bound-bound-free transitions were observed¹⁶ belonging to

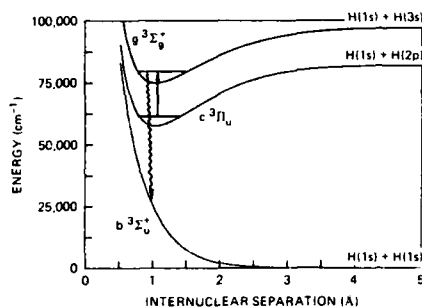


FIGURE 4
Bound Free Radiation
of Excited State

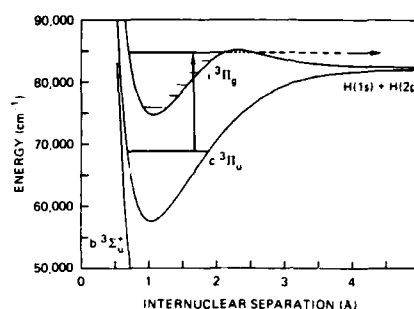


FIGURE 5
Dissociation by Tunneling
of Excited State

the $i^3\Pi + c^3\Pi_u$, $g^3\Sigma^+ + c^3\Pi_u$, $j^3\Delta_g + c^3\Pi_u$ and $h^3\Sigma_g^+ + c^3\Pi_u$ systems. Figure 3a shows an example of the continuous fragment-energy distribution which is obtained when we pump the R1 line of the $i+c$ transition in the (3,3) band. The measured energy distribution represents the lower-energy portion of the total distribution produced, fragments with separation energies > 1.25 eV falling outside the current detection geometry and time window. The small structure which appears in the continuum energy distribution in Figure 3a arises from an underlying bound-free photodissociation which is discussed below.

(2) Bound-quasibound excitation followed by predissociation.

The $i^3\Pi_g$ and $h^3\Sigma_g^+$ states correlate to the energetically higher lying 3p and 3s united atom limits. This correlation leads to initially repulsive electronic states, the repulsion being overcome by the Rydberg character imposed by the H_2^+ core at molecular distances. As a result these states develop intrinsic barriers in their potential energy curves which can support quasibound vibrational levels lying above the asymptotic dissociation limit $H(1s) + H(2l)$ (Fig. 5). These quasibound levels can decay by tunneling through the potential barrier. We observed several transitions to quasibound levels which we have assigned to the (4,4) and (5,5) bands of the $i+c$ system.^{14,16} Figure 3b shows as an example the kinetic-energy spectrum of photofragments produced by pumping the R1 line of the (4,4) band ($W \sim 160$ meV).

In addition to predissociation by barrier tunneling predissociation by rotational coupling to the continuum of a lower electronic state has been observed for the $j^3\Delta_g$ state.¹⁸ Figure 6 shows the dissociative path for this case at the example of $v=6$.

(3) Bound-free photodissociation.

Underlying the discrete photodissociation spectrum a continuous background of laser-induced dissociation was observed which arises from bound-free

photodissociation. At a fixed laser wavelength, bound-free transitions produce photofragments at discrete energies, $W = h\nu - D^{v,N}$, where $D^{v,N}$ is the dissociation energy of the rovibrational level with quantum numbers v, N from which the optical absorption occurs (see Figure 7). Bound-free photodissociation at fixed wavelength leads to fragment energy distributions that reflect

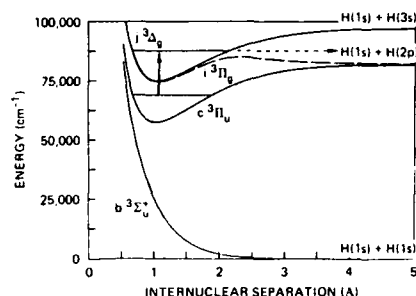


FIGURE 6
Predissociation of Excited State

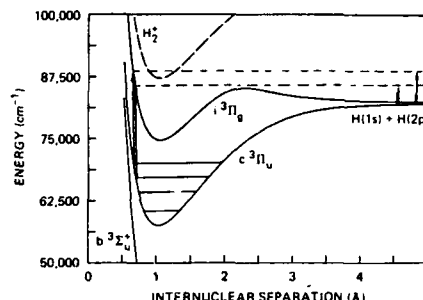


FIGURE 7
Direct Photodissociation

directly the lower-state rotational and vibrational spacings. Because of the very high energy resolution of the time and position-sensitive detector we were able to resolve this distribution experimentally. Figure 3c shows such an energy distribution obtained at a fixed frequency near 16480 cm^{-1} , where no noticeable peak occurs in the absorption spectrum. As indicated in this figure, bound-free transitions are observed from the vibrational levels $v'' = 5, 6, 7$, and 8 of the $c^3\Pi_u$ state, with individual rotational levels being resolved in the kinetic energy spectrum. The intensity distribution over the individual rovibrational bound-free transitions which appear in the kinetic energy spectrum reflects the population in the lower-state levels multiplied by the v - and N -dependent photodissociation cross section. The 3:1 intensity alternation levels belonging to ortho and parahydrogen respectively is clearly apparent from the spectrum in Fig. 3c.

Note that the upper state involved in the direct photodissociation from $v'' = 8$, and 9 of the c -state lies at energies above the $\text{H}_2^+(v=0)$ ionization limit. However, in the visible wavelength range investigated here, ionization was not observed to be a measurable competitor to the dissociative path due to the unfavorable overlap between the continuum wavefunction of the dissociative channel with the vibrational wavefunction of the lowest bound vibrational level of H_2^+ .

The data in Figure 3 demonstrate that a time and position sensitive detector extends the capabilities of fast-beam photofragment spectroscopy¹³ to neutral molecules, permitting very high resolution, at the level of meV, in the translational energy of neutral fragments. The detection arrangement necessarily requires a crossed laser-neutral beam configuration. For such a configuration the ultimate optical apparatus resolution is determined by the angular divergence of the fast neutral beam and the precision at which the laser and neutral beam can be held perpendicular. For a neutral beam

divergence of 1 mrad the residual Doppler broadening for perfect perpendicular alignment amounts to 3 GHz at 7.5 keV beam energy and 6000 Å.

The intrinsic high optical resolution of a fast beam can more easily be exploited in the coaxial configuration (see Figure 1) though at the expense of simultaneous determination of the translational energy of neutral fragments.

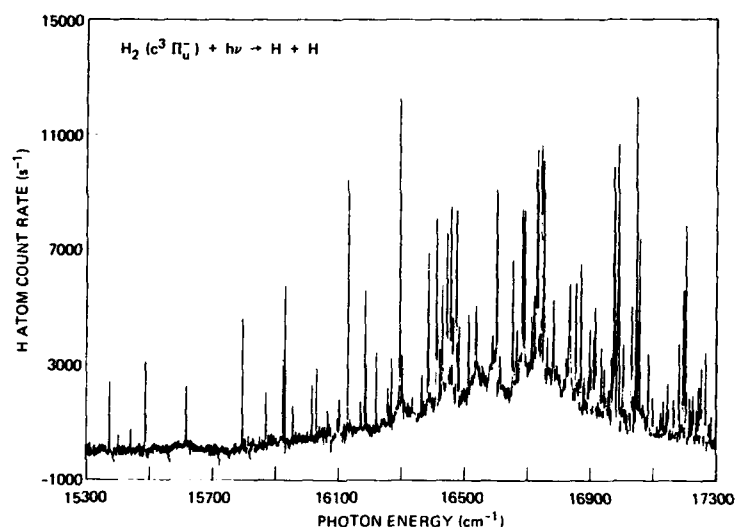


FIGURE 8 Low-Resolution Photodissociation Spectrum of $H_2 c^3\Pi_u^-$.

Figure 8 gives a low-resolution absorption spectrum from the c-state which leads to photodissociation in the visible wavelength range, obtained in the coaxial configuration¹⁴ shown in Figure 1. Here only a small portion of photofragments are detected, namely those which happen to fall into the solid angle seen by the off-axis channeltron. The low efficiency of the small solid angle is compensated for by the fact that the photon interaction region is now 100 cm long. Using a single frequency laser, an optical resolution of 80 MHz was achieved in this configuration. This is illustrated in Figure 9 which gives a high resolution spectrum of the of the Q(1) line of the (2,2) band of the $g^3\Sigma_g^- + c^3\Pi_u^-$ system at 6134.28 Å. The observed splitting of this line arises from the fine-structure and the hyperfine-structure in the c and g states.¹⁴ It should be noted however that the resolution achieved in our fast beam so far is lower than that obtained by Lichten, Wik and Miller¹⁹ in a crossed laser-thermal beam study of the lowest triplet states of H_2 (35-50 MHz).

The photodissociation studies described here can naturally be extended to probe the higher n members of the triplet Rydberg series by using shorter wavelength excitation. For the higher n members at least one additional decay path opens, namely autoionization. In principle also ion-pair formation into

$H^+ + H^-$ might occur via spin-orbit coupling of the triplet Rydberg states to the $1\Sigma_g^+$ terms.

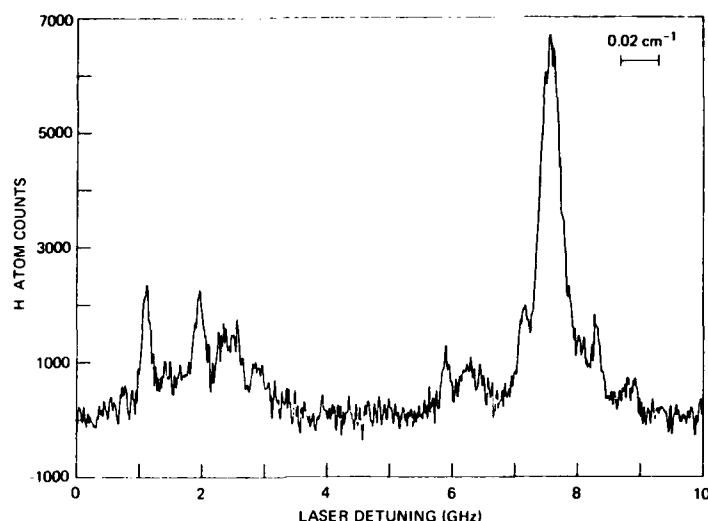


FIGURE 9

High-resolution photodissociation spectrum near 6134.28 Å. The Q(1) transition of the (2,2) band of the g+c system is shown at an apparatus resolution of 0.1 GHz (0.003 cm⁻¹). Fine and hyperfine structure is resolved. The excited state radiates to the H₂b³Σ_u⁺ state, which dissociates into H(1s) + H(1s).

PHOTOIONIZATION

Using the experimental setup shown in Figure 1 we have obtained the excitation spectrum of high lying Rydberg states by detecting the appearance of H₂⁺ formed in autoionization and field-ionization.²⁰ In these experiments, the molecules are excited in the 100 cm long field-free drift region (see Fig. 1), by a collinear dye laser beam. The dye laser operates at 10 Hz and has an energy of typically 50 μJ/pulse after frequency doubling. The 5 ns pulses have a spectral width of 1 cm⁻¹ (.1 cm⁻¹) in the low (medium) resolution mode.

Ionizing states are detected by separating the product H₂⁺ ions from the parent neutral beam into a channeltron using the electrostatic quadrupole deflector at the end of the beam line in Fig. 1. The channeltron output is shaped into 10 ns long pulses and counted with a gated scaler. The gate is opened 200 ns following the dye laser pulse and closed after 3 μs (corresponding to the flight time of 1 keV H₂ molecules over a distance of 100 cm) ensuring that only molecules excited in the field free region of the apparatus are detected. In the absence of the laser, there are practically no H₂⁺ counts (<10⁻⁴ counts/gate width), while the maximum observed count rate for the strong transitions is up to 10 counts/laser pulse, corresponding to a count rate of 4 MHz.

A typical photoionization spectrum observed by scanning the dye laser with 1 cm^{-1} linewidth, from 3360 to 3550 Å is shown in Figure 10. The photoion signal shows contributions from direct photoionization, vibrational autoionization, and field-ionization. The threshold for direct photoionization (in $\Delta v = 0$ transitions, where $\Delta v = v' - v''$) from the $N''=1, v''=0$ level of the c-state lies at 3386 Å, decreasing to 3480 Å for the $N''=1, v''=6$ level. The gradual increase in the continuous portion of the spectrum in Figure 10 with decreasing wavelength reflects the consecutive opening of continuum channel for the individual vibrational levels of the c-state. At wavelengths shorter than ~ 3400 Å the continuum background appears constant, reflecting the wavelength independence of the direct photoionization cross section near threshold. Superimposed on this background roughly one thousand discrete peaks occur, their linewidths apparently being limited by the laser bandwidth (1 cm^{-1}). At wavelengths longer than the $v=0$, direct-ionization threshold, these peaks correspond to the $\Delta v=0$ excitation of the vibrationally autoionizing Rydberg

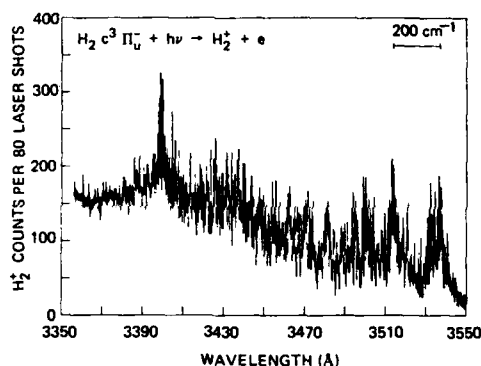


FIGURE 10
Low Resolution Photoionization Spectrum

series converging to vibrationally excited levels, $v > 1$, of the H_2^+ core. A smaller number and less intense series of discrete transitions which populate vibrationally autoionizing levels in $\Delta v \neq 0$ transitions are dispersed over the entire wavelength range covered. Finally, the group of intense discrete peaks near 3400 Å arise from the field ionization of Rydberg series converging to the lowest vibrationally level of the H_2^+ core. The field ionization is accomplished in the 2kV/cm field region of the electrostatic deflector employed to separate the H_2^+ ions from the H_2 beam. (see Fig. 1).

A portion of the ionization spectrum is shown under increased resolution in Figure 11. We have found²⁰ that the general appearance of the experimental spectrum is reproduced in calculations which use a non-interacting single channel Rydberg electron model. Significant shifts from the calculated level positions appear at high resolution. In the light of the simplicity of the model calculation these differences are however not unexpected. It should be noted in the experimental spectra of Figure 11 that all peaks display a

splitting at the level of $\sim 0.2 \text{ cm}^{-1}$. This splitting is due to the fine-structure splitting¹ of the c-state levels.

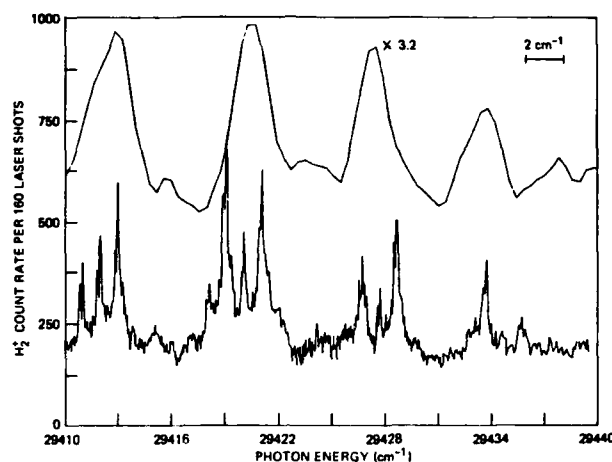


FIGURE 11 Medium-Resolution Ionization Spectrum near 3400 Å. The top trace gives the low resolution spectrum.

CONCLUSION

The experiments described here demonstrate that a time and position sensitive detector can be used in photofragment spectroscopy in a fast molecular beam, allowing high resolution translational spectroscopy on electronic states that are coupled to the dissociation continuum. With this device we are able to investigate bound, quasibound and continuum states of H_2 in the vicinity of its dissociation limit $\text{H}(1s) + \text{H}(2s)$. The same states were investigated under high optical resolution using a coaxial laser-fast neutral beam configuration. These experiments revealed fine and hyperfine structure in some dissociative transitions, proving that for H_2^+ on Cs a very monoenergetic metastable neutral beam is formed in charge transfer. The coaxial configuration was also used in conjunction with a pulsed laser and permitted a first high resolution study of photoionization processes of the triplet H_2 molecule. The coaxial fast beam spectrometer at SRI has since been used successfully in excitation studies of metastable H_3 and N_2 molecules.²¹

ACKNOWLEDGEMENTS

It is a pleasure to acknowledge the contributions of coworkers to the experimental work described here: The measurements on the kinetic energy distribution of the photofragments were performed at FOM in collaboration with Dr. D. P. de Bruijn and Dr. J. Los. The high resolution photodissociation studies were performed at SRI in collaboration with Dr. Nis Bjerre. The photoionization studies were performed at SRI in collaboration with

Dr. R. Kachru. It is also a pleasure to thank Dr. D. L. Huestis for helpful discussions.

The quintessential factor enabling this work is financial support through the National Science Foundation under grant No. PHY 84-11517.

REFERENCES

- 1) W. Lichten, J. Chem. Phys. 26, (1957) 306; Phys. Rev. 120, (1960) 848; Phys. Rev. 126 (1962) 1020.
- 2) W. Lichten, Bull. Am. Phys. Soc. 7, (1963) 43.
- 3) P. R. Brooks, W. Lichten, and R. Reno, Phys. Rev. A 4, (1971) 2217.
- 4) G. Herzberg, Sci. Light (Tokyo) 16, (1967) 14.
- 5) D. K. Bhattacharyya and L.Y.C. Chiu, J. Chem. Phys. 67, (1977) 5727.
- 6) R. P. Freis and J. R. Hiskes, Phys. Rev. A 2, (1970) 573.
- 7) C. E. Johnson, Phys. Rev. A 5, (1972) 1026.
- 8) B. Meierjohann and M. Vogler, Phys. Rev. A 17, (1978) 47.
- 9) D. P. de Bruijn, J. Neuteboom, and J. Los, Chem. Phys. 85, (1984) 233.
- 10) G. Comtet and D. P. de Bruijn, Chem. Phys. 94, (1985) 365.
- 11) L. D. Landau and E. M. Lifschitz, "Quantum Mechanics" Pergamon Press (Oxford, 1976).
- 12) When electron spin is taken into account, this selectivity pertains to all three fine-structure components $J=N-1$, N , $N+1$, which derive from a given value of N .
- 13) H. Helm, in "Electronic and Atomic Collisions," Editors: J. Eichler, I. V. Hertel, and N. Stolterfoht (North Holland, 1984) page 275, and references therein.
- 14) H. Bjerre and H. Helm, ECAP 1985 (Amsterdam), contr. papers p. 444, and XIV ICPEAC (1985, Palo Alto) contr. papers p. 56.
- 15) D. P. de Bruijn and J. Los, Rev. Sci. Instr. 53, (1982) 1020.
- 16) H. Helm, D. P. de Bruijn, and J. Los, Phys. Rev. Lett. 53, (1984) 1642.
- 17) E. E. Eyler and F. M. Pipkin, Phys. Rev. Lett. 47, (1981) 1270; J. Chem. Phys. 77 (1982) 3315; Phys. Rev. A 27, (1983) 2452.
- 18) D. P. de Bruijn, H. Helm, and J. Los, in preparation.
- 19) W. Lichten, T. Wik, and T. A. Miller, J. Chem. Phys. 71, (1979) 2441.
- 20) R. Kachru and H. Helm, Phys. Rev. Lett. 55, (1985) 1575.
- 21) H. Helm, in preparation.

QUANTUM MECHANICAL TIME-INDEPENDENT THEORY OF MOLECULAR PHOTODISSOCIATION

J. Alberto BESWICK

L.U.R.E. - CNRS and Université de Paris Sud, 91405 Orsay, France.

The quantum mechanical time-independent theory of molecular photodissociation is presented. Exact numerical as well as approximate methods are discussed. The theory provides state-to-state photodissociation probabilities and it addresses to the following questions: 1) what factors determine the energy and momentum disposal in the fragments, 2) what is the effect of the dynamics (final state interactions) on the lineshapes and final distributions.

1. INTRODUCTION

Motivation for theory of photodissociation dynamics in polyatomic molecules arises for several reasons:

- a) Molecular photofragmentation in an isolated molecule is a basic reactive process which constitutes one of the primary steps in a large number of photochemical phenomena. Knowledge of the dissociation products and their detailed energy distributions is extremely important in order to understand the reactions in which they may participate in subsequent collisions.
- b) It provides a mean for studying molecular dynamics on excited potential energy surfaces (1,2). In particular, it allows the study of electronic non-adiabatic interactions in half-collisions (3).
- c) It also provides a means for relating features of the potential energy surfaces (steepness, anisotropy, etc.) to the experimentally measured observables.

The detailed theoretical description of photodissociation in a diatomic molecule is relatively simple if only a single repulsive potential energy surface is involved. However, this is very often not the case and many questions concerning non-adiabatic interactions (3) in the photodissociation of diatomic molecules are still under investigation (4). On the other hand, the few degrees of freedom of diatomic molecules usually allow a complete quantum mechanical calculation to be performed if the relevant potential energy curves and couplings are known.

Consider, on the contrary, the photodissociation of a polyatomic molecule. Even if the potential energy surfaces and couplings were known, the problem is almost intractable numerically because of the many degrees of freedom (in parti-

cular rotations) which participate in the dynamics. This was the main reason why for many years quantum mechanical calculations were restricted to collinear triatomic molecules in which rotations and bending degrees of freedom were neglected (5). Only recently, approximate (6-8) and exact (9-16) quantum mechanical calculations in 3-dimensions have started to emerge.

2. GENERAL THEORY

The quantum mechanical partial cross section for photofragmentation from a well-defined initially bound state $|\psi_i\rangle$ to a well-defined final dissociative state $|\psi_{fE}\rangle$, E being the relative kinetic energy of the fragments in the channel f , is given by:

$$\sigma_{i \rightarrow fE} \propto |\langle \psi_i | \vec{\mu} \cdot \vec{e} | \psi_{fE} \rangle|^2 \quad (1)$$

where $\vec{\mu}$ is the dipole moment operator and \vec{e} is the light polarization vector. Eq. (1) is not restricted to direct photodissociation or to only one dissociative surface, and can also be applied to predissociation or to more complex cases (17).

In the case of slow predissociation, however, it is possible to express Eq. (1) in terms of a Lorentzian lineshape. Slow predissociation corresponds to a lifetime much longer than a vibrational period. In that case, it is possible to separate the photon excitation of the intermediate bound state ψ_s , from the decay of ψ_s into the continuum states. The partial rate for predissociation will then be given by the well known Golden Rule expression:

$$\Gamma_{s \rightarrow fE} = \pi |\langle \psi_s | X | \psi_{fE} \rangle|^2 \quad (2)$$

where X is the interaction operator inducing the predissociation (spin-orbit interaction, for instance). The total rate will be given by the sum of the individual rates calculated by Eq. (2) over all possible final channels f . Its value in energy units will correspond to the half-width of the Lorentzian lineshape at half-maximum (HWHM).

There is a striking similarity between Eqs. (1) and (2). Both involve the calculation of the matrix elements of an interaction operator (the radiation and matter coupling in the case of Eq. (1), and the intramolecular coupling X in the case of Eq. (2)), between a bound and a continuum wavefunction. Very often the Condon approximation is invoked implying that the operators are slowly varying functions of the internuclear distances. In that case both Eqs. (1) and

(2) reduce to the calculation of a bound-continuum overlap factor, between nuclear ro-vibrational wavefunctions for the initial and final states.

The rigorous calculation of those matrix elements (or eventually overlaps) for a polyatomic molecule is only possible through a numerical solution of the Schrödinger equation, usually by the integration of coupled equations. Several approximate solutions can also be implemented: distorted-wave diabatic (5) and adiabatic (18), local basis sets (19, 20), half-collision (21) and sudden (8) approximations. All these treatments have in common that the wave function for the continuum state is constructed as a product of a function depending on the internal degrees of freedom of the fragments and a function describing the translational motion along the dissociative coordinate (or the reaction path). This amounts to decouple the motion along the dissociation coordinate from the internal motion of the fragments. The neglected couplings are referred to as "final state interactions".

In order to write the rigorous coupled equations, first we consider a general photodissociation process $AB + h\nu \rightarrow A + B$, where A and B can be atoms or molecules. The coordinate system which is usually chosen in the calculations is the Jacobi dissociation one: the internuclear distance between the two center of mass of the fragments, \vec{R} , and a collection of internal coordinates, \vec{r} , describing the fragments A and B and their orientations with respect to \vec{R} (body-fixed system of coordinates). We shall describe the total wavefunctions as linear combinations of appropriate basis functions describing the internal motion of A and B at $R \rightarrow \infty$, and the rotation of the \vec{R} axis. This basis set is characterized by the quantum numbers $vJM\Omega$, where J is the total angular momentum quantum number, M its projection on the laboratory z-axis, Ω its projection on the R axis (the body-fixed axis), while v is a collection of quantum numbers describing vibrations, rotations and electronic degrees of freedom of the fragments. Expanding the total wavefunction in terms of this basis set:

$$|\psi\rangle = R^{-1} \sum_{v\Omega} \Phi_{v\Omega}(R) |vJM\Omega\rangle \quad (3)$$

and introducing into the Schrödinger equation $H\Psi = E\Psi$, one gets the familiar coupled equations:

$$\begin{aligned} & - \left[\frac{\hbar^2}{2\mu} \frac{d^2}{dR^2} + \langle vJM\Omega | (V + \frac{\hbar^2}{2\mu R^2}) | vJM\Omega \rangle + E_{v\Omega} - E \right] \Phi_{v\Omega}(R) = \\ & = - \sum_{v'\Omega'} \langle vJM\Omega | (V + \frac{\hbar^2}{2\mu R^2}) | v'JM\Omega' \rangle \Phi_{v'\Omega'}(R) \end{aligned} \quad (4)$$

where V is the interfragment interaction defined by $V = H - H_A - H_B$, with H_A and H_B being the Hamiltonians for the free molecules. Thus V goes to zero as R goes to infinity. In Eq. (4) we have denoted by $E_{v\Omega}$ the asymptotic internal energy of the fragments, i.e., the eigenvalue of $H_A + H_B$.

A set of coupled equations have to be solved for the initial bound as well as for the final dissociative state. The matrix elements involved in Eqs. (1) and (2) can then be computed. Eqs. (4) can be solved by the use of scattering integrators with the appropriate boundary conditions (22). The first exact method which has been developed to treat photodissociation in polyatomics was the "artificial channel algorithm" (23, 1). Other methods have also been proposed (24). In what follows, we shall provide two examples of the application of the "artificial channel method" to study the role of the anisotropy of the potential energy surface on the final rotational distribution of the fragments.

3. EXAMPLES

The first example (11) is a case of electronic predissociation of a triatomic molecule and it models the predissociation of the zero-point level of $N_2O^+(A)$. The initial bound state A is linear and predissociation proceeds through spin-orbit coupling to a ${}^4\Pi$ surface, the strength of the interaction being estimated to be of the order of 3 cm^{-1} (11). The predissociation lifetimes are very long compared with the vibrational and rotational periods and therefore Eq. (2) is valid. Furthermore, the spin-orbit interaction can be considered to be a slowly varying function of the nuclear displacements and can be taken out of the matrix element in Eq. (2).

The potential energy surface for the final dissociative state was taken of the form:

$$U = A e^{-\alpha R} f(\theta) + D + \frac{1}{2} k (r - r_e)^2 \quad (5)$$

with

$$f(\theta) = 1 - \frac{\chi}{2} \sin^2 \theta \quad (6)$$

θ being the angle between the two vectors \vec{R} and \vec{r} .

Let us consider the results obtained with an anisotropy parameter $\chi = 1$. In figure 1 the partial rates for predissociation into different rotational states of the NO fragment in the $v = 0$ vibrational state, are represented. It is seen that the final rotational distribution is rather broad with a maximum at $j \sim 7$.

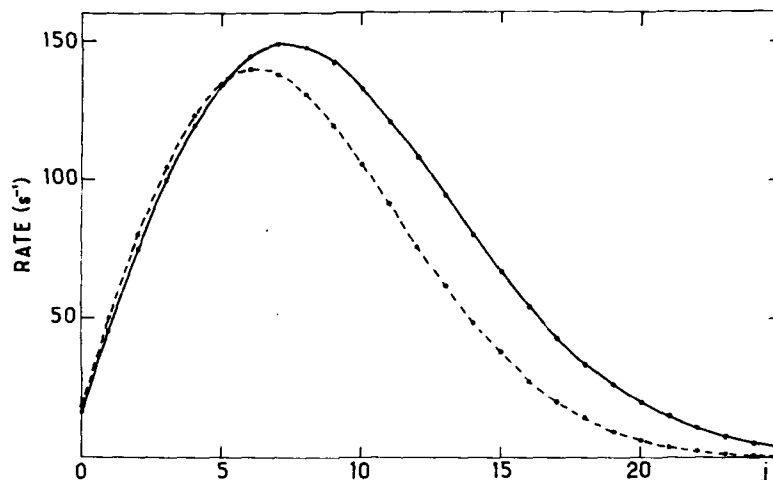


FIGURE 1

Partial rates for predissociation into different rotational states of the fragments. — $\chi = 1$, --- $\chi = 0$.

As a comparison the calculation with $\chi = 0$ (isotropic potential) is also presented in fig. 1. We notice that the effect of the anisotropy in the final potential energy surface is to shift the rotational distribution to larger j but the overall distributions are quite similar. This has been already found in other calculations (10), and seems to be a general result for dissociative surfaces which are purely repulsive such as the one used in this calculation. A very different result is expected for surfaces which present a barrier for the angular orientation corresponding to the initial geometry of the molecule. Then in order to dissociate, the molecule has to bend and the fragments acquire large rotational excitation. The $\text{H}_2\text{O(A)}$ dissociative continuum is a well known case of this type and the OH fragments are produced with very large rotational excitation (9). On the other hand the first dissociative continuum of H_2O , which is a direct (purely repulsive) process leads to rotationally cold OH fragments (25).

The fact that even without anisotropy in the final dissociative energy surface there is a whole distribution of rotational states in the fragments is well understood and has been extensively discussed in the literature (6, 7). Briefly, the initial state has a zero point bending. Associated to it is a distribution of geometries around equilibrium with a width $\Delta\theta$. After dissociation (if no additional torques are exerted as in the case $\chi = 0$) this initial state projects

onto the free rotor states of the fragments. Hence there will be a distribution of rotational states with a total width Δj such that $\Delta j \Delta \theta \sim 1$.

The second example corresponds to vibrational predissociation in the $(\text{HF})_2$ dimer. The $(\text{HF})_2$ dimer is possibly the simplest of all hydrogen bonded molecules. The first calculations for vibrational predissociation in this system was performed by Ewing (26) using a collinear model. This calculation gives lifetimes many orders of magnitude larger than those observed experimentally (27). Ewing suggested that this apparent contradiction does not exist in the real three dimensional world where the effect of rotations may speed up the dissociation.

In the calculations of ref. (16), the proton acceptor monomer was constrained to its equilibrium position and the quasi-triatomic system $\text{FH}-(\text{FH})$ was treated fully, including stretching and bending degrees of freedom. The linewidth (lifetime) and the final rotational distribution of the fragments have been obtained by converged close-coupling quantum mechanical calculations using the artificial channel method. The potential energy surface of Cournoyer and Jorgensen (28) was used.

The results are drastically different from those obtained in the collinear model, reflecting the importance of the rotational-vibrational coupling in systems with high anisotropy and low moment of inertia. The lifetime obtained is now in good agreement with experiment. The final rotational state distribution of the HF fragment is highly inverted as can be seen from figure 2 where the individual linewidths for vibrational pre-

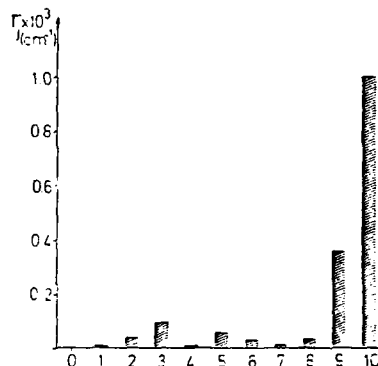


FIGURE 2

dissociation as a function of the rotational quantum number j is presented. These calculations clearly point out that clusters may play an important role in inducing rotational population-inversion in the HF hydrogen bonded molecules, and this may also be true for other systems as well.

4. CONCLUSIONS

Recently several quantum mechanical 3-dimensional studies of photodissociation of small polyatomic molecules have been conducted. This opens a new generation of detailed comparisons between exact and approximate treatments in this area. It also provides a mean for relating features of the system to the experimental

rotational distributions, angular distributions and polarization which can now be measured experimentally thanks to the combination of lasers and supersonic beams.

REFERENCES

- 1) G. Balint-Kurti and M. Shapiro, in: Photodissociation and Photoionization, ed. K.P. Lawley (J. Wiley, New-York, 1985).
- 2) J.P. Simons, *J. Phys. Chem.* 88 (1984) 1287.
- 3) S. Singer, K.F. Freed and Y. Band, *J. Chem. Phys.* 79 (1983) 6060.
- 4) M. Glass-Maujean and J.A. Beswick, to be published.
- 5) K.F. Freed and Y. Band, in: Excited States, Vol.3, ed. E.C. Lim (Academic Press, New-York, 1977) p. 109, and references therein.
- 6) M. Morse, K.F. Freed and Y. Band, *Chem. Phys. Lett.* 44 (1976) 125; *J. Chem. Phys.* 70 (1979) 3604 and 3620; *Chem. Phys. Lett.* 67 (1979) 294; *J. Chem. Phys.* 74 (1981) 4395.
- 7) J.A. Beswick and W.M. Gelbart, *J. Phys. Chem.* 84 (1980) 3148.
- 8) S. Miret-Artes, G. Delgado-Barrio, O. Atabek and J.A. Beswick, *Chem. Phys. Lett.* 98 (1983) 554.
- 9) E. Segev and M. Shapiro, *J. Chem. Phys.* 73 (1980) 2001.
- 10) R.W. Heather and J.C. Light, *J. Chem. Phys.* 78 (1983) 5513.
- 11) O. Atabek, J.A. Beswick and G. Delgado-Barrio, *J. Chem. Phys.* in print.
- 12) V. Engle and R. Schinke, to be published.
- 13) J.M. Hutson, C.J. Ashton and R.J. LeRoy, *J. Phys. Chem.* 87 (1983) 2713; J.M. Hutson and R.J. LeRoy, *J. Chem. Phys.* 78 (1983) 4040.
- 14) I.F. Kidd and G. Balint-Kurti, *Chem. Phys. Lett.* 101 (1983) 419; *J. Chem. Phys.* in print.
- 15) D. Chuljian, J. Ozment and J. Simons, *J. Chem. Phys.* 80 (1984) 176.
- 16) N. Halberstadt, Ph. Bréchignac, J.A. Beswick and M. Shapiro, to be published.
- 17) J.A. Beswick and J. Durup, in: Chemical Photophysics, eds. P. Glorieux, D. Leclerc and R. Vetter (CNRS, Paris, 1979).
- 18) V. Kresin and W.A. Lester Jr., *Int. Journal of Q. Chem.* 15 (1981) 703; *J. Phys. Chem.* 86 (1982) 2182.
- 19) C.E. Caplan and M.S. Child, *Mol. Phys.* 23 (1972) 249.
- 20) A.J. Lorquet, J.C. Lorquet and W. Forst, *Chem. Phys.* 51 (1980) 241, 253 and 261.
- 21) O. Atabek, J.A. Beswick, R. Lefebvre, S. Mukamel and J. Jortner, *J. Chem. Phys.* 65 (1976) 4035.
- 22) G. Balint-Kurti and M. Shapiro, *Chem. Phys.* 61 (1981) 137.
- 23) M. Shapiro, *J. Chem. Phys.* 56 (1972) 2582.
- 24) a: R.W. Numrich and K.G. Kay, *J. Chem. Phys.* 70 (1979) 4343; b: J.E. Grabenstetter and R.J. LeRoy, *Chem. Phys.* 42 (1979) 41; c: K.C. Kulander and J.C. Light, *J. Chem. Phys.* 73 (1980) 4337; d: S. Chu, *J. Chem. Phys.* 73 (1980) 4772; e: Y.B. Band, K.F. Freed and D.J. Kouri, *J. Chem. Phys.* 74 (1981) 4380; f: O. Atabek and R. Lefebvre, *Chem. Phys.* 55 (1981) 395, *ibid.* 56 (1981) 195; g: K. Kodaa and A.D. Bandrauk, *Chem. Phys.* 57 (1981) 461.
- 25) P. Andresen, G.S. Ondrey, B. Titze and E.W. Rothe, *J. Chem. Phys.* 80 (1984) 2548; R. Schinke, V. Engels and V. Staemmler, to be published.
- 26) G.E. Ewing, *J. Chem. Phys.* 72 (1980) 2096.
- 27) a: T.R. Dyke, B.J. Howard and W. Klemperer, *J. Chem. Phys.* 56 (1972) 2442; b: W. Klemperer, *Ber. Bunsenges. Phys. Chem.* 78 (1974) 1281; c: D.A. Dixon, D.R. Herschbach and W. Klemperer, *Faraday Discuss. Chem. Soc.* 62 (1977) 341; d: A.S. Pine and W.J. Lafferty, *J. Chem. Phys.* 78 (1983) 2154; e: A.S. Pine, W.J. Lafferty and B.J. Howard, *J. Chem. Phys.* 81 (1984) 2939; f: R.D. Suenram, F.J. Lovas and W.J. Lafferty, to be published.
- 28) M.E. Cournoyer and W.L. Jorgensen, *Mol. Phys.* 51 (1984) 119.

ANALYTIC MULTICHANNEL THEORY OF MOLECULAR DISSOCIATION

Paul S. JULIENNE and Frederick H. MIES

Molecular Spectroscopy Division, National Bureau of Standards, Gaithersburg,
MD 20899*

A generalized multichannel quantum defect analysis of the close coupled molecular wavefunction for arbitrary potentials gives a unified description of the bound and scattering states of the diatomic molecule AB by defining a real symmetric matrix $Y(E)$ which can be analytically continued across a dissociation threshold. The theory also leads to a half collision analysis of weak predissociation and photodissociation whereby the transition amplitude matrix is separated into factors representing short range Franck-Condon transitions and long range final state interactions. For sufficiently high fragment separation velocity, the effects of final state interactions on product distributions are well approximated by small departures from the recoil limit as prescribed by pure frame transformations among Hund's coupled electronic-rotational states.

1. INTRODUCTION

The process with which we are concerned here is that of molecular dissociation, that is, the formation of an unstable state of the molecule AB which separates to fragments A and B. There are a variety of ways by which a dissociative continuum state can be excited: through initial preparation of a bound metastable state which predissociates, through direct photoexcitation, or perhaps through some collisional excitation process. Generally the items of interest for measurement or calculation are the total rate at which the process occurs and the branching ratios which describe the distribution of particular final states.

The dissociative states of the species AB are also the collisional or scattering states of the fragments A + B. Therefore there has been a considerable amount of interest and success recently in generalizing close coupling scattering algorithms for the numerical calculation of photodissociation transition amplitudes (1-7). The theory (8-13) which we will summarize here is complementary to these numerical approaches. It is based on an analysis of the structure of the close coupled, or multichannel, time independent scattering wavefunction. It will hopefully lead to useful insights concerning molecular dissociation and also lend itself to the development of quantum and semiclassical approximations. Although our development has concentrated on application to neutral atom scattering, that is, diatomic dissociation, many of the features of the theory are general and need not be restricted to this case.

We call our approach a generalized multichannel quantum defect analysis (MCQDA) (10), since it is strongly motivated by the concepts of standard multichannel quantum defect theory (MQDT) (14,15). The latter is designed to treat problems associated with bound Rydberg states, autoionizing resonances, and electron-ion scattering. It has not only been successfully applied to many

*This work was sponsored in part by the Air Force Office of Scientific Research.

atomic problems, but has also been extended to treat molecular bound and dissociative states in the vicinity of an ionization threshold (16,17). This standard MQDT makes heavy use of the properties of the Coulomb potential and its solutions. The generalized MCQDA has been developed by us (10,11) and others (17-19) to apply to systems described by arbitrary potentials, for example, the Born-Oppenheimer potentials for the interaction of A and B.

There are two features of the theory which we will emphasize in this paper. First, the theory enables us to define a real, symmetric matrix $Y(E)$ that can be analytically continued across thresholds and thereby relate the properties of open channel scattering states above threshold and predissociating closed channel resonances below threshold (10,11). Second, we will explicitly consider the case of weak coupling between an initial state and a manifold of final states, and show how a half-collision factorization of transition amplitudes for predissociation and photodissociation can be developed (12). This analysis will be illustrated by interpreting photodissociation and radiative redistribution experiments in which an aligned 1P atom is produced following molecular absorption of a polarized photon.

2. MCQDA FORMULATION

In general the wavefunction that describes the diatomic species AB at total energy E can be expanded as

$$\psi_{\alpha}(E) = \sum_{\alpha} |\alpha\rangle F_{\alpha\alpha}(E, R)/R \quad (1)$$

where the basis functions $|\alpha\rangle$ span all coordinates except the AB interfragment separation R . This may also be written in the following matrix notation, where $|\alpha\rangle$ is a row vector:

$$\psi = |\alpha\rangle F(E, R)/R \quad (2)$$

Introduction of eq. 1 into the Schrodinger equation, $H\psi = E\psi$, generates the standard matrix Schrodinger equation, or equivalently, the set of close coupled equations,

$$\frac{d^2}{dR^2} F + \frac{2\mu}{\hbar^2} [E \cdot 1^0 - W(R)] F = 0, \quad (3)$$

where 1^0 is the unit matrix [In this paper diagonal matrices are always indicated by a superscript zero]. The symmetric normally nondiagonal matrix W , which describes the potentials and couplings among the various states α , is found by taking matrix elements of the total Hamiltonian over the basis function $|\alpha\rangle$.

Although it is possible to set up and solve such equations using a variety of choices of basis $|\alpha\rangle$, the scattering boundary conditions in the limit of large R must be applied using a particular basis set, namely, the channel state basis $|\gamma\rangle$. These basis states are eigenstates of total angular momentum, $\hat{J} = \hat{j} + \hat{\ell}$, where $\hat{j} = \hat{j}_A + \hat{j}_B$ is total fragment angular momentum and $\hat{\ell}$ is the relative angular momentum of A and B. For the case of atom-atom scattering this basis corresponds to Hund's case (e) of diatomic angular momentum coupling. The potential matrix W^{∞} in the channel state representation is asymptotically diagonal, having elements

$$W_{\gamma\gamma}^{\infty}(R \rightarrow \infty) = E_{\gamma}^{\infty} + \frac{\hbar^2 \ell_{\gamma}(\ell_{\gamma} + 1)}{2\mu R^2} \quad (4)$$

The channel energy E_Y^∞ is the total asymptotic fragment energy, not including kinetic energy.

The expansion basis must always be truncated with only a finite number of states, hopefully chosen to represent the physics adequately. The total number of channels N_T is divided into N_O open and N_C closed channels, depending on total energy. The channel wave vector

$$k_Y = [2\mu(E - E_Y^\infty)/\hbar^2]^{1/2} \quad (5)$$

is real for open channels, for which the fragments can separate asymptotically with kinetic energy $E - E_Y^\infty$. But k_Y is pure imaginary for closed channels, i.e., $E < E_Y^\infty$, so that the fragments can not separate in channel Y . If $E < E_Y^\infty$ for all Y , $N_T = N_C$ and the only possible states of AB are bound states. If $E > E_Y^\infty$ for all Y , $N_T = N_O$ and inelastic collisions can couple any two channels. If E is such that some channels are open, some closed, then it is possible to have metastable bound states, or resonances, which can decay by predissociation.

The MCQDA gives a unified way to describe open and closed channel properties and gives new insights into the decay of predissociating resonances. The basic idea of the analysis is to introduce a set of diagonal reference potentials W° such that

$$W(R) = W^\circ(R) + V(R), \quad (6)$$

and $V(R)$ vanishes asymptotically. Each reference potential $W_{\alpha\alpha}(R)$ gives rise to two linearly independent solutions of the Schrodinger equation, f_α° and g_α° . In matrix form the diagonal matrices f° and g° are each solutions of the diagonal (or uncoupled) set of equations

$$\frac{d^2}{dR^2} F^\circ + \frac{2\mu}{\hbar^2} (E - W^\circ) F^\circ = 0. \quad (7)$$

The general solution to the coupled equations 3 can be written as a linear combination of these reference solutions, with R -dependent coefficients A and B ,

$$F(E, R) = \hat{F}^\circ(E, R) A(E, R) + \hat{g}^\circ(E, R) B(E, R). \quad (8)$$

If \hat{F}° and \hat{g}° are carefully chosen to be analytic in E , then the $N_T \times N_T$ dimensional matrix defined by the asymptotic quantity

$$Y(E) = B(E, \infty) A(E, \infty)^{-1} \quad (9)$$

can be analytically continued across dissociation thresholds (i.e., like a "quantum defect") and quantitatively relates the scattering and bound state properties of $\psi(E, R)$. In addition, the complex matrix

$$t^\pm(E) = [A(E, \infty) \pm iB(E, \infty)]^{-1} \quad (10)$$

may be used to define "half collision" amplitudes which describe final state distributions in photodissociation and weak predissociation processes. Note that no approximations are involved in writing eq. 8. In fact, the original second order differential equations 3 can be rewritten as two coupled first order differential equations for A and B , or equivalently, for R -dependent analogs of Y and t^\pm (9-12). Thus our analysis is related to amplitude density and phase amplitude methods in scattering theory (20,21). Our contribution is to emphasize the intrinsic analytic properties of the wavefunction that can be projected from such an analysis.

Although the MCQDA is a nonperturbative analysis, its usefulness will often depend on making a judicious choice of reference potentials W^0 . The reference basis $|\alpha\rangle$ is derived from the channel state basis $|\gamma\rangle$ by an orthogonal transformation

$$|\alpha\rangle = |\gamma\rangle \tilde{m}(R) \quad (11)$$

$$W = W^0 + V = \tilde{m} W^0 m \quad (12)$$

Normally the transformation m will be chosen for physical reasons to suggest reference potentials W^0 which isolate particular effects by making V small or vanishing at some value of R . For example, if we want to be able to generate an energy insensitive $Y(E)$ for extrapolating across thresholds, we would seek a transformation that gives a coupling $V(R)$ that operates only in a short range zone of R , typically in the R_e region of Born-Oppenheimer potentials. On the other hand, for describing a photodissociation process, we would want to choose a V which is negligible in the zone of R near R_e which determines the Franck-Condon absorption, whereas there may be strong inelastic couplings due to V in an intermediate range of R that determine the distribution of atomic fragment states. Depending on the specific application, some choices of suitable reference functions for diatomic processes could be: a pure Hund's coupling case, such as the standard case (a) states; a set of intermediate coupled states; an adiabatic-electronic-rotational (AER) basis, which continuously diagonalizes the electronic-rotational Hamiltonian as a function of R and smoothly transforming from one Hund's case to another (8b,9).

Several types of reference solutions may be defined, depending on boundary conditions chosen (10,18). The solutions useful for extrapolating across thresholds are the functions \hat{f} and \hat{g} , respectively regular and irregular as $R \rightarrow 0$. They are defined quantum mechanically but have the following semiclassical interpretation in a classical region of phase space:

$$\hat{f}_\alpha = \sin \beta_\alpha(R)/k_\alpha^{1/2}(R) \quad \text{and} \quad \hat{g}_\alpha = \cos \beta_\alpha(R)/k_\alpha^{1/2}(R) \quad , \quad (13)$$

where $\beta_\alpha(R)$ is the WKB phase angle (a is the classical turning point)

$$\beta_\alpha(R) = \int_a^R k_\alpha(R) dR - \frac{\pi}{4} \quad . \quad (14)$$

Each reference potential $W_{\alpha\alpha}(R)$ uniquely defines two energy-dependent phase angles $\xi_\alpha(E)$ and $\nu_\alpha(E)$. Above a channel threshold the open channel solutions define the reference phase shifts (we ignore subtle threshold effects discussed in detail in references 10 and 11)

$$\hat{f}_\alpha(R \rightarrow \infty) \sim k_\alpha^{-1/2} \sin(k_\alpha R - \frac{\pi}{2} \ell_\alpha + \xi_\alpha) \quad . \quad (15)$$

Below a channel threshold the regular solutions $\hat{f}_\alpha(E, R)$ are asymptotically divergent except at closed channel eigenvalues $E = E_n^\alpha$ defined by the modular π values of $\nu_\alpha(E)$

$$\tan \nu_\alpha(E) = 0 \quad \text{or} \quad \nu_\alpha(E_n^\alpha) = n\pi \quad . \quad (16)$$

The semiclassical approximation to ν

$$\nu_\alpha + \frac{\pi}{2} = \int_a^b k_\alpha(R) dR \quad (17)$$

gives the standard Bohr-Sommerfeld quantization rules.

The MCDWA analysis of Mies (10) shows how to define the symmetric real matrix $Y(E)$ in eq. 9. If all channels are open, the $N_T \times N_T$ scattering matrix S is simply related to Y as follows

$$S = e^{i\xi^0} (1^0 + iY) (1^0 - iY)^{-1} e^{i\xi^0}. \quad (18)$$

If we calculate S and the reference phase shift diagonal matrix ξ^0 above threshold, then we can calculate the $N_T \times N_T$ Y matrix. If Y is sufficiently energy insensitive, then it may be extrapolated below thresholds to predict the resonance scattering and closed channel properties. For example, if we take the case $N_T=2$ with channel 1 closed and channel 0 open, then the elastic scattering phase shift of the open channel is modified due to predissociation originating from the bound states located at $v_1(E) = n\pi$ (11),

$$\eta_0(E) = \xi_0(E) + \tan^{-1} \left[Y_{00} - \frac{Y_{01} Y_{10}}{\tan v_1(E) - Y_{11}} \right] \quad (19)$$

If both channels are closed, the bound state eigenvalues are given by the expression

$$(\tan \gamma_0(E_n) + Y_{00}) (\tan \gamma_1(E_n) + Y_{11}) = Y_{01}^2. \quad (20)$$

Eqs. 19 and 20 are valid for arbitrarily strong coupling and are only limited by our ability to obtain the reference phases and the matrix $Y(E) = \text{constant}$.

In the limit of weak coupling when $Y \rightarrow 0$, eq. (19) transforms into the usual Lorentzian expression for an isolated resonance. The weak coupling width Γ_n and shift ΔE_n of the predissociating level at $E = E_n$ are

$$\Gamma_n = \frac{2\Delta G_n}{\pi} Y_{01}^2 \quad \text{and} \quad \Delta E_n = - \frac{\Delta G_n}{\pi} Y_{11}, \quad (21)$$

where we have introduced the approximation

$$\left(\frac{\partial v_1}{\partial E} \right)_{E=E_n} = \frac{\pi}{\Delta G_n} \quad (22)$$

where ΔG_n is the vibrational spacing.

We have carried out a number of test calculations on 2 state models, i.e., 2 open or 1 open and 1 closed channels, and have demonstrated the success of the analysis over a wide range of conditions (11). These include an analysis of Cd_2 $^3\Sigma_u^+$ state predissociation to $\text{Cd}(^3P_0) + \text{Cd}(^1S_0)$ using AER reference states, and an analysis of the O_2 $^3\Sigma_u^-$ predissociation using diabatic reference states. Model strong coupling cases based on the latter were used to demonstrate the nonperturbative nature of the analysis. The $Y(E)$ matrix was found to be most energy insensitive for short range inner potential wall curve crossings or near crossings where two reference potentials remain nearly parallel over a range of R . Its greatest energy sensitivity will occur for sharp outer crossings due to the more rapid energy variation of Franck-Condon overlaps.

3. WEAK COUPLING HALF COLLISION ANALYSIS

Let us now consider a special case which covers a wide variety of actual phenomena and for which the MCQDA allows us to develop a number of useful insights or approximations. Assume that we have a manifold of N_I channels

which may be strongly coupled among themselves and a similar manifold of N_F final channels, but that the coupling between the initial and final manifolds, described by the $N_F \times N_I$ V_{FI} submatrix, is very weak. For simplicity we will consider the case here where $N_I = 1$, i.e., there is only a single nondegenerate initial channel. If the initial channel is open, as well as the final channels, the free-free transition amplitudes are given by the $N_F \times N_I$ subblock of the S matrix, described to first order in V_{FI} by the Born distorted wave approximation,

$$S_{FI}(E) = -2\pi i \langle \psi_F^-(E) | V | \psi_I^+(E) \rangle, \quad (23)$$

when ψ^\pm are energy normalized wavefunctions calculated in the absence of the weak coupling and the \pm refer to incoming and outgoing scattering boundary conditions. Similarly, if the initial channel is closed, the bound-free predissociation transition amplitudes for decay of the closed channel resonance at $E=E_n$ are

$$\tau_{FI}(E_n) = -2\pi i \langle \psi_F^-(E_n) | V | E_n \rangle \quad (24)$$

where $|E_n\rangle$ is the unit normalized bound state wavefunction.

There are numerous examples of weak predissociations in molecular spectroscopy. One special case is predissociation induced by a radiation field, namely, photodissociation. If the initial state basis functions are molecule-radiation-field states $|\alpha_I\rangle |nq\rangle$, with n photon of frequency ω and polarization q , and the final states have $n-1$ photons $|\alpha_F\rangle |n-1, q, \omega\rangle$, then the free-free process, eq. 23, describes line broadening and radiative redistribution phenomena and the bound-free process, eq. 24, describes photodissociation (22). For the case of radiative coupling the weak coupling matrix is just (22,23).

$$V_{FI}(\text{rad}) = \left(\frac{2\pi\hbar\omega\phi}{c} \right)^{1/2} \langle \alpha_F | \hat{e}_q \cdot \hat{\mu} | \alpha_I \rangle \quad (25)$$

where ϕ is the field intensity (photons $\text{cm}^{-2}\text{sec}^{-1}$), \hat{e}_q the polarization vector of the light, and $\hat{\mu}$ the molecular dipole operator.

When we impose scattering boundary conditions on the asymptotic wavefunction in the channel state basis $|\gamma\rangle$, we find (using eq. 11) that the energy normalized wavefunctions for the respective initial and final manifolds are

$$\psi^\pm = |\alpha\rangle \kappa (\hat{F} \cdot \mathbf{A} + \hat{G} \cdot \mathbf{B}) \mathbf{N}^\pm, \quad (26)$$

where $\kappa = (2\mu/\hbar^2\pi)^{1/2}$ and the normalization matrix \mathbf{N}^\pm is

$$\mathbf{N}^\pm = [\mathbf{t}^\mp(\omega)]^{-1} e^{\pm i\mathbf{E}^0}, \quad (27)$$

with \mathbf{t} given by eq. 10. (12) We now wish to make one more assumption. Assume that the weak coupling V_{FI} which couples the two manifolds is only significant in some short range zone of R near R_0 and that the final state interactions V_{FF} which determine the final state distribution are important in a longer range zone of R . Since \mathbf{B} must vanish at the origin and does not become large until $R > R_0$, the weak transition occurs in a zone of R where to a good approximation we may take $\mathbf{A}=\mathbf{1}$, $\mathbf{B}=\mathbf{0}$. We immediately see from eqs. 23, 24, 26 that the weak coupling amplitudes are

$$S_{FI} = -2\pi i \tilde{\mathbf{N}}_F^+(E) \hat{S}_{FI}(E) \mathbf{N}_I^+(E) \quad (28a)$$

$$\tau_{FI}(E_n) = -2\pi i \tilde{\mathbf{N}}_F^+(E_n) \hat{\mathbf{t}}_{FI}(E_n) \quad (28b)$$

where

$$S_{FI}(E) = \kappa^2 \langle f_F^O(E) | V_{FI} | f_I^O(E) \rangle \quad (29a)$$

$$T_{FI}(E_n) = \kappa \langle f_F^O(E_n) | V_{FI} | E_n \rangle \quad (29b)$$

and we have used the result $N_F^+ = N_F^{-*}$.

The results, eq. 28, show how a very useful factorization of the weak coupling transition amplitudes can be achieved. The S and T amplitudes are real Franck-Condon amplitudes which describe the excitation process. The N_F matrix is a "half collision" dynamical matrix which incorporates the effect of final state interactions and provides the correlation between the short range reference states excited by V_{FI} and the asymptotic distribution of fragments which could be measured experimentally. The initial state matrix N_I is a simple phase factor for a single initial channel, whereas for a manifold of initial channels, it would describe the formation of the reference states from the asymptotic states. We see that the physical picture implicit in the factorization, eq. 28b, is the time-independent analog of the time-dependent wavepacket viewpoint of photodissociation of Lee and Heller (24). According to this viewpoint, photodissociation is described as the initial creation of an excited state wavepacket through a "Franck-Condon" excitation from the initial bound state due to weak radiative coupling. The time evolution of this wavepacket leads to the distribution of final states.

We have shown two important properties of the N^+ matrix (12). First, as long as no nonclassical regions are encountered by the fragments between the excitation region, $R \approx R_0$, and the detection region, $R = \infty$, then N^+ is unitary to a very good approximation. Second, the N^+ matrix can be further factored as

$$N^+ = O^+ U^+ \quad (30)$$

The factor U^+ , the so-called frame transformation matrix, depends only on the reference solutions and the orthogonal basis transformation matrix \mathbf{m} . If an AER reference basis is used, it takes on the form

$$U^+ = L(R_S) e^{i\mathbf{F}^0} \quad (31)$$

$$\text{with } L(R) = e^{i\mathbf{B}^0} \mathbf{m}(R) e^{-i\mathbf{B}^0} \quad (32)$$

where \mathbf{B}^0 is the matrix of WKB reference phases, eq. 14. The distance R_S is a characteristic switching distance at which the final state interactions begin to become important as the fragments separate. The matrix O^+ in eq. 30 incorporates the effect of final state interactions in causing deviations from the pure frame transformation, eq. 31. It is possible to obtain a first order differential equation for O^+ by which these deviations can be calculated (12).

A special limiting case which has been used to predict final state distributions in diatomic photodissociation is the recoil approximation, or more specifically, the J -independent recoil approximation (25). This amounts to ignoring any J dependence of final state Franck-Condon factors and phase development. This limit will always apply at sufficiently high fragment kinetic energy. In our formulation, this limit corresponds to setting $N^+ = \mathbf{m}(R_0)$. If, however, we set $N^+ = U^+$, thereby ignoring the nonadiabatic corrections in O^+ but incorporating the effect of adiabatic phase development, and continue to ignore any J -dependence in the Franck-Condon amplitudes, S or T , we obtain an improved approximation which allows us to incorporate the effect of molecular axis rotation into orientation/alignment experiments. We thus see that the factorizations, eqs. 28 and 30, are very powerful tools which enable us to introduce a hierarchy of approximations for successively introducing various dynamical effects into the interpretation of photodissociation or predissociation product distributions.

In our earlier discussion we emphasized the Y matrix and its continuity across a dissociation threshold. For our present example of a single initial channel weakly coupled to a manifold of final channels, the Y_{FI} submatrix to first order in V_{FI} is

$$Y_{FI}(E) = -\pi A_F^{-1}(E, \infty) \hat{S}_{FI}(E). \quad (33)$$

The continuity of Y across the initial state threshold is thus reflected by the well known continuity of Franck-Condon amplitudes \hat{S} . The connection between \hat{S}_{FI} and \hat{T}_{FI} in eq. 29 is readily seen when we write the unit normalized initial bound state function as

$$|E_n\rangle = (\Delta G_n)^{1/2} \kappa \hat{P}_I(E_n) \quad (34)$$

where we have used eq. 22 and the results of references 8 and 10. Thus,

$$\hat{T}_{FI}(E_n) = (\Delta G_n)^{1/2} \hat{S}_{FI}(E_n) \quad (35)$$

shows the relation between the nonanalytic \hat{T} and the analytic \hat{S} .

One important consequence of the unitarity of N^+ is that the total predissociation decay rate, given by the following scalar dot product,

$$A_n = \tilde{\tau}_F^* \tau_F / h = (4\pi^2 \hat{S}_{FI}^* \hat{S}_{FI}) (\Delta G_n / h), \quad (36)$$

depends only on the excitation Franck-Condon factors \hat{S} , and not on the half-collision dynamical matrix. This justifies the usual adiabatic approximation for continuum spectroscopy and weak predissociation, i.e., given our assumptions, it is only necessary to take into account the local interactions in the Franck-Condon region to calculate the total rate of decay. Since when the initial channel is open the first factor in parenthesis in eq. 36 is interpreted as the total inelastic transition probability from I to the F manifold, we see that the closed channel decay rate is simply interpreted as a single cycle transition probability times the oscillation frequency $\Delta G_n / h$. The continuity of \hat{S} across threshold and this interpretation of eq. 36 has recently been discussed by Tellinghuisen and Julienne (26) in relation to the inverse of the phenomena considered here, namely, for radiative association and bound state radiative decay.

We have carried out specific calculations for the case where polarized absorption from a $^1\Sigma^+$ state through either a $^1\Sigma$ or $^1\Pi$ molecular Born-Oppenheimer reference state leads to $^1P + ^1S$ fragment atoms (23,27). The 1P atom may be aligned ($q=0$) or oriented ($q=\pm 1$). This describes both Sr or Ba + rare gas radiative redistribution experiments (28) and the Ca_2 photodissociation experiment of Vigué, et. al. (29). Our full close coupled results for Sr + Ar are in good agreement with the radiative redistribution experiments. The half collision analysis leads to an especially simple and pleasing physical picture of the product alignment.

The same angular momentum transfer formalism applies to both radiative redistribution (23) and photodissociation (30). The transfer cross sections require a coherent sum of transition amplitudes resulting from P, Q, and R type radiative transitions, i.e, those having $\Delta J = 1, 0$, and $+1$ respectively. The transfer cross sections that result from applying the factored form of the N_F^+ matrix can be expressed in terms of an angle

$$\theta_A = \alpha_A / 2 - \Delta_S / 2.$$

The angle $\alpha_A/2$ originates from the frame transformation matrix U^+ in eq. 30 and represents the effect of adiabatic motion on the Born-Oppenheimer potential Λ . Semiclassically, it is the angle through which the molecular axis rotates in a complete half collision in the final state, that is, $(\pi - \theta_c)/2$, where θ_c is the final state classical deflection function. The classical deflection function enters since it is $2\partial\xi_A/\partial J$ and the adiabatic phases ξ_A vary slightly with J_F for adiabatic evolution following P, Q, and R excitation. The angle $\Delta_S/2$ originates from the effect of nonadiabatic Coriolis coupling between Σ and Π states in the nonadiabatic correction matrix O^+ . It represents the decoupling of electronic angular momentum from the rotating axis beyond a switching distance R_S .

This model leads to the same polarization ratio as found by Lewis, et al. (31) on the basis of an ad hoc geometric model. This model corresponds to the picture that angular momentum projection Λ rotates with the internuclear axis inside of some characteristic internuclear separation R_S but is decoupled and fixed in space for $R > R_S$. If molecular axis rotation is neglected, our half collision analysis predicts the J-independent recoil limit results (25,29), namely, respective $q = 0$ polarization ratios of 1/2 and 7/9 for Σ and Π excitation. The usefulness of the complete half collision analysis is that corrections to this simple J-independent recoil approximation are possible by introducing additional effects into M_F^+ . In the present case it happens to be simple to isolate the separate effects of adiabatic and nonadiabatic dynamics.

We have also used the half collision analysis to interpret Na + rare gas radiative redistribution experiments (31) in which the Na $^2P(j=1/2)/^2P(j=3/2)$ ratio was measured following wing absorption to the $^2\Sigma$ and $^2\Pi$ states (32). The recoil limit result is approached for fragment kinetic energy of about 2000 cm^{-1} for an argon collision partner, but at a much lower kinetic energy for the lighter He collision partner. The large departures of the fine structure branching ratio from the recoil limit for low (thermal) separation energies reflects the influence of the adiabatic potentials and their curve crossings.

REFERENCES

- 1) M.S. Shapiro, J. Chem. Phys. 56 (1972) 2582.
- 2) E. Segev and M.S. Shapiro, J. Chem. Phys. 73 (1980) 2001.
- 3) K.C. Kulander and J.C. Light, J. Chem. Phys. 73 (1980) 4337.
- 4) R.W. Heather and J.C. Light, J. Chem. Phys. 78 (1983) 5513.
- 5) S. Singer, K.F. Freed, and Y. B. Band, J. Chem. Phys. 77 (1982) 1942.
- 6) S. Singer, K.F. Freed, and Y. B. Band, J. Chem. Phys. 81 (1984) 3091.
- 7) J.A. Beswick, Quantum mechanical time-independent treatment of photo-dissociation dynamics, this volume.
- 8) F.H. Mies, Mol. Phys. 41 (1980) 953; Mol. Phys. 41 (1980) 973.
- 9) P.S. Julienne and F.H. Mies, J. Phys. B14, (1981) 4335.
- 10) F.H. Mies, J. Chem. Phys. 80 (1984) 2514.
- 11) F.H. Mies and P.S. Julienne, J. Chem. Phys. 80 (1984) 2526.
- 12) F.H. Mies and P.S. Julienne, A molecular half collision analysis of atomic lineshapes, in Spectral Lineshapes, Vol. 3, ed. F. Rostas (de Gruyter, Berlin, 1985) pp. 393-420.
- 13) P.S. Julienne and F.H. Mies, Half collision analysis of 1P polarization redistribution, in Spectral Lineshapes, Vol. 3, ed. F. Rostas (de Gruyter, Berlin, 1985) pp. 525-526.
- 14) M.J. Seaton, Rept. Prog. Phys. 46 (1983) 167.
- 15) U. Fano, Comm. At. Mol. Phys. 10 (1981) 223; J. Opt. Soc. Am. 65 (1975) 979.
- 16) Ch. Jungen and O. Atabek, J. Chem. Phys. 66 (1977) 5584.
- 17) A. Guisti, J. Phys. B13 (1980) 3867; A. Guisti-Suzor and U. Fano, J. Phys. B17 (1984) 4267.

- 18) C.H. Greene, A.R.P. Rau, and U. Fano, *Phys. Rev. A* 26 (1982) 2441; C.H. Greene, U. Fano, and G. Strinati, *Phys. Rev. A* 19, (1978) 1485
- 19) R. Colle, *J. Chem. Phys.* 74 (1981) 2910.
- 20) F. Calogero, *Variable Phase Approach to Potential Scattering* (Academic Press, NY, 1967).
- 21) R.D. Levine, *Mol. Phys.* 22 (1971) 497.
- 22) F.H. Mies, Quantum theory of atomic collisions in intense laser fields, in *Theoretical Chemistry: Advances and Perspectives*, Vol. 6B, ed. D. Henderson (Academic Press, NY, 1981) pp. 127-198.
- 23) P.S. Julienne and F.H. Mies, *Phys. Rev. A* 30 (1984) 831.
- 24) S.Y. Lee and E.J. Heller, *J. Chem. Phys.* 76 (1982) 3035.
- 25) S.J. Singer, K.F. Freed, and Y.B. Band, *J. Chem. Phys.* 79 (1983) 6060; *J. Chem. Phys.* 81 (1984) 3064.
- 26) J. Tellinghuisen and P.S. Julienne, *J. Chem. Phys.* 81 (1984) 5779.
- 27) P.S. Julienne, Nonadiabatic theory of line broadening, in *Spectral Line Shapes*, Vol. 2, ed. K. Burnett (de Gruyter, Berlin, 1983) pp. 769-786.
- 28) P. Thomann, K. Burnett, and J. Cooper, *Phys. Rev. Lett.* 45 (1980) 1325; W.J. Alford, K. Burnett, and J. Cooper, *Phys. Rev. A* 27 (1983) 1310; W.J. Alford, N. Anderson, M. Belsley, J. Cooper, D. M. Warrington, and K. Burnett, *Phys. Rev. A* 31 (1985) 2096.
- 29) J. Vigué, P. Grangier, G. Roger, and A. Aspect, *J. de Physique Lett.* 42 (1981) L532; J. Vigué, J. A. Beswick, and M. Broyer, *J. Physique* 44 (1983) 1225.
- 30) C.H. Greene and R.N. Zare, *Ann. Rev. Phys. Chem.* 33 (1982) 119.
- 31) M.D. Havey, G.E. Copeland, and W.J. Wang, *Phys. Rev. Lett.* 50 (1983) 1767.
- 32) L. Vahala, P. S. Julienne, and M.D. Havey, to be submitted (1985).

TRANSITIONS WITHIN THE CONTINUUM IN HIGH-INTENSITY LASER FIELDS

M.J. VAN DER WIEL and H.-G. MULLER

FOM-Institute for Atomic and Molecular Physics, Kruislaan 407, Amsterdam,
The Netherlands

The current status of experimental and theoretical work on 'Above-Threshold Ionization' (ATI) in multiphoton processes is reviewed. Some features of the low-intensity regime are treated in order to provide a basis for discussion of the phenomena in the high-intensity, non-perturbative regime. It is shown how saturation of continuum-continuum transitions leads to a distribution of photoelectrons over a range of continuum states. Furthermore, we consider how AC Stark shifts of the atomic levels, and the ponderomotive force, affect the position and width of the photoelectron peaks, for various conditions of laser pulse length vs. photoelectron escape time.

1. INTRODUCTION

The process of multiphoton ionization has been studied extensively over the past two decades, an important item of investigation being the rate dependence on the intensity of the laser light, i.e. the order of non-linearity of the process. It can be stated that in practically all cases the observed order of non-linearity does not exceed the minimum number of photons N needed to cross the ionization potential (I.P.):

$$\text{I.P.} < N \cdot h\nu < \text{I.P.} + h\nu \quad (1)$$

This is the dependence one would expect in the regime of validity of lowest-order perturbation theory, for a process which is terminated once N photons have been absorbed; indeed, this has been the accepted picture for a considerable period.

Nevertheless, it is against reason to accept that ionization can take place through fully non-resonant absorption of a large number of photons, and then disregard the possibility of further absorptions by what could be considered 'quasi-resonant steps' in the continuum. This actually was one of the reasons for undertaking the analysis of photoelectron energies. Over the past five years, extensive evidence for the generation of photoelectrons with energies $[(N+S)h\nu - \text{I.P.}]$, S being an integer, has been collected (see reviews [1] and [2]). Of the various names that have been proposed for the process, Above-Threshold-Ionization at least has the advantage of allowing a short abbreviation: ATI.

This paper attempts to bring out the most salient physics that has emerged from these studies. Firstly, a few features of the low-intensity regime are briefly discussed in order to provide a framework for thinking about ATI. The main part of the paper is concerned with the high-intensity regime and discusses several experiments as well as recent theoretical approaches, using non-perturbative methods.

2. LOW-INTENSITY REGIME

One objective criterion for distinguishing between a low- and high-intensity regime is whether $(N+1)$ -photon ionization has a considerably lower probability than N -photon ionization. If so, lowest-order perturbation theory can be expected to be valid.

ted to hold. A schematic representation of an $(N+1)$ -photon ionization ($N=2$) is given in fig. 1a, on the conceptually convenient basis of a stepwise excitation via virtual intermediate states separated by $\hbar\omega$. In this example, one tends to think in terms of a two-photon transition to the continuum, followed by a one-photon continuum-continuum (CC) transition to the final state.

A proper lowest-order perturbation description replaces this simple picture by a coherent sum (with appropriate energy denominators) over all allowed three-photon paths (fig. 1b), of which the energy-conserving case is just one. An obvious question arises: what is the relative importance of the energy-conserving, quasi-resonant CC step in fig. 1a with respect to the full amplitude? It is a simple matter to show that the transition amplitude is a complex quantity [3], the energy-non-conserving paths contributing the real part, while the energy-conserving path yields the imaginary part. It has been found for the case of hydrogen [4] that real and imaginary parts are of the same order of magnitude for a wide range of parameters. A two-step hypothesis, consisting of a two-photon ionization followed by a CC transition, is therefore not strictly applicable, but it does provide a crude estimate. For instance, for the case of five-photon ionization of Xe at $\lambda = 440$ nm, the ratio of $(5+1)$ - to 5-photon ionization is underestimated by a factor of four, when taking only the fig. 1a path into account.

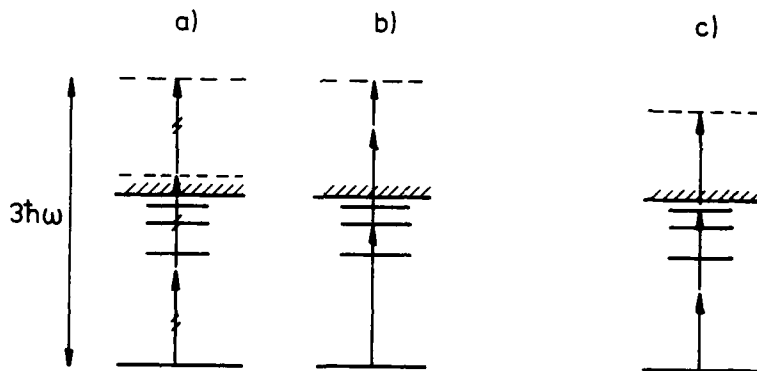


FIGURE 1

Energy diagrams showing various 3-photon ionization pathways; a) and b) for ATI. a) energy-conserving path; b) one of the energy non-conserving paths; c) 3-photon path without ATI, through high Rydberg state.

A second point of interest is the behaviour of $(N+1)$ -ionization with laser intensity. It is by now well established that in the low-intensity regime perturbation theory correctly predicts [1] an order of non-linearity equal to $(N+1)$, or equivalently, a ratio of $(N+1)/N$ -ionization linear with intensity. An example is shown in fig. 2. The figure is taken from ref. [5], in which a special method is described to circumvent problems of intensity determination in multimode laser operation. The method relies on a detuning from exact (three-photon) resonance, such that only specific local, momentary intensities create a dynamic resonance through AC Stark shifting. Out of the resonance, two- and three-photon ionization occurs at the same selected intensity, which depends linearly on the detuning. It will be clear that in the low-intensity regime, $(N+S)$ -processes contribute little to the total ionization rate; experimental accuracies are usually insufficient to detect the correspondingly small deviations from I^N behaviour (I = intensity).

Finally, let us consider the behaviour of the ATI signal in fig. 1, when the photon energy is lowered such that $2\hbar\omega$ no longer exceeds the I.P. Obviously,

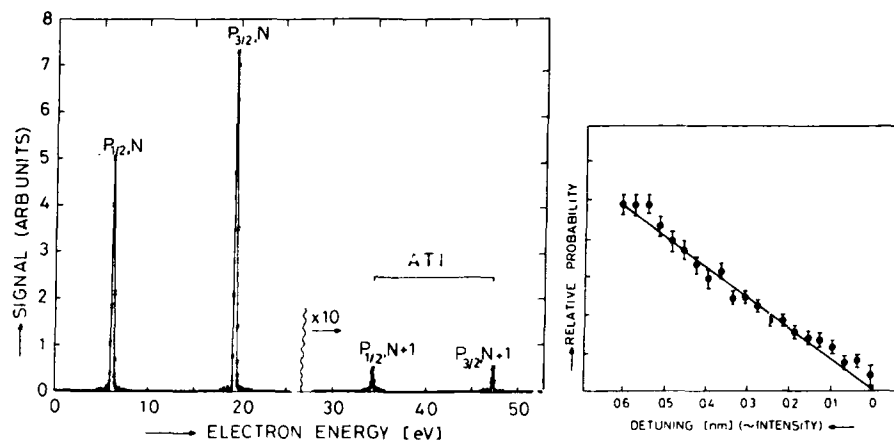


FIGURE 2

- a) Electron energy spectrum from 5-photon and (5+1)-photon ionization of Xe ($P_{3/2}$ and $P_{1/2}$ ion states) at $\lambda = 440$ nm. Intensity $\sim 10^{11}$ W cm $^{-2}$.
 b) Ratio of (5+1)- to 5-photon $P_{3/2}$ signal as function of detuning. Relation between detuning and intensity discussed in text.

the 2-photon ionization signal disappears, but in the 3-photon signal no sign of a threshold is present (fig. 3). This is just another manifestation of the general phenomenon of continuity across the threshold: the density of transition strength in the high-Rydberg region always joins smoothly into that of the corresponding continuum.

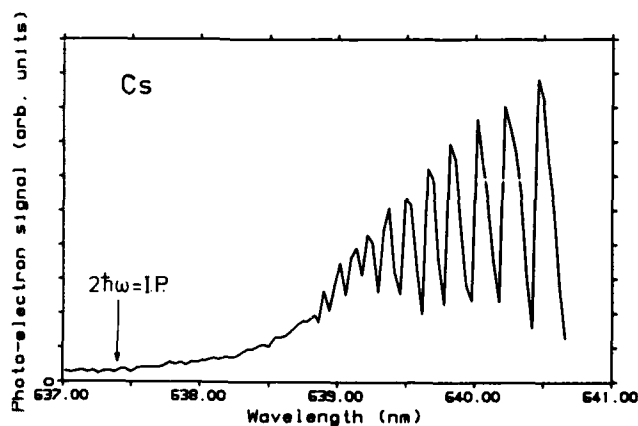


FIGURE 3

3-photon ionization signal of Cs. Arrow indicates where 3-photon ionization according to fig. 1c, through Rydberg states, goes over into the ATI case of figs. 1a,b.

3. HIGH-INTENSITY REGIME

3.1. Observations

It is interesting to note that several of the peculiar features of high-intensity ATI observations, which are presently the subject of a strong theoretical effort, were actually predicted already in 1980 by Reiss [6], for multiphoton detachment of H^- by an intense CO_2 laser.

The first detailed study, under well-defined conditions, of ATI in the high-intensity regime ($\sim 10^{13} \text{ W cm}^{-2}$), was that of Kruit et al. [7], on 11-photon ionization of Xe by 1064 nm photons (fig. 4). The main observations were:

- the disappearance of low-order peaks,
- a total order of non-linearity of 10 ± 1 , i.e. close to the minimum number of photons,
- the envelope of the spectrum peaks at an energy which shifts upwards with increasing intensity,
- no peak shift connected with the ponderomotive force (see below),
- considerable peak broadening ($\sim 200 \text{ meV}$).

The experiment of ref. [7] was later confirmed and extended by Humpert et al. [8], under similar experimental conditions of intensity and pulse length. However, there are two recent reports of seemingly conflicting measurements, in which ps pulses were used. One is by Lompré et al. [9], in which a simple retarding-field analyser separates different continuum energies. It was observed that for increasing continuum energies, increasing orders of non-linearity occur. The numbers found are close to the minimum number of photons needed to reach the corresponding continuum state. Again no shift of peak energies was observed. Contrary to this, Freeman [10] reports preliminary ps pulse measurements, which show significant shifts and broadening of the electron peaks.

3.2. Qualitative interpretation

Most of the features of fig. 4, including the apparent conflict with later ps data, can be understood when adopting the following qualitative picture which was developed by Muller and Tip [11,12] and later refined by Mittleman et al. [13,14]. We first consider a CW laser field of limited spatial extent. In this field the atomic energy levels undergo AC Stark shifts, the magnitude and direction of which depend on wavelength and local intensity. For the I.P., the shift is upwards and amounts to $\frac{1}{2} a^2$ (a.u.), where a is the vector potential. As an example, $\Delta(\text{I.P.}) [\text{eV}] = 10^{-13} I [\text{W cm}^{-2}]$ for $\lambda = 1064 \text{ nm}$. These

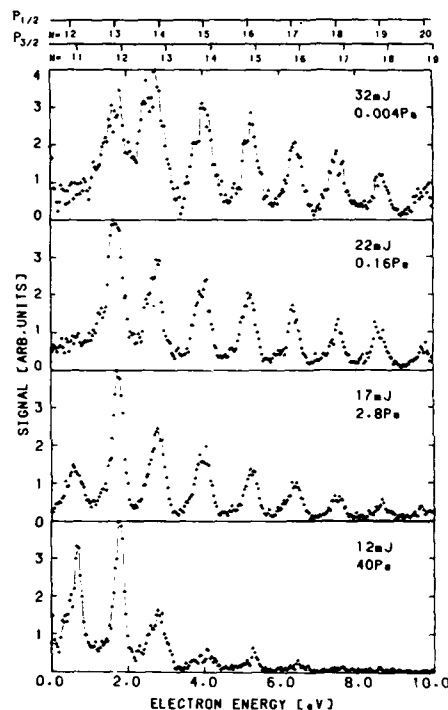


FIGURE 4
Electron energy spectra of Xe ionized by 1064 nm photons. Vertical scales adjusted to equal height. Pulse energies and target pressures are given in each panel. No depletion of ground state up to highest intensity. Estimated effective intensity of multimode pulses $6 \times 10^{13} \text{ W cm}^{-2}$ for upper panel.

local shifts determine the minimum number of photons needed to ionize; in the case of Xe at $\lambda = 1064$ nm, clear evidence exists (fig. 4) that at intensities around 10^{13} W cm $^{-2}$ eleven photons no longer suffice for ionization.

With regard to the electron energy at arrival on the detector, this is determined not only by the above shifts, but additionally by the ponderomotive force accelerating the electron during its escape from the focus to the field-free region. It turns out [11] that the energy gain due to the ponderomotive force exactly cancels the shift of the I.P., such that only the ground state shift is noticeable in the final electron energy. Since ionization events take place throughout the laser focus, there is a distribution of shifts resulting in broadening of the peaks.

The above picture requires the field to be constant during escape of the photoelectron, which takes place on the order of 10 ps for a 1 eV electron. Thus, the CW description holds for pulselengths longer than 10 ps. Note that in multi-mode pulses not the overall pulselength, but the duration of individual spikes counts. E.g. in a 0.1 nm bandwidth YAG laser, intensity fluctuations on a 10 ps time scale are possible. For short pulses the electron energy depends on how the electron emerges from the field pulse [14]. For escape out of the side of the pulse, again the CW case applies. During escape from the rear of the pulse, however, the acceleration acts very briefly and the initial electron velocity hardly changes. Thus, electrons created with equal energies inside the focus, may show an asymptotic energy difference as large as the full energy gain of the ponderomotive force. This clearly could result in excessive peak broadening, of several eV and more. It is worth noting that the higher the initial velocity, the larger the probability for escape out of the side of the pulse, and therefore the narrower the energy spread. This effect has not been observed yet.

The next problem concerns the orders of non-linearity. It is clear from fig. 4 that, although the total (unsaturated!) ionization rate depends on intensity I approximately as I^{11} (experiment $I^{10 \pm 1}$), we are dealing with the non-perturbative regime. The qualitative explanation given in [7] is the following: The eleven-photon step into the continuum limits the total rate for ionization. Further steps in the continuum are (nearly) saturated, such that a range of higher continuum states is populated.

Support for this reasoning is obtained from a calculation of CC matrix elements for Xe [4], using a one-electron model potential. Matrix elements on the order of 10 a.u. for 3 eV photons have been obtained. Using the well-known scaling with $1/\omega^2$, values at 1 eV would be 100 a.u. At intensities of 10^{13} W cm $^{-2}$, transition rates are on the order of 10^{17} s $^{-1}$. Such rates clearly compete with 'direct' ionization, and thus are capable of populating higher final states.

This interpretation is in conflict with the recent data of Lompré et al. [9], for reasons that are as yet not clear. Possibly the small angle of acceptance of the photoelectrons, combined with intensity-dependent angular distributions, plays a role.

3.3. Quantitative theory

As regards more quantitative descriptions, we already mentioned the calculation by Reiss [6], which is based on a revision of the Keldysh approximation. Although limited to systems with short-range potentials (e.g. H $^{-}$), the predictions are remarkable close to a number of the later observations, as listed in 3.1, including the upward shift of the I.P. with $\frac{1}{2} a^2$. The next non-perturbative approach was that of Muller and Tip [11,12], who treated the exactly soluble case of a one-electron atom in a circularly polarized field. A numerical evaluation for a zero-range potential (fig. 5) gave results which reproduce the essential features of the experiment.

Three more recent theories [15-17] basically replace the N-photon ground state-to-continuum step by some effective coupling, and then treat the interactions in the continuum to all orders in the intensity. Spectral distributions and orders of non-linearity are obtained by making simplifying assumptions with

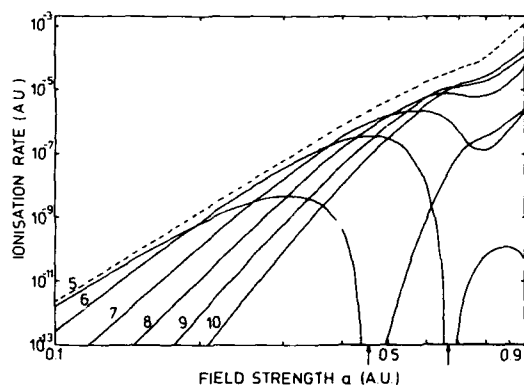


FIGURE 5
Calculated rates for absorption of 5 to 10 photons by a zero-range potential model atom, as function of field strength. A minimum of 5 photons is needed to ionize. Arrows indicate field strengths at which AC Stark shift pushes the ionization potential beyond 5, resp. 6 times the photon energy. The dashed curve represents the total rate and has order of non-linearity close to five.

regard to the CC matrix elements, such that the equations governing the time evolution of the multiphoton process become analytically soluble. The assumption is that the CC matrix elements can be factorized into a product of two terms:

$$\langle \psi_{\epsilon} | D | \psi_{\epsilon'} \rangle = f(\epsilon) \cdot g(\epsilon') \quad (2)$$

The simplest and most elementary of these theories, by Deng and Eberly [15], supposes that both f and g , and therefore all CC matrix elements, are constants. CC transitions then connect an infinite set of structureless continua as a linear chain, the first continuum of that chain being connected to the ground state by an effective coupling proportional to I^N .

This model gives rise to an ionization rate

$$R_i = \frac{I^N}{1 + \frac{Z_{12}^2}{1 + \frac{Z_{12}^2}{1 + \dots}}} \quad (3)$$

the

$$Z_{k,k+1} = \pi^2 I^2 |\langle \psi_{\epsilon_k} | D | \psi_{\epsilon_{k+1}} \rangle|^2$$

describing the coupling between continua k and $k+1$. For all Z equal, R_i can be shown to behave as I^{N-1} for large I , i.e. in close agreement with the observed $I^{10 \pm 1}$ (for $N=11$). When Z varies with k , it turns out that the lowest transition which saturates, i.e. for which $Z > 1$ (see also 3.2), acts as a bottleneck for the order of non-linearity of the ATI process. Since in real atoms the first CC matrix elements are usually the largest, these transitions saturate first and thus block the growth of the order of non-linearity.

The paper by Edwards et al. [16] deals with general forms of f and g in eq. (2) and justifies the use of only a single 'staircase' of continua when using circularly polarized light. Again they find orders of non-linearity of approximately $N-1$ at large I , for all peaks in the ATI spectra except the first. The behaviour of the first peak depends strongly on the coupling with the bound state (observed value 7.7 [7]). A similar approach by Bialynicka-Birula [17] treats the effect of more bound states, including resonances between them, and the splitting of the electron peaks due to Rabi oscillations.

Although successful in explaining the orders of non-linearity, the three papers have the serious shortcoming that approximation (2) is unrealistic: CC matrix elements are known to behave as $1/(\epsilon - \epsilon')^2$. This strong singularity of the interaction with the field gives rise to interesting effects near the I.P., which the three theories lack. Indeed, the first even lacks the threshold itself. Note that it is this singularity which in the work of Muller and Tip [12] leads

to the shift of the I.P. and its pronounced consequences.

3.4. Experiment in progress

We conclude this section by mentioning present efforts at the FOM-Institute to measure ATI in a 'pure' case, i.e.:

- using atomic hydrogen as a target, for which exact calculations are feasible;
- performing 'two-colour' excitation: a weak $3\omega_1$ transition to the 3p level, followed by $2, 3, \dots \omega_2$ ionization, so including ATI, ω_2 being the fundamental YAG frequency;
- detuning ω_1 from exact zero-field $3\omega_1$ resonance, and bringing the process back into resonance by the AC Stark shift of the 3p level due to the ω_2 beam. The specific ω_2 intensity which then produces ionization, can be calculated exactly from the accurately known AC Stark shift parameter of the 3p level for ω_2 .

A pilot experiment on Xe (fig. 6) shows many of the desired characteristics, except that the $3\omega_1$ excitation occurs to the dense region of Rydberg states, where AC Stark broadening precludes selection of a single level. It is worth noting that the ω_2 beam couples a chain of continua not only by absorption, i.e. $(3\omega_1 + n\omega_2)$, but also through stimulated emission, starting from an $4\omega_1$ continuum: $(4\omega_1 \pm m\omega_2)$.

Finally, the atomic hydrogen target has already been used in a one-colour 3-photon resonant experiment. A first result of the same nature as that of fig. 2b for Xe, yields a $(4+1)/4$ photon ionization ratio of $(1.6 \pm 0.2) \times 10^{-6}$ per GW cm^{-2} . This result should provide a stringent test for theory, as it is not subject to the usual uncertainties in averaging over a wide intensity distribution in a laser focus.

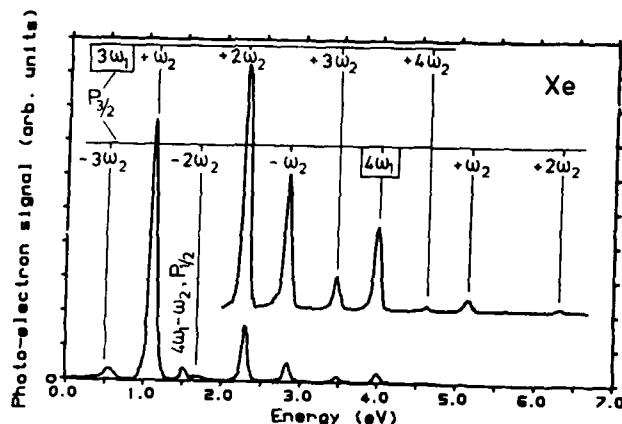


FIGURE 6

Electron energy spectrum of $(3\omega_1 + n\omega_2)$ and $(4\omega_1 \pm m\omega_2)$ processes in Xe. The two series belong to the $P_{3/2}$ ion state; one $P_{1/2}$ transition is indicated separately, while $4\omega_1$, $P_{1/2}$ is visible as a shoulder on the 2.8 eV peak. ω_1 : 308 nm; ω_2 : 1064 nm; $3\hbar\omega_1$ just below I.P.; intensity of ω_2 approxim. $10^{12} \text{ W cm}^{-2}$.

4. CONCLUSION

Summarizing, we note that:

- in the low-intensity regime, ATI is quantitatively accounted for by perturbation theory;
- in the high-intensity regime, behaviour of the total intensity rate with $\sim I^N$ does not imply lowest-order perturbation theory is applicable;
- most of the ATI features obtained with ns pulses, like peak positions, widths, spectral envelopes and orders of non-linearity, can be understood semi-quantitatively;
- some features in ps experiments still require further study.

ACKNOWLEDGEMENTS

We acknowledge the contribution of Dr. H.B. van Linden van den Heuvell to the experiments mentioned in 3.4. This work is part of the research program of the Stichting voor Fundamenteel Onderzoek der Materie (Foundation for Fundamental Research on Matter) and was made possible by financial support from the Nederlandse Organisatie voor Zuiver-Wetenschappelijk Onderzoek (Netherlands Organization for the Advancement of Pure Research).

REFERENCES

- [1] G. Petite, F. Fabre and P. Agostini, Collisions and Half-Collisions with Lasers, Edts. N.K. Rahman and C. Guidotti, Harwood Acad.Publ. (Chur, 1984) p.203.
- [2] M.J. van der Wiel, *ibidem*, p.217.
- [3] P. Kruit, H.-G. Muller, J. Kimman and M.J. van der Wiel, J.Phys.B. 16 (1983) 2359.
- [4] A. Maquet, Resonances-Models and Phenomena, Lecture Notes in Physics 211, Edts. S. Albeverio, L.S. Ferreira and L. Streit, Springer (Berlin 1984) p.257.
- [5] P. Kruit, J. Kimman, H.-G. Muller and M.J. van der Wiel, J.Phys.B 16 (1983) 937.
- [6] H.R. Reiss, Phys.Rev.A 22 (1980) 1786.
- [7] P. Kruit, J. Kimman, H.-G. Muller and M.J. van der Wiel, Phys.Rev.A 28 (1983) 249.
- [8] H.J. Humpert, H. Schwier, R. Hippler and H.O. Lutz, Abstracts of 2nd Europ. Conf.At.and Mol.Physics, Edts. A.E. de Vries and M.J. van der Wiel (Amsterdam 1985), p.305.
- [9] L.A. Lompré, A. L'Huillier, G. Mainfray and C. Manns, postdeadline paper at 3rd Int.Conf.on Multiphoton Processes, Crete, 1984.
- [10] R.R. Freeman, private communication.
- [11] H.-G. Muller, A. Tip and M.J. van der Wiel, J.Phys.B 16 (1983) L 679.
- [12] H.-G. Muller and A. Tip, Phys.Rev.A 30 (1984) 3039.
- [13] M.H. Mittleman, Phys.Rev.A 29 (1984) 2245.
- [14] E. Fiordilino and M.H. Mittleman, J.Phys.B (1985), to be published.
- [15] Z. Deng and J.H. Eberly, Phys.Rev.A (1985), to be published.
- [16] M. Edwards, L. Pan and L. Armstrong, to be published.
- [17] Z. Bialynicka-Birula, J.Phys.B 17 (1984) 3091.

MULTIPHOTON MULTIPLE IONIZATION OF ALKALINE-EARTH ATOMS

Pierre AGOSTINI and Guillaume PETITE

Service de Physique des Atomes et des Surfaces, Centre d'Etudes Nucléaires
de Saclay, 91191 Gif-sur-Yvette Cedex, France.

Recent results on single, double and triple ionization of alkaline-earth atoms irradiated by intense picosecond pulses are reported. For single ionization, features characteristic of two-electron atoms multiphoton ionization are emphasized: intermediate-resonance with bound two electron states, resonances with autoionizing states either as final states or as intermediate states. For double ionization, observations confirm that the most probable mechanisms are stepwise, resonant processes. For triple ionization, results are compared with similar findings in rare gas ionization as well as in double ionization of alkali.

1. INTRODUCTION

Experimental studies of multiphoton ionization of complex atom are as old as the field of multiphoton ionization itself since rare gases, for instance, were among the first targets used in experiments (1). However, multiphoton ionization of such atoms was found, suprisingly enough, to behave as predicted on the basis of one-electron models. For example, resonances with intermediate one-electron states (2) as well as power dependence compatible with such a simple model (3) were observed. Recent studies of the photoelectron energy spectra have somehow complicated this simple picture by showing that the ejected electron could keep absorbing photons in the continuum part of the spectrum (above the ionization limit: a process called Above-Threshold Ionization (4), (5)). But, even in the presence of this higher order process there was no evidence of any "core" excitation, i.e. that more than one electron was involved in the transition.

The discovery that alkaline-earth atoms could be doubly ionized (6), (7) and that rare gases could be ionized up to the complete stripping of the outer-shell (8), (9), with a relatively small increase of the laser intensity, was the starting point of new investigations in multiphoton ionization of complex atoms. Even in the simplest case of single multiphoton ionization of an alkaline-earth atom it can be realized that new processes involving some core excitation can be expected: intermediate resonance with bound two-electron states, resonances with autoionizing states (i.e. two-electron states imbedded in the continuum) either as final states of the ionization or as intermediate states in higher-order transitions. In all cases, new interference effects have been predicted (10). Regarding the double-ionization of alkaline-earth atoms, from experiments on Ba, Sr and Eu (6) it could be concluded that it was a "direct" multiphoton process driving the two electrons from the ground state up to the second ionization limit through two-electron excited states. However, other experiments on Sr (7) lead to the opposite conclusion that it was mainly a "stepwise" process. In this paper, we report recent results on multiphoton ionization of Ca and Sr with intense picosecond laser pulses using both ion detection and electron energy analysis. The results are divided in three main sections after a brief description of the experiment. Thus, Section 3 is dealing with single multiphoton ionization of Sr when the two-outer electrons are involved. In Section 4 we summarize our observations on double ionization

of Ca and Sr and show that, in most cases, it is a stepwise (or resonant) process. Finally, in Section 5 we present and discuss briefly preliminary results on triple ionization of Ca.

2. EXPERIMENT

The primary laser source used in these experiments is a Quantel picosecond, 10 pps, oscillator/amplifiers system. It has been used either directly at 1060 nm and 530 nm or as a pumping source for a synchronously pumped oscillator/amplifier, Fourier-limited, dye laser (11). This system provides after focusing ($f = 100$ to 200 cm) intensities up to 10^{13} W.cm $^{-2}$ at 1060 nm, $3 \cdot 10^{12}$ W.cm $^{-2}$ at 530 nm and 10^{12} W.cm $^{-2}$ between 557 nm and 585 nm, the tuning range of Rhodamine 6 G. The target is an atomic beam effusing from a resistively heated oven. Ions are analyzed in a time-of-flight charge spectrometer while electron-spectroscopy is performed in a combined time-of-flight/retarding potential spectrometer (12). The average power of the laser is stabilized to within $\pm 5\%$ while tuning and data acquisition are computer controlled.

3. MULTIPHOTON SINGLE IONIZATION OF STRONTIUM

Fig. 1 shows the Sr^+ ion signal as a function of the laser wavelength between 559 and 567 nm. The resonance at 560.7 nm can be assigned to the two-photon resonance with the $5p^2\ ^3P_2$ state (13), (14). Upon the absorption of a third photon, either a continuum $5s\ \epsilon 1$ or configurations with a $5p$ or $4d$ core (due to electron correlations) can be reached. This illustrates the simplest "core"-excitation effect in multiphoton ionization of an alkaline earth, namely a resonance with a bound two-electron state. These resonance can be Stark-shifted by the laser field in much the same way as single-electron states as shown on Fig. 2 where the shifts of the two-photon resonances with the $5p^2\ ^3P_0$ and $5s\ 5d\ ^3D_2$ can be compared. The resonances A, B, C, D on Fig. 1 have been assigned to three-photon resonances with autoionizing states with $J = 3$ (13), lying above the ionization limit. These states can autoionize to a $5s\ \epsilon 1$ continuum : this is the second "core"-excitation effect : resonances with final states in the continuum, which can be sharp as in the above mentioned cases, or much broader (6) depending on the autoionizing rate of the state. In theory, this rate can be strongly modified by interferences between the configuration interaction and the dipole coupling to the same continuum (10). However no experiment, so far, has been able to demonstrate this effect. One of the reasons for this failure might be that the autoionizing state is also coupled to other continua by absorption of one more photon. For instance states belonging to the $5p\ n1$ and $4d\ n1$ configurations can be coupled to $5p\ \epsilon 1$ and $4d\ \epsilon 1$ continua, thus leaving the ion in the excited states $5p_{1/2,3/2}$ or $4d_{3/2,5/2}$ respectively. That such processes do exist is demonstrated by electron spectra of Fig. 3 and Fig. 4. Fig. 3 shows an electron peak associated to the process labelled (4) on Fig. 6. This process is identified not only by the electron energy but also by the threshold behavior clearly displayed on Fig. 5 (15). Furthermore, the study of the wavelength dependence of electron peaks (4) of Fig. 3 and (3) of Fig. 4 shows that the autoionizing states reached upon the absorption of the third photon are inducing resonances for the four-photon absorption processes (3) and (4) on Fig. 6. This is the third "core" excitation effect mentioned above, namely resonance on an intermediate two-electron state in multiphoton ionization of alkaline-earth atoms. To conclude this section, let us remark that four-photon ionization leaving the ion in the ground state (process (2) on Fig. 6) (so-called Above-Threshold Ionization (4), (12) is much less probable than the processes just discussed, as shown by the small component (2) in the spectrum of Fig. 4. In other words, transitions involving

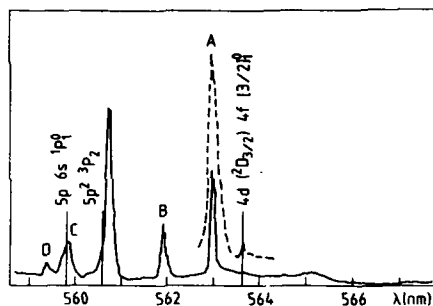


FIGURE 1
 Sr^+ ion spectrum taken at 10 GW.cm^{-2} (full curve) and 50 GW.cm^{-2} (broken curve). The peak between B and C is a two-photon resonance with the two-electron state $5p^2 \ 3p_2$ while peaks A, B, C, D are three-photon resonances on autoionizing final states (13).

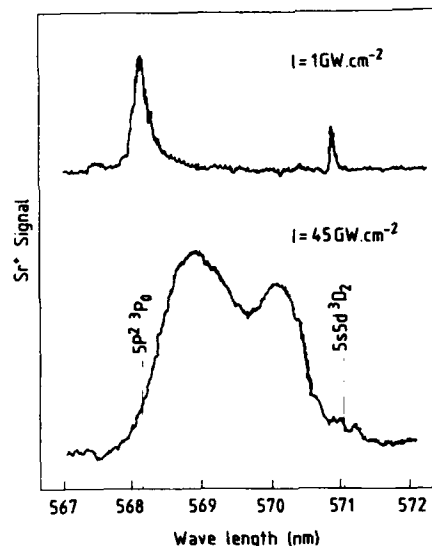


FIGURE 2
 Intensity effects on two-photon resonances with a two-electron state ($5p^2 \ 3p_0$) and a single electron state ($5s \ 5d \ 3D_2$).

the excitation of a single electron above the ionization limit are much less probable than transitions involving two excited electrons. The reason for this is certainly that the single-electron excitation channel ($5s^2 - 5s5p - 5sn1 - 5sn1'$) is less probable than the two-electron excitation channel ($5s^2 - 5s5p - 5p^2 - n1, n1'$) due to the proximity of two-photon resonances with the $5p^2 \ 3p$ states and of the three-photon resonances with, for instance $4d \ 4f$ states. Although the transitions leaving the ions in excited states $5p_{1/2, 3/2}$ or $4d_{3/2, 5/2}$ (after absorption of four photons) imply the absorption of one photon above the ionization limit, they are of a different nature than Above-Threshold Ionization in single electron atoms (12). The probability of process (2) (see Fig. 6) relative to the three-photoionization is quite comparable to the corresponding transitions (5-photon and 4-photon ionization respectively) observed in Cesium (12).

In conclusion, it can be said that single multiphoton ionization of Strontium can exhibit several "core"-excitation processes. In our case, it seems that the two electrons keep comparable levels of excitation, rather than one being excited while the other one remains a spectator, but the use of other wavelengths could have produced the reverse situation, for instance by resonantly exciting Rydberg states $5s \ np$. Finally it should be pointed out that photoelectron spectroscopy and laser tunability are very valuable tools in understanding these processes since information obtained from intensity variations is seldom unambiguous.

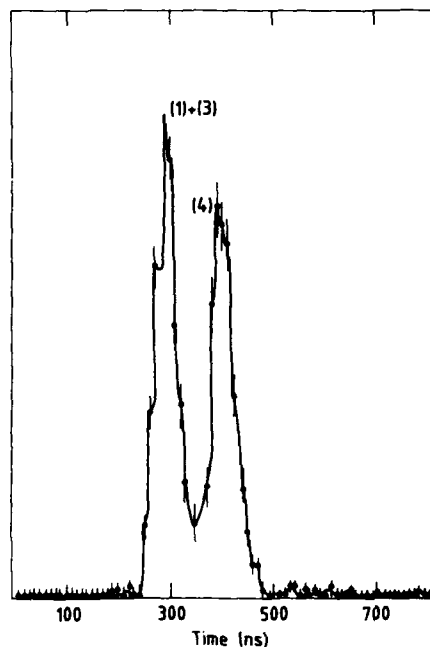


FIGURE 3
Electron energy spectrum taken at 100 GW.cm^{-2} . The numbers in parenthesis refer to processes shown on Fig. 6. (One volt acceleration has been added to the kinetic energy of the electrons).

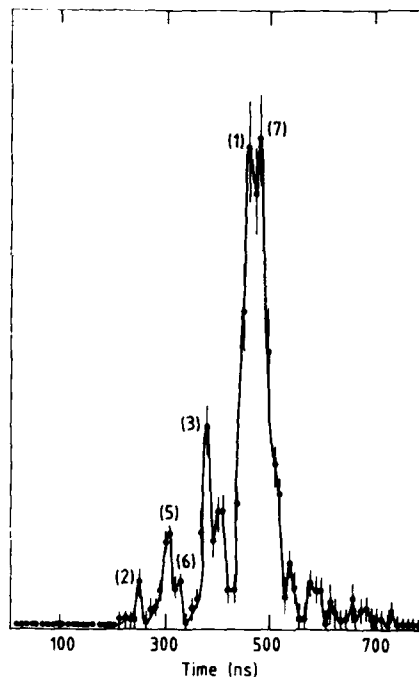


FIGURE 4
Electron energy spectrum taken at 2.8 TW.cm^{-2} showing electrons from the second ionization (5) and from ATI (2) (see Fig. 6).

4. MULTIPHOTON DOUBLE IONIZATION OF CALCIUM AND STRONTIUM

Two mechanisms have been proposed from the beginning (see references in (6)) to explain the formation of doubly charged ions when an atom A is irradiated by a strong laser beam : either a "direct" multiphoton absorption from the ground state of the neutral atom ($A \rightarrow A^{++}$) or a two-step process ($A \rightarrow A^+$, $A^+ \rightarrow A^{++}$) although it is not always clear how to experimentally distinguish between the two processes when a single laser pulse is used. The intensity dependences of the singly and doubly charged signals can sometimes partly answer the question as in the situation illustrated by Fig. 7. At 532 nm in Calcium (16) Ca^{++} ions appear only for intensities higher than $7.10^{11} \text{ W.cm}^{-2}$ (average power 10 mW) at which the Ca^+ ion signal is completely saturated : it means that practically all the neutral atoms in the interaction volume have

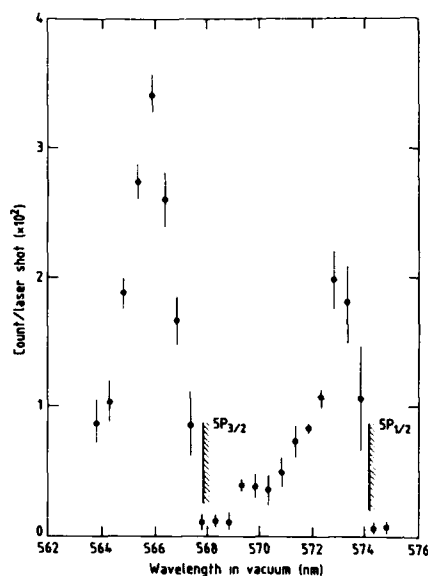


FIGURE 5
Wavelength dependence of component (4)
around $5P_{1/2}$ and $5P_{3/2}$ thresholds.

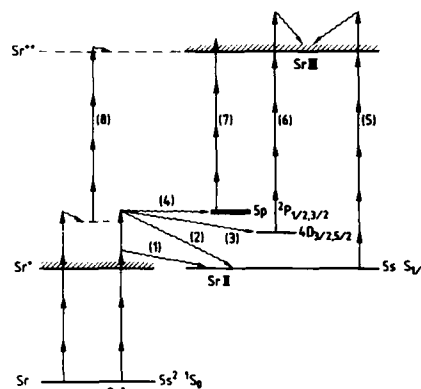


FIGURE 6
Energy levels of Sr I and Sr II relevant to the processes discussed in Sections 3 and 4.

been ionized during the first part of the pulse and that Ca^{++} ions can be formed only from Ca^+ ions. This is clearly a two-step process although there is still not enough information to know if the Ca^+ ions are in the ground state or in some excited state. In principle, one could measure the slopes ($d \log |\text{Ca}^{++}| / d \log P$) to determine the number of photons absorbed in the transition but the precision would not be sufficient for an unambiguous determination. A more complex situation is met at 1064 nm (Fig. 8). The two ions signals not only appear at the same intensity but have comparable intensity dependences and amplitudes. It can only be said that the double ionization probabilities are much larger than what could be estimated on the basis of what has been measured for non resonant ionization of alkali (for a more quantitative argument see ref. (6)). However many reasons can be invoked to explain a large cross-section: for instance a resonance can occur in the double ionization process and not in the single ionization. Such a resonance is shown on Fig. 9 obtained by scanning the wavelength of a picosecond dye laser (16). Unfortunately, due to Stark shifts and broadening of the line, it is not easy to assign it without uncertainty. In particular, it is not possible to decide if it is a resonance with doubly excited state, as described in Section 3, or a resonance in the ion spectrum, i.e. between two states of the ion*. In the case of Strontium, Fig. 10 shows the Sr^{++} ion signal as a function of the laser wavelength between 559 and 567 nm. They all can be assigned to resonances in the ion spectrum either between ground state and excited states (I) or between excited states (II), (III). Additional proof of these processes has already been presented in Section 3 by identifying the corresponding components in the photoelectron spectra, namely

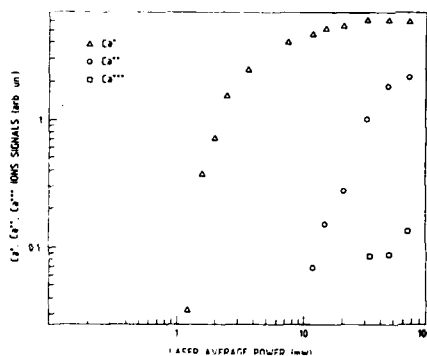


FIGURE 7
Intensity dependence of Ca ion signals
at 532 nm.

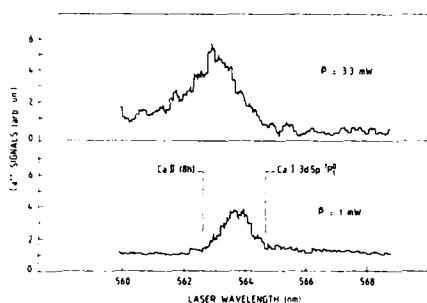


FIGURE 9
Wavelength dependence of the Ca^{++}
signal at two different intensities.

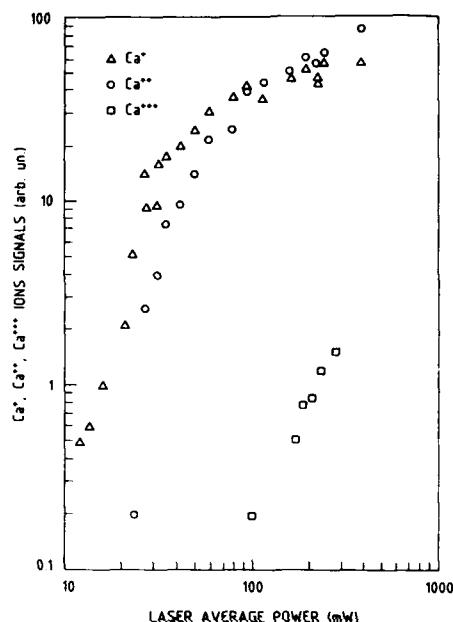


FIGURE 8
Intensity dependence of Ca ion signals
at 1064 nm.

components (5), (6), (7) in Fig. 4 and Fig. 6 together with the threshold dependence of Fig. 5. Therefore, it seems that the most probable mechanism producing doubly ionized Strontium is the following: the two outer electrons are excited on low-lying di-electron states by absorption of the first three or four photons. These states (auto) ionize rapidly towards continua $5s\ \epsilon l$, $5p\ \epsilon l$, $4d\ \epsilon l$ while the remaining electron is removed by absorption of additional photons in a transition which can be resonant. Resonances appearing in the first step (Fig. 1) do not show up in step (2) (Fig. 10) because of the larger intensity used to detect Sr^{++} ions ($60\ \text{GW}\cdot\text{cm}^{-2}$) which is enough to saturate the spectrum of Fig. 1. There is no evidence, so far, in such experiments for the excitation of high lying di-electronic states (double Rydberg states) although these states have probably some influence at least for wavelengths outside the ionic resonances (I), (II) and (III) of Fig. 10. Moreover, resonances on double Rydberg states have been shown (18) to be much smaller than the ionic resonances like the ones showing on Fig. 10. If no special care is taken to select-

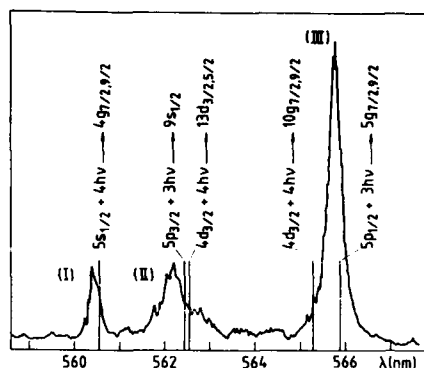


FIGURE 10
 Sr^{2+} ion spectrum taken at 60 GW.cm^{-2} .

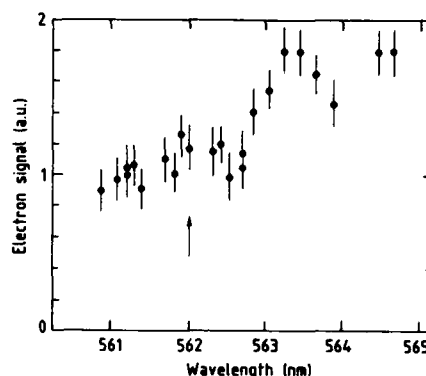


FIGURE 11
 "Avoided" threshold behavior in 5-6
 photon ionization of Sr^+ .

tively excite such states, the most likely path towards double ionization is the one just mentioned. Another way to state this is to say that resonant processes like (1) + (5), (3) + (6), (4) + (7) on Fig. 6 are dominant over non resonant processes like the one labelled (8) (17). In order to preferentially observe the latter, the best way would be to excite so-called Wannier states (18), (19) but there is no efficient scheme to do that, so far, mainly because their positions are completely unknown.

In the tuning range of Rhodamine 6 G, the threshold at which the 5-photon ionization of $5s \text{ } S_{1/2}$ of Sr^+ becomes a 6-photon ionization, can be crossed (562 nm). By monitoring the corresponding photoelectrons (peak (5) on Fig. 4) as a function of the laser wavelength one could expect to observe a threshold behavior similar to the one reported on Fig. 5. The peak (5) should disappear as soon as the energy of 5-photons becomes large enough to ionize Sr^+ and be replaced by a very low energy component. Fig. 11 shows the experimental result. The arrow shows the theoretical position of the threshold, and obviously no threshold behavior is observed. This interesting enough "avoided"-threshold is probably due to Above-Threshold Ionization: the wavelength dependence of the electron peak is expected to be that of the 6-photon cross-section when the 5-photon intermediate state crosses the continuum limit (15). Due to the continuity of the wavefunctions for Rydberg States when $n \rightarrow \infty$ and continuum states when $k \rightarrow 0$ there is no rapid variation of this ATI cross-section when crossing the continuum limit (20). Here, due to the high intensity used (2.8 TW.cm^{-2}) six-photon ionization takes place even when 5-photon ionization is possible.

5. MULTIPHOTON TRIPLE IONIZATION OF CALCIUM

We have observed triple ionization of Calcium for the first time using a YAG laser with intensities of about $10^{13} \text{ W.cm}^{-2}$ (1064 nm) and $10^{12} \text{ W.cm}^{-2}$ (532 nm) as shown on Fig. 7 and Fig. 8. These processes require respectively 60 and 30 photons and there is, so far, no known mechanisms to explain this

ionization. Since the experimental data is very poor it is very difficult to guess a reasonable explanation. We would just like to mention that ionization of Ca II is comparable to ionization of Argon (21) and to double ionization of Na and K as observed in (22). Understanding of this process obviously require more experiments.

REFERENCES

- 1) N.B. Delone and G.S. Veronov, JETP Lett. (Eng. Transl.) 1 (1965) 42 ; JETP 50 (1966) 78.
- 2) P. Agostini and C. Lecompte, Phys. Rev. Lett. 36 (1976) 1131.
- 3) L.A. Lompré, G. Mainfray, C. Manus, S. Repoux and J. Thebault, Phys. Rev. Lett. 36 (1976) 949.
- 4) P. Agostini, F. Fabre and G. Petite, Above-Threshold Ionization : Multiphoton ionization involving continuum-continuum transitions, in : Multiphoton Ionization of Atoms, eds. S.L. Chin and P. Lambropoulos (Academic Press, Toronto, 1984) pp. 133-154.
- 5) M. van der Wiel, Transitions within the continuum at high intensity laser fields, this volume.
- 6) N.B. Delone, V.V. Surin and B.A. Zon, Many electron processes in Non-linear Ionization of Atoms, in : Multiphoton Ionization of Atoms, eds. S.L. Chin and P. Lambropoulos (Academic Press, Toronto, 1984) pp. 235-264.
- 7) D. Feldman, M.J. Krautwald and K.H. Welge, Creation of doubly charged Strontium ions, in : Multiphoton Ionization of Atoms, eds. S.L. Chin and P. Lambropoulos (Academic Press, Toronto, 1984) pp. 223-233.
- 8) A. L'Huillier, L.A. Lompré, G. Mainfray and C. Manus, Phys. Rev. Lett. 48 (1982) 1814.
- 9) T.S. Luk, H. Pommer, K. Boyer, M. Shadidi, M. Egger and C.K. Rhodes, Phys. Rev. Lett. 51 (1983) 110.
- 10) P. Lambropoulos and P. Zoller, Multiphoton Autoionization in : Multiphoton Ionization of Atoms, eds. S.L. Chin and P. Lambropoulos (Academic Press, Toronto 1984) pp. 189-222.
- 11) G. Petite, P. Agostini and C.K. Wu, Revue de Physique Appliquée 20 (1985).
- 12) G. Petite, F. Fabre, P. Agostini, M. Crance and M. Aymar, Phys. Rev. A 29 (1984) 2677.
- 13) D. Feldman and K.H. Welge, J. Phys. B : At. Mol. Phys. 15 (1982) 1651.
- 14) P. Agostini and G. Petite, J. Phys. B : At. Mol. Phys. 18 (1985) L281.
- 15) P. Agostini and G. Petite, submitted.
- 16) P. Agostini and G. Petite, J. Phys. B : At. Mol. Phys. 17 (1984) L811.
- 17) M. Crance and M. Aymar, to be published Jour. Phys. Paris (Oct. 1985).
- 18) P. Camus, P. Pillet and J. Boulmer, J. Phys. B : At. Mol. Phys. (1985) in press.
- 19) G.H. Wannier, Phys. Rev. 90 (1953) 817.
- 20) M. Gavrilă, Europhysics Study Conference on Multiphoton Processes, Benodet, (France) (1979) unpublished.
- 21) A. L'Huillier, L.A. Lompré, G. Mainfray and C. Manus, J. Phys. B : At. Mol. Phys. 16 (1983) 1363.
- 22) S.L. Chin, K.X. He and F. Yergeau, J. Opt. Soc. Am. B 1 (1984), 505.
- 23) C.L. Cramer and Charles W. Clark, J. Phys. B (1985) in press.

*Nota : After this was written, it has been proposed (23) that this resonance would be the first observation of the $3d5p\ ^1F_0$ state of Ca, i.e. a doubly excited state.

MULTIPHOTON INNER-SHELL ATOMIC EXCITATION AND MULTIPLE IONIZATION

U. JOHANN, T.S. LUK and C.K. RHODES

University of Illinois at Chicago, Department of Physics, P.O. Box 4348,
Chicago, Illinois 60680, USA

Studies of multiphoton ionization of atoms have revealed several unexpected characteristics. The nonlinear coupling of 193 nm radiation to a range of atomic and molecular materials has been experimentally explored up to a maximum intensity on the order of $\sim 10^{17}$ W/cm². On the basis of observations of ion charge state spectra and electron energy distributions, the experimental evidence points to an ordered atomic motion involving several electrons, possibly an entire shell, as the main physical mechanism governing the coupling. Therefore, states representing multiple excitations appear to play a central role in the coupling, a consideration that fundamentally distinguishes the nonlinear interaction of a multielectron atom from that of a single-electron system. In the important regime, for which the radiative field strength E is greater than an atomic unit (e/a_0^2), the interaction can be viewed in approximate correspondence with the physics of fast (~ 10 MeV/amu) atom-atom scattering.

1. INTRODUCTION

Studies of multiphoton ionization involve the examination of the general class of reactions denoted by



Of particular significance, are the ion charge state spectra (X^{q+}) and the electron energy distributions produced in the interaction. Certain aspects of both of these types of data obtained with 193 nm radiation are discussed below.

Among the most important results is the finding that a multielectron atom, under intense irradiation with a coherent ultraviolet wave, having an electric field magnitude on the order of an atomic unit (e/a_0^2), exhibits a nonlinear response which is fundamentally different from that of a single-electron system. Furthermore, it can be shown that the interaction has, in several important respects, features in common with fast (~ 10 MeV/amu) atom-atom and ion-atom collisions(1). With the conclusion that a sufficiently strong radiative field can simulate the electronic environment corresponding to energetic atomic encounters, it follows that highly charged ions (2-4) arising from multiple electron ejection and inner-shell (5,6) excited states should be directly produced by atom-field interaction.

2. DISCUSSION OF RESULTS

Multiple ionization of atoms under collision-free conditions has been observed to occur readily with sufficiently intense irradiation at optical (3) and ultraviolet wavelengths (2,4). In particular, it was found (2,4) that the heavier atomic materials often presented the strongest coupling. In the ultraviolet studies, which were conducted at 193 nm, the highest charge state observed was

U^{10+} , a species requiring the transfer of more than 630 eV of energy(7), or equivalently, a minimum of 99 quanta. An example of the data taken on ion charge state distributions, Fig. 1 exhibits the results obtained with atomic thorium, a material that was studied with the use of an experimental technique involving laser-induced evaporation (8) to provide the sample.

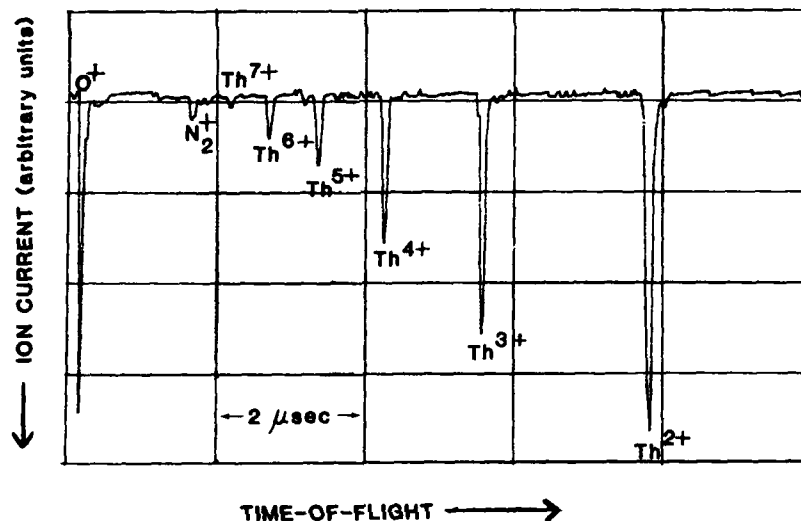


FIGURE 1

Time-of-flight ion spectrum of thorium produced under collision-free conditions with 193 nm radiation having a pulse width of ~ 5 ps and an intensity in the range of $10^{15} - 10^{16}$ W/cm 2 . The Th^+ peak is not shown. Impurity peaks arising from N_2^+ and O^+ are also evident.

A significant implication (4) of the ion production experiments was that the atomic shell structure is a principal determinant of the observed nonlinear response. Indeed, the hint provided by the role of the shell structure led to the hypothesis that it was mainly the number of electrons in the outer subshells that governed the coupling. A measurement of the response of elements in the lanthanide region enabled this view to be checked. As one moves from La ($Z = 57$) to Yb ($Z = 70$) in the lanthanide sequence, aside from slight rearrangements (9) involving the 5d shell for Gd ($Z = 64$), 4f electrons are being added to interior regions (10) of the atoms. The data showed (4) that for Eu ($4f^7 6s^2$) and Yb ($4f^{14} 6s^2$), which differ by seven 4f electrons, these inner 4f electrons play a negligible role in the direct radiative coupling, a fact that is in rapport with the observed dependence on the outer-shell structure.

A measurement of the electrons produced as a consequence of the ionization is also informative. In particular, on the basis of studies (11) of the electron energy distributions produced with 193 nm radiation, the excitation of inner-shell levels may have been established by the observation (5,11) in Xe of high energetic electron lines, which have been tentatively identified as $N_{4,5}O_0$ Auger electrons arising from 4d vacancies. The Auger photoelectron features appear in the range from 8 to about 40 eV at a laser peak intensity of $\sim 10^{15}$ W/cm 2 . The most prominent lines are those associated with $N_{4,5}O_1O_1$ transitions of neutral xenon which terminate on the $4d^{10}5s^05p^6$ double-hole state. A total of eight electron lines is observed (5,11), representing a quartet of pairs of

transitions, all of which exhibit the known (12,13) $4d_{3/2} - 4d_{5/2}$ fine structure splitting in xenon of ~ 2 eV.

The results on the 4d-shell excitation in xenon are significant, since theoretical results obtained by quantitative calculations (14) based on the time dependent Hartree-Fock method confirm (i) the fundamental character of the atomic motion, represented in the analogy with fast atom-atom collisions (1,15-17), and (ii) provide quantitative agreement as well. For the latter, the intensity levels at which 4d Auger electrons should be observable in xenon correspond, within a factor of approximately two, for both (1,6,14) theoretical approaches. Importantly, these results are also in accord with the experimental figure (5,11) to within the same rather small level of uncertainty.

The Xe electron energy spectrum exhibits another salient change with increasing intensity of the 193 nm radiation in the range of 10^{14} to 10^{15} W/cm². The first ionization line, which corresponds to two-photon absorption with a corresponding photoelectron energy of 0.7 eV, nearly disappears, while the three-photon process, arising from continuum-continuum transitions (18-20) develops greater strength. The suppression of the lowest order photoelectron line can be understood as arising from the influence of the pondermotive potential (19-22) and predicts that the 0.7 eV line in xenon should vanish at an intensity (21) of 2×10^{14} W/cm², a value in reasonable agreement with the experimental figure (5,6,11).

Another important characteristic of the 0.7 eV feature is the width of the line in the range of intensity below 2×10^{14} W/cm², since that line breadth can be interpreted in terms of the lifetime of the excited atomic level that is imbedded in the ionization continuum at the energy corresponding to two 193 nm quanta (~ 12.8 eV). This width, which is measured (11) to be ~ 0.2 eV with an instrumental resolution (5,11) of $\sim 4 \times 10^{-2}$ eV, corresponds to a lifetime of $\tau \sim 3.3 \times 10^{-15}$ sec, a duration on the order of ~ 5 periods of the ultraviolet wave. This lifetime τ can be compared with the one estimated from the transition rate calculated (23) by standard perturbation theory for two-photon absorption at 193 nm in xenon. At an intensity of $\sim 10^{14}$ W/cm², the lifetime that results is $\sim 1.2 \times 10^{-15}$ sec, a value approximately three times shorter than that characteristic of the measured width (11) at the comparable intensity of irradiation.

On the basis of the observation of Auger lines in the electron spectrum characteristic of the neutral atom and the disappearance of the lowest order photoelectron feature at 0.7 eV, it appears that a considerable fraction of the neutral atoms in the focal volume of the 193 nm laser beam are exposed to the peak intensity of the laser pulse (21).

3. MECHANISM OF COUPLING

From an analysis of the data now at hand, the following hypothesis can be considered as an approximate description of the basic character of the electronic motions involved in these processes. Overall, the data strongly indicate that an organized motion of an entire shell, or a major fraction thereof, is directly involved in the nonlinear coupling. With this picture, the outer atomic subshells are envisaged as being transiently driven in coherent oscillation by the intense ultraviolet wave. With this type of electronic motion, the observed increase in the multiphoton coupling strength can be qualitatively correlated (4) with the larger magnitude of the effective charge involved in the interaction. In quantum mechanical language, an oscillating shell would be represented by a wave function of a multiply excited configuration.

The coherence of the electronic motion in the outer region of the atom has important consequences for the coupling of energy to atomic inner-shells. In terms of a simple model, it has been possible to describe this interaction (1)

by correspondence with certain properties of fast atom-atom collisions (15-17). Formulated in this way, the atomic inner-shell interaction can be viewed as a form of dynamic configuration interaction in which the fields of the participating outer electrons sum constructively. Constructive addition naturally results if the scale of the momentum transfer Δq communicated in the interaction is sufficiently small so that the length $\hbar/\Delta q$ is greater than the spatial scale of the scattering system. The physical origin of this effect is the same as that which generates the coherent forward scattering (24) observed in nuclear collisions (25).

4. CONCLUSIONS

Basic physical studies of collision-free nonlinear atomic processes, through an analysis involving combined measurement of ion charge state distributions (2,4), photoelectron energy spectra (5,11), and photon spectra (6,26-28) arising from intense ultraviolet irradiation, have produced data that strongly indicate that multielectron atoms respond in a manner basically different from single-electron counterparts. The confluence of the evidence suggests that, under appropriate circumstances, the outer atomic subshells can be driven in coherent oscillation, and this ordered electronic motion can, by direct intra-atomic coupling, lead to the rapid excitation of atomic inner-shell states. Quantum mechanically, such states of motion for the outer-shell electrons would be described by multiply excited configurations. Two direct consequences of this type of motion are (i) that the maximum magnitude of the oscillating intra-atomic electric field can approach several atomic units, since the fields of all the participating outer electrons combine constructively, and (ii) that the harmonic content of the resulting field can, because of the nonlinear character of the electron-electron $1/r^2$ coulombic interaction, become large. A strong, highly nonlinear coupling to the atom results, and enhanced rates of nonlinear absorption leading to multiple ionization and inner-shell excitation are expected.

In the near future, ultraviolet laser technology will enable basic physical studies to be performed in the $10^{20} - 10^{21}$ W/cm² range with pulse lengths on the order of $\sim 10^{-13}$ sec. At such an intensity, the peak electric field of the coherent driving wave approaches the unprecedented value of ~ 100 e/a₀. In such an extreme environment, it is likely that physical processes never previously observed will be detected. This would include certain mechanisms involving the production of electron-positron pairs (1).

ACKNOWLEDGEMENTS

The authors wish to acknowledge fruitful discussions with H. Egger, A.P. Schwarzenbach, K. Boyer, and A. Szöke. This work was supported by the Office of Naval Research, the Air Force Office of Scientific Research under contract number F49620-83-K-0014, the Innovative Science and Technology Office of the Strategic Defence Initiative Organization, the Department of Energy under grant number DE-AC02-83ER13137, the Lawrence Livermore National Laboratory under contract number 5765705, the National Science Foundation under grant number PHY 84-14201, the Air Force Office of Scientific Research, Department of Defense University Research Instrumentation Program under grant number USAF 840289, the Defense Advanced Research Projects Agency, and the Los Alamos National Laboratory under contract number 9-X54-C6090-1.

REFERENCES

- 1) K. Boyer and C.K. Rhodes, *Phys. Rev. Lett.* **54**, 1490 (1985).
- 2) T.S. Luk, H. Pummer, K. Boyer, M. Shahidi, H. Egger, and C.K. Rhodes, *Phys. Rev. Lett.* **51**, 110 (1983).

- 3) A. L'Huillier, L.-A. Lompré, G. Mainfray, and C. Manus, *Phys. Rev. Lett.* **48**, 1814 (1982); *ibid.*, *Phys. Rev.* **A27**, 2503 (1983).
- 4) T. S. Luk, U. Johann, H. Egger, H. Pummer, and C. K. Rhodes, *Phys. Rev.* **A32**, 214 (1985).
- 5) U. Johann, T. S. Luk, H. Egger, H. Pummer, and C. K. Rhodes, "Evidence for Atomic Inner-Shell Excitation in Xenon from Electron Spectra Produced by Collision-Free Multiphoton Processes at 193 nm," *Conference on Lasers and Electro-Optics '85*, Baltimore, Maryland, p. 152.
- 6) Charles K. Rhodes, "Multiphoton Ionization of Atoms," *Science*, in press.
- 7) T. A. Carlson, C. W. Nestor, Jr., N. Wasserman, and J. D. McDowell, *Atomic Data* **2**, 63 (1970).
- 8) J. F. Ready, *J. Appl. Phys.* **36**, 462 (1965).
- 9) T. D. Cowan, *The Theory of Atomic Structure and Spectra* (University of California Press, Berkeley, 1981); I. I. Sobel'man, *Introduction to the Theory of Atomic Spectra* (Pergamon Press, Oxford, 1972).
- 10) F. Herman and S. Skillman, *Atomic Structure Calculations* (Prentice Hall, Inc., Englewood Cliffs, 1963).
- 11) U. Johann, T. S. Luk, H. Egger, and C. K. Rhodes, "Measurement of Electron Energy Distributions Produced by Collision-Free Multiquantum Processes," manuscript in preparation.
- 12) S. Southworth, U. Becker, C. M. Truesdale, P. H. Kobrin, D. W. Lindle, S. Owaki, and D. A. Shirley, *Phys. Rev.* **A28**, 261 (1983).
- 13) L. O. Werme, T. Bergmark, and K. Siegbahn, *Phys. Scr.* **6**, 141 (1972).
- 14) A. Szöke and C. K. Rhodes, "A Theoretical Model of Inner-Shell Excitation by Outer-Shell Electrons," submitted to *Physical Review Letters*.
- 15) J. S. Briggs and K. Taulbjerg, in *Structure and Collision of Ions and Atoms*, edited by I. A. Sellin (Springer-Verlag, Berlin, 1978) p. 105.
- 16) George H. Gillespie and Mitio Inokuti, *Phys. Rev.* **A22**, 2430 (1980).
- 17) J. H. McGuire, N. Stolterfoht, and P. R. Simony, *Phys. Rev.* **A24**, 97 (1981).
- 18) P. Kruit and F. H. Read, *J. Phys.* **E16**, 373 (1983).
- 19) H. G. Muller and A. Tip, *Phys. Rev.* **A30**, 3039 (1984); P. Kruit, J. Kimman, H. G. Muller and M. J. van der Wiel, *Phys. Rev.* **A28**, 248 (1983).
- 20) P. Kruit, J. Kimman, H. G. Muller, and M. J. van der Wiel, *J. Phys. B: At. Mol. Phys.* **16**, 937 (1983); H. G. Muller, A. Tip, and M. J. van der Wiel, *J. Phys. B: At. Mol. Phys.* **16**, L679 (1983).
- 21) A. Szöke, *J. Phys. B: At. Mol. Phys.* **18**, L427 (1985).
- 22) Marvin H. Mittleman, *Phys. Rev.* **A29**, 2245 (1984).
- 23) E. J. McGuire, *Phys. Rev.* **A24**, 835 (1981).
- 24) L. Rosen, in *High-Energy Physics and Nuclear Structure--1975*, edited by D. E. Nagle, A. S. Goldhaber, C. K. Hargrave, R. L. Burman, and B. G. Storms, AIP Conference Proceedings No. 26 (American Institute of Physics, New York, 1975) p. 265.
- 25) J. M. Blatt and V. F. Weisskopf, *Theoretical Nuclear Physics* (Wiley, New York, 1952).
- 26) T. Srinivasan, H. Egger, T. S. Luk, H. Pummer, and C. K. Rhodes, in *Laser Spectroscopy VI*, edited by H. P. Weber and W. Lüthy, (Springer-Verlag, Berlin, 1983) p. 385.
- 27) H. Egger, T. S. Luk, W. Müller, H. Pummer, and C. K. Rhodes, in *Laser Techniques in the Extreme Ultraviolet*, AIP Conference Proceeding No. 119, edited by S. E. Harris and T. B. Lucatorto (AIP, New York, 1984) p. 64; H. Egger, K. Boyer, T. S. Luk, W. Müller, H. Pummer, and C. K. Rhodes, *SPIE* **476**, 52 (1984).
- 28) K. Boyer, H. Egger, T. S. Luk, H. Pummer, and C. K. Rhodes, *J. Opt. Soc. Am.* **B1**, 3 (1984).

MULTIPHOTON STRIPPING OF ATOMS

Michele CRANCE

Laboratoire Aime Cotton, C.N.R.S. II,
Bat.505, 91405 Orsay cedex, France

Multiphoton stripping of atoms seems to concern only outershell electrons. The formation of multicharged ions results from the competition of direct and stepwise processes. The pulse duration and the number of photons involved are the essential parameters. Depending on the intensity required to saturate single ionisation, different behaviours are observed: in weak field, resonance structure is observed; in strong field, the memory of the energy spectrum seems to be "lost" except for the characteristics of the initial state. The distribution of charge states can be calculated from the knowledge of ionisation potential and electronic orbital size.

1 INTRODUCTION

Formation of multiply charged ions by multiphoton absorption is observed when an atom is irradiated by a strong light field. Evidence of this process has been given ten years ago by pioneer experiments on alkaline earths and rare earths (1). The simultaneous emission of singly charged and doubly charged ions has been detected for Strontium (1), Barium (2), Europium (3) excited by a Neodymium YAG laser delivering nanosecond pulses of intensity up to 10^{11} W cm⁻² at 9450 cm⁻¹. In the same conditions, no doubly charged ions have been detected for Samarium (4), Calcium (5), Magnesium and Lead (3). Following this first experiment, several studies on Barium (6-9) and Strontium (10-13) have provided a number of results on the behaviour of alkaline earths excited by nanosecond light pulses. Additional informations have been given by recent experiments using picosecond pulses (14,15). Many results obtained for nanosecond pulses excitation have, in fact, been confirmed by the latter work. Qualitatively, the behaviour of alkaline earths is very similar to the behaviour of alkalis and reflects the typical features of multiphoton processes in atoms excited by a light field of moderate intensity (16).

Recently, a series of experiments carried out on noble gases and some other complex atoms have shed a new light on multiphoton stripping of atoms. For noble gases, several charge states are observed: up to five for excitation by a Neodymium YAG laser (17-22) or a CO₂ laser (23,24), up to eight for U.V. excitation by an excimer laser (25-28). However, for Caesium, only the singly charged ion is obtained even if the intensity is increased up to 10^{13} W cm⁻². Experimental data show that the intensity required to remove several electrons is hardly larger than the intensity required to remove one electron, as long as outershell electrons are concerned. However, the range of intensity required for observation of single ion varies strongly with atoms. As we shall discuss in next section, the efficiency of excitation can be characterised by the saturation intensities I_{sat} for a pulse of duration τ . For picosecond pulses delivered by a Neodymium YAG laser, saturation intensities are of the order of 10^{11} W cm⁻² for alkalis and alkaline earths, a few 10^{13} W cm⁻² for noble gases.

For all the species studied, everything happens as if only outershell electrons were involved in multiphoton absorption process. However, strong differences between two outershell electron atoms and more complex atoms appear

which are related to the difference in intensity required for ionisation. Two types of behaviour are observed:

- a "weak field" behaviour which reflects the detail of the energy spectrum and can be analysed in the frame work of perturbation theory,
- a "strong field" behaviour where the memory of the atomic spectrum seems to be "lost" except for the characteristics of the initial state (energy and size of the electronic orbitals).

In next sections, we shall present both points of view and discuss what mechanisms can be considered as responsible for the formation of multicharged ions. Most observations on alkaline earths correspond to a "weak field" behaviour while most observations on noble gases correspond to a strong field behaviour. However, both points of view must be considered for a better understanding of all experimental data.

2. MULTIPHOTON STRIPPING IN WEAK FIELD

In the dressed atom picture, the evolution of the system atom plus field is governed by the Hamiltonian $H = H_0 + V$, where $H_0 = H_A + H_F$. H_F is the field Hamiltonian, V is the atom field interaction. H_A is the atomic Hamiltonian: H_A describes the interaction of the nucleus plus its Z electrons and thus, the energy spectrum of H_A contains the states of the neutral atom as well as the states of multicharged ions plus ejected electrons. The resolvent of the unperturbed system is $G_0(z) = (z - H_0)^{-1}$. The initial state, $|g\rangle$, is the neutral atom dressed by N_0 photons, its energy is E_0 , the transition probability to state $|f\rangle$ is given by

$$P_{gf} = (2\pi/\hbar) \langle f | G_0(E_f) V | g \rangle \langle g | G_0(E_g) V | f \rangle \quad (1)$$

In this formula, $|f\rangle$ is supposed to be a continuum state with energy E_f , that is any state above the first ionisation threshold dressed by the suitable number of photons. When perturbation theory is applied at minimum non vanishing order, only the lowest term of V expansion is kept in Eq.1, q is then the minimum number of photons required for energy conservation. For an atom with ionisation potential E_0 , irradiated by a light field of frequency ω , the minimum number of photon absorption required for single ionisation is n , the integer part of $E_0/\hbar\omega - 1$. Ionisation probability calculated at minimum non vanishing order is obtained by taking for $|f\rangle$, the singly charged ion in ground state and an electron of energy $n\hbar\omega - E_0$. At order $q > n$, different types of terms appear in Eq.1. Transition probabilities for Above threshold ionisation are obtained by taking for $|f\rangle$ the singly charged ion in ground state and an electron with energy $(n+q)\hbar\omega - E_0$. Another possibility for $|f\rangle$ is the singly charged ion in excited state with energy E_a and an electron with kinetic energy $q\hbar\omega - E_a$, the corresponding processes lead to single ionisation. One can also take for $|f\rangle$ a state belonging to a continuum of multiple ionisation. All the probabilities mentioned above correspond to competing processes which lead to the depletion of the ground state of neutral atom. Once an ion has been created, it interacts with the light field and may eject one or more electrons after multiphoton absorption. The probabilities for such processes are calculated by equations similar to Eq.1.

For the sake of simplicity, we shall neglect the formation of ions in excited states. It is thus possible to calculate a set of probabilities $P_{ab}(t)$, with a, b , corresponding to the transition $H^{a+} \rightarrow H^{b+}$. The probabilities for an atom to be neutral, N_0 , or in charge state q , N_q , at time t , are governed by rate equations involving the probabilities P_{ab} defined above (33);

$$\dot{N}_0 = -(P_{01} + P_{02} + \dots) N_0 \quad (2a)$$

$$\dot{N}_1 = P_{01} N_0 - (P_{12} + P_{13} + \dots) N_1 \quad (2b)$$

the hierarchy of Eqs.2 can be solved formally for any pulse shape. However, in order to understand the most important features of the process, we shall discuss the solution of Eqs.2 under some simplifying assumptions. We suppose that the P 's are calculated by perturbative treatment at minimum non vanishing order and thus the following treatment will be valid for moderate intensities only. For the sake of simplicity, we consider a rectangular pulse shape with duration t . The solution of Eq.2a is

$$N_0 = \exp(-(P_{01} + P_{02} + \dots)t) \quad (3)$$

From Eq.3, we define the saturation intensity for single ionisation, I_s by

$$(P_{01}(I_s) + P_{02}(I_s) + \dots) t = 1 \quad (4)$$

For intensities I_m smaller than I_s , the solution of Eqs.2 reduces to

$$\begin{aligned} N_1(t) &= P_{01} t \\ N_2(t) &= P_{02} t + P_{01} P_{12} t^2/2 \\ N_3(t) &= P_{03} t + (P_{01} P_{13} + P_{02} P_{23}) t^2/2 + P_{01} P_{12} P_{23} t^3/6 \end{aligned} \quad (5)$$

The time-dependence reflects the nature of the contribution to each N_i : contribution of direct process is proportional to t , contribution of two-step process is proportional to t^2 , contribution of three-step process is proportional to t^3 ... Multicharged ions are formed by several competing processes. For doubly charged ions, direct and two-step process are possible. They correspond to the transitions: $A \rightarrow A^{++}$, for direct process and $A \rightarrow A^+$ followed by $A^+ \rightarrow A^{++}$ for stepwise process. For a given intensity, the ratio of the contributions of both processes depends on t . Direct process is favoured by short pulses. The variation of doubly charged ion yield with the pulse duration has been studied experimentally for Xenon excited by the first harmonics of a Neodymium YAG laser (20). For 5ps pulses, Xe^{++} is detected before single ionisation saturates, while for 200ps pulses, Xe^{++} is observed only for an intensity larger than saturation intensity of single ionisation.

Direct and stepwise processes do not necessarily involve the same number of photons. Defining E_1 as the energy difference between the ground states of A^+ and A^{++} , the number of photons required for direct process is n_0 , the integer part of $(E_0 + E_1)/h\nu + 1$. The number of photons required for stepwise process is $n_1 + n_2$ where n_1 is the integer part of $E_0/h\nu + 1$ and n_2 is the integer part of $E_1/h\nu + 1$. In a direct process, two electrons are ejected at the same time, sharing the energy

$$e_0 = n_0 h\nu - E_1 \quad (6)$$

In a stepwise process, two electrons are ejected successively, the energy of the first electron being

$$e_1 = n_1 h\nu - E_0 \quad (7)$$

The energy of the second one is

$$e_2 = n_2 h\nu - E_1 \quad (8)$$

If $e_1 < e_0$, the same number of photons is involved in the stepwise and the direct process: $n_0 = n_1 + n_2$. If e_1 is already larger than e_0 , the second step requires one more photon and $n_1 + n_2 = n_0 + 1$. In the latter case, the competition between direct and stepwise processes is also the competition between two processes of different order. In weak field, the most probable process is certainly the one requiring the smallest number of photons.

There is a more fundamental difference between direct and stepwise processes which is related to the coherence of successive photon absorptions in a multiphoton process. In a direct process, n_0 photons are absorbed simultaneously. In a stepwise process, n_1 photons are absorbed simultaneously and then, at any time later in the pulse, n_2 photons are absorbed simultaneously. It is possible to study coherence properties of multiphoton absorption by using pulses with different statistical properties (34). It has been shown that the ion yield obtained with chaotic light is larger than the ion yield obtained with coherent light by a factor of $n!$ for a n -photon process. In the same way, different enhancements are expected for direct and stepwise processes: $n_0!$ and $n_1! n_2!$ respectively. Both processes could be distinguished by another method: the study of time correlation between emitted electrons.

In the previous discussion, we have considered that the intensity was weak enough for a perturbative treatment at minimum non vanishing order to be valid. The validity of this assumption can be tested by measuring, for each process, the effective order of non linearity, k . In a log-log plot, k is the slope of the curve giving the number of ions in charge state q as a function of the field intensity.

Table 1:
Effective order of nonlinearity for single ionisation.

species	n_1	k	frequency (cm ⁻¹)	reference
Ba	5	4.0±0.1	9450	3
Sr	5	5.0±0.2	9450	3
Eu	5	5.0±0.2	9450	3
La	6	5.9±0.1	9450	3
Mg	7	5.0±0.3	9450	3
Pb	7	5.9±0.2	9450	3
Sr	5	5.6±1	9395	11
Br	5	5.6±1	9395	11
Sr	3	3.5±1	18790	11
Sr	2	2.3±0.3	28185	11
Br	2	1.6±0.4	37580	11
Xe	11	10.8±0.5	9395	17
Kr	13	12.9±0.5	9395	17
Ar	14	13.6±0.7	9395	17
Ne	19	19.±2	9395	17
He	22	21.±2	9395	17
Xe	6	6.±0.5	18790	19
Ne	10	9.6±0.5	18790	19

As shown by the data given in table 1, the effective order of non linearity measured for singly charged ion yield is approximately equal to the number of photons required for the transition $A \rightarrow A^+$.

When doubly charged ions are observed, two types of curves are obtained depending whether they are detected above or below saturation intensity for single ionisation. In the latter case, one expects direct process to occur and the effective order of non linearity to be equal to n_D (see Table 2). In the former case, doubly charged ions are produced by stepwise process and the effective order of non linearity is to be compared with n_2 (see Table 3).

Table 2:
Effective order of non linearity for double ionisation by direct process.

species	n_D	k	frequency (cm ⁻¹)	reference
Ba	15	2.9	9450	3
Sr	15	10.1	9450	3
Eu	14	4.9	9450	3
Sr	15	8.	9395	11
Sr	4	3.7	37580	11
Xe	15	15.	18790	20

Table 3:
Effective order of non linearity for double ionisation by stepwise process.

species	n_2	k	frequency (cm ⁻¹)	reference
Sr	5	5.5	18790	11
Ne	18	17.	18790	19

The structure of Eq.1 allows one to relate the orders of magnitude of processes involving different numbers of photon absorptions. When no interference (constructive or destructive) occurs, the ratio between the probability for a process involving q photons and a process involving $q-1$ photons has a typical order of magnitude of $r=10^{-14}$ 1, for an optical frequency (ω is expressed in $W\text{ cm}^{-2}$). When Above threshold Ionisation or stripping is detected, it means that processes involving more than n photons have become noticeable. Due to the magnitude of r , one expects to observe high order processes in two situations, either the intensity is large, this is the case of experiments on noble gases, or one of the quantum paths leading to a high lying state is enhanced by a resonance, this could be the situation for alkaline earths. Systematic studies of ion yield as a function of frequency have shown a structure of resonances which have not been always identified. According to the previous analysis, when direct process is detected, one expects to observe resonances with doubly excited states lying above the first ionisation threshold. When stepwise process is responsible for double ionisation, resonance states should belong to the energy spectrum of the singly charged ion. Another type of enhancement might be observed at the transition between direct and stepwise process. Let the frequency ω_0 correspond exactly to the ionisation threshold to excited state a of the singly charged ion. Then

$$e_1 = 0, e_2 = e_D \quad \text{and} \quad n_1 + n_2 = n_D$$

for this channel. For frequency ω smaller than ω_0 , direct process along this channel dominates; its probability is proportional to $(\omega_0 - \omega)^{-2}$ and, thus, increases when ω tends to ω_0 . For frequency larger than ω_0 , the same channel is a stepwise process which probability decreases when $\omega - \omega_0$ increases. The result should be an asymmetric peak in A^{++} yield.

3 MULTIPHOTON STRIPPING IN STRONG FIELD

In weak field, multiphoton processes are governed by power laws with an index equal to the number of photons absorbed, except in the close vicinity of exact resonance. When the intensity is increased, resonances shift and broaden, but the resonance structure of the energy spectrum still survives. Light shifts have comparable orders of magnitude in all atoms. For strong field, typically $10^{13} \text{ W cm}^{-2}$, the shift of resonances along the light pulse smooths the resonance structure and measured ion yields hardly depend on the frequency. That is the range of intensity considered in this section. Most experiments on noble gases are concerned; for alkaline earths, only the highest range of intensity in experiments using picosecond pulses might correspond to strong field excitation.

The complexity of calculations based on first principles is so formidable that nobody has tried to calculate non perturbative ionisation probabilities for complex atoms. Several authors have proposed treatments based on statistical considerations. A first approach consists in assuming that all outershell electrons have the same probability to be ejected, this probability being taken as a parameter. This treatment leads to a binomial law for charge state distribution which can be used to analyse experimental results (35). This idea has been reinvestigated recently to analyse experiments involving different ranges of intensity and wavelength (36). While the latter works propose a parametric analysis of experimental data, we have built a heuristic model, based on semiclassical considerations (37). Multiphoton ionisation consists in a series of virtual absorptions which are equally allowed in a time $T = \hbar/E_0$. The outershell electrons appear as a target, the geometrical size of which is approximately determined by the mean radius of electronic orbitals. From this data, saturation intensity is calculated for an interaction time T , allowing the prediction of cross section for any type of process, direct or stepwise, in which one or more electrons are ejected.

Saturation intensity for single ionisation has been measured for noble gases excited by a Neodymium YAG laser (17) and its first harmonics (19) and by CO_2 laser (23,24). The predictions of statistical model are in good agreement with experimental data obtained at intensities of the order of $10^{13} \text{ W cm}^{-2}$ or larger (38,39). The discrepancy observed for lower intensity can be partly understood as related to the ratio of the kinetic energy gained by the electron and the energy of one photon (40). Experimental data obtained with an excimer laser on various species (25-28) can be interpreted by statistical calculations (41). It is also possible to predict the energy spectrum of emitted electrons (42) when Xenon (32) or Helium (43,44) are excited by a Neodymium YAG laser.

For alkaline earths, statistical considerations lead to a rough order of magnitude for saturation intensities measured with nanosecond pulses. However, for larger intensities (about $10^{13} \text{ W cm}^{-2}$), the relative yield of singly and doubly charged ions obtained when Calcium is excited by picosecond pulses at the same frequency are well reproduced by statistical calculations. Statistical models are based on the simple picture of an atom having lost any memory of its energy spectrum between the ground state and the threshold. All these results support the validity of this picture and suggest the use of simplifying assumptions in calculations based on first principles.

4 CONCLUSION

Up to now, two opposite approaches have been considered to interpret multiphoton stripping of atoms: consideration of very weak or very strong intensities. The essential mechanisms have been identified and qualitatively explained. In the intermediate range of intensity where most experiments on alkaline earths have been carried out, a number of problems remain unsolved. One of the

reasons is the lack of precise spectroscopic data, experimental as well as theoretical, on doubly excited states. Experiments in progress with picosecond pulses (15) should improve the situation shortly.

ACKNOWLEDGEMENTS

The author is grateful to Prof. S.L.Chin for communicating experimental data prior to publication.

REFERENCES

- 1 V.V. Suran, I.P. Zapesochny JETP Lett. 1 (1975) 973
- 2 I.S. Alexakhin, I.P. Zapesochny V.V. Suran Ukr.Fiz.Zh. 21 (1976) 1383
- 3 I.S. Alexakhin, N.D. Delone, I.P. Zapesochny, V.V. Suran Sov. Phys. JETP 49 (1979) 447
- 4 V.V. Suran Opt. Spectrosc. 41 (1976) 901
- 5 V.V. Suran Ukr. Fiz. Zh. 22 (1977) 2055
- 6 N.B. Delone, I.P. Zapesochny, B.A. Zon, V.V. Suran Izv. Akad. Nauk. SSSR Ser. Fiz. 45 (1981) 1081
- 7 I.I. Bondar, N.B. Delone, I.P. Zapesochny, V.V. Suran JETP Lett. 7 (1981) 243
- 8 I.I. Bondar, N.B. Delone, B.A. Zon, V.V. Suran Opt. Comm. 40 (1982) 268
- 9 I.I. Bondar, A.I. Gomonay, N.B. Delone I.P. Zapesochny, V.V. Suran J. Phys. B17 (1984) 2049
- 10 D. Feldmann, K.H. Welge J. Phys. B15 (1982) 1651
- 11 D. Feldmann, J. Krautwald, S.L. Chin, A. von Hellfeld, K.H. Welge J. Phys. B15 (1982) 1663
- 12 D. Feldmann, J. Krautwald, K.H. Welge J. Phys. B15 (1982) L529
- 13 S.L. Chin, A. von Hellfeld, J. Krautwald, D. Feldmann, K.H. Welge ICOMP Proceedings Budapest (1980)
- 14 F. Agostini, G. Petite J. Phys. B17 (1984) L811
- 15 F. Agostini, G. Petite J. Phys. B18 (1985) L281
- 16 G. Mainfray, C. Manus Multiphoton ionisation of atoms ed. S.L. Chin and P. Lambropoulos Academic Press (1984)
- 17 A.L. Huillier, L.A. Lompre, G. Mainfray, C. Manus J. Phys. B16 (1983) 1363
- 18 A.L. Huillier, L.A. Lompre, G. Mainfray, C. Manus Phys. Rev. Lett. 48 (1982) 1814
- 19 A.L. Huillier, L.A. Lompre, G. Mainfray, C. Manus Phys. Rev. A27 (1983) 2503
- 20 A.L. Huillier, L.A. Lompre, G. Mainfray, C. Manus J. de Physique 44 (1983) 1247
- 21 L.A. Lompre, G. Mainfray Multiphoton processes ed. P. Lambropoulos and S.J. Smith Springer Verlag (1984)
- 22 L.A. Lompre, A.L. Huillier, G. Mainfray, J.Y. Fan J. Phys. B17 (1984) L817
- 23 S.L. Chin, G. Farkas, F. Vergeau J. Phys. B16 (1983) L223
- 24 S.L. Chin, F. Vergeau, P. Lavigne J. Phys. B18 (1985) L213
- 25 I.S. Luk, H. Pummer, K. Bover, M. Shahidi, H. Egger, C.K. Rhodes Phys. Rev. Lett. 51 (1983) 110
- 26 K. Bover, H. Egger, I.S. Luk, H. Pummer, C.K. Rhodes JOSA B1 (1984) 1
- 27 C.K. Rhodes Multiphoton processes 31 (1984) Springer Verlag
- 28 C.K. Rhodes Fundamentals of laser interactions p.111 (1985) Ubergangl Austria
- 29 M. Lrance Multiphoton ionisation of atoms ed. S.L. Chin and P. Lambropoulos Academic Press (1984)
- 30 J. Moreillec, D. Normand, G. Petite Phys. Rev. Lett. 14 (1976) 300
- 31 L.A. Lompre, G. Mainfray, C. Manus J. Phys. B13 (1980) 85
- 32 P. Krut, J. Fimman, H.G. Muller, M.J. Van der Wiel Phys. Rev. A28 (1983) 248
- 33 M. Lrance J. Phys. B17 (1984) 4323
- 34 L.A. Lompre, G. Mainfray, C. Manus, J.P. Mariniier J. Phys. B14 (1981) 4307
- 35 I. Aberg, A. Blomberg, J. Tuikkari, O. Gosdzinski Phys. Rev. Lett. 52 (1984) 1207
- 36 S. Beitman Phys. Rev. Lett. 54 (1985) 1905

- 37 M.Crance J.Phys. B17 (1984) 4333
- 38 M.Crance J.Phys. B17 (1984) 3503
- 39 M.Crance Fundamentals of laser interactions p.136 (1985) Ubergurgl Austria
- 40 M.Crance J.Phys. B17 (1984) L635
- 41 M.Crance J.Phys. B17 (1984) L155
- 42 M.Crance J.Phys. B17 (1984) L355
- 43 B.W.Boreham and J.L.Hughes Sov.Phys. JETP 53 (1981) 252
- 44 B.W.Boreham and B.Luther Davies J.Appl.Phys. 50 (1979) 2533

THEORY OF MULTIPHOTON IONIZATION AND AUTOIONIZATION OF Xe^{*}

Pradip GANGOPADHYAY, Xian TANG, P. LAMBROPOULOS[†] and Robin SHAKESHAFT

Department of Physics, University of Southern California,
Los Angeles, California 90089-0484

1. INTRODUCTION

Although the rare gases and especially Xe have, for several years now, been serving as testing ground for experimental multiphoton ionization studies, relevant calculations^{1,2} have been very rare. The complexity of these atoms is of course the main reason for the scarcity of such calculations. The problem can not, however, be avoided for ever and it is our belief that one must make some attempts even if they have to be not very accurate at first. Two types of experiments during the last three or four years make this unattractive task even more imperative. One has to do with above threshold ionization³⁻⁵ or continuous-continuous transitions in which the electron keeps absorbing photons even after having absorbed the minimum number of photons necessary to cross the threshold. These are observations with either 1,064 nm or 532 nm radiation and intensities around 10^{13} W/cm². The other type of experiments⁶ deal with multiphoton, multiple ionization under much higher intensity (10^{14} - 10^{16} W/cm²) and shorter wavelengths (193 nm). Multiple ionization has also been observed⁷ at $\lambda=1,064$ nm and $\lambda=532$ nm. The atom of Xe has figured prominently in both types of experiments. For radiation of $\lambda=193$ nm, one electron is ejected from Xe by two-photon ionization and a second electron by a four-photon process. In fact the first (two-photon) process falls within the autoionizing region between the $P_{3/2}$ and $P_{1/2}$ thresholds. It is at this type of process that we are aiming at first with the undertaking of the calculations reported in this paper. The only other calculations in rare gases, except He, that we are aware of, are those of Pindzola and Kelly¹ dealing with many-body theory of 2-photon ionization of Ar and of McGuire² dealing with 2- and 3-photon ionization of rare gases using a Green's function based on a single-electron model. To deal with the autoionizing region, however, we must include the channel couplings which cause the wave-function to depart substantially from the single-electron model.

As in any multiphoton calculation⁸, we need good wavefunctions and a method for performing the infinite summations over the intermediate states or equivalently the Green's function. The latter is not practical to construct if the channel couplings are to be included. The approach we have chosen is multichannel quantum defect theory (MQDT) especially in the form employed by Lu and Fano in the analysis of photoabsorption in Xe. The summation over intermediate states is performed by truncating the sum to a finite number of terms. By employing MQDT, we can account for the channel couplings, thus obtaining relatively accurate matrix elements. Truncation is the price we pay which, however, is expected to be not too serious an approximation since none of the calculations we report fall within a deep minimum where the complete summation becomes essential. In any case, it is with trial and

[†]Also, Department of Physics, University and Research Center of Crete, Iraklion, Crete, Greece

Work supported by NSF Grants PHY-8306263 and PHY-8119010.

error that the level of accuracy is ultimately assessed in such complex calculations.

This is not the place to review MQDT, summaries of which abound in the literature³. For Xe, far from the ionic core, the excited electron channels are described by *jj* coupling. But these asymptotic channel states $|i\rangle$ are not eigenstates of the electron ion system at small distances. In that region, close coupling eigenchannels $|\alpha\rangle$ are defined which are appropriate to the short-range interaction. Two asymptotic channel states $|i\rangle$ and $|j\rangle$ are connected through the $|\alpha\rangle$ - states and this connection is expressed through the scattering matrix S_{ij} which can be written in terms of diagonal matrix elements $\exp(2i\pi\mu_\alpha)$ as

$$S_{ij} = \sum_{\alpha} U_{i\alpha} \exp(2i\pi\mu_\alpha) U_{\alpha j}^{\dagger} \quad (1)$$

The $U_{i\alpha}$'s form the so-called frame transformation matrix and the μ_α 's are the eigenphase shifts of the scattering eigenstates $|\alpha\rangle$. In a heavy atom like Xe, where the spin orbit interaction is strong, the main contribution to $U_{i\alpha}$ comes from the (LS/*jj*) transformation coefficients. The spin-orbit interaction in Xe gives rise to two ionization thresholds $I_{3/2}$ and $I_{1/2}$ labelled by the *j* of the residual ion which is either $P_{3/2}$ or $P_{1/2}$, respectively, with $I_{3/2}$ being energetically lower. In the MQDT formalism, the final state of the excited electron plus ion system can be written in terms of known functions, if the parameters $U_{i\alpha}$, μ_α , $I_{3/2}$ and $I_{1/2}$ are known. They can be determined from experimentally obtained spectroscopic data or, in principle, by *ab initio* calculations. In this paper, the parameters are obtained from experimental information through the Lu-Fano¹⁰ plots or extrapolations thereof.

The final electron state is expanded in terms of the usual angular momentum partial waves with somewhat different expressions being necessary inside the autoionizing region (extending from 12.20 eV to 13.45...eV) and outside where all continuum channels are open. In the open region, the expression for the total (angle-integrated) transition probability is given by

$$\begin{aligned} \int_{\Omega} M_{fg}^{(N)}(\theta) d\Omega = (4\pi)^2 \sum_i \left| \sum_{\alpha} D_{\alpha}^{(N)} e^{-i\pi\mu_{\alpha}} U_{\alpha i}^{\dagger} \right|^2 [J_c = 3/2] + \\ + (4\pi)^2 \sum_i \left| \sum_{\alpha} D_{\alpha}^{(N)} e^{-i\pi\mu_{\alpha}} U_{\alpha i}^{\dagger} \right|^2 [J_c = 1/2] \end{aligned} \quad (2)$$

where $D_{\alpha}^{(N)} = \langle \alpha | r^{(N)} | g \rangle$ is an *N*th order dipole matrix element connecting the ground state with the channel states $|\alpha\rangle$ which obey $\langle \alpha | i \rangle = U_{\alpha i}^{\dagger}$. The incoherent summation over core final states *J* is included under the assumption that only the electron is observed. Simultaneous observation of the ion state corresponds to only one of the terms in Eq. (2).

For the expressions inside the autoionizing region, we need a third set of channel states $\psi_p(r)$ which behave as open channels for large *r* but have bound character for small *r*. This set of wavefunctions introduces another set of transformation coefficients $\langle p | \alpha \rangle = A_{\alpha} / N_p$ where N_p is a normalization factor (containing most of the energy dependence) and the coefficients A_{α} satisfy the relations

$$\sum_{\alpha} U_{i\alpha} \sin(\mu_{\alpha} - \tau_p) A_{\alpha} = 0 \quad (3)$$

for all i with π_i being the eigenphase shifts of the collision eigenfunction ψ_ρ . The total phase shift is $\delta_{\rho(l)} = \eta_l + \pi_i$ where μ_l is the Coulomb phase shift of the l th partial wave. In the calculation of the total transition probability, the sums over ρ, i, α and partial waves l contribute coherently. The final expression has the form

$$\int |M_{fg}^{(N)}(\theta)|^2 d\Omega_{\vec{k}} = (4\pi)^2 \sum_{\rho} \left| \sum_{\alpha, l} D_{\alpha(l)}^{(N)} \frac{A_{\alpha}}{N_{\rho}} \right|^2 \quad (4)$$

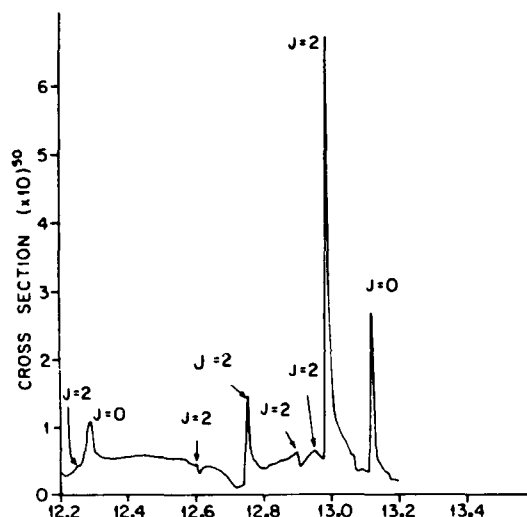


FIGURE 1.

Two photon autoionizing cross section. Total cross section in units of $\text{cm}^2 \text{sec}$ is plotted against total energy in eV. The various peaks have been identified with various angular momenta (J) channels as shown in the figure.

The generalized cross section (gcs) $\hat{\sigma}_N$ is expressed* in terms of $\int |M(\theta)|^2 d\Omega_{\vec{k}}$ multiplied by the appropriate constants and the N th power of the photon frequency. The photoelectron angular distribution is proportional to $|M(\theta)|^2$.

A sample of our results is shown in Figs. 1-3. The first two figures summarize the structure of the two- and three-photon ionization gcs inside the autoionization region. The background in both cases is of a magnitude typical for the respective order without the deep minima found in single-electron atoms. In 3-photon ionization, for example, the deep minima can be as low as $10^{-33} \text{ cm}^2 \text{sec}^2$ while the background in Fig. 2 is about three orders of magnitude larger. The main reason for the absence of deep minima is the relatively large number of contributing channels whose interference

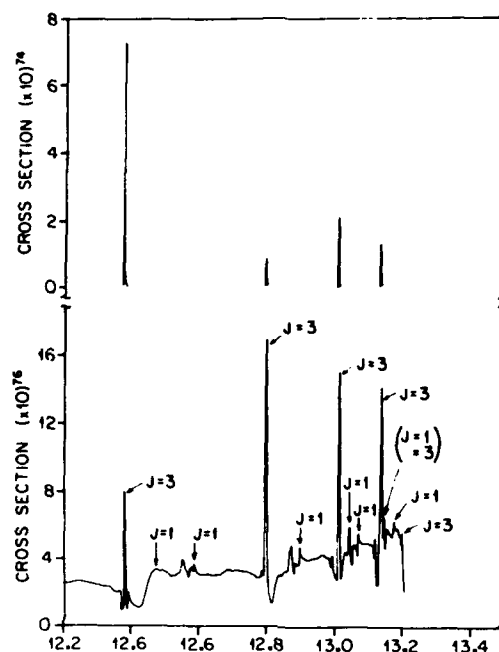


FIGURE 2.

Three photon autoionizing cross section. Total cross section in units of $\text{cm}^6 \text{sec}^2$ is plotted against total energy in eV. The various peaks have been identified with various angular momenta (J) channels as shown in the figure.

smooths out the deep minima. The peaks represent autoionizing resonances and correspond to energies at which π_f changes by π . Each peak is characterized by a total angular momentum J . Only the $J=1$ peaks of Fig. 2 could have been observed in single-photon UV photoionization experiments. It appears that the $J=1$ peaks at around 12.5 eV and 12.9 eV correspond to those observed by Heinzmann¹¹. Their line-shape, however, is not identical to that observed by Heinzmann. There is in fact no strict requirement for a $J=1$ autoionizing peak reached by a 3-photon process to have the same line-shape it has in a single-photon process; even without taking into account laser intensity effects which can cause distortion of a different nature¹². Effects of this type are not included in Figs. 1 and 2. All peaks of Fig. 1 and the $J=3$ peaks of Fig. 2 represent new predictions as they could not have been seen in single-photon processes. Above the autoionizing region, the gcs for both 2- and 3-photon ionization, has the expected smooth character with peaks appearing when the photon frequency is in resonance with intermediate bound atomic states.

In Fig. 3 we show four examples of photoelectron angular distributions corresponding to energies of selected autoionizing peaks. Each of these

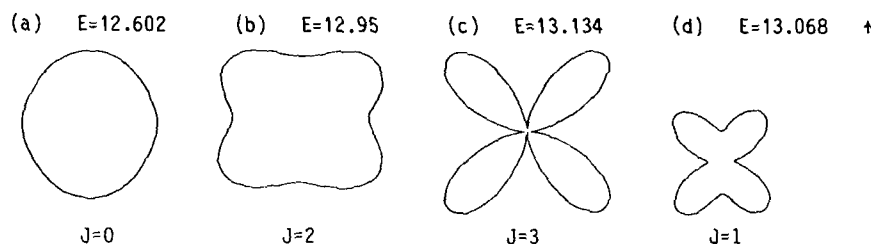


FIGURE 3.

Angular distribution of the outgoing electron at peaks (a) and (b) correspond to 2-photon Xe autoionizing angular distributions. (c) and (d) correspond to 3-photon Xe autoionization. The direction of light polarization is shown by the arrow.

distributions corresponds to a peak with a different J . We find that the main features of the distributions are determined by the order of the process (as expected) and by J . In all of these examples, the distributions exhibit a rather unusual form which is not typical of distributions for the same order in other atoms. Thus the 2-photon ionization distributions show an unusually large isotropic component while the 3-photon distributions exhibit unusually large anisotropy. In the open continuum, the distributions tend to be more typical, although they still retain a rather unusual blend of anisotropy. Overall, it is clear that the distributions are fairly sensitive to the channel couplings and as such provide a sensitive probe of the model.

The results of this and related work, whose details will be published elsewhere, implies that multiphoton multiple ionization under intensities above 10^{13} W/cm² occurs through successive stripping of electrons during the rise of the pulse¹³.

REFERENCES

- 1) M. S. Pindzola and H. P. Kelly, Phys. Rev. A **11**, 1543 (1975).
- 2) E. J. McGuire, Phys. Rev. A **24**, 835 (1981).
- 3) P. Agostini, M. Clement, F. Fabre and G. Petite, J. Phys. B **14**, L491 (1981).
- 4) P. Kruit, H. G. Muller, J. Kimman and M. J. van der Wiel, J. Phys. B **16**, 937 (1983).
- 5) R. Hippler, H. J. Humpert, H. Schwier, S. Jetzke and H. O. Lutz, J. Phys. B **16**, L713 (1983).
- 6) T. S. Luk, H. Pummer, K. Boyer, M. Shakidi, H. Egger and C. K. Rhodes, Phys. Rev. Lett. **51**, 110 (1983).
- 7) A. L'Huillier, L.-A. Lompre, G. Mainfray and C. Manus, Phys. Rev. Lett. **48**, 1814 (1982); also Phys. Rev. A **27**, 2503 (1983).
- 8) P. Lambropoulos, Adv. At. Mol. Phys. **12**, 87 (1976).
- 9) U. Fano, J. Opt. Soc. Am. **65**, 979 (1975).
- 10) K. T. Lu, Phys. Rev. A **4**, 579 (1971).
- 11) U. Heinzmann, J. Phys. B **13**, 4353 (1980); also J. Phys. B **13**, 4367 (1980).
- 12) Y. S. Kim and P. Lambropoulos, Phys. Rev. A **29**, 3159 (1984).
- 13) P. Lambropoulos, submitted to Phys. Rev. Lett.

TWO PHOTON IONIZATION OF METASTABLE HELIUM

Hellmut HABERLAND, Jens HÖHNE, Michael OSCHWALD

Fakultät für Physik, Universität Freiburg, D 7800 Freiburg, Germany
and

John BROAD

Fakultät für Chemie, Universität Bielefeld, D 4800 Bielefeld, Germany

Two photon ionization of $\text{He}(2^1\text{S})$ and $\text{He}(2^3\text{S})$ has been measured using a pulsed dye-laser. A simple theory can account for most of the observed experimental features.

1. INTRODUCTION

Two photon ionisation of metastable helium atoms ($\text{He}(1s2s, 2^1\text{S}$ and $2^3\text{S})$) has been studied with a pulsed dye laser. Ionisation via the 3P (dipole) and 3D (quadrupole) resonances in $\text{He}(2^1\text{S})$ and $\text{He}(2^3\text{S})$ has been measured. The energy levels and pumping schemes are shown schematically in Fig. 1. Several noteworthy features are observed:

- 1) The dipole allowed $2^1_{1/2}\text{S} \rightarrow 3^1_{1/2}\text{P} \rightarrow \text{K}$ resonances are very broad, up to 10 Å for the highest intensities used. K denotes a continuum state.
- 2) The peak shape of the $2^1_{1/2}\text{S} \rightarrow 3^1_{1/2}\text{P} \rightarrow \text{K}$ transition depends strongly on the pulse shape of the dye laser.
- 3) A high and flat background is observed away from the resonance.
- 4) The dipole forbidden, but quadrupole allowed resonances $2^1_{1/2}\text{S} \rightarrow 3^1_{3/2}\text{D} \rightarrow \text{K}$ have nearly the same intensities as the dipole allowed ones at resonance, but are much narrower.
- 5) For the triplet system some results (peak shape, structure on the red side of dipole resonance) are not understood presently.

Some related experiments have been performed earlier. The first experiments on this system have been performed by a group¹⁾ at Rice University. Their experimental set-up is similar to ours, only the laser intensity was about 3 orders of magnitude lower. The Saclay group²⁾ crossed a powerful Ruby laser with a He^* beam and measured total cross sections. The experiments of the Moscow³⁾ and the Bell Labs group⁴⁾ were performed with gas discharges.

2. APPARATUS

The experimental set-up is shown schematically in Fig. 2. A beam of metastable He atoms (He^*) is produced in a gas discharge source. The intensity of the He^* flux as measured by secondary electron emission is about $10^{14} \text{ s}^{-1} \text{ sr}^{-1}$ resulting in a He^* density of 10^6 cm^{-3} or about 10^{-10} Torr in the ionisation volume. The background pressure is four orders of magnitude higher. About 10% of the metastables are in the singlet state. The mean distance between the He^* atoms is about 0.1 mm. They are ionised by photons from an excimer laser pumped dye laser. Two different dye lasers are used, each consisting of an oscillator and two amplifier stages. Unless otherwise stated all data have been taken with a Lambda Physik FL2002 dye laser, which has a bandwidth of 0.2 to 0.3 cm^{-1} and delivers energies up to several tens of mJ/pulse. An energy of

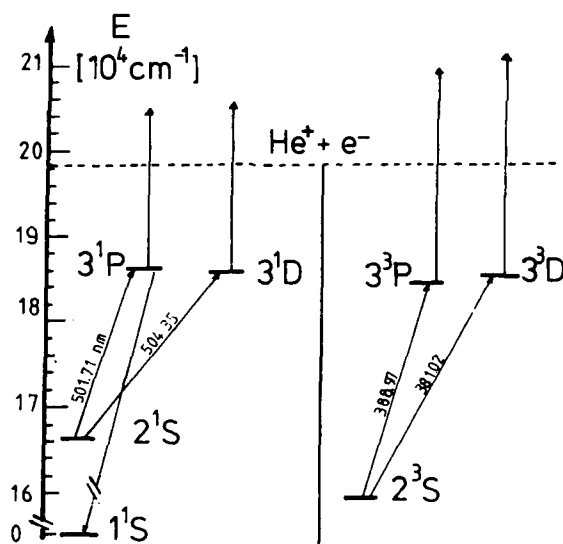


FIGURE 1

He energy levels and pumping schemes. The wavelength of the resonant transitions are given in nanometers.

1 mJ per pulse gives a power density of about 7 MW/cm^2 for an unfocused beam and 1.5 GW/cm^2 in the waist of the focus region for the lens used ($f=6 \text{ cm}$). The resulting He^+ ions are extracted by a static electric field and mass selected via time-of-flight in order to discriminate against background.

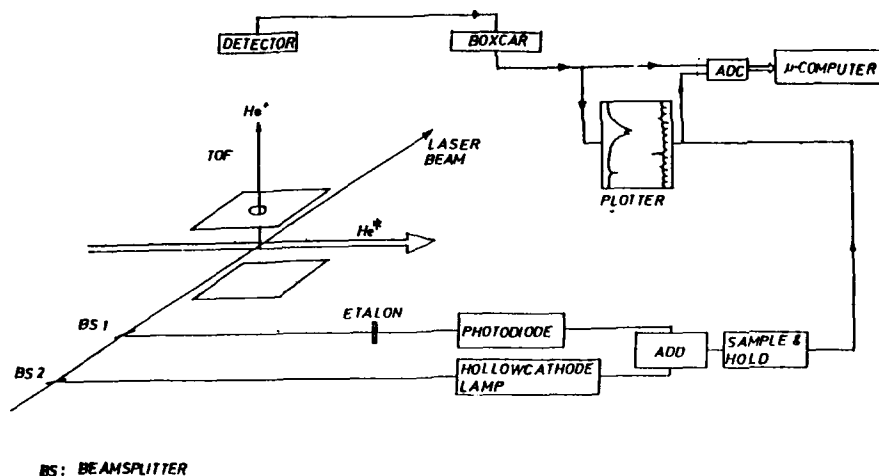


FIGURE 2

Experimental set-up. The total ion signal is measured as a function of the laser frequency and laser flux.

3. EXPERIMENTAL RESULTS FOR SINGLET He^*

The total ion signal is shown in Fig.3 as a function of the laser frequency, for a focused laser energy of 1mJ/pulse. The broad resonance is due to the $2^1\text{S} \rightarrow 3^1\text{P}$ resonance (501.71 nm) in the first step in the ionization process. The sharp peak at 504.35 nm results from the corresponding quadrupole transition. The results shown in Fig.4 were obtained for the same system, but with a different dye laser: homebuilt, Littman type, bandwidth 0.6 cm^{-1} , 70% linear polarization, cavity length a factor 2.5 shorter, higher ASE (amplified spontaneous emission) background. The line shapes of the two dipole resonances differ somewhat, but what is unexpected, is that a dip occurs in only one of the measurements. It is probable that this is due to the different temporal behaviour of the two dye laser pulses, as discussed below.

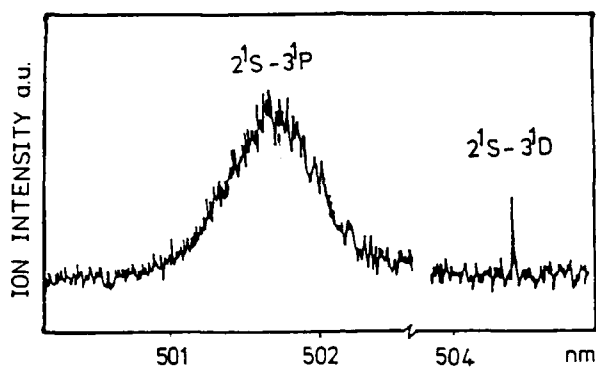


FIGURE 3

Two photon ionization of $\text{He}(2^1\text{S})$ at a focused laser power of 1mJ/pulse using the Lambda Physik dye laser.

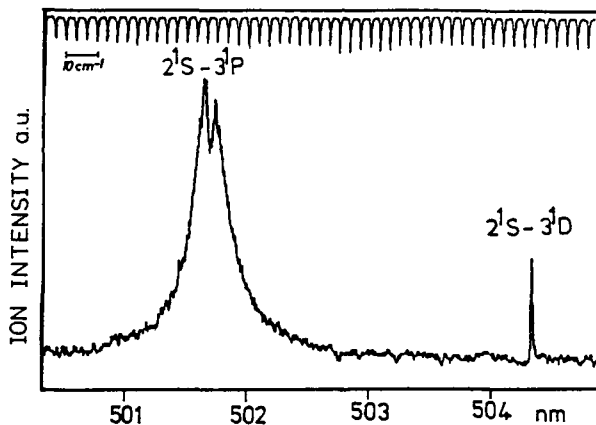


FIGURE 4

The same experimental situation as in Fig.3, but for the homebuilt laser. Note the difference in the wavelength scale. The better signal to noise ratio compared to Fig.3 was due to a higher He^* intensity.

4. DISCUSSION OF THE SINGLET RESULTS

The relevant levels and transition rates are shown in Fig.5. The metastable 2^1S level is pumped to the 3^1P level with the rate Γ_P , whose value is given in the table for 3 different intensity levels. There are four different decay channels for the P state as listed below, only the first two being field dependent:

- 1) induced transitions back to the 2^1S state leading to Rabi oscillations (up to 10^4 during the pulse duration of 5ns),
- 2) ionizing transitions to the continuum,
- 3) spontaneous decays back to the metastable state,
- 4) spontaneous decays to the ground state.

The direct two photon ionization of 2^1S can be neglected. Note that the ionization rate is always about 4 orders of magnitude smaller than the Rabi frequency. For low to medium fluxes it is also smaller than the inverse pulse width. The loss rate to the ground state, which is responsible for the dip on the resonance of Fig.4, is larger the ionization rate for fluxes less than 20 MW/cm^2 . The relative importance of the rates changes during the laser pulse.

	1 GW/cm^2	10 MW/cm^2	0.1 MW/cm^2
Γ_R	67 THz	670 GHz	6.7 GHz
$\bar{\Gamma}_R$	67 THz	670 GHz	6.7 GHz
Γ_I	25 GHz	250 MHz	2.5 MHz
γ_1	13 MHz		
γ_2	566 MHz		

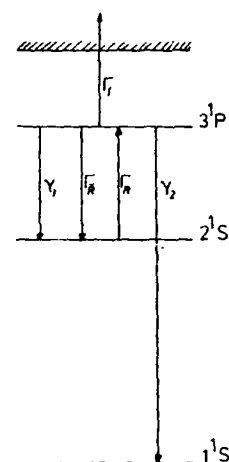


FIGURE 5

Atoms in the 2^1S state are pumped by laser radiation to the 3^1P state with the rate Γ_R as given in the table. The 3^1P state can decay via four different channels, two of them being field dependent. Numerical values for the rates for three different laser fluxes. Note that the inverse pulse width of the laser pulse is 200 MHz, comparable with some of the rates.

A simple theoretical model has been developed to account for the experimental data⁵. Calculations for this system have been performed earlier by two groups^{6,7}. Briefly two dressed states coupled to one ionization continuum are treated. Their propagation is calculated using the time independent Floquet Hamiltonian⁸. An average over the Rabi frequencies is performed, the result is integrated over photoelectron energies, and the experimental arrangement is modeled closely. Especially the inhomogeneous laser field distribution is taken into account. The calculated ion signal reproduces the salient features of the experimental signal. Fig.6 shows the calculated ion signal for a focused laser pulse having a Gaussian time distribution of 5ns length. The pronounced deep dip on the resonance is decreasing for steeper rise times and is absent for a nearly rectangular pulse. The following interpretation results:

- 1) The dips in Fig.4 and 6 are due to loss of the atoms by spontaneous emission to the ground state, which occurs during pulse turn-on, when the width of the dressed intermediate state is still narrow.
- 2) The broad, flat background comes from the intensity maximum of the laser pulse, where this width is large.
- 3) Much of the signal near the resonance maximum does not come from the region of maximum laser intensity, but from the wings. The moderate intensity there requires small detuning, but the number of atoms is large. This delicate structure occurs

because the pulse length and spontaneous emission time are comparable with the time needed to ionize. We have so far no definite experimental proof that the dips in fig.4+6 are due to the different time dependence of the light pulses from the two different dye lasers. But this is very plausible according to the theoretical calculations. The mean width of both light pulses is the same and also their rise-time, as measured by a fast photodiode. But if the pulse of the homebuilt laser would have a small foot ($\approx 10^{-4}$ of the peak intensity), this would be sufficient to produce the dip.

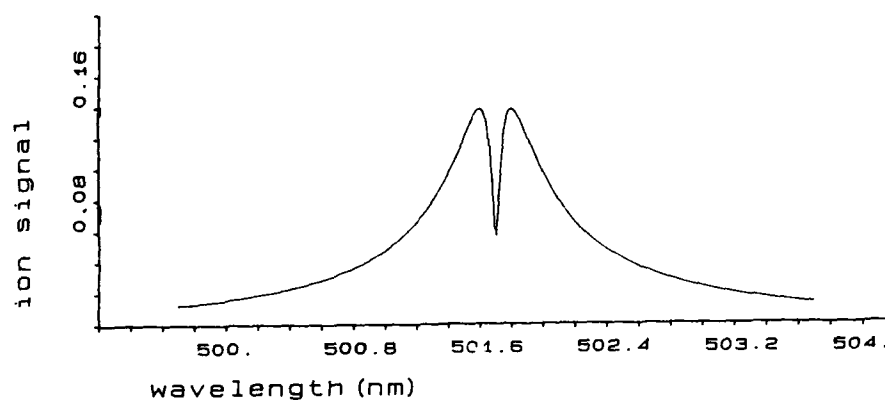


FIGURE 6

Calculated signal for the experimental situation of Fig.3 and 4, assuming a Gaussian pulse width of 5ns. For steeper rise times the dip on the dipole resonance becomes smaller and vanishes for a near sudden turn-on of the laser pulse.

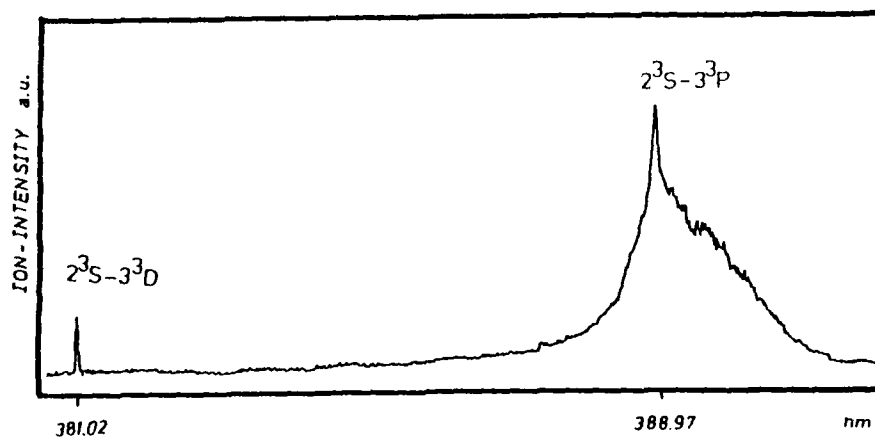


FIGURE 7

Two photon ionization of $\text{He}(2^3\text{S})$ at 1.6mJ/pulse focused laser radiation. The broad structure on the red side of the resonance changes for an unfocused beam, comp.Fig.8.

5. EXPERIMENTAL RESULTS FOR TRIPLET He*

The dipole resonance 2^3S-3^3P appearing at 388.97nm is again very broad. The resonance peak is asymmetric with a long tail to the red, even at laser intensities of 0.02mJ/pulse (30MW/cm²). A Stark effect would shift the resonance and due to the spatial distribution of the laser field intensity in the focus region would give an asymmetric line shape. A calculation by Aymar and Crance⁷ predict a dynamic polarizability that would shift the resonance to the blue. Their results cannot explain our asymmetry via an AC-shift. With unfocused laser, i.e. 5MW/cm², the asymmetry vanishes, but then there is a structured background over which the resonance peak appears. The structure on the red side of the resonance peak exceeds the signal to noise ratio. No known molecular transitions correspond to these peaks. Also no signal has been observed on mass 8, so that transitions in He₂ are improbable. It seems as if this structure is correlated with the asymmetry of the resonance peak at high laser intensities. The lineshape of the 2^3S-3^3D quadrupole resonance at 381.01nm is determined again by the bandwidth of the laser. The intensity dependence of the quadrupole resonance is less than linear, indicating saturation effects.

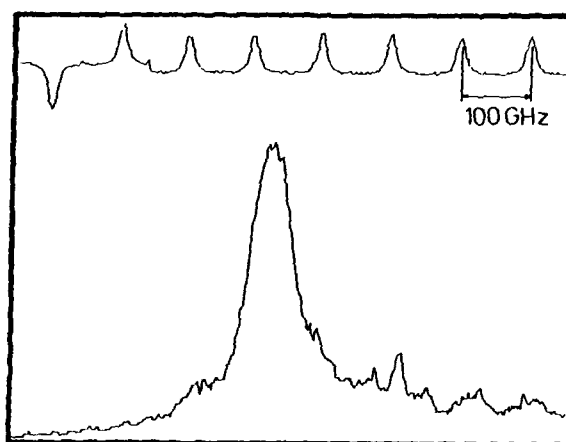


FIGURE 8

Same as Fig. 7 but with unfocused beam (about 5MW/cm²). The reproducible structure on the red side of the dipole resonance is not understood presently.

REFERENCES

- 1) F. B. Dunning and R. F. Stebbings, Phys. Rev. Lett. 32 (1974) 1286
- 2) L.-A. Lompre, G. Mainfrej, B. Mathieu, G. Watel, M. Aymar, and M. Crance, J. Phys. B: Atom. Molec. Phys. 13 (1980) 1799
- 3) J. Bakos, N. B. DeLone, A. Kiss, N. L. Mankov, and M. L. Nagaeva, Sov. Phys. JETP 44 (1976) 168
- 4) R. Panock, R. R. Freeman, J. C. White, and R. H. Storz, Opt. Lett. 5 (1980) 16
- 5) J. Broad, Fakultät für Chemie, Bielefeld, to be published
- 6) K. C. Mathur and R. K. Sharma, IEEE QE 14 (1978) 771
- 7) M. Aymar and M. Crance, J. Phys. B: Atom. Molec. Phys. 13 (1980) 2527
- 8) A. Maquet, Shin-I Chu and W. P. Reinhardt, Phys. Rev. A27 (1983) 2946

THE HIGHLY EXCITED HYDROGEN ATOM IN STRONG MAGNETIC FIELDS

K.H. WELGE and A. HOLLE

Fakultät für Physik, Universität Bielefeld, D4800 Bielefeld 1, F.R.G.

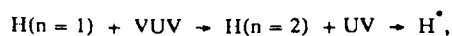
1. INTRODUCTION

In the physics of highly excited atoms in external electric and magnetic fields [1] under strong force mixing conditions [2], that is where the external forces are comparable with, or larger than the internal electronic binding forces, the hydrogen atom with its purely Coulombic field plays naturally a fundamental role. While the non-relativistic H atom in homogeneous static electric fields may be considered a solved problem [3], the situation is basically different for the atom in magnetic fields with dominant diamagnetic interaction [4]. The Schrödinger equation even with the Hamiltonian in the simplest form, $H = -1/r + 1/8a^2B^2r^2 \sin^2 \Theta$ is not separable, and there apparently exists no quantitative theory for the diamagnetism of the atom in the high n-mixing and quasi-Landau regime. Also, no experiments are known with H around the ionization limit, or even in the lower L- and n-mixing regimes, except most recent ones carried out in our laboratory [5].

In this paper we report some of the results of our work. Since only a fraction of the work can be covered here, we concentrate on a few new observations in the quasi-Landau regime, which is the most interesting and challenging one, theoretically as well as experimentally. For more complete information we must refer to publications soon forthcoming.

2. EXPERIMENTAL

Like in our experiments with the H atom in electric fields [3], the excitation was performed in two steps,



with pulsed ($\sim 10\text{ns}$, 10Hz) tunable laser radiation in the VUV around 121.6nm and in the uv. A crossed laser-atomic beam configuration (Figure 1) was used, in which the atomic and two laser beams are perpendicular to each other and the atomic beam parallel to the magnetic field. The electric field arrangement served to field ionize H^* atoms and to extract electrons from the excitation zone for detection by a surface barrier detector. Excitation-ionization spectra have been obtained by keeping the VUV fixed in resonance with the first excitation step and recording signals as function of the UV wavelength in increments of typically 0.1cm^{-1} . The resolution in the second-step excitation was 0.3cm^{-1} , mostly given by the UV laser bandwidth

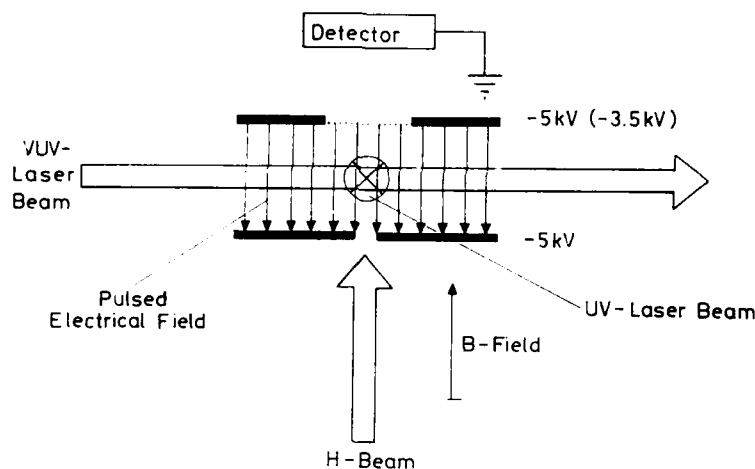


Figure 1: Scheme of experimental setup.

and to a smaller degree by the residual Doppler width perpendicular to the atomic beam.

Depending on which energy range of H^* atoms was to be investigated, two different experimental procedures have been employed. At low excitation energies, i.e., $E \lesssim 20\text{cm}^{-1}$ H^* atoms have been detected through field ionization by applying electric fields of KV/cm strength in pulsed fashion, after the laser excitation. At energies $E \gtrsim 20\text{cm}^{-1}$ a weak constant electric field ($\sim 1\text{ V/cm}$) was continuously on also during the excitation. However, while this

field was strong enough to extract electrons from the excitation zone and also for field ionization down to about -20cm^{-1} , it was still sufficiently weak so that the Stark interaction by the electric field was small compared to the diamagnetic interaction. In this paper we are not concerned with the experiments by the first mode of operation, that is at low energies in the Z- and n-mixing regime.

3. RESULTS

According to the constants of motion for the diamagnetic interaction in a static homogeneous field, i.e. the energy, parity and z-component of the angular momentum in the final state, the excitation must be performed state selectively with respect to the magnetic

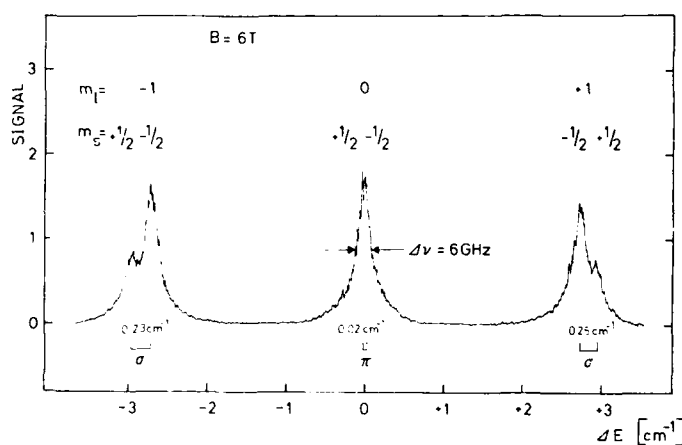


Figure 2: Paschen-Back splitting of $H(n=1) \rightarrow H(n=2)$ transition with linearly polarized VUV laser radiation at about 45° to the B-field. Field Strength $B=6\text{T}$.

quantum number m_l in all steps. At field strengths applied in these experiments the first-step transition, $H(n=1) \rightarrow H(n=2)$, is governed by the Paschen-Back splitting with the three m_l states $|m_l = 0, \pm 1\rangle$ in $n=2$ (Figure 2). Each of these states was individually excited by employing linearly polarized VUV radiation, either parallel (π) or perpendicular (σ) to the B-field, with a resolution of $\sim 6\text{GHz}$. Starting from these initial states, three different types of final states with $m_l = 0 \pm 1, \pm 2$ could be reached employing the UV radiation also either

π or σ polarized. Examples of transitions are:

$|m_f^i = 0\rangle \xrightarrow{\pi} |m_f^f = 0\rangle$, $|m_f^i = +1\rangle \xrightarrow{\pi} |m_f^f = +1\rangle$, and

$|m_f^i = +1\rangle \xrightarrow{\sigma} |m_f^f = +2\rangle$. Because of the relative orientation of the UV beam and B-field directions, the σ excitation allows both $\Delta m = \pm 1$ transitions. This means that in the third case also $|m_f^f = 0\rangle$ states are excited. However the transition to $|m_f^f = 0\rangle$ is less probable than $|m_f^f = +2\rangle$ by an order of magnitude. We have observed all three kinds of final state spectra of $m_f^f = 0, \pm 1, \pm 2$ and even parity.

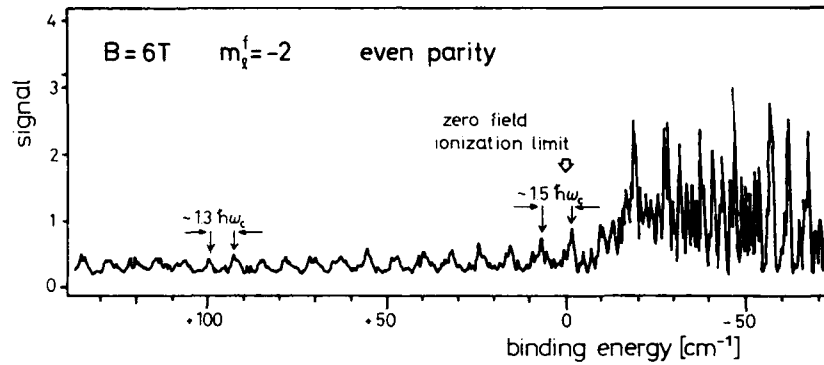


Figure 3: Excitation-ionization spectrum of the H atom previously taken [5] at low resolution ($\sim 2\text{cm}^{-1}$). Excitation of final states $|m_f^f = -2\rangle$ from $|n = 2, m_f^i = -1\rangle$ with σ polarized UV radiation. Magnetic field strength $B=6\text{T}$.

Figure 3 shows a first example of a spectrum with $|m_f^f = -2\rangle$ (with a small admixture of $|m_f^f = 0\rangle$) at $B=6\text{T}$, previously obtained [3]. It clearly exhibits quasi-Landau resonance structures. As to be expected from theory [1,2,6], their energy spacing is $1.5 \times \hbar\omega_c$ at $E = 0$, decreasing with increasing excitation energy. Figure 4 shows spectra obtained more recently with improved signal quality and higher resolution (0.3cm^{-1}). The measured spectra (light line) exhibit line structure of the quasi-Landau resonances, observed here for the first time with the H atom. The width of the sharpest features at $E \geq 0$ corresponds to the experimental resolution limit of 0.3cm^{-1} , which indicates actual ionization lifetimes of these states of $\geq 10^{-11}$ s.

The solid line curves are the result of averaging the measured spectra by a Gaussian line shape with a bandwidth of 2cm^{-1} FWHM. In the spectra with $m_f^f = 0$ and $m_f^f = +2$ this yields

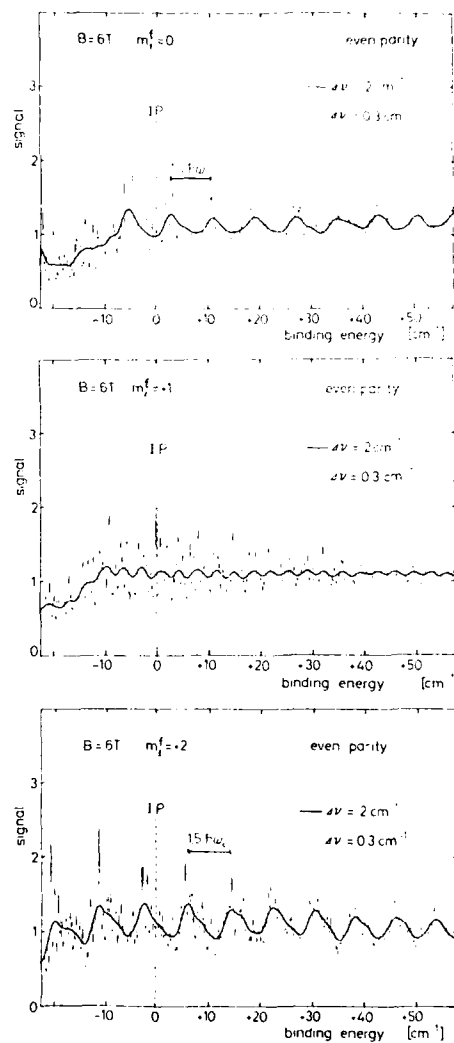


Figure 4: Excitation-ionization spectra of the H atom with final states $|m_f^f = 0\rangle$, $|m_f^f = +1\rangle$, $|m_f^f = +2\rangle$ at B-6T. Light line: measured spectra taken with 0.3cm^{-1} resolution. Heavy line: light line spectra averaged with 2cm^{-1} bandwidth (see text).

smooth quasi-Landau oscillations with a periodicity of $1.5 \times \hbar\omega_c$ at $E=0$. Quite unexpectedly, however, in the $m_l = +1$ averaged spectrum oscillations are observed with a $\sim 0.64 \times \hbar\omega_c$ periodicity at $E = 0$ instead.

According to the WKB [2] and time-dependent wavepacket [6] treatments resonances with the "normal" periodicity of $1.5 \times \hbar\omega_c$ are expected when the electronic motion is confined to the $z=0$ plane, i.e. perpendicular to the magnetic field. This is an appropriate approximation for electrons initially excited to the $|m_l = +2\rangle$ since the wavefunction is localized oriented in the $(z=0, x-y)$ plane with a node in the z -direction. This is similarly true also for $|m_l = 0\rangle$ states where some part of the wavefunction is in the $(z=0, x-y)$ plane. The $|m_l = +1\rangle$ state wavefunction however is conically distributed with an angle of 45° to the z -axis, and has nodes along z and in the $(z=0, x-y)$ plane. Using the time-dependent wavepacket concept [6], the recurrence time, or the corresponding period of oscillation of an $|m_l = +1\rangle$ electron is evidently different from that of electrons bound in the $(z=0, x-y)$ plane by a factor $1.5/0.64$. As of now, no theory is available that accounts quantitatively for this observation, though the WKB method may be adapted to motions of electrons initially excited to states at angles different from 90° to the z axis. Even more open is the theoretical treatment of the fine structure of quasi-Landau states observed in these experiments.

REFERENCES

- [1] The field of highly excited atoms in strong external fields has been extensively reviewed. For references see ref. [5].
- [2] A.R.P. Rau, J. Phys. **B12**, L193 (1979); A.R.P. Rau and K.T. Lu, Phys. Rev. **A21**, 1057 (1980).
- [3] See for example H. Rottke and K.H. Welge, Phys. Rev. A, in press (1985).
- [4] D. Kleppner, M.G. Littman, and M.L. Zimmerman, in "Rydberg States of Atoms and Molecules", ed. R.F. Stebbings and F.B. Dunning; Cambridge Univ. Press (1983).
- [5] A. Holle, H. Rottke, and K.H. Welge, "Lecture Notes in Physics," Vol. 229, "Fundamentals of Laser Interaction", ed. F. Ehlotzky, Springer-Verlag (1985); A. Holle and K.H. Welge, Conf. Proceedings of the "Seventh Intl. Conf. Laser Spectroscopy", Hawaii, Springer-Verlag (1985).
- [6.] W.P. Reinhardt, J. Phys. **B16**, L635 (1983).

STATE SELECTIVE LASER DETECTION OF RYDBERG ATOMS

Wolfgang SANDNER

Fak. für Physik, Universität Freiburg, D7800 Freiburg, West Germany

1. INTRODUCTION

One of the main reasons for the recent advances in the field of Rydberg atoms is the experimentalists' ability to excite single high lying states of atoms with tunable dye lasers. The necessity for a spectrally narrow excitation light source becomes immediately obvious if we consider the decreasing energy spacing between neighbouring Rydberg states for increasing principal quantum number n . We find, for n around 50, that the excitation light source must have a resolution $\Delta E/E \approx 4 \times 10^{-5}$, if we assume a typical excitation energy of about 5 eV. This is an easy task for lasers, while it is not for other excitation mechanisms.

At the same time it appears to be true that there is still a considerable demand for an efficient *detection* method for atoms in high Rydberg states, which allows to distinguish between single n states. So far, people have usually resorted to electric field ionization, in spite of the fact that ionization of single Rydberg states in an increasing electric field displays a multiple threshold behaviour. While it is well predictable (1) this behaviour makes it difficult or even impossible to unravel the field ionization signal from a dense mixture of states once n considerably exceeds values around $n \approx 30$.

Experiments which suffer most from this dispair in quality between excitation and detection mechanisms are collision experiments with Rydberg atoms. Whether it be state changing collisions between high Rydberg states, or collisions which produce Rydberg atoms in their final state (like dielectronic or radiative recombination), they all require a highly selective and efficient detection method in order to focus on the dynamics of the collision itself. Hereby the restriction to $n \leq 30$ is a remarkable one if we only think of "natural" Rydberg atoms in astrophysics, where creation and collisional redistribution typically takes place around $n \approx 100$, or even higher (2).

2. STATE SELECTIVE DETECTION BY OFF RESONANT CORE EXCITATION: THE RYDBERG FILTER

2.1 Basic principles of operation

In the following, we present a laser based detection method for Rydberg atoms which has already shown to be state selective at $n \geq 30$, and which is anticipated to work well beyond $n = 100$, provided the right lasers are used. The method requires a strong *core transition* to be present in the Rydberg atom, which can be driven by tunable, narrowband dye lasers.

It is well known that after a core transition the whole system contains enough energy to autoionize, which is usually a very rapid process and by far dominates the radiative decay back to the ground state of the core. As a consequence one can, for any nonvanishing core excitation cross section, always ionize *all* Rydberg atoms with near 100% efficiency, if only the product of core excitation cross section and laser photon flux is kept sufficiently large (3,4). Hence we are left with charged fragments, autoionization electrons and ions, either of which may conveniently be detected to witness the past existence of the Rydberg atoms. While this detection method is very efficient, it is not yet state selective. The average spatial separation between the Rydberg electron and its own core is so huge that the resonance frequency ω_0 of the core is rather

insensitive to the state or even to the presence of the Rydberg electron itself.

State selectivity comes in if we detune the laser from the exact core transition frequency ω_0 (*off resonant core excitation*). Energy conservation now requires the Rydberg electron to change its orbit, where it is no longer restricted to discrete energy values since the final state of the whole system is continuously (though not homogeneously) broadened by autoionization. The process has been described before as a dipole excitation of the core and a simultaneous monopole ("shake") transition of the Rydberg electron (3,4). The latter is simply the overlap integral $\langle \psi_{\nu_0} | \psi_{\nu} \rangle$ between the initial and final Coulomb wave function of the Rydberg electron, which are characterized by their effective quantum numbers ν_0 and ν , respectively (the effective quantum number ν is the difference between the principal quantum number n and the quantum defect μ : $\nu = n - \mu$). Orthogonality of the Coulomb wave functions forces this integral to vanish whenever ν and ν_0 differ by an integer value. In this case the off resonant core excitation and the subsequent autoionization cannot take place and, hence, the Rydberg atom remains unaffected by the laser.

We can easily show that, on the frequency scale of the core transition laser, these zero cross section points occur at frequencies $\omega(k, \nu_0)$ given by (5)

$$\omega(k, \nu_0) = \omega_0 + (R/h) \frac{k(2 + k/\nu_0)}{\nu_0^3 (1 + k/\nu_0)^2} \quad (1)$$

where k is a label counting the number of consecutive cross section zeroes, and R/h is the Rydberg frequency, $4.1341 \times 10^{16} \text{ sec}^{-1}$.

So far, several assumptions went into the derivation of equation 1. First, we have tacitly assumed that we are dealing with hydrogenic Coulomb wave functions, whose orthogonality is determined by $\nu - \nu_0 = k$ (k integer). Thereby we neglected the presence of the atomic core, where the wave function is not only strongly non-hydrogenic, but will, in general, be not the same for the ground and the excited core state. For the purpose of evaluating an overlap integral this is a good approximation, since for high n the size of the core is negligible when compared with the spatial region $r \approx n^2$ (a.u.) over which the orthogonality integral is evaluated. On the other hand, the transition from the ν scale to the laser frequency scale ω is determined by the large r properties of the potential. Here we have assumed a pure Coulomb potential without any corrections due to the core polarization in the initial and final core state, which is again a generally acceptable approximation for high Rydberg states. Finally, we have neglected the possibility of direct photoionization of the Rydberg electron by the core transition laser. This is an excellent approximation in the vicinity of the resonant core transition frequency ω_0 . However, since the off resonant core transition amplitude decreases rapidly with increasing detuning (3,4) one will eventually arrive at a point where the Rydberg photoionization can no longer be neglected, and the cross section will be influenced by interference between the two processes.

Any of the above mentioned effects yields small corrections to equation 1, which can be accounted for in a rigorous treatment, but which will be neglected for the sake of transparency in the present discussion.

Equation 1 is the basis for the state selective laser detection of Rydberg atoms since it predicts the cross section zeroes to occur at *different laser frequencies for different initial Rydberg states* ν_0 . Let us consider an ensemble of atoms in an unknown distribution of Rydberg states. We can easily measure the relative population of the particular state ν_0 by tuning a powerful, narrowband "selection laser" to any frequency given by equation 1; in particular, we may use the first "red" ($k=1$) cross section zero. The state ν_0 will not be affected by the laser, whereas all atoms in other states will eventually be core excited and autoionize. The number of remaining neutral Rydberg atoms in the state ν_0

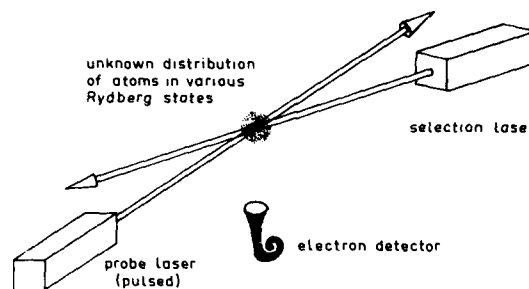


FIGURE 1
A Rydberg Filter Apparatus (schematic)

may be determined from the subsequent autoionization electron signal of a comparably weak "probe laser". This laser is tuned to the resonant core excitation frequency ω_0 and thus ionizes all remaining Rydberg atoms. The experimental setup, which has been termed a "Rydberg filter" (5), is shown on fig. 1.

2.2 Experimental results and discussion

The quality of such a filter can be demonstrated by successively preparing atoms in various Rydberg states and then exposing them to the Rydberg filter, which is tuned to one particular state, say $6s32d(^1D_2)$ in Barium. This state has a known effective quantum number $\nu_0 \approx 29.334$. As a core transition we have used the $6s \rightarrow 6p_{3/2}$ transition in Ba, occurring at $\lambda \approx 455.4$ nm. The selection laser, set to the first red zero of the $6s32d$ state, then had a wavelength $\lambda = 455.606$ nm.

The probe laser signal, normalized to the total number of Rydberg atoms prepared in each state, is shown on fig. 2. The curve shown may be identified as the "transmission curve" $T(n)$ of the filter, where we would ideally expect $T(n) = \delta_{n,32}$. For all n except $n = 41$ the actual curve deviates only slightly from the ideal one, where the deviations can be attributed to the finite bandwidth (0.3 cm^{-1}) and energy flux ($50 \mu\text{J}/\text{mm}^2$) of the selection laser, and to statistics. The agreement with a calculated transmission curve, taking into account the laser properties, is generally very good for all n .

The feature around $n = 41$ is easily explained if we consider that, for increasing n or ν_0 , the cross section zeroes move closer to the central frequency ω_0 , as can be seen from equation 1. As a consequence, the second red zero ($k=-2$) for the $n = 41$ state coincides with the first red zero of $n = 32$, leading to the small additional transmission peak in fig. 2. Such unwanted coincidences are expected to occur periodically for higher states $\nu > \nu_0$; however, they can either be neglected if only a moderate n -range is to be investigated, or eliminated through a coarse preselection of the n -range under consideration, e.g. by electric field ionization.

So far we have demonstrated that the state selective laser detection scheme works satisfactorily around $n = 32$. While this performance already compares favourably with electric field ionization, it is certainly of interest to explore the basic limitations of the new method for selective detection of much

higher states. The most obvious limitations arise from the selection laser performance. It can be shown that the selection laser bandwidth Δ_L must satisfy the approximate condition $\Delta_L \leq |6Rk\nu_0^{-4}|$, if the filter is to be operated in the k -th cross section zero of the state ν_0 . At the same time, the laser energy flux Φ_L must be adjusted according to $\Phi_L \propto \Delta_L^{-2}$ for saturation of the core transition of all other states $\nu \neq \nu_0$. By extrapolation of the experiment displayed on fig. 2 we can estimate that today's state of the art excimer or Nd:YAG pumped pulsed dye lasers allow filter operation up to $\nu_0 \approx 100$. Flash-lamp pumped dye lasers may even work at considerably higher ν_0 , due to their lower fourier-transform limited bandwidth and higher energy flux (5).

At the present time these considerations are still theoretical, but experiments are under way to explore the performance of the Rydberg filter in more detail and apply it to actual problems.

3. OTHER APPLICATIONS OF THE OFF RESONANT CORE EXCITATION

In the previous section we have investigated the possibility of preparing atoms in specific states ν_0 out of a random sample of Rydberg atoms, using off resonant core excitation. With some variations the same technique may be applied to detect other properties of Rydberg atoms with high precision, which will be outlined in the following (see also reference 5).

First, one may address the obvious question of also measuring the angular momentum quantum number ℓ of Rydberg atoms. This is by far not a trivial task for conventional detection methods, and in many cases only works if the ℓ -degeneracy is sufficiently removed as to allow conclusions about the ℓ -value by the measured energy of the Rydberg state. This is a rather unsatisfactory approach, since for $\ell \geq 3$ all Rydberg levels are practically degenerate. On the other hand, ℓ -measurement via spontaneous optical decay of Rydberg states suffers from extremely low efficiency, since Rydberg atoms are rather stable. Here it appears as if off resonant core excitation also offers an interesting alternative.

We have already made an experiment where the core transition laser was detuned so far towards high energies that the Rydberg electron had to make a monopole transition *into the continuum* ("shake off transition") in order to fulfil the energy conservation law. Since the shake off transition is still

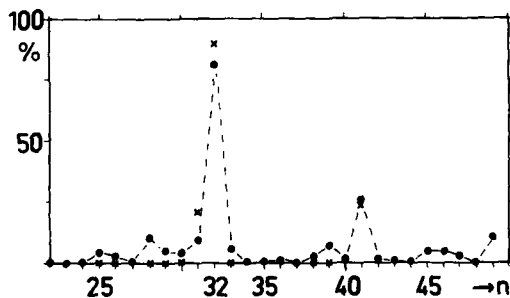


FIGURE 2
"Transmission curve" of the Rydberg filter. (●) Experiment (X) Theory

governed by the selection rule $\Delta l = 0$, such an experiment offers the possibility of measuring the initial l -value by determination of the angular distribution of shake off electrons. The difficulty of such an approach lies in the fact that the electrons tend to have rather low energies, since the shake off probability decreases rapidly with increasing detuning of the core transition laser. The preliminary data obtained so far suggest, however, that a reasonable compromise can be found between sufficient electron energy on the one hand and sufficient intensity of the other to make this method a valuable spectroscopic tool for the investigation of high Rydberg states.

As a final remark we may mention that equation 1 also provides a simple recipe to measure the effective quantum number ν_0 of a Rydberg state to a very high accuracy. One simply has to evaluate the measured pattern $\omega(k, \nu_0)$ of cross section zeroes when the laser is continuously detuned from the resonant core transition. Most accurate results are obtained if one evaluates the frequency distances between the zero cross section points and compares them with a reference etalon, thereby eliminating the need of measuring absolute laser wavelengths. Provided that all corrections to equation 1 are properly taken into account and that a sufficient number of zeroes is evaluated, one can obtain extremely accurate values for the effective quantum number ν_0 . In a first experiment, we have measured the effective quantum number of the $6s42d\ 1D^2$ state in Ba to a relative accuracy of few times in 10^{-4} , by evaluation of some 50 to 60 cross section zeroes.

There are two interesting aspects of such an approach. First, the method is insensitive to multi channel interaction effects in complicated atoms. Second, it requires no knowledge of the ionization limit of the system, in contrast to usual methods of ν_0 -determination. Hence, we may obtain accurate quantum defects for QDT analysis even in those systems where the ionization limit is only poorly known (like some open shell atoms). Moreover, we may even use the obtained ν_0 -value, together with the excitation energy $E(\nu_0)$ of the initial Rydberg state to determine the ionization energy I_0 of the atom according to Rydberg's law $E(\nu_0) = I_0 - R/\nu_0^2$. Experiments along these lines are in progress.

4. CONCLUSION

This paper focuses on the various possibilities of investigating and detecting atomic Rydberg states by off resonant core excitation. While the process itself is far from being new, we have tried to demonstrate that it may still bear some interesting aspects as a laser spectroscopic tool for the study of the initial bound Rydberg state. First experimental studies yielded some promising results along these lines.

ACKNOWLEDGEMENT

The present work has been supported by the Deutsche Forschungsgemeinschaft.

REFERENCES

- 1) F.G. Kellert, T.H. Jeys, G.B. McMillian, K.A. Smith, F.B. Dunning and R.F. Stebbings Phys. Rev. A 23 (1981) 1127.
- 2) A. Dalgarno in "Rydberg states of atoms and molecules", eds. R.F. Stebbings and F.B. Dunning, Cambridge (1983) pp. 1-30.
- 3) N.H. Tran, R. Kachru and T.F. Gallagher Phys. Rev. A 26 (1982) 3016.
- 4) S.A. Bhatti and W.E. Cooke Phys. Rev. A 28 (1983) 756.
- 5) W. Sandner, G.A. Ruff, V. Lange and U. Eichmann (submitted for publication).

PHOTODETACHMENT SPECTROSCOPY OF FeO^-

T. ANDERSEN,* K. R. LYKKE, D. M. NEUMARK and W. C. LINERBERGER

Joint Institute for Laboratory Astrophysics, University of Colorado and
National Bureau of Standards, and Department of Chemistry, University of
Colorado, Boulder, Colorado 80309 USA

High-resolution autodetachment spectroscopy of FeO^- has been used to study the ionic ground state as well as electronically excited states located in the vicinity of the $\text{FeO}(^5\Delta_4)$ thresholds. The observed autodetachment resonances suggest two qualitatively different types of electronic states in this region, a $^4\Delta$ valence state and two negative ion complexes consisting of an $\text{FeO}(^5\Delta_3)$ core and an s or p electron primarily bound by the dipolar electric field of the neutral core. The dependence of autodetachment lifetimes upon the rotational quantum numbers of the excited states shows markedly different properties for the two types of states. A significant difference in autodetachment lifetimes is observed for the two Λ -doublet components assigned to the FeO-p electron complex. We propose that a difference in the location of the electron density of the detaching electron with respect to the plane of rotation is responsible for the Λ -doublet effect.

1. INTRODUCTION

The recent observation (1) of dipole-bound excited states in the acetaldehyde enolate negative ion has opened up new possibilities for structural and dynamical studies of molecular anion systems by means of photodetachment spectroscopy. In addition to valence states, some negative ions may exhibit dipole-bound excited states where the extra electron is bound primarily by interaction with the electric dipole moment of the neutral core. Dipole-bound states are predicted (2) to exist in a number of anion systems since all molecules with dipole moments larger than approximately 2 D should be able to support dipole-bound states. These states are characterized by the small binding energy of the electron, the presence of the electron in a diffuse orbital with large radius, and by the weak perturbation of the core.

Dipole-bound states can be viewed as the next step beyond Rydberg states, since the binding is caused by an electric dipole field rather than by an electric monopole field. The orbital of the dipole-bound electron must be orthogonal to the orbitals of the core (3-5), introducing nodal structures not seen in point-charge systems. Even the existence of dipole-bound states was suggested from electron scattering by polar molecules (6,7) or from low-resolution photodetachment of highly polar negative polyatomic ions (8,9) dipole-bound states were first identified unambiguously from high-resolution photodetachment spectroscopy data last year (1,10).

To gain more insight into the properties of dipole-bound excited states it would be valuable to study a few selected diatomic systems. Such a study would not only yield information about structural properties, but would also

*1984-85 JILA Visiting Fellow. Permanent address: Institute of Physics,
University of Aarhus, Denmark.

enable some insight to the dynamics of these states. Rotational levels of dipole-bound states located energetically above the electron affinity limit may decay by autodetachment. The dynamical aspect of this process, which involves the transfer of energy from the core of the molecule to the loosely bound electron, is controlled by the coupling between rotational energy and electronic energy. This coupling mechanism is also known to play an important role in some autoionization processes (11), but rotational autoionization is often difficult to study in detail due to lack of rotationally resolved autoionization lifetimes.

In this brief report we describe some of the main results of the first study of dipole-bound states in a diatomic system, the FeO^- molecule. A more detailed description will be published elsewhere (12). In order to select diatomic systems for dipole-bound state studies two prerequisites must be taken into account. The dipole moment of the neutral molecule should be approximately 2 D or larger and the electron affinity of the molecule should both be known and be within the wavelength region accessible by tunable lasers. Many diatomic molecules with large dipole moments have electron affinities (13) too small to be studied at the present time due to lack of suitable tunable infrared lasers. At the time we began this study, these two prerequisites limited our possibilities to one system, the FeO^- molecule. The FeO molecule is known to have a $^5\Delta$ ground state (14), an electron affinity reported to be 1.492 ± 0.020 eV (15), and a calculated dipole moment on ~ 3.3 D (16).

The experimental equipment, a coaxial beam photodetachment apparatus and a laser system have been described in detail before together with the experimental procedures (1,12,17). For further experimental details, the reader is referred to the previously published information.

2. RESULTS

In order to be able to perform dynamical studies involving molecular anions, such as rotational or vibrational autodetachment, it is necessary first to characterize the structural properties of the excited negative ion states. For a molecule such as FeO^- it can be expected that besides dipole-bound excited states also valence states can be located energetically close to the electron affinity limit.

2.1. Low and medium resolution data

The photodetachment of FeO^- near threshold was investigated at successively higher levels of resolution ranging from 1 cm^{-1} to 20 MHz (0.0007 cm^{-1}). The most structured region of the spectrum (at 1 GHz resolution) is shown in Fig. 1. The typical rotational structure seen in this figure consists of well-resolved and equally intense R and P branches separated by an unresolved Q branch. This intensity pattern is consistent with transitions between states with the same angular momenta (18), such as π - π or Δ - Δ . A similar rotational system, but with the P branch more intense than the R branch, was observed at higher (222 cm^{-1}) frequencies. Rotational analysis (12) of the two-band systems showed that the ~ 100 broad autodetachment resonances ($>1 \text{ GHz}$) observed could be assigned to transitions between the $X^4\Delta_i$ ($i = 7/2, 5/2$) ground state of FeO^- and an excited $A^4\Delta_{5/2}$ valence state. The effective structural parameters for these two states are given in Table 1 together with results for excited states described in the following.

2.2. High-resolution data

A significant part of the energy region 11700 - 12200 cm^{-1} above the FeO^- $^4\Delta_{7/2}$ ground level was studied with the laser operating single mode, yielding data from the photoelectron spectrometer at its Doppler-limit resolution of 20 MHz ($\sim 0.0007 \text{ cm}^{-1}$). More than 300 well-resolved and narrow resonances ($<1 \text{ GHz}$) were observed. The observation of two markedly different sets of autodetaching resonances in the vicinity of the $\text{FeO}(^5\Delta_i)$ thresholds strongly

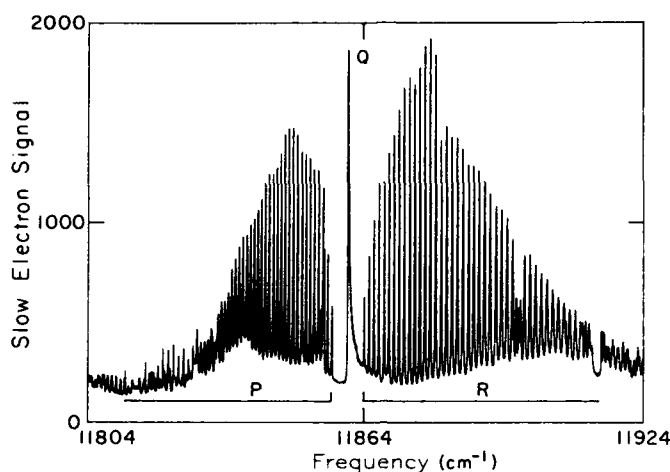


FIGURE 1.

Medium resolution (1 GHz or 0.03 cm^{-1}) scan of the slow electron cross section in the $11804\text{--}11924 \text{ cm}^{-1}$ frequency region. The rotational spectrum is due to transitions between the $X^4\Delta_{5/2}$ ground state of FeO^- and the $A^4\Delta_{5/2}$ state.

Table 1. Effective parameters for the observed FeO^- states (cm^{-1}).

State	Ω	T_Ω	R	$10^6 \eta$
$X^4\Delta$	7/2	0	0.4971(2)	0.91(32)
	5/2	222.52(3)	0.4996(2)	0.96(23)
	3/2	459.75(5)	0.5017(9)	1.21(33)
$A^4\Delta$	5/2	12081.75(5)	0.5043(1)	1.34(21)
	3/2	12291(3)		
$[^5\Delta_3]\text{-s}$	7/2	12011.21(46)	0.5044(3)	3.63(64)
$[^5\Delta_3]\text{-p}$	5/2	12221.23(5)	0.4806(9)	1.40(31)

Error limits are one standard deviation in units of the last significant figure quoted. The $\text{FeO}(^5\Delta_4)$ and $\text{FeO}(^5\Delta_3)$ states are located $12042 \pm 40 \text{ cm}^{-1}$ (Ref. 19) and $12227 \pm 40 \text{ cm}^{-1}$, respectively above the $\text{FeO}^-(^4\Delta_{7/2})$ state with $B = 0.5168 \text{ cm}^{-1}$ and $D = 0.725 \times 10^{-6} \text{ cm}^{-1}$ (Ref. 14).

indicates that we are observing two qualitatively different types of electronic states in FeO^- , valence states and dipole-bound states. The large majority of the narrow resonances can be assigned to transitions from the FeO^- ground state to two dipole-bound states, best characterized as negative ion complexes consisting of an $\text{FeO}(^5\Delta_4)$ core and a loosely bound s or p electron. In the present study we have only observed the complexes with an $\text{FeO}(^5\Delta_3)$ core. A detailed discussion of the assignment of these dipole-bound states will be given elsewhere (12).

An energy level diagram for FeO^- and FeO showing the transitions observed in FeO^- is given in Fig. 2. The FeO energy scale is based upon recent

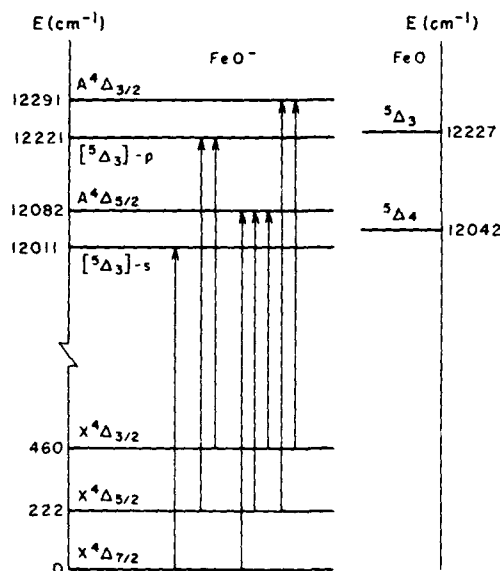


FIGURE 2.

Energy level diagram of FeO^- and FeO with the observed transitions indicated.

photoelectron spectroscopy data from this laboratory (19) yielding the $\text{FA}(\text{FeO})$ to be $12042 \pm 40 \text{ cm}^{-1}$ and Merer's spectroscopic studies of FeO (14). Figure 2 shows that the binding energies are $\sim 220 \text{ cm}^{-1}$ and $\sim 6 \text{ cm}^{-1}$, respectively, for the s and p electron. To explain the large binding energy for the s electron or the existence of a p complex for which calculations (20) had predicted that the dipole moment should be $\geq 9 \text{ D}$, it is necessary to assume that short-range forces, in addition to the dipole field effects, are playing a significant role in the binding of the outer electron in these FeO^- s or p electron complexes. The short-range forces may also explain the fact that we have not been able to observe any of the dipole-bound levels located below the detachment limit by means of electric field effects (1).

2.3. Linewidths and lifetimes

The widths of many autodetaching lines belonging to the identified band systems have been measured with the highest resolution available. Different transitions terminating in the same upper state have been observed to have identical linewidths. The line shapes, when not limited by the 20 MHz instrumental resolution, are Lorentzian. The results presented in Figs. 3 and 4 are obtained by fitting the lines to a Lorentzian function.

The rotational dependence of the FeO^- autodetachment rates for the $\text{A}^4\Delta_{5/2}$ valence state is shown in Fig. 3. The detachment rate increases linearly with rotational energy. A similar behavior has previously been seen for valence states in C_2^- (17). The detachment rate seems not to be influenced by the $\text{FeO}(^5\Delta_3)$ threshold, indicating that the autodetachment process occurs to the $\text{FeO}(^5\Delta_4) + e$ continuum. Even though rotational-to-electronic energy coupling plays an important role in the overall photodetachment process, the main contribution at low J is due to another coupling mechanism. In order to detach to the $\text{FeO}(^5\Delta_4) + e$ continuum, realignment of the spins in the $\text{A}^4\Delta_{5/2}$ state is

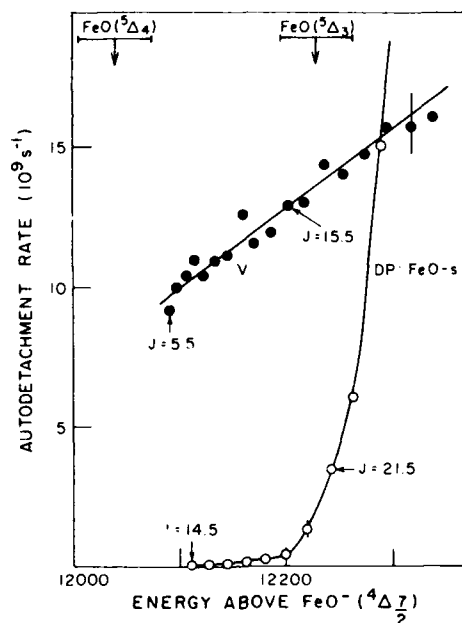


FIGURE 3.

Rotational dependence of the FeO^- autodetachment rates for the $A^4\Delta_{5/2}$ valence state (v) and the dipole-bound $\text{FeO}(^5\Delta_3)$ -s electron complex (DP). The $\text{FeO}(^5\Delta_4)$ and $^5\Delta_3$ thresholds are indicated.

needed. It is therefore likely that the spin-orbit coupling mechanism is of primary importance in transforming internal-to-electronic energy.

Figure 3 also shows the rotational dependence of the autodetachment rates for the $\text{FeO}(^5\Delta_3)$ -s electron complex. The detachment rates increase nearly linearly with rotational energy for the levels located below the $\text{FeO}(^5\Delta_3)$ threshold. Above this threshold a fast rise in detachment rates sets in. The slowly detaching levels can only decay to the $\text{FeO}(^5\Delta_4)$ level system, whereas the faster detaching levels also can detach to the $\text{FeO}(^5\Delta_3)$ level system. A very fast rise in detachment rates has previously (1) been seen for the dipole-bound states of acetaldehyde enolate just above the detachment limit. The rapid rise in detachment rate just above the $\text{FeO}(^5\Delta_3)$ threshold most likely reflects nearly identical structural properties of the core of the dipole-bound state and of $\text{FeO}(^5\Delta_3)$.

Any autodetachment process must conserve energy and angular momentum. The rotational angular momenta for the autodetaching state and for the neutral molecule must satisfy the triangular conditions with the electron orbital angular momentum. For the J levels of the $\text{FeO}(^5\Delta_3)$ -s complex located above the $\text{FeO}(^5\Delta_3)$ threshold ($J \geq 21.5$) these requirements can only be fulfilled for the rotational autodetachment process by the transfer of a rather large number of quanta of rotational energy to electronic motion. The much lower detachment rates observed for the J levels located below the $\text{FeO}(^5\Delta_3)$ threshold ($J \leq 19.5$) are considered to be associated with the spin rearrangement process in the core of the complex. Whereas the $^5\Delta_3 \rightarrow ^5\Delta_4$ rearrangement process is thought to play an important role in the detachment of the $A^4\Delta_{5/2}$ valence

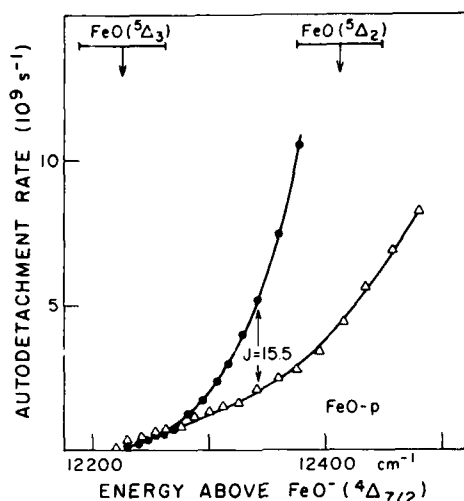


FIGURE 4.

Rotational dependence of the FeO^- autodetachment rates for the two $p\pi$ Λ -doublet components assigned to the $\text{FeO}(^5\Delta_3)$ - p electron complex. Triangles represent the lower doublet component. The $\text{FeO}(^5\Delta_3)$ and $^5\Delta_2$ thresholds are indicated.

state, it may be much less effective in causing fast detachment from dipole-bound states.

Figure 4 shows the rotational dependence of the autodetachment rates for the two $p\pi$ Λ -doubling components assigned to the $\text{FeO}(^5\Delta_3)$ - p electron complex. The detachment rates are nearly identical at low J , but differ at high J with the upper Λ -doublet component detaching faster than the lower one. The different detachment rates may be attributed to different structural properties of the two Λ -doublet levels. For molecules such as OH the different dynamical properties of Λ -doublet levels are assumed (21) to be due to a difference in the π electron wave function in the Λ -doublet levels. The electron density of the single occupied OH π orbital forms lobes either in the plane of rotation or perpendicular to this plane. Accordingly, the former state shows a much greater rotational energy dependent deformation than the latter. Markedly different detachment rates for Λ -doublet components in NH^- have recently (22) been accounted for by an analogous mechanism. We believe that a similar description is valid for the Λ -doublet levels of the $\text{FeO}(^5\Delta_3)$ - p complex. A difference in the location of the electron density of the detaching electron with respect to the plane of rotation would be most noticeable at high J levels, in agreement with the experimental observations.

3. DISCUSSION AND CONCLUSION

The present study has shown that it is possible to obtain detailed structural and dynamical information from studies of autodetachment resonances in rather complex negative molecular ions. The prediction (15) that the ground state of FeO^- is a $^4\Delta$ state is in agreement with the present data, whereas the

$6z^+$ ground state proposed by Krauss and Stevens (16) is inconsistent with the experimental observations. The structural properties of the ground states of FeO^- and FeO are found to be very similar. The dipole-bound states observed support the prediction (2) from the dipole field model that molecules with dipole moments larger than ~ 2 D are able to support dipole-bound states. The structural properties of the dipole-bound states reflect properties well known from Rydberg- π complexes (18,23). Contrary to theoretical predictions (2) the rotational energies of dipole-bound states observed to date are well described by the usual $J(J+1)$ dependence. The properties of the $\text{FeO}(^5\Delta_3)$ -s or p electron complexes clearly deviate from the predictions based upon the simple dipole-field model. The binding energies of these complexes can only be accounted for taking short-range forces into account and the simplicity characterizing the spectra of dipole-bound states in acetaldehyde enolate (1) is lacking due to insufficient rotational coupling.

Recent studies (24) involving rotational autoionization of Rydberg states in molecules such as K_2 have shown that the dynamical process occurs by transfer of large amounts of quanta of rotational energy to electronic motion. The rotational autodetachment of the $\text{FeO}(^5\Delta_3)$ -s electron complex seems to exhibit the same properties. Broyer et al. (24) have attributed this phenomenon to the nonspherical character of the potential energy seen by the loosely bound electrons. This effect would be even more important for negative ions than for neutral molecules. Further studies of rotational-to-electronic energy transfer seem to be needed to obtain a better understanding of the physical mechanisms involved in these processes. The present investigation shows that rotational-to-electronic energy transfer for valence and dipole-bound states in the same molecule can exhibit markedly different energy dependence. This difference in behavior may be useful for identification of the two types of states in future studies of molecular anions.

Even though the present study has yielded insight into a number of questions related to the presence of dipole-bound states in the diatomic systems, future studies of dipole-bound states in diatomic systems should be directed toward molecules with simpler structures. Both molecules with large dipole moments, such as the alkali halides, and molecules with dipole moments close to the limit for binding an electron are of interest.

ACKNOWLEDGMENTS

This work was supported by the National Science Foundation under grants CHE83-16628 and PHY82-00805. TA thanks the Danish Natural Science Council for a travel grant.

REFERENCES

- 1) K. R. Lykke, R. D. Mead and W. C. Lineberger, *Phys. Rev. Lett.* 52 (1984) 2221.
- 2) W. R. Garrett, *Chem. Phys. Lett.* 5 (1970) 393; *Phys. Rev. A* 3 (1971) 961; *J. Chem. Phys.* 73 (1980) 5721; *ibid.* 77 (1982) 3666.
- 3) K. D. Jordan and W. Luken, *J. Chem. Phys.* 64 (1976) 2760.
- 4) K. D. Jordan and J. J. Wendoloski, *Chem. Phys.* 21 (1977) 145.
- 5) E. A. McCullough, *J. Chem. Phys.* 75 (1981) 1579.
- 6) S. F. Wong and G. J. Schulz, *Phys. Rev. Lett.* 33 (1974) 134.
- 7) K. Rohr and F. Linder, *J. Phys.* B 9 (1976) 2521.
- 8) A. H. Zimmerman and J. I. Brauman, *J. Chem. Phys.* 66 (1977) 5823; *ibid.* 71 (1979) 2088.
- 9) R. L. Jackson, P. C. Hiberty and J. I. Brauman, *J. Chem. Phys.* 74 (1981) 3705.

- 10) R. D. Mead, K. R. Lykke, W. C. Lineberger, J. Marks and J. I. Brauman, *J. Chem. Phys.* 81 (1984) 4883.
- 11) G. Herzberg and Ch. Jungen, *J. Mol. Spectrosc.* 41 (1972) 425; Ch. Jungen and D. Dill, *J. Chem. Phys.* 73 (1980) 3338.
- 12) T. Andersen, K. R. Lykke, D. M. Neumark and W. C. Lineberger, *J. Chem. Phys.*, submitted.
- 13) CRC Handbook of Chemistry and Physics, 1985 edition, section on Electron Affinities.
- 14) A. S-C. Cheung, R. M. Gordon and A. Merer, *J. Mol. Spectrosc.* 87 (1981) 289; A. S-C. Cheung, N. Lee, A. M. Lyrre, A. J. Merer and A. W. Taylor, *J. Mol. Spectrosc.* 95 (1982) 213.
- 15) P. C. Engelking and W. C. Lineberger, *J. Chem. Phys.* 66 (1977) 5054.
- 16) M. Krauss and W. J. Stevens, *J. Chem. Phys.* 82 (1985) 5584; H.-J. Werner and P. Rosmus, to be published.
- 17) U. Hefter, R. D. Mead, P. A. Schulz and W. C. Lineberger, *Phys. Rev. A* 28 (1983) 1429.
- 18) G. Herzberg, *Spectra of Diatomic Molecules* (Van Nostrand, New York, 1950).
- 19) D. G. Leopold, private communication.
- 20) O. H. Crawford, *Proc. Phys. Soc. London* 91 (1967) 279.
- 21) P. Andresen and E. W. Rothe, *J. Chem. Phys.* 82 (1985) 3634.
- 22) D. Neumark, K. R. Lykke, T. Andersen and W. C. Lineberger, *J. Chem. Phys.* in press.
- 23) I. Kovács, *Rotational Structure in the Spectra of Diatomic Molecules* (Adam Hilger Ltd., London, 1969).
- 24) M. Broyer, J. Chevalere, G. Delacretaz, S. Margin and L. Wöste, *Chem. Phys. Lett.* 99 (1983) 206.

MODIFIED PHOTODETACHMENT THRESHOLD BEHAVIOR NEAR RESONANCES

Young K. BAE and James R. PETERSON

Molecular Physics Department, SRI International, Menlo Park, CA 94025

Modified formulae for photodetachment threshold behavior affected by three different types of resonances, such as shape, Feshbach, and virtual state resonances been studied and applied to available experimental results.

1. INTRODUCTION

The energy dependences of scattering cross sections near resonances, and near new channel thresholds, have each been the subject of extensive theoretical and experimental studies in the fields of atomic, nuclear, and elementary particle physics. However, little attention has been given to the effects that result when thresholds are close to resonances. Until recently, observation of these effects has probably been inhibited because experiments have not had sufficient energy resolutions. The development of laser photodetachment techniques has now removed that barrier and the combined effects have already been seen.¹

The negative ion resonances that are observed frequently in electron scattering have provided both stimulus and test in the development of the theory of the short-range correlation interactions that cause them. In atomic systems, these resonances occur commonly at energies in the vicinity of the excited states of the neutral target, where the loosely bound excited electron can share the attractive force of the ion core with the low-energy scattered electron to form a loosely bound temporary compound state. Thus it is more the rule than the exception that negative ion resonances lie close to threshold, and it is not surprising that their combined effects have now been observed in photodetachment experiments.

Wigner² first derived threshold laws for opening channels that yield a pair of outgoing products, and showed that the behavior is independent of the excitation mechanism and depends only on the long-range interaction between the product particles. Thus the threshold laws are the same for photodetachment as for electron scattering. Both of these reactions are characterized by short-ranged correlation forces and, ignoring other effects, the cross sections near threshold should follow the Wigner law for neutral products, namely

$$\sigma \sim k^{2l+1} \quad (1)$$

where k and l are the linear and angular momentum of the outgoing state. In terms of energies, this expression becomes

$$\sigma \sim (E - E_0)^{l+1/2}, \quad (2)$$

where E and E_0 are the total and threshold energies of the system. Although the threshold laws are the same for the two types of excitation, unlike electron scattering, photodetachment has well-defined final angular momentum states due to optical selection rules, a property that simplifies the analysis of experimental results.

Similar to the resonance phenomena in other short-range potential systems (atom-atom, neutron-nucleus, etc.),³ electron scattering and photodetachment resonances are of three types. In the electron-atom (molecule) systems they are caused by the short-ranged attractive correlation potentials that commonly exist in the collision complex at energies near the thresholds of excited-state channels. If the correlation potential is sufficiently strong that the compound state is "bound" below the continuum of the excited channel state, it is a "bound," "closed-channel," or "Feshbach" resonance. If the attractive potential is not quite strong enough to form a Feshbach resonance, a "virtual state"⁴ can exist for an s -wave channel ($l=0$), or a "shape" resonance can exist if $l \gg 1$. The scattering phase changes rapidly and passes through $(n+1/2)\pi$ as the total energy passes through the levels of Feshbach and shape resonances, but it does not quite reach $(n+1/2)\pi$ in the case of a virtual state.

Dramatic interference effects due to Feshbach resonances were first observed by Patterson et al.⁵ in the photodetachment of K^- , Cs^- and Rb^- just below the thresholds of the first excited neutral product channels. In later experiments,⁶ departures from the Wigner threshold law for the production of these excited s -wave channels were found to exist within about 120 μ eV for K and Cs . In later experiments,¹ deviations were found within 25 μ eV for Cs . Frey et al.⁷ have observed similar deviations in their 2P partial cross section measurements on Rb^- . We have recently observed and analyzed⁸ the deviations due to a shape resonance near the $He(2^3P)$ threshold in He^- photodetachment and also⁹ the effects of a virtual state on the Wigner cusp in Li^- photodetachment at the 2P threshold. Here, based on that work^{8,9} we derive parametric threshold formulae which show explicitly the characteristics of neighboring resonances. We treat the effects of shape and Feshbach resonances on the behavior of a single opening channel; the effects of a virtual state are treated for a two-channel system.

2. SINGLE CHANNEL THRESHOLD BEHAVIOR NEAR SHAPE OR FESHBACH RESONANCE

The total cross section for the photoexcitation of a single opening detachment channel may be written as

$$\sigma_l \sim k |M_l|^2, \quad (3)$$

where M_l is the dipole matrix element connecting the initial (negative ion) and final (atom + electron) states. M_l contains only contributions from a small finite region of space because of the localization of the initial wave function. Since we are concerned only with the behavior of the opening channel near its threshold, the asymptotic energy of the final state wave function can be considered infinitesimal compared to the interaction energy in this localized region, the only characteristic of the local final state wave

function that is sensitive to small variations of the asymptotic energy is the amplitude, which is proportional to the inverse of the (volume) normalization factor of the asymptotic wave function. Following this idea, O'Malley¹⁰ factored M_λ as

$$M_\lambda = N_\lambda^{-1} M', \quad (4)$$

where N_λ is the normalization factor of the asymptotic final state electron wave function and M' is a constant to lowest order in k^2 . O'Malley¹⁰ also noted, with reference to Gillespie¹¹ that N_λ is connected to the Jost function $f_\lambda(k)$ by

$$N_\lambda = |f_\lambda(k)| k^{-\lambda}, \quad (5)$$

and we note that the Jost function is related to the scattering matrix S_λ by $S_\lambda(k) = f_\lambda(-k)/f_\lambda(k)$.^{11,12} Here, the Jost function describes the half collision process. Now, from Eqns. (3-5), we see that the cross section of the new opening channel near its threshold may be written as

$$\sigma_\lambda \sim k^{2\lambda+1} |f_\lambda(k)|^{-2}. \quad (6)$$

We note that a resonance can be identified^{12,13} with a pole of the scattering matrix (or a zero of the Jost function) in the complex k -plane. If there is no resonance near the threshold, then $f_\lambda(k)$ is not close to a zero and can be regarded as constant for small values of k , and the cross section Eq. (6) follows the Wigner threshold law. However, if there is a zero of $f_\lambda(k)$ near $k \sim 0$, then $f_\lambda(k)$ can vary strongly, and Eq. (6) can deviate from the Wigner law very close to the threshold.

In order to see how $f_\lambda(k)$ depends on k when it has a zero close to the threshold, $k=0$, we let the interaction potential of the final state be $\mathcal{W}(r)$, where $V(r)$ describes only the form of the potential, and λ represents its strength. We assume that $V(r)$ is short ranged (for large $V(r) \sim -r^{-n}$, where $n > 2$), and strength is such that if $\lambda = \lambda_0$, the zero of $f_\lambda(k)$ occurs at the threshold, $k=0$ (zero energy resonance). Since we want to treat the cases where the resonances occur close to $k=0$, not only is k small but so is $|\lambda - \lambda_0|$. Therefore $f_\lambda(k)$ can be expanded as

$$f_\lambda(k) \sim \beta_\lambda k^2 + i\gamma_\lambda k^{2\lambda+1} + \eta_\lambda(\lambda - \lambda_0) + \text{higher order terms}, \quad (7)$$

where β_λ , γ_λ , and η_λ , are real constants that depend only on the shape of the potential (not on its strength). Thus we have

$$|f_\lambda(k)|^2 = \beta_\lambda^2 (k^2 - k_1^2)^2 + \gamma_\lambda^2 k^{4\lambda+2} + \text{higher order terms}, \quad (8)$$

where $k_1^2 = -\eta_\lambda(\lambda - \lambda_0)/\beta_\lambda$ and $\gamma = \gamma_\lambda/\beta_\lambda$. For $\lambda=0$, the dominant terms in Eq. (8) are quadratic in k^2 , and using the relation $k^2/2 = E - E_0$ and $k_1^2/2 = E_R - E_0$ we can transform Eq. (8) into

$$|f_\lambda(k)|^2 = F(E - E_0) [(E - E_R)^2 + (\Gamma/2)^2] \quad (9)$$

where E_0 is the threshold energy, $F(E - E_0)$ is a slowly varying function of $E - E_0$, and E_R and $\Gamma/2$ are the real and imaginary parts of pole position in the

complex E -plane. For $l=1$, dominant terms in Eq. (8) are cubic in k^2 , and we can transform Eq. (8) into

$$|f_l(k)|^2 = G(E-E_0)(E-E_0+A) [(E-E_R)^2 + (\Gamma/2)^2] \quad (10)$$

where $G(E-E_0)$ is a slowly varying function of $E-E_0$, and $|A| \gg |E-E_0|$, if there is only one pole affecting the threshold behavior. For $l \geq 2$, if there is only one pole affecting the threshold, it is possible to transform Eq. (8) into a similar form to Eq. (9). Therefore, for any l , we have

$$|f_l(k)|^2 \sim (E - E_R)^2 + (\Gamma/2)^2 \quad (11)$$

Finally, by combining Eqns. (6) and (11), we conclude that near the threshold cross section for a single opening channel (for any l) is approximately

$$\sigma \sim \frac{(E - E_0)^{l+1/2}}{(E - E_R)^2 + (\Gamma/2)^2} \quad (12)$$

which is simply a product of the Wigner threshold law and the Breit-Wigner resonance formula. We now present some applications.

a. Shape Resonance

Eq. (12) was first derived to account for difficulties encountered in trying to use the Wigner law to fit our He^- photodetachment data near the $\text{He}(2^3\text{P})$ threshold.⁸ Figure 1 shows the data and a least-squares fit (dashed curve) of the first seven data to the Wigner threshold law. Due to the strong effects of the shape resonance the cross section rapidly deviates from the Wigner law, and we found that the threshold value E_0 obtained by fitting the data to it increased substantially as more data above the threshold were included in the fitting procedure. Thus the Wigner law could not be used with these data. On the other hand, equation (12) which gave quite good fits not only to the threshold data as shown in Figure 1, but to the entire resonance peak as well, as is seen in Figure 2. The fit to the entire resonance yielded $E_R = +10.8 \pm 0.3$ meV and $\Gamma = 7.4 \pm 0.3$ meV. These values were then used in equation (12) to determine E_0 from the data in Figure 1, and yielded $E_0 = 1222.1 \pm 1.0$ meV, from which we obtained an electron affinity for $\text{He}(2^3\text{S})$ of 77.6 ± 1.0 meV.

b. Feshbach Resonance

We also have found that equation (12) can also be applied to partial cross sections previously obtained in Rb^- (reference 7) and Cs^- photodetachment.¹ In the derivation of the equation (11) there is no restriction on the positions of the resonance poles, thus it can be applied to threshold behaviors affected by poles located either above the thresholds ($E_R > E_0$, i.e. shape resonances,) or below the thresholds ($E_R < E_0$, i.e. Feshbach resonances). Figure 3 and Figure 4 show the squares of the partial cross sections for the first opening $2\text{P} + \text{cs}$ channel in Rb^- photodetachment by Frey et al.⁷ and in Cs^- photodetachment by Mead et al.¹ Because there are s -wave thresholds, the Wigner law is $\sigma^2 \sim (E-E_0)$, and in these figures non-Wigner behavior due to the presence of Feshbach resonances that lie below the thresholds, shows up as deviations from linearity of σ^2 vs. $h\nu$ (dashed curves). The Wigner law holds for an energy range less than the experimental resolutions ($\sim 0.2 \text{ cm}^{-1}$). The solid curves represent fits to Equation (12), which yielded the fit parameters

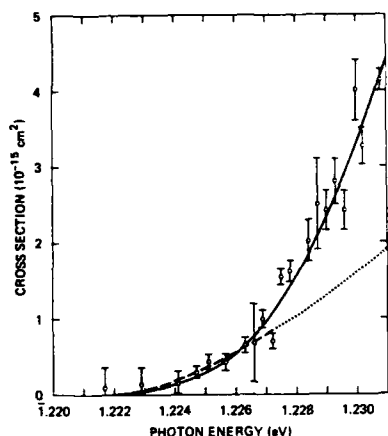


FIGURE 1

He^- photodetachment cross sections near the $\text{He}(2^3\text{P})$ threshold which is strongly affected by the $\text{He}^-(4p^e)$ shape resonance. Dashed curve: least-square fit of the first seven data to Wigner threshold law. Solid curve: least-square fit to the modified form.

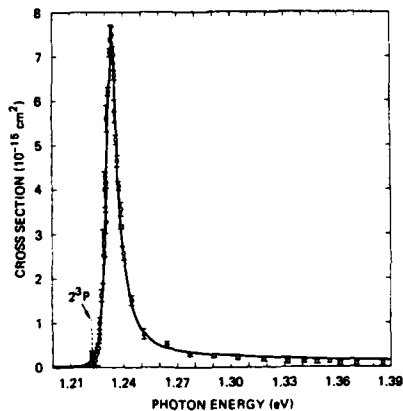


FIGURE 2

He^- photodetachment cross sections near the $\text{He}^-(4p^e)$ shape resonance. Solid curve: least-square fit to the modified form.

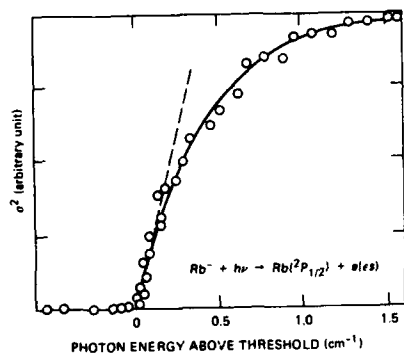


FIGURE 3

The square of the partial cross sections for Rb^- photodetachment to the $\text{Rb}(^2P_{1/2})$ by Frev et al.⁷ Dashed curve: visual fit of near-threshold data to Wigner threshold law. Solid curve: least-square fit to the modified form.

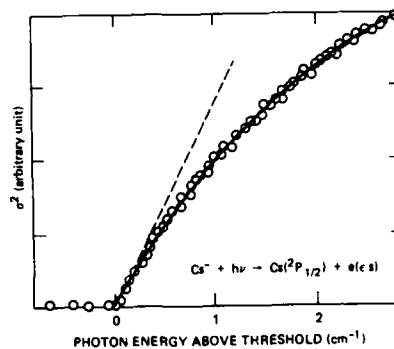


FIGURE 4

The square of the partial cross sections for Cs^- photodetachment to the $\text{Cs}(^2P_{1/2})$ by Mead et al.¹ Dashed curve: visual fit near threshold to Wigner threshold law. Solid curve: least-square fit of all data to the modified form.

$E_R \sim -17 \text{ cm}^{-1}$ and $\Gamma \sim 1 \text{ cm}^{-1}$ for Rb^- , and $E_R \sim -27 \text{ cm}^{-1}$ and $\Gamma \sim 8 \text{ cm}^{-1}$ for Cs^- .

3. TWO-CHANNEL THRESHOLD BEHAVIOR NEAR A VIRTUAL STATE

The negative alkali-metal ions have the valence electronic configuration ns^2 , so the first excited state in Li^- photodetachment occurs as $h\nu + \text{Li}^-(2^1S) \rightarrow \text{Li}(2^2P) + e$. Moores and Norcross¹⁴ performed an *ab initio* calculation of the total photodetachment cross section for Li^- . They also used effective-range theory to generalize the Wigner threshold law for the many-channel case and compared it to their calculations near the "Wigner cusp" that occurs at the opening of the s-wave channel at the 2^2P threshold. They found that their partial cross sections could not be adequately described by the Wigner law even 0.07 meV away from the threshold and attributed this deviance to "resonant behavior," taking note of the rapid variation in the phase shift of their final-state wave functions. In rearranged form, the Wigner law for the photodetachment cusp derived by Moore and Norcross¹⁴ can be expressed as

$$\sigma = \sigma_0 (1 - A \sqrt{E_0 - E}) \quad (13a)$$

below the threshold, and by

$$\sigma = \sigma_0 (1 - B \sqrt{E - E_0}) \quad (13b)$$

above the threshold. Here, σ_0 is the total cross section at the threshold energy, $E=E_0$, and A and B are constants.

We have measured the cross sections for Li^- photodetachment in the region of the $\text{Li}(2^2P)$ threshold.⁹ An examination of the results showed that the cross section rapidly deviates from Equations (13a) and (13b), in agreement with the findings of Moores and Norcross.¹⁴ Noting that their calculated phase shift although changing rapidly just below the 2^2P threshold, did not quite reach $\pi/2$, we sought to interpret the deviations from the Wigner law as resulting from the near presence of a virtual state. In this case we were able to use the theoretical work of Nesbet¹⁵ on multichannel s-wave threshold structure in electron scattering. We derived an appropriate parametric formulation of the cross-section behavior that contains corrective terms to Equations (13a) and (13b) accounting for these effects.

We consider a two-channel scattering system, in which channel 1 is continually open, and the channel 2, with $k=0$ outgoing, is open above a threshold energy E_0 . By applying Equations (1), (2), (13), and (16) of Nesbet¹⁵ to this system and neglecting second order terms, the total cross section $E < E_0$ can be shown to be approximated by

$$\sigma \sim \sigma_0 [1 - (2 \tan \eta_0) |\gamma|^2 \beta \left(\frac{\kappa}{\kappa + \beta} \right)] \quad (14a)$$

for energies $E < E_0$, and by

$$\sigma \sim \sigma_0 [1 - (1 - \cot^2 \eta_0) |\gamma|^2 \beta^2 \left(\frac{\kappa}{\kappa^2 + \beta^2} \right)] \quad (14b)$$

for energies $E > E_0$. Here, σ_0 and η_0 are the total cross section and the phase shift of channel 1 at E_0 , k and κ are defined by $k^2 = -\kappa^2 = 2(E - E_0)$, and $E_0 - \beta^2/2$ is the energy level of the virtual state, for which $\beta > 0$. The above equations can be transformed so that for $E < E_0$,

$$\sigma \sim \sigma_0 \left[1 - \frac{A \sqrt{E_0 - E}}{\sqrt{E_0 - E} + \sqrt{E_0 - E_v}} \right], \quad (15a)$$

and for $E > E_0$,

$$\sigma \sim \sigma_0 \left[1 - \frac{B \sqrt{E - E_0}}{(E - E_0) + (E_0 - E_v)} \right], \quad (15b)$$

where A and B are constants, and $E_v = E_0 - \beta^2/2$. We note that Equations (15a and 15b) are equivalent to the normal Wigner "cusp" formulae as expressed by Moores and Norcross,¹⁴ but modified in the denominator of the second terms to include the effects of the virtual state. When $|E_0 - E_v| \gg |E - E_0|$, i.e., when the virtual state is far removed from E_0 , they become the same. The phase shift η_0 of channel 1 at $E = E_0$ can be obtained from the relation

$$B/A = [\beta (1 - \cot^2 \eta_0) \cot \eta_0] / 2 \sqrt{2}. \quad (16)$$

Figure 5 shows our results of Li^- photodetachment near $\text{Li}(2^2\text{P}) + e$ threshold where a Wigner cusp is expected. While the Wigner-law (Equations

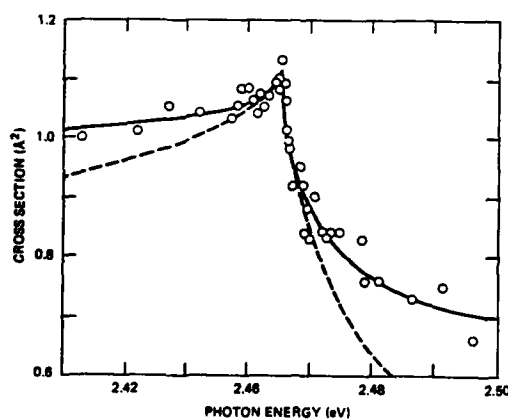


FIGURE 5

Li^- total photodetachment cross sections near the $\text{Li}(2^2\text{P})$ threshold, where the Wigner cusp is affected by a virtual state. Dashed curve: visual fit of near-threshold data to Wigner form. Solid curve: least-square fit of all data to the modified form.

(13a) and (13b)) fit deviates rapidly from the data, a very good fit is given by Equations (15a) and (15b). These equations not only give an accurate value of E_0 , but also provide information on the resonance state. The fitting yielded $E_0 = 2.4652 \pm 0.0006$ eV and $\beta^2/2 = 55 \pm 10$ meV with $\beta > 0$ (a virtual state). The phase shift η_0 at threshold obtained from the present result is 1.4 ± 0.1 radian, which is in good agreement with the value calculated by Moores and Norcross (~ 1.3 radian).¹⁴ Although random fluctuations in the data from this brief experiment do not allow more accurate and detailed analysis near the threshold, the general shape of the cross section still reveals a Wigner cusp in good detail and shows that it is strongly affected by the virtual-state. Because most excited opening electron scattering and photodetachment channels are accompanied by neighboring negative ion resonances, these effects would seem to be quite common, and virtual state resonance effects can be generally expected near excited s-wave channel thresholds where Feshbach resonances are not observed below the thresholds.

(Note: In the course of this work we were unaware of a recent analytical theory of resonances, virtual states and bound states in electron-molecule scattering, by Domcke.¹⁶ His treatment is more general than ours, and would doubtless yield similar results when adapted to our specific problems.)

We are grateful to T. F. O'Malley and D. L. Huestis, and D. W. Norcross for helpful theoretical discussions and information, and to R. D. Mead, W. C. Lineberger and H. Hotop and coworkers for enthusiastically offering their data for our analysis. This work was supported by the NSF under Grant No. PHY-81-11912 and by the AFOSR under Contract No. F49620-82-K-0030.

REFERENCES

- 1) R. D. Mead, K. R. Lykke, and W. C. Lineberger, in "Electron and Atomic Collisions," XIII ICPEAC Invited Papers, J. Eichler et al., Eds. (North Holland Pub. Co., 1984), p. 721.
- 2) E. P. Wigner, Phys. Rev. 73, (1948) 1002.
- 3) T. W. Wu and T. Ohmura, Quantum Theory of Scattering, Prentice-Hall Inc. NJ (1962).
- 4) S. T. Ma, Rev. Mod. Phys. 25, (1953) 853.
- 5) T. W. Patterson, H. Hotop, A. Kasdan, D. W. Norcross, and W. C. Lineberger, Phys. Rev. Lett. 32, (1974) 189.
- 6) J. Slater, F. H. Read, S. E. Novick, and W. C. Lineberger, Phys. Rev. A 17, (1978) 201.
- 7) P. Frey, M. Lawen, F. Breyer, H. Klar, and H. Hotop, Z. Phys. A 304, (1982) 155.
- 8) J. R. Peterson, Y. K. Bae, and D. L. Huestis, Phys. Rev. Lett. 55, (1985) 692.
- 9) Y. K. Bae and J. R. Peterson, Phys. Rev. A (to be published).
- 10) T. F. O'Malley, Phys. Rev. 137, (1965) A1668.
- 11) J. Gillespie, Phys. Rev. 135, (1964) A75.
- 12) J. R. Taylor, Scattering Theory (Wiley, New York, 1972).
- 13) R. G. Newton, Scattering Theory of Waves and Particles (McGraw-Hill Book Co. New York, 1966).
- 14) D. L. Moores and D. W. Norcross, Phys. Rev. A 10, (1974) 1646.
- 15) R. K. Nesbet, J. Phys. B 13, (1980) L193.
- 16) W. Domcke, J. Phys. B. 14, (1981) 4889.

EXPERIMENTS ON MASS-RESOLVED CLUSTERS OF SEMICONDUCTORS

L. A. BLOOMFIELD, M. E. GEUSIC, R. R. FREEMAN, and W. L. BROWN

AT&T Bell Laboratories, Murray Hill, NJ 07974

An experimental technique that produces both neutral and ionized semiconductor clusters is described. Cluster ions of from 2 to several hundred atoms are observed. Positive and negative cluster ions are mass-selected and studied by photofragmentation or photodetachment.

1. INTRODUCTION

The study of small atomic clusters has developed recently as a means for understanding the connection between the properties of solids and those of their constituent atoms. These clusters of from 2 to a few hundred atoms bridge the gap between atomic and molecular physics and the physics of solid state. One of the most interesting observations about clusters is the existence of "magic numbers," sizes which are more easily produced and less fragile than clusters differing in size by one or more atoms (1-8). Knowing which clusters are the most stable is extremely helpful in understanding the structure of these tiny pieces of matter.

Until now, most "magic numbers" have been found indirectly by producing a mixture of various clusters and then counting them to see which clusters are unusually common. But the process of detecting and counting the clusters involves ionizing them, a procedure which is likely to break the cluster as it removes an electron (9). Thus most previous studies have involved some initial assumptions about the fragility of the clusters and the correspondence between a strong signal of ionized clusters and a "magic number" in the original neutral species.

To avoid these ambiguities, we have employed two new techniques in our attempt to understand the structure of the semiconductor clusters. First, we have produced beams of positively ionized clusters (silicon, carbon, and germanium) which have been purified so as to contain only a single cluster size. A laser beam is used to study the photofragmentation of these cluster ions, both to measure the intensity of light needed to break them as well as to observe the fragments which remain after the original clusters break. In this manner, we have measured the total photofragmentation cross sections for positive silicon cluster ions of between 2 and 11 atoms (Fig. 1), along with the branching ratios of these clusters to smaller fragments (Fig. 2). These studies give clear indication that clusters of Si_6^+ and Si_{10}^+ are "magic." Similar experiments in carbon have demonstrated that C_2 is a "magic fragment" during the breakup of larger cluster ions.

The second technique which we have developed for use with refractory materials such as the semiconductors, is one in which the clusters are produced as ions rather than as neutrals.

Removal of the photoionization step eliminates the ambiguities introduced by photofragmentation during photoionization. Furthermore, negative cluster ions are easily produced and provide considerable information concerning the effect of charge (positive or negative) on the "magic numbers" and thus on the structure of the cluster ions themselves.

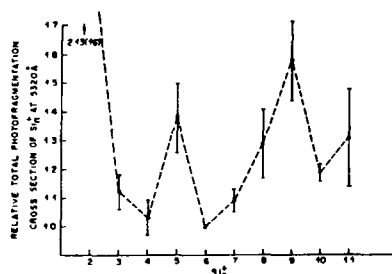


Figure 1
Relative total photofragmentation cross sections for silicon positive cluster ions at 532 nm. One unit is equal to $7(3) \times 10^{-19}$.

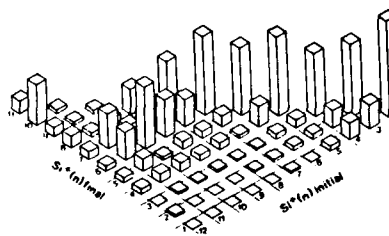


Figure 2
The branching ratios for photo-fragmentation of silicon positive cluster ions with 532 nm light.

2. APPARATUS

The apparatus is shown schematically in Fig. 3. The clusters, both neutral and ions, are produced by laser vaporization of the sample rod by the focused beam of a Nd:YAG laser (532 nm). These clusters are entrained in a pulse of carrier gas, usually helium, which undergoes a supersonic expansion into the first of a series of vacuum chambers. The version of the apparatus drawn in Fig. 3 is specialized to the observation of ions produced in the cluster source. The ions enter the acceleration region undeflected following which the plates are raised to high voltage. The ions are accelerated to a constant energy and dispersed in time along the horizontal time-of-flight region. A similar version, which is specialized to the observation of neutrals, involves an excimer laser for photoionization. In this case, the acceleration plates are kept at high voltage, excluding the ions, and only the neutral clusters enter undeflected. The neutrals are then photoionized and the resultant positive clusters are accelerated and dispersed in time.

Mass selection of the accelerated cluster beam is possible using the pulsed mass isolation plates. By switching the field present on these plates, it is possible to deflect all but the desired cluster ion packet away from the axis of the time-of-flight tube. Thus only the selected cluster packet continues undeflected through the apparatus. Further experiments, either photofragmentation for positive ions or photodetachment for negative ions, can be carried out in the deacceleration and

reacceleration region of the time-of-flight path. A laser is used to change the mass or charge of the cluster ions and the resultant fragments are reaccelerated to a different potential. The fragments again disperse in time and are observed at the microchannel plate detector. Neutral fragments are not reaccelerated and simply coast into the detector, which registers them weakly.

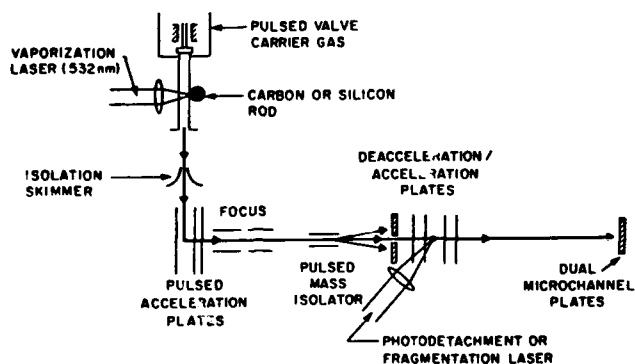


Figure 3

Experimental apparatus: Cluster neutrals and ions are produced in the source by laser vaporization of a sample rod. These particles are (ionized and) accelerated in the acceleration region and dispersed by a time-of-flight technique. Individual masses can be selected for photofragmentation or photodetachment.

3. OBSERVATIONS

Spectra of the clusters produced by laser vaporization are shown in Fig. 4 (carbon) and Fig. 5 (silicon). The upper two traces in each figure are the negative cluster ions (top) and positive ions (second) produced in the source. The positive ion trace can be compared with the signals observed when the neutral clusters are ionized and the resultant positive clusters are accelerated toward the detector (third trace). In both carbon and silicon, photoionization increases the contrast between strong, "magic" peaks and the weaker peaks corresponding to less common clusters. This increased contrast is due in part to a greater photofragmentation of the less common, more fragile clusters. The extreme example of this effect is visible in the carbon positive ions, where the ionized neutrals contain no odd cluster ions for masses larger than 30 atoms. The positive ions produced in the source do contain large odd clusters, showing only a weak even/odd alternation above mass 30.

The fourth trace for carbon shows the photofragmentation of a large carbon cluster (C_{60}^+) with very intense light. The intensity of the light permits multiple fragmentation of the

clusters. The spectrum produced by this breakup closely resembles that of ionized neutrals (for cluster ions larger than about 8 atoms) and indicates that photoionization of the neutral probably involves considerable photofragmentation as well.

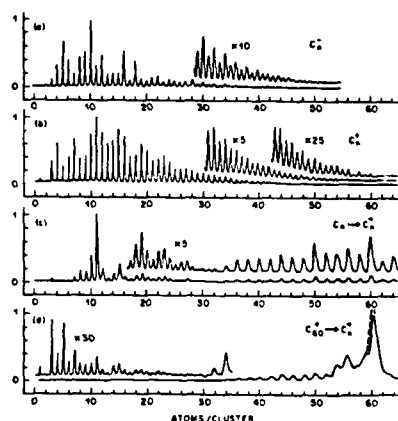


Figure 4

Spectra of carbon cluster ions. (a) and (b) are negative ions and positive ions produced in the source, (c) are ionized neutral clusters, and (d) are the fragments produced by photofragmentation of C_{60} .

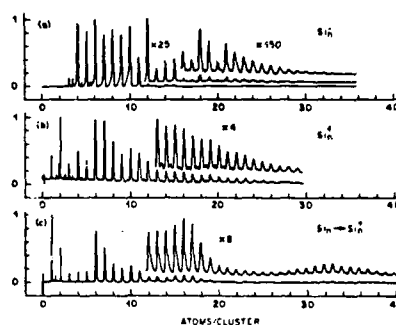


Figure 5

Spectra of silicon cluster ions. (a) and (b) are negative ions and positive ions produced in the source, and (c) are ionized neutral clusters.

Photofragmentation measurements (10), shown in Figs. 1 and 2 for silicon, have given additional information about the "magic numbers" in the semiconductor clusters. The strong rows at Si_4^+ and Si_{10}^+ as final states indicate that these cluster ions are either unusually stable energetically, or are more easily produced than adjacent cluster sizes. The structure in the breakup of Si_{11}^+ into clusters with from 4 to 7 atoms also indicates that the initial cluster structure may play a role in determining which fragments are produced. Photofragmentation of carbon clusters indicates that the principal decay mode for the light positive cluster ions (4 to 20 atoms) is to emit a neutral C_3 . Again, C_3 is either an unusually stable fragment or a basic building block of the larger cluster ions.

Photodetachment measurements of the negative clusters ions are also possible. The electron is easily removed with a laser pulse and the neutralized clusters coast into the detector at a speed which is independent of accelerating voltages. No charged photofragments of negative cluster ions are observed.

4. CONCLUSION

We have demonstrated a technique which produces neutral and charged clusters of semiconductors and have measured the relative abundances of the cluster ions produced in the source or by photoionization of the neutrals. We have also studied the photofragmentation and photodetachment of the cluster ions and have obtained additional information about the structure and stabilities of the various cluster sizes.

REFERENCES

1. P.W. Stephens and J.C. King, *Phys. Rev. Lett.* 51 (1983) 1538.
2. I.A. Harris, R.S. Kidwell, and J.A. Northby, *Phys. Rev. Lett.* 53 (1984) 2390.
3. A. Ding and J. Hesslich, *Chem. Phys. Lett.* 94 (1983) 54.
4. O. Echt, K. Sattler, and E. Recknagel, *Phys. Rev. Lett.* 47 (1981) 1121.
5. T.T. Tsong, *App. Phys. Lett.* 45 (1984) 1149.
6. E.A. Rohlfing, D.M. Cox, and A. Kaldor, *J. Chem. Phys.* 81 (1984) 3322.
7. W.D. Knight, K. Clemenger, W.A. de Heer, W.A. Saunders, M.Y. Chou, and M.L. Cohen, *Phys. Rev. Lett.* 52 (1984) 2141.
8. M.M. Kappes, R.W. Kunz, and E. Schumacher, *Chem. Phys. Lett.* 91 (1982) 413.
9. U. Buck and H. Meyer, *Phys. Rev. Lett.* 52 (1984) 109.
10. L.A. Bloomfield, R.R. Freeman, and W.L. Brown, *Phys. Rev. Lett.* 54 (1985) 2246.

THE VIBRATIONAL PREDISSOCIATION SPECTROSCOPY OF HYDROGEN CLUSTER IONS

L. I. YEH, Mitchio OKUMURA, and Y. T. LEE

Materials and Molecular Research Division, Lawrence Berkeley Laboratory and
Department of Chemistry, University of California, Berkeley, CA 94720 USA

Low resolution vibrational predissociation spectra of hydrogen cluster ions H_n^+ ($n=5,7,9,11,13,15$) have been obtained in the gas phase. These ions have been shown to have H_2 molecules attached to the apexes of H_3^+ in the ab initio calculations. Two vibrational modes have been observed. One, corresponding to an H-H stretch of an H_2 attached to H_3^+ , occurs at 3910 cm^{-1} in H_5^+ and shifts to higher frequencies for the larger cluster ions. The second mode, which has only been seen in H_5^+ , is located at 3532 cm^{-1} and corresponds to an H_3^+ symmetric ring stretch. The experimental results are compared with ab initio theory.

1. INTRODUCTION

The vibrational predissociation spectra of gas phase hydrogen cluster ions have been obtained in our laboratory. The stimulus for this particular work was provided by recent ab initio predictions of the structures and frequencies of H_5^+ , H_7^+ , and H_9^+ by Yamaguchi, Gaw, and Schaefer (1). The predicted structures are composed of an H_3^+ ion with H_2 moieties complexed around it. The first three hydrogen molecules are bound directly to the apexes of the H_3^+ ion with the H-H bond perpendicular to the H_3^+ plane. The study of cluster ion spectroscopy is of fundamental importance toward the goal of understanding solvation phenomena at the molecular level.

Although little has been done on the spectroscopy of ion clusters, a fair amount of work has gone toward the study of the kinetics and thermodynamics of such ions. The hydrogen cluster ions have been the target of many such projects. The dissociation energy of H_5^+ has been studied by many groups with varying results (2-5). One of the difficulties in measuring such a quantity has been the requirement that equilibrium be reached between the relevant ions and hydrogen molecules. Recently, Elford (6) has used a variable length drift-tube to ensure that his measurements are reliable. Beuhler, Ehrenson, and Friedman (7) have also carried out careful measurements of dissociation energies avoiding previous sources of error. These two groups have obtained values of $\sim 6\text{ kcal/mole}$ and $\sim 3\text{ kcal/mole}$ for the dissociation energies of the reactions $H_5^+ \rightarrow H_3^+ + H_2$ and $H_7^+ \rightarrow H_5^+ + H_2$, respectively. These values are in excellent agreement with the theoretical results of Yamaguchi, et al. (1).

In this paper, we report on the observation of two vibrational modes in the hydrogen cluster ions. One of the modes detected was that corresponding to excitation of an H-H stretching motion of an H_2 attached to the apex of H_3^+ . This mode was seen in the ions H_n^+ ($n=5,7,9,11,13,15$). The second mode observed corresponds to excitation of the H_3^+ symmetric stretch. To date, this mode has only been observed in H_5^+ .

2. EXPERIMENTAL

The apparatus is shown in Fig. 1. The ion source consists of a supersonic expansion of ultra high purity hydrogen (stagnation pressure of 20-40 atm,

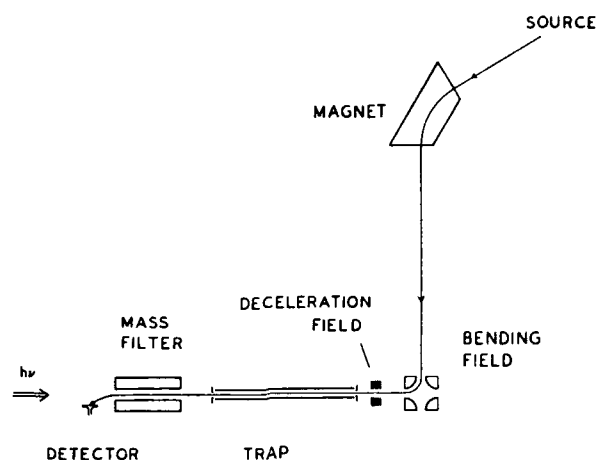


FIGURE 1
Schematic of the apparatus.

130 K) through a 10 μm diameter nozzle followed by electron bombardment ionization of the neutral clusters formed in the expansion process. A sector magnet selects the desired ion mass which then is directed into a radio frequency octupole trap. After the tunable infrared laser interacts with the parent ions, fragment ions travel through a quadrupole mass filter into our detector. Thus, "absorption spectroscopy" can be carried out by scanning the laser frequency and monitoring the dissociation product ion signal.

Two laser systems were used. The initial laser system was a Nd:YAG pumped LiNbO₃ optical parametric oscillator (OPO) (8). This was tuned from 3800 to 4200 cm^{-1} with a linewidth of roughly 10 cm^{-1} . The pulses were generally 8 nsec long and gave us 4 to 6 mJ per pulse at a 10 Hz repetition rate. The OPO was selected as the initial laser partly because its wide linewidth made scanning over a large frequency range in a reasonable amount of time practical and partly because it provides relatively high power. We found the location of the peaks corresponding to the H-H stretch in H_5^+ , H_7^+ , H_9^+ , ..., H_{15}^+ with the low resolution OPO.

The second laser system used was a Burleigh F-center laser which has much higher resolution. Without its intracavity etalon the resolution was 0.5 cm^{-1} ; with the etalon the resolution became $\sim 3 \times 10^{-5} \text{ cm}^{-1}$. In these experiments, it became advantageous to have the ions travel continuously through the machine rather than trapping them. To vary the Doppler width, which was estimated to be $< 0.2 \text{ cm}^{-1}$ when trapping, the ion energy in the interaction region ranged from 1 to 100 eV.

3. RESULTS AND DISCUSSION

The spectra of H_5^+ , H_7^+ , and H_9^+ shown in Fig. 2 and 3 were taken with the optical parametric oscillator (OPO) and correspond to excitation of the mode resembling an H-H stretch. No rotational structure has been resolved, although the rotational spacing calculated from the CI geometry of ref. 1 for the $\Delta J = \pm 1$ transitions is estimated to be 6 to 7 cm^{-1} . An initial hypothesis to explain the broadness of the peaks, which in some cases exceeded 100 cm^{-1} , was a com-

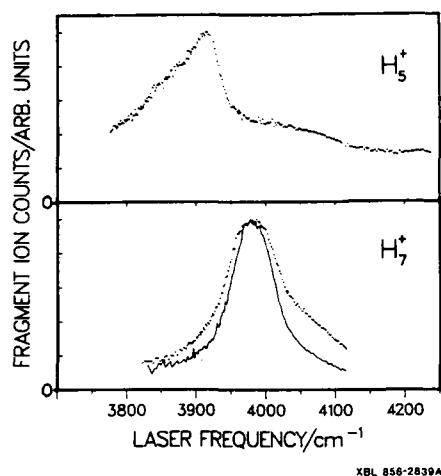


FIGURE 2
Predissociative spectra of H_5^+ and H_7^+ taken at a resolution of ~ 10 cm^{-1} . Upper plot: spectrum of H_5^+ detecting H_3^+ fragments. Lower plot: spectrum of H_7^+ detecting H_5^+ (solid curve) and H_3^+ (dotted curve).

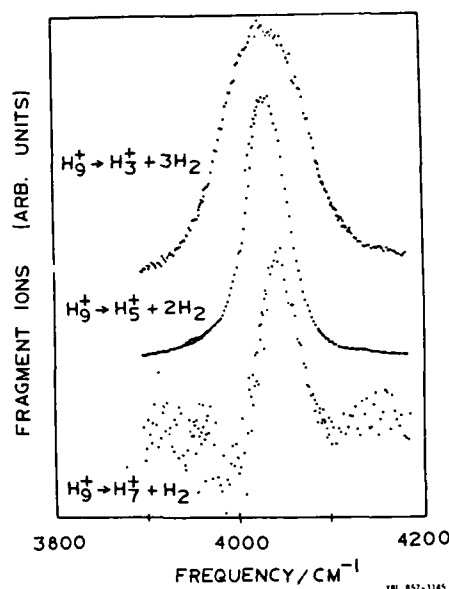


FIGURE 3
Predissociative spectra of H_9^+ detected by monitoring fragment ion signal for all three channels ($\Delta\nu = 10$ cm^{-1}).

bination of the broad linewidth (~ 10 cm^{-1}) of the OPO and the population of a large number of rotational states. This possibility has been ruled out by the experiments done with the F-center laser which also yielded broad spectra. Two other explanations that would account for the broadness of the peaks are an extremely short predissociative lifetime of the parent ion and the high internal excitation of the ions causing spectral congestion. The first of these alternatives seems quite improbable because to obtain homogeneous broadening of 100 cm^{-1} necessitates a predissociative lifetime on the order of 0.03 psec. The second hypothesis will be tested using a corona discharge source where the ionic clusters will be formed in the expansion process through a 70 μm nozzle. The clusters formed will be much colder than the original source where neutral clusters were ionized by electron bombardment to form the cluster ions.

The spectrum of H_5^+ is qualitatively different from that of the larger cluster ions. The long tail on the blue side may arise from combination bands involving the low frequency motion of the center hydrogen atom as it oscillates between two equivalent structures, e.g. $H_3^+ \cdot H_2 \rightleftharpoons H_2 \cdot H_3^+$. Because the center of charge oscillates across the center of mass, the transition moment will be very large. The larger cluster ions, in the analogous motion, would not be oscillating between two equivalent structures.

Figure 2 also shows the spectra of H_7^+ fragmenting to H_5^+ and H_3^+ scaled to equal maximum peak heights. Both peaks are significantly narrower than that of H_5^+ and the peak on the blue side much smaller, especially for the H_5^+ fragment.

Table 1. Infrared Absorption Frequencies in cm^{-1} for the Hydrogen Cluster Ions.

	Experimental ^a	Calculated Origin ^b
H_5^+	3532	--
	3910	3844 ^c
H_7^+	3980	3992, 3995 ^d
H_9^+	4020	4015 ^d
H_{11}^+	4028	--
H_{13}^+	4037	--
H_{15}^+	4040	--

a) This work. Peak of the observed band, to within 10 cm^{-1} .

b) Ab initio calculations from References 1 and 9. The frequencies reported are harmonic frequencies obtained by analytic gradient SCF and CI calculations. The frequencies in this column have been corrected for anharmonicity and systematic deviations by subtracting the difference between the harmonic frequency calculated for H_2 and the experimental H_2 ($1 \leftarrow 0$) origin.

c) DZ+P basis set, full CI, see Ref. 9.

d) DZ+P basis set, SCF, see Ref. 1.

The absorption spectra from H_9^+ dissociating to H_7^+ , H_5^+ , and H_3^+ is shown in Fig. 3. A small depletion peak is evident in the $\text{H}_9^+ \rightarrow \text{H}_7^+ + \text{H}_2$ spectrum. Its location corresponds to the H_7^+ absorption peak. In comparing the peak position of the H_7^+ fragment spectra with those of H_5^+ and H_3^+ , the slight apparent shift may actually be due to the H_7^+ depletion. Note that once again the smaller fragment ion (H_3^+) has the broadest peak shape.

A comparison of the experimentally found peak positions with the theoretical predictions is shown in Table 1. The calculated values, which include a semi-empirical correction, coincide with the experimental maxima within 70 cm^{-1} . As the rotational structure is not resolved, it is uncertain whether the peak maxima correspond to the vibrational band centers. Thus, the comparison with theory needs to be interpreted with caution. The absorption peak locations as a function of cluster size are plotted in Fig. 4. The laser used to find peak positions was the F-center laser. Although the peak locations are subject to some uncertainty due to the broadness of the peaks, an interesting trend is evident in inspecting this plot. Although the peak positions change substantially in going from H_5^+ to H_7^+ to H_9^+ , the frequency change for the higher cluster ions is marginal. The most likely explanation of this observation is that, even in the higher cluster ions, the H-H stretch excited is in one of the three H_2 moieties bound to an apex of the H_3^+ . The remaining H_2 groups, which are more loosely coordinated to the H_3^+ ring, may very well have frequencies closer to that of free H_2 , but are very weakly infrared allowed.

The fragmentation distribution of the hydrogen cluster ions has also been monitored. Results are shown in Fig. 5. One point to note is that dissociation of many H_2 units takes place when energetically allowed. For example, in the case of H_{11}^+ , the dominant product ions is H_5^+ which requires three H_2 moieties to detach.

In addition to the mode corresponding to a H-H stretching motion in one of the H_2 moieties, we have also seen an absorption band identified as originating from the H_3^+ symmetric stretch. This spectra is shown in Fig. 6. Once again a rather broad peak is evident; however, now a significant shoulder exists on the red side rather than on the blue side as described earlier for the absorption

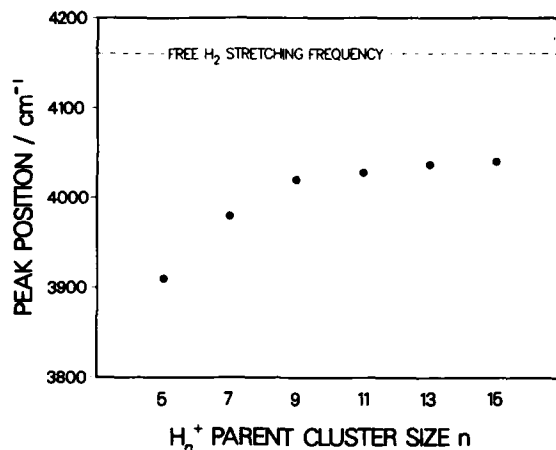
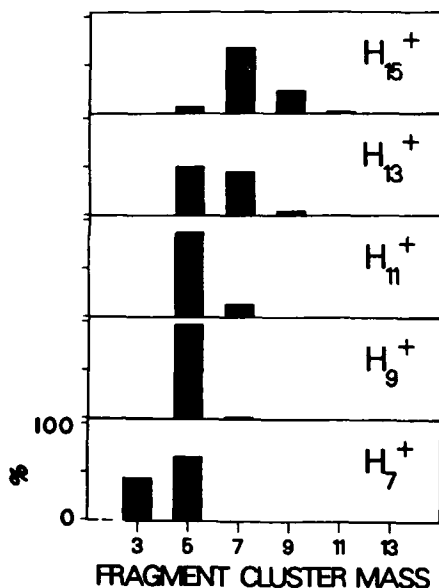


FIGURE 4

Frequencies of hydrogen stretching band absorption maxima as a function of cluster size. Uncertainty in peak position is $\Delta\nu = \pm 10 \text{ cm}^{-1}$.

spectra due to the excitation of the H-H stretching mode. We were not able to find the band arising from the H_3^+ symmetric stretching mode in H_7^+ . *Ab initio* theory (9) has predicted this intensity to be a factor of sixteen lower in H_7^+ as compared to the H-H stretching mode in H_7^+ . In the case of H_5^+ , the H_3^+ symmetric stretching mode is predicted to be only a factor of four lower in intensity than the H-H stretching mode.



ZBL 857-3146

FIGURE 5

Distribution of fragment ion mass for each parent hydrogen cluster ion.

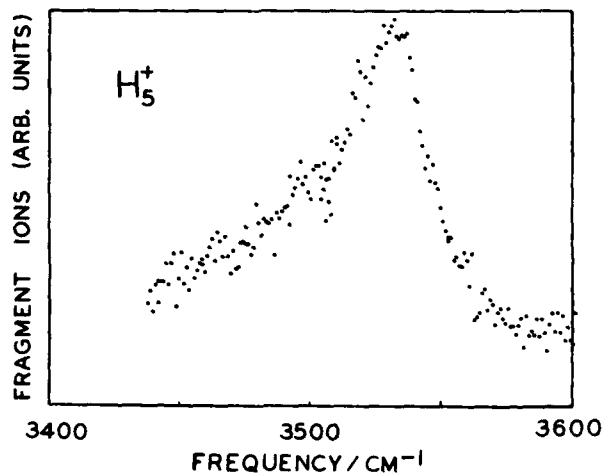


FIGURE 6
Predissociation spectrum of H_5^+ exciting the H_3^+ symmetric stretching mode ($\Delta v \sim 0.5 \text{ cm}^{-1}$).

ACKNOWLEDGMENT

This work was supported by the Director, Office of Energy Research, Office of Basic Energy Sciences, Chemical Sciences Division of the U.S. Department of Energy under Contract No. DE-AC03-76SF00098. The F-center laser was on loan from the San Francisco Laser Center, a National Science Foundation Regional Instrumentation Facility, NSF Grant No. CHE79-16250 awarded to the University of California at Berkeley in collaboration with Stanford University. LIY acknowledges a National Science Foundation Fellowship. We also would like to thank J.F. Gaw, Y. Yamaguchi, and H.F. Schaefer III for providing us with results of unpublished calculations.

REFERENCES

- 1) Y. Yamaguchi, J.F. Gaw and H.F. Schaefer III, *J. Chem. Phys.* 78 (1983) 4074.
- 2) K. Hiraoka and P. Kebarle, *J. Chem. Phys.* 63 (1975) 746.
- 3) R. Johnsen, C. Huang and M.A. Biondi, *J. Chem. Phys.* 65 (1976) 1539.
- 4) U.A. Arifov, S.L. Pozharov, I.G. Chernov and Z.A. Mukhamediev, *High Energy Chem.* 5 (1971) 69.
- 5) M.T. Elford and H.B. Milloy, *Aust. J. Phys.* 27 (1974) 795.
- 6) M.T. Elford, *J. Chem. Phys.* 79 (1983) 5951.
- 7) R.J. Beuhler, S. Ehrenson and L. Friedman, *J. Chem. Phys.* 79 (1983) 5982.
- 8) Stephen J. Brosnan and Robert L. Byer, *IEEE J. Quantum Electron.* QE-15 (1979) 415.
- 9) Y. Yamaguchi, J.F. Gaw and H.F. Schaefer III, unpublished results.

AUTHOR INDEX

- AGOSTINI, P., 743
 AGUER, P., 377
 ANDERSEN, L.H., 365
 ANDERSEN, N., 57
 ANDERSEN, T., 791
 ANDRIAMONJE, S., 377
 ANHOLT, R., 245

 BAE, Y.K., 799
 BE, S.H., 417
 BERKNER, K.H., 425
 BERKOWITZ, J., 631
 BERNSTEIN, E.M., 425
 BESWICK, J.A., 717
 BIZAU, J.M., 493
 BLOOMFIELD, L.A., 607
 BOBASHEV, S.V., 479
 BREGEL, T., 577
 BREGER, P., 493
 BREINIG, M., 555
 BRIAND, J.P., 685
 BROAD, J., 771
 BROWN, W.L., 807
 BRUANDET, J.F., 377
 BUBERT, W., 577

 CARRÉ, B., 493
 CELOTTA, R.J., 239
 CHEMIN, J.F., 377
 CIRIĆ, D., 445
 CLARK, M.W., 425
 COCKE, C.L., 453
 CRANCE, M., 757
 CUBAYNES, D., 493

 De BRUIJN, D.P., 697
 De HEER, F.J., 445
 De REUS, T., 389
 DEVI, K.R. Sandhya, 263
 DIJKKAMP, D., 445
 DOMCKE, W., 195
 DUBÉ, L.J., 345
 DUNN, G.H., 23

 EICHLER, J., 257
 ELSTON, S.B., 331
 ESAULOV, V.A., 175

 FREEMAN, R.R., 807
 FROMME, D., 233

 GAITHER, III, C.C., 555
 GALLAGHER, J.W., 57

 GALLAGHER, T.F., 609
 GANGOPADHYAY, P., 765
 GANZ, J., 577
 GARCIA, J.D., 263
 GENTRY, W.R., 13
 GÉRARD, P., 493
 GERLICH, D., 541
 GEUSIC, M.E., 807
 GIESE, J.P., 453
 GOHIL, P., 425
 GRAHAM, W.G., 425
 GREGORY, D.C., 205
 GREINER, W., 389
 GUEZET, D., 377

 HABERLAND, H., 771
 HALE, M.O., 585
 HANNACHI, F., 377
 HATANO, Y., 153
 HEINZMANN, U., 37
 HELM, H., 705
 HERTEL, I.V., 57, 561, 585
 HÖHNE, J., 771
 HOLLE, A., 779
 HOTOP, H., 577
 HUETZ, A., 141

 ITOH, A., 671

 JOHANN, U., 751
 JOHNSON, B.M., 425
 JONES, K.W., 425
 JULIENNE, P.S., 725

 KAMBARA, T., 417
 KASE, M., 417
 KATO, T., 529
 KAUPPILA, W.E., 105
 KELLER, W., 605
 KELLEY, M.H., 239
 KIMURA, M., 431
 KIMURA, Masahiro, 471
 KING, G.C., 215
 KOHNO, I., 417
 KONDOW, T., 517
 KOYANO, I., 529
 KUMAGAI, H., 417
 KWONG, N.H., 263

 LAMBROPOULOS, P., 765
 LASLEY, S.E., 555
 LEE, Y.T., 561, 813
 LEONE, S.R., 585

- LI, J.-M., 621
LIN, C.D., 643
LINEBERGER, W.C., 791
LUK, T.S., 751
LYKKE, K.R., 791
LYNN, K.G., 227
MAZEAU, J., 141
McCLELLAND, J.J., 239
McCULLOUGH, R.W., 463
McFARLAND, R.H., 425
MERON, M., 425
MESTDAGH, J.-M., 507
MIES, F.H., 725
MILLS, Jr., A.P., 227
MORGAN, T.J., 425
MORGNER, H., 605
MULLER, A., 425
MÜLLER, B., 389
MULLER, H.-G., 735
MÜLLER, U., 389
MÜLLER, W.A., 605
MÜNDEL, C., 195

NASON, J., 425
NEUMARK, D.M., 791
NEUSCHÄFER, D., 585
NIEHAUS, A., 657
NIENHUIS, G., 569

OKUMURA, M., 813
OSCHWALD, M., 771

PETERSON, J.R., 799
PETITE, G., 743
PICQUÉ, J.L., 493
PRITCHARD, D.E., 593

RAITH, W., 233
RAMSEY, N.F., 3
REINHARDT, J., 389
RHODES, C.K., 751
RIERA, A., 319
ROELLIG, L.O., 227
ROUSSEL, F., 493
RUF, M.-W., 577

SANDNER, W., 785
SCHÄFER, A., 389
SCHEURER, J.N., 377
SCHIWETZ, G., 671
SCHLACHTER, A.S., 425
SCHLÜTER, P., 389
SCHMIDT, H., 561
SCHNEIDER, D., 671
SCHNEIDER, T., 671
SCHRAMM, S., 389
SCHUCH, R., 297
SCHWEPPE, J., 405
SELLES, P., 141
SHAKESHAFT, R., 765
SHIBATA, H., 417
SHIMAMURA, I., 93
SHMAENOK, L.A., 479
SINAPIUS, G., 233
SOFF, G., 389
SPIESS, G., 493
STEARNS, J.W., 425
STEIN, T.S., 105
STOCKLI, M.P., 425
STOLTERFOHT, N., 671

TANAKA, K., 529
TANG, X., 765
TANIS, J.A., 425
TAWARA, H., 417
THIBAUD, J.P., 377
TONUMA, T., 417
TRAJMAR, S., 77
TUNNELL, L.N., 453

VARGHESE, S.L., 453

WAGGONER, W., 453
WEBER, M., 227
WEIGOLD, E., 125
WELGE, K.H., 779
WILLE, U., 273
WIEL, M.J. van der, 735
WUILLEUMIER, F.J., 493

YEH, L.I., 813

ZEITZ, W., 671
ZOUROS, T., 671